VOLUME 2

TREATISE ON
PROCESS METALLURGY
Process Phenomena

VOLUME 2

TREATISE ON
PROCESS METALLURGY
Process Phenomena

Editor-in-Chief

SESHADRI SEETHARAMAN
Royal Institute of Technology
Stockholm, Sweden

Co-editors-in-Chief

ALEXANDER McLEAN
Department of Materials Science and Engineering
University of Toronto,
Toronto, Ontario, Canada

RODERICK GUTHRIE
McGill Metals Processing Centre,
Montreal, Quebec, H3A 2B2, Canada

SEETHARAMAN SRIDHAR
Royal Academy of Engineering / Tata Steel Research Chair
in Low Carbon Materials Technologies
University of Warwick
Coventry, UK



ELSEVIER Amsterdam • Waltham • Heidelberg • London • New York • Oxford
Paris • San Diego • San Francisco • Sydney • Tokyo

Elsevier
The Boulevard, Langford Lane, Kidlington, Oxford OX5 1GB, UK
225 Wyman Street, Waltham, MA 02451, USA

Copyright © 2014 Elsevier Ltd. All rights reserved.

No part of this publication may be reproduced, stored in a retrieval system or transmitted in any form or by any means electronic, mechanical, photocopying, recording or otherwise without the prior written permission of the publisher.

Permissions may be sought directly from Elsevier's Science & Technology Rights Department in Oxford, UK: phone (+44) (0) 1865 843830; fax (+44) (0) 1865 853333; email: permissions@elsevier.com. Alternatively you can submit your request online by visiting the Elsevier web site at http://elsevier.com/locate/permissions, and selecting *Obtaining permission to use Elsevier material*.

Notice
No responsibility is assumed by the publisher for any injury and/or damage to persons or property as a matter of products liability, negligence or otherwise, or from any use or operation of any methods, products, instructions or ideas contained in the material herein. Because of rapid advances in the medical sciences, in particular, independent verification of diagnoses and drug dosages should be made.

British Library Cataloguing in Publication Data
A catalogue record for this book is available from the British Library

Library of Congress Cataloging in Publication Data
A catalog record for this book is available from the Library of Congress

ISBN: 978-0-08-096984-8

For information on all Elsevier publications
visit our website at store.elsevier.com

Printed and bound in United Kingdom.
14 15 16 17 10 9 8 7 6 5 4 3 2 1



This book is dedicated to the Memory of former Chief Co-editor Professor Masanori Iwase, Kyoto University, Japan



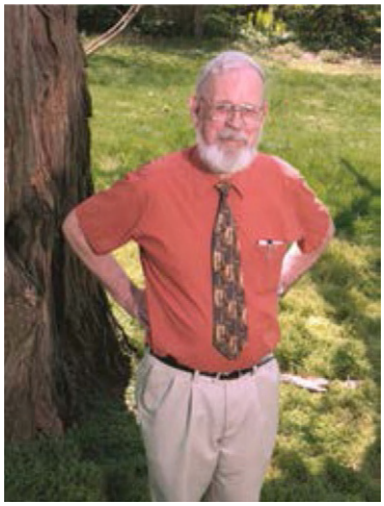
January 10, 1948 to September 29, 2011

Professor Masanori Iwase, known to his friends as "Masa," was a beacon of knowledge with respect to the thermochemistry of metallurgical systems. He graduated from Kyoto University with his Bachelor's Degree in 1971, obtained his Master's Degree in 1973, and his Doctor of Engineering Degree in 1979, by which time he had already published 14 papers. From 1979 through 1981, he was a Post-Doctoral Fellow with Professor Alexander McLean's Group within the Department of Metallurgy and Materials Science at the University of Toronto. He was appointed Associate Professor in the Department of Ferrous Metallurgy, now the Department of Energy Science and Technology, at Kyoto University in 1985 and became Full Professor in 1996. On several occasions he served as Department Chair. He held visiting Professorships at the University of Toronto, the University of New South Wales, and the Royal Institute of Science and Technology in Stockholm and was granted the title of Honorable Professor by North Eastern University in China. He was a member of the International Editorial Board of "Transactions of the Iron and Steel Society of AIME" and "High Temperature Materials and Processes." He presented numerous courses on metallurgical chemistry to steelmaking engineers and researchers in Japan and countries overseas. He published over 200 technical papers and 2 books and obtained over 30 patents. He had a strong interest in the development of electrochemical sensors for the measurement of the chemical potentials of species in

molten copper as well as in molten iron and steel and steelmaking slags. He was the inventor of a "Silicon Sensor" and an "FeO Activity Determinator" both of which are manufactured commercially and currently utilized by a number of steel companies in different parts of the world. In the area of slags, he made a number of major contributions by combining excellent experimental measurements with a sound knowledge of thermodynamics. During his later years, he was deeply engaged in the environmental problems associated with the metallurgical industries and conducted studies on waste incineration in the blast furnace. His research findings on the reduction of steelmaking slag volume and fluorspar consumption have been applied within several steel plants in Japan. In recognition of his many achievements, he received the Silver Medal Award from the Japan Institute of Metals in 1991 and the Nishiyama Memorial Award from the Iron and Steel Institute of Japan in 1993. During his last days, he was Co-Editor-in-Chief for this Treatise on Process Metallurgy. May it serve as a tribute to his numerous contributions.

David R. Gaskell, (1940 – 2013)

A Memorial Tribute



David Robert Gaskell was born in Glasgow, Scotland where he attended Glasgow University and The Royal College of Science and Technology. He received his B.Sc. and A.R.C.S.T. with First Class Honors in Metallurgy and Technical Chemistry in 1962 after which he spent two years working in England with the chemical industry. He married Sheena Morrow in 1964 and they had three children, Sarah, Claire and Drew. Shortly after their marriage they immigrated to Hamilton, Canada where David

conducted graduate studies at McMaster University under the supervision of Professors R. G. Ward and A. McLean. His Ph.D. degree was awarded in 1967 with a thesis entitled: "The Densities of Liquid Silicates Containing Iron Oxide at 1410°C." Following his Doctoral studies, David joined the University of Pennsylvania as an Assistant Professor where he worked closely with Professor Geoff Belton. In 1982 he moved to Purdue University as a Professor of Metallurgical Engineering. During his career, Dr. Gaskell served as a Visiting Professor working with Dr. Charles Masson at the Atlantic Regional Laboratory of the National Research Council of Canada in Halifax, Nova Scotia (1975–1976) and as a Visiting Professor at the G.C. Williams Co-operative Research Centre for Extraction Metallurgy at the University of Melbourne (1995).

Professor Gaskell was gifted with an exceptional combination of intellect and curiosity and particularly enjoyed his teaching, his research and his discussions with students. He served as thesis advisor for numerous graduate students as well as faculty mentor for dozens of undergraduate student projects. He was the recipient on several occasions of the Schuhmann Best Teaching Award in Materials Engineering. Dr. Gaskell was a prolific writer with numerous publications in journals and conference proceedings. He was known internationally for his classic textbooks "Introduction to Metallurgical Thermodynamics", "An Introduction to the Thermodynamics of Materials", and "An Introduction to Transport Phenomena in Materials Engineering". He was also involved in professional activities, including the Metallurgical Society of AIME, Alpha Sigma Mu (President, 1985–1986) and the Iron and Steel Society Transactions International Advisory Board. In 1977 Dr. Gaskell was named a Distinguished Alumnus of McMaster University and in 2000 was the recipient of the John F. Elliott Memorial Lectureship Award from the Iron and Steel Society of AIME. At the time of his death, David was serving as one of four distinguished reviewers for this Treatise on Process Metallurgy. He will be remembered with great fondness by many friends around the world not only for his intellectual achievements, and they were many, but also for his laughter, his sense of fun and his ability to play the bagpipes.

PREFACE

This book, "Treatise on Process Metallurgy", consisting of three volumes, aims to provide a comprehensive work that is intended to be a reference source for industrial and academic researchers and to provide material for teachers of process metallurgy. This effort was inspired by the successful series on Treatise for Physical Metallurgy by Robert Cahn and Peter Haasen published by Elsevier that has become a standard text found on the shelves of most academics and industrial metallurgists. We hope to mirror this success in the field of Process Metallurgy. This work is intended to provide the most pertinent contemporary developments within process metallurgy and offer a single complete collection of information on metal extraction processes from atomic level to industrial production.

The book is an important milestone in the development of technologies in metal extraction and refining that have evolved over the past millennia. After humans discovered fire and started using this energy source for metal extraction, the field of process metallurgy has grown from an art to an area of advanced technology. Growth has been significant over the past 200 years, and over the past five decades it has been exponential. Although there are books available describing well-defined aspects of the subject, it is rather surprising that we do not yet have a comprehensive volume which covers the broad spectrum of topics that constitute "process metallurgy". The current endeavor is aimed at addressing this deficiency.

An important phenomenon that has happened over the years is the separation of the subject of process metallurgy into ferrous and non-ferrous extraction processes. While the underlying principles are the same for both areas, the enormous impact of iron and steel on human civilization has given ferrous metallurgy a special place. Process design in the case of non-ferrous metals such as copper, lead and zinc, has often lagged behind that in iron and steelmaking. Over the course of time, the synergistic effects of the interactions between these two major areas of process metallurgy were lost. The present work is designed to bridge this knowledge gap.

Another development, which has manifested itself especially in Europe, is the division between "Theoretical Process Metallurgy" and "Applied Process Metallurgy". Fortunately, this division is not encountered to the same extent within Northern America. This division between theory and practice can be attributed in large part to the eagerness of industry to solve their immediate problems within tightly defined conditions and within the shortest possible time frame. As a consequence, in the absence of proper theoretical foundations, the solutions tend to be empirical in character and of limited applicability. In this context, it is worth emphasizing that no solution is generally applicable without proper theory, and no theory is particularly helpful, if it cannot be applied.

Another objective of this Treatise therefore, is to provide a bridge between fundamental concepts and practical applications.

The current work aims to present a comprehensive overview of the broad field of process metallurgy, bridging the above-mentioned gaps. It begins with a historical perspective of the development of metal extraction processes from the earliest of times to today's state-of-the art. There are thirteen chapters with about twenty five editors and eighty specialists, who have contributed to particular subject areas within which they

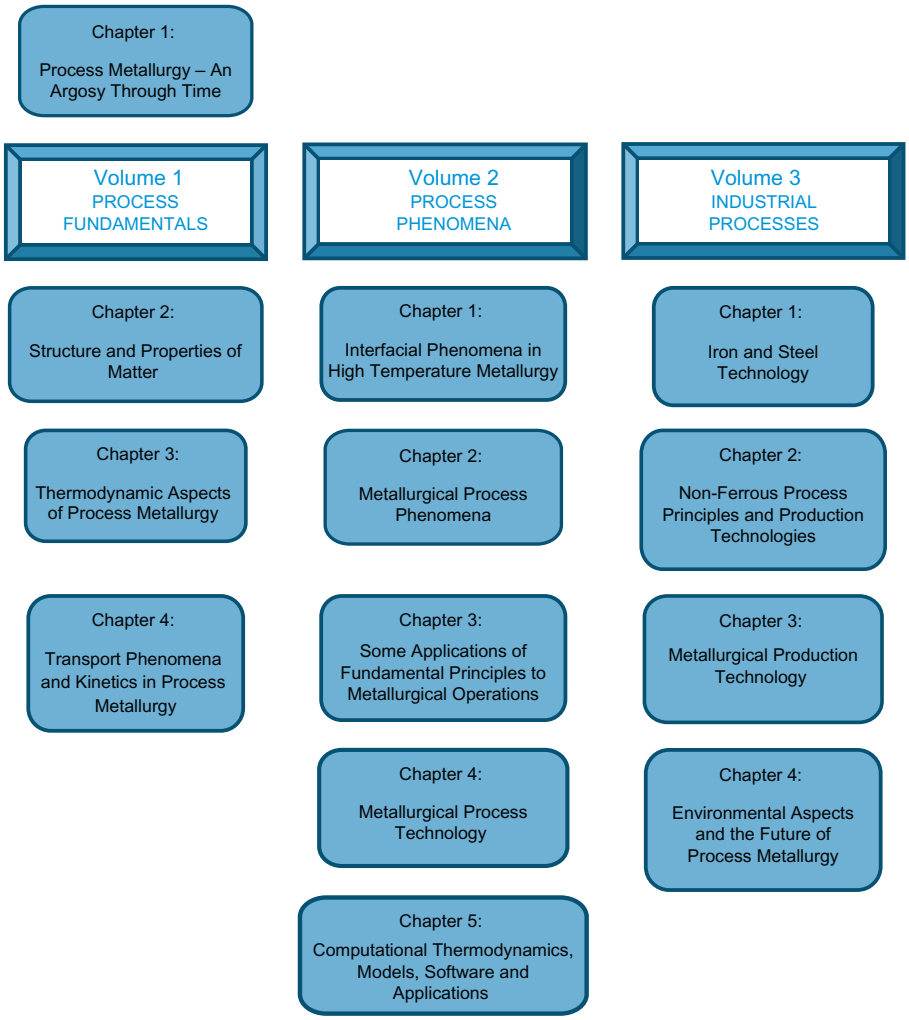


Figure. The flowchart of chapters in the Treatise.

are recognized experts. The development of the subject through these chapters is outlined in the following flow-chart.

The book is divided into three main streams. Following the first chapter which presents a birds-eye view of the history of metal extraction from stone-age to modern times, Chapters 2–4 present the process fundamentals. The second group of chapters on Process Phenomena, *viz*. Chapters 1–5, link the micro-modeling of process phenomena to macro-modeling of industrial processes, reactor technologies and computational models for process simulations. The third group deals with Industrial Processes. Chapters 1 and 2 present details of modern industrial practice for the extraction and refining of ferrous and non-ferrous metals respectively. Chapter 3 describes the design of metallurgical plants including the logistics, economics, intellectual property rights, upscaling and some case studies. The last chapter, Chapter 4, addresses the environmental problems existing today and the directions we should take for a better future. All chapters use the same nomenclature and symbols so that the reader can more readily see the links between related areas.

As the subject area is broad, the Treatise was designed as a multi-author work. The editors were asked to choose their contributors so that one red-thread passed through any particular chapter. While the potential problem of different schools of thought in each area had to be resolved, the editors took care that, where necessary, other schools of thought were presented, without causing confusion. The editors and contributors are from all parts of the world and formed a virtual forum of noted metallurgists who have worked in harmony for a period of more than two years. As the Board of Editors-in-Chief, it has been a distinct privilege to bring these leading members of the process metallurgy community together. We were also fortunate to obtain four world-famous metallurgists to review the chapters, so that their views could be implemented before the manuscripts were printed.

The publication of this Treatise is timely, as many of the present younger generation do not perceive Process Metallurgy as a "high-tech" area compared to more recent technologies, such as electronic-, bio- and nano-materials. The work is intended to show to the coming generations that Process Metallurgy is a continuously evolving subject area, like a flowing river, collecting tributaries from adjoining areas: sensor developments, signal processing, physical and mathematical modeling, automation, robotics and business management. It can be said, without exaggeration, that Process Metallurgy has had a major impact on the development of human civilization, and will continue to exert a powerful influence on metals production and the generation of advanced materials, for many decades to come.

The Board of Editors-in Chief expresses its deep gratitude to Staff Members at Elsevier who proposed the concept of a treatise on Process Metallurgy and who encouraged and assisted it throughout this activity. The generous support of Chief Editor, Seshadri Seetharaman, by the Swedish Steel Producers Association is also greatly

appreciated. Finally, the Editors-in-Chief express their sincere thanks to the chapter editors, contributors and reviewers, for providing their valuable time and expertise, in order to bring this endeavor to a successful conclusion.






Seshadri Seetharaman
Stockholm

Alexander McLean
Toronto

Roderick Guthrie
Montreal

Seetharaman Sridhar
Warwick

EDITOR IN CHIEF



Seshadri Seetharaman received his Ph.D. degree in Metallurgy from Indian Institute of Science, Bangalore, India, in the year 1971. He joined the Royal Institute of Technology, Stockholm, in 1973 as Senior Research Associate and became Associate Professor in 1981. Dr. Seetharaman was installed in the Chair of Theoretical Metallurgy in 1990 and he retired from this position at the end of 2010. Professor Seetharaman has about 350 peer-reviewed publications in leading journals in Metallurgy, about 150 conference presentations, and 10 patents. His major scientific interests are the fundamentals of Process Metallurgy that covers thermodynamics, transport phenomena, thermophysical properties of high temperature systems, and interfacial phenomena. He was also involved in the teaching of the above subjects.

Professor Seshadri Seetharaman has been nominated eight times as the best teacher in Materials Design teaching program at the Royal Institute of Technology. He has been awarded the President's Award in 1994 for meritorious contributions in teaching. He was selected as the best teacher of the Royal Institute of Technology in 2004.

Professor Seshadri Seetharaman has been awarded the Brimacombe Prize for the year 2010. He is an Honorary member of the Iron and Steel Institute of Japan, Honorary doctor at the Aalto University in Finland, Honorary Professor at the Metallurgical Academy of Ukraine as well as at The University of Science and Technology Beijing. He also received the Distinguished Alumni Award of the Indian Institute of Science, Bangalore, in the year 2013.

CO-EDITORS-IN-CHIEF



Alexander McLean

Following graduation with degrees in Applied Chemistry and Metallurgy from the Royal College of Science and Technology and the University of Glasgow, Dr. McLean spent 5 years at McMaster University before moving to Jones and Laughlin Steel Corporation in Pittsburgh. He joined the University of Toronto in 1970, and in 1984 the Ferrous Metallurgy Research Group was formed with Professor McLean as Director. He served as Department Chair from 1992 through 1997 and was appointed Professor Emeritus in 2002. He is an Honorary Member and elected Fellow of several organizations including AIME, The Iron and Steel Institute of Japan, the Royal Society of Canada, and the Canadian Academy of Engineering. He is a recipient of the Queen Elizabeth II Diamond Jubilee Medal and received Honorary Doctorates from the University of Miskolc and the University of Strathclyde. He has published extensively in the areas of iron and steelmaking and materials processing.



Roderick Guthrie

Roderick I.L. Guthrie, Ph.D. (Imperial College), ARSM, Eng., is the Macdonald Professor of Metallurgy and Director of the McGill Metals Processing Centre. An Honorary Member of ISIJ, Distinguished Member of AIST, Fellow of the Canadian Institute of Mining and Metallurgy, Fellow of the Royal Society of Canada, and Fellow of the Canadian Academy of Engineering, he is the author of two text books concerning *Engineering in Process Metallurgy* and *The Physical Properties of Liquid Metals*. The winner of the 2006 Killam Prize for Engineering, he was co-inventor of the successful LiMCA process for detecting inclusions in liquid metals, and also of the HSBC process for casting steel and aluminum alloy sheets. As a researcher, he has been keenly interested in the application of fluid flow, heat, and mass transfer phenomena in the description of metallurgical processes. A long-time consultant to the steel industry, Dr. Guthrie has worked in all segments of an integrated steelplant, from blast furnaces through steelmaking and hot rolling mills, to annealing and finishing lines.



Seetharaman Sridhar is currently the Tata Steel/RAEng Joint Chair for Research into Low Carbon Materials Technology. He was until recently the POSCO Professor of Steelmaking at Carnegie Mellon University and the co-director of the Industry–University Consortium, Center for Iron and Steelmaking Research (CISR) of which Tata is a member. He received his Ph.D. from the Massachusetts Institute of Technology and his undergraduate degree from the Royal Institute of Technology in Sweden.

His research and teaching interests lie in the physical chemistry of metal processing. He has published over 125 journal papers in the areas of secondary refining, casting and mold slags, coal gasification, oxidation, and hot-shortness. He has received the following best paper awards: Marcus Grossman Award from ASM, the Herty Award from ISS, The Spriggs Phase Equilibria Award from ACERS, and the Jerry Silver Award from AIST. He has also received the Friedrich Wilhelm Bessel Research Prize from the Alexander Von Humboldt Foundation and the NSF Career Award, both for his general contributions in research. As a teacher, he was recognized by the Benjamin Teare Teaching Award by Carnegie Institute of Technology, the Philbrook Prize by the MSE Department at CMU, and he was the recipient of the 2011 J.F. Elliott Lecturer Award for AIST. He is the editor for *AIST Transactions* and an associate editor for *Metallurgical and Metals Transactions A, B, and E*. He is also on the International Advisory Board for *Steel Research International* and *ISIJ International*.

CONTRIBUTORS TO VOLUME 2

Joonho Lee
Department of Materials Science and Engineering, Korea University, Anam-dong, Seongbuk-gu, Seoul, Republic of Korea

Toshihiro Tanaka
Division of Materials and Manufacturing Science, Graduate School of Engineering, Osaka University, Osaka, Japan

Piotr R. Scheller
Technical University Bergakademie Freiberg, Freiberg, Germany

Takeshi Yoshikawa
Institute of Industrial Science, The University of Tokyo, Tokyo, Japan

P. Chris Pistorius
Center for Iron and Steelmaking Research, Carnegie Mellon University

Richard J. Fruehan
Center for Iron and Steelmaking Research, Carnegie Mellon University

Kimihisa Ito
Department of Applied Mathematics, Waseda University, Tokyo, Japan

A. McLean
Department of Materials Science and Engineering, University of Toronto, Toronto, Ontario, Canada

Y.D. Yang
Department of Materials Science and Engineering, University of Toronto, Toronto, Ontario, Canada

Lidong Teng
Division of Materials Process Science, Royal Institute of Technology, Stockholm, Sweden

Mansoor Barati
Department of Materials Science and Engineering, University of Toronto, Toronto, Ontario, Canada

Stavros A. Argyropoulos
Department of Materials Science and Engineering, University of Toronto, Toronto, Ontario, Canada

Zhi Li
Department of Materials Science and Engineering, University of Toronto, Toronto, Ontario, Canada

Roderick I.L. Guthrie
McGill Metals Processing Centre (MMPC), Montreal, Canada

Mihaiela Isac
McGill Metals Processing Centre (MMPC), Montreal, Canada

Kinnor Chattopadhyay
HATCH (formally PDF with the MMPC)

Klaus Hack
GTT Technologies, Kaiserstrasse, Herzogenrath, Germany

Jean Lehmann
ArcelorMittal, Global R&D, Maizières-lès-Metz Cedex, France

In-Ho Jung
Department of Mining and Materials Engineering, McGill University, Montreal, Canada

Evgueni Jak
School of Chemical Engineering, University of Queensland, Queensland, Australia

Marie-Aline Van Ende
Department of Mining and Materials Engineering, McGill University, Montreal, Canada

ACKNOWLEDGEMENT

The Editors-in Chief express their sincere gratitude to
"Jernkontoret"- the Swedish Steel Producers' Association

for their generous support to Professor Seshadri Seetharaman towards the production of this book.

The support from the Iron and Steel Institute of Japan is gratefully acknowledged.

THE REVIEW COMMITTEE

The various chapters of the Treatise were distributed for review between the following internationally renowned metallurgists: Professors T. Emi (Japan), D. R. Gaskell (USA), D. C. G. Robertson (USA) and O. Wijk (Sweden). After the sad demise of Professor Gaskell, the review of his assigned material was completed by the Board of Editors-in-Chief and Dr. V.I. Lakshmanan (Canada). The Editors-in-Chief express their gratitude to the Reviewers for their invaluable contributions in improving the quality of the book.

CHAPTER 1

Interfacial Phenomena in High Temperature Metallurgy

Toshihiro Tanaka[a] **and Piotr R. Scheller**[b]

[a]Division of Materials and Manufacturing Science, Graduate School of Engineering, Osaka University, Osaka, Japan
[b]Technical University Bergakademie Freiberg, Freiberg, Germany

Contents

1.1. Surfaces and Interfaces 2
1.2. Surface Tension and Contact Angle 11
1.3. Experiments 19
1.4. Surface Tension Models 35
1.5. Interfacial Free Energy and Wettability 61
1.6. Some Aspects of Electrochemistry of Interfaces 79
1.7. Interfacial Convection and Its Effect on Material Processing 95
1.8. Stability of Interface Between Liquid Steel and Molten Slag 111
1.9. Applications of Interfacial Phenomena in Process Metallurgy 119

CHAPTER 1.1

Surfaces and Interfaces

Joonho Lee[a] **and Toshihiro Tanaka**[b]

[a]Department of Materials Science and Engineering, Korea University, Anam-dong, Seongbuk-gu, Seoul, Republic of Korea
[b]Division of Materials and Manufacturing Science, Graduate School of Engineering, Osaka University, Osaka, Japan

1.1.1. DEFINITION OF SURFACES AND INTERFACES

Interface is a dividing plane of two contacting phases. When two phases contact, a certain plane arises where the continuity of physical and/or chemical properties of each phase does not maintain anymore. This plane is defined as interface, and surface is an interface between gas and condensed phase (solid or liquid). High-temperature reactions take place at or through these interfaces, namely, slag–metal, slag–refractory, metal–inclusion, slag–inclusion, slag–gas, metal–gas interfaces, and grain boundary.

The physical interface is three dimensional and only a few atoms thick. Thanks to the technical improvements of high-resolution transmission electron microscopes, we may investigate some solid–solid and solid–liquid interfaces [1] (see Figure 1.1.1). But still we cannot investigate liquid–liquid and liquid–gas interfaces at high temperatures, yet. Therefore, explanation of such interfaces cannot be made from direct observations.

Gibbs suggested an imaginary two-dimensional dividing interface (so-called Gibbs interface or Gibbs surface) to explain macroscopic interfacial behaviors from a thermodynamic point of view [2]. Figure 1.1.2a shows a physical interface θ between α and β phases. The concentration profile of solute i, c_i (mol/m^3) is shown in Figure 1.1.2b. If we simply assume that the concentration of i in α and β phases are constant in each phase to the Gibbs interface, the excess numbers of moles of solute i is given by Equation (1.1.1).

$$n_i^{\sigma} = n_i - \left(c_i^{\alpha} V^{\alpha} + c_i^{\beta} V^{\beta}\right) \tag{1.1.1}$$

where n_i^{σ}, n_i, c_i^{ν}, and V^{ν} are the numbers of moles of i at the interface, the total numbers of moles of i in the whole system, the concentration of i in the phase ν, and the volume of the phase ν, respectively. n_i^{σ} divided by the interface area A yields the superficial density of i at the interface, namely the adsorption of i.

Treatise on Process Metallurgy, Volume 2
http://dx.doi.org/10.1016/B978-0-08-096984-8.00029-X
© 2014 Elsevier Ltd.
All rights reserved.

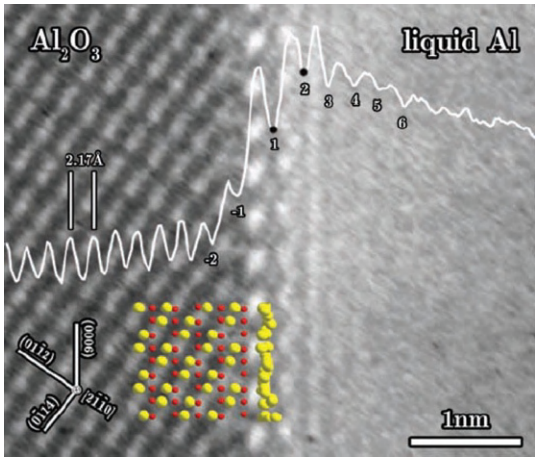


Figure 1.1.1 An example of the HREM investigation at solid–liquid interface [1].

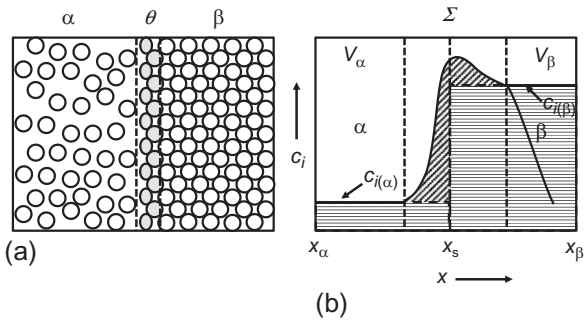


Figure 1.1.2 A physical interface θ between α and β phases, and the concentration profile of solute *i*, c_i (mol/m^3).

$$\Gamma_i = n_i^\sigma / A \tag{1.1.2}$$

The adsorption of *i* may have different value depending on the exact location of the Gibbs interface. Consequently, it may also have positive or negative value.

In order to avoid the variation of the adsorption with respect to the position of the dividing interface, the relative adsorption concept is introduced. Combining Equations (1.1.1) and (1.1.2), one may obtain Equation (1.1.3).

$$\Gamma_i = \frac{n_i^\sigma}{A} = \frac{1}{A}\left(n_i - \left(c_i^\alpha V^\alpha + c_i^\beta V^\beta\right)\right) = \frac{1}{A}\left(n_i - c_i^\alpha V - \left(c_i^\beta - c_i^\alpha\right) V^\beta\right)\right) \tag{1.1.3}$$

Similarly, the adsorption of solvent 1 is given by Equation (1.1.4).

$$\Gamma_1 = \frac{1}{A}\left(n_1 - c_1^{\alpha} V - \left(c_1^{\beta} - c_1^{\alpha}\right) V^{\beta}\right) \tag{1.1.4}$$

In Equations (1.1.3) and (1.1.4), V^{β} is the only quantity depending on the position of the dividing interface and $V = V^{\alpha} + V^{\beta}$. By eliminating V^{β}, we may introduce an invariant value, the relative adsorption of solute i with respect to solvent 1 ($\Gamma_{i(1)}$).

$$\Gamma_{i(1)} = \Gamma_i - \Gamma_1 \frac{c_i^{\alpha} - c_i^{\beta}}{c_1^{\alpha} - c_1^{\beta}} = \frac{1}{A}\left(\left(n_i - c_i^{\alpha} V\right) - \left(n_1 - c_1^{\alpha} V\right)\frac{c_i^{\alpha} - c_i^{\beta}}{c_1^{\alpha} - c_1^{\beta}}\right) \tag{1.1.5}$$

$\Gamma_{i(1)}$ and Γ_i may have the same value when we choose the interface that Γ_1 is zero. This interface is called as "zero interface."

For a surface (interface between gas and condensed phase), Equation (1.1.5) can be simplified to Equation (1.1.6).

$$\Gamma_{i(1)} = \Gamma_i - \Gamma_1 \frac{c_i^{\alpha}}{c_1^{\alpha}} = \Gamma_i - \Gamma_1 \frac{X_i^{\alpha}}{X_1^{\alpha}} \tag{1.1.6}$$

When the concentration ratios of bulk and surface are identical ($\Gamma_i/\Gamma_1 = c_i^{\alpha}/c_i^{\beta}$), the relative adsorption becomes zero. If the concentration ratio of surface is higher than that of bulk, the relative adsorption becomes positive. On the contrary, if the concentration ratio of surface is lower than that of bulk, the relative adsorption becomes negative.

In many metallurgical processes, surface tension and interfacial tension drastically change by the adsorption of surface active elements, solute that is more abundant (preferentially adsorbed) at the interface. A monolayer model is widely accepted to describe the thermodynamic behavior of liquid alloys containing surface active elements. The monolayer model assumes that the interface is located just below the surface monolayer [3] (Figure 1.1.3). The adsorption of solute i in the monolayer is given by Equation (1.1.7).

$$\Gamma_i^{*} = \frac{n^{(\mathrm{m})}}{A} X_i^{(\mathrm{m})} \tag{1.1.7}$$

where $n^{(\mathrm{m})}/A$ is the number of moles of solute i in the monolayer per unit area, and $X_i^{(\mathrm{m})}$ is the mole fraction of i in the monolayer. Therefore, the relative adsorption of solute i can be given by Equation (1.1.8).

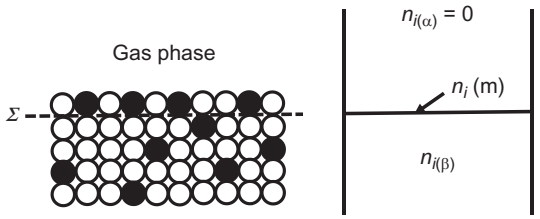


Figure 1.1.3 Selection of dividing surface Σ in the case of a monolayer model [3].

$$\Gamma_{i(1)} = \frac{n^{(\mathrm{m})}}{A}\left(X_i^{(\mathrm{m})} - X_1^{(\mathrm{m})}\frac{X_i^{\alpha}}{X_1^{\alpha}}\right) \tag{1.1.8}$$

1.1.2. GIBBS ADSORPTION ISOTHERM

The energy of a system in Figure 1.1.2 is given by Equation (1.1.9).

$$\begin{aligned} U = S\left(\frac{\partial U}{\partial S}\right)_{V^{\alpha},V^{\beta},n_i,A} + V^{\alpha}\left(\frac{\partial U}{\partial V^{\alpha}}\right)_{S,V^{\beta},n_i,A} + V^{\beta}\left(\frac{\partial U}{\partial V^{\beta}}\right)_{S,V^{\alpha},n_i,A} \\ + \sum_{i=1}^{m} n_i\left(\frac{\partial U}{\partial n_i}\right)_{S,V^{\alpha},V^{\beta},n_j,A} + A\left(\frac{\partial U}{\partial A}\right)_{S,V^{\alpha},V^{\beta},n_i} \end{aligned} \tag{1.1.9}$$

Equation (1.1.9) can be rewritten by Equation (1.1.10).

$$U = TS - P^{\alpha}V^{\alpha} - P^{\beta}V^{\beta} + \sum_{i=1}^{\mathrm{m}} n_i\mu_i + \sigma A \tag{1.1.10}$$

where μ_i is the chemical potential of solute i and σ is the interfacial tension.

The energy of phases α and β are given by Equations (1.1.11) and (1.1.12), respectively.

$$U^{\alpha} = TS^{\alpha} - P^{\alpha}V^{\alpha} + \sum_{i=1}^{m} n_i^{\alpha}\mu_i \tag{1.1.11}$$

$$U^{\beta} = TS^{\beta} - P^{\beta}V^{\beta} + \sum_{i=1}^{m} n_i^{\beta}\mu_i \tag{1.1.12}$$

The interfacial energy is given by Equation (1.1.13).

$$U^{\sigma} = U - U^{\alpha} - U^{\beta} = TS^{\sigma} + \sum_{i=1}^{m} n_i^{\sigma}\mu_i + \sigma A \tag{1.1.13}$$

Since

$$\mathrm{d}U^{\sigma} = T\mathrm{d}S^{\sigma} + \sum_{i=1}^{m}\mu_i\mathrm{d}n_i^{\sigma} + \sigma\mathrm{d}A \tag{1.1.14}$$

Equation (1.1.15) is then obtained.

$$S^{\sigma}\mathrm{d}T+\sum_{i=1}^{m}n_i^{\sigma}\mathrm{d}\mu_i+A\mathrm{d}\sigma=0 \tag{1.1.15}$$

By rearranging Equation (1.1.15), Equation (1.1.16) is obtained.

$$\mathrm{d}\sigma=-\frac{S^{\sigma}}{A}\mathrm{d}T-\sum_{i=1}^{m}\Gamma_i\mathrm{d}\mu_i \tag{1.1.16}$$

This equation is known as the Gibbs adsorption equation.

Choosing an interface that Γ_1 is zero at a constant temperature ($\Gamma_i=\Gamma_{i(1)}$), we may obtain Equation (1.1.17).

$$\mathrm{d}\sigma=-\sum_{i=2}^{m}\Gamma_i\mathrm{d}\mu_i \tag{1.1.17}$$

For a binary condensed system contacting gas phase, Equation (1.1.17) can be simplified to Equation (1.1.18).

$$\Gamma_2=-\left(\frac{\partial\sigma}{\partial\mu_2}\right)_T=-\frac{1}{RT}\left(\frac{\partial\sigma}{\partial\ln a_2}\right) \tag{1.1.18}$$

Therefore, when the surface tension of a binary alloy is measured by changing the concentration, the adsorption of solute 2 can be obtained from the slope of the curve in Figure 1.1.4.

For a ternary system, Equation (1.1.17) will be rewritten by Equation (1.1.19).

$$\mathrm{d}\sigma=-\Gamma_2\mathrm{d}\mu_2-\Gamma_3\mathrm{d}\mu_3 \tag{1.1.19}$$

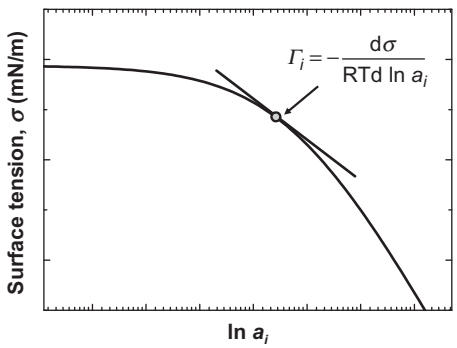


Figure 1.1.4 Determination of surface adsorption of solute *i* from the dependence of surface tension on the activity of solute *i* in the bulk.

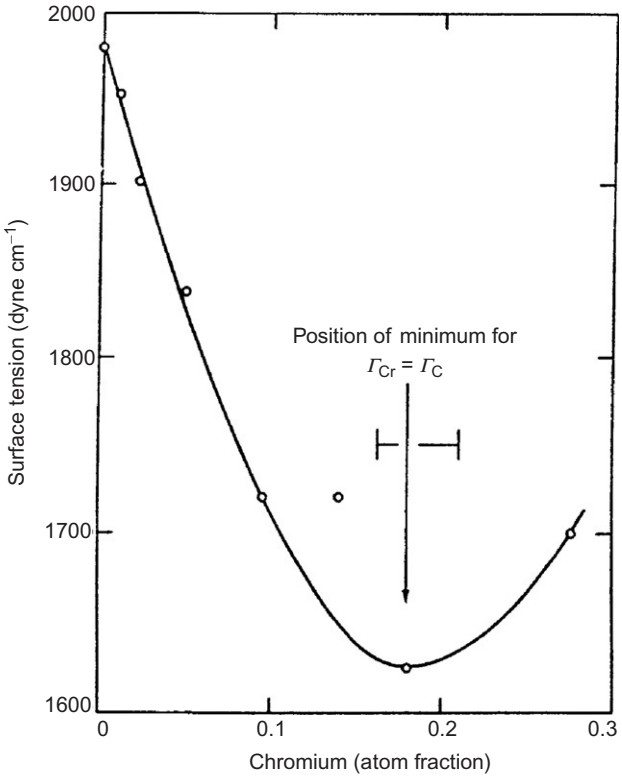


Figure 1.1.5 Determination of a compound type associative adsorption using Equation (1.1.20) [4].

The chemical potential of i is given by $\mu_i = \mu_i^o + RT \ln \gamma_i X_i$. If we simply assume that the activity coefficient is given by the first order interaction parameter, namely, $\varepsilon_i^j = \partial \ln \gamma_i / \partial X_j$, differentiating Equation (1.1.19) by $\ln X_2$ may yields Equation (1.1.20).

$$-\frac{1}{RT}\left(\frac{\partial \sigma}{\partial \ln X_2}\right)_{X_3} = \Gamma_2\left(1 + X_2\varepsilon_2^2\right) + \Gamma_3 X_2 \varepsilon_3^2 \tag{1.1.20}$$

Equation (1.1.20) is useful to determine the compound type associative adsorption [4] (Figure 1.1.5). When $d\sigma/d \ln X_2$ equals zero, one gets the ratio of Γ_2 to Γ_3.

1.1.3. LANGMUIR'S ISOTHERM

The adsorption of surface active elements is generally described by the Langmuir's model. Langmuir's model assumes that surface monolayer is composed of solute atoms and vacancies, and the total number of reaction sites is constant at a certain temperature (Figure 1.1.6). In addition, the original Langmuir's model considers that there are no mutual interactions between adsorbed atoms.

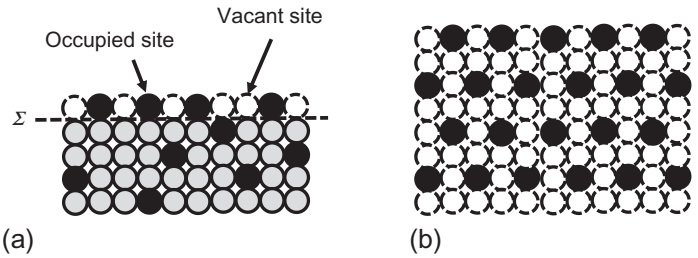


Figure 1.1.6 Cross-section (a) and top-view (b) of the surface monolayer in the Langmuir model.

For a binary system, the equilibrium at the interface is described by Equation (1.1.21).

$$\underline{i} + \mathrm{vac}^{\sigma} = i^{\sigma} \tag{1.1.21}$$

where $\underline{i}$, vac^{σ}, i^{σ} are solute i in the bulk, the vacant site at the interface, the site occupied by solute i. The equilibrium constant of Equation (1.1.21) is expressed by Equation (1.1.22).

$$K = \frac{\Gamma_i}{a_i\left(\Gamma_i^{\mathrm{sat}} - \Gamma_i\right)} \tag{1.1.22}$$

where a_i is the activity of solute i in the bulk (with a Henrian standard state reference). $\Gamma_i^{\mathrm{sat}} - \Gamma_i$ is the concentration of vacancies at the surface. This expression contains the assumption of Lucassen–Reynders convention ($\sum \Gamma_j = \Gamma_i^{\mathrm{sat}}$) [5].

At an interface that Γ_1 is zero ($\Gamma_i = \Gamma_{i(1)}$), Equation (1.1.18) may be combined with Equation (1.1.22) to yield Equation (1.1.23).

$$\sigma = \sigma_1 - RT\Gamma_{i(1)}^{\mathrm{sat}} \ln(1 + Ka_i) \tag{1.1.23}$$

where σ_1 is the surface tension of pure 1 (solvent). Equations (1.1.5)–(1.1.23) was firstly suggested by Szyszkowski as an empirical equation and later derived thermodynamically by Belton. Therefore, it was named as Szyszkowski's equation or more generally known as Belton's equation. Sahoo *et al.* showed that surface tension of several metals containing surface active elements can be expressed by Equation (1.1.23) (Figure 1.1.7) [6], but Lupis asserted that this simple ideal adsorption isotherm could not express the adsorption of surface active elements properly [3].

It is more reasonable to consider that the adsorbed atoms have mutual interactions. This nonideal adsorption isotherm can be described by Equation (1.1.24) [7].

$$K = \frac{\gamma_i^{\sigma}\Gamma_i}{a_i\gamma_v^{\sigma}\left(\Gamma_i^{\mathrm{sat}} - \Gamma_i\right)} = \frac{\gamma_i^{\sigma}\theta_i}{a_i\gamma_v^{\sigma}(1 - \theta_i)} \tag{1.1.24}$$

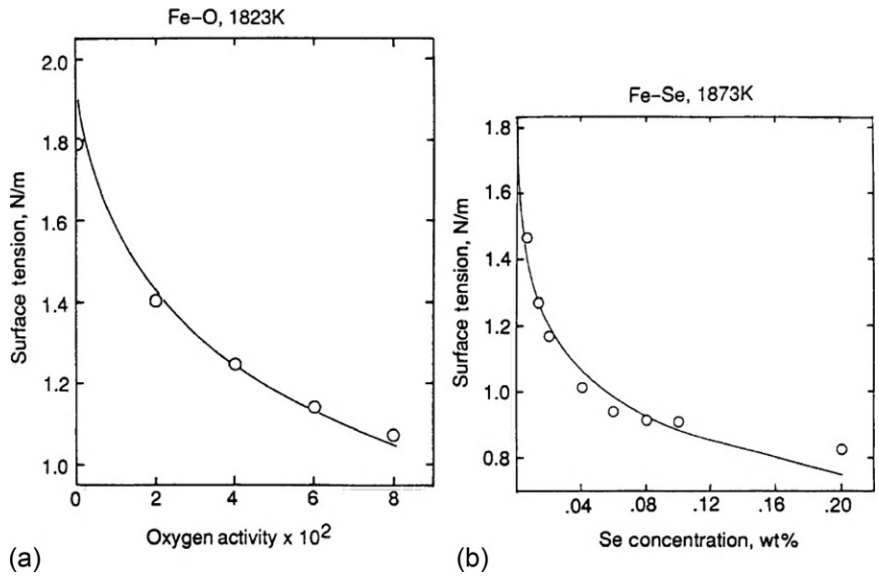


Figure 1.1.7 Surface tension of liquid iron containing surface active elements [6].

where γ_i^{σ}, γ_v^{σ}, θ_i denote the activity coefficient of the surface sites occupied by i, the activity coefficient of the surface vacant sites, and the surface fraction of i. If we assume a regular solution model for simplicity, Equation (1.1.24) can be rewritten by Equation (1.1.25) by introducing the interaction parameter Ω.

$$\ln K - \ln a_i = \frac{\Omega}{RT}(1-\theta_i)^2 + \ln \theta_i - \frac{\Omega}{RT}\theta_i^2 - \ln (1-\theta_i) \tag{1.1.25}$$

Differentiation of Equation (1.1.25) yields Equation (1.1.26).

$$\mathrm{d}\ln a_i = \left(-\frac{2\Omega}{RT} + \frac{1}{\theta_i(1-\theta_i)}\right)\mathrm{d}\theta_i \tag{1.1.26}$$

Instituting Gibbs adsorption isotherm (Equation 1.1.18) yields Equation (1.1.27).

$$\mathrm{d}\sigma = -\frac{RT}{A}\left(-\frac{2\Omega}{RT}\theta_i + \frac{1}{1-\theta_i}\right)\mathrm{d}\theta_i \tag{1.1.27}$$

Integrating from $\theta_i = 0$ to $\theta_i = \theta_i$ gives Equation (1.1.28).

$$\sigma = \sigma_1 + \frac{RT}{A}\left(\frac{\Omega\theta_i^2}{RT} + \ln(1-\theta_i)\right) \tag{1.1.28}$$

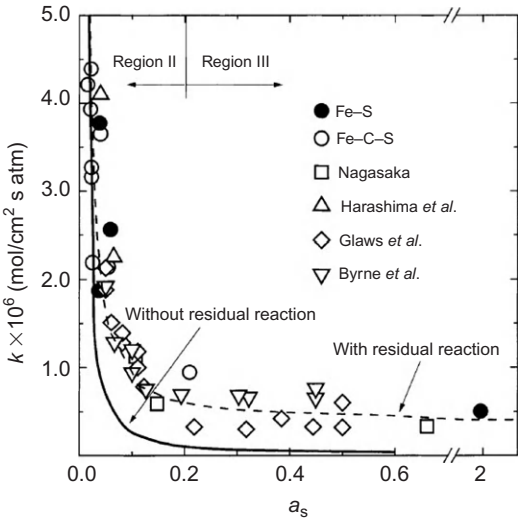


Figure 1.1.8 Residual reaction rate constant of the nitrogen dissociation on the surface of liquid iron at high sulfur activity [7].

For a more generalized form, Equation (1.1.28) can be written by Equation (1.1.29).

$$\sigma = \sigma_1 + \frac{RT}{A}\left(\ln\gamma_\nu^\sigma + \ln(1-\theta_i)\right) = \sigma_1 + \frac{RT}{A}\ln a_\nu^\sigma \tag{1.1.29}$$

If we assume a binary system, the surface tension may change from σ_1 to σ_2, and the activity of the surface vacant sites will be varied from $e^{-\frac{A(\sigma_1-\sigma_2)}{RT}}$ to unity. It means that there should be a residual reactivity of the surface vacant sites even after the surface was fully saturated with solute 2. Many researchers reported the existence of the residual reactions in gas-liquid reactions (see Figure 1.1.8). Nonideal adsorption isotherm also can be derived from Butler's equation, which will be discussed in Section 1.4.2.

REFERENCES

[1] S.H. Oh, Y. Kauffmann, C. Scheu, W.D. Kaplan, M. Ruhle, Science 310 (2005) 661.
[2] J.W. Gibbs, Collected Works vol. 1 Yale University Press, New Haven, CT, 1948.
[3] C.H.P. Lupis, Chemical Thermodynamics of Materials, North-Holland, New York, 1983, p. 394.
[4] G.R. Belton, Metall. Trans. 3 (1972) 1465.
[5] E.H. Lucassen-Reynders, J. Phys. Chem. 70 (1966) 1777–1785.
[6] P. Sahoo, T. Debroy, M.J. McNallan, Metall. Mater. Trans. B 19 (1988) 483–491.
[7] J. Lee, K. Morita, ISIJ Int. vol.43 (2003) 14–19.

CHAPTER 1.2

Surface Tension and Contact Angle

Joonho Lee
Department of Materials Science and Engineering, Korea University, Anam-dong, Seongbuk-gu, Seoul, Republic of Korea

1.2.1. SURFACE TENSION

1.2.1.1. Definition of Surface Tension

Let us recall the reversible variation of the system of Figure 1.1.2.

$$dU = dU^{\alpha} + dU^{\beta} + dU^{\sigma} \tag{1.2.1}$$

$$dU^{\alpha} = TdS^{\alpha} + \sum_{i=1}^{m} \mu_i dn_i^{\alpha} - P^{\alpha} dV^{\alpha} \tag{1.2.2}$$

$$dU^{\beta} = TdS^{\beta} + \sum_{i=1}^{m} \mu_i dn_i^{\beta} - P^{\beta} dV^{\beta} \tag{1.2.3}$$

Since the interface tension σ is the work for reversible creation of a new interface instead of PV work of bulk phases, the energy of interface is given by Equation (1.2.4).

$$dU^{\sigma} = TdS^{\sigma} + \sum_{i=1}^{m} \mu_i dn_i^{\sigma} + \sigma dA \tag{1.2.4}$$

Incorporating Equations (1.2.2)–(1.2.4) in Equation (1.2.1), we may obtain Equation (1.2.5).

$$\begin{aligned} dU &= T\left(dS^{\alpha} + dS^{\beta} + dS^{\sigma}\right) + \sum \mu_i \left(dn_i^{\alpha} + dn_i^{\beta} + dn_i^{\sigma}\right) - P^{\alpha} dV^{\alpha} - P^{\beta} dV^{\beta} + \sigma dA \\ &= TdS + \sum_{i=1}^{m} \mu_i dn_i - P^{\alpha} dV^{\alpha} - P^{\beta} dV^{\beta} + \sigma dA \end{aligned} \tag{1.2.5}$$

From Equation (1.2.5), the interface tension can be defined thermodynamically by Equation (1.2.6).

$$\sigma = \left(\frac{dU}{dA}\right)_{S, n_i, V^{\alpha}, V^{\beta}} \tag{1.2.6}$$

However, it is difficult to fix the entropy term as bulk phases. Therefore, the interface tension is generally defined using Helmholtz free energy (F) or Gibbs free energy (G).

http://dx.doi.org/10.1016/B978-0-08-096984-8.00028-8
© 2014 Elsevier Ltd.
All rights reserved.

$$\sigma = \left(\frac{dF}{dA}\right)_{T,n_i,V^\alpha,V^\beta} \tag{1.2.7}$$

$$\sigma = \left(\frac{dG}{dA}\right)_{T,n_i,P^\alpha,P^\beta} \tag{1.2.8}$$

Assuming that α is a gas phase and β is a condensed phase (solid or liquid), the surface tension is defined by Equation (1.2.9).

$$\sigma = \left(\frac{dU}{dA}\right)_{S,n_i,V} = \left(\frac{dF}{dA}\right)_{T,n_i,V} = \left(\frac{dG}{dA}\right)_{T,n_i,P} \tag{1.2.9}$$

Therefore, the surface tension σ can be defined as the work for isothermal reversible creation of a new surface of a condensed phase β. However, it should be noted that the creation of a new surface may take place by two different processes.

Figure 1.2.1 shows the two possible processes for the creation of a new surface: cleavage and elastic deformation [1]. Generally, the first energy is called surface tension σ, and the second one is surface stress ξ. For a liquid phase, the surface tension and the surface stress are identical. On the other hand, for a solid phase, the surface tension and the surface stress have the relation expressed by Equation (1.2.10) [2,3].

$$\zeta = \sigma + \frac{d\sigma}{d\varepsilon} \tag{1.2.10}$$

where ε is a macroscopic elastic strain. At very high temperatures, the second term of the right hand side of Equation (1.2.10) is much smaller than the first term [1].

1.2.1.2. Temperature Dependence of Surface Tension

From the convention of the Helmholtz free energy, the free energy of a unit surface area of a pure substance can be expressed by Equation (1.2.11).

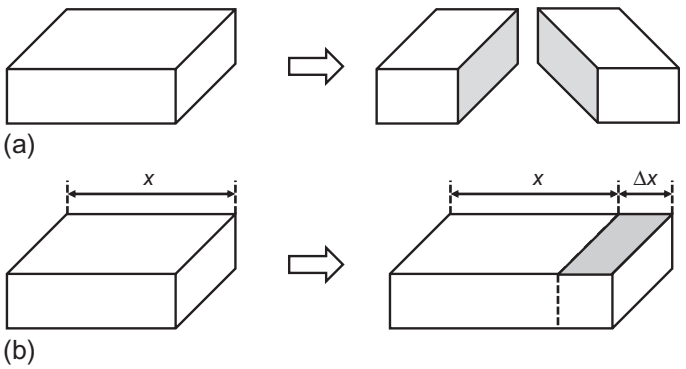


Figure 1.2.1 Two possible processes for the creation of a new surface: cleavage and elastic deformation [1].

$$f^{\sigma} \equiv u^{\sigma} - Ts^{\sigma} \tag{1.2.11}$$

where u^{σ} and s^{σ} denote the surface energy and surface entropy of the unit surface area. Consequently, surface tension σ $(=f^{\sigma})$ is composed of the internal energy and entropy terms.

Derivation of Equation (1.2.11) is given by Equation (1.2.12).

$$\left(\frac{\partial f^{\sigma}}{\partial T}\right) = \left(\frac{\partial \sigma}{\partial T}\right) = -s^{\sigma} \tag{1.2.12}$$

Since the surface entropy is positive, as temperature increases, the surface tension decreases.

According to Oriani, Equation (1.2.11) can be rewritten by Equation (1.2.13) [4].

$$\sigma = \frac{1}{A}\left\{\left(\frac{Z_i - Z_s}{Z_i}\right)\Delta_s^{g}H_0 - \frac{Z_s\phi}{2}\right\} + T\left(\frac{\mathrm{d}\sigma}{\mathrm{d}T}\right) \tag{1.2.13}$$

where Z_i is the coordination number of the bulk atom i, Z_s the coordination number of the surface atom i, $\Delta_s^{g}H_0$ the sublimation enthalpy of i at 0 K, ϕ the excess binding energy (the difference in the pair-wise interaction energy within the bulk and that on the surface layer).

Experimentally, the temperature dependence of the surface tension was suggested by Eötvös law [5] as:

$$\sigma = \frac{k}{V_{\mathrm{m,(l)}}^{2/3}}(T_{\mathrm{c}} - T) \tag{1.2.14}$$

where $V_{\mathrm{m,(l)}}$ is the molar volume of a liquid, T_{c} the critical temperature, and k a constant (approximately $6.4 \times 10^{-8}\,\mathrm{J/K\,mol^{2/3}}$ for all liquid metals). Consequently, the temperature dependence of surface tension of pure metals is negative.

On the other hand, the temperature dependence of alloys is not always negative [6]. Rearranging Equation (1.1.14), we may obtain Equation (1.2.15).

$$\mathrm{d}\sigma = -\frac{S^{\sigma}}{A}\mathrm{d}T - \sum_{i=1}^{m}\Gamma_i \mathrm{d}\mu_i = -s^{\sigma}\mathrm{d}T - \frac{\mathrm{d}G^{\sigma,\mathrm{mix}}}{A} \tag{1.2.15}$$

Accordingly,

$$\frac{\mathrm{d}\sigma}{\mathrm{d}T} = -s^{\sigma} - \frac{\mathrm{d}G^{\sigma,\mathrm{mix}}}{A\mathrm{d}T} \tag{1.2.16}$$

The first and second terms on the right hand side are the surface entropy (s^{σ}) and the ordering effect by the surface segregation in unit area. Therefore, when the temperature

coefficient ($d\sigma/dT$) is zero, the surface entropy is equal to the surface mixing entropy. A positive temperature coefficient can be obtained for the surface segregation especially of the surface active elements, or of the component elements having much lower surface tension.

1.2.2. CONTACT ANGLE

1.2.2.1. Young's Equation

Once a nonreactive liquid is in contact with a solid surface, which is flat, undeformable, perfectly smooth and chemically homogeneous, under a vapor atmosphere, the liquid surface will intersect the solid surface at a contact angle θ (see Figure 1.2.2). The equilibrium value of θ_e is determined by the Young's equation (1.2.17) [7].

$$\cos\theta_e = \frac{\sigma_{SV} - \sigma_{SL}}{\sigma_{LV}} \tag{1.2.17}$$

where σ_{SV}, σ_{SL}, and σ_{LV} denote the solid surface tension, the solid–liquid interface tension, and the liquid surface tension, respectively.

Equation (1.2.17) can be derived by the variation of interfacial free energy per unit length of the $S/L/V$ triple line δF^{σ} by a small linear displacement δz of the triple line [1].

$$F^{\sigma}(z+\delta z) - F^{\sigma}(z) = \delta F^{\sigma} = (\sigma_{SL} - \sigma_{SV})\delta z + \cos\theta \cdot \sigma_{LV}\delta z \tag{1.2.18}$$

The equilibrium condition is obtained as $d(\delta F^{\sigma})/d(\delta z) = 0$, yielding Equation (1.2.17).

1.2.2.2. Smith's Equation

At high temperatures, the assumption of undeformable solid surface is not valid. Therefore, the equilibrium contact angle obtained from Equation (1.2.17) is a metastable value. If we consider the displacement of the triple line, δh, is composed of the vector perpendicular to the L/V interface (δh_1) and that perpendicular to the S/L interface (δh_2) (see Figure 1.2.3). The interfacial free energy change for the direction of δh_1 is given by Equation (1.2.19).

$$\delta F^{\sigma} = \sigma_{SV}\sin(\phi_2)\delta h_1 - \sigma_{SL}\sin(\phi_1)\delta h_1 \tag{1.2.19}$$

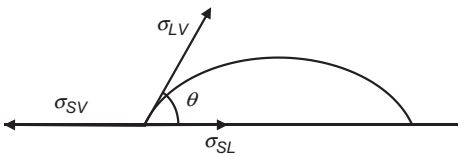


Figure 1.2.2 Equilibrium contact angle determined by the Young's equation.

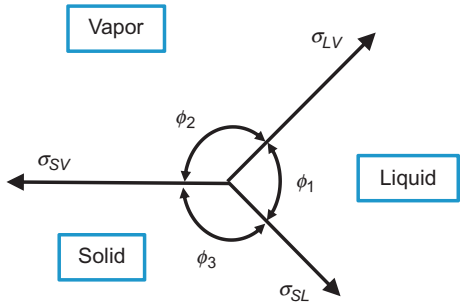


Figure 1.2.3 Equilibrium contact angles determined by the Smith's equation [8].

The equilibrium condition is obtained as $d(\delta F^s)/d(\delta h_1) = 0$, yielding Equation (1.2.20).

$$\sigma_{SV} \sin \phi_2 = \sigma_{SL} \sin \phi_1 \tag{1.2.20}$$

Similarly, at the condition of $d(\delta F^s)/d(\delta h_2) = 0$, Equation (1.2.21) is derived.

$$\sigma_{SV} \sin \phi_3 = \sigma_{LV} \sin \phi_1 \tag{1.2.21}$$

Combining Equations (1.2.20) and (1.2.21), we may obtain Equation (1.2.22).

$$\frac{\sigma_{SV}}{\sin \phi_1} = \frac{\sigma_{SL}}{\sin \phi_2} = \frac{\sigma_{LV}}{\sin \phi_3} \tag{1.2.22}$$

where $\phi_1, + \phi_2 + \phi_3 = 360^\circ$. Equation (1.2.22) is known as Smith equation [8].

1.2.2.3. Effect of Surface Roughness

The roughness of solid surface affects the contact angle due to an increased surface area. Small displacement of a triple line on a rough surface δx may yield the variation of interfacial free energy per unit length, δF^σ (see Figure 1.2.4)

$$\delta F^\sigma = (\sigma_{SL} - \sigma_{SV}) s_r \delta x + \sigma_{LV} \cos(\theta_M) \delta x \tag{1.2.23}$$

where s_r and θ_M are the ratio of the actual to the planar area and the apparent macroscopic contact angle, respectively. The equilibrium condition is obtained as $d(\delta F^\sigma)/d(\delta x) = 0$, yielding Equation (1.2.24).

$$\cos \theta_M = s_r \cos \theta_e \tag{1.2.24}$$

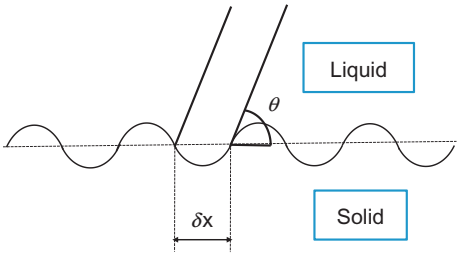


Figure 1.2.4 Displacement of a triple line on a rough surface by δx.

Equation (1.2.24) is known as Wenzel equation [9].

The roughness of solid surface may yield pinning effect of the triple line by sharp edges. Therefore, the apparent contact angle can be measured between the maximum advancing (θ_a(max)) and the receding (θ_r(min)) angles [1].

$$\theta_r(\min) \leq \theta_e \leq \theta_a(\max) \tag{1.2.25}$$

The maximum advancing and the minimum receding angles can be expressed by Equations (1.2.26) and (1.2.27), respectively.

$$\theta_a(\max) = \theta_e + \beta_{\max} \tag{1.2.26}$$
$$\theta_r(\min) = \theta_e - \beta_{\max} \tag{1.2.27}$$

A schematic illustration of the maximum advancing angle and the minimum receding angle on a rough surface is given in Figure 1.2.5.

1.2.3. WETTING

Generally, wetting is defined as "coating behavior of liquid phase on a solid surface." Wetting is important phenomena in many pyro-metallurgical processes. Types of wetting are spreading wetting, immersion wetting, and adhesion wetting, as illustrated in Figure 1.2.6 [10]. In all the wetting phenomena, a new solid–liquid interface is made by consuming a gas–solid interface of the same area. Therefore, the wetting energy can be described by the interface tensions.

$$W_s = \sigma_s - \sigma_l - \sigma_{sl} \tag{1.2.28}$$
$$W_i = \sigma_s - \sigma_{sl} \tag{1.2.29}$$
$$W_a = \sigma_s + \sigma_l - \sigma_{sl} \tag{1.2.30}$$

Instituting Young's equation, Equations (1.2.31)–(1.2.33) are obtained.

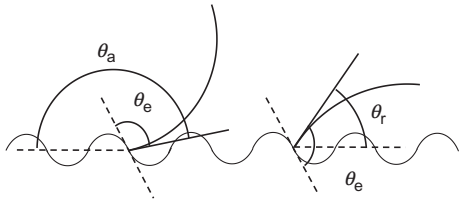


Figure 1.2.5 The maximum advancing contact angle and the minimum receding contact angle on a rough surface [1].

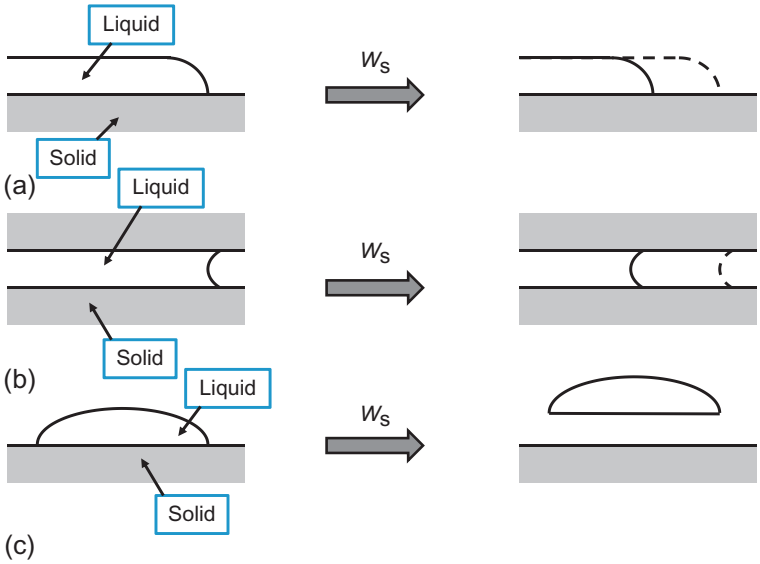


Figure 1.2.6 Three types of wetting: (a) spreading, (b) immersion, and (c) adhesion [10].

$$W_s = \sigma_l(\cos\theta - 1) \tag{1.2.31}$$

$$W_i = \sigma_l \cos\theta \tag{1.2.32}$$

$$W_a = \sigma_l(\cos\theta + 1) \tag{1.2.33}$$

REFERENCES

[1] N. Eustathopoulos, M.G. Nicholas, B. Drevet, Wettability at High Temperatures, Pergamon, Amsterdam, 1999, p. 1.
[2] R. Shuttleworth, Proc. Phys. Soc. (Lond.) A63 (1950) 444.
[3] C. Herring, in: R. Gomer, C.S. Smith (Eds.), Structure and Properties of Solid Surfaces, University of Chicago, Chicago, 1953, p. 5.
[4] R.A. Oriani, J. Chem. Phys. 18 (1950) 575.

[5] T. Iida, R.I.L. Guthrie, The Physical Properties of Liquid Metals, Clarendon Press, Oxford, 1988, p. 131.
[6] J. Lee, W. Shimoda, T. Tanaka, Mat. Trans. 45 (2004) 2864–2870.
[7] T. Young, Phil. Trans. R. Soc. Lond. 94 (1805) 65.
[8] C.S. Smith, Trans. AIME 175 (1948) 15.
[9] R.N. Wenzel, Ind. Eng. Chem. 28 (1936) 988.
[10] K. Mukai, ISIJ Int. 32 (1992) 19–25.

CHAPTER 1.3

Experiments

Toshihiro Tanaka[a] **and Joonho Lee**[b]

[a]Division of Materials and Manufacturing Science, Graduate School of Engineering, Osaka University, Osaka, Japan

[b]Department of Materials Science and Engineering, Korea University, Anam-dong, Seongbuk-gu, Seoul, Republic of Korea

Outlines on fundamental experimental procedures for measurement of surface tension of liquid metals, alloys and molten slag and flux are explained in this chapter. Detail issues related to each procedure can be found in the references [1–3]. Fundamental explanations for each method were quoted from those references [1–3].

Many methods to determine surface tension σ at high temperatures are based on the Laplace equation, which relates the excess pressure (ΔP) at a curved surface or interface, with the principal radii of curvature (R_1 and R_2) at a point on the surface, namely

$$P_1 - P_2 = \Delta P = \sigma\left(\frac{1}{R_1} + \frac{1}{R_2}\right) \tag{1.3.1}$$

where P_1 and P_2 are, respectively, the pressure on the concave and the convex side of the meniscus.

This is the fundamental equation which describes the equilibrium shape of menisci such as drops and bubbles. Analysis of Equation (1.3.2) shows that where the meniscus is spherical, i.e., $R_1 = R_2 = R$

$$\Delta P = \frac{2\sigma}{R} \tag{1.3.2}$$

1.3.1. SESSILE DROP

Sessile drop method has proved to be one of the most popular techniques to determine σ of liquid metals in spite of its limitations with regard to possible contamination of the sample during the experiment. The sessile drop method has been used most extensively for measuring the surface tension of liquid metals and alloys because of the following advantages. The sessile drop method allows simultaneous measurements of contact angle, spreading coefficient, work of adhesion, and density. Furthermore, both mathematical treatment for calculating surface tensions from measured drop dimensions, as well as the experimental equipment needed for providing a sessile drop, are relatively simple.

Treatise on Process Metallurgy, Volume 2
http://dx.doi.org/10.1016/B978-0-08-096984-8.00027-6

© 2014 Elsevier Ltd.
All rights reserved.

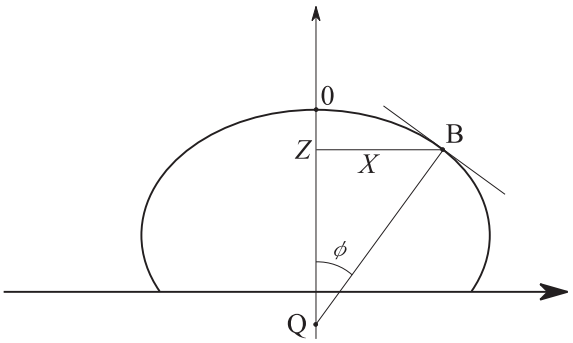


Figure 1.3.1 Sessile drop method.

It also allows more accurate determination of surface tensions over wide ranges of temperature.

Figure 1.3.1 shows the equilibrium profile of a sessile drop of liquid at rest on a horizontal solid surface. At any point, B on the surface, the principal radii of curvature are R_1 and R_2. The excess pressure due to surface curvature is given by the Laplace equation

$$\Delta P = \sigma\left(\frac{1}{R_1}+\frac{1}{R_2}\right) = \rho g Z + C \tag{1.3.3}$$

where Z, vertical distance of point B from the apex (0); ρ, density difference between the two phases; and C, constant.

If ϕ is the angle the normal at B makes with the axis of symmetry at Q, then the two principal radii of curvature at B can be designated as R and $(X/\sin\phi)$, respectively. At the apex (0), the two principal radii of curvature are equal $(=b)$ and the parameter b, which depends on the dimensions of the drop, is termed to the "size factor." The constant C is given by the ratio $2\sigma/b$. Equation (1.3.3) can be mathematically transformed into a non-dimensional form, namely

$$\Delta P = \sigma\left(\frac{1}{R}+\frac{\sin\phi}{X}\right) = \rho g Z + \frac{2\sigma}{b} \tag{1.3.4}$$

$$\frac{b}{R}+\frac{b\sin\phi}{X} = \frac{\rho g Z b}{\sigma} + 2 \tag{1.3.5}$$

Equation (1.3.5) describes mathematically the surface curvature of a meridian section of a sessile drop, and is a second order, second degree differential equation which can only be solved numerically by using approximation procedures such as computer curve fitting programs.

Measurements of sessile drop dimensions are usually obtained from photographic images. Recent developments have seen the application of the computer curve fitting technique for the analysis of drop images obtained by high resolution CCD camera equipment. The accuracy of the data should be improved particularly since the

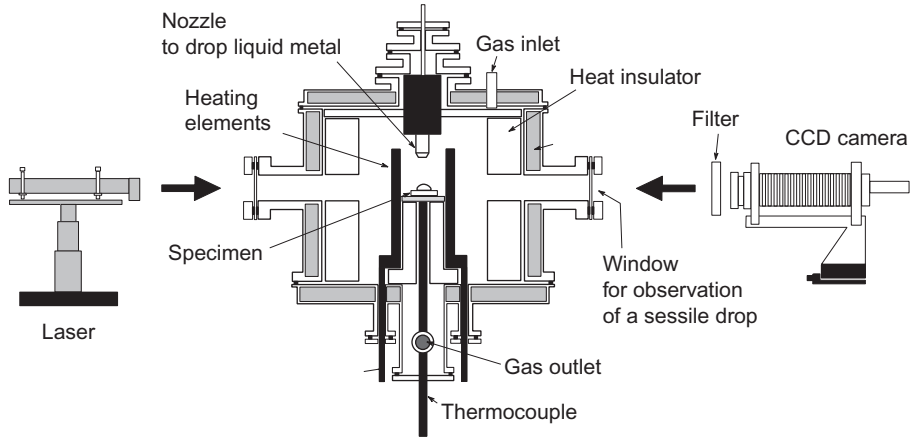


Figure 1.3.2 An apparatus for sessile drop method.

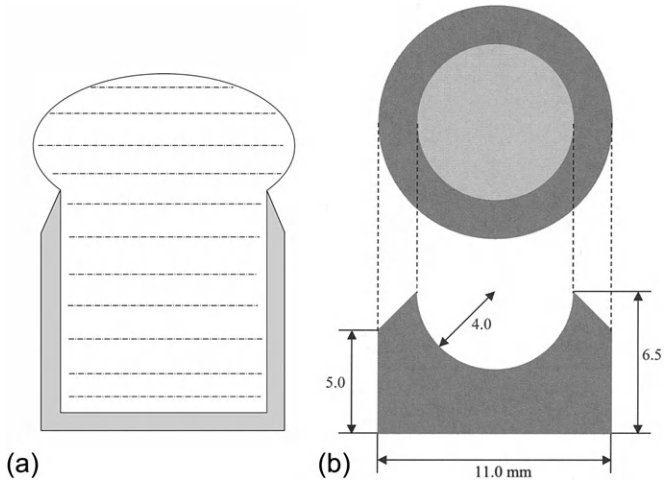


Figure 1.3.3 Large drop method.

coordinates of a considerable number of points along the drop perimeter can be accurately located. Especially when a laser is used as a light source, a very clear contour of a droplet can be measured to improve more accurate the surface tension of the liquid. Figure 1.3.2 shows one example of a setup of a sessile drop method in a furnace with a laser and a CCD camera equipment [4].

Ideally, measurements should be made on the profiles of nonwetting sessile drops ($\theta > 90\,^{\circ}$). Large sessile drops should be used for the best accuracy, but in practice, it is usually difficult to obtain large drops in isolation that are truly axisymmetric. To overcome problems of asymmetry, the "large drop" method can be used as shown in Figure 1.3.3. This modification of the sessile drop technique has two advantages in that

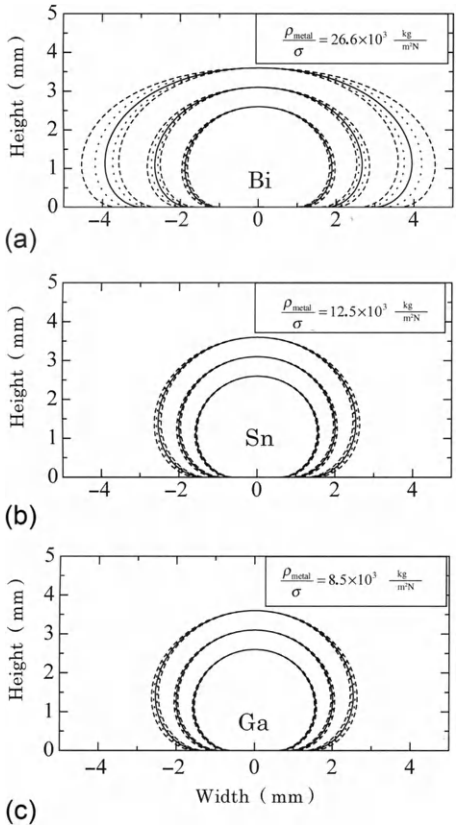


Figure 1.3.4 Contours of droplets for Bi, Sn and Ga.

it produces a large axisymmetric meniscus and can be used with both wetting and non-wetting systems. A circular crucible or cup which has its upper circumferential edge chamfered to an acute angle is overfilled with fluid so that an axisymmetric meniscus is produced which stand proud of the rim. Figure 1.3.4 shows the contour of the droplet for some liquid metals at fixed height of the droplet [5]. The solid curves in this figure show the profile of the droplet of liquid Bi, Sn and Ga at their melting points for $h = 2.6$, 3.1, and 3.6 mm when the recommended values σ_{rec} of the surface tension are used. The dotted curves and broken curves in this figure indicate the profiles obtained from the conditions for $\sigma_{rec} \times (1 \pm 0.05)$ and $\sigma_{rec} \times (1 \pm 0.10)$, respectively These curves correspond to the profiles of the droplet, which are obtained when the value of the surface tension has 5% or 10% of the uncertainty from the values of σ_{rec}. As can be seen from Figure 1.3.4, the shape for σ_{rec} can be distinguished more clearly from that for $\sigma_{rec} \times (1 \pm 0.05)$ and $\sigma_{rec} \times (1 \pm 0.10)$ as the size of the droplet increases. In other words, if a small droplet is investigated, the measured value of the surface tension contains easily 5% or 10% uncertainty. In addition, the change in the profile due to the uncertainty of the

surface tension depends on the capillary constant, i.e., the ratio of ρ/σ where ρ is the density and σ is the surface tension of a metal. The values of the ratio ρ/σ for each metal are indicated in Figure 1.3.4. If the liquid has s smaller capillary constant, a larger droplet is necessary to obtain high accuracy of the surface tension of liquid metals. Thus, a highly reliable value of the surface tension can be obtained if a large drop can be made as a sessile drop. It is, however, difficult to make a large droplet of liquid metal and keep it stable on a flat substrate which is not wetted by liquid metals. Therefore, a crucible is generally used for the large drop method. One example of a crucible actually used for the large drop method is shown in Figure 1.3.3b [5].

1.3.2. MAXIMUM BUBBLE PRESSURE

A capillary tube of known radius r is immersed in the fluid to a known depth h. A gas/liquid meniscus is produced at the capillary tip by progressively increasing the gas pressure in the tube until the applied pressure is sufficient for the meniscus to form an independent bubble which detaches from the orifice. The maximum pressure at this point is recorded by a suitable transducer system, and from this value, σ can be calculated. If the tip of the capillary is immersed to a depth h in the fluid as shown in Figure 1.3.5, the total pressure $P_{\max}$ acting at the point of bubble detachment is given by

$$P_{\max} = \frac{2\sigma}{r} + \rho g h \tag{1.3.6}$$

where ρ is the density difference between the fluid and gas and g the acceleration due to gravity.

In Equation (1.3.6), $P_{\max}$ varies linearly with h and from a straight line plot, σ can be determined by extrapolation to the intercept on the $P_{\max}$ axis at which point $P_{\max} = 2\sigma/r$. The density of the fluid can be derived from the slope ($=\rho g$) of the line.

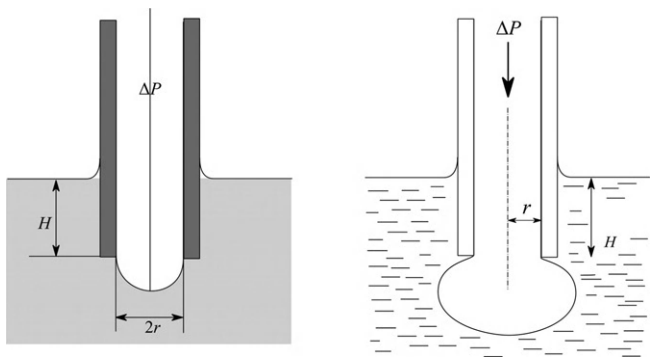


Figure 1.3.5 Maximum pressure method.

Equation (1.3.6) pertains only to the limiting case of menisci which possess spherical contours, but in many practical situations the shape of the meniscus is modified by gravitational effects and it is necessary to account for the deviation from spherical shape. Several methods have been proposed for correcting experimental data to give absolute surface tension value σ. The most widely used correction is the approximation derived by Schrödinger, namely

$$\sigma = \frac{P_{\max} r}{2}\left\{1 - \frac{2}{3}\left(\frac{r\rho g}{P_{\max}}\right) - \frac{1}{6}\left(\frac{r\rho g}{P_{\max}}\right)^2\right\} \tag{1.3.7}$$

The expression in the braces is the correction factor for $P_{\max}$. The Schrödinger equation has proved to be accurate for systems in which

$$r \cdot \left(\frac{2\sigma}{\rho g}\right)^{-1/2} < 0.2 \tag{1.3.8}$$

The rate of bubble formation in the maximum bubble pressure (MBP) technique is very important, since high rates of bubble formation can lead to erroneous results. For liquids with high viscosity the pressure required to detach a bubble depends strongly on the bubble rate and for the best accuracy, rates of one bubble every 1–2 min are common. The selection of materials of a capillary for a target liquid is important to measure an accurate surface tension. For example, as shown in Figure 1.3.6, if the material of a capillary is not wet with liquid specimen, the diameter of a bubble is expanded to the outer edge of the capillary, which means that we adjust the value of r for Equations (1.3.6) or (1.3.7). Thus, generally we select a material of a capillary wet well with a target liquid specimen. When we try to measure the surface tension of liquid metals and alloys by

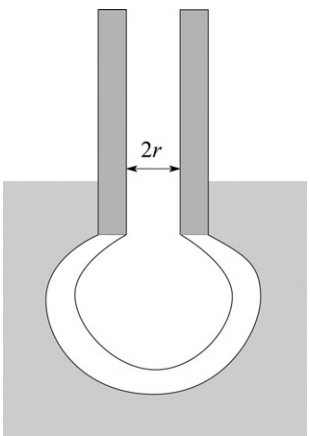


Figure 1.3.6 Maximum pressure method (wettability of liquid with capillary).

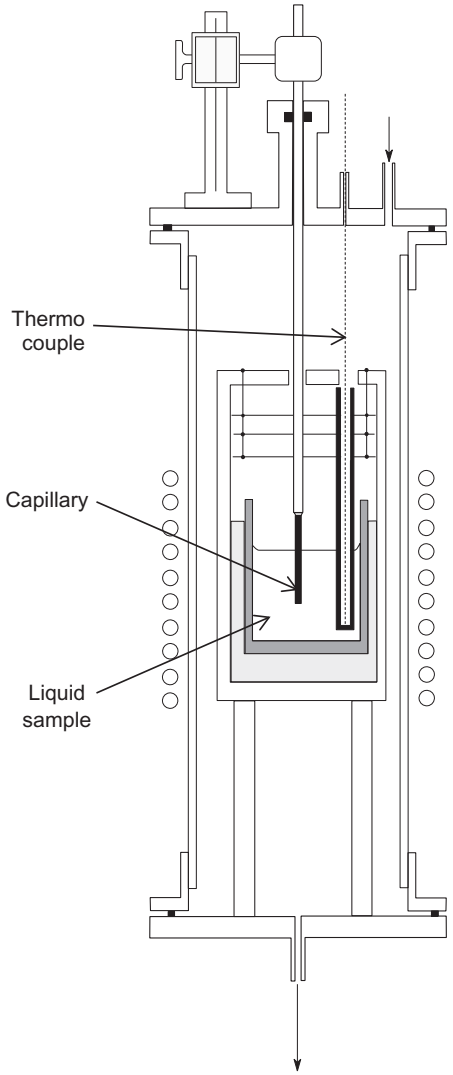


Figure 1.3.7 An apparatus for maximum pressure method.

MBP method, it is difficult to find an adequate material of a capillary. Figure 1.3.7 shows an example of a setup of a maximum pressure method in a furnace [6].

1.3.3. PENDENT DROP

When a liquid drop hangs freely from an orifice of a capillary tube, it will adopt a shape which is generally similar to that shown in Figure 1.3.8 [7,8]. If the forces of gravity and surface tension are balanced in a static pendant drop, the liquid surface tension is given by

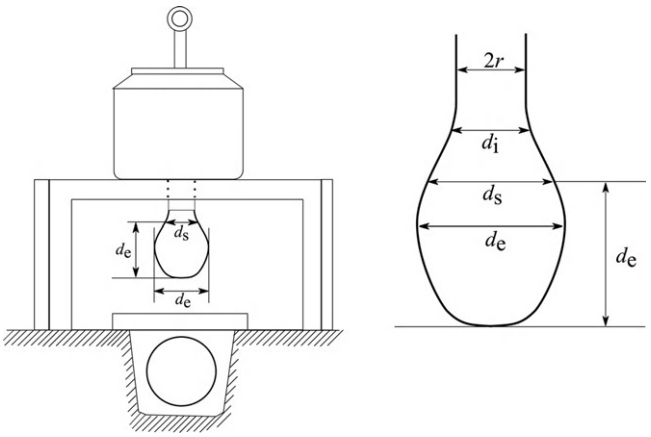


Figure 1.3.8 Pendant drop method.

$$\sigma = \frac{\rho g X^2}{H} \tag{1.3.9}$$

in which X is the maximum drop diameter and $1/H$ is the shape factor of the drop. Values of $1/H$ have been calculated as a function of the experimentally determined parameters X^1/X, and usually vary between 0.3 and 1.0 [7].

1.3.4. DROP WEIGHT

The experimental basis of this drop weight (DW) method is to produce a liquid drop slowly at the end of a capillary tube and increase the size of the drop until it ultimately detaches from the tip [8,9]. When a liquid drop formed at the tip of a vertical cylindrical rod or capillary grows large enough, the liquid drop falls as a result of its weight. The surface tension of the liquid can be computed from the mass of the drop which falls. If m is the mass of the drop separating from a vertical rod or capillary tube of radius r as a result of gravitational forces, the surface tension of the liquid is given by

$$\sigma = \frac{mg}{2\pi r f_D} \tag{1.3.10}$$

where f_D: a function of $(r/V^{1/3})$, V: the volume of the falling drop.

A drop whose weight is equal to $2\pi r\sigma$ (when $f_D = 1$ and $2\pi r\sigma = mg$) is called the "ideal drop." Both observation and theory indicate that, while the major fraction of the drop falls, a part remains attached to the capillary. Equation (1.3.10) may be rewritten as follows:

$$\sigma = \frac{mgF_D}{r} \tag{1.3.11}$$

in which F_D is a function of (V/r^3) or $(m/\rho r^3)$. The values of F_D corresponding to given values of V/r^3 have been given in Ref. [9].

1.3.5. DETACHMENT METHOD

The determination of σ by detachment methods is generally based on measurement of the maximum force exerted on a body as it is withdrawn from the surface of a liquid. The shape of the body used in the experiment can take a variety of forms, e.g., ring, thin plate, rod hollow cylinder. When the body is slowly pulled from the surface of a fluid, then, providing the wetting conditions are appropriated, a meniscus of the liquid adheres to the base and continually extends as the body is withdrawn. As the failure point of the meniscus is approached, the force required to draw the body away from the surface goes through a maximum and from measurement of this maximum force it is possible to calculate σ. Detachment techniques have not often been employed to determine the σ of liquid metals.

The method commonly used for melts at high temperatures is the maximum pull on a hollow cylinder. A thin walled cylindrical tube is attached by one end to a continuously recording balance and the ring of the opposite end is dipped just below the surface of the melt (Figure 1.3.9). The liquid level is slowly lowered and the meniscus attached to the rim of the cylinder gradually extends (Figure 1.3.9) until it ultimately fails. The maximum excess weight recorded by the balance is W_{max} then σ can be calculated from the relation

$$\sigma = \frac{W_{max} g}{4\pi r} F \tag{1.3.12}$$

where r is the mean radius of the cylinder and F correction factor, which allows for the shape of the meniscus and the dimensions of the cylinder. The factor F can be established by, e.g., calibration of the system with liquids of known σ. Nakashima *et al.* used the ring method to measure the surface tension of various molten oxide systems [10].

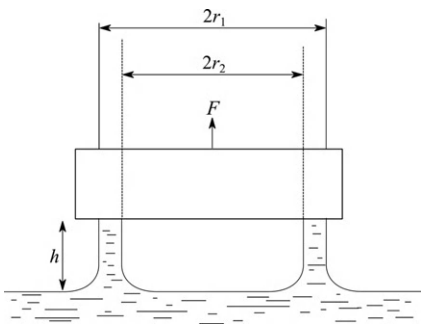


Figure 1.3.9 Detached method.

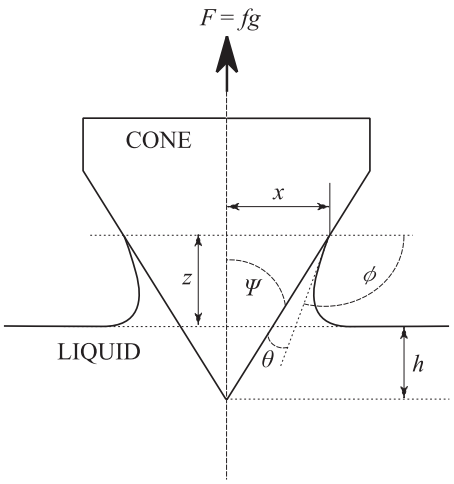


Figure 1.3.10 Padday's Cone Technique.

As another type of the detachment method, Padday *et al.* [11] has described a novel equilibrium method which allows determination of the surface tension of a liquid by measuring the maximum excess force exerted on a cone during its immersion in or withdrawal from the liquid. The excess force acting on the partially immersed cone, shown in Figure 1.3.10, arises from the surface tension at the line of contact with the meniscus, the weight of the volume of liquid raised above the general level of the liquid, and the buoyancy effect. For a cone of half-angle Ψ and a liquid which has a contact angle of θ, this force, F, is given by

$$F = 2\pi x\sigma\cos(\phi-\theta)+\pi z x^2\rho g-\frac{1}{3}\pi x^2(z+h)\rho g \tag{1.3.13}$$

and the axisymmetric meniscus follows Laplace's capillary equation

$$\frac{\mathrm{d}^2z/\mathrm{d}x^2}{\left[1+\frac{\mathrm{d}z}{\mathrm{d}x}\right]^{3/2}}+\frac{k\sin\Psi}{x}=\frac{z}{k} \tag{1.3.14}$$

in which k, the capillary constant, is given by $k^2=\sigma/\rho g$, and σ and ρ are, respectively, the surface tension and the density of the liquid. Equation (1.3.14) is reduced to dimensionless form by dividing by σk to give

$$\frac{F}{\sigma k}=\frac{2\pi x\cos(\varphi-\theta)}{k}+\frac{\pi x^2 z}{k^3}-\frac{\pi x^2(x+h)}{3k^3}=\frac{V}{K^3} \tag{1.3.15}$$

In Equation (1.3.15), V is the volume of liquid raised above the general level of the liquid minus the volume displaced by the part of the cone which is below the general level of the surface.

If a cone is immersed in a liquid, or, after immersion, is withdrawn from the interface, the excess force exerted on the cone passes through a maximum value before the meniscus is broken. The corresponding maximum value of V/k^3 in Equation (1.3.15) have been calculated by Padday for a series of values of Ψ (and $\theta = 0$). The maximum value of V/k^3 defines the cone constant, i.e.,

$$C = \frac{V_{\max}}{k^3} \tag{1.3.16}$$

Thus if $F = fg$ is experimentally measured as the maximum excess force on the cone, the surface tension is obtained from

$$\frac{fg}{\sigma k} = C \tag{1.3.17}$$

as

$$\sigma = g\rho^{1/3}\left(\frac{f}{C}\right)^{2/3} \tag{1.3.18}$$

One example of the application of the above technique was given by Kidd and Gaskell for the measurement of the surface tensions of Fe-saturated iron silicate and Fe-saturated calcium ferrite melts in [12].

1.3.6. LIQUID SURFACE CONTOUR METHOD

Mukai *et al.* [13] proposed a unique experimental method to determine of molten slag from the surface contour as described in this section. In order to measure the surface tension of liquid by this method, a crucible in Figure 1.3.11 is filled with the liquid and a cylinder is immersed vertically into the liquid. Then, the contour of a meniscus of the liquid formed around the cylinder is measured. The contour is analyzed on the basis of Laplace's equation to determine the surface tension of the liquid. The meniscus is recognized to be a symmetrical solid of revolution around Z axis in Figure 1.3.11. The contour of the meniscus is described by the following Laplace equation:

$$\sigma\left(\frac{1}{R_1} + \frac{1}{R_2}\right) = \rho g z + C_0 \tag{1.3.19}$$

$$\frac{1}{R_1} = \frac{\left(\frac{\partial^2 z}{\partial x^2}\right)}{\left(1 + \left(\frac{\partial z}{\partial x}\right)^2\right)^{2/3}} \tag{1.3.20}$$

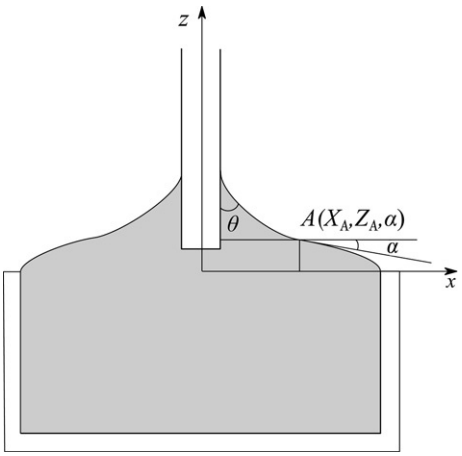


Figure 1.3.11 Liquid surface contour method.

$$\frac{1}{R_2}=\frac{\left(\frac{\partial z}{\partial x^2}\right)}{x\cdot\left(1+\left(\frac{\partial z}{\partial x}\right)^2\right)^{1/2}} \tag{1.3.21}$$

Here, σ is the surface tension, R_1 and R_2 are two main curvature radii, z is the height of a point along the contour, g is the gravitational constant, C_0 is a constant. As shown in Figure 1.3.11, at an inflection point A,

$$z=Z_{\mathrm{A}},\quad x=X_{\mathrm{A}},\quad R_1=\infty,\quad R_2=-\frac{\sin\alpha}{X_{\mathrm{A}}} \tag{1.3.22}$$

When the above equations are inserted to Equation (1.3.19), the value of C_0 is determined as follows:

$$C_0=-\frac{\sigma\sin\alpha}{X_{\mathrm{A}}+\rho g Z_{\mathrm{A}}} \tag{1.3.23}$$

By inserting Equation (1.3.23) into Equation (1.3.19), the following equation is obtained:

$$\frac{1}{R_1}+\frac{1}{R_2}=\left(\frac{\rho g}{\sigma}\right)(z-Z_{\mathrm{A}})-\frac{\sin\alpha}{X_{\mathrm{A}}} \tag{1.3.24}$$

By using the boundary conditions in Equation (1.3.22), Equation (1.3.24) is solved computationally. The contour obtained from Equation (1.3.24) is a function of $(\rho g/\sigma)$. Therefore, we can determine the value of $(\rho g/\sigma)$ to fit the contour obtained experimentally. When the value of the density ρ is given, the surface tension can be determined.

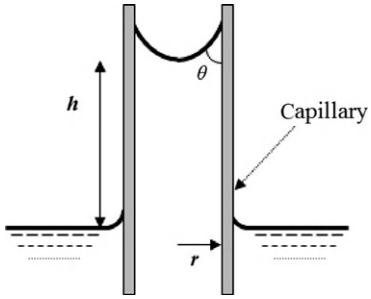


Figure 1.3.12 Capillary rise method.

1.3.7. CAPILLARY RISE METHOD

Capillary rise method represents an application of the well-known phenomenon of capillary action. The liquid surface tension can be computed from the expression

$$\sigma = \frac{\rho g h r}{2\cos\theta} \tag{1.3.25}$$

where h is the difference in height between the liquid surface within the capillary and the surface of the bulk liquid metal outside the capillary (liquid head), r is the radius of the capillary, and θ is the contact angle between the liquid and the capillary wall as shown in Figure 1.3.12.

The theory of the capillary rise method is simple. However, the technique requires an exact knowledge of contact angles. Since this information is lacking for most metals, this angle is often more difficult to measure than surface tension. As a result, the method is not commonly used for metallic liquids. However, measurement of σ for some low-melting-point metals, i.e., indium, tin, and the lead, have been made up to about 1000 K using this technique (e.g., [9,14]).

1.3.8. LEVITATING DROP

A sample of electrically conducting material is introduced into the electromagnetic field of an induction coil, where it levitates and melts as shown in Figure 1.3.13 [15,16]. Small perturbations in the system cause the drop to oscillate continuously at its natural frequency ω_n, which is related to the surface tension. To determine the oscillation frequency, an image of the drop is focused on to a photo detector system, and the frequency content of the resultant electrical signal is displayed as a spectrum from a Fourier analyzer. Provided the viscosity of the levitated liquid is low and the amplitude

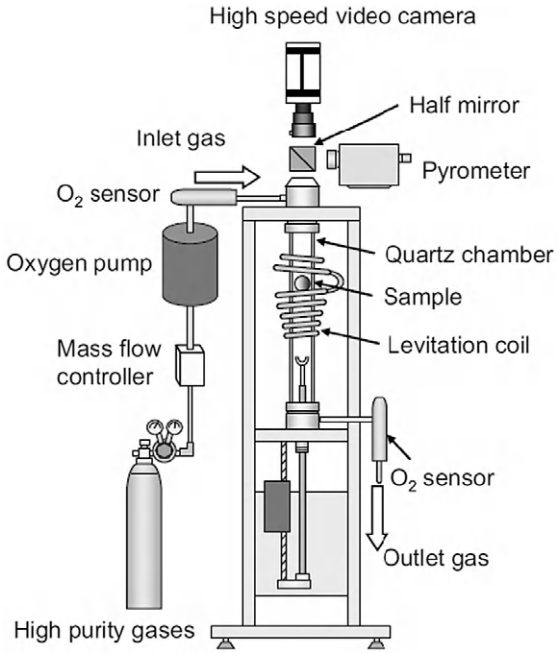


Figure 1.3.13 Apparatus for electromagnetic levitation drop method [15].

of the oscillations is small, then the relation between ω_n and σ for a drop of mass m is given by the Rayleigh equation [16].

$$\sigma = \frac{3}{8}\pi m \omega_n \tag{1.3.26}$$

In practice, the drops are aspherical and additional vibrational modes are present. Figure 1.3.14 is a record of a typical frequency spectrum (for molten iron) and shows five major peaks. The modified Rayleigh Equation (1.3.26) is used to calculate the surface tension [17].

$$\sigma = \frac{3}{8}\pi m \left[\frac{1}{5} \sum_{m=-2} \omega_m^2 - \omega_t^2 \left\{ 1.9 - 1.2 \left(\frac{g}{8\pi^2 \omega_t^2 R_0} \right)^2 \right\} \right] \tag{1.3.27}$$

where ω_m [Hz] is the surface oscillation frequency for $m = 0, \pm 1$ and ± 2 for the $l = 2$ mode, ω_t [Hz] is the translation frequency of center of gravity, g $[m \cdot s^{-1}]$ is the gravitational acceleration and R_0 [m] is the sample radius.

A unique advantage of this technique is that there is no contact between the molten material and a solid medium and consequently, sample contamination by this means is not possible. Because of the two basic requirements that the sample material is an electrical conductor and has low viscosity, applications of the levitating drop method at high

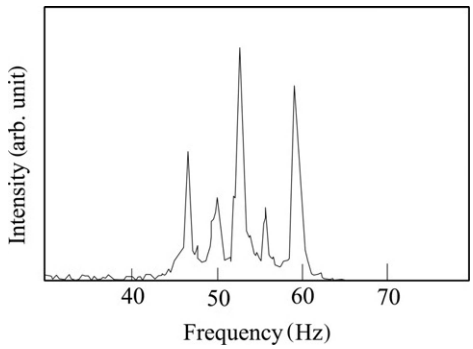


Figure 1.3.14 Typical frequency spectrum in levitation drop method.

temperatures have been confined to metallic systems. It is anticipated that as a consequence of the relatively low electrical conductivity, it would be difficult to use the levitating drop technique with semiconductor-type materials, such as silicon or germanium. In such cases, it may be possible to increase the conductivity by preheating the sample before introduction into the electromagnetic field. A possible alternative to electromagnetic levitation is the electrostatic levitation or the acoustic techniques. In this case the sample does not need to be an electrical conductor. Hibiya, Ozawa, Watanabe and Fukuyama *et al.* reported the surface tension measurements of liquid metals accurately by the levitating drop method considering the effect of oxygen on the surface tension [15–19].

APPENDIX A. SOFTWARE FOR EVALUATION OF SURFACE TENSION FROM SESSILE DROP

The computer software for evaluation of surface tension of a sessile drop was developed by Rotenberg *et al.* [20]. This software was updated by Jimbo and Cramb later [21]. The algorithm to calculate the surface tension of a sessile drop is to find the theoretical profile with Equation (1.3.5) to minimize the objective function Equation (A1). Here $dx/ds = \cos\varphi$ and $dz/ds = \sin\varphi$, where x and z are coordinates of the theoretical profile with the origin in the apex, and ϕ is the turning angle with respect to the arc-length parameter s.

$$E = \frac{1}{2}\sum_{n=1}^{N}[d(u_n, v)]^2 \tag{A1}$$

where $d(u_n,v)$ is the normal distance between u_n and the curve v (see Figure A1). Details of the computer software for evaluation of surface tension of a sessile drop can be found in

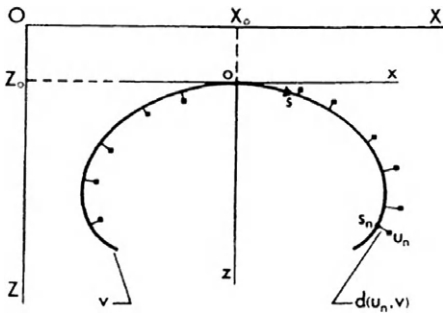


Figure A1 Schematic of the calculated surface profile of a liquid droplet using Eq. (1.3.24) with measured points [20].

[20–24]. In order to get a reliable surface tension value, computer software to get a clear image of a sessile drop is more important. Details can be found in [4]. The most recent improvements of the computer software was made by Taniguchi *et al.* [25].

REFERENCES

[1] T. Iida, R.I.L. Guthrie, The Physical Properties of Liquid Metals, Clarendon Press, Oxford, 1988.
[2] B.J. Keene, Int. Mater. Rev. 38 (1993) 157–192.
[3] A.I. Rusanov, V.A. Prokhorov, Interfacial Tensiometry, Elsevier, Amsterdam, 1996.
[4] J.-H. Lee, A. Kiyose, S. Nakatsuka, M. Nakamoto, T. Tanaka, ISIJ Int. 44 (2004) 1793–1799.
[5] T. Tanaka, M. Nakamoto, R. Oguni, J.-H. Lee, S. Hara, Z. Metallkde. 95 (2004) 818–822.
[6] T. Tanaka, A. Niino, N. Hirai, S. Hara, High. Temp. Mater. Processes 22 (2003) 151–156.
[7] S. Fordham, Proc. R. Soc. A194 (1948) 1.
[8] B.C. Allen, Trans. Met. Soc. AIME 227 (1963) 1175.
[9] W.D. Harkins, F.E. Brown, J. Am. Chem. Soc. 41 (1919) 499.
[10] F. Shimizu, H. Tokunaga, N. Saito, K. Nakashima, ISIJ Int. 46 (2006) 388–393.
[11] J.F. Padday, A.R. Pitt, R.M. Pashley, J. Chem. Soc. Faraday Trans. I 71 (1975) 1919.
[12] M. Kidd, D.R. Gaskell, Metall. Trans. B 17 (1986) 771.
[13] Z. Yu, K. Mukai, J. Jpn. Inst. Metals 59 (1995) 806–813.
[14] D.A. Melford, T.P. Hoar, J. Inst. Metals 85 (1956–1957) 197.
[15] S. Ozawa, S. Suzuki, T. Hibiya, H. Fukuyama, J. Appl. Phys. 109 (2011) 014902.
[16] L. Rayleigh, Proc. R. Soc. London 29 (1879) 71.
[17] D.L. Cummings, D.A. Blackburn, J. Fluid Mech. 224 (1991) 395.
[18] S. Ozawa, K. Morohoshi, T. Hibiya, H. Fukuyama, J. Appl. Phys. 107 (2010) 014910.
[19] K. Morohoshi, M. Uchikoshi, M. Isshiki, H. Fukuyama, ISIJ Int. 51 (2011) 1580–1586.
[20] Y. Rotenberg, L. Boruvka, A.W. Neumann, J. Colloid Interface Sci. 93 (1983) 169–183.
[21] I. Jimbo, A.W. Cramb, ISIJ Int. 32 (1991) 26–35.
[22] P. Cheng, A.W. Neumann, Colloids Surf. 62 (1992) 297.
[23] F.K. Hansen, J. Colloid Interface Sci. 160 (1993) 209.
[24] A.S. Krylov, A.V. Vvedensky, A.M. Katsnelson, A.E. Tugovikov, J. Non-Cryst. Solids 156–158 (1993) 845.
[25] Y. Taniguchi, S. Seetharaman, Metall. Mater. Trans. B 43 (2012) 587–597.

CHAPTER 1.4

Surface Tension Models

Toshihiro Tanaka
Division of Materials and Manufacturing Science, Graduate School of Engineering, Osaka University, Osaka, Japan

Modeling of surface tension is described for liquid metals & alloys and molten ionic materials including molten slag in this chapter.

1.4.1. MODELING OF SURFACE TENSION OF LIQUID PURE METALS AND MOLTEN SALTS

The surface free energy of pure element i is discussed from the thermodynamic point of view in this section. The surface free energy σ_i of pure element i consists of the surface energy σ_i^{H} and the surface entropy σ_i^{S} as follows:

$$\sigma_i = \sigma_i^{\mathrm{H}} - T\cdot\sigma_i^{\mathrm{S}} \tag{1.4.1}$$

First of all, we focus on the surface energy σ_i^{H}, and this term is defined as the difference of the binding energy of atoms at a surface with that in a bulk divided by the surface area A_i in Equation (1.4.2).

$$\sigma_i^{\mathrm{H}} = \frac{1}{A_i}\left(E_i^{\mathrm{Surface}} - E_i^{\mathrm{Bulk}}\right) \tag{1.4.2}$$

The surface area A_i for dense configuration of atoms can be expressed by

$$A_i = 1.091\cdot\left(\frac{V_i}{N_0}\right)^{2/3}\cdot N_0 = 1.091\cdot\left(V_i\right)^{2/3}\cdot\left(N_0\right)^{1/3} \tag{1.4.3}$$

where V_i, molar volume of element i; N_0, Avogadro number. The value of 1.091 is a geometric factor.

The binding energies E_i^{Bulk} and E_i^{Surface} of 1mole atoms in the bulk and the surface are given by

$$E_i^{\mathrm{Bulk}} = \frac{1}{2}\varepsilon\cdot Z^{\mathrm{Bulk}}\cdot N_0 \tag{1.4.4}$$

$$E_i^{\mathrm{Surface}} = \frac{1}{2}\varepsilon\cdot Z^{\mathrm{Surface}}\cdot N_0 \tag{1.4.5}$$

Treatise on Process Metallurgy, Volume 2
http://dx.doi.org/10.1016/B978-0-08-096984-8.00026-4
© 2014 Elsevier Ltd.
All rights reserved.

where ε, a binding energy of one pair of two atoms, Z^{Bulk} and Z^{Surface}, coordination numbers in the bulk and the surface.

Then we obtain

$$\begin{aligned}\sigma_i^{\mathrm{H}} &= \frac{1}{A_i}\left(\frac{1}{2}\varepsilon\cdot Z^{\mathrm{Surface}}\cdot N_0 - \frac{1}{2}\varepsilon\cdot Z^{\mathrm{Bulk}}\cdot N_0\right) \\ &= \frac{1}{A_i}E_i^{\mathrm{Bulk}}\left(\frac{Z^{\mathrm{Surface}}}{Z^{\mathrm{Bulk}}} - 1\right)\end{aligned} \tag{1.4.6}$$

The binding energy E_i^{Bulk} can be approximately replaced by the heat of vaporization $\Delta H_i^{\mathrm{Vap}}$ as follows:

$$\begin{aligned}\sigma_i^{\mathrm{H}} &= \frac{1}{A_i}\Delta H_i^{\mathrm{Vap}}\left(1 - \frac{Z^{\mathrm{Surface}}}{Z^{\mathrm{Bulk}}}\right) \\ &= \frac{1}{A_i}\Delta H_i^{\mathrm{Vap}}(1-\beta)\end{aligned} \tag{1.4.7}$$

When we increase temperature, the configuration and the vibration of atoms at the surface increase and the effect of the surface entropy cannot be ignored. Then, the surface free energy is expressed by

$$\sigma_i = \frac{1}{A_i}\Delta H_i^{\mathrm{Vap}}(1-\beta) - T\cdot\sigma_i^{\mathrm{S}} \tag{1.4.8}$$

If we assume that the above procedure for σ_i^{H} can be applied to the term σ_i^{S}, and that the entropy of vaporization is proportional to the heat of vaporization, we obtain the following equation at a given temperature:

$$\sigma_i = \frac{1}{A_i}\Delta H_i^{\mathrm{Vap}}(1-\beta) - \frac{1}{A_i}\Delta H_i^{\mathrm{Vap}}\varsigma = \frac{1}{A_i}\Delta H_i^{\mathrm{Vap}}(1-\beta^*) \tag{1.4.9}$$

Figure 1.4.1 shows the relationship between the surface tension σ_i of pure liquid metals and $\Delta H_i^{\mathrm{Vap}}/A_i$ for various pure metals at their melting points. As can be seen in Figure 1.4.1, there is a linear relation between σ_i and $\Delta H_i^{\mathrm{Vap}}/A_i$ as follows:

$$\sigma_i = \frac{1}{A_i}\Delta H_i^{\mathrm{Vap}}(1-\beta^*) = \frac{1}{A_i}\Delta H_i^{\mathrm{Vap}}(1-0.83) = 0.17\frac{1}{A_i}\Delta \mathrm{H}_i^{\mathrm{Vap}} \tag{1.4.10}$$

When we consider only the surface energy σ_i^{H} for dense configuration of atoms, the following equation is obtained:

$$\sigma_i^{\mathrm{H}} = \frac{1}{A_i}\Delta H_i^{\mathrm{Vap}}\left(1 - \frac{Z^{\mathrm{Surface}}}{Z^{\mathrm{Bulk}}}\right) = \frac{1}{A_i}\Delta H_i^{\mathrm{Vap}}\left(1 - \frac{9}{12}\right) = 0.25\frac{1}{A_i}\Delta H_i^{\mathrm{Vap}} \tag{1.4.11}$$

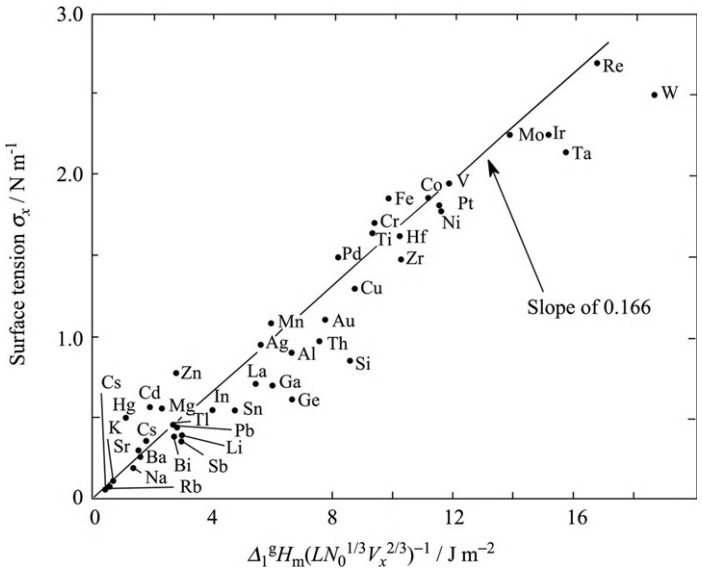


Figure 1.4.1 Correlation of surface tension of liquid metals with heat of evaporation per unit surface area.

That is to say, $Z^{\text{Surface}}/Z^{\text{Bulk}}$ is 0.75. However, the value of β^* is obtained to be 0.83 from Figure 1.4.1 since it is affected by the surface entropy.

When we apply the above procedure to pure molten salts, we obtain the following relationship between σ_i and $\Delta H_i^{\text{Vap}}/A_i$ at their melting points as shown in Figure 1.4.2:

$$\sigma_i = \frac{1}{A_i}\Delta H_i^{\text{Vap}}(1-\beta^*) = \frac{1}{A_i}\Delta H_i^{\text{Vap}}(1-0.94) = 0.06\frac{1}{A_i}\Delta H_i^{\text{Vap}} \tag{1.4.12}$$

Consequently, the surface free energy, in other words the surface tension for liquids, is related to the heat of vaporization which is an energy to make a new surface. Strictly speaking, the effect of the surface entropy should be considered, but the evaluation of this contribution is very difficult.

1.4.2. MODELING OF SURFACE TENSION OF LIQUID ALLOYS

First of all, the evaluation of the surface tension σ of liquid alloys is discussed in this section. The following Equations (1.4.13) and (1.4.14) have been often used to evaluate the surface tension of liquid A–B binary alloys. The formula is called Butler's model [1]. The fundamental concept and derivation for Butler's equation is described in Section 1.4.5.1 in detail.

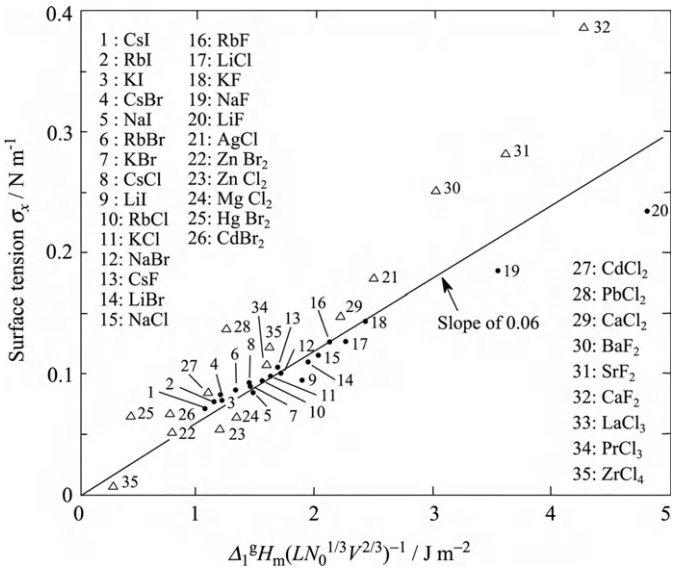


Figure 1.4.2 Correlation of surface tension of molten salts with heat of evaporation per unit surface area.

$$\sigma = \sigma_A^{\mathrm{Pure}} + \frac{RT}{A_A}\ln\frac{N_A^{\mathrm{Surf}}}{N_A^{\mathrm{Bulk}}} + \frac{1}{A_A}\left\{G_A^{\mathrm{E,Surf}}\left(T,N_B^{\mathrm{Surf}}\right) - G_A^{E,\mathrm{Bulk}}\left(T,N_B^{\mathrm{Bulk}}\right)\right\} \tag{1.4.13}$$

$$\sigma = \sigma_B^{\mathrm{Pure}} + \frac{RT}{A_B}\ln\frac{N_B^{\mathrm{Surf}}}{N_B^{\mathrm{Bulk}}} + \frac{1}{A_B}\left\{G_B^{E,\mathrm{Surf}}\left(T,N_B^{\mathrm{Surf}}\right) - G_B^{E,\mathrm{Bulk}}\left(T,N_B^{\mathrm{Bulk}}\right)\right\} \tag{1.4.14}$$

In Equations (1.4.13) and (1.4.14), σ_i^{Pure} is the surface tension of pure component i, $A_i = LN_0^{1/3}V_i^{2/3}$ (N_0, Avogadro's number; $L = 1.091$ for liquid metals; V_i, molar volume of pure component i) is the molar surface area of pure component i. Superscripts *Bulk* and *Surf* show bulk and surface, respectively. Here, the surface is assumed to be an outermost monolayer of a material. N_i^P is mole fraction of component i in the bulk ($P = Bulk$) and the surface ($P = Surf$). $G_i^{E,P}(T,N_B^P)$ is partial excess Gibbs energy of component i in the bulk ($P = Bulk$) and the surface ($P = Surf$), which is a function of temperature T and the mole fraction of component B N_B. In Equations (1.4.1) and (1.4.2), $G_i^{E,\mathrm{Bulk}}(T,N_B^{\mathrm{Bulk}})$ in the bulk can be obtained directly from thermodynamic databases, but $G_i^{E,\mathrm{Surf}}(T,N_B^{\mathrm{Surf}})$ for the surface can be estimated on the following approximation proposed by Speiser *et al.* [2,3].

$$G_i^{E,\mathrm{Surf}}\left(T,N_B^{\mathrm{Surf}}\right) = \beta^{\mathrm{MIX}} \cdot G_i^{E,\mathrm{Bulk}}\left(T,N_B^{\mathrm{Surf}}\right) \tag{1.4.15}$$

The above equation means that the excess Gibbs energy in the surface has the same function of temperature and composition as that in the bulk, but the mole fraction is

replaced by N_B^{Surface}. β^{MIX} is a parameter related to the ratio of the coordination number in the surface to that in the bulk $Z^{\text{Surf}}/Z^{\text{Bulk}}$. For example, Speiser *et al.* [2,3] proposed $\beta^{\text{MIX}} = Z^{\text{Surf}}/Z^{\text{Bulk}} = 9/12 = 0.75$ by assuming a closed packed solid structure. However, since the value β^{MIX} for liquid can not be evaluated exactly, Tanaka *et al.* determined the apparent ratio of $(Z^{\text{Surf}})'/Z^{\text{Bulk}}$ for liquid metals and alloys, as described in the preceding section, from the relationship between the surface tension of pure metals and the binding energy per unit area [4]:

$$\beta^{\text{MIX}} = \frac{(Z^{\text{Surf}})'}{Z^{\text{Bulk}}} = 0.83 : \text{for pure metals and alloys} \tag{1.4.16}$$

The procedure to calculate the surface tension of liquid alloys σ in Equations (1.4.13) and (1.4.14) is as follows [4–7]:

1. After the surface tensions, the molar volumes of pure components and excess Gibbs energies in the bulk of components A and B are substituted in Equations (1.4.13) and (1.4.14) at a given temperature and bulk composition.
2. Equations (1.4.13) and (1.4.14) are the equations having two unknowns; the surface tension of liquid alloys σ and the surface composition N_B^{Surface}.
3. These equations are solved numerically to determine σ and N_B^{Surface}.

As shown in Figure 1.4.3a–c, the calculated results [4–7] of the surface tension of liquid alloys (solid curves) in Fe—Si, Fe—Cu, and Cu—Pb systems agree well with the experimental values [8–12]. It was found from Figure 1.4.3a–c that when alloys have negative excess Gibbs energy, e.g., Fe—Si alloy, the surface tension deviates positively from the surface tension in ideal solution. On the other hand, when alloys have positive excess Gibbs energy, e.g., Fe—Cu and Cu—Pb alloys, the surface tension deviates negatively from that in ideal solution [4–7]. These thermodynamic characteristics can be generally applied to liquid alloys. The relationship between N_B^{Bulk} and N_B^{Surface} are indicated in small squares in Figure 1.4.3a–c. When we look at the relationship between $N_{\text{Pb}}^{\text{Bulk}}$ and $N_{\text{Pb}}^{\text{Surface}}$ in Figure 1.4.3c, $N_{\text{Pb}}^{\text{Surface}}$ indicates 0.99 even for $N_{\text{Pb}}^{\text{Bulk}} = 0.2$. This means that the surface of liquid Cu—Pb alloy is covered by almost pure Pb although the bulk concentration of Pb is only 20%. Therefore the surface tension at $N_{\text{Pb}}^{\text{Bulk}} = 0.2$ shows almost the same value as pure Pb. In other words, the surface tension seems to be determined from very thin layers at the surface.

1.4.3. MODELING OF SURFACE TENSION OF MOLTEN IONIC MATERIALS INCLUDING MOLTEN SLAG

1.4.3.1. Some Issues on the Evaluation of Molten Ionic Mixtures

By applying the above procedure for liquid alloys, the surface tension of molten ionic mixtures was tried to be evaluated so far [13]. Some of the results [13] are shown as solid curves in Figure 1.4.4 although we used $\beta^{\text{MIX}} = (Z^{\text{Surf}})'/Z^{\text{Bulk}} = 0.94$, which

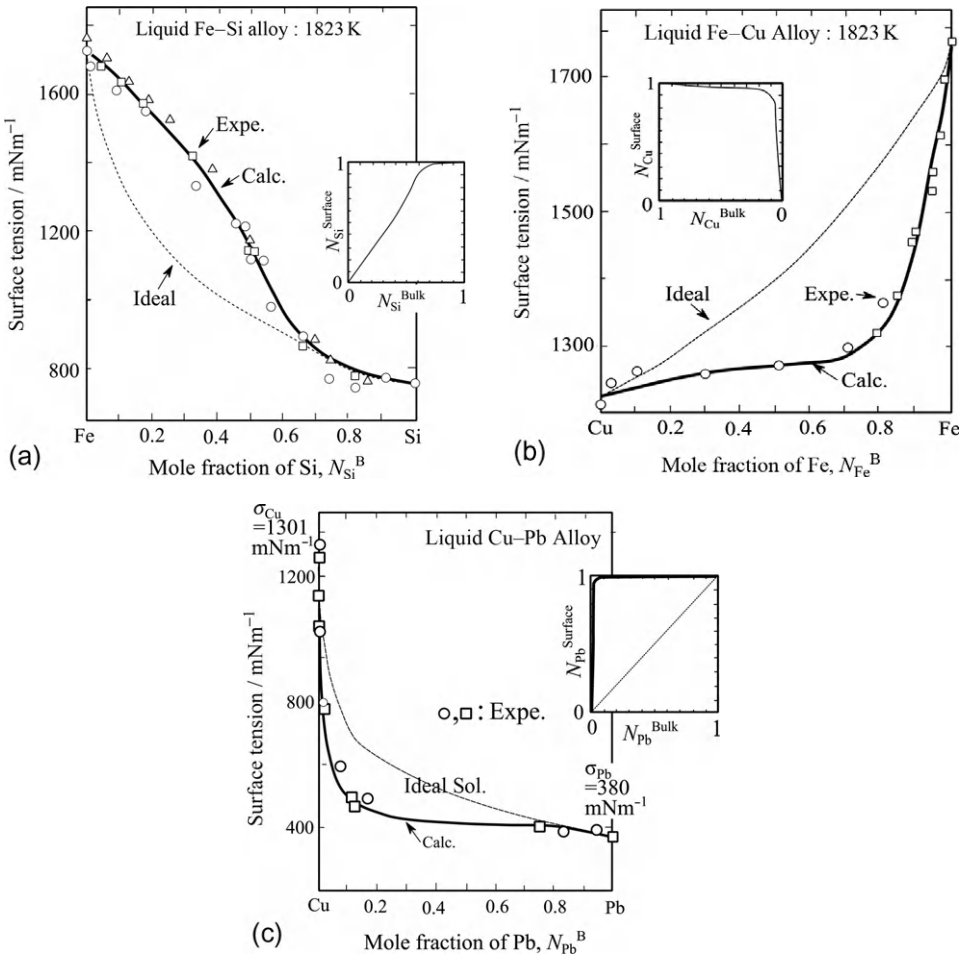


Figure 1.4.3 (a) Composition dependence of surface tension of liquid Fe—Si binary alloy. (b) Composition dependence of surface tension of liquid Cu—Fe binary alloy. (c) Composition dependence of surface tension of liquid Cu—Pb binary alloy.

had been obtained for ionic mixtures [4] by applying the same procedure to obtain the above equation (1.4.16). As can be seen in Figure 1.4.4, the calculated results (solid curves) [13] do not agree with the experimental values (▪) [14]. Especially, although those molten ionic mixtures have negative excess Gibbs energies, the experimental values of the surface tension deviate negatively from that in the ideal solution [13], which do not obey the above thermodynamic characteristics of the composition dependence of the surface tension in liquid alloys. In other words, the calculated results exist at the opposite sides against the surface tension of ideal solutions, which means that we can not evaluate the surface tension of molten ionic

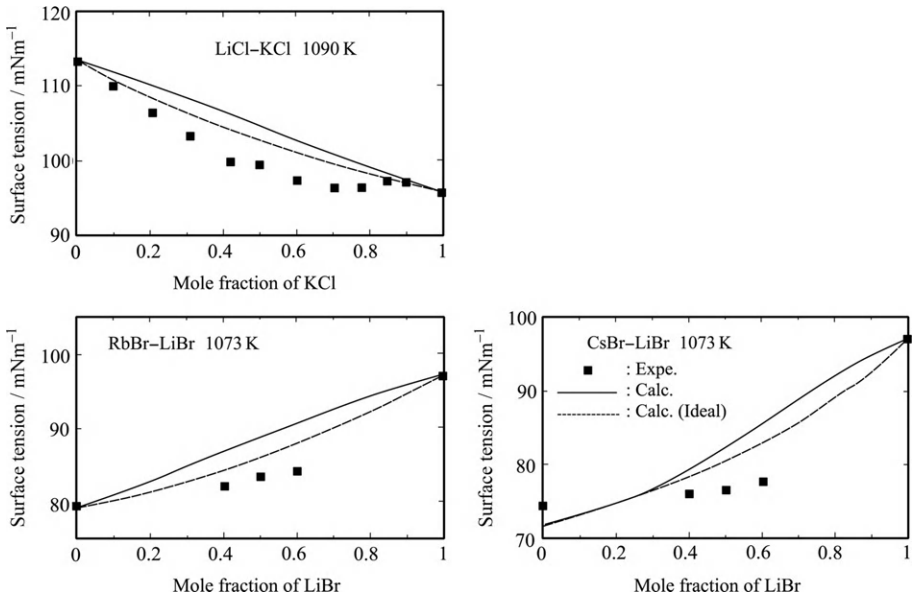


Figure 1.4.4 Comparison of calculated results of surface tension of molten binary ionic mixtures with experimental values.

mixtures by considering only the ratio of the coordination number in the surface to that in the bulk [13].

1.4.3.2. Evaluation of Surface Tension of Molten Ionic Mixtures

In order to cope with the problems on the evaluation of the surface tension of molten ionic mixtures, Tanaka *et al.* [13] have derived the following semiempirical equations to evaluate the surface tension σ of molten ionic mixtures:

$$\sigma = \sigma_{AX}^{\text{Pure}} + \frac{RT}{A_{AX}} \ln \frac{M_{AX}^{\text{Surf}}}{M_{AX}^{\text{Bulk}}} \tag{1.4.17}$$

$$\sigma = \sigma_{BY}^{\text{Pure}} + \frac{RT}{A_{BY}} \ln \frac{M_{BY}^{\text{Surf}}}{M_{BY}^{\text{Bulk}}} \tag{1.4.18}$$

Here,

$$M_{AX}^{P} = \frac{(R_A/R_X)\cdot N_{AX}^{P}}{(R_A/R_X)\cdot N_{AX}^{P} + (R_B/R_Y)\cdot N_{BY}^{P}},$$

$$M_{BY}^{P} = \frac{(R_B/R_Y)\cdot N_{BY}^{P}}{(R_A/R_X)\cdot N_{AX}^{P} + (R_B/R_Y)\cdot N_{BY}^{P}}$$

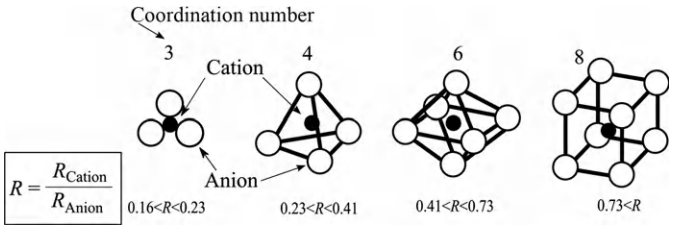


Figure 1.4.5 Correlation of ratio of cation radius to anion radius with crystal structure.

In the above equations, the effect of radii of cations and anions are considered because it is well known in the science for ionic systems that the coordination number and ionic structure depend upon the ratio of the radius of cation to that of anion as shown in Figure 1.4.5, which affects various physicochemical properties of ionic melts.

In the above equations, subscripts A and B are cations, and X and Y are anions. Superscripts $P = Surf$ and $Bulk$ indicate the surface and the bulk, respectively. R_A and R_B are the radius of cations, and R_X and R_Y are the radius of anions. The information on the radius of ions can be obtained from the compilation by Shannon [15]. $A_i = N_0^{1/3} V_i^{2/3}$ (N_0, Avogadro's number; V_i, molar volume of pure component i) is the molar surface area of pure component i.

The calculated results of the surface tension in various alkaline–halide ionic mixtures obtained from Equations (1.4.17) and (1.4.18) are shown by solid curves in Figure 1.4.6. In all of the systems in Figure 1.4.6, the calculated results (solid curves) agree well with the experimental values (▪) [14]. In addition, the model reproduces the characteristics of the composition dependence quite well in common ionic mixtures. That is to say, the composition dependence tends to show almost linear change in common cation systems, and on the other hand, the composition dependence of common anion systems shows large downward curvature as can be seen in Figure 1.4.6. Furthermore, this model can be applied to molten salt mixtures with complex anions such as sulfate systems. In those ionic mixtures, we used the apparent effective radii of complex anions proposed by Jenkins *et al.* [16,17], who derived the radii to investigate other bulk properties. Some of the calculated results on sulfate systems are shown in Figure 1.4.7.

1.4.3.3. Evaluation of Surface Tension of Molten SiO_2 based Binary and Ternary Slag

The model for the surface tension of molten ionic mixtures [13] are described in the preceding section. This model has been extended to molten SiO_2 based binary and ternary slag [18,19]. The models and the procedures to evaluate the surface tension of molten slag are as follows:

The surface tension for the AX–BY–CZ melt is expressed on the basis of Equations (1.4.17) and (1.4.18) as follows:

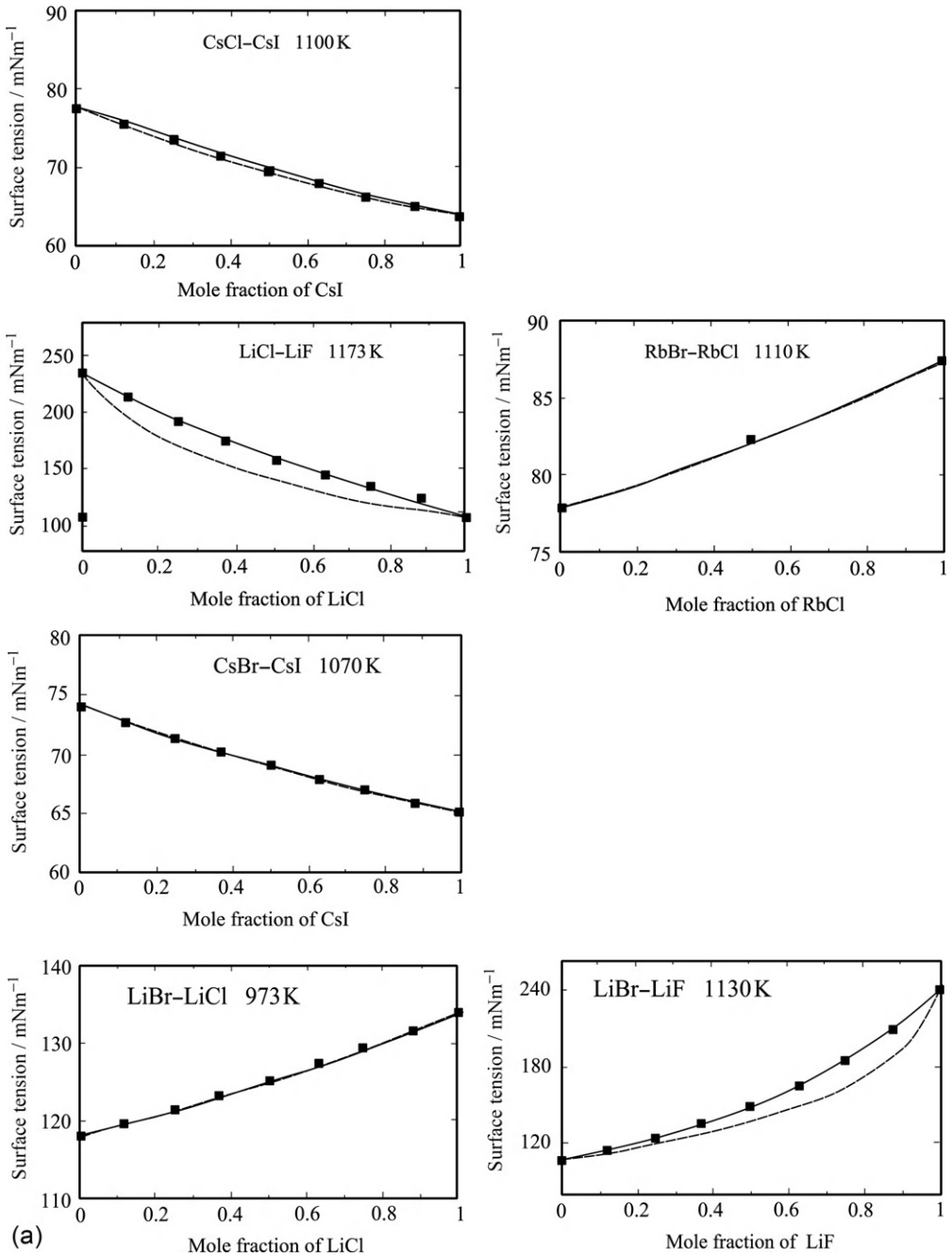


Figure 1.4.6 (a) Comparison of calculated results of surface tension of molten binary ionic mixtures with experimental values in common cation systems.

(Continued)

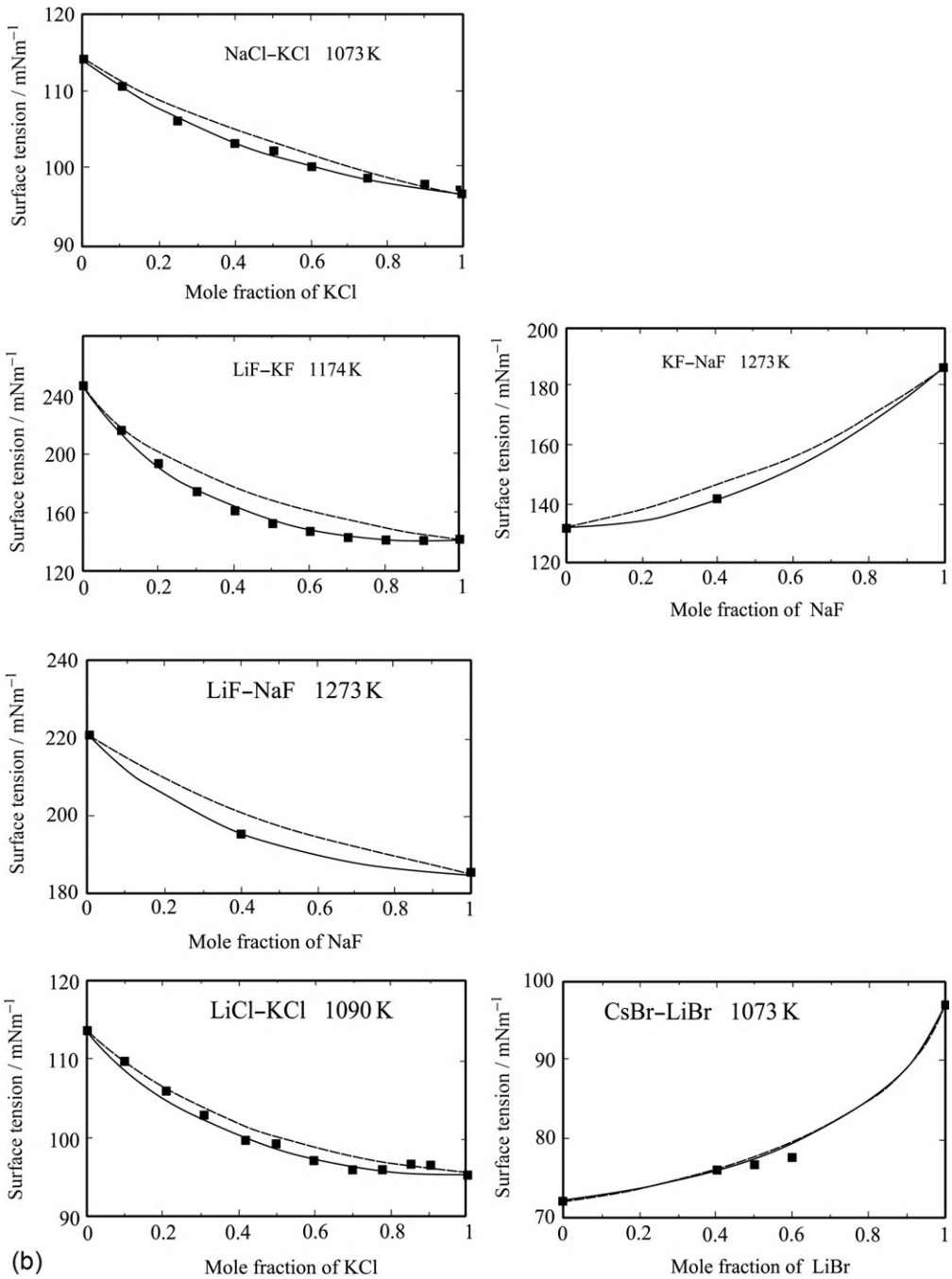


Figure 1.4.6, cont'd (b) Comparison of calculated results of surface tension of molten binary ionic mixtures with experimental values in common anion systems.

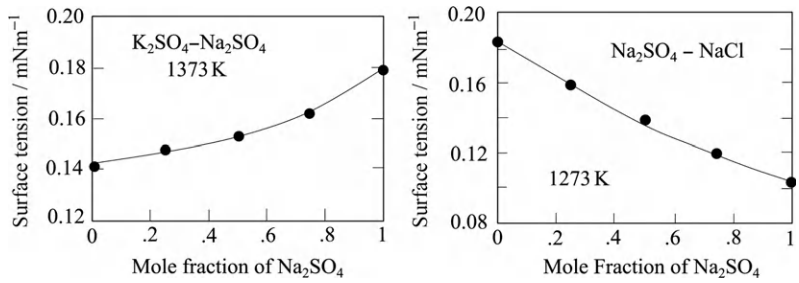


Figure 1.4.7 Comparison of calculated results of surface tension of molten binary ionic mixtures with experimental values in complex anion systems.

$$\sigma = \sigma_{AX}^{\text{Pure}} + \frac{RT}{A_{AX}} \ln \frac{M_{AX}^{\text{Surf}}}{M_{AX}^{\text{Bulk}}} \tag{1.4.19}$$

$$\sigma = \sigma_{BY}^{\text{Pure}} + \frac{RT}{A_{BY}} \ln \frac{M_{BY}^{\text{Surf}}}{M_{BY}^{\text{Bulk}}} \tag{1.4.20}$$

$$\sigma = \sigma_{CZ}^{\text{Pure}} + \frac{RT}{A_{CZ}} \ln \frac{M_{CZ}^{\text{Surf}}}{M_{CZ}^{\text{Bulk}}} \tag{1.4.21}$$

where $M_{AX}^{P} = \frac{\frac{R_A}{R_X} \cdot N_{AX}^{P}}{\frac{R_A}{R_X} \cdot N_{AX}^{P} + \frac{R_B}{R_Y} \cdot N_{BY}^{P} + \frac{R_C}{R_Z} \cdot N_{CZ}^{P}}$, $M_{BY}^{P} = \frac{\frac{R_B}{R_Y} \cdot N_{BY}^{P}}{\frac{R_A}{R_X} \cdot N_{AX}^{P} + \frac{R_B}{R_Y} \cdot N_{BY}^{P} + \frac{R_C}{R_Z} \cdot N_{CZ}^{P}}$, $M_{CZ}^{P} = \frac{\frac{R_C}{R_Z} \cdot N_{CZ}^{P}}{\frac{R_A}{R_X} \cdot N_{AX}^{P} + \frac{R_B}{R_Y} \cdot N_{BY}^{P} + \frac{R_C}{R_Z} \cdot N_{CZ}^{P}}$.

Subscripts A, B, and C correspond to cations, while X, Y, and Z correspond to anions. R is the gas constant, T is the absolute temperature. σ_i^{Pure} is the surface tension of pure molten compound i ($i = AX$, BY, or CZ), which is treated as a model parameter. $A_i = N_0^{1/3} \cdot V_i^{2/3}$ corresponds to the molar surface area in a monolayer of pure molten compound i (N_0, Avogadro's number; V_i, molar volume of pure molten oxide i). N_i^P is the mole fraction of compound i in phase P (P = Surf or Bulk). 'Surf' and 'Bulk' indicate the surface and the bulk, respectively. R_A, R_B, and R_C correspond to the radii of cations A, B, and C, while R_X, R_Y, and R_Z correspond to the radii of anions X, Y, and Z. For example, in the case of the SiO_2—CaO—MgO system:

$$R_A = R_{\text{Si}}{}^{4+}, R_B = R_{\text{Ca}}{}^{2+}, R_C = R_{\text{Mg}}{}^{2+} \tag{1.4.22}$$

$$R_X = R_{\text{SiO}_4}{}^{4-}, R_Y = R_{\text{O}}{}^{2-}, R_Z = R_{\text{O}}{}^{2-} \tag{1.4.23}$$

where it is assumed that Si^{4+} is cation, and SiO_4^{4-} is anion unit in order to evaluate the ratio of cationic and anionic radii for SiO_2 because the complex ion SiO_4^{4-} exists in molten SiO_2 system. Thus, $R_{\text{Si}}{}^{4+}/R_{\text{SiO}_4}{}^{4-}$ is treated as a parameter in this model since there is no precise information on the apparent effective radii of complex anion

$R_{SiO_4}{}^{4-}$. The $R_{Si}{}^{4+}/R_{SiO_4}{}^{4-}$ ratio was assessed to be 0.5 to fit many experimental results on binary and ternary SiO_2-based melts [13,18,19].

The ionic radii data were taken from the data compiled by Shannon [15], while the molar volumes of the pure oxides, as recommended by Mills and Keene [20], were used in the present calculations.

The values of the surface tensions for pure oxides were used as parameters in the present model because most of pure liquid oxides, which are components in molten slag, do not exist at around 1873 K except for SiO_2 and some alkaline oxides. Then, the values of the surface tensions for pure oxide were evaluated by minimizing the differences between the calculated results and the literature values [21–35]. For this purpose, it is advisable to use the literature data in as many systems as possible, and for as many temperatures. Therefore, for evaluation purposes, almost all of the available literature data for ternary silicate systems containing Al_2O_3, CaO, FeO, MgO, MnO, CaF_2, or Na_2O, were collected over the wide composition and temperature ranges in SLAG ATLAS second edition [21]. The value σ_{SiO_2} (mN/m) = 243.2 + 0.031 T (K) was used as the surface tension of molten pure SiO_2, as suggested by NIST [14]. Table 1.4.1 shows the equations corresponding to the temperature dependence of the surface tension values for pure oxides obtained in this evaluation with $R_{Si}{}^{4+}/R_{SiO4}{}^{4-} = 0.5$ [18,19].

The surface tension values calculated in the binary and ternary silicates melts are shown in Figures 1.4.8–1.4.14. It is found that the experimental surface tensions [21–35] in the ternary systems targeted in this study decrease mainly with increasing the content of SiO_2 while the effects of the exchange of other two components on

Table 1.4.1 Data for Calculation of Surface Tension of Molten Slag

	Molar Volume (m^3/mol)	Temp. Dependence (K) of Surface Tension (N/m)	Cationic and Anionic Radii (Å)	
SiO_2	$27.516 \cdot \{1 + 1 \cdot 10^{-4}(T - 1773)\} \cdot 10^{-6}$	$243.2 + 0.031 \cdot T$	Si^{4+}	0.42
Al_2O_3	$28.3 \cdot \{1 + 1 \cdot 10^{-4}(T - 1773)\} \cdot 10^{-6}$	$1024 - 0.177 \cdot T$	Al^{3+}	0.51
CaO	$20.7 \cdot \{1 + 1 \cdot 10^{-4}(T - 1773)\} \cdot 10^{-6}$	$791 - 0.0935 \cdot T$	Ca^{2+}	0.99
FeO	$15.8 \cdot \{1 + 1 \cdot 10^{-4}(T - 1773)\} \cdot 10^{-6}$	$504 - 0.0984 \cdot T$	Fe^{2+}	0.74
MgO	$16.1 \cdot \{1 + 1 \cdot 10^{-4}(T - 1773)\} \cdot 10^{-6}$	$1770 - 0.636 \cdot T$	Mg^{2+}	0.66
MnO	$15.6 \cdot \{1 + 1 \cdot 10^{-4}(T - 1773)\} \cdot 10^{-6}$	$988 - 0.179 \cdot T$	Mn^{2+}	0.80
Na_2O	$33.0 \cdot \{1 + 1 \cdot 10^{-4}(T - 1773)\} \cdot 10^{-6}$	$438 - 0.116 \cdot T$	Na^{+}	0.97
CaF_2	$31.3 \cdot \{1 + 1 \cdot 10^{-4}(T - 1773)\} \cdot 10^{-6}$	$1604.6 - 0.72 \cdot T$	Ca^{2+}	0.99
			O^{2-}	1.44
			F^{-}	1.33

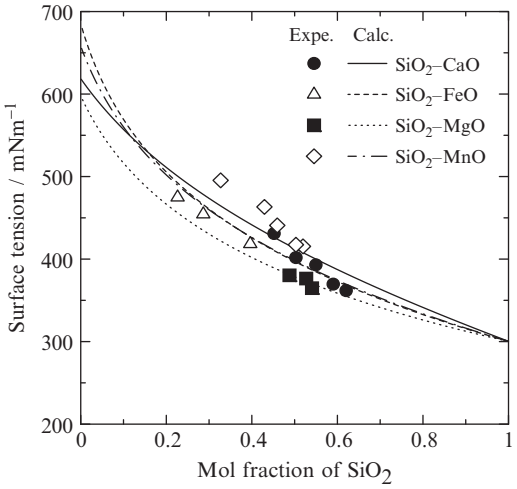


Figure 1.4.8 Surface tension of molten SiO_2-based binary system at 1843 K. Expe. [22].

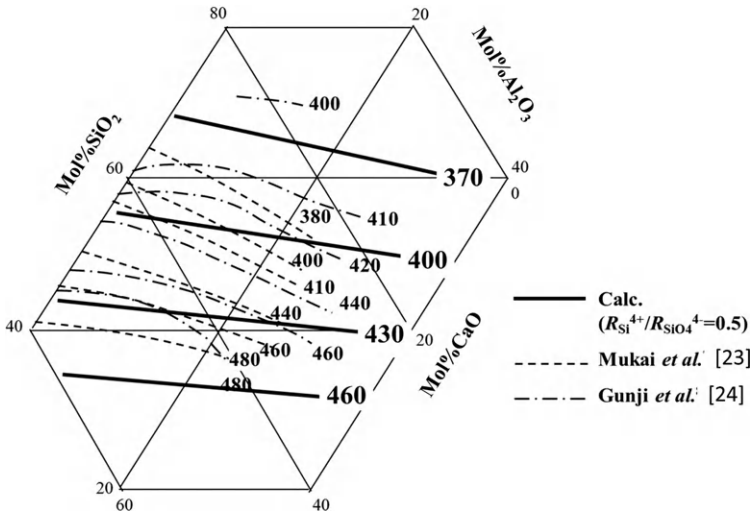


Figure 1.4.9 Surface tension (mN/m) of molten SiO_2—Al_2O_3—CaO system at 1873 K. Comparison between the calculated results obtained for $R_{Si}{}^{4+}/R_{SiO_4}{}^{4-} = 0.5$.

the surface tension depend on the systems. Although the present model is the simplest model in which the surface tension of molten slag can be calculated from information relating to the surface tension and molar volume of pure oxides, as well as from the cationic and anionic radii in the system, the results reproduce the composition dependence of the experimental data at various temperatures in binary and ternary silicates.

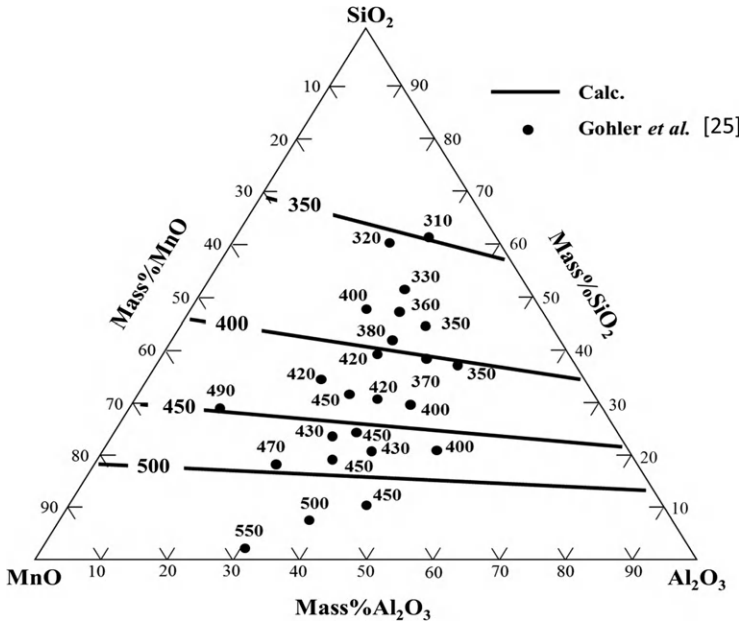


Figure 1.4.10 Surface tension (mN/m) of molten SiO_2—Al_2O_3—MnO system at 1873 K.

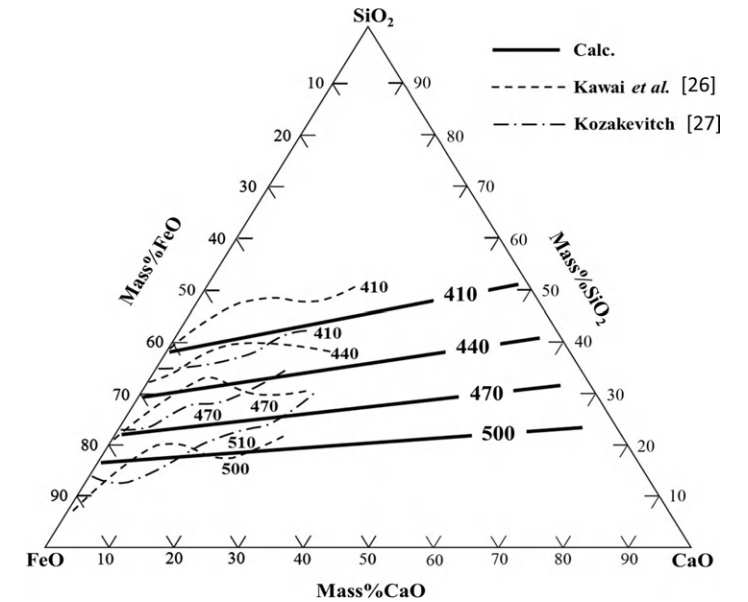


Figure 1.4.11 Surface tension (mN/m) of molten SiO_2—CaO—FeO system at 1673 K.

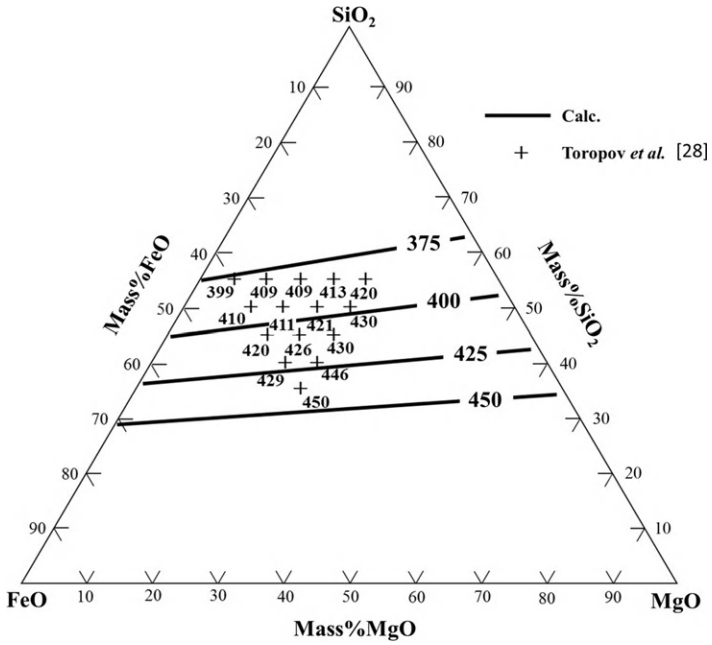


Figure 1.4.12 Surface tension (mN/m) of molten SiO_2—FeO—MgO system at 1823 K.

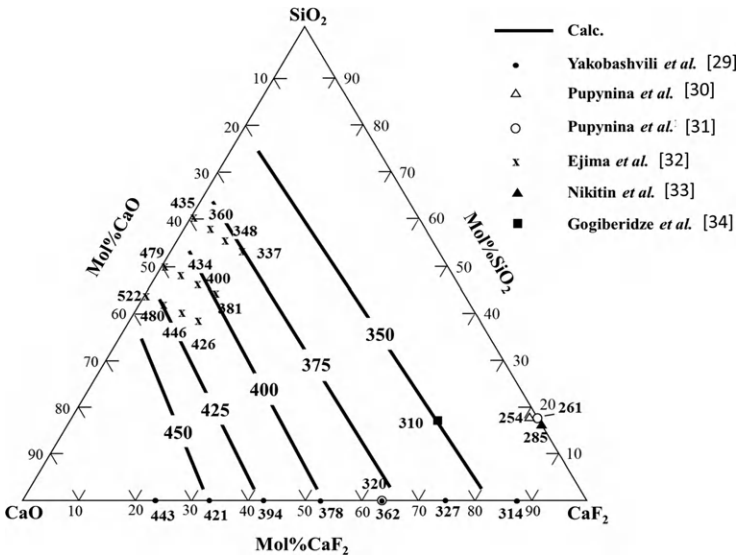


Figure 1.4.13 Surface tension of molten SiO_2—CaO—CaF_2 system at 1773 K.

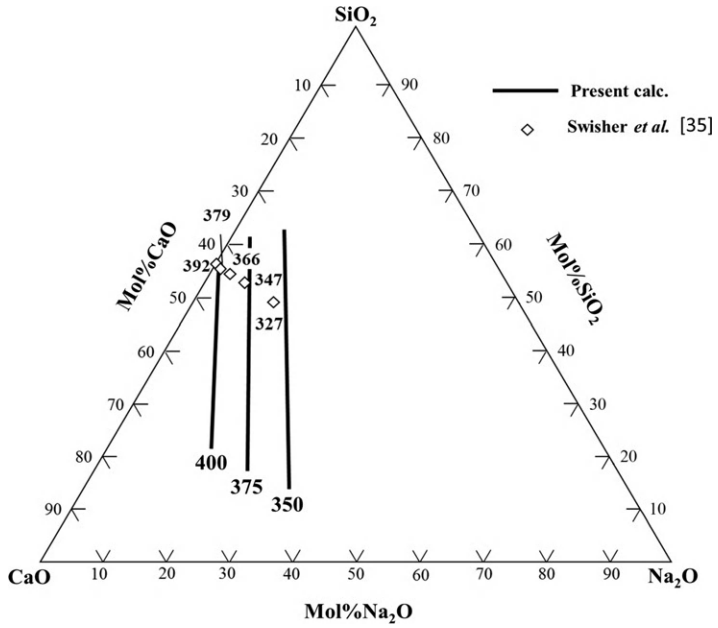


Figure 1.4.14 Surface tension of molten SiO_2—CaO—Na_2O system at 1863 K.

1.4.4. EVALUATION OF INTERFACIAL TENSION BETWEEN LIQUID STEEL AND MOLTEN SLAG

There have been a number of attempts to develop models for the calculation of interfacial free energies in steel slag systems. One approach by Cramb *et al.* [36] is described in this section, they applied the approach of Gilifalco and Good [37] where the values of surface tension of the initial phases are used to calculate the interfacial energy of the combined phases.

$$\sigma_{m-s} = \sigma_m + \sigma_s - 2\Phi\cdot(\sigma_m\sigma_s)^{1/2} \tag{1.4.24}$$

The interaction coefficient (Φ) from the Gilifalco and Good equation is a measure of an interaction between two condensed phases and is defined as work of adhesion (W_{ad}) between two phases divided by the square root of work of cohesion of each phase (W_{co}^{m} and W_{co}^{s}) as follows:

$$\Phi = \frac{W_{ad}}{\left(W_{co}^{m}\cdot W_{co}^{s}\right)^{1/2}} = \frac{\sigma_m + \sigma_s - \sigma_{m-s}}{s\sqrt{(\sigma_m\cdot\sigma_s)}} \tag{1.4.25}$$

The interaction coefficient (Φ) varies from 1, which indicates strong attraction between the two liquid phases, to 0, which indicates weak attraction between the two liquid phases.

Humenik and Kingery [38] first developed a predictive model for the work of adhesion of solid based on a thermodynamic approach. They suggested that the ability of metals to form low energy interfaces could be related to the oxygen affinity of the metals, as described in Equation (1.4.26).

$$W_{\mathrm{ad}} = f(\Delta G_{\mathrm{mo}}) \tag{1.4.26}$$

where ΔG_{mo} is the Gibbs free energy of formation of the oxide of the liquid metal.

McDonald and Eberhart [39] developed a model for the work of adhesion of Al_2O_3 considering Van der Waals ionic metal–oxygen bonding, as described in Equation (1.4.27).

$$W_{\mathrm{ad}} = \frac{n}{2a}(\Delta G_{\mathrm{mo}}) + n\left[\frac{3}{2}\left(\frac{\alpha_{\mathrm{m}}\alpha_{\mathrm{o}}}{R^6}\right)\right]\left[\frac{I_{\mathrm{m}}I_{\mathrm{o}}}{I_{\mathrm{m}}+I_{\mathrm{o}}}\right] \tag{1.4.27}$$

where n is the density of ionic bond sites; a is the number of bonds in a mole of metal oxide; α_{m} and α_{o} are the polarizabilities of the metal and oxygen ions; I_{m} and I_{o} are ionization potentials of the metals and oxygen ions; R is the separation distance of Van der Waals metal–oxygen bond. Cramb *et al.* [36] found from their experiments that the first term represented a much larger contribution to the bonding than the second term, thus, the work of adhesion of Al_2O_3 increases with increasing affinity of a metal for oxygen, namely, with increasing stability of the metal oxide.

Adhesion of metal to various oxides is also correlated with Gibbs free energies of formation of oxides. Sveshkov *et al.* [40] showed that work of adhesion of liquid metals on SiO_2, Y_2O_3, and Al_2O_3 substrates increased with respect to increasing Gibbs free energy of formation of the oxides. A general equation was proposed as follows:

$$W_A = W_{\mathrm{o}} + A(\Delta F^{\mathrm{o}}) \tag{1.4.28}$$

where W_{o} is the contribution to bonding by dispersion forces and (ΔF^{o}) is the Gibbs free energy of formation due to chemical interaction between liquid metal and the oxygen of the oxide at the surface. Cramb *et al.* [36] suggested that the slope, A, could depend on the screening action of the cations on the respective oxide surfaces.

The molar Gibbs free energy of formation of liquid oxides is estimated from adding the two terms.

$$G_i^{\mathrm{m}} = \sum_i X_i \cdot G_i^{\mathrm{o}} + \Delta G_{\mathrm{m}} \tag{1.4.29}$$

where $\sum_i X_i \cdot G_i^{\circ}$ is the molar Gibbs free energy before mixing, and ΔG_m is the Gibbs free energy of mixing. The Gibbs free energy of mixing is generally small compared to the formation energy, and to a first approximation, it can be ignored.

The molar Gibbs free energy of formation of liquid oxides per oxygen atom (ΔG_i^m) can be expressed as

$$\Delta G_i^{\mathrm{m}} = \sum_i X_i \cdot \Delta G_{i-o} \tag{1.4.30}$$

where X_i is mole fraction of liquid oxide i, and ΔG_{i-o} is the molar Gibbs free energy of formation of oxide i per oxygen atom. If the Gibbs free energy of formation of FeO is taken as a reference state, a new term, formation energy difference, can be defined as follows:

$$\Delta G_i^{\mathrm{D}} = \Delta G_{\mathrm{FeO}} - \Delta G_i^{\mathrm{m}} \tag{1.4.31}$$

Figure 1.4.15 shows the interaction coefficient as a function of formation energy difference of various slag systems as measured by several investigators [36]. As seen in the figure, there is a linear correlation between the interaction coefficient and the formation energy difference, and the interaction coefficient decreases with increasing formation energy difference. Because all data fit a linear relationship between the interaction coefficient and formation energy difference, the relation can be rewritten as the following linear regression:

$$\Phi = \Phi_{\mathrm{D}} + B \cdot \Delta G_i^{\mathrm{D}} \tag{1.4.32}$$

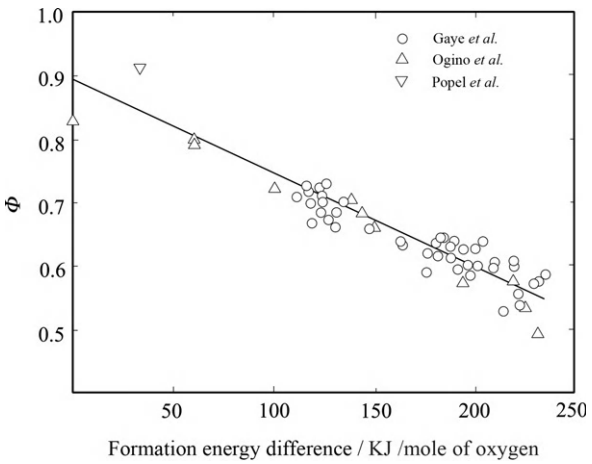


Figure 1.4.15 Relationship between Φ and the formation energy difference.

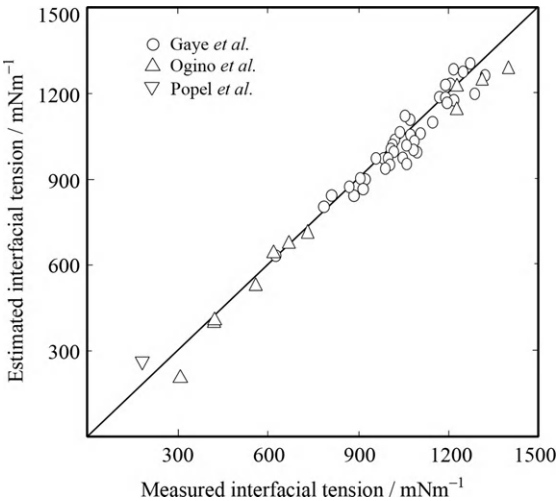


Figure 1.4.16 Calculated and measured interfacial tension between liquid steel and molten slag.

where Φ_D is the interaction coefficient for the reference state, namely, 100% FeO slag; B is an empirical slope obtained from the figure. Thus, the following relation between Φ and the formation energy difference can be developed [36]:

$$\Phi = 0.89 - 0.0015 \cdot \Delta G_i^D \tag{1.4.33}$$

The relationship in Equation (1.4.33) can then be used in the Gilifalco and Good equation along with a knowledge of the surface energies of the slag and the metal to predict equilibrium interfacial energies in liquid steel–slag systems that contain oxides. An example is given in Figure 1.4.16 where the calculated values are plotted against the measured values [36]. The above model allows an accurate calculation of the interfacial energies of measured oxide metals in contact with liquid iron alloys.

1.4.5. APPLICATION OF CONSTRAINED GIBBS ENERGY MINIMIZATION APPROACH TO EVALUATE SURFACE TENSION OF LIQUID ALLOYS

In the preceding section for prediction of surface and interfacial tensions of liquid metals, alloys and molten slag, those models can be easily applied to binary or ternary systems. However, industrial alloys and molten slag are usually multicomponent systems. When the models in the preceding sections are applied to multicomponent systems, the calculation is very complicated to solve simultaneous equations. Fortunately in order to calculate chemical reactions and phase equilibria from thermodynamic databases, there exist several computer programs and software which can be applied to evaluate those subjects in multicomponent systems. In these calculations,

the Gibbs energy of a total system is minimized to evaluate equilibrium state, in other words, composition, temperature, phases, etc. Koukarri and his group extended those thermodynamic approaches to a material system including surface [41,42]. That is to say, they tried to minimize Gibbs energy of a total system including surface or interface, and successfully evaluated surface free energy in the system. Their procedure is called constrained Gibbs energy minimization approach. In this section, their approach is described with some calculated results [42].

1.4.5.1. Basic Thermodynamic for Constrained Gibbs Energy Minimization Approach

If a system containing a surface is considered as being comprised of two parts (phases), a surface layer (s) and an isotropic bulk (b), the total Gibbs energy of the system can be written as

$$G = \sum_i n_i \mu_i + A\sigma = \sum_i n_i^{\mathrm{b}} \mu_i + \sum_i n_i^{\mathrm{s}} \mu_i + A\sigma \tag{1.4.34}$$

where n_i is the molar amount and μ_i the chemical potential of species i, σ the surface tension in the system and A the surface area. If the surface phase is considered to be of a monolayer thickness, Equation (1.4.34) can be rewritten in a form

$$G = \sum_i n_i^{\mathrm{b}} \mu_i + \sum_i n_i^{\mathrm{s}} (\mu_i + A_i\sigma) \tag{1.4.35}$$

where A_i is the molar surface area of the species i. The chemical potential of species i in the bulk phase can be written as

$$\mu_i = \mu_i^{\mathrm{o}} + RT \ln a_i^{\mathrm{b}} \tag{1.4.36}$$

and in the surface phase as

$$\mu_i = \mu_i^{\mathrm{o,s}} + RT \ln a_i^{\mathrm{s}} - A_i\sigma \tag{1.4.37}$$

By applying Equations (1.4.36) and (1.4.37) for the case of a pure one-component system, a relationship between the standard states of the bulk and surface phase can be derived:

$$\mu_i^{\mathrm{o,s}} = \mu_i^{\mathrm{o}} + A_i\sigma_i \tag{1.4.38}$$

By combining Equations (1.4.34) and (1.4.36), the total Gibbs energy of the system can be given in a simple form that does not explicitly include the surface tension term:

$$G = \sum_i n_i^{\mathrm{b}} \left(\mu_i^{\mathrm{o}} + RT \ln a_i^{\mathrm{b}}\right) + \sum_i n_i^{\mathrm{s}} \left(\mu_i^{\mathrm{o,s}} + RT \ln a_i^{\mathrm{s}}\right) \tag{1.4.39}$$

while from Equations (1.4.36)–(1.4.38) one obtains

$$\mu_i^{\circ} + A_i\sigma_i + RT\ln a_i^{s} - A_i\sigma = \mu_i^{\circ} + RT\ln a_i^{b}$$
$$\therefore \quad \sigma = \sigma_i + \frac{RT}{A_i}\ln\frac{a_i^{s}}{a_i^{b}} \tag{1.4.40}$$

an equation first derived by Butler [1] and used extensively in calculating surface tension in various mixtures, including metal alloy systems.

1.4.5.2. Use of Gibbs Energy Minimizer for Surface Equilibria Calculations

When a Gibbs energy minimizer is used to solve chemical equilibrium states, the total Gibbs energy is usually calculated as

$$G = \sum_{\alpha}\sum_{i} n_i^{\alpha}\mu_i \,(\text{over all phases } (\alpha) \text{ and species } (i) \text{ present in the system}) \tag{1.4.41}$$

where the chemical potentials of the species are calculated from supplied thermodynamic data using an equation of the type of equivalent to

$$\mu_i^{\alpha} = \mu_i^{\circ,\alpha}(T,p) + RT\ln\gamma_i^{\alpha}x_i^{\alpha} \tag{1.4.42}$$

Comparing Equations (1.4.35), (1.4.37), and (1.4.42), one can see that the chemical potential for a species in the surface phase as calculated by a Gibbs energy minimizer would really be the total molar Gibbs energy of the surface species, marked here with μ_i^{*}:

$$\mu_i^{*} = \mu_i + A_i\sigma \tag{1.4.43}$$

For a traditional chemical equilibrium calculation the mass balance relations restricting the possible states can be given in the form

$$\sum_{\alpha}\sum_{i} \nu_{ik}n_i^{\alpha} - b_k = 0 \,(\text{for all components } k) \tag{1.4.44}$$

where b_k is the total molar amount of component k and ν_{ik} the stoichiometric coefficient between species i and component k. The condition of constant total surface area can be stated in a similar form as

$$\sum_{i} A_i n_i^{*} - A = 0 \tag{1.4.45}$$

or alternatively as

$$\sum_{\alpha}\sum_{i} A_i^{\alpha} n_i^{\alpha} - A = 0 \tag{1.4.46}$$

where the molar surface for any species in any nonsurface phase α is zero. A is the total surface area of the system. As the constant surface area condition (Equation 1.4.46) is of the same form as the traditional mass balances (Equation 1.4.44), it can for the

Table 1.4.2 Presentation in a Matrix of Stoichiometries in a System with a Bulk and a Surface, *N* Species and *M* Components

		Component (1)	**Component (2)**		**Component (*M*)**	**Area**
Bulk	Species (1)	v_{11}	v_{12}	$\cdots$	v_{1M}	0
	Species (2)	v_{21}	v_{22}	$\cdots$	v_{2M}	0
	$\vdots$	$\vdots$	$\vdots$	$\ddots$	$\vdots$	$\vdots$
	Species (N)	v_{N1}	v_{N2}	$\cdots$	v_{NM}	0
Surface	Species (1)	v_{11}	v_{12}	$\cdots$	v_{1M}	A_1/A_0
	Species (2)	v_{21}	v_{22}	$\cdots$	v_{2M}	A_2/A_0
	$\vdots$	$\vdots$	$\vdots$	$\ddots$	$\vdots$	$\vdots$
	Species (N)	v_{N1}	v_{N2}	$\cdots$	v_{NM}	A_N/A_0

mathematical handling of the system be combined with them by considering the surface area as a new component in the system. In Table 1.4.1 this is presented in a matrix form; the species in the system are presented as rows and the conserved components as columns.

In Table 1.4.2, A_0 is a normalization constant with dimensions of m^2/mol. The numerical value of A_0 is in principle arbitrary, but for the best numerical performance of Gibbs energy minimizers it is generally best to choose the value so that the resulting A_i/A_0 values are fairly near to unity.

In a chemical equilibrium state, in addition to species and phases, chemical potentials can also be defined for the different components in the system. The chemical potential of individual species are related to the chemical potentials of the components by Equation (1.4.47).

$$\mu_i = \sum_k v_{ik}\pi_k \tag{1.4.47}$$

where π_k is the chemical potential of the component k, and v_{ik} the stoichiometric coefficient between species i and component k.

Applied to the surface system, Equation (1.4.47) can be stated for a bulk species as

$$\mu_i = \sum_{k=1}^{M+1} v_{ik}\pi_k = \sum_{k=1}^{M} v_{ik}\pi_k \tag{1.4.48}$$

and for the surface species as

$$\mu_i^* = \sum_{k=1}^{M+1} \nu_{ik}\pi_k = \sum_{k=1}^{M} \nu_{ik}\pi_k + \frac{A_i}{A_0}\pi_{\text{area}} \tag{1.4.49}$$

where π_{area} is the chemical potential of the new component defined to fix the total surface area of the system.

Finally, from Equations (1.4.48), (1.4.43), and (1.4.49) we have the equalities

$$\frac{\pi_{\text{area}}}{A_0} = \frac{\mu_i^* - \mu_i}{A_i} = \sigma \tag{1.4.50}$$

The chemical potential (divided by the normalization constant Ao) of the new 'area' component is equal to the surface tension of the system.

1.4.5.3. Some Results

As examples we consider a binary and ternary alloy system in the liquid state. The method described above is applied to calculate the surface tension and composition of Bi—Sn and Ag—Au—Cu melts in temperatures where experimental surface tension data are available for these mixtures [42].

The calculations were made using the ChemSheet program [43] that is based on the ChemApp [43] thermodynamic program library. The calculated results are shown in Figures 1.4.17 and 1.4.18.

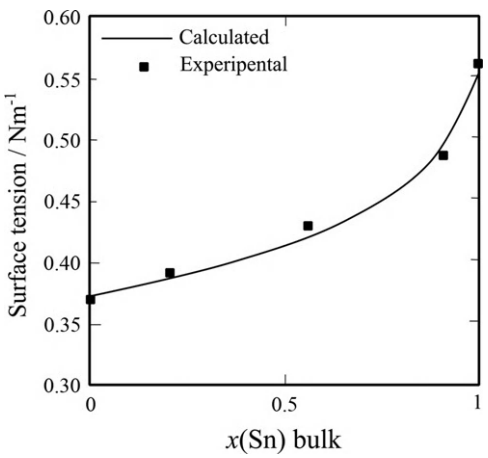


Figure 1.4.17 Calculated and measured surface tension of liquid Bi—Sn alloy.

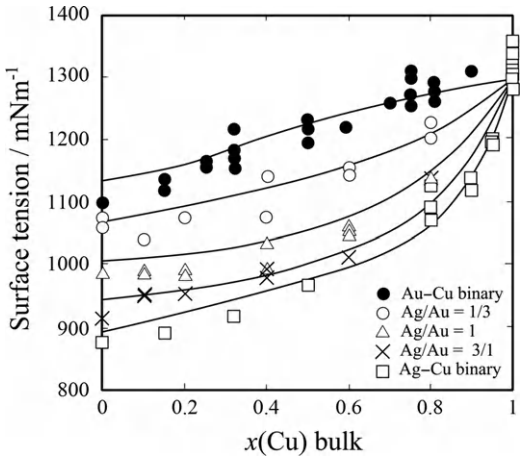


Figure 1.4.18 Calculated and measured surface tension of liquid Au—Ag—Cu alloy.

REFERENCES

[1] J.A.V. Butler, Proc. R. Soc. A. 135 (1932) 348.
[2] R. Speiser, D.R. Poirier, K. Yeum, Scripta Metall. 21 (1987) 687.
[3] K.S. Yeum, R. Speiser, D.R. Poirier, Metall. Trans. B 20B (1989) 693.
[4] T. Tanaka, K. Hack, T. Iida, S. Hara, Z. Metallkunde 87 (1996) 380.
[5] T. Tanaka, K. Hack, S. Hara, MRS Bull. 24 (1999) 45.
[6] T. Tanaka, K. Hack, S. Hara, CALPHAD 24 (2001) 465.
[7] T. Tanaka, J. Lee, N. Hirai, in: T. Letcher (Ed.), Chemical Thermodynamics for Industry, Advancing the Chemical Science, Royal Society of Chemistry, Cambridge, UK, 2004.
[8] N.K. Dzhemilev, S.I. Popel, B.V. Tsarevskii, Fiz. Metal. Metalloved 18 (1) (1964) 83.
[9] L.M. Shergin, S.I. Popel, B.V. Tsarevskii, in: V.N. Eremenko (Ed.), Fiz. Khim. Poverkl. Yavlenii rasp, Naukova Dumka, Kiev, 1971, p. 569.
[10] Y. Kawai, K. Mori, M. Kishimoto, K. Ishikawa, T. Shimoda, Tetsu-to- Hagane 60 (1974) 29.
[11] A. Kasama, T. Inui, Z. Morita, J. Jpn. Inst. Metals 42 (1978) 1206.
[12] B.F. Dyson, Trans. TMS-AIME 227 (1963) 1098.
[13] T. Tanaka, T. Kitamura, I.A. Back, ISIJ Int. 46 (2006) 400.
[14] NIST Molten Salt Database, National Institute of Standards and Technology (1987).
[15] R.D. Shannon, Acta Cryst. A32 (1976) 751.
[16] H.D.B. Jenkins, H.K. Roobottom, J. Passmore, L. Glasser, J. Chem. Ed. 76 (1999) 1570.
[17] H.D.B. Jenkins, H.K. Roobottom, Handbook of Chemistry and Physics, eightieth ed., CRC Press, 1999–2000.
[18] M. Nakamoto, A. Kiyose, T. Tanaka, L. Holappa, M. Hamalainen, ISIJ Int. 47 (1) (2007) 38–43.
[19] M. Nakamoto, T. Tanaka, L. Holappa, M. Hamalainen, ISIJ Int. 47 (2) (2007) 211–216.
[20] K.C. Mills, B.J. Keene, Int. Mater. Rev. 32 (1987) 1.
[21] B.J. Keene, Slag Atlas, second ed., Verlag Stahleisen GmbH, Dusseldorf, 1995, p. 403.
[22] R.E. Boni, G. Derge, J. Metals 206 (1956) 53.
[23] K. Mukai, T. Ishikawa, J. Jpn. Inst. Met. 45 (1981) 147.
[24] K. Gunji, T. Dan, Trans. Iron Steel Inst. Jpn. 14 (1974) 162.
[25] M. Gohler, Freiburger Forschungsh B92 (1963) 41, Slag Atlas, second ed., Verlag Stahleisen GmbH, Dusseldorf, 1995, p. 435.
[26] Kawai, K. Mori, Y. Shiraishi, N. Yamada, Tetsu-to-Hagane 53 (1976), Slag Atlas, second ed., Verlag Stahleisen GmbH, Dusseldorf, 1995, p. 439.0029.

[27] P. Kozakevitch, Rev. Metall. 46 (1949) 572, Slag Atlas, second ed., Verlag Stahleisen GmbH, Dusseldorf, 1995, p. 439 and 443.
[28] N.A. Toropov, B.A. Bryantsev, Strukt. Prevrash. v. Stekla. Pri. Povyshen. Pub. Nauka. Temp. (1965) 205, Slag Atlas, second ed., Verlag Stahleisen GmbH, Dusseldorf, 1995, p. 442.
[29] S.B. Yakobashvili, I.I. Frumin, Autom. Weld. (USSR) 15 (1962) 33.
[30] S.M. Pupynina, S.E. Volkov, O.S. Bobkova, V.S. Petukhov, Sb. Tr. Tsent. Inst. Chernaya Metal. 70 (1967) 47.
[31] S.M. Pupynina, S.E. Volkov, Teoriya Metallurgicheskikh Protsessov, Metallurgizdat, Moscow, 1971, p. 156.
[32] A. Ejima, M. Shimoji, Trans. Faraday Soc. 66 (1970) 99.
[33] Yu.P. Nikitin, A.N. Safonnikov, Sb. Nauchn. Tr. Uralsk. Politekh. Inst. 126 (1963) 68.
[34] Yu.M. Gogiberidze, T.I. Dzhincharadze, Sh.M. Mikiashvili, Soob. Akad. Nauk Gruz. SSR (3) (1968) 695.
[35] J.H. Swisher, C.L. McCabe, Trans. Metall. Soc. AIME 230 (1964) 1669.
[36] Y. Chung, A.W. Cramb, Metall. Trans. B 31B (2000) 957–971.
[37] L.A. Gilifalco, R.J. Good, J. Chem. Phys. 61 (1957) 904–909.
[38] M. Humenik, W.D. Kingery, J. Am. Ceram. Soc. 37 (1954) 18.
[39] L.E. MacDonald, J.G. Eberhart, Trans. AIME 233 (1965) 512.
[40] Y.V. Sveshkov, V.I. Mogilenskii, Y.A. Polonskii, O.A. Valman, Z. Prikl. Khim. 49 (1976) 2629.
[41] P. Koukkari, R. Pajarre, Calphad 30 (2006) 18–26.
[42] R. Pajarre, P. Koukkari, T. Tanaka, J.-H. Lee, Calphad 30 (2006) 196–200.
[43] http://www.gtt-technologies.de/.

CHAPTER 1.5

Interfacial Free Energy and Wettability

Toshihiro Tanaka[a], Joonho Lee[b] and Piotr R. Scheller[c]

[a]Division of Materials and Manufacturing Science, Graduate School of Engineering, Osaka University, Osaka, Japan
[b]Department of Materials Science and Engineering, Korea University, Anam-dong, Seongbuk-gu, Seoul, Republic of Korea
[c]Technical University Bergakademie Freiberg, Freiberg, Germany

It is significant to understand deeply interfacial properties and interfacial phenomena appeared in high temperature metallurgical processing. In particular, highly purified steel production is a clear and important goal to be aimed at in steelmaking processes. In order to produce highly purified steel, there are a lot of subjects which we should cope with, such as generation and growth of nonmetallic inclusions and their wettability with liquid steel, and furthermore engulfing small droplets of molten slag or CC molten flux into liquid steel. Those subjects are strongly related to interfacial properties and interfacial phenomena of liquid steel, solid oxides, and molten slag. In addition, solidification of metals and alloys are also related to interfacial phenomena between solid and liquid phases.

In this chapter, we focus on (1) wettability between liquid metals and solid oxide, (2) interfacial free energy between solid and liquid phases in metals and alloys, and (3) interfacial tension between liquid steel and molten slag and some fundamental information on them are explained.

1.5.1. WETTABILITY

Although wettability of liquid steel with solid oxides is one of the typical wetting behaviors between liquid and solid phases in metallurgical processing, the wettability of molten slag with refractories is another important phenomenon in steelmaking processing.

In general, the wettability between solid and liquid phases is expressed by the following Young–Laplace's equation:

$$\sigma^{\mathrm{Solid}} = \sigma^{\mathrm{Liquid}} \cdot \cos\theta + \sigma^{\mathrm{Solid-Liquid}} \tag{1.5.1}$$

where σ^{Solid}, σ^{Liquid}, $\sigma^{\mathrm{Solid-Liquid}}$, and θ are surface free energy of solid phase, surface tension of liquid phase, interfacial free energy between solid and liquid phases, and contact angle, respectively.

The balance of the above three interfacial tensions are drawn in Figure 1.5.1.

The wettability can be evaluated by the contact angle. That is to say, the wettability is recognized to be good when the contact angle is smaller than 90°. On the other hand, the wettability becomes bad when the contact angle is larger than 90°. The contact angle is affected

http://dx.doi.org/10.1016/B978-0-08-096984-8.00025-2
© 2014 Elsevier Ltd.
All rights reserved.

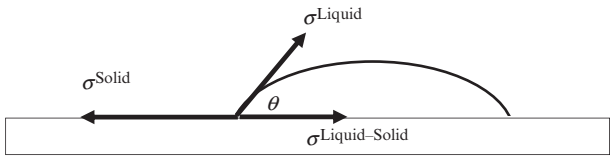


Figure 1.5.1 The balance of surface tension of liquid, surface free energy of solid, and interfacial free energy between solid and liquid.

by various factors except for the above three interfacial properties appeared in Young–Laplace's equation. For example, the contact angle is affected by physic–chemical properties such as chemical reactions between liquid alloy and solid oxide, oxygen partial pressure, crystal structure of oxide phase as well as surface roughness of solid oxide.

Eustathopoulos *et al.* [1] reported the correlation between the contact angle and the following chemical reaction for the wettability of liquid metals (M) and solid oxides (XO):

$$M(l) + XO(s) = \underline{X}_{\text{in liquid } M} + \text{MO}(l \text{or} s) \tag{1.5.2}$$

Figure 1.5.2 shows the relationship between the contact angle and the standard Gibbs energy change for the above chemical reaction plus the effect of partial enthalpy change of element X in liquid M. The indication M/XO in this figure shows the combination of liquid metal M and solid oxide XO. Furthermore, Eustathopoulos *et al.* [2] focused on the effect of oxygen content on the wettability of liquid metals with solid oxides and they reported the correlation between the contact angle and equilibrium oxygen content when solid oxide XO is decomposed and dissolved into liquid metal M. The results are indicated in Figure 1.5.3 [2].

In Figures 1.5.2 and 1.5.3, several important factors have been considered to control the wettability of liquid metals with solid oxides. However, some additional factors should be taken into account. In particular, mutual soluble reactions between liquid metal and solid oxide are supposed to be related to interfacial phenomena, but the correlations in Figures 1.5.2 and 1.5.3 are mainly focused on the dissolution reactions into liquid phases. Actually, the tiny dissolution reaction of elements from liquid phase into solid oxide phases might be significant to determine the wettability. We should investigate the correlations of the wettability with some physical properties of solid oxide phases.

The wettability of liquid metals and alloys with solid oxides has been studied extensively and many literatures have been published so far. The references in this section include some representative reviews on this subject.

The wettability of molten slag with solid oxides is another important subject in high temperature metallurgical engineering. Generally, we get the good wettability between materials which have the same type of bond, e.g., mutual metallic bond, ionic bond and covalent bond etc.

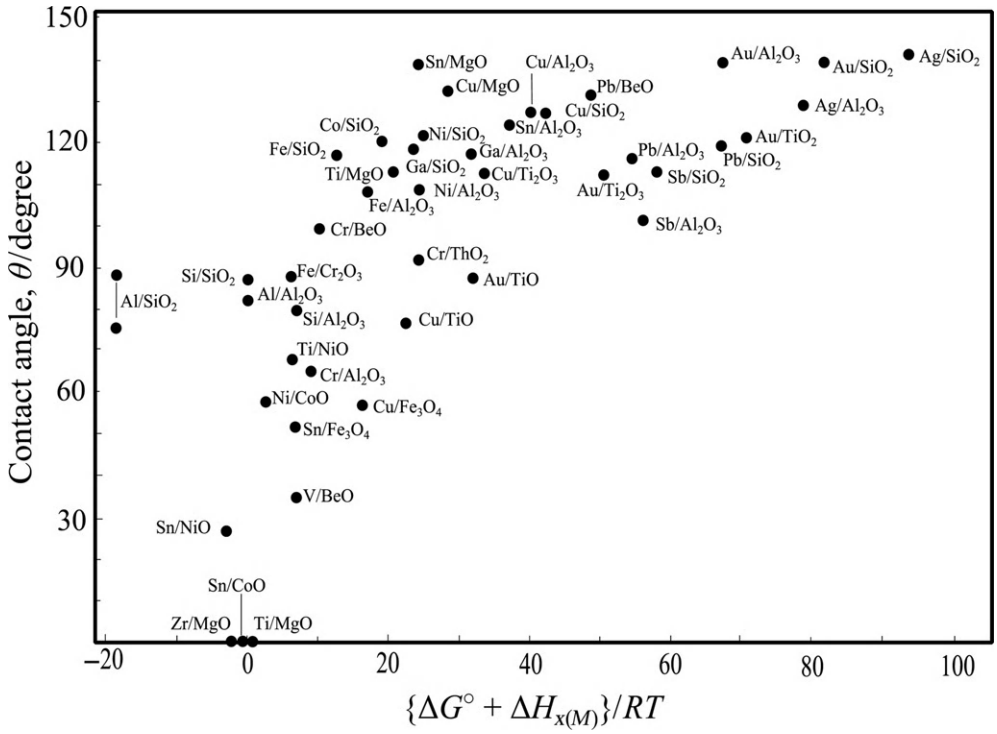


Figure 1.5.2 Correlation of contact angle with Gibbs free energy between liquid metals and solid oxide substrates.

1.5.2. INTERFACIAL FREE ENERGY BETWEEN SOLID AND LIQUID PHASES IN METALS AND ALLOYS

We describe here the interfacial free energy between solid and liquid phases in pure metals and some alloy systems. The wettability between those phases is generally well because both phases have the same metallic bond. A lot of information on the interfacial free energy between solid and liquid phases in pure metals has been reported so far and they can be summarized as shown in Table 1.5.1 [3]. On the other hand, the information on the interfacial free energy between solid and liquid phases in alloy systems is very limited. Eustathopoulos [3] summarized the information on it in 1983, but since then, additional information is not enough to understand the interfacial property in alloys more deeply. Most of the information has been reported on alloy systems, of which interactions between different elements are repulsive. Some examples of the interfacial free energy between solid and liquid phases in alloys are shown in Figure 1.5.4 [4].

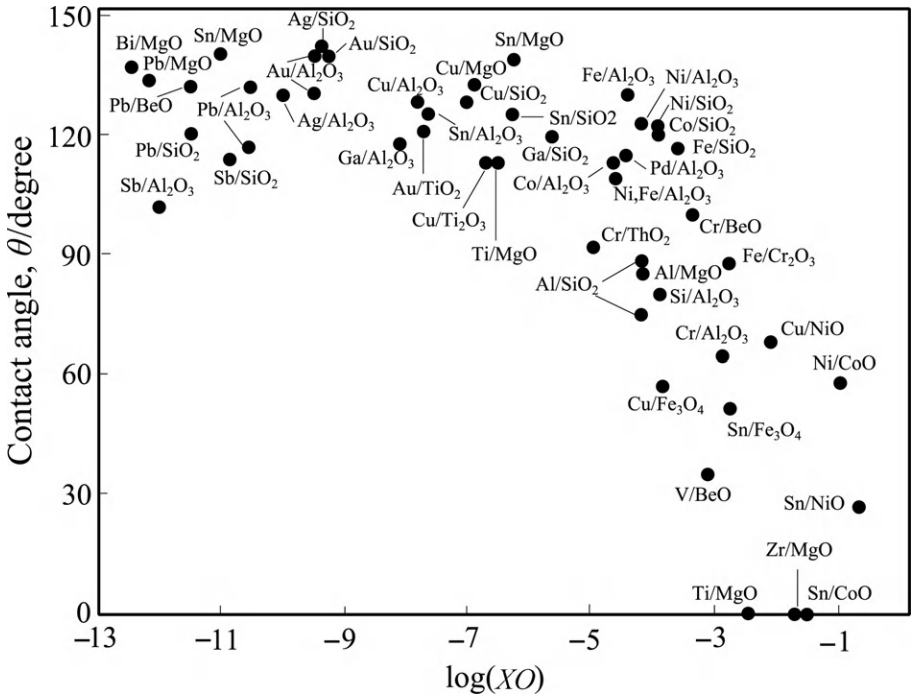


Figure 1.5.3 Correlation of contact angle with oxygen solubility between liquid metals and solid oxide substrates.

Table 1.5.1 Interfacial Free Energy Between Solid and Liquid Phases in Pure Substance

Metal	Crystal Structure	Interfacial Free Energy (mJ/m^2)
Hg	Hexagonal	24.4
H_2O	Hexagonal	32.1
Ga	Orthorhombic	55.9
Sn	Tetragonal	54.5
Bi	Rhombohedral	54.4
Pb	Fcc	33.3
Sb	Rhombohedral	101
Al	Fcc	93
Ge	Diamond cubic	181
Ag	Fcc	126
Au	Fcc	132
Cu	Fcc	177
Mn	Tetragonal	206
Ni	Fcc	255
Co	Fcc	234
Fe	Bcc	204
Pd	Fcc	209
Pt	Fcc	240

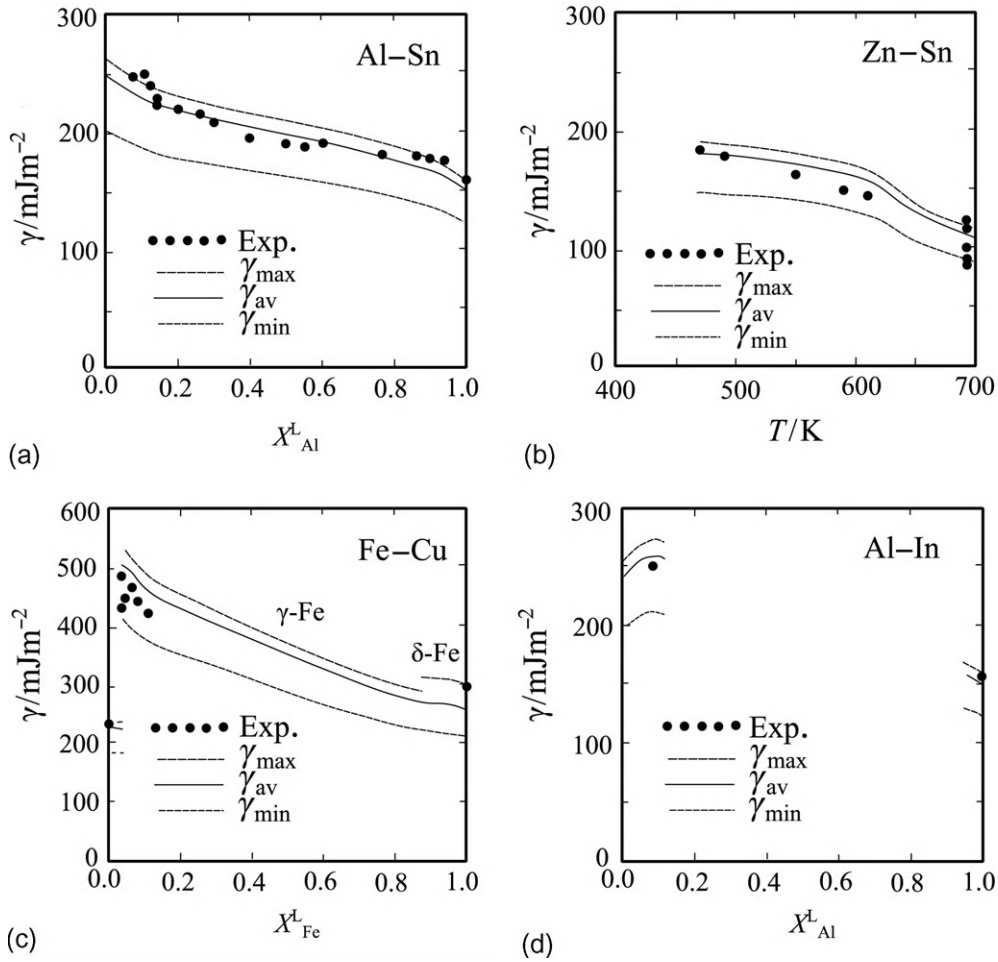


Figure 1.5.4 Interfacial free energy between solid and liquid phases in binary alloys [4].

1.5.3. INTERFACIAL TENSION BETWEEN LIQUID STEEL AND MOLTEN SLAG

The wettability between liquid steel and molten slag is generally good and the interfacial tension between those phases have been investigated extensively so far. The measurements on the interfacial tension are based on the following three procedures:

(1) When a droplet of liquid steel is placed on the bottom of a crucible which contains molten slag, the contour is recorded by an X-ray to determine the interfacial tension.

(2) When a droplet of molten slag is placed on a flat surface of liquid steel which is put in a shallow crucible, the contact angle of the molten slag with liquid steel is measured to determine the interfacial tension.

(3) Measurement of the drop weight when metal rod immersed in slag melts down or is introduced through the capillary.

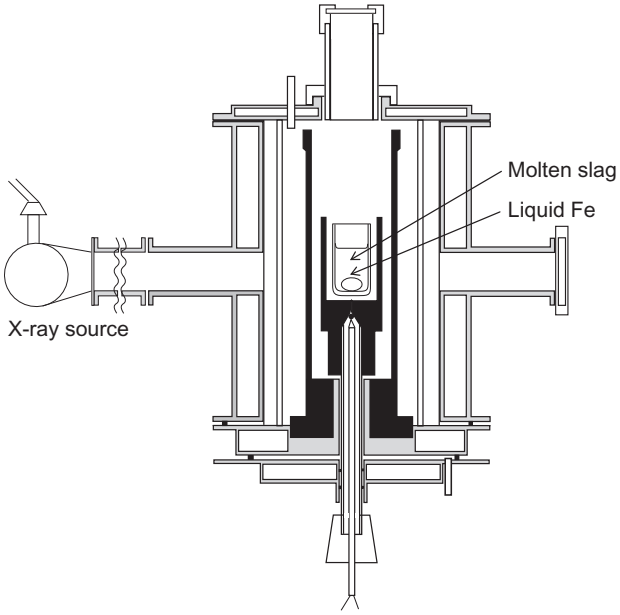


Figure 1.5.5 An apparatus for sessile drop method to measure interfacial tension between liquid steel and molten slag.

An apparatus as shown in Figure 1.5.5 is used for the method (1). The procedure to determine the interfacial tension is the same as that used to the measurement of a sessile drop method to determine the surface tension of liquid metals.

An example of an apparatus for the method (2) is shown in Figure 1.5.6a. After the contact angle $\theta_{2\alpha}$ is measured, the interfacial tension is determined from the following equation:

$$\sigma_{\mathrm{Fe/Slag}} = \sqrt{(\sigma_{\mathrm{Fe}})^2 + (\sigma_{\mathrm{Slag}})^2 - 2\cdot\sigma_{\mathrm{Fe}}\cdot\sigma_{\mathrm{Slag}}\cdot\cos\theta_{2\alpha}} \tag{1.5.3}$$

where $\sigma_{\mathrm{Fe/Slag}}$, σ_{Fe}, σ_{Slag}, and $\theta_{2\alpha}$ are the interfacial tension between liquid steel and molten slag, the surface tension of liquid steel, the surface tension of molten slag, and the contact angle in Figure 1.5.6a, respectively. As shown in the above equation, the data on the surface tensions of liquid steel and molten slag are needed to determine the interfacial tension in this method.

An apparatus for the estimation of the interfacial tension via metal drop weight (method 3) is shown in Figure 1.5.6b. In this method, the choice of the capillary material with as low as possible reactivity with metal and slag, and the preparation of the capillary end is essential for correct measurements. The interfacial tension is then calculated from the following equation:

$$\sigma_{\mathrm{Metal/Slag}} = \frac{mg}{2\pi r\psi}, \tag{1.5.4}$$

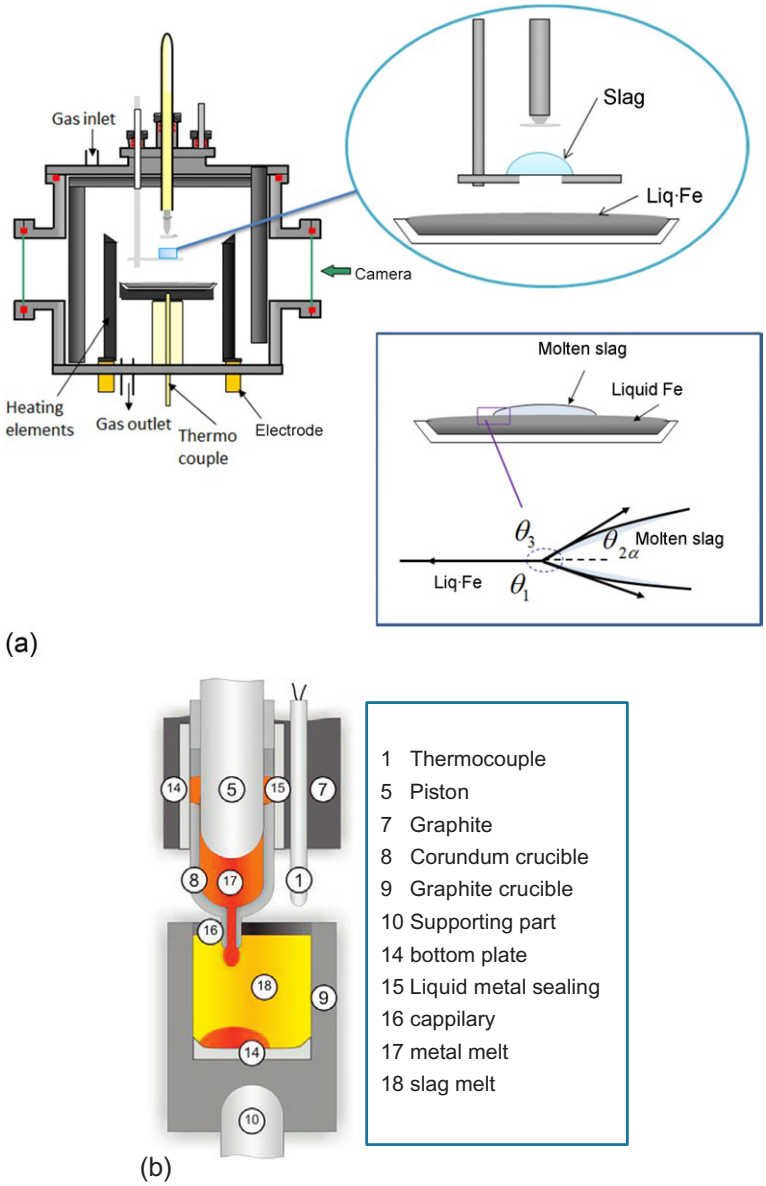


Figure 1.5.6 (a) An apparatus to measure interfacial tension between liquid steel and molten slag from contact angle of molten slag on liquid steel. (b) Drop weight method for measurement of interfacial tension.

where m mass of the drop, g gravity, r radius of the capillary, and ψ the correcting factor which depends on the drop generation frequency (or flow rate through the capillary):

$$\Psi = f(\delta) = f\left(\frac{r}{V_{\text{drop}}^{1/3}}\right) \tag{1.5.5}$$

If the capillary radius r and the drop volume V_{drop} are chosen in such way that the resulting δ lies between 0.6 and 1.2 then Ψ remains nearly constant [5]. The results obtained with this method are reported in [6–9].

Some examples [10,11] of the measured interfacial tension between liquid steel and molten slag are shown in Figures 1.5.7(a)-(i) [10] and Figure 1.5.7(j) [11]. The values in parentheses in these figures indicate oxygen contents in Fe (ppm). Oxygen and sulfur in liquid steel affect the interfacial tension between liquid steel and molten slag as they have the effect on the surface tension of liquid steel. As shown in Figure 1.5.8 [10], the interfacial tension between liquid steel and molten slag can be summarized by the contents of oxygen in liquid steel even for various molten slag which have different chemical compositions. Furthermore, as Nakashima *et al.* [10] reported and shown in Figure 1.5.9, the Belton's approach [12], which has been applied to express the effect of oxygen or sulfur on the surface tension of liquid steel, can be applied to the effect of oxygen on the interfacial tension between liquid steel and molten slag as follows:

$$\gamma^{0}_{Fe/Slag} - \gamma_{Fe/Slag} = R \cdot T \cdot \Gamma \ln(1 + K \cdot a_O) \tag{1.5.6}$$

where $\gamma_{Fe/Slag}$, $\gamma^{0}_{Fe/Slag}$, Γ, K, and a_o are interfacial tension of liquid Fe with molten slag, interfacial tension between liquid Fe without dissolution of oxygen and molten slag, adsorption coefficient at the interface, equilibrium constant of adsorption reaction of oxygen at the interface, and activity of oxygen in liquid Fe.

The measured values on the interfacial tension between liquid metals except for Fe and molten slag have been reported so far. Some of the examples are shown in Figure 1.5.10 [13].

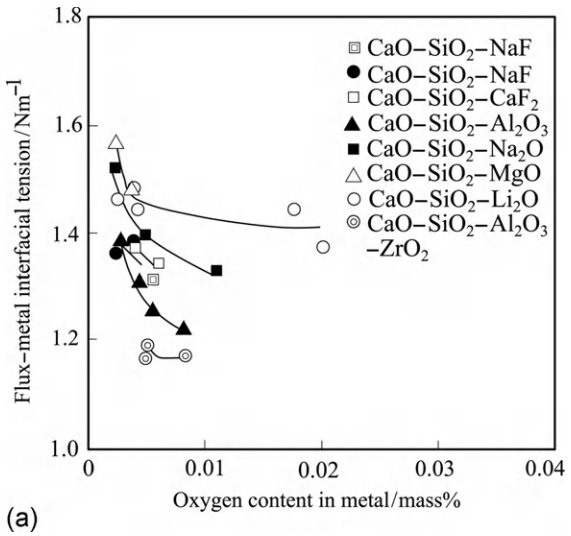


Figure 1.5.7 (a) Interfacial tension versus oxygen content in molten iron at 1580 °C.

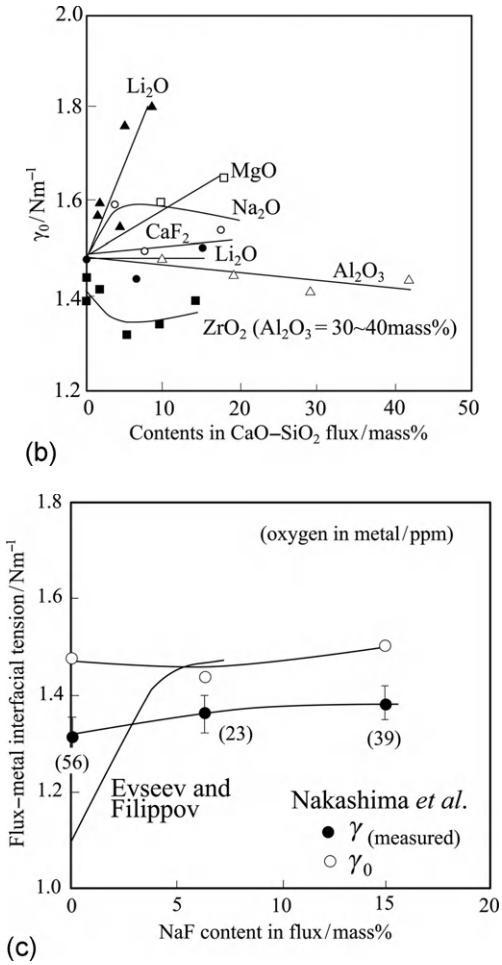
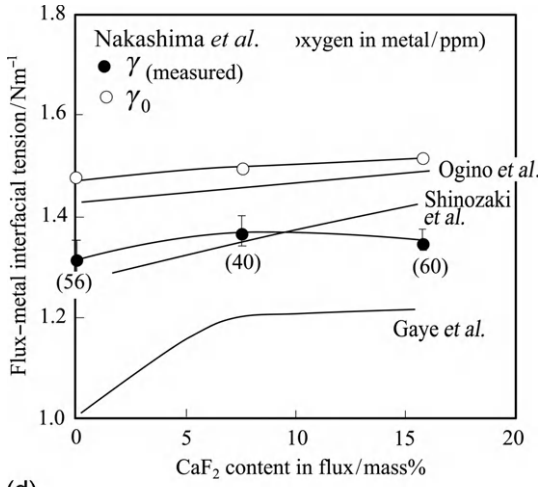
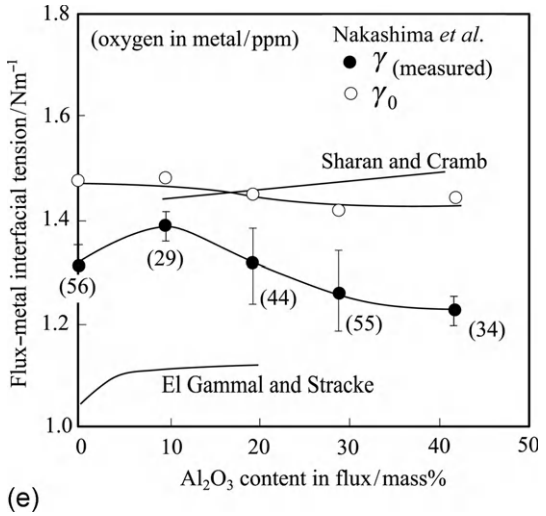


Figure 1.5.7, cont'd (b) Influence of additions in CaO—SiO_2 flux (%CaO/%SiO_2 = 1) on the interfacial tension between liquid iron and flux at 1580 °C. (c) Effect of NaF in flux on the interfacial tension between liquid iron and flux. Nakashima *et al.*: CaO—SiO_2 flux, zirconia crucible, 1580 °C. Evseev and Filippov: CaO—Al_2O_3 flux.

(Continued)

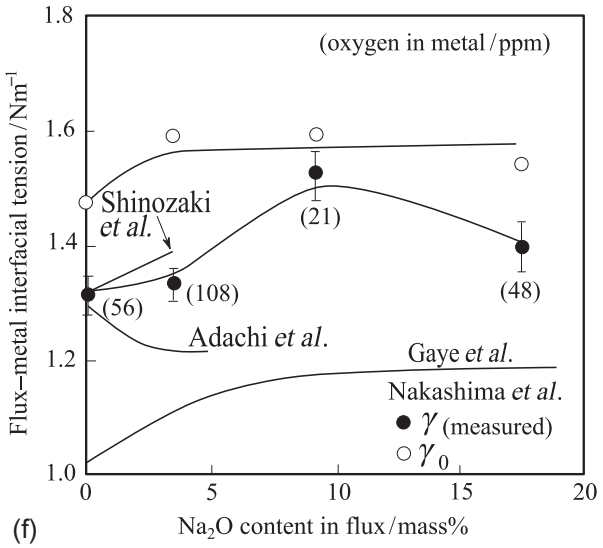


(d)



(e)

Figure 1.5.7, cont'd (d) Effect of CaF_2 in flux on the interfacial tension between liquid iron and flux. Nakashima *et al.*: CaO—SiO_2 flux, zirconia crucible, 1580 °C. Ogino *et al.*: CaO—Al_2O_3 flux, lens method, 1600 °C. Shinozaki *et al.*: CaO—SiO_2—Al_2O_3 flux, alumina or magnesia crucible, 1600 °C. Gaye *et al.*: CaO—SiO_2—Al_2O_3 flux, alumina crucible, 1600 °C. (e) Effect of Al_2O_3 in flux on the interfacial tension between liquid iron and flux. Nakashima *et al.*: CaO—SiO_2 flux, zirconia crucible, 1580 °C. El Gammel and Stracke: CaO—SiO_2—Al_2O_3 flux, drop weight method, 1570 °C. Sharan and Cramb: CaO—SiO_2—Al_2O_3 flux and Fe–20%Ni alloy, alumina crucible, 1550 °C.



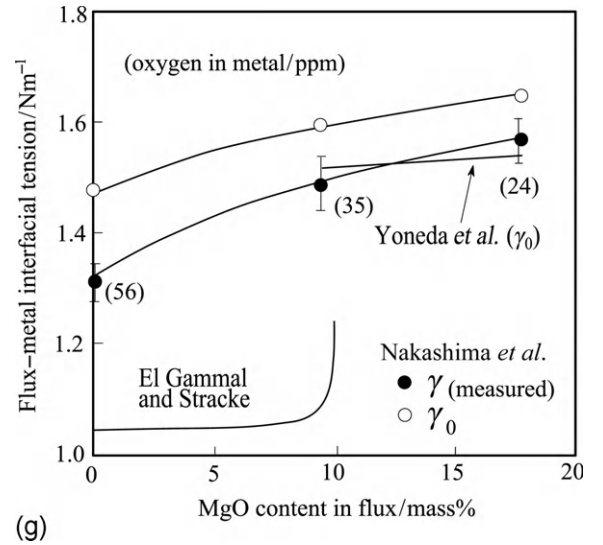
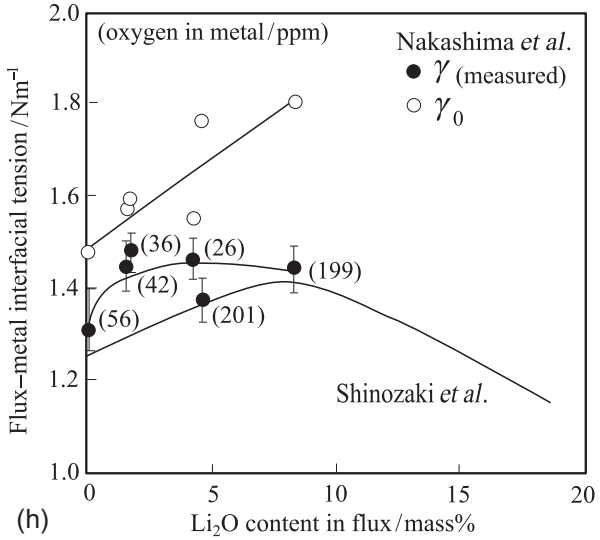


Figure 1.5.7, cont'd (f) Effect of Na_2O in flux on the interfacial tension between liquid iron and flux. Nakashima *et al.*: CaO—SiO_2 flux, zirconia crucible, 1580 °C. Shinozaki *et al.*: CaO—SiO_2—Al_2O_3 flux, magnesia crucible, 1600 °C. Adachi *et al.*: CaO—MgO—Al_2O_3 flux, lens method, 1600 °C. Gaye *et al.*: CaO—SiO_2—Al_2O_3 flux, lens method, 1600 °C. (g) Effect of MgO in flux on the interfacial tension between liquid iron and flux. Nakashima *et al.*: CaO—SiO_2 flux, zirconia crucible, 1580 °C. Yoneda *et al.*: CaO—SiO_2 flux, zirconia crucible, 1580 °C. El Gammel and Stracke: CaO—SiO_2—Al_2O_3 flux, drop weight method, 1570 °C.

(Continued)



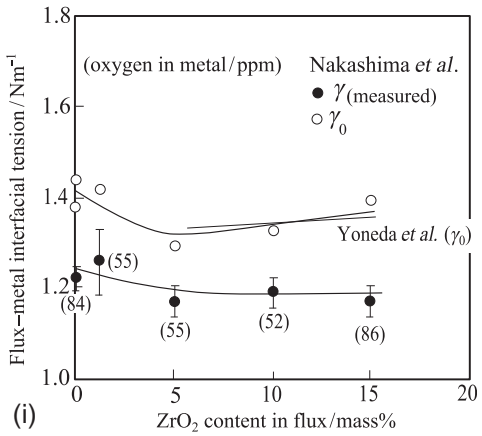


Figure 1.5.7, cont'd (h) Effect of Li_2O in flux on the interfacial tension between liquid iron and flux. Nakashima *et al.*: CaO—SiO_2 flux, zirconia crucible, 1580 °C. Shinozaki *et al.*: CaO—SiO_2—Al_2O_3 flux, magnesia crucible, 1600 °C. (i) Effect of ZrO_2 in flux on the interfacial tension between liquid iron and flux. Nakashima *et al.*: CaO—SiO_2—Al_2O_3 flux, alumina crucible, 1580 °C. Yoneda *et al.*: CaO—SiO_2—Al_2O_3 flux, alumina crucible, 1580 °C.

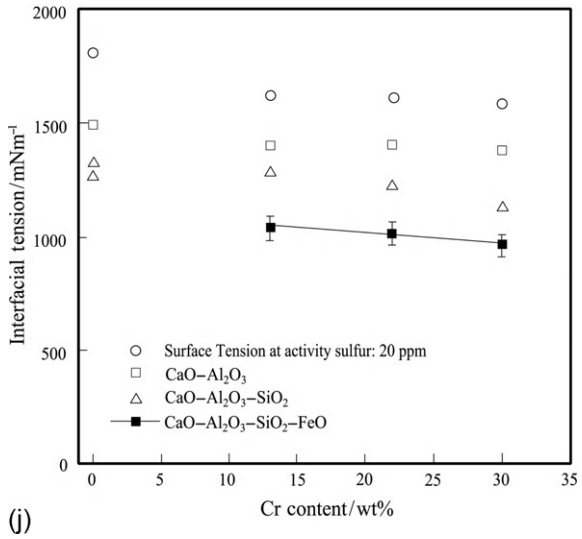


Figure 1.5.7, cont'd (j) Effect of slag chemistry on interfacial tension for Fe—Cr alloys.

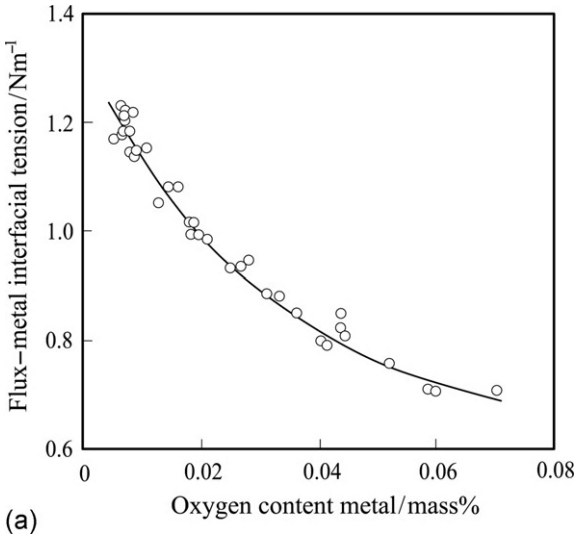


Figure 1.5.8 (a) Dependence of 35CaO—35SiO_2—30Al_2O_3 + FeO (=0–12.1 mass%) flux and molten iron interfacial tension on oxygen content in molten iron at 1580 °C.

(Continued)

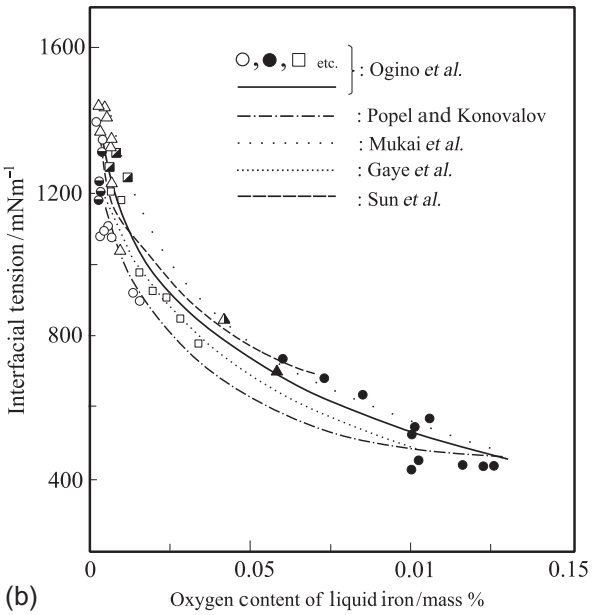


Figure 1.5.8, cont'd (b) Correlation of interfacial tension between liquid steel and molten slag with oxygen content in liquid steel.

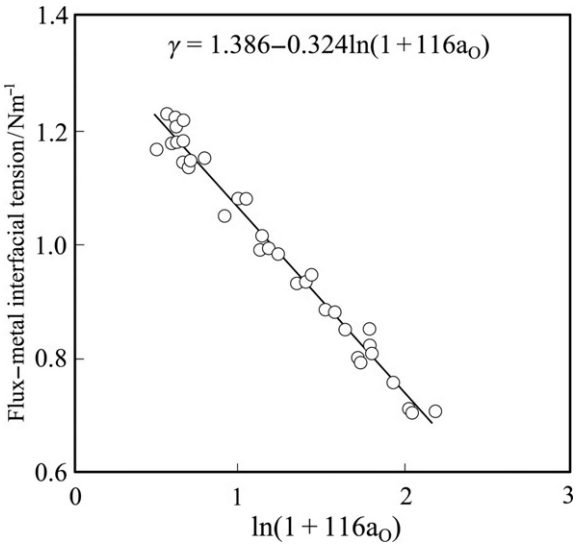


Figure 1.5.9 Measured interfacial tension values at 1580 °C against oxygen activity based on Equation (1.5.6) in Section 1.5.3.

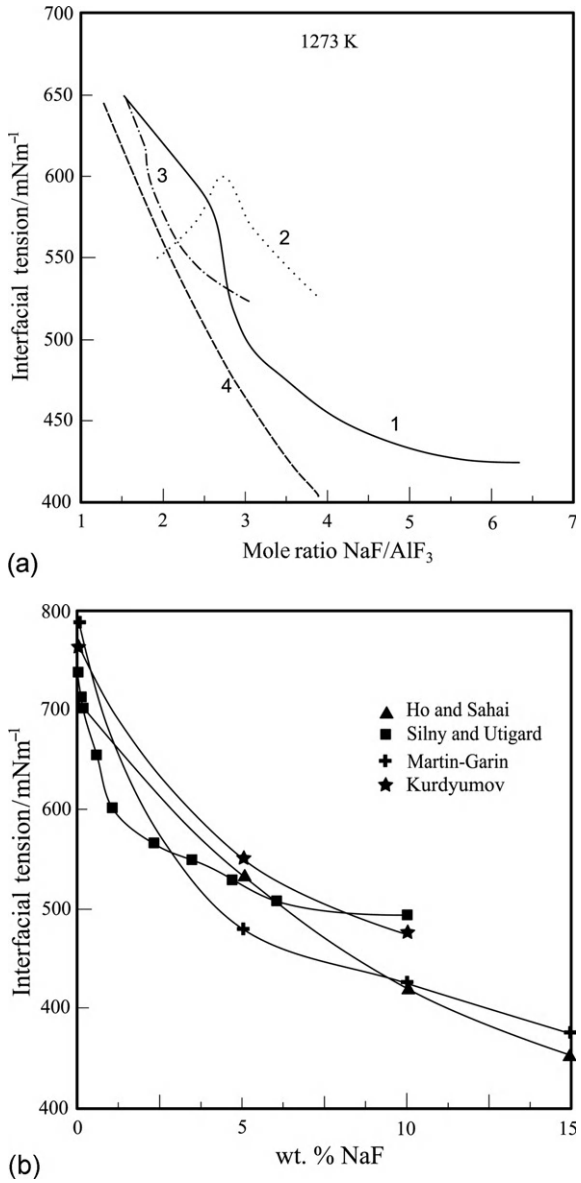
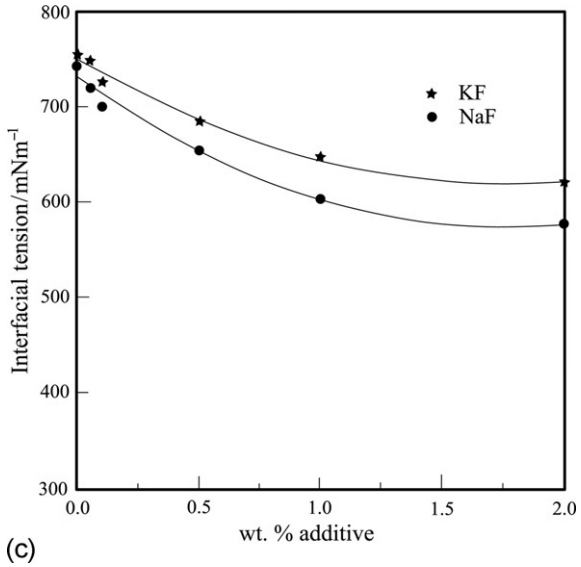
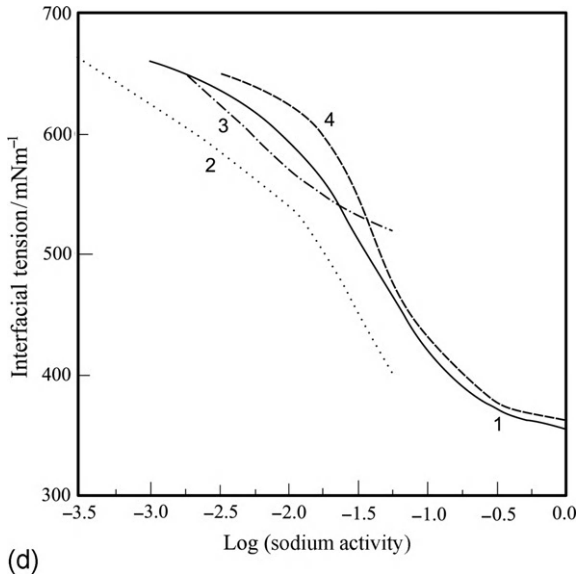


Figure 1.5.10 (a) Interfacial tension of aluminum in cryolite: 1, Utigard and Toguri; 2, Zhechuzhina and Belyaev; 3, Gerasimo and Belyaev; 4, Dewing and Desclaux. (b) Variation of interfacial tension between aluminum and equimolar NaCl—KCl as a function of NaF addition at 1013 K.

(Continued)



(c)



(d)

Figure 1.5.10, cont'd (c) Variation of interfacial tension between aluminum and NaCl with addition of NaF and KF at 1123 K. (d) Interfacial tension of aluminum in cryolite melts at 1273 K [13]: 1, calculated; 2, Dewing and Desclaux; 3, Gerasimo and Belyaev; 4, Utigard and Toguri.

REFERENCES

[1] N. Eustathopoulos, B. Drevet, J. Phys. III 4 (1994) 1865–1881.
[2] N. Eustathopoulos, B. Drevet, M.L. Muolo, Mater. Sci. Eng. A 300 (2001) 34–40.
[3] N. Eustathopoulos, Intern. Metal Rev. 28 (1983) 189–210.
[4] L. Granasy, M. Tegze, Mater. Sci. Forum 77 (1991) 243–256.
[5] A.W. Adamson, A.P. Gast, Physical Chemistry of Surfaces, sixth ed., Wiley-Interscience, New York, (1977) 19970-471-14873-3.
[6] S. Lachmann, Diss. Thesis, Electrochemical investigation of steel-slag interfaces, TU Bergakademie Freiberg, 2011.
[7] B. Vinet, J.P. Garandet, L. Cortella, J. Appl. Phys. 73 (8) (1993) 3830–3834.
[8] B. Vinet, S. Schneider, J.P. Garandet, B. Marie, Int. J. Thermophys. 25 (6) (2004) 1889–1903.
[9] B. Vinet, J.P. Garandet, B. Marie, L. Domergue, Int. J. Thermophys. 25 (3) (2004) 869–883.
[10] H. Sun, K. Nakashima, K. Mori, ISIJ Int. 37 (4) (1997) 323–331.
[11] Y. Chung, A.W. Cramb, Metall. Mater. Trans. B 31 (2000) 957–971.
[12] G.R. Belton, Metall. Trans. B 7 (1976) 35–42.
[13] R. R. Roy, T.A. Utigard, Metall. Mater. Trans. B 29 (1998) 821–827.

CHAPTER 1.6

Some Aspects of Electrochemistry of Interfaces

Piotr R. Scheller
Technical University Bergakademie Freiberg, Freiberg, Germany

1.6.1. BASICS OF ELECTROCHEMISTRY OF INTERFACES

If two in each other immiscible liquids (one of them ionic solution) contact, then segregations at the interface occur and electric potential between both phases is generated. This is the case, e.g., when liquid metal contacts with liquid slag. Using electrochemical measurements the reaction course, reaction kinetics and adsorption mechanisms can be investigated. In chemical practice, current–potential dependencies of interfacial tension are frequently recorded. Their course and characteristic points deliver the information about the adsorption phenomena at the interface. Measurements using a.c. current and using nonstationary methods as, e.g., galvano or potentiostatic impulse, are applied to get more information about the nature of the adsorbed layers and the migration of ions near the interface. Electrochemical potential and electrochemical double layer are shortly discussed as well as the effect of adsorption on the electric potential and the interfacial tension. Finally some practical aspects of electrocapillarity phenomena are presented.

1.6.1.1. Electrochemical Equilibria

An electrochemical system contains usually two phases, which are separated by the interface. In the metallurgical systems these are the liquid metal α, which is treated as the electrode, and liquid slag β, which is treated as the electrolyte. In the electrode, the atoms and electrons are transported and in the electrolyte the ions, some neutral molecules and under certain conditions also electrons.

The interfaces can be polarized and nonpolarized. The charge exchange at the full polarized interfaces is not possible and they behave as condenser. The capacity depends among other things on the degree of polarization. In real systems, the interfaces are partially not polarized. In this case, the electrons and ions can partially move throughout the interface. Even at small electric potentials high currents can be measured [1]. The resulting difference of the Galvani potentials $\Delta\varphi^{\alpha\beta}$ of both phases is therefore characteristic for the analyzed system and depends on the chemical composition of phases and the temperature [2,3].

Treatise on Process Metallurgy, Volume 2
http://dx.doi.org/10.1016/B978-0-08-096984-8.00023-9
© 2014 Elsevier Ltd.
All rights reserved.

When both phases come into contact the electrochemical reactions at the interface starts. For example, the cations of the electrode will be transferred to the electrolyte with parallel negative charge of the electrode. This negative charge of the electrode prevents the generation of new cations and their transfer to the electrolyte. On the side of the electrolyte the cations or anions generate adsorption layers at the interface (see Section 1.6.1.2). This process is running until no more current is transferred through the interface [3]. At this stage, the electrochemical equilibrium is reached, the double layer is developed and the Galvani potentials $\Delta\varphi^{\alpha\beta}$ (or contact potential) becomes a stable value. The electrochemical equilibrium is therefore then reached, when besides the chemical potential equilibrium resulting from reaction or mass transport also the electrical potentials of reacting species are taken into account for the estimation of equilibrium. Therefore the energy equation (1.1.10–1.1.12) in the Section 1.1.2 and the chemical potentials μ_i of the species i must be extended. The electrochemical potential after Nernst is therefore defined as

$$\mu_i^* = \mu_i + z_i F\varphi = \mu_i^0 + RT\ \ln\ a_i + z_i F\varphi \tag{1.6.1}$$

where μ_i^0 the chemical standard potential and a_i the chemical activity of the species i, R the gas constant, T temperature in Kelvin, z_i the electro valence, F Faraday constant, and φ the Galvani potential.

The equilibrium is then reached if the electrochemical potentials μ^* are equal in both reacting phases:

$$\mu_\alpha^* = \mu_\beta^* \tag{1.6.2}$$

and

$$\mu_\alpha^* = \mu_\alpha^0 + RT\ \ln\ a_\alpha + z_i F\varphi_\alpha = \mu_\beta^* = \mu_\beta^0 + RT\ \ln\ a_\beta + z_i F\varphi_\beta. \tag{1.6.3}$$

From these can be derived

$$\varphi_\alpha - \varphi_\beta = \frac{\mu_\alpha^0 - \mu_\alpha^0}{z_i F} + \frac{RT}{z_i F}\ln\left(\frac{a_\alpha}{a_\beta}\right) \tag{1.6.4}$$

and

$$\Delta\varphi = \Delta\varphi^0 + \frac{RT}{z_i F}\ln\ a_\alpha/a_\beta \tag{1.6.5}$$

$\Delta\varphi$ is the equilibrium Galvani potential and $\Delta\varphi^0$ the standard Galvani potential.

The electrochemical equilibrium is a dynamic equilibrium, i.e., even in equilibrium the charge exchange at the interface between the electrode (metal) and the electrolyte (slag) will take place. In equilibrium, both there and back reaction rates are equal.

1.6.1.2. Electrochemical Double Layer

At interfaces between metal and electrolyte or between two electrolytes, an electrochemical double layer of charge carrier is formed. It is generated by the displacement of the charge carrier near the interface. After both phases are brought into contact, the charge carrier (electrons or ions) can be transferred between them. The charge on the metal side is estimated through the moving electrons or by nonmoving metal cations. Because of this the difference in the electrical potential is established. The properties of the double layer are determined not only by the concentration of elements (adsorption and desorption) but additionally by their electrical properties and structure. A part of the charge carrier is adsorbed as a rigid layer at the interface. This layer acts as a plate condenser and causes the decrease of the electrical potential φ toward the interface. The local structure for metal–electrolyte is schematically drawn in the Figure 1.6.1. The rigid charge carrier layer directly at the interface is called inner Helmholtz layer (Hermann von Helmholtz investigated the electrokinetic transport in the nineteenth century and found the charged layers at phase interfaces). Toward the bulk the next charge carrier layer follows which can still interact with the metal electrode (outer Helmholtz layer). It was found that the model of the outer Helmholtz layer was too simple and valid only for high ion concentrated solution in which the movement of ions is limited. Gouy, Chapman and then in 1924 Otto Stern [4] analyzed the possible ion transport in this area and postulated the layer with diffuse movement of ion in this layer. In slags, the nature of this layer is until now not known because of the complex nature of slag melts and because of experimental

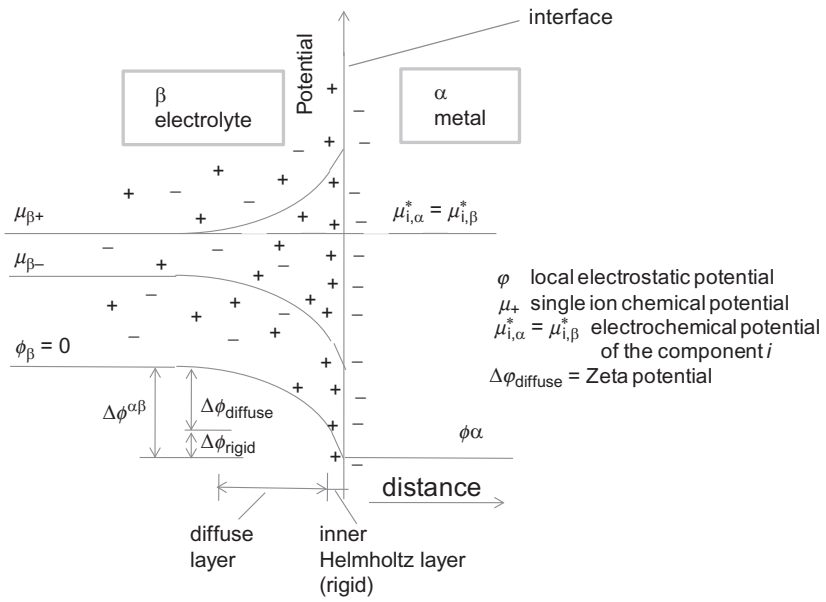


Figure 1.6.1 Equilibrium local structure for metal–electrolyte interfaces.

problems. It can be assumed that in the slag phase the inner Helmholtz layer containing adsorbed charge carrier exists and the ion solution [5]. The thickness of such layers can reach few ion diameter.

The direct measurement of the Galvani potential $\Delta\varphi^{\alpha\beta}$ between the electrode and the electrolyte is not possible. The reason for this is that metallic conductor for the measurement is necessary between both phases and it generates an additional conductor–electrolyte electrochemical equilibrium (the Galvani potential between the metal electrode and the metallic conductor can be neglected, so far equal metals are used). Following the measurement the difference of two Galvani potentials is registered which represent the electromotoric force (EMF) of the following electrochemical cell:

$$\mathrm{Me^{I}/electrode}(\alpha)//\mathrm{electrolyte}(\beta)/\mathrm{Me^{II}} \tag{1.6.6}$$

The EMF E_0 of the cell can be measured current less using the compensation method or high ohmic instruments. The result does not give any information about the processes leading to the measured values [5].

In the chemistry, the reference electrode is used to define the electromotive series. For liquid slags and metals at high temperature such reference electrodes are not defined. Molybdenum and graphite seems to be suitable for this application as they have good high temperature resistivity and the solubility in liquid slags is very low. For the estimation of the oxygen partial pressure p_{O2} in slags the graphite/CO could be used [6].

1.6.2. ELECTROCAPILLARY PHENOMENA

The electrocapillarity is an electrochemical phenomenon which describes the dependency of the interfacial tension at the interface electron conductor/electrolyte solution on the electrode potential. In the case of the excess of electric charge carrier at the interface, they repulse themselves independent on the polarity and decrease the interfacial tension. The charged ions migrate toward the interface and charge the double layer with certain density. If small change of the electric potential is additionally applied, then the charge density of the double layer changes and influence directly the interfacial tension. The dependency between both these parameters has a parabolic character. The electric potential at the maximum value of the interfacial tension is called "zero charge potential," $\Delta\varphi_{zc}^{\alpha\beta}$. At this condition, the external potential nullifies completely the charge of the double layer. From the change of the interfacial tension with the electric potential the differential double layer capacity can be estimated.

In the simplified description, the double layer represents the plate condenser. Its capacity increases linearly with the charge of the double layer. Each interfacial phenomenon can produce the specific capacities, which depend on, e.g., the adsorption,

generation of reaction products, delayed charge transfer, etc. [7]. In modern descriptions, the equivalent-circuit diagram is used, in which besides ohmic also inductive resistances are used. Using the frequency dependent impedance measurements the double layer capacity–potential relations are recorded which allow more exact information about the properties of the double layer [8].

1.6.2.1. Electrocapillary Equation

At electrochemical equilibrium, the interfacial tension γ depends on the thermodynamic parameters and the electrical potential:

$$\gamma = f(\Delta)\left(\Delta\varphi^{\alpha\beta}\right) \text{ at } T,p,\mu_i = \text{const.} \tag{1.6.7}$$

The electrocapillarity equation is therefore

$$\mathrm{d}\gamma = -\sum_i \Gamma_i^{\alpha}\cdot \mathrm{d}\mu_i^{\alpha} - \sum_i \Gamma_i^{\beta}\cdot \mathrm{d}\mu_i^{\beta} + q\cdot \mathrm{d}E \tag{1.6.8}$$

where q = charge density at the interface, Γ = interface concentration of the species i and E the measurable electrical potential.

In this form, the equation describes the change of the interfacial tension with the change of the chemical potentials of neutral components and ions as well as with the change of the electrical potentials between the phases. It is well known for ideally polarized electrodes [9] and was defined for nonpolarized electrodes by Mohliner [3] and then further developed [10].

1.6.2.2. Adsorption and Electrocapillary Curves

At the constant chemical potentials, Lippmann defined (for "ideal"—fully polarized system) on the basis of the electrocapillary equation the dependency between the interfacial tension, electric potential and the charge density at the interface [11]

$$\left(\frac{\partial\gamma}{\partial E}\right)_{T,p,\mu} = q \tag{1.6.9}$$

This equation is called *Lippmann equation*. The plot of the interfacial tension against the electrical potential delivers so-called electrocapillary curves. The real metal/slag interfaces are not polarizable. Following, because of the electrochemical reactions the certain value of the equilibrium electrical potential is reached. In opposite, the change of the electric potential via external sources leads to the change of the chemical potential at the interface.

In Figure 1.6.2, the effect of charge carrier adsorption on the $\gamma - \Delta\varphi^{\alpha\beta}$ (or E) relation is schematically shown [12]. If no adsorption exists, the maximum of interfacial tension lies at potential of zero, dotted line. If anions are adsorbed in the double layer in the

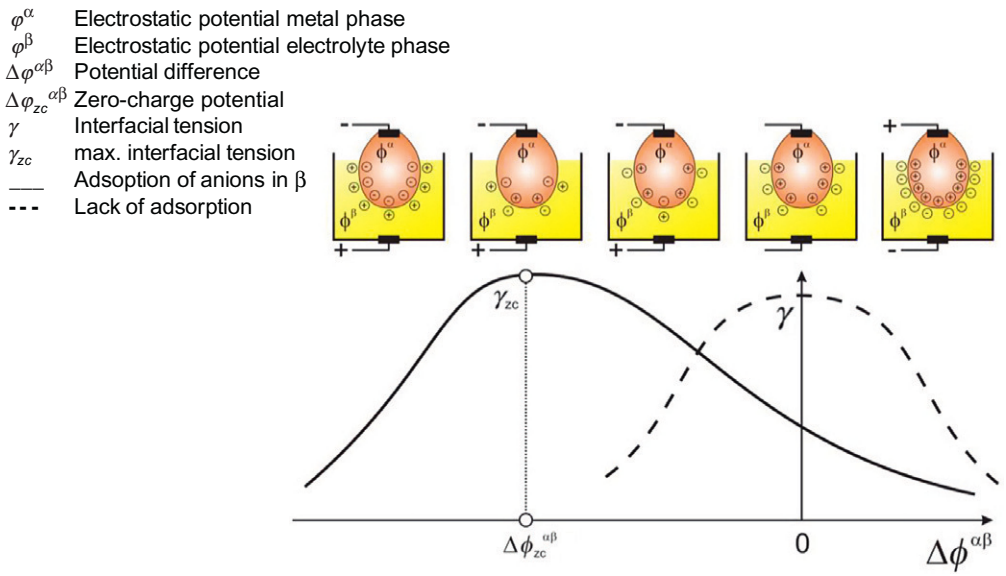


Figure 1.6.2 Effect of charge carrier adsorption on the $\gamma - \Delta\varphi^{\alpha\beta}$ (or *E*) relation, schematically.

electrolyte at the interface, the maximum of the interfacial tension moves to the negative values of the potential, full line. The maximum value of γ in this case determines the zero charge potential [13,14]. In real systems, like metal and slag, even if maximum of γ lies at $\Delta\varphi^{\alpha\beta} = 0$ there is still increased density of the charge carrier at the interface which reduces the interfacial tension. They are mainly compensated by the charge carrier adhered from the diffuse part of the layer [15]. In Figure 1.6.3, the effect of different charge carrier and neutral species on the position of the electrocapillary curve in the $\gamma - \Delta\varphi^{\alpha\beta}$ coordinates [12].

In polarized electrodes, it is possible from the value of γ_{zc} and the position of the electrocapillary curve to deduce which kind of ions are adsorbed [16]; this is valid only if one kind of ions is adsorbed. The position of γ maximal value at negative or positive potential values point to the adsorption of anions or cations at the interface. The exact value of zero charge depends on the work function of electrons which is characteristic for each kind of metal, as shown for water systems [17].

1.6.2.3. Electrocapillarity at the Slag/Metal Interface

Experimental measurements of electrocapillary properties are extremely difficult at high temperatures. Therefore only a very limited number of measurements exists. For carbon saturated iron and varied slag compositions, Patov found that with increasing CaO content the maximum of the interfacial tension will move to the positive values of the potential [18–20], Figure 1.6.4. The replacement of Al_2O_3 through SiO_2 increases the

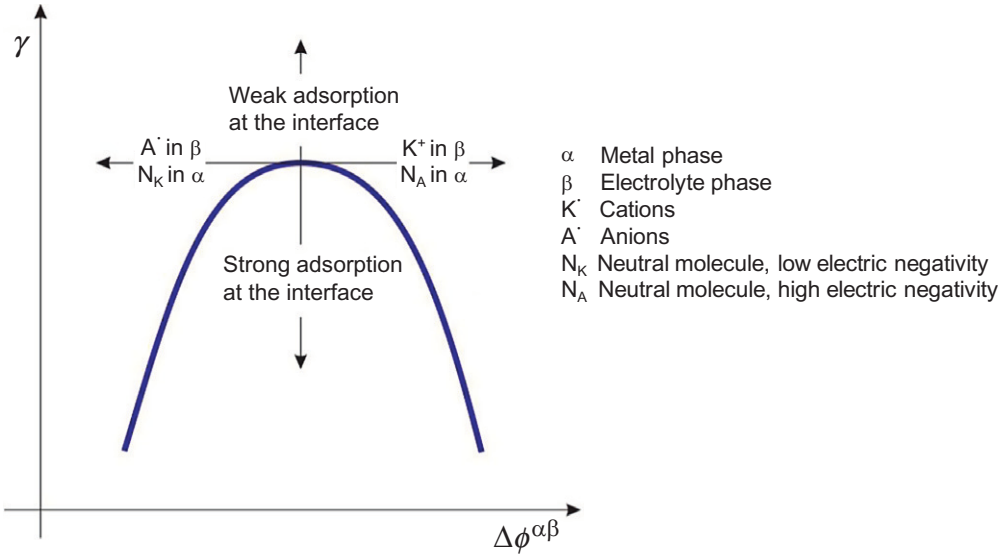


Figure 1.6.3 Effect of different charge carrier and neutral species on the position of the electrocapillary curve in the $\gamma - \Delta\varphi^{\alpha\beta}$ coordinates.

interfacial tension and not shift the zero charge potential, Figure 1.6.4 [18]. For the same slag composition (50% CaO, 50% Al_2O_3), the electrocapillary curves were recorded for low alloyed steel and for copper [21] using the metal drop weight method, Figure 1.6.5 [12]. In contact with steel, the maximum in interfacial tension lies at +50 mV and in contact with copper −90 mV. Besides ±200 mv from the γ maximum no effect of the potential on γ was registered. This shows that in contact with steel obviously the anions as O^{2-} and S^{2-} on the metal side are adsorbed and Ca^{2+} cations on the slag side. In contact with copper Cu^{2+} on the metal side and O^{2-} on the slag side [22]. In the case of steel, this adsorption supports the generation of CaS and therefore the desulfurization. In previous investigations on carbon reach Si and Fe melts as well P enriched Fe melts with SiO_2—Al_2O_3 slags the enrichment of carbon and phosphor in metal at the interface was registered [23,24,19,20].

Recently new electrocapillary measurement in steel–slag melts were performed [12]. The metal drop weight in liquid slag method was used for investigation. The schematic representation of the experimental apparatus is drawn in the Figure 1.6.6 [12]. Using this method the interfacial tension and the potential can be measured simultaneously. As an example, the effect of the oxygen and sulfur in the steel and of the slag basicity, CaO/SiO_2, on the interfacial tension and the zero charge potential is shown [300]. Two low

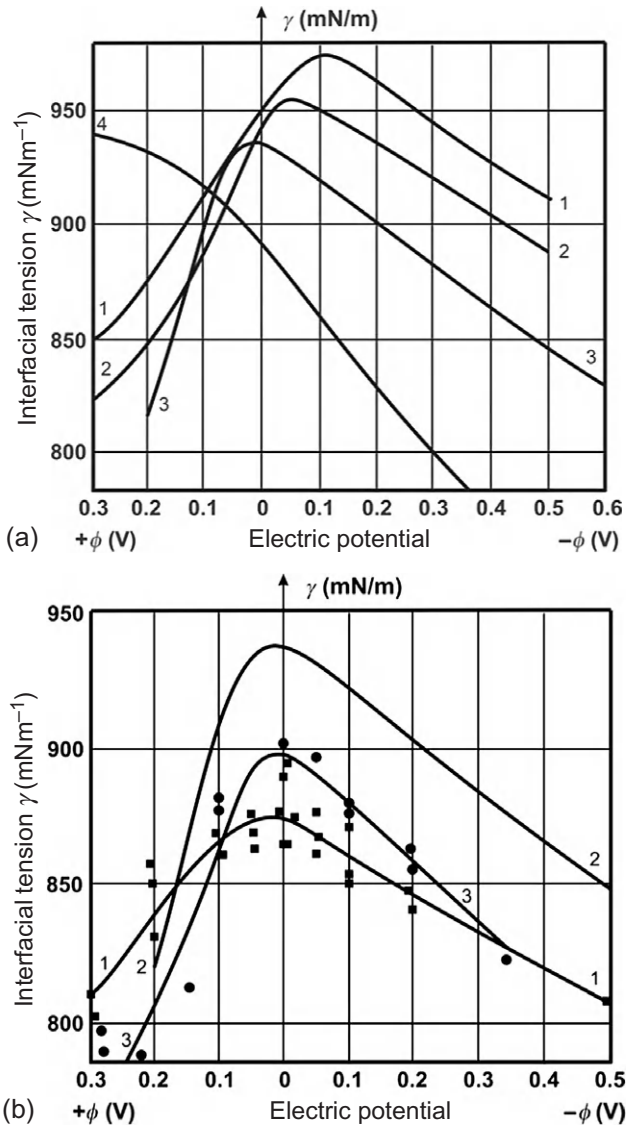


Figure 1.6.4 Electrocapillary curves for the interface Fe—C—Si—Mn/CaO—SiO_2—Al_2O_3. (a) CaO/SiO_2 increases from 1 to 4. (b) SiO_2/Al_2O_3 increases from 1 to 3.

alloyed steels with similar composition, expected O and S, were used and slag with 30.6% CaO, 50.3% SiO_2, 19% Al_2O_3 ($B=0.61$) and 43.8% CaO, 37.2% SiO_2, 19% Al_2O_3 ($B=1.18$). The results in Figure 1.6.7a and b [12] show that with a_O and a_S of 125 and 510, respectively, in steel the $\Delta\varphi_{zc}$ lies at −100 mV for $B=0.61$ and −50 mV for $B=1.18$. The interfacial tension increases with increasing basicity. At low oxygen and

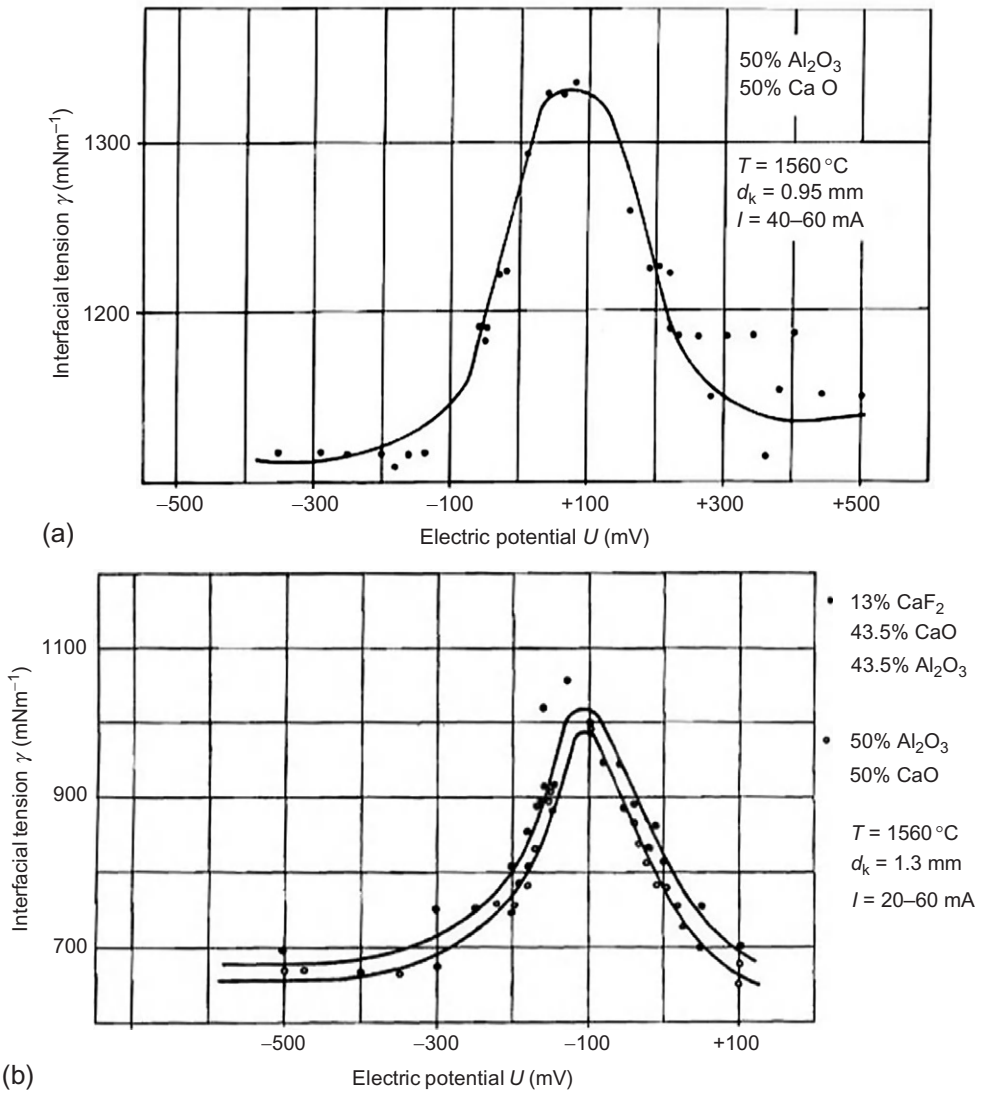


Figure 1.6.5 Electrocapillary curves for the slag in contact with (a) low alloyed steel Ck 45. (b) Copper (additional curve for slag CaO—Al_2O_3—CaF_2).

sulfur content of steel, γ increases clearly whereas the $\Delta\varphi_{zc}$ do not change. At lower basicity negative charged ions, probably silica anions with negative charged oxygen ends directed toward the metal phase, are adsorbed at the slag side of the interface. With increasing basicity the content of Ca^{2+} ions increases which displace silica ion fragments from the interface and are adsorbed. The increased adsorption of Ca^{2+} ions decreases the

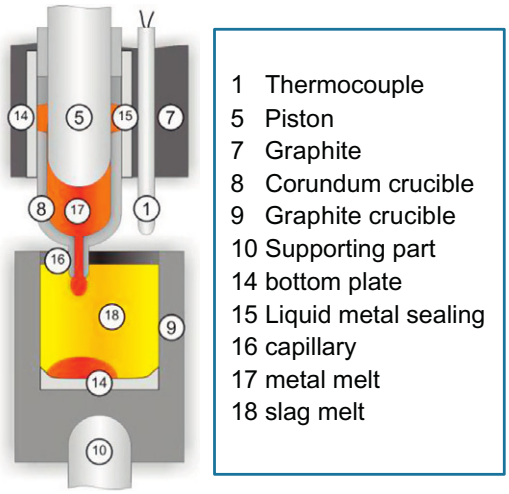


Figure 1.6.6 Drop weight method experimental arrangement used for electrocapillary measurement.

total charge in the double layer and therefore the potential with smaller negativity is necessary to reduce the adsorption and increase the interfacial tension. At lower O and S contents, the adsorption of O^{2-} and S^{2-} ions in double layer at the metal side [25] decreases as well as the total charge in the double layer on both sides of the interface. Following the interfacial tension increases and the effect of basicity is reduced.

Similar effect shows S in Cu melts. The electrocapillary curves recorded for Cu melts without S and with 0.05% S in contact with B_2O_3—Al_2O_3 slags show that γ is reduced at higher S content in the metal [26]. Points of inflection in the electrocapillary curve indicate more complex interaction between adsorbed species.

Electrocapillary phenomena were also observed by Mukai [27] when lead melts are in contact with Pb—SiO_2 slags. With the increase of the electronegative potential of the lead the interfacial tension increased.

Between molten oxides and molten salts a number of similarities exist. Especially the alkalinehalogenides and alkalinitrates were intensively investigated mainly in contact with lead because of the low melting point [7,28–32]. The inconsistent behavior can be explained by the impurities and the choice of the reference electrode [31]. At metal–salt interfaces electrochemical reactions with high mass transfer density are running. This process reduces strongly the charge separation and the capacity of the double layer. The focus in the investigation of the electrocapillarity was then the estimation of the double layer capacity and the value of the $\Delta\varphi_{zc}^{\alpha\beta}$. The electrocapillary curves are then mainly estimated by integrating of the double layer capacity–potential relations. An important role in this interfacial reaction plays the electron emittivity of the metal electrode.

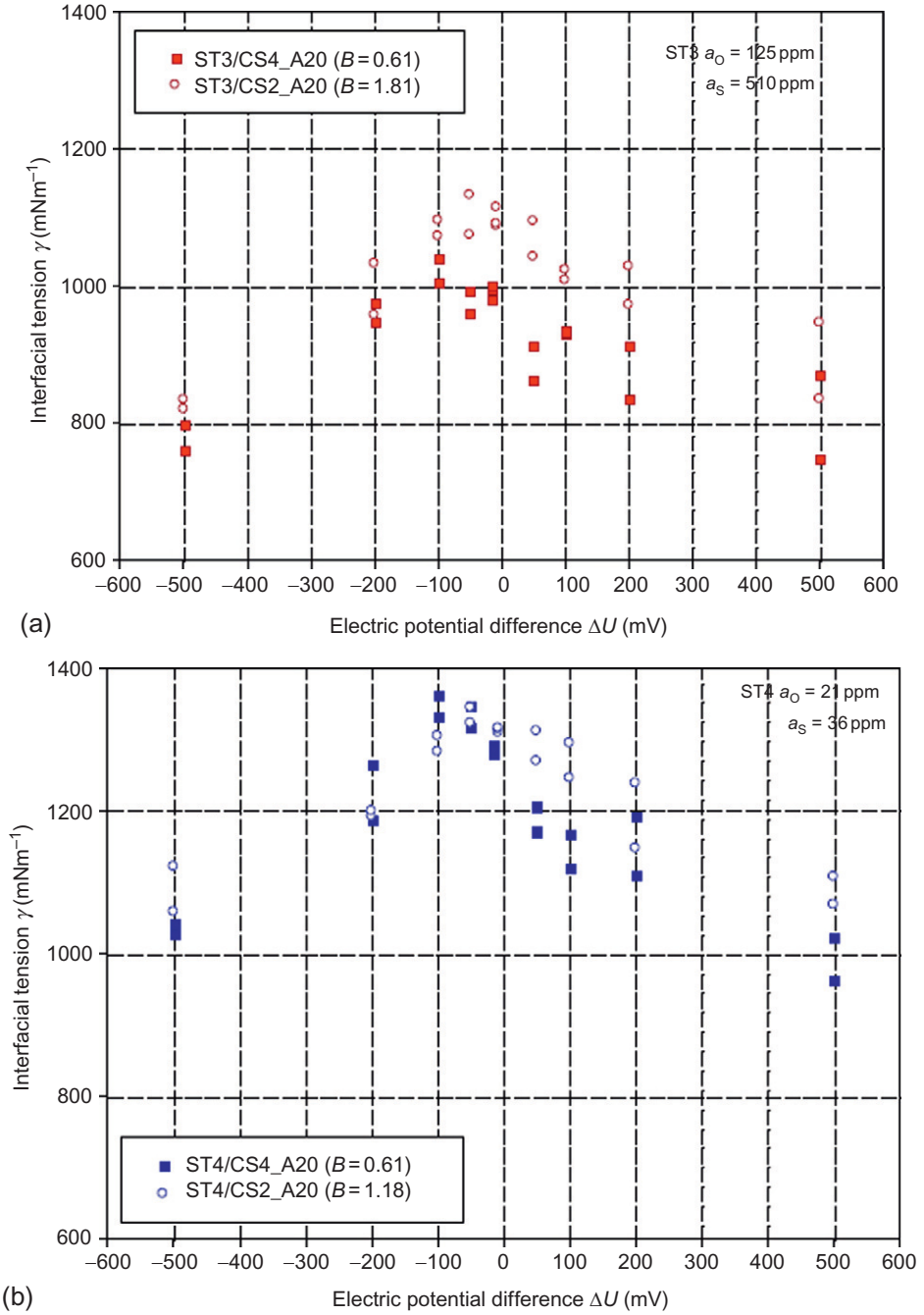


Figure 1.6.7 Dependence of the interfacial tension on the electrical potential for steel/slag. (a) at high oxygen and sulfur activity. (b) at low oxygen and sulfur activity.

1.6.2.4. Some Practical Aspects of Electrocapillary Phenomena

All reactions take place at interfaces between the phases. Therefore the interfacial phenomena play an important role not only in the thermodynamic equilibrium but also in the reaction kinetics. Some aspects in practical metallurgy will be described below.

1.6.2.5. Wettability and Wear of Refractory Materials

The roughness and porosity of the refractory material is an important parameter influencing the dynamic of the contact angle. Therefore the systematic observation of wetting behavior on real materials is connected with big scatter of results. The effect of the interfacial tension and the wetting angle is explained in other chapters. Iguchi et al. [33] pointed out that the electrochemical reactions at the interface are the real reason for the dissolution of the refractory materials. In this process, the ions produced in one place diffused and discharged in another place. Additionally, Marangoni convection is generated because of nonuniform distribution of electric charge at interfaces. This convection supports the mass transport and therefore the refractory dissolution.

1.6.2.6. Clogging in Casting Processes

The sticking and clogging of nonmetallic particles (NMI) to the walls of casting nozzles and channels disturb the casting process. This is mainly alumina which can be generated at the interface liquid steel/refractory material and others which separate from the steel melt and stick to the refractory wall or to other particles already clogged. The application of the electrochemical reactions can help to reduce this problem. In the laboratory scale, the effect of the electrical potential on the thickness of the alumina layer adhered to the refractory material immersed in moved liquid steel was investigated [34]. Applying the electric current flow the local electrochemical deoxidation and transport of oxygen ions through refractory material containing zirconia takes place. The oxygen activity is reduced at the interface refractory/steel melt. Following the *in situ* formation of NMI is prevented and clogging build-up is reduced. The experimental results show that the thickness of the alumina layer separated on the refractory (SEN) material was much lower when electrical potential with current flow was applied, Figure 1.6.8 [34]. Nowadays there are some submerged entry nozzle (SEN) producers which use this technique in the industrial production.

1.6.2.7. Emulsification of Metal and Slag

Mechanical work is necessary to emulsify one phase in the other one. In this process, the interfacial area will be increased by orders of magnitude. Because of the high values of the interfacial tension between slag and metal the emulsification is only possible if the

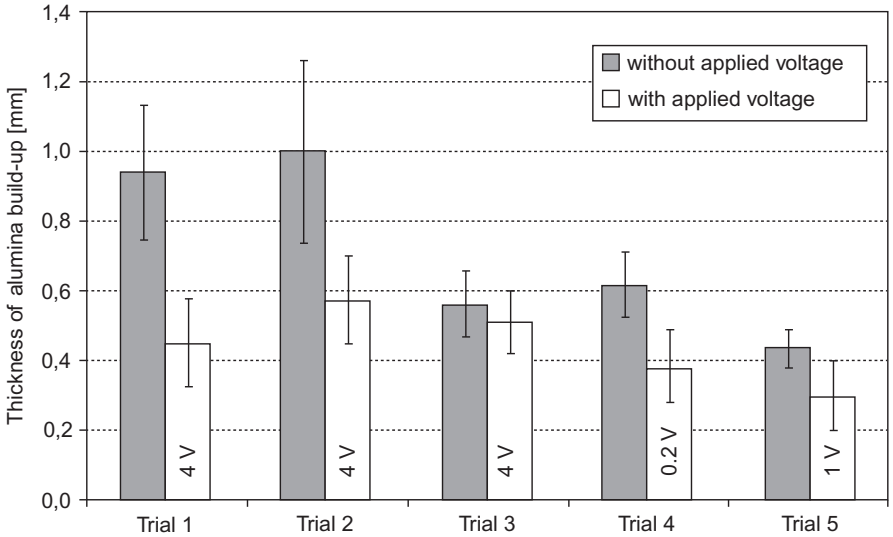


Figure 1.6.8 Thickness of alumina layers on reference sample and electrode sample with applied voltage.

interfacial tension is reduced nearly to zero. This precondition is fulfilled, if intense reactions between both phases with mass and charge transfer takes place and high level of surfactants (e.g., oxygen, sulfur) is present. In real material systems, the distribution of these parameters at the interface in small scale is never homogeneous. Because of this local gradients of interfacial tension exist which leads to interfacial convection. Besides large scale convection, the interfacial convection contributes strongly to the emulsification processes [34,35]. On the one hand the emulsification can produce defects by the emulsification of microscopic slag droplets in the solidified strand of slabs, compare Figure 1.9.11 in chapter 1.9 [36]. On the other hand the emulsification of metal in the BOF increases the reaction rate of decarburization.

1.6.2.8. Separation Technology

The coagulation of emulsified droplets can be supported by the application of electric fields [37]. The probability of the coagulation and therefore the separation will be increased in this way. The movement of emulsified species will be supported by electric fields in the processes of electrophoreses or electroosmoses in the filtration or separation technology. The application of electric fields cause not only the charge of the interfaces but also generate the gradients of the interfacial tensions which in turn lead to the electrocapillary movement [38,39]. The movement of the drops can be than increased from μm/s (electrophoresis) to cm/s (electrocapillarity). Successful trials in separation technology were demonstrated in the nonferrous metallurgy [40]. The gradient of the interfacial

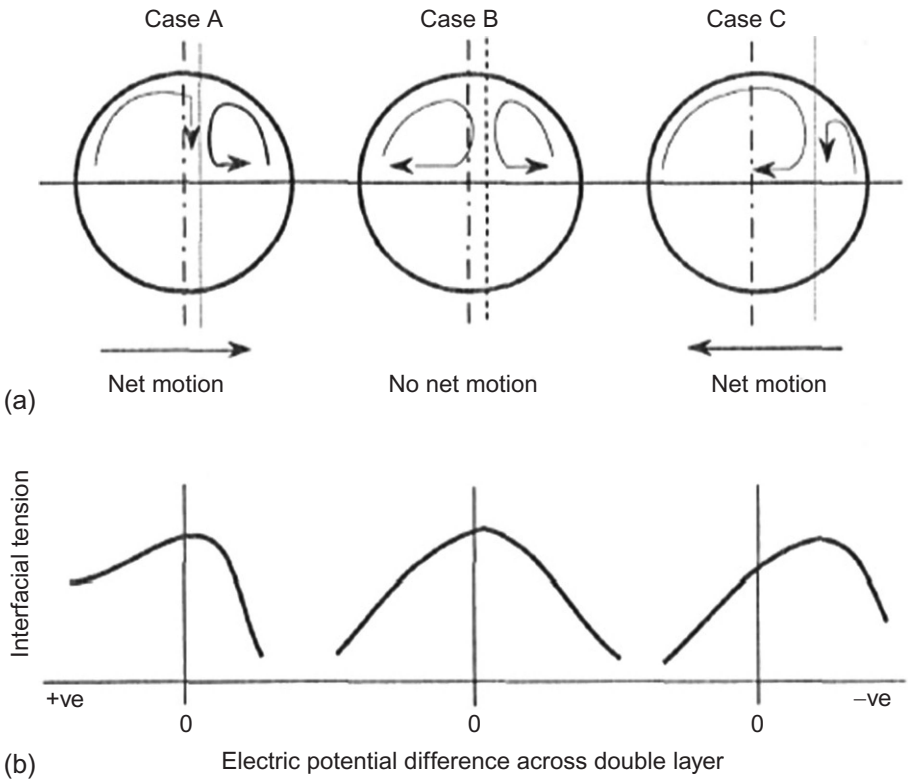


Figure 1.6.9 Principals of (a) electrocapillar movement of drops at (b) different shapes of electrocapillary curves. Case A, movement to the right; case B, no movement; case C, movement to the left.

tension causes electrocapillary convection within the drops which then move along the electric field gradient (see Figure 1.6.9) [41].

REFERENCES

[1] T. Utigard, J.M. Toguri, Metall. Mater. Trans. B 17B (1986) 547–552.
[2] A.G. Volkov, D.W. Deamer, D.L. Tanelian, V.S. Markin, Liquid Interfaces in Chemistry and Biology, first ed., Wiley Interscience, New York, 1998.
[3] D.M. Mohliner, J. Electroanal. Chem. 534 (2) (2002) 99–106.
[4] O. Stern, Z. Elektrochem. 30 (1924) 508.
[5] C.H. Hamann, W. Vielstich, Elektrochemie. 3, Wiley-VCH, Weinheim, 1998.
[6] J. Pötschke, German Institute of Refractory and Ceramics, Bonn, Germany, personal, communication, 2013.
[7] A. Kisza, J. Electroanal. Chem. 534 (2) (2002) 99–106.
[8] M. Karolczak, J. Electroanal. Chem. 402 (1–2) (1996) 37–46.
[9] D.C. Grahame, R.B. Whitney, J. Am. Chem. Soc. 64 (1942) 1548.
[10] V.S. Markin, A.G. Volkov, Electrochim. Acta 35 (4) (1990) 715–724.
[11] G. Lippmann, Ann. Phys. 149 (1873) 546.
[12] S. Lachmann, Electrochemical investigation of steel-slag interfaces, TU Bergakademie Freiberg, Germany. Diss. Thesis, 2011.

[13] A.N. Frumkin, Zero Charge Potentials, Nauka, Moskau, 1979.
[14] P. Rüetschi, P. Delahay, J. Chem. Phys. 23 (4) (1955) 697–699.
[15] H. Wendt, P. Riemenschneider, Chem. Ingen. Techn. 4 (1978) 250–258.
[16] P. Delahay, Double Layer and Electrode Kinetics, Wiley Interscience, New York, 1965.
[17] S. Trasatti, J. Electroanal. Chem. 33 (2) (1971) 351–378.
[18] B.V. Patrov, in: A.E. Belyaev (Ed.), Surface Phenomena in Metallurgical Processes, Consultants Bureau, New York, 1965, pp. 129–133.
[19] B.V. Patrov, Izvestija Vyssich Ucebnych Zavedenij/Cernaja Metallurgija 6 (1959) 3.
[20] B.V. Patrov, Izvestija Vyssich Ucebnych Zavedenij/Cernaja Metallurgija 7 (1961) 33.
[21] O.R. Mayer, Interfacial phenomena in liquid metals in molten electrolytes at high temperature under consideration of electric parameter, Dr. Diss., RWTH Aachen, 1981.
[22] T. El-Gammal, in: Proc. of MMT 2000, Ariel, ISR, 2000, pp. 547–557.
[23] Y.P. Nikitin, O.A. Esin, Phys. Chem. Sect. 107 (1956) 847.
[24] A.E. Vanyukov, I.I. Kirillin, V.Y. Saizev, Izv. Vyssich Uceb. Zav./Tzvet. Met (4) (1970) 38.
[25] P. Kozakevitch, J. Metals 21 (1969) 57–68.
[26] O.A. Kobelev, A.I. Sotnikov, A.V. Kobelev, Z. Phys. Chem. 203 (1) (1998) 143–158.
[27] K. Mukai, J.M. Toguri, I. Kodama, J. Yoshitomi, Can. Metall. Q. 25 (3) (1986) 225–231.
[28] E.A. Ukshe, N.G. Bukun, D.I. Leikis, A.N. Frumkin, Electrochim. Acta 9 (4) (1964) 431–439.
[29] A.D. Graves, J. Electroanal. Chem. 25 (3) (1970) 349–356.
[30] A.D. Graves, D. Inman, J. Electroanal. Chem. 25 (3) (1970) 357–372.
[31] M.V. Smirnov, V.P. Stepanov, Electrochim. Acta 24 (6) (1979) 651–655.
[32] G.J. Hills, P.D. Power, Trans. Faraday Soc. 64 (1968) 1629–1637.
[33] Y. Iguchi, G.J. Yurek, J.F. Elliott, in: Proc. of the 3rd Int. Iron and Steel Congress 1978, Chicago, Illinois, USA, 1978.
[34] P.R. Scheller, S. Lachmann, in: UNITECR Conf. Proc., Dresden, Sept. 18-21, 2007, pp. 334–337.
[35] M.A. Rhamdhani, K.S. Coley, G.A. Brooks, Metall. Mater. Trans. B 36B (5) (2005) 591–604.
[36] P.R. Scheller, Ironmak. Steelmak. 29 (2) (2002) 154–160.
[37] K.J. Ptasinski, P.J. Kerkhof, Sep. Sci. Technol. 27 (8/9) (1992) 995–1021.
[38] C. Christiansen, Ann. Phys. 12 (4) (1903) 1072.
[39] O.A. Kobelev, A.I. Sotnikov, Trans. JWRI 30 (2001) 311–315.
[40] R. Kammel, Erzmetall 27 (3) (1974) 135–144.
[41] R.T.C. Choo, J.M. Toguri, Can. Metall. Q. 31 (2) (1992) 113–126.

CHAPTER 1.7

Interfacial Convection and Its Effect on Material Processing

Piotr R. Scheller[a] **and Takeshi Yoshikawa**[b]
[a]Technical University Bergakademie Freiberg, Freiberg, Germany
[b]Institute of Industrial Science, The University of Tokyo, Tokyo, Japan

Convective heat and mass transports are important in the high-temperature metallurgical processing in order to optimize the reaction process as well as to ensure the material quality during solidification and during the crystal growth process. Besides of forced and natural convection, the interfacial convection in the vicinity of the interfaces plays an important role in total transport process.

In this chapter, the basic explanations on interfacial convection are provided at first and the effect of interfacial flow in the reaction technique (liquid–liquid, gas–solid, liquid–solid) and in solidification process are then presented.

After the basic explanations, the effect of interfacial flow in the reaction technique (liquid–liquid, gas–liquid, liquid–solid) and in solidification process will be presented.

1.7.1. SOME BASICS OF THE INTERFACIAL CONVECTION

Forced and natural convection as well as the mixing processes have been intensively studied and can be well described in most cases. The capillary phenomena were observed and registered since the eighteenth century and become extensively to be investigated in the second half of the nineteenth century. The first publication describing the surface flow was published by J. Thomson 1855 [1] who observed the movement of wine on the glass wall during evaporation of alcohol. Marangoni [2] described the movements of liquid surfaces as a result of the change of potential energy of liquid surfaces resulting from differences of temperature and composition. Later, the interfacial or surface flow caused by this reason was called after his name and is commonly used today as "Marangoni flow".

In contrast to the large scale natural or forced convection, the interfacial convection acts in small scale range near to the interface. Because of the experimental and observation difficulties, the interfacial phenomena became to be investigated until the last decades.

Reactions between the phases take place at interfaces, followed by transport of species from or to the interface. In the vicinity of the interface, the heat or mass transport takes place by thermal or mass diffusion within the temperature or diffusion layer. In most cases of high–temperature processes, the diffusion is the slowest step in the overall reaction.

Treatise on Process Metallurgy, Volume 2
http://dx.doi.org/10.1016/B978-0-08-096984-8.00020-3
© 2014 Elsevier Ltd.
All rights reserved.

Therefore the interfacial convection starting from the interface increases strongly the transport in this area. In solidification processes, especially in crystal growth, the control of interfacial convection is essential to obtain the needed product quality.

The interfacial energy between the phases reaches the smallest value in the equilibrium state and the total energy of the system becomes minimum (Chapter 1.1). In real material systems, only the dynamic equilibrium can be reached; in this state, the forward and reverse reactions are equal. Because a number of parameters affect the interfacial energy and they are inhomogeneously distributed at the interface, gradients of the interfacial energy or interfacial tension exist. The gradients of the interfacial tension generate the shear stress τ_x in the adhered layer and can be produced by local differences of temperature T, species concentration C_i, ion concentration $C_{I(\pm)}$, electrical potential Φ, and species transfer rate through the interface $\dot{m}_i$ at the length distance x at the interface:

$$\tau_x = \frac{\partial \sigma}{\partial x} = \frac{\partial \sigma}{\partial T}\frac{\partial T}{\partial x} + \frac{\partial \sigma}{\partial C_i}\frac{\partial C_i}{\partial x} + \frac{\partial \sigma}{\partial C_{I(\pm)}}\frac{\partial C_{I(\pm)}}{\partial x} + \frac{\partial \sigma}{\partial \Phi}\frac{\partial \Phi}{\partial x} + \frac{\partial \sigma}{\partial \dot{m}_i}\frac{\partial \dot{m}_i}{\partial x}. \tag{1.7.1}$$

The flow in the liquid caused by this surface shear stress can be derived from the equations governing the conservation of mass, momentum, and energy with the boundary condition of the surface shear stress. Commonly the two first gradients are used to describe the shear stress at the interface as other ones are extremely difficult to estimate.

Marangoni number is employed as a dimensionless number to feature the extent of Marangoni convection of the system. For the case of the thermal Marangoni convection, it is expressed as Equation (1.7.2) from the ratio of the energy transportation by the convection to that by the thermal diffusion,

$$\mathrm{Ma} = \left|\frac{\partial \sigma}{\partial T}\right| \cdot \frac{\Delta T \cdot L}{\mu \cdot \alpha} \tag{1.7.2}$$

Here, $|\partial \sigma / \partial T|$, μ, and α are the temperature coefficient of surface tension, viscosity, and thermal diffusivity of the liquid, respectively. ΔT and L are the temperature difference and the characteristic length of the system, respectively. In the case of local differences at the interface in the chemical composition, the so-called solutal Marangoni convection occurs. For this case, the Marangoni number is expressed as Equation (1.7.3) from the ratio of the mass transfer by the convection to that by the mass diffusion.

$$\mathrm{Ma} = \left|\frac{\partial \sigma}{\partial c}\right| \cdot \frac{\Delta c \cdot L}{\mu \cdot D} \tag{1.7.3}$$

Here, $|\partial \sigma / \partial c|$ and D are the concentration coefficient of surface tension and the diffusion coefficient of the liquid, respectively. Δc is the concentration difference in the system.

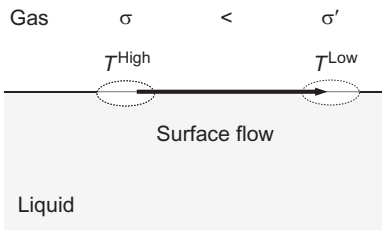


Figure 1.7.1 Surface tension driven flow.

Figure 1.7.1 shows the situations with the temperature gradients at the free surface. When the temperature difference exists at the melt surface as shown in Figure 1.7.1, the convection is generated from the high-temperature region to the low temperature region as the surface tension decreases with increasing temperature. This type of the convection is called as thermocapillary flow. The hot spot at the surface can be generated by, e.g., welding burner or by thermal convection from the bulk of liquid metal. The liquid is then sucked from the inner part through the hot spot to the colder boundary. This type of the convection is defined as Marangoni flow or thermocapillary flow. Although the above explanation is given for the temperature gradient of the surface tension (thermal Marangoni convection), the solutal Marangoni convection works in the similar way and is induced by the local change of interfacial tension caused by different content of solute species.

As Marangoni number becomes larger (e.g., by increasing the temperature difference), Marangoni flow will be accelerated and change from stationary to oscillatory, further turbulent type flow. In the stationary flow conditions, regular structures of flow pattern arise as shown in Figure 1.7.2 [3]. In the liquid heated from below the heated volumes ascend to the surface and decrease locally the surface tension. This gradient of surface tension is a motor for the surface flow. As a number of hot spots exist after short time hexagonal cells are generated and they organize themselves to the regular flow pattern structure, which can be seen in the view from the top. The flow pattern is made

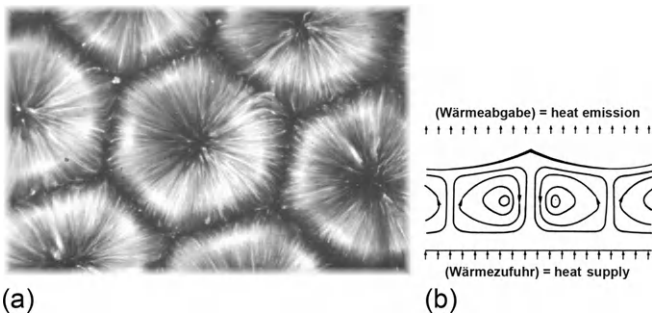


Figure 1.7.2 Surface-tension-driven (Bénard) convection: (a) view from the top on the surface, (b) flow pattern in the square section. *After: Scientific American, July 1980.*

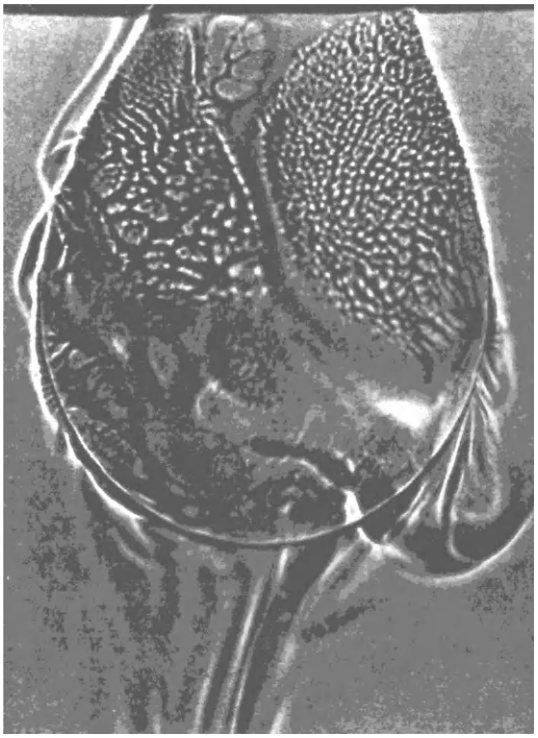


Figure 1.7.3 Schlieren photograph of hanging diethylether droplet during mass transfer of buthanol from the surrounding water into the droplet; turbulences in the interfacial layer generated by mass transfer through the interface.

visible by the addition of tracer particles. With increasing driving force for interfacial convection structures become irregular and can change to the turbulent flow. In many cases, the separation of the origin of the convection—gradient of the interfacial tension or thermal convection—is not possible as they cause each other (e.g., local thermal spot caused by thermal convection generate the local decrease of the interfacial tension). Figure 1.7.3 shows the turbulent fluid movement in the interfacial layer, which is generated by fluctuating interfacial tension as a result of intense mass transfer between two liquids [4]. The generated interfacial convection increases the mass transport and therefore the mass transfer rate between the phases. In this coupled system, the material parameter and the reaction rate plays an important role.

1.7.2. EFFECT OF INTERFACIAL FLOW IN LIQUID–LIQUID REACTIONS

In metallurgical processing the liquid–liquid reactions are very common as slag–metal reactions. Slag is used as the extracting, oxidizing, and protecting phase. Reactions taking place at the slag–metal interface lead at the interface to gradients of all parameters

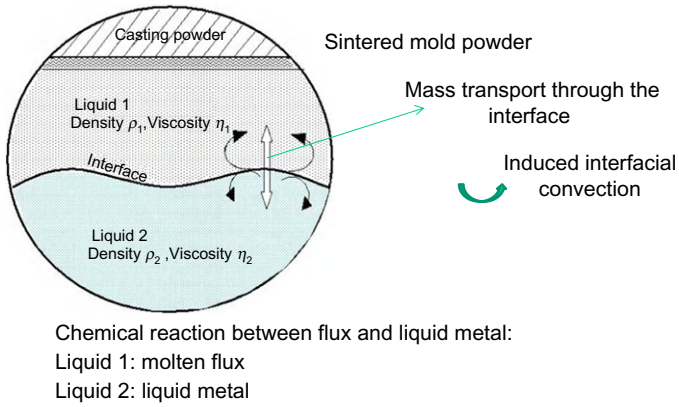


Figure 1.7.4 Mass transfer between slag and metal induce the interfacial convection.

given in Equation (1.7.1) and therefore gradients of the interfacial tension. The induced flow pattern in the vicinity of the interface is drawn schematically in Figure 1.7.4 in the case of reaction between flux and metal in the continuous casting process. For the description of the flow in the vicinity of the interface up to few millimeters from the interface another dimensionless number, the *Steinmetz-number* Ste, was developed [5]. The generation of the driving force $\Delta\sigma$ can have different reasons (see Equation 1.7.1) and the movement of the liquid layer with the interface as the boundary on one side is determined by the local liquid density ρ, dynamic viscosity η, and the thickness of the moved (slag) layer L_c:

$$\mathrm{Ste} = L_c \Delta\sigma \rho \eta^{-2} \equiv \frac{F_\sigma F_\rho}{F_\eta^2} = \frac{\text{interface tension force} \times \text{inertia force}}{\text{viscous force}} \tag{1.7.4}$$

By the definition the *Ste-number* represents the relation of the product of interfacial tension force by inertia force to the viscous force. (Rem.: dimensionless number with similar definition, where σ instead of $\Delta\sigma$ is used, are the Laplace number La, also known as Suratman number Su, which are derived from the Ohnesorge number Oh; $\mathrm{La} = \mathrm{Su} = \mathrm{Oh}^{-2}$. La and Oh number are used in fluid dynamics for the description of the free surface liquid jet breakup, where the jet diameter is inserted as a characteristic length; the Su number is more familiar in the emulsification and drop breakup processes). In nonforced fluid flow, this number can be used for the description of flow near the interface, if the Ra-number is below the critical one (1701); therefore $\Delta\sigma$ is the dominating driving force for fluid convection near the interface. At higher Ra-numbers the thermal convection occurs additionally. The highest value of $\Delta\sigma$ is given by the value of interfacial tension. The evaluation of the experimental results obtained in the industrial continuous casting process shows that the mass transport is strongly influenced by the flow conditions near the interface and defined by the *Ste-number*,

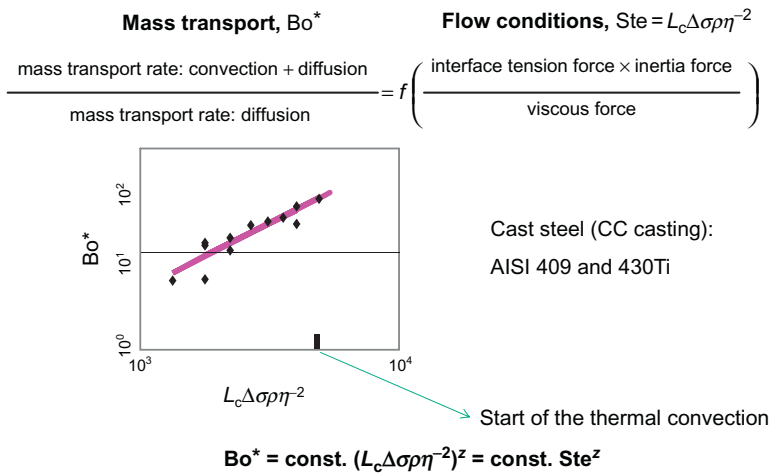


Figure 1.7.5 Bo*-number for TiO_2-absorption into the casting flux as a function of the $L_c\Delta\sigma\rho\eta^{-2}$-number (Ste).

Figure 1.7.5 [5]. The mass transport is described by the modified *Bodenstein-number* Bo*, which is defined as

$$\mathrm{Bo}^* = \frac{\text{mass tr.rate by convection} + \text{mass tr.rate by diffusion}}{\text{mass tr.rate by convection}} = \frac{\dot{m}_{i,\Sigma}}{\dot{m}_{i,D}} \qquad (1.7.5)$$

and represents the relation of mass transport rate of the species *i* by convection and diffusion to that one caused only by diffusion. The total mass transport rate can be experimentally measured (time dependent concentration change) and mass transport caused by diffusion can be measured in diffusion experiments or be calculated using known diffusion coefficients for the investigated material. If the estimated *Bo* number* is higher than unity at Ra number < 1701, then it is a clear indication on the existence of the interfacial convection. When exchange reactions between slag and metal are running, the interfacial tension can decrease (locally) down to nearly zero [6,7]. The resulting interfacial convection supports the mass transport near the interface and can also generate the emulsification process. The experimental results plotted in Figure 1.7.5 show that the *Bo* number* increases to the value up to 20 with increase in *Ste-number* before the thermal convection starts (the thick stroke on the *x*-axis, Ra = 1701). These results indicate clearly that the interfacial convection exists and increases the mass transport in the case investigated up to 20 times compared to the transport by diffusion. This is clear evidence about the contribution of the interfacial convection to the mass transport [5].

Movement velocity at the interface is influenced on the one hand by the local gradient of the interfacial tension along the interface as driving force and on the other hand by the

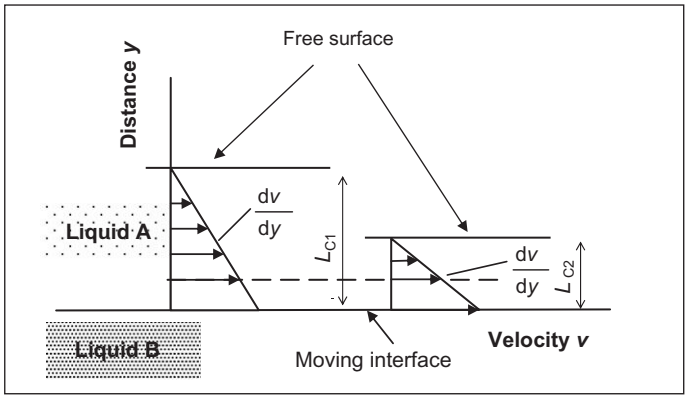


Figure 1.7.6 The fluid movement in the boundary layer at the interface.

retarding force, the surface and liquid viscosity. The liquid properties change starting from the interface towards the bulk (see Chapter 1.4) but represent still the properties of the continuous phase. Therefore the momentum of the movement at the interface is transported via viscosity to the next layers and can produce vortices because of the flow separation [8]. The involved liquid volume is characterized by L_c in the Ste-number and causes the velocity gradient perpendicular to the interface in the moved layer, Figure 1.7.6 [5]. The maximum shear stress at the interface is defined by Equation (1.7.6) and the change of the velocity perpendicular to the interface depends on the liquid viscosity:

$$\tau_x = \frac{\partial \sigma}{\partial x} = -\eta \frac{\Delta v}{\Delta y} \tag{1.7.6}$$

In physical cold models the movement of the fluid in the vicinity of the interface between two liquids after the local addition of surfactant was measured. The results obtained for the combination of fluids with various physical properties shows that the movement of the liquid layer adhered to the interface increases with the dimension less *Ste-number* [9]. With the *Ste-number* of 2.7×10^3 to 5.4×10^3 for liquid fluxes the flow velocity at the interface to liquid metal can be estimated from the interpolation of results to approx. 20×10^{-3} to 25×10^{-3} ms^{-1}. Similar values were measured by X-ray observation, when sulfur introduced via slag reached the surface of the metal drop surrounded by slag [10].

1.7.3. EFFECT OF INTERFACIAL FLOW IN LIQUID–GAS REACTIONS

When reacting gas is blown onto the metal surface for the oxidation or reduction (deoxidation) as seen in Figure 1.7.7, there exists the surface tension gradient from the reacting center and the surrounding area. During the oxidation and the deoxidation in the oxygen-bearing system, the outward and inward surface flow takes place due to the oxygen content distribution at the melt surface.

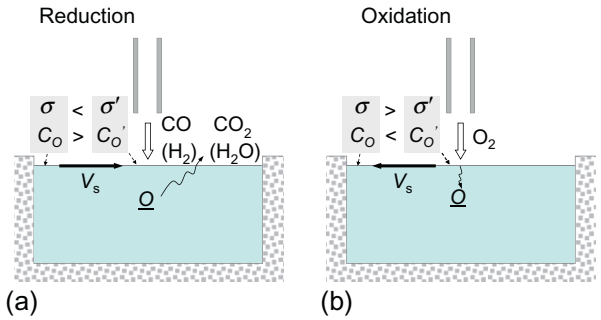


Figure 1.7.7 Flow at the melt surface caused by reduction and oxidation.

Brimacombe *et al.* [11,12] conducted the oxygen blowing to the surface of molten Sn, Cu, and Fe. The oxide particles were formed just below the gas lance and then moved radially. The velocity of the particle movement was largest in case for the Sn melt, and was as much as 1.5 m/s. Such a surface flow was estimated to be caused by the oxygen content gradient. They measured the oxygen absorption rate in molten Cu and determined the extremely large mass transfer coefficient in the liquid phase caused by surface flow. Otsuka *et al.* [13] carried out the deoxidation of Cu by CO and/or H_2 gas and obtained the enhanced reaction by the surface flow at the initial stage of reaction, where the change in the surface tension by the reduction is significant. They also found the surface movements toward the gas nozzle below with the addition of alumina particles just after starting to blow the reducing gas. Yamamoto and Kato [14] found the effect of the surface flow during the vacuum treatment. They measured the rates of evaporations of alloying elements from Fe—Cu, Fe—Sn, and Fe—Cr melts. For example in the Fe—Sn system, Sn can work as a surfactant due to its smaller surface tension than that of Fe. They observed the high evaporation rate and also the surface movement from the Marangoni effect caused by the surface tension gradient due to Sn evaporation.

On the other hand, Sano and Mori [15] conducted the deoxidation of Ag melted in the induction furnace by argon blowing and found the retardation of the reaction by the thermocapillary effect. Generally, the electromagnetic stirring promotes the convection in the liquid metal, but the gradient of the surface tension during the deoxidation works to the opposite direction of the electromagnetic force, which results in the retardation of the surface movement. Such a retardation effect was significant at the high oxygen concentration.

1.7.4. EFFECT OF INTERFACIAL FLOW IN LIQUID–SOLID REACTIONS

It often appears that refractories are corroded locally at the meniscus edge of the slag or the slag–metal interface in iron- and steel-making processes. Local corrosion is the significant issue in considering the lifetime of refractories. It is affected at least partly

by the Marangoni effect with combining the dissolution of refractory components into slag or metal (comp. also Chapter 1.9). Mukai *et al.* [16–18] has described the corrosion mechanism of refractories by the Marangoni effect. A summary of different metallurgical investigations is given by Mukai in 1998 [19].

Refractory corrosion at the meniscus edge of the slag has been investigated by immersing a solid oxide (quartz, MgO, Al_2O_3) rod into various kinds of slags [16,17]. When the dissolution of the solid oxide changes the surface tension of slag, the motion of the film on the oxide rod was observed and severe corrosion was found. In case of SiO_2 partial immersion into PbO—SiO_2 slag [16], immediate creeping up of the slag film after the immersion, followed by the slag film circulation with the "rising" wide zones and "falling" narrow zones on the SiO_2 rod above the slag within the surrounding gas atmosphere, were observed, Figure 1.7.8a and b. Dissolution of SiO_2 into slag increases the slag surface tension, and induced surface tension gradient results in the upward Marangoni flow. Such a slag film motion leads the increased local corrosion of solid oxide just above the slag level. In case of SiO_2 immersion into FeO—SiO_2 slag [17] in the similar arrangement, where SiO_2 dissolution into slag decreases its surface tension, the

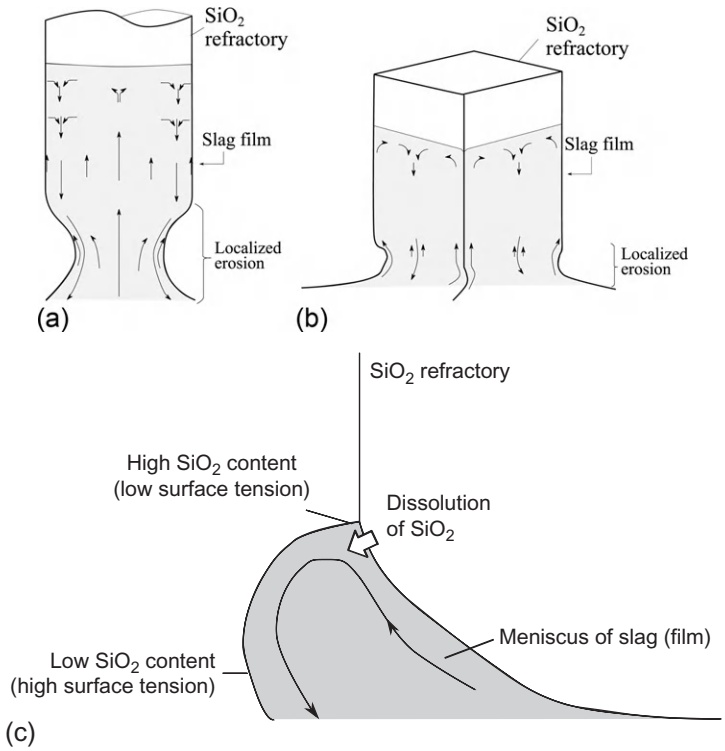


Figure 1.7.8 Marangoni flow of molten PbO—SiO_2 along the surface of column (a) and rectangular (b) SiO_2 refractory. (c) Explanation for Marangoni flow of molten FeO—SiO_2 along the surface of SiO_2 refractory.

up-down motion of the slag film free surface was observed. Explanation on such a motion was given as: (1) the SiO_2 dissolution leads the downward Marangoni flow and the meniscus edge is pulled down, (2) the descended slag film is mixed with the surrounding bulk slag, which reduces the surface tension gradient, (3) wetting of slag to SiO_2 raises the meniscus edge, see Figure 1.7.8c. Such an up-down motion of the slag film brings a severe necking of the solid oxide.

First systematic studies on wear of refractory materials were performed on Submerged Entry Nozzles (SEN) used for continuous casting, which were made of alumina graphite [20]. The results are presented in Chapter 1.9. In laboratory the refractory corrosion at the slag–metal interface has been investigated by melting the slag and iron in the crucible made from magnesia-chrome refractory material [21]. The up-down motion of the slag–metal interface and the local corrosion of the crucible were observed by X-ray observation. The dissolution of the crucible increases the oxygen concentration in the iron and decreases the slag/metal interfacial tension at the three phase interface. As it causes the inward Marangoni flow at the slag/metal interface, the metal is pulled away from the crucible wall and the slag fills in the gap. After oxygen content in the metal becomes uniform, the metal comes down due to gravity and pushes up the slag. This motion of slag/metal interface enhances the mass transfer around the interface in the slag, resulting in the local corrosion there.

In the last decade efforts have been made to quantify the local corrosion rate and to model the time dependence of the produced groove [21,22]. The shape of the groove in the refractory wall and the capillary flow condition in the crucible filled with molten glass and with steel and slag are shown in Figure 1.7.9. The flow behavior is determined by the wetting condition of the refractory material and by gravity. Glass and slag wet the refractory wall and the melt is pulled upward the wall. Considering the solutal and thermal

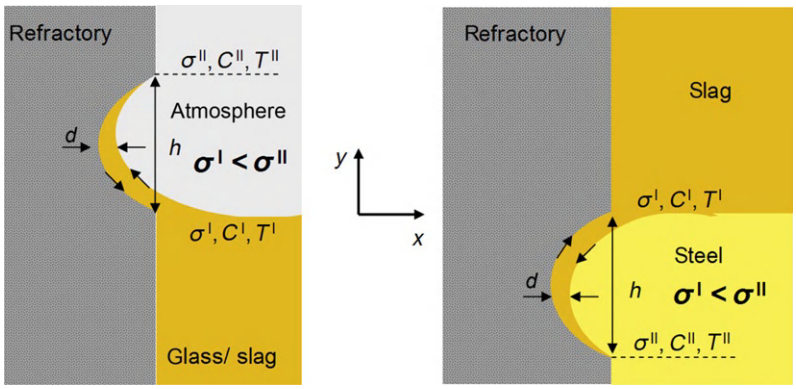


Figure 1.7.9 Corrosive groove in the refractory in contact with glass (left) and slag (right).

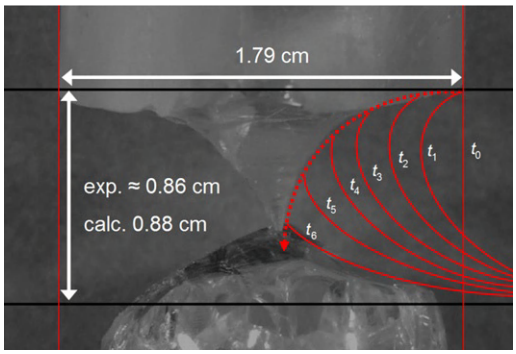


Figure 1.7.10 Corrosion of fused, polycrystalline MgO in lime-aluminate slag at 1650 °C.

capillary convection, the diffusion of solute species, and the concentration difference in the corroding liquid between the initial concentration and the saturation concentration with refractory material, the development of the groove was calculated, Figure 1.7.10 [22]. The calculated results describe well the shape of the groove in the final stage.

If the dissolution of solid material into the liquid phase takes place, the possibility always exists that the composition change induces the Marangoni flow and thereby enhances the local dissolution. Looking additionally to the electrochemical processes at interfaces (see Chapter 1.6) it can be stated that there must be numerous numbers of unnoticed phenomena relating to Marangoni effect in high-temperature material processes.

1.7.5. EFFECT OF INTERFACIAL FLOW IN SOLIDIFICATION PROCESSES AND CRYSTAL GROWTH

During the solidification and the melting of the materials, there exists temperature and concentration gradients near the solid/liquid interface. Marangoni flow is induced by such gradients, especially in the case of the system containing the surface active components.

Kimura *et al.* [23] carried out the laser microscope observation of the solid–liquid interface of the steel. They found the rapid escape of inclusion particles from the solidification front by Marangoni effect when the steel contains 100 ppm oxygen. They estimated that the contribution of solutal Marangoni effect is larger than thermal Marangoni effect. Yin and Emi [24] conducted similar observation, varying the cooling rate. They also found the Marangoni flow affecting the movements of inclusion particles at the melt surface during the solidification and the increase in the flow velocity with the increase of the cooling rate, which was explained by the steep concentration profile near the solidification front with rapid cooling. The Marangoni flow induced by the solidification

should be of importance for inclusions dispersion during the solidification although such observations are limited to the surface phenomena.

In crystal growth processes as melt or solution growth methods such as Czochralski (CZ) and the floating zone (FZ) are employed for growing the semiconductor and other high quality materials. The crystal quality (including impurity distributions, dislocations) is strongly affected by convection, and an electromagnetic convection and a natural convection are regarded as most important factors to control the mass transport in the liquid. However, a large temperature gradient of the order of several 10 s K cm^{-1} is generally applied to the melt in the vicinity of the solid/liquid interface. This large temperature gradient is directed also along the free surface of the melt, and induces Marangoni convection.

Especially in the field of crystal growth of silicon, the spoke-pattern formation at the melt surface and the dopant inhomogeneities to form striations in the grown crystals have been problematic, and considered to relate with the Marangoni effect. After Eyer *et al.* [25] confirmed the existence of oscillatory Marangoni flow during the silicon growth for the first time at the microgravity experiment on the space shuttle SL-1 in 1983, the significance of Marangoni effect was accepted in the crystal growth field.

Prior to the above finding of the Marangoni convection in the crystal growth of silicon, Schwabe [26,27] performed the visualization of Marangoni flow using a transparent melt of $NaNO_3$ for conditions of FZ [26] and CZ [27] methods. Besides the transparency, the similarity of the Marangoni numbers between $NaNO_3$ and silicon was paid attention.

To determine the flow in a FZ method [26], the liquid bridge of 6 mm long and 6 mm diameter was fabricated, and the inner streamlines were marked with small gas bubbles or were photographically recorded using suspended Pb—Mg particles. When a liquid bridge was heated by a surrounding Pt ring heater, it was found that the two couples of vortexes existed in both the upper and lower halves of the bridge, and streamlines concentrated at the surface as shown in Figure 1.7.11a. The surface velocity was as much as

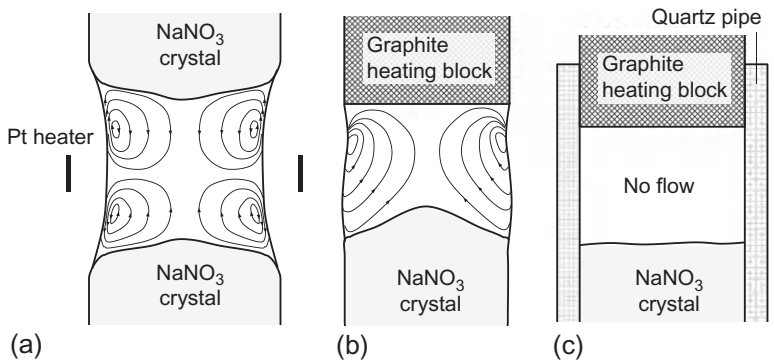


Figure 1.7.11 Observed streamlines in the $NaNO_3$ liquid bridge at the condition of FZ method.

17 mm/s. In case of heating top of the liquid bridge (Figure 1.7.11b), a couple of vortexes appeared. On the other hand, no flow was observed with a quartz cylinder cover fitting to the melt (Figure 1.7.11c). Surface flow (Marangoni convection) was always found from the high to low temperature region at the surface as far as the liquid bridge had a free surface. They also mentioned the instability of Marangoni convection and found oscillations of the temperature and flow velocity with increasing the temperature gradient.

Schwabe and Scharmann [27] reported the model experiments with a $NaNO_3$ melt to understand flows in an open boat and Czochralski growth conditions. They prepared the sample setup described in Figure 1.7.12a, where a quartz boat ($L=180$ mm, $W=20$ mm, $H=20$ mm) was used as a container and the two graphite blocks were used as heat reservoirs. Flow in a $NaNO_3$ melt was visualized by illuminating "tracer" hollow quartz spheres. Figure 1.7.12b–d shows a summary of observed streamlines in a $NaNO_3$ melt. When both ends of the melt were heated to same temperature and the middle was in low temperature (Figure 1.7.12b), inward surface flow and the downward flow at the middle of the melt to form symmetric vortexes were observed. In cases of central heating and cooling both ends to reproduce the crystal growth there (Figure 1.7.12c), vortexes became upside down. When one end was kept higher than the other end (Figure 1.7.12d), a single vortex was observed. On the other hand, the addition of oil layer onto a $NaNO_3$ melt surface decreased the flow velocity in one order of magnitude. Hence, they determined the flow was dominated by the surface tension gradient due to the temperature difference and not by the natural (buoyant) convection. Observed

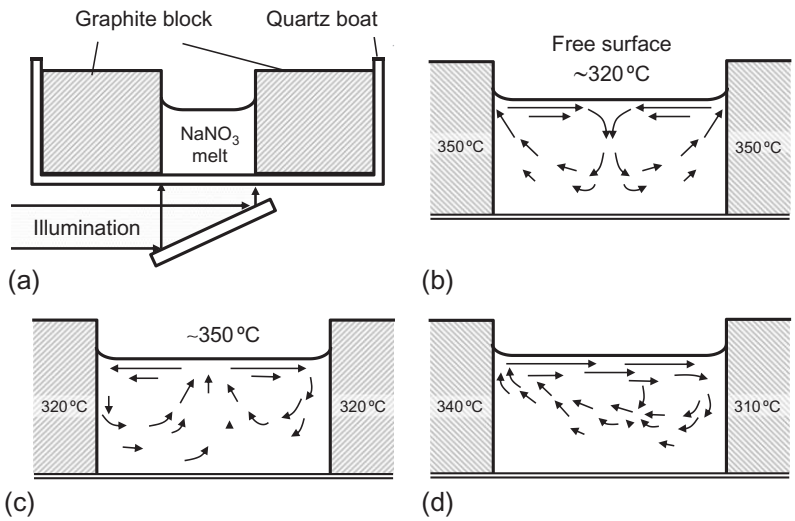


Figure 1.7.12 Observed streamlines in the $NaNO_3$ melt at the condition for simulating CZ crystal growth.

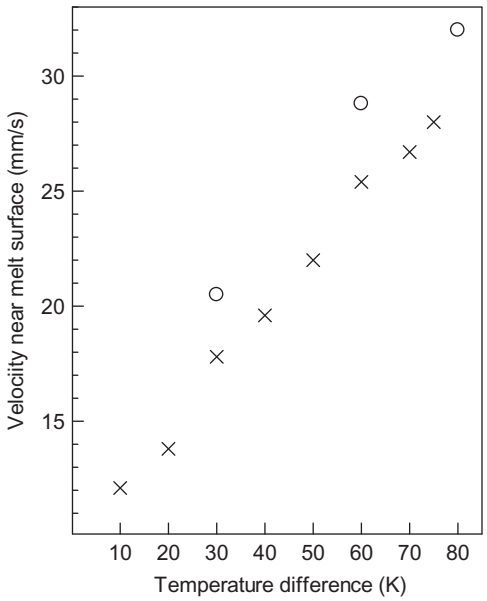


Figure 1.7.13 Relationship between flow velocity just below the free surface and the temperature difference between heating blocks in the condition of Fig. 1.7.12d.

surface flow velocity in the condition of Figure 1.7.12d is shown in Figure 1.7.13 and is in the linear relationship with the temperature difference between both ends. Thus, even in the open boat and Czochralski growth conditions, where the temperature gradient along the melt surface is generally smaller than in the float zone growth, Marangoni flow becomes the major convection especially just below the melt surface.

In order to understand the Marangoni convection in the crystal growth condition, the microgravity experiments to eliminate the buoyancy force effect [28,29] and also numerical approaches [30,31] have been conducted. The importance of the critical Marangoni number is clarified to discuss the transition of the steady to the oscillatory Marangoni convection. However, further research is required as it has not been fully established to reproduce the crystal growth condition on earth where the complex phenomena occur from the combination of the Marangoni convection with the buoyancy effect or the other forces.

REFERENCES

[1] J. Thomson, Phil. Mag. Ser. 4 (10) (1855) 330–333.
[2] C. Marangoni, Nuovo Cim. Ser. 3 (3) (1878) 97–115.
[3] M.G. Velarde, C. Normand, Sci. Am. 243 (1980) 92–108.
[4] H. Linde, E. Schwarz, Z. Phys. Chem. 224 (1963) 331.
[5] P.R. Scheller, Ironmak. Steelmak. 29 (2) (2002) 154–160.
[6] P.V. Riboud, L.D. Lucas, Can. Metall. Q. 20 (1981) 199.
[7] P.R. Scheller, Steel Res. Int. 81 (9) (2010) 886–890.

[8] P.R. Scheller, in: Proceedings of SANO Symposium, University of Tokyo, Tokyo Oct. 1–3, 2008, pp. 84–95.
[9] P.R. Scheller, B. Sahebkar, O. Volkova, in: Proceedings of Clean Steel 2007, Balatonfüred, June 04-06, Hungary, 2007, pp. 173–182.
[10] W. Cao, L. Muhmood, S. Seetharaman, Metall. Mater. Trans. B 43 (2012) 363–369.
[11] J.K. Brimacombe, F. Weinberg, Metall. Trans. 3 (1972) 2298–2299.
[12] R.G. Barton, J.K. Brimacombe, Metall. Trans. 8B (1977) 417–427.
[13] S. Otsuka, H. Tanabe, Z. Kozuka, J. Jpn. Inst. Metals 41 (1977) 117–123.
[14] M. Yamamoto, E. Kato, Tetsu-to-Hagane 66 (1980) 608–617.
[15] M. Sano, K. Mori, Tetsu-to-Hagane 60 (1974) 10–20.
[16] K. Mukai, T. Harada, T. Nakano, K. Hiragushi, J. Jpn. Inst. Metals 49 (1985) 1073–1082.
[17] Z. Yu, K. Mukai, J. Jpn. Inst. Metals 56 (1992) 1137–1144. (a) F. Hauck, J. Pötschke, Arch. Eisenhüttenw. 53 (1982) 133–138.
[18] Z.F. Yuan, W.L. Huang, K. Mukai, J. Colloid. Interface Sci. 253 (2002) 211–216.
[19] K. Mukai, Marangoniflows and corrosion of refractory walls, Philos. Trans. R. Soc. Lond. 365 (1998) 1015–1026.
[20] F. Hauck, J. Pötschke, Arch. Eisenhüttenw. 53 (1982) 133–138.
[21] J. Pötschke, in: Proc. UNITECR', Salvador, Brazil, 13-16. Oct., 2009, pp. 902–905.
[22] J. Pötschke, C. Brüggemann, Steel Res. Int. 83 (2012) 637–644, http://dx.doi.org/10.1002/srin.201100294.
[23] S. Kimura, Y. Nabeshima, K. Nakajima, S. Mizoguchi, Metall. Mater. Trans. B 31 (2000) 1013–1021.
[24] H. Yin, T. Emi, Metall. Mater. Trans. B 34 (2003) 483–493.
[25] A. Eyer, H. Leiste, R. Nitsche, in: Proceedings of 5th European Symposium on Materials Sciences under Microgravity, ESA-SP222, Schloß, Elmau, 1984, p. 173.
[26] D. Schwabe, A. Scharmann, F. Preisser, F. Oeder, J. Crystal Growth 49 (1978) 305–312.
[27] D. Schwabe, A. Scharmann, J. Crystal Growth 52 (1981) 435–449.
[28] A. Cröll, W. Müller-Sebert, R. Nitsche, Mater. Res. Bull 24 (1989) 995–1004.
[29] S. Nakamura, T. Hibiya, K. Kakimoto, N. Imaishi, S. Nishizawa, A. Hirata, K. Mukai, S. Yoda, T.S. Morita, J. Cryst. Growth 186 (1998) 85.
[30] C.E. Chang, W.R. Wilcox, Int. J. Heat Mass Transf. 19 (1976) 355–366.
[31] T. Kaiser, K.W. Benz, J. Cryst. Growth 183 (1998) 564–572.

CHAPTER 1.8

Stability of Interface Between Liquid Steel and Molten Slag

Piotr R. Scheller[a], Joonho Lee[b] and Toshihiro Tanaka[c]

[a]Technical University Bergakademie Freiberg, Freiberg, Germany
[b]Department of Materials Science and Engineering, Korea University, Anam-dong, Seongbuk-gu, Seoul, Republic of Korea
[c]Division of Materials and Manufacturing Science, Graduate School of Engineering, Osaka University, Osaka, Japan

Macroscopic flow near the metal–slag interface as well as the microscopic interfacial flow (Marangoni flow) generates shear forces at the interface. Depending on the local flow velocity and the physical properties of both liquid phases, the interface can become unstable and the phases are dispersed in each other. Emulsion is a disperse system of immiscible liquid phases in which the small droplets of the disperse phase exist in the continuous phase (dispersion medium). From the thermodynamic point of view, emulsions are not stable and separate with time. The process of separation is accompanied by the coagulation of the dispersed droplets. The electrochemistry on interfaces plays a crucial role in the emulsification process and in the stability of the emulsion. In the first steps of the process metallurgy, the emulsification processes increase the reaction rate by the enlargement of the interfacial area. In the last step, in the casting and solidification process, the emulsification of slag in liquid metal generates defects in the cast products and has to be avoided.

In metallurgical processes there are two types of high-temperature emulsions:

(1) dispersion of metal (or matte) droplets in a molten slag (or salt)

(2) dispersion of molten slag (or nonmetallic inclusions) in a molten metal

It is understood that most emulsions take place due to chemical reactions or mechanical stirring. When chemical reactions take place the chemical composition of phases change and following their physical and chemical properties the interfacial tension is strongly reduced. The reduction of the interfacial tension in metallurgical systems is a necessary precondition before the emulsification processes starts. If it is not fulfilled, only big droplets (bigger than approx. half a mm) can be generated which can separate quickly due to buoyancy forces.

In the emulsification process, the droplets of the dispersed phase moves in the continuous phase in the turbulent flow, i.e., the droplet is the object with strong shear stress forces acting on it. The value of shear stress depends on the energy supplied to the system. In a simplified version neglecting the viscosity and the density of the dispersed phase, the maximum droplet diameter D_{max} which can exist in the shear stress flow can be calculated from the relation

Treatise on Process Metallurgy, Volume 2
http://dx.doi.org/10.1016/B978-0-08-096984-8.00021-5

© 2014 Elsevier Ltd.
All rights reserved.

$$D_{\max}\left(\frac{\rho_c}{\sigma}\right)^{3/5}\varepsilon^{2/5}=\text{const.} \tag{1.8.1}$$

where ρ_c is the density of the continuous phase, σ the interfacial tension, and ε the supplied energy to the system. It is evident that for given density of the continuous phase, the stable droplet diameter can be decreased with increasing the supplied energy and decreasing the interfacial tension.

Microscopic slag inclusions near to the surface of the cast products are a serious problem in the material quality. They are emulsified in liquid metal because of reactions running at the interface with following instability of the interface and additionally the shear stress produced by metal flow near to the interface. Mechanical forces produced by macroscopic flow and transferred via viscosity to the interface and by interfacial convection produce the microscopic droplets of both phases which are dispersed on both sides of the interface. Physical cold model experiments have been carried out to quantify the dependences between the liquid properties and acting forces leading to the emulsification. The flow velocity of the lower liquid was adjusted using rotating roller near to the interface. The densities and viscosities of both interacting phases were taken into account as they are very different in the metallurgical systems. From the dimension analysis, two dimension free numbers were defined, the capillary number

$$\text{Ca}=\frac{u\eta_c}{\sigma} \tag{1.8.2}$$

and the material number

$$\Lambda=\frac{v_d}{v_c} \tag{1.8.3}$$

where u is the flow velocity in the vicinity of the interface in the continuous phase, η_c the dynamic viscosity of the continuous phase, v_d and v_c are kinematic viscosities of the dispersed and continuous phase respectively. Plotting the relation $\text{Ca}=f(\Lambda)$ the parameter areas were defined where the emulsification can take place and where not, Figure 1.8.1 [1]. The line dividing both parameter areas represents the critical Ca number Ca^* as a function of the material number. In the range $0.001<v_1/v_2<10$, the capillary number is independent of v_1/v_2 and at the values $v_1/v_2>10$, the critical capillary number increases. Beyond $v_1/v_2=500$ a drastic increase of Ca^*. For practical use, it can be derived from this relationship that if the emulsification should be prevented, the viscosity of the upper liquid and/or the interfacial tension should be increased and the flow velocity decreased. Harman and Cramb [2] observed in similar investigations that the critical fluid velocity decreases with increasing thickness of the upper layer. This is in accordance with the relationships defined by the *Steinmetz number Ste* [3], see Chapter 1.6. Assuming the usual physical properties of casting fluxes and liquid steel is Λ in the range 50–500; furthermore, assuming the interfacial tension at quasi equilibrium conditions and the flow

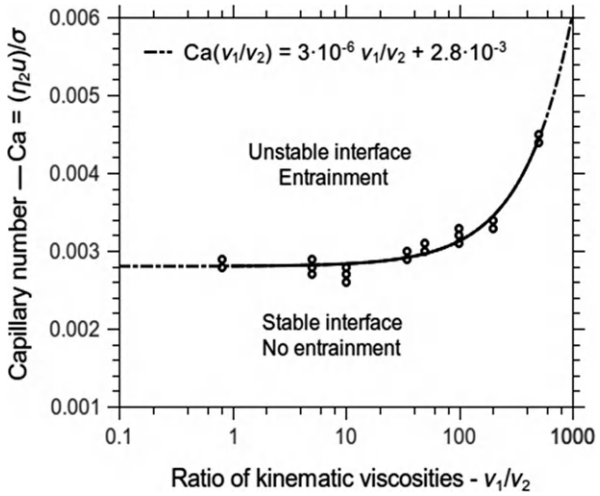


Figure 1.8.1 Capillary number as a function of the ratio of kinematic viscosities for the start of upper phase entrainment in the lower liquid.

velocity near the flux/metal interface (0.4 m/s) the estimated Ca-number will be in the range of 2×10^{-3} and with this value significantly lower than the critical value of Ca needed for emulsification. In the real casting processes, the emulsification of flux near the solidified surface is frequently observed [3] (see Chapter 1.6) which indicate that the interfacial tension decreases strongly. The reason is reactions between steel and flux at the interface (see also below). The dispersion of slag droplets due to a decrease of interfacial tension caused by exchange reactions and induced interfacial flow at the slag/metal interface was reported in some previous papers [3–8].

During the continuous casting process, soluble Al (or Ti) may react with SiO_2 in molten slag. This chemical reaction generates the interfacial instability, and emulsion of small droplets of molten slag into liquid steel occurs. This behavior is called as "micro-emulsion." The engulfing of small droplets of molten slag into liquid steel at the interface between liquid steel and molten flux is one of the important subjects to produce highly purified steel in continuous casting molds. This phenomenon is related to the stability of the interface between liquid steel and molten slag. The stability at the interface between liquid metals and molten oxides has been investigated so far and the effect of chemical reactions on the stability has been reported by several researchers. Some examples are described on this subject.

Figure 1.8.2 [9] shows the change in the contour of liquid steel in molten slag when SiO_2 in molten slag was reduced by Al in liquid steel as follows:

$$2\underline{Al}_{\text{in Fe}} + \frac{3}{2}SiO_{2\text{in Slag}} = 2\underline{Si}_{\text{in Fe}} + Al_2O_{3\text{in Slag}}$$

Although the liquid Fe contained 4 mass% Al initially, the concentration of Al was decreased by the reaction with SiO_2 in molten slag. The interfacial tension between

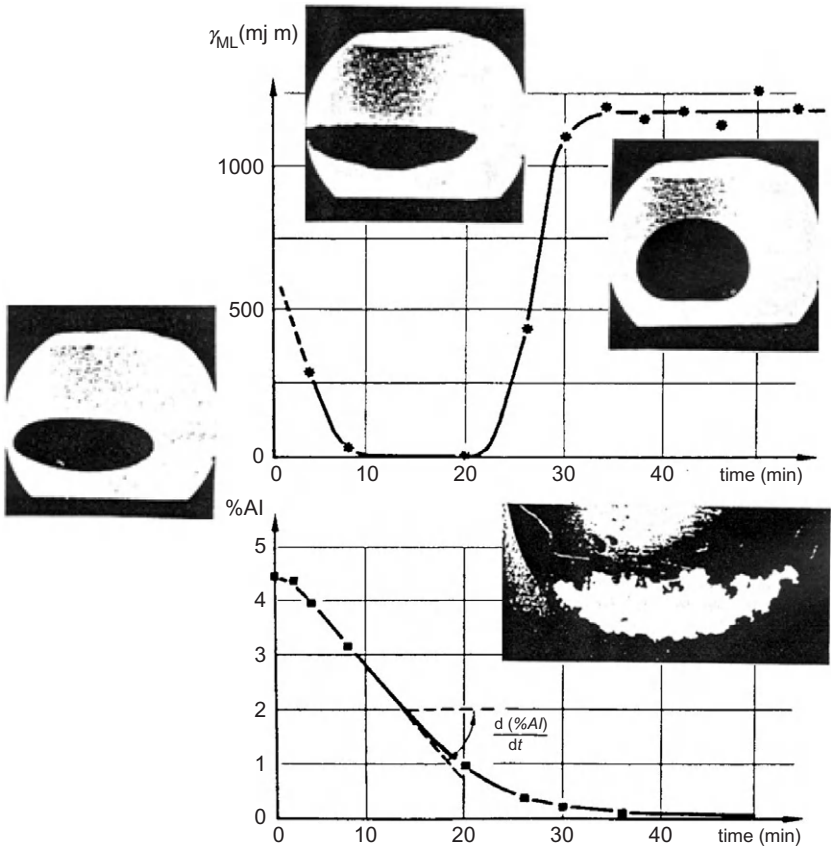


Figure 1.8.2 Change in the interfacial tension between liquid Fe—Al alloy and molten silicate slag when Al in liquid Fe alloy is oxidized.

liquid steel and molten slag decreased and then the interfacial tension increased after the reaction as shown in Figure 1.8.2. In particular, while the chemical reaction occurs, the interfacial tension tends to decrease, and sometimes the interface of liquid Fe is disturbed. Since the interface areas increase due to the interface disturbance with chemical reactions and it causes the increase of the reaction rate, the exact correlation between kinetics of the reaction and the interfacial tension cannot be determined from the results in Figure 1.8.2. However, it is clear that the interfacial tension between liquid steel and molten slag decreases with the chemical reactions between those two phases.

The same results were confirmed by Ooi *et al.* [10] for liquid Fe—Al and Fe—Ti alloys with molten CaO—SiO_2—Al_2O_3 slag.

Chung and Cramb reported the decrease of the interfacial tension between liquid Fe—Ti alloy and molten slag with the chemical reactions between those two phases as shown in Figure 1.8.3 [11]. They explained that the local gradient in interfacial tension

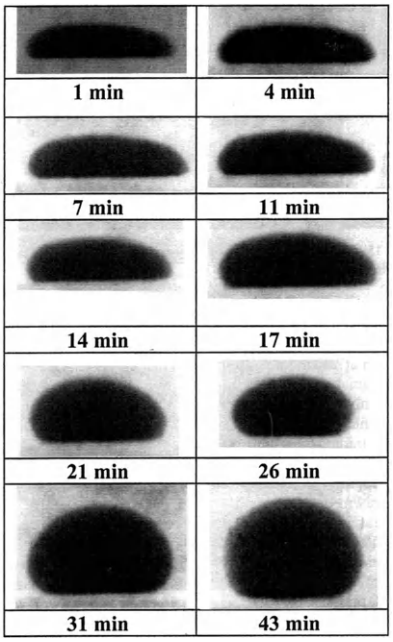


Figure 1.8.3 Scanned X-ray pictures of 11.0 pct Ti alloy droplets in contact with 40 pct CaO–40 pct SiO_2–20 pct Al_2O_3 slag.

due to chemical reaction yield Marangoni flow along the slag–metal interface. Since the Marangoni flow in slag surface is slower than that of metal surface, interfacial instability may increase, Figure 1.8.4. According to the Kelvin–Helmholtz instability model, it is considered that as the instability of the interface increases, a nipple is formed and it extends in the direction normal to the slag–metal interface, Figure 1.8.5 [12]. Finally, the head of the nipple tends to decrease its surface area to form a spherical shape, and it is consequently detached from the bulk phase (metal or slag) and belongs to the other side phase (or becomes a suspended particle in the other phase), Figure 1.8.6 [13]. Chung and Cramb reported some evidence of the emulsified phases in slag and metal phases, Figure 1.8.7 [11].

For the above examples, the interfacial tension between liquid steel and molten silicate slag decreases while chemical reactions occur with oxides and oxygen in liquid steel. However, Takeuchi *et al.* [14] and Ooi *et al.* [10] reported that the interfacial tension does not always decrease when desulfurization reaction occurs between liquid steel containing sulfur and CaO base molten slag as shown in Figure 1.8.8 [10].

The overview about emulsification in casting processes including own model experiments are described by Feldbauer and Cramb [16]. Emulsions are stabilized by the

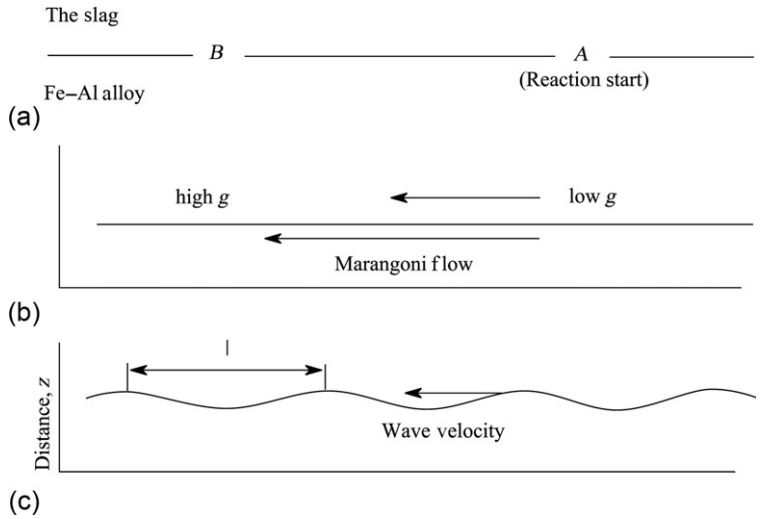


Figure 1.8.4 (a)–(c) Suggested mechanism of the generation of the Marangoni flow and its role in the interfacial instability at the steel–slag interface during reaction [4].

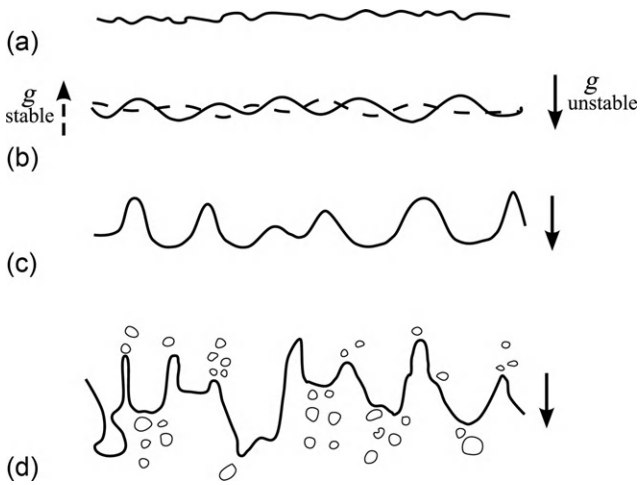


Figure 1.8.5 (a)–(d) Formation of perturbation and emulsification by Kelvin–Helmholtz instability [5].

existence of ionic double layer (see Chapter 1.4). Such double layer was expected for steel/slag emulsions by Kozakevitch [16]. Electrochemical measurements described in Chapter 1.6 reveal via Lipmann electrocapillary dependences the existence of double layers.

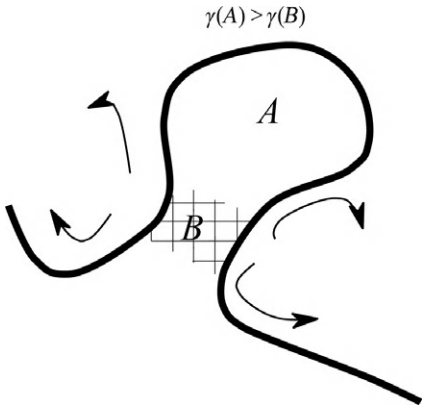


Figure 1.8.6 Emulsification enhanced by Marangoni flow [6].

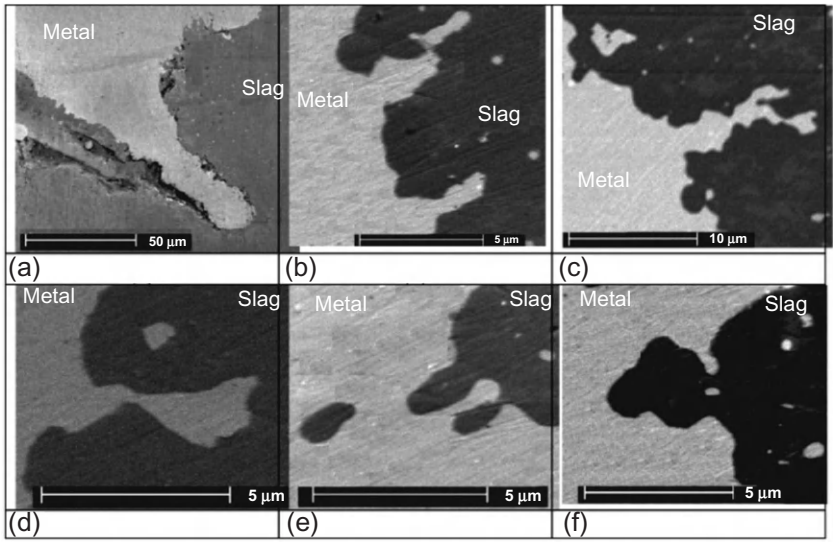


Figure 1.8.7 (a)–(f) Feature of initiation of emulsification at the alloy–slag interface [4].

During the oxygen steelmaking process, the ultrasonic gas injection yields considerable chemical reactions as well as strong stirring. Accordingly, emulsion happens due to both the chemical reactions with resulting strong interfacial flow and the strong stirring. Once the gas injection stops, droplets sink to the bottom due to gravity and coagulate with each other. Kozakevitch reported that the emulsion stability is affected by slag viscosity, existence of solid particles, adsorption layer, and slag–metal interfacial tension [17].

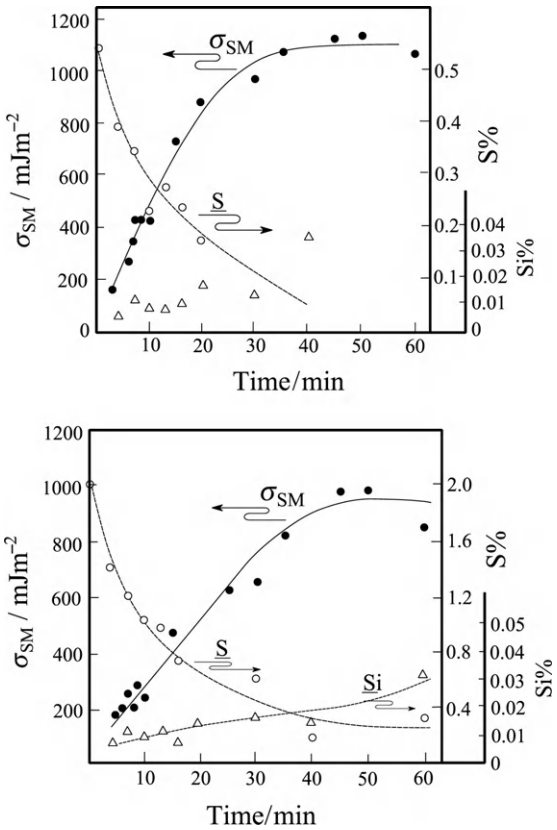


Figure 1.8.8 Change in the interfacial tension between liquid Fe—Si—S alloy and molten Cao-based slag.

REFERENCES

[1] R. Hagemann, R. Schwarze, P. Heller, P.R. Scheller, Metall. Mater. Trans. B (2012)http://dx.doi.org/10.1007/sl 1663-012-9749-9, Nov.
[2] J. Harman, A. Cramb, in: Steelmaking Conference Proceedings, 1996, pp. 773–783.
[3] P.R. Scheller, Ironmak. Steelmak. 29 (2) (2002) 154–160.
[4] H. Gaye, L.D. Lucas, M. Olette, P.V. Riboud, Can. Metall. Q. 23 (1984) 179–191.
[5] A. Sharan, A.W. Cramb, Metall. Mater. Trans. B 26 (1995) 87–94.
[6] A. Jakobsson, N. Viswanathan, D. Sichen, S. Seetharaman, Metall. Mater. Trans. B 31 (2000) 973–980.
[7] P.R. Scheller, Steel Res. Int. 76 (2005) 581–587.
[8] P.R. Scheller, R. Hagemann, CAMP-ISIJ 24 (2011) 509.
[9] P.V. Riboud, L.D. Lucas, Can. Metall. Q. 20 (1981) 199–208.
[10] H. Ooi, T. Nozaki, H. Yoshii, Trans. ISIJ 14 (1974) 9–16.
[11] Y. Chung, A.W. Cramb, Metall. Mater. Trans. B 31 (2002) 957.
[12] E.S.R. Gopal, in: P. Sherman (Ed.), Emulsion Science, Academic Press, London, 1968, p. 1.
[13] G.S. Bainbridge, H. Sawistowski, Chem. Eng. Sci. 19 (1964) 992.
[14] E. Takeuchi, M. Kishimoto, K. Mori, Y. Kawai, Tetsu-to-Hagane 64 (1978) 1704–1713.
[15] P. Kozakevitch, J. Metals 211 (1969) 57–68.
[16] S. Feldbauer, A.W. Cramb, in: Proc. 13th Process Technology Conf. 1995, Nashville, US, 1995, pp. 327–340.
[17] P. Kozakevitch, in: Open Hearth Proceedings, 1969, pp. 64–75.

CHAPTER 1.9

Applications of Interfacial Phenomena in Process Metallurgy

Piotr R. Scheller[a], Joonho Lee[b], Takeshi Yoshikwa[c] and Toshihiro Tanaka[d]

[a]Technical University Bergakademie Freiberg, Freiberg, Germany
[b]Department of Materials Science and Engineering, Korea University, Anam-dong, Seongbuk-gu, Seoul, Republic of Korea
[c]Institute of Industrial Science, The University of Tokyo, Tokyo, Japan
[d]Division of Materials and Manufacturing Science, Graduate School of Engineering, Osaka University, Osaka, Japan

Various interfacial phenomena in steelmaking processes affect the quality of steels, and the following subjects related to the interfacial phenomena are still investigated extensively nowadays:

(1) Interfacial convection in welding processes
(2) Engulfing small droplets of molten slag into liquid steel
(3) Erosion or dissolution loss of refractories
(4) Separation of metallic droplets from slag
(5) Engulfing nonmetallic inclusions into solidified interface
(6) Generation of gas bubbles in liquid steel
(7) Nucleation during solidification
(8) Slag foaming

In this chapter, some examples of the investigation on the above subjects are explained by referring to the relationship with interfacial properties.

1.9.1. MARANGONI FLOW DURING THE WELDING PROCESS

In general, the surface tension decreases with increasing temperature as is the case for pure metals. However, it is not always the case when a metal contains the surface active element. If the elements of the VIth group in the periodic system are dissolved in iron, the temperature dependency of the surface tension changes as shown with example of S content in Figure 1.9.1 [1].The change of the temperature coefficient of surface tension is shown in Figure 1.9.2 for liquid iron with oxygen and sulfur addition. Similar results were reported earlier by Popel et al. and Scheller et al. [2,3]. The temperature coefficient is negative at low oxygen and sulfur concentrations while it becomes positive at their larger concentrations. Modification of the repulsive interaction between iron and the surface active element with temperature increase is considered to be responsible for the positive temperature coefficient. Therefore, the concentration of minor elements in steels is significant to control the Marangoni convection in the welding pool, and the

Treatise on Process Metallurgy, Volume 2
http://dx.doi.org/10.1016/B978-0-08-096984-8.00022-7
© 2014 Elsevier Ltd.
All rights reserved.

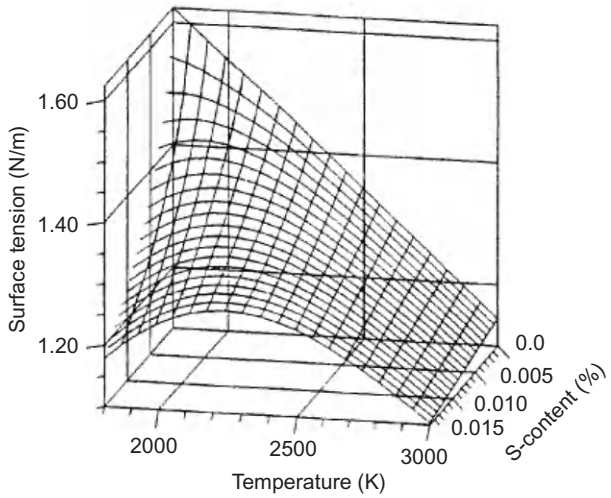


Figure 1.9.1 Surface tension of 304 stainless steel as a function of temperature and sulfur content.

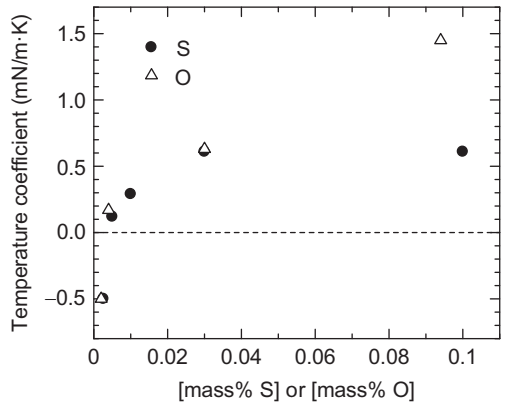


Figure 1.9.2 Temperature coefficients of surface tension of Fe—O and Fe—S alloys.

consecutive weld penetration. Here, it should be noted to distinguish the total and soluble oxygen and sulfur concentrations. Although total concentration, which includes both soluble and combined (as compounds) concentrations, mostly appears in the material (steel) composition, the surface tension (or any other properties in matrix phase) is determined by the soluble concentration. Especially for the case of oxygen, it tends to form oxide inclusions with the alloying element so that the effect of total oxygen concentration is generally smaller than the total sulfur concentration. In the practical process, it must be taken into account that below the welding electrode temperatures up to 2000 K and more exist, and even the oxidic compounds dissociate and precipitate in modified composition during solidification. In the dissociate state, the free oxygen or other surface active elements affect the surface tension as described above.

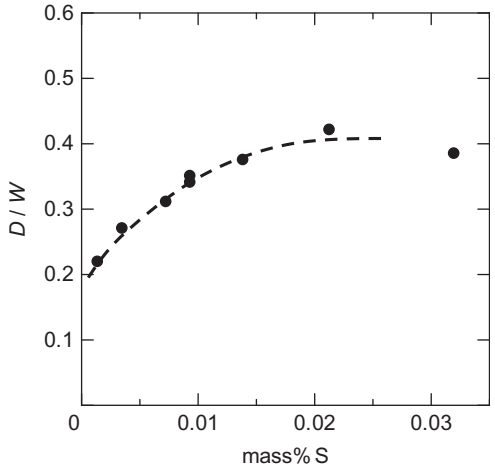


Figure 1.9.3 Effect of sulfur on *D*/*W* ratio in the weld pool.

Heat-to-heat variations in the weldability during the welding of ferritic and stainless steels were recognized in the 1960s. Minor elements in steels have been known to affect the penetration of the weld pool. The penetration is often discussed with the depth (D)/width (W) ratio, and the significant effect of the sulfur can be seen in Figure 1.9.3 [4]. Several theories have been proposed to explain the difference in weldability with varying the steel compositions. Ishizaki [5] pointed out that the surface flow is caused by the temperature gradient along the melt surface during welding and affects the weld pool geometry. Heiple and Roper [6] postulated the model of the flow direction in the weld pool to describe the change in the weld penetration depth. Since the 1980s, it is widely accepted that the Marangoni effect contributes the weld penetration and in addition, minor elements, especially surface active elements, in steels affect the Marangoni flow during the welding process. The forces acting on the liquid metal pool during TIG welding are depicted in Figure 1.9.4 [1]. The fluid flow in a weld pool is illustrated in Figure 1.9.5. The center of the weld pool is heated highest and the edge is cooled, resulting in the temperature gradient along the surface of the pool. If the temperature coefficient of the surface tension of the pool is negative ($\partial\gamma/\partial T<0$), the outward flow occurs at the surface. Heat transported by the surface flow dissolves the edge of the pool, and forms a shallow weld. In contrast, if the temperature coefficient of the surface tension is positive ($\partial\gamma/\partial T>0$), the inward surface flow leads the central downward flow of hot melt and the bottom is preferentially melted to form the deep weld penetration.

The strongest and therefore controlling force for the flow in the liquid metal pool is the Marangoni force. The investigation of the topography of the quenched metal pool shows clearly the effect of the sulfur content on the flow direction, Figure 1.9.6 [7]: at S content of 20 ppm the liquid metal is pulled from the hot center to the cold edge whereas

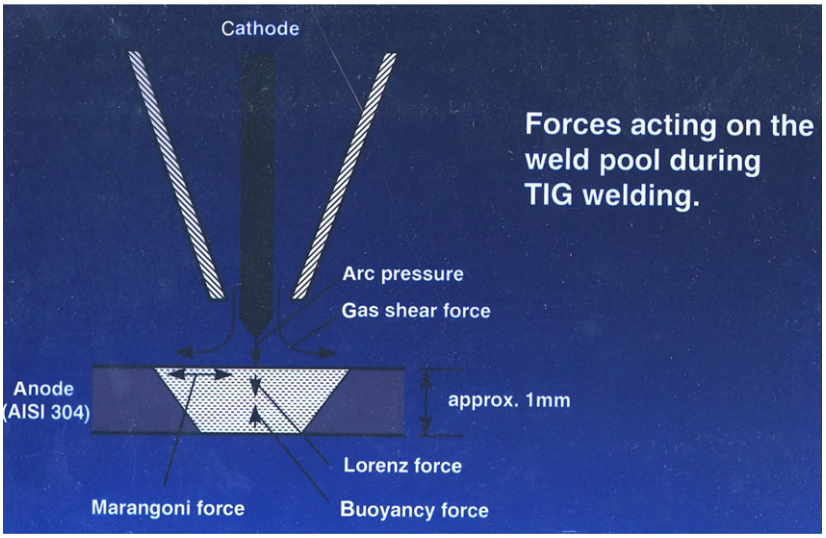


Figure 1.9.4 Forces acting on the weld pool during TIG welding.

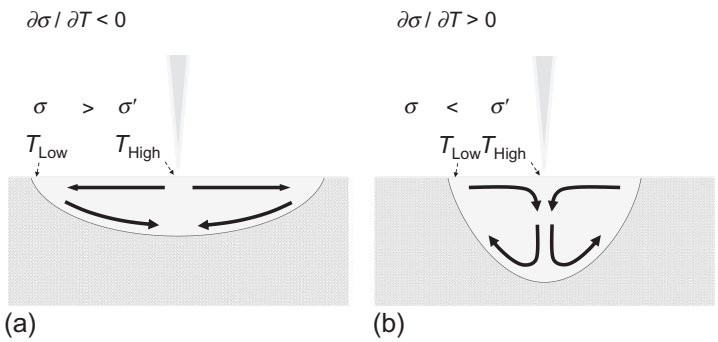


Figure 1.9.5 Flow direction and the weld geometry during the welding process.

at 100 ppm S content the acting force has a quite opposite direction and the liquid metal is sucked to the hot center and then flows to the center of the ~1 mm thick steel sheet. The flow pattern at different S contents is schematically shown in Figure 1.9.7 [7]. At S contents of 40–50 ppm, at which $\partial\gamma/\partial T$ is nearly zero more complex flow pattern is induced, Figure 1.9.7c. Based on this measurement of the pool shape at the 1 mm thick sheet it is confirmed, that the Marangoni force is the strongest one acting on the pool even at the conditions of full gravity force.

Besides the surface active elements contained in materials, their addition to the shielding gas affecting the Marangoni convection has been noticed. The effects of SO_2 and O_2/CO_2 addition to the shielding gas on the D/W ratio are shown in Figure 1.9.8 [1,8,9]. The ratio increases with the concentration of SO_2 up to its value

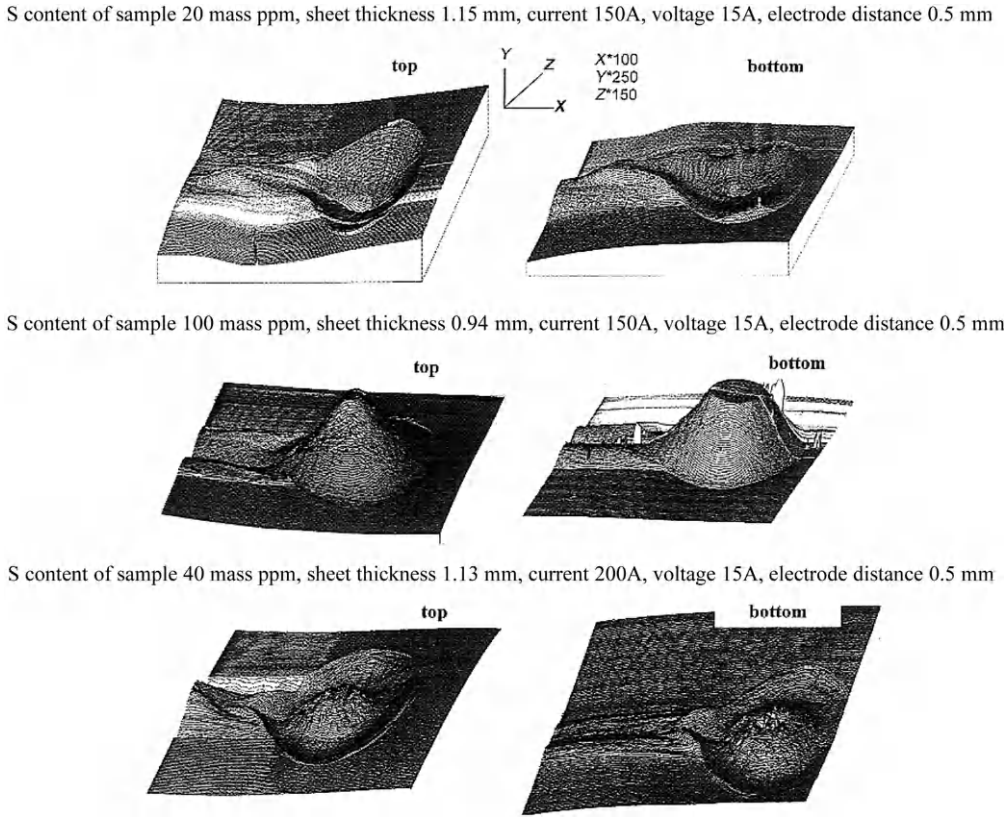


Figure 1.9.6 Topographies of the weld pool surface (end center).

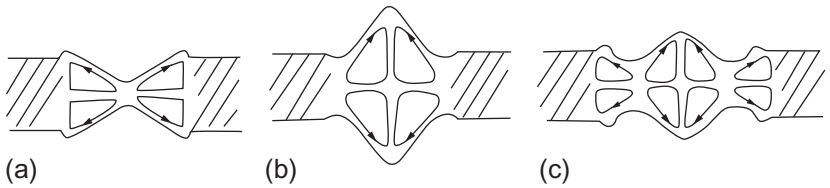


Figure 1.9.7 Flow conditions in the liquid pool in Figure 1.9.6. S content in mass ppm: (a) 20, (b) 100, and (c) 40.

of 0.07%, where the sulfur pick up into the weld pool increased to 30 ppm. The ratio also increases with the concentration of O_2 or CO_2 up to 0.3–0.5%, where the oxygen pick up increased to 200 ppm. However, D/W ratio decreased at the concentration of O_2 or CO_2 larger than 0.5% after the oxide film formation on the surface. Increase of the D/W ratio can be explained with the inward surface flow caused by the positive temperature coefficient of surface tension due to the dissolved sulfur or oxygen. In addition, the oxide film suppresses the surface flow, resulting in the shallow weld penetration under the atmosphere with the excess amount of oxygen.

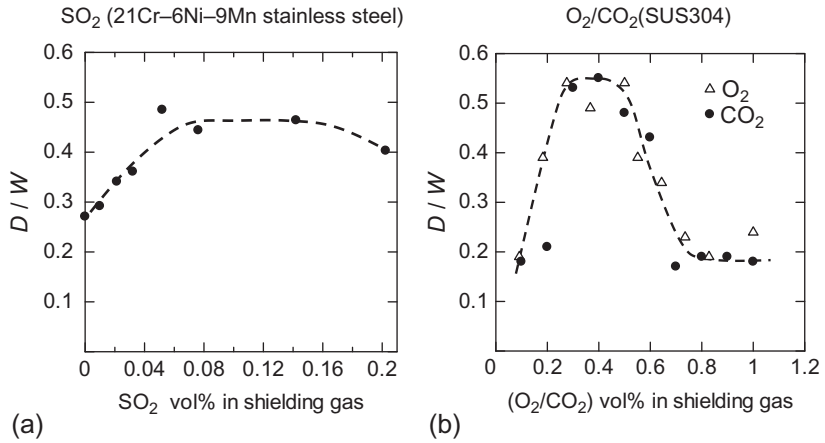


Figure 1.9.8 Effect of SO_2 and O_2/CO_2 in the shielding gas on *D/W* ratio in the weld pool.

The Marangoni effect can be seen when a filler metal is used in welding process such as gas–metal arc welding. The major driving force is difference in the surface tension between filler metal and weld pool (see detail in the literature [10]).

Accordingly, in the welding process, understanding the surface properties of the weld pool combined with the minor element concentrations is indispensable to control the convection in the inside of weld pool.

1.9.2. ENGULFING OF SMALL DROPLETS OF MOLTEN SLAG INTO LIQUID STEEL

As mentioned in Chapters 1.7 and 1.8, this subject has been often investigated so far. The physical or kinematical similarity between high temperature and low temperature systems can only be obtained using dimension free numbers derived using similarity theory, as described in Chapter 1.7. For qualitative visualization of the effect of the interfacial tension on the engulfing of one liquid in the other one some water/oil experiments have been performed. In Figure 1.9.9 [11], the experimental arrangement for investigation of the trapping of liquid oil into liquid water is shown. *J*-type nozzle is equipped just under the interface between oil and water to suck water and oil through the nozzle. The distance between the tip of the nozzle and the interface was measured when oil is sucked for various conditions such as low viscosity of oil and low interfacial tension with surfactant added. The long distance measured under such conditions means that engulfing of oil into water does not occur easily. As shown in the results in Figure 1.9.10 [11], when the interfacial tension decreases with the addition of surfactants, the engulfing occurs easily. In addition to the investigation on the effect of the interfacial tension on the engulfing, the effect of the viscosity of oil was studied to show that the high viscosity of oil prevents the engulfing of oil into water, which is in accordance with results presented in Chapter 1.8 (compare Figure 1.8.1). In the full scale processes, besides of large

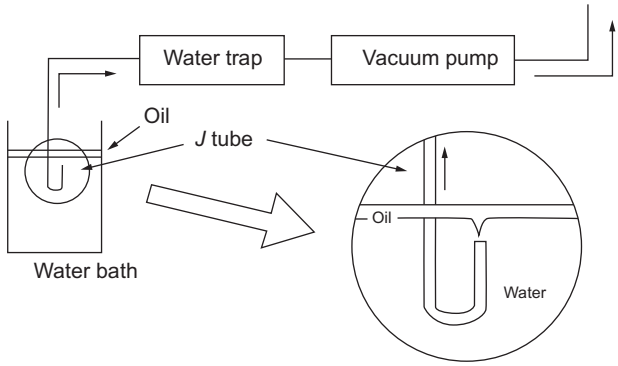


Figure 1.9.9 Experimental apparatus to trap liquid oil into liquid water from the interface between oil and water.

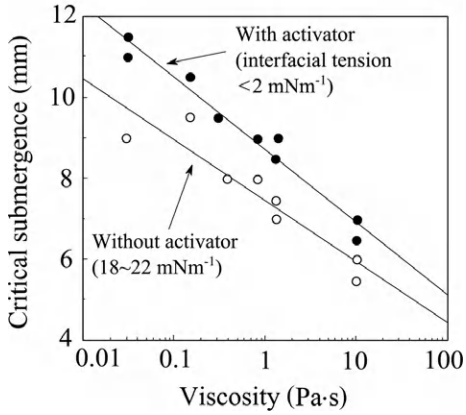


Figure 1.9.10 The effect of viscosity of oil and interfacial tension between oil and water on the trapping of oil into water from the interface.

scale convection, the interfacial convection contributes strongly to the engulfment of slag droplets in steel. The most frequent slag particles found in the industrial continuously cast products are situated near the surface and have a diameter of less than 50 μm. The reason for the engulfment is strong local marangoni flow at the meniscus before the metal solidifies. Samples taken in the industrial continuous casting process show such inclusions, Fig. 1.9.11 [12], which cannot separate from liquid metal in a short time because of their micro size.

1.9.3. EROSION OR DISSOLUTION OF REFRACTORIES

It often appears that refractories are corroded locally at the slag meniscus edge or slag–metal interface in iron- and steelmaking processes. Local corrosion is a significant issue requiring preventive measures to extend the lifetime of refractories. It is affected

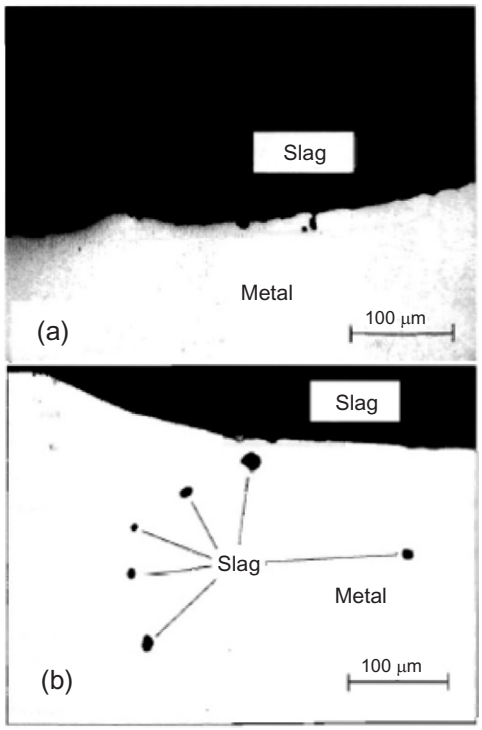


Figure 1.9.11 Interface between metal and casting flux. (a) Deformation metal/slag interface. (b) Slag droplets dispersed in solidified metal.

at least partially by the Marangoni effect with a combination of the dissolution of refractory components into slag or metal.

Although the example of Marangoni flow of slag on SiO_2 material described in Chapter 1.7 is a case of erosion at the interface between refractory and molten slag, actual process accompanies the interface among refractory, molten slag, and liquid metal. In such a case, the following explanation is given to prove the effect of Marangoni flow on the erosion as shown in Figure 1.9.12 which is an example for the system of SiO_2 refractory– ($PbO—SiO_2$) slag–liquid Pb [13]. Molten slag is generally wetted well with solid oxide refractory as well as with liquid metal. On the other hand, liquid metal is not wetted with solid oxide refractory. Then, molten slag penetrates into a small gap between SiO_2 refractory and liquid Pb due to capillary penetration. After the penetration, SiO_2 of the refractory dissolves into molten slag and increases the interfacial tension between solid SiO_2 and molten slag as well as molten slag and liquid Pb. The slag film pulls the molten slag into the gap, but the thickness of the film increases gradually and the capillary effect is weakened. Thus the slag film moves toward the bulk of molten slag. Such repetition of the flow causes the erosion of SiO_2 at the interface among SiO_2 refractory, molten slag, and liquid Pb.

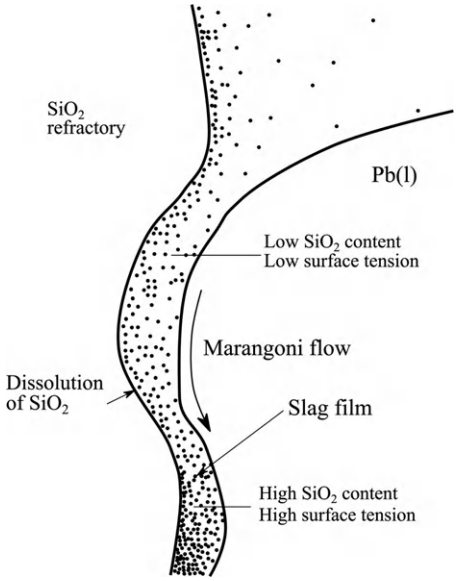


Figure 1.9.12 Explanation for Marangoni flow of molten PbO—SiO_2 slag along the surface of SiO_2 refractory in liquid Pb and molten PbO—SiO_2 slag system.

On the other hand, molten slag of steelmaking process contains SiO_2 and other components, in which SiO_2 decreases the surface tension and the interfacial tension [14]. In such a case, a meniscus is formed at the interface of molten slag with SiO_2 refractory as shown in Figure 1.9.13. As described above, SiO_2 of the refractory dissolves into molten slag to decrease the surface tension of molten slag. Then, there exists the difference of the surface tension along the surface of molten slag; low surface tension at the meniscus and high surface tension at the surface of the bulk of molten slag generate Marangoni flow along the surface.

Actually, alumina–graphite refractory is often used in steelmaking process. In such a case, molten slag penetrates into a gap between the refractory and liquid steel as shown in Figure 1.9.14 [15]. Alumina of the refractory dissolves into molten slag to increase the thickness of the slag film. Simultaneously, the surface of the refractory becomes composed of graphite, which is not wetted well with molten slag. Then, molten slag recedes to the bulk of molten slag. After that, the graphite at the surface of the refractory dissolves into liquid steel and alumina appears again at the surface which is not wetted well with liquid steel. Thus, the penetration of molten slag restarts to repeat the above phenomena. Mukai [16] proposed that those repetitions cause the erosion of the refractory at the interface among refractory, molten slag, and liquid steel.

The square section of the submerged entry nozzle SEN used in the continuous casting process is shown in Figure 1.9.15 [17,18]. The strong erosion at the three phase area, refractory–steel–flux, is clearly visible. In practical process, the corrosion is reduced if

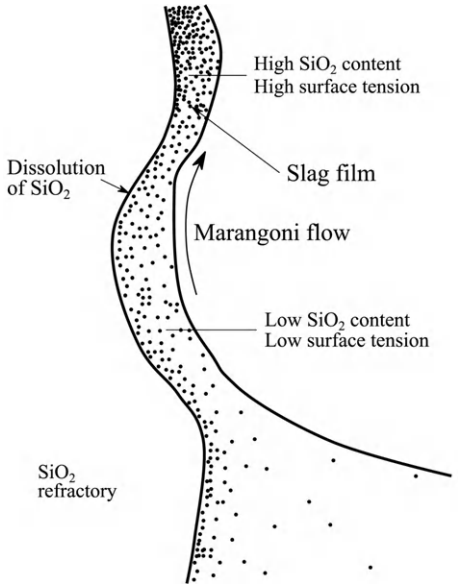


Figure 1.9.13 Explanation for Marangoni flow of molten SiO_2 slag along the surface of SiO_2 refractory in steelmaking process.

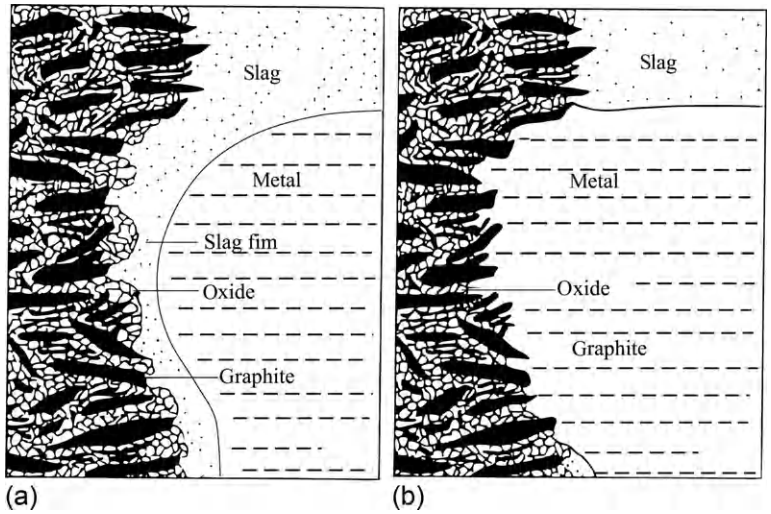


Figure 1.9.14 Explanation for Marangoni flow of molten SiO_2 slag along the surface of Al_2O_3–graphite refractory in steelmaking process.

stable materials such as zirconia are implemented in this area of the SEN. For the safety of the casting process, the immersion depth of the SEN is changed at certain time intervals during casting. In Figure 1.9.16 [18,19], the premature wear and the corrosion groove in three phase areas of both steel–refractory–slag and slag–refractory–air, produced in the

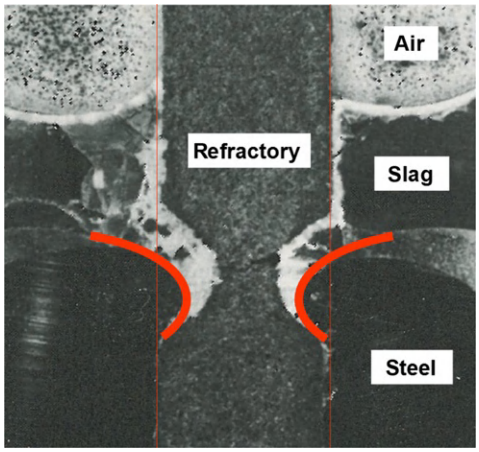


Figure 1.9.15 Corrosion of submerged entry nozzle material in slag/steel at 1650 °C.

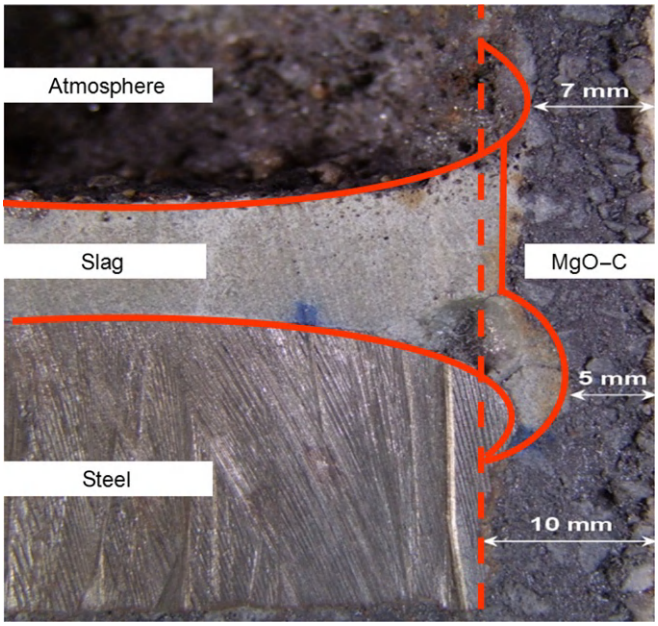


Figure 1.9.16 Square section in the area refractory–steel–slag–air in the induction furnace.

induction furnace are presented. The corrosion rate of different refractories used for lining are plotted in Figure 1.9.17 as a function of chemical driving force defined as the difference of the saturation solubility (c_s) of the refractory oxides in the slag to the starting concentration (c_0) [19]. In this experimental study, the slags of ones employed in the secondary metallurgy were used. The Marangoni convection in the system

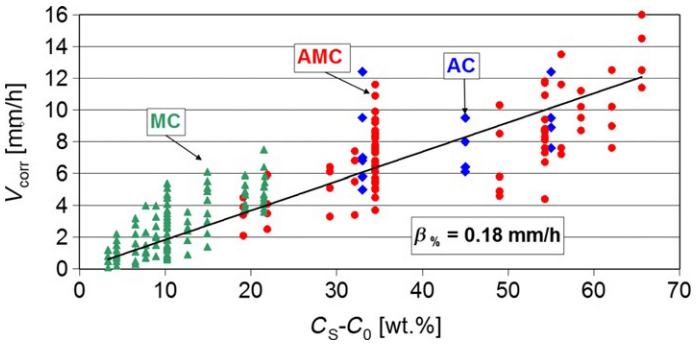


Figure 1.9.17 Corrosion of Al_2O_3—C, MgO—C, and Al_2O_3—MgO—C linings in an laboratory induction furnace (20 kg of steel, 2 kg of slag) at 1550–1650 °C.

alumina–graphite/iron depends strongly on the carbon content of iron: at C-saturation the convection stops [17].

1.9.4. SEPARATION OF METALLIC DROPLETS FROM SLAGS

In the separation technology, the movement caused by electrocapillarity plays an important role. In the copper production, the movement of Cu_2S—FeS droplets in FeO—CaO—Al_2O_3—SiO_2 slag was investigated [20,21]. The results show that the movement direction depends on the chemical composition of droplets and of slag. The positive movement direction toward the anode and the negative toward the cathode is in accordance with the physical flow of electrons. The movement velocity increases with increasing droplet radius, which results in the coalescence with small droplets and further increase of big droplets.

1.9.5. ENGULFING NONMETALLIC INCLUSIONS AND GAS BUBBLES INTO SOLIDIFIED INTERFACE

Generally solid nonmetallic inclusions are not wetted well with liquid steel. Those inclusions and small gas bubbles distributed in liquid steel are sometimes engulfed into the solidification interface and become defects in steel products. Therefore, the behavior of those inclusions and gas bubbles at the interface should be investigated in detail. Mukai *et al.* [22–26] pointed out that those behaviors are related to interfacial properties. Actually, when the gradient of the interfacial tension exists around a gas bubble or a small liquid inclusion, those particles move from a position with higher interfacial tension to other positions with lower interfacial tension. For solid particles such movement is not possible as the adhering liquid layer has still the velocity equal to zero. They follow the general (turbulent) flow in the liquid phase.

Figures 1.9.18–1.9.20 show the results on the behaviors of small gas bubbles at the interface between solid ice and aqueous solution, which was reported by Mukai *et al.* [22–25]. Since solute component NaCl does not work as a surfactant for water, the gradient of the interfacial tension is not generated even when NaCl is enriched at the solidification interface in water. On the other hand, when a strong surfactant, $C_8H_{17}SO_3Na$ (see Figure 1.9.20), is added to water, small concentration gradient of $C_8H_{17}SO_3Na$ occurs in the vicinity of the solidification interface. The large gradient of the interfacial tension is thus generated so that gas bubbles are drawn toward the interface and are engulfed in solid ice (Figure 1.9.19).

The similar phenomenon occurs at the interface between refractory and liquid steel. When Si and C dissolve into liquid steel from the refractory, the concentration gradient of them is formed to decrease the interfacial tension between inclusions and liquid steel.

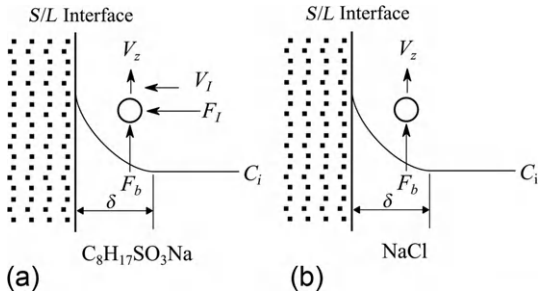


Figure 1.9.18 The effect of Marangoni force on a bubble in liquid aqua solutions just near the interface of solidified phase.

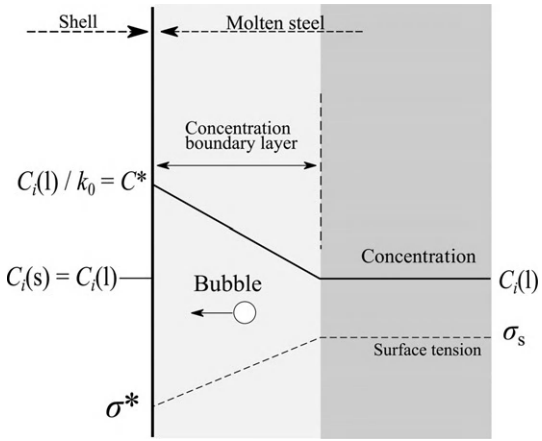


Figure 1.9.19 The effect of Marangoni force on a bubble in liquid aqueous solutions just near the interface of solidified phase for adding surfactant into solution.

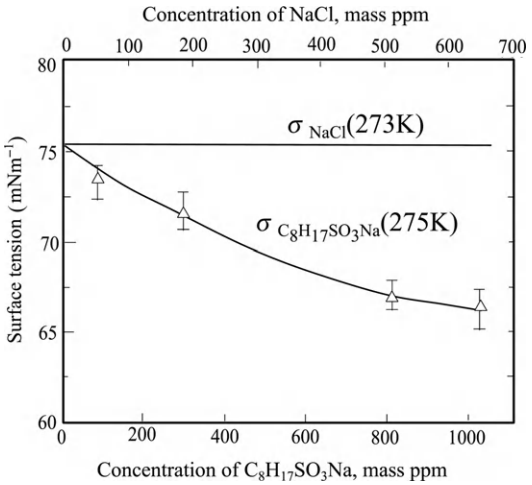


Figure 1.9.20 Change of surface tension of aqueous solutions with NaCl and $C_8H_{17}SO_3Na$ addition.

Mukai *et al.* [25,26] reported that this phenomenon causes the movement of inclusions toward the interface and the accumulation of small inclusions onto the surface of the refractory. If it occurs in SEN nozzle for continuous casting, it may be a cause of nozzle clogging which is one of the serious problems in steelmaking processing. In this solid particle, agglomeration process also other phenomena, as Van der Waals force and electrostatic force can play an important role and should be taken into account.

1.9.6. GAS BUBBLE FORMATION IN LIQUID STEEL

Gas injection into molten metal is an important process to enhance the removal rate of gaseous component from metal by increasing the reaction interface and lead to stirring in the metal. The gas bubble may grow to a certain critical size at the nozzle tip and it will be detached and rise vertically upward due to the buoyancy force. The ascending bubble swarm stirs the liquid steel and increases the mass transfer in the vessel.

The gas bubble size detaching (D_b) at the tip of a submerged nozzle is determined by Equation (1.9.1) [27]

$$D_b = \left(\frac{6 d_o \sigma}{g\left(\rho_l - \rho_g\right)} \right)^{1/3} \tag{1.9.1}$$

where d_o is the nozzle diameter, σ is the surface tension, g is the gravitational acceleration, ρ_l is the density of liquid steel, and ρ_g is the density of gas. Here, the contact angle between liquid steel and the nozzle is assumed 180° (a nonwetting system).

The rising velocity of gas bubbles is determined by balancing the buoyancy force and the drag force. If the bubble size is small enough (less than ~2 mm) and Reynolds number is less than unity, a terminal velocity (u_t) is determined by Stoke's law;

$$u_t = g\left(\frac{D_b^2}{18\mu_l}\right)\left(\rho_l - \rho_g\right) \tag{1.9.2}$$

where μ_l is the viscosity of the liquid steel. As the bubble size increases, the rise velocity becomes greater than the predicted value by Stokes's law.

As the gas flow rate increases considerably, the gas bubble size depends on the gas flow rate. Mori reported that the bubble size (cm) generated at the orifice can be described by Equation (1.9.3) [28]

$$D_b = \left[\left(\frac{6d_o\sigma}{g\left(\rho_l - \rho_g\right)}\right) + 0.0242\left(\dot{V}_g^2 d_o\right)^{0.867}\right]^{1/6} \tag{1.9.3}$$

where $\dot{V}_g$ is gas flow rate (cm^3/s). Then the rising gas velocity (u_b) can be calculated by Equation (1.9.4) [29]:

$$u_b = \left(\frac{2\sigma}{\rho_l D_b} + \frac{1}{2}gD_b\right)^{1/2} \tag{1.9.4}$$

In metallurgical processes, the metal flow is always highly turbulent. Therefore Equation (1.9.1) is not applicable for three reasons: (1) the metal flow is always turbulent, (2) the gas flow rates are always in the jetting and not bubbling region independent on kind of gas introduction, and (3) the gas expansion while entering into the liquid metal is not taken into account. The size of the gas bubbles in the process is then estimated by the surface tension and shear stresses in the turbulent flow [30,31], see Equation (1.8.1) in Chapter 1.8. The ascending velocity of single bubbles in the infinite liquid are different compared to the movement within the bubble swarm. Within the bubble swarm the single bubbles are affected by additional turbulences produced by surrounded bubbles and their movement; their subsequent flow velocity will be smaller compared to that of single bubbles in the infinite liquid. The measurements in the industrial scale show that the average relative ascending velocity of single bubbles (slip velocity) in the center of the bubble swarm are ~37 cm s^{-1} [30,31], Figure 1.9.21. They generate a steady-state recirculation flow in the ladle where flow velocity increases with increasing the flow rate of gas introduced into the liquid steel, Figure 1.9.22. From these data obtained in the industrial process the average equivalent argon-bubble diameter could be estimated to ~2.5 cm in the deoxidized steel melts [30]. The higher oxygen content in the liquid steel, as, e.g., during the converter process, reduces the surface tension and leads finally to

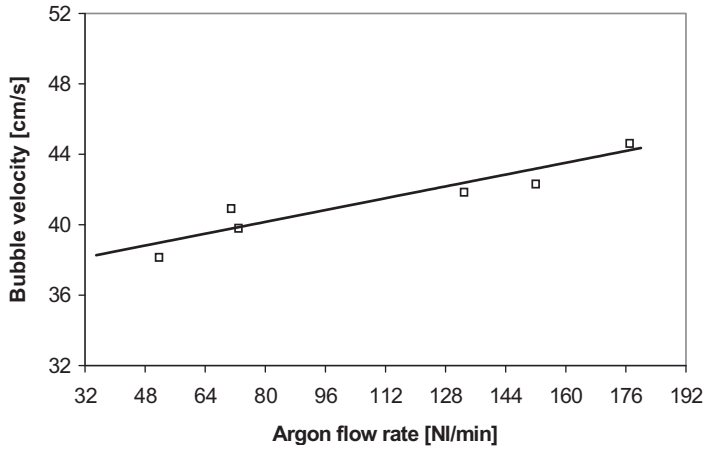


Figure 1.9.21 Ascending velocity of single bubbles within the swarm 30t melts.

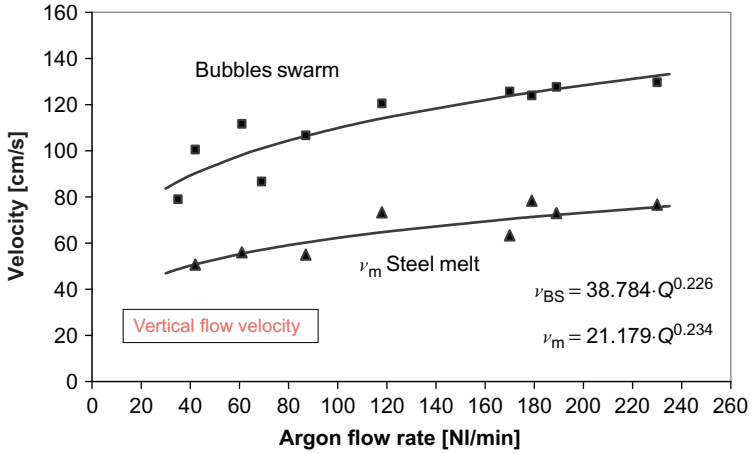


Figure 1.9.22 Ascending velocity of bubble swarm and of steel in the center of the swarm, 30t melts.

the production of smaller (CO) bubbles, Figure 1.9.23 [32]. This situation is convenient for instance if dissolved gases should be removed from the melt [33]. The equivalent bubble diameter is calculated using the dependency [32]:

$$D_b = \left(\frac{3}{C_d \rho_g \rho_l^2}\right)^{1/3} \frac{2\sigma}{U_b^2} \tag{1.9.5}$$

were C_d is the drag coefficient, ρ_g and ρ_l are gas and liquid densities, respectively, σ the surface tension, and U_b is the bubble ascending velocity. ε is the gas hold up within the plume.

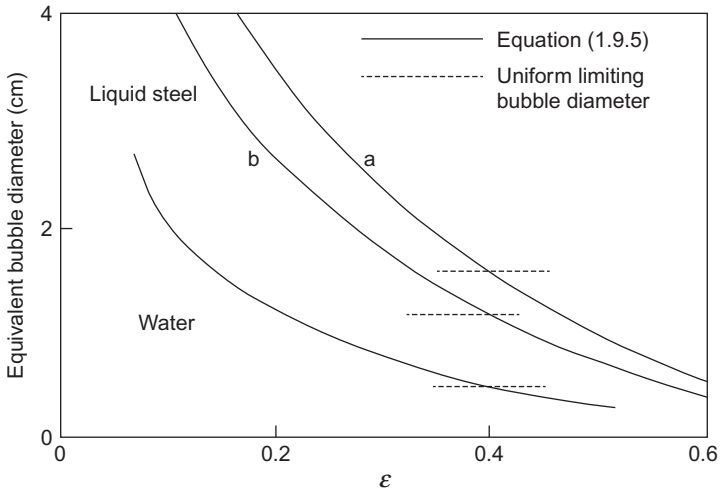


Figure 1.9.23 Calculated bubble diameter for bubble fragmentation mechanism Equation (a-1) compared with uniform limiting diameter at higher *e* values for water and liquid steel; (a) for O <4 ppm and 40 ppm S; (b) for 600 ppm O and 120 ppm S. ε = gas hold up.

1.9.7. NUCLEATION DURING SOLIDIFICATION

Microstructure in metal and alloy products is initially dominated by nucleation during solidification process. The basic theory of homogeneous and inhomogeneous nucleation is given in this section.

According to the classical nucleation theory, the homogeneous steady-state nucleation rate per mole is expressed by Equation (1.9.6) [34–36]

$$I^{\mathrm{st}} = \frac{24Dn^{*2/3}N_A}{\lambda^2}\left(\frac{|\Delta\mu|}{6\pi k_{\mathrm{B}}Tn^*}\right)^{1/2}\exp\left(-\frac{\Delta G^*}{k_{\mathrm{B}}T}\right) \tag{1.9.6}$$

Equation (1.9.6) can be rewritten by Equation (1.9.7) as the steady-state nucleation rate per unit volume

$$I^{\mathrm{st}} = \frac{8n^{*2/3}k_{\mathrm{B}}TN_{\mathrm{A}}}{\pi\lambda^3\eta}\left(\frac{|\Delta\mu|}{6\pi k_{\mathrm{B}}Tn^*}\right)^{1/2}\exp\left(-\frac{\Delta G^*}{k_{\mathrm{B}}T}\right) \tag{1.9.7}$$

where D, n^*, N_{A}, λ, k_{B}, T, $\Delta\mu$, ΔG^*, and η denote the diffusivity, the number of atoms in the critical nucleus, the Avogadro's number, the average atomic jump distance, Boltzmann constant, the temperature, the change in chemical potential per atom for the phase transition (α to β), the work of critical cluster formation, and the viscosity.

When a spherical nucleus is assumed, the Gibbs energy change to form a cluster of radius r can be described by Equation (1.9.8) [37].

$$\Delta G = G(r=r) - G(r=0) = \frac{4}{3}\pi r^3 \frac{\Delta\mu}{\bar{\nu}} + 4\pi r^2 \sigma_{\alpha\beta} \tag{1.9.8}$$

where $\bar{\nu}$ and $\sigma_{\alpha\beta}$ are the average atomic volume and the α–β interfacial tension. Figure 1.9.24 shows a schematic illustration of the Gibbs energy change with respect to the cluster size [37]. The critical radius r^* and the work of critical cluster formation ΔG^* are then determined at $\partial \Delta G/\partial r = 0$.

$$r^* = -\frac{2\sigma_{\alpha\beta}}{\Delta\mu/\bar{\nu}} \tag{1.9.9}$$

$$\Delta G^* = \frac{16\pi\sigma_{\alpha\beta}^3}{3(\Delta\mu_{l\to s}/\bar{\nu})^2} \tag{1.9.10}$$

In many practical applications, contact with other impurities such as inclusions or refractory materials are inevitable. These impurities may play a role as a heterogeneous nucleation site. If we consider a heterogeneous nucleation of a new phase β from phase α on the surface of phase N, the Gibbs energy change can be expressed by Equation (1.9.11) [38]:

$$\Delta G = G(r=r) - G(r=0) = \left\{\frac{4}{3}\pi r^3 \frac{\Delta\mu_{l\to s}}{\bar{\nu}} + 4\pi r^2 \sigma_{\alpha\beta}\right\} f(\phi) \tag{1.9.11}$$

where the volume ratio between a heterogeneous nucleus and a homogeneous one with the same radius of curvature r is given by Equation (1.9.12), see Figure 1.9.25

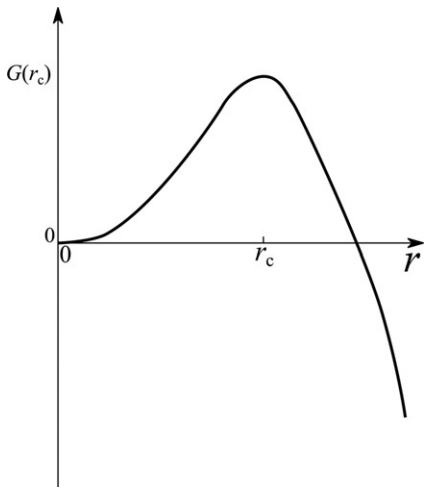


Figure 1.9.24 Schematic illustration of the Gibbs energy change with respect to the cluster size.

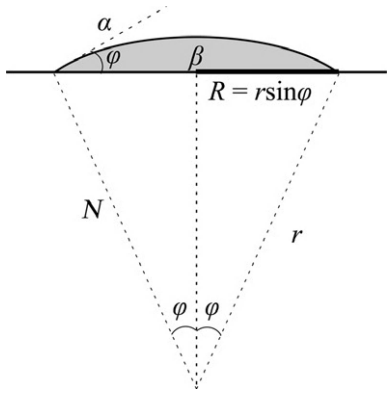


Figure 1.9.25 A spherical embryo has a lateral radius, where *r* is the radius of curvature of the α–β interface.

$$f(\phi) = \frac{(2 - 3\cos\phi + \cos^3\phi)}{4} \tag{1.9.12}$$

Likely, the area of the α–β interface of the heterogeneous nucleus can be obtained by multiplying the area factor expressed by Equation (1.9.13) by the surface area of a homogeneous nucleus.

$$\alpha(\phi) = \frac{(1 - \cos\phi)}{2} \tag{1.9.13}$$

At $\partial \Delta G/\partial r = 0$, the critical radius and the work of critical cluster formation are determined. The critical radius r^* is the same as the homogeneous nucleation, but the work of critical cluster formation ΔG^* is given by

$$r^* = -\frac{2\sigma_{\alpha\beta}}{\Delta\mu_{l\to s}/\bar{v}} \tag{1.9.14}$$

$$\Delta G^* = \frac{16\pi\sigma_{\alpha\beta}^3}{3(\Delta\mu_{l\to s}/\bar{v})^2} f(\phi) \tag{1.9.15}$$

Generally, the nucleation rate of a homogeneous nucleus, Equation 1.9.6 or 1.9.7 is simply expressed by Equation (1.9.16):

$$I^{st} = A^* \exp\left(\frac{-\Delta G^*}{k_B T}\right) \tag{1.9.16}$$

The heterogeneous steady-state nucleation rate is closely related to the homogeneous one

$$I_{\text{het}}^{\text{st}} = A^* \frac{N_S}{N_V} \frac{\alpha(\phi)}{\sqrt{f(\phi)}} \exp\left(-\frac{\Delta G^*}{k_B T} f(\phi)\right) \tag{1.9.17}$$

where N_s and N_v are the number of excess surface atoms in contact with substrate per unit area of original phase and the number of molecules per unit volume. The term $\alpha(\phi)/\sqrt{f(\phi)}$ is almost unity except for small angles less than 10°.

1.9.8. SLAG FOAMING

When the gas evolution is extensive, slag foaming can occur. In order to evaluate the foaminess of molten slag, Ito and Fruehan first suggested the foam index, which is defined as the average traveling time of the gas in the foam [39]

$$\Sigma = \frac{H_f}{V_g^s} \tag{1.9.18}$$

where H_f is the foam height and $V_g{}^s$ is the superficial gas velocity. Jiang and Fruehan considered that the foaminess is determined by balancing the effects of surface tension and viscosity [40]. From the dimensionless analysis with experimental data, Zhang and Fruehan reported that the foam index is described by Equation (1.9.19) [41]:

$$\Sigma = 1.83 \frac{\mu^{1.2}}{\sigma^{0.2} \rho D_b^{0.9}} \tag{1.9.19}$$

where μ is the viscosity, σ is the surface tension, ρ is the density of the molten slag, and D_b is the diameter of the foam bubbles. In many practical cases, slag foaming occurs as a result of the reduction of FeO in the slag by carbonaceous particles. In such applications, the exact mechanisms have not been elucidated yet due to the existence of carbonaceous particles in the molten slag.

The above examples show that the understanding of interfacial properties and phenomena is a key to cope with various problems in high temperature metallurgical processing and give the wide field for future research.

REFERENCES

[1] P.R. Scheller, in: Proc. Int. Congress Stainless Steel ´96, 3-5 June 1996, Düsseldorf/Neuss, 1996, pp. 73–78.
[2] S.I. Popel, B.V. Tsarevskii, V.V. Pavlov, E.L. Furman, Iszvestiia Nauk SSSR (1975) 54–58.
[3] P.R. Scheller, R.F. Brooks, K.C. Mills, Welding J. Res. Suppl. 74 (2) (1995) 69s–75s.
[4] A.A. Shirali, K.C. Mills, Welding J. 72 (1993) 347s–352s.
[5] K. Ishizaki, N. Araki, H. Murai, J. Jpn. Welding Soc. 34 (1960) 146s–153s.
[6] C.R. Heiple, J.R. Roper, Welding J. 61 (1982) 97s–102s.
[7] P.R. Scheller, Steel Res. 72 (3) (2001) 76–80.
[8] C.R. Heiple, P. Burgardt, Welding J. 64 (1985), 159s-162s.
[9] S. Lu, H. Fujii, K. Nogi, Mater. Sci. Eng., A 380 (2004) 290–297.

[10] T. Takasu, J.M. Toguri, Philos. Trans. R. Soc. B 356 (1998) 967–980.
[11] K. Watanabe, K. Tsutsumi, M. Suzuki, M. Nakada, T. Shiomi, ISIJ Int. 49 (2009) 1161–1169.
[12] P.R. Scheller, Ironmaking and Steelmaking 29 (2) (2002), 154–160.
[13] K. Mukai, T. Masuda, K. Gouda, T. Harada, J. Yoshitomi, S. Fujimoto, J. Jpn. Inst. Met. 48 (1984) 726–734.
[14] Z. Yu, K. Mukai, J. Jpn. Inst. Met. 56 (1992) 1137–1144.
[15] K. Mukai, J.M. Toguri, J. Yoshitomi, Can. Metall. Q. 25 (1986) 265–275.
[16] K. Mukai, Philos. Trans. R. Soc. Lond. 365 (1998) 1015–1026.
[17] F. Hauck, J. Pötschke, Arch. Eisenhüttenw. 53 (1982) 133–138.
[18] J. Pötschke, C. Brüggmann, Steel Res. Int. 83 (2012) 637–644.
[19] J. Pötschke, T. Deinet, The Corrosion of AMC—Refractories by Steel and Slag, UNITECR—2005—Congress, Orlando, USA, 2005, pp. 75–79.
[20] R.T. Choo, A. Warczock, J.M. Toguri, Copper (91, IV), pp 409–424.
[21] R. Kammel, Erzmetall 27 (1974) 135–144.
[22] K. Mukai, W. Lin, Tetsu-to-Hagane 80 (1994) 527–532.
[23] K. Mukai, W. Lin, Tetsu-to-Hagane 80 (1994) 533–538.
[24] Z. Wang, K. Mukai, I.J. Lee, ISIJ Int. 39 (1999) 553–562.
[25] K. Mukai, M. Zeze, Steel Res. Int. 74 (2003) 131.
[26] T. Matsushita, K. Mukai, M. Zeze, ISIJ Int. 53 (2013) 18–26.
[27] B. Deo, R. Boom, Fundamentals of Steelmaking Metallurgy, Prentice Hall Int, New York, 1993, pp. 3–10.
[28] K. Mori, Trans. Iron Steel Inst. Jpn 28 (1988) 246–261.
[29] H.D. Mendelson, Am. Inst. Chem. Eng. J. 13 (1967) 250–253.
[30] E. Steinmetz, P.R. Scheller, Stahl. Eisen 9 (1987) 57–65.
[31] P.R. Scheller, in: Proc. R.I.L. Guthrie Honorary Symposium Proc., June 6–9, 2011, Montreal, Canada, 2011, pp. 424–428.
[32] E.T. Turkdogan, Fundamentals of Steelmaking, (1996).
[33] P.R. Scheller, E. Steinmetz, in: Proc. 2nd Int. Congr. On the Sci. &Technol. of Steelm., ICS 2001, 10-11 April 2001, Univ. of Swansea, UK, 2001, pp. 197–206.
[34] K.F. Kelton, A.L. Greer, Nucleation in Condensed Matter—Application in Materials and Biology, Elsevier, Oxford, UK, 2010, pp. 19–83.
[35] G.W. Lee, A.K. Gangopadhyay, T.K. Croat, T.J. Rathz, R.W. Hyers, J.R. Rogers, K.F. Kelton, Phys. Rev. B 72 (2005) 174107.
[36] J. Lee, K. Sim, Calphad (2013). http://dx.doi.org/10.1016/j.calphad.2013.07.008.
[37] C.H.P. Lupis, Chemical Thermodynamics of Materials, North-Holland, Amsterdam, 1983, p. 94.
[38] K.F. Kelton, A.L. Greer, Nucleation in Condensed Matter—Application in Materials and Biology, Elsevier, Oxford, UK, 2010, pp. 165–226.
[39] K. Ito, R.J. Fruehan, Metall. Trans. B 20 (1989) 509–521.
[40] R. Jiang, R.J. Fruehan, Metall. Trans. B 22 (1991) 481–489.
[41] Y. Zhang, R.J. Fruehan, Metall. Trans. B 26 (1995) 803–812.



CHAPTER 2

Metallurgical Process Phenomena

Richard J. Fruehan and P. Chris Pistorius
Center for Iron and Steelmaking Research, Carnegie Mellon University

Contents

2.1. The importance of metallurgical process phenomena 142
2.2. Kinetics of gas-liquid and liquid-liquid reactions 143
2.3. Bubbles in process metallurgy 179
2.4. Foams and foaming 197
2.5. Applications 217

CHAPTER 2.1

The Importance of Metallurgical Process Phenomena

P. Chris Pistorius
Center for Iron and Steelmaking Research, Carnegie Mellon University

The rather broad concept of "metallurgical process phenomena" here has a quite specific meaning, namely the kinetics of fluid-based (gas–liquid and liquid–liquid) reactions, with an emphasis on the effects of gas flow. In many process metallurgy reactions, gas is a reagent or product; additional gas is often added as diluent or to stir the system. Argon well suited to this purpose: it has very low solubility in condensed phases, is inert, and makes up approximately 1% of the earth's atmosphere.

This chapter first summarizes the relevant kinetic principles, reviews both bubble formation by gas injection into liquid metal and slag foaming, and finally presents five process examples to illustrate the kinetic principles. These examples reflect our particular interests in ferrous pyrometallurgy, but should be of interest to process metallurgists generally.

Reactions in process metallurgy are manipulated in several fundamental ways. The following affect reaction *equilibria*:

- Temperature
- Redox conditions (e.g., concentrations of reducible species such as the FeO content of slag, or of reactive elements—deoxidizers—dissolved in liquid metal)
- Activity and activity coefficients of species dissolved in slag (affected by slag basicity)
- Mass balance (e.g., the relative masses of slag and metal)
- Gas phase: change in total pressure; dilution with an inert gas

These all affect the *equilibrium* state of reactions. This chapter considers some of the reaction steps which affect *rates*. Reaction kinetics is manipulated by stirring, particle size and porosity (gas–solid reactions), heat transfer rate, reactor size and shape, and fluid flow.

These multiple equilibrium and kinetics factors offer several ways of achieving desired process outcomes; they also constitute a list of those variables which must be controlled or known to ensure stable and predictable production.

Treatise on Process Metallurgy, Volume 2
http://dx.doi.org/10.1016/B978-0-08-096984-8.00019-7
© 2014 Elsevier Ltd.
All rights reserved.

CHAPTER 2.2

Kinetics of Gas–Liquid and Liquid–Liquid Reactions

Richard J. Fruehan
Center for Iron and Steelmaking Research, Carnegie Mellon University

2.2.1. INTRODUCTION

In many metallurgical processes, equilibrium is not achieved because one or more of the reactions involved are relatively slow. In this section, the rates of chemical reactions are examined. In particular, gas–liquid and liquid–liquid reactions are examined; gas–solid reactions are discussed in detail in Chapter 4 in Volume 1. In this section, the concept of the rate-controlling process is reviewed. The processes considered are gas-phase mass transfer (GPMT), liquid-phase mass transfer (LPMT), and heat transfer and chemical kinetics at the surface. For chemical kinetics, the critical rate-controlling step for the chemical reaction is examined. In addition, mixed control by two of more of the above processes, parallel reactions, and the role of gaseous intermediates are discussed.

2.2.2. RATE-CONTROLLING PROCESS

Most metallurgical reactions occur at surfaces between phases. For example, reactions involving gas–solid, gas–liquid, or liquid–liquid phases occur at the interface. Consider the following reaction that is occurring at the surface between a condensed phase (solid or liquid) and a gas phase as shown in Figure 2.2.1

$$\mathrm{A(g)} + \mathrm{B(c)} = \mathrm{C(g)} + \mathrm{D(c)} \tag{2.2.1}$$

where (g) and (c) represent the gas and condensed phases, respectively. Assuming the reactions have a positive heat of reaction (ΔH), the rate of the reaction can be controlled by:

(1) GPMT of A gas to the surface.
(2) LPMT of B in solution to the surface.
(3) Chemical kinetics of the reaction at the surface.
(4) Heat transfer through the gas or condensed phases that is required for the reaction.
(5) GPMT of C gas away from the surface.
(6) LPMT of D in solution away from the surface.

Treatise on Process Metallurgy, Volume 2
http://dx.doi.org/10.1016/B978-0-08-096984-8.00001-X
© 2014 Elsevier Ltd.
All rights reserved.

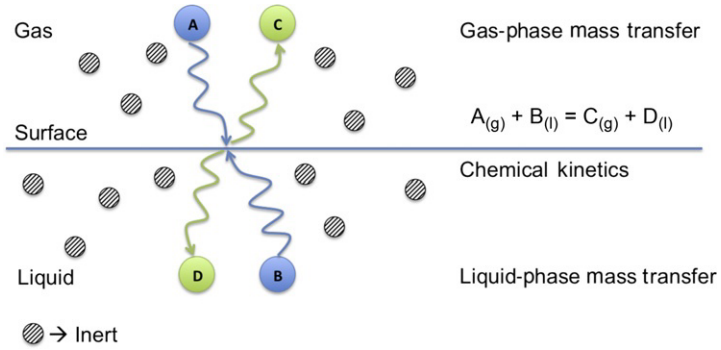


Figure 2.2.1 Schematic diagram indicating possible rate-controlling processes.

If one of the above processes is considerably slower that the others, then that is the rate-controlling process. If this is the case, the rate can be computed from the rate equations for the individual process. However, in general, simultaneous mass transfer to and from the surface is occurring. Also, very often if the rates of the individual processes are similar, there can be a "mixed control" of two of more processes. For example, GPMT and chemical kinetics could be jointly controlling the rate. Mixed control will be discussed later in this chapter.

For gas–liquid and liquid–liquid reaction, it is possible to state Rules (1) and (2):

1. If one process is significantly slower than any of the other possible processes, that process is controlling and it determines the rate of the reaction.
2. If one process is considerably slower than the other processes, the other processes are fast and close to equilibrium. For example, if the rate is controlled by GPMT, the reaction at the surface will be at equilibrium for the surface concentrations. Conversely, if the rate is controlled by chemical kinetics at the surface, the surface concentrations and bulk concentrations are equal.

2.2.3. THE DIFFERENCE BETWEEN THERMODYNAMICS AND KINETICS

Thermodynamics determines if a reaction can occur but not how fast. For a reaction to occur, the free energy change (ΔG) must be negative. Thermodynamic equilibrium helps determine the driving force for a reaction, defined as the difference between the instantaneous condition and equilibrium condition. However, the driving force alone does not define the rate of a reaction.

Consider the oxidation of iron by oxygen

$$\mathrm{Fe} + \frac{1}{2}\mathrm{O_2} = \mathrm{FeO} \tag{2.2.2}$$

The ΔG of the reaction is more negative at low temperature than at high temperature, but in general the rate is slower at lower temperatures due to kinetics limitation.

Comparing the thermodynamics for the oxidation of iron and nickel at low oxygen pressures, the free energy for iron oxidation is considerably more negative.

$$\mathrm{Ni} + \frac{1}{2}\mathrm{O_2} = \mathrm{NiO} \tag{2.2.3}$$

However, the initial rate of both reactions at oxygen pressures much greater than the equilibrium will be controlled by GPMT of oxygen and will be nearly the same at a given oxygen pressure.

The enthalpy change (ΔH) of a reaction defines the amount of heat given off or required by the reaction. It therefore defines the heat required to sustain the reaction, but if the rate is controlled by another slower process ΔH does not affect the rate of the reactions.

Therefore, whereas the thermodynamics determines if a reaction will occur and takes part in defining the driving force for the reaction, it does not indicate how fast the reaction will occur.

2.2.4. GAS-PHASE MASS TRANSFER

2.2.4.1. Flux Equations

For many reactions in metallurgical processes and laboratory experiments, GPMT plays a major role. In most cases, it is mass transfer through a boundary layer at the surface of the condensed phase with a turbulent well-mixed gas in the bulk gas as illustrated in Figure 2.2.2. Consider the simple reaction in which A reacts at the surface to produce B in an inert gas (I)

$$\mathrm{A(g)} = \mathrm{B(g)} \tag{2.2.4}$$

A and B are used as a simplification to indicate different species.

A(g) diffuses through the boundary layer and reacts to produce B(g) which is transferred into the bulk gas. In this case, the reaction is equimolar meaning for each mole of A reacting, 1 mol of B is produced. In this case, there is no mass transfer due to bulk flow. The more general case with bulk gas flow will be discussed later.

In this case, Fick's First Law can be applied.

$$J_\mathrm{A} = D_\mathrm{A}\frac{\partial C_\mathrm{A}}{\partial Z} \tag{2.2.5}$$

where J_A = flux of A

D_A = diffusivity of A in the gas

C_A = concentration of A

Z = the flux direction

With boundary layer diffusion, a steady state is quickly developed and the flux is given by

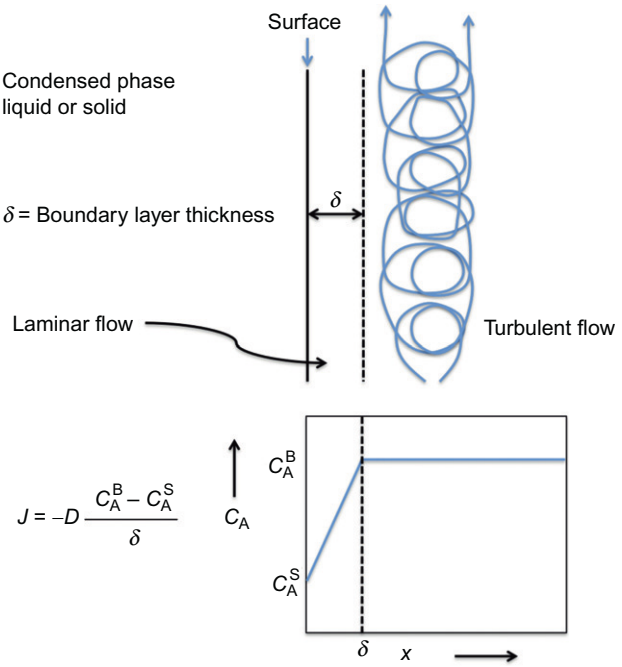


Figure 2.2.2 Schematic diagram illustrating gas-phase mass transfer through a boundary layer.

$$J_A = -D_A \frac{\left(C_A^B - C_A^S\right)}{\delta} \tag{2.2.6}$$

where C_A^B and C_A^S are the concentrations of A in the bulk gas and on the surface, respectively, and δ is the boundary layer thickness. Assuming an ideal gas and the units given below, it follows that

$$J_A\left(\text{moles m}^{-2}\text{s}^{-1}\right) = -\frac{k_g^A\left(\text{ms}^{-1}\right)\left(p_A^B - p_A^S\right)}{RT} \tag{2.2.7}$$

where p_A^B and p_A^S are the bulk and surface pressure of A, R is the gas constant, and k_g^A is the average mass transfer coefficient of A in the gas to the surface. Using film theory to approximately represent the transport through the boundary layer, the mass transfer coefficient is given by (2.2.8).

$$k_g^A = \frac{D_A}{\delta} \tag{2.2.8}$$

It is also possible to transfer component A with the bulk flow of gas due to the reaction. In general, the flux of A is given by

$$J_A = -D_A \frac{\partial C_A}{\partial Z} + \sum J_i C_A \tag{2.2.9}$$

The second term in Equation (2.2.9) is often referred to as the bulk flow term. The reaction given by (2.2.2) is an equimolar reaction, there is no bulk flow of gas, the bulk flow term is zero, and Equation (2.2.7) is valid. If the reaction is not equimolar, the bulk flow contributes to the mass transfer. Consider the following reaction

$$A(g) = 2B(g) \tag{2.2.10}$$

From the stoichiometry of the reactions

$$J_A = -2J_B \tag{2.2.11}$$

$$J_A = D_A \frac{\partial C_A}{\partial Z} + J_A C_A \tag{2.2.12}$$

For an ideal gas using film theory, it follows that

$$J_A = \frac{k_g^A}{RT} \mathrm{In} \left| \frac{1 + p_A^B}{1 + p_A^S} \right| \tag{2.2.13}$$

If the reacting gas A is dilute, Equation (2.2.13) is approximately the same as Equation (2.2.7). Therefore, the bulk flow term can be neglected for an equimolar reaction or a dilute reaction gas.

2.2.4.2. Properties of Gases and Mass Transfer Coefficient Relationships

Diffusivities in gases are much greater than for condensed phases. Diffusivities vary greatly and are functions of temperature. Typical ranges of values are given for solids, liquids, and gases below.

Solids	$10^{-14} - 10^{-9}$	$m^2 s^{-1}$
Liquids	$10^{-9} - 10^{-7}$	$m^2 s^{-1}$
Gases	$10^{-5} - 10^{-3}$	$m^2 s^{-1}$

Whereas it is not possible to accurately calculate diffusivities in condensed phases, it is possible to estimate those for gases from the kinetic theory of gases. The details of their calculations and the required parameters are given elsewhere [1]. For example, interdiffusivity of a binary gas of components (1) and (2) is given by

$$D_{12} = 1.585 \times 10^{-7} \frac{T^{3/2}}{P \sigma_{12}^2 \Omega} \left(\frac{1}{M_1} + \frac{1}{M_2} \right)^{1/2} \tag{2.2.14}$$

where D_{12} = the interdiffusivity of gases 1 and 2 ($m^2\ s^{-1}$)

P = total pressure

σ_{12} = collision diameter related to the size of the molecules

Ω = the collision integral related to the frequency of collisions
M_1 and M_2 = molecular weight of components (1) and (2)
Similar type expressions exist for viscosity and thermal conductivity [2,3].

2.2.4.3. Mass Transfer Correlation Relationships

Correlations have been developed to predict the mass transfer coefficient from the properties of the gas and the gas flow conditions using dimensional analysis. Primarily using the following dimensionless numbers, the mass transfer coefficient can be estimated for several geometries.

$$Re = \frac{ud}{\nu} \tag{2.2.15}$$

$$Sc = \frac{\nu}{D} \tag{2.2.16}$$

$$Sh = \frac{k_G d}{D} \tag{2.2.17}$$

The Reynolds's number (Re) is related to the flow conditions, the Schmidt number (Sc) is related to the flow conditions, and the Sherwood number (Sh) is related to the mass transfer coefficient. For a range of conditions and geometries, correlations or relationships have been developed relating primarily to these three numbers. For some common geometries, the following relationships have been developed.

Flow around a sphere (Ranz-Marshall equation)

$$Sh = \left(2 + 0.6 Re^{1/2} Sc^{1/3}\right) \tag{2.2.18}$$

Flow over a flat plate:

$$Sh = 0.664 Sc^{1/3} Re^{1/2} \tag{2.2.19}$$

In this case, the characteristic dimension d is the length of the plate in the direction of flow. Also, this relationship is only valid at high values of Re since it does not have a term for zero flow as does (2.2.18). Therefore, sometimes this expression underpredicts the mass transfer coefficient.

Gas jet impinging perpendicular to the surface

$$Sh = 0.4 \left(\frac{d}{r}\right) Re^{2/3} Sc^{1/3} \tag{2.2.20}$$

In this case, d is the diameter of the jet at its nozzle and r is the radius of the condensed phase.

Details of the correlations given above, correlations for other geometries, and those for heat transfer are given in more detail elsewhere [2,3].

Whereas the GPMT coefficient (k_G) depends on gas properties and flow conditions, there are some typical ranges of values. At 1873 K for common gases (CO, CO_2, N_2, Cl_2, HCl, Ar, etc.), the value of k_G for a sphere or flat plate is on the order of 0.02–0.1 m s^{-1} and 0.5–2 m s^{-1} for a gas jet. For lighter gases such as H_2 and He, the values are three to five times higher.

2.2.4.4. Characteristics of GPMT-Controlled Reactions

GPMT-controlled reactions uniquely depend on the following variables.

1. The gas velocity: In general, the rate increases with gas velocity because it increases the Reynolds number (*Re*) and therefore k_G increases.
2. Type of dilution gas: Often, the reacting gas is diluted with inert gas such as Ar, He, or N_2. The diffusivity is significantly higher when He or a light gas is used and hence the rate increases.
3. The geometry of the condensed phase: In general, the mass transfer coefficient increases with a decrease in the size of the condensed phase and hence the rate per unit area increases.

Whereas the value of the mass transfer coefficient increases only slowly with temperature (roughly proportional to $T^{3/2}$ from Equation 2.2.14), the rate of reaction may increase greatly with temperature. For example, if the rate is controlled by transfer of the product gas away from the sample, its pressure can increase significantly with temperature and hence the driving force and reaction rate increase.

2.2.4.5. Examples of GPMT

Consider the reaction of Cl_2 with nickel from about 1100 to 1240 K

$$\mathrm{Ni} + \mathrm{Cl_2} = \mathrm{NiCl_2(g)} \tag{2.2.21}$$

This reaction was examined using small Ni plates ($2.5 \times 1.0 \times 0.1$ cm), Ar–Cl_2, and He–Cl_2 gas mixtures and a conventional weight loss technique [4]. It was found that the rate was proportional to the pressure of Cl_2 and not a strong function of temperature (Figure 2.2.3). The rate was faster when He was used as dilution gas. The rate for transfer of Cl_2 to the surface was computed using equations and was found to be slightly higher (25%) than the calculated rate. This was assumed to be because Equation (2.2.19) slightly underpredicts the rate for the conditions used (i.e., relatively low *Re* numbers).

At lower temperatures, the experimental evidence showed that a thin layer of $NiCl_2$ formed on the surface and then it vaporized. In this case, the rate was controlled by transport of $NiCl_2$ gas away from the surface and the flux equation is given by

$$J_{\mathrm{NiCl_2}} = \frac{k_g^{\mathrm{NiCl_2}}}{RT} p_{\mathrm{NiCl_2}}^{S} \tag{2.2.22}$$

Since it assumed the rate is controlled by mass transfer, the vaporization reaction at the surface is close to equilibrium and the surface pressure of $NiCl_2$ is the equilibrium

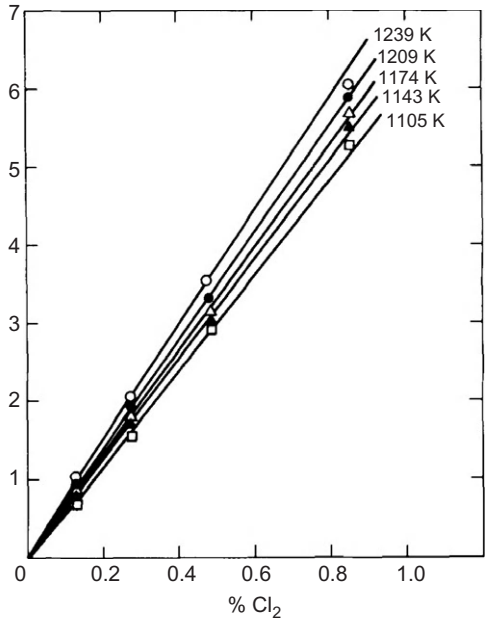


Figure 2.2.3 The rate of reaction of Cl_2 with Ni at higher temperatures (115–1229 K) indicating the rate is controlled by mass transfer (Fruehan and Martonik [4]).

vapor pressure of $NiCl_2$ at the given temperature. In this case, the rate is a strong function of temperature even though the rate is controlled by GPMT (Figure 2.2.4). Specifically, the mass transfer coefficient $\left(k_g^{NiCl_2}\right)$ does not increase rapidly with temperature but the pressure of $NiCl_2$ does. The rate increases with gas velocity because the Reynolds number and hence the mass transfer coefficient increase. The rate increases rapidly with temperature because the equilibrium vapor pressure of $NiCl_2$ increases. The computed rate agreed with the measured rate.

If the temperature dependence of the rate is examined in the usual manner using the following relationship

$$\frac{d\ln(\text{rate})}{d\left(\frac{1}{T}\right)} = -\frac{\text{“}Q\text{”}}{R} \tag{2.2.23}$$

where “Q” is often referred to as the apparent activation energy, in this case, “Q” would be approximately equal to the heat of vaporization of $NiCl_2\left(\Delta H^v_{NiCl_2}\right)$ since the temperature dependence of the pressure of $NiCl_2$ is

$$\frac{d\ln p_{NiCl_2}}{d\left(\frac{1}{T}\right)} = -\frac{\Delta H^v_{NiCl_2}}{R} \tag{2.2.24}$$

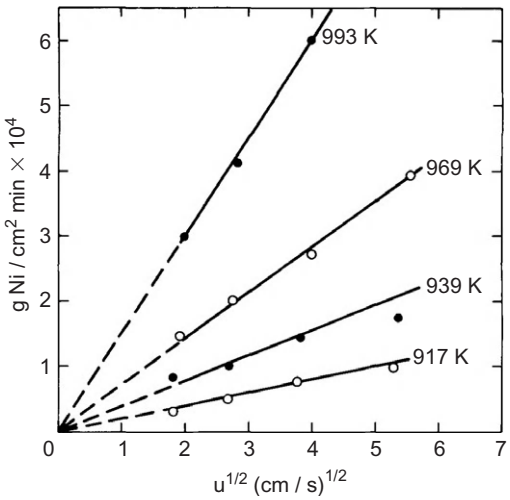


Figure 2.2.4 The rate of reaction of Cl_2 with nickel at low temperature (917–993 K) indicating the rate is controlled by vaporization of $NiCl_2$ from the surface which is a function of temperature and gas velocity (Fruehan and Martonik [4]).

It should be noted "Q" is not the chemical kinetic activation energy as discussed later, but simply the temperature dependence of the rate.

At higher temperatures, $NiCl_2$ solid does not form but rather reaction (2.2.21) occurs. The driving force for the reaction is the equilibrium pressure of $NiCl_2$ for the reaction. In this case, the temperature dependence ("Q") of the rate determined by Equation (2.2.23) is one half of the heat of reaction. This is because thermodynamics indicates that the pressure of $NiCl_2$ is proportional to $K^{1/2}$ and the following thermodynamic relationship holds

$$\frac{d\left(\ln K^{1/2}\right)}{d(1/T)} = -\frac{\Delta H^{o}}{2R} \tag{2.2.25}$$

where ΔH is enthalpy of reaction (2.2.21).

2.2.4.6. Coupled Mass Transfer

In general for GPMT, both transport to the surface and away from the surface should be considered. For example, consider the reaction of nickel with HCl in Ar [5]. The pressures are all low and the bulk flow term can be neglected.

$$Ni + 2HCl = NiCl_2(g) + H_2 \tag{2.2.26}$$

The three fluxes are given by

$$J_{HCl} = \frac{k_g^{HCl}}{RT}\left(p_{HCl} - p_{HCl}^{S}\right) \tag{2.2.27}$$

$$J_{H_2} = \frac{k_g^{H_2}}{RT}\left(p_{H_2}^S\right) \tag{2.2.28}$$

$$J_{NiCl_2} = \frac{k_g^{NiCl_2}}{RT}\left(p_{NiCl_2}^S\right) \tag{2.2.29}$$

There are six unknowns, the three pressures and the three fluxes. However, there are three more valid relationships. First, there are two relationships between the fluxes

$$J_{H_2} = J_{NiCl_2} \tag{2.2.30}$$

$$J_{NiCl_2} = -\frac{1}{2}J_{HCl} \tag{2.2.31}$$

Also since the rate is controlled by GPMT, the chemical reaction at the surface is at equilibrium

$$K = \frac{P_{NiCl_2}^S P_{H_2}^S}{\left(P_{HCl}^S\right)^2} \tag{2.2.32}$$

where K is the equilibrium constant for reaction (2.2.26)

This set of six equations can be solved for the six unknowns. For example, the pressure of HCl at the surface is given by

$$p_{HCl}^S = \frac{k_g^{HCl} p_{HCl}}{p_g^{HCl} + 2\left(k_g^{H_2} k_g^{NiCl_2}\right)K^{1/2}} \tag{2.2.33}$$

The pressure of HCl at the surface can then be used to compute the flux of HCl using (2.2.33) and the other fluxes can be computed.

It is useful to examine the limiting cases: At high temperatures, K is large. In this case, the pressure of HCl on the surface is approximately equal to zero and the rate can be expressed in terms of the mass transfer of HCl to the surface. The rate is not a strong function of temperature and varies with gas velocity and sample size, and is faster when He is used in place of Ar as the dilution gas.

At low temperature (K is small ($K \ll 1$)), the pressure of HCl at the surface is the same as in the bulk phase. Using Equations (2.2.32–2.2.33), it can be seen that

$$p_{NiCl_2}^S = K^{1/2}\left(\frac{k_g^{H_2}}{k_g^{NiCl_2}}\right)^{1/2} p_{HCl} \tag{2.2.34}$$

The flux of $NiCl_2$ is then given by

$$J_{NiCl} = -\frac{1}{RT}\left(k_g^{H_2} k_g^{NiCl_2}\right)^{1/2} K^{1/2} p_{HCl} \tag{2.2.35}$$

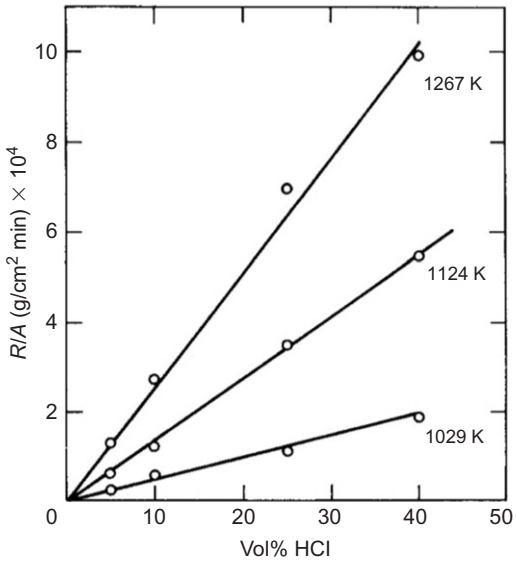


Figure 2.2.5 The rate of chlorination of Ni with HCl demonstrating the rate is controlled by gas-phase mass transfer and is a function of temperature [5].

In this case, the rate also depends on gas velocity, dilution gas, and sample size but is a strong function of temperature. This illustrates an important point that the rate can be a function of temperature because the equilibrium pressure is a function of temperature. Temperature is not greatly affecting the mass transfer coefficient but rather the driving force. The rate of reaction of HCl with Ni in Figure 2.2.5 shows it is controlled by GPMT of $NiCl_2$ from the surface and a strong function of temperature.

2.2.4.7. Reactions with Bulk Flow

The rate of reaction of CO_2 with carbon in liquid iron has been extensively studied. At low sulfur contents under conditions of low or moderate flow, the rate is controlled by GPMT. In this case, the reaction (2.2.36) is not equimolar nor is the reactant dilute

$$\underline{C} + CO_2 = 2CO \tag{2.2.36}$$

Baker *et al.* [6] used levitated drops to study the reaction. The equation below described the flux of CO_2 to the surface of the drop.

$$J_{CO_2} = \frac{k_G^{CO_2}}{RT} \ln\left(\frac{1 + p_{CO_2}}{1 + p_{CO_2}^e}\right) \tag{2.2.37}$$

where D_{CO_2} is the diffusivity of CO_2 and $p_{CO_2}^e$ is the equilibrium pressure of CO_2 with carbon in the melt, which is close to zero. With levitated drops, the surface of the drop is

close to the melt temperature, about 1650° C, and the bulk gas temperature close to room temperature (20° C). Baker et al. used the Ranz-Marshall equation (2.2.37) and the properties of the gas for the average temperature, about 830° C, to calculate $k_G^{CO_2}$. The temperature gradient around the drop is linear and similar to the concentration gradient so this assumption is not unreasonable. Also, it was shown the assumption only leads to an uncertainty of 25%. The experimental rate of carbon reaction agreed with that for GPMT of CO_2 controlling the rate.

2.2.5. FREE VAPORIZATION

As indicated by Equation (2.2.14), the diffusivity becomes very high as the pressure approaches zero. Consider the rate of vaporization of a metal in an inert gas measured as a function of total pressure

$$A = A(g) \tag{2.2.38}$$

$$J_A = \frac{kA}{RT} p_A^o \tag{2.2.39}$$

At some low total pressure, the rate of free vaporization becomes slower than that for GPMT control because the diffusivity increases and therefore k_g and the resulting flux are very high.

When the diffusivity get very large because the pressure is approaching zero, the rate of reaction (2.2.38) becomes controlled by free vaporization, which is the fastest rate possible. The rate of free vaporization can be calculated from the kinetic theory of gases. In practical units, the flux of A in terms of (kg m^{-2} s^{-1}) for free vaporization is given by

$$J_A = 443.4 \left(\frac{M_A}{T}\right)^{1/2} p_A^o \tag{2.2.40}$$

where M_A is the molecular weight of A and p_A^o is measured in atmospheres.

If A is in solution, the equilibrium pressure is used in Equation (2.2.40).

To illustrate, consider the rate of free vaporization of Cu from liquid Fe in vacuum. In addition to free vaporization, LPMT could control the rate but for the present case, we will assume LPMT of Cu is fast. The vapor pressure of Cu in Fe is given by

$$p_{cu} = X_{cu} \gamma_{cu} p_{cu}^o \tag{2.2.41}$$

where γ_{cu} is the activity coefficient of Cu and X_{cu} is the mole fraction of Cu. For a dilute solution

$$X_{cu} = \frac{[\%Cu] M_{Fe}}{100 M_{Cu}} \tag{2.2.42}$$

and $\gamma = \gamma^{o}_{Cu}$

where γ^{o}_{Cu} = activity coefficient of Cu at infinite dilution

M_{Cu} and M_{Fe} are the molecular weights of Cu and Fe, respectively. It follows that

$$\frac{d(\%Cu)}{dt} = -4.43 \times 10^4 \frac{A\gamma^{o}_{Cu} M_{Fe}}{W M_{Cu}} \left(\frac{M_{Cu}}{T}\right)^{1/2} p^{o}_{Cu}[\%Cu] \tag{2.2.43}$$

where W is the total weight of metal and A is the surface area

Integrating from $t = 0$ to $t = t$

$$\ln \frac{[\%Cu]}{[\%Cu]_o} = -4.43 \times 10^4 \frac{A\gamma^{o}_{Cu} M_{Fe} p^{o}_{Cu}}{(M_{Cu} T)^{1/2}} t \tag{2.2.44}$$

Iron is of course also vaporizing but due to much higher concentration, its vaporization does not affect the Cu content significantly. If reasonable values of the area A are used in Equation (2.2.44), it indicates that it is impractical to remove Cu in any industrial process at a reasonable rate from Fe by vacuum despite its higher vapor pressure than Fe for the pure elements. The equilibrium pressure for Cu at low concentrations is too low.

2.2.6. LIQUID-PHASE MASS TRANSFER

2.2.6.1. Flux Equations and Correlations

LPMT plays an important role in several metallurgical reactions. Since liquids are fluids like gases, well-stirred liquids follow the same relationships as gases with respect to mass transfer. The flux of A to the surface of a liquid is given by

$$J_A = k^{A}_{L}\left(C_A - C^{s}_{A}\right) \tag{2.2.45}$$

where k^{A}_{L} = the LPMT coefficient of A

C_A and C^{S}_{A} are the bulk and surface concentration of A.

The correlations for LPMT are somewhat similar as those for GPMT. For example, for a solid sphere in a flowing liquid, the Ranz-Marshall equation can be used. For metallurgical systems, two of the more useful correlation are for stirred liquids and gas bubbles.

A liquid metal can be stirred by induction, by a gas, or other means. For this case, the mass transfer coefficient (k_L) is given by

$$k_L = 2\left(\frac{Du}{\pi R}\right)^{1/2} \tag{2.2.46}$$

where D = the diffusivity

u = surface velocity of the melt at R

R = radius of the container

Mass transfer to gas bubbles in metals is also a major reaction mechanism. In this case, the mass transfer coefficient is given by

$$k_L = 1.28\left(\frac{Dv_B}{d_B}\right)^{1/2} \tag{2.2.47}$$

v_B = velocity of bubbles in m s^{-1}

d_B = equivalent diameter of the bubble (assuming the bubble is spherical) in m

Since k_L depends on diffusivities, reaction geometries and flow conditions it can vary significantly. However, for metallurgical systems, typical values are about 10^{-4} to 10^{-3} (m s^{-1}). For details and other correlations for LPMT as well as the behavior of bubbles, others books deal with these in more detail [2,3].

2.2.6.2. An Example of LPMT Control

Consider the reactions of pure nitrogen with liquid iron at low oxygen and sulfur contents. Since pure nitrogen is used, GPMT will not be limiting the rate. Oxygen and sulfur are surface-active elements that reduce the rate of the chemical reaction as will be discussed later in detail. However, if oxygen and sulfur are low (<20 ppm), the chemical rate is fast, there is equilibrium at the surface, and the rate is controlled by LPMT. The reaction sequence is

$$N_2(g) = 2N_S \quad \text{fast} \tag{2.2.48}$$

$$N_S = N_B \quad \text{slow} \tag{2.2.49}$$

where N_S and N_B represent nitrogen at the surface and in the bulk, respectively.

The flux equation is given by

$$J_N = k_L^N\left(C_N^S - C_N^B\right) \tag{2.2.50}$$

where C_N^S and C_N^B are the concentrations of nitrogen at the surface and in the bulk, respectively.

In terms of mass percent [%N], it follows that

$$C_N = \frac{[\%N]\rho_{Fe}}{100} \tag{2.2.51}$$

$$\frac{d\%N}{dt} = \frac{AJ_N(100)}{W} \tag{2.2.52}$$

where ρ_{Fe} = density of iron

A = surface area of the melt

W = weight of the melt

Combining (2.2.51) and (2.2.52) and since the chemical rate at the surface is fast, the surface concentration is the equilibrium concentration with the gas phase it follows that

$$\frac{\mathrm{d}\%\mathrm{N}}{\mathrm{d}t} = \frac{A\rho_{\mathrm{Fe}}k_{\mathrm{L}}^{\mathrm{N}}}{W}[\%\mathrm{N}_{\mathrm{e}} - \%\mathrm{N}] \tag{2.2.53}$$

It is possible to integrate Equation (2.2.53) from $t=0$ to $t=t$.

$$\ln\left\{\frac{\%\mathrm{N}_{\mathrm{e}} - \%\mathrm{N}}{\%\mathrm{N}_{\mathrm{e}} - \%\mathrm{N}_{\mathrm{o}}}\right\} = -\frac{A\rho_{\mathrm{Fe}}k_{\mathrm{L}}^{\mathrm{N}}}{W}t \tag{2.2.54}$$

where $\%\mathrm{N}_{\mathrm{e}}$, $\%\mathrm{N}$, and $\%\mathrm{N}_{\mathrm{o}}$ are the equilibrium, instantaneous, and initial nitrogen contents, respectively.

Experiments were performed in an induction-stirred system in which the amount of nitrogen absorbed into the melt was determined from a small change in pressure at constant volume. The results are shown in Figure 2.2.6. From the slope of the line, the value of $k_{\mathrm{L}}^{\mathrm{N}}$ can be calculated from (2.2.54). To prove the rate is controlled by LPMT, the form of the rate equation must agree with the results, and the computed LPMT coefficient should agree with the experimentally determined value [6].

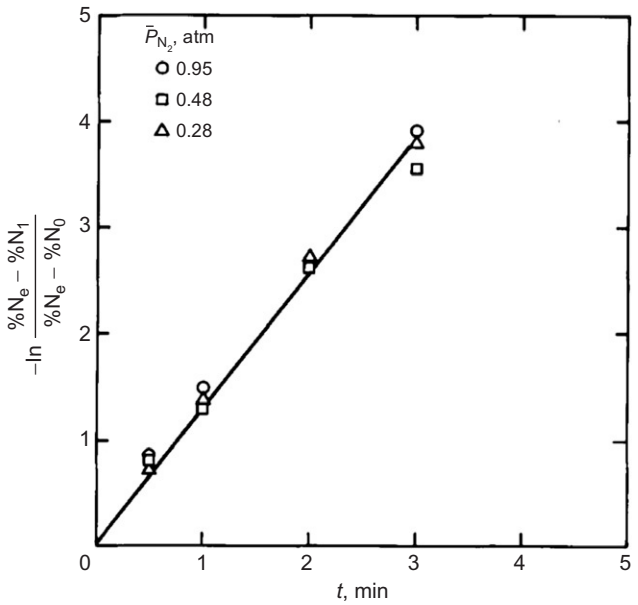


Figure 2.2.6 The rate of nitrogen pick up in liquid iron at 1873 K indicating the rate is controlled by liquid-phase mass transfer at low oxygen and sulfur (<30 ppm) [7].

2.2.6.3. Two-Phase LPMT

In several metallurgical processes involving a slag and a metal, mass transfer in both phases must be considered. Consider a metal (M) and slag (S) in which an element (A) is being transferred from metal to slag. The flux of A in the metal phase must equal that in the slag phase because A cannot accumulate at the surface.

$$J_A = k_M^A \left(C_M^A - C_M^{A(s)} \right) = k_S^A \left(C_S^{A(s)} - C_S^A \right) \tag{2.2.55}$$

where k_M^A, k_S^A = mass transfer coefficient of A in metal and slag

C_M^A, C_S^A = concentration of A in metal and slag. The superscript (s) indicates surface.

Since the rate is controlled by mass transfer, the rate at the surface is fast and the surface reaction is at equilibrium. From the thermodynamics, an equilibrium partition ratio P_A can be computed.

$$P_A = \frac{C_S^{A(s)}}{C_M^{A(s)}} \tag{2.2.56}$$

It shall be noted the concentrations are in mass per unit volume and P_A is similar to the equilibrium constant, but in terms of concentration.

By combining (2.2.55) and (2.2.56), the surface concentrations can be computed.

For example:

$$C_M^{A(s)} = \frac{k_M^A C_M^A + k_S^A C_S^A}{k_M^A + P_A k_S^A} \tag{2.2.57}$$

By substituting Equation (2.2.57) into (2.2.55), it can be shown that

$$J_A = \frac{1}{1/P_A k_S^A + 1/k_M^A} \left[C_M^A - \frac{C_S^A}{P} \right] \tag{2.2.58}$$

In terms of mass percent, it follows that

$$J_A = \frac{1}{\dfrac{\rho_S}{\rho_M K k_S^A} + \dfrac{1}{k_M^A}} \frac{\rho_M}{100} \left[[\%A] - \frac{(\%A)}{K} \right] \tag{2.2.59}$$

The equilibrium constant is for the reaction of A going from metal into slag. If mass transfer in the slag is not rate-determining, the equation can be simplified to

$$J_A = k_M^A \frac{\rho_M}{100} \left[[\%A] - \frac{(\%A)}{K} \right] \tag{2.2.60}$$

Equation (2.2.59) is similar to having two resistances in series in an electric circuit.

2.2.7. HEAT TRANSFER CONTROL

Several important metallurgical reactions are endothermic and heat must be applied to have the reaction proceed. A good example of such a reaction is the reduction of iron oxide (e.g., FeO) with carbon which is endothermic

$$\mathrm{FeO} + \mathrm{C} = \mathrm{CO} + \mathrm{Fe} \tag{2.2.61}$$

Consider a pellet of iron oxide and carbon. As will be discussed in detail later, the reaction proceeds by means of two gas–solid reactions

$$\mathrm{FeO} + \mathrm{CO} = \mathrm{Fe} + \mathrm{CO_2} \tag{2.2.62}$$

$$\mathrm{CO_2} + \mathrm{C} = 2\mathrm{CO} \tag{2.2.63}$$

If these reactions are relatively fast, the rate will be controlled by the heat flux (J_H). The rate $\dot{n}_{FeO}$ will simply be given by

$$\dot{n}_{FeO} = \frac{\Delta H^o}{J_H} \tag{2.2.64}$$

There are several types of heat transfer—convection, radiation, or conduction. Details of these are given in several books including Refs. [2,3]. The simplified equation for convection is:

$$J_H = k_H^C (T_S - T_o) \tag{2.2.65}$$

where k_H^C is the convection heat transfer coefficient T_o and T_S are the furnace temperature and surface temperature.

Correlations similar to those for mass transfer exist to predict k_H.

At high temperature, radiation is a major mode of heat transfer. The heat flux is given by

$$J_H = \varepsilon\sigma\left(T_S^4 - T^4\right) \tag{2.2.66}$$

where

σ = Stefan-Boltzmann constant

ε = emissivity

The emissivity of a black body, a metallic surface, and an oxidized metal is about 1, 0.1–0.2, and 0.5–0.7, respectively.

In some cases, the convection and radiation heat transfer coefficients are combined

$$k_H^r = \frac{\varepsilon\sigma\left(T_S^4 - T^4\right)}{T_S - T} \tag{2.2.67}$$

$$k_H = k_H^r + k_H^C \tag{2.2.68}$$

$$J_H = k_H(T_S - T) \tag{2.2.69}$$

Heat transfer correlations and details are given in various textbooks including Refs. [2] and [3].

2.2.8. CHEMICAL KINETICS

2.2.8.1. Absorption of Surfaces

Most metallurgical reactions occur on surfaces. Homogeneous kinetics is relatively slow and chemical reactions occur more rapidly on catalytic surfaces. In general, metal surfaces, such as Pt, Fe, Cu, Ni, etc., are good catalysts for reactions. However, certain elements such as oxygen and sulfur segregate to the surface of the metal and block active sites for chemical reactions. Therefore, these elements retard the rate of reaction. These elements are referred to as surface-active elements and with regard to chemical reactions as "surface poisoners."

Surface-active elements segregate to the surface because in doing so they reduce the energy of the system. This manifests itself as reductions in the surface energy or surface tension. The Gibbs Absorption Isotherm expresses the number of sites occupied by the surface-active element

$$\Gamma_i = \frac{1}{RT}\left(\frac{\partial\sigma}{\partial \ln a_i}\right) \tag{2.2.70}$$

where Γ_i = excess surface sites occupied by element i in solution

σ = surface tension of melt

a_i = activity of element i in solution

An example of the relationship is shown in Figure 2.2.7 (from Belton [25]) for the effect of oxygen on the surface tension of liquid iron. At moderate activities (e.g., 0.01% for the 1 wt standard state), the slope of the curve in Figure 2.2.7 becomes constant indicating the surface is becoming saturated with the surface-active species and the value of the surface excess is $\Gamma^{(s)}$. The fraction of sites occupied by i (θ_i) is therefore given approximately by

$$\theta = \frac{\Gamma_i}{\Gamma^{(s)}} \tag{2.2.71}$$

The value of θ_i at a concentration of (i) is therefore the value of the slope of the curve at the concentration divided by the limiting slope at high concentrations.

$$\theta_i = \frac{\text{slope}}{\text{limiting slope}} \tag{2.2.72}$$

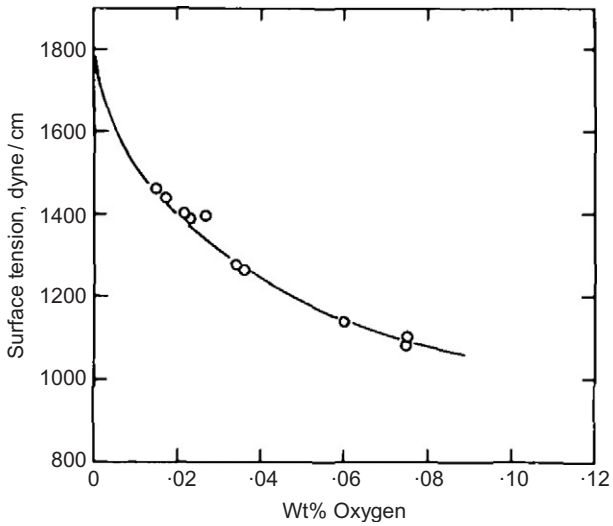


Figure 2.2.7 The effect of oxygen on the surface tension of liquid iron according to the Gibbs Absorption Isotherm (Belton [7]).

When considering the relationship between the activity and the surface coverage of an element in solution, there are a limited number of surface sites. The relationship is expressed as

$$a_i = \frac{\varphi_i \theta_i}{(1-\theta_i)} \tag{2.2.73}$$

$$\varphi_i = \frac{1}{K_i} \tag{2.2.74}$$

where $(1-\theta_i)$ = the fraction of vacant sites

K_i = adsorption coefficient

By combining (2.2.73) and (2.2.74), it follows that

$$(1-\theta_i) = \frac{1}{1+K_i a_i} \tag{2.2.75}$$

If specie (i) is absorbed, ideally K_i is constant.

Belton [7] has shown that, by combining the above equations, the relationship between surface tension and adsorption is

$$\left(\sigma^{\mathrm{P}} - \sigma\right) = RT\Gamma_0 \ln(1+K_i a_i) \tag{2.2.76}$$

2.2.8.2. Rate Equations and Activated Complexes

The absolute rate theory proposes that reactions proceed by means of an activated complex. The formation of the activated complex is the critical rate-controlling process for the reaction. Once this complex forms, it reacts and the system proceeds to equilibrium.

An example of an activated complex is the reaction of nitrogen gas on an iron surface to put nitrogen into solution

$$N_2(g) = 2\underline{N}(\text{in Fe}) \tag{2.2.77}$$

The overall reaction sequence is

$$N_2(\text{gas}) \rightarrow N_2(\text{adsorbed}) \tag{2.2.78}$$
$$N_2(\text{adsorbed}) = N_2{}^* \tag{2.2.79}$$
$$N_2{}^* \rightarrow 2N(\text{adsorbed}) \tag{2.2.80}$$
$$2N(\text{adsorbed}) = 2N(\text{in Fe}) \tag{2.2.81}$$

The slow rate-controlling step is (2.2.79) the formation of an activated N_2 molecule. A physical description is a vibrating N_2 molecule and the activated complex is one that has almost enough energy and is just ready to dissociate. The metallic iron surface is a good catalyst for the reaction, whereas a surface site occupied by a surface-active element such as oxygen and sulfur is not. Oxygen and sulfur essentially block sites for the reaction and are often referred to as "surface poisoners."

From these considerations and the absolute rate theory, the rate equation is given by

$$\text{Rate} = k_p(\text{net driving force})(1 - \Sigma\theta_i) \tag{2.2.82}$$

where

k_p = rate constant on a pure metal surface

$(1 - \Sigma_i\theta_i)$ = number of vacant sites not occupied by a surface-active element (i)

For the case of the nitrogen reaction, the rate equation is given by

$$R = k_p(1 - \Sigma_i\theta_i)(p_{N_2} - p^e_{N_2}) \tag{2.2.83}$$

where the rate (R) is in moles of N_2 per unit area per second. The overall rate constant k_o for a given alloy is given by

$$k_o = k_p(1 - \Sigma_i\theta_i) \tag{2.2.84}$$

By combining (2.2.75) and (2.2.84), the overall rate constants is given by

$$k_o = \frac{k_p}{1 + K_i a_i} \tag{2.2.85}$$

A more detailed discussion of the absolute rate theory is given in Chapter 4 in Volume 1 and elsewhere.

2.2.8.3. Relationship Between Forward and Reverse Reaction

Consider a simple reaction. Again, this is a simplified expression and A and B merely indicating different species.

$$aA = bB \tag{2.2.86}$$

Further assume the activated complex is $(aA)^*$. The rates of the forward R_f and reverse reaction R_r are given by

$$R_f = k_f\, a_A^a (1-\theta) \tag{2.2.87}$$

$$R_f = k_r a_B^b (1-\theta) \tag{2.2.88}$$

where k_f and k_r are the rate constants for the forward and reverse reactions, respectively.

At equilibrium, the rates of the forward and reverse reactions are equal. Equaling (2.2.89) and (2.2.90), it follows that

$$\frac{k_f}{k_r} = \frac{a_B^b}{a_A^a} = K_{eq} \tag{2.2.89}$$

K_{eq} = the equilibrium constant for the reaction
k_f, k_r = rate constant for the forward and reverse reaction, respectively

Equation (2.2.89) indicates that if you know the rate constant for the forward reaction and the K_{eq}, then you know the rate constant for the reverse reaction.

The rate of the net or observable reaction (R) is given by

$$R = R_f - R_r \tag{2.2.90}$$

$$R = k_f a_A^a - k_r \left(a_B^b\right) \tag{2.2.91}$$

Combining the above equations, it follows that

$$R = k_f \left(a_A^a - (a_A)_e^a\right) \tag{2.2.92}$$

where $(a_A)_e^a$ = the activity of A in equilibrium with B at that instance

This concept can be explained with a simple equation: the decarburization of carbon in liquid iron.

$$CO_2 + \underline{C} = 2CO \tag{2.2.93}$$

As discussed later, the rate-controlling step in the dissociation of CO_2 and the activated complex can be considered to be $(CO_2)^*$ and the reaction sequence

$$\text{Slow} \quad CO_2 = CO_2{}^* \tag{2.2.94a}$$

$$\text{Fast} \quad CO_2{}^* = CO(g) + O \tag{2.2.94b}$$

$$\text{Fast} \quad C + O = CO \tag{2.2.94c}$$

Since reactions (2.2.93) and (2.2.94a–2.2.94c) are fast, they are at equilibrium

$$K_{2.2.94b} = \frac{P_{CO} a_o}{P_{CO_2}} \tag{2.2.95}$$

$$K_{2.2.94c} = \frac{p_{CO}}{a_C a_O} \tag{2.2.96}$$

$$R = R_f - R_r = (k_f P_{CO_2} - k_r P_{CO} a_o)(1 - \theta) \tag{2.2.97}$$

where $a_o = \dfrac{P_{CO}}{a_C K}$

By combining the above equations and (2.2.86), it can be shown that

$$R = k_f \left(P_{CO_2} - P^e_{CO_2} \right)(1 - \theta) \tag{2.2.98}$$

where

$P^e_{CO_2}$ = pressure of CO_2 in equilibrium with carbon in the metal and the CO pressure

It is interesting to note that although carbon takes part in the overall reaction, it does not take part in the formation of the activated complex and hence the rate equation. This is because the rate-controlling step is the dissociation CO_2. Carbon affects the net driving force through $P^e_{CO_2}$ because as carbon decreases the equilibrium pressure of CO_2 increases.

2.2.8.4. Examples of Gas–Metal Reactions

2.2.8.4.1 N_2 Reaction with Liquid Iron

The reaction of nitrogen has been extensively studied using dynamic measurements where nitrogen is absorbed into iron in an isotope technique [7–9]. One of the pioneering studies was conducted by Pelke and Elliott [8] using a modified Sieverts apparatus to measure the rate of nitrogen absorption. They showed sulfur could reduce the rate of the reaction.

If we assume an ideal absorption of oxygen or sulfur, the rate expression in terms of mass percent nitrogen in iron at moderate oxygen and sulfur contents is given by (2.2.99)

$$\frac{d[\%N]}{dt} = \frac{A k_p 2800}{W} \left(\frac{1}{1 + K_i a_i} \right) \left(P_{N_2} - P^e_{N_2} \right) \tag{2.2.99}$$

where

A = area of reaction

W = weight of melt

K_i and a_i = absorption coefficient and activity of surface-active elements

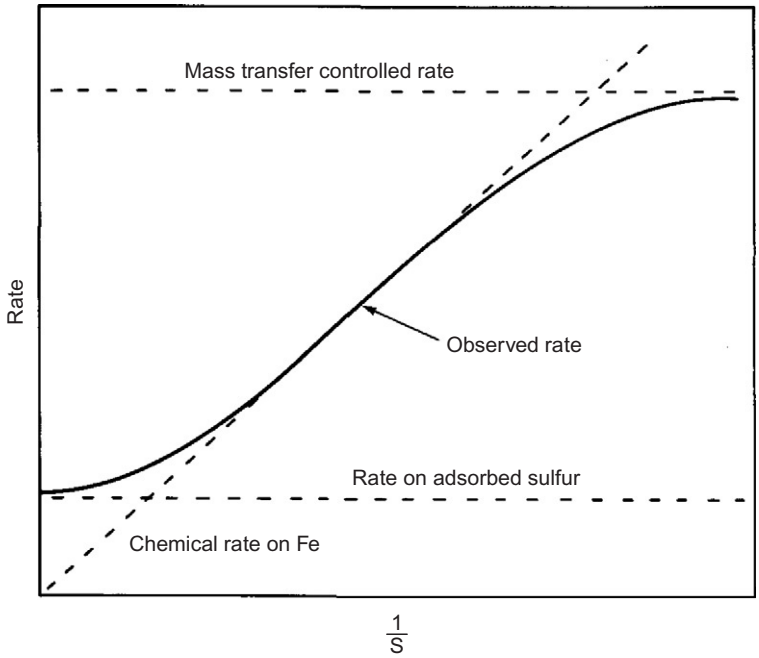


Figure 2.2.8 The rate of the nitrogen reaction on liquid iron (1873 K) as a function of reciprocal of sulfur content (Fruehan and Martonik [6]).

At high concentration of oxygen and sulfur, the number of available sites and hence the rate of reaction will be inversely proportional to the oxygen and sulfur contents.

A schematic diagram of the overall rate constant was plotted versus the reciprocal of the sulfur content in Figure 2.2.8. At low sulfur, the rate was influenced by LPMT. At intermediate sulfur contents, the rate is approximately inversely proportional to the sulfur content. However, at high sulfur contents, the rate did not approach zero as predicted but approached a limiting rate. This effect is referred to as the residual rate. The residual rate for sulfur has been observed for other reactions and is discussed elsewhere in detail. The exact reason is not known but could represent the rate of the reaction on sulfur sites that cover most of the surface.

The reverse reaction was also measured by measuring the removal under a reduced pressure of nitrogen. The rate is plotted versus the driving force in Figure 2.2.9. Also shown is the rate calculated from the forward or nitrogen absorption rate using (2.2.86). The actual measurements are in good agreement with the calculated rate. This supports the fact if you know the rate of a reaction, it is possible to calculate the rate of the reverse reaction.

One problem with measuring the rate by measuring the increase in nitrogen content is that the rate can be influenced by LPMT of nitrogen from the surface to the bulk phase. Bryne and Belton [9] overcame this problem by measuring the rate of dissociation of

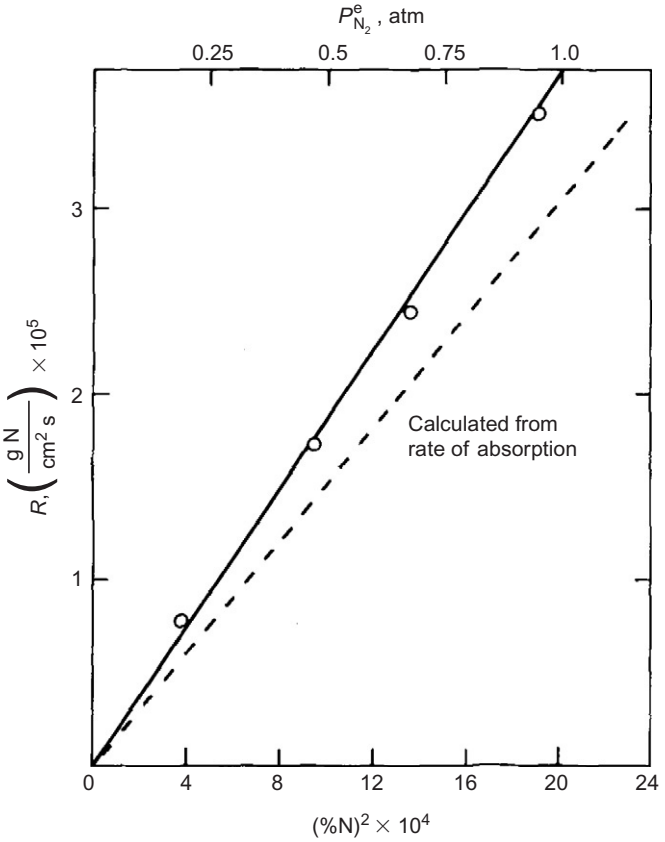


Figure 2.2.9 The measured and calculated rate of nitrogen removal from liquid iron (Fruehan and Martonik [6]).

nitrogen using the N_2^{30} isotope. In this technique, normal N_2^{28} is doped with about 1% of a N_2^{30} double isotope. The reaction is run at equilibrium so there is no net absorption of nitrogen and hence no problems with mass transfer. By measuring the change in the N_2^{30} after the reaction, the rate of dissociation of the N_2 molecule can be determined. If this is the rate-controlling step in the overall reaction sequence for nitrogen absorption, the two rates, the rate of absorption and the rate of dissociation of N_2^{30} should be the same. Byrne and Belton compared their measured rate of dissociation with other dynamic measurements that support the hypothesis that dissociation of the molecule is rate controlling.

Fruehan and Martonik measured the rate of nitrogen absorption into Fe–Cr alloys. The rate increased with Cr content but was affected by LPMT. Glaws and Fruehan [10] used both the dynamic nitrogen absorption and isotopic exchange techniques in the same equipment and conditions for Fe, Fe–Cr, and Fe–Cr–Ni alloys. They showed the rate was controlled by dissociation of N_2, that sulfur reduced the rate, there was a residual rate at high sulfur contents, and Cr increased the rate. It should be noted that

whereas the isotope exchange technique eliminates LPMT as a possible rate-controlling step, it does not eliminate GPMT since the isotope $\left(N_2^{30}\right)$ must be transferred through the normal nitrogen.

The rate of the N_2 reaction on Fe–Ni–S, Fe–Cr–Ni–S, and Fe–C (saturated) [11] melts using the isotope exchange has been measured. In recent years, the technique was used for looking at the effect of Al, Ti, and other elements on the rate [12].

2.2.8.5. The CO_2 Reaction on Iron–Carbon Alloys

2.2.8.5.1 The CO_2 Reaction with Liquid Fe–C

Early work on rate of the reaction of CO_2 with liquid iron was run under experimental conditions where GPMT or LPMT was controlling the overall rate. Sain and Belton [13] used an experimental technique using a gas jet and maintaining carbon saturation that overcame mass transfer limitations. They showed the rate was proportional to the CO_2 pressure and decreased with sulfur content. They proposed the rate was controlled by dissociation of the CO_2 molecule and sulfur decreased the rate by blocking surface sites. Furthermore, the adsorption coefficient calculated from the rate as a function of sulfur content was in agreement with that computed from surface tension measurements.

Mannion and Fruehan [14] also investigated the CO_2 reaction with carbon-saturated iron using a mass spectrometer to measure the change in CO_2 after the reaction. They used a gas jet geometry to increase the GPMT coefficient of CO_2. They developed a mixed control model to correct for GPMT. Their results also indicated a residual rate of high sulfur contents as shown in Figures 2.2.10 and 2.2.11.

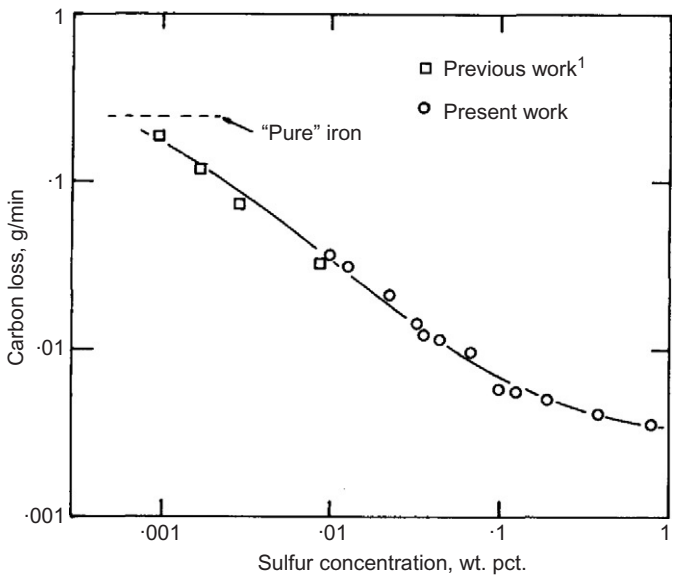


Figure 2.2.10 The rate of decarburization of liquid iron by CO_2 (Sain and Belton [12]).

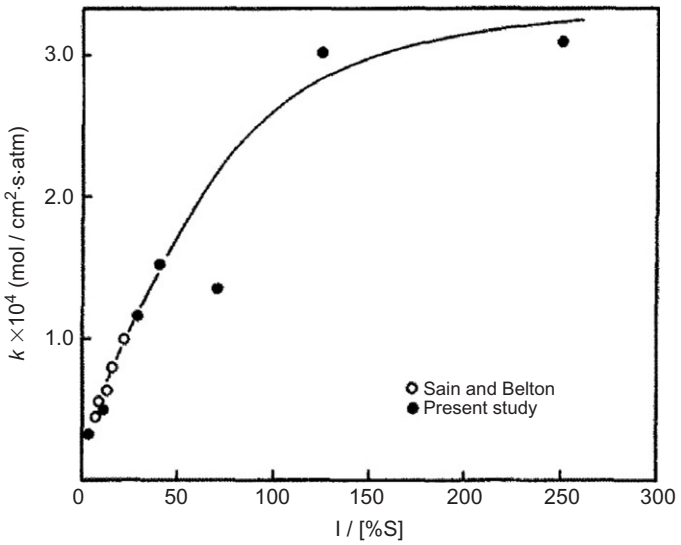


Figure 2.2.11 The rate of decarburization of liquid iron by CO_2 indicating a residual rate (Mannion and Fruehan [13]).

Petit and Fruehan [15] examined the effect of chromium and nickel on the CO_2 reaction on liquid iron–carbon alloys also containing sulfur. They found that, at a given sulfur activity, the rate was not influenced by the presence of Cr or Ni. However, Ni and Cr affect the activity coefficient of sulfur and at constant sulfur content the coverage by sulfur increased with increasing Cr or Ni, and therefore, these elements reduced the rate in this case.

2.2.8.5.2 The H_2O Reaction with Liquid Iron–Carbon Alloys

The reaction of H_2O on liquid iron–carbon alloys is very fast as compared to the CO_2 and N_2 reactions. Consequently, early work on reaction (2.2.100) was highly influenced by GPMT

$$H_2O + \underline{C} = H_2 + CO \tag{2.2.100}$$

Nagasaka and Fruehan [16] used a gas jet with a high mass transfer coefficient and corrected for mass transfer using a mixed control model. They found the chemical rate was controlled by the dissociation of H_2O and that sulfur in the metal reduces the rate. In the limiting case, the rate should be inversely proportional to the sulfur content as show in Figure 2.2.12. The results also indicate there is a residual rate when the surface is almost saturated with adsorbed sulfur.

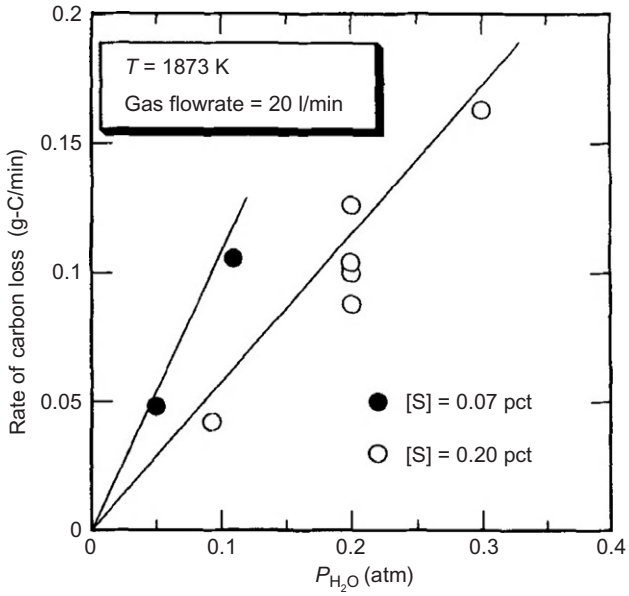


Figure 2.2.12 The effect of sulfur on the dissociation of H_2O on liquid iron–carbon alloys (Nagasaka *et al.* [15]).

The rates of the N_2, CO_2, and H_2O reactions depend on sulfur and exhibit a residual rate. Furthermore, the dissociation of H_2O is an order of magnitude faster than for CO_2 and two orders of magnitude faster than for N_2 (Figure 2.2.13).

2.2.8.5.3 The CO, H_2, C_2H_6, and CH_4 Reaction with Liquid Iron

The rate of dissociation of CO measured using a double isotope (C^{14} C^{18}) was extremely fast even when using a gas jet with a high GPMT coefficient [16]. The measured rates were in agreement with GPMT control. Therefore, the chemical rate of

$$CO = \underline{C} + \underline{O} \tag{2.2.101}$$

is so fast that it cannot be measured using current experimental methods.

Fruehan and Martonik [17] measured the rate of hydrogen absorption in Fe–S alloys. They found the rate was independent of sulfur content and controlled by LPMT in induction-stirred melts. Apparently, the dissociation of H_2 is very fast and cannot be measured using conventional techniques.

Sekino *et al.* [18,19] measured the rate of CH_4 and C_2H_6 reaction with iron containing sulfur, found sulfur reduced the rate, and concluded the rates were controlled by dissociation of the hydrocarbon molecules.

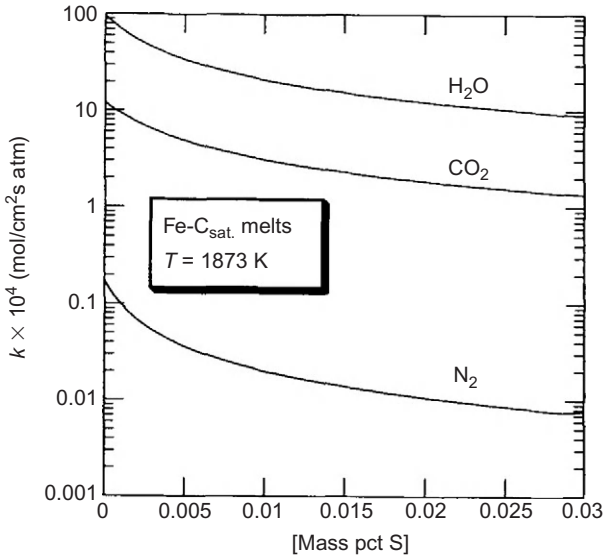


Figure 2.2.13 The effect of sulfur on the rate constant for the dissociation of N_2, H_2O, and CO_2 on liquid iron–carbon alloy at 1873 K (Nagasaka *et al.* [15]).

2.2.8.5.4 Parallel Reaction and Mixed Control

In actual processes, two or more reactions could be occurring at the surface. An example of this is the carburization of iron in CO–H_2 gas mixtures. The two reactions put carbon into solution or deposit carbon onto the metal.

$$2CO = \underline{C} + CO_2 \tag{2.2.102}$$

$$CO + H_2 = \underline{C} + H_2O \tag{2.2.103}$$

By measuring the rates of carburization of iron and CO–Ar and CO–H_2 gas mixtures, Fruehan [20,21] demonstrated that the two reactions proceeded independently and the rate-controlling reactions were the formation of CO_2 and H_2O, respectively. It is speculated that the fraction of surface sites occupied by the activated complex is very small and hence do not affect the rate of the other reaction. Also, the rate of the H_2–CO reaction is considerably faster than the CO reaction which is consistent with the fact that H_2O dissociates and hence forms at a faster rate than CO_2. This is demonstrated in Figure 2.2.14 which gives the initial rate of carburization as a function of gas composition of a H_2–CO gas mixture. For 100% H_2, obviously there is no carburization; at 100% CO, the rate is for reaction (2.2.104) only. The rate reaches a maximum which is much faster than for CO only, at about an equimolar composition. The initial rate of the two reactions (R) can be expressed as

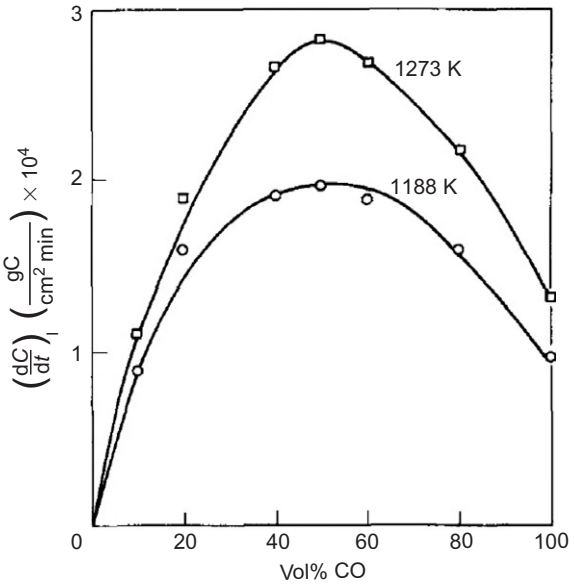


Figure 2.2.14 The rate of carburization of solid iron in CO–H_2 gas mixtures (Fruehan [22]).

$$R = \left(k_{CO} p_{CO}^2 + k_{CO-H_2} p_{CO} p_{H_2}\right)(1-\theta) \tag{2.2.104}$$

where k_{CO},k_{CO-H_2} are the rate constants for the respective reactions.

For the initial rate, there is no carbon in the metal so the reverse reaction can be neglected.

Another example of parallel reactions was studied by Sekino *et al.* [18] who measured the rate of decarburization of liquid iron in CO–CO_2–CO gas mixtures. They showed that the rate was the sum of the two reactions.

$$CO_2 + \underline{C} = 2CO \tag{2.2.105}$$

$$O_2 + 2\underline{C} = 2CO \tag{2.2.106}$$

2.2.9. MIXED CONTROL

2.2.9.1. Chemical Kinetics—GPMT

Very often a chemical reaction is controlled by two processes in sequence, for example, GPMT and chemical kinetics. If the two rates are similar, for example, are of the same order of magnitude, both processes must be considered.

For example, Nagasaka and Fruehan [16] examined the rate of reaction of H_2O in argon with carbon in liquid iron. Despite using a gas jet to obtain high GPMT mass

transfer coefficients of over 1 m s^{-1}, GPMT contributed to the overall reaction rate. The rate of the chemical reaction (R_C) and of mass transfer J_{H_2O} are given by

$$R_C = k_{H_2O} p^S_{H_2O} \tag{2.2.107}$$

$$J_{H_2O} = \frac{k_G^{H_2O}}{RT}\left(p_{H_2O} - p^S_{H_2O}\right) \tag{2.2.108}$$

where

k_{H_2O} = the rate constant for dissociation of H_2O including any effect of surface-active elements

$k_G^{H_2O}$ = the mass transfer coefficient

p_{H_2O}, $p^S_{H_2O}$ = the bulk and surface pressure of H_2O

For high carbon activities such as at or close to saturation, the back reaction can be neglected. Since H_2O at steady state cannot accumulate at the surface R_C and be set equal to J_{H_2O}, the resulting equation can be solved for $p^S_{H_2O}$. The pressure at the surface can then be put into either Equation (2.2.107) or (2.2.108) to give the following

$$R_C = J_{H_2O} = \frac{p_{H_2O}}{\frac{RT}{k_G^{H_2O}} + \frac{1}{k_{H_2O}}} \tag{2.2.109}$$

In the limiting cases of $\left(\frac{k_G^{H_2O}}{RT}\right) \gg k_{H_2O}$, the rate is essentially controlled by chemical kinetics and if k_{H_2O} is greater, it is controlled by GPMT.

In experimental studies, usually $k_G^{H_2O}$ is calculated from appropriate correlations, the rate experimentally measured, and k_{H_2O} computed from these parameters and the measured rate. In general, at high temperatures the chemical rate is faster than GPMT and the rate is controlled by GPMT and at low temperatures by kinetics.

Fruehan [21] examined the rate of decarburization of solid iron–carbon thin plates by CO_2. The observed rate constant is plotted versus the reciprocal of temperatures in Figure 2.2.15. At low temperature, the rate is independent of gas flow, has a significant temperature dependence, and is controlled by chemical kinetics. At high temperature, the rate depends on flow rate, depends on gas flow rate, and controlled primarily by GPMT [21].

2.2.9.2. Chemical Kinetics—LPMT

An example of mixed control with chemical kinetics and LPMT control is the pure nitrogen reaction at moderate oxygen and sulfur levels [6]. At high contents of these surface-active elements, the rate is controlled by chemical kinetics while at low contents by LPMT. However, in general, it is controlled by mixed control. The rate of the chemical reaction (R) and the flux of N (J_N) are given by

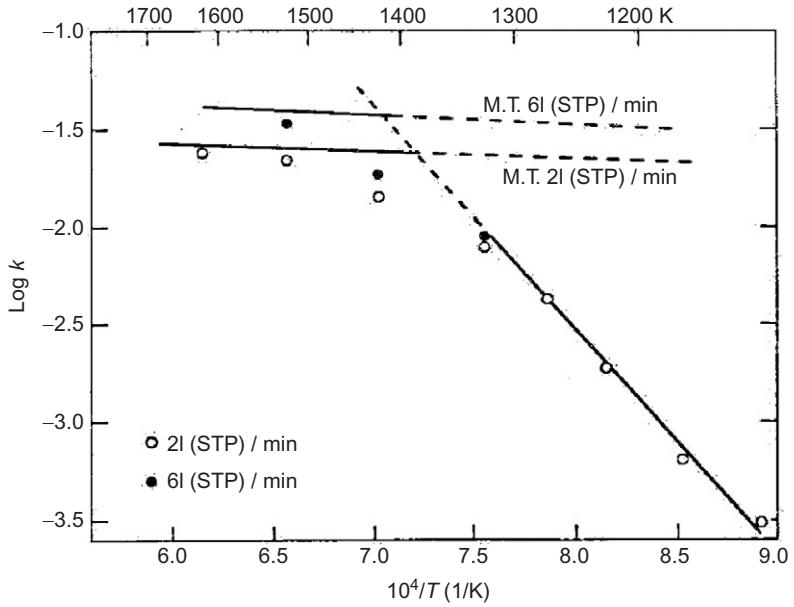


Figure 2.2.15 The rate of dissociation of CO_2 on solid iron as a function of reciprocal temperature indicating chemical kinetics at low temperatures and mass transfer control at high temperatures (Fruehan [21]).

$$R = k_{N_2}\left[p_{N_2} - \frac{[\%N^S]^2}{K}\right] \tag{2.2.110}$$

$$J_N = \frac{k_L^N \rho}{100}[\%N_S - \%N] \tag{2.2.111}$$

where k_{N_2} = rate constant for dissociation of N_2 including the effect of any surface-active elements (kg m^{-2} s^{-1} $(atm)^{-1}$)

k_L^N = mass transfer coefficient of nitrogen in liquid Fe

$\%N^S$ = nitrogen content on the surface

K_N = the equilibrium constant for the overall reaction

ρ = density of iron

The change in nitrogen content with time is given by (2.2.112) and (2.2.113).

$$\frac{d[\%N]}{dt} = \frac{k_L^N A \rho}{W}[\%N^S - \%N] \tag{2.2.112}$$

$$\frac{d[\%N]}{dt} = \frac{k_{N_2} A}{W(100)}\left(p_{N_2} - \frac{[\%N_S]^2}{K}\right) \tag{2.2.113}$$

where A = surface area

W = total weight of iron

Again, imposing the fact that nitrogen cannot accumulate at the surface the flux and chemical reaction rate can be equated to obtain an expression from which the surface concentration of nitrogen can be calculated

$$\frac{k_{N_2}}{K_N}[\%N_S]^2 = \frac{k_L^N \rho}{100}[\%N_S] = k_{N_2} p_{N_2} + \frac{k_L^N \rho}{100}[\%N] \tag{2.2.114}$$

There is no analytical solution but Equation (2.2.114) can be solved numerically for $\%N_S$. Then, the computed value of $\%N_S$ is used to compute the instantaneous rate in Equation (2.2.112) or (2.2.113). This model and equation have been substantiated experimentally and used for various processes.

2.2.9.3. Gaseous Intermediates

Several metallurgical reactions proceed by means of gaseous intermediates. These gaseous species are not part of the overall reactant or product, but take part in the reactions. The classic case is the reduction of solid iron oxide by carbon. For example, for FeO

$$C + FeO = CO + Fe \tag{2.2.115}$$

Since both reactants are solid and the product is gas and a solid, there is very limited contact. It has been speculated, and reasonably well proven, that CO_2 plays a role as a gaseous intermediate. The CO_2 oxidizes the carbon and the resulting CO reduces the iron oxide producing the CO_2.

$$C + CO_2 = 2CO \tag{2.2.116}$$

$$CO + FeO = CO_2 + Fe \tag{2.2.117}$$

This solid–solid reaction is discussed in detail elsewhere and in Chapter 4 in Volume 1.

A similar reaction mechanism plays a role in the reaction of C carbon dissolved in liquid iron and FeO dissolved in slag.

Min and Fruehan [23] investigated the reaction by measuring the rate of CO evolution and by viewing the reaction using X-ray fluoroscopy.

The first observation was when the metal drop entered the slag, it did not sink to the bottom as would be expected based on the density difference. The preheated drop began reacting and a gas halo surrounded the drop within 1–2 s. The drop remained suspended in the slag until the reaction stopped and then it sank. A complex mixed control model was developed based on the chemical kinetics and mass transfer. The model predicted that at high sulfur activities, the oxidation rate of carbon was

controlling the rate, more specifically, the rate of dissociation of CO_2 on the iron surface.

The rate of FeO reduction was computed using independent data on the dissociation of CO_2 on the Fe–C–S metal surface. The rate equation is given by (2.2.118)

$$\text{Rate} = k_{CO_2} AKC(\text{wt\%FeO}) \tag{2.2.118}$$

where k_{CO_2} = rate constant for dissociation of CO_2

A = area of metal drop

K = equilibrium constant for (2.2.117)

C = constant relating the activity of FeO to wt% FeO

In deriving (2.2.118), it is assumed the reduction reaction (2.2.117) is fast, at equilibrium, and thus determines the CO_2 pressure for oxidation (2.2.116).

For high sulfur contents based on the measurements of Sain and Belton and Mannion and Fruehan, the rate constant $\left(\frac{\text{moles}}{\text{cm}^2\text{s(\%FeO)}}\right)$ is given by

$$k_{CO_2} = \frac{1.5 \times 10^{-6}}{[\text{wt\%S}]} + k^{r}_{CO_2} \tag{2.2.119}$$

$k^{r}_{CO_2}$ = the limiting rate constant at high sulfur contents (i.e., residual rate)

In Figure 2.2.16, the rate of reduction of FeO is plotted according to (2.2.118). The calculated line is then calculated using the independent results of the CO_2 metal reaction.

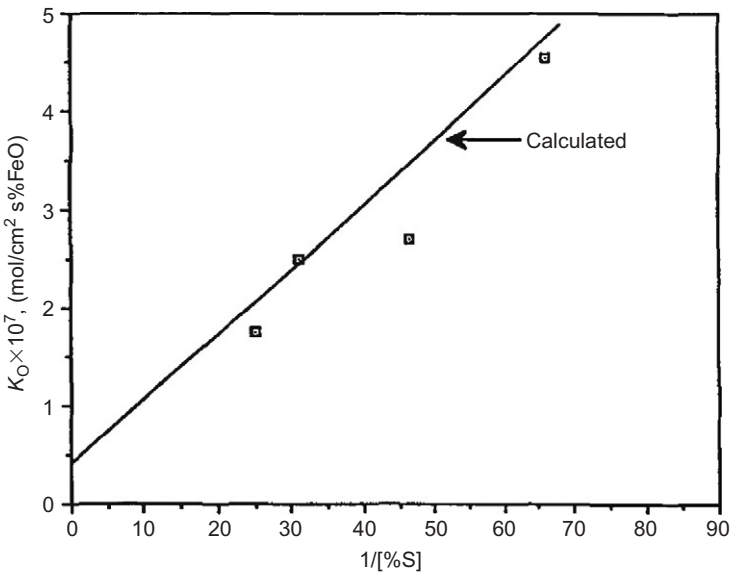


Figure 2.2.16 The rate of reaction of FeO in liquid slag with Fe–C droplets and the predicted rate assuming dissociation of CO_2 is controlling (Min and Fruehan [24]).

The agreement is very close indicating that, at reasonably high sulfur activities, CO_2 is a gaseous intermediate and the overall rate of reduction of FeO is controlled by the CO_2 reaction with carbon producing the CO for reduction reaction.

2.2.10. CONCLUDING REMARKS

During the past several decades, our knowledge of and ability to calculate rates of metallurgical reactions has increased significantly. Essentially, all reactions occur at interfaces between phases. Most reactions involving two condensed phases are controlled by diffusion or LPMT. If the flow conditions are known, reasonable estimates of the rate can be made using the flux equations and correlations to predict the mass transfer coefficients.

Gas–metal and gas–slag reactions are controlled by true chemical kinetics, LPMT, or GPMT. Again for mass transfer, the rates can be estimated using existing correlations. For chemical kinetics, the rates must be measured. Also, for chemical kinetics, the rates depend on the presence of surface-active elements in the metal such as oxygen and sulfur which reduce the number of sites available on the surface for the reaction to occur.

For determining the rate-controlling process, experimental strategies can be used. For example, for GPMT, the rate depends on gas flow conditions and the specific properties of the gas. For chemical kinetics, the rate will depend on the concentration of surface-active elements. Under the conditions existing in actual metallurgical processes, the rate is often controlled by two processes in series, or mixed control, such as GPMT and chemical kinetics. The cases of mixed control can be addressed using mathematical models or equations which account for two or more processes in series.

The kinetics are reasonably well known for many reactions. However, in a real process, the reaction area is not well defined. For example, the reaction area for slag–metal mixtures and gas bubbles in metal for actual processes are not accurately known and additional research is required on these aspects.

REFERENCES

[1] J.O. Hirschfelder, C.F. Curtis, R.B. Bird, Molecular Theory of Gases and Liquids, John Wiley and Sons, Inc., New York, 1954.
[2] G.H. Geiger, R.R. Poirier, Transport Phenomena in Metallurgy, Addison-Wesley, Reading, Mass, 1973.
[3] R.I.L. Guthrie, Engineering in Process Metallurgy, Clarendon Press, Oxford, 1989.
[4] R.J. Fruehan, Metall. Trans. 3 (1972) 2585–2592.
[5] R.J. Fruehan, L.J. Martonik, Metall. Trans. 4 (1973) 2789–2792.
[6] L.A. Baker, N.A. Warner, A.E. Jenkins, Trans. TMS-AIME 230 (1964) 1228–1235.
[7] R.J. Fruehan, L.J. Martonik, Metall. Trans. B 11B (1980) 615–621.
[8] R.D. Pelke, J.F. Elliott, Trans. TMS-AIME 227 (1963) 844–855.
[9] M. Bryne, G.R. Belton, Metall. Trans. B 14B (1983) 441–449.
[10] P.C. Glaws, R.J. Fruehan, Metall. Trans. B 16B (1985) 317–322.
[11] F. Tsukihashi, R.J. Fruehan, Trans. ISIT 27 (1987) 858–863.

[12] K. Moreta, T. Hirosumi, N. Sano, Belton Memorial Symposium, Sydney Australia, ISS Warrendale, PA, 2000, pp. 31–39.
[13] D.R. Sain, G.R. Belton, Metall. Trans. B 9B (1978) 403–407.
[14] F.J. Mannion, R.J. Fruehan, Metall. Trans. B 20B (1989) 853–861.
[15] C.P. Petit, R.J. Fruehan, Metall. Mater. Trans. B 28B (1997) 639–645.
[16] T. Nagasaka, R.J. Fruehan, Metall. Mater. Trans. B 25B (1994) 245–253.
[17] R.J. Fruehan, L.J. Martonik, Metall. Trans. B 123B (1981) 379–384.
[18] K. Sekino, T. Nagasaka, R.J. Fruehan, Metall. Mater. Trans. B 26B (1995) 317–324.
[19] K. Sekino, T. Nagasaka, R.J. Fruehan, ISIJ 40 (2000) 315–320.
[20] R.J. Fruehan, Metall. Trans. B 4 (1973) 2123–2127.
[21] R.J. Fruehan, Metall. Trans. B 4 (1973) 2585–2592.
[22] R.J. Fruehan, S. Antolin, Metall. Trans. B 18B (1987) 415–419.
[23] D.J. Min, R.J. Fruehan, Metall. Trans. B 23B (1992) 29–36.
[24] R.J. Fruehan, High Temp. Sci. 2 (3) (1971) 244–256.
[25] G.R. Belton, Metall. Trans. B 7B (1976) 35–42.

CHAPTER 2.3

Bubbles in Process Metallurgy

P. Chris Pistorius
Center for Iron and Steelmaking Research, Carnegie Mellon University

2.3.1. INTRODUCTION

Injected gas is commonly used to stir melts for thermal and chemical homogenization and to increase the rate of metal–slag and metal–gas reactions. Inadvertent gas–metal reactions occur when gas is entrained into the metal by a tapping stream [1], or at leaks at a slide gate. In this section, the focus is on intentional injection of gas, typically through a tuyère or porous plug.

Injected gas naturally rises through the molten metal, matte, or slag, because of the much lower density of the gas. The rate at which the bubbles rise depends on bubble size, and on bulk flow (in a "plume") driven by gas flow. The average bubble size and residence time determine the gas–liquid contact area. Calculating the expected effect of gas stirring or injection on reaction kinetics therefore relies on the ability to predict bubble dynamics.

Interaction of gas with melts is a much-studied topic, which lends itself to imaging with high-speed cameras, use of model systems (often water and air) at room temperature, and computational flow modeling. However, despite the large volume of work on injection of gas into liquids, it is not currently possible to calculate exactly what type of flow would result (jetting or bubbling; periodic or aperiodic bubbling), nor what the total gas–liquid contact area would be. However, some useful correlations and fundamental trends are known; these are briefly reviewed. The intention is to provide an update and extension to the previous concise review by Oeters [2], and the useful and thorough compilation of Mazumdar and Guthrie [3].

2.3.2. BUBBLE FORMATION

2.3.2.1. Quasi-Stationary Bubbling

At low gas flow rates, the size of a gas bubble upon its release from the orifice depends only on the gas–liquid surface tension, orifice diameter, and the degree of wetting of the container bottom by the liquid. The bubble is released from the orifice when the buoyancy

Treatise on Process Metallurgy, Volume 2
http://dx.doi.org/10.1016/B978-0-08-096984-8.00002-1
© 2014 Elsevier Ltd.
All rights reserved.

force on the bubble is equal to the surface tension force on the curved bubble surface. To a first approximation, the bubble diameter at detachment is then given by [2]:

$$d_B = [6\sigma d_o/g\rho_L]^{1/3} \tag{2.3.1}$$

where σ is the liquid–gas surface energy, d_o is the orifice diameter, g is gravitation acceleration, and ρ_L is the liquid density. Substitution of values for pure liquid iron ($\sigma = 1.8$ N/m and $\rho_L = 7000$ kg/m^3) gives a bubble diameter of 1.5 cm if the orifice diameter is 2 cm.

For small orifices (0.5–2 mm diameter) and quasi-stationary bubbling in water, consideration of the surface tension and buoyancy allows accurate calculation of the bubble shape [4]; examples are shown in Figure 2.3.1, for the case where the liquid wets the chamber bottom around the orifice. In cases where the liquid does not wet the bottom, the bubble spreads laterally from the orifice before the bubble detaches and hence grows larger than in the wetting case. The nonwetting condition is relevant to processing conditions, since in general liquid metals do not wet refractories (Figure 2.3.2) [5].

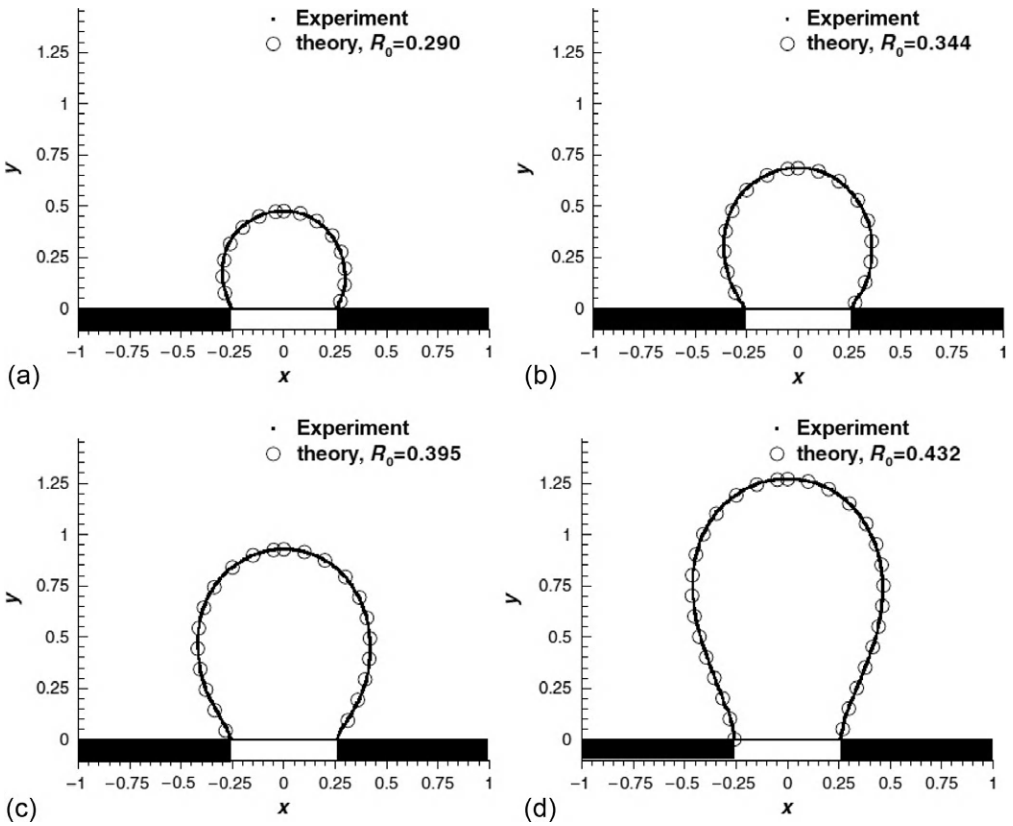


Figure 2.3.1 Quasi-stationary growth of an air bubble in water. R_o is the radius of curvature at the bubble apex; dimensions are relative to the Laplace constant, $a = \{2\sigma/[g(\rho_L - \rho_G)]\}^{0.5}$ (Ref. [4]). (a) to (d) show consecutive stages of bubble growth.

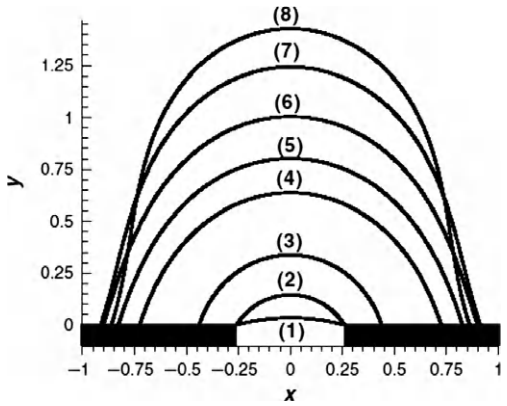


Figure 2.3.2 Spreading of bubble around the orifice before detaching, for the case where the liquid does not wet the solid [4].

For quasi-stationary bubbling, the bubbling frequency is simply the gas flow rate divided by the bubble volume. At somewhat elevated gas flow rates, a number of effects can arise: interaction between bubbles can cause frequency doubling (where two bubble release frequencies are observed) [6] and also aperiodic (chaotic) bubbling [7]. Bubbles can also merge before or shortly after release [7].

2.3.2.2. Effect of Drag on Bubble Detachment Size

In addition to bubble–bubble interference effects, at higher flow rates drag on the bubble increases the force keeping the bubble attached to the orifice, and hence each bubble grows larger before detachment. The effect of drag on bubble size can be approximated by

$$d_B = [3\sigma d_o/(g\rho_L)]^{1/3}\left[1+\left(1+1.028We^2/Fr\right)^{1/2}\right]^{1/3} \qquad (2.3.2)$$

where the Weber number is given by $We = u_o^2 d_o \rho_L/\sigma$ and the Froude number by $Fr = u_o^2/g d_o$.

Calculated bubble sizes using this expression are shown in Figure 2.3.3, for argon flow into liquid iron at 1873 K, and for two different nozzle sizes. In ladle metallurgy, gas flow rates are typically in the range 1.5–20 Ndm^3/ton/min [2,8]. For these flow rates, the bubble diameter upon release from the orifice is predicted to be around 0.2 m, much larger than practically observed bubbles in steel. Practical bubbles are much smaller because of breakup, as discussed below. (For bubbles in viscous liquids, the inertia of the injected gas has little effect on bubble size, as shown by Davidson and Schüler [9].)

2.3.2.3. Bubble Breakup

As a bubble rises from the orifice and expands as the static pressure decreases, breakup can occur; instability of the Rayleigh–Taylor (RT) type (caused by buoyancy acting against

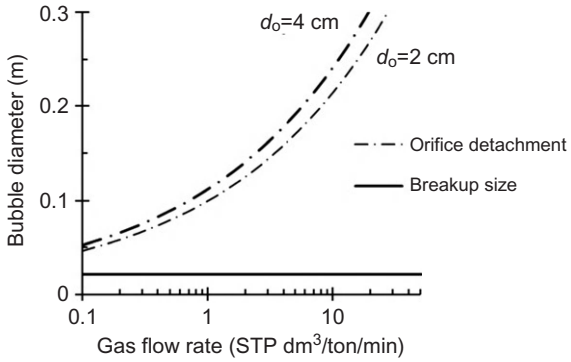


Figure 2.3.3 Calculated bubble diameter for argon bubbling into liquid iron at 1873 K (mass of liquid iron 150 ton; pressure at orifice 3 atm). The lines marked "Orifice detachment" give the bubble size upon release from the orifice. The line marked "Breakup size" indicates the critical bubble size for bubble breakup.

surface tension) and the Kelvin–Helmholtz (KH) type (shear acting against surface tension) can both contribute to breakup [10,11]. The following simple relationship for the "critical bubble size" (the size above which bubble breakup can occur) was given by Zhou and Brimacombe [12]:

$$d_{\mathrm{B-crit}} = 4.044\{\sigma/[g(\rho_{\mathrm{L}} - \rho_{\mathrm{G}})]\}^{0.5} \tag{2.3.3}$$

This expression implies that the critical size for bubble breakup is approximately three times the Laplace constant, $a = \{2\sigma/[g(\rho_{\mathrm{L}} - \rho_{\mathrm{G}})]\}^{0.5}$. A similar critical size was estimated by Wichterle [13].

For argon injection in pure liquid iron, this give a critical bubble size of approximately 2 cm. Figure 2.3.3 demonstrates that the breakup diameter is small compared with the bubble diameter upon release from the orifice; bubbles are expected to break up shortly after release from the nozzle. As pointed out by Mazumdar and Guthrie, this observation implies that the inlet conditions (such as nozzle diameter) have little effect on the development of the bubble plume [3].

2.3.2.4. Effect of Flow Conditions on Bubble Breakup and Coalescence

It is expected that the flow conditions in the bubble plume will affect the distribution of bubble sizes, through collision of bubbles (which may lead to bubble coalescence), and fragmentation of bubbles. The experimental results of Anagbo and Brimacombe illustrate that both coalescence and breakup occur in the plume: for a 1/6 length scale water model of a ladle, the bubble sizes *decreased* with height in the plume, indicating breakup of bubbles (for the water model, static pressure differences would have been insignificant over the height of the ladle); bubble sizes *increased* with increased flow rate, suggesting that more bubble coalescence occurred [14].

Models for bubble breakup and coalescence (mostly based on water) are available in the chemical engineering literature; see Alexiadis [15] for an overview of such models. While these models have not been validated for liquid metals nor for the bubble sizes encountered in ladle stirring, recent use of a breakup and coalescence model in computational modeling of a gas-stirred ladle yielded promising results [16]. Following Alexiadis *et al.* [15,16], the correlations for bubble breakup and coalescence are considered here as examples.

Bubble breakup was considered to be the result of the opposing actions of turbulent forces (tending to distort the bubble) and surface tension (restoring the bubble shape) [17]. The difference between turbulent forces and surface tension forces results in a wave of shape disturbance which propagates around the bubble; the breakup frequency is then given by the speed at which the disturbance travels, divided by the distance traveled around the bubble (which is proportional to bubble diameter) [17]:

$$f_B = 0.25 \frac{\sqrt{8.2(\varepsilon d_B)^{2/3} - 12\sigma/(\rho_L d_B)}}{d_B} \tag{2.3.4}$$

In this expression, ε is the energy dissipation rate per unit mass of liquid. For gas injection into liquid metal, it is assumed that the stirring power arises from expansion of the gas as it rises from the higher static pressure at the injection point to the lower static pressure at the metal surface. This stirring power (P) is hence given by [18]:

$$P = (n/t) R T_L \ln\left(p_{in}/p_{top}\right) \tag{2.3.5}$$

where (n/t) is the molar flow rate of gas, R the ideal gas constant, T_L the metal temperature, and p_{in} and p_{top} the pressures at the injection point and at the top of the ladle.

The energy dissipation rate is then given by $\varepsilon = P/W_L$, where W_L is the mass of the liquid in which the energy is dissipated.

The rate of bubble coalescence depends on the rate at which bubbles collide, and the likelihood that bubbles will coalesce if they do collide (the collision efficiency). Based on Ref. [21], the resulting coalescence rate for a theoretical monodisperse collection of bubbles is given by:

$$f_C = 5.77 \alpha^2 \varepsilon^{1/3} {d_B}^{-11/3} \exp\left(-1.29 \varepsilon^{1/3} {d_B}^{5/6} \sqrt{\rho_L/\sigma}\right) \tag{2.3.6}$$

where α is the volume fraction of bubbles. In this expression, the pre-exponential term is the collision frequency, and the exponential term gives the likelihood of coalescence.

These expressions do predict reasonable bubble sizes, as illustrated by Figure 2.3.4. To calculate these figures, it was assumed that the stirring power of the gas is uniformly dissipated within the plume, using the correlations of Krishnapisharody and Irons [13] to estimate the plume shape and bubble void fraction.

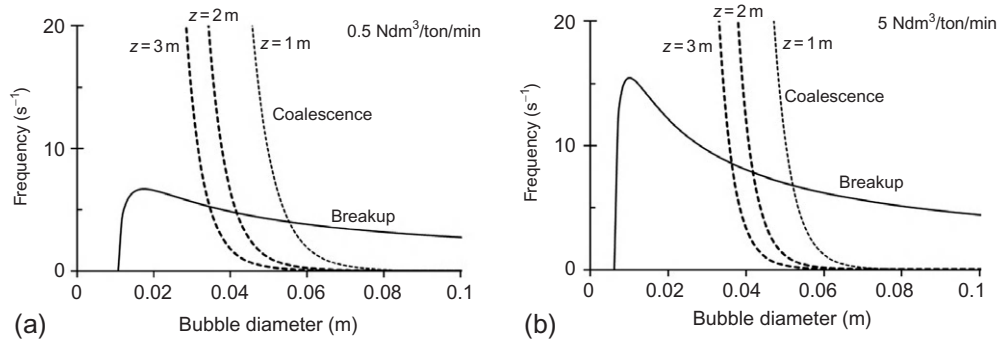


Figure 2.3.4 Predicted rates of bubble breakup (solid lines) and coalescence (broken lines) for argon injection into a 150-ton steel ladle at 1873 K (ladle diameter 3 m), for two argon flow rates: (a) 0.5 Ndm^3/ton/min and (b) 5 Ndm^3/ton/min.

In Figure 2.3.4, the steady-state bubble size is given by the intersection of the breakup and coalescence curves. Bubbles larger than the steady-state size have a higher rate of breakup than coalescence and hence would decrease in size; bubbles smaller than the steady-state size grow by coalescence (since their coalescence rate is higher than their breakup rate). The rates are large enough to allow each bubble to undergo several breakup or coalescence events during its residence time in the plume, which is around a second. The bubble sizes (several centimeters in diameter) and trends (small bubbles higher in the ladle; somewhat larger bubbles at a higher gas flow rate) agree with what is expected, indicating that this is a promising approach to bubble size prediction.

2.3.3. BUBBLE SHAPES

The steady-state shape of bubbles depends on the balance between drag (which tends to deform bubbles) and surface tension (which tends to restore the bubble to a spherical shape). For this reason, the Weber number (the ratio of inertial to surface tension forces) has been used to map possible bubble shapes (Figures 2.3.5 and 2.3.6) [20,22]. Bubbles in liquid metals typically have $We \sim 10^2$ and $Re \sim 10^4$, in the spherical-cap region of the bubble-shape map. (This map was originally drawn with the Eötvös [Bond] number as the abscissa. For spherical-cap bubbles, the Froude number is 1 [23], and hence the Eötvös number is numerically equal to the Weber number.)

2.3.4. PLUME SHAPE

Based on the discussion this far, the main features of subsonic gas flow from a porous plug or orifice can be summarized simply: spherical-cap bubbles with a diameter of a few centimeters are expected to be present, with little effect of the injector condition

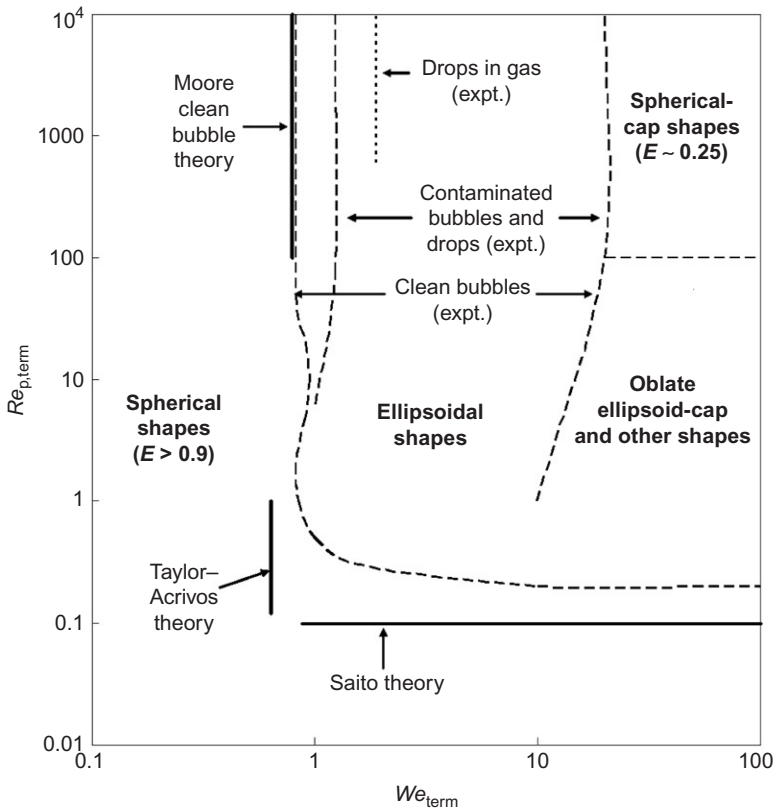


Figure 2.3.5 Expected bubble shapes, for different Reynolds and Weber numbers [22].

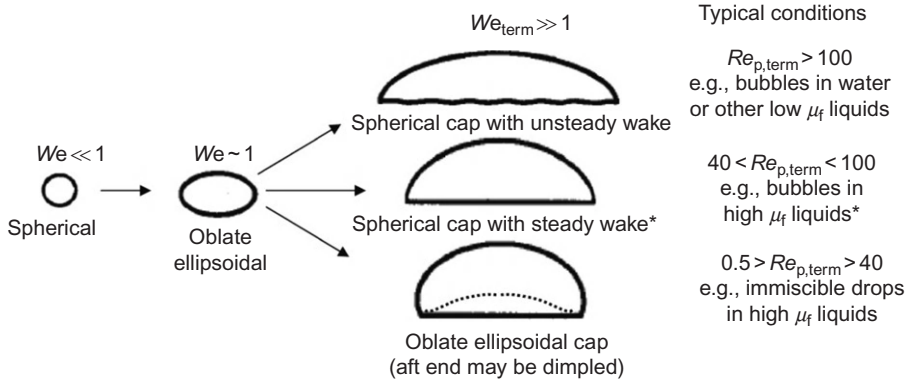


Figure 2.3.6 Examples of bubble shapes [22].

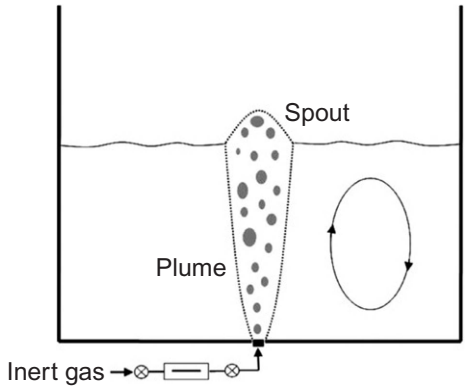


Figure 2.3.7 Schematic diagram of a bubble plume and liquid circulation in a gas-stirred ladle [13].

on bubble size and shape. Of practical importance in reaction kinetics are the gas hold-up in the liquid bath, liquid circulation rate, liquid velocity in the plume, and the total bubble–liquid contact area.

Here, "plume" refers to the expanding column of bubbles over the injection point (see Figure 2.3.7). Within the plume, the radial distributions of the vertical velocity and the gas content of the liquid are both Gaussian; the width of the velocity distribution is wider (by a factor of approximately 1.4) than that of the gas distribution [2]. The plume boundary is often assumed to be conical, although Krishnapisharody and Irons have suggested that the shape is actually parabolic [24], and presented useful correlations which obey rational scaling laws [13]. The correlations are as follows (for SI units):

$$r = 0.55 Q^{0.2} z^{0.5} \tag{2.3.7}$$

$$\alpha = 0.55 Q^{0.63} z^{-1.57} \tag{2.3.8}$$

$$u_L = 2.57 Q^{0.31} z^{-0.28} \tag{2.3.9}$$

$$u_G = 7.3 Q^{0.37} z^{-0.43} \tag{2.3.10}$$

where Q is the gas flow rate, z is the distance from the bottom of the ladle, and r is the plume radius. The values for the three other parameters are averages for the plume cross-section and are the gas volume fraction (α), the vertical liquid velocity (u_L), and the vertical gas velocity (u_G). As an example of the use of these equations, Figure 2.3.8 shows the calculated plume width, gas fraction, and vertical velocities for a typical steelmaking ladle. (In performing this calculation, gas flow rate [Q] is calculated for conditions at ladle mid-height.) The expected trends are observed, namely a sharp decrease in the gas concentration with vertical distance, and nearly constant gas and liquid velocities [2].

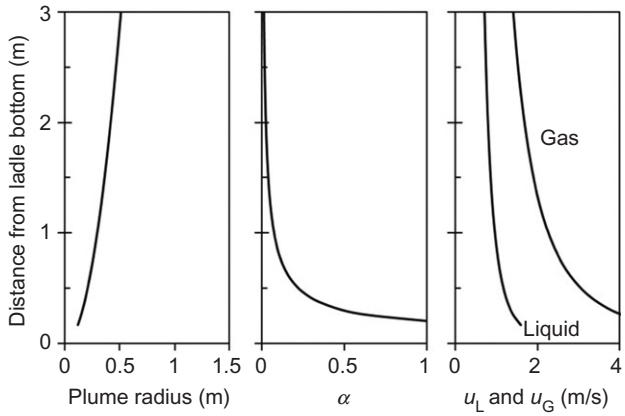


Figure 2.3.8 Example of calculated plume properties, using the correlations of Krishnapisharody and Irons [13] (cylindrical steel ladle, 150 ton steel mass, inner diameter 3 m, at 1873 K; argon flow rate 5 Ndm^3/ton/min).

2.3.5. MIXING TIME

One of the functions of gas stirring is to homogenize the temperature and composition in the liquid. Various correlations are available to estimate the "mixing time" (the time to achieve a certain percentage of the change in composition; this percentage is often taken to be 95%). The correlation of Mazumdar and Guthrie is convenient [25]:

$$\tau_m = 25.4R^{7/3}\left(Q^{1/3}H\right) \tag{2.3.11}$$

where τ_m is the 95% mixing time, R the vessel radius and H its depth, and Q the gas flow rate (at the average temperature and pressure in the bath), all in SI units. As an example, this expression predicts a mixing time of 56 s for the conditions of Figure 2.3.8.

While such correlations are useful, it should be recognized that the mixing time is not the same everywhere in a ladle. For an axially placed porous plug, a dead volume is present at the bottom of the ladle along the wall; an asymmetrically placed plug (or use of multiple plugs) can greatly increase the flow rate in this region (Figure 2.3.9) [8,26].

2.3.6. BUBBLE RUPTURE

Bubbles rising to the surface of the liquid bath rupture or can move into an overlying liquid layer (such as slag). If the bubbles rupture, droplets of liquid are ejected; this mechanism is a major source of sea water aerosols (forming from bubbles produced by breaking waves) [27] and is estimated to form 60% of the dust in electric arc furnace steelmaking (from carbon monoxide bubbles) [28]. Smaller droplets form by rupture of

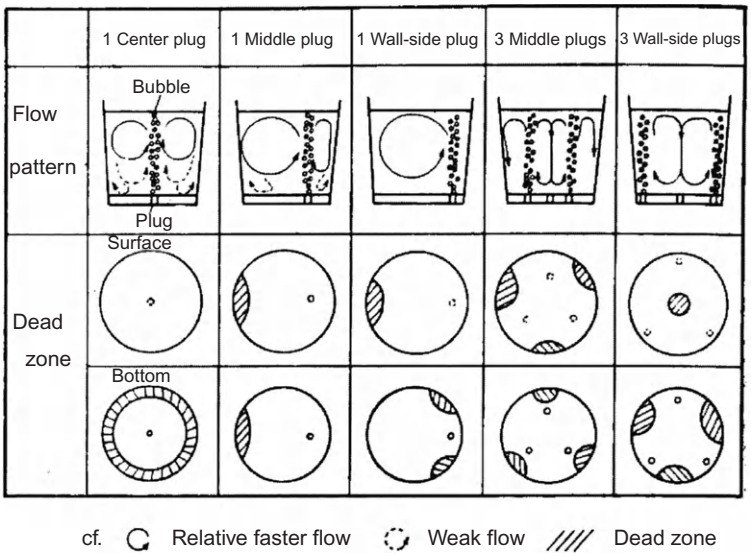


Figure 2.3.9 Effect of porous plug number and placement on flow in gas-stirred ladles [26].

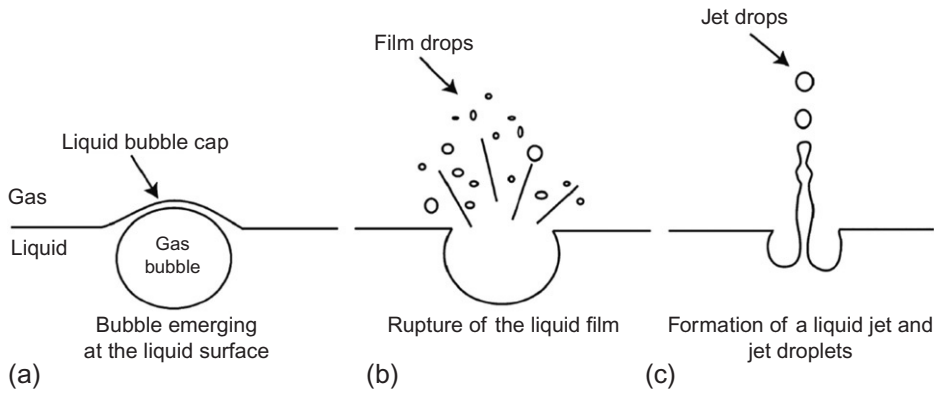


Figure 2.3.10 Bubble rupture leading to ejection of film droplets and jet droplets [28].

the liquid film covering the bubble, and larger droplets result from a jet which arises when the liquid cavity relaxes under the effects of buoyancy and surface tension (Figure 2.3.10). The large (jet) droplets are around one-tenth the diameter of the bubble, and the number of jet droplets decreases strongly with bubble size [28]. The amount of material which can be ejected is 20–30 g/m^3 of gas flow, for argon bubbles bursting at the surface of liquid steel [28].

If the liquid metal surface is covered by a slag layer, metal droplets can be transferred into the slag by a similar mechanism (Figure 2.3.11) [29].

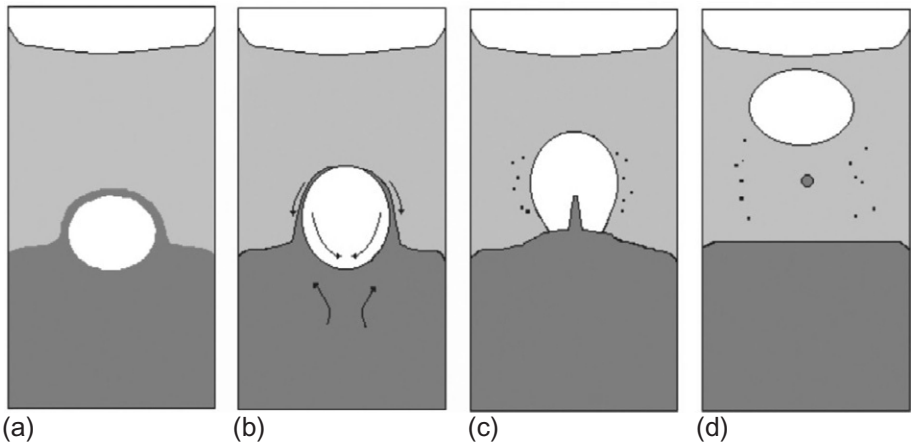


Figure 2.3.11 Mechanism of metal droplet transfer into the slag layer when a gas bubble ruptures at the metal–slag interface [29]. (a) to (d) show consecutive stages of rupturing and bubble escape.

2.3.7. BUBBLING–JETTING TRANSITION

As noted in the previous section, at increased gas flow rates, interference between bubbles increases. If the gas flow rate is sufficiently high, bubbles coalesce at the orifice, and the gas stream remains unbroken, and in permanent contact with the orifice. Such permanent contact is one definition of jetting flow [30]. Mori suggested that jetting flow starts to dominate if the gas velocity at the nozzle exit exceeds the sonic velocity [31]. The transition is not sharp; rather, jetting flow starts to occur for some of the time as the gas speed exceeds the sonic velocity (Figure 2.3.12). The conclusion that jetting starts to predominate at Mach numbers around 1 (transonic flow) was confirmed by a recent study that found (for water model experiments) that jet penetration sharply increased if the gas flow rate approached or exceeded the sonic velocity [30].

Unlike the case for bubbling flow through a porous plug, jetting appears to be very sensitive to inlet conditions. This sensitivity can be used advantageously, for example, by changing the tuyère configuration to promote jetting flow, so avoiding metal penetration into the tuyères; such metal penetration leads to tuyère wear [32].

However, some studies found that the transition to jetting does not coincide with sonic flow in the tuyère, in the case of low-density gases (hydrogen and helium) [33]. Lee *et al.* suggested that transition to jetting is better correlated with a critical value of the "nondimensional mass velocity" (N_G), defined as follows [33]:

$$N_G = \rho v / \rho^* v^* \tag{2.3.12}$$

where ρ and v are the gas density and velocity at the nozzle exit, and ρ^* and v^* are the gas density under standard conditions (taken to be 1 bar and 293 K) and the sonic velocity

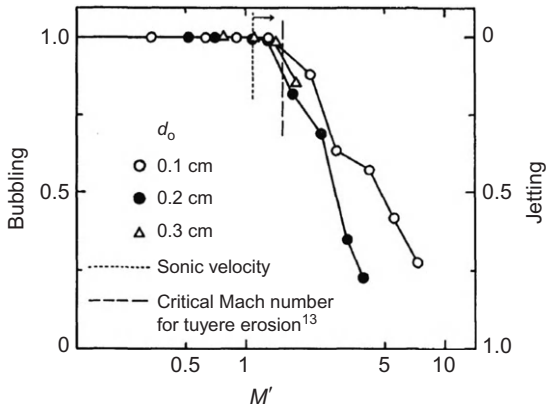


Figure 2.3.12 Time fractions of bubbling and jetting flow at different Mach numbers, for gas injected into mercury [31].

under standard conditions. This means that the nondimensional mass velocity (NDMV) is closely related to the Mach number:

$$N_G = (\rho/\rho*)Ma \tag{2.3.13}$$

This approach therefore simply compensates for departure of the gas temperature and pressure from standard conditions. Increased pressure at the nozzle exit is associated with underexpanded flow, with resulting shock waves, which may well tend to disturb jetting flow.

It is not clear that the NDMV approach improves prediction of jetting flow; the available data suggest that assuming the transition to occur when *Ma* is around 1 is sufficient in most cases. Certainly, jetting flow is not expected for the typical gas flow rates employed in ladle stirring. Jetting is expected in the case of converters that use submerged tuyères.

Some of the ambiguity concerning the transition to jetting flow may be related to uncertainty as to what the sonic velocity is, since the sonic velocity depends on gas temperature and is strongly affected by entrained liquid.

2.3.7.1. Effects of Temperature and Entrained Liquid on the Sonic Velocity

For the case of adiabatic flow, the sonic velocity in gas is given by

$$c = (\gamma RT/M)^{1/2} \tag{2.3.14}$$

where $\gamma = C_p/C_v$ (note that $\gamma \approx 1.4$ for diatomic gases at room temperature; $\gamma = 5/3$ for argon), R is the ideal gas constant, T the absolute temperature, and M the molar mass of the gas.

As this expression shows, the gas temperature at the nozzle exit is important, because the sonic velocity is proportional to the square root of the absolute temperature. For flow

through porous plugs, Oeters [2] suggested that gas heating occurs before the gas leaves the porous plug. In contrast, for injection through nozzles in relatively shallow baths of liquid steel (laboratory experiments; bath depth approximately 0.17 m), Sharma [32] estimated the gas exit temperature to be barely above ambient (approximately 80 °C). Wraith and Chalkely similarly suggested that the gas would remain cold close to the injection point [34]. Hence, it does not appear that uncertainty in the gas temperature could account for any large departure from the $Ma = 1$ criterion for the onset of jetting flow. However, entrained liquid can have a strong effect.

When gas is injected into a liquid, it appears likely that some of the liquid is entrained into the gas stream. The speed of sound in such a gas–liquid mixture is much lower than in the gas alone, at even modest liquid contents in the gas. For the case where the pressure in the gas is equal to that in the liquid (that is, with a negligible effect of surface tension), the sonic velocity in the mixture is given by [35]:

$$\frac{1}{c^2} = [\rho_L(1-\alpha) + \rho_G\alpha]\left[\frac{\alpha}{kp} + \frac{(1-\alpha)}{\rho_L c_L^2}\right] \tag{2.3.15}$$

where ρ_i is the density of phase i (where i can be "L" or "G") α is the volume fraction of gas, p is the pressure, and c_L is the sonic velocity in the liquid. $k = 1$ for isothermal flow, and $k = 1.4$ for adiabatic flow (in diatomic gas at room temperature). For small volume fractions of liquid, and in the general case where $kp/\rho_L c_L^2 \ll 1$, the expression can be simplified to

$$\frac{1}{c^2} = \frac{\alpha}{kp}[\rho_L(1-\alpha) + \rho_G\alpha]. \tag{2.3.16}$$

This expression reveals the origin of the strong effect of entrained liquid on the sonic velocity of gas. The sonic velocity is inversely proportional to the square root of mixture density; because the liquid density is around 10^4 times larger than the gas density (for gas injected into liquid iron), even a small amount of entrained liquid has a large effect on the density of the mixture, while the bulk elastic modulus of the mixture remains nearly unchanged. (For an ideal gas, and for the mixture of gas with a small fraction of liquid, the bulk elastic modulus is simply equal to kp.) The large effect of even a small volume of entrained liquid is illustrated by Figure 2.3.13.

Liquid can be entrained into jetting flow if a converging–diverging nozzle is used (whether by design or due to wear of the nozzle during use) and if the flow is "overexpanded." In the overexpanded case, the static pressure at the nozzle exit is lower than in the surrounding liquid; this occurs if the gas flow rate through a converging–diverging nozzle reaches sonic velocity in narrowest part of the nozzle, but the flow is lower than the design flow.

In the recent study of Weiland and Vlachos, care was taken to ensure that gas jets were perfectly expanded at the nozzle exit [30]. In other studies, discrepancies in observations

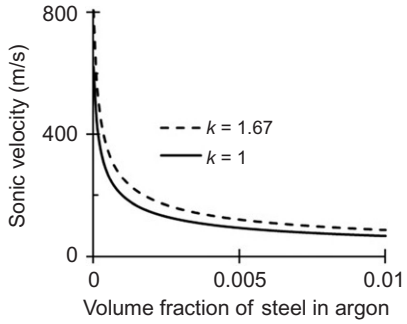


Figure 2.3.13 Effect of entrained liquid steel in argon, on the sonic velocity. Calculated for a gas temperature of 1873 K and pressure of 3 atm; liquid steel density taken as 7000 kg/m^3.

regarding the effect of gas flow rate on bubble-to-jetting transition may well be related to overexpanded or underexpanded conditions during the tests. Based on water model experiments (with a single injection orifice), it was suggested that droplets are carried away by the gas flow [34]. Zhao and Irons suggested that droplets form by flow instability at the gas–liquid interface, and that the gas jet is stabilized by the droplets [36]. If it is indeed the case—as suggested by several researchers—that stabilization of jetting flow is associated with the gas flow rate achieving sonic velocity, then decrease of the sonic velocity by entrained liquid (Figure 2.3.13) may well serve to stabilize jet flow.

2.3.7.2. Jet Breakup

In the case of jetting flow, the stream of gas breaks up into numerous small bubbles downstream. This process has been studied carefully for a water model and tested against predictions regarding stability of fluid interfaces [30]. Fluid interfaces can break up by the KH mechanism when the fluids move relative to one another in shear; this is the mechanism by which wind raises ripples on water. Where a less dense fluid is trapped beneath a denser fluid (as is the case for gas injection into liquid metal), the interface can break up even if the fluids are initially at rest (RT instability). Figure 2.3.14 illustrates interface breakup by the two mechanisms.

Quantitative analysis of jet movement (and taking into account the gas and liquid densities and interfacial tension) indicates that the KH and RT mechanisms are equally important in jet breakup, in line with the previous conclusion of Zhao and Irons [36].

2.3.8. MODELING

Much of the insight into bubble and plume behavior has come from physical modeling (often using water) and computer modeling of flow. Quantitative predictions require reliable ways to scale between experimental and practical conditions, that is, consideration of appropriate dimensionless groups.

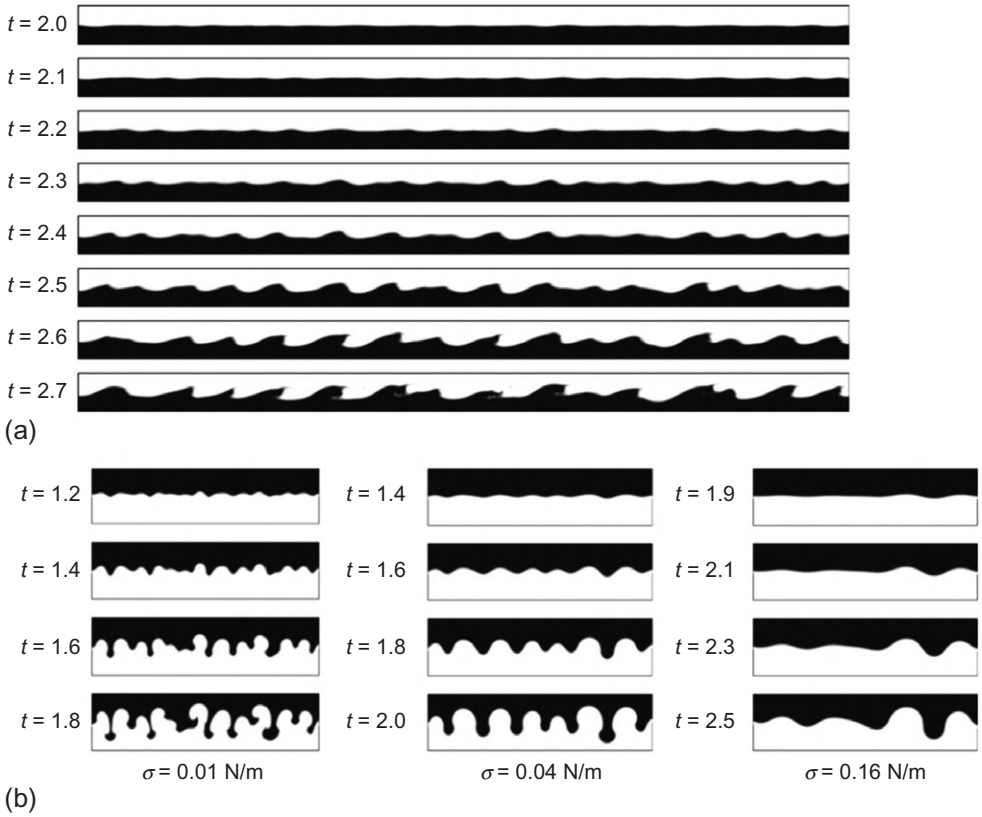


Figure 2.3.14 Development (with increased time) of unstable interfaces. (a) Kelvin–Helmholtz instability due to shear flow between two fluids. (b) Rayleigh–Taylor instability (layer of denser liquid lying on top of less dense liquid); note how increased interfacial tension suppresses instability [11].

Flow in gas-stirred ladles is Froude dominated, that is, the effect of the buoyancy of the injected gas on the inertia of the liquid in the ladle determines flow [37,38]. Dynamic scaling should hence be based on the Froude number and not on the Reynolds number (which gives the ratio of inertial to viscous forces) [37].

The Froude number is the ratio of the square of a characteristic velocity to a characteristic length ($Fr = u^2/gL$); appropriate scaling requires use of the correct velocity and length dimension. In the bubbling regime, ladle flow is not strongly affected by inlet conditions, and hence the orifice diameter is not the correct characteristic length. Rather, the plume Froude number is used for scaling, containing the plume length (typically the ladle depth, H) and the average liquid velocity in the plume:

$$Fr = \frac{\bar{U}_L^2}{gH} \tag{2.3.17}$$

It has been suggested that, for full similarity, the plume Froude number should also contain the average void fraction in the plume [13]:

$$Fr = \frac{\bar{U}_L^2}{\bar{\alpha} g H} \tag{2.3.18}$$

One of the implications of Froude dynamic similarity and the observed effect of size and flow rate on mixing time and the plume spout is that the gas flow rate should be scaled by $\lambda^{2.5}$, where λ is the linear geometric scaling factor [13,38]. This is the same scaling factor previously used by Kim and Fruehan [39].

In addition to appropriate geometric and dynamic scaling, the effect of model fluids should be considered. The $[\sigma/(\rho g)]^{0.5}$ ratio (calculated in Table 2.3.1 below) defines a characteristic length for flow affected by surface tension (such as deformation of bubbles) and hence appears in the Weber number. Water turns out to be an appropriate medium for modeling gas-stirred metals, because the ratio of surface tension to density of water is of the same order as that of liquid metals; see Table 2.3.1.

There are many examples of computer modeling of gas-stirred ladles in the literature. It is currently not possible to model the free surfaces of individual bubbles within a larger ladle flow model. Rather, multiscale models are employed, modeling bubble evolution in a smaller domain and then transferring bubble behavior as an input to ladle models (see Figure 2.3.15). For modeling of flow of individual bubbles (prediction of interface shape evolution and breakup), benchmark test cases have been proposed for quantitatively testing the accuracy of the results from different codes [41].

Both Euler–Lagrange and Euler–Euler (two-fluid) models have been used for ladle flow modeling [13,42]. All such models require a large number of inputs (turbulence model, bubble size and breakup, and bubble drag and lift coefficients), which would affect the accuracy of model outputs [13]. For example, it has been shown that neglecting bubble breakup leads to incorrect plume flow predictions [13]. Using correlations for

Table 2.3.1 Density and Surface Tension of Selected Liquids

Liquid	Temperature (K)	Density (kg/m^3)	Surface Tension (N/m)	Length Scale $[\sigma/(\rho g)]^{0.5}$ (m)
Iron	1873	7000	1.8	5.1×10^{-3}
Water	298	1000	0.073	2.7×10^{-3}
Mercury	298	13,500	0.46	1.9×10^{-3}
Wood's metal	353	10,600	0.40	2.0×10^{-3}
Tin	523	7000	0.48	2.6×10^{-3}
Hexane	298	650	0.018	1.7×10^{-3}

Adapted from Ref. [19].

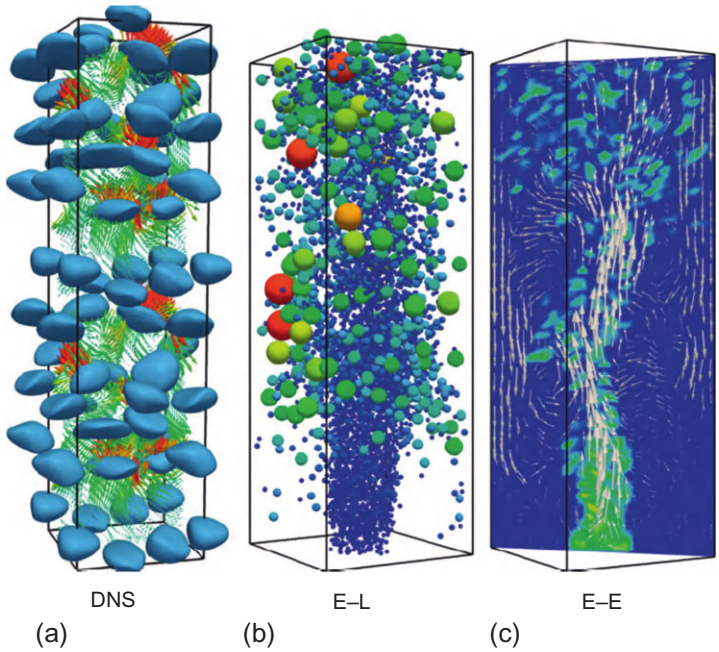


Figure 2.3.15 Illustration of different length scales of modeling: (a) direct numerical simulation of bubble shapes, (b) Euler–Lagrange model (with input bubble characteristics), and (c) Euler–Euler (two-fluid) model [40].

bubble breakup and coalescence appears to be a promising approach for predicting bubble size, rather than having to rely on bubble sizes measured by water modeling [16].

REFERENCES

[1] K. Iwata, T. Choh, M. Inouye, Trans. ISIJ 23 (1983) 218–227.
[2] F. Oeters, Metallurgy of Steelmaking, Verlag Stahleisen, Düsseldorf, 1989.
[3] D. Mazumdar, R.I.L. Guthrie, ISIJ Int. 35 (1995) 1–20.
[4] D. Gerlach, G. Biswas, F. Durst, V. Kolobaric, Int. J. Heat Mass Transf. 48 (2005) 425–438.
[5] K. Mori, M. Sano, T. Sato, Trans. Iron Steel Inst. Jpn. 19 (1979) 553–558.
[6] D. Gerlach, N. Alleborn, V. Buwa, F. Durst, Chem. Eng. Sci. 62 (2007) 2109–2125.
[7] L. Zhang, M. Shoji, Chem. Eng. Sci. 56 (2001) 5371–5381.
[8] K.W. Lange, Int. Mater. Rev. 33 (1988) 53–89.
[9] J.F. Davidson, B.O.G. Schüler, Trans. Inst. Chem. Eng. 38 (1960) 335–342.
[10] J. Kitscha, G. Kocamustafaogullari, Int. J. Multiphase Flow 15 (1989) 573–588.
[11] L. Štrubelj, I. Tiselj, Nucl. Eng. Des. 241 (2011) 1018–1023.
[12] M. Zhou, J.K. Brimacombe, Metall. Mater. Trans. B 25B (1994) 681–693.
[13] K. Krishnapisharody, G.A. Irons, ISIJ Int. 50 (2010) 1413–1421.
[14] P.E. Anagbo, J.K. Brimacombe, Metall. Trans. B 21B (1990) 637–648.
[15] A. Alexiadis, Appl. Math. Model. 31 (2007) 1534–1547.
[16] A. Alexiadis, P. Gardin, J.F. Domgin, Metall. Mater. Trans. B 35B (2004) 949–956.
[17] C. Martínez-Bazán, J.L. Montañés, J.C. Lasheras, J. Fluid Mech. 401 (1999) 157–182.

[18] Y. Sundberg, Scand. J. Metall. 7 (1978) 81–87.
[19] K. Wichterle, Steel Res. Int. 81 (2010) 356–361.
[20] J.R. Grace, Trans. Inst. Chem. Eng. 51 (1973) 116–120.
[21] M.J. Prince, H.W. Blanch, AIChE J. 36 (1990) 1485–1499.
[22] E. Loth, Int. J. Multiphase Flow 34 (2008) 523–546.
[23] P.P. Wegener, J.-Y. Parlange, Annu. Rev. Fluid Mech. 5 (1973) 79–100.
[24] K. Krishnapisharody, G.A. Irons, Metall. Mater. Trans. B 38B (2007) 377–388.
[25] D. Mazumdar, R.I.L. Guthrie, Metall. Trans. 17B (1986) 725.
[26] K. Narita, A. Tomita, Y. Hirooka, Y. Satoh, Tetsu-to-Hagané 57 (1971) 1101–1108.
[27] E.M. Mårtensson, E.D. Nilsson, G. de Leeuw, L.H. Cohen, H.-C. Hansson, J. Geophys. Res. 108 (D9) (2003) 4297.
[28] A.-G. Guézennec, J.-C. Huber, F. Patisson, P. Sessiecq, J.-P. Birat, D. Ablitzer, Powder Technol. 157 (2005) 2–11.
[29] Z. Han, L. Holappa, Metall. Mater. Trans. B 34B (2003) 525–532.
[30] C. Weiland, P.P. Vlachos, Int. J. Multiphase Flow 48 (2013) 46–57.
[31] K. Mori, Y. Ozawa, M. Sano, Trans. Iron Steel Inst. Jpn. 22 (1982) 377–384.
[32] S.K. Sharma, Transactions of the ISS, I&SM 14 (3) (1987) 73–85.
[33] M.S. Lee, T.J. Evans, N.A. Molloy, Ironmaking Steelmaking 28 (2001) 329–336.
[34] A.E. Wraith, M.E. Chalkely, in: M.J. Jones (Ed.), Advances in Extractive Metallurgy 1977, The Institute of Mining and Metallurgy, London, 1977.
[35] C.E. Brennen, Fundamentals of Multiphase Flow, Cambridge University Press, New York, 2005.
[36] Y.-F. Zhao, G.A. Irons, Metall. Trans. B 21B (1990) 997–1003.
[37] D. Mazumdar, R.I.L. Guthrie, Metall. Mater. Trans. B 30B (1999) 349–351.
[38] D. Mazumdar, H.B. Kim, R.I.L. Guthrie, Ironmaking Steelmaking 27 (2000) 302–309.
[39] S.-H. Kim, R.J. Fruehan, Metall. Trans. B 18B (1987) 381–390.
[40] I. Roghair, Y.M. Lau, N.G. Deen, H.M. Slagter, M.W. Baltussen, M. Van Sint Annaland, J.A.M. Kuipers, Chem. Eng. Sci. 66 (2011) 3204–3211.
[41] S. Hysing, S. Turek, D. Kuzmin, N. Parolini, E. Burman, S. Ganesan, L. Tobiska, Int. J. Numer. Methods Fluids 60 (2009) 1259–1288.
[42] M.T. Dhotre, B.L. Smith, Chem. Eng. Sci. 62 (2007) 6615–6630.

CHAPTER 2.4

Foams and Foaming

Kimihisa Ito
Department of Applied Mathematics, Waseda University, Tokyo, Japan

2.4.1. FOAMING IN METALLURGICAL PROCESSES

Foams are very complex systems consisting of dispersed gas bubbles separated by draining films. In metallurgical processes, slag foaming involves the expansion of slag layer by injected gas or by gas generated by chemical reactions. The precise control of this dynamic phenomenon is crucial for the success of some metallurgical processes.

2.4.1.1. Study of Slag Foaming

Observation of slag foaming has been carried out by two different techniques. In the pneumatic method, bubbles are injected into a molten slag through one or more orifices. In the chemical reaction method, gas formation reactions, such as the reduction of iron oxide in slag by carbonaceous materials, are used to supply the bubbles to obtain the foaming slag. The pneumatic method offers the advantage of facilitating the control of the supply rate and mean diameters of the bubbles by varying the experimental conditions like the gas flow rate and orifice diameter. Hence, this method has been widely used for the study of slag foaming. However, the range over which the bubble sizes can be varied is rather limited, especially for small bubbles less than 10 mm in diameter.

Figure 2.4.1 shows a typical experimental arrangement used for the study of slag foaming using the pneumatic method [1]. An inert gas is introduced through an orifice into a molten slag placed in a crucible. The surface position of the slag is detected by an electric probe. The foam height is usually defined as the increment in the slag surface level from the original (i.e., when gas flow rate is zero) to that formed after foaming, which is measured at a steady state while the gas is bubbling. The foam life is defined as the time for the foam height decay to some fractions of its initial value after the gas is turned off at the steady state. The bubble formation frequency is determined by a pressure transducer connected to the bubbling nozzle to calculate the mean bubble size from the gas flow rate.

Cooper and Kitchener [2] studied the foaming of $CaO–SiO_2$ slag at temperatures ranging from 1748 to 1998 K. They measured the life of a specific volume of foam and found that the foam life increased when the temperature and basicity decreased. It was also observed that the addition of a small amount of P_2O_5 increased the foam

Treatise on Process Metallurgy, Volume 2
http://dx.doi.org/10.1016/B978-0-08-096984-8.00003-3
© 2014 Elsevier Ltd.
All rights reserved.

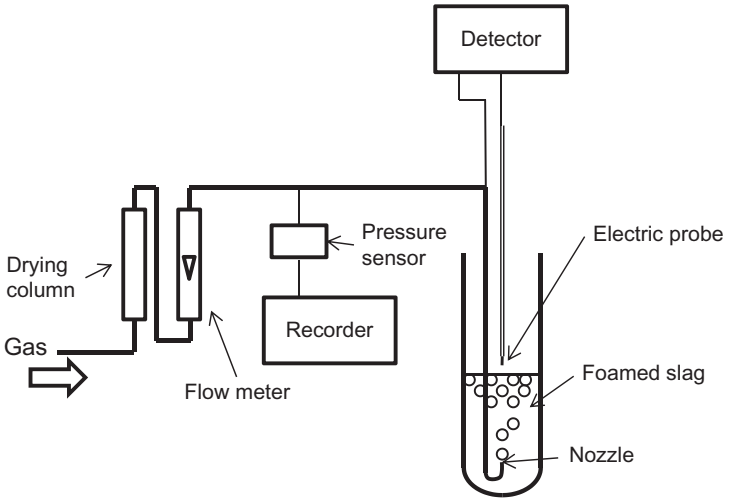


Figure 2.4.1 Schematic representation of the typical experimental setup used for generating slag foams by pneumatic method [1].

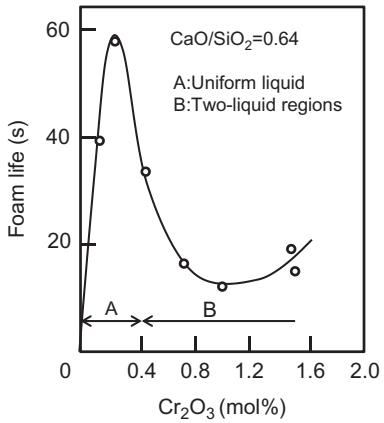


Figure 2.4.2 Variation in the foam life in CaO–SiO_2 slag after the addition of Cr_2O_3 [3].

life. Swisher and McCabe [3] studied the effect of Cr_2O_3 on the foaming of slags in the temperature range 1853–1913 K by using the technique employed by Cooper and Kitchener. Their studies indicated that Cr_2O_3 increased the foam life only within the regions of slag compositions that were completely in a single liquid state, but the foam life was decreased in the two-liquid region, as shown in Figure 2.4.2. Hara *et al.* [4] measured the foam life and foam height in CaO–FeO, SiO_2–FeO, and CaO–SiO_2–FeO slag systems at 1523 and 1573 K. The foam life was defined in an identical manner as mentioned in the previous studies. Their studies showed that the foam life increased with increasing foam height and decreasing surface tension of the slag.

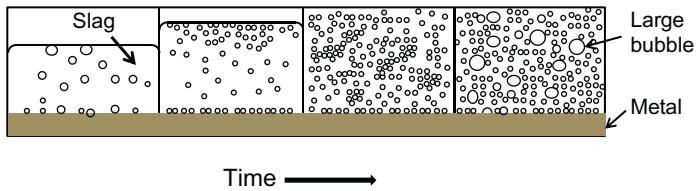


Figure 2.4.3 Slag foaming caused by slag–metal reactions as observed by X-ray fluoroscopic method [6].

The chemical reaction method, on the other hand, is favorable to investigate the dynamic phenomena that occur during the actual metallurgical slag foaming process. Ogawa and Tokumitsu [5,6] observed the slag foaming caused by slag–metal reactions in a graphite crucible with the aid of X-ray fluoroscopic apparatus to clarify the effect of the bubble sizes on the foam height and distribution of bubbles in the slag. X-Ray images of slag foaming caused by the slag–metal reaction are shown in Figure 2.4.3. The foam layer was observed to develop when the diameter of the CO bubbles, evolved at the slag–metal interface, became lesser than around 2 mm. The foam height increased with a decrease in the bubble size for a particular gas evolution rate. The size of the bubbles decreased with an increase in the iron oxide and sulfur contents in the slag.

Yokoyama *et al.* [7] studied slag foaming in $CaO–SiO_2–Al_2O_3–MgO$ systems formed during the reduction of chromite ore by $Fe–C_{sat}$ melts. They assumed the bubble life, the average residence time of CO gas, to be equal to the foam life and calculated it from the CO gas generation rate. The foam life was found to decrease with an increase in the MgO content, and by increasing the ratio of CaO to SiO_2 in the slag, the foam life was also strongly affected by the slag viscosity.

Kapilashrami *et al.* [8] analyzed the phenomenon of slag foaming under dynamic conditions on the basis of the results from X-ray image analysis. The mismatch between the gas generation rate and gas escape rate was found to significantly affect the foam height, which was attributed to the rate of the chemical reaction. Khanna *et al.* [9] have developed novel video-processing software for the sessile drop technique for the rapid and quantitative estimation of slag foaming, which could be used for determining the extent of formation and stability of the foam as a function of time.

2.4.1.2. Foam Stability

The stability of the foam is strongly governed by the resistance forces operating against film thinning. These resistance forces are caused by the surface viscosity of the liquid. The underlying concept is that the viscosity of the inner layer is equal to that of the bulk, but the viscosity of the exterior layers on both sides is much higher than that of the bulk [10]. The surface viscosities of various aqueous solutions and several slag systems have

been measured [11]. According to the results of experiments conducted on several binary oxide melts carried out by Hara *et al.*, the foaminess of the slags strongly depended on the surface viscosities [12].

In addition, the surface elasticity is also an important contributor to the resistance forces operating against film thinning. Let us assume that the bulk liquid containing the surface active species is initially in equilibrium with the slag surface, and a portion of the surface is locally extended by an external force. In such a system, according to Gibbs [13], the elasticity of the surface E (N m^{-1}) is expressed by Equation (2.4.1):

$$E = \frac{a\mathrm{d}\sigma}{\mathrm{d}a} = \frac{\mathrm{d}\sigma}{\mathrm{d}lna} \tag{2.4.1}$$

In the above equation, a denotes the surface area (m^2) and σ (N m^{-1}) is the surface tension of the slag.

As the diffusion of surface active species from the bulk to the surface requires a definite amount of relaxation time, the surface concentrations of the surface active species in the extended portion will be lower than the equilibrium concentration. Therefore, the surface tension of the extended portion becomes larger than that of the surrounding surface that is in equilibrium with the bulk. This difference in the surface tensions tends to push the adjacent surrounding surface toward the extended region. When such a surface flow is generated, an accompanying bulk flow is produced by the viscous drag on the underlying bulk liquid. This viscoelastic phenomenon, the Marangoni effect, is illustrated in Figure 2.4.4, which is thought to be the major mechanism of slag foam stabilization [1,3,4,14].

2.4.1.3. Foam Drainage

Usually, three foam films meet along an edge termed as the "Plateau border," through which drainage of the liquid from the film occurs due to gravitational force. Although, in

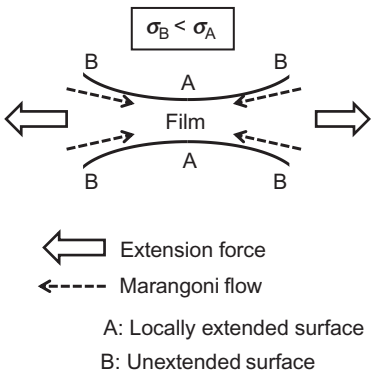


Figure 2.4.4 Stabilization of foam by Marangoni effect [10].

principle, foam drainage and foam collapse are independent, foam drainage does make the films thinner. As the critical film thickness for rupture of slag foams is thought to be much higher than that of aqueous foams, it is reasonable to assume that the collapse of foams can be expressed in terms of the drainage of liquid from the foam. Assuming first-order kinetics for the drainage, the rate of drainage is given by Equation (2.4.2):

$$\frac{\mathrm{d}v}{\mathrm{d}t} = k\left(V^0 - v\right) \tag{2.4.2}$$

where k (s^{-1}) represents the rate constant of foam drainage, V^0 (m^3) is the initial volume of liquid in the foam, and v (m^3) is the drained liquid volume. By integrating Equation (2.4.2) from $t=0$ to t, Equation (2.4.3) is obtained as follows:

$$kt = -\ln\left(\frac{V^0 - v}{V^0}\right) \tag{2.4.3}$$

When the container is cylindrical and the void fraction α (−), which is the volumetric fraction of gas in the foamed layer, is assumed to be a constant, Equation (2.4.3) can be written as given below:

$$kt = -\ln\left(\frac{h}{h^0}\right) \tag{2.4.4}$$

In Equation (2.4.4), h (m) is the foam height after a duration of t (s) and h^0 (m) is the initial foam height. The average foam life, τ (s), can be shown to be equal to $1/k$.

According to Equation (2.4.4), if the decay of foam height is measured and $-\ln(h/h^0)$ is plotted against time, the gradient represents the average foam life, which is one of the physical parameters of foaming. On the other hand, the foam life introduced in 2.4.1.1 according to the early studies is only an empirical index and cannot be used for a qualitative analysis. Figure 2.4.5 shows the variation of logarithmic relative foam height with time for CaO–SiO_2–FeO slag at 1573K. In this case, the slag foam was prepared by the

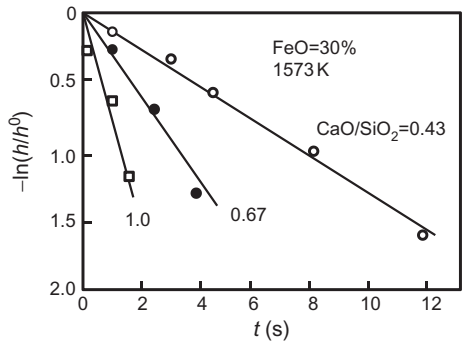


Figure 2.4.5 Variation of foam height with time [1].

pneumatic method, and the bubble diameters ranged from 10 to 15 mm [1]. All the data points showed a good linear relationship, and the foam life increased with decreasing basicity index, i.e., the ratio CaO/SiO_2. Mukai *et al.* [15] directly observed the foaming of $CaO–SiO_2–Al_2O_3–FeO$ slag in reaction with Fe-4.5 wt% C alloy at 1773 K using a X-ray radiographic technique. They measured the decay of foam with time after the formation of CO bubbles ceased and confirmed the validity of Equation (2.4.4) for slag foaming caused by chemical reactions.

2.4.1.4. Physical Model of Slag Foaming

Ogawa *et al.* [16] developed a physical model to describe slag foaming using the results of cold and hot model experiments. The bubble size at the slag–metal interface, the void fraction of the foam, and the film life of a bubble at the top surface of the slag were calculated. These studies confirmed that the bubble size at the slag–metal interface is essentially determined by the static balance between the buoyancy force and the adhesive force at the slag–metal interface.

Ito and Fruehan [1] treated slag foaming as a dynamic phenomenon and a special case of one-dimensional two-phase flow, and they measured the foaming index, Σ (s) [10,17], to make quantitative predictions about foaming in practical operations. A more detailed explanation about the foaming index will be furnished in Section 2.4.2. Ghag *et al.* [18] proposed a general model to describe foaming, which relates the structure of the foams stabilized by viscoelastic forces to the bubble rupturing processes. In this model, the effective elasticity resulting from the dynamic adsorption of surface active species was considered. Hong *et al.* [19] investigated the behavior of slag foaming in $CaO–Li_2O–SiO_2–Al_2O_3$ slag systems formed during iron oxide reduction by graphite at 1573 K. To fit their experimental results, they developed a simple model, termed as "drift-flux analysis," based on the fluid mechanics of a one-dimensional two-phase flow. Gou *et al.* [20] developed a one-dimensional multiphase fluid-dynamics-based model to determine the relationship between superficial gas velocity and void fraction in liquids when gases are injected at high rates. This model can be used to calculate slag heights in bath smelting vessels, as shown Figure 2.4.6. Although nonfoaming aqueous systems and expanded slag show similar tendencies, the foaming regime is different in these systems. Further, Gou *et al.* pointed out that the behavior of slag foam at high rates of gas injection is markedly different from the foams observed at low flow rates. The advances in the construction of physical models to describe slag foaming in metallurgical processes have been reviewed by Zhu *et al.* [21].

2.4.2. FOAMING INDEX

The dynamic method for measuring the foaminess of aqueous solutions involves the supply of gas bubbles having well-defined diameters at a constant rate. The foaming index Σ (s) is used as the unit of foaminess [10,17] and is defined by Equation (2.4.5):

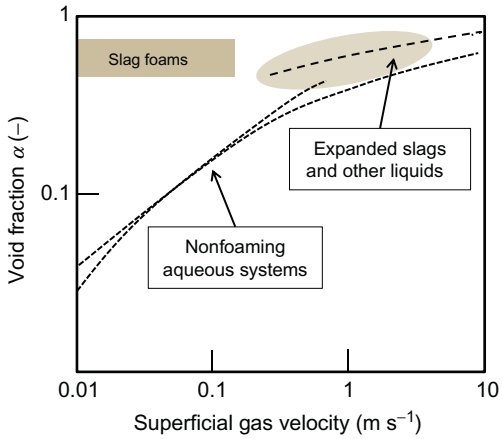


Figure 2.4.6 Relationship between superficial gas velocity and void fraction in foaming and non-foaming systems [20].

$$\Sigma = \frac{V^{\mathrm{f}}}{Q} \tag{2.4.5}$$

In the above equation, V^{f} (m^3) is the volume of the foam layer and Q is the rate of gas flow ($m^3\ s^{-1}$).

The foaming index of molten slags is defined by modifying the definition of foam index used for aqueous foams [10], which will be explained in detail in the subsequent sections.

2.4.2.1. Theory

Let us suppose that gas bubbles are continuously generated in the molten slag bath held in a cylindrical container of cross-sectional area A (m^2), the foamed slag is in a steady state, and the foam formation and collapse are at equilibrium. The foam height h (m) and foam layer thickness L (m) are defined as shown in Figure 2.4.7.

The superficial gas velocity u_{s} ($m\ s^{-1}$) is defined by Equation (2.4.6):

$$u_{\mathrm{s}} = \frac{Q}{A} \tag{2.4.6}$$

Ito and Fruehan [1] investigated a system in which gas bubbles with a definite diameter (10–15 mm) were continuously injected at a constant rate into a molten slag bath. Their experimental observations revealed that the foam height increased linearly with increasing superficial gas velocity, and the slope of this linear relation became constant after the flow rate reached a particular value, as shown in Figure 2.4.8. The slope of the line was found to be independent of the crucible diameter, provided the crucible

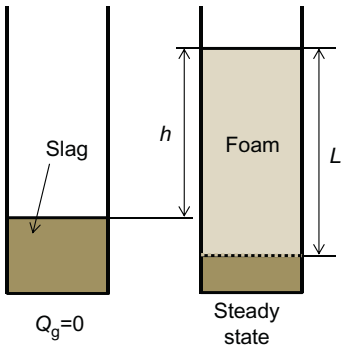


Figure 2.4.7 Illustration of foaming that defines foam height and foam layer thickness L (m).

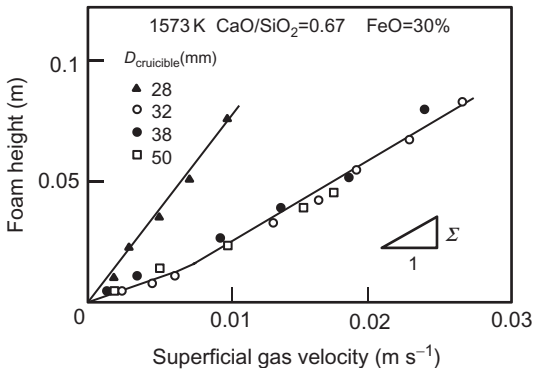


Figure 2.4.8 Relationship between foam height h (m) and superficial gas velocity u_s (m s^{-1}) for various crucible sizes [1].

was large enough to eliminate the wall effects. Consequently, the foaming index Σ, as defined by Equation (2.4.7), denotes the characteristic foaminess of the slag:

$$\Sigma = \frac{\Delta h}{\Delta u_s} \tag{2.4.7}$$

The superficial gas velocity is also correlated to the void fraction and to the actual gas velocity u (m s^{-1}) by Equation (2.4.8):

$$u_s = \alpha u \tag{2.4.8}$$

The foam height is expressed as a function of the void fraction and foam layer thickness by Equation (2.4.9), if the void fraction is assumed to be independent of the foam height:

$$h = \alpha L \tag{2.4.9}$$

Consequently, Σ can be expressed in terms of the foam layer thickness and the actual gas velocity as

$$\Sigma = \frac{\Delta L}{\Delta u} \tag{2.4.10}$$

From Equation (2.4.10), it is clear that Σ signifies the average travelling time of the gas through the foamed layer.

If the foam formation rate is proportional to the rate of gas flow and the collapse rate of the foam is proportional to its height, the rate equation describing the change in foam height can be represented by Equation (2.4.11):

$$\frac{\mathrm{d}h}{\mathrm{d}t} = K_1 Q - K_2 h \tag{2.4.11}$$

where K_1 and K_2 in the above equation are the formation and collapse rate constants of the foam, respectively. When the system is in steady state,

$$\frac{\mathrm{d}h}{\mathrm{d}t} = 0 \tag{2.4.12}$$

Therefore,

$$K_1 Q = K_2 h \tag{2.4.13}$$

However, if the gas flow is halted (i.e., $Q=0$) when the system is in steady state, Equation (2.4.11) reduces to Equation (2.4.14):

$$\frac{\mathrm{d}h}{\mathrm{d}t} = -K_2 h \tag{2.4.14}$$

Integrating Equation (2.4.14) from $t=0$ to $t=t$ and from $h=h^0$ to $h=h$ yields the variation of foam height as a function of time, as shown in Equation (2.4.15):

$$K_2 t = -\ln\left(\frac{h}{h^0}\right) \tag{2.4.15}$$

From Equations (2.4.4) and (2.4.15), it is clear that the collapse rate constant K_2 and the drainage rate constant k, are equivalent and are equal to $1/\tau$.

In a system where the void fraction can be assumed to be constant, the foaming index can be related to the foam life τ. The rate equation that describes foam formation is written as

$$\frac{\mathrm{d}h}{\mathrm{d}t} = \alpha \frac{\mathrm{d}L}{\mathrm{d}t} = \frac{\alpha}{A}\frac{V^{\mathrm{f}}}{\mathrm{d}t} = \frac{Q}{A} \tag{2.4.16}$$

From Equations (2.4.11), (2.4.13), and (2.4.16), Equation (2.4.17) is obtained:

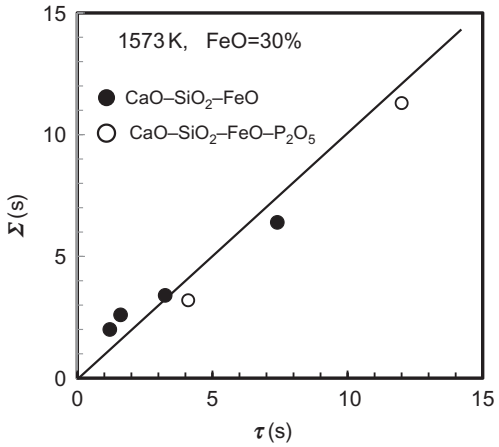


Figure 2.4.9 Relationship between the foam life τ and foaming index Σ for $CaO–SiO_2–FeO$ slags [1].

$$\frac{\tau}{A}=\frac{h}{Q} \tag{2.4.17}$$

From Equations (2.4.6), (2.4.7), and (2.4.17), the foaming index can be related to the average foam life by Equation (2.4.18):

$$\tau=\frac{\Delta h}{\Delta(Q/A)}=\frac{\Delta h}{\Delta u_s} \tag{2.4.18}$$

Therefore, for foams with a uniform void fraction profile, the foaming index Σ is equal to the average foam life τ. Figure 2.4.9 shows a comparison of the foaming index with foam life for $CaO–SiO_2–FeO$ slags at 1573 K, and experiments confirmed that the two values are in good agreement with each other [1].

2.4.2.2. Experimental Measurements

Experimental measurements of the foaming index have been reported for iron and steelmaking slags under various conditions [1,22–28]. The effect of the concentration of FeO on the foaming index of $CaO–SiO_2–FeO–MgO$ slags is shown in Figure 2.4.10 [22–24]. The foaming index decreased when the FeO content increased to up to about 20%. When the FeO concentration was increased further from 20% to 32%, the foaming index nearly remained constant. This is explained on the basis of the viscosity becoming almost constant when the FeO concentration increased above 25%.

Figure 2.4.11 shows the effect of slag basicity on the foaming index of $CaO–SiO_2–FeO–MgO–Al_2O_3$ slags [1,24]. The foaming index decreased with increasing basicity index $[(CaO+MgO)/(SiO_2+Al_2O_3)]$ up to 1.4, at which point the slag was expected to be in the liquidus composition. However, the foaming index increased at higher

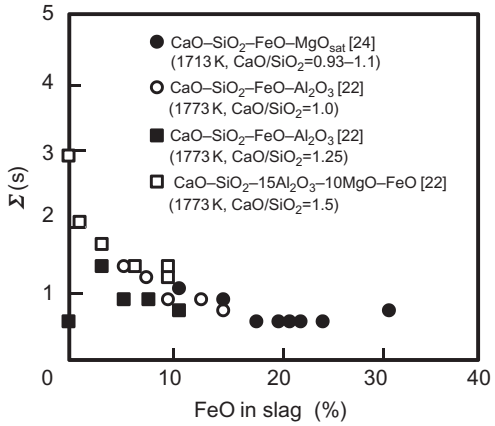


Figure 2.4.10 Variation of foaming index Σ of the $CaO–SiO_2–FeO–MgO_{sat}$ slags with the FeO content in the slag [24].

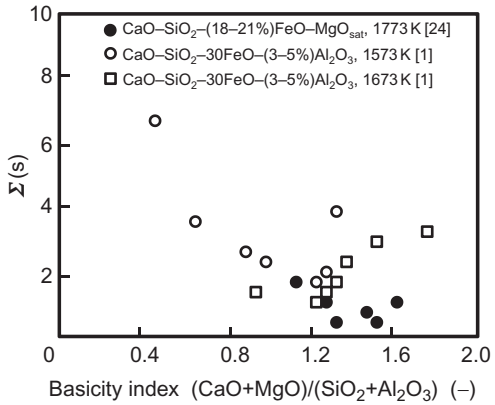


Figure 2.4.11 Variation of foaming index Σ of the $CaO–SiO_2–FeO–MgO_{sat}$ slags with the basicity index $[(CaO + MgO)/(SiO_2 + Al_2O_3)]$, at 1713 K [24].

basicities, due to the precipitation of solid phases like $2CaO{\cdot}SiO_2$ or (Fe,Mg)O, which stabilized the foam.

The temperature dependence of the foaming index for the $CaO–SiO_2–FeO–MgO$ slag system is shown in Figure 2.4.12 [24]. The logarithm of foaming index decreased with increasing temperature. From the data shown in Figure 2.4.9, the dependence of the foaming index on temperature T can be expressed by Equation (2.4.19):

$$\log \Sigma = \frac{6610}{T} - 3.90 \tag{2.4.19}$$

The apparent activation energy for the foam decay was estimated to be 126.5 kJ mol^{-1} for $CaO–SiO_2–FeO–MgO$ slag, and as 160 kJ mol^{-1} for 35%CaO–

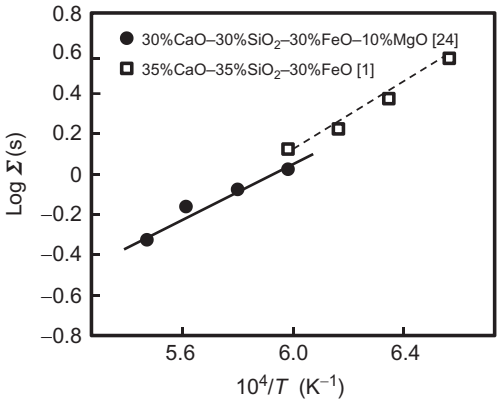


Figure 2.4.12 Dependence of foaming index Σ on temperature T for $CaO–SiO_2–FeO–MgO$ slags [24].

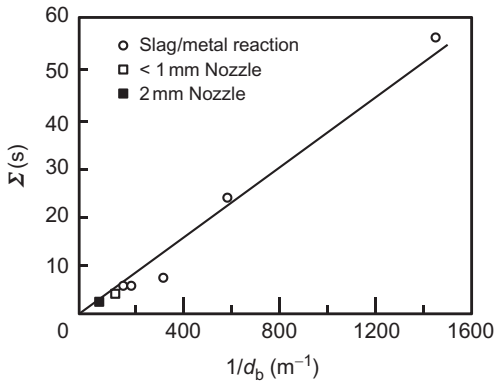


Figure 2.4.13 Variation of foaming index Σ as a function of the reciprocal of average bubble diameter [23].

35%SiO_2–30%FeO slag [1]. The value reported for 48%CaO–32%SiO_2–10% FeO–10%Al_2O_3 slag at temperatures ranging from 1723 to 1873 K was 139.6 kJ mol^{-1}. It can be noted that there was no significant difference in these activation energies.

Zhang and Fruehan [23] measured the effect of the bubble size on the foaming index as shown in Figure 2.4.13, in which the foaming index is plotted against the reciprocal of average bubble diameter. In order to vary the sizes of the bubbles widely, foams were generated either by injecting argon gas or by inducing slag–metal reactions. The foaming index was found to be inversely proportional to the bubble diameter for a particular slag system, and therefore, smaller bubbles stabilized slag foaming.

The effects of the type of the gas and its pressure on slag foaming were also studied by Zhang and Fruehan [26]. The foaming index was found to depend on the physical

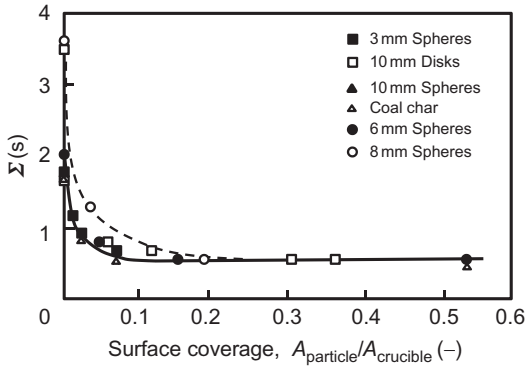


Figure 2.4.14 Variation of foaming indexes of slags exhibiting initial foaming indexes of 1.8 and 3.6 s, as a function of the surface coverage by coke [28].

properties of the gas used for foaming. However, the foaming index was not affected by gas pressures ranging from 1 to 2 atm.

Zhang and Fruehan also studied the effect of the presence of coke and coal char particles on the foaming index [28]. They used two different slags, 30%CaO–60%SiO_2–10%CaF_2 and 25.5%CaO–51%SiO_2–8.5%CaF_2–150%Al_2O_3, with foaming indexes of 1.8 and 3.6 s, respectively at 1773 K, for their experiments. The foaming indexes of these slags were experimentally measured in the presence of coke spheres or coke disks. The foaming index plotted as a function of the coverage ratio of the slag surface by the carbonaceous materials is shown in Figure 2.4.14. Foaming was drastically suppressed when the coverage by carbonaceous materials increased, in both the slag systems, although the initial foaming indexes of the systems differed from each other by a factor of two.

2.4.2.3. Dimensional Analysis and Empirical Equations

It is expected that the foaming index can be related to the physical properties of the slag. Hence, dimensional analysis was applied to derive a relationship which describes the foaming index as a function of slag properties [22,23,29].

It can be assumed that foaming index, as described in Equation (2.4.20), is based on the information obtained from pneumatic experiments, in which the injected bubble diameters were varied within a specific range:

$$\Sigma = f(\rho, \mu, \sigma, g) \tag{2.4.20}$$

In the above equation, ρ is the density (kg m^{-3}) of the liquid slag, μ is the slag viscosity (N s m^{-2}), σ is the slag surface tension (N m^{-1}), and g is gravitational acceleration (m s^{-2}). With five variables and three fundamental dimensions, two dimensionless

numbers, N_Σ and Mo (expressed in Equations 2.4.21 and 2.4.22), were obtained by Jiang and Fruehan [22]:

$$N_\Sigma = \frac{\Sigma g \mu}{\sigma} \tag{2.4.21}$$

$$\mathrm{Mo} = \frac{g\mu^4}{\rho\sigma^3} \tag{2.4.22}$$

Mo is the Morton number, which is generally used to describe the motion of bubbles in a liquid. The relationship between the two dimensionless numbers was calculated from the experimentally measured foaming indexes and the physical properties of the slag, and consequently, Equation (2.4.23) was derived:

$$\log \mathrm{Mo} = 2\log N_\Sigma + 5.11 \tag{2.4.23}$$

The final equation derived that related the foaming index with slag viscosity, density, and surface tension is shown in Equation (2.4.24). The units used in this equation are SI units as used in Equation (2.4.20):

$$\Sigma = 115\frac{\mu}{\sqrt{\rho\sigma}} \tag{2.4.24}$$

Kim *et al.* [27] proposed similar relationships (such as those shown in Equations 2.4.25 and 2.4.26), based on the foaming index measurements they carried out on CaO–SiO_2–FeO–MgO_{sat}–X systems (X was Al_2O_3, MnO, P_2O_5, and CaF_2):

$$\Sigma = 214\frac{\mu}{\sqrt{\rho\sigma}} (\text{for CaO based slags}) \tag{2.4.25}$$

$$\Sigma = 999\frac{\mu}{\sqrt{\rho\sigma}} (\text{for MgO saturated slags}) \tag{2.4.26}$$

Skupien and Gaskell [30] repeated Jiang and Fruehan's [22] dimensional analysis and correlated N_Σ and Mo by using experimentally obtained surface tensions and viscosities to derive Equation (2.4.27):

$$\Sigma = \frac{100\mu^{0.54}}{\rho^{0.39}\sigma^{0.15}} \tag{2.4.27}$$

Since equations from (2.4.24) to (2.4.27) are obtained from the data of pneumatic foaming experiments with similar geometries, in which the bubble diameters in the foam are estimated to be around 10 mm. It should be noted that above four equations are applicable only for the slag foam containing bubbles with diameters about 10 mm.

Based on the experimental data shown in Figure 2.4.13, Zhang and Fruehan [23] reconsidered the dimensional analysis to include the average bubble diameter d_b(m) as

a new independent variable. Now, with six independent variables, another dimensionless number Ar was obtained, in addition to N_Σ and Mo. Ar, the Archimedes number, signifies the ratio of the buoyancy force to the viscous force and is related to the slag properties by Equation (2.4.28):

$$\mathrm{Ar} = \frac{g d_b^3 \rho^2}{\mu^2} \tag{2.4.28}$$

Subsequently, Equation (2.4.29) was obtained by regression analysis:

$$N_\Sigma = 900 \mathrm{Mo}^{0.39} \mathrm{Ar}^{-0.28} \tag{2.4.29}$$

The final mathematical description of the foaming index is represented in Equation (2.4.30):

$$\Sigma = 115 \frac{\mu^{1.2}}{\sigma^{0.2} \rho {d_b}^{0.9}} \tag{2.4.30}$$

The viscosity used in these correlations should be the bulk viscosity including the effect of second phase particles. If the particles are small compared to the bubble size, they will increase the bulk viscosity, decreasing the drainage rate, and hence increase the foam index. This was discussed in detail by Ito and Fruehan [1] and Zhu *et al.* [21].

Ghag *et al.* [18] proposed a different type of relationship based on a foaming model in which the structure of the foam is stabilized by viscoelastic forces. The final relationship that included the effective elasticity E_{eff} (N m^{-1}), resulting from the dynamic adsorption of surface active species, was derived from the data of cold model studies using water–glycerol–SDBS solutions at 293 K; however, there is no direct evidence for the applicability of their model to the foaming of metallurgical slags.

2.4.2.4. Mass-Limited Foaming

When the foam index and the gas flow rate are high enough to foam all of the available slag, the foam height will no longer increase with the gas flow rate but will be relatively constant with increasing flow rate. This is discussed by Zhu *et al.* [21] in more detail. Depending on a number of slag properties and the gas flow rate, the gas fraction cannot exceed 80–90% of the foam. This means the foam volume cannot exceed 4–10 times the static slag volume.

2.4.3. SLAG FOAMING IN INDUSTRIAL PROCESSES

If the void fraction α is kept constant in the foamed slag and the flow regime is maintained unchanged with the gas velocity, the foam height h in practical metallurgical

processes can be estimated using the foaming index of the slag from Equation (2.4.31), which can be derived by integrating Equation (2.4.7):

$$\Sigma = \frac{\Delta h}{\Delta u_s} \tag{2.4.7}$$

$$h = \Sigma\left(u_s - u_s^*\right) + h^* \tag{2.4.31}$$

where u_s^* (m s^{-1}) is the superficial gas velocity and h^* (m) is the foam height when the foaming begins. Both u_s^* and h^* are usually expected to be negligibly small in real processes, and consequently, the foam height in the furnace, H_f (m), is given by Equation (2.4.32):

$$H_f = \Sigma u_s \tag{2.4.32}$$

If the cross-sectional area of the furnace A (m^2) is known, H_f (m) can be estimated from the total gas flow rate in the furnace and the foaming index of the slag, by using Equations (2.4.6) and (2.4.32):

$$u_s = \frac{Q}{A} \tag{2.4.6}$$

2.4.3.1. Electric Arc Furnace

The control of slag foaming is important in an electric arc furnace (EAF) operation, as the slag foam protects the refractory from the high intensity arc, allowing for high power input and productivity. Carbon is injected into the slag to make slag foam by the generation of CO bubbles, which are formed by the reaction of the carbon with FeO in the slag. The CO bubbles used for slag foaming can also be produced by the decarburization of the metal. The foam height can be estimated by substituting the values of the generation rate of CO and foaming index in Equations (2.4.6) and (2.4.32).

Matsuura and Fruehan [31] examined slag foaming in a steelmaking EAF aimed at achieving high productivities with a mathematical model of the EAF, to compute the CO generation rate and slag chemistry for evaluating Equation (2.4.32). They calculated the effects of the amounts of pig iron, carbon, oxygen, and slag on the foam height and concluded that the foam was usually essentially limited by the amount of slag in the furnace. When the amount of total carbon (pig iron, coke, and coal) and oxygen was reduced, the foam height, limited by the CO generation rate, decreased.

Oosthuizen *et al.* [32] estimated the slag foam depth using a dynamic EAF model describing the time evolution of the EAF and the off-gas system variables. Industrial data on foaming of basic slags in an EAF were used to estimate the relationship between the foam index and FeO content in the slag.

As discussed in Section 4.2.4 and by Zhu *et al.* [21] and Matsuura and Fruehan [31], when the gas rate is high, the foam is simply limited by the volume of slag available. For the EAF, it was assumed the volume fraction of gas in the foam cannot exceed 80% so the foam volume cannot be greater than four times the slag volume. This restriction applies to much of the EAF process when high pig iron and oxygen amounts are used. At lower CO rates, the foam index can be used to calculate the foam volume.

2.4.3.2. Bath Smelting Furnace

During bath smelting (a smelting process that reduces thick layered slags), it is important to stably maintain the slag height and avoid any abnormal slag foaming. Therefore, the prediction and the control of slag foaming is one of the key requirements of this process.

Jiang and Fruehan [22] calculated the foam height in a bath smelting furnace using Equation (2.4.32) and compared their results with real pilot trials [33]. The results obtained from the calculations are summarized in Figure 2.4.15. In Figure 2.4.15, PRD and PCR denote the prereduction degree of the iron ore and the postcombustion ratio, respectively. The calculated foam height increased with increasing T. Fe content in the slag. The predicted foam height was in good agreement with the observed values, when PRD = 0% and PCR = 40%, which were close to the real conditions. The dotted curve shows the calculated foam heights when excess coke was present. These values were obtained by using the observation that the presence of carbonaceous materials reduced the foaming index by a factor of 2 (Figure 2.4.14). The calculated values also agreed well with the observations obtained from real slag foaming trials.

Ogawa *et al.* [34] experimentally investigated the mechanism of controlling slag foaming by the use of carbonaceous materials using a 1-ton bath smelting furnace.

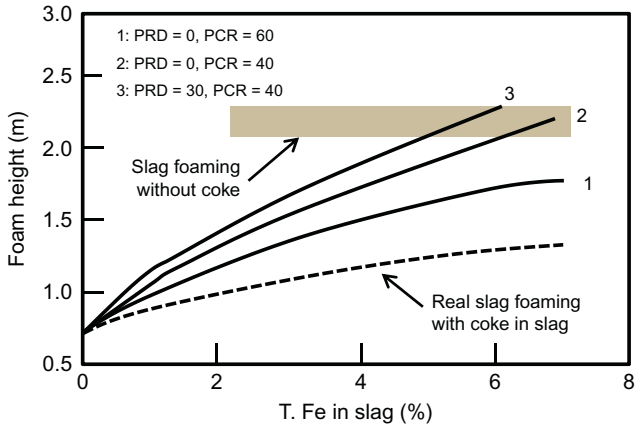


Figure 2.4.15 Comparison of the estimated and real foaming heights in a bath smelting process that uses a 5-ton converter [22].

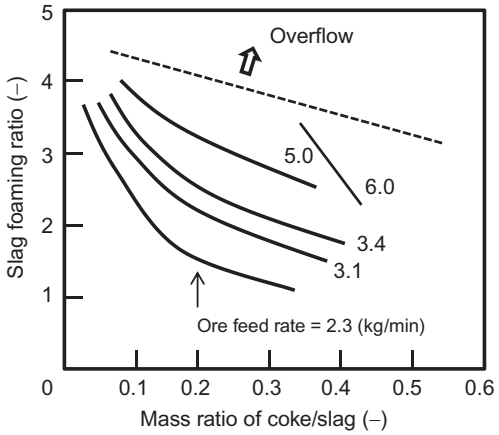


Figure 2.4.16 Effect of coke to slag mass ratio on the slag foaming ratio [34].

Figure 2.4.16 shows the relationship between the coke to slag mass ratio in the furnace and the slag foaming ratio which is defined by Equation (2.4.33), for various iron ore feed rates:

$$\text{slag foaming ratio} = \frac{V^{\text{s}} + V^{\text{g}}}{V^{\text{g}}} \tag{2.4.33}$$

In the above equation, V^{s} (m^3) is the volume of slag and V^{g} (m^3) is the volume of gas in the foamed slag. The slag foaming ratio increased with increasing iron ore feed rate and decreasing amount of coke, which suggested that the presence of coke exerted a suppression effect on slag foaming. It was experimentally confirmed that the stable operation of bath smelting in a 100-ton scale furnace was possible, as far as sufficient carbonaceous material was present in the slag.

2.4.3.3. Basic Oxygen Furnace

In hot metal pretreatment processes, slag foaming has been a key challenge both in desiliconization and dephosphorization processes. Kitamura and Okohira [35] investigated the slag foaming caused by the reaction between the FeO-containing slag and hot metal in the $CaO–SiO_2–Al_2O_3–P_2O_5–TiO_2–MnO–MgO–CaF_2$ system. The maximum slag foam height was observed when the basicity index [CaO/SiO_2] was around 1.2, which slightly increased with increasing temperature and CaF_2 concentration. The achievement of maximum values can be attributed to the combination of decreasing foaming index and increasing CO generation rate that accompany the increase in slag basicity. In the high basicity region, the slag foaming height increased with the increase in temperature and CaF_2 concentration.

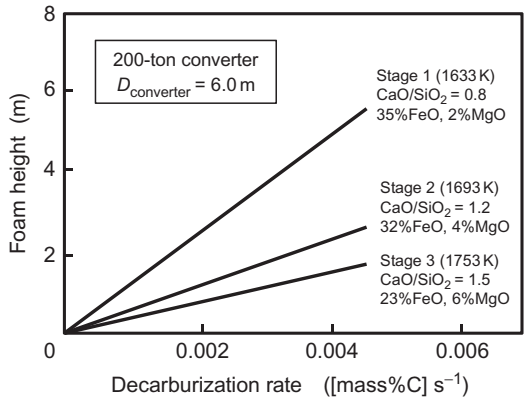


Figure 2.4.17 Variation of calculated foam heights during the first half of the blowing process in the BOF, as a function of the decarburization rate [24].

Jung and Fruehan [24] estimated the foam height of slags during the first half of the blowing process in the basic oxygen furnace (BOF). The superficial gas velocity of a 200-ton converter (6.0 m in diameter) was assumed to be dominated by the decarburization reaction of steel. The results of the calculations using Equation (2.4.32) are shown in Figure 2.4.17. The foam height linearly increased with increasing decarburization rate and decreased with the progress of the stages.

Bramming *et al.* [36] developed a vessel vibration measurement technique that employed a triaxial accelerometer mounted on a trunnion. The transfer of kinetic energy from the foaming slag to the vessel resulted in vibration excitation at the vessel walls. Consequently, the frequency band with the best correlation to the foam level was determined by FFT analysis. The results showed a correlation between vessel vibrations and foam heights, which can be used for the control of dynamic foam levels and slopping.

2.4.3.4. Suppression of Foaming

Zhang and Fruehan [28] found that coke and coal char have the same strong antifoam effect on the liquid slag. The foaming index of the slag was drastically decreased when the coverage of liquid slag surface by carbonaceous materials increased.

In the case of slag foams generated by the reaction of FeO with coke, X-ray characterization revealed that small bubbles coalesced on the interface between the carbonaceous materials such as coke and the slag [34] because of the poor wettability between them. The large bubbles formed by the coalescence of the small bubbles can rise through the foaming slag layer at relatively high speeds, leading to lower foam heights.

REFERENCES

[1] K. Ito, R.J. Fruehan, Metall. Trans. B 20B (1989) 509.
[2] C.F. Cooper, J.A. Kitchener, JISI 230 (1959) 48.

[3] J.H. Swisher, C.L. McCabe, TMS-AIME 230 (1964) 1669.
[4] S. Hara, M. Ikuta, M. Kitamura, K. Ogino, Tetsu-to-Hagane 69 (1983) 1152.
[5] Y. Ogawa, N. Tokumitsu, in: Proceedings of 6th International Iron and Steel Congress, ISIJ, Nagoya, 1990, p. 147.
[6] Y. Ogawa, N. Tokumitsu, Tetsu-to-Hagane 87 (2001) 14.
[7] S. Yokoyama, M. Takeda, K. Ito, M. Kawakami, Tetsu-to-Hagane 78 (1992) 223.
[8] A. Kapilashrami, A.K. Lahiri, M. Gornerup, S. Seetharaman, Metall. Mater. Trans. B 37B (2006) 145.
[9] R. Khanna, M. Rahman, R. Leow, V. Sahajwalla, Metall. Mater. Trans. B 38B (2007) 719.
[10] J.J. Bikerman, Foams, Springer-Verlag, New York, NY, 1973.
[11] S. Hara, M. Kitamura, K. Ogino, Tetsu-to-Hagane 75 (1994) 2174.
[12] S. Hara, T. Yunoki, K. Ogino, Tetsu-to-Hagane 75 (1989) 2182.
[13] J.W. Gibbs, The Scientific Papers of J. Willard Gibbs, Longmans, London, 1906.
[14] P. Kozakevitch, J. Metals 21 (1969) 57.
[15] K. Mukai, T. Nakamura, H. Terashima, Tetsu-to-Hagane 78 (1992) 1682.
[16] Y. Ogawa, D. Huin, H. Gaye, N. Tokumitsu, ISIJ Int. 33 (1993) 224.
[17] B.J. Akers, Foams, Academic Press, London, 1976, p. 1.
[18] S.S. Ghag, P.C. Hayes, H.-G. Lee, ISIJ Int. 38 (1998) 1208.
[19] L. Hong, M. Hirasawa, M. Sano, ISIJ Int. 38 (1998) 1339.
[20] H. Gou, G.A. Irons, W.-K. Lu, Metall. Mater. Trans. B 27B (1996) 195.
[21] T.X. Zhu, K.S. Coley, G.A. Irons, Metall. Mater. Trans. B 43B (2012) 751.
[22] R. Jiang, R.J. Fruehan, Metall. Trans. B 22B (1991) 481.
[23] Y. Zhang, R.J. Fruehan, Metall. Mater. Trans. B 26B (1995) 803.
[24] S.-M. Jung, R.J. Fruehan, ISIJ Int. 40 (2000) 348.
[25] B. Ozturk, R.J. Fruehan, Metall. Mater. Trans. B 26B (1995) 1086.
[26] Y. Zhang, R.J. Fruehan, Metall. Mater. Trans. B 26B (1995) 1088.
[27] H.S. Kim, D.J. Min, J.H. Park, ISIJ Int. 41 (2001) 317.
[28] Y. Zhang, R.J. Fruehan, Metall. Mater. Trans. B 26B (1995) 813.
[29] K. Ito, R.J. Fruehan, Metall. Trans. B 20B (1989) 515.
[30] D. Skupien, D.R. Gaskell, Metall. Mater. Trans. B 31B (2000) 921.
[31] H. Matsuura, R.J. Fruehan, ISIJ Int. 49 (2009) 1530.
[32] D.J. Oosthuizen, J.H. Viljoen, I.K. Craig, P.C. Pistorius, ISIJ Int. 41 (2001) 339.
[33] N. Tokumitsu, M. Matsuo, K. Hatayama, H. Ishikawa, Y. Yamamoto, Y. Hayashi, in: Process Technol. Conf. Proc., Toronto, ISS of AIME, vol. 7, 1988, p. 99.
[34] Y. Ogawa, H. Katayama, H. Hirata, N. Tokumitsu, M. Yamauchi, ISIJ Int. 32 (1992) 87.
[35] S. Kitamura, K. Okohira, ISIJ Int. 32 (1992) 741.
[36] M. Bramming, S. Millman, A. Overbosch, A. Kapilashrami, D. Malmberg, B. Bjorkman, ISIJ Int. 51 (2011) 71.
[37] D. Lotun, L. Pilon, ISIJ Int. 45 (2005) 835.

CHAPTER 2.5

Applications

Richard J. Fruehan and P. Chris Pistorius
Center for Iron and Steelmaking Research, Carnegie Mellon University

2.5.1. RATE PHENOMENA IN DIRECT IRONMAKING

The iron blast furnace is an efficient counter current reactor, which produces the vast majority of liquid hot metal in the world. The problems with the process are that it requires coke and has high capital cost. Coke requires a separate environmentally challenged process and special coals. The furnace also has a relatively low specific production rate (tonnes/m^3 day) leading to high capital cost. From roughly 1990 to 2010, there was a major worldwide effort to develop a new ironmaking process, which uses coal directly and is carried out in a liquid melt of slag and metal resulting in significantly higher productivity.

Several different approaches were employed that led to significant advances and appear promising: DIOS (Direct Iron Ore Smelting) in Japan, HIsmelt in Australia, ROMELT in Russia, and AISI (American Iron and Steel Institute) Direct Steelmaking in the United States. Detailed descriptions of these processes are given elsewhere [30,31,32]. Briefly, iron ore is added to a melt of slag and metal. The AISI, DIOS, HIsmelt, and ROMELT use simple gravity feeding into the slag while HIsmelt injects ore into the melt. The ore may be partially prereduced using the off-gas from the system; for example, removal of about 33% of the oxygen producing FeO. The ore dissolves into the slag and is reduced out of the slag by solid carbon or carbon dissolved in liquid iron. The energy and reducing agent are supplied by coal which is injected in the HIsmelt process and gravity fed in the others [1]. A schematic diagram of the processes indicating the chemical reactions is given in Figure 2.5.1. The CO and H_2 from primary combustion and the reduction reaction are postcombusted to CO_2 and H_2O above the melt and the energy from these reactions is transferred back to the melt, which heats materials and supplies some of the energy for reactions. HIsmelt and ROMELT use oxygen-enriched air while DIOS and AISI use oxygen for combustion.

Two of the most critical steps in the process are the reduction and postcombustion reactions. The rate of reduction and the effect of volatiles in the coal on postcombustion are examined using the fundamentals presented earlier in this chapter. Laboratory and pilot plant results from DIOS, AISI, and HIsmelt are used in the analysis [1].

http://dx.doi.org/10.1016/B978-0-08-096984-8.00004-5
© 2014 Elsevier Ltd.
All rights reserved.

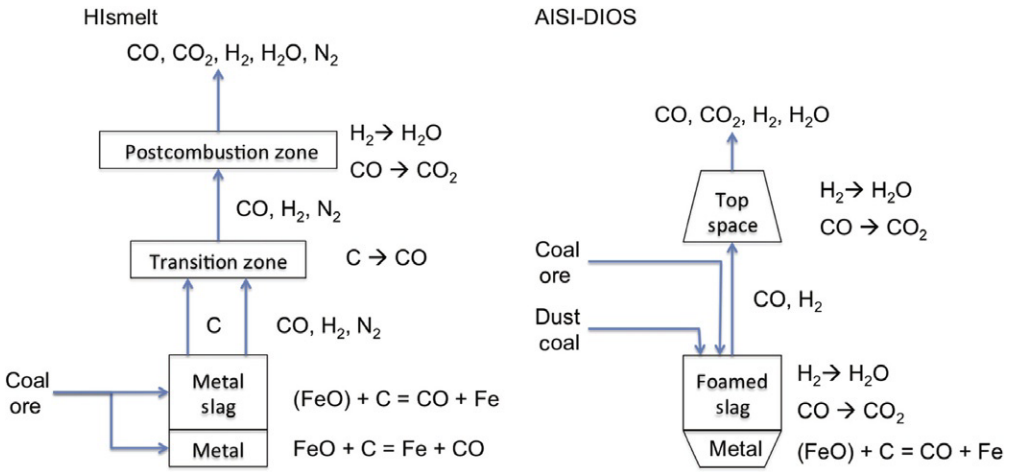


Figure 2.5.1 Schematic diagram of the HIsmelt, AISI, and DIOS iron smelting indicating reactions.

Coal char and carbon in metal droplets in the slag reduce the FeO in the slag

$$(\mathrm{FeO}) + \mathrm{C} = \mathrm{Fe} + \mathrm{CO} \tag{2.5.1}$$

$$(\mathrm{FeO}) + \underline{\mathrm{C}}(\mathrm{Fe}) = \mathrm{Fe} + \mathrm{CO} \tag{2.5.2}$$

The rate of reaction (2.5.1) has been shown to be controlled by mass transfer of FeO to the char surface. For reaction (2.5.2), the rate mechanism is as described in Section 6.2 in this chapter. Namely CO_2 is produced by the reduction of FeO by CO. The CO_2, which is a gaseous intermediate, reacts with carbon in iron drops producing CO for reduction. For each reaction, the rate depends on the surface area of char and metal droplets reacting which is roughly proportional to the slag weight. Furthermore, the rates in both cases depend on the FeO content of the slag. Therefore, the production rate (PR) is proportional to the slag weight (W_s) and the FeO or Fe_T (total Fe) dissolved in the slag. For DIOS and AISI, the PR is therefore given by

$$\mathrm{PR} = (k_s + k_M) W_s (\%\mathrm{Fe_T}) \tag{2.5.3}$$

where k_s is the rate constant for the char reaction (2.5.1) involving a mass transfer coefficient and k_M is the rate constant for the dissolved carbon in the metal reaction (2.5.2), including the chemical rate constant for the reaction of CO_2 with carbon in iron.

The PR for AISI per unit slag weight is plotted in Figure 2.5.2. The rate is proportional to the FeO content of the slag as indicated by relationship (2.5.3). The PR for the DIOS process divided by the FeO content of the slag is plotted versus slag weight in Figure 2.5.3. The rate increases with slag weight as indicated by (2.5.3). The PR for DIOS and AISI follows Equation (2.5.3) and is fairly similar.

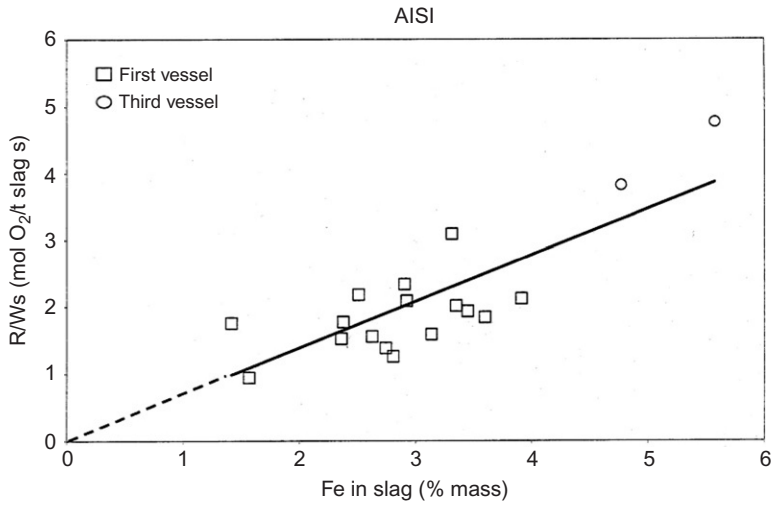


Figure 2.5.2 The production rate in the AISI smelter as a function of Fe_T content of the slag [1].

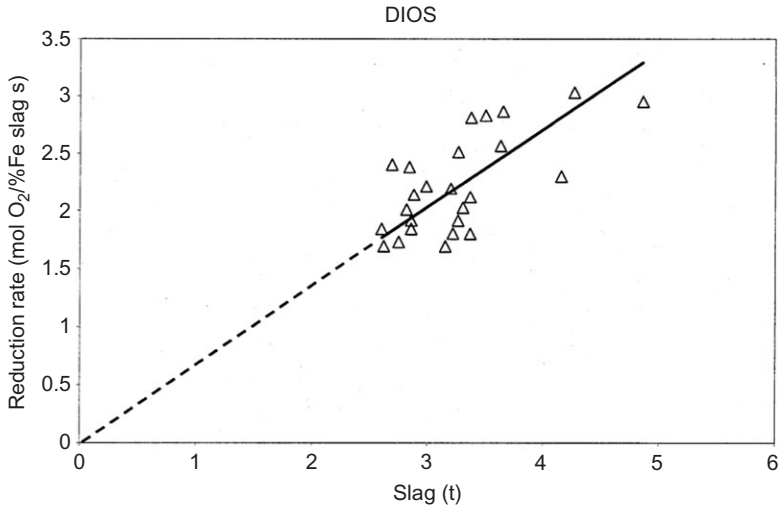


Figure 2.5.3 The production rate for the DIOS 100-t smelter as a function of slag weight [1].

For HIsmelt, there is a third reaction mechanism: the reaction of FeO_X particles with carbon in the iron melt as they are injected into the metal and rise to be dissolved in the slag. The reaction is given by

$$FeO_X + \underline{C} = CO + Fe \tag{2.5.4}$$

where FeO_X is iron oxide in the injected feed material and $\underline{C}$ is carbon dissolved in the iron melt. In this case, PR is given by

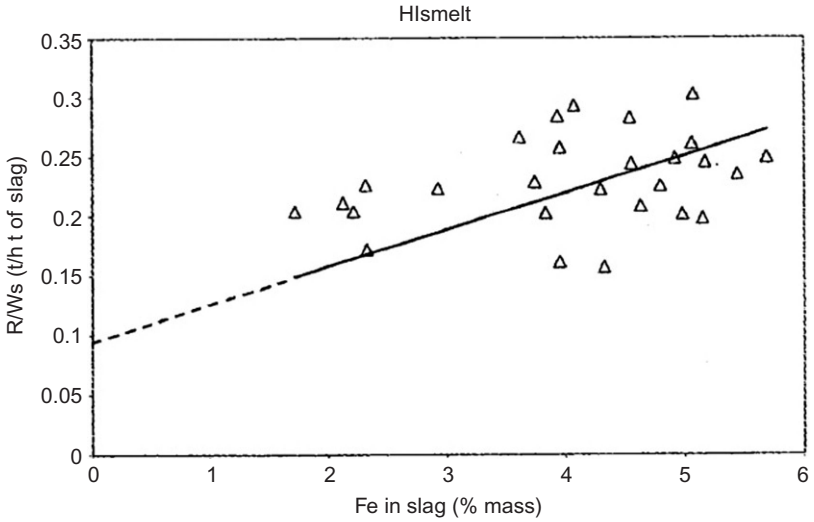


Figure 2.5.4 The production rate for the HIsmelt smelter as a function of Fe_T content in the slag [1].

$$PR = (k_s + k_M) W_s (\%Fe_T) + R_i \tag{2.5.5}$$

where R_i is the rate of reduction of the injected ore particle. The PR for HIsmelt is given as a function of slag weight W_s in Figure 2.5.4. In this case, there is an intercept at zero slag due to the reduction of ore in the melt. The results from the three processes give about the same rate constants k_s and k_M, and for HIsmelt, about 40% of the reduction is by the reaction of the ore particle with the iron–carbon melt.

The postcombustion reactions provide most of the energy for the process.

$$CO + \frac{1}{2}O_2 = CO_2 \tag{2.5.6}$$

$$H_2 + \frac{1}{2}O_2 = H_2O \tag{2.5.7}$$

However, the CO_2 and H_2O can react with char or carbon in iron, reducing the degree of postcombustion and the energy generated. When high-volatile coals are used, generally more H_2 reacts compared to low-volatile coals. It has been shown that when higher volatile coals are used, the postcombustion ratio (PCR) achieved decreases for all three processes.

$$PCR = \frac{H_2O + CO_2}{H_2O + CO_2 + H_2 + H_2O}$$

As shown in Figure 2.5.5, the degree of postcombustion decreases with the amount of volatiles.

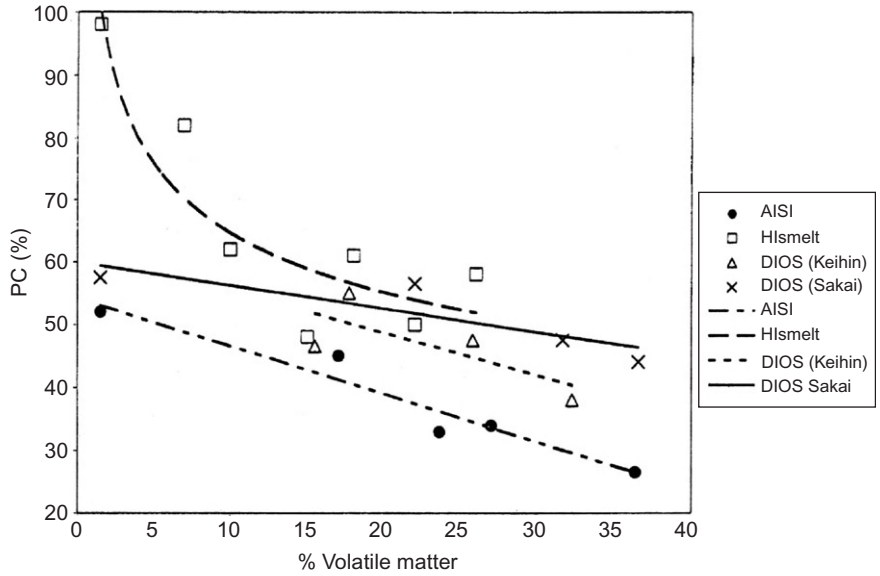


Figure 2.5.5 The postcombustion ratio as a function of the volatiles in the coal for AISE, DIOS, and HIsmelt processes [1].

This can be explained by the fact that the H_2O reaction with carbon is faster than for CO_2.

$$H_2O + \underline{C} = CO + H_2O \tag{2.5.8}$$

$$CO_2 + \underline{C} = 2CO \tag{2.5.9}$$

This is discussed in Section 6.2 of this chapter. Specifically, the rate of dissociation of H_2O is faster than for CO_2 and hence reaction (2.5.8) is faster than reaction (2.5.9). Therefore, the more hydrogen, or volatiles in coal, the lower the PCR.

2.5.2. LADLE DESULFURIZATION KINETICS

2.5.2.1. Principles and Equilibrium Relationships

Ladle desulfurization is commonly used in electric steelmaking plants to decrease the dissolved sulfur content of aluminum-killed steel [2]. The desulfurization reaction is often written as follows:

$$\frac{2}{3}[Al] + [S] + (CaO) = \frac{1}{3}(Al_2O_3) + (CaS) \tag{2.5.10}$$

In Equation (2.5.10), species in square brackets are dissolved in the liquid steel, and slag species are indicated by round brackets. This is only one of several reactions which

can occur during ladle refining (others are reduction of FeO, MnO, SiO_2, and MgO from the slag). The effect of these parallel reactions can be readily understood by considering how these reactions change the oxygen activity at the slag–steel interface. The importance of oxygen activity is shown by the ionic version of Equation (2.5.10):

$$[S] + (O^{2-}) = (S^{2-}) + [O] \tag{2.5.11}$$

As Equation (2.5.11) shows, any reaction which lowers the oxygen activity at the slag–steel interface would tend to improve desulfurization.

A change in the interfacial oxygen content appears to be a reasonable explanation for the role of silicon in ladle desulfurization, as studied recently [3,5]. While Equation (2.5.10) does not indicate any direct role of silicon in the steel, plant engineers reported an effect of silicon, namely that steels with lower silicon contents are desulfurized more readily. Silicon can exert an effect on desulfurization if it changes the activity of dissolved oxygen. In steels with sufficiently high silicon contents, in contact with slags with sufficiently low silica (SiO_2) contents, the Si/SiO_2 buffer can be as effective as the Al/Al_2O_3 buffer at promoting a low oxygen activity. To illustrate the slag and steel compositions where this would be the case, Figure 2.5.6 shows the equilibrium Al content of steel and the equilibrium sulfur distribution coefficient between slag and metal. The sulfur distribution coefficient is the ratio of the sulfur contents of slag and steel:

$$L_S = \frac{(\%S)}{[\%S]} \tag{2.5.12}$$

In Equation (2.5.12), the compositions are given as mass percentages.

Figure 2.5.6 illustrates that a silicon content of 0.2% in liquid steel is sufficient to ensure a sulfur distribution coefficient of 1000, if the slag contains some 5% SiO_2 and is CaO saturated (i.e., the slag composition lies along the left-hand boundary of the fully liquid region in Figure 2.5.6). As Figure 2.5.6 shows, use of this slag and silicon content would result in an equilibrium Al content of approximately 0.05%.

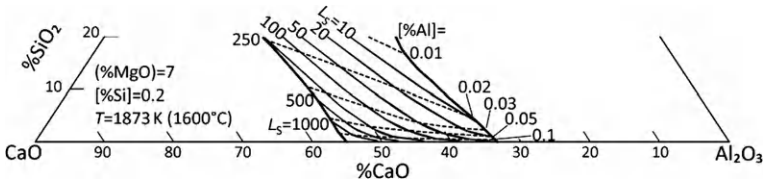


Figure 2.5.6 Equilibrium Al content (broken lines) in steel (containing 0.2% Si) in contact with fully liquid ladle slag containing 7% MgO (by mass); CaO, SiO_2, and Al_2O_3 mass percentages normalized to 100%. Full lines give sulfur distribution coefficient between slag and steel. The region where the Al and sulfur distribution coefficient isopleths are shown is where the slag is fully molten. Calculated with FactSage [6].

The equilibrium extent of desulfurization can be calculated with a simple mass balance; the equilibrium sulfur content of the steel is then given by Equation (2.5.13):

$$[\%S]_{equilib} = \frac{[\%S]_0}{\left(1 + L_S W_{slag}/W_{steel}\right)}, \tag{2.5.13}$$

where $[\%S]_0$ is the total sulfur content of steel and slag, expressed as a mass percentage of the steel, W_{slag} is the slag mass, and W_{steel} is the steel mass.

For ladle metallurgy, a typical (W_{slag}/W_{steel}) ratio is 0.01. If an L_S of 1000 is achieved, then more than 90% of the sulfur can be removed to the slag (as calculated with Equation 2.5.13).

The equilibrium relationships in Figure 2.5.6 demonstrate that, for lime-saturated slags with suitably low SiO_2 contents, steel containing as little as 0.2% Si can be viewed as being desulfurized by silicon and lime. That is, instead of the Al-driven desulfurization reaction of Equation (2.5.10), the desulfurization reaction can be written as follows:

$$\frac{1}{2}[Si] + [S] + (CaO) = \frac{1}{2}(SiO_2) + (CaS) \tag{2.5.14}$$

In addition, if the aluminum content of the steel is less than the equilibrium amount shown in Figure 2.5.6, the steel would tend to pickup Al, by the following reaction:

$$3[Si] + 2(Al_2O_3) = 3(SiO_2) + 4[Al] \tag{2.5.15}$$

It was shown experimentally [3] that reactions (2.5.14) and (2.5.15) do indeed occur in parallel, in steels of appropriate composition: dissolved silicon can simultaneously desulfurize the steel and cause aluminum pick up by the steel.

2.5.2.2. Kinetic Effects

Whether desulfurization thermodynamics are determined by the aluminum or silicon content of the steel, desulfurization approximately follows first-order kinetics [4]. Full description of the desulfurization kinetics needs to take into account changes in oxygen activity and slag composition (which change the sulfur distribution coefficient) [4], but a simple analytical approach as shown here gives a good approximation [5].

As discussed in Section 6.2 of this chapter, the rate of sulfur removal from the steel must equal the rate of sulfur pickup by the slag:

$$k_{steel} A \rho_{steel} \left([\%S]_{steel} - [\%S]_{int}\right) = k_{slag} A \rho_{slag} \left[(\%S)_{int} - (\%S)_{slag}\right] \tag{2.5.16}$$

where k is the mass transfer coefficient (in steel and slag), ρ the density, $[\%S]_{steel}$ the bulk sulfur content of the steel, $[\%S]_{int}$ the sulfur content in the steel at the slag–steel interface, $(\%S)_{int}$ the sulfur content in the slag at the interface, and $(\%S)_{slag}$ the sulfur content of the bulk slag.

Because local equilibrium holds at the slag–steel interface, $(\%S)_{int}/[\%S]_{int} = L_S$ (Equation 2.5.12). A further constraint is that the total mass of sulfur in slag and steel remains

constant. Substitution of these constraints allows the change in sulfur content of the steel to be calculated analytically for the case where L_S does not change with time (or remains high during the whole process).

The result is that the sulfur content of the steel decays exponentially to the equilibrium sulfur content given by Equation (2.5.13); the rate constant of the exponential decay is given by:

$$a = \frac{k_{steel} A \rho_{steel}}{W_{steel}} \left(\frac{L + \frac{W_{steel}}{W_{slag}}}{L + \frac{k_{steel}\rho_{steel}}{k_{slag}\rho_{slag}}} \right) \tag{2.5.17}$$

For ladle desulfurization, L is typically in the range 500–1000, which implies (based on Equation 2.5.17) that mass transfer in the slag is not expected to limit the desulfurization rate: the ratio $(k_{steel}\rho_{steel})/(k_{slag}\rho_{slag})$ is typically in the range 30–100, much smaller than L.

The prediction that mass transfer in the slag is not rate limiting was tested by comparing the results of the kinetic model when full mixing of the slag was assumed, with the case where limited slag mass transfer was quantified using k_{slag}; as predicted, there was little difference in the results (except in somewhat artificial cases where slags with low CaO contents and hence low L_S were modeled) [5].

2.5.2.3. Desulfurization Mass Transfer Constant

A complete description of ladle desulfurization would require consideration of multiphase flow in the ladle and dispersion of slag droplets into the steel [9]. However, the simple "two-film" model as described here has been found to give an adequate description of practical desulfurization. Such a description requires information on the reaction equilibrium (L_S) and the mass transfer constant ($k_{steel}A$). The mass transfer constant depends strongly on gas stirring, following the general relationship

$$k_{steel} A \propto Q^n \tag{2.5.18}$$

where Q is the gas flow rate; the exponent n is smaller than 1 at low gas flow rates [8,10]. Water-model measurements (using a layer of oil to simulate slag) showed that kA increases abruptly above a certain flow rate (with a large increase in n; see Figure 2.5.7); this increase was associated with "emulsification"—droplets of slag sheared off from the oil and mixed into the upper regions of the underlying denser liquid (water) [7]. This means that the true area is much larger than the apparent area A of the steel–slag interface. Experimentally, the effects of stirring on k and A are not readily distinguished, and hence the product kA (which can be found directly from experiments) is given in Equation (2.5.18).

Emulsification is more readily achieved in such water-model experiments (with a small density difference between oil and water); however, consideration of the

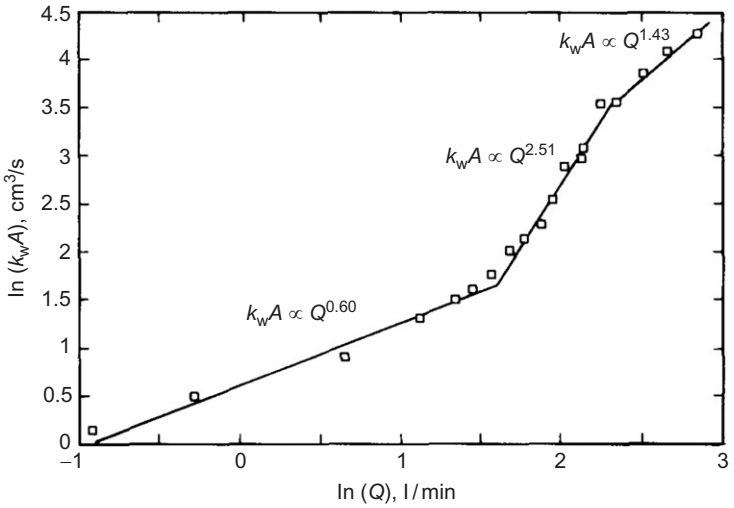


Figure 2.5.7 Relationship between the mass transfer constant *kA* and gas flow rate, for water-model measurements simulating steel–slag reactions [7].

appropriate density difference, interfacial tension, and gas flow rates for ladle metallurgy conditions indicates that emulsification occurs under plant desulfurization conditions [7,11]. Ishii *et al.* [33] showed the rate constant for desulfurization to be approximately proportional to the stirring power ε (which is proportional to the gas flow rate), hence $n = 1$; this large value of n similarly indicates that slag emulsification occurs during practical ladle desulfurization.

2.5.3. RATE PHENOMENA IN VACUUM DEGASSING

The use of vacuum degassing has increased dramatically in the past 25 years. Vacuum degassing removes hydrogen, nitrogen, oxygen, and carbon as H_2, N_2, and CO gasses which form at low pressures.

Schematic diagrams of three types of degassers are shown in Figure 2.5.8. Ladle-to-ladle degassing is when the steel from a ladle is introduced into a second ladle under vacuum. The metal stream is converted into a "spray" in the vacuum ladle, which exposes a large surface area for the degassing reactions. This process is usually used to remove hydrogen from relatively small heat sizes (<100 t).

In a ladle or tank degasser, the ladle is placed under vacuum or in a vacuum tank. Ar is used to stir the metal and provide reaction area associated with the Ar bubbles. These are sometimes referred to as VAD (vacuum argon degassing) or VOD (vacuum oxygen degassing) when oxygen is used to decarburize the steel. These units are widely used for heat sizes ranging from 50 to 200 t. They are used to remove hydrogen, nitrogen, and carbon.

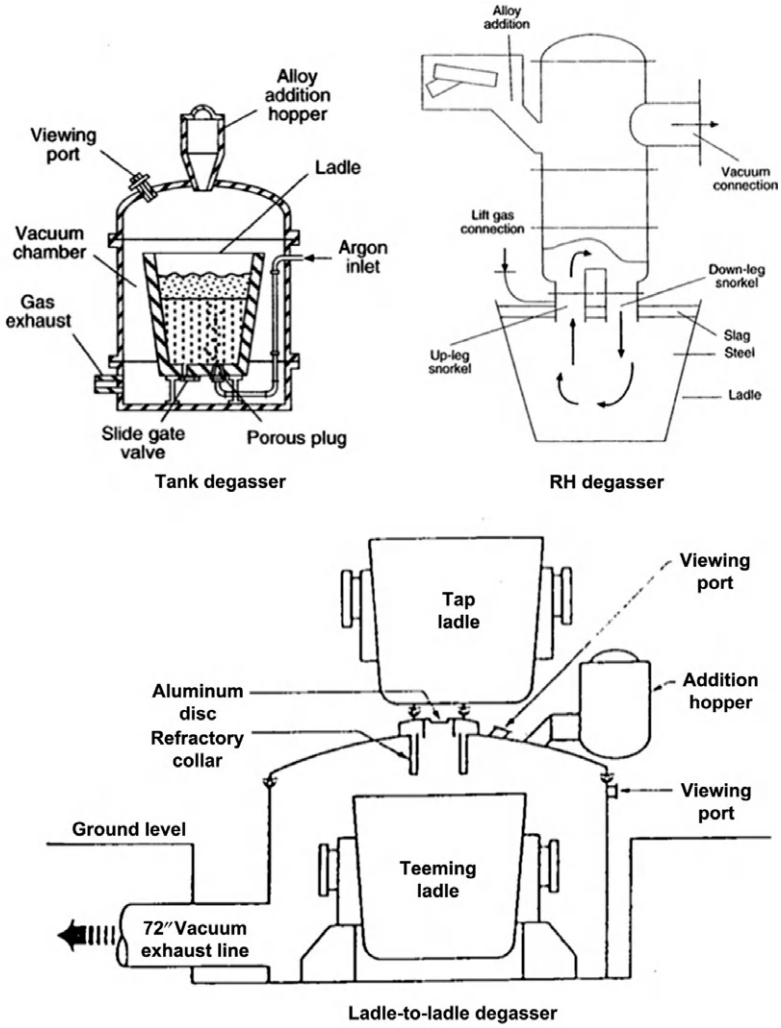


Figure 2.5.8 Schematic diagram of several degassing processes [14].

RH and RH-OB (oxygen blowing) are used primarily to produce low-carbon flat-rolled steels. The RH unit is placed above steel in a ladle. Two nozzles enter the steel. Ar is injected into one of the nozzles and lifts the metal into the degasser forming a spray or fountain of steel with a high surface area. The steel then returns to the ladle through the second nozzle.

In the ladle-to-ladle degasser, hydrogen is removed by the reaction

$$2H = H_2 \tag{2.5.19}$$

As shown in Section 2.2, liquid-phase mass transfer controls the rate, and the rate equation is given by

$$\ln\frac{\%H-\%H_0}{\%H_e-\%H_0}=-\frac{A\rho k}{W}t \tag{2.5.20}$$

where $\%H_0$ and $\%H_e$ are the initial and equilibrium hydrogen contents, A is the surface area of the drops, and t is the residence time of the drops exposed to the vacuum. The terms on the right hand side of (2.5.21) are constant so

$$\ln\frac{\%H-H_0}{\%H_e-\%H_0}=\beta \tag{2.5.21}$$

where β is a constant depending on the process. Typically, 50–70% of the hydrogen is removed in the process.

An important consideration is the $\%H_e$. It is not necessarily determined by the hydrogen pressure in the vacuum ladle, which is very low. The H_2O pressure may determine it. For example, for Al or Si being used as a deoxidizer, the equilibrium hydrogen is determined by the equilibrium for the following reactions.

$$3H_2O+2\underline{Al}=Al_2O_3+6\underline{H} \tag{2.5.22}$$

$$2H_2O+Si=SiO_2+4\underline{H} \tag{2.5.23}$$

The value of $\%H_e$ for (2.5.22) and (2.5.23) is usually much higher than reactions (2.5.19). Therefore, on more humid days, hydrogen removal may be slower.

Tank degassing has been used to remove hydrogen, nitrogen, and oxygen, and carbon as CO. It has achieved significant nitrogen removal while the other processes have had limited denitrogenization. There are two major reasons. First, there is a lower total pressure and hence lower N_2 pressures, which give lower equilibrium nitrogen contents. Second, there usually is extensive desulfurization with sulfur contents 10 ppm or lower which increases the rate of the nitrogen reaction.

Liquid-phase mass transfer of nitrogen and the chemical rate at the surface control the nitrogen reaction as discussed in detail in Section 2.2 of this chapter. The rate equations are given by 2.2.113 and 2.2.114 and the equation to compute the nitrogen content at the surface is given by 2.2.115. Bannenberg *et al.* [12] developed a similar model and made measurements on a 185-t vacuum tank facility. In the rate equations, a critical input is the reaction surface area. They demonstrated that the reaction surface is primarily that of the argon bubbles as they rise in the vessel. The surface area of the bubbles is very large, in part because of the extensive expansion due to the low pressure, and the bubble area far exceeds the surface area of the normal top of the melt. A schematic diagram demonstrating an Ar bubble expansion and the nitrogen concentration is seen in Figure 2.5.9. The rate of removal of nitrogen as a function of Ar gas used for several different sulfur levels is shown in Figure 2.5.10. The figure demonstrates that to go from 50 to 30 ppm N requires about twice as much Ar at 200 ppm S as compared to 5 ppm S.

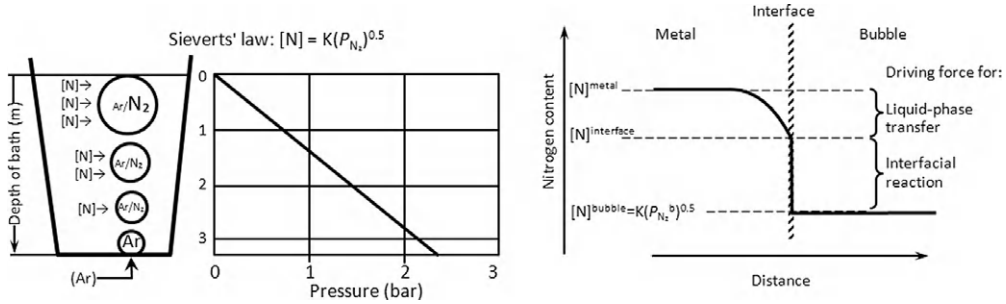


Figure 2.5.9 Schematic diagram of expansion of the argon bubbles and concentration gradient of nitrogen [12].

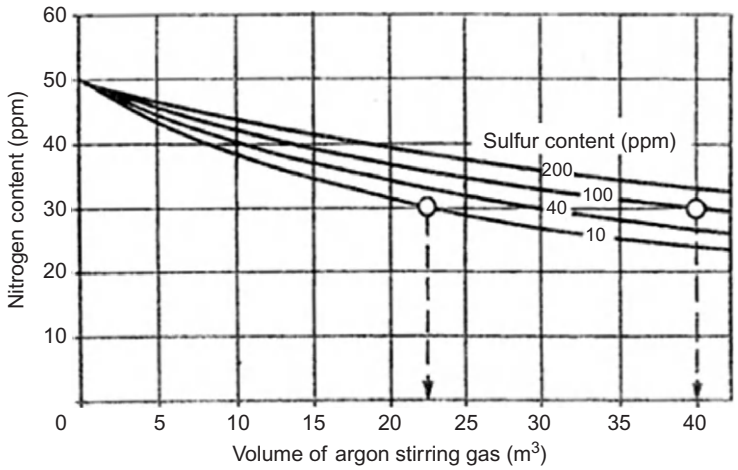


Figure 2.5.10 Nitrogen removal in a tank degassing varying sulfur content [12].

The RH degasser is primarily used to produce low- and ultra low-carbon flat-rolled steels. The rate of the reaction is controlled by liquid-phase mass transfer but is complicated by the circulation of metal from the ladle to the vacuum vessel on the top of the melt. Kondo *et al.* [13] have developed rate equations to describe the rate of carbon removal in an RH degasser. They showed that an appropriate rate expression is given by

$$\%C = \%C_O \exp(-Kt) \tag{2.5.24}$$

$$K = \frac{Ak}{\frac{Q}{\rho} + Ak} \tag{2.5.25}$$

where Q = circulation rate from the ladle into the RH (t/s); Ak = surface area times the mass transfer coefficient (m^3/s); ρ = density of iron.

If the circulation rate is high ($Q \gg Ak$), the rate is controlled by liquid-phase mass transfer. If $Ak \gg Q$, then the rate is controlled by the circulation rate. Increasing the nozzle diameter can increase the circulation rate. The rate of decarburization increases with the Ar flow rate, which increases the surface area and the mass transfer coefficient. The actual reaction sites are the Ar bubbles and the metal droplets that spray into the RH vessel.

This is demonstrated in Figure 2.5.11 in which Ak is plotted versus Q showing the resulting value of K. Also shown are the approximate conditions for reaction, circulation, and mixed control. Increasing K is also demonstrated. By increasing the nozzle diameter and argon flow rate, both Q and Ak increase as indicated by condition I going to condition II. Further increases are obtained by additional Ar increasing Ak as indicated by III.

The same equation (Equation 2.5.24) holds for hydrogen removal. For hydrogen, the value of Ak is higher than for carbon since the diffusivity of hydrogen is higher. For hydrogen, circulation control plays a more important role. In the RH, nitrogen removal is limited due to lower initial nitrogen content in the metal, and the N_2 pressure in the RH is higher than for a tank degasser, lowering the driving force for nitrogen removal.

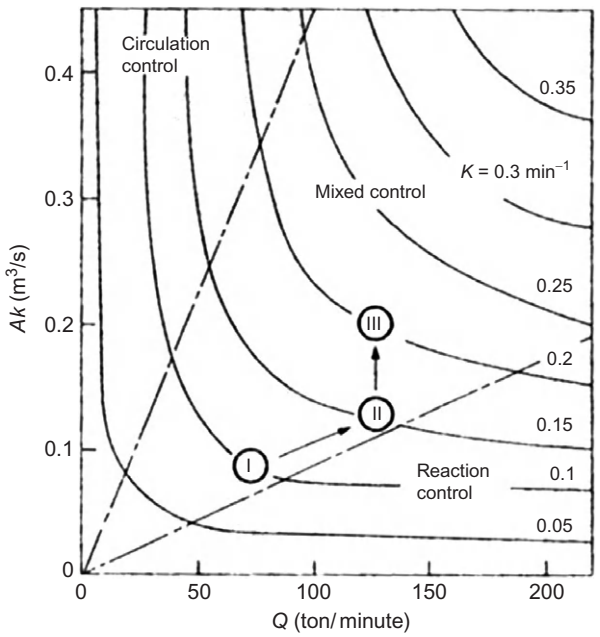


Figure 2.5.11 Rate constant for decarburization in an RH degasser as a function of circulation rate and mass transfer parameter [13].

2.5.4. RATE PHENOMENA IN AOD STAINLESS STEEL PRODUCTION

The vast majority of stainless steelmaking is by the AOD or argon–oxygen decarburization process. First stainless scrap, carbon steel scrap, and high-carbon ferrochrome are melted in an EAF. Then the melt is charged into the AOD converter.

The melt has to be decarburized by injection of oxygen resulting in two competing reactions: oxidation of carbon and chromium.

$$\underline{C} + \frac{1}{2}O_2 = CO \tag{2.5.26}$$

$$2\underline{Cr} + \frac{3}{2}O_2 = Cr_2O_3 \tag{2.5.27}$$

Depending on condition, CrO may be the reaction product.

To determine if carbon or chromium will be oxidized, reactions (2.5.26) and (2.5.27) can be combined

$$3\underline{C} + Cr_2O_3 = 2\underline{Cr} + 3CO \tag{2.5.28}$$

By examining the thermodynamics of this reaction, it is predicted that at 1600 °C for a steel containing 18% Cr carbon will be preferentially oxidized until its content decreases to 0.4% at which point Cr will be oxidized. Consequently, prior to the development of the AOD, it was difficult to produce low-carbon stainless steels. It required the use of more expensive low-carbon ferrochrome and much higher temperature (>1700 °C) where the thermodynamics of (2.5.28) is more favorable for the oxidation of carbon.

Examining reaction (2.5.28) indicates that if the CO pressure is reduced below 1 atm, the critical carbon content can be lowered. This can be achieved by using a vacuum such as the VOD (vacuum oxygen decarburization) or by dilution of the oxygen with an inert gas such as Ar as in the AOD process [14]. Due to higher productivity and lower cost, the AOD is primarily used for stainless steel production. In the AOD, the O_2–Ar gas mixture is injected via a series of tuyères located near the bottom of the reactor as shown in Figure 2.5.12. For early stages of the process, N_2 can be used in place of Ar to reduce cost. The nitrogen will be flushed out by the argon and CO gases in the later stages.

Early studies of the AOD process indicated that for the Ar to be effective, it must be injected deep into the melt and Cr was still oxidized at carbon contents higher than predicted by (2.5.28), indicating equilibrium for reaction (2.5.28) is not observed [35]. Laboratory experiments using relatively small melts (7.5 cm deep) into which O_2–Ar gas mixtures were injected indicated that Cr was primarily oxidized and little carbon was oxidized. Also in laboratory experiments, it was found that the rate of reaction (2.5.28) was controlled by liquid-phase mass transfer. These observations led to a model of the AOD, which assumes when oxygen is first introduced it primarily oxidizes Cr. Iron may also be oxidized but is quickly reduced by Cr. The (CrO_x) is then reduced by reaction (2.5.28) and the rate is controlled by mass transfer of carbon to the reaction

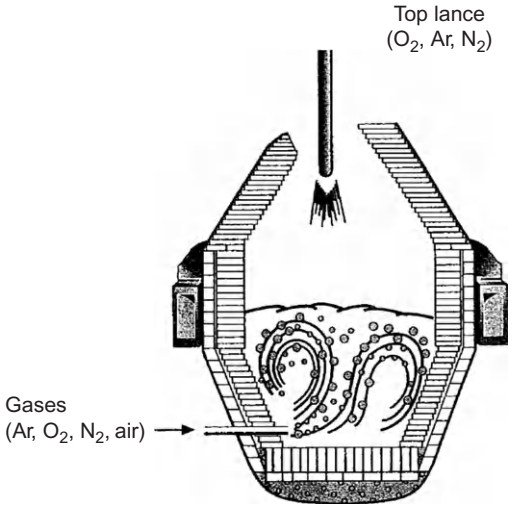


Figure 2.5.12 Schematic diagram of AOD stainless steelmaking [34].

site of the rising bubbles or by metal droplets in the slag. The small-scale experiment described above in which Cr was primarily oxidized is indicative of the tuyère zone in the AOD, not the entire converter.

Based on the assumption given above, a very simple model was developed to predict carbon and chromium oxidation rates [36]. Since the temperature is changing, this introduces some error. More complex models have been developed which take into account these effects.

The rate of decarburization is given by

$$\frac{\mathrm{d}\%\mathrm{C}}{\mathrm{d}t} = -\alpha[\%\mathrm{C} - \%\mathrm{C_e}] \tag{2.5.29}$$

$$\alpha = \frac{A\rho k}{W} \tag{2.5.30}$$

$\%C_e$ = equilibrium carbon content for reaction (2.5.28).

This equation assumes mass transfer of carbon is controlling the rate. Similar expressions were derived and the symbols defined in Section 2.2 of this chapter.

$\%C_e$ depends on the equilibrium constant for (2.5.28) and the prevailing pressure of CO (p_{CO}). The pressure of CO is given by

$$p_{\mathrm{CO}} = \frac{N_{\mathrm{CO}} p}{N_{\mathrm{CO}} + N_{\mathrm{Ar}}} \tag{2.5.31}$$

where p is the total pressure and N_{CO} and N_{Ar} are the molar flow rates of CO and Ar. N_{CO} depends on the rate of decarburization.

$$N_{CO} = -\frac{\mathrm{d\%C}\, 10^{-2} W}{\mathrm{d}t} \frac{}{M_c} \tag{2.5.32}$$

where M_c is the molecular weight of carbon. By combining the above equations, it follows that

$$\frac{d(\%C)}{dt} = \alpha \left[\%C - \frac{\frac{[a_{Cr}]^{2/3} \mathrm{Wp}}{K^{1/3} M_{Fe} \gamma_c} \left(\frac{d(\%C)}{dt} \right)}{\left(N_{AR} - \frac{W}{100 \mathrm{M}_c} \left(\frac{d(\%C)}{dt} \right) \right)} \right] \tag{2.5.33}$$

γ_c = activity coefficient of carbon; M_c = molecular weight of carbon; M_{Fe} = molecular weight of iron; a_{Cr} = activity of Cr in the metal.

The rate of oxidation of Cr can be computed based on a mass balance for oxygen. Specifically, the oxygen used for decarburization as predicted by (2.5.33) is deducted from the total oxygen injected and the remaining oxygen is used for Cr oxidation.

The value of α and more specifically the mass transfer parameter "Ak," the surface area for the reaction times the mass transfer coefficient, is process specific. Since it is extremely difficult to compute A and k accurately, the mass transfer parameter (Ak) is usually derived from the operating data for the process. For the 90 t AOD used in this particular investigation, the value of α was computed to be 0.015 s^{-1}. The carbon content predicted for a 409 grade stainless (9% Cr) is plotted versus the observed content in Figure 2.5.13. In the calculation, the value of α (0.015 s^{-1}) was computed from an independent set of data. The agreement between the calculated and observed carbon contents

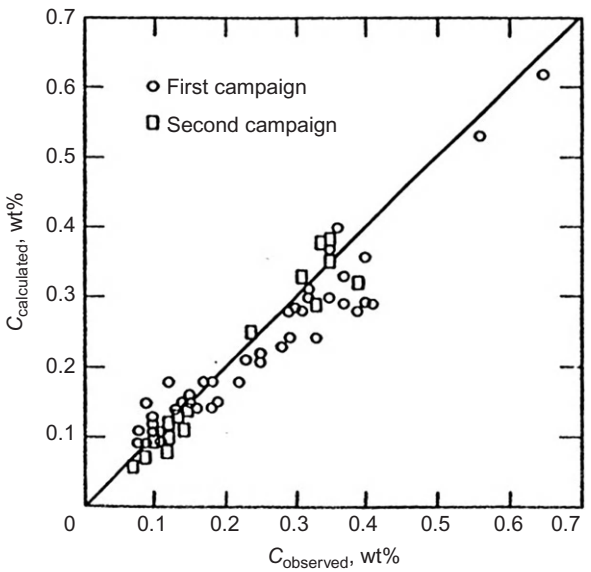


Figure 2.5.13 The predicted versus the measured carbon content for the production of 409 stainless steel [36].

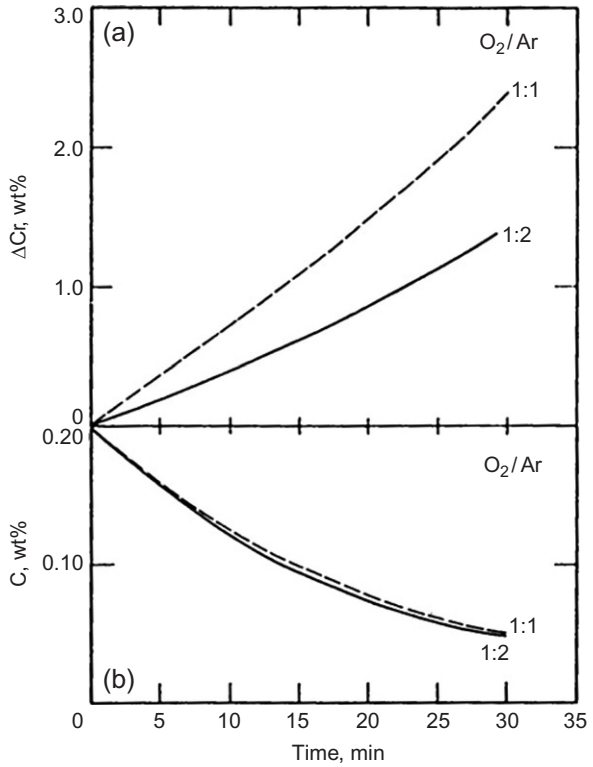


Figure 2.5.14 Predicted rates of oxidation of carbon and chromium for an 18-8-type stainless steel for 1:1 and 1:2 ratios of oxygen to argon [36].

is reasonably good and allows the prediction for different operating conditions so it can be used for process optimization. For example in Figure 2.5.14, the predicted carbon content and Cr oxidation predicted for an 18%C–9% Ni stainless steel are shown. The results indicate that by changing the O_2/Ar ratio from 1:1 to 1:2 results in a slightly faster decarburization rate and reduces the Cr oxidation in half, from 2.2% to 1.1% in 30 min. The Cr oxidized to the slag can be recovered in the metal by reduction using ferrosilicon. The operator must weigh the cost of argon versus the cost of ferrosilicon in making a decision as to what gas composition to use.

The model presented is relatively simple, and steel producers, gas suppliers, and researchers have made improvements. However, the basic mechanism and equation have not changed.

2.5.5. INCLUSION FLOTATION IN ARGON-STIRRED STEEL

Argon stirring is commonly applied to remove nonmetallic inclusions from liquid steel. The density of inclusions is lower than that of liquid steel, and hence the inclusions

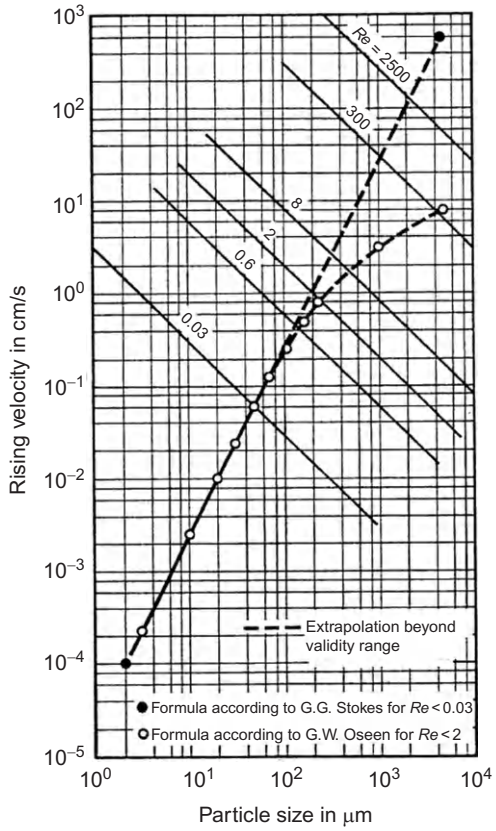


Figure 2.5.15 Terminal velocity of spherical alumina particles in liquid steel [16].

tend to float under the influence of buoyancy (Stokes flotation). However, for typical inclusion sizes (in the range of microns to tens of microns), the terminal velocity is so small that bulk flow of the steel has a much larger effect on inclusion movement than does Stokes flotation [15]. For illustration, Figure 2.5.15 gives the calculated terminal velocities of alumina spheres in liquid steel [16], showing that even a very large inclusion—100 μm in diameter—would require approximately 10 min to rise 1.5 m (half the depth of steel in a typical ladle); smaller inclusions would requires much longer to float, because the terminal velocity is proportional to the square of the particle diameter (for the small Reynolds numbers relevant to Stokes flow).

The actual terminal velocity of alumina inclusions in steel would be even lower than shown in Figure 2.5.15, because alumina inclusions are present as clusters rather than spheres. The inclusions and the liquid steel in such a cluster move as a unit; hence, the effective density of the cluster is (significantly) higher than that of the inclusion. The result is that even large clusters have very low terminal velocities (Figure 2.5.16).

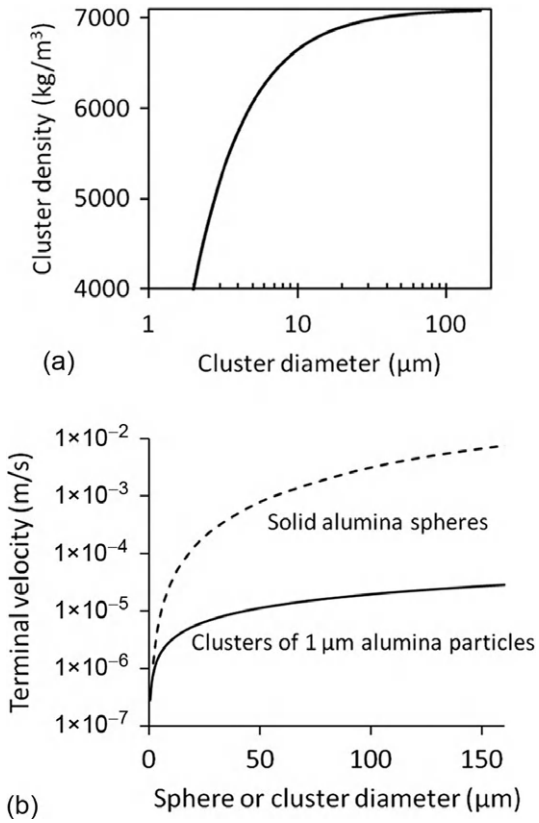


Figure 2.5.16 Stokes flotation behavior of clusters of 1-μm alumina particles. (a) Effective density of cluster; (b) terminal velocities of clusters compared with solid alumina spheres. *After Tozawa* et al. *[17]*.

Transport of inclusions toward the slag layer that covers the steel (and toward the refractory walls, where they can also be captured) [18] therefore relies on bulk flow of the steel. Gas stirring of the melt promotes inclusion removal (at least in part) simply by moving steel (and the inclusions contained in the steel) toward the slag–steel interface, where the inclusions can be absorbed in the slag. Schwerdtfeger suggested that the flow effect of gas stirring can be expressed by a simple first-order relationship (Figure 2.5.17) [19]:

$$\frac{\mathrm{d}[\mathrm{O}]}{\mathrm{d}t} = -(k_{\mathrm{eff}} A/V)\{[\mathrm{O}] - [\mathrm{O}]_{\infty}\}$$

where [O] is the inclusion concentration in the steel (expressed as total oxygen, for example), k_{eff} is the effective mass transfer coefficient, A the surface area, V the volume of steel, and $[\mathrm{O}]_{\infty}$ is the steady-state inclusion concentration at long times.

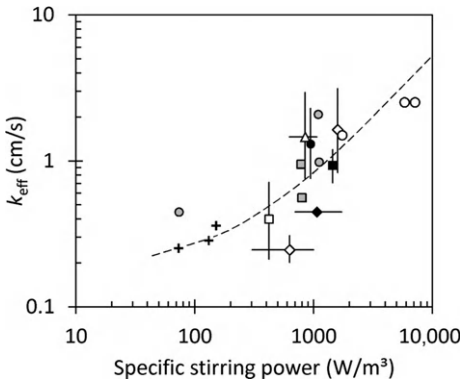


Figure 2.5.17 Effect of stirring power (related to the argon bubbling rate) on the mass transfer coefficient for alumina removal from liquid steel (open symbols, symbols filled with gray, and crosses). Filled symbols are the rate constants for desulfurization. Collated by Schwerdtfeger from different sources [19].

The steady-state inclusion concentration $[O]_\infty$ reflects the balance between inclusion removal and processes which create new inclusions or return inclusions to the steel. Processes which create new inclusions or return inclusions to the steel are reoxidation, washing of inclusions resting at the steel–slag interface back into the bulk steel, erosion of ladle walls [37], and (possibly) emulsification.

New inclusions form by reoxidation: gas stirring opens an "eye" where the steel is not covered by slag [8,20,21]. Oxygen from air comes into contact with steel in the eye, forming new inclusions (alumina, in aluminum-killed steel).

Washing of inclusions from the steel–slag interface, returning the inclusions to the bulk steel, is to be expected because inclusions are not immediately absorbed into the slag upon reaching the slag–steel interface; the inclusions remain at the slag–steel interface for several seconds before being absorbed into the slag [22,23]. During this sedentary period, inclusions could be removed by the eroding action of the steel flow.

In principle, emulsification at the slag–steel interface—forming slag droplets which can be entrained in the flowing liquid steel—can contribute to the steady-state inclusion content of the steel. However, the slag droplets which result from emulsification are unlikely to be smaller than around 1 mm in diameter, and hence should have rather short residence times in the steel [9], precluding a significant contribution to $[O]_\infty$.

Both reoxidation and inclusion washing occur at higher rates if stirring is stronger. Hence, stronger stirring has two opposing effects on inclusion removal: the rate constant (k_{eff}) is larger at higher gas flow rates, but $[O]_\infty$ is also larger; Figure 2.5.18 illustrates these two effects for an induction-stirred ladle. A result of these two opposing effects of stirring is an optimal stirring rate which gives the lowest inclusion content; at lower stirring rates the smaller k_{eff} dominates, and at higher stirring rates the larger $[O]_\infty$ plays a larger role (Figure 2.5.19).

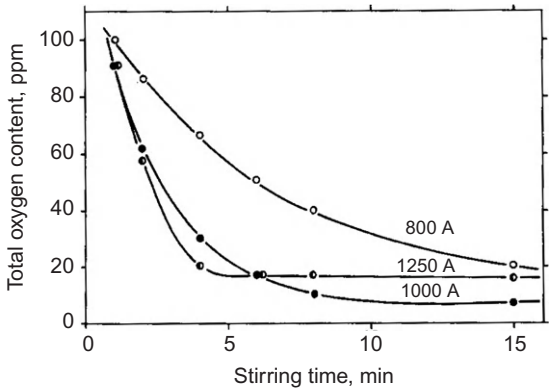


Figure 2.5.18 Alumina oxide removal by induction stirring in an ASEA-SKF ladle furnace. The numbers on the curves refer to the stirring current (which is an indication of the stirring power) [38].

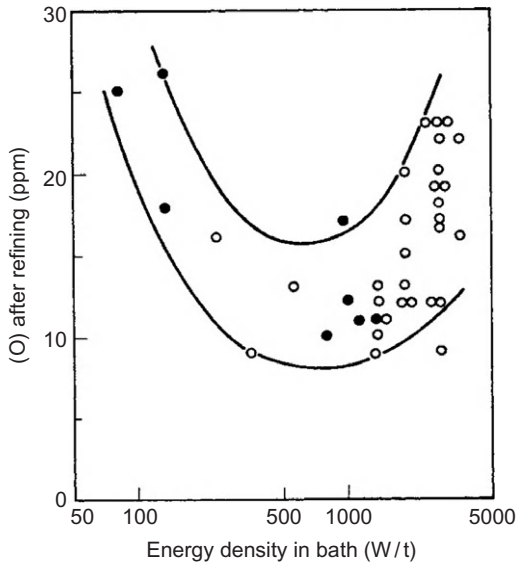


Figure 2.5.19 Effect of stirring power (in an argon-stirred ladle) on the total oxygen content after 7–15 min of treatment [38].

For gas-stirred ladles, direct interaction of inclusions with gas bubbles may also contribute to inclusion removal. Inclusions are not wetted by steel; hence, inclusions would tend to attach to gas bubbles if inclusions collide with bubbles. This is similar to froth flotation of hydrophobic minerals. Quantitative descriptions are available for each of the fundamental steps of froth flotation—collision of particles with bubbles, attachment to bubbles, and detachment from bubbles—and quantification of these steps shows good

correspondence with actual mineral flotation rates [25]. In principle, the same approach can be used to predict rates of inclusion attachment to and removal by bubbles, as was done by Zhang and Taniguchi [26]. Their analysis shows that inclusion removal by direct bubble-inclusion interaction can only be expected if the bubbles are quite small, in the millimeter size range; actual bubbles in ladle processing are about an order of magnitude larger and would not give any significant inclusion removal through direct collection of inclusions.

A similar conclusion was reached by Arcos-Gutierrez *et al.* regarding inclusion removal in the tundish [27]. Bubbles injected through a porous insert in the tundish floor, to form a bubble curtain, are effective in promoting inclusion removal to the tundish slag [28]. However, the mechanism of inclusion removal does not rely on any specific inclusion-bubble interaction; rather, the bubbles direct the steel flow upward to the slag–steel interface [27]. Similarly, Schwerdtfeger [19] has observed that the rate constant for ladle desulfurization (for which transport in the steel to the slag–steel interface is generally rate determining) is approximately equal to the rate constant for inclusion removal (Figure 2.5.17).

Quantitative description of inclusion removal during ladle stirring requires mathematical descriptions of inclusion agglomeration (to form clusters or larger inclusions), bulk steel flow, inclusion transfer into the slag, and inclusion source terms. Progress has been made to formulating practically useful models [29,39].

REFERENCES

[1] R.J. Fruehan, Trans. ISS, Ironmaking Steelmaking 2 (2003) 48–59.
[2] R.J. Fruehan, ISS Trans. 6 (1985) 43–49.
[3] D. Roy. PhD thesis, Carnegie Mellon University, 2012.
[4] D.G.C. Robertson, B. Deo, S. Ohguchi, Ironmaking Steelmaking 11 (1984) 41–55.
[5] D. Roy, P.C. Pistorius, R.J. Fruehan, Metall. Mater. Trans. B, 44B (2013) 1086–1094 and 1095–1104.
[6] C.W. Bale, P. Chartrand, S.A. Decterov, G. Eriksson, K. Hack, R. Ben Mahfoud, J. Melançon, A.D. Pelton, S. Petersen, Calphad 62 (2002) 189.
[7] S.-H. Kim, R.J. Fruehan, R.I.L. Guthrie, Iron Steelmaker 20 (11) (1993) 71–76.
[8] S.-H. Kim, R.J. Fruehan, Metall. Trans. B 18B (1987) 381–390.
[9] D. Sichen, Steel Res. Int. 83 (2012) 825–841.
[10] K.W. Lange, Int. Mater. Rev. 33 (1988) 53–89.
[11] J. Mietz, S. Schneider, F. Oeters, Steel Res. 62 (1991) 10–15.
[12] N. Bannenberg, B. Bergman, H. Wagner, H. Gaye, Proceedings of 6th International Iron and Steel Congress, vol. 3, ISIJ, Nagoya Japan, 1990, pp. 603–611.
[13] H. Kondo, K. Kameyama, H. Nishekowa, K. Hamagami, T. Fiyi, in: 72nd Steelmaking Conference ISS, Chicago, IL, 1989, pp. 191–199.
[14] R.J. Fruehan (Ed.), 11th ed., The Making Shaping and Treating of Steel, Steelmaking Volume, AIST, Pittsburgh, PA, 1998.
[15] A.W. Cramb, in: C.L. Briant (Ed.), Impurities in Engineering Materials; Impact, Reliability and Control, Marcel Dekker, New York, 1999, pp. 49–89.
[16] F. Oeters, Metallurgy of Steelmaking, Verlag Stahleisen, Düsseldorf, 1989, pp. 221–225.
[17] H. Tozawa, Y. Kato, K. Sorimachi, T. Nakanishi, ISIJ Int. 39 (1999) 426–434.
[18] T.A. Engh, N. Lindskog, Scand. J. Metall. 4 (1975) 49–58.
[19] K. Schwerdtfeger, Arch. Eisenhüttenwes. 54 (1983) 87–98.

[20] K. Yonezawa, K. Schwerdtfeger, ISIJ Int. 44 (2004) 217–219.
[21] K. Krishnapisharody, G.A. Irons, ISIJ Int. 48 (2008) 1807–1809.
[22] P. Misra, V. Chevrier, A.W. Cramb, Metall. Mater. Trans. B 31B (2000) 1135–1139.
[23] M. Magnelöv, U. Sjöström, D. Sichen, in: VII International Conference on Molten Slags Fluxes and Salts, The South African Institute of Mining and Metallurgy, Johannesburg, 2004, pp. 577–584.
[24] K.-H. Tacke, J. Iron Steel Res. 18 (Suppl. 2) (2011) 211–219.
[25] J. Ralston, D. Fornasiero, S. Grano, J. Duan, T. Akroyd, Int. J. Miner. Process. 84 (2007) 89–98.
[26] L. Zhang, S. Taniguchi, Int. Mater. Rev. 45 (2000) 59–82.
[27] H. Arcos-Gutierrez, J. de J. Barreto, S. Garcia-Hernandez, A. Ramos-Banderas, J. Appl. Math. 2012 (2012) 16, paper 534275.
[28] Y. Sahai, T. Emi, Tundish Technology for Clean Steel Production, World Scientific, Hackensack, NJ, 2008, p. 199.
[29] M. Hallberg, P.G. Jönsson, T.L.I. Jonsson, R. Eriksson, Scand. J. Metall. 34 (2005) 41–56.
[30] E. Aukrust, DOE—Report ID/12847-7. AISI Direct Steelmaking Final Report, August 1994.
[31] R. Dry, C.P. Bates, D.P. Price, Ironmaking Conf. Proc. ISS 58 (1999) 361–366.
[32] T. Ibaraki, et al., Iron Steelmaker, ISS 22 (3) (1995) 83–98.
[33] A. Ishii, M. Tate, T. Ebisawa, K. Kawakami, Iron Steelmaker 10 (7) (1983) 35–42.
[34] R.J. Choulet, Can. Met. Quart. 10 (1972) 129–135.
[35] J.C. Fulton, S. Ramachandran, AIME Electric Furnace Steel Conference Proceedings, vol. 30, 1972, pp. 43–49.
[36] R.J. Fruehan, Ironmaking Steelmaking 3 (3) (1976) 153–158.
[37] L. Zhang, B.G. Thomas, ISIJ Int. 43 (2003) 271–291.
[38] G. Yuasa, S. Sugiura, M. Fujine, N. Demukai, Electric Furnace Conference Proceedings, 1982 vol. 40, (1982) 197–206.
[39] V. De Felice, I.L.A. Daoud, B. Dussoubs, A. Jardy, J.-P. Bellot, ISIJ Int. 52 (2012) 1273–1280.

CHAPTER 3

Some Applications of Fundamental Principles to Metallurgical Operations

A. McLean
Department of Materials Science and Engineering, University of Toronto, Toronto, Ontario, Canada

Contents

3.0. Introductory Comments: Some Perspectives on the Process of Innovation 241
3.1. Some Metallurgical Considerations Pertaining to the Development of Steel Quality 251
3.2. Refractory Corrosion during Steelmaking Operations 283
3.3. Application of Slag Engineering Fundamentals to Continuous Steelmaking 305
3.4. Kinetics of Assimilation of Additions in Liquid Metals 359

3.0. INTRODUCTORY COMMENTS: SOME PERSPECTIVES ON THE PROCESS OF INNOVATION

In 1890, Henry Marion Howe published his classic text entitled "The Metallurgy of Steel" [1]. In this prestigious volume, he emphasized the vital necessity of monitoring the process with words that carry the weight of a commandment!

> *The very pliancy of the steelmaking processes, demands increased watchfulness to prevent and detect unsought variation.*

With respect to the importance of measurements, the words attributed to Lord Kelvin convey a similar strident, uncompromising tone:

> *When you can measure what you are speaking about and express it in numbers, you know something about it. When you cannot measure it, your knowledge is meager and unsatisfactory.*

In his 1987 Extractive Metallurgy Lecture, the late Julian Szekely, a distinguished Professor at MIT and a pioneer in the mathematical modeling of metallurgical processes, reviewed the state of extractive metallurgy and its important place within the national economy [2]. In this excellent paper, he enunciated the following concepts:

> *Both process optimization and process control require a quantitative representation of the process. Calculations and measurements are not alternatives, but most often must be pursued in a complementary fashion.*
> *The main barrier to the implementation of these concepts tends to be the non-availability of suitably trained personnel.*

Treatise on Process Metallurgy, Volume 2
http://dx.doi.org/10.1016/B978-0-08-096984-8.00024-0
© 2014 Elsevier Ltd.
All rights reserved.

At an International Conference in Tokyo on Computer-Assisted Materials Design and Process Simulation, the late Professor J.K. Brimacombe, an internationally renowned expert in the field of Process Metallurgy, emphasized the importance of:

> *—balancing the application of sophisticated computer models with painstaking measurements [3].*

Professor Brimacombe went on to state:

> *Without careful companion measurements, both in the laboratory and in-plant, to characterize thermophysical properties and complicated boundary conditions, as well as to validate the mathematical models, the power of the computer is severely blunted [3].*

Today this message is more relevant than ever. The importance of observations and measurements from the laboratory and the plant, together with the validation and application of models in the production process, cannot be overemphasized. These individual activities cannot be carried out in isolation. They must be conducted in a collaborative mode and when this happens, the successful application of knowledge within the manufacturing sector is achieved.

The interrelationships between measurements, models, and manufacturing are shown in Figure 3.1 as the triumvirate for knowledge exchange. In efforts to characterize and improve the performance of an existing process or in the quest to generate fundamental information as a basis for the development of new manufacturing routes, measurements and models should be considered as two interdependent requirements. Without actual measurements, the models are incomplete and unsatisfactory. Without models, the real significance of the measurements may not be fully appreciated.

Back in the 1930s, the construction of the Queen Mary provides a fine example of the importance of measurements and models. In this case, physical models were used to

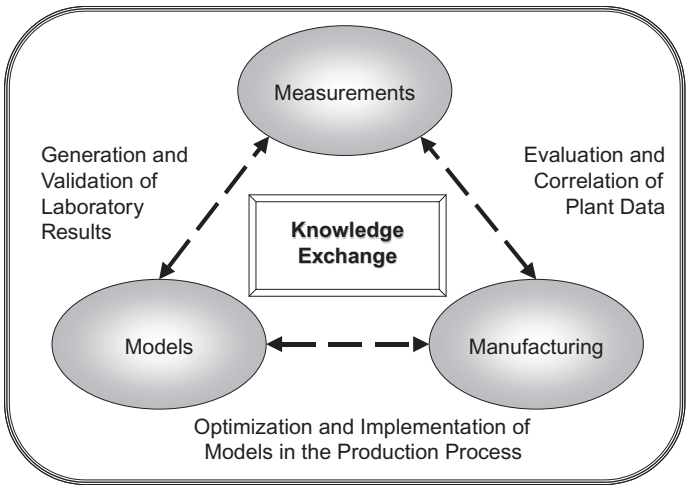


Figure 3.1 The triumvirate for knowledge exchange.



Figure 3.2 In 1936, the Queen Mary was the world`s largest liner.

obtain data for the design and construction of what was then the world's largest liner (Figure 3.2). Built before the age of computers, the design was developed based on approximately 8000 experiments conducted in a water tank 400 ft long and 20 ft wide with 22 scale models of the proposed vessel, each over 16 ft long. The performance of the different models under weather conditions that simulated the worst Atlantic storms was recorded on 16 mm film and the data subsequently analyzed. A wind tunnel was used to monitor the flow behavior of smoke from different funnel designs and under different wind conditions in order to ensure the smoke was blown clear of the decks. After over 30 years in service, the Queen Mary is now docked at Long Beach in California and functions as a hotel and conference center.

Sometimes in our enthusiasm, we construct sophisticated elegant models and forget the reality of the actual system. In this computer age, we need to remember again the importance of observations and accurate measurements. With these thoughts in mind, the basic philosophy woven within the fabric of each of the topics discussed in the following subchapters can be summarized by the simple concept:

You cannot control what you cannot measure.

The generation of experimental data on the physical and chemical properties of metallic melts and oxide systems combined with the careful development of appropriate models has considerably enhanced our understanding of the phenomena that occur between gas, metal, slag, and refractory phases during metallurgical processing. For a cost-effective and energy-efficient operation, the interactions between these different phases must be optimized.

In the quest to generate steel of consistent quality, considerable effort is devoted to control of the chemical, physical, and thermal behavior of the liquid metal and molten

slag phases. These properties are frequently interdependent so that when changes are made with respect to one parameter, the others are also affected. For example in the steelmaking furnace, by changing the lime/silica ratio of the slag, the melting characteristics and the viscosity are affected as well as the ability to absorb sulfur and phosphorus from the molten steel. If the slag is not sufficiently basic, the slag will not properly absorb these harmful species and will adversely affect the behavior of the refractories. These interrelationships provide a fundamental basis for the development of appropriate control strategies. The characteristics of different slags and their influence on steel quality and on refractory performance are discussed in more detail in the following subchapters.

While it cannot be overemphasized that considerable research together with in-plant evaluation is required in order to transform a fundamental scientific concept into a reliable operating system, when all of these aspects are integrated together, they constitute the process of knowledge exchange. The technological benefits and innovative developments that can accrue from knowledge exchange are well exemplified by the steel railway bridge that was constructed over the River Forth on the East Coast of Scotland in 1890, the same year Henry Marion Howe published his classic text "The Metallurgy of Steel" [1]. The Forth Bridge was noteworthy for several reasons [4]. At the time of construction, it was the largest structure ever built with steel, a relatively new material. In addition, it was based on a novel design. It was the first time a bridge of this size had been built using the cantilever principle (Figure 3.3).

In order to illustrate this concept, a model was constructed, involving two men sitting on chairs with a third gentleman suspended between them (Figure 3.4). This model was shown at a lecture presented to the Royal Institute in London in 1887.



Figure 3.3 The Forth Bridge built in 1890 [4].

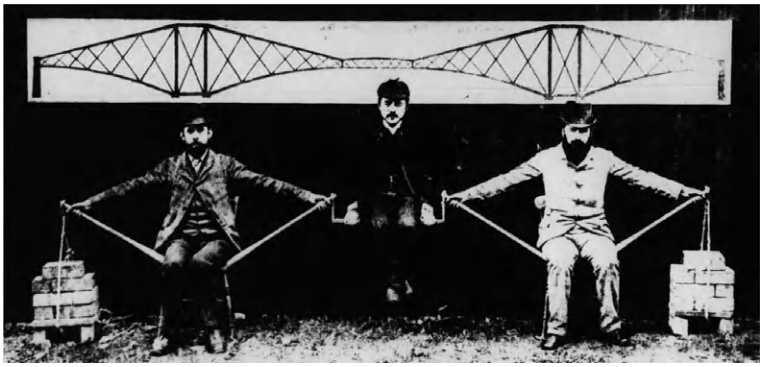


Figure 3.4 The Forth Bridge: The human model devised to explain the cantilever principle at a Royal Institution Lecture in 1887 [4].

It is interesting to note that the gentleman representing the center span of the bridge was in fact a Japanese engineer called Mr. Watanabe, who had been sent to Britain for the purpose of studying the engineering aspects of bridge construction. He was included as part of this human model in order to pay tribute to the fact that the cantilever design had originated not in the United Kingdom, but in the Orient, where for many centuries it had been used as the basic design for bridges made with bamboo. The Forth Bridge is still in use today and is an integral part of the rail system that connects Aberdeen and the North of Scotland with London and the South of England [4].

In his 1993 Howe Memorial Lecture to The Iron and Steel Society of AIME, Professor J.K. Brimacombe [5] stated the following:

> *A never-ending challenge to the competitiveness of the steel industry is the application of knowledge on the shop floor where, finally, productivity and quality are realized.*

The manufacturing systems for metal production generally consist of several metallurgical reactors linked together by a number of transfer operations each of which can be considered as an individual component within a communication network transmitting different types of signals that may be physical, chemical, thermal, or electrical in character. With appropriate methods for detection, interpretation, and response, these signals can permit the development of new process control strategies for the monitoring and optimization of specific aspects of metallurgical operations in order to obtain consistent quality products with associated benefits related to metal yield, environmental aspects, and operating costs. In this chapter, some examples are provided from laboratory studies and plant investigations of signals and sensors that pertain to metal quality and slag chemistry. From these illustrative examples, it is apparent that synergistic interactions between the research and manufacturing communities can enhance the generation and validation of new knowledge and facilitate the implementation of innovative technologies on a regular production basis.

For many decades, control strategies have been based upon samples taken from liquid steel, molten slag, and the gas phase as well as from solid products. This is very much a static control system. With major advances in the areas of computational models, artificial intelligence, expert systems, and signal processing technologies, there has been increasing activity with respect to the development of dynamic systems based on diagnostic sensors which permit online, continuous monitoring of metallurgical operations.

A good illustration of the advantages that can accrue from a dynamic rather than a static system can be found in the story of the Battle of Trafalgar when the British fleet under the command of Lord Horatio Nelson aboard HMS Victory, on October 21, 1805, defeated the combined sea forces of France and Spain. The Battle of Trafalgar ended Napoleon Bonaparte's plans to invade England and established Britain as the ruler of the seas for over 200 years. Lord Nelson lost his life at Trafalgar but it is appropriate to remember that at Trafalgar, for the first time, detailed messages were transmitted between vessels using flag signals (Figure 3.5). This method of communication permitted important changes to be made in the attack plan while the battle was actually in progress and gave the British fleet a significant advantage over the enemy ships. Prior to this time, sea battles were fought based on a fixed strategy between the different ships of the fleet that was determined before the commencement of battle. Because the ships were unable to communicate with each other, the strategy remained unchanged throughout the battle. It has been recorded by historians that Nelson's victory at Trafalgar was in large measure due to the successful implementation by the British fleet of the use of flag signals for the transmission of strategic messages during the course of the engagement. This is an early example of the benefits associated with "continuous monitoring."



Figure 3.5 For the first time, messages were transmitted between ships with flag signals.

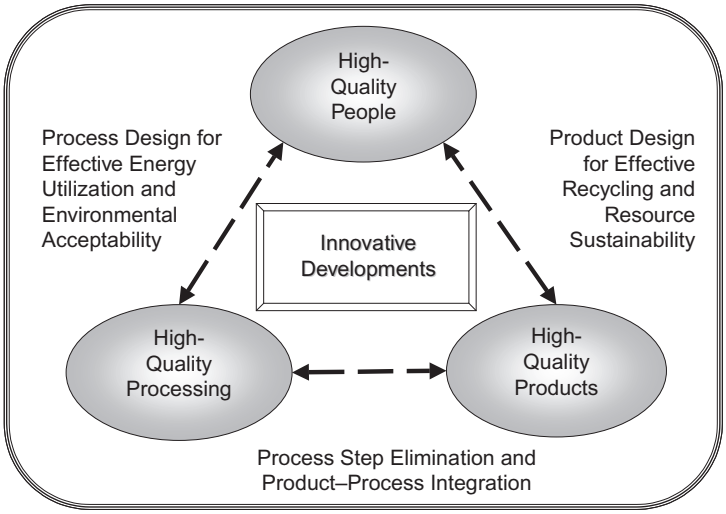


Figure 3.6 The HQPs for Innovative Developments.

Novel sensor technologies including nonintrusive monitoring systems are finding increasing application for the continuous evaluation of metallurgical operations so that the occurrence of any detrimental variations due to perturbations or imperfections within the processing system can be detected and corrected at an early stage. Several examples of these diagnostic systems are presented in the following subchapter.

High-quality products require high-quality processing and both require high-quality people (Figure 3.6). In order to promote and encourage collaborative partnerships that will not only enhance the exchange of knowledge and experience between the laboratory and the production plant but also facilitate the development and utilization of new materials and new processes, well-educated people will always constitute the vital link. Ensuring the availability of skilled personnel is perhaps our greatest challenge for the future. In the final analysis, improvements in existing processes and the development and implementation of new technologies depend on the availability of men and women with a sound understanding of the fundamental aspects and practical implications of their discipline and who are fully equipped with the behavioral attributes and communicative skills that will enable them to apply their knowledge, with wisdom and integrity, within this most challenging field of endeavor, the science and technology of metallurgical processing.

The pace of innovative developments can be greatly accelerated by synergistic interactions if basic studies performed by the research community are conducted in close collaboration with the user community and the resource community, the provider of equipment and the supplier of materials (Figure 3.7).

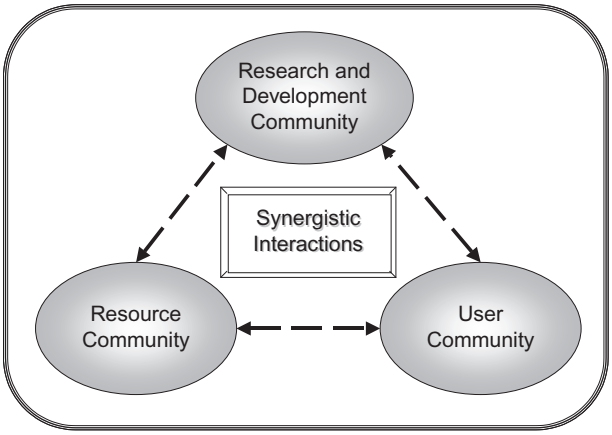


Figure 3.7 Synergistic interactions between different communities.

It must be recognized and acknowledged that these three communities represent quite distinct cultures, with very different objectives, and mutual interaction combined with effective collaboration is not always an easy task. In this collaborative process, the exchange of knowledge between the different communities is perhaps the most difficult step since it not only requires a willingness to share knowledge but also a willingness to receive knowledge. In this process of knowledge exchange, the receptor capacity of the individual is frequently the rate-limiting step. Nevertheless, when meaningful communication is established between the members of this triumvirate of diverse cultures, there is a powerful driving force for the synergistic development of innovative technologies.

An example of the ingenuity and flexibility of thinking which is sometimes required for effective communication between different cultures can be found on the West Coast of Scotland, where, separated from the mainland by less than 100 m, there is a small island called Seil Isle. Connecting the island with the mainland, there is an ancient, stone bridge (Figure 3.8). In a fine display of Scottish modesty, it is called "Bridge over the Atlantic." On the island side of the bridge, there is a small inn called "Tigh-Na-Truish." Translated, this means, "Place of the Trousers."

After the defeat of the Scots by the English in 1745, every effort was made to introduce an English culture to the mainland and the wearing of the kilt was declared illegal. Nevertheless on the island, there remained a strong sense of Scottish culture and the men of the island continued to wear the kilt. However, when they had business to conduct with the "foreign" culture on the mainland, they first paid a visit to Tigh-Na-Truish where they exchanged their kilts for trousers and then crossed over the bridge to the mainland. After their business was complete, the Scotsmen crossed back over the bridge to the island again and back into the inn where the despised trousers were discarded and proudly replaced with the kilt.



Figure 3.8 "Bridge over the Atlantic," on the West Coast of Scotland as depicted by Artist C. John Taylor.

On our technological journey through the twenty-first century, we will cross a number of bridges that will span our knowledge gaps, bring a new understanding of existing processes, and permit the development of new processing routes, new diagnostic systems, new materials, and new partnerships between people. Regardless of whether we work in industry, government, or academia, we have the great privilege of participating in the bridge-building process:

- Bridges of education that will enhance knowledge exchange
- Bridges of innovation that will transform industrial operations
- Bridges of friendship that will facilitate communication between different cultures

Let us therefore build with vision, with enthusiasm, with integrity, and with wisdom. In this way, the torch of knowledge, the light of innovation, and the flame of friendship will be passed on from one generation to the next and together we can enlighten the road that leads to understanding and set ablaze the imagination and minds of the young engineers and teachers of tomorrow on their journey toward technological discovery. In all of our endeavors aimed at knowledge exchange, a process that encompasses quality communications, innovative developments, international collaborations, and the training of people, let us resolve to emulate the highest standards of achievement and professionalism so well exemplified by the giants of our profession who have gone on before and on whose shoulders we have the privilege to stand.

In the following subchapters, discussions are presented on aspects pertaining to the physical chemistry of steelmaking processes and the thermochemical behavior associated with the addition of alloying elements to both ferrous and nonferrous melts. Examples are provided of relationships between measurements, models, and manufacturing, based on laboratory investigations, pilot plant studies, and results from production operations. The individual contributions provide detailed descriptions of process development, the generation of product quality, and innovative technologies that have been applied for the evaluation and control of specific aspects of metallurgical operations.

REFERENCES

[1] H.M. Howe, The Metallurgy of Steel, The Scientific Publishing Company, New York, 1890.
[2] J. Szekely, Metall. Trans. B 19B (1988) 525.
[3] J.K. Brimacombe, I.V. Samarasekera, S.L. Cockcroft, in: Proceedings of the International Conference on Computer-Assisted Materials Design and Process Simulation, ISIJ, 1993, p. 102.
[4] A. McLean, T. Emi, Tetsu-to-Hagane 77 (1991) N196 (in Japanese).
[5] J.K. Brimacombe, Metall. Trans. B 24B (1993) 917.

CHAPTER 3.1

Some Metallurgical Considerations Pertaining to the Development of Steel Quality

Y.D. Yang and A. McLean
Department of Materials Science and Engineering, University of Toronto, Toronto, Ontario, Canada

3.1.1. INTRODUCTION

Toward the end of the nineteenth century, Henry Marion Howe, a distinguished steelmaker, an eminent professor of metallurgy and President of AIME, published his classic text entitled "The Metallurgy of Steel" [1]. In spite of the time difference, much of the material contained in this volume is still worthy of study today. Howe had the great gift of being able to express in vivid terms, some of the basic truths of iron and steelmaking technology. An example of this may be found in his use of the term "The Treachery of Steel," which he employed in a very graphic manner to discuss what we today would call, "The Management of Quality": "Owing to the very nature of the processes by which steel and wrought iron are made, carelessness and ignorance, whether in selecting materials, in conducting the processes, or examining the product, is likely to lead to the making and selling of treacherous steel, treacherous simply because it is unsuited to the purpose for which it is sold."

Major technological changes have transformed the iron and steel industry during the past century. These changes have had a profound effect on process intensification, energy utilization, metal yield, and product quality. They include: high productivity blast furnaces, external treatment of hot metal, oxygen steelmaking, alternate ironmaking processes, ultra high power arc furnaces, ladle metallurgy, vacuum processing, continuous casting, thermomechanical processing, and novel coating technologies.

Coupled with the implementation of advanced production technologies, there have been ever-increasing demands for improved steel performance which in turn have strongly influenced changes in steel chemistry and steel quality. For example, in 1911 at the time of the launch of the Titanic, the steel plates used for construction of the hull met all of the required standards. The ship was built by Harland & Wolff at Belfast in Northern Ireland. The steel was manufactured using the open-hearth process by David Colville & Company in Scotland, the same company that 25 years later provided steel for the construction of the world's largest passenger liners, the Queen Mary and the Queen

Treatise on Process Metallurgy, Volume 2
http://dx.doi.org/10.1016/B978-0-08-096984-8.00005-7
© 2014 Elsevier Ltd.
All rights reserved.

Elizabeth. On April 14, 1912 at 11.40 PM, the Titanic struck an iceberg and sank 2 h and 40 min later, with a loss of 1517 men, women, and children. In 1992, metallurgists at the Metals Technology Laboratories, CANMET, in Ottawa, Canada, published a report on their investigation of a number of cast iron, wrought iron, and steel samples recovered from the Titanic wreck site, on the bed of the Atlantic, over 4000 m below the surface of the ocean [2]. Chemical analysis of a section of hull plate, which was approximately 25 mm thick, indicated that the steel contained 0.2%C, 0.52%Mn, 0.025%Si, 0.065% S, 0.010%P, <0.005%Al, and 0.004%N. The high sulfur content is of particular significance. Microstructural examination indicated extensive carbon banding, typical of hot-rolled 0.2%C steel and more importantly, elongated in the rolling direction, long MnS stringers, some of which exceeded 25 mm in length (Figure 3.1.1).

The results of Charpy tests performed on samples taken in the longitudinal direction are compared with data for a semi-killed steel of similar composition but with lower sulfur content that would be typical of steel produced in the early 1950s (Figure 3.1.2). With a seawater temperature of approximately 0 °C and because of the elongated manganese sulfide inclusions, the hull plates of the Titanic had essentially no ductility at the time of impact with the iceberg. A major thrust in current steelmaking technology is the production of steel with lower residual concentrations of sulfur. Today, high-quality steels are produced for demanding applications such as Arctic pipelines, offshore platforms, ice-breaker vessels, and ships for the transportation of liquid natural gas. These steels are produced with extremely low inclusion contents and residual sulfur levels can be less than 10 ppm.

The system for successful production of quality steel can be viewed as a "chain of quality" consisting of a number of metallurgical reactors linked together by a series of transfer operations. In this context, the furnace and ladles are batch reactors, while the tundish and the casting molds are continuous reactors. In recent years, it has become increasingly evident that transfer operations between one reactor and the next must be carefully controlled; otherwise they become destroyers of quality and constitute "weak links" in this "chain of quality." During the manufacturing process, the objective must be to continuously improve quality as the metal moves from one reactor to the next.



Figure 3.1.1 Carbon banding and elongated manganese sulfide inclusions in plate steel from the Titanic [2].

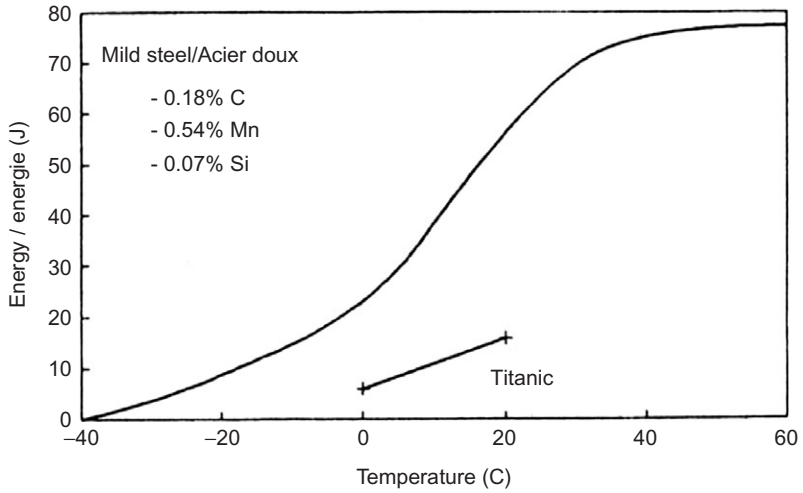


Figure 3.1.2 Charpy tests on specimens of plate steel from the Titanic and similar steel produced in the 1950s [2].

In each case, the reactor can be designed to include a series of operations involving chemical, physical, and thermal control, arranged in such a way that the interactions between steel, gas, slag, and refractory phases within each reactor are optimized so that each unit functions as a refiner rather than a contaminator. These control parameters are frequently interdependent so that when changes are made with respect to one parameter, the others are also affected. For example, during ladle stirring operations, the injection of argon induces fluid flow within the molten steel and slag phases, and by this means, chemical and thermal uniformity are obtained.

Since oxygen and sulfur have a profound influence on the formation of inclusions and hence on the properties of steel in service, considerable attention has been directed toward the development of a thorough understanding of the chemical behavior of these solutes in molten steel. Factors which influence the formation of inclusions include interactions within the molten steel itself, interactions between steel and molten slag, interactions between steel and refractory materials, and finally interactions between molten steel and air during transfer operations from one vessel to another. These aspects together with methods for evaluating steel quality are discussed in more detail in the following sections.

3.1.2. GENERATION OF STEEL QUALITY

3.1.2.1. Oxygen Control in Molten Steel

In discussions of steel quality, interactions between oxygen and elements such as carbon, manganese, chromium, silicon, aluminum, and calcium are of particular interest. The same is true with respect to reactions involving the elements sulfur, phosphorus,

hydrogen, and nitrogen. Control of the oxygen potential throughout steelmaking operations is in fact essential. Without oxygen control, it is impossible to control the behavior of the other elements. In this context, control of the composition, properties and performance of steelmaking slags, and refractories, is also a mandatory requirement for the production of quality steel.

In steelmaking processes, molten steel is inevitably brought into direct contact with air. Little *et al.* have shown that large inclusions are primarily due to reoxidation of the metal during transfer operations [3]. An exposed metal meniscus in the ladle or tundish, a molten stream, and turbulence of the metal in the mold cavity, all provide ample opportunity for liquid steel to react with air, which is an unlimited supplier of oxygen [4]. In addition, these conditions can also contribute to the absorption of nitrogen as well as hydrogen particularly when the humidity content of the atmosphere is high.

Reactions between molten steel and the surrounding atmosphere have been investigated using levitation melting and a falling droplet technique (Figure 3.1.3) [5,6].

The quenched droplet is analyzed for oxygen and nitrogen contents to determine the effects of different solutes on the reoxidation and nitrogen absorption behavior. Studies have been made of the solutes oxygen and sulfur and the interrelationships that exist

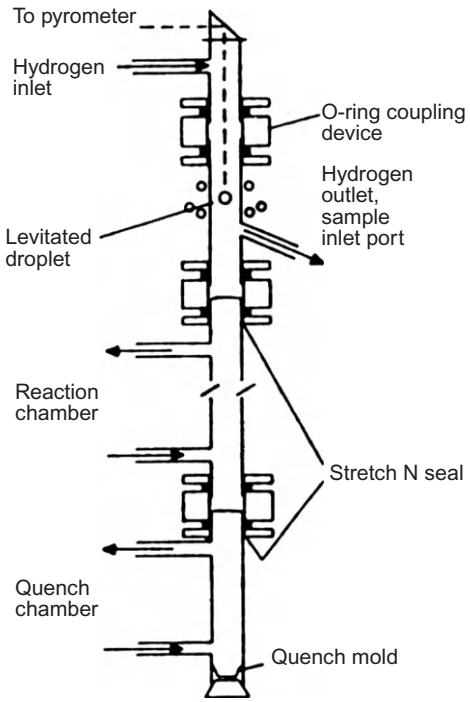


Figure 3.1.3 Levitation melting and falling droplet facility for the investigation of reactions between molten steel and gas atmospheres [5,6].

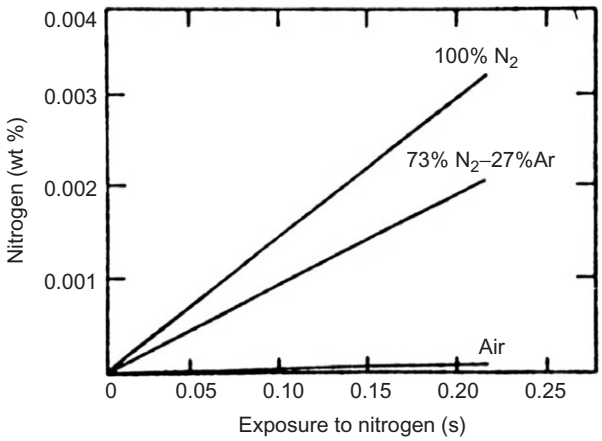


Figure 3.1.4 Absorption of nitrogen by steel droplets after falling for various times through different gas atmospheres [5].

between these solutes and the elements nitrogen and hydrogen. When present in molten steel, oxygen and sulfur behave as surface-active elements. This implies that oxygen and sulfur concentrate at the surface of liquid steel and block surface sites that would otherwise be available for the adsorption of nitrogen.

Experiments have shown that both oxygen and sulfur drastically decrease the rate of nitrogen absorption [5]. The effect of oxygen is illustrated in Figure 3.1.4, where the rate of nitrogen absorption from an argon–73% nitrogen gas mixture is actually greater than that from air which in fact contains a higher concentration of nitrogen, 79%. This is due to the rapid pick-up of oxygen from air which then inhibits the slower absorption of nitrogen. The strong inhibiting effect of sulfur on the pick-up of nitrogen is shown in Figure 3.1.5. Similar behavior has been observed with respect to the effects of oxygen and sulfur on the absorption of hydrogen.

Thus if steel is produced with very low oxygen and sulfur contents, then the molten steel is more susceptible to the absorption of nitrogen and hydrogen. For example, during ladle desulfurization treatments, it has been found that the nitrogen absorption may be about 15 ppm when the final sulfur level is 90 ppm. However, when the final sulfur level is 20 ppm, the nitrogen absorption may be as high as 50 ppm [7]. This implies that while problems associated with the presence of sulfides may be avoided by producing low sulfur steels, new problems may be introduced due to high nitrogen contents and possibly even high hydrogen contents. For this reason, there are advantages in producing steel with final sulfur concentrations that are at the higher end of the sulfur specification rather than at the lower end. In this way, the absorption of nitrogen and hydrogen can be minimized. By the same logic, delaying the addition of deoxidizers and/or desulfurizing treatments will also decrease the opportunities for absorption of nitrogen and hydrogen.

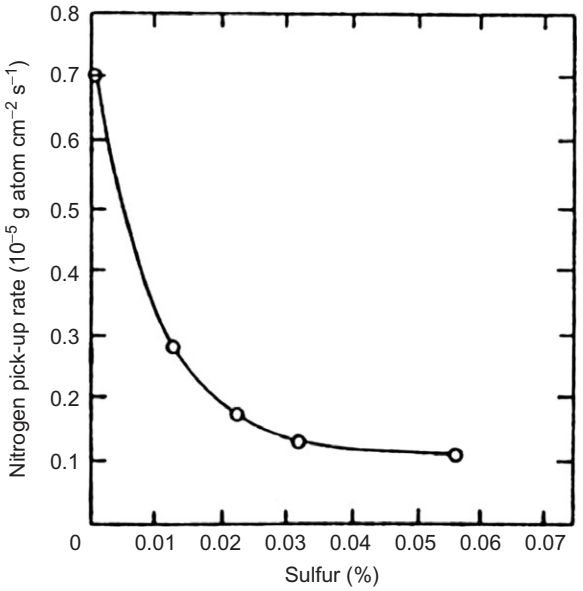


Figure 3.1.5 Decrease in the rate of nitrogen absorption by steel droplets with increase in sulfur content [5].

On the other hand, Figure 3.1.6 shows that in the case of oxygen absorption, the rate is not affected by the sulfur content of the steel or by the presence of strong deoxidizers such as aluminum or titanium [6]. The line shown in Figure 3.1.6 corresponds to the predicted rate of oxidation based on diffusion control in the gas phase and is in good agreement with the results obtained from the falling droplet experiments.

3.1.2.2. The Characterization of Refining Slags

In discussing the refining capacity of slags, the characterization of slag basicity is an important consideration. The ratio of basic oxides to acidic oxides expressed in weight percent, or sometimes as a molar ratio, is traditionally used as a measure of slag basicity. However, the simple (CaO/SiO_2) ratio ignores the effects of other oxides, and the ratio $(CaO + MgO)/(Al_2O_3 + SiO_2)$ implies that lime and magnesia behave as equivalent basic oxides and that alumina and silica have the same degree of acidity, neither of which is the case. To some degree, this can be offset by the use of empirical coefficients, although the modified ratios are somewhat restricted in their applicability. Optical basicity provides a good foundation for a better understanding of the behavior of molten slags than the conventional basicity ratios. The concept of optical basicity was developed by two glass scientists Duffy and Ingram [8] and introduced to the metallurgical community by Duffy *et al.* in the late 70s [9]. This approach has proved to be a valuable tool for designing slags or fluxes which will have the required characteristics with respect to the behavior of, for example, sulfur, phosphorus, hydrogen, magnesia, and alkalis [10–15].

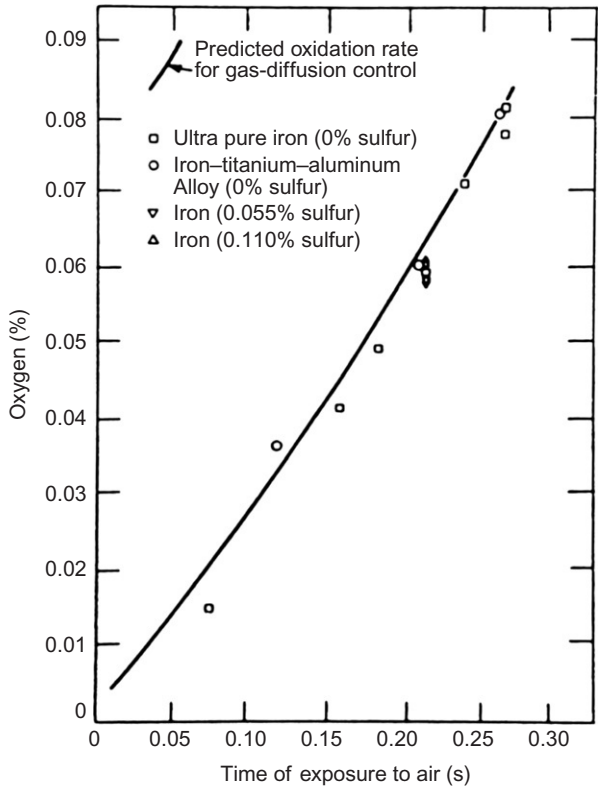


Figure 3.1.6 Absorption of oxygen by steel droplets containing different amounts of sulfur, aluminum (0.1%), and titanium (0.1%), after falling for various times through air [6].

The optical basicity scale is constructed on the basis that the optical basicity value of calcium oxide, Λ(CaO), is unity, and the Λ values for all other components in the slag are measures of the "lime character" or "lime equivalence." The values can be used in systems which do not contain lime. This approach allows basicity values to be ascribed to slags which may not contain lime or any "acidic" constituents. The optical basicity of molten slag can be calculated using the following relationships:

$$\Lambda = \sum_{i=1}^{n} \Lambda_i N_i \tag{3.1.1}$$

$$N_i = \frac{X_i n_{O_i}}{\sum_{i=1}^{n} X_i n_{O_i}} \tag{3.1.2}$$

Here Λ: optical basicity of the slag; Λ_i: optical basicity value of component "i"; N_i: compositional fraction; X_i: mole fraction of component "i" in the slag; n_{O_i}: number of oxygen atoms in component "i."

On the basis of the experimentally measured values of optical basicity, correlations have been developed which allow extension of this approach to other components and systems. For nontransition metal oxides, Duffy and Ingram [8] deduced an excellent correlation between the optical basicity of the oxide, Λ, and the Pauling electronegativity, x of the cation. This has proved an extremely useful correlation, which has allowed application of optical basicities to many more systems than have been measured spectroscopically.

Nakamura *et al.* [16] developed an alternative scale based on average electron density which provides values for the transition metal oxides and also a fair number of halides as well as for the main series oxides. Values calculated from Pauling electronegativities and from average electron densities for oxides of interest in iron and steelmaking are compared in Table 3.1.1.

Table 3.1.1 Different Optical Basicity Scales for Oxides [10]

Oxide	Ion-Oxygen Attraction, $I=(2Z)/d^2$	Ionic Bond Fraction	Optical Basicity, Λ Derived from Pauling Electronegativity	Optical Basicity, Λ Derived from Average Electron Density	Optical Basicity, Λ, Recommended Values
K_2O	0.27	0.68	1.40	1.15	1.4
Na_2O	0.36	0.65	1.15	1.10	1.2
Li_2O	0.50	0.63	1.07	1.05	1.05
BaO	0.53	0.65	1.15	1.08	1.10
SrO	0.63	0.61	1.07	1.04	1.05
CaO	0.70	0.61	1.00	1.00	1.00
MnO	0.83	0.47	0.59	0.95	0.95
FeO	0.87	0.38	0.51	0.93	0.93
MgO	0.95	0.54	0.78	0.92	0.85
Cr_2O_3	1.44	0.41	0.55	0.69	0.69
Fe_2O_3	1.50	0.36	0.48	0.69	0.69
Al_2O_3	1.66	0.44	0.61	0.68	0.65
TiO_2	1.85	0.41	0.61	0.64	0.65
B_2O_3	2.34	0.31	0.42	0.42	0.42
SiO_2	2.44	0.36	0.48	0.47	0.48
P_2O_5	3.31	0.28	0.40	0.38	0.40

The agreement between the two scales is reasonable for the main series oxides, but not for the transition metal oxides [10]. Clearly, the values for these latter oxides calculated from the average electron densities are more reasonable, and therefore this scale may well be the preferred one for metallurgical slags which tend to contain at least small quantities of one or more of these transition metal oxides.

Based on the above considerations, Sommerville and Yang [10] have suggested what they consider to be an appropriate scale of values for the various oxides. These are listed as recommended values in the end column of Table 3.1.1.

3.1.2.3. Slag Chemistry and the Control of Sulfur

The sulfide capacity of a slag is a useful chemical parameter for comparing the desulfurization ability of different slags. Once the sulfide capacity of the slag is known, a quantitative evaluation of desulfurization using this slag under a fixed condition can be made. It is also possible to design a slag with an appropriate composition in order to achieve a desirable desulfurization result. The definition of sulfide capacity is commonly derived from the slag–gas exchange reaction:

$$1/2\ S_2(g) + O^2 = S^2 + 1/2O_2(g) \tag{3.1.3}$$

$$K_3 = \frac{a_{S^{2-}} \cdot p_{O_2}^{1/2}}{a_{O^{2-}} \cdot p_{S_2}^{1/2}} \tag{3.1.4}$$

The sulfide capacity of the slag is defined as:

$$C_{S^{2-}} = (\text{wt\% S})\frac{p_{O_2}^{1/2}}{p_{S_2}^{1/2}} = \frac{K_3 a_{O^{2-}}}{f_{S^{2-}}} \tag{3.1.5}$$

Equation (3.1.5) can be rewritten in terms of the sulfur distribution ratio, L_S equal to (wt% S)/[wt% S]:

$$\log L_S = \log C_{S^{2-}} + \log f_S - \frac{1}{2}\log p_{O_2} - \frac{7055}{T} + 1.224 \tag{3.1.6}$$

By introducing the free energy change for the dissolution of gaseous oxygen into liquid iron, Equation (3.1.6) can be rewritten as:

$$\log L_S = \log C_{S^{2-}} + \log f_S - \log a_{[O]} - \frac{935}{T} + 1.375 \tag{3.1.7}$$

Dependence of final sulfur content $[S]_f$ in liquid steel on the initial sulfur content $[S]_i$, the sulfur distribution ratio between molten slag and liquid metal, L_S, and the ratio of slag to metal quantities, Q, is expressed as:

$$[S]_f = \frac{[S]_i}{1 + L_S \cdot Q} \tag{3.1.8}$$

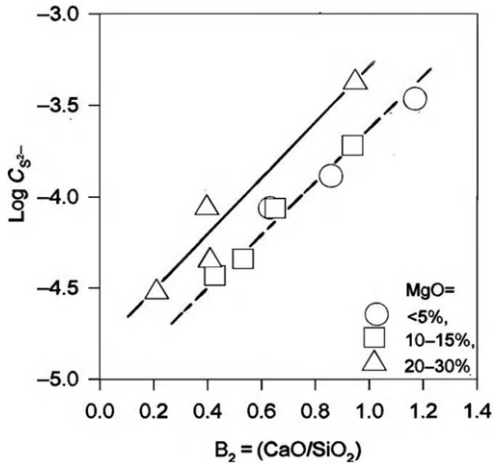


Figure 3.1.7 Dependence of sulfide capacity on CaO/SiO_2 ratio of $CaO–MgO–SiO_2$ slags at 1873 K derived [19] from experimental results of Nzotta *et al.* [17,18].

Equations (3.1.7) and (3.1.8) can be used to calculate the extent of desulfurization of hot metal and liquid steel that is attainable under a range of operating conditions. In order to design a slag for effective desulfurization, the sulfide capacity of that slag must be known or predicted. For this reason, a considerable number of studies have been carried out to evaluate the sulfide capacity of metallurgical slags. Figure 3.1.7 shows the correlation of sulfide capacity of $CaO–MgO–SiO_2$ slag with the ratio of CaO/SiO_2. Data used in the figure were derived from the work of Nzotta *et al.* [17,18].

As shown in this figure, the sulfide capacity of the slags increases with increasing CaO/SiO_2 ratio as expected. Figure 3.1.7 also shows that slags with 20–30% MgO content have a higher sulfide capacity than slags with the same CaO/SiO_2 ratio but lower MgO content. However, when slag basicity is described in terms of the ratio $(CaO + MgO)/SiO_2$, as shown in Figure 3.1.8, the opposite tendency is observed, slags with a lower magnesia content have a higher sulfide capacity. This apparent contradiction can be rationalized by noting that in Figure 3.1.7, an increase in magnesia content in a slag with a fixed CaO/SiO_2 ratio represents an increase in slag basicity, and consequently an increase in ability to absorb sulfur. In Figure 3.1.8, an increase in magnesia content in a slag with a fixed $(CaO + MgO)/SiO_2$ ratio actually constitutes a decrease in slag basicity, since CaO, a strong basic oxide, is being replaced by MgO, a weaker basic oxide. Under these circumstances, an increase in MgO yields a slag with a lower ability to absorb sulfur.

The potential for confusion, and the possibility of reaching a wrong conclusion, with respect to the effect of magnesia on the sulfide capacity of slag, or for that matter, other constituents such as hydrogen or phosphorus, highlights the disadvantage of using variable, empirical ratios as indicators of slag basicity.

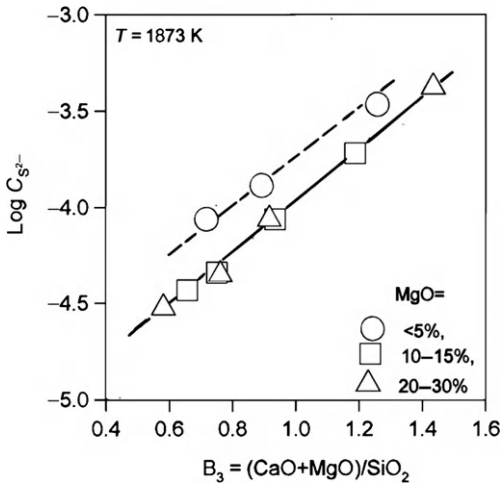


Figure 3.1.8 Dependence of sulfide capacity on (CaO + MgO)/SiO_2 ratio of CaO–MgO–SiO_2 slags at 1873 K derived [19] from experimental results of Nzotta *et al.* [17,18].

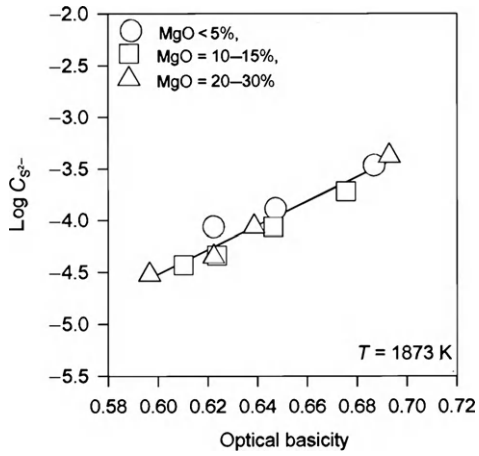


Figure 3.1.9 Dependence of sulfide capacity on optical basicity of CaO–MgO–SiO_2 slags at 1873 K derived [19] from experimental results of Nzotta *et al.* [17,18].

Figure 3.1.9 shows the relation between sulfide capacity and optical basicity of slags using the same data as those shown in Figures 3.1.7 and 3.1.8. A good linear relation is found between the two parameters for the slags with different MgO contents [19]. The increase in sulfide capacity with increasing basicity of slags with different compositions is consistent with the acidic character of the sulfide ion.

Figure 3.1.10 from the work of Sosinsky and Sommerville [11] shows the sulfide capacity of different slag systems as a function of optical basicity at 1773 K.

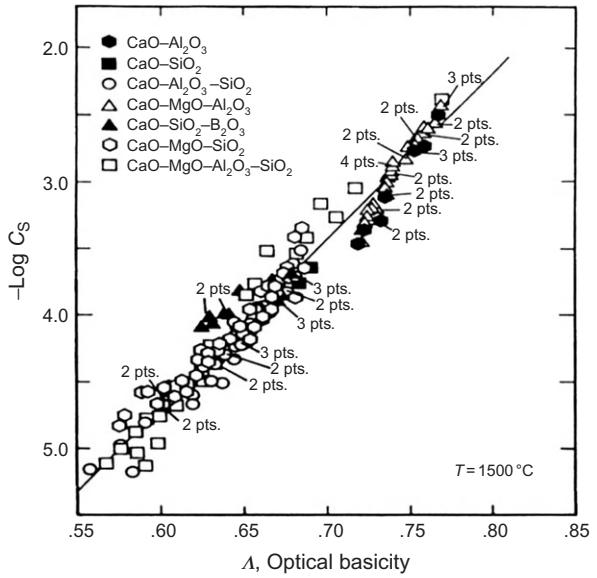


Figure 3.1.10 The sulfide capacity of different slag systems as a function of optical basicity at 1773 K [11].

Based on these data, the following correlation between the sulfide capacity of slags at 1773 K and their optical basicity is obtained [11]:

$$\log C_{S^{2-}} = 12.630\Lambda - 12.30 \tag{3.1.9}$$

Figure 3.1.11 shows lines of iso-sulfide capacity derived from optical basicity calculations for lime–alumina–silica slags at 1873 K [11].

From this diagram, it can be deduced that a binary slag consisting of 50% lime and 50% silica has a sulfide capacity of approximately 5×10^{-4}. On the other hand, a binary slag consisting of 50% lime and 50% alumina has a sulfide capacity of approximately 8×10^{-3} which is 16 times greater than the sulfide capacity of the equivalent lime–silica slag. Thus, by replacing part of the silica with alumina, the desulfurizing power of the slag is increased. On the other hand, to minimize sulfur loss from the metal, for example, during the production of high-sulfur machining grades, a lime–silica slag would be more effective than a lime–alumina slag.

3.1.2.4. Water Vapor Dissolution in Molten Slags

The absorption of hydrogen by molten steel has adverse effects on steel quality and is strongly influenced by the composition of the slag phase. This has important implications with respect to ladle slags as well as the selection of tundish fluxes and continuous casting mold powders. At this point, tribute must be paid to the pioneering studies on water

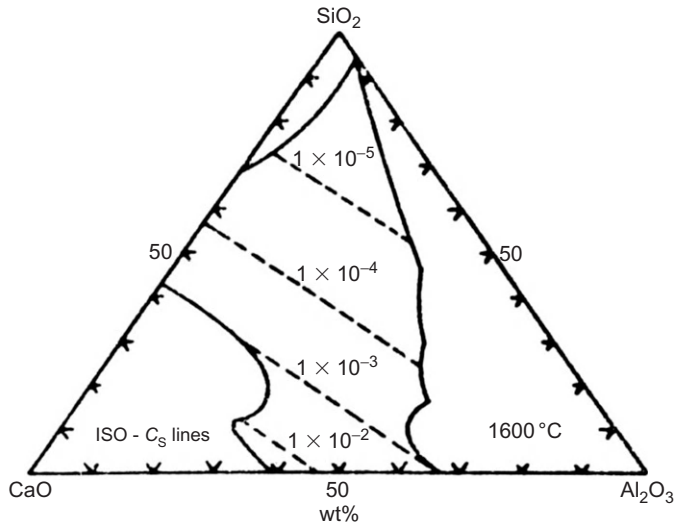


Figure 3.1.11 Iso-sulfide capacity lines derived from optical basicity calculations for liquid slags in the lime–alumina–silica system at 1873 K [11].

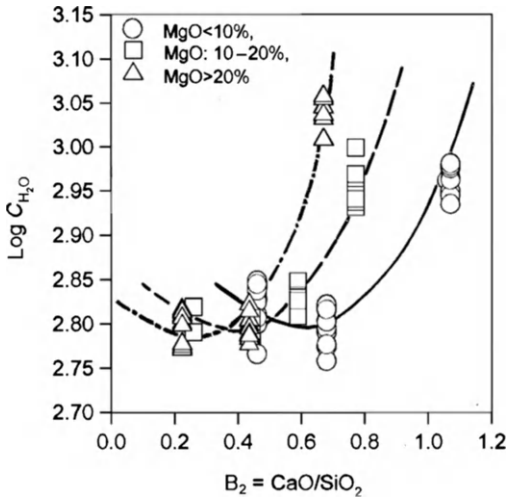


Figure 3.1.12 Dependence of water vapor capacity on CaO/SiO_2 ratio and MgO concentration of synthetic slags at 1723–1873 K derived [19] from results of Zuliani *et al.* [24] and Sosinsky *et al.* [25].

vapor dissolution in slags by Chipman *et al.* at M.I.T. [20], Imai *et al.* at Kawasaki Steel Corporation [21], and T. Fuwa *et al.* at Tohoku University [22,23].

In Figure 3.1.12, the water vapor capacity of molten slags is plotted as a function of the basicity ratio CaO/SiO_2 using the experimental data of Zuliani *et al.* [24] and Sosinsky *et al.* [25]. As shown in this figure, in a similar manner to that described for sulfur, different

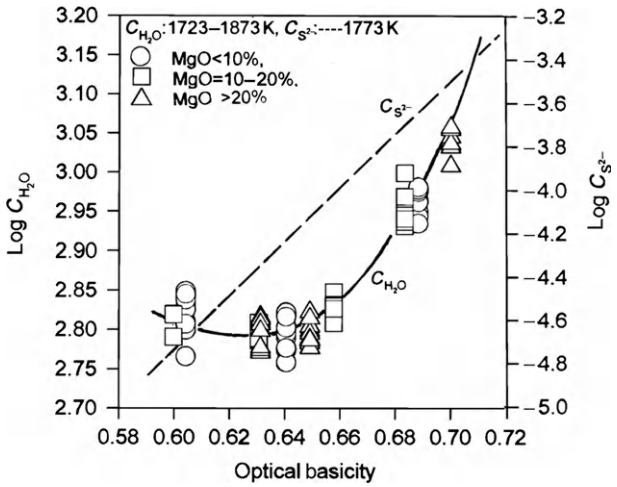


Figure 3.1.13 Dependence of water vapor capacity of molten CaO–MgO–SiO_2 slags on optical basicity at 1723–1873 K derived [19] from results of Zuliani *et al.* [24] and Sosinsky *et al.* [25].

lines are obtained for different slag systems. In this case, however, the relationships are curvilinear rather than linear due to the amphoteric behavior of water vapor in molten slags. In acidic slags, the water vapor content actually decreases with increasing basicity, while with basic slags the reverse is true. As shown in Figure 3.1.12, for basic slags with a fixed CaO/SiO_2 ratio, slag water vapor capacity increases with increasing MgO concentration, while the reverse is true for acidic slags [19].

When the water vapor capacity is plotted against optical basicity, Figure 3.1.13, the curvilinear relationship is again observed; however, all of the data for different slag systems can be represented by a single line. From a quantitative evaluation of water vapor data for a number of different slag systems at temperatures around 1723–1873 K, the following correlation was established [19]:

$$\log C_{H_2O} = +41.92 - 164.92\Lambda + 226.42\Lambda^2 - 100.31\Lambda^3 \quad \left(r^2 = 0.87\right) \qquad (3.1.10)$$

In acidic slags, $\Lambda < 0.6$, water vapor reacts as a basic oxide and the water vapor capacity of the slags decreases with increasing slag basicity. In highly basic slags, $\Lambda > 0.65$, water vapor reacts as an acidic oxide and water vapor capacity increases with increasing slag basicity. In slags with $\Lambda = 0.6$–0.65, the water vapor capacity remains essentially constant with increasing slag basicity, due to a mixture of basic and acidic reactions. For comparison purposes, the relationship between slag sulfide capacity and optical basicity at 1773 K, Equation (3.1.9), is shown in Figure 3.1.13 by a broken line [19].

Figure 3.1.14 shows iso-water vapor capacity lines derived from optical basicity calculations for the lime–alumina–silica system at 1873 K [12]. In moving away from the

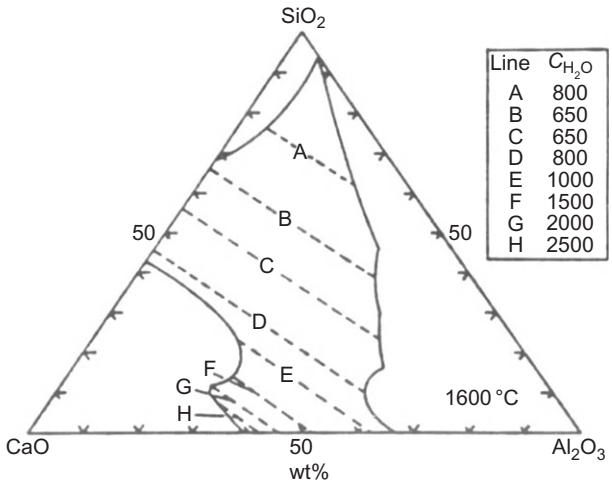


Figure 3.1.14 Iso-water vapor capacity lines derived from optical basicity calculations for liquid slags in the lime–alumina–silica system at 1873 K [12].

silica-rich region of the diagram, the water vapor capacity initially decreases from line A to line B, passes through a minimum to line C and then increases to line H as the system becomes progressively more basic. This is again a reflection of the amphoteric behavior of water vapor in molten slags. A binary slag consisting of 50% lime and 50% silica has a water vapor capacity of approximately 730. On the other hand, a binary slag consisting of 50% lime and 50% alumina has a water vapor capacity of approximately 1500.

Thus, a lime–alumina slag is more likely to absorb moisture from the atmosphere and transfer hydrogen into the steel than a lime–silica slag. In order to minimize hydrogen pickup by the steel, a lime–silica slag would be more effective than a lime–alumina slag. Unfortunately, these conditions are the opposite of those that would be most appropriate for good sulfur removal. Thus, for those grades of steel which require desulfurization and where hydrogen pickup could be a problem, an appropriate slag composition should be selected from within the ternary system, taking these conflicting considerations into account. On the other hand, to minimize sulfur loss from the metal, for example, during the production of high-sulfur machining grades, a slag with a lower optical basicity value would be appropriate which would be also beneficial in minimizing hydrogen absorption by the steel.

3.1.3. PRESERVATION OF STEEL QUALITY

During transfer from furnace to ladle, ladle to tundish, and tundish to mold, oxygen, nitrogen, and hydrogen absorbed from entrained moist air can be destroyers of quality. In light of current trends to produce steel with lower residual concentrations

of oxygen and sulfur, it is important to note that, as the concentrations of these two surface-active solutes decrease, the rate at which the steel picks up nitrogen and hydrogen increases.

An important consideration during steel transfer operations is the formation of vortices in the furnace, ladle, tundish, or mold by means of which molten slag can be drawn from one vessel into the next. As a general principle, although there are exceptions, furnace slag is inappropriate in the ladle, ladle slag is inappropriate in the tundish, tundish slag is inappropriate in the mold, and mold slag is always inappropriate in the final product. Slag, which is a refining agent in one reactor, if transferred inadvertently to the next reactor, becomes a contaminator. In this context, vortex formation which draws slag from one vessel to another can be a serious destroyer of quality.

3.1.3.1. Furnace to Ladle Transfer

During furnace tapping, an uncontrolled and variable amount of air is entrained by the tapping steam and carried into the ladle. This air entrainment has a direct bearing on fluid flow patterns in the ladle which in turn determine whether an alloy additive dissolves in the steel or is carried up to the surface to be lost by oxidation due to contact with the atmosphere. For this reason, the timing, location, and method of deoxidizer and other alloy additions all influence alloy recovery and final steel quality. As mentioned previously, in addition to reoxidation, it is also possible for the steel to pick up nitrogen and hydrogen from a humid atmosphere during this transfer operation.

Improvements in furnace tapping operations to minimize slag carryover into the ladle and to promote the formation of a more compact tapping stream include the use of slide-gate valves and bottom tapping systems. With more compact streams, it is easier to protect the steel from contamination with air, by gas shrouding the stream with a protective atmosphere.

When elements with a high affinity for oxygen and sulfur such as calcium or magnesium are added to the ladle, the effectiveness of the added element is strongly influenced by the quantity and composition of the slag carried over from the furnace. This furnace slag can constitute a major source of oxygen which then transfers to the steel during ladle processing. This transfer of oxygen from slag to metal is enhanced during any gas stirring operation which brings fresh metal into contact with the slag. In addition, as the steel is poured from the ladle, the interaction which takes place between the descending slag layer and the refractory ladle walls can produce a reaction product or glaze, which serves as a reservoir for oxygen and perhaps sulfur. These elements can then transfer into the next batch of steel during ladle processing and have an adverse effect on steel quality. If there is substantial carryover of slag from the furnace, the iron oxide, and manganese oxide content of which is likely to be high, then a reducing agent may need to be added in order to minimize the use of expensive deoxidizing agent or loss of alloying elements which may be added to the steel. Calcium carbide can be used as a reducing agent for

the slag phase. If phosphorus oxide is present in the slag carried over from the steelmaking vessel, then during slag reduction or steel deoxidation, phosphorus may revert to the steel from the slag phase, and again this is a destroyer of quality.

With respect to slag compositions for ladle desulfurizing treatments, a highly basic slag is generally used. While such slags have a high capacity for absorbing sulfur, they also have a strong ability to transfer hydrogen from moisture-containing atmospheres into molten steel at a faster rate than would be the case with a more acidic slag. It has also been found that steel with a very low inclusion content is less able to tolerate hydrogen. For these reasons, special processing steps such as inert gas shrouding, vacuum treatment, stream protection, and controlled cooling may be required if problems attributable to hydrogen are to be avoided.

3.1.3.2. Ladle to Tundish Transfer

It is important to recognize that the tundish, like the ladle, is a metallurgical reactor involving interactions between molten steel, slag, and refractory phases as well as the atmosphere. It is now accepted that the tundish is not only a distributing vessel but also a continuous reactor. This is particularly significant because the tundish links together the ladle that is a batch reactor with the casting molds, which are themselves continuous reactors. A major challenge for the steelmaker is to ensure that the tundish is in fact a continuous refiner and not a continuous contaminator [26]. In this context, tundish slags play an important role. There are three requirements for a good tundish flux:

- Thermal insulation of the molten steel.
- Protection of the steel from reaction with the atmosphere.
- Absorption of nonmetallic inclusions from the molten steel.

Thermal insulation is best obtained with a solid powder layer. On the other hand, prevention of reoxidation, nitrogen, and hydrogen absorption from the atmosphere by the molten steel and absorption of nonmetallic inclusions from the steel are all best achieved by the presence of a liquid layer. The viscosity of the tundish flux is also important for the production of clean steel. If the viscosity is too high, this will limit the ability of the flux to absorb inclusions. If the viscosity is too low, then flux may be drawn down into the mold, particularly during ladle transfer operations, when conditions are unstable. Tundish slags can now be designed using the concept of optical basicity to obtain a flux which has the required characteristics in terms of chemical properties as well as viscosity in order to ensure that the tundish will function as a refining vessel and not a contaminator [12].

Methods of preventing reoxidation during metal transfer between ladle and tundish and tundish and mold by extended refractory nozzles and/or gas-shrouding devices are now well-established practices. However, significant contamination can still occur during ladle-change operations, when exposure of steel to air for even a few seconds can lead to the casting of inferior steel over the next several minutes. An increase in the nitrogen

content of the steel by a few ppm is a valid indicator that reoxidation has occurred. Since the rate of oxygen dissolution is about 200 times faster than that of nitrogen [5], analysis of samples for oxygen can yield values of several hundred ppm. This represents massive reoxidation and the generation of very large inclusions. Much of this reoxidation material will separate in the tundish and collect in the tundish flux. In so doing, the iron oxide and the manganese oxide contents of the tundish flux may be markedly increased.

The influence of thermal effects on liquid steel flow in tundishes during a ladle-change operation and during steady-state conditions have been reported by Lowry and Sahai based on results from an elegant one-third scale water modeling study together with in-plant tracer measurements on the six-strand bloom caster at the Kansas City Works of Armco Inc. [27]. From residence time distribution diagrams pertaining to the actual steel casting tundish, it was concluded that the steel flow following a ladle change is radically different from that under almost isothermal, steady-state conditions during the latter half of a ladle pour. During a ladle change, the new steel entering the tundish is at a higher temperature than the steel already present in the tundish. The new higher temperature steel actually reaches the nozzles at the end of the tundish before it reaches the nozzles closest to the incoming ladle stream. This behavior is the reverse of that observed under steady-state conditions. Steady-state flow is reestablished when the new steel displaces the previous steel. This requires almost 2.5 times the mean residence time for the tundish. This time period could amount to 25% or more of the ladle casting time depending on the tundish capacity and casting rate. This is a significant portion of the casting time during which the metal flow is in a reverse mode. These effects will clearly have a profound influence on factors such as alloy additions, inclusion flotation, and intergrade mixing and should be included in any consideration and analysis of tundish design for improvement in steel quality.

During the casting operation, ladle slag can be drawn by vortex formation into the tundish as the metal level in the ladle decreases. Again this is an example where slag which is a refining agent in one vessel becomes a contaminating agent in the next. Some of this entrained slag may enter the tundish flux and consequently alter its behavior, while other portions may be carried over into the mold and end up adversely affecting the performance of the mold flux or generating defects in the final product. From flotation considerations, there may also be a higher content of inclusions in the last portion of steel to leave the ladle. In a typical ladle-change operation, the total oxygen content in the tundish can change quite drastically, both at the entrance to the tundish close to the incoming ladle stream and at the exit above the mold. In addition, the weight of metal in a tundish under stable operating conditions may drop by about half during the ladle-change operation, and this in turn can have an adverse effect on the quality of steel entering the casting molds. It is significant that while the ladle change may require approximately 2 min, the effect on the quality of the steel leaving the tundish could extend for over 15 min [28].

3.1.3.3. Tundish to Mold Transfer

In recent years, there has been increasing awareness of the critical importance of "meniscus control" because of the direct correlation that has been established between fluid flow behavior at the metal meniscus in the mold and the surface quality of the cast products [29,30]. When the metal delivery system involves the use of submerged entry refractory nozzles, the behavior of fluid flow in the mold as well as at the meniscus is extremely important. The design of the nozzle as well as the depth of submergence has a direct influence on fluid flow within the casting mold, behavior at the meniscus, vortex formation, and the distribution and location of inclusions in the final product.

In order to minimize nozzle blockage and enhance the flotation of nonmetallic inclusions, argon gas is sometimes injected down the submerged entry nozzle. This can have a pronounced effect on fluid flow behavior. If argon injection is excessive, mold slag can be drawn into the molten steel and end up as defects in the product. Even in the absence of argon injection, if the submerged entry nozzle has not been properly fired and is porous, or if cracks are present in the nozzle wall caused by damage during handling, or if cracks form during use, air can be drawn into the nozzle, the oxygen from which will cause reoxidation while the nitrogen will behave essentially like argon and cause considerable disturbance of the mold powder at the meniscus. In addition, if the formation of reoxidation material is excessive, the composition of the mold flux can change and this can adversely affect subsequent performance.

The behavior of synthetic fluxes in the casting mold is a critical parameter for the production of quality steel. This is the last slag with which the molten steel has contact before solidification. All of the previous work which has been conducted in the furnace, ladle, and tundish to generate quality steel can be destroyed in the casting mold. For this reason, the mold can be considered as the "heart" of quality and the mold slag must be designed to perform a range of functions which is considerably greater than that required of any of the previous slags in the furnace, ladle, or tundish. These functions include prevention of reoxidation, provision of thermal insulation, availability as a flux to dissolve impurities, performance as a lubricant, and possession of good heat transfer characteristics to enhance solidification. Since the flux forms a glass during the casting process, this glass can also influence heat transfer in the spray chambers. The interaction of the mold flux with refractory nozzles and the behavior with respect to the absorption of hydrogen from the atmosphere and subsequent pickup of hydrogen by the steel are also important considerations when designing the most appropriate composition of the flux for a particular application.

A comparison of water-simulated tundish streams with open steel streams is shown in Figure 3.1.15 [31].

In the case of billet molds with small cross section, the use of submerged entry nozzles may not be possible. Reoxidation of open streams by direct contact with air will result

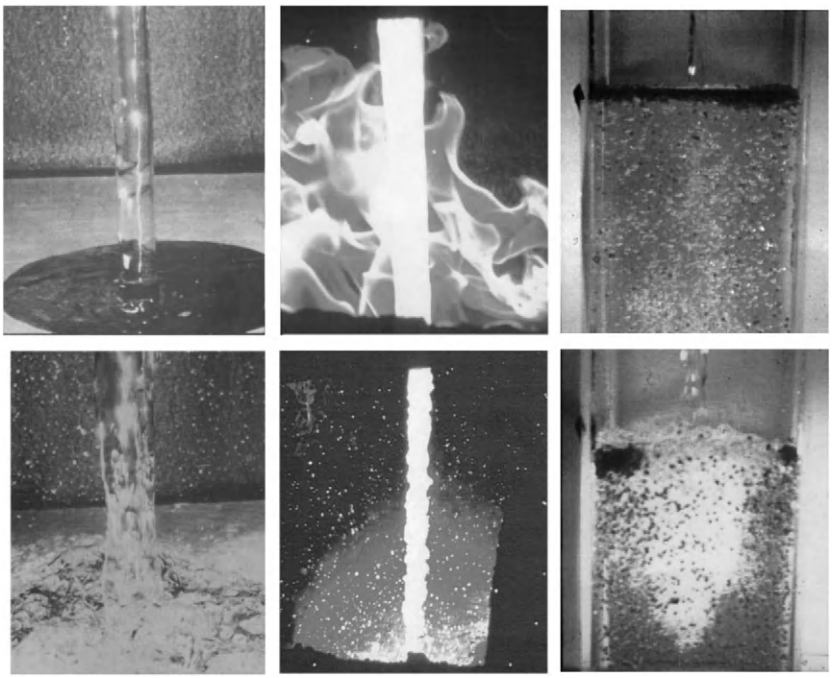


Figure 3.1.15 Smooth tundish streams with little air entrainment, quiescent conditions at the meniscus, no splashing and deep penetration in the mold pool, compared with rough tundish streams, massive air entrainment, turbulent conditions at the meniscus, considerable splashing, droplet formation and shallow penetration within the mold pool [31].

in the formation of oxide slag within the mold. If this oxide material is drawn down into the solidifying steel, it can produce large centerline defects. If it is entrapped as a solid crust between the solidifying steel shell and the mold wall, then large surface slag defects can be generated [30]. While open streams can be protected by gas-shrouding systems, differences in stream character between strands or even instability at different times on the same strand can adversely affect meniscus behavior, fluid flow patterns, surface quality, pinholes, and the location of inclusions in the final product.

With multistrand billet casting and a central ladle stream, smooth streams are usually found at the ends of the tundish. Such streams entrain very little air and the steel meniscus is quiescent with a slow motion from the outside of the mold toward the stream. In this case, mold scum will float on the surface but could be driven deep within the steel pool by the incoming tundish stream. Rough streams, such as those issuing from tundish nozzles located nearest to the ladle stream, have not only a higher surface-to-volume ratio than a smooth stream but will also entrain more air causing increased turbulence in the mold and excessive splashing at the meniscus. Within a turbulent mold pool, new steel is continuously brought to the surface where further contact with the air can occur. Turbulent

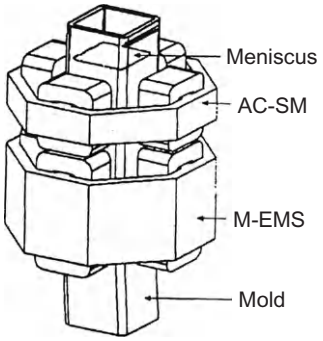


Figure 3.1.16 Dual-coil electromagnetic stirring system for billet casting [32].

pools give little opportunity for proper separation of reoxidation products. These oxides, in the form of mold scum, are thrown to the outside of the mold where they can be entrapped in the freezing interface at the surface of the billet and give rise to surface slag defects [4].

Based on advances in the understanding of electromagnetic force fields and their effects on liquid metal flow, together with parallel developments in mathematical modeling and induction power units, novel systems for steel flow control in the mold have been developed. These technologies are applicable for open stream pouring between the tundish and mold and also in cases where submerged entry nozzles are used to protect the steel from reoxidation. One example of an in-mold electromagnetic stirring system developed by Beitelman and Limoges incorporates two sets of stirring coils with independent control of each of the electromagnetic fields [32]. The stirring coil in the lower region of the mold (M-EMS) provides the main stirring action while the coil in the meniscus region has a more localized effect and is termed the auxiliary coil-stirring modifier (AC-SM) (Figure 3.1.16).

Depending on the casting requirements, the stirring intensity at the meniscus can be enhanced, diminished, or essentially eliminated by adjusting the current input to the AC-SM and controlling the direction of the magnetic field relative to that of the M-EMS [32]. Since this system provides independent control of liquid steel flow at the meniscus and within the lower region of the mold, electromagnetic stirring conditions can be optimized to achieve maximum benefits in each of these locations. Operating experience has confirmed that the dual-coil system has major beneficial implications with respect to the quality of continuously cast steel as well as productivity [33].

Other EMS systems have been implemented to achieve similar objectives. It has been established that appropriate electromagnetic stirring in the mold promotes good surface quality, reduces the incidence of pinholes, decreases segregation of elements such as carbon, sulfur, and phosphorus, and diminishes crack formation and center line defects. In addition, when over-stirring at the meniscus is prevented, mold powder entrapment

and accelerated wear of the submerged entry nozzle can be avoided [34]. As might be expected, the actual position of EMS within the copper mold will significantly affect the quality of the cast product. The optimum location will depend on several factors including cross section and length of the copper mold, immersion depth of the submerged entry nozzle (if used), meniscus position, type of steel being cast, and associated measuring sensors. Zhang *et al.* have made use of computer simulations in order to study the effects of stirring power, frequency, and location of EMS within the mold on steel quality [34]. The optimum conditions generated during the model studies were then validated with plant trials, and it was confirmed from sulfur prints and inclusion analysis that an optimized location for EMS will facilitate meniscus control, promote removal of nonmetallic inclusions from the molten steel, and enhance quality of the final product.

3.1.4. EVALUATION OF STEEL QUALITY

In the quest for steel quality, it is imperative that detrimental variations during processing be prevented. In addition to traditional sampling methods, it is also important that sensor technologies be developed that will permit monitoring of the metallurgical operations so that the occurrence of any detrimental variations due to perturbations or imperfections within the processing system can be detected and evaluated at an early stage.

3.1.4.1. Ferrous Oxide in Molten Slag

To a large extent, oxygen control in steelmaking is affected by the composition and properties of the slag phase. Without oxygen control, the behavior of the other elements cannot be managed. Steelmaking slag systems involve at least seven important components: CaO, MgO, MnO, FeO, SiO_2, Al_2O_3, and P_2O_5, and often a number of others such as CaF_2, Na_2O, TiO_2, and Cr_2O_3. One of the greatest obstacles to the application of physical chemistry principles to the elucidation of slag–metal and slag–gas reactions is a lack of knowledge of activities of the reacting species. Since iron oxide in slag participates in numerous reactions between metal, slag, and gas phases and important steelmaking reactions such as desulfurization and dephosphorization are related to the ferrous oxide activity, the evaluation of the activity of this component is particularly important. For example, consider the reoxidation of aluminum in the steel by ferrous oxide in molten slags:

$$2[\mathrm{Al}] + 3(\mathrm{FeO}) = \mathrm{Al_2O_{3(s)}} + 3\mathrm{Fe_{(l)}} \tag{3.1.11}$$

where [i] and (i) indicate components dissolved in molten steel and slag, respectively. Reaction (3.1.11) will proceed to the right-hand side with an increase in FeO activity and a consequent loss of aluminum from the steel. Manganese oxide can also reoxidize aluminum. Hara *et al.* have shown that the total oxygen concentration in steel after

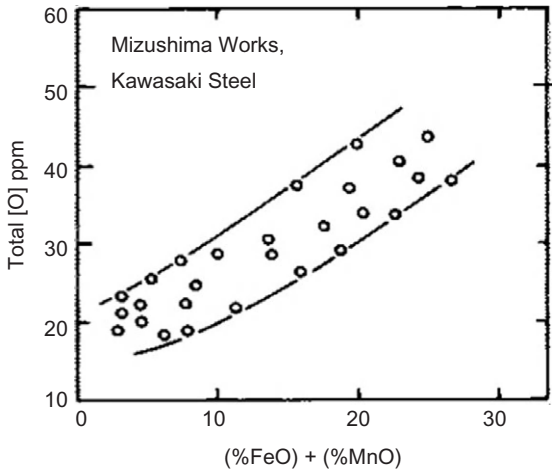


Figure 3.1.17 Relationship between total oxygen content in steel after degassing and slag chemistry [35].

RH degassing increased with an increase in (%FeO) + (%MnO) in the slag phase (Figure 3.1.17) [35].

Thus, it is important to lower the FeO and MnO contents in molten slag, especially in secondary refining vessels, to avoid the oxidation of aluminum. To achieve this objective, aluminum or calcium carbide can be added to the slag phase. Generally, control strategies for such practice are based on samples taken from the molten slag during ladle treatment. However, chemical analysis for FeO and MnO in slags usually requires at least 20 min, while ladle treatment is generally completed within 15–20 min. Hence, a knowledge of (%T.Fe) + (%MnO) based on chemical analysis cannot really assist plant operators to control the molten slag of a particular heat during actual production.

In view of the industrial significance of ferrous oxide activity, numerous experimental determinations have been conducted by many laboratories during the past five decades. Nevertheless, our knowledge of the activity of FeO in multicomponent industrial slags is still far from satisfactory. The conventional experimental technique for determination of ferrous oxide activity consists of equilibrating molten slags with liquid iron. Chemical analysis for oxygen made on samples taken from liquid iron yields values of ferrous oxide activities. Alternatively, molten slags contained in an iron crucible are brought into equilibrium under a stream of $CO–CO_2$ or $H_2–H_2O$. These techniques, however, require a relatively complex experimental set-up and long duration.

3.1.4.1.1 Activity Determinator for Ferrous Oxide

To facilitate the evaluation of ferrous oxide activities, Iwase and his co-workers have developed a "shop floor" activity determinator based on the principles of zirconia sensors [36]. This equipment makes use of samples taken from the slag phase. However,

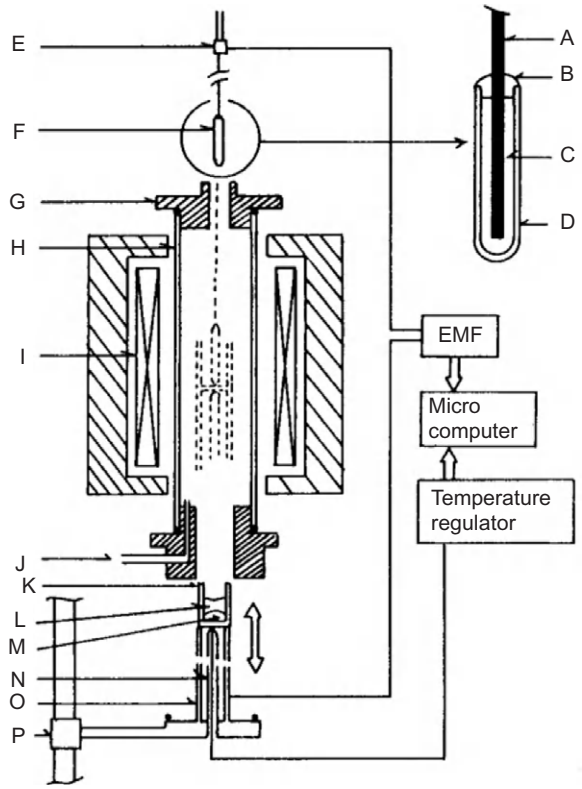


Figure 3.1.18 Schematic diagram of automatic activity determinator. A, Mo rod; B, zirconia cement; C, $Mo + MoO_2$ reference electrode; D, reference electrode; E, elevator mechanism; F, zirconia cell; G, water-cooled brass flange; H, transparent silica tube; I, tungsten filament; J, Ar inlet; K, iron crucible; L, slag sample; M, silver; N, Pt-PtRh 13 thermocouple; O, stainless steel pedestal; P, elevator mechanism [37].

knowledge of sample weight is not required and activity measurements can be completed within 5 min. This electrochemical technique based on magnesia-stabilized zirconia permits rapid determination of ferrous oxide activity within homogeneous and heterogeneous slag systems [37–40].

This research led to the manufacture of an analytical instrument for the determination of FeO activities [36,40]. A schematic diagram of the automatic activity determinator is shown in Figure 3.1.18. For operating this system, a solid-state sensor F is attached to the elevator mechanism E and an iron crucible K is placed on the steel pedestal O. The electrical contact to the outer electrode of the zirconia cell is made via this pedestal. Pure silver M is premelted within the iron crucible. A sample of slag L, 1–3 g, is placed in the iron crucible. The iron crucible is moved upward, via an elevator mechanism P, into a transparent silica reaction tube H. The furnace is subsequently heated to a temperature of

1750 K under a stream of argon within 2.5 min in accordance with a computer program. The electrochemical cell is lowered until it contacts both the molten silver and the slag. Open-circuit cell voltages generated are monitored on the LCD of the microcomputer. The cell potential is then converted to the FeO activity and displayed on the LCD. In this way, a single activity measurement is completed within 5 min. This analytical instrument is manufactured commercially and used by several steel companies in different parts of the world. The activity determinator has permitted new control strategies to be developed for the behavior of phosphorus and sulfur in liquid iron and for the reduction in steelmaking slag volume.

3.1.4.1.2 Application of Activity Determinator for Desulfurization Control

An example of the industrial application of the activity determinator by Hamm *et al.* [41] relates to control of the desulfurization reaction, which can be expressed as:

$$(\mathrm{CaO}) + [\mathrm{S}] + \mathrm{Fe} = (\mathrm{CaS}) + (\mathrm{FeO}) \tag{3.1.12}$$

Equation (3.1.12) implies that if the activity of CaO (i.e., the basicity of the slag) is kept constant, a logarithmic plot of the sulfur partition ratio against FeO activity should be a straight line with a slope of -1. The relationship obtained by Hamm *et al.* is shown in Figure 3.1.19. Although the slope is different from the theoretical value, there is a good correlation between the two parameters indicating that the sulfur partition ratio can be monitored and therefore controlled through FeO activity measurements.

3.1.4.1.3 Application of Activity Determinator for Cleanliness Control

Figure 3.1.20 shows the relationship between a_{FeO} determined by the activity determinator and (%T.Fe) + (%MnO) obtained by chemical analysis for industrial slags taken

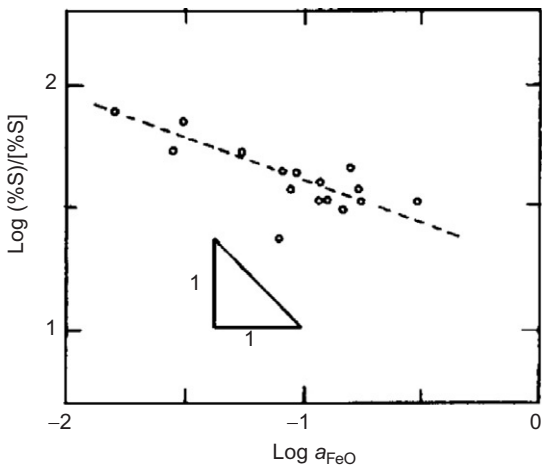


Figure 3.1.19 Relationship between sulfur partition ratio and FeO activity [41].

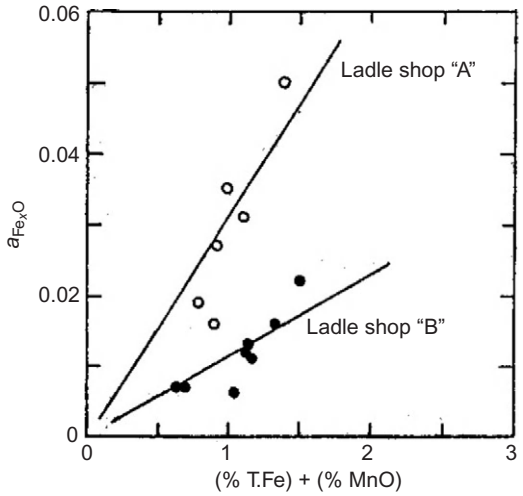


Figure 3.1.20 Relationship between FeO determined by the activity sensor and (%T.Fe) + (%MnO) [41].

from different ladle steelmaking operations [41]. As shown in this figure, the empirical parameter, (%T.Fe) + (%MnO), is proportional to the FeO activities. However, FeO activities of slags from one melt-shop are different from those at another, even although the empirical parameter, (%T.Fe) + (MnO), is the same.

From a thermochemical point of view, this behavior is quite understandable if differences in slag basicity are taken into account. In other words, it can be stated that the empirical parameter is not an appropriate model for close control of the FeO activity. Oh-nuki *et al.* have reported that improved slag reduction together with increased steel cleanliness was achieved at the ladle furnace with the aid of measurements obtained by the FeO activity determinator [42].

3.1.4.1.4 Application of Activity Determinator for Manganese Control

Manganese control during steelmaking is governed by the equilibrium reaction:

$$[\mathrm{Mn}] + (\mathrm{FeO}) = (\mathrm{MnO}) + \mathrm{Fe} \tag{3.1.13}$$

The partition ratio is expressed as follows:

$$\log\{(\%\mathrm{Mn})/[\%\mathrm{Mn}]\} = \log a_{\mathrm{FeO}} + (\mathrm{constant}) \tag{3.1.14}$$

where (%Mn) and [%Mn] are the weight pct. concentrations of manganese in the slag and metal phases, respectively. According to Equation (3.1.14), a logarithmic plot between (%Mn)/[%Mn] and the a_{FeO} should yield a straight line with a slope of unity. Hamm *et al.* have shown such a relationship based on actual data from practical steelmaking operations (Figure 3.1.21) [41]. These authors also reported that a_{FeO} measurements can be used to

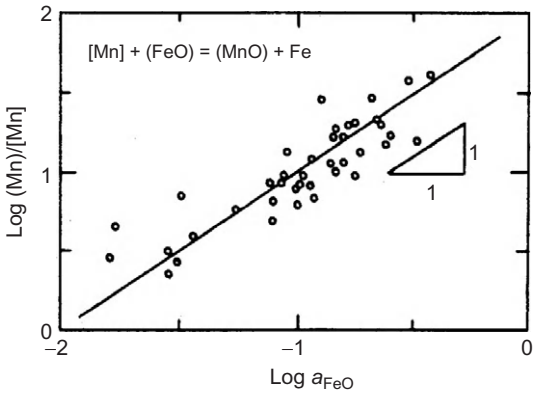


Figure 3.1.21 Plant data showing relationship between manganese partition ratio and FeO activity [41].

calculate alloying efficiency with a higher degree of precision, thus resulting in significant cost reduction and more accurate heat chemistries.

3.1.4.2. Continuous Monitoring of Metallurgical Processes

One of the critical factors determining the quality of cast products, in addition to chemical composition, homogeneity, and appropriate microstructure, is the cleanliness of the liquid metal. Considerable progress has been made in the development of online sensors for the evaluation of the inclusion content of molten metals prior to solidification. A comprehensive review of *in situ* sensors for the evaluation of liquid metal quality has been published by Guthrie and Isac [43].

3.1.4.2.1 Online Sensors for Evaluation of Liquid Metal Cleanliness

In the early 1980s, Guthrie and Doutre at McGill University in collaboration with industrial partners pioneered the development of the Liquid Metal Cleanliness Analyser system [44]. This approach is based on passing an electrical current through a sensing zone within which passes the liquid metal to be tested. Interaction between the liquid metal and the imposed field provides information on the number and size distribution of inclusions. Following a number of developments, this continuous sensing technology has found extensive application within the aluminum industry, and more recently, an adaptation of the technology has been evaluated as an online inclusion determination system within liquid steel [45].

Another approach that has been developed by Mountford and co-workers at the University of Toronto makes use of an ultrasonic sensor [46]. Sound waves essentially render opaque liquids transparent and can therefore be used to make assessments of liquid quality. The principles used in the ultrasonic evaluation of liquid metals are similar to those used in standard NDT ultrasonic flaw detection. One practical difference is that

it is necessary to use guide rods to introduce the sound pulses into the liquid metal and to receive the reflected signals, since the piezoelectric crystals must be prevented from overheating.

When high-frequency sound pulses are passed into the liquid, since the nonmetallic particles have different acoustic properties from the liquid, they reveal their presence by both attenuation and reflection of the sound pulse. The former is a measure of the general level of cleanliness, while the latter yields a size distribution of the particles large enough to produce reflections. It has been established empirically that the minimum particle size detectable in liquid metal is determined by the frequency and power level of the sound wave.

The electronics generate extremely high signal-to-noise ratios so that particles in the 10–15 μm range can be detected and counted using the relatively modest crystal frequency of 2.25 MHz. Detection and counting become easier as particle size increases so that particles in the 100–1000 μm range, which could cause very serious product defects, are easily detectable. Since the pulse rate used is 100 per second, the data ultimately presented on the monitor screen is the result of around 5000 measurements per minute, with the exact number depending on the cleanliness of the liquid metal. The technique has been used on a trial basis to evaluate the cleanliness of molten steel in pilot-scale ladles and to provide online and in real time, a comparative rating of the cleanliness of liquid steel in the tundish during sequence casting. It has also been used in conjunction with pressure die-casting, the direct casting of billets or logs for extrusion, and in lost foam casting of nonferrous metals and alloys. The results clearly indicate that an ultrasonic sensor could form the basis of a liquid metal control system [47,48].

3.1.4.2.2 Continuous Nonintrusive Monitoring of Steelmaking Operations

In recent years, acoustic technology and vibration analysis to continuously monitor and control metallurgical processes have found increasing application. It has been established that the sound emitted during certain metallurgical operations reflects the corresponding operating conditions and thus the acoustic response may be used to monitor and control the process. Accelerometers have been used to detect the vibrations generated by gas–solid interactions within the blast furnace; in torpedo cars during hot metal treatment; within steelmaking furnaces during decarburization and slag foaming; and in ladles, tundishes and submerged nozzles during steel processing [49].

Pioneering studies conducted within the Hungarian steel industry demonstrated that it is possible to continuously monitor with the aid of a remote microphone, the rate of desulfurization of hot metal or molten steel during injection of appropriate reagents with a carried gas by measuring the change in sound caused by the bubbles (Figure 3.1.22) [50].

As the desulfurization reaction proceeds, the surface tension of the metal phase increases, and this is accompanied by a change in the sound emitted by the bubbles. It is also possible to continuously monitor the desulfurization process by measuring with an

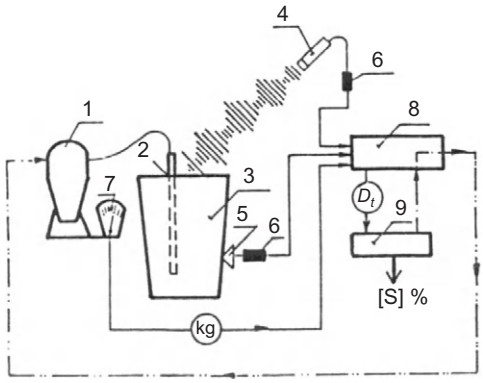


Figure 3.1.22 Continuous monitoring of desulfurization: 1—powder injector; 2—lance; 3—ladle; 4—microphone; 5—accelerometer; 6—preamplifier; 7—balance; 8—basic instrument; 9—computer [50].

accelerometer the vibrations caused by gas injection. An investigation of factors such as temperature and surface tension which influence the sound emitted by bubbles when gas is injected into a liquid has been conducted by Zhang [51] and more recently by Barati and co-workers [52].

The term "ladle metallurgy" is widely used to describe a number of processes which include steel reheating, deoxidation, alloying, desulfurization, modification of inclusions, and various techniques for promoting thermal and chemical uniformity within the steel by injecting argon or nitrogen through porous refractory units located within the base of the ladle or through submerged lances. However, the gas bubbling process is often highly variable and frequently excessive. This can lead to slag entrainment, steel reoxidation, and accelerated refractory attack. An early application of vibration monitoring to control argon stirring during ladle processing at the Hilton Works of Stelco Inc. has been described by Minion and co-workers [53].

During the treatment of steel in a ladle-arc-furnace, it is also important to minimize refractory attack caused by arc flare. This is achieved by ensuring that sufficient slag is present with appropriate foaming characteristics to enclose the arc discharge. A unique technology has been developed by Kemeny to control this process by monitoring the vibrations generated not only by the rising gas bubbles but also by the arc flare (Figure 3.1.23) [54].

These two quite separate processes, gas bubbling and arc flare, create pressure waves which can be independently monitored by measuring the vibrations on the outside steel shell of the ladle. Separate characteristic frequency ranges can be identified which relate to the rising gas bubbles and the arc flare. If there is insufficient slag present, this will be indicated by a high reading on the arc flare indicator. As synthetic flux is added to the ladle, the arc flare value will progressively decrease until an acceptable level of flux addition is achieved. Using this nonintrusive, continuous monitoring technology to

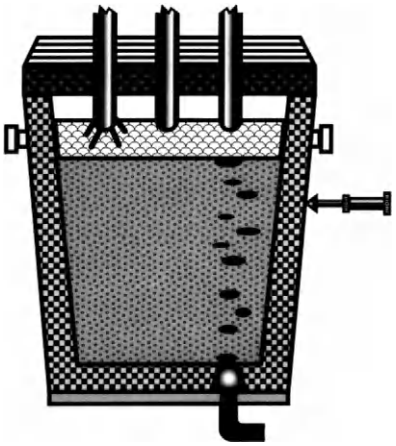


Figure 3.1.23 Vibration monitoring of gas rinsing and arc flare during ladle furnace processing [54].

independently control both the bubbling and arc heating processes, the following benefits have been achieved: consistent stirring practice; predictable alloy recovery; less aluminum fade; predictable desulfurization; clean steel with low total oxygen content; less nozzle clogging; less arc flare and slag overheating; improved refractory performance; and reduced argon consumption.

Several nonintrusive techniques have been employed to detect slag carryover from one vessel to another. These include electromagnetic devices, optical measurements, and vibration sensors. Because of the significant difference in density between metal and slag, there is a change in momentum transfer to a submerged refractory nozzle from molten steel when slag is entrained by the stream. This change in momentum is reflected by a change in vibrational movement of the submerged nozzle and also the tundish [55–57]. By continuously sensing these vibrational signals with accelerometers, it is possible to monitor the transfer operation and thus detect the onset of slag carryover. In some instances, it may be possible to detect the onset of vortex formation before slag has left the ladle or tundish, thus permitting the operator to implement corrective measures before slag carryover has actually taken place.

3.1.5. SUMMARY

There is good evidence from plant observations that quality achieved within one reactor can be lost during transfer to the next. In addition, short intermittent variations during the transfer process can have relatively long-time, adverse effects. All of these factors can influence the formation of inclusions and ultimately their location and distribution within the cast product. They can also affect surface quality and segregation. Improvements in our understanding of the importance of these phenomena have led

to developments in processing technologies that have had a pronounced beneficial effect on steel quality.

ACKNOWLEDGMENTS

To former students, research staff, and colleagues within academia and industry, sincere appreciation is expressed for their excellent contributions to so much of the work described in this chapter. Their efforts have advanced our understanding of the fundamental and applied aspects of steelmaking processes. For their friendship shared over so many years, we are deeply grateful.

REFERENCES

[1] H.M. Howe, The Metallurgy of Steel, The Scientific Publishing Company, New York, 1890.
[2] R.J. Brigham, Y.A. Lafreniere, Titanic specimens. Report No. 92-32 (TR). Metals Technology Laboratories, CANMET, Ottawa, Canada, 1992.
[3] J. Little, M. Van Oosten, A. McLean, Can. Met. Quart. 7 (1968) 235.
[4] W.J. Maddever, A. McLean, J.S. Luckett, G.E. Forward, Can. Met. Quart. 12 (1973) 79.
[5] L.A. Greenberg, A. McLean, Steelmaking Conf. Proc., ISS-AIME 63 (1980) 201.
[6] L.A. Greenberg, A. McLean, Trans. ISIJ 14 (1974) 395.
[7] J.D. Young, A. McLean, I.D. Sommerville, Proc. Vol. Japan-Canada Seminar on Secondary Steelmaking, CSIRA-ISIJ, Tokyo, 1985, pp. C4, 1.
[8] J.A. Duffy, M.D. Ingram, J. Am. Ceram. Soc. 93 (1971) 6448.
[9] J.A. Duffy, M.D. Ingram, I.D. Sommerville, J. Chem. Soc. Faraday Trans. 74 (6) (1978) 1410.
[10] I.D. Sommerville, Y.D. Yang, Aus. IMM Proc. 306 (1) (2001) 71.
[11] D.J. Sosinsky, I.D. Sommerville, Metall. Trans. B 17B (1986) 331.
[12] Y.D. Yang, Z.A. Daya, I.D. Sommerville, A. McLean, J. Iron Steel Res. Int. 5 (2) (1998) 7.
[13] Y.D. Yang, A. McLean, I.D. Sommerville, J.J. Poveromo, Iron Steelmaker 27 (10) (2000) 103.
[14] K. Karsrud, Scand. J. Metall. 13 (1984) 98.
[15] A. Bergman, Steel Res. 60 (9) (1989) 383.
[16] T. Nakamura, Y. Ueda, J.M. Toguri, Trans. JIM 50 (1986) 456.
[17] M.M. Nzotta, R. Nilsson, D. Sichen, S. Seetharaman, Ironmaking Steelmaking 24 (4) (1997) 300.
[18] M.M. Nzotta, D. Sichen, S. Seetharaman, ISIJ Int. 38 (11) (1998) 1170.
[19] E. Wei, Y.D. Yang, I.D. Sommerville, A. McLean, Proc. Vol. Ladle and Tundish Metallurgy, Met. Soc. C.I.M., Montreal, 2002, p. 27.
[20] J.H. Walsh, J. Chipman, T.B. King, N.J. Grant, J. Metals 8 (1956) 1574.
[21] M. Imai, H. Ooi, T. Emi, Tetsu-to-Hagane 48 (1962) 111, (in Japanese).
[22] T. Fukushima, Y. Iguchi, S. Ban-ya, T. Fuwa, Trans. ISIJ 6 (1966) 19.
[23] Y. Iguchi, T. Fuwa, Trans. ISIJ 10 (1970) 29.
[24] D.J. Zuliani, D.J. Sosinsky, A. McLean, Proc. Vol. Second Int. Symposium on Metallurgical Slags and Fluxes, AIME, 1984, p. 625.
[25] D.J. Sosinsky, M. Maeda, A. McLean, Metall. Trans. B 16B (1985) 61.
[26] A. McLean, in: Steelmaking Conference Proc., ISS-AIME, vol. 71, 1988, p. 2.
[27] M.I. Lowry, Y. Sahai, Iron Steelmaker 19 (3) (1992) 81.
[28] H. Kimura, Curr. Adv. Mater. Processes, ISIJ 4 (1991) 1198.
[29] J.K. Brimacombe, Metall. Mater. Trans. B 30B (1999) 553.
[30] I.V. Samarasekera, J.K. Brimacombe, S. Kumar, A. McLean, Proc. Vol. International Symposium on Near-Net-Shape Casting in the Mini Mills, Met. Soc. C.I.M., 1995, p. 135.
[31] A. McLean, Metall. Mater. Trans. B 37B (2006) 319.
[32] J. Limoges, L. Beitelman, Iron Steelmaker 24 (11) (1997) 49.
[33] L. Beitelman, in: Electric Furnace Conf. Proc., ISS-AIME, vol. 55, 1997, p. 333.
[34] G.-F. Zhang, Y.D. Yang, P. Wu, A. McLean, Proc. Vol. Iron & Steel Technology Conference, AIST-AIME, Indianapolis, IN, 2011, p. 1567.

[35] Y. Hara, S. Idogawa, T. Sakuraya, S. Hiwasa, H. Nishikawa, Curr. Adv. Mater. Processes, ISIJ 4 (1991) 1202.
[36] T. Ogura, R. Fujiwara, R. Mochizuki, K. Kawamoto, T. Oishi, M. Iwase, Metall. Trans. B 23B (1992) 459.
[37] M. Iwase, Y. Uchida, Y. Tomii, A. McLean, K. Katogi, High Temp. Mater. Processes 20 (3–4) (2001) 269.
[38] V. Espejo, M. Iwase, Metall. Mater. Trans. B 26B (1995) 257.
[39] H. Hoshino, M. Iwase, Metall. Mater. Trans. B 27B (1996) 595.
[40] M. Iwase, T. Ogura, R. Tsujino, Steel Res. 65 (1994) 90.
[41] A. Hamm, R. Cundiff, W. McCauley, G. Frigm, Steelmaking Conf. Proc., ISS-AIME 77 (1994) 153.
[42] K. Oh-nuki, T. Isono, K. Umezawa, Curr. Adv. Mater. Processes, ISIJ 6 (1) (1993) 220.
[43] R.I.L. Guthrie, M. Isac, High Temp. Mater. Processes 31 (4/5) (2012) 633.
[44] D. Doutre, R.I.L. Guthrie, U.S. Patent No. 4,555,662, Issued November 26, 1985.
[45] R.P. Stone, C.C. Liu, P.C. Glaws, Iron Steel Technol., AIST-AIME July (2009) 42.
[46] N.D.G. Mountford, I.D. Sommerville, A. Simionescu, C. Bai, Trans. Am. Foundrymen's Soc. 105 (1997) 939.
[47] I.D. Sommerville, N.D.G. Mountford, A. Simionescu, Proc. Vol. Alex McLean Symp., I.S.S.-A.I.M. E., 1998, p. 87.
[48] N.D.G. Mountford, P.H. Mountford, I.D. Sommerville, B. de Walle, Proc. Gerald Heffernan Inter. Symposium on Innovative Technologies for Steel and Other Materials, Met. Soc. C.I.M., 2001, p. 227.
[49] X.F. Zhang, A. McLean, I.D. Sommerville, Steelmaking Conf. Proc., ISS-AIME 74 (1991) 659.
[50] G. Pal, U.S. Patent No. 4,617,830, Issued October 21, 1986.
[51] X.F. Zhang, PhD Thesis, University of Toronto, 1991.
[52] H.L. Yu, L. Tafaghodi, M. Barati, Metall. Mater. Trans. B 42 (2011) 516.
[53] R.L. Minion, C.F. Leckie, K.J. Legeard, B.D. Richardson, Iron Steelmaker 25 (1998) 25.
[54] F.L. Kemeny, Proc. Vol., Alex McLean Symp., I.S.S.-A.I.M.E., 1998, p. 103.
[55] T. Itoh, et al., Trans. Iron Steel Inst. Jpn. 22 (1982) B90.
[56] F. Fitzgerald, Steel Research, British Steel Corp., June, 1983.
[57] M. Downey, et al., in: Proc. 6th International Conference on Refining Processes, Scaninject VI, Luleå, Sweden, 1992, p. 489.

CHAPTER 3.2

Refractory Corrosion During Steelmaking Operations

Lidong Teng
Division of Materials Process Science, Royal Institute of Technology, Stockholm, Sweden

3.2.1. INTRODUCTION

Heating and melting furnaces, smelting and refining furnaces, and the vessels used to carry hot metal and molten steel are all lined with refractories. Refractories have a high melting point and good heat-insulating properties. Their basic composition comprises chemically stable substances such as magnesia, alumina, and silica which do not easily react with steel slags or fluxes. When binders are mixed with these refractories, the mixture, when used as it is, is called an unshaped/monolithic refractory; when pressurized, compacted, and fired, it is called firebrick. Refractories for iron and steel production are used under very severe conditions, which include not only elevated temperatures but also thermal shock caused by abrupt temperature changes. Further, they must possess high-temperature strength and wear resistance to counter the large momentum of impinging and turbulent metal flow. Refractories must also have the chemical stability to withstand attack by hot metal, slag, and various fluxes.

The steel industry is the major customer of the refractories industry, consuming 50–80% of the total annual refractory production, depending upon the country. However for a variety of reasons, we have seen a continuing decline in the consumption of refractories by the steel industry. In 1970, the steel industry in Japan and the United States consumed 25–30 kg of refractory per ton of steel produced. Currently, this figure has dropped to about 10 kg of refractory per ton of steel produced. The steelmakers in other industrialized nations of the world have likewise achieved a similar decrease in refractory consumption. The continuing decrease in the refractory consumption results from two main reasons: (i) changes in blowing and casting processes, which are typified by the change from the open hearth furnace to the BOF, and the replacement of ingot casting by the continuous casting process; and (ii) the extension of the life of refractories by improvement in their quality as well as progress in application techniques.

Melt corrosion of refractories is a serious problem in iron and steelmaking processes because the corrosion shortens the service life of the refractory and therefore limits the service life of furnaces and vessels. Corrosion of refractories is a complex phenomenon

Treatise on Process Metallurgy, Volume 2
http://dx.doi.org/10.1016/B978-0-08-096984-8.00006-9
© 2014 Elsevier Ltd.
All rights reserved.

involving not only chemical wear but also physical/mechanical wear (such as erosion/abrasion) processes which may act synergistically. Corrosion of refractories by molten liquids involves reactant contact and product transport to allow it to proceed. Therefore, the refractories' composition, physical texture, and product transport nature of the bond phase (which is the first to be penetrated by liquid), and the characteristics of the melt and reaction products affect the rate of the reaction. Consequently, to understand the corrosion mechanisms, refractory microstructure (in particular, composition and texture of grain and bond phases, the linkage of grain to bond), internal or residual stress, melt properties (especially composition and viscosity as a function of temperature), and their wetting and interaction at high temperatures should be examined together. Almost all liquid metals do not wet ceramics while almost all slags and fluxes do, so local corrosion at the interfaces of the slag–gas and slag–metal is frequently a serious problem in iron and steelmaking processes. Tar-bonded ceramics are not wetted by silicate liquids, behavior which has led to their extensive use in iron- and steelmaking refractories.

In general, phases of dissimilar chemical nature tend to react at high temperature [1]. Therefore, to limit the extent of dissolution, the refractory and liquid in contact should be of similar nature. In other words, acid refractories tend to resist acid slags better than basic slags, and conversely, basic refractories tend to resist basic slags better than acid slags. SiO_2 (B_2O_3, P_2O_5, and V_2O_5) are acidic so that high silica refractories are used with acid liquids (some steelmaking, coal gasifiers, and glass melts). MgO and CaO are basic and so are used in contact with basic melts (e.g., basic oxygen steelmaking, cement production). Some refractories, e.g., $MgCr_2O_4$ and carbon, are neutral resisting acid and basic slags to a similar degree.

This review aims at giving the reader a basic knowledge of the corrosion mechanisms between solid refractories and liquid melts (slag or metal).

3.2.2. THEORETICAL CONSIDERATIONS

The corrosion of refractory may take place by either a dissolution process at the liquid–solid interface or by the penetration of liquid into solid grains or grain boundaries or pores, with a subsequent sloughing off of discrete pieces of solid. The theoretical models of penetration and dissolution are described in the following sections.

3.2.2.1. Penetration of Melt into Refractories

Capillaries, such as open pores and microcracks, are the main channels of initial slag penetration into a refractory. Then, penetration of slag into a porous refractory can be described with a model of liquid penetration into a vertical cylindrical capillary (referred to as capillary model) as shown in Figure 3.2.1 [2]. The rate (variation of penetration height with time) V of slag penetration into the capillary with the radius r can be expressed by Equation (3.2.1) which is derived from the equations given by Washburn [3].

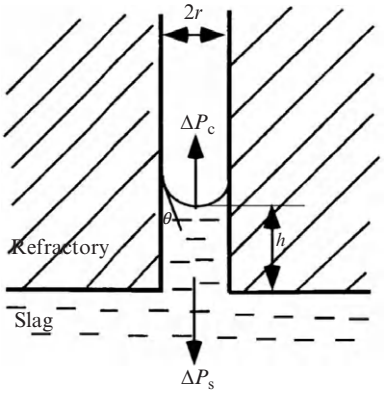


Figure 3.2.1 Schematic illustration of slag penetration model into a vertical capillary [2].

$$V = \frac{\mathrm{d}h}{\mathrm{d}t} = \frac{r^2 \Delta P}{8\mu h} \tag{3.2.1}$$

$$\Delta P = \Delta P_\mathrm{c} + \Delta P_\mathrm{s} \tag{3.2.2}$$

where h (m) is the penetration height from the slag surface, ΔP (N m^{-2}) is the pressure difference between the two ends of the capillary, ΔP_c (N m^{-2}) is the capillary pressure, ΔP_s (N m^{-2}) is the hydrostatic pressure caused by the penetrated slag, μ (Pa) is the viscosity of the penetrated slag in the refractory, and t (s) is the penetration time.

The capillary pressure ΔP_c is given by Equation (3.2.3).

$$\Delta P_\mathrm{c} = \frac{2\gamma \cos\theta}{r} \tag{3.2.3}$$

where σ (N m^{-1}) and θ (rad) are the surface tension and the contact angle of the slag with the refractory, respectively.

The hydrostatic pressure ΔP_s is given by Equation (3.2.4).

$$\Delta P_\mathrm{s} = -\rho g h \tag{3.2.4}$$

where ρ (kg m^{-3}) is the density of the penetrated slag and g is the gravitational acceleration.

Substituting Equations (3.2.2)–(3.2.4) into Equation (3.2.1), then

$$V = \frac{\mathrm{d}h}{\mathrm{d}t} = \frac{r^2}{8\mu h}\left(\frac{2\sigma \cos\theta}{r}\right) - \rho g h \tag{3.2.5}$$

The hydrostatic pressure ΔP_s may be neglected in comparison with ΔP_c because of $\Delta P_\mathrm{s} \ll \Delta P_\mathrm{c}$ in the initial stage of penetration. The physicochemical properties of the penetrated slag, such as σ, θ, ρ, μ, are assumed to remain constant in the initial penetration

stage. Then, the relationship between the penetration height and time are obtained as Equations (3.2.6) and (3.2.7) by integrating Equation (3.2.5) from $h=0$ at $t=0$ to h at t.

$$h = k_c t^{1/2} \tag{3.2.6}$$

$$k_c = \left(\frac{r\sigma\cos\theta}{2\mu}\right)^{1/2} \tag{3.2.7}$$

Equations (3.2.6) and (3.2.7) indicate that the rate of slag penetration increases with increasing pore radius and surface tension of the slag. The rate also increases with decreasing contact angle ($\theta < \pi/2$ rad) of the slag with the refractory and decreasing slag viscosity. Although not directly included in Equation (3.2.1), the temperature has a big effect on the penetration depth through its effect on μ. In the initial penetration stage, the penetration height is proportional to the square root of penetration time ($t^{1/2}$) [2]. Figures 3.2.2 and 3.2.3 show the influences of total Fe (T·Fe) concentration and temperature on the rate of slag penetration. Increasing T·Fe concentration of CaO–FeO–SiO_2 slag in the concentration range increases the surface tension and decreases the viscosity of the slag, which results in an increase in the slag penetration rate into MgO refractory. In general, increasing temperature lowers the slag viscosity and decreases the surface tension of the slag although the change of the surface tension of the slag is small. Thus, the rate of slag penetration increases with increasing temperature, as shown in Figure 3.2.3.

k_c in Equation (3.2.7) can be regarded as a theoretical penetration coefficient, while the constant in the equations for Figures 3.2.2 and 3.2.3 is the observed penetration coefficient (k_o). The practical penetration coefficient should be different from the theoretical penetration coefficient because the penetration model shown in Figure 3.2.1 differs from the actual penetration process in the following points [2]: (1) The actual penetration path

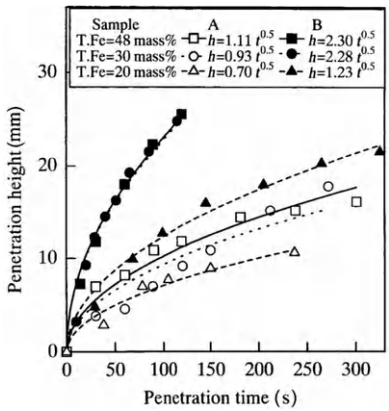


Figure 3.2.2 Relationship between penetration height and penetration time for the slag of C/S = 1.0, T·Fe = 20, 30, 48 mass% at 1593 K. The pore size in sample B is larger than that in sample A [2].

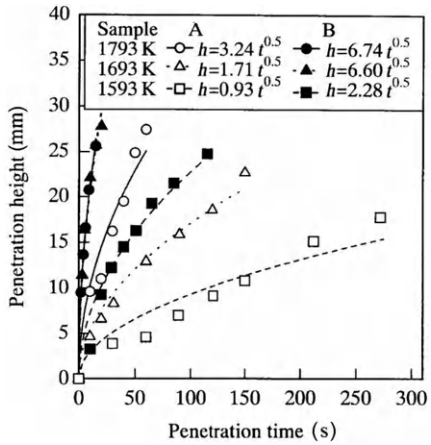


Figure 3.2.3 Relationship between penetration height and penetration time for the slag of C/S = 1.0, T·Fe = 30 mass% at 1593, 1693, and 1793 K [2].

in the sample is not straight but zigzag. The observed penetration height is therefore smaller than the length of the actual penetration. (2) The pores in the samples are not uniform. (3) The composition of the penetrated slag is different from that of the initial bulk slag due to reaction between the refractory and the penetrated slag, especially in the late stage of penetration.

In view of the poor wetting properties of refractories by molten steel, the penetration mechanism can usually be neglected in dealing with the metal–refractory reactions. However, if external pressure is applied to the metal–refractory system, the penetration of molten steel into porous refractory should be considered. Following Equation (3.2.1), Matsushita *et al.* developed a modified capillary model obtained by introducing labyrinth (or tortuosity) factor ξ into the capillary model [4]

$$V = \frac{\mathrm{d}h}{\mathrm{d}t} = \frac{r^2}{8\mu h}\left(\left(\Delta P_\mathrm{o} + \frac{2\sigma\cos\theta}{r}\right)\xi - \rho g h\right) \tag{3.2.8}$$

where ΔP_o (N m^{-2}) is the pressure applied to the liquid metal. By direct observation of molten steel penetration into porous refractory [4], it was reported that molten steel could not penetrate into the porous brick below the critical pressure. Above the critical pressure, the maximum height of molten steel penetration increases linearly with the external pressure. The value of ξ is expected to depend not only on the porosity of the porous refractory but also on the distribution of the pores and the properties of molten metal.

3.2.2.2. Dissolution of Refractories into Melt

Dissolution at refractory/melt interfaces is governed by three consecutive steps: (1) transport (or diffusion) of reactants from melt to the refractory/melt interface,

(2) chemical reaction (or solution) at the refractory/melt interface, and (3) transport of products from the refractory/melt interface to the melt.

In general, the process involving a series of steps is governed by the virtual maximum rate of the slowest step when that step is much slower than any other [5]. The rate-determining step is used to define the types of dissolution which are termed transport or diffusion controlled for step (1) or (3) and interface reaction controlled for step (2). When neither reaction nor diffusion is the rate-controlling factor, it is called "mixed controlled." In the iron and steelmaking process, the chemical reaction rates are usually very fast while the diffusion coefficients in the refractory–slag systems are low. Therefore, the dissolution rate of refractory in the slag is usually controlled by the transport process.

Suppose a situation where the rate of removal of reaction products by diffusion is slower than the rate of chemical reaction, a solute-rich boundary layer builds up, whose interface with the refractory is saturated with reaction products. The dissolution process is then controlled by the diffusion of reactants to, or the products away from, the interface through the boundary layer. The concentration distribution at the interface of a static melt and solid refractory is illustrated in Figure 3.2.4.

Here, the rate of corrosion can be expressed in terms of the Noyes–Nernst equation [6]:

$$\frac{\mathrm{d}n}{\mathrm{d}t} = -A \cdot D \frac{\mathrm{d}c}{\mathrm{d}x} = -A \cdot D \frac{C^{\mathrm{o}} - C^{\mathrm{s}}}{\delta^*} \tag{3.2.9}$$

where n is the mole of dissolved material, D ($\mathrm{m^2\,s^{-1}}$) is the diffusion coefficient for the slowest ion participating in the liquid, C^{o} the concentration in the bulk melt, C^{s} the saturation concentration of refractory in the melt (kmol $\mathrm{m^{-3}}$), A ($\mathrm{m^2}$) the area of interface, t (s) the time, and δ^* (m) the effective boundary thickness for diffusion, defined by the tangent to the concentration profile at the interface, as shown in Figure 3.2.4. δ^* is defined as

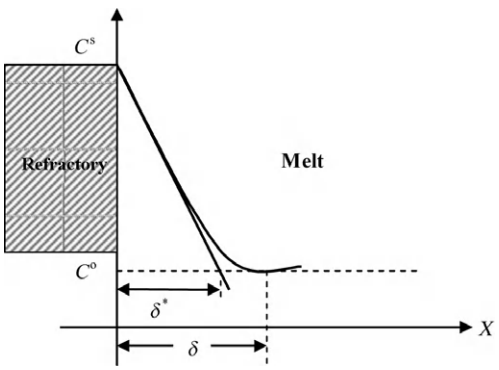


Figure 3.2.4 The concentration distribution at the interface of a static melt and solid refractory.

$$\delta^* = \frac{C^s - C^o}{\left(\frac{dc}{dx}\right)} \tag{3.2.10}$$

where dc/dx is the concentration gradient over the interface.

By including the interface reaction rate constant, $K(s^{-1})$, Berthoud derived the following equation [7]:

$$\frac{dn}{dt} = -A \cdot \frac{K}{1 + \left(\frac{K\delta^*}{D}\right)} \cdot (C^o - C^s) \tag{3.2.11}$$

It should be pointed out that, in some cases, the dissolution process also includes the transport in the solid interlayer which is precipitated between the melt and the refractory. Figure 3.2.5 illustrates the growth of solid interlayer between refractory and slag during dissolution. In this case, solid-state diffusion of the reaction species from the melt through the solid interlayer has to be considered. The interlayer will change its thickness so that the rate of transport through the interlayer and through the liquid boundary layer is the same at quasi-steady-state conditions (assuming rapid chemical reaction).

Stirring the melt or rotating the refractory sample will increase the rate of indirect dissolution (or effectively converts it to direct dissolution) by reducing the thickness of any liquid boundary layer (or breaking up any solid layer). In the case of a flat slab held vertically in the melt, the dissolution rate depends on the boundary layer thickness which is limited by such variables as the degree of convective flow caused by thermal and density

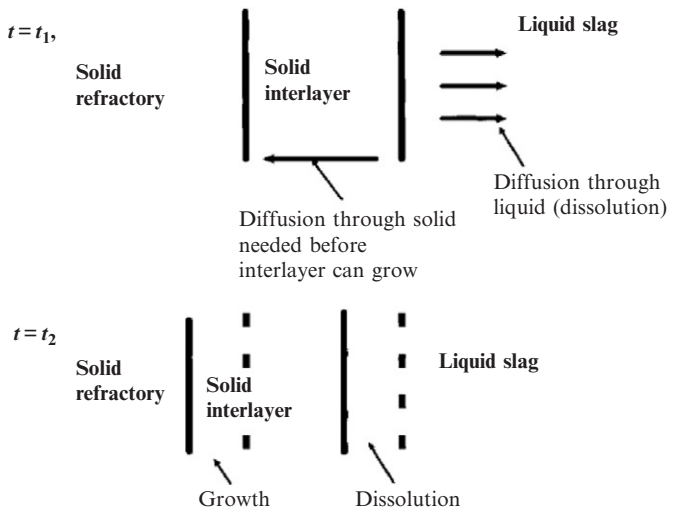


Figure 3.2.5 Growth of solid interlayer between refractory and slag leads to indirect dissolution; $t_1 < t_2$ [1].

gradients, the liquid viscosity, the mean diffusion coefficient, and the container size. Wagner [8] first used an equation taking into account these variables on dissolving a thin plate and the rate of dissolution under natural convection given by Levich [9], this is

$$\frac{dn}{dt} = -0.5D(C^o - C^s)\cdot\left(\frac{\Delta\rho g}{D\nu x}\right)^{1/4} \tag{3.2.12}$$

where $\Delta\rho$ is the density difference between saturated and bulk melt (g cm^{-3}), ν is kinematic viscosity (m^2 s^{-1}), g the gravitational constant (m s^{-2}), and x the distance from the leading edge of the slab (m).

Under forced convection where the melt is agitated, the fluid velocity U replaces $\Delta\rho$ as a variable. The dissolution rate for a rotating disc geometry can then be rearranged as

$$\frac{dn}{dt} = -2^* W^* x^* D^* B^* \left(\frac{U}{\nu x}\right)^{1/2}\left(\frac{\nu}{D}\right)^{1/3}(C^s - C^o) \tag{3.2.13}$$

where B is a constant, x is the distance along the plate, W is the width of the flat plate, and the effective boundary layer thickness $1/\delta^* = B(U/\nu x)^{1/2}(\nu/D)^{1/3}$, U is the bulk velocity of the fluid (m s^{-1}) and ν its kinematic viscosity (m^2 s^{-1}). It is clear that the value of $(C^s - C^o)$ has a great influence on the dissolution rate. If the refractory oxide in the bulk slag has been saturated, then $dc/dt = 0$. Naturally, to minimize the dissolution rate, $(C^s - C^o)$ must be minimized. For example, increased MgO content in slag decreases the corrosion of periclase, the primary phase in many basic refractories. If $C^o = 0$, then the value of $(C^s - C^o)$ reaches a maximum, and thus so does the dissolution rate. Consequently, the solubility of refractory oxides in molten slag and the saturation concentration at the interface between refractory and slag are very important in refractories corrosion.

It is worth noting that, in practical situations, dissolution is often under mixed control and it is difficult to distinguish between first-order reaction and diffusion control. Experiments must be performed over a wide range of hydrodynamic conditions to demonstrate the dissolution mechanism convincingly.

3.2.3. CORROSION TESTING OF REFRACTORIES [1]

Many different methods have been used to attempt to simulate the environment to which a refractory is exposed during commercial service. Each has benefits and limitations and can be categorized as either static where there is no attempt to simulate motion of the corroding fluid or dynamic where the fluid moves relative to the refractory. These tests are shown schematically in Figure 3.2.6 [1]. In all of them, changes will occur in the slag during the test due to different oxidation states (especially Fe), preferential penetration of specific elements into the brick, and dissolution of brick into the slag. These tests are essentially comparative but still useful for assessing the corrosion mechanisms.

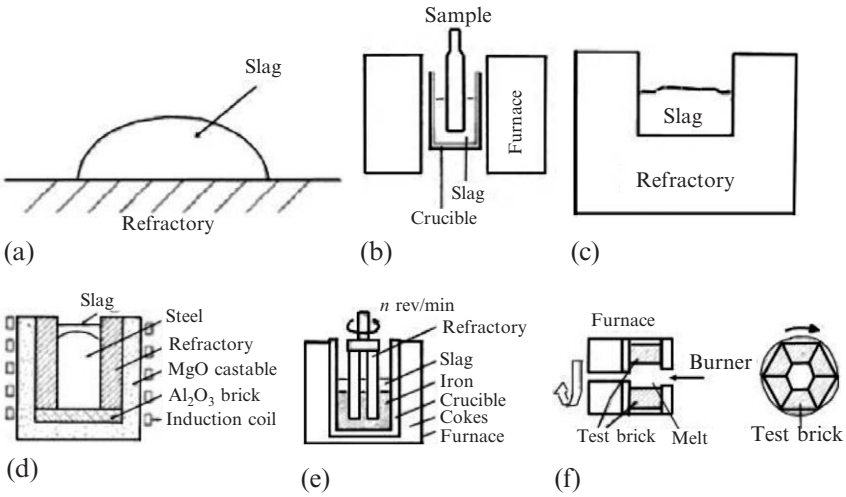


Figure 3.2.6 Schematic diagrams of common laboratory corrosion tests. (a) Sessile drop test. (b) Finger test. (c) Crucible test. (d) Induction furnace test. (e) Rotating finger test. (f) Rotary slag test. [1].

3.2.3.1. Static Corrosion Tests

All of the static tests have the drawback of the corroding medium (usually slag) rapidly becoming saturated with products of reaction with the solid. In the button or sessile drop test (Figure 3.2.6a), shaped slag is placed on a refractory substrate, heated to temperature, and held for a fixed time to allow the slag to wet and react with the refractory. The sessile drop technique is used to measure interface and surface energies in systems where the liquid is fluid and does not react with the solid but becomes more complicated when reactions occur such as when hot viscous slag is on a refractory solid. In the dipping, immersion, or finger test (Figure 3.2.6b), one or more cylindrical or square pillar-shaped refractory samples are held in the corrosive slag for a certain period in an electric resistance or induction furnace. In this method, the atmosphere is easily controlled and the composition variation of the slag, associated with rapid saturation with reaction products, can be minimized by using a large volume of slag relative to the size of the samples. However, as in the button test, no temperature gradient exists in the refractories; they are isothermal, i.e., at the same temperature through their volume. This is not the case in commercial practice where a temperature gradient between the hot face of the contact lining and the cold face or safety lining exists. In the crucible, cavity, cup, or brick test (Figure 3.2.6c), a cored out refractory brick is filled with slag and exposed to high temperature to promote slag refractory interaction. This method is popular since it is simple and many samples can be tested in a short time. However, it suffers from the drawbacks associated with static tests, i.e., no temperature gradient, rapid saturation of slag composition with reaction products (often all slag is absorbed into the brick), and no slag flow. In the induction furnace test (Figure 3.2.6d), refractory samples are set in the shape of a

polygonal crucible in an induction furnace. Since the contents need to conduct electricity, metal and slag are placed in the crucible and melted by induction heating. In this method, a temperature gradient can be established, atmosphere and temperature are easily controlled, and rapid and vigorous corrosion can occur at the melt/slag line since the less dense slag floats on the metal. An induction furnace test induces some motion of the metal and slag on heating and so has some dynamic aspect. The results of such a test can therefore effectively simulate the situation in a practical furnace except that flow is uncontrolled.

3.2.3.2. Dynamic Tests

Relative motion of liquid slag and solid refractory is particularly important since it can remove most of the boundary layer and increase any active corrosion process so that dynamic tests are needed to simulate such behavior. The dipping test can be made dynamic by rotating the samples in the molten slag, a rotating finger test (Figure 3.2.6e). Perhaps the most popular corrosion test procedure is the rotary slag test (Figure 3.2.6f) in which the slag is melted with an oxypropane flame in a cylindrical drum lined with sections of refractory and rotating about a horizontal axis. The slag is refreshed at periods throughout the test by tilting to remove old slag, returning to horizontal, and adding new slag. The advantages of this method include the fact that many samples can be compared in a single test, a temperature gradient can be established, and the composition and fluidity of the slag is partially controlled although during the test the slag composition (especially the oxidation state of iron oxide) may change. However, since this is what happens during practical steelmaking procedures, it is not necessarily a disadvantage. Nonetheless, the purpose of refreshing the slag is to keep it as constant in composition as possible. Clearer drawbacks are that temperature is difficult to control and that the reproducibility is not good.

It should be pointed out that a high-temperature X-ray radiographic technique developed by Kii *et al.* [10] has been widely used for the corrosion test. This experimental apparatus uses an electric resistance furnace combined with an X-ray transmission apparatus (Figure 3.2.7). This allows observation of corrosion phenomena as they occur during the test enabling valuable information for clarifying the mechanism and revealing the main factors affecting the corrosion. Another major advantage of such a test is that the corrosion rate of localized wear at different boundary conditions can be determined.

3.2.4. CORROSION OF OXIDE–CARBON REFRACTORIES

Carbon-containing refractories are used throughout the steel industry. Benefits of carbon include its nonwettability by slag and its high thermal conductivity which facilitates use of cooling systems and improves thermal shock resistance. Carbon is used in two forms.

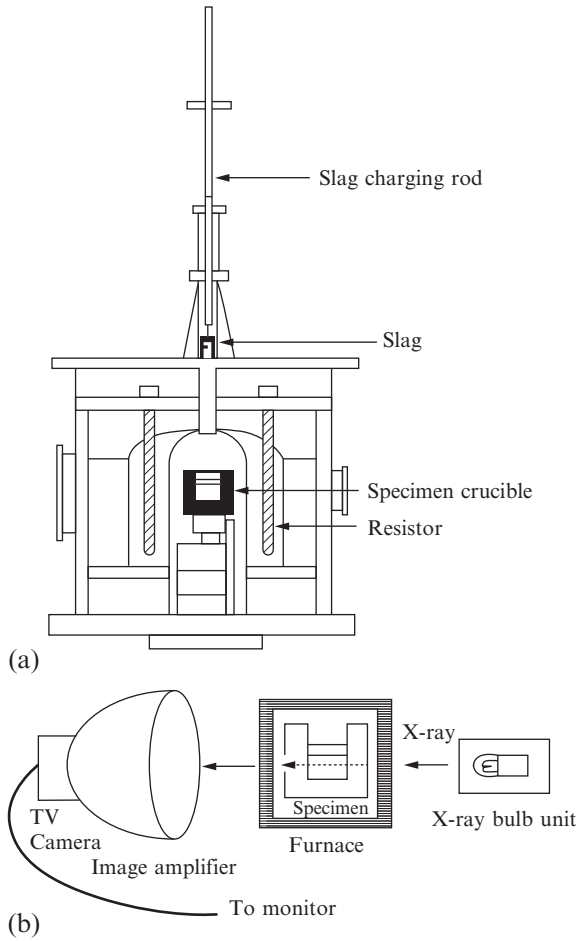


Figure 3.2.7 Schematic diagram of slag test allowing *in situ* observation of corrosion. *After Ref. [10].*

Pyrolytic carbon derived from pitch or resin binders which is located in the matrix and is fine and reactive or as graphite flakes which could be categorized as part of the aggregate system. Carbon in both forms is used with many refractory oxides such as $A1_2O_3$, SiO_2, ZrO_2, and MgO. Figure 3.2.8 shows a typical microstructure in which large sintered MgO grains (M) are bonded to gray edge-on graphite flakes (G) by a carbon bond. Light antioxidant metal grains are clearly visible.

Different types of oxide–C refractories have emerged for use in different areas of iron- and steelmaking. MgO–C refractories are used in BOF and EAF steelmaking furnace linings for the whole lining in the former and at the slag line in the latter. At present, the BOF and EAF are lined mainly with fired magnesia–carbon brick which is a composite material that maintains the high corrosion resistance to basic slag and molten metal

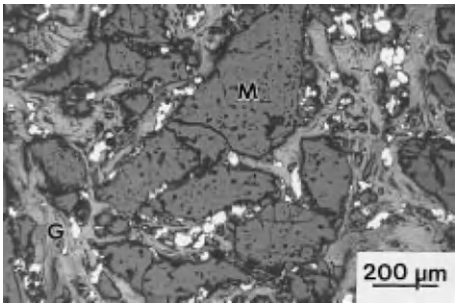


Figure 3.2.8 Microstructure of incompletely fired MgO–C composite refractory [1].

of magnesia, while enhancing thermal shock resistance, which was the weak point of magnesia brick, by adding carbon. Porosity is reduced by firing this brick at high temperatures in reducing atmosphere to prevent penetration by slag and molten steel. As an example, the chemical composition and physical properties of the refractories used for an EAF lining are listed in Table 3.2.1. Figure 3.2.9 illustrates the refractory lining of EAF

Table 3.2.1 The Chemical Composition and Physical Properties of Refractories Used for an EAF Lining [11]

Position	Refractory	Chemical Composition (Mass%)						Physical Property		
		CaO	Al_2O_3	SiO_2	MgO	SiC	C	Apparent Porosity (%)	Bulk Density (kg/cm^3)	Compressive Strength (MPa)
Furnace cover	High alumina	1.3	86.2	9.6	–	–	–	18.3	2.86	53
Furnace wall	MgO–C	1.1	0.1	0.8	74.8	–	19.5	3.4	2.84	33
Furnace hearth	Sintered MgO	1.2	1.1	2.1	94.3	–	–	3.5	2.92	73
	Stamped MgO	1.4	0.1	1.2	96.3	–	–	–	–	–
Taphole	Al_2O_3–SiC–C	–	78.0	3.0	–	15.0	3.0	12.5	3.05	50
Repairing materials	MgO	1.6	1.5	6.8	87.4	–	–	–	2.43	15
Tuyere	Alumina	1.1	91.0	1.5		–		13.7	3.20	55
	MgO–C		0.2	0.5	74.9	–	17.9	3.1	2.88	48
EBT	MgO–C	–	–	–	77.3	–	15.3	3.1	2.86	38

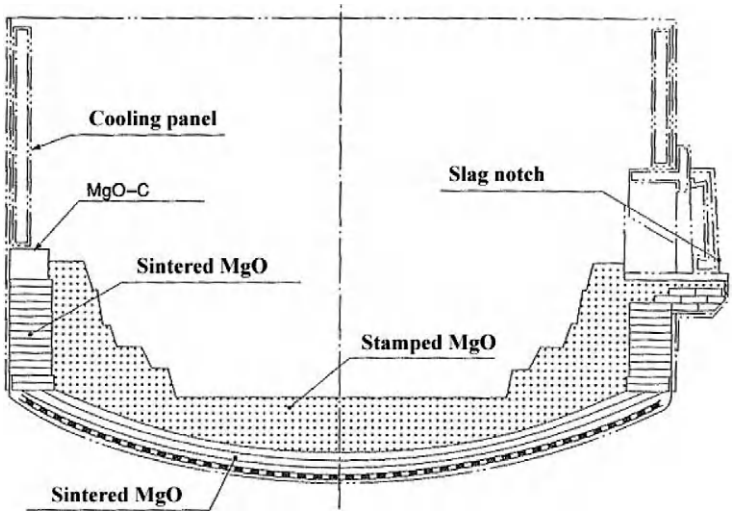


Figure 3.2.9 The lining design for the hearth of electric arc furnace (EAF) [11].

hearth [11]. Al_2O_3–C refractories are used predominantly in submerged entry pour tubes and shrouds (hollowware) in continuous steel casting and in sliding gate valves; ZrO_2–C inserts are used in areas where severe erosion or corrosion may occur in the continuous casting hollowware; Al_2O_3–SiC–C and Al_2O_3–SiO_2–SiC–C find many uses in iron- and steelmaking, such as for blast furnace tapholes and troughs and torpedo ladles (see Figure 3.2.10); doloma (MgO–CaO)–C refractories are in common use in Europe in steel refining ladles. However, by far the most extensively studied oxide–carbon refractories are those based on MgO grain so the following discussion is concentrated on MgO–C refractory.

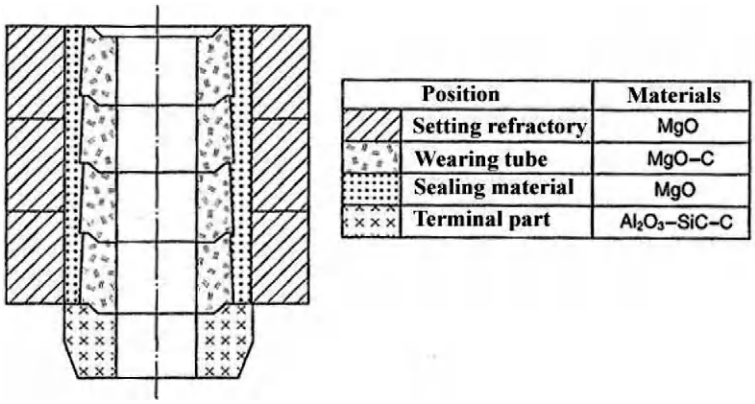


Figure 3.2.10 The lining design of taphole for eccentric bottom tapping (EBT) [11].

3.2.4.1. Corrosion Mechanism of MgO–C

Several mechanisms for the good slag resistance of carbon-bonded MgO refractories have been proposed as follows:

(1) Nonwettability of carbon: This limits the liquid penetration to the refractories.

(2) Reduction of MgO by carbon: $MgO + C = Mg(g) + CO(g)$, the gaseous products Mg(g) and CO(g) will inhibit the penetration.

(3) The reoxidation of Mg(g): $Mg(g) + 0.5O_2 = MgO$, MgO product deposits as a dense layer of secondary MgO at the slag/brick interface physically preventing penetration.

(4) Reduction by C of iron oxides to Fe metal so that they do not attack the oxides forming low-melting phases, and formation of CO vapor by oxidation of C provides overpressure resisting slag/metal ingress.

Which of these mechanisms is the most significant is still unclear, and obviously, only some of them may apply when the oxide grain is other than MgO. While carbon confers many of the desired properties on oxide–C refractories, it also has the drawback of being highly vulnerable to oxidation. Consequently, lifetimes of carbon containing refractories in oxygen-rich atmospheres depend, to a large extent, on their oxidation resistance. Furthermore, the weak nature of the carbon bond between the oxide and graphite leads to relatively low strengths. To inhibit oxidation and provide stronger (ceramic) matrix bonding at high temperatures, metallic or carbide powder additions are made and the thermochemical and microstructural changes arising from their presence as a function of temperature are well known.

Corrosion of oxide–C refractories follows the following general scheme (as shown in Figure 3.2.11) although some of these stages may occur simultaneously:

(a) formation of a decarburized layer due to oxidation of graphite/pyrolytic C mainly by FeO in the slag or oxygen in the furnace atmosphere (Figure 3.2.11a);

(b) infiltration of slag into the decarburized layer and erosion of the oxide grain by slag penetration aided by high-temperature softening of any intragranular silicate bond and reaction and dissolution of the oxide grain into slag and molten steel (Figure 3.2.11b);

(c) reduction of oxide grain by high temperature ~1873 K (~1600 °C) reaction with carbon (in MgO systems, this is termed the MgO–C reaction) resulting in its exposure and further erosion (Figure 3.2.11c).

As can be seen from Figure 3.2.8, the microstructures of MgO–C refractories contain MgO grain phases, graphite or pyrolytic carbon, as well as various phases derived from the antioxidant additions (see the discussion on antioxidants below). Simplistically, it can be considered that once the C has gone, the wear of grain phases will be similar to those of the corresponding oxide. However, this picture is complicated by the fact that the atmosphere may be reducing (although in some cases locally oxidizing) and the liquids may contain low levels of carbon. Furthermore, several reactions may occur and lead to

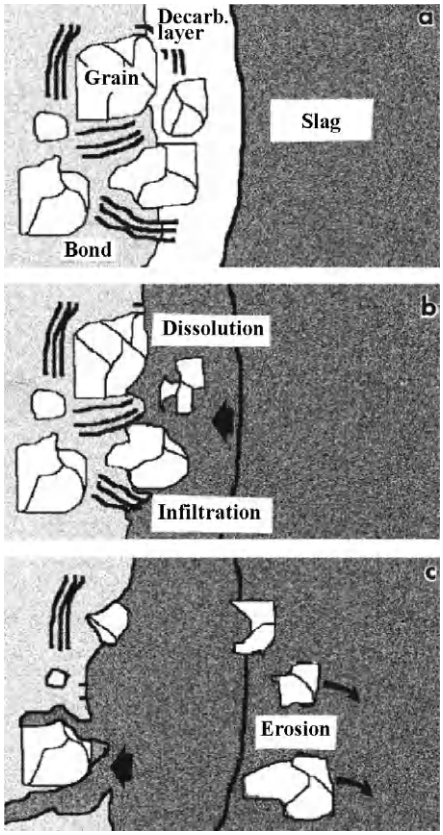


Figure 3.2.11 Schematic of general corrosion mechanism of oxide–carbon refractories. (a) Formation of a decarburized layer due to oxidation of carbon. (b) Infiltration of slag into the decarburized layer and erosion of the oxide grain by slag penetration. (c) Reduction of oxide grain by high temperature reaction with carbon [1].

generation of vapor species. The thermodynamic situation is thus rather complex and may vary depending on location in the brick, i.e., whether the hot (slag) face is being considered or the inside of the brick away from liquid penetration.

Many studies have indicated the beneficial protective effect of a secondary MgO dense layer formed at the hot face of MgO–C bricks first detected by Herron *et al.* [12]. In both dolomite and MgO refractories, this arises from reduction of MgO by C to Mg vapor which is transported to the hot face where it subsequently reoxidizes to fine grained, dense MgO helping to prevent slag/metal ingress. This dense layer does not always form. Careful control of conditions both inside and outside the refractory is required to maintain this dense layer.

For example, a high CaO/SiO_2 ratio slag is required which maintains the delicate balance between dense layer dissolution and formation by limiting the former.

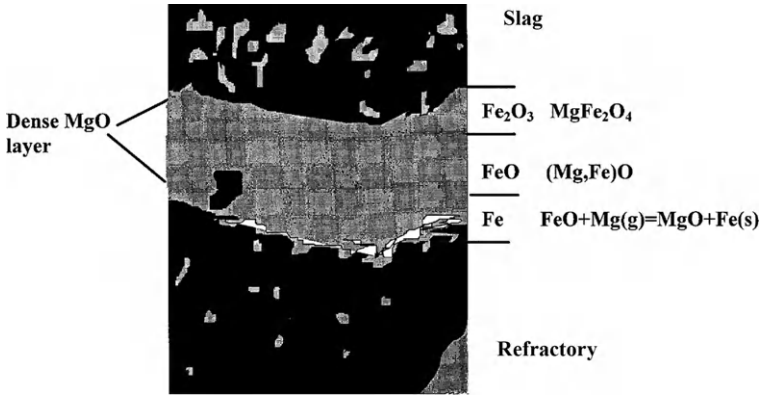


Figure 3.2.12 State of Fe in MgO dense layer of MgO–C refractory [13].

Furthermore, the presence of iron oxide in the slag is beneficial as it diffuses into the MgO layer forming $MgFe_2O_4$ in contact with the slag, (Mg,Fe)O further in the refractory and Fe metal inside the brick (Figure 3.2.12). This observation suggests that oxygen is continuously supplied from the slag to the dense layer by reduction of iron oxides. Inside the brick, the following reaction occurs

$$FeO_l + Mg_v = Fe_s + MgO_s$$

This reaction helps the MgO dense layer to grow while causing precipitation of metallic Fe. It is now realized that dense layer formation can be promoted by metallic additions to the MgO–C brick (see the last paragraph in this section).

It should be pointed out that the microstructure and composition of MgO–C refractory will have significant effect on the corrosion resistance. The quality (i.e., purity, porosity, and crystallite size) of the oxide grain used in oxide–C refractories has significant effects on the corrosion resistance of the refractories. MgO grain usually contains various second phases arising from impurities or deliberate additions (such as SiO_2, Al_2O_3, Fe_2O_3, Cr_2O_3, FeO, and CaO) to provide a silicate bonding phase. To improve the refractories' corrosion resistance, the purity of the MgO grain must be enhanced. Larger crystallite size within the magnesia grain means fewer secondary phase containing grain boundaries which can be penetrated by liquid leading to improved corrosion resistance. The large crystallite size (typically over 100 μm) may also decrease the extent of the MgO–C reaction by limiting the surface area of contact. Fused magnesia grain has higher purity and larger grain size than sintered grain and hence fused grain MgO–C bricks show better corrosion resistance than those containing sintered MgO.

The influence of graphite content on corrosion of MgO–C bricks has also been extensively studied. Yoshino *et al.* found that the wear rate decreased with increasing graphite content from 10 to 35 wt% but increased above 35% presumably because the

graphite flake content was so high that the flakes were acting as flaws opening up the microstructure to penetration [14].

The antioxidants are usually used to improve the corrosion resistance in the oxide–C refractories. Two main types of additive are used: metals/alloys (such as Al, Si, Mg, and Al–Mg) and boron-based compounds (such as B, B_4C, CaB_6, ZrB_2, $Mg_3B_2O_6$, and SiB_6). These two additive types work in different ways. Metal/alloy additives act as CO reducing agents contributing to carbon oxidation inhibition and/or improving hot strength by forming high-temperature ceramic bonds. The ceramic phases forming are a strong function of the temperature and environment but, for example, Si may react to form SiO_2, Mg_2SO_4, SiC, or Si_3N_4 and Al to form Al_2O_3, $MgAl_2O_4$, $A1_4C_3$, or AlN as fine bonding phases which act to hold the microstructure together thus improving hot strength. Furthermore, metal additives have been observed to facilitate dense layer formation both at the slag/refractory interface as described above and locally inside the brick leading to earlier in service protection. Boron-based additives, on the other hand, act to block open pores to reduce the oxidation of carbon by formation of liquid phases. This has the drawback of lowering the hot strength and corrosion resistance. SiC and Si_3N_4 have also been used to improve the corrosion resistance with SiC additionally observed to retard carbon oxidation although the mechanism has not been specified. When the SiC content is below about 5%, the wear rate of the bricks decreases with increasing SiC content but above about 5%, owing to excessive formation of SiO_2, the corrosion resistance begins to decrease.

3.2.4.2. Local Corrosion of Refractories

Local corrosion of refractories at the interfaces of slag–gas and slag–metal is one of the important factors shortening the service life of the refractory in iron and steelmaking processes. Considerable research work has been carried out to understand the corrosion mechanism of local corrosion, the major contributions coming from Mukai and his group [15–17]. Based on their experimental results, Mukai *et al.* proposed that local corrosion of refractories at the slag surface is essentially caused by the active motion of the slag film formed by the wettability between the refractory and slag, since the slag film motion accelerates the dissolution rate of the refractory and also induces the abrasion of some refractories. The active film motion is dominantly induced by the Marangoni effect and/or change in the form of the slag film (slag meniscus) due to the variation of the surface tension and the density of the slag film. Figure 3.2.13 shows a typical local corrosion profile of the SiO_2(s)–(PbO–SiO_2) slag system [16]. It can be seen from this figure that the local corrosion progresses in the area where the slag film moves directly. The slag film forms characteristic flow patterns, principally composed of wide zones of rising film and narrow zones of falling film, according to the contour of the specimen, as shown in Figure 3.2.14a and b [16]. In the case of a cylindrical specimen, the position

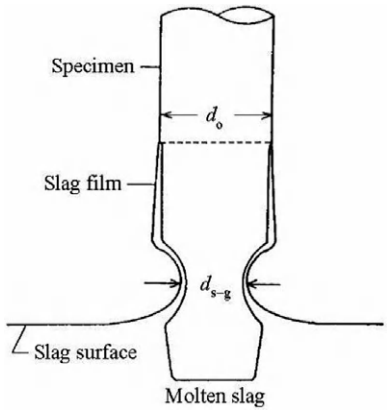


Figure 3.2.13 Typical local corrosion profile of the SiO_2(s)–($PbO–SiO_2$) slag system.

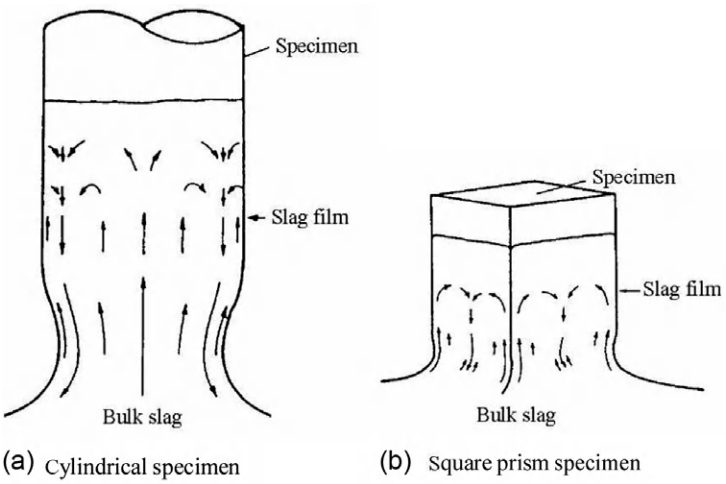


Figure 3.2.14 Typical flow pattern of the slag film on (a) the 6-mm OD rod and (b) the 6-mm square prism silica specimen dipped in $PbO–SiO_2$ slag [16].

of the falling zone moves gradually on the surface of the specimen. However, the prism-shaped specimen always has one zone of rising film at, and around, each corner of the specimen and one narrow zone of falling film at each plane side of the specimen, as shown in Figure 3.2.14b.

It was reported that the rising-zone films were several times thinner than falling-zone films [16]. The concentration distribution of the SiO_2 component in a rapidly solidified slag film was detected perpendicular to the specimen surface and also along the surface of the specimen in the vertical direction. Since contact time of the upper film with the

specimen is longer than that for the lower film, the upper film has a higher SiO_2 content, due to the dissolution of SiO_2 from the specimen into the film. The difference in SiO_2 content causes a surface tension gradient in the vertical direction. The surface tension of PbO–SiO_2 slag increases with SiO_2 content. Thus, the slag film is continuously pulled up by the surface tension gradient, i.e., the rising zone of the film is generated by the Marangoni effect due to the concentration gradient. Since the film motion in the upper part of the specimen is slower than the lower part due to its high viscosity coefficient, the risen slag is accumulated in the upper part. The thickened film caused by the accumulation begins to fall down when its weight exceeds the surface tension gradient, i.e., a film falling zone is formed. Hydrodynamic analysis of the film motion, using the observed surface tension gradient along the surface of the film, results in good agreement between the calculated and observed film velocities. The velocity distribution in the slag film obtained from the analysis shows that the slag film motion in the local corrosion zone is still active even in a thin slag film with a thickness of several tens of microns (Figure 3.2.15). The film has a concentration gradient of SiO_2 perpendicular to the surface of the solid silica, which means that a diffusion layer is formed over the whole range of the slag film. The corrosion rate in the rising zone of the slag film is well described by the rate equation derived from the conditions that the rate is controlled by mass transport

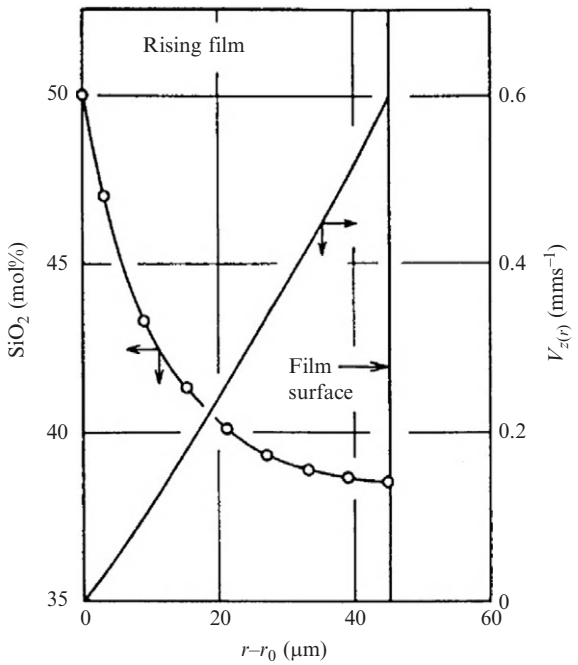


Figure 3.2.15 Distribution of velocity and SiO_2 content in the slag film for a 6-mm OD specimen dipped for 0.3 ks in a PbO–30 mol% SiO_2 slag at 1073 K [11].

of the dissolved component SiO_2 in the slag film under the Marangoni flow of the film. Therefore, the Marangoni flow in the slag film results in breakdown of the diffusion layer and is the main cause of local corrosion. In other words, the local corrosion proceeds largely as a result of the wall-washing of solid silica with a fresh thin, rising slag film induced by the Marangoni effect. The corner of a prism specimen that is continuously washed always by the rising film, as shown in Figure 3.2.14, is thus corroded much faster than the plane side, which leads to the formation of a round horizontal specimen cross section from an initial square-shaped cross section. On the other hand, a cylindrical specimen retains its initial round horizontal cross section in the local corrosion zone, because the rising zone of the slag film shifts its location with time on the surface of the specimen horizontally, resulting in an almost even corrosion rate at the same level in the local corrosion zone.

Local corrosion of Al_2O_3–C refractory at Fe(l) – (CaO–Al_2O_3–SiO_2) slag system has been investigated by Mukai *et al.* [18]. The corrosion of alumina–graphite immersion nozzles can be explained qualitatively with the aid of Figure 3.2.14. As shown in Figure 3.2.16, when the wall of the Al_2O_3–C refractory is initially covered with a slag film (Figure 3.2.16a), the film not only wets the oxides but dissolves them in preference to graphite. This changes the interface to a graphite-rich layer. Since the metal phase wets graphite better than the slag, the metal phase creeps up the surface of the specimen, as indicated in Figure 3.2.16b, and dissolves graphite in preference to the oxides. Once the graphite-rich layer disappears due to dissolution into metal, the slag can again

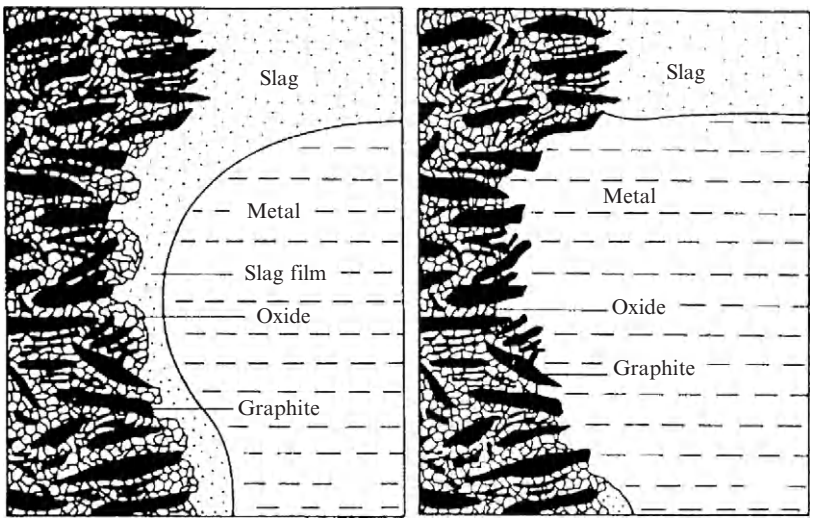


Figure 3.2.16 Schematic representation of the manner in which local corrosion of the immersion nozzle at the slag–metal interface proceeds [18].

penetrate the boundary between the metal and the specimen, and the process is repeated. This cycle produces a local corrosion zone at the metal–slag interface. The up-and-down motion of the slag–metal interface shown in Figure 3.2.16 was clearly observed using X-ray radiographic techniques [18]. The Marangoni flow of the slag film is also considered to play an important role in the local corrosion of Al_2O_3–C immersion nozzles at the metal–slag interface during the stage shown in Figure 3.2.16a.

3.2.5. SUMMARY

Refractory corrosion during steelmaking operations is a complex phenomenon involving not only chemical wear but also physical/mechanical wear (such as erosion/abrasion) processes which may act synergistically. In this chapter, the corrosion mechanisms between solid refractories and liquid melts have been discussed. The refractory corrosion test methods have been briefly summarized. The main discussion focused on the tar-bonded alkaline oxide refractories which are widely used in steelmaking practice and their corrosion mechanism. Local corrosion of refractories at slag–metal interfaces is one of the important factors shortening the service life of the refractory in steelmaking processes. The Marangoni effect plays an important role in the local refractory corrosion at the slag–metal interface.

REFERENCES

[1] W.E. Lee, S. Zhang, Int. Mater. Rev. 44 (3) (1999) 77.
[2] K. Mukai, Z.N. Tao, K. Goto, Z.S. Li, T. Takashima, J. Tech. Assoc. Refract. Jpn. 21 (1) (2001) 3.
[3] E.D. Washburn, Phys. Rev. 17 (1921) 273.
[4] T. Matsushita, T. Ohuchi, K. Mukai, I. Sasaka, J. Yoshitomi, J. Tech. Assoc. Refract. Jpn. 23 (1) (2003) 15.
[5] A.R. Cooper, W.D. Kingery, in: W.D. Kingery (Ed.), Kinetics of High-Temperature Process, Wiley, New York, 1959, p. 85.
[6] A.A. Noyes, W.R. Whitney, Z. Phys. Chem. 23 (1897) 689.
[7] A. Berthoud, J. Chem. Phys. 10 (1912) 624–635, Cited from: R.A. McCauley, Corrosion of Ceramic and Composite, 2004, second ed., New York, p. 9.
[8] C. Wagner, J. Phys. Colloid Chem. 53 (1949) 1030.
[9] V.G. Levich, Physicochemical Hydrodynamics, Prentice Hall, Englewood Cliffs, NJ, 1962, p. 66.
[10] T. Kii, K. Hiragushi, H. Yasui, K. Mukai, in: Proc. Unified Int. Tech, Conf. Refractories, Kyoto, Japan, 1995, Technical Association of Refractories, Japan, p. 379.
[11] The Technical Association of Refractories, Refractories Handbook, The Technical Association of Refractories, Tokyo, Japan, 1999, p. 336.
[12] R.H. Herron, C.R. Beechan, R.C. Padfield, Bull. Am. Ceram. Soc. 46 (1967) 1163.
[13] A. Yamaguchi, Taikabutsu Overseas 4 (1) (1984) 32.
[14] S. Yoshino, H. Kyoden, H. Nishio, T. Matsumoto, J. Watanabe, Taikabutsu Overseas 3 (1983) 21–23.
[15] K. Mukai, Z.N. Tao, Recent Res. Dev. Metall. Mater. Sci. 2 (1998) 17.
[16] K. Mukai, Philos. Trans. R. Soc. Lond. A 356 (1998) 1015.
[17] Z.S. Li, K. Mukai, Z.N. Tao, ISIJ Int. 40 (2000) S101, Suppl..
[18] K. Mukai, J.M. Toguri, N.M. Stubina, J. Yoshitomi, ISIJ Int. 29 (1989) 469.

CHAPTER 3.3

Application of Slag Engineering Fundamentals to Continuous Steelmaking

Mansoor Barati
Department of Materials Science and Engineering, University of Toronto, Toronto, Ontario, Canada

3.3.1. INTRODUCTION

The ever-increasing demand for the mineral resources together with the scarcity of fossil fuels and the environmental problems associated with their use have posed new challenges to the metallurgical industry that include lowering the dependence on natural resources (energy and minerals) through conservation and recycling, ability to process low-grade ores and recycled materials with complex chemistries, and reducing the environmental footprint of the technologies involved. Driven by the higher demand, these need to be accompanied by larger production rate.

A look at the historical evolution of steel industry in the United States, with respect to specific energy consumption, Figure 3.3.1, reveals that major improvements in energy saving have been achieved up to the present day. It is not surprising that such success has been possible by introducing breakthrough technologies such as preparation of blast furnace (BF) feed, introduction of basic oxygen furnace (BOF) steelmaking, and continuous casting. An analysis by Fruehan *et al.* [2] indicates that 20–99% additional energy savings and cuts in CO_2 footprint can be realized in various steelmaking steps, based on the difference between minimum practical energy requirement and the current industry norms.

Iron and steelmaking has traditionally been based on linking a series of continuous and batch operations through proper scheduling of the feed/product transfer and treatment time. For example, in the integrated plants producing steel from iron ore and coal, the BF and caster are operated continuously whereas BOF and coke ovens treat their feed in batches. Similarly, in the steelmaking based on the use of direct reduced iron (DRI), the continuous direct reduction furnace is coupled with a batch electric arc furnace (EAF) that produces liquid steel for the continuous caster. In an ideally streamlined flowsheet, the steelmaking in BOF or EAF would also take place continuously, facilitating the materials transfer and reducing the operating costs. Replacing batch operations with continuous processes has been the general trend in the metallurgical industry because of

Treatise on Process Metallurgy, Volume 2
http://dx.doi.org/10.1016/B978-0-08-096984-8.00015-X
© 2014 Elsevier Ltd.
All rights reserved.

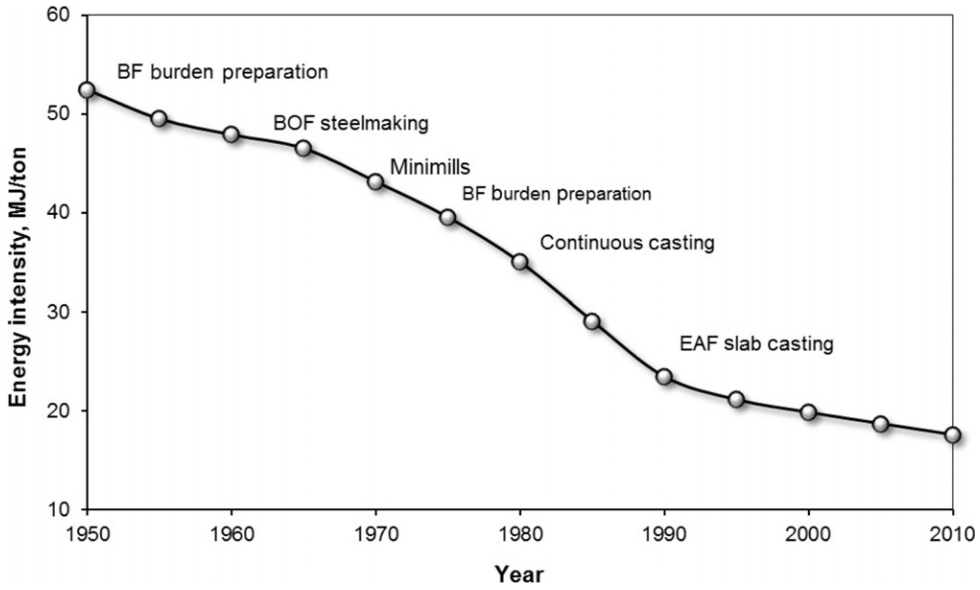


Figure 3.3.1 Specific energy consumption in the U.S. steel industry [1].

the proven benefits [3]. The implementation of new technologies however has been proven to be challenging. A recent survey of 23 new technology-based metallurgical plant start-ups [4] has shown that 70% of these plants failed or had difficulty in completion of the project and/or reaching the designed capacity within the predefined time frames. It has been indicated that the key to minimizing the risk in implementing a new technology is gradual scale-up to commercial scale with proper test work and pilot trials. Adham *et al.* [5] have discussed that a development path involving conceptual studies, laboratory testing, pilot trials, and full-scale demonstration plant has the highest likelihood of succeeding.

In this chapter, through a case study of continuous steelmaking based on the use of DRI, the practical significance of prior knowledge and properly designed test work in development of new technologies is demonstrated. Particular attention will be paid to understanding process requirements and translating them to questions that can be answered by theoretical analysis, laboratory experiments, or pilot tests.

3.3.2. CONTINUOUS STEELMAKING: AN OVERVIEW

3.3.2.1. Review of Previously Proposed Technologies

The primary driver for continuous operation of a unit is the economic advantages over a comparable batch process. For example, in a study, Goršek and Glavič [6] have shown that, from economic standpoint, continuous operation of a single-purpose equipment is superior to a batch scheme, regardless of the production rate. Steelmaking is no exception in this regard, with well-recognized economic benefits associated with continuous processes.

The early attempts for continuous steelmaking date back to 1860s [7]. Since then, over 80 different processes have been proposed, with several reaching pilot-scale and commercial testing. Currently, a few scrap melting EAFs are in operation where the feed is continuously charged. However, the extent of metal refining in such processes is very limited and a true, fully continuous process has yet to be successfully commercialized [8].

In a recent article, Peter *et al.* [8] reviewed the historical evolution of continuous steelmaking technologies, their current status, and the type of furnaces they used, divided into two simplified categories: plug flow reactor (PFR) and completely stirred tank reactor (CTSR). In a PFR, the steel is refined as it travels through the reactor, creating compositional gradients with time and position inside the vessel, whereas in a CTSR, the extent of mixing is sufficient to eliminate such gradients. A summary of the classification presented by Peter *et al.* is provided in Table 3.3.1, and an illustration of the type and configuration of reactors proposed for continuous steelmaking is shown in Figure 3.3.2.

Table 3.3.1 Evolution and Overall Characteristics of Continuous Steelmaking Technologies [8]

Period	# Of Processes	Starting Material	Extent of Development	Principal Reactor	Major Characteristic
1860s–1930s	3	Hot metal	Pilot plant	CSTR/PFR	Modified open-hearth furnace
1930s–1950s	1	Scrap	Pilot plant	PFR	Counter flow
	1			CSTR	Single vessel
	1		Proposal		Series of vessels
	1	Hot metal			
	1				Fully continuous
	2			PFR	Single vessel
	2				Series of vessels
1950s–1960s	3	Hot metal	Pilot plant	CSTR	Spray refining
	1				Emulsion
	2				Single vessel
	1		Proposal		Series of vessels
1960s–1970s	9	Hot metal	Pilot plant	PFR	Counter flow
	3				Concurrent flow
	1				Series of vessels
	2		Proposal		Counter flow
	2				

Continued

Table 3.3.1 Evolution and Overall Characteristics of Continuous Steelmaking Technologies [8]—cont'd

Period	# Of Processes	Starting Material	Extent of Development	Principal Reactor	Major Characteristic
1970s–1980s	6	Scrap	Pilot plant	CSTR	Semi-continuous EAF
	4				Series of vessels
	2		Proposal	PFR	
	1				Fully continuous
	1				Rotary furnace
	2	Hot metal	Pilot plant		Concurrent flow
	1				Series of vessels
	1		Proposal	CSTR	
	1				Fully continuous
	1				Vacuum refining
1980s–1990s	2	Hot metal	Pilot plant	CSTR	Series of vessels
	5			PFR	Counter flow
	2		Proposal		
	4				Series of vessels
	2			CSTR	
	1				Fully continuous
	1				Single vessel
1990s–2000s	2	Scrap	Commercial	CSTR	Semi-continuous EAF
	2		Proposal		
	2			PFR	Counter flow
	1	Scrap/ore	Pilot plant		Induction furnace

The continuous steelmaking concepts can be alternatively categorized based on the way the refining process is satisfied. Essentially, in all processes, crude iron must be refined with respect to the concentration of C, Si, etc., to achieve the final product specifications. A fundamental challenge is to achieve the highest reaction rate, while avoiding back-mixing of the refined metal with the fresh feed. This imposes a limitation, that is, to increase the localized rate of reactions, while avoid mixing in a larger domain. The solutions are to either split the process into several compartments or make a very long and narrow vessel. The former design ensures that each compartment can be thoroughly

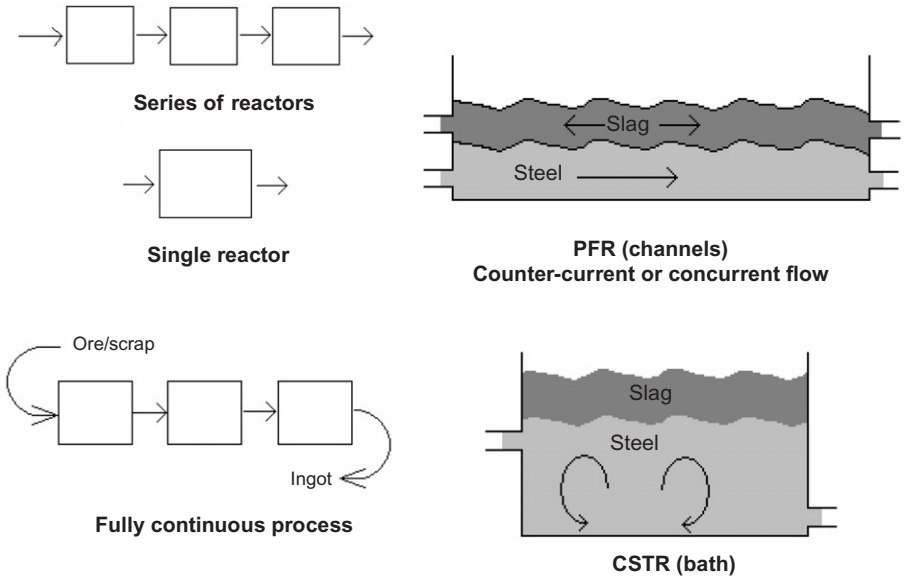


Figure 3.3.2 Schematic of reactor type (PFR/CSTR) and configuration (single vessel, series of vessels, fully continuous) applicable to continuous steelmaking [8].

mixed for a high rate of refining, while the mixing between the products of individual compartments is minimized. The single-vessel approach employs a channel reactor (PFR) that creates a natural concentration gradient along the reactor length.

3.3.2.2. Fundamental Challenges for Continuous Refining of Steel

The generic barriers against the success of the continuous steelmaking technologies were recognized by Abel *et al.* [9] to be the following.

1. Large variations in the product composition.
2. Refractory erosion and wear.
3. Low reaction rates due to the insufficient mixing between slag and metal, particularly in the channel type reactors.
4. Controlling flow of slag and metal in a series of vessels.
5. Loss of metal to slag.
6. Back-mixing of refined steel and fresh feed.
7. Substantial energy loss because of air entrainment and/or large exposed area of the slag/metal.
8. Process control.

The above challenges are reduced to two fundamental problems in continuous conversion of crude iron, as hot metal, scrap, or DRI, to steel. First and foremost, furnace integrity that is primarily dictated by the refractory stability must be maintained in order to achieve

uninterrupted operation. This is however difficult, as the reactive slags that are required for refining of metal also tend to be aggressive toward the refractory. Second, refining the feed material to the desired steel chemistry must be met, leading to compositional variations with time. This essentially prevents "perfect" mixing regardless of the number of vessels used. As a consequence, the refining must take place between inlet and outlet, while minimizing the mixing in PFR vessels or transfer of feed from one furnace to another in the CSTR arrangement. The implications are that, in CSTR, process control is difficult and of prime importance while the reactions are rapid. In PFR, on the other hand, the refining must take place in a "low-intensity" regime, thus longer processing times and larger furnaces are required. This will lead to design challenges to reduce the energy loss.

3.3.3. CONTINUOUS STEELMAKING BASED ON THE USE OF DRI

3.3.3.1. Direct Reduced Iron

DRI, also known as sponge iron, is the product of reducing iron oxide in the form of iron ore and steel plant wastes into metallic iron, below the melting point of iron and typically in the range of 800–1200 °C. Iron oxide is charged into shaft furnace, rotary kiln, or fluidized beds in the form of pellet, iron ore lumps, or fines. The reduction takes place using gaseous reductants ($CO + H_2$) which are generated through partial oxidation of coal (Reaction 3.3.1), reforming of methane by CO_2/H_2O (Reactions 3.3.2 and 3.3.3), or partial combustion of natural gas (Reaction 3.3.4).

$$C + \frac{1}{2}O_{2(g)} = CO_{(g)} \tag{3.3.1}$$

$$CH_4 + CO_{2(g)} = 2CO_{(g)} + 2H_{2(g)} \tag{3.3.2}$$

$$CH_4 + H_2O_{(g)} = CO_{(g)} + 3H_{2(g)} \tag{3.3.3}$$

$$CH_4 + \frac{1}{2}O_{2(g)} = CO_{(g)} + 3H_{2(g)} \tag{3.3.4}$$

DRI is a highly metallized iron-bearing material with some iron being present as cementite and wustite, in addition to gangue. Table 3.3.2 shows a range of compositions for DRI products based on the reductants used.

Table 3.3.2 Range of Chemical Composition for Natural Gas- and Coal-Based Produced DRI [10]

Reduction Method	Degree of Metallization	Total Fe	Carbon Content (%)	Acid Gangue (%)[a]	Basic Gangue (%)[a]
NG based	92–96	91–93	1.0–2.5	2.5–5.0	0.5–2.7
Coal based	92–93	90.4–93.7	0.1–0.2	3.2–7.6	0.1–0.35

[a]Acid gangue: $SiO_2 + Al_2O_3 + TiO_2 + P_2O_5 + Cr_2O_3$; basic gangue: $CaO + MgO + Na_2O + K_2O$.

It is evident from this table that 4–8% of the DRI iron is nonmetallic, in the form of FeO. Carbon is also present in two forms, primarily as cementite and the remainder as elemental carbon deposited in the pores of DRI.

3.3.3.2. Use of DRI in Steelmaking

DRI is a major iron feedstock for many of today's steelmaking operations. Since commercial production of DRI in late 60s, its use as a high-quality iron-bearing source has been investigated for virtually all major iron and steelmaking processes including as a coolant in BOF [11], a substitute for scrap, impurity diluter in the EAF [12–18], and pre-reduced iron feed for BF [19]. Driven by the rising scrap prices and the market's demand for high-quality clean steel, there has been a trend toward increasing the DRI charge into the EAF. As a result, the DRI production has experienced a substantial increase in the past few decades from 0.8 million tons/year in 1970 to over 70 million tons/year in 2010 and is expected to grow even more rapidly in the next decade [20]. More than 95% of the DRI produced is used in the EAF and its share in the global EAF feedstock has sharply grown to over 14% in 2006 (Figure 3.3.3). The portion of DRI in the metallic feed of those operations using DRI typically exceeds 50%, while in some cases, 100% DRI has been used.

As a source of uncontaminated iron units, DRI is a prime quality EAF feed for lowering the concentration of liquid steel impurities that are associated with using scrap

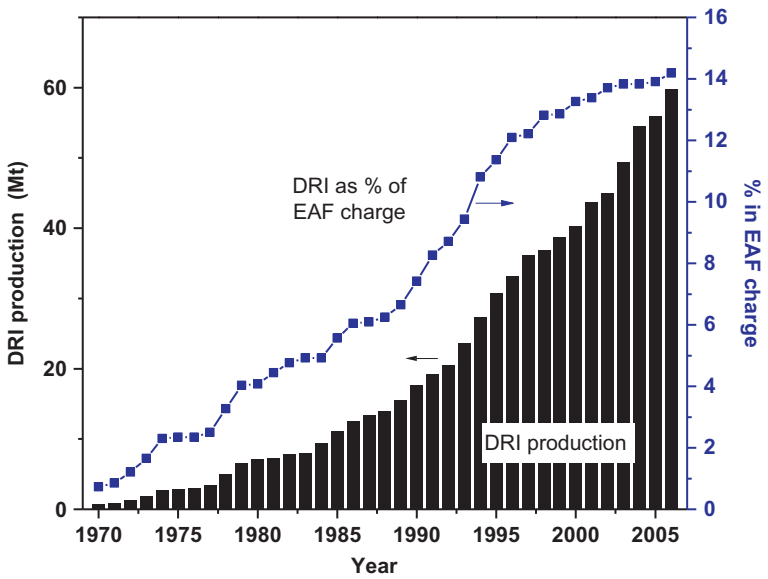


Figure 3.3.3 Evolution of DRI as a major EAF feedstock [21].

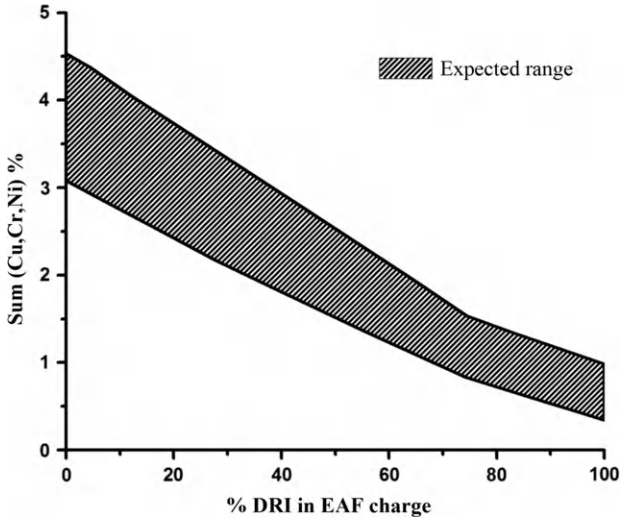


Figure 3.3.4 Expected range of some impurities in steel produced in EAF vs. %DRI of EAF charge [22].

(Figure 3.3.4). In addition, the high carbon content of DRI has been advantageously employed to induce slag foaming and increase the chemical energy input into EAF. The kinetics of interactions between DRI and steelmaking slags is known to affect the foaming behavior, furnace productivity, and steel quality. Compared to scrap, DRI has a much larger gangue content that is primarily acidic, as evident in Table 3.3.2. To satisfy the EAF slag basicity requirements, this gangue must be neutralized by addition of lime and/or dolomitic lime in the EAF, resulting in an increase in energy consumption. In addition, the reduction of residual FeO with carbon in DRI adds to the energy requirement. A combination of these two effects results in increased power-on and tap-to-tap times as well as the electrical energy consumption. As one example, a compilation of data from 16 EAFs [10] has shown furnaces using a mix of 80% DRI–20% scrap have a tap-to-tap time of 68 min and specific energy consumption of 570 kWh/ton_{steel}, compared to 52 min and 391 kWh/ton_{steel} for those consuming 100% scrap.

A conventional flowsheet for steel production from DRI includes the reduction unit, DRI handling facilities, electric furnace, ladle, and continuous caster. The original DR plants were dependent on reforming of natural gas to generate the reducing gases and were able to discharge DRI only at temperatures close to the ambient. The cold DRI would then be periodically charged to an EAF, melted, and tapped into the ladle.

In the past two decades, direct reduction iron-making technologies have transformed dramatically in accepting alternative fuel sources (coal, natural gas, and waste plastic), increasing capacity of furnaces, and also offering various product options to the downstream meltshop. Today's leaders of direct reduction technology, Midrex and Hylsa, have demonstrated that the DRI can be produced at independently controlled levels of carbon

and metallization, thus providing the steelmaker with a proper feed to adjust the final carbon content based on the availability of oxygen.

One of the major advancements in DRI-based steelmaking has been the introduction of "hot charge" technology that allows feeding DRI directly into the EAF at temperatures up to 650 °C [23–25]. A recent evaluation by one of the plants employing this technology has shown [26] that shifting from a 100% cold DRI feed to 90% hot DRI–10% cold DRI blend results in substantial benefits: reduction in tap-to-tap time from 59 to 46 min and saving in electrical energy consumption of 26% (from 533 to 392 kWh/ton_{steel}). While in the 1970s, the charging of hot DRI directly to the EAF was practiced first in the Purofer plants in Brazil and Iran [27], it took about three decades before the technological challenges of hot charging were rectified, and its implementation received wide acceptance. The high energy prices of recent years have acted as a catalyst toward further utilization of the technology. The majority of the new integrated DR-EAF installations employ hot charging as a standard technology, while the existing operations can benefit from the advantages by retrofitting.

Two hot DRI transport systems which are currently being employed in the various plants were introduced in 1980s and 1990s: HYTEMP® by HYL [28] and HOTLINK® by Midrex [23]. In HYTEMP®, hot DRI is discharged from DR plant via a pneumatic transport pipe to the EAF meltshop. The pneumatic system utilized a transport gas (inert or process gas) to transfer the hot DRI to a bin located above the EAF. On the other hand, HOTLINK® transfers DRI from a Midrex shaft furnace to the EAF by gravity transport. Using the gravity as the transfer mechanism is only possible when the DR furnace is placed above the EAF. Both technologies provide the possibility of transferring the hot DRI with the temperature up to 650 °C. The earlier users of the technology had relied on transport of DRI to meltshop in sealed containers.

Despite the obvious advantages of charging hot DRI into the EAF, the maximum energy saving and productivity increase potentials may not be achieved using the conventional EAFs due to the different operation mode of DR furnace and EAF. While the former continuously produces HDRI, the latter is a batch process and can only receive the feed for the power-on time of the furnace. The concept of a continuous EAF was put forward to streamline the flow of material from DR plant to caster without any interruption.

3.3.3.3. DRI-Based Continuous Steelmaking

3.3.3.3.1 Process Characteristics

In order to overcome the mismatch in the operation mode of the conventional, batch EAFs and the continuous direct reduction furnace, a continuous steelmaking technology was introduced by Gordon and Wheeler [29,30]. The process flowsheet of this technology is shown in Figure 3.3.5, and, as seen, is very similar to the existing DRI-based steel mills. The difference is however in the design of the electric furnace. While the

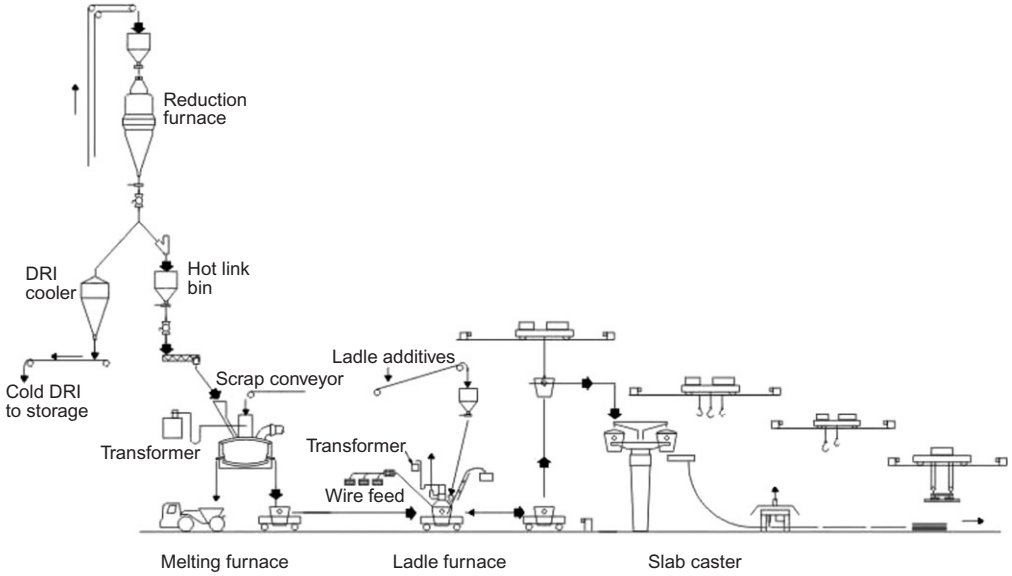


Figure 3.3.5 Process flowsheet of DR-CRISP steelmaking [31].

conventional EAFs are 3-electrode, tilting furnaces that operate batch-wise, the melting vessel of this process is a stationary furnace with 6 (or more) in-line electrodes. The furnace receives DRI (cold or hot) as well as scrap on a continuous basis, melts the feed, and reduces the carbon to acceptable levels. The steel and slag are discharged periodically through designated tapholes, in a fashion similar to the BF. In this respect, it might be categorized as a semi-continuous process, as the tapping is periodic. Liquid steel from this furnace is further processed in the conventional downstream facilities: ladle metallurgy furnace (LMF) and continuous caster. The characteristic operation of the continuous EAF places it among the single-vessel, PFR reactors where the refining of steel occurs under low-intensity conditions. A long residence time inside the furnace allows the refining to take place, with limited mixing between slag and steel.

This novel steelmaking process known as CRISP (continuous reduced iron steelmaking process) close-couples two continuous operations, DR (direct reduction) and continuous casting, that are otherwise linked through to a rather unfit batch EAF.

The continuous EAF is rectangular-shaped and is equipped with feed points located in the roof, allowing continuous discharge of hot DRI and shredded scrap into the furnace. While the production rate is comparable with the conventional EAFs, the bath size is approximately 10 times the heat size by design [32]. Several advantages have been attributed to the large furnace and bath size. First, at power input rate similar to or smaller than the conventional EAFs, the power density (defined as power input per unit area of furnace hearth) is about one fifth of the conventional EAFs: 400–500 kW/m^2 as compared to 2500–3000 kW/m^2. Figure 3.3.6 shows nominal power rating versus furnace

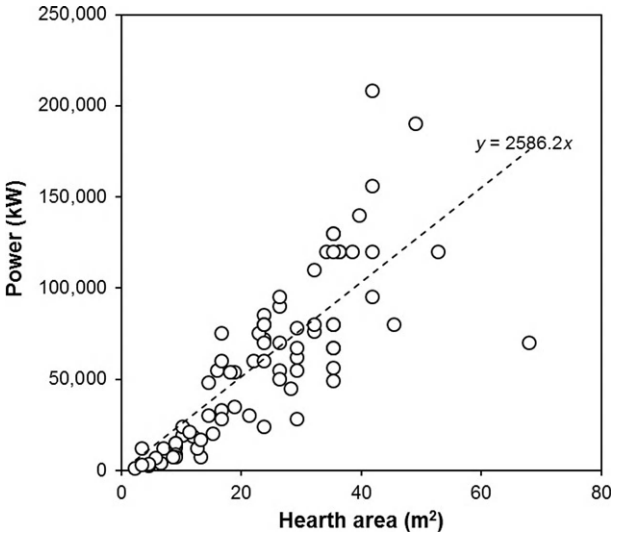


Figure 3.3.6 Power rating against hearth area for several conventional EAFs [33].

hearth area for several conventional EAFs, with an average power density of 2590 kW/m^2. The reduced power density is expected to contribute to an extended refractory life, as the furnace walls are exposed to significantly lower radiation from arc and thermal shocks. Second, the large bath to heat size gives the material a much longer residence time in the furnace. Accordingly, the state of the reactions will be closer to equilibrium and the refining can be carried out in a less intense regime. For example, it is expected that the slag will contain less FeO, resulting in reduced corrosiveness and lower iron loss. Third, the large bath will have a flywheel effect, resulting in consistent metal composition despite fluctuations in the feed. A thick slag layer is expected to contribute in several ways to process improvements: (a) it covers the electrodes, reducing radiation and thermal degradation of the furnace wall and roof, (b) higher energy efficiency due to the submerged arc, and (c) longer residence time of DRI feed in the slag, allowing for larger degree of refining before the material reaches the metal bath. The latter is an important feature of the process as it facilitates reducing the concentration gradients in the metal bath. The drawback of a large bath is however slow transition to a different steel grade when required. For that reason, ladle furnace (LMF) has a key role in the integrated process for adjusting the steel composition, particularly during transitions from one grade of steel to another.

3.3.3.3.2 Process Requirements

Melting of DRI in the absence of externally added carbon or oxygen produces a medium carbon steel with 0.3–0.7% C. Noting that the structural steels typically contain <0.1% C, it is clear that partial decarburization is the most important refining reaction for a DRI-based steelmaking process. In essence, this means that oxidizers must be added, and a

combination of mixing between slag and metal, and contact time between the two phases should produce a steel of desired carbon level. Decarburization should be accompanied by slag foaming to use the associated benefits such as arc shielding, reduced electrode and refractory consumption, and lower energy intensity. Furnace integrity, in particular the durability of the refractory during long operation times, is also critical. Among various steelmaking furnaces, EAFs have the highest refractory wear, 0.8 kg of bricks and 4.5 kg of ramming materials per ton of steel, on average. In a continuous process, such severe degradation is detrimental and must be avoided.

It is apparent that, to satisfy the two key process requirements of this technology (good furnace life and refining as discussed in Section 3.3.2.2), slag optimization has to be carried out. They impose significant, often conflicting demands on the physical and chemical properties of the slag. For example, on one side, the slag should be fairly oxidizing, to satisfy decarburization, whereas on the other side, highly oxidizing slags tend to be aggressive toward the refractory. Also, the design relies on slag foaming for reducing arc flare, but this foaming should be achieved with virtually zero oxygen injection, as otherwise the FeO would be driven up excessively, causing damage to the refractory. The engineering of an appropriate slag was thus vital to the viability of the CRISP technology. It is this aspect of the technology development that is described in the following subsections.

3.3.4. FUNDAMENTAL CONSIDERATIONS

As discusses earlier, the slag chemistry must satisfy two basic requirements: decarburize the melting DRI to the desired levels and be compatible with the refractory. The slag should also support good foaming. These requirements for slag are discussed in this section from fundamental points of view, aiming to establish the basis for slag design practice.

3.3.4.1. Melting and Decarburization of DRI

3.3.4.1.1 Behavior of DRI in Slag

Behavior of DRI pellets in slag affects their melting and decarburization kinetics. For example, in an electric furnace with limited mixing between slag and metal, decarburization at the slag/metal interface is a rather slow process and is rate limited by transport of C (in metal) or FeO (in slag). Consequently, it is important to understand the rate of such phenomena, which in turn will allow designing a reactor with sufficient residence time and mixing intensity to achieve the desired degree of refining.

The critical aspects of the process are the mechanisms and rates of decarburization and the melting of the DRI pellets as they are fed from the direct reduction module and pass through the slag phase.

In a set of experiments, the behavior of DRI in slag has been visualized by X-ray fluoroscopy technique [34]. Simultaneous measurement of the gas evolution rate by constant volume pressure increase method allows relating the pellet dynamics to the gas release rate. Examples of the captured images and the gas evolution curve are provided in Figures 3.3.7 and 3.3.8.

Direct observation of the DRI–slag interactions revealed that, depending on the slag viscosity and gas evolution rate, pellets behave differently [34]. Majority of the DRI pellets float inside the slag and remain buoyant for a period of up to 30 s (Figure 3.3.7a). The pellet is surrounded by a relatively thick gas halo, while the rapid rate of gas evolution moves the pellet within the top layer of slag. It appears that the reaction once started is accelerated quickly, causing the slag to expand substantially for a relatively short period. The pellet then shrinks and falls to the bottom of the crucible, while the slag foam collapses at the same time. An analysis of gas evolution rate and slag properties has shown that, for this behavior to be seen, large gas release rate and medium slag viscosity are required. These observations are consistent with the previous findings by Goldstein *et al.* [36] in that during the period when DRI is *active*, i.e., generating gas, it remains buoyant in the slag phase.

Under the condition of small gas evolution rate, the pellet settles to the bottom of the crucible immediately once dropped into the slag. The pellet is partially covered with a thin gas film so that the apparent density of the pellet–gas is not low enough to float the pellet (Figure 3.3.7b). Finally, for very viscous slags, the pellet remains at the slag surface until it is fully melted, regardless of the gas release rate (Figure 3.3.7c).

The position of a pellet within the slag while its reactions are proceeding affects the steel quality and slag foaming behavior. Clearly, gas has to be released below the slag surface to bring about foaming. Therefore, while high viscosity is shown to improve foamability [37], a slag that is too *heavy* prevents the pellets from reaching slag depth, thus does not support foaming. The observation of DRI behavior in slag also reveals the mechanism of nitrogen removal that will be discussed in Section 3.3.5.3.2.3.

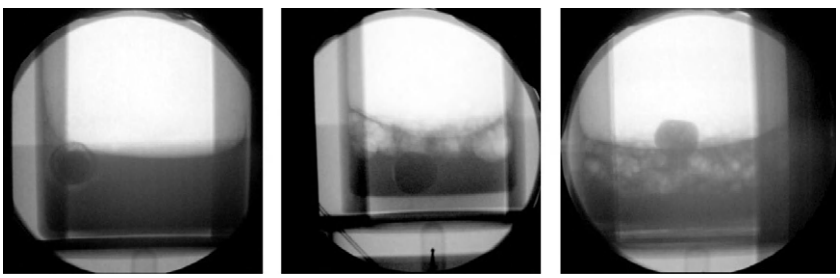


Figure 3.3.7 Pellet positions inside slag (a) suspended in the slag, (b) sinking to the bottom of crucible, and (c) resting at the surface [34].

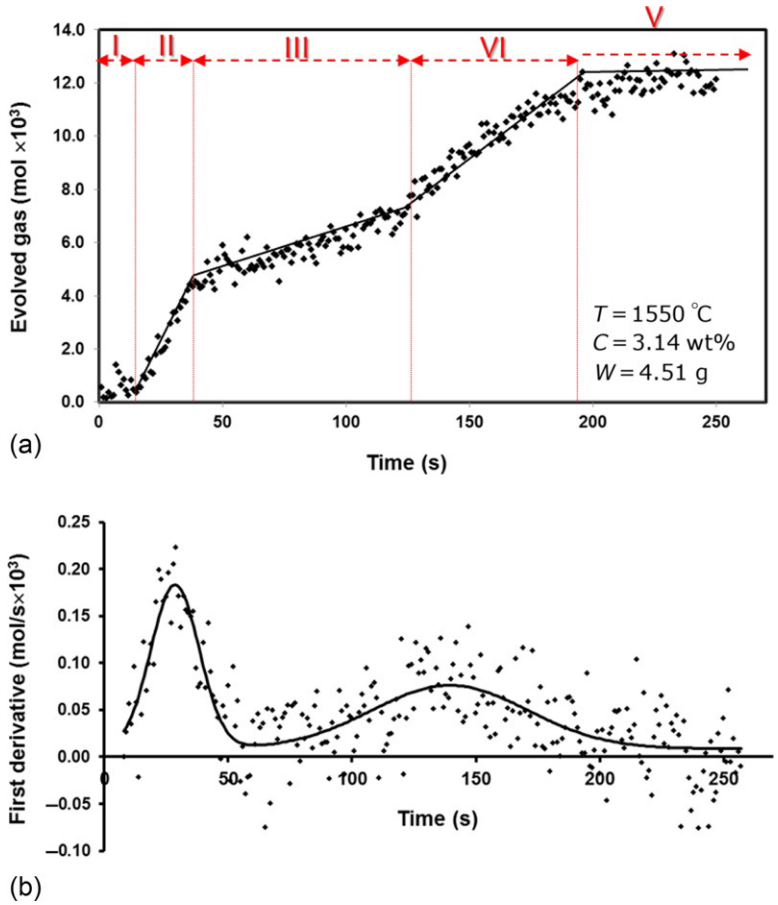


Figure 3.3.8 Variations with time of the moles of gas released and the reaction rate [35].

3.3.4.1.2 Reaction Mechanism and Kinetics

The pellet dynamics in slag explained above could be justified by the trend of gas generation shown in Figure 3.3.8. On dropping a DRI pellet into slag bath, five distinct regimes of reaction may be developed (Figure 3.3.8.a). Stage I constitutes an initial incubation period of up to 10 s, when little gas is generated. This stage is followed by a rapid gas evolution regime, that lasts 20–30 s [34,36] (Stage II). During this period, a gas halo forms around the pellet, giving rise to its flotation. Slag foams up substantially and the pellet moves about rapidly. Following this stage, there is a *pause*, or slow activity period, in which the gas flow rate drops sharply. This quiet period is followed by a sudden increase in the reaction rate in Stage VI, although the rate is smaller than Stage II. Finally, the gas evolution appears to reach steady state at a very small rate (Stage V). The variations in the amount of evolved gas and the five regimes are shown in Figure 3.3.8a. By taking the first derivative of gas amount to obtain the rate of gas evolution and using Gaussian

multipeaks fitting, these five regions are revealed more clearly, as depicted in Figure 3.3.8b. The duration of each of these reaction stages depends on the pellet characteristics including its carbon content, as well as heat and mass transfer conditions between the slag and DRI. For example, Stage III is not seen for many of the test conditions due to its very short occurrence. The following sections discuss the reaction rate and the dominating mechanisms for these phases.

3.3.4.1.2.1 Stage I—Incubation Period

In a set of experiments by Sharifi and Barati [38], a DRI pellet was suspended inside the furnace under an inert atmosphere to study the interactions within the pellet in a slag-free environment. Figure 3.3.9 shows the relationship between the amount of gas generated and the pellet core temperature. It is evident that gas evolution becomes appreciable only when the pellet core temperature exceeds ~900 °C. Therefore, it may be justified that the *inactive* period in the beginning of pellet immersion in slag is required for it to reach the reaction initiation temperature. In order to simulate the heat transfer conditions to pellet, Sadrnezhaad and Elliot [39] submerged nickel spheres in liquid slag and measured the thickness of the slag shell forming at the surface. At the same time, they measured the center temperature of the spheres under two conditions, when no gas was escaping the pellet surface and when 6000 cm^3/min of gas was purged into the pellet through narrow channels. Based on their findings, presented in Figure 3.3.10, the slag shell begins to disappear when the pellet core temperature approaches 900 °C, regardless of the gas escape rate. This temperature coincides well with the measurements presented in Figure 3.3.9,

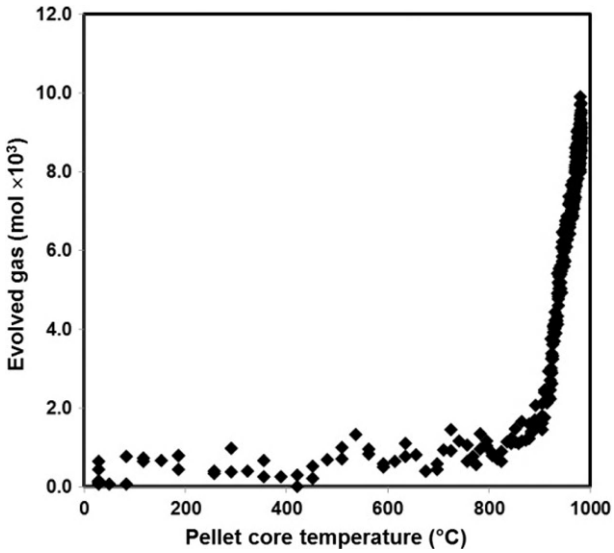


Figure 3.3.9 Variations of pellet core temperature and released gas amount [38].

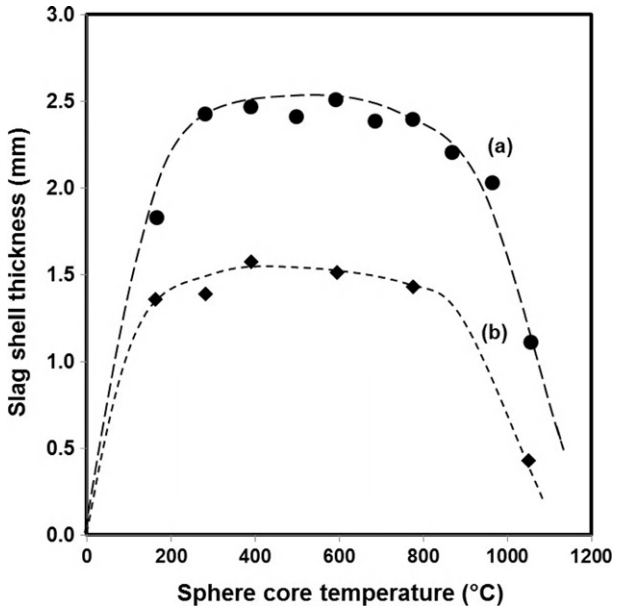


Figure 3.3.10 Thickness of slag shell formed on 1.5-cm nickel sphere under various gas escape rates: (a) 0 cm^3/min and (b) 6000 cm^3/min. Slag temperature = 1275 °C [39].

indicating that the initial incubation period is related to the time required for melting of the rather insulating slag shell and heating of the pellet. Melting this slag shell accelerates the rate of heat transfer to pellet, allowing rapid evolution of gas.

3.3.4.1.2.2 Stage II: Rapid Gas Evolution Period—Decarburization Within DRI Pellet

According to several researchers [34,36,39–41], the rapid gas evolution of this stage is because of the reaction between residual FeO and carbon within the DRI pellet, $FeO + C = Fe + CO$. Sadrnezhaad has reported that the reaction commences at around 800 °C and approaches completion when the pellet core temperature is around 1200 °C. The reaction stops when FeO or carbon are fully consumed, while for the majority of the commercial DRI, it is the FeO that is consumed first, i.e., carbon is present in excess amounts. After completion of this reaction, the gas release rate drops substantially, leading to the collapse of slag foam and settling of pellets to the bottom of slag. Provided that DRI pellet was FeO deficient, the remaining carbon continues to react with the iron oxide from slag (Stage VI). Stages II and VI are separated by the lull stage (III) that is sometimes too short to be detected.

The endothermic nature of FeO reduction by carbon implies that its overall rate may be limited by heat transfer from slag to the pellet. Also, chemical reaction itself or transport of gas species may become the rate-limiting step. Goldstein *et al.* [36], Sadrnezhaad and Elliot [39], and Sharifi and Barati [38] developed heat transfer-based models for this

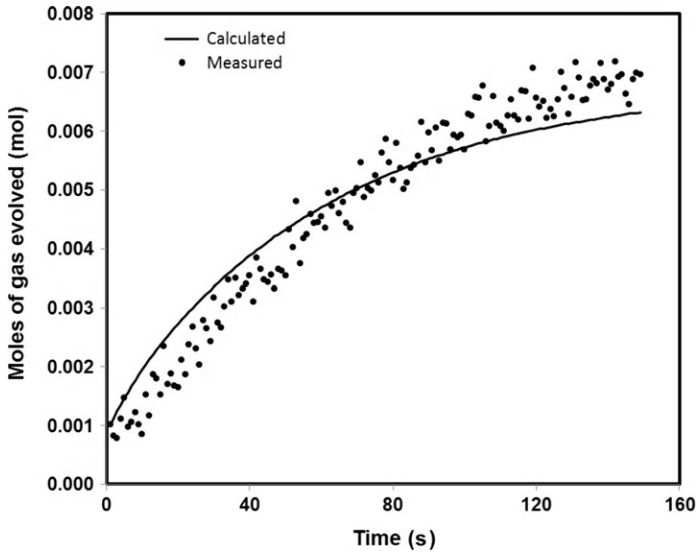


Figure 3.3.11 Measured and calculated rates of CO generation from a DRI pellet 4.5 g [38].

stage of reaction and computed reaction rates that were in agreement with the experimental measurements and therefore concluded that the rate of FeO–C reaction within the pellet is limited by heat transfer. An example of such comparisons is displayed in Figure 3.3.11, where the gas evolution rates calculated based on heat transfer rate are presented together with those measured for a DRI pellet heated in the absence of slag.

In an extensive study involving immersion of DRI pellets in slag, the dependence of the rate of the reaction at Stage II on DRI carbon content, slag temperature, and DRI preheating temperature [41,42] has been evaluated. One of the interesting observations was that the gas evolution rate depends on the initial temperature and carbon content of DRI (Figure 3.3.12). The positive effect of preheating temperature on the reaction rate supports a heat transfer-controlled reaction. However, it is expected that the chemical composition of DRI including its carbon content should not affect the rate, unless heat transfer is limited by thermal conduction within the pellet and its conductivity is significantly affected by its carbon content. The results presented in Figure 3.3.12 do not support a reaction rate that is controlled by heat transfer. This is based on the fact that the role of carbon in heat transfer, if any, should be decreasing thermal conductivity of the pellet by forming more iron carbide at the expense of iron. Therefore, carbon should in fact decrease the rate, if its role was solely on the heat transfer rate. The inconsistency may be explained by noting that the heat-transfer-based models have been confirmed in a slag-free atmosphere, whereas the carbon dependence of the rate was observed for the experiments involving slag. The overall rate seen in Stage II may be a result of two simultaneous reactions, where one reaction (FeO and C within pellet) is controlled by heat

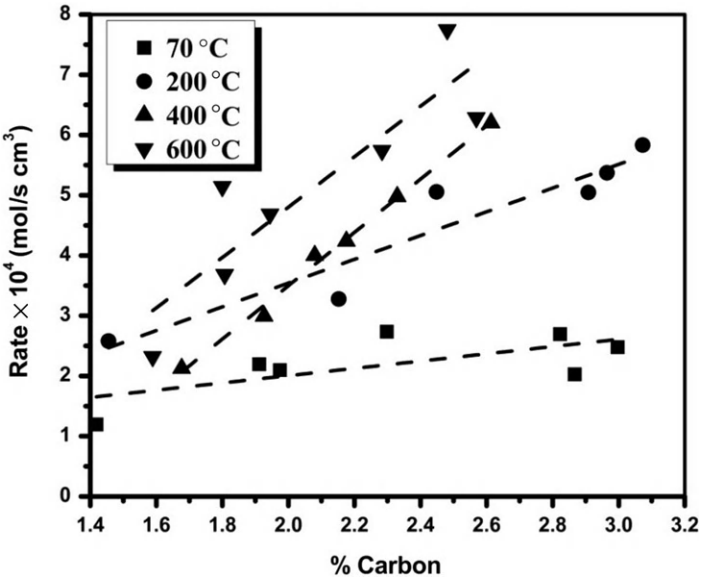


Figure 3.3.12 Rate of gas evolution in Stage II as a function of DRI carbon content and preheating temperature [41].

transfer and the other (FeO of slag and C of pellet) is limited by chemical reaction at the pellet–slag interface. Clearly, by eliminating the slag, such as those in Figure 3.3.11, a model based on the rate of heat transfer proves sufficient for predicting the reaction kinetics. On the other hand, when DRI is in contact with slag, a mixed control mechanism involving heat transfer and slag–C reaction is most pertinent.

3.3.4.1.2.3 Stage III: Lull Period—Interface Replenishment

After the primary decarburization stage within DRI, the excess carbon is removed by FeO of slag (Stage VI). As discussed earlier, during Stage II, in addition to the reduction of FeO with carbon inside pellet, the outer layers also react with slag to form CO. Therefore, once reaction within the pellet stops, the excess carbon is mostly present inside the pellet and away from the slag–pellet interface. Maintaining the reaction of slag FeO and carbon requires that the DRI outer layer be replenished with carbon from the pellet bulk. At the same time, the slag layer around the pellet has to be supplied with FeO from the liquid bulk. Both processes are diffusion controlled and therefore hinder the reaction. Also, it is possible that the pellet is melted at the end of Stage II and reacts with slag in a fashion similar to Fe–C drops. In a work by Gare and Hazeldean [43] on kinetics of decarburization of Fe–C drops with slag, a similar lull period has been observed. In this case, one possible mechanism for the reaction stoppage may be the time required for diffusion of oxygen into the drop that will lead to formation of CO bubbles and

expansion of the drop. In the case of DRI pellets, a similar mechanism could be effective when the DRI pellet becomes liquid.

3.3.4.1.2.4 Stage IV: Continued Decarburization by Slag

This stage represents the reaction between FeO of slag and remaining carbon from DRI. It has been shown that the rate of this stage increases significantly with the FeO content of slag, with its rate constant being consistent with the typical slag phase mass transport [34]. An examination of the role of DRI carbon and slag temperature on the rate of this stage reveals that both increase the rate (Figure 3.3.13). The higher carbon leads to higher rates for the first stage (Figure 3.3.12), which in turn increases the rate of FeO mass transfer within the slag, due to more intense gas evolution and pellet movement. The temperature increase also plays a positive effect since it reduces the slag viscosity, hence larger a mass transfer coefficient. On the other hand, the pellet preheating temperature does not have any effect on this rate (Figure 3.3.14), indicating that only Stage II can be shortened by preheating the DRI. Essentially, when this decarburization mechanism takes over, the pellet has already reached a temperature well above the preheating temperatures.

3.3.4.1.3 Slag Oxidizing Power

For a typical DRI with $Fe_t = 92$, metallization degree of 90%, and carbon content of 2%, the flat-bath carbon content in the absence of any oxidizer addition is around 0.5–0.6%. Decreasing the carbon level to the low carbon steel requires moderate decarburization. This is accompanied by increasing the slag FeO level according to the following reaction:

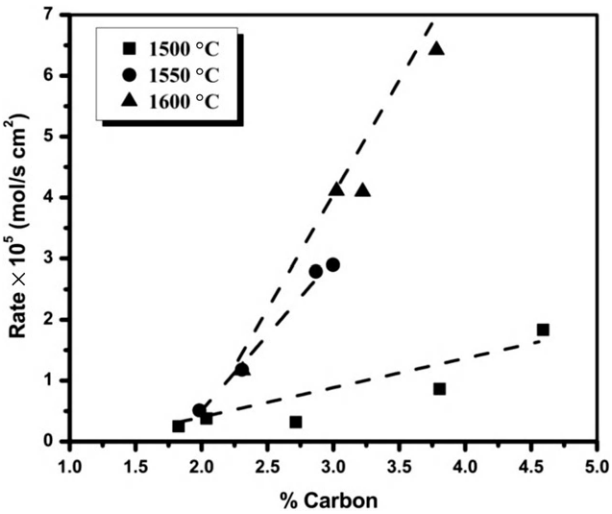


Figure 3.3.13 Effect of DRI carbon content and slag temperature on the rate of gas evolution in Stage VI [41].

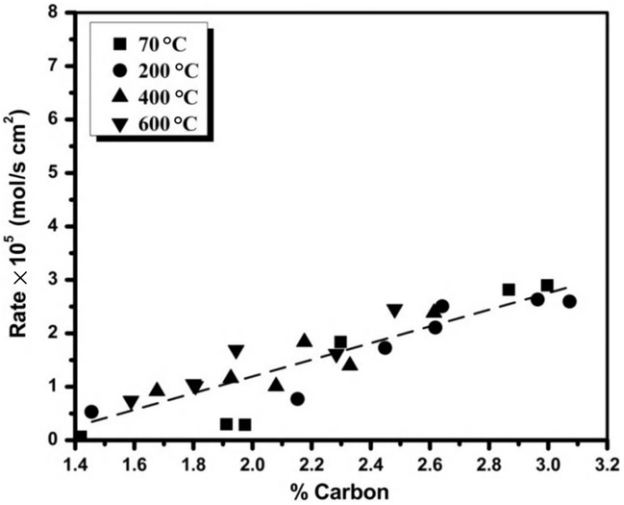


Figure 3.3.14 Rate of gas evolution in Stage VI as a function of carbon content, for various preheating temperatures [41].

$$(\mathrm{FeO}) + [\mathrm{C}] = [\mathrm{Fe}] + \mathrm{CO}_{(\mathrm{g})}. \tag{3.3.5}$$

In equilibrium, this reaction yields a relationship of the form presented below:

$$\%\mathrm{FeO} = \frac{k'}{\%\mathrm{C}}, \tag{3.3.6}$$

where k' in this equation is a function of the slag chemistry and temperature. Controlled by kinetic limitations, the practical FeO content of slag for a given C level depends on the extent of slag–steel mixing, the contact time, and method of oxygen introduction. The rate of decarburization when direct oxidation of metal bath is not the dominant mechanism and slag plays the intermediate role may be limited by the rate of mass transfer of FeO in slag or that of carbon in metal. In either case, excess oxygen is supplied to the system, resulting in higher than equilibrium FeO levels. As a rule of thumb, the FeO requirement in the EAF slag for a given carbon level is estimated by the following formula [44]:

$$\%\mathrm{FeO} = 10 + \frac{1}{\%\mathrm{C}}. \tag{3.3.7}$$

Based on this relationship, for low carbon steels, FeO levels in excess of 20% are required in a typical EAF. This value is dependent on the basicity and the temperature of the bath and will be examined later for the case of continuous steelmaking in EAF.

3.3.4.2. Slag Foaming

Slag foaming occurs during steelmaking as well as the iron smelting processes, where the slag is expanded by the rising flow of gases injected to the melt and/or generated from the reactions inside the furnace. In BOF steelmaking, for example, slag slopping during decarburization is a frequent problem. In EAF steelmaking however, slag foaming is known to improve the process performance. As a result of reduced thermal shock and radiations to the refractories and roof, energy efficiency is improved and at the same time the furnace wall refractory life is extended. Also, a foamy slag is known to reduce electrical and acoustic noises due to its dampening effect. In a study by Morales *et al.* [45], significant reductions in tap-to-tap time, and consumption of energy and electrode have been realized, as a result of introducing foamy slag practice in the EAF. In essence, the slag foaming contributes to increasing slag volume, without an increase in its mass. It may thus be considered as an ideal way of covering the electrodes and improving the process performance, without facing energy loss associated with a larger slag volume.

The effective volume of the slag during the process is dictated by its mass (i.e., volume at rest), gas release characteristics (gas flow rate, distribution of the flow, bubble size), and the ability of the slag to "hold" the bubbles, known as slag "foamability." Essentially, the longer the bubbles remain in the slag, the more expanded it becomes.

The slag foaming index (Σ) can be used to obtain a quantitative measure of slag foamability. It is in principle the average traveling time of the gas bubbles through the slag and is closely related to the physical properties of the melt [46,47]. One expression is given in Equation (3.3.1) [46].

$$\Sigma = 115\left(\frac{\mu^{1.2}}{\rho\sigma^{0.2}D_b^{0.9}}\right) \tag{3.3.8}$$

where Σ is the foaming index, μ is the slag viscosity, ρ is the melt density, σ is surface tension, and D_b represents the gas bubble diameter.

The dependence of foaming index to these parameters can be readily realized, noting that Σ essentially represents the ease of drainage of slag film between the bubbles. Higher viscosity, lower density, and smaller surface tension all contribute to the film being held more strongly by the bubbles. On the other hand, smaller bubbles hold a thinner slag film between them, which is harder to drain.

Although the above equation suggests a direct relationship with the slag viscosity, this dependence is valid only in a certain range. It has been shown that a slag that is "too" viscous suppresses foaming, as gas bubbles cannot escape the slag, resulting in their coalescence, forming large cavities that hinder uniform expansion of the slag. Accordingly, neither fully liquid slags nor crusty ones sustain a good foam. It is well known that the presence of a small amount of suspended solid phases results in a moderate slag viscosity that is appropriate for foaming. The effect of second-phase particles on foaming has been

studied by Ito and Fruehan [48–50]. They discussed that the larger foaming index is because of higher viscosity of these slags, as solid particles are known to increase the viscosity according to the Einstein–Roscoe equation [51] or its modified versions by Brinkman [52] and Happel [53] presented below:

$$\mu = \mu_0(1 - 1.35f)^{-2.5} \tag{3.3.9}$$

$$\mu = \mu_0(1 + 5.5f) \tag{3.3.10}$$

$$\mu = \mu_0(1 - f)^{-2.5} \tag{3.3.11}$$

with f being the volume fraction of solid particles, μ viscosity, and μ_0 viscosity of fully liquid slag.

In addition to increasing the slag viscosity, second-phase particles improve foaming by serving as gas nucleation sites, leading to a large number of bubbles, which is preferred over a few large bubbles. In an attempt to define the optimum range of slag composition for foaming, Pretorius and Carlisle [54] developed Isothermal Saturation Diagrams. The diagram is essentially a "predominance diagram" and maps the stability regions of various phases in multicomponent slags as a function of concentration of slag constituents, for a given basicity and slag temperature. An example of such diagrams is shown in Figure 3.3.15. In this figure plotted for $CaO–SiO_2–MgO–FeO$ system, the fully liquid

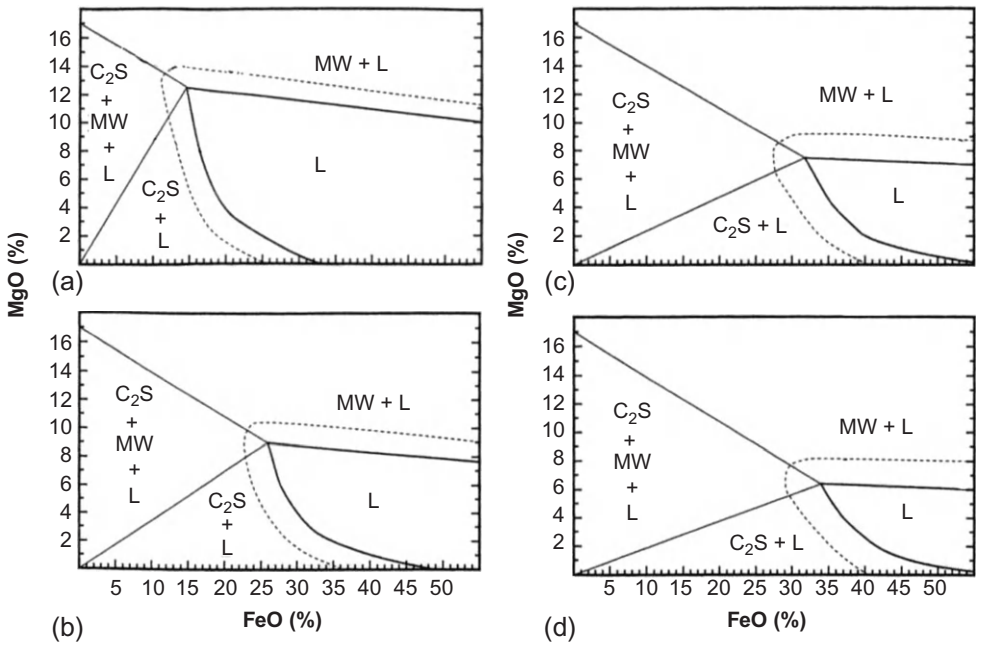


Figure 3.3.15 The isothermal saturation diagram for $CaO–SiO_2–MgO–FeO$ system at 1600 °C at various basicity ratios ($B_3 = CaO/(SiO_2 + Al_2O_3)$) is 1.5 in (a), 2.0 in (b), 2.5 in (c), and 3.0 in (d) [54].

domain of slag shrinks as the basicity increases. As seen, outside this region the slag is saturated with (Mg,Fe)O solid solution (magnesiowustite, MW) or Ca_2SiO_4 (C_2S), or both. From the standpoint of foaming, formation of a certain volume fraction of solids is desired, regardless of the type of the solids. A dashed line surrounding the liquidus region corresponds to the slag compositions with optimum viscosity for foaming. As seen, such slags would have 1–1.5% MgO above the saturation limit or 3–7% FeO below the liquidus composition, to form MW or C_2S solid phases, respectively [54,55]. Slags containing higher MgO or lower FeO contain excessive amounts of solid so that foaming is suppressed. On the other hand, slags within the liquid domain are too fluid to sustain the foam. It should be noted that lowering FeO content of slag may not be a practical solution to improve foaming for two reasons. First, slag FeO is dictated by the requirement for the carbon level of steel and the intensity of refining in the furnace. Second, a certain amount of FeO is required in the slag to promote *in situ* generation of gas bubbles through Reaction (3.3.5). As Figure 3.3.15 illustrates, for a given FeO concentration, the slag may be saturated with C_2S by increasing the basicity through addition of lime. This also reduces the MgO requirement for saturation with MW.

From continuous processing perspective, a foamy slag is highly desired as it reduces the radiation from arc/electrode to the walls to extend the refractory life. Also, in an expanded slag with low apparent density, DRI is suspended in the slag for a longer time, thus the refining reactions take place to a larger extent by the time the metal reaches the steel bath. Inducing a foamy slag in a continuous process, particularly one using DRI, would be normally more straightforward than the batch counterpart. This is because, in a batch process, there are substantial changes in the slag chemistry from the beginning to the end of the process, making it difficult to adjust the fluxes so that a slag for optimum foaming be formed. In addition, gas generation from reactions as DRI pellets react with slag, the consistency in the chemical composition of the DRI (compared to scrap), and simultaneous charging of flux and iron-bearing feed all contribute to stable foam throughout the process. In conventional EAFs, on the other hand, the increase in the FeO during the final stages of refining leads to a slag that is too fluid to sustain a good foam.

3.3.4.3. Refractory Degradation

3.3.4.3.1 EAF Refractories and Their Degradation Mechanisms

Magnesia-based refractory materials are widely used in the wall lining of EAFs due to their excellent thermal resistance and high-temperature strength. Figure 3.3.16 illustrates various zones of a typical eccentric bottom-tapping EAF. The refractory at the hearth of the furnace consists of two layers. The steel shell is first lined with approximately 20–25 cm of magnesia bricks containing up to 97% MgO. This safety lining is protected by a thicker layer, 25–60 cm, of monolithic magnesite that acts as the working layer. To form this layer, dry ramming material containing 60–95% magnesia is compacted against

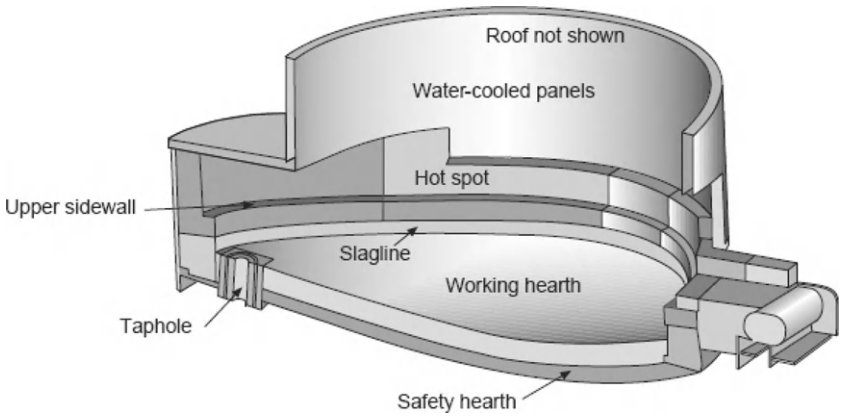


Figure 3.3.16 Cut-out view of an eccentric bottom-tapping EAF [56].

the underlying safety lining. The material becomes hard and fused together once it is subjected to the high temperature of liquid steel.

The slagline lies above the furnace hearth and below the upper sidewall. This area is most prone to severe damages caused by slag attack, erosion, and radiation from electric arc. The slagline refractory includes two layers: an overlaying monolithic material and a backing refractory lining with a thickness of 30–50 cm. The bricks are made from magnesite and carbon (10–20% graphite), bonded by a carbonaceous resin. The role of carbon is to reduce the porosity of the bricks and lower the wetting between slag/refractory, hence lessen the chemical attach. Also, it increases the thermal conductivity of the material, reducing its susceptibility to thermal shocks. The protective layer is made of magnesite and/or dolomite gunning materials that are injected onto the bricks. This layer is repaired frequently, and whenever the bricks are exposed to slag, a complete relining is prescribed.

The lining of upper sidewall consists of MgO–C bricks with 5–20% C. Chemical attack by slag is not severe in this area. However, high temperatures due to arc flare and physical damage by impinging scrap are common causes of damage.

The wear in EAF refractories takes place as a result of several mechanisms in various zones of the furnace [56]

- Chemical attack by slag: This is the most important form of degradation and can cause severe damages to the refractory even in one heat, if the operating conditions are not controlled. The rate and extent of corrosion are increased by the higher concentration of oxidizing and/or acidic components such as SiO_2, Al_2O_3, FeO, and MnO. In addition to dissolving MgO from refractory, the slag also oxidizes the refractory carbon, subjecting the refractory to slag penetration and faster disintegration.
- Erosion: Flow of metal/slag during refining or discharge as well as Marangoni-induced flow at the slag–metal interface gives rise to wearing away of the refractory, known as erosion. This phenomenon is particularly common at the taphole and slagline.

- Melting and spalling: EAF refractories are subjected to high temperature, thermal shocks, and frequent thermal cycles. Unshielded arc is a major cause of such damage that can be reduced by submerging the arc in a thick or foamy slag layer.
- Chemical attack by atmosphere: Oxidation of carbon with oxygen weakens the refractory lining leading to faster wear. Also, any water leak in the furnace can cause hydration and swelling of the material that under thermal and physical stresses is degraded readily.

Resistance to slag, wear, and thermal shocks should be maintained for extended operation times as otherwise interruptions for maintenance and rebuilding the refractory prevent continuous processing. The methods to improve refractory life include the following:

- Optimization of refractory material: As discussed earlier, magnesia- and dolomite-based refractory bricks are widely used in the wall lining of EAFs. Optimization of micro and macrostructure of the material as well as addition of carbon to close the pores have shown to reduce the rate of wear.
- Proper maintenance and operation: Continuous or frequent inspection of the furnace, monitoring the refractory thickness, and repairing the damaged sections all contribute to improved refractory life and reduced furnace downtime. Also, the use of cooling devices embedded in the refractory (such as copper fingers) has shown a positive effect on the refractory life.
- Reduced thermal shock: This may be achieved by covering the arc (foamy slag), decreasing power density, and improving the operation so that the temperature fluctuations within the refractory are minimized.
- Slag optimization: Making the slag chemically compatible with the refractory will have a significant impact on reduction of the chemical attack.

3.3.4.3.2 Refractory Corrosion

The degradation of refractory by slag attack occurs in two ways. First is uniform corrosion that involves dissolution and loss in thickness of the bricks over their entire area in contact with slag. The second mechanism that has a more severe impact consists of penetration of slag into the refractory pores, localized corrosion to widen the pores that accelerates penetration of slag, and eventually disintegration of the bricks. Larger pore size, higher surface tension, and lower viscosity are all known to intensify the penetration rate and subsequent structural degradation of the refractory. The empirical correlation of Endell *et al.* [57] for the rate of refractory corrosion in slag is very useful to explore the role of various parameters on the corrosion rate

$$R = CL_0\left(\frac{T^{2/3}}{\mu^{8/9}}\right)(fHA)^{1/9} \tag{3.3.12}$$

In this equation, the following terms are used:

R: attack rate of refractory by slag (cm/s)
L_0: solubility of refractory in slag (g/g)
T: absolute temperature of the refractory hot face (K)
μ: slag viscosity (poise)
f: fraction of slag adhered to the refractory wall
H: rate of heat liberation in the furnace chamber (kJ/m^3/h)
C: a constant for the furnace geometry

The correlation shows a strong dependence of refractory corrosion rate on the solubility in slag, temperature, and slag viscosity.

A more fundamentally based correlation can be developed for the situation where the mass transfer of MgO in slag controls the rate of refractory dissolution. In this case, the rate is given by

$$J = D(C_i - C_b)/\delta \tag{3.3.13}$$

where D is the diffusion coefficient (m^2/s), C_i and C_b are the concentrations at slag–refractory interface (g/m^3) and slag bulk, respectively, and δ is the effective thickness of the boundary layer (m). There is experimental evidence that the mass transfer to a large extent controls the overall rate of dissolution even under forced convection [58,59]. Under these conditions, the concentration of the refractory component in the slag at the interface is equal to its solubility limit in slag.

Equation (3.3.13) indicates that both kinetic factors (diffusivity and boundary layer thickness) and thermodynamic properties of the system (solubility) influence the rate. In order to reduce the rate of solid degradation, one needs to either minimize mass transport in the slag (limited agitation, high viscosity, low temperature) or increase the concentration of the refractory component in the slag bulk. If the slag is saturated as it forms, the driving force of dissolution (C_i–C_b) will be zero, resulting in protection of the refractory. Addition of MgO to slag plays two roles. First, it shifts the composition toward saturated slags, lowering (C_i–C_b), and second, it changes the mass transport rate by varying the slag viscosity. In a fluid slag, the dissolved oxide is carried faster to the bulk, preventing the formation of a saturated layer at the interface. On the other hand, increased viscosity gives rise to lower diffusivity and a thicker diffusion layer. A slag oversaturated with MgO will contain solid phases such as Al_2O_3·MgO spinel or MW ((Fe·Mg)O) solid solution, that increase slag viscosity, and reduce its degradation rate. As Figure 3.3.15 depicts, increasing MgO concentration leads to formation of MW that is expected to lower the dissolution rate.

Formation of Al_2O_3·MgO spinel can lead to formation of a barrier against dissolution; however, it has been shown [58] that the mechanism is only effective in temperatures below 1530 °C and under static conditions, where the layer remains at the interface.

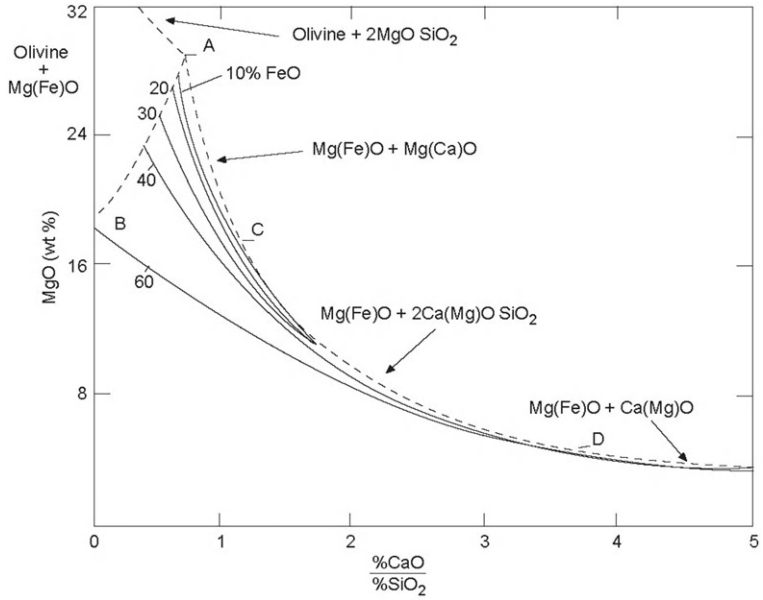


Figure 3.3.17 Solubility of MgO in FCSM slags at 1600 °C [60].

Higher temperature or more intense flow close to the interface removes this coating, exposing the MgO surface to the corrosive slag.

With the constraints that a viscous slag imposes on handling, foaming, and refining ability of slag (promoted by mixing), it appears that limiting the thermodynamic driving force of the dissolution, i.e., saturating the slag with MgO, is the most convenient way of lowering slag attack. Tromel *et al.* [60] made a thorough study of MgO solubility in FeO–SiO_2–CaO–MgO slags equilibrated with pure iron at 1600 °C. The solubility limit was obtained as a function of FeO and CaO/SiO_2 content of the slag (Figure 3.3.17). With the aid of this figure, one can determine the amount of MgO required to saturate a given slag with magnesiowustite.

3.3.4.3.3 Effect of Slag FeO on Refractory Degradation

Figure 3.3.17 generated from the results of Tromel *et al.* [60] shows increased solubility of MgO at lower FeO level and C/S ratios. This was confirmed later by Jung [61] who observed a significant decrease in MgO solubility with the increase of slag FeOx level, in slags saturated with dicalcium silicate (Figure 3.3.18). The effect of FeO becomes less pronounced at higher basicity so that when C/S exceeds 2, the saturation concentration of MgO becomes essentially independent of FeO level.

Despite the positive effect of FeO on lowering MgO solubility (C_b), the slags containing high FeO are known to be very aggressive toward the refractory. It is believed that

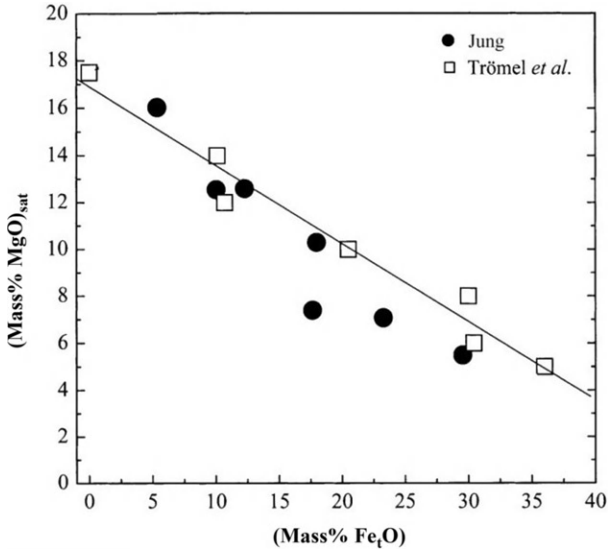


Figure 3.3.18 Dependence of MgO concentration at saturation FeO in $CaO–SiO_2–Fe_tO–MgO$ slags saturated with dicalcium silicate at 1600 °C [61].

Table 3.3.3 Temperature for Full or Partial Melting of Reaction Products in Steelmaking Slags [62]

System $CaO–MgO–Al_2O_3–SiO_2$		System $FeO–MgO–Al_2O_3–SiO_2$	
Mineral	**Melting Temperature (°C)**	**Mineral**	**Melting Temperature (°C)**
$2MgO·SiO_2$ (forsterite)	1900	$FeO·SiO_2$ (fayalite)	1205
$CaO·MgO·SiO_2$ (monticellite)	1485	$FeO·MgO·SiO_2$ (iron monticellite)	1230
$3CaO·MgO·2SiO_2$ (merwinite)	1575	$2CaO·(Fe_2O_3·Al_2O_3)·SiO_2$ (iron gehlenite)	1285
$2CaO·SiO_2$ (dicalcium silicate)	2130	$FeO·Al_2O_3·5SiO_2$ (iron cordierite)	1210
$3CaO·SiO_2$ (tricalcium silicate)	2070	$2CaO·Fe_2O_3$ (tricalcium silicate)	1489
$CaO·Al_2O_3·2SiO_2$ (anorthite)	1553	$4CaO·Al_2O_3·Fe_2O_3$ (anorthite)	1395

the high corrosion rate is because FeO combines with refractory oxides to form compounds with low melting temperature that under the operating conditions are washed away rather easily (Table 3.3.3). This fluxing effect also increases the slag fluidity, resulting in a larger mass transfer rate (D/δ). A more oxidizing slag can also result in

oxidation of carbon in refractory, which leads to even faster degradation. Numerous observations in industry confirm that the overall impact of FeO increase is more severe refractory attack. The effect is magnified at lower basicity as, with respect to MgO solubility, FeO has only a secondary effect and the solubility is dominantly controlled by basicity (Figure 3.3.17). A combination of low basicity and high FeO will be severe and result in rapid degradation of the refractories.

3.3.5. SLAG DESIGN STEPS

The fundamental considerations pertaining to the continuous steelmaking process discussed in Section 3.3.4 revealed that the slag design requires meeting several significant and often conflicting demands on the physical and chemical properties of the slag. For example, on one hand, the slag should be fairly oxidizing, to satisfy decarburization, whereas on the other hand, slags with high FeO tend to be aggressive toward the refractory. Also, the design relies on slag foaming for shielding the electric arc, but this foaming should be achieved with virtually zero oxygen injection, as otherwise the FeO would be driven up excessively, causing refractory corrosion. The engineering of an appropriate slag was thus vital to the viability of the proposed continuous steelmaking technology. The slag optimization exercise consisted of four major phases that are discussed in this section. This exercise may be considered as an example of a classical approach to employing process metallurgy principles in technology development.

3.3.5.1. Thermodynamic Evaluation

A thermodynamic evaluation was performed with the objective of calculating the minimum FeO required for sufficient decarburization. In order to reduce slag corrosiveness, FeO has to be maintained at the lowest possible concentration for a given steel carbon level. The carbon level of steel and tap temperature are primarily decided by product specifications and downstream processing steps (i.e., not related to slag). Therefore, slag chemistry, particularly the dependence of FeO requirement (for a given C%) on basicity, and MgO content are of interest.

Turkdogan [63] compiled a set of experimental data on the activity coefficient of FeO in slags with a wide range of compositions. The results, presented in Figure 3.3.19, indicate that there is a strong correlation between the activity coefficient (with pure liquid FeO as the standard state) and the slag basicity, expressed as $B = (\%CaO + 1.4\%MgO)/(\%SiO_2 + 0.84\%P_2O_5)$. The activity coefficient, γ_{FeO}, peaks at $B = 1.8$, implying that there exists an optimum basicity at which FeO concentration can be minimized. For example, increasing the basicity of slag from 1.0 to 1.8, the FeO content of slag may be reduced to half for the same carbon content in steel. The practical implication is that an optimum basicity for operating under minimum FeO concentration is between 1.8 and 2.2.

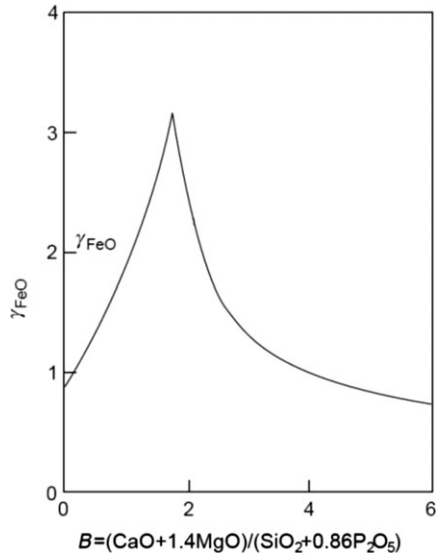


Figure 3.3.19 Dependence of FeO activity on slag basicity at 1600 °C [63].

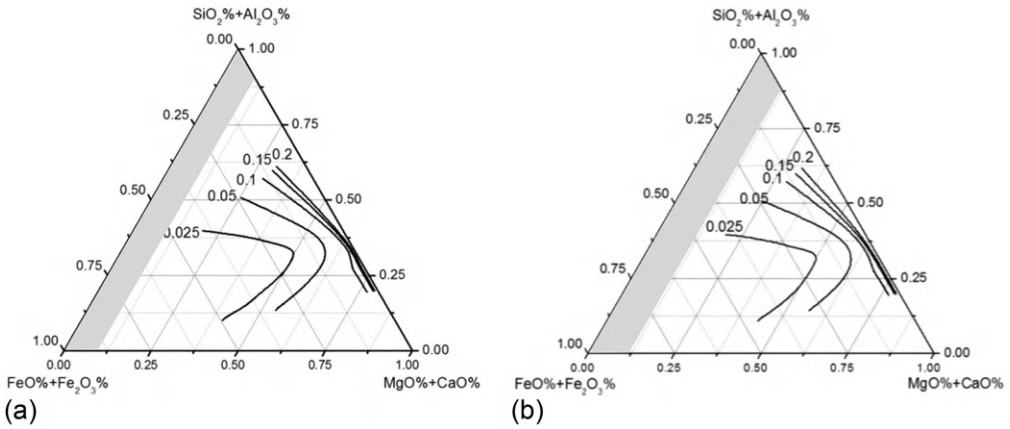


Figure 3.3.20 Isocarbon curves in SiO_2–Al_2O_3–CaO–MgO–FeO system with (a) MgO = 8% and (b) MgO = 12%.

A more detailed analysis was carried out on the slag–metal equilibrium using the FactSage™ thermodynamic modeling package [64,65]. The calculations involved determination of the carbon content of steel in equilibrium with FeO–CaO–MgO–SiO_2–Al_2O_3 slags of various basicity, and MgO and FeO concentrations. The results were presented as isocarbon curves on a ternary slag phase diagram. As seen in such diagrams, Figure 3.3.20, the required FeO content for a specific C% depends on the slag composition and goes through a minimum at basicity

($V = [CaO + MgO]/[SiO_2 + Al_2O_3]$) of 1.5–2.0, indicating a large activity coefficient of FeO in this range. This is consistent with the data presented in Figure 3.3.19, noting the small difference is because of the slightly different definition of basicity in the two works.

Based on this analysis, the basicity of slag should be maintained around 1.5–2.0 for minimizing the FeO content. In addition, this V ratio is lower than the typical basicity of the conventional EAFs (2.5–3.5) and thus will result in smaller slag volume and lower consumption of fluxes such as lime or dolomite. Additional benefits of operating in this low basicity regime include reduced amount of FeO in the slag (due to smaller slag volume) and higher activity coefficient, resulting in higher iron yield and also lower energy loss associated with the slag thermal energy. It however must be noted that a higher MgO concentration is required to saturate low basicity slags with MW and/or C_2S, as depicted in Figure 3.3.17. As discussed earlier, slight oversaturation to form solid particles is beneficial for foaming, with MW being the preferred solid as it serves two purposes: improved foaming and reduced slag affinity for the MgO-based refractories.

In the basicity range of 1.5–2.0 and for a typical low carbon steel with 0.05–0.1% C, the FeO content of slag at equilibrium is 3–8% (Figure 3.3.20). In steelmaking, higher FeO concentrations are however required to maintain a driving force for the decarburization reaction. Also, due to the limited mixing of the bath in electric furnaces and short residence time, the equilibrium condition is far from being reached. It is believed that, due to the expected longer residence time in the proposed CRISP furnace, the required FeO content is lower than that in the conventional EAF practices. A kinetic study as discussed in the next section provides the actual minimum FeO and the refining time required for sufficient decarburization.

3.3.5.2. Bench-Scale Experiments

It was discussed in Section 3.3.4.1.2 that decarburization of DRI takes place in several steps. The majority of carbon is removed rapidly within the first 30 s upon immersion of DRI in slag. The final carbon content of metal is however controlled by a slower reaction step that involves decarburization through slag. It is this period that determines the practical minimum FeO requirement in slag for sufficient decarburization within the given processing times. Bench-scale experiments were useful in determining this critical FeO level and also the rate and mechanism of the reactions. In these experiments, 500 g of commercial DRI (composition provided in Table 3.3.4) was melted and subjected to an oxidizing slag.

A wide range of slag composition has been chosen in which the initial FeO content is from 20% to 34% (20%, 27%, and 34%) and for each FeO concentration, the basicity (V ratio) is maintained at three levels, 1.5, 2.0, and 2.5. MgO concentration is approximately 1–2% above the solubility limit for all slags.

Table 3.3.4 Chemical Composition (wt%) of the DRI Used in Bench-Scale Experiments [66]

Fe_{tot}	92.0	P	0.025
Fe_{met}	87.4	SiO_2	2.15
Metallization	95.0	Al_2O_3	0.50
C	2.2	CaO	0.71
S	0.006	MgO	0.39

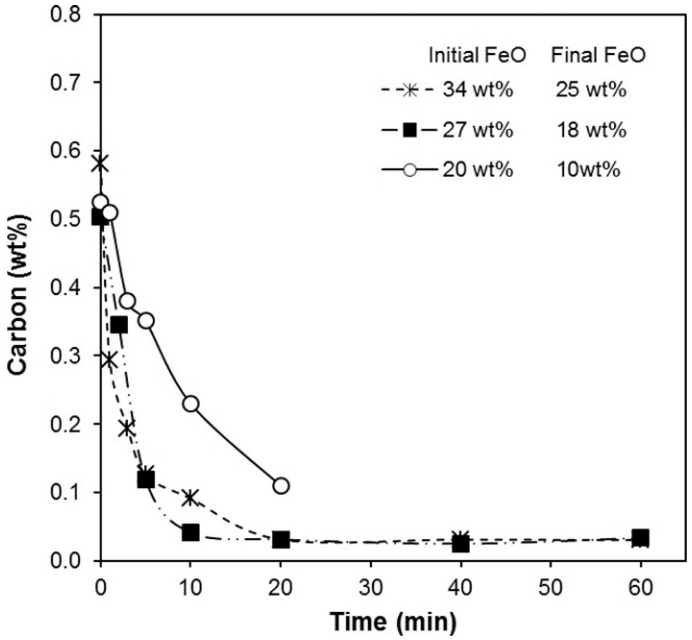


Figure 3.3.21 Decarburization of DRI melt with slags ($V = 1.5$, $T = 1600$ °C).

Figure 3.3.21 presents the variations with time of C% for various FeO concentrations for slags with basicity of 1.5. The initial carbon is at 0.5–0.6 wt%, lower than the amount initially present in the DRI. The reduction in the carbon upon melting is because of the reaction with DRI residual FeO. On addition of slag, as seen, C% falls to 0.1% or lower within 20 min for all three initial FeO concentrations. The decarburization rate increases with the increase in initial FeO content. Initially, carbon content drops rapidly as the decarburization is very fast (primary decarburization stage). After the transition, decarburization becomes extremely slow (secondary decarburization stage). Therefore, instead of equilibrium carbon content, this quasi-steady C% could be the final carbon content in a real steelmaking practice, as the residence time cannot be long enough to achieve equilibrium. As seen, the quasi-steady carbon content increases with decreasing FeO content

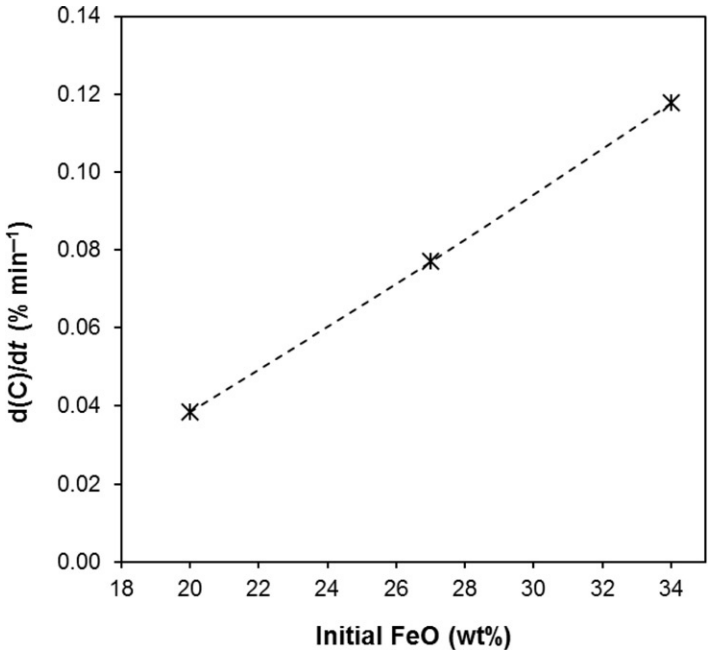


Figure 3.3.22 Decarburization rate as a function of initial FeO content of slag ($V = 1.5$, $T = 1600\ ^\circ C$).

in the slag. It is further noticed that, for a batch containing 0.1 wt% C, the FeO of the slag phase is 10%. This is significantly higher than the 1–3% FeO determined based on the thermodynamic evaluation, which is anticipated as in a commercial-scale operation, an "active" slag bath that drives the decarburization must contain higher FeO levels than equilibrium.

The results for $V = 2.0$ and 2.5 followed similar trends but the decarburization rates and the steady-state carbon contents were different. In all the experiments, the majority of bath carbon was removed early after addition of slag. The rate of decarburization thus can be obtained from the slopes of the curves in the first few sampling intervals. These "apparent" decarburization rates were obtained and plotted against the initial FeO content (Figure 3.3.22), where a linear dependence was observed. Considering a flat interface between slag and metal, and the mass of metal, the rate constant of decarburization is obtained that varies between 6.2×10^{-7} and 9.9×10^{-7} mol/(cm^2 s pct FeO) depending on the basicity.

It is generally agreed that the reaction between FeO in the slag and solid or dissolved carbon in metal occurs via an intermediate gas film. At the slag–gas interface, FeO is reduced by CO, to produce CO_2. The CO_2 then reacts with carbon at the gas–metal interface to regenerate CO through the Boudouard reaction. This reaction path suggests that there could be four elementary steps involved in the overall reaction: (a) FeO mass

Table 3.3.5 Rate Constants for Possible Rate-Limiting Steps [67]

Reaction Step	Rate Constant mol/(cm^2 s pct FeO)
(a) Mass transfer of FeO	4×10^{-7} to 4×10^{-6}
(b) Gas–slag reaction	2.6×10^{-5}
(c) Gas diffusion	5×10^{-7} to 5×10^{-6}
(d) Gas–metal reaction	2.5×10^{-6}

transfer in the slag, (b) interfacial gas–slag reaction, (c) diffusion of CO and CO_2 in the gas halo, and (d) Boudouard reaction. The rate constants for each of the four possible rate-limiting steps given by Min and Fruehan [67] are summarized in Table 3.3.5.

Min and Fruehan suggested a mixed control model consisting of CO_2 transport in the gas phase and FeO transport in the slag phase in the case that the sulfur content in the melt is lower than 0.01%, which is the case in this study. The rate constants for these two mechanisms are given in Table 3.3.5. The calculated rate constant values of the DRI experiments by Li *et al.* [66] fall within the rate constant range of these two mechanisms. However, their experiments were performed at higher temperatures (1600 °C compared to 1400 °C in Min and Fruehan's study). It is expected that the rates of chemical reactions, i.e., steps (b) and (d) are higher at this temperature than those presented in Table 3.3.5. Therefore, the measured rate constants (6.2×10^{-7} to 9.9×10^{-7}) may be too small for a "reaction control" mechanism, and mass transfer is the more likely rate-limiting step. Also, the dependence of the rate on FeO content shows that the gas-phase mass transport cannot likely be the rate-determining step as otherwise it should not be related to the slag chemistry. As a result, FeO mass transport in the slag is the most likely rate-determining step of the overall reaction. The practical implication of this is that decarburization of DRI should take place as much as possible while the pellet is sinking in slag and before it reaches the metal bath as otherwise mass transfer of iron oxide from bulk to the FeO-depleted region of slag–metal interface will play a hindering role in decarburization. In other words, the pellet travel time through the slag layer should be adequate so that its carbon content approaches the desired levels. This can be achieved by maintaining a thick slag layer and/or inducing slag foaming. Slag foaming will have the added benefit of agitating the bath, diminishing the FeO gradient, hence accelerating the decarburization.

3.3.5.3. Pilot Trials

Based on the theoretical and experimental studies discussed above, two sets of pilot trials were carried out in an AC 3-electrode EAF with rated power of 3 MW, inner pot diameter of 2.1 m, and heat size of 8 tons. The objectives of these trials were the following:

1. To narrow down the optimum slag composition and define an operating window for commercial-scale testing of the technology.
2. To determine the relationship between slag FeO and steel carbon in a semi-industrial setting, pertaining to this continuous operation. Of particular interest was to achieve the desired carbon levels with the minimum FeO possible.
3. To practice extended operation of EAF in continuous mode during a several-day campaign.
4. To examine the stability of the refractory, as well as the foaming behavior of slag.
5. To investigate the responsiveness of the process to different product specification, i.e., how the process may be manipulated to produce steel with various carbon levels.

Considering the second objective, it should be noted that due to the longer than normal residence time of metal pellets and slag in the proposed technology, it is anticipated that a certain degree of steel refining can be achieved under a low-intensity refining regime. That is, to avoid intense refining typically practiced in the conventional EAFs for increasing productivity. To achieve this, oxygen injection was ruled out; instead, addition of solid oxidants (iron ore, pellet, or mill scale) was practiced to achieve the desired slag FeO levels.

The pilot trials consisted of two phases. The first campaign was undertaken, aiming to define an optimum operating window for the slag composition. The second set of trials was aimed at satisfying objectives 2–5, with a fewer number of slag compositions.

3.3.5.3.1 Phase I

The slag compositions in Table 3.3.6 were selected for testing in this phase. Three V ratios and three FeO levels were chosen to be examined for understanding the effects of basicity and FeO content on the decarburization rate and slag foaming.

Table 3.3.6 The Selected Slag Compositions for the First Pilot Trials

Test #	FeO (wt%)	B_4	MgO (wt%)
S_1	25	2.0	12.0
S_2	18	2.0	12.0
S_3	10	2.0	12.0
S_4	25	1.5	14.0
S_5	18	1.5	14.0
S_6	10	1.5	14.0
S_7	25	2.5	8.5
S_8	18	2.5	8.5
S_9	10	2.5	8.5

In order to determine the slag chemistry for these trials, the following considerations were made:

1. The V ratio, slag basicity, remains between 1.5 and 2.5. Below 1.5, the refractory corrosion rate would be severely high or a very high concentration of MgO is required to saturate the slag. For example, as seen in Figure 3.3.18, to saturate the slag with MW, a decrease in CaO/SiO_2 ratio from 2 to 1 will result in an increase in MgO requirement from ~9% to ~20%. On the other hand, a slag with $V > 2.5$ is considered highly basic. Such slag that also contains high concentration of MgO will be too viscous (crusty) to support good foaming, also its removal from the intended stationary furnace will be difficult. These considerations determined the upper and lower limits of basicity. This range was also more favorable as FeO has the highest activity within this range (Figures 3.3.19 and 3.3.20), indicating that a lower concentration of FeO is required for a certain degree of decarburization.
2. The MgO content of all the slags was maintained 1–2% above their saturation concentration. This was to (a) ensure a reduced affinity of slag for refractory, thus minimizing chemical attack and (b) sustain a good slag foam, according to the discussions in Section 3.3.4.2.
3. The lower level of FeO (10%) was selected based on the bench-scale experiments, showing that for 0.1% C, just over 10% FeO is required. Higher FeO concentrations may be needed due to the specific kinetic conditions pertaining to this larger furnace. The upper level of FeO (25%) was based on the need for decarburization rate on one side and the limitation on slag corrosiveness on the other side. Slags with FeO above 25% cause severe damage to the refractory.

Each test began by charging DRI together with required slag forming materials to a steel heel of 2 tons from the previous heat. The average composition of DRI is presented in Table 3.3.7. For each heat, a mixture of flux materials was prepared to form the slag of the target composition. The individual materials used to create a given mixture were lime, dolomitic lime, and mill scale. The relative amount of each material was calculated using an optimization program that minimizes the slag weight while maintaining the desired composition. The gangue constituents introduced to the furnace with the DRI were taken into consideration in these calculations.

The materials were fed continuously from an overhead feed system, at the rate of 3000 kg/h. The furnace power was set at 2 MW and the feed rate was adjusted to maintain a liquid steel bath temperature of 1600 °C. The furnace power density was 500–600 kW/m^2 of hearth area, which is substantially lower than the typical EAF values and is close to the power density rating for the CRISP furnace. When the steel level in the bath reached the maximum capacity, feeding was stopped and the bath was held at the temperature for approximately 15 min to determine whether the decarburizing reaction would continue as the slag FeO and bath carbon ratio approach steady state. Steel and slag samples were taken every 30 min for LECO and XRF analysis, respectively.

Table 3.3.7 DRI Composition in the Pilot Trials

Total Fe	91.0%
Metallic Fe	86.0%
Metallization	94.5%
C	2.0%
FeO	6.43%
SiO_2	2.66%
Al_2O_3	0.70%
CaO	1.06%
MgO	0.64%
TiO_2	0.19%
MnO	0.09%
Na_2O	0.10%
K_2O	0.03%
P_2O_5	0.05%
V_2O_5	0.04%

Oxygen concentration of steel and temperature were also measured every 30 min using dip-in probes. DRI feeding and power were stopped before sampling and *in situ* measurements. At the end of each test, running for ~2–3 h, the slag was skimmed off, metal was tapped, and heel of ~2 tons was retained in the furnace for the subsequent heat.

In the course of the 4 days of trials, 14 tests were conducted. Table 3.3.8 lists actual slag compositions for all the examined conditions. As can be seen, deviations exist between the target and actual slag compositions, which are because of difficulty in process control, especially oxidation of metal due to air ingress, as well as fluctuations in the feed composition. The control of FeO was particularly challenging as each heat (except those in day 4) began with a bare metal surface to examine a new slag mix. This caused excessive FeO levels in some tests. In day 4 (heats H_{10}–H_{14}), the slag was not skimmed off and was left to flow out of the furnace as its volume increased. This allowed better protection of metal bath. The main objective of this last day test was to explore the relationship between slag FeO and metal carbon, in a regime where the contact is extended.

Figure 3.3.23 presents the variations with time of carbon input rate and decarburization rate for these tests. As seen, the decarburization rate generally follows the same trend of carbon input rate (from the DRI). The decarburization rate is 5–10 kg/h higher than

Table 3.3.8 Test Results in the First Pilot Trials [68]

Test #	C%	FeO%		*V* ratio		MgO%		Slag	Slag
		Target	Actual	Target	Actual	Target	Actual	Fluidity	Foaming
Day 1/H_1	0.065–0.08	25	16.8–22.2	2.0	1.8–1.9	12	11.1–14.3	Viscous	Good
Day 1/H_2	0.03–0.1	18	17.6–32.9	2.0	1.6–2.0	12	10.6–14.5	Creamy	Good
Day 1/H_3	0.05–0.077	10	29.6–32.0	2.0	1.9–2.0	12	12.8–16.0	Watery	Poor
Day 2/H_4	0.054–0.11	25	13.5–18.4	1.5	1.4–1.6	14	11.1–16.8	Creamy	Good
Day 2/H_5	0.056–0.084	18	16.8–20.7	1.5	1.5–1.6	14	14.6–15.9	Thinner	Moderate
Day 2/H_6	0.032–0.082	10	16.9–27.2	1.5	1.4–1.6	14	15.2–16.9	Creamy	Good
Day 3/H_7	0.037–0.059	10	28.5–29.7	2.5	1.7–2.2	8.5	6.8–8.6	Watery	Poor
Day 3/H_8	0.025–0.062	18	28.7–33.8	2.5	1.9–2.0	8.5	8.2–10.0	Watery	Poor
Day 3/H_9	0.025–0.046	25	32.5–38.9	2.5	2.1–2.6	8.5	4.9–7.0	Watery	Very poor
Day 4/H_{10}	0.03–0.08	Var[a]	16.1–22.9	2.0	1.7–1.8	12	7.6–9.9	Creamy	Excellent
Day 4/H_{11}	0.07–0.10	Var[a]	14.6–19.5	2.0	1.7–1.8	12	10.4–11.5	Creamy	Excellent
Day 4/H_{12}	0.09–0.15	Var[a]	11.1–15.7	2.0	1.7–1.8	12	12.4–13.6	Creamy	Excellent
Day 4/H_{13}	0.16–0.26	Var[a]	8.5–10	1.5	1.6	14	13.5–15.0	Moderate	Good
Day 4/H_{14}	0.273	Var[a]	7.34	1.5	1.6	14	13.1	Moderate	Good

[a]Attempt was to gradually increase the bath C by lowering FeO level, in order to establish a relationship between the two.

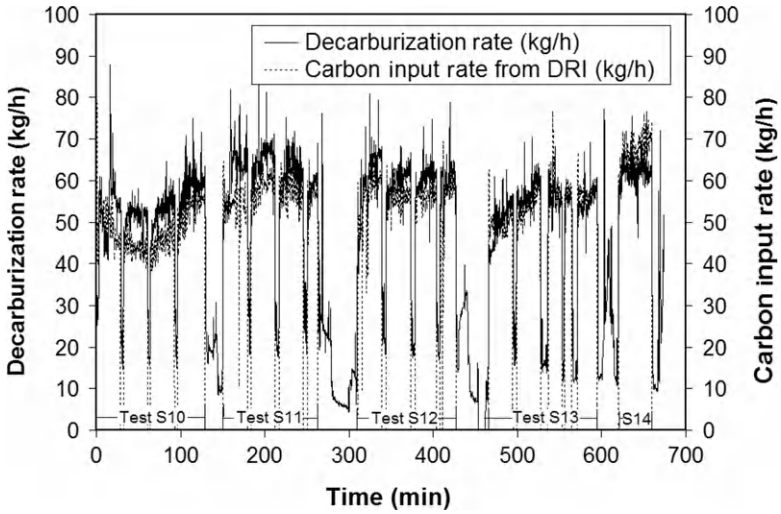


Figure 3.3.23 Carbon input rate and decarburization rate for the last day tests.

the input rate in the first three tests, which is about the same as the consumption rate of graphite electrodes in the furnace. In the last two heats, the decarburization rate is very close to the carbon input rate because the final carbon content in the liquid steel is much higher due to lower FeO contents, i.e., more carbon stayed in the liquid steel instead of leaving the furnace as off-gas. Figure 3.3.23 also indicates that the decarburization was completed in a very short time (less than 1 min) after DRI was fed so that the decarburization rate could follow the trend of carbon input rate. As discussed earlier, the decarburization is a multistep process. The first step, the reduction of FeO inside DRI pellets, is in part controlled by heat transfer and should complete in 20–30 s. Since in DRI the FeO content was 6.43% and carbon was 2.0%, 1.07% of carbon is consumed in this step for the reduction of FeO. With final carbon being 0.1%, during the second step another 0.83% of the DRI carbon is removed by the FeO from slag. Since the entire decarburization was completed in a short period, the second step decarburization should have been quick, indicating that melting of DRI pellets occurred as it was fed, without buildup of unmelted DRI ("pellet bergs") in the furnace. Buildup of unmelted DRI floating on slag was observed in one occasion when the feed rate exceeded 3200 kg/h (Figure 3.3.24).

Figure 3.3.23 shows that decarburization rate curves always follow those of the carbon input rate despite the fact that FeO content in the slag varied. It reveals that the effect of FeO content on the decarburization rate is not so significant to be measurable in the tests. This points to heat transfer being the primary controlling mechanism of the rate of decarburization. Also, noting that decarburization was achieved entirely by dissolved FeO, without any gaseous oxygen injection, it can be considered that dissolution of iron oxide in the slag was fast enough to not limit decarburization.



Figure 3.3.24 Buildup of unmelted DRI pellet.

Visual observations were made to characterize the slag foaming conditions qualitatively. Several measurements on collapse of slag foam when the feeding stopped and power was turned off indicated that for slags showing "poor" foaming, the collapse took place within 30 s. For slags with moderate foaming, this time was 30–60 s, whereas the ones with "good" and "excellent" foaming showed very stable foam that lasted over 1 min, sometimes up to 2 min. As shown in Table 3.3.8, the FeO content has a strong effect on the foaming properties of slags. The slag was too fluid (watery) in tests H_2, H_7, H_8, and H_9 because FeO content was between 28.5% and 38.9% even if MgO content was up to 16%. The best slag foaming appeared in tests H_{10}, H_{11}, and H_{12} when FeO was between 11.1% and 22.9%, basicity 1.7–1.8, and MgO 7.6–13.6. No refractory loss was observed under these conditions. In several tests with excessive FeO (e.g., H_7–H_9), the slagline was visibly damaged. However, with better control of FeO and MgO in subsequent runs, the damage was repaired, by presumably deposition of MW rich slag.

The measured carbon content in the liquid steel increased with decreasing FeO content in the slag as shown in Table 3.3.8. This can be explained by the fact that the transition carbon content increases with the decreasing FeO content in the slag. The carbon content in the melt represents the transition carbon content described in Section 3.3.5.2.

3.3.5.3.2 Phase II

3.3.5.3.2.1 Trials

The Phase II pilot testing was a logical extension of the Phase I trials. Having established workable slag compositions in the first trials, the Phase II trials were expected to examine the feasibility of continuous steelmaking using DRI as the metallic charge. The objectives were to (a) obtain predefined carbon levels in the range 0.04–0.1 wt% with minimal or no use of gaseous oxygen, (b) prove stability and controllability of the process for a minimum 4 days of operation, (c) practice a slag compatible with the refractory, i.e.,

minimum refractory wear, and (d) sustain good slag foaming. The target conditions based on the previous slag engineering works were defined as following:

- Basicity: 2.0
- Bath carbon content: three levels (0.04, 0.06, 0.1 wt%)
- FeO of slag: as low as possible for each carbon level
- MgO of slag: slightly oversaturated (1–2%) [55,69] for the basicity and given FeO
- Steel bath temperature: 1600 °C

The raw materials used for the trials were DRI (average composition similar to that in Phase I), fluxes (lime, dolomite), and solid oxidizers (iron oxide, as mill scale and iron ore pellets). The ratio of materials in the mix except the oxidizer was calculated using an optimization program that minimizes the slag weight based on the constraints (basicity and MgO). The proportion of iron oxide in the mix was adjusted by an iterative procedure, to achieve the minimum FeO required for specified carbon contents. The raw materials were premixed and fed to a bin located above the furnace. The furnace power was set at 2.0 MW and the mix feed rate was manipulated around 3000 kg/h using a vibratory feeder, to maintain a bath temperature of 1600 °C. Feeding stopped only for periodical tapping of steel and slag that took less than 5 min each time. Steel and slag samples were taken every hour. The steel samples were analyzed for carbon by LECO and the slag composition was determined by XRF analysis. Oxygen activity and temperature were also measured using oxygen and temperature probes every hour. DRI feeding was continued during sampling and temperature measurement. The trials were continued for 115 h in a 5-day campaign. A total of 254 tons of DRI was melted during this campaign and 52 heats were made, producing 243 tons of steel.

The variations of slag FeO and melt C during this continuous steelmaking test are shown in Figure 3.3.25. The DRI was first melted and allowed to reach its steady-state carbon level without any addition of oxidant. As seen, the carbon increases to a relatively steady-state value of 0.5–0.6 wt% in about 14 h. Due to accumulation of slag and inherent foaming by melting of DRI, air ingress to the steel bath is reduced at this stage, and the carbon concentration observed may be considered as the bath carbon associated with natural melting of DRI. Similar carbon levels were obtained in the laboratory studies by melting of DRI under argon purging. Following this step, addition of iron oxide in the form of mill scale began by mixing the material with other slag forming oxides. Adding iron oxide at a constant rate, it took about 15 h to lower the carbon to the desired level (0.1%). Faster decarburization could be achieved by increasing the oxide addition rate, but it was deliberately kept low to avoid exceeding the minimum FeO required. As seen in Table 3.3.9, for this carbon level, the slag FeO has to remain within a range of 14–20%, with an average of 16%. As expected, it was noted that there is a strong inverse relationship between the steel carbon and the slag FeO. This feature of the process will be discussed further in the section on FeO–C relation. The target carbon of 0.1% was maintained for about 33 h (second period), indicating easy control and stability of the

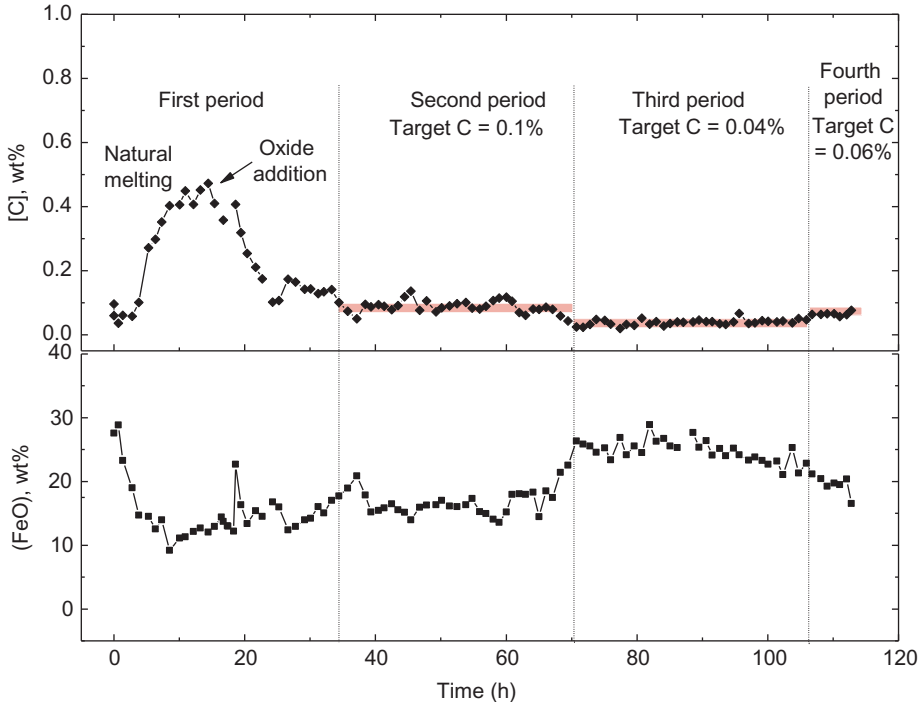


Figure 3.3.25 Variation of carbon and FeO content during the campaign [70].

process. After the second period, melt carbon content was varied to 0.04% and 0.06%, by changing the rate of iron oxide addition. Table 3.3.9 presents the slag parameters and their variations during these trials.

3.3.5.3.2.2 State of Reactions Between Slag and Metal

In the course of the trials, particularly in the first period, a relatively wide range of carbon concentration was obtained. At the same time, it was found that the carbon and FeO follow a mirror image of each other versus time, i.e., one is inversely related to the other. This relationship can be clearly seen in Figure 3.3.26, where all data obtained for carbon and FeO are presented in a single graph. The results are also compared with the data obtained in the first trials as well as typical conditions of the conventional steelmaking processes.

In the range of carbon concentration from 0.02% to 0.2%, the following empirical correlation between FeO and C is obtained:

$$\%\mathrm{FeO} = -8.2 \ln [\%\mathrm{C}] - 2.644 R^2 = 0.8 \tag{3.3.14}$$

Table 3.3.9 Distribution of Carbon and FeO in Samples Taken During Periods 2–4 of Continuous Operation

Parameter	Target	Actual			
		Min	Max	Avg	STD
Second period—target C of 0.1%					
C	0.1 wt%	0.050	0.136	0.090	0.018
MgO	12 wt%	8.90	13.13	10.74	1.096
V ratio	2.0	1.72	1.98	1.850	0.072
FeO	Lowest possible	13.6	20.9	16.45	1.65
Third period—target C of 0.04%					
C	0.04 wt%	0.020	0.067	0.038	0.009
MgO	14 wt%	11.0	17.13	13.89	1.480
V ratio	2.0	1.76	2.31	2.06	0.13
FeO	Lowest possible	21.07	28.92	24.92	1.63
Fourth period—target C of 0.06%					
C	0.06 wt%	0.047	0.076	0.061	0.009
MgO	14 wt%	12.62	18.06	14.73	1.63
V ratio	2.0	1.99	2.22	2.08	0.08
FeO	Lowest possible	16.53	22.83	20.13	1.74

The relationship between FeO and C concentrations can be theoretically established through Reaction (3.3.5). In equilibrium state, this reaction yields a relationship of the form presented below:

$$K = \frac{p_{CO}}{[\%C]a_{FeO}} \tag{3.3.15}$$

With the equilibrium constant being [63]

$$\log K = -\frac{5730}{T} + 5.096 \tag{3.3.16}$$

At 1600 °C, we obtain $K = 108.8$. An estimation of the CO gas pressure can be made as following.

Supposing that CO gas is released at the slag–metal interface, its pressure has to be just over the static pressure of the slag layer. For a steelmaking slags, the density may be estimated based on the correlation by Mills and Keene [72]:

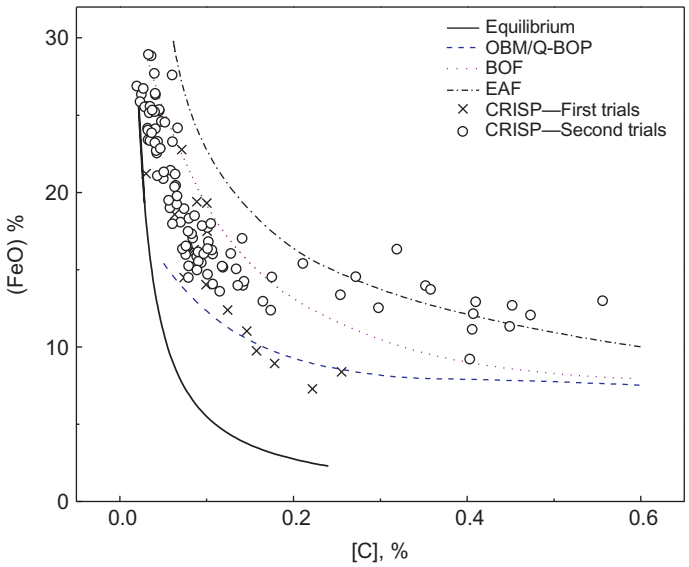


Figure 3.3.26 Relationship between slag FeO and steel C [63,71].

$$p\left(\mathrm{g\ cm^{-3}}\right) = 2.46 + 0.018\,(\%\mathrm{FeO} + \%\mathrm{MnO}) \tag{3.3.17}$$

For slags containing 10–25% FeO, the density is approximately 2.6–2.9 g/cm^3. For a typical slag depth of 0.4 m, the minimum partial pressure of CO gas is 1.2 atm. Equation (3.3.15) will yield:

$$[\%\mathrm{C}]\,a_{\mathrm{FeO}} = 0.011 \tag{3.3.18}$$

Using $\gamma_{\mathrm{FeO}} \cong 2.5$ for a slag with $V = 2.0$ (based on previous data on activity coefficient of iron), one obtains $a_{\mathrm{FeO}} = 2.5X_{\mathrm{FeO}}$ with X_{FeO} being the mole fraction of FeO in slag. For a slags with 10–15% MgO, 10–25% FeO, and basicity of 2.0, $X_{\mathrm{FeO}} \cong 0.008\,(\%\mathrm{FeO})$. Therefore, the equilibrium relationship between the metal C and slag FeO is established as:

$$[\%\mathrm{C}] \times (\%\mathrm{FeO}) = 0.55 \tag{3.3.19}$$

This is shown by the solid line labeled "equilibrium" in Figure 3.3.26. As shown, the FeO–C curve for these trials is generally above the equilibrium data but approaches them at low carbon levels. The curve lies between those for BOF and Q-BOP, and below that of typical EAF operations, indicating that the desired carbon content can be obtained with a less oxidizing slag. Under the operating conditions of the pilot EAF (bath size of 8 tons, heat size of ~2 tons), the average residence time of the metal in the furnace is approximately 4 h, that is much longer than the conventional EAFs (0.5–1.0 h). On

the other hand, the mixing of slag and metal in the continuous operation is very limited compared to well-stirred Q-BOP reactor. Therefore, the observed relationship is expected, as both mixing and residence time greatly influence the extent of reactions, with slag–metal mixing playing a greater role. Compared to the conventional EAFs, the lower slag FeO for a given C presents several advantages: (a) reduced affinity of slag toward refractory, i.e., lower refractory corrosion, (b) higher yield of iron, and (c) smaller slag volume (reduced energy loss, slag handling works, etc.).

During the trials, oxygen content of the steel was also measured. The relationship between the dissolved oxygen and carbon of steel bath in the trials is compared with BOF and Q-BOP typical trends as well as the equilibrium values in Figure 3.3.27. In the ternary Fe–O–C system, the equilibrium relationship between carbon and oxygen concentrations at 1600 °C can be established as following, using the interaction coefficients of Sigworth and Elliott [73]:

$$\begin{aligned}\log[\text{ppmO}] + \log[\%\text{C}] + 0.09[\%\text{C}] - 2.97 \times 10^{-5}[\text{ppmO}] \\ = 1.322 + \log(p\text{CO})\end{aligned} \tag{3.3.20}$$

When comparing the results of the trials with the equilibrium values (Figure 3.3.27), it can be seen that the data generated from the pilot works demonstrated an

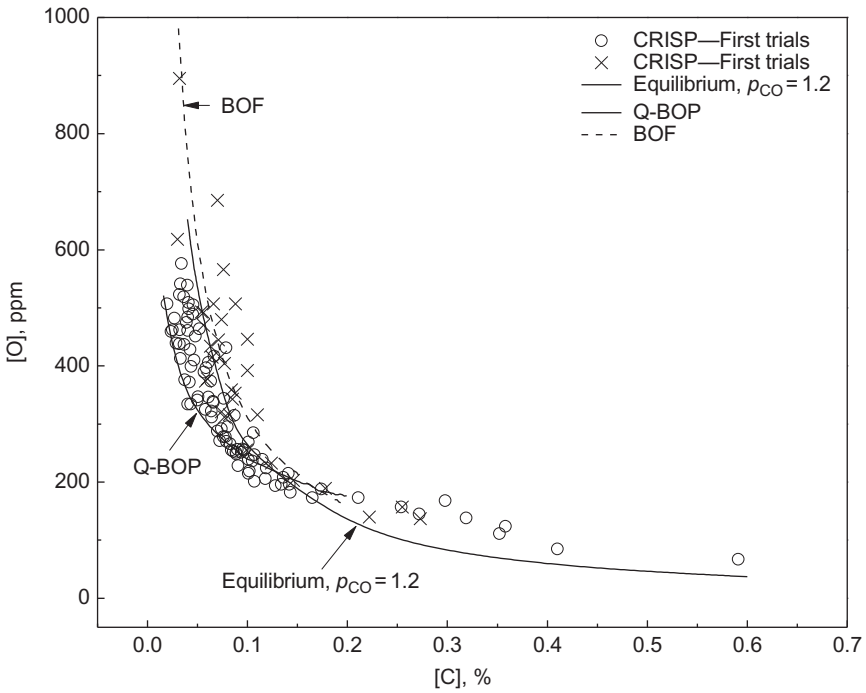


Figure 3.3.27 Relationship between dissolved oxygen and carbon in steel.

oxygen–carbon relationship close to the equilibrium state with pressure of CO about 1.2 atm. This is consistent with the CO gas pressure calculated earlier.

The figure also shows that C–O relation is closer to the state of reactions in Q-BOP process, i.e., equilibrium at lower pressure of CO gas. It has been discussed [63] that, at low carbon contents, the partial pressure of CO is smaller in Q-BOP than in BOP, due to higher fraction of hydrogen (in Q-BOP) than argon (in BOP) in the gas bubbles. The lower pressure of CO in the continuous steelmaking trials can be attributed to the fact that decarburization of molten DRI takes place primarily in the slag phase, where the static pressure is smaller than inside a deep metal bath. Thus, the CO bubbles at a lower pressure.

3.3.5.3.2.3 Slag Foaming and Steel Nitrogen Content

Good slag foaming was achieved throughout the trials, with foam collapse time over 100 s when the power was turned off for steel tapping. The foam covered the electrodes up to the slag door level. The slag flowed out of the furnace when its level rose above the slag door.

In addition to reduced electric and acoustic noise, lowering electrical energy and electrode consumptions, and improved refractory stability, foaming is known to result in steel with lower nitrogen content. The steel nitrogen was measured for 33 samples in the pilot trials and the results are presented in Figure 3.3.28. As seen, 85% of the steel samples have below 20% ppm N, with 63% below 10 ppm. In an examination of effect of DRI on nitrogen content of steel, Anghelina *et al.* [17] reported that, in a commercial EAF,

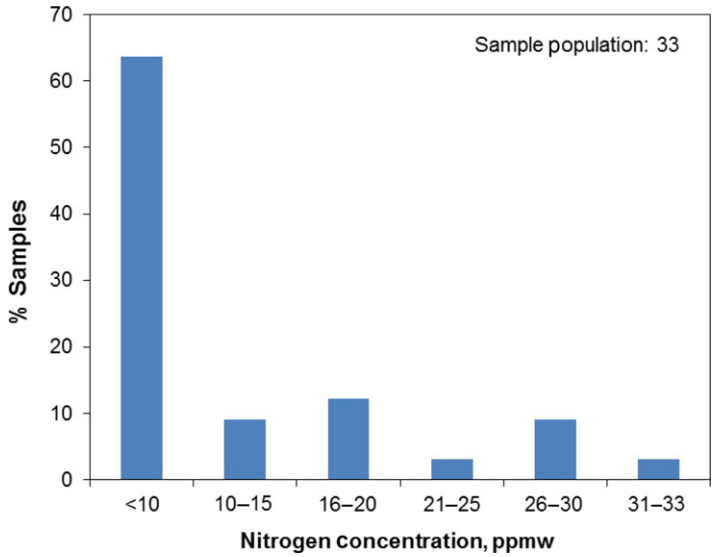


Figure 3.3.28 Distribution of nitrogen concentration in various steel samples.

the nitrogen dropped from 68 to 20 ppm, when the charge was changed from 100% scrap to 100% DRI. The positive effect of DRI on reducing nitrogen has been confirmed by other authors [16,18,36], and several mechanisms have been proposed. For example, Golstein *et al.* [36] concluded that the reduction in nitrogen level is primarily because of the dilution effect of low-nitrogen DRI. Their X-ray fluoroscopy observations revealed that the CO gas from the reduction of residual FeO within pellet is released in the slag layer rather than the metal bath, hence little role in nitrogen removal from steel. Anghelina *et al.* [17], on the other hand, have discussed that it is the CO gas bubble that flushes out the nitrogen. Based on the X-ray fluoroscopy observations presented earlier, DRI pellets melt and lose their carbon while sinking in the slag and also when they rest at the slag–metal interface. They will have little effect on nitrogen pick up from the bath depth. On the other hand, a larger effect of DRI use is sustaining a slag foam. DRI may be one of the best materials for slag foaming as it presents an intimate mix of FeO and C in the place where gas generation should take place, i.e., slag. The inherent foaming associated with DRI–slag reactions diminishes the dissolution of nitrogen into the metal by creating a thick slag layer that covers the electric arc. A submerged arc results in reduced nitrogen dissociation, while gas release within slag generates a positive pressure at the slag surface, both of which reduce the exposure of metal to the atmosphere. Therefore, it may be concluded that the low-nitrogen levels associated with the use of DRI are because of two mechanisms (a) diluting the steel with a low-nitrogen feed and (b) reducing the dissociation and absorption of nitrogen to steel, caused by a thicker slag layer and slag foaming. The conditions that promote faster reaction of DRI–slag are therefore beneficial for steel quality in addition to the obvious advantage of higher productivity.

3.3.5.3.2.4 Refractory Stability

An evaluation of the refractory health during the trials was performed, as stability of refractory during extended runs is a determining factor in viability of the technology. The profile of the EAF lining before and after the campaign was measured. Figure 3.3.29 depicts the furnace wall profile at three stages: before the first trials when the furnace was just re-bricked, between the two trials, and after the second trial. The average variations in the thickness of the refractory for each section are also provided in Table 3.3.10. The values are in mm with positive numbers showing deposition on the wall and negative numbers representing wear. From Figure 3.3.29 and Table 3.3.10, along with the observations made during the trials, the conclusions were drawn.

- The overall effect of the first set of trials was small deposition on the refractory. However, visual observations made during the trials revealed that this overall effect is in fact the result of deposition–wear cycles depending on the slag chemistry. In some instances when the FeO content increased to about 30 wt pct, the slagline wear was clearly seen whereas in the subsequent heats with lower FeO and high MgO,

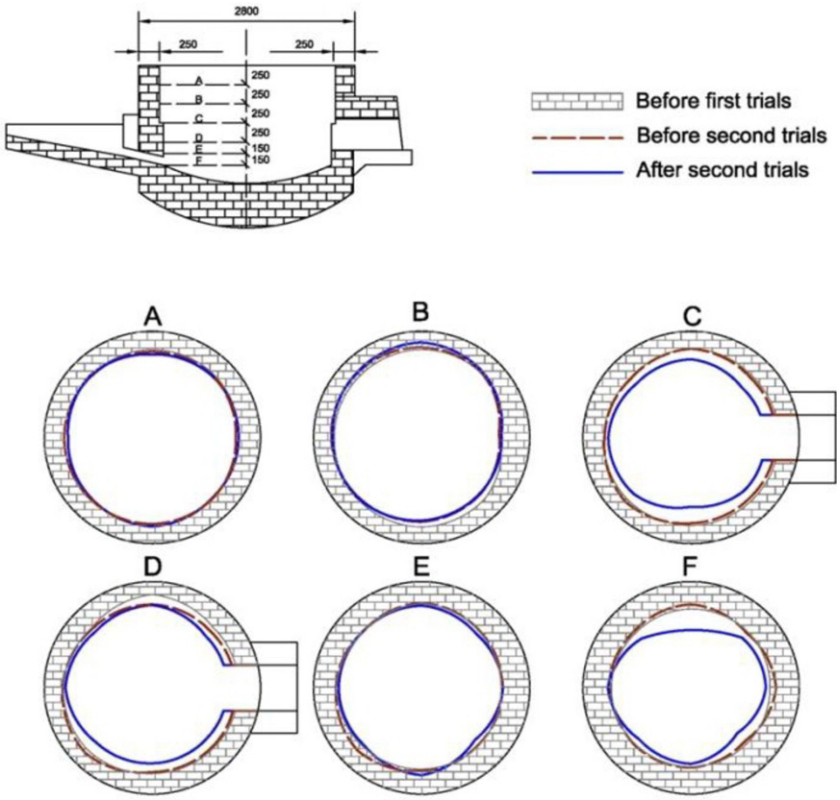


Figure 3.3.29 Refractory profiles before and after the two trials [70].

Table 3.3.10 Variation of the Furnace Refractory Thickness (in mm) Across Each Section [70]

Section →	A	B	C	D	E	F	Average
After first trials	12.5	10.0	15.0	28.1	−18.1	−20.6	4.5
After second trials	3.7	−11.5	135.5	92.2	29.9	120.0	61.6
After both campaigns (combined effect)	16.2	−1.5	150.5	120.3	11.8	99.4	66.1

the refectory repaired itself to its original profile. The slight erosion around the slagline (Sections E and F) for this campaign is believed to be the result of several heats with highly oxidized slag (caused by significant air ingress and the slag being removed after each heat, leaving a bare metal surface). Nevertheless, the wall condition after the trials is excellent, particularly in view of the not fully controllable periods of oxidized slags experienced in the Phase I trials. Also, the fact that the refectory can self-repair

itself by proper control of the slag chemistry indicates that the refractory can be maintained without a need for interrupting the process.

- In the second trials, the slag overoxidation was minimized and a thick layer of slag was always retained in the furnace. The result on the refractory appears to be very good, as in this phase, a net deposition of 62 mm is seen. More interestingly, the slagline (Section E), which is the area most prone to refractory loss, has gained an average thickness of 30 mm. The only point where the slagline has experienced a wear is opposite Phase B, the "hot" phase. This could be expected as it is customarily experienced in this area for conventional AC arc furnaces and is caused by the arc deflection toward the transformer. The CRISP six-in-line furnace geometry and electrics are however different and this phenomenon should not occur.
- The overall effect of the two campaigns together lasting about 200 h of operation is a net deposition of 66 mm. This is regarded as one of the most promising outcomes of the CRISP trials, showing an excellent corrosion resistance of the refractory. These encouraging results can be attributed primarily to the properties of the slag: good foaming action with low FeO levels and MgO saturation.

The results of the tests can be used to define an optimum operating window for CRISP technology per following:

- FeO: defined as a function of target carbon content (Equation 3.3.14).
- MgO: slightly above the saturation limit, that is about 11–15% for the slags studied in this research
- Basicity expressed as V ratio, 1.5–2.0.

3.3.6. PROCESS ANALYSIS

The operating conditions obtained from the pilot tests together with the results of a materials and energy balance model were used to evaluate the energy consumption and greenhouse gas (GHG) footprint of the process [74]. The analysis was based on CRISP furnace treating a charge of 90% hot DRI (HDRI) fed at 600 °C and 10% scrap. The results are compared with the conventional CDRI-EAF (cold DRI charged EAF) and the rather recent HDRI-EAF (hot DRI charged EAF) in Table 3.3.11. The method of analysis is discussed in detail elsewhere [74].

The results of the energy balance are summarized in Figure 3.3.30 as Sankey diagrams, displaying the distribution and the total energy for each process. The energy values presented in this figure represent the energy at the use point. In other words, inefficiencies in production of electricity or energy equivalents of the materials and reagents used in each process are not considered here. As shown, the total energy demand of CRISP process is about 10% lower than both hot and cold charged conventional EAFs. This is chiefly due to the lower off-gas and slag rates as well as the reduced energy loss. It is clear from Figure 3.3.30 that the total energy demand of the conventional EAFs is essentially constant

Table 3.3.11 Typical Operating Parameters of Three DRI-Based Steelmaking Scenarios [74]

Parameter	Unit	HDRI-CRISP	HDRI-EAF	CDRI-EAF
Electrode consumption	kg/ton Ls	1.7	1.7	2.1
Refractory consumption	kg/ton Ls	1.8	3.6	3.6
Carbon injection	kg/ton Ls	0	9	9
Oxygen source	–	Iron oxide	O_2	O_2
Natural gas	Nm^3/ton Ls	0	6	6
DRI/scrap ratio	–	9	9	9
Off-gas CO/CO_2	–	9	1	1
Hot DRI Temp	°C	600	600	25
Off-gas Temp	°C	1625	1625	1625
Steel Temp	°C	1630	1630	1630
Slag Temp	°C	1650	1650	1650
% Hot DRI		100	90	0
% Cold DRI		0	10	100
Slag parameters				
FeO	wt%	22	30	30
MgO	wt%	12	8	8
Basicity (V ratio)	–	1.75	2.5	2.5

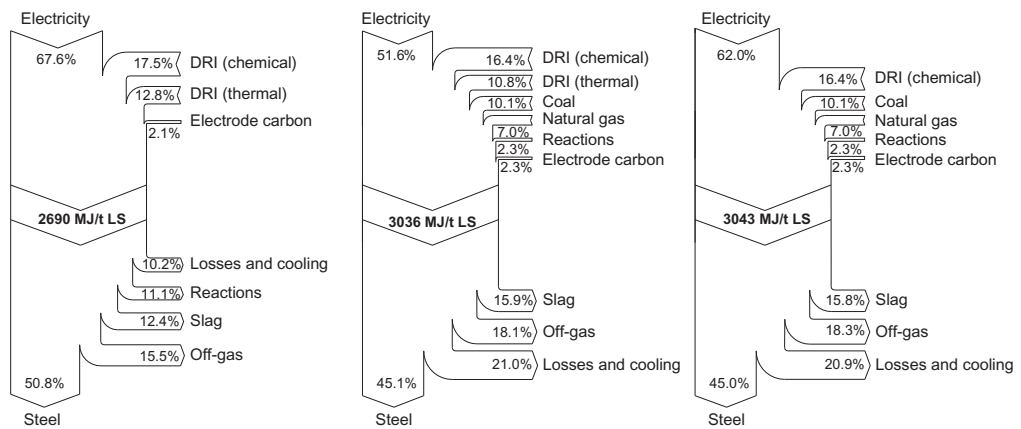


Figure 3.3.30 Energy distribution in the three steelmaking scenarios [74].

Table 3.3.12 Total Energy Intensity of DRI-Based Steelmaking Processes (MJ/ton) [74]

	HDRI-CRISP	HDRI-EAF	CDRI-EAF
Electrical	5589	4812	5798
Fuels	–	492	492
Energy equivalent of supplies	579	996	1018
Energy equivalent of by-products	−167	–	–
Energy equivalent of DRI and scrap	14,909	15,694	15,450
Energy equivalent of liquid steel	20,910	21,995	22,759

Table 3.3.13 GHG Footprint of Various Steelmaking Routes [74]

Process	HDRI-CRISP	HDRI-EAF	CDRI-EAF	BF-BOF
GHG footprint (CO_{2-e}/ton liquid steel)	1310	1409	1452	1922

regardless of the temperature of the charged DRI. However, charging 90% of DRI as hot DRI at the temperature of 600 °C at the specific ratio of 90% DRI to 10% CDR results in a saving of about 17% in the electrical energy consumption (from 524 to 435 kWh/ton_{steel}). The advantage of charging HDRI however may be fully realized using a continuous process, where hot DRI is charged to the EAF without any interruption.

By considering the energy value of all materials and fuels used in the process as well as inefficiency of electricity conversion, one can obtain a life cycle and inclusive measure of the energy value of the product (liquid steel) in each process. The results of such analysis are presented in Table 3.3.12, indicating that the overall energy intake through HDRI-CRISP technology is lower than the conventional and comparable processes. However, if one only considers the net electricity use, CRISP tends to be more energy intensive due to the fact that no supplemental chemical energy (coal/NG and oxygen) is considered for this process.

The results of a life cycle analysis on the generation of GHGs presented as $kgCO_{2-e}$ per ton of liquid steel are shown in Table 3.3.13. They indicate that the DRI-based technologies are more environmentally friendly, having 25–30% smaller CO_2 footprint than the currently dominant BF-BOF steelmaking route. Reliance of BF on coke as the major fuel gives rise to the high rate of CO_2 for this process. Between the three processes using DRI, CRISP-based integrated steelmaking is the least GHG-emitting process, presenting a 10% reduction in CO_2 against the conventional CDRI-EAF.

REFERENCES

[1] J.R. Stubbles, Conference of Metallurgists, Greenhouse Gases in the Metallurgical Industries: Policies, Abatement and Treatment, Toronto, Canada, MeSoc, 2001, pp. 103–116.

[2] R.J. Fruehan, O. Fortini, H.W. Paxton, R. Brindle, Theoretical Minimum Energies to Produce Steel for Selected Conditions, prepared for the U.S. Department of Energy, 2000, 2000).
[3] U.N. Publications, The Increasing Use of Continuous Processes in the Iron and Steel Industry and Their Techno-Economic Aspects. United Nations Publications, 1987.
[4] B. Wasmund, N. Voermann, B. Haneman, J. Sarvinis, G. Sheehan, 50th Conference of Metallurgists (COM2011): New Technology Implementation in Metallurgical Processes Symposium, Metallurgical Society of CIM, Montreal, Canada, pp. 37–54.
[5] K. Adham, A. Tohn, L. May, 50th Conference of Metallurgists (COM2011): New Technology Implementation in Metallurgical Processes Symposium, Metallurgical Society of CIM, Montreal, Canada, pp. 3–15.
[6] A. Goršek, P. Glavič, Chem. Eng. Res. Des. 75 (7) (1997) 709–717.
[7] W. Crookes, E. Röhrig, in: A Practical Treatise on Metallurgy, Steel, Fuel, Supplement, vol. 3, John Wiley and Son, New York, 1870, p. 87.
[8] J. Peter, K.D. Peaslee, D.G.C. Robertson, Iron Steel Technol. 2 (2) (2005) 53–60.
[9] C.A. Abel, R.J. Fruehan, A. Vassilicos, Iron Steelmaker (I and SM) 22 (7) (1995) 47–56.
[10] M. Kirschen, K. Badr, H. Pfeifer, Energy 36 (10) (2011) 6146–6155.
[11] N.N. Jha, R.K.P. Singh, K.P. Jagannathan, S. Jha Ajit, R.P. Singh, B.A. Kumar, S.R. Sahu, S.B. Singh, P.K. Bose, A.M. Pande, S.K. Biswas, K.N. Gupta, NML Tech. J. 29 (1–4) (1987) 25–32.
[12] M. Hein, M. Abel, SEAISI Q. 38 (2) (2009) 68–73.
[13] R. Verma, SEAISI Q. 20 (4) (1991) 54.
[14] M. Klemm, K. Stercken, Wire J. Int. 31 (12) (1998) 88–94.
[15] G.L. Dressel, Iron Steelmaker (I and SM) 26 (1) (1999) 53–55.
[16] D. Trotter, D. Varcoe, R. Reeves, S.H. Anderson, SEAISI Q. 31 (2) (2002) 39–50.
[17] D. Anghelina, G.A. Irons, G.A. Brooks, Charlotte, NC, United States, Association for Iron and Steel Technology, AISTECH, pp. 403–412.
[18] R. Lule, F. Lopez, J. Espinoza, R. Torres, R.D. Morales, St. Louis, MO, United States, Association for Iron and Steel Technology, AISTECH, pp. 489–498.
[19] P. Kaushik, R.J. Fruehan, Metall. Mater. Trans. B Process Metall. Mater. Process. Sci. 37B (5) (2006) 715–725.
[20] Midrex, 2010 World Direct Reduction Statistics, 2007, 4.
[21] J. Kopfle, R. Hunter, Ironmaking Steelmaking 35 (4) (2008) 254–259.
[22] E. Blondelot, EAF Technology: State of the Art & Future Trends, International Iron and Steel Institute, Belgium, 2000, p. 62.
[23] S.C. Montague, W.D. Häusler, Direct from Midrex 4th Quarter 1999, pp. 3–7.
[24] R. Bailey, Direct from Midrex 2nd Quarter 2001, pp. 7–8.
[25] R.M. Klawonn, G.E. Hoffman, Charlotte, NC, United States, Association for Iron and Steel Technology, AISTECH, pp. 383–393.
[26] P. Razza, D. Patrizio, Millennium Steel, London, UK, Millennium Steel, pp. 39–44.
[27] A. Tavano, B. Franco, A. Martinis, D. Taylor, AISTech 2004—Iron and Steel Technology Conference Proceedings, Nashville, USA, Association for Iron & Steel Technology, pp. 525–533.
[28] P.E. Duarte, R. Lopez, Iron Steel Eng. 73 (1996) 38–41.
[29] I. Gordon, F.M. Wheeler, Continuous Steelmaking Process, in: United States Patent, US 6,875,251, 2005.
[30] I. Gordon, F.M. Wheeler, Continuous Steelmaking Process, in: United States Patent, US 7,449,142, 2008.
[31] F.M. Wheeler, Y.M. Gordon, J.G. Wheeler, AISE Conference, Pittsburgh, PA, USA, 2003
[32] G. Traquair, F.M. Wheeler, Y.M. Gordon, METEC Conference, Düsseldorf, Germany, 2007.
[33] EAF Roundup, Iron Steel Technol. 9 (1) (2012) 100–120.
[34] J. Li, M. Barati, Metall. Mater. Trans. B 40 (1) (2009) 17–24.
[35] M. Barati, Physical Chemistry of Sustainable Metals (Richard J. Fruehan Symposium), Pittsburgh, PA, USA, AIST and TMS, pp. 11–20.
[36] D.A. Goldstein, R.J. Fruehan, B. Ozturk, Iron Steelmaker 26 (1999) 49–61.
[37] Y. Zhang, R. Fruehan, Metall. Mater. Trans. B 26 (4) (1995) 803–812.

[38] M. Barati, E. Sharifi, Metall. Mater. Trans. B 43 (2012) 680–685.
[39] K. Sadrnezhaad, J.F. Elliott, Iron Steel Int. 53 (1980) 327–339.
[40] K. Sadrnezhaad, Iron Steel Int. 54 (6) (1981) 309–314.
[41] E. Sharifi, M. Barati, Metall. Mater. Trans. B 41 (5) (2010) 1018–1024.
[42] E. Sharifi, M. Barati, M.D. Johnston, Pittsburgh, PA, Association for Iron & Steel Technology, pp. 875–883.
[43] T. Gare, G.S.F. Hazeldean, Ironmaking Steelmaking 8 (1981) 169–181.
[44] G.L. Dressel, Iron Steelmaker 25 (1998) 47–48.
[45] R.D. Morales, R. Lule, G.F. Lopez, J. Camacho, J.A. Romero, ISIJ Int. 35 (9) (1995) 1054–1062.
[46] R. Jiang, R.J. Fruehan, Metall. Trans. B Process Metall. 22 (4) (1991) 481–489.
[47] Y. Zhang, R.J. Fruehan, Metall. Mater. Trans. B Process Metall. Materials Process. Sci. 26 (5) (1995) 1088–1091.
[48] K. Ito, R.J. Fruehan, Iron Steelmaker 16 (8) (1989) 55–60.
[49] K. Ito, R.J. Fruehan, Metall. Trans. B Process Metall. 20 (4) (1989) 509–514.
[50] K. Ito, R.J. Fruehan, Metall. Trans. B Process Metall. 20 (4) (1989) 515–521.
[51] R. Roscoe, Br. J. Appl. Phys. 3 (1952) 267–269.
[52] H.C. Brinkman, J. Chem. Phys. 20 (4) (1952) 571–581.
[53] J. Happel, J. Appl. Phys. 28 (11) (1957) 1288–1292.
[54] E.B. Pretorius, R.C. Carlisle, Iron Steelmaker 26 (10) (1999) 79–88.
[55] D. LeMar, E.B. Pretorious, 58th Electric Furnace Conference, pp. 401–414.
[56] R.J. Fruehan (Ed.), The Making, Shaping and Treating of Steel, in: E.T. Turkdogan, R.J. Fruehan (Eds.), Steelmaking and Refining Volume, AISE Steel Foundation, Pittsburgh, PA, 2003.
[57] K. Endell, R. Fehling, R. Kley, J. Am. Ceram. Soc. 2 (4) (1939) 105–116.
[58] S.A. Nightingale, G.A. Brooks, B.J. Monaghan, Metall. Mater. Trans. B 36 (2005) 453–461.
[59] S. Jansson, V. Brabie, P. Jönsson, Scand. J. Metall. 34 (5) (2005) 283–292.
[60] G. Trömel, K. Koch, W. Fix, N. Großkurth, Arch. Eisenhüttenwes. 40 (1969) 969.
[61] S.-M. Jung, ISIJ Int. 43 (2) (2003) 216–223.
[62] M.A. Brosnan, in: C.A. Schacht (Ed.), Refractories Handbook, CRC Press, New York, 2004, p. 62 (Chapter 3).
[63] E.T. Turkdogan, Fundamentals of Steelmaking, The Institute of Materials, London, UK, 1996.
[64] C.W. Bale, P. Chartrand, S.A. Degterov, G. Eriksson, K. Hack, R. Ben Mahfoud, J. Melançon, A.D. Pelton, S. Petersen, Calphad 26 (2) (2002) 189–228.
[65] C.W. Bale, E. Bélisle, P. Chartrand, S.A. Decterov, G. Eriksson, K. Hack, I.H. Jung, Y.B. Kang, J. Melançon, A.D. Pelton, C. Robelin, S. Petersen, Calphad 33 (2) (2009) 295–311.
[66] J. Li, M. Barati, Y. Yang, in: The 4th International Congress on the Science and Technology of Steelmaking (ICS 2008), Gifu, Japan, 2008, pp. 526–529.
[67] D.J. Min, R.J. Fruehan, Metall. Mater. Trans. B 23 (1992) 29–37.
[68] F.M. Wheeler, F. Atkinson, Y.M. Gordon, B. Stephan, V. So, M. Barati, SCANMET III. 3rd International Conference on Process Development in Iron and Steelmaking, Luleå, Sweden, pp. 203–212.
[69] E.B. Pretorious, R.C. Carlisle, Iron Steelmaker 26 (10) (1999) 79–88.
[70] M. Barati, J. Li, F.M. Wheeler, G.M. Yakov, F. Atkinson, S. Broek, in: VIII International Conference on Molten Slags, Fluxes and Salts, MOLTEN 2009, Santiago, Chile, 2009, pp. 875–885.
[71] E.T. Turkdogan, in: R.D. Pehlke, W.F. Porter, R.F. Urban, J.M. Gaines (Eds.), BOF Steelmaking, vol. 2, Iron and Steel Society of AIME, 1975 (Chapter 4).
[72] K.C. Mills, B.J. Keene, Int. Mater. Rev. 32 (1987) 1–120.
[73] G.K. Sigworth, J.F. Elliott, Metal Sci. 8 (1) (1974) 298–310.
[74] M. Barati, Energy 35 (9) (2010) 3731–3737.

CHAPTER 3.4

Kinetics of Assimilation of Additions in Liquid Metals

Stavros A. Argyropoulos and Zhi Li
Department of Materials Science and Engineering, University of Toronto, Toronto, Ontario, Canada

LIST OF NOMENCLATURE

C_A concentration
C_A^* dimensionless concentration
c_{in} solid/liquid interface specific heat capacity (J kg^{-1} $°C^{-1}$)
c_l liquid-phase specific heat capacity (J kg^{-1} $°C^{-1}$)
$C_{p,l}^{Si}$ heat capacity of liquid silicon
$C_{p,l}^{W}$ heat capacity of water
c_s solid-phase specific heat capacity (J kg^{-1} $°C^{-1}$)
D_A diffusion coefficient (m^2 s^{-1})
g gravitational acceleration (m s^{-2})
g_z gravitational acceleration (m s^{-2})
Gr heat transfer Grashof number
Gr_C Grashof number due to the concentration gradients
$Gr_{Effective}^{Macroexothermic}$ effective Grashof number during macroexothermic phenomena
Gr_{mC} modified mass transfer Grashof number
Gr_{mT} modified heat transfer Grashof number
Gr_T Grashof number due to the density gradients
h enthalpy (J kg^{-1})
h^* dimensionless enthalpy (J kg^{-1})
$h_{Effective}^{Macroexothermic}$ average effective heat transfer coefficient during macroexothermic phenomena
H_f latent heat (J kg^{-1})
H_f^{Si} latent heat of Si
H_f^{W} latent heat of ice
$\overline{\Delta H}_{Macroexothermicity}$ macroexothermicity during assimilation of exothermic addition (J kg^{-1})
$\overline{\Delta H}_{Element}$ heat released from exothermic reaction during addition (J kg^{-1})
$\overline{\Delta H}_{Si}$,$\overline{\Delta H}_{Silicon}$ exothermic heat released from reaction Si/steel (J kg^{-1})
$\overline{\Delta H}_{W}$,$\overline{\Delta H}_{Water}$ exothermic heat released from reaction sulfuric acid/water (J kg^{-1})
$\Delta\overline{H}_W$ exothermic heat of mixing
k thermal conductivity (W m^{-1} $°C^{-1}$)
k_{in} solid/liquid interface thermal conductivity (W m^{-1} $°C^{-1}$)
k_l liquid-phase thermal conductivity (W m^{-1} $°C^{-1}$)
k_s solid-phase thermal conductivity (W m^{-1} $°C^{-1}$)
L length (m)
L length of immersed cylinder (m)
$LH_{Element}$ addition element latent heat (J kg^{-1})

Treatise on Process Metallurgy, Volume 2
http://dx.doi.org/10.1016/B978-0-08-096984-8.00016-1
© 2014 Elsevier Ltd.
All rights reserved.

$\mathbf{LH_{Silicon}}$ silicon latent heat (J kg^{-1})
$\mathbf{LH_{Water}}$ water latent heat (J kg^{-1})
Me1 first reactant metal
Me2 second reactant metal
$Nu_L^{\mathbf{Macroexothermic}}$ effective average Nusselt number for exothermic heat transfer
$Nu_L^{\mathbf{Natural\ Convection}}$ Nusselt number for natural convection heat transfer
p pressure (Pa)
p^* dimensionless pressure (Pa)
Pr Prandtl number
r cylindrical coordinate direction
r^* dimensionless cylindrical coordinate direction
r_1, r_2 radius (m)
R cylinder radius
Sc Schmidt number
S_E, S_1, S_2 source term
S_1^*, S_2^* dimensionless source term
t time (s)
t^* dimensionless time (s)
T temperature (°C)
T_{ref} reference temperature (°C)
T_m melting point temperature (°C)
ΔT average temperature difference between melting point of the addition and the temperature of the fluid
$\Delta T'$ average increase in the temperature around the moving interface
z cylindrical coordinate direction
z^* dimensionless cylindrical coordinate direction
z_1, z_2 height (length) (m)

GREEK SYMBOLS

α_{in} solid/liquid interface thermal diffusivity (m s^{-1})
α_l liquid-phase thermal diffusivity (m s^{-1})
α_s solid-phase thermal diffusivity (m s^{-1})
β_C concentration volumetric expansivity
β_T thermal volumetric expansivity
γ coefficient
$\Gamma_\alpha, \Gamma_D, \Gamma_\mu$ coefficients
λ liquid-phase fraction
ρ density (kg m^{-3})
ρ^* dimensionless density (kg m^{-3})
ρ_{in} solid/liquid interface density (kg m^{-3})
ρ_l liquid-phase density (kg m^{-3})
ρ_l^{Si} density of liquid Si
ρ_l^{W} density of water
ρ_{ref} reference density (kg m^{-3})
ρ_s solid-phase density (kg m^{-3})
ρ_S^{Si} density of solid Si
ρ_S^{W} density of ice
μ dynamic viscosity (N s m^{-2})

$\boldsymbol{\nu_l}$ kinematic viscosity ($m^2\ s^{-1}$)
$\boldsymbol{v_r}$ velocity in r direction ($m\ s^{-1}$)
$\boldsymbol{v_r^*}$ dimensionless velocity in r direction ($m\ s^{-1}$)
$\boldsymbol{v_z}$ velocity in z direction ($m\ s^{-1}$)
$\boldsymbol{v_z^*}$ dimensionless velocity in z direction ($m\ s^{-1}$)

SUBSCRIPTS

A component
C concentration
D diffusion coefficient related
in solid/liquid interface
l liquid phase
m melting point
r cylindrical coordinate direction
ref reference value
s solid phase
Si silicon
T temperature
W water
z cylindrical coordinate direction
$\boldsymbol{\alpha}$ thermal diffusivity related
$\boldsymbol{\mu}$ viscosity related

SUPERSCRIPTS

Si silicon
W water
* dimensionless

3.4.1. INTRODUCTION

This chapter deals with the assimilation kinetics of various additions in ferrous and nonferrous liquid metals. It starts with an exhaustive review of published experiments of solid metals into different liquid metals. This review is summarized in two tables, describing different assimilation experiments that focus on nonferrous (Table 3.4.1) and ferrous (Table 3.4.2) liquid metals. Both of these tables present information regarding:

(1) Reported temperature range;
(2) The shape of the specimen used;
(3) Experimental method (i.e., static or dynamic);
(4) Assimilation mechanism (i.e., reaction controlled, mixed controlled, or liquid-phase diffusion (LPD) controlled);
(5) Activation energy whenever reported.

Table 3.4.1 Assimilation Experiments in Nonferrous Liquid Metals

System		Temperature (°C)	Specimen Type	Method	Assimilation Mechanism	Activation Energy (kJ mol^{-1})	Reference
Solid	Liquid						
Ni	Ag–Cu–Pd	1050	Crucible	Static	Reaction	NA	[1]
Al–Sr	Al	665–780	Cylinder	Static	LPD/mixed	41.84–83.68	[2–4]
Cr–steel	Al	750, 800, 950	Cylinder	Static	LPD	125.94	[5]
Steel	Al	775	Cylinder	Dynamic	LPD	NA	[6]
Steel	Al	775	Rod	Dynamic	LPD (low velocity) Mixed (high velocity)	NA	[7]
Steel	Al	800 ± 5 (793–803)	Cylinder	Dynamic	LPD	NA	[8]
Steel	Al	700–820	Cylinder	Static	LPD	NA	[9]
Steel	Al	800 ± 5	Cylinder	Dynamic	LPD	NA	[10]
Steel	Al	700–820	Cylinder	Static	LPD	NA	[10]
Co	Al	700–800	Cylinder	Static/dynamic	LPD	132.63	[11]
Co	Al	700–900	Disc	Dynamic	LPD	NA	[12]
Cr	Al	700–800	Cylinder	Static/dynamic	LPD	135.14	[11]
Cr	Al	700–900	Disc	Dynamic	LPD	NA	[13]
Cr	Al	700–915	Disc	Dynamic	LPD	58.7 ± 0.7	[14]
Fe	Al	700–800	Cylinder	Static/dynamic	LPD	100	[11]
Fe	Al	700–900	Disc	Dynamic	LPD	NA	[12]
Fe	Al	700–800	Cylinder	Static	Mixed	NA	[15]

Fe	Al	700–800	Cylinder	Dynamic	LPD	NA	[16]
Fe	Al	800–1300	Disc	Dynamic	Mixed	NA	[17]
Fe	Al	700, 750, 800	Disc	Dynamic	NA	NA	[18]
Fe–C	Al	700–800	Cylinder	Static	Reaction	NA	[15]
Fe–C	Al	700–800	Cylinder	Dynamic	Mixed	NA	[16]
S45C	Al	700–800	Cylinder	Dynamic	LPD	NA	[16]
Fe–Cr	Al	700–800	Cylinder	Static	LPD	NA	[15]
Fe–Cr	Al	700–800	Cylinder	Dynamic	LPD	NA	[16]
Fe–Cu	Al	700–800	Cylinder	Static	LPD	NA	[15]
Fe–Mn	Al	700–800	Cylinder	Static	Mixed	NA	[15]
Fe–Ni	Al	700–800	Cylinder	Static	LPD	NA	[15]
Fe–Ni	Al	700	Disc	Dynamic	LPD	NA	[19]
Fe–Si	Al	700–800	Cylinder	Static	LPD	NA	[15]
Fe–Si	Al	700–800	Cylinder	Dynamic	LPD	NA	[16]
Mo	Al	700–850	Disc	Dynamic	LPD	25.8 ± 0.2	[20]
Mo	Al	700–915	Disc	Dynamic	LPD	18.5 ± 0.1	[14]
Nb	Al	700–850	Disc	Dynamic	LPD	26.8 ± 0.5	[20]
Nb	Al	700–915	Disc	Dynamic	LPD	41.7 ± 0.7	[14]
Ni	Al	700–800	Cylinder	Static/dynamic	LPD	78.24	[11]
Ni	Al	675	Cylinder	Static	LPD	NA	[21]
Ni	Al	700–900	Disc	Dynamic	LPD	NA	[12]

Continued

Table 3.4.1 Assimilation Experiments in Nonferrous Liquid Metals—cont'd

System		Temperature (°C)	Specimen Type	Method	Assimilation Mechanism	Activation Energy (kJ mol^{-1})	Reference
Solid	Liquid						
Re	Al	700–900	Disc	Dynamic	LPD	NA	[22]
Sr	Al	665–780	Cylinder	Static	LPD/mixed	NA	[2–4]
Ta	Al	700–850	Disc	Dynamic	LPD	28.0 ± 0.2	[20]
Ti	Al	700–800	Cylinder	Static/dynamic	LPD	105.02	[11]
Ti	Al	800–1300	Disc	Dynamic	LPD	NA	[17]
V	Al	700–800	Cylinder	Static/dynamic	LPD	93.30	[11]
W	Al	700–850	Disc	Dynamic	LPD	28.3 ± 0.5	[20]
Y	Al	700–915	Disc	Dynamic	LPD	32.1 ± 0.2	[14]
Cu	Al–Cu	600–750	Cylinder	Static	LPD	30	[23]
Ti	Al–Fe	800–1300	Disc	Dynamic	LPD	NA	[17]
Al	Al–Si	585–625	Cylinder	Static	LPD	313.8	[24]
Al	Al–Si	585–600	Cylinder	Dynamic	LPD	NA	[24]
Al	Al–Si	585–640	Cylinder	Static/dynamic	LPD	NA	[25]
Cr–steel	Al–Si–Fe	750, 800, 950	Cylinder	Static	LPD	135.56	[5]
Al	Al–Si–Mg	571–603	Cylinder	Static	LPD	83.68–301.25	[26]
Al–Sr	A356	640–780	Cylinder	Static	LPD/mixed	41.84–83.68	[2–4]
Sr	A356	640–780	Cylinder	Static	LPD/mixed	NA	[2–4]
Al	Bi	300–600	Cylinder	Dynamic	LPD	NA	[27]
Ag	Bi	300–500	Cylinder	Static	LPD	NA	[28]

Cu	Bi	300–500	Cylinder	Static	LPD	NA	[28]
Cu	Bi	360–510	Cylinder	Static	LPD	NA	[29]
Cu	Bi	360–460	Cylinder	Dynamic	LPD	NA	[30]
Ni	Bi	300–450	Cylinder	Static	LPD	NA	[31]
Zn	Bi	300–400	Cylinder	Dynamic	LPD	26.36	[32]
Al	Cu	NA	Cylinder	Static	Melting	NA	[33]
Co	Cu	1200–1340	Cylinder	Dynamic	LPD	53.14–57.32	[34]
Co	Cu		Wire	Static	LPD	NA	[35]
Cu	Cu	NA	Cylinder	Static	Melting	NA	[33]
Fe	Cu	1220–1370	Cylinder	Dynamic	LPD	NA	[36]
Fe	Cu		Wire	Static	LPD	NA	[35]
Fe	Cu		Disc	Dynamic	LPD	NA	[37]
Ni	Cu		Wire	Static	LPD	NA	[35]
Ti	Cu	800–1300	Disc	Dynamic	LPD	NA	[17]
Co	Cu–Co	1200–1340	Cylinder	Dynamic	LPD	53.14–57.32	[34]
Fe	Cu–Fe	1220–1370	Cylinder	Dynamic	LPD	NA	[36]
Fe	Cu–Sn		Disc	Dynamic	LPD	NA	[37]
Fe	Cu–Zn		Disc	Dynamic	LPD	NA	[37]
Cd	Ga	80	Foil	Static	LPD	NA	[35]
Ag	Hg	59, 85	Cylinder	Dynamic	LPD	NA	[38]
Low carbon steel	Hg	482–649	NA	Dynamic	LPD	NA	[39]

Continued

Table 3.4.1 Assimilation Experiments in Nonferrous Liquid Metals—cont'd

System		Temperature (°C)	Specimen Type	Method	Assimilation Mechanism	Activation Energy (kJ mol^{-1})	Reference
Solid	Liquid						
Cd	Hg	Room temp.	Horizontal cylinder	Static	LPD	NA	[40]
Iron	Hg	Room temp.	NA	Static	LPD	NA	[39]
Pb	Hg	Room temp.	Horizontal cylinder	Static	LPD	NA	[40]
Pb	Hg	Room temp.	Beds of sphere	Dynamic	LPD	NA	[40]
Pb	Hg	30–40	Rod	Dynamic	LPD	NA	[41]
Pb	Hg	-36-50	Disc	Dynamic	LPD	NA	[42]
Sn	Hg	Room temp.	Horizontal cylinder	Static	LPD	NA	[40]
Sn	Hg	30–40	Rod	Dynamic	LPD	NA	[41]
Sn	Hg	3, 30	Cylinder	Dynamic	LPD	NA	[38]
Sn	Hg	20, 30	Cylinder	Static	LPD	NA	[9]
Sn	Hg	20, 30	Cylinder	Static	LPD	NA	[10]
Zn	Hg	Room temp.	Horizontal cylinder	Static	LPD	NA	[40]
Zn	Hg	Room temp.	Tube	Dynamic	LPD	NA	[40]
Zn	Hg	30–40	Rod	Dynamic	Reaction	NA	[41]
Zn polycrystalline	Hg	3, 30, 45, 59	Cylinder	Dynamic	Mixed	NA	[38]
Zn single crystal	Hg	30	Cylinder	Dynamic	Mixed	NA	[38]

Zn–Hg	Hg	30	Cylinder	Dynamic	Mixed	NA	[38]
Zn	Hg	20, 30	Cylinder	Static	LPD	NA	[9]
Zn	Hg	20, 30	Cylinder	Static	LPD	NA	[10]
Zn	Hg	50	Disc	Dynamic	Reaction	NA	[27]
Cu	Mg–Cu	600–750	Cylinder	Static	LPD	32–40	[23]
Ag	Na	380	Wire	Static	LPD/reaction	NA	[35]
Au	Na	380	Wire	Static	LPD/reaction	NA	[35]
310 Stainless steel	Na	760	NA	Static	Reaction	NA	[39]
C–steel	Na	400	NA	Static	Reaction	NA	[39]
Cu	Pb	360–510	Cylinder	Static	LPD	NA	[29]
Cu	Pb	360–460	Cylinder	Dynamic	LPD	NA	[30]
Cu	Pb	527, 727	Cylinder	Dynamic	LPD (low velocity) Mixed (high velocity)	NA	[43]
Cu	Pb	450 ± 5	Cylinder	Dynamic	LPD	NA	[10]
Cu–Ni	Pb	527, 727	Cylinder	Dynamic	LPD (low velocity) Mixed (high velocity)	NA	[43]
Ni	Pb	527, 727	Cylinder	Dynamic	LPD (low velocity) Mixed (high velocity)	NA	[43]
Au	Sn–Pb	190–260	Stud	Static	LPD	NA	[44]
Cu	Sn–Pb	400	Disc	Static	LPD	NA	[45]
Cu	Sn–Pb	400	Cylinder	Static/dynamic	Mixed	NA	[46]

Continued

Table 3.4.1 Assimilation Experiments in Nonferrous Liquid Metals—cont'd

System		Temperature (°C)	Specimen Type	Method	Assimilation Mechanism	Activation Energy (kJ mol^{-1})	Reference
Solid	Liquid						
Pb	Pb–Sn	248–320	Semi-cylinder	Static (no stirring)	LPD	NA	[47]
Pb	Pb–Sn	204–273	Cylinder	Dynamic (high stirring)	Reaction	8.37 ± 4.18	[47]
Ag	Sn	300–400	Wire	Static	NA	NA	[48]
Cu	Sn	340–508	Disc	Static	LPD	NA	[49]
Cu	Sn	260–450	Coupon	Static	LPD	NA	[50]
Cu	Sn	300–400	Wire	Static	NA	NA	[48]
Fe	Sn	445–780	Cylinder	Static	Reaction ($\forall\ T < 496\ ^\circ C$) LPD ($\forall\ T > 496\ ^\circ C$)	23.60–57.74	[51]
Nb	Sn	800–1200	Disc	Dynamic	LPD	NA	[52]
Nb–Sn	Sn	800–1200	Disc	Dynamic	LPD	NA	[52]
Nb–Sn–C	Sn	800–1200	Disc	Dynamic	LPD	NA	[52]
Ni	Sn	270–400	Wire	Static	N/A	41	[53]
Ni	Sn	278–530	Cylinder	Static	LPD ($\forall\ T < 355\ ^\circ C$) Mixed ($\forall\ T = 408\ ^\circ C$) Reaction ($\forall\ T > 462\ ^\circ C$)	NA	[54]
Ni–Sn	Sn	825	Cube	Static	LPD	NA	[55]

Ag	Sn–Ag	300–400	Wire	Static	NA	NA	[48]
Cu	Sn–Ag	300–400	Wire	Static	NA	NA	[48]
Ag	Sn–Ag–Cu	300–400	Wire	Static	NA	NA	[48]
Cu	Sn–Ag–Cu	300–400	Wire	Static	NA	NA	[48]
Ag	Sn–Zn	300–400	Wire	Static	NA	NA	[48]
Cu	Sn–Zn	300–400	Wire	Static	NA	NA	[48]
Fe	Zn	465	Disc	Dynamic	LPD	NA	[56]
Steel	Zn	600	Cylinder	Dynamic	LPD	NA	[6]
Steel	Zn	600	Cylinder	Static	LPD	NA	[6]
Steel	Zn	550–650	Cylinder	Static	LPD	33.3	[57]
Steel	Zn	600	Cylinder	Dynamic	LPD	NA	[57]
Steel	Zn	600	Rod	Dynamic	LPD (low velocity) Mixed (high velocity)	NA	[7]
Steel	Zn	475–600 (475–590)	Cylinder	Dynamic	LPD	NA	[8]
Steel	Zn	488–650	Cylinder	Static	LPD	NA	[9]
Steel	Zn	475–600	Cylinder	Dynamic	LPD	NA	[10]
Steel	Zn	488–650	Cylinder	Static	LPD	NA	[10]
Ni	Zn	450–550	Plate	Dynamic	LPD	NA	[58]
Various solid metals	Various liquid metals	–	–	–	–	–	[59]

Table 3.4.2 Assimilation Experiments in Ferrous Liquid Metals

System		Temperature (°C)	Specimen Type	Method	Assimilation Mechanism	Activation Energy (kJ mol^{-1})	Reference
Solid	Liquid						
BN	Fe	1550	Rod	Dynamic (rotating in resistance furnace)	LPD	NA	[60]
Cr	Fe	1650	Disc	Dynamic	LPD	NA	[61]
Cr	Pure Fe	1650	Disc	Dynamic	LPD	NA	[62]
FeMo	Fe	1650	Disc	Dynamic	LPD	NA	[61]
FeMo (62%Mo)	Pure Fe	1650	Disc	Dynamic	LPD	NA	[62]
FeNb	Fe	1650	Disc	Dynamic	LPD	NA	[61]
FeNb (60%Nb)	Pure Fe	1600	Disc	Dynamic	LPD	NA	[62]
FeW	Fe	1650	Disc	Dynamic	LPD	NA	[61]
FeW (74%W)	Pure Fe	1600	Disc	Dynamic	LPD	NA	[62]
Mo	Fe	1650	Disc	Dynamic	LPD	NA	[61]
Mo	Pure Fe	1650	Disc	Dynamic	LPD	NA	[62]
Mo	Fe	NA	Cylinder	Dynamic/static	LPD	NA	[63]
Mo	Fe	1590–1680	Rod	Dynamic/static	LPD	273	[64]
Ti	Fe	1650	Disc	Dynamic	LPD	NA	[61]
Ti	Pure Fe	1650	Disc	Dynamic	LPD	NA	[62]
TiN	Fe	1550–1650	Disc	Dynamic	LPD	NA	[65]

W	Fe	NA	Cylinder	Dynamic/static	LPD	NA	[63]
W	Pure Fe	1650	Disc	Dynamic	LPD	NA	[62]
BN	Fe–B	1610, 1685, 1760	Disc	Static (induction)	LPD	NA	[60]
Fe–C	Low carbon steel	1600	Cylinder	Dynamic	Melting	NA	[66]
Fe–Cr	C–steel	1600	Irregular piece	Dynamic	NA	NA	[67]
Fe–Cr–Mn	Low carbon steel	1600	Cylinder	Dynamic	Melting	NA	[66]
Fe–Cr–Mn–Si	Low carbon steel	1600	Cylinder	Dynamic	Melting	NA	[66]
Fe–Mn	Low carbon steel	1600	Cylinder	Dynamic	Melting	NA	[66]
Fe–Mn	C–steel	1575, 1600	Irregular piece	Dynamic	NA	NA	[67]
Fe–Mn–Si–Al	Low carbon steel	1600	Cylinder	Dynamic	Melting	NA	[66]
Fe–Si–Mn	C–steel	1575, 1600	Irregular piece	Dynamic	NA	NA	[67]
Fe–Ti	C–steel	1575, 1600	Irregular piece	Dynamic	NA	NA	[67]
Fe–V	C–steel	1575, 1600	Irregular piece	Dynamic	NA	NA	[67]

Continued

Table 3.4.2 Assimilation Experiments in Ferrous Liquid Metals—cont'd

System		Temperature (°C)	Specimen Type	Method	Assimilation Mechanism	Activation Energy (kJ mol^{-1})	Reference
Solid	Liquid						
Fe–Cr	Steel	1600, 1630, 1660	Lump	NA	LPD	NA	[68]
Fe–Mn	Steel	1600	Cylinder	Static	Melting	NA	[69]
Fe–Mn	Steel	1560–1650	Lump	Dynamic/static	Melting	NA	[70]
Fe–Nb	Steel	1600	Lump	Static	LPD	NA	[71]
Fe–Nb	Steel	1600	Cylindrical compact	Static	Melting	NA	[72]
Fe–Nb	Steel	1610–1630	Lump	Dynamic/static	LPD	NA	[73]
Fe–B	Steel	1580–1610	Lump	Static	Melting	NA	[73]
Fe–Si	Steel	1590	Cylinder	Static	Melting	NA	[74]
Fe–Si	Steel	1596–1614	Lump	Static	Melting	NA	[71]
			Cylinder				
Fe–80%V	Steel	1615–1620	Lump	Static	LPD	NA	[71]
Fe–50%V	Steel	1600	Cylinder	Static	Melting	NA	[75]
Fe–43%V	Steel	1600	Lump	Dynamic	Melting	NA	[76]
Fe–Zr	Steel	1590–1635	Lump	Static	Melting	NA	[73]
Mo	Steel	1630	Bar, rod	NA	NA	NA	[77]
Nb	Steel	1596–1664	Cylinder	Dynamic/static	LPD	172 ± 15	[78]
Nb–Ni	Steel	1605–1634	Lump	Static	Melting	NA	[73]

Si	Steel	1618	Lump	Static	Melting	NA	[71]
Si–Mn	Steel	1600	Cylinder	Static	Melting	NA	[60]
Si–Mn	Steel	1560–1650	Lump	Dynamic/static	Melting	NA	[70]
Ti	Steel	1560–1625	Cylinder	Static	LPD/melting	296.3	[75,79]
Ti	Steel	1450–1650	Disc	Dynamic	LPD	NA	[80]
V	Steel	1576–1634	Cylinder	Static	LPD	300.6	[75,76]
Zr	Steel	1600	Cylinder	Dynamic/static	Reaction	340 ± 26.4	[81,82]
Al	Fe–C_{sat}	1254	Hemisphere	Static	Melting	NA	[83]
Al_2O_3	Fe–C_{sat}	1550–1650	Crucible	Static	LPD	NA	[84]
Al_2O_3	Fe–C_{sat}	1500, 1560, 1600	Cylinder	Dynamic/static	LPD	NA	[85]
Ce	Fe–C_{sat}	1400	NA	Static	LPD	NA	[86]
Cu–Mg	Fe–C	NA	NA	Static	LPD	NA	[87]
Fe	Fe–C_{sat}	1374–1500	Cylinder	Dynamic	LPD	NA	[88]
Fe	Fe–C_{sat}	1185–1406	Cylinder	Dynamic/static	LPD	NA	[89]
Fe	Fe–C	1185–1406	Cylinder	Dynamic/static	LPD	NA	[89]
Fe–Mn	Fe–C	NA	Lump	Static	Melting	NA	[83]
Fe–Si	Fe–C	NA	Lump	Static	Melting	NA	[83]
Graphite	Fe–C	1550, 1590	Cylinder	Static	LPD	NA	[90]
Graphite	Fe–C	1470–1640	Cylinder	Dynamic	LPD	NA	[91]
Graphite	Fe–C	1270–1550	Rod	Dynamic/static	LPD	NA	[92]

Continued

Table 3.4.2 Assimilation Experiments in Ferrous Liquid Metals—cont'd

System		Temperature (°C)	Specimen Type	Method	Assimilation Mechanism	Activation Energy (kJ mol^{-1})	Reference
Solid	Liquid						
Graphite	Fe–C	1400	Granule	Static (resistance furnace)	NA	NA	[93]
Graphite	Fe–C	1350–1450	Granule	Dynamic (induction furnace)	NA	NA	[93]
Mo	Fe–C_{sat}	1315–1425	Cylinder	Dynamic	LPD	83.68	[94]
Mo	Fe–C	1590–1680	Rod	Dynamic/static	LPD	108	[64]
Nb	Fe–C	1250–1450	Disc	Dynamic	LPD	NA	[95]
SiC	Fe–C_{sat}	1400–1600	Cylinder	Static	LPD	205.02–359.82	[96]
Si–C	Fe–C	1350–1450	Granule	Dynamic (induction furnace)	NA	NA	[93]
SiC	Fe–C	1376–1525	Rod	Dynamic	LPD	100.42	[97]
Steel	Fe–C	1400 (1385–1410)	Cylinder	Static	LPD	NA	[10]
Steel	Fe–C	1400 (1403–1415)	Cylinder	Dynamic	LPD	NA	[10]
Steel	Fe–C_{sat}	1560	Hemisphere	Static	Melting	NA	[83]
C–Steel	Fe–C_{sat}	1374–1500	Cylinder	Dynamic	LPD	NA	[88]
C–Steel	Fe–C	1300–1500	Cylinder	Dynamic/static	LPD	NA	[98]
C–Steel	Fe–C_{sat}	1185–1406	Cylinder	Dynamic/static	LPD	NA	[89]
Mo	Fe–C_{sat}–Mo	1315	Cylinder	Dynamic	LPD	NA	[94]

CaC_2	Fe–C_{sat}–S	1250, 1350, 1450	Cylinder	Dynamic (rotating in induction furnace)	LPD	NA	[99]
Ce	Fe–C–S	1400	NA	Static	LPD	NA	[86]
Coal	Fe–C–S	1550	Particle	Dynamic	LPD	NA	[100]
Graphite	Fe–C–S	1550	Particle	Dynamic	Mixed	NA	[100]
Ce	Fe–C–Si	1400	NA	Static	LPD	NA	[86]
SiC	Fe–C–Si	1400–1600	Cylinder	Static	LPD	221.75–301.25	[96]
BN	Fe–N_{sat}	1610, 1685, 1760	Disc	Static (induction)	LPD	NA	[60]
C	Pig iron	1475–1550	NA	Static	LPD	NA	[101]
1020 Steel	Pig iron	1260–1454.4	Cylinder	Dynamic/static	LPD	NA	[102]
C–steel	Pig iron	1363–1428	Cylinder	Dynamic	LPD	NA	[103]
Steel	Pig iron	1371–1526	Cylinder	Static	LPD	NA	[104]
Co	Cast iron	1400	Disc	Dynamic	LPD	NA	[62]
Cr	Cast iron	1370	Disc	Dynamic	LPD	NA	[62]
Mo	Cast iron	1400	Disc	Dynamic	LPD	NA	[62]
Ni	Cast iron	1400	Disc	Dynamic	LPD	NA	[62]
Si	Cast iron	1400	Disc	Dynamic	LPD	NA	[62]
Ti	Cast iron	1400	Disc	Dynamic	LPD	NA	[62]
W	Cast iron	1370	Disc	Dynamic	LPD	NA	[62]

Subsequently, a broad classification of various additions is made, and they are classified into three groups. The additions are considered to be in the lump or briquette form, and they are at room temperature prior to immersion into the liquid metal. The processing characteristics of assimilation were identified according to the various routes which these additions follow. Six routes were identified and depicted schematically along with the conditions which promote each individual route. This description is accompanied with relevant photographs, and in some cases, mathematical modeling predictions are included.

Exothermicity represents an important factor which can affect the assimilation kinetics. Various examples are provided to illustrate the two classifications of exothermicity, namely, as microexothermicity and macroexothermicity.

Finally, aspects of recovery of additions are presented and a parameter, rate of recovery, is introduced. Tabulated results on additions' rate of recovery in liquid aluminum and liquid steel are presented.

3.4.2. FUNDAMENTALS OF ASSIMILATION

Two types of mass transfer, melting and dissolution, take place when a solid addition is immersed into a liquid metal. The former occurs when the melting temperature range of the addition is below that of the liquid metal temperature, whereas the latter takes place when the solid addition has a melting temperature range which is higher than that of the liquid metal. Solid additions in liquid metals can be classified into three groups. Group I follows mass transfer characterized by melting. Ferromanganese additions in liquid steel are a typical case of this first group. Group II obeys mass transfer characterized by dissolution. Silicon additions in liquid aluminum denote a representative case from this second group. Group III is comprised of exothermic additions having melting points higher than the liquid metal temperatures. These exothermic additions can release substantial amounts of heat. Furthermore, their mass transfer in a liquid metal can start as dissolution and under special conditions can progress to melting. Titanium additions in liquid steel denote an example of this third group.

Tables 3.4.1 and 3.4.2 list a plethora of different types of assimilation experiments reported in nonferrous and in ferrous liquid metals, respectively. The descriptions of specimen type and method used are identical to the depictions given in the original reference cited. LPD is cited as the assimilation mechanism, for the majority of cases shown in Tables 3.4.1 and 3.4.2. Reaction mechanism is reported for very few cases shown in these tables. It is worth mentioning that in the cases in which activation energy is reported and LPD is considered as the assimilation mechanism, the values of activation energy vary widely (i.e., from 41.84 to 359.82 kJ mol^{-1}). A plausible explanation for this wide range of reported activation energies is given later on in this chapter. For the very few cases for which reaction is cited as the assimilation mechanism, the dissolution of Zr into liquid steel exhibits an activation energy of 340 ± 26.4 (kJ mol^{-1}). It should be pointed out that

the value of activation energy alone does not characterize the assimilation mechanism involved. Quite often, there is a need for supplementary experiments, such as stirring the metal bath, which provide the necessary information for the characterization of the assimilation mechanism.

3.4.3. ROUTES OF ASSIMILATION

A common characteristic exhibited by all of the previously mentioned groups of additions is the formation of a solid metal shell around the cold addition immediately upon immersion. Heat transfer phenomena are responsible for the shell formation. In particular, the difference between the convective heat flux from the metal bath to the addition and the conductive heat flux absorbed by the cold addition is the reason for the shell formation. It should be stated here that the thickness and duration of the solidified shell is not only a function of the difference in the heat fluxes but is also a function of the thermal conductivity of the addition, the density of the liquid metal, and the thermal resistance at the addition–shell interface. The period of time during which there is a shell around the immersed addition is called the shell period, while the period of time during which there is no shell around the addition is called the free assimilation period. The shell period together with the free assimilation period corresponds to the assimilation time of the immersed addition. In some cases, the time of the shell duration represents nearly all, while in other cases it corresponds to a small fraction, of the addition's assimilation time.

In an effort to present the various characteristics of assimilation of additions in liquid metals, six routes of assimilation will be presented. In the subsequent analysis, the immersed addition is considered to be a long cylinder or sphere at room temperature prior to submersion into the liquid metal. The schematics shown subsequently depict cross-section views of the cylinders and spheres. In the case of the cylinder, the cross section is perpendicular to its vertical axis, while in the case of the sphere it is through its center. Furthermore, the dipping of the addition into the metal bath is assumed to be instantaneous. During the subsequent analysis of the six routes, predictions which are based on mathematical modeling work [105] will also be presented. In making these predictions, thermal resistance was considered between the shell and the solid addition interface. More details on the magnitude of this thermal resistance can be found in Ref. [106].

In all the routes described and depicted subsequently, r_1 corresponds to the radius of the addition prior to immersion while r_2 represents the radius of the addition with the corresponding shell around it. The part of the addition which is still solid is indicated by r_3. During the course of assimilation, r_2 and r_3 are changing.

3.4.3.1. Route One

Figure 3.4.1 depicts various stages of addition assimilation in route one. The addition following this route belongs to Group I, and it melts inside the shell. Conditions which

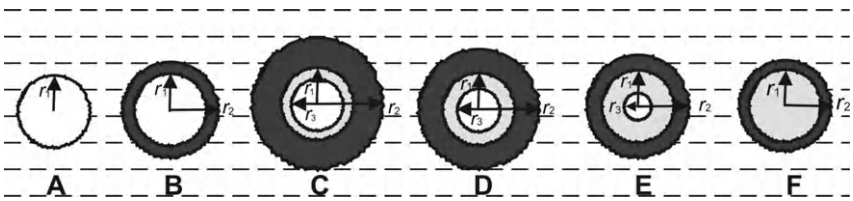


Figure 3.4.1 Various stages of route one. The addition starts to melt inside the shell (stage C) and it is only released to the bath once the protective shell has melted back.

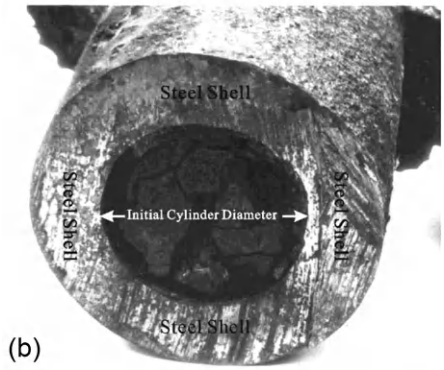
promote this route are a low liquid metal superheat and/or a high thermal conductivity of the addition. In this case, the assimilation of the addition in the liquid metal takes place only when the protective shell has melted back. Figure 3.4.2a shows a specifically manufactured ferromanganese cylinder. This cylinder was immersed into liquid steel of 30 °C superheat for 30 s and afterward withdrawn and sectioned. The resulting cross section is presented in Figure 3.4.2b. An enlargement of a portion of the cross section of Figure 3.4.2b is shown in Figure 3.4.2c. Figure 3.4.2c displays the solid ferromanganese, the steel shell, and the melting zone of the ferromanganese engulfed between the steel shell and the solid ferromanganese. The assimilation of this addition under the specified liquid steel conditions follows route one. Figure 3.4.3 displays predicted results for the melting of ferromanganese and silicomanganese additions following route one. For both of these additions, the inflection points B and F are due to loss of the thermal resistance. Figure 3.4.4 presents predicted results for an aluminum spherical addition following route one in its assimilation in liquid steel and the steel bath superheat is 100 °C. In this case, the aluminum follows route one despite the high superheat. This is possible due to the high thermal conductivity of aluminum. It should be pointed out here that the thermal conductivity of aluminum is approximately 37 times higher than that of solid ferromanganese. The two lines shown in Figure 3.4.4 correspond to two different thermal resistances. The shell with thermal resistance $R = 0.0001\ \mathrm{m^2\ K\ W^{-1}}$ melts faster (i.e., segment AEFG) than the shell with $R = 0\ \mathrm{m^2\ K\ W^{-1}}$ (i.e., segment ABC). The other two lines depict melting of Al sphere inside the steel shell for two different resistances (AD for $R = 0\ \mathrm{m^2\ K\ W^{-1}}$) and (HI for $R = 0.0001\ \mathrm{m^2\ K\ W^{-1}}$).

3.4.3.2. Route Two

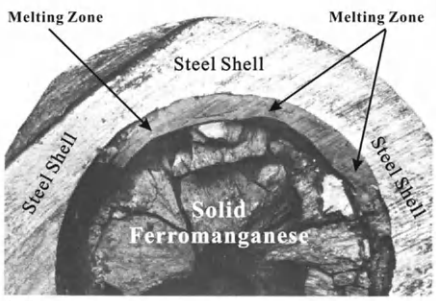
Figure 3.4.5 shows the different stages of assimilation of an addition following route number two. Figure 3.4.6 displays predicted results of the assimilation of ferromanganese and silicomanganese additions following route two. In this case, the steel bath superheat was 50 °C. The inflexion point, B, in the ferromanganese predictions, Figure 3.4.6, indicates the melting of a portion of ferromanganese which is in contact with the steel shell. This melting results in the disappearance of interfacial thermal resistance between the ferromanganese and steel shell, which in turn makes the steel shell



(a)



(b)



(c)

Figure 3.4.2 (a) Ferromanganese cylinder 3.8 cm in diameter and 15.2 cm in length. (b) Cross section of ferromanganese cylinder following immersion in liquid steel at superheat 30 °C for 30 s. (c) An enlargement of a portion of the cross section shown in (b).

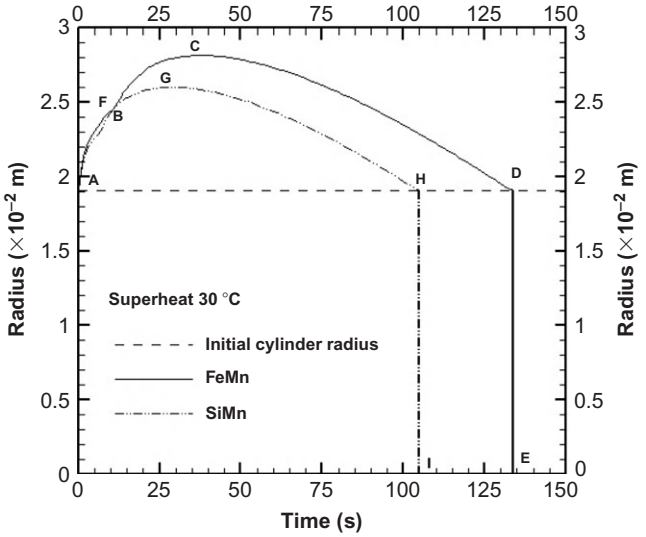


Figure 3.4.3 Predictions for assimilation time of ferromanganese and silicomanganese cylinders immersed into liquid steel having superheat 30 °C. In this case, route one is followed.

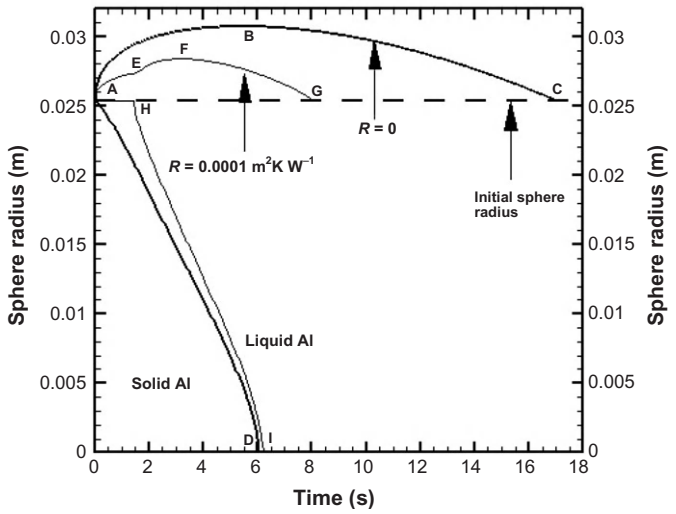


Figure 3.4.4 Predictions for assimilation time of aluminum sphere immersed into liquid steel having superheat 100 °C. In this case, route one is followed.

grow faster—segment BC. In the subsequent segment, CDE, the shell thickness decreases and has zero thickness at a point in time, D. Segment DE signifies the release of liquid ferromanganese in the steel bath and the following segment, EF, indicates a relatively fast melting process of the remaining ferromanganese. Segment EF is illustrated in Figure 3.4.5 by the stages D, E, and F.

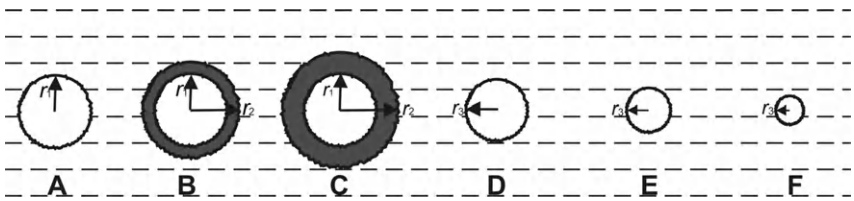


Figure 3.4.5 Various stages of route two. A shell is solidified around the addition and upon melting back of the shell the addition is very close to its melting temperature and stages D, E, and F are taking place in very short period of time.

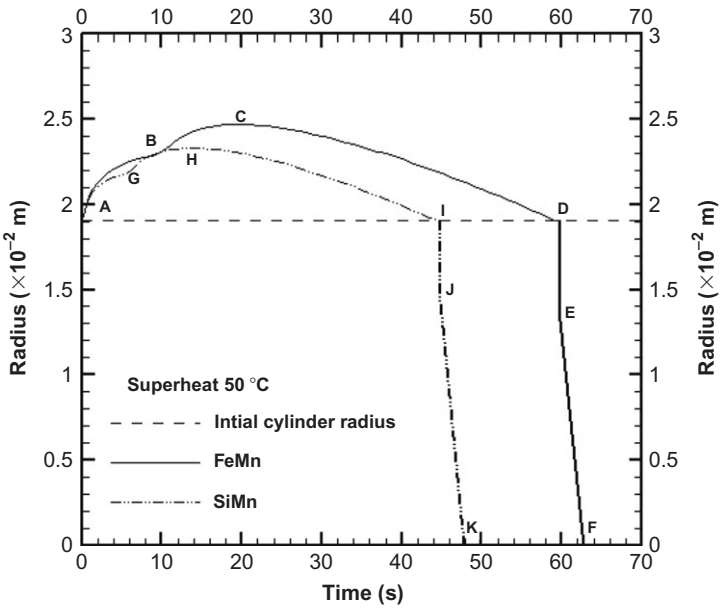


Figure 3.4.6 Predictions for assimilation time of ferromanganese and silicomanganese into liquid steel having superheat 50 °C. In this case, route two is followed.

3.4.3.3. Route Three

Figure 3.4.7 presents various stages of assimilation when route three is involved. For an addition to follow this route, it must be relatively large, have a low thermal conductivity, and must be immersed into a liquid metal with high superheat. In this case, the first shell, stage B, melts back quickly and subsequently a second shell is formed (stage E), with an even shorter duration than the first shell.

Support for the claim that a second shell forms is provided by two experiments. In the first case, specimens of ferromanganese cylinders, 2.54 cm in diameter and 17.8 cm in length, equipped with thermocouples located close to the centerline, were immersed into liquid steel. In these experiments, the temperatures of the steel bath as well as that of the

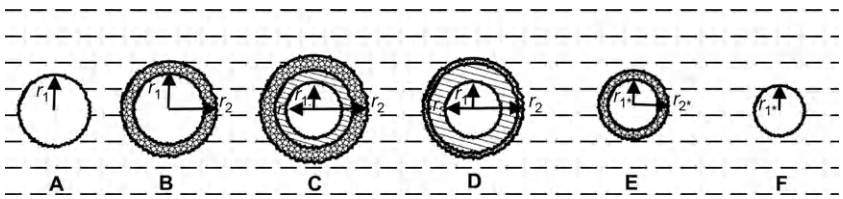


Figure 3.4.7 Various stages of route three. This route takes place when an addition with low thermal conductivity is immersed into metal bath having large superheat. A first shell solidifies around the addition and melts back fast and then a second shell forms, stage E. The light gray of stages C and D corresponds to a layer of molten addition formed under the first shell.

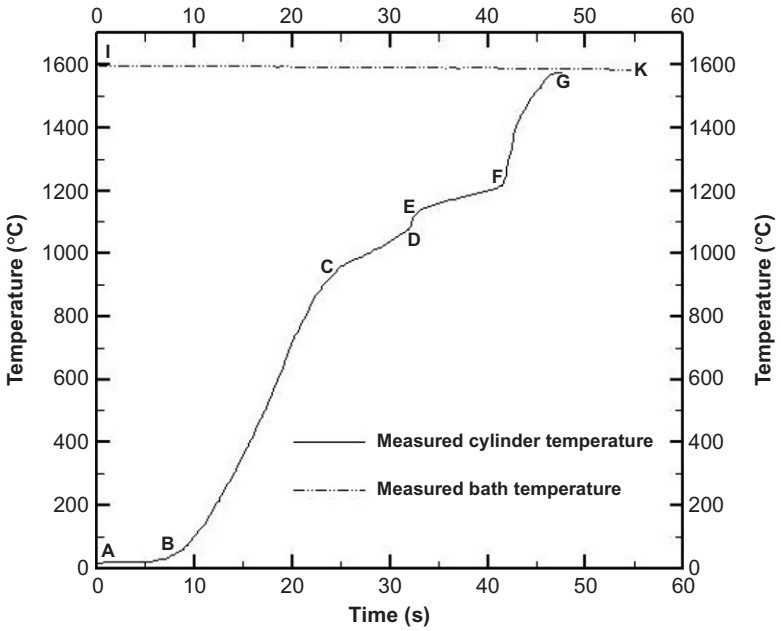


Figure 3.4.8 Experimental results about immersing ferromanganese cylinder in liquid steel.

centerline of the cylinder were recorded. Figure 3.4.8 depicts a typical experimental result, tracing the addition's temperature history from the time of its immersion into the liquid steel (point A) until its assimilation into the steel bath (point G). Segment ABCD corresponds to the formation and subsequent melting of the first steel shell. Segment DE corresponds to the removal of a small segment of the ferromanganese cylinder that has melted. Segment EF corresponds to the formation and subsequent melting of the second shell. Segment FG represents the ferromanganese cylinder which has been assimilated into the liquid steel, thereby the centerline temperature is approaching that of the steel bath temperature very quickly (i.e., segment FG).

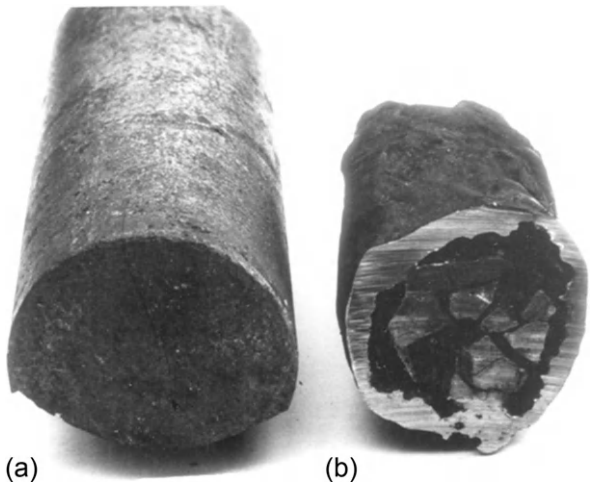


Figure 3.4.9 (a) Size of ferromanganese cylinder prior to immersion in steel bath. (b) Ferromanganese cylinder after withdrawal from steel having second shell.

Further support of the formation of a second steel shell is provided in a second set of tests, using ferromanganese cylinders of 3.81 cm in diameter and 15.20 cm in length immersed into liquid steel and then withdrawn and sectioned. Figure 3.4.9 is a photograph of one of these cylinders prior to immersion (a) and sectioned following immersion (b). As seen, the sectioned cylinder after immersion has a smaller diameter than the original one. This is indicative that the shell that is visible must be the second shell, because if it were the first shell it would have had a larger diameter than the original cylinder. Figure 3.4.10 displays predictions for the formation of the first and second shell, around an immersed ferromanganese cylinder under conditions of high liquid metal superheat of 100 °C. The first shell is indicated by the segment ABCDF. The segment FE relates to part of ferromanganese which has melted at point F. Segment EGH corresponds to the second shell formation, and as seen, this second shell in comparison with the first shell lasts a shorter period of time.

3.4.3.4. Route Four

Figure 3.4.11 displays the various assimilation stages of route four. In this route, an exothermic reaction is triggered between the shell and the addition (stage B). It was found that this exothermic reaction generates heat fluxes of 251 and 397 kW m^{-2} for 50 wt% ferrosilicon and titanium metals, respectively. The net result of this reaction is to make the shell that was formed to melt back very fast, stages B and C. Upon shell melting, the assimilation of the addition proceeds extremely fast, stages D, E, and F with simultaneous agitation of the liquid metal adjacent to the addition. In some cases, this agitation can proceed in a quickening manner resulting in an acceleration of the addition's assimilation.

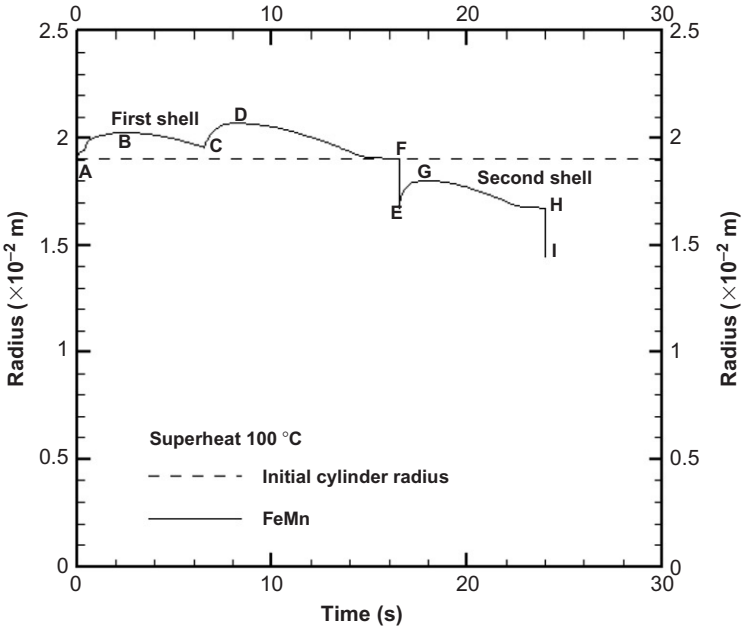


Figure 3.4.10 Predictions for melting of the first shell and second shell.

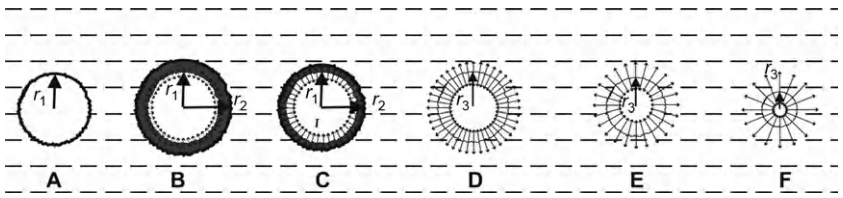


Figure 3.4.11 Schematic representation of various stages of route four.

Both groups of additions (i.e., I and II) can follow this route. Figure 3.4.12 shows various experimental results of additions in liquid steel following route four. In these experiments, various types of additions were immersed into liquid steel for short time periods and then withdrawn and sectioned. In all of these experimental results, the developed reaction zone is sandwiched between the addition and the steel shell. Figure 3.4.13 presents various stages of titanium assimilation into liquid steel. In this figure, segments ABC and CDE of line 1 denote the steel shell period and the free dissolution period, respectively. During the steel shell period, the interface reaction between the steel shell and the titanium (i.e., Figure 3.4.12d) was observed. In Figure 3.4.13, line 3 also depicts the deduced free dissolution speed. In this line, segment FG indicates a relative constant dissolution speed. In the following segment, GHIJK, the dissolution speed increases more than five times and signifies the observed acceleration. In tandem with this acceleration,

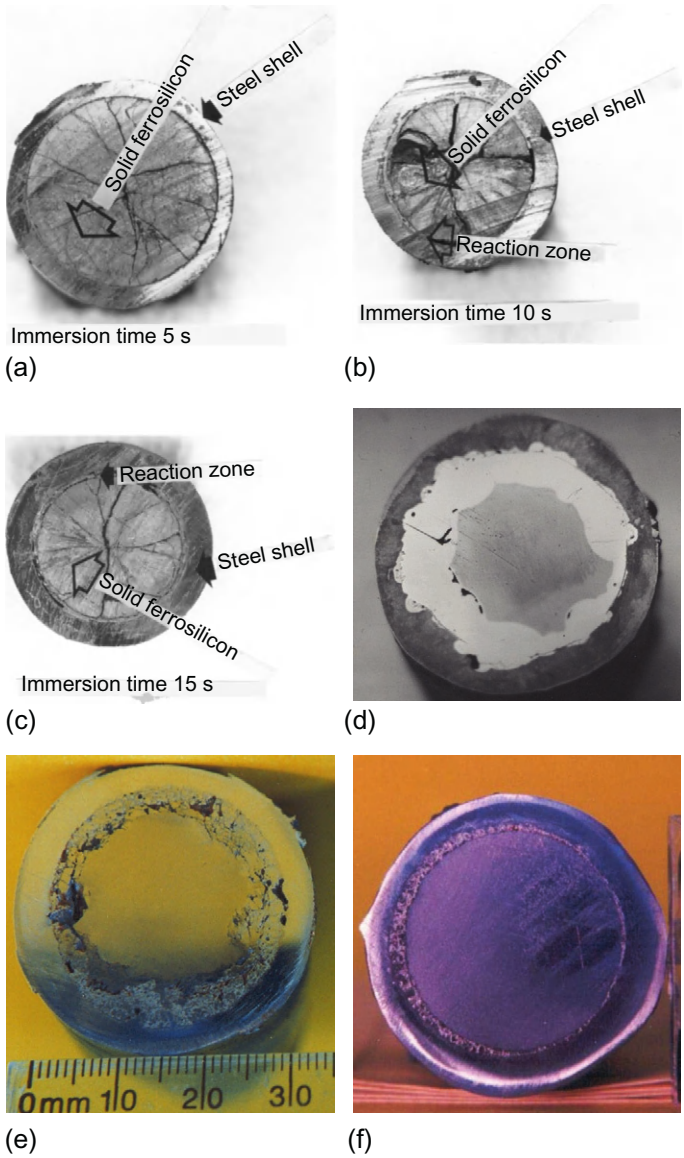


Figure 3.4.12 Experimental results with additions immersed in liquid steel following route four. (a–c) 50 wt% ferrosilicon [74], (d) titanium [79], (e) zirconium [81], and (f) niobium [78].

an increased agitation was observed in the liquid steel which was adjacent to the dissolving titanium cylinder. Figure 3.4.14 displays predictions on the effect of the liquid metal superheat on the steel shell melting time under two different conditions, using a 2.54-cm diameter 50-wt% ferrosilicon cylinder. In the first condition, the reaction at

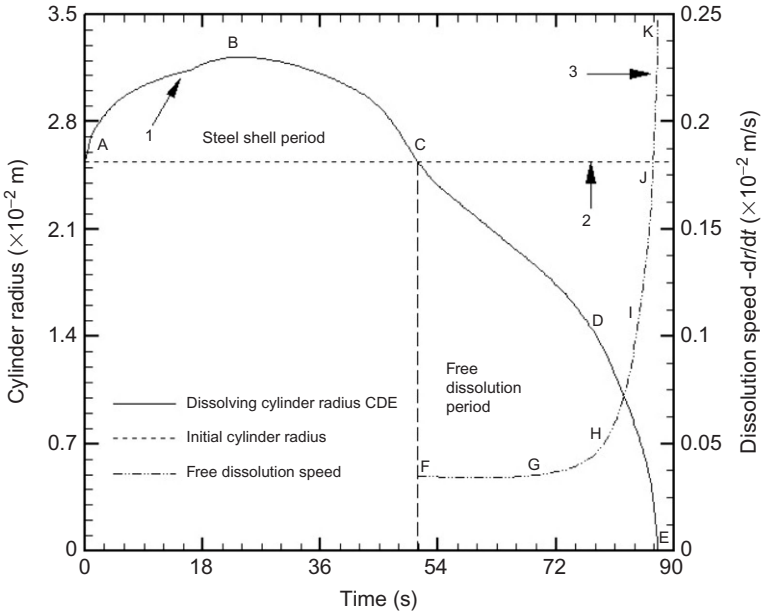


Figure 3.4.13 Various stages of assimilation of titanium cylinder in liquid steel with the measured free dissolution speed.

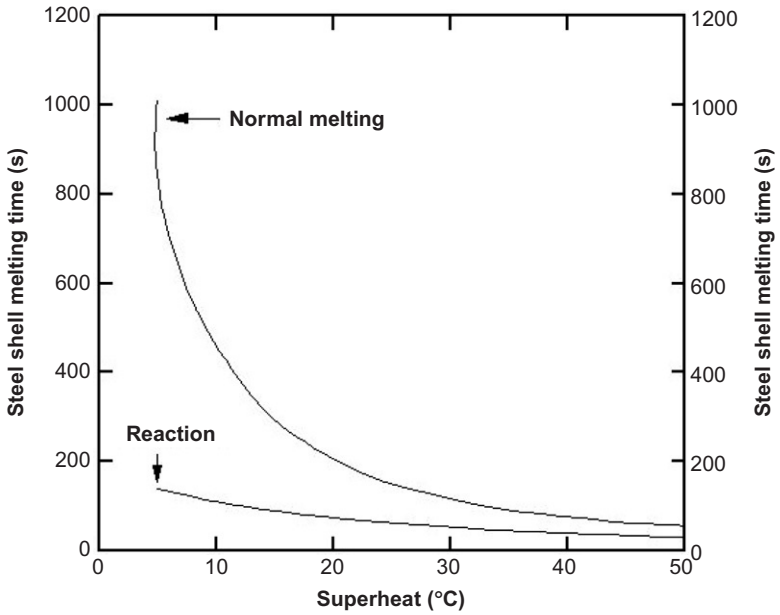


Figure 3.4.14 Predicted steel shell melting time versus steel bath superheat for 2.54-cm diameter cylinder of 50 wt% ferrosilicon.

the steel shell cylinder interface is considered while in the second condition, normal melting (i.e., no reaction) was assumed at that interface. As seen, at low liquid steel superheats, the melting of the steel shell is very different from normal melting when reaction is considered. However, this difference is diminished at high superheats. The much lower convective flux from the steel bath at low superheats is responsible for these phenomena.

3.4.3.5. Route Five

Various stages of route five are displayed in Figure 3.4.15. In this case, a shell (i.e., stage B) is formed. The melting back of this shell is followed by a liquid-phase diffusion process (i.e., stages C, D, E, and F). For additions following this route, the shell period might be a small fraction of the whole assimilation process. Figure 3.4.16 displays predictions of a small part of the assimilation history of manganese into liquid magnesium. As seen,

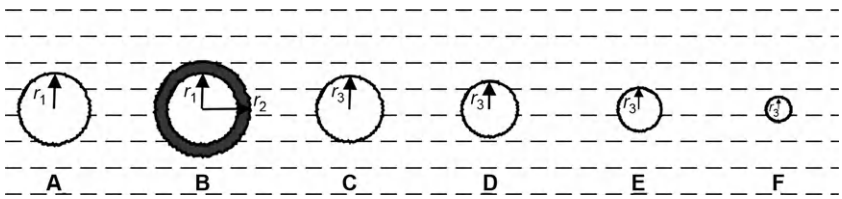


Figure 3.4.15 Various stages of route five.

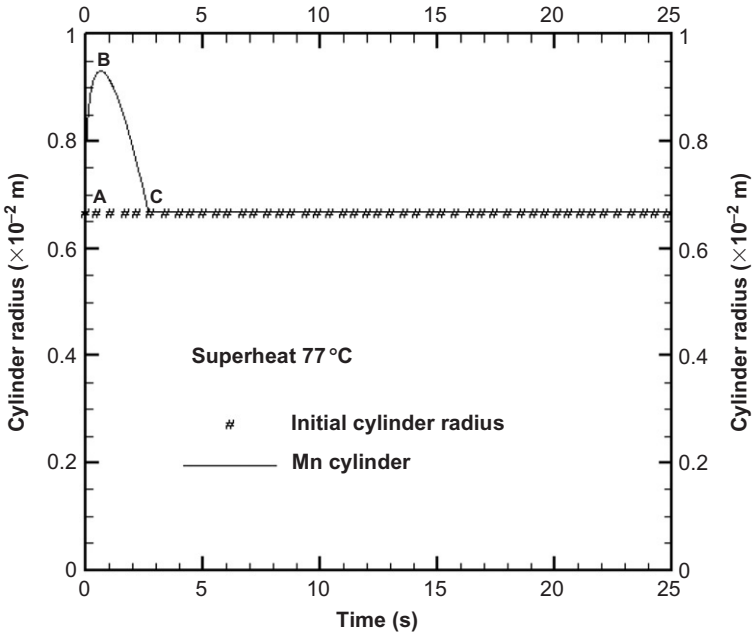


Figure 3.4.16 Predictions of assimilation of solid manganese cylinder into liquid magnesium.

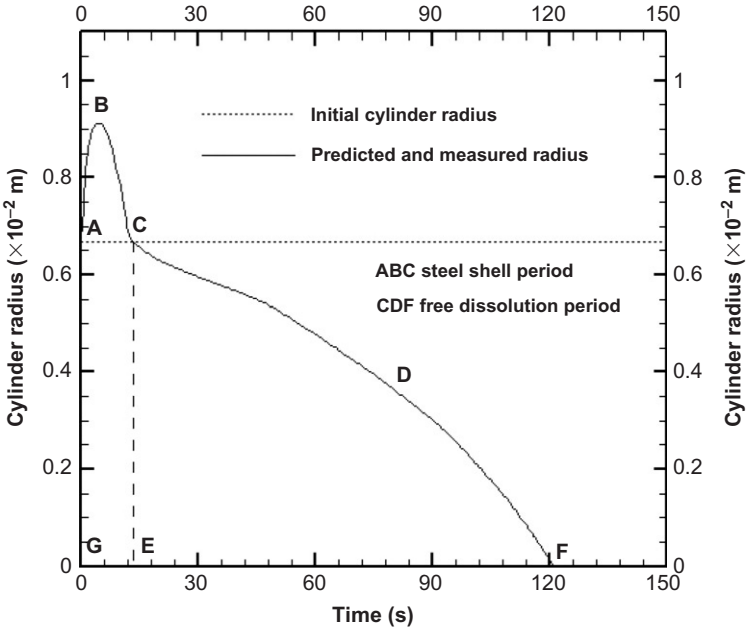


Figure 3.4.17 Assimilation of vanadium in liquid steel experimental and predicted results.

the magnesium shell will last only a few seconds (i.e., segment ABC) around the addition. It should be pointed out here that the whole assimilation of the manganese cylinder will last for hours. Consequently and in this case, the shell period would represent an extremely small fraction of the whole assimilation period. Figure 3.4.17 shows typical predicted and experimental results of the assimilation of pure vanadium in liquid steel. In this case, segment ABC represents the steel shell period while CDF displays the free dissolution period. The steel shell period corresponds to approximately 10% of the assimilation period.

3.4.3.6. Route Six

Various stages of route six are displayed in Figure 3.4.18. This route is followed by additions in the form of compacted powder mixtures or briquettes. Upon immersion of these additions into the liquid metal, a shell is formed around the addition and melts back quickly due to the low thermal conductivity of these types of additions, shown by stage B in this route. Then, the addition is heated up and expands, stage C, in Figure 3.4.18. Various exothermic reactions are taking place and an intensive exothermicity is observed. This exothermicity is due to the formation of various types of intermetallic compounds. Following this enlargement, the addition starts to fragment. This disintegration proceeds rather stochastically (i.e., stages DEF). An idea of compact swelling can be gained in Figure 3.4.19. It illustrates the volumes of a compact before and after triggering the

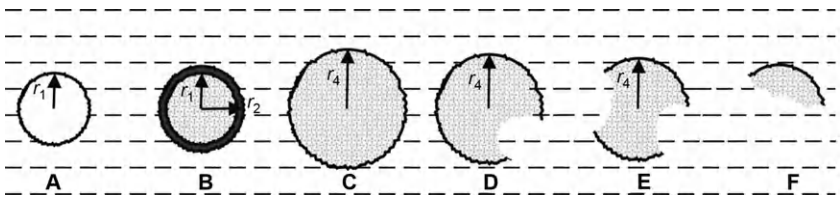


Figure 3.4.18 Various stages of route six.

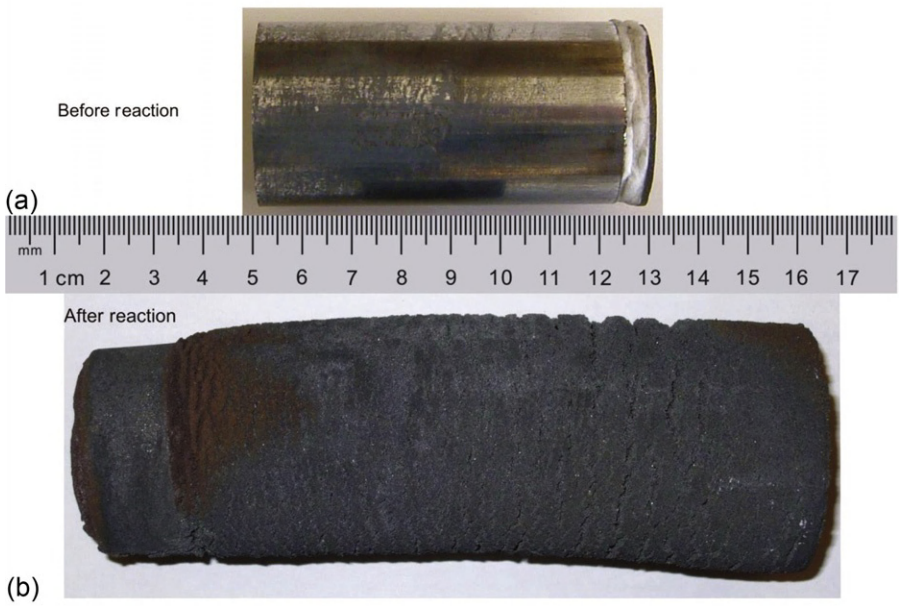


Figure 3.4.19 A 75 wt%Mn–25 wt%Al compact before and after the intermetallic reactions in a 750 °C argon protective environment.

intermetallic reactions in a 750 °C argon protective environment. The explanation for the swelling of the compact is given in Ref. [107]. Fe–Mn compacts were fabricated and their assimilation into liquid magnesium was examined. The interested reader can find more details on the fabrication of these compacts in Ref. [108]. Figure 3.4.20 illustrates various essentials of these assimilation experiments. Figure 3.4.21 shows results of a typical assimilation experiment in liquid magnesium. In this case, the data acquisition started to record data for more than 110 s prior to the compact's immersion into the liquid magnesium. Segment EF of line 2 indicates the time period during which the cylinder started to be lowered toward magnesium bath. The subsequent segment, FG, denotes the time when the compact was immersed into the liquid metal. At that moment, the bath temperature exhibited a certain decrease, as indicated in segment BC of line 1. At

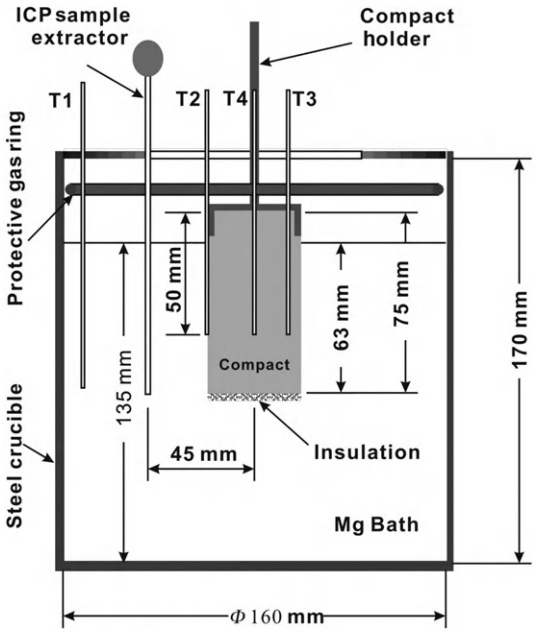


Figure 3.4.20 Cross-sectional details of the crucible used in this experimental work.

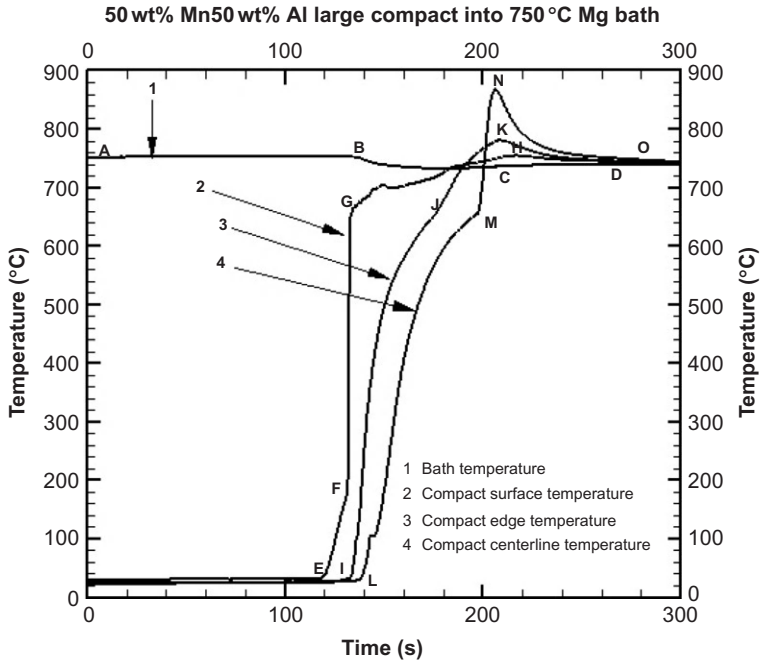


Figure 3.4.21 Experimentally recorded temperature–time history of Mn–Al compact immersed into liquid magnesium.

this moment, the liquid metal acted as a heat source to the immersed compact and for this reason there is such a decrease in line 1. From segment GHO, of line 2, it is clear that the temperature at H exceeds the bath temperature. In fact, similar phenomena are observed in lines 3 and 4 at points K and N, respectively. Points H, K, and N provide undisputable proof that heat is generated inside the compact. From that moment, the magnesium bath reverses its role and acts as a heat sink [108].

An addition can follow different routes in the same liquid metal, depending on the liquid metal superheat and flow conditions. An example of this case can be ferromanganese additions in liquid steel. In this case, ferromanganese can follow the first three routes of assimilation. Moreover, a given addition in different metal baths may be categorized as belonging to Group I, or Group II, or Group III. For example, Si metal addition in liquid steel belongs to Group I. The same addition in liquid Al is a member of the Group II, whereas Si metal in high carbon liquid iron (HCLI) is placed in Group III.

3.4.4. EXOTHERMIC PHENOMENA DURING ASSIMILATION

The exothermic phenomena during assimilation of additions in liquid metals have been classified as microexothermic and macroexothermic.

3.4.4.1. Microexothermic Phenomena

Exothermicity is observed in a variety of different metals when they are mixed with other metals. The formation of an intermetallic compound is usually associated with a certain amount of heat release. When small finite amounts of two metals are mixed to produce an intermetallic, the reaction that will take place can be written as:

$$x{*}\mathrm{Me1} + y{*}\mathrm{Me2} \rightarrow \mathrm{Me1}_x\mathrm{Me2}_y \tag{3.4.1}$$

The term microexothermicity was coined [72] to indicate exothermicity that is released from reactions of type (3.4.1). Microexothermic reactions similar to (3.4.1) have been observed in ferrous [72,109] and in nonferrous metallurgy [2,110]. These reactions have also captured the attention of researchers in the area of thin films in the microelectronics industry [111]. Depending on the context where these reactions occur, the impact of microexothermic reactions can range from desirable [112,113] to catastrophic [110].

The starting temperature of type (3.4.1) reactions has attracted much research. In the area of metallurgy, it was observed that type (3.4.1) reactions proceed at lower temperatures when the reactants (i.e., Me1 and Me2) are in powder form, while they proceed at higher temperatures when the reactants are in larger form. Kubaschewski and Dench [114] observed that equiatomic powder mixtures of iron and titanium reacted at about 1090 °C (1363 K), the eutectic temperature. In another study, using larger samples of steel and titanium 2.54 cm in diameter, starting temperature was reported to be

1185 °C (1458 K) [75,79]. Similar phenomena have been observed in the iron–niobium system [72,78]. In general, two factors are primary in the triggering of microexothermic reactions. Foremost is the temperature at the interface between the steel shell and the specific addition. Of secondary importance is the surface roughness of the specimens involved. When the addition's surface is smooth, the triggering temperature approaches the eutectic temperature; when the surface is rough, the triggering temperature may be marginally lower than the eutectic temperature [78,79,81,115].

Since microexothermic reactions proceed rather swiftly and are substantially adiabatic, the initial temperature of reactants is important for the state of products in type (3.4.1) reactions. For example, if the following reaction:

$$0.667\mathrm{Fe}_{(\gamma)} + 0.333\mathrm{Nb}_{(s)} \rightarrow \mathrm{Fe}_{0.667}\mathrm{Nb}_{0.333(\varepsilon)} \tag{3.4.2}$$

were to take place at a temperature of 1600 °C, typical of steelmaking, the heat that reaction (3.4.2) would release would be capable of increasing the temperature of the resultant intermetallic compound $\mathrm{Fe}_{0.667}\ \mathrm{Nb}_{0.333(\varepsilon)}$ close to its melting point [72]. This phenomenon was used in the development of the microexothermic ferroalloy additions [72,113]. It should be pointed out here that similar microexothermic phenomena were observed with Mn–Al compact additions immersed into liquid metals such as magnesium [107] and aluminum [116]. The microexothermic compact additions belong to class III and they follow route six. The various pictures shown in Figure 3.4.12 depict microexothermic phenomena involving steel with different metal additions. Figure 3.4.22a displays a steel cylinder immersed in a 50 wt% ferrosilicon bath and then withdrawn and quenched in water with visible 50 wt% ferrosilicon shell. In Figure 3.4.22b, the same cylinder as Figure 3.4.22a is shown but in this case 50 wt% ferrosilicon shell and microexothermic reaction products were removed. The extent of microexothermic reaction is clearly seen [117].

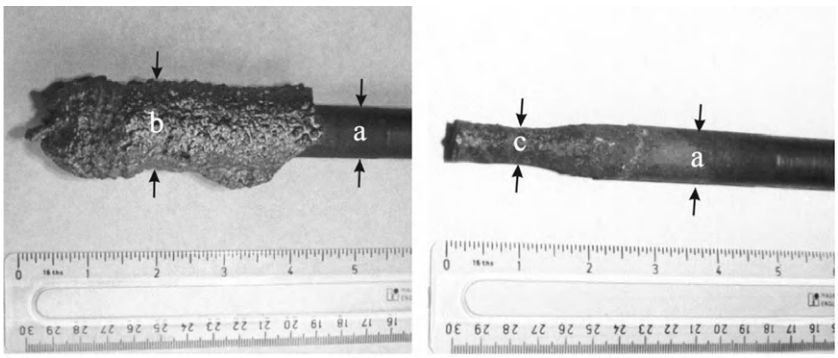


Figure 3.4.22 (a) Steel cylinder with ferrosilicon shell around it. (b) The same cylinder with the ferrosilicon shell removed.

During the course of a research study focusing on assimilation of zirconium–aluminum powder compacts into liquid aluminum, it was deemed necessary to study the microexothermicity involved during heating in an argon protective atmosphere of Zr–Al compacts [115]. Figure 3.4.23 depicts schematic representation of this experimental setting. Figure 3.4.24 presents the results of a 60 wt%Zr–40 wt%Al cylindrical compact heating. That compact had a 1.905 cm diameter and 6.4 cm length and its weight was 71.7 g. During heating, the centerline temperature was recorded using a R-type sacrificial thermocouple. As seen from the segment PQ of line 3, there is an approximately 1000 °C temperature increase. This increase was due to microexothermic events that occurred.

The microexothermicity concept was applied in the development of a new family of additions with superior assimilation characteristics. Conventional ferromolybdenum, ferroniobium, and ferrochromium alloys were modified with minor quantities of silicon in order to achieve improved assimilation rates in liquid steel. Both the modified and unmodified ferroalloys were compacted into cored-wire forms. The microexothermicity involved can be attributed to the formation of intermetallic compounds, which results in a certain amount of heat being released. This heat is sufficient to melt the compound and form a liquid alloy which is, in turn, more rapidly assimilated by the molten steel. It has been found that silicon-modified core-wire additions based on FeMo, FeNb, and FeCr powders exhibit markedly superior solution characteristics when compared to unmodified

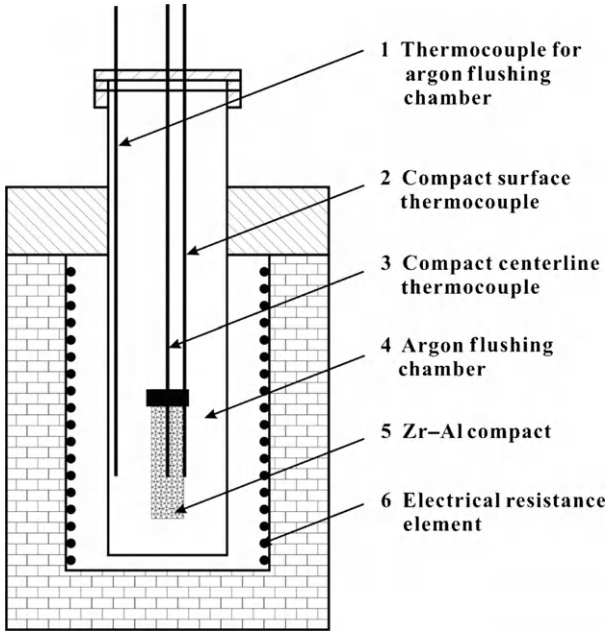


Figure 3.4.23 Schematic of experimental setting of heating Zr–Al compacts in an argon protective atmosphere.

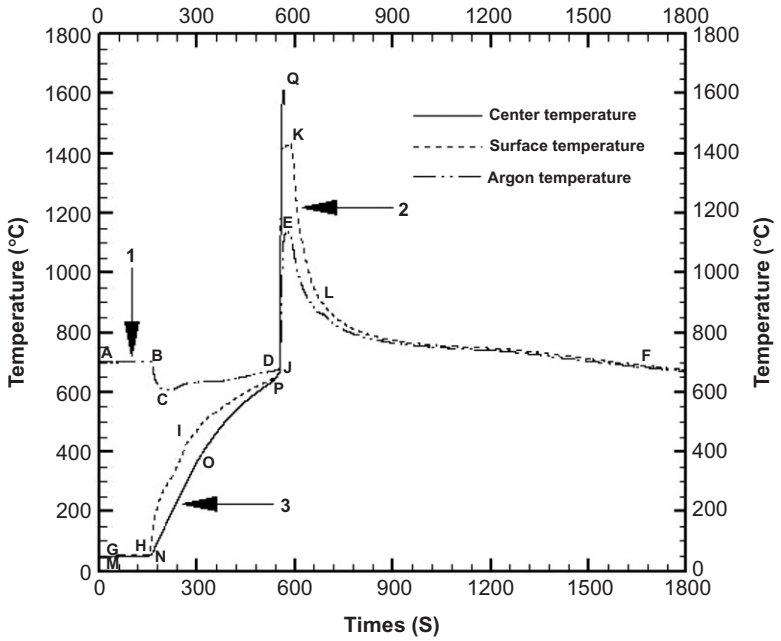


Figure 3.4.24 Experimental results of heating Zr–Al compact into an argon protective atmosphere.

cored-wired additions. The significantly shorter time required for assimilation of microexothermic cored-wires into liquid steel suggests that alloys of this type would be well suited for addition in the tundish, where residence time restrictions demand a very rapid rate of solution [118,119].

There is an interest in microexothermic reactions from another area of Materials Engineering, because these reactions are used in the synthesis of advanced materials. A symposium on *in Situ* Reactions for Synthesis of Composites, Ceramics, and Intermetallics has summarized the advances in this area, and more details can be found in Ref. [120].

3.4.4.2. Macroexothermic Phenomena

When a small amount of a solid metal, Me2, is mixed with very large amounts of a liquid metal, Me1, and if the mixing happens to be exothermic, a certain amount of heat is released. In order to quantify this phenomenon, it is important to recall that when a small amount of Me2 is mixed with a large quantity of liquid Me1, the heat of mixing should closely approximate the partial enthalpy of mixing. In this case, the relevant reaction can be written as follows:

$$\mathrm{Me1} + \mathrm{Me1}_m\mathrm{Me2}_n \rightarrow \mathrm{Me1}_{m+1}\mathrm{Me2}_n \tag{3.4.3}$$

In the case of Equation (3.4.3), the ratio of m/n is equal to the ratio of x/y in Equation (3.4.1), but the magnitude of m and n is such that $(m+1)$ practically equals m.

The term macroexothermicity was coined [72] to indicate exothermicity that is released from reactions of this type (3.4.3). These macroexothermic phenomena are observed during the free dissolution period of some additions, such as titanium, exhibiting large exothermic heat of mixing, as illustrated by segment CDE of line 1 in Figure 3.4.13. Most importantly, these phenomena present a unique feature that the dissolution speed accelerates significantly, as depicted by line 3, segment GHIJK. During the free dissolution period, the relative proportions of dissolution and melting depend upon the steel bath temperature; that is, the higher the steel bath temperature, the larger the proportion of cylinder which is molten when it is assimilated in liquid steel. From the analysis of numerous experimental results, it was found that when the inward radial velocity of the titanium interface was less than 0.045 cm s^{-1}, dissolution dominated, while above this number melting occurred [75]. The acceleration phenomena observed during the free dissolution of zirconium cylinders in liquid steel [81,82] were even more intensive than those in titanium.

The stages D, E, and F in route four of Figure 3.4.11 schematically represent these macroexothermic phenomena, while in the same figure stages B and C represent microexothermic phenomena. During the assimilation of exothermic additions in liquid steel, it is possible for both microexothermic and macroexothermic events to take place. The interested reader can find more details on these simultaneous events in Ref. [117].

For a given element assimilating into liquid steel, its macroexothermicity can be quantified using the following equation:

$$\overline{\Delta H}_{\text{Macroexothermicity}} = \overline{\Delta H}_{\text{Element}} + (\text{LH}_{\text{Element}}) \tag{3.4.4}$$

Experimental data from a number of studies examining the average mass transfer rates involving the free dissolution of various elements in liquid steel were compiled. All these studies used liquid steel at 1600 °C under natural convection conditions, utilizing approximately similar specimens of comparable size. The purity of these cylindrical specimens was at least 99 wt%. The experimental data are tabulated in Table 3.4.3 according to increasing mass transfer rates. As seen, the metal with the smallest rate is tungsten and with the highest is silicon. In increasing order, the metals were W–Cr–Mo–V–Nb–Ti–Zr–Si. In the same table, the corresponding activity coefficients of different elements in dilute solutions in liquid steel (i.e., γ^0_{Me}) are also shown. Nearly all the elements exhibit negative deviation from Raoultian ideal behavior, with W being the only exception, displaying a positive deviation and the smallest mass transfer rate. As seen in Table 3.4.3, as the negative deviation from ideal Raoultian behavior increases the corresponding mass transfer rates also rise. Using Equation (3.4.4), the macroexothermicity of each element displayed in Table 3.4.3 was estimated. As seen from this table, the estimated macroexothermicity decreases in the order of W–Cr–Mo–V–Nb–Ti–Zr–Si which is in tandem

Table 3.4.3 Experimental Results from Various Studies Dealing with Assimilation of Different Elements in Liquid Steel

Assimilated Cylindrical Specimen	Mass Transfer Rate (Natural Convection) (g cm^{-2} s^{-1})	Raoultian Activity Coefficient at Infinite Dilution (γ_M^0)	Macroexothermicity (J g^{-1})
W	0.0059 [63]	2.9 [121]	283
Cr	0.0079 [122]	0.63 [121]	190
Mo	0.0080 [63]	0.43 [121]	150
V	0.025 [75,76]	0.21 [121]	−64
Nb	0.37 [78]	0.080 [121]	−136
Ti	0.40 [75,79]	0.037 [123]	−666
Zr	0.44 [81,82]	0.022 [81,82]	−721
Si	3.5 [117]	0.0013 [124]	−2970

with the observed increase of mass transfer rates. Another important feature of this table is the drastic change of mass transfer rates between Si and the rest of the elements. This drastic change, approximately an order of magnitude, is due to the fact that between various elements shown in Table 3.4.3 only Si belongs to Group I of additions and as such follows melting. All the other elements belong to Group II.

In Table 3.4.2, very large apparent activation energies of Ti, V, Nb, and Mo in liquid steel are registered. Despite these large activation energies, LPD is reported as the assimilation mechanism during the free dissolution. These uncommonly high values are most likely being explained on the basis of macroexothermic phenomena exhibited during their free dissolution in liquid steel. For such elements as Ti, V, Nb, and Mo, the temperature at the dissolving interface is higher than the temperature of the bulk steel and tends to increase during the course of free dissolution. Consequently, their dissolution in liquid steel can be regarded as being nonisothermal. Since it is very difficult or might be impossible to accurately measure the temperature of the dissolving interface, supplementary experiments are needed to determine the assimilation mechanism. In fact, for Nb and Mo, these supplementary experiments have been carried out. In the case of Nb, the liquid steel was static (i.e., natural convection) and dynamic (i.e., steel inductively stirred) with the latter exhibiting 30–70% increase in mass transfer coefficients over the former [78,82]. In the case of Mo, the crucible with liquid steel was stationary (i.e., natural convection) and subsequently different levels of vibration were imposed. It was reported [64] that the mass transfer coefficient for stationary crucible was 1.7×10^{-3} cm s^{-1} while at a vibration frequency of $n = 40$ impulses min^{-1} the mass transfer coefficient was 2.4×10^{-3} cm s^{-1} and at $n = 90$ impulses min^{-1} the mass transfer

coefficient was 3.2×10^{-3} cm s^{-1} [64]. In fact, these supplementary experiments for Nb and Mo provide unquestionable proof that LPD is the assimilation mechanism. In contrast, the supplementary experiments of Zr assimilation into liquid steel have shown no difference in the measured mass transfer rates between induction stirring and no stirring of the liquid steel [81]. As such, the activation energy of assimilation of Zr in liquid steel reported in Table 3.4.2 (340 ± 26.4 kJ mol^{-1}) indicates that, under the experimental conditions performed, reaction is the assimilation mechanism.

3.4.4.3. Transport Phenomena During Exothermic Assimilation

The exothermic phenomena during the assimilation of additions in liquid metals set in motion various heat, mass, and momentum transport phenomena, which are strongly coupled. The investigation of such exothermic phenomena from a fundamental viewpoint is motivated by its representation of a unique moving boundary problem, which is characterized by specific physical phenomena. An analysis of these phenomena indicates that this moving boundary problem is further complicated by the presence of a heat source. The reason for this complication is the fact that a heat sink (i.e., melting of a solid) and a heat source (i.e., exothermic heat of mixing) occur simultaneously within close proximity. The presence of the heat source in this kind of moving boundary problem has two effects. First, it makes the moving boundary move faster (i.e., melting faster). Second, it enhances the fluid movement in the vicinity of the moving boundary (i.e., accelerated fluid flow conditions).

3.4.4.4. Mathematical Formulation and Computational Approach

Initially, the energy equation was used in combination with experimental work and inverse heat transfer procedures to characterize and quantify the convective heat transfer conditions during the free dissolution of zirconium and titanium in liquid steel [105]. Figure 3.4.25 presents the predicted heat fluxes during the free dissolution period of Ti and Zr in liquid steel. Segment BC, representing the heat flux released during Ti dissolution, corresponds to the period during which Ti melts inside the liquid steel. Similar phenomena take place during segment EF, representing Zr melting in liquid steel. It should be pointed out that, in the cases of these ultra large macroexothermic phenomena, the liquid steel acts as a heat sink. Comparable phenomena where the liquid metal has acted as heat sink around the assimilating addition have been observed in liquid metals such as aluminum [115] and magnesium [108].

Following this initial work, a major advancement ensued. This involved the development of a rigorous mathematical model capable of predicting the coupled heat, mass, and momentum phenomena that occur when a solid has been assimilated exothermically in a stagnant (i.e., natural convection) liquid metal. In this case, the mathematical modeling work was validated in two stages, using experimental work. First, extensive

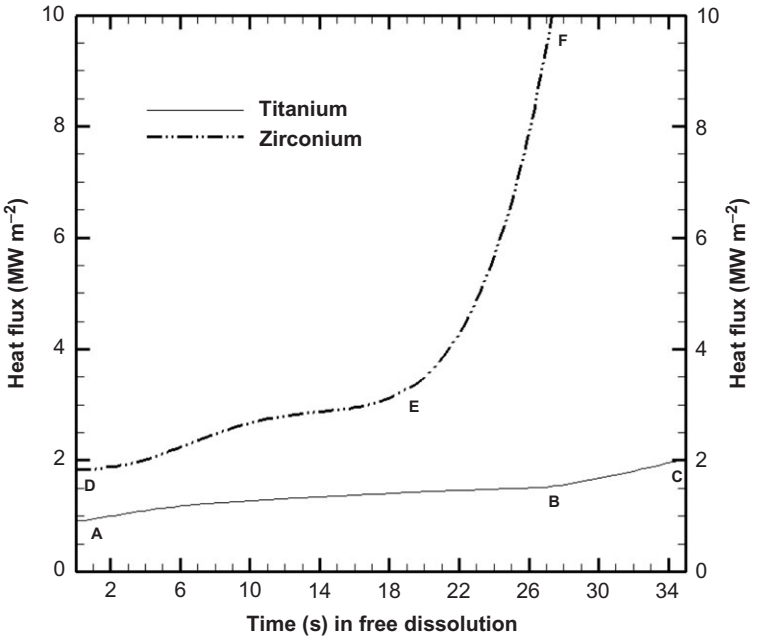


Figure 3.4.25 Predicted heat fluxes during the free dissolution period at the dissolving front interface for Ti and Zr.

low-temperature experimental work involving melting of ice cylinders in different concentrations of sulfuric acid solutions was undertaken, followed by high-temperature experimental study involving melting cylindrically shaped metallurgical-grade silicon in liquid high carbon iron.

In an attempt to develop a mathematical formulation for such a complex system, the immersion of a cylindrical sample into a cylindrical container with liquid solution was considered. Figure 3.4.26 shows schematically the physical system. In this case, the sample undergoes an inward melting process in a cylindrical container.

In order to develop the mathematical formulation for this complex case in the presence of natural convection, heat source, and heat sink, certain simplifying assumptions were made:

(i) The fluid motion of the liquid solution is two-dimensional laminar incompressible flow;
(ii) The volume variations associated with phase change and the viscous dissipation are ignored;
(iii) The liquid solution is a Newtonian fluid;
(iv) The immersion of the specimen into liquid solutions is assumed to take place instantaneously.

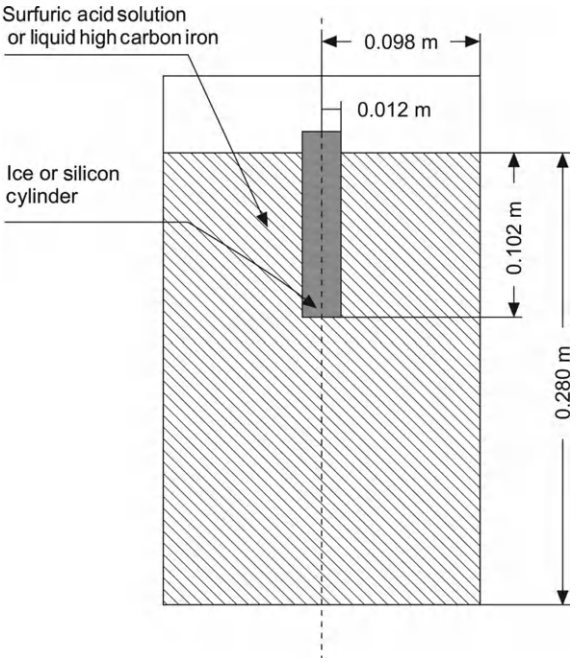


Figure 3.4.26 Schematic of sulfuric acid–ice experimental setup.

Regression analyses were carried out with the thermophysical data provided in Refs. [125–130]. The resulting relationships describing the variation of thermophysical properties of the solutions are listed in Refs. [131,132].

The governing differential equations for the laminar and incompressible flow with no viscous dissipation in a cylindrical polar coordinate system can be represented as follows:
Continuity equation:

$$\frac{\partial \rho}{\partial t}+\frac{1}{r}\frac{\partial}{\partial r}(\rho r v_r)+\frac{\partial}{\partial z}(\rho v_z)=0 \tag{3.4.5}$$

Momentum equation:
r-component:

$$\frac{\partial}{\partial t}(\rho v_r)+v_r\frac{\partial}{\partial r}(\rho v_r)+v_z\frac{\partial}{\partial z}(\rho v_r)=-\frac{\partial p}{\partial r}+\left[\frac{1}{r}\frac{\partial}{\partial r}\left(\mu r\frac{\partial v_r}{\partial r}\right)+\frac{\partial}{\partial z}\left(\mu\frac{\partial v_r}{\partial z}\right)\right]+\left(-\frac{\mu}{r^2}\right)v_r \tag{3.4.6}$$

z-component:

$$\frac{\partial}{\partial t}(\rho v_z)+v_r\frac{\partial}{\partial r}(\rho v_z)+v_z\frac{\partial}{\partial z}(\rho v_z)=-\frac{\partial p}{\partial z}+\left[\frac{1}{r}\frac{\partial}{\partial r}\left(\mu r\frac{\partial v_z}{\partial r}\right)+\frac{\partial}{\partial z}\left(\mu\frac{\partial v_z}{\partial z}\right)\right]+\rho g_z \tag{3.4.7}$$

Energy equation:

$$\frac{\partial}{\partial t}(\rho h)+\upsilon_r\frac{\partial}{\partial r}(\rho h)+\upsilon_z\frac{\partial}{\partial z}(\rho h)=\left[\frac{1}{r}\frac{\partial}{\partial r}\left(kr\frac{\partial T}{\partial r}\right)+\frac{\partial}{\partial z}\left(k\frac{\partial T}{\partial z}\right)\right] \tag{3.4.8}$$

Diffusion equation:

$$\frac{\partial C_A}{\partial t}+\upsilon_r\frac{\partial C_A}{\partial r}+\upsilon_z\frac{\partial C_A}{\partial z}=\left[\frac{1}{r}\frac{\partial}{\partial r}\left(D_A r\frac{\partial C_A}{\partial r}\right)+\frac{\partial}{\partial z}\left(D_A\frac{\partial C_A}{\partial z}\right)\right] \tag{3.4.9}$$

Since the energy equation consists of both convective and diffusive terms in which two dependent variables are included, temperature T and enthalpy h, the Enthalpy Transforming Model [133,134] is used to convert the energy equation into a nonlinear equation with only one dependent variable, enthalpy, and as such the existing SIMPLER (Semi-Implicit Method for Pressure Linked Equations Revised) [135] algorithm can easily be implemented. Temperature and enthalpy are related via the following state equation based on thermodynamics.

$$\frac{\mathrm{d}h}{\mathrm{d}T}=C(T) \tag{3.4.10}$$

If a constant specific heat for each phase is considered, $h=0$ is chosen to correspond the phase change phase in its solid state at the temperature of the solid, then the relation between temperature and enthalpy, when introducing the exothermic heat of mixing $(\Delta\overline{H_W})$, becomes

$$T=\begin{cases} T_m+\dfrac{h}{C_s}; & h\le 0 \\ T_m; & 0<h<H_f \\ T_m+\dfrac{(h-H_f+\Delta\overline{H_W})}{C_l}; & h\ge H_f \end{cases} \tag{3.4.11}$$

The energy equation can be rewritten as follows:

$$\frac{\partial}{\partial t}(\rho h)+\upsilon_r\frac{\partial}{\partial r}(\rho h)+\upsilon_z\frac{\partial}{\partial z}(\rho h)=\left[\frac{1}{r}\frac{\partial}{\partial r}\left(\gamma r\frac{\partial h}{\partial r}\right)+\frac{\partial}{\partial z}\left(\gamma\frac{\partial h}{\partial z}\right)\right]+S_E \tag{3.4.12}$$

where

$$S_E=\left[\frac{1}{r}\frac{\partial}{\partial r}\left(r\frac{\partial S_1}{\partial r}\right)+\frac{\partial^2 S_1}{\partial z^2}\right]+\left[\frac{1}{r}\frac{\partial}{\partial r}\left(r\frac{\partial S_2}{\partial r}\right)+\frac{\partial^2 S_2}{\partial z^2}\right]$$

and where

$$\begin{cases} \text{Solid phase } h \le 0; & \gamma = \dfrac{k_s}{C_s}; S_1 = 0; S_2 = 0 \\ \text{Solid/liquid phase } 0 < h < H_f; & \gamma = \dfrac{k_{in}}{C_{in}}; S_1 = 0; S_2 = 0 \\ \text{Liquid phase } h \ge H_f; & \gamma = \dfrac{k_l}{C_l}; S_1 = -\dfrac{H_f k_l}{C_l}; S_2 = \dfrac{\Delta \overline{H_W} k_l}{C_l} \end{cases}$$

$$\begin{aligned} k_{in} &= \lambda k_l + (1-\lambda) k_s \\ C_{in} &= \lambda C_l + (1-\lambda) C_s \\ \rho_{in} &= \lambda \rho_l + (1-\lambda) \rho_s \\ \lambda &= \frac{h}{H_f} \end{aligned}$$

As shown, Equation (3.4.12) is expressed only in terms of a single dependent variable, h, and two source terms of heat sink S_1 and heat source S_2. The transformation of the energy equation simplifies the numerical solution of the present complex case and makes it possible to use the existing SIMPLER algorithm. In order to solve this problem in a more general way, the governing equations should be nondimensionalized. The following dimensionless variables are defined

$$\begin{aligned} z^* &= \frac{z}{L}; \quad r^* = \frac{r}{L}; \quad \upsilon_r^* = \frac{\upsilon_r L}{\alpha_l}; \quad \upsilon_z^* = \frac{\upsilon_z L}{\alpha_l} \\ h^* &= \frac{h}{H_f}; \quad \rho^* = \frac{\rho}{\rho_{ref}}; \quad t^* = \frac{t\alpha_l}{L^2}; \\ P^* &= \frac{P}{\rho\left(\dfrac{\alpha_l}{L}\right)^2}; \quad S_1^* = \frac{S_1 C_l}{H_f k_l}; \quad S_2^* = \frac{S_2 C_l}{H_f k_l} \end{aligned} \tag{3.4.13}$$

Since the gravity terms in the momentum equations may have a substantial effect on the fluid flow, the density in the buoyancy forces is dependent on temperature and concentration, based on the assumption that it follows the Boussinesq approximation. Density, temperature, and concentration are related via

$$\rho = \rho_{ref}[1 - \beta_T(T - T_{ref}) + \beta_C(C_A - C_{ref})] \tag{3.4.14}$$

The governing equations can be expressed as the following dimensionless forms by substituting the dimensionless variables from Equation (3.4.13) into Equations (3.4.5)–(3.4.7), (3.4.9), and (3.4.12):

Continuity equation:

$$\frac{\partial \rho^*}{\partial t^*}+\frac{1}{r^*}\frac{\partial}{\partial r^*}\left(\rho^* r^* v_r^*\right)+\frac{\partial}{\partial z^*}\left(\rho^* v_z^*\right)=0 \tag{3.4.15}$$

Momentum equation:
r-component:

$$\frac{\partial v_r^*}{\partial t^*}+v_r^*\frac{\partial v_r^*}{\partial r^*}+v_z^*\frac{\partial v_r^*}{\partial z^*}=\left[\frac{1}{r^*}\frac{\partial}{\partial r^*}\left(\Gamma_\mu r^*\frac{\partial v_r^*}{\partial r^*}\right)+\frac{\partial}{\partial z^*}\left(\Gamma_\mu\frac{\partial v_r^*}{\partial z^*}\right)\right]+\left(-\frac{\Gamma_\mu}{r^{*2}}\right)v_r^* \tag{3.4.16}$$

z-component:

$$\frac{\partial v_z^*}{\partial t^*}+v_r^*\frac{\partial v_z^*}{\partial r^*}+v_z^*\frac{\partial v_z^*}{\partial z^*}=\left[\frac{1}{r^*}\frac{\partial}{\partial r^*}\left(\Gamma_\mu r^*\frac{\partial v_z^*}{\partial r^*}\right)+\frac{\partial^2}{\partial z^{*2}}\left(\Gamma_\mu v_z^*\right)\right]-Gr_{\mathrm{mT}}(h^*-1)+Gr_{\mathrm{mC}} \tag{3.4.17}$$

Energy equation:

$$\frac{\partial h^*}{\partial t^*}+v_r^*\frac{\partial h^*}{\partial r^*}+v_z^*\frac{\partial h^*}{\partial z^*}=\left[\frac{1}{r^*}\frac{\partial}{\partial r^*}\left(r^*\Gamma_\alpha\frac{\partial h^*}{\partial r^*}\right)+\frac{\partial}{\partial z^*}\left(\Gamma_\alpha\frac{\partial h^*}{\partial z^*}\right)\right]+S_{\mathrm{E}} \tag{3.4.18}$$

where

$$S_{\mathrm{E}}=\left[\frac{1}{r^*}\frac{\partial}{\partial r^*}\left(r^*\frac{\partial S_1^*}{\partial r^*}\right)+\frac{\partial^2 S_1^*}{\partial z^{*2}}\right]+\left[\frac{1}{r^*}\frac{\partial}{\partial r^*}\left(r^*\frac{\partial S_2^*}{\partial r^*}\right)+\frac{\partial^2 S_2^*}{\partial z^{*2}}\right]$$

Diffusion equation:

$$\frac{\partial C_{\mathrm{A}}^*}{\partial t^*}+v_r^*\frac{\partial C_{\mathrm{A}}^*}{\partial r^*}+v_z^*\frac{\partial C_{\mathrm{A}}^*}{\partial z^*}=\left[\frac{1}{r^*}\frac{\partial}{\partial r^*}\left(\Gamma_D r^*\frac{\partial C_{\mathrm{A}}^*}{\partial r^*}\right)+\frac{\partial}{\partial z^*}\left(\Gamma_D\frac{\partial C_{\mathrm{A}}^*}{\partial z^*}\right)\right] \tag{3.4.19}$$

$$\begin{cases}\text{Solid phase } h^*\le 0; & \Gamma_\mu=\infty;\\ \text{Solid/liquid phase } 0<h^*<1; & \Gamma_\mu=Pr\times 10^{10(1-h^*)};\\ \text{Liquid phase } h^*\ge 1; & \Gamma_\mu=Pr;\end{cases}$$

$$\Gamma_\alpha=\frac{\alpha_{\mathrm{s}}}{\alpha_{\mathrm{l}}};\ \ \Gamma_D=0;\ \ S_1^*=0;\ \ S_2^*=0$$

$$\Gamma_\alpha=\frac{\alpha_{\mathrm{in}}}{\alpha_{\mathrm{l}}};\ \ \Gamma_D=0;\ \ S_1^*=0;\ \ S_2^*=0$$

$$\Gamma_\alpha=1;\ \ \Gamma_D=\frac{Pr}{Sc}=\frac{D_{\mathrm{A}}}{\alpha_{\mathrm{l}}};\ \ S_1^*=-1;\ \ S_2^*=\frac{\Delta\overline{H_{\mathrm{W}}}}{H_{\mathrm{f}}}$$

$Pr=\dfrac{v_{\mathrm{l}}}{\alpha_{\mathrm{l}}}$ is the Prandtl number; $Sc=\dfrac{v_{\mathrm{l}}}{D_{\mathrm{A}}}$ is the Schmidt number; $Gr_{\mathrm{mT}}=\dfrac{g\beta_{\mathrm{T}}L^3H_{\mathrm{f}}}{\alpha_{\mathrm{l}}^2\rho^*C_{\mathrm{l}}}$ is a modified heat transfer Grashof number; and $Gr_{\mathrm{mC}}=\dfrac{g\beta_C C_{\mathrm{A}}L^3}{\rho^*\alpha_{\mathrm{l}}^2}$ is a modified mass transfer Grashof number.

The initial and boundary conditions are as follows:

3.4.4.5. Initial Conditions

In the domain of calculation, the velocity for the momentum equations is set to zero; the temperature in the ice is set to its melting point; the temperature of the acid solution is specified to be at room temperature (22 °C); and the concentration is set to the desired value.

3.4.4.6. Boundary Conditions

The radial velocity gradient at the free surface and the vertical velocity gradient on the plane of symmetry are zero. The velocity is set to zero at all solid walls. The temperature and concentration are kept constant at all the solid walls. An adiabatic condition is assumed for the temperature gradient and the concentration gradient at the top surface due to minor changes of temperature and concentration during and after the melting process.

They can be represented in mathematical forms as: Initial conditions: at initial interface between the ice and the solution;

$$v_r = 0,\ \ v_z = 0,\ \ T = 0^\circ\mathrm{C},\ \ C_\mathrm{A} = 0,\ \ \text{for } t = 0, r = r_1, z = z_1;$$

in the ice,

$$v_r = 0,\ \ v_z = 0,\ \ T = 0\ ^\circ\mathrm{C},\ \ C_\mathrm{A} = 0,\ \ \text{for } t = 0, 0 < r < r_1, (z_2 - z_1) < z < z_2;$$

in the solution,

$$\begin{gathered} v_r = 0,\ \ v_z = 0,\ \ T = 22^\circ\mathrm{C},\ \ C_\mathrm{A} = \text{constant},\ \ \text{for } t = 0, \\ r > r_1, 0 < z < z_2,\ \ \text{and}\ \ 0 < r < r_1, 0 < z < z_2 - z_1; \end{gathered}$$

Boundary conditions:
at the axis of symmetry,

$$v_r = 0,\ \ \frac{\partial v_z}{\partial r} = 0,\ \ \frac{\partial T}{\partial r} = 0,\ \ \frac{\partial C_\mathrm{A}}{\partial r} = 0,\ \ \text{for } r = 0, 0 < z < z_2;$$

at the free surface,

$$\frac{\partial v_r}{\partial z} = 0,\ \ v_z = 0,\ \ \frac{\partial T}{\partial z} = 0,\ \ \frac{\partial C_\mathrm{A}}{\partial z} = 0,\ \ \text{for } 0 < r < r_2, z = z_2;$$

at the bottom wall and side wall,

$$\begin{gathered} v_r = 0,\ \ v_z = 0,\ \ T = 22\ ^\circ\mathrm{C},\ \ C_\mathrm{A} = \text{constant}, \\ \text{for } 0 < r < r_2, z = 0,\ \ \text{and}\ \ r = r_2, 0 < z < z_2. \end{gathered}$$

In the Si–high carbon iron system, both initial and boundary conditions are the same as those used in the ice–sulfuric acid system except those initial conditions for the energy

and diffusion equations in the silicon cylinder and liquid high carbon iron. In the initial conditions, the temperature in the silicon is set to be at room temperature (22 °C), the temperature of the liquid high carbon iron is specified to be 1500 °C, and the concentration is set to the desired value. In boundary conditions, the temperature and concentration are kept constant at all the solid walls. Due to the extremely fast melting of silicon in liquid high carbon iron, the immersion experiments were completed within 25 s as soon as the power of the induction furnace was turned off. Zero heat flux condition is introduced and an adiabatic condition is assumed for the concentration gradient at the top surface [132].

The governing equations are discretized with the control volume implicit finite difference procedure referred to as SIMPLER [135]. The computational domain actually is half the experimental area shown in Figure 3.4.1 owing to axisymmetric conditions of the current case. The computation is done on a domain with 62 by 102 nodes. The convergence for each iteration was assured with the dimensionless time step under 8×10^{-7}. The mass source term is within the order of 10^{-5} in the pressure equation, which was used as an indicator of convergence in the fluid flow solution.

In tandem with this advancement, the predictions of the mathematical model were validated by an extensive, two-stage, experimental work [131,132]. In the first stage, the model was validated in a low-temperature physical system involving ice melting in sulfuric acid solutions of different concentrations. And in this first stage flow visualization, laser Doppler velocimetry and detection of the moving boundary were undertaken. In the second stage, the model was validated in a high-temperature system involving silicon melting in liquid high carbon iron having very large superheat. For this second stage, the mass transfer of a solid silicon cylinder and the surface velocity of the liquid high carbon iron were measured [131,132,136]. Figure 3.4.27 shows the vertical velocities predicted by the model and those measured experimentally on the three different levels at the 93 wt% solution. The results indicate that there is a peak value at all three levels, and the vertical velocity in the 93 wt% solution is upward, indicated by the minus sign. The peak value of the vertical velocity in the 93 wt% solution is around $0.06\ \mathrm{m\ s^{-1}}$. By comparing the predicted output to experimental results, it is seen that they are in good agreement. Figure 3.4.28 displays typical results of the flow visualization work. The three photographs shown were obtained at various times during the ice melting in the 93 wt% sulfuric acid solution. In this case, the acid solution was initially at room temperature. It is apparent that the flow patterns consist of a strong upward flow present around the moving interface between the ice and the solution and a recirculating zone located high in the cylindrical container. The recirculating flow tends to spread radially and vertically as the immersion time of the ice cylinder increases. The vertical expansion of the recirculating flow produces a downward flow adjacent to the predominant upward flow along the moving interface. As a result of the encounter between the upward and downward flows, a weak secondary recirculating flow forms at the bottom of the ice cylinder.

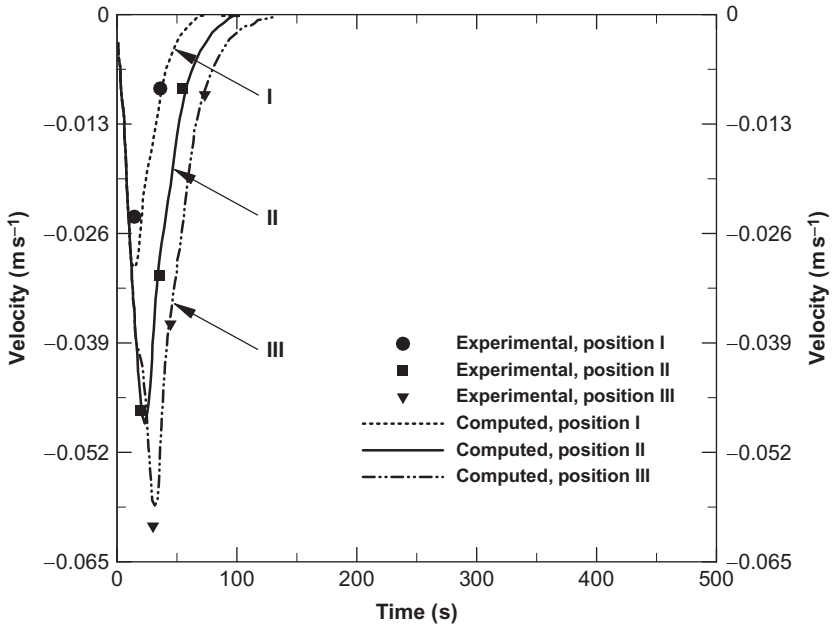


Figure 3.4.27 Comparisons of the predicted and experimental results of the vertical velocity at the initial positions of the moving interface as an ice cylinder melts in 93 wt% solution.

Figure 3.4.29 displays predicted and experimental results of ice cylinders immersed in different concentrations of sulfuric acid solutions. There are two features to be observed in this figure. First, there was an excellent agreement between experimental measurements and modeling predictions. Second, it is clear from these results that as the sulfuric acid concentration increased, there was a drastic decrease in melting time. Between 93% sulfuric acid solution and 0% (i.e., pure water), there was more than a fourfold decrease in the ice-melting time. This phenomenon can be best understood with the concept of macroexothermicity. Mathematically, the parameter of macroexothermicity can be deduced from the following equation (3.4.20):

$$\overline{\Delta H}_{\text{Macroexothermicity}} = \overline{\Delta H}_{\text{Water}} + (\text{LH}_{\text{Water}}) \tag{3.4.20}$$

Figure 3.4.29 also displays the variation of the parameter of macroexothermicity as a function of sulfuric acid concentrations. As seen, this parameter at zero sulfuric acid concentration has the highest positive value. As the sulfuric acid concentration increases, this parameter becomes gradually smaller and finally becomes progressively more negative at very high sulfuric acid concentrations. The very big variation of the partial heat of mixing of water in different concentrations of sulfuric acid was responsible for the very large variation in macroexothermicity. A very wide variety of fluid flow patterns has been seen around the melting of the ice cylinder [131,132,136]. In an earlier research work, Szekely

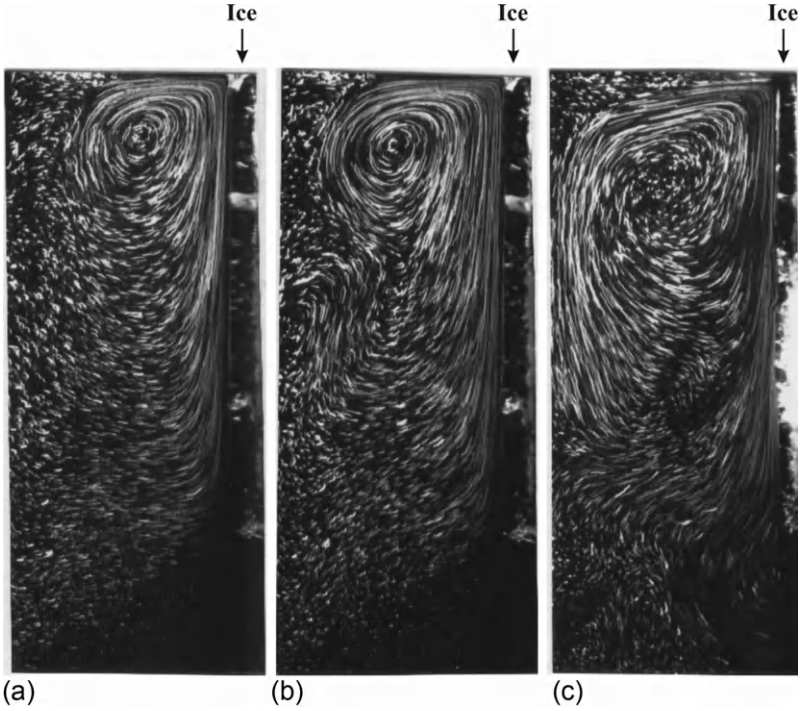


Figure 3.4.28 Experimentally observed flow fields during melting of an ice cylinder in a 93 wt% sulfuric acid solution (a), (b), and (c) at 20, 40, and 80 s, respectively.

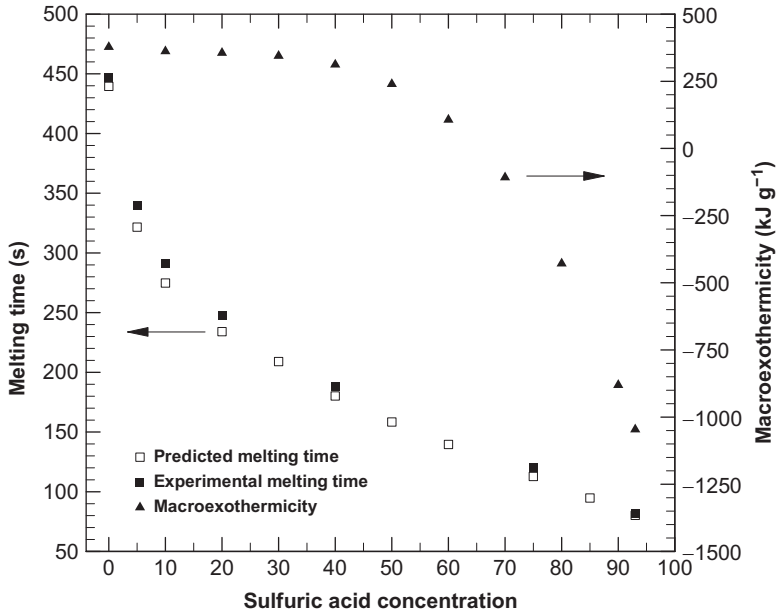


Figure 3.4.29 Left vertical axis: variation of melting time of ice as a function of sulfuric acid concentration, experimental measurements, and modeling predictions. Right vertical axis: deviation of macroexothermic parameter versus sulfuric acid concentration.

and Chuang [137], immersing ice spheres in different concentrations of sulfuric acid solutions, observed similar trends on the effects of macroexothermic reactions. This is despite the fact that Szekely and Chuang [137] used different shapes of immersing objects than the ones used in Refs. [131,132,136]. The similar trends of the results with immersing objects of different shapes lend even greater support to the macroexothermic concepts that have been discussed.

Figure 3.4.30 shows melting predictions and experimental results of a silicon metal cylinder in HCLI. In making these predictions, the temperature of HCLI was set to be 1773 K (1500 °C). As it was mentioned before, the HCLI at this temperature had a superheat in excess of 300 °C. Consequently, the duration of the shell period is extremely short (i.e., much less than 1 s) and for all practical purposes negligible [71]. The silicon cylinder had a diameter of 2.286 cm and 12.7 cm length. The solid lines in Figure 3.4.30 represent predictions, while the broken lines depict measurements. The cylinder melted in HCLI in about 11 s (dashed line). The same cylinder immersed in HCLI with 6 wt% Si melted in 16 s (dashed-dot-dot line). The difference in melting times can be attributed to the different levels of macroexothermicity. In this case, the macroexothermicity can be deduced from the following formula:

$$\overline{\Delta H}_{\text{Macroexothermicity}} = \overline{\Delta H}_{\text{Silicon}} + (\text{LH}_{\text{Silicon}}) \tag{3.4.21}$$

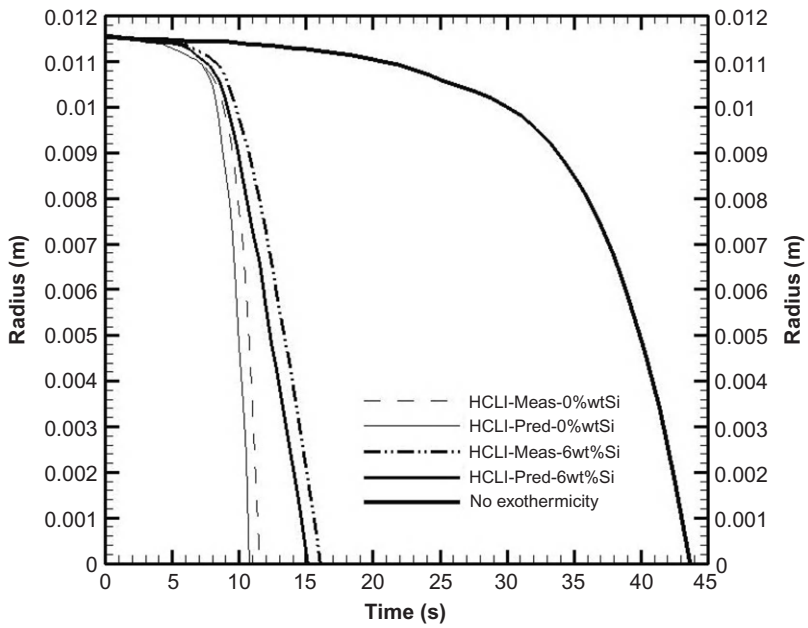


Figure 3.4.30 Predicted and experimentally determined radii of silicon cylinder immersed in high carbon liquid iron having different silicon compositions.

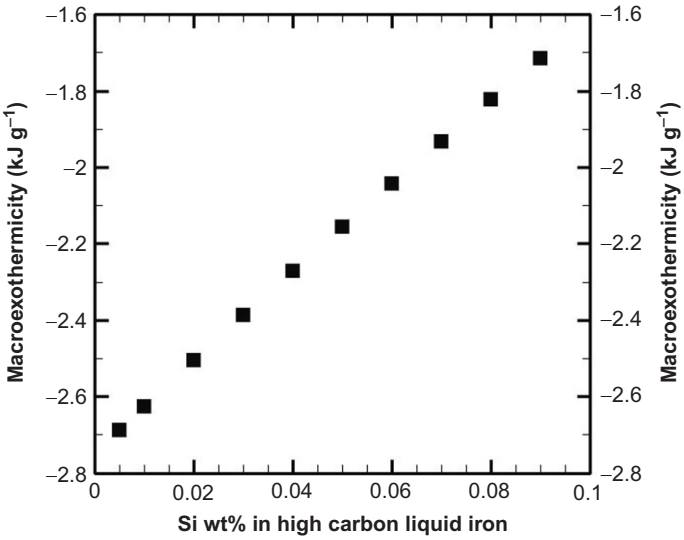


Figure 3.4.31 The amount of energy released due to macroexothermic reaction versus the Si mass content in high carbon liquid iron.

As seen in Figure 3.4.30, the model predictions are in good agreement with the experimental results. In mixing silicon in HCLI, the partial heat of mixing of silicon depends upon the silicon content of HCLI. In general, the smaller the silicon content in HCLI, the larger the partial heat of mixing of silicon in HCLI. Figure 3.4.31 presents the amount of energy released due to the macroexothermic reaction of silicon in HCLI. It is evident from Figure 3.4.31 that the lower the silicon level in HCLI, the more negative the macroexothermic energy release becomes. In Figure 3.4.30, the solid thick line corresponds to a purely hypothetical case where the Si melting in HCLI occurs with no exothermicity. As seen, the melting time of the silicon cylinder is about four times longer than the equivalent silicon melting time which melts under exothermicity conditions. Consequently, it can be stated that macroexothermicity plays a significant role in various transport phenomena.

3.4.4.7. Acceleration of Assimilation During Macroexothermic Phenomena

In Figure 3.4.13, there is clear evidence of the acceleration of dissolution speed of a titanium cylinder in liquid steel. These accelerating phenomena were experimentally and mathematically investigated in great detail in the system involving ice in sulfuric acid [131,132]. Figure 3.4.32 depicts model predictions and experimental measurements of rate of ice melting (dR/dt) as a function of immersion time. In this case, the melting of an ice cylinder in a 93 wt% sulfuric acid solution was considered. As seen in

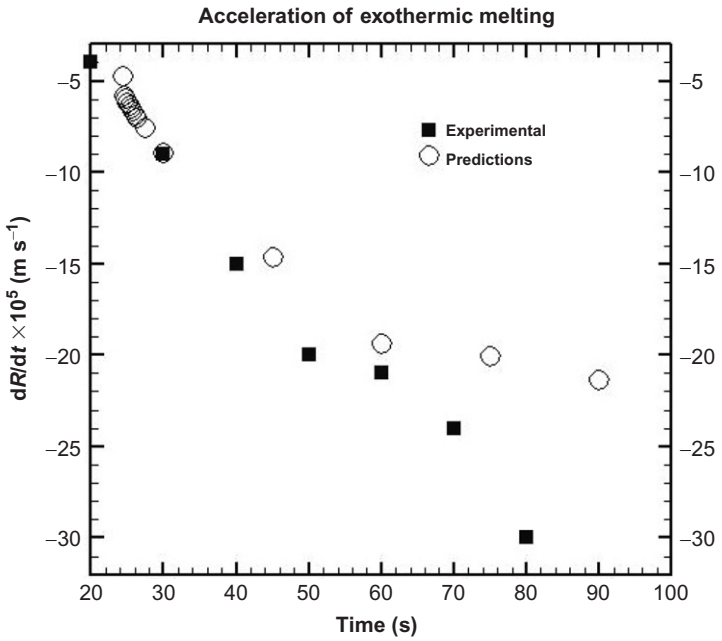


Figure 3.4.32 The rate of ice melting as a function of time.

Figure 3.4.32, the predicted and the experimentally measured rates of melting agreed very well up to 60 s. Then, a gradual deviation was observed. In this case, the experimental measurements were carried out by removing the ice cylinders from the sulfuric acid solution at specific times and then measuring the cylinder radius. For ice cylinders held over long time periods in sulfuric acid, this type of measurement tends to measure rates of melting which are higher than the rate of melting *in situ* inside the sulfuric acid. This is due to the fact that initially, the ice cylinder melted under natural convections condition, and as such, the melting rate was relatively small. During this period, there was no substantial macroexothermicity involved. In fact, in order for the macroexothermic phenomena to be started, the ice cylinder must start melting. Once the ice cylinder has started melting, then the macroexothermic phenomena are triggered. Initially, these phenomena have a relatively small impact on the rate of ice melting. However, with time, the impact of those macroexothermic phenomena intensifies. This intensification over time is the result of ice melting, thereby more water is being mixed with sulfuric acid. The net result of this intensification is depicted in Figure 3.4.32. The predicted and measured rates of ice melting became progressively faster. In tandem with the melting acceleration, there was an intensification of flow in the vicinity of the ice/sulfuric acid interface. This intensification of flow was the direct result of macroexothermic phenomena. Comparable phenomena were observed in a high-temperature system, namely, melting of silicon metal in HCLI and the results are shown in Figure 3.4.30. In this figure, the rate of

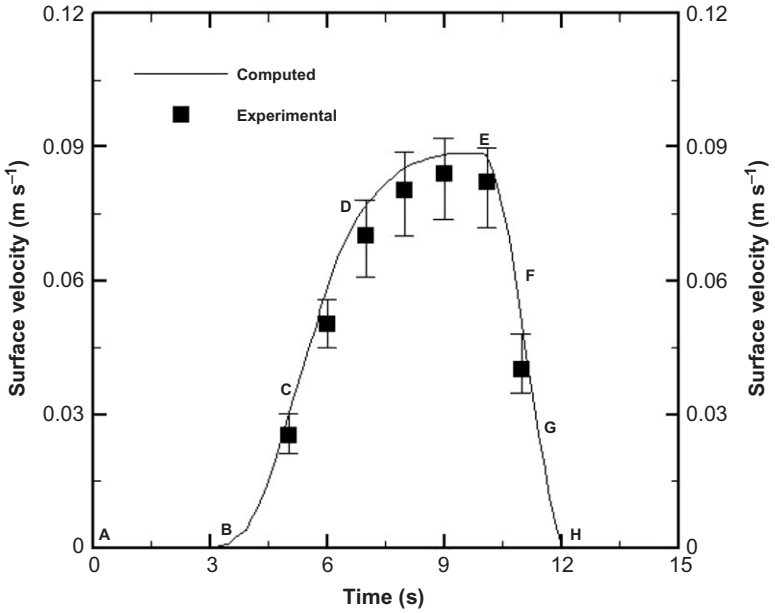


Figure 3.4.33 Comparison of predicted and experimental results of the surface velocities during the assimilation of silicon into high carbon liquid metal.

melting is low at the early stages and increases later on. Figure 3.4.33 illustrates a comparison of the experimental measurements with the numerical predictions for the velocities of the melt at the initial position of the interface on the top free surface of the liquid high carbon iron. It is worth noting that the surface velocities predicted by the model remain very close to zero within the first 3 s after immersion, segment AB. It was also observed experimentally that during this period, the top free surface of the liquid high carbon iron bath was almost motionless. This indicates that prediction is consistent with the experimental observation during the first few seconds of the silicon immersion. The increase of surface velocities, segment BCD, corresponds to the initial melting of the silicon cylinder. The subsequent segment, DE, corresponds to the period during which the remaining part of the silicon melted. The last segment, EFGH, denotes the period during which the silicon cylinder has melted and the surface velocity subsides, since there are no more macroexothermic phenomena. More details on the various aspects of this flow are given in Refs. [131,132,136,137].

3.4.4.8. Dimensionless Heat Transfer Equations for Macroexothermic Phenomena

The driving force of a melting process where exothermic phenomena do not exist is the temperature gradient in the thermal boundary. However, in the case of melting

where macroexothermic phenomena are involved (i.e., ice–sulfuric acid and silicon–HCLI), the temperature gradient is strengthened by the existence of exothermic heat. This was observed by the sharp increase in the temperature around the moving interface [131,132,136]. As such, none of the existing dimensionless heat transfer correlations for natural convection can be used when macroexothermic phenomena are taking place. In this work, a new formulation is introduced which presents dimensionless convection equations for additions exhibiting macroexothermic phenomena.

The exothermic heat of mixing (i.e., ice–sulfuric acid) is dependent on the variation of acid concentrations. Thus temperature, concentration gradient, and exothermic heat must be considered together as the effective Nusselt number is calculated.

The estimation of an effective average Nusselt number is carried out as follows:

$$Nu_L^{\text{Macroexothermic}} = \frac{h_{\text{Effective}}^{\text{Macroexothermic}} L}{k} = \frac{L}{k\Delta T}\left(\rho_S^W H_f^W \frac{dR}{dt} + \rho_l^W C_{p,l}^W \Delta T' \frac{dR}{dt}\right) \quad (3.4.22)$$

where: $h_{\text{Effective}}^{\text{Macroexothermic}}$, the average effective heat transfer coefficient during macroexothermic phenomena; k, the thermal conductivity of the solution; L, length of the immersed cylinder; ρ_S^W, density of ice; H_f^W, latent heat of ice; ρ_l^W, density of water; $C_{p,l}^W$, heat capacity of water; ΔT, average temperature difference between melting point of the addition and the temperature of the fluid; $\Delta T'$, average increase in the temperature around the moving interface; R, cylinder radius.

The first term in the right-hand bracket of Equation (3.4.22) results from the evolution of latent heat. The second term, $(\rho_l^W C_{p,l}^W \Delta T' dR/dt)$ in Equation (3.4.22) arises because of the instantaneous increase in temperature, $\Delta T'$, around the moving interface as a result of the heat of mixing. The $\Delta T'$ can be measured experimentally or predicted from the present computer model developed.

The experimental and theoretical studies of natural convection assumed either that there is a uniform heat flux between the convecting fluid and solid plate or that the surface temperature is uniform. The latter case corresponds to the conditions of the present study, the constant temperature being the melting point of the solid in contact with the liquid. In addition, laminar convection from a constant temperature vertical cylinder can be considered to be the same as from a vertical plate if curvature effects are negligible. Minkowycz and Sparrow [138] have suggested a criterion which can determine if the curvature effects of the immersed cylinder are negligible [138]. This criterion involved estimation of a parameter ξ. Applying this parameter to the present work, it was found to be $\xi \approx 0.3$. This number indicates that the curvature effects are indeed negligible. Since natural convection in a vertical cylinder in the current case is similar to that on a vertical plate, in an effort to compare the results computed from Equation (3.4.22), the Nusselt numbers were recalculated. This recalculation was based on the dimensionless correlation

[139] which is applicable for a wide range of Prandtl numbers ($0.00835 \leq Pr \leq 1000$) for laminar flow conditions, with $10^4 < Gr\ Pr < 10^{10}$:

$$Nu_L^{\text{Natural convection}} = \sqrt[4]{\frac{Gr}{4}}\left(\frac{0.902Pr^{0.5}}{[0.861+Pr]^{0.25}}\right) \tag{3.4.23}$$

Equation (3.4.23) estimates the natural convection imposed on the cylinder driven only by temperature gradients. To apply Equation (3.4.23) to the present case involving melting of ice in sulfuric acid solutions, the convection in the acid solution should be quantified in terms of both concentration and temperature gradients. Since the concentration gradients dominate density gradients, an effective Grashof was introduced for the present case and defined as:

$$Gr_{\text{Effective}}^{\text{Macroexothermic}} = Gr_C + Gr_T \tag{3.4.24}$$

where: $Gr_{\text{Effective}}^{\text{Macroexothermic}}$, effective Grashof number during macroexothermic phenomena; Gr_C, Grashof number due to the concentration gradients; Gr_T, Grashof number due to the density gradients.

Reference [140] describes the detailed calculations performed. From various calculations of $Nu_L^{\text{Macroexothermic}}$ and $Nu_L^{\text{Naturalconvection}}$, the following correlation was deduced:

$$Nu_L^{\text{Macroexothermic}} = 3.031\left(\frac{|\overline{\Delta H_{\text{W}}}|}{H_{\text{f}}^{\text{W}}}\right)^{0.363} Nu_L^{\text{Natural convection}} \tag{3.4.25}$$

Equation (3.4.25) shows the necessary parameters which must be introduced in order to express the Nusselt number under exothermic conditions (i.e., $Nu_L^{\text{Macroexothermic}}$) as a function of Nusselt number under natural convection conditions (i.e., $Nu_L^{\text{Naturalconvection}}$, natural convection driven only by temperature gradients). The parameter $|\overline{\Delta H}_{\text{W}}|/H_{\text{f}}$ determines the flow pattern around the moving boundary. From various experimental and predicted results, the ratio of $Nu_L^{\text{Macroexothermic}}/Nu_L^{\text{Naturalconvection}}$ is plotted against $|\overline{\Delta H}_{\text{W}}|/H_{\text{f}}$ in Figure 3.4.34. The line represents values deduced from Equation (3.4.25).

A similar procedure was followed for the silicon–HCLI system. However, the data used were predicted using the validated model. Equation (3.4.22) was modified for the case of Si–HCLI system as follows:

$$Nu_L^{\text{Macroexothermic}} = \frac{h_{\text{Effective}}^{\text{Macroexothermic}} L}{k} = \frac{L}{k\Delta T}\left(\rho_{\text{S}}^{\text{Si}} H_{\text{f}}^{\text{Si}} \frac{\text{d}R}{\text{d}t} + \rho_{\text{l}}^{\text{Si}} C_{\text{p,l}}^{\text{Si}} \Delta T' \frac{\text{d}R}{\text{d}t}\right) \tag{3.4.26}$$

where: $h_{\text{Effective}}^{\text{Macroexothermic}}$, the average effective heat transfer coefficient; k, the thermal conductivity of the HCLI; L, length of the immersed cylinder; $\rho_{\text{S}}^{\text{Si}}$, density of solid Si; H_{f}^{Si}, latent heat of Si; $\rho_{\text{l}}^{\text{Si}}$, density of liquid Si; $C_{\text{p,l}}^{\text{Si}}$, heat capacity of liquid Si; ΔT, average temperature difference between melting point of the addition and the temperature of

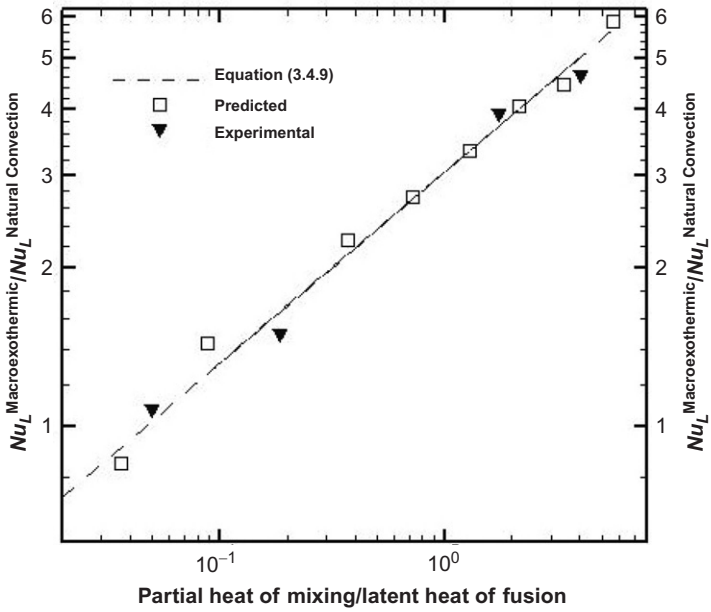


Figure 3.4.34 Experimental and predicted and regression analysis results for the ice–sulfuric acid system.

HCLI; $\Delta T'$, average increase in the temperature around the moving interface; R, cylinder radius.

Reference [140] describes the detailed calculations performed. From various calculations of $Nu_L^{\text{Macroexothermic}}$ and $Nu_L^{\text{Naturalconvection}}$, the following correlation was deduced:

$$Nu_L^{\text{Macroexothermic}} = 0.18\left(\frac{|\overline{\Delta H_W}|}{H_f^W}\right)^{2.70} Nu_L^{\text{Naturalconvection}} \tag{3.4.27}$$

The Si range in HCLI where Equation (3.4.27) can be applied is $0 \leq \text{Si} \leq 10$ wt%.

From various experimental and predicted results, the ratio of $Nu_L^{\text{Macroexothermic}}/Nu_L^{\text{Naturalconvection}}$ is plotted against $|\overline{\Delta H_{Si}}|/H_f^{Si}$ in Figure 3.4.35. The line represents values deduced from Equation (3.4.27).

As seen from Equations (3.4.25) and (3.4.27), the exothermic ratio $|\overline{\Delta H}|/H_f$ impacts on the ratio of $Nu_L^{\text{Macroexothermic}}/Nu_L^{\text{Naturalconvection}}$. There is a large difference between the respective exponents of the exothermic ratio of Equations (3.4.25) and (3.4.27). The reasons for this difference are twofold. First, the vast difference between the Prandtl numbers of HCLI and sulfuric acid. Second, Equation (3.4.27) is applicable to a very narrow Si range where the partial heat of mixing exhibits an extreme negative value, in contrast to Equation (3.4.25), which is applicable for the mixing of ice with practically the whole

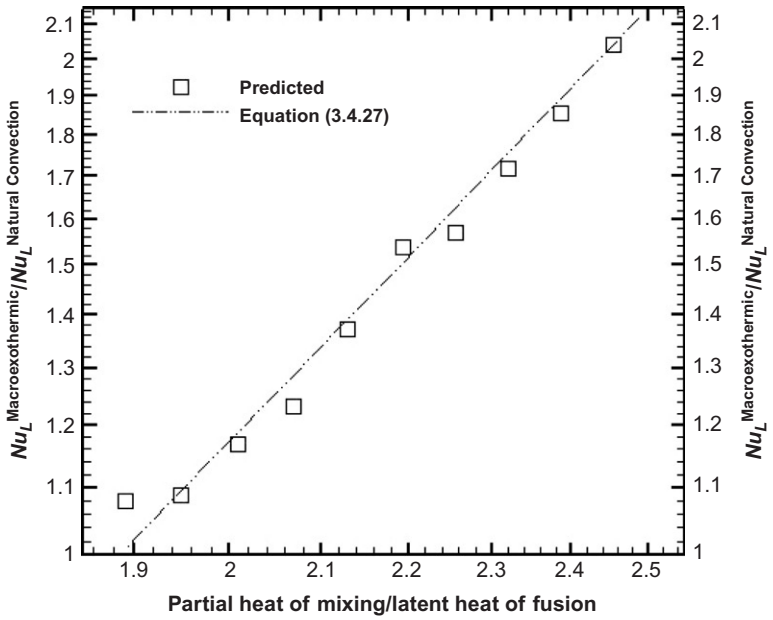


Figure 3.4.35 Predicted and regression analysis results from Equation (3.4.27) for silicon in the HCLI system.

range of sulfuric acid concentrations. In both systems examined, the exothermic ratio $|\overline{\Delta H}|/H_f$ determines the intensity of the flow patterns around the moving boundary.

3.4.5. RECOVERY

The data on addition assimilation kinetics offer a valuable parameter describing how fast a given addition enters the metal bath. These data may be expressed as g m^{-2} s^{-1} of additive for a set of experimental conditions which might include bath temperature and degree of bath agitation among others. However, the liquid metal processing practitioner is more interested in the recovery of additions. In other words, the point of interest is the percentage of the used addition entering the metal bath. Ideally, the addition recovery can reach the 100% level. However, in practice the addition recovery never or rarely reaches that level. Many factors can contribute to this. Some of these factors can be slow assimilation kinetics, addition density, addition practice, turbulence of the melt, etc. In some cases, sloppy addition practices can contribute to low recoveries, or even worse, to erratic recoveries. Despite the fact that numerous research works on the assimilations kinetics of various additions in liquid metals exist, only a tiny proportion of them focused on addition recovery.

3.4.5.1. Liquid Light Metals

The effects of temperature on the recovery of various additions used in liquid Al alloys differ widely. For example, strontium is added in a variety of grades, which can vary from 90 wt%Sr all the way to 10 wt%Sr. In contrast to what might have been anticipated, the addition with a higher level of Sr has very unexpected behavior relative to the addition with a lower level Sr. Figures 3.4.36 and 3.4.37 present published results on the recovery of reactive [2] and nonreactive [3] strontium, respectively, in aluminum alloy melts. The unexpected behavior of reactive Sr is that an increase of melt temperature has a negative effect on recovery as shown in Figure 3.4.36 [2]. Moreover, in the case of nonreactive Sr addition, an increase in bath temperature has a positive effect on recovery, as seen in Figure 3.4.37 [3]. In an effort to maximize the recovery of these additions in Al melts, diametrically opposite melt practices must be exercised. The reactive Sr additions must be immersed into low-temperature Al melts while the nonreactive strontium into high-temperature Al melts. Comparable phenomena are reported from industrial practice of using Mn–Al exothermic briquettes to alloy liquid aluminum alloys. In this case, the Mn–Al exothermic briquettes exhibit the best recoveries in the temperature range of 725–740 °C [108]. Above and below this range, the recovery is very low [108]. It appears that the formation of certain phases is either promoted or retarded at different

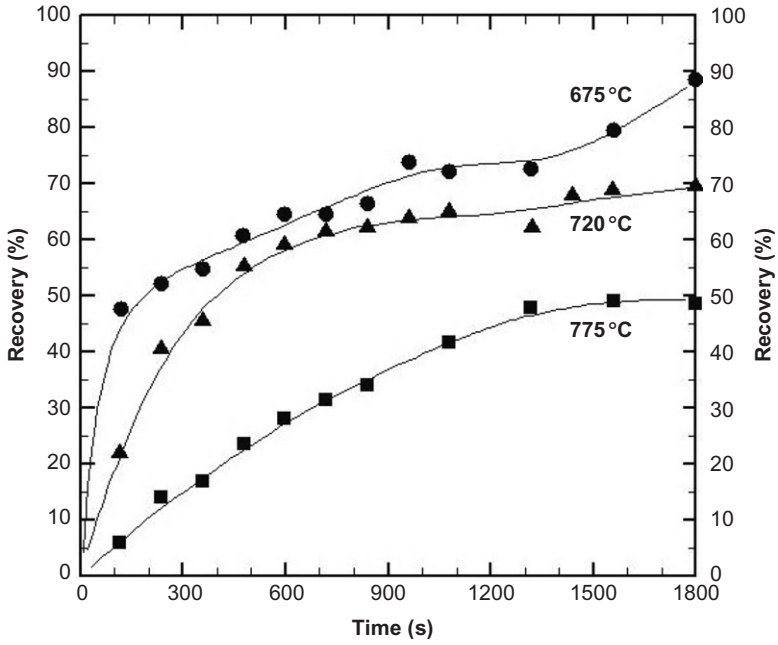


Figure 3.4.36 Recovery of reactive 90 wt%Sr–10 wt%Al in liquid A356 under different bath temperatures.

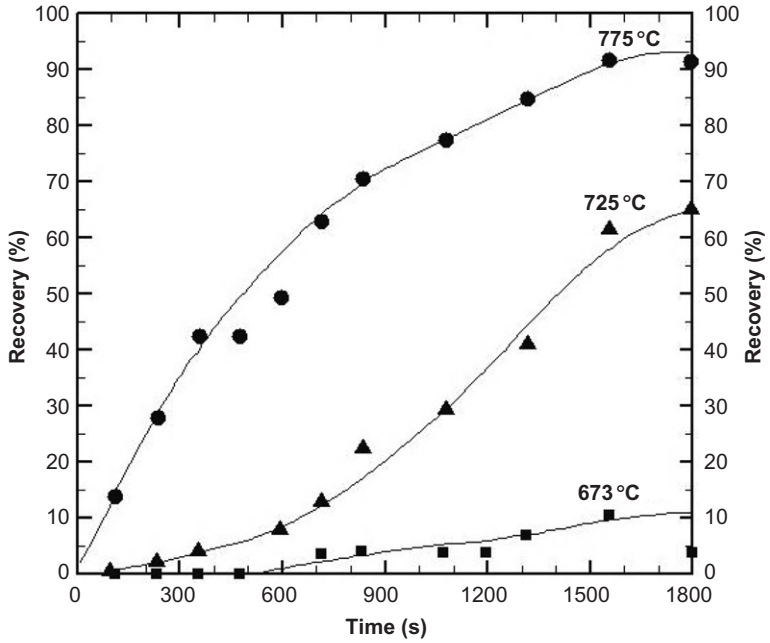


Figure 3.4.37 Recovery of nonreactive ternary alloy (10 wt%Sr–14 wt%Si–76 wt%Al) in liquid A356 under different bath temperatures.

temperatures [108]. In some cases, the size of exothermic additions plays a significant role in the observed recoveries. The interested reader can find results from industrial practice as well as from research work in Ref. [108].

While the highest addition recovery is a principal parameter, the time needed for the addition to reach the highest recovery level is very important too. As such a parameter was introduced here, called rate of recovery (RR). This parameter was defined as:

$$\text{Rate of recovery} = \frac{\text{maximum recovery attained}}{\text{time required to achieve maximum recovery in minutes}} \quad (3.4.28)$$

It brings to bear the liquid metal processing practices, as well as the physicochemical properties of the addition in question.

Figure 3.4.38 displays some data collected on the recovery of an alloy with 10 wt%Sr–90 wt%Al in liquid aluminum [141]. The graph in Figure 3.4.38 clearly displays how the RR is estimated for one case in which the bath temperature is 775 °C. In this case, the maximum recovery and the time to achieve this maximum recovery are clearly noted by the dashed lines. For a given additive, a large value for RR means that it takes a shorter time for that additive to achieve maximum recovery. In a similar manner, the RR has been estimated for different alloying additives in liquid aluminum alloys. Table 3.4.4 shows the results for 42 additives. The additives numbered 1–29 represent various types of strontium

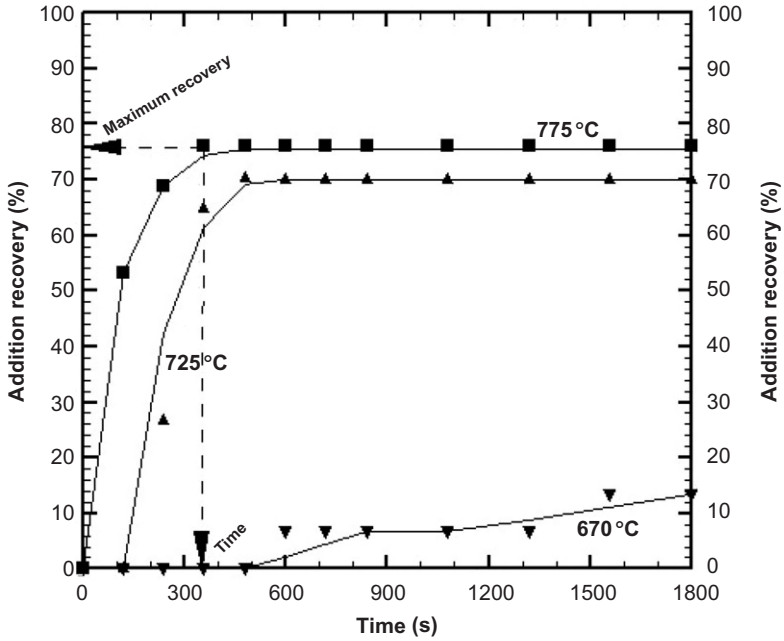


Figure 3.4.38 Typical estimation of the rate of recovery parameter for a 10 wt%Sr–90 wt%Al alloy immersed in liquid aluminum at a temperature of 775 °C.

additives, which are further subdivided into reactive (R) and nonreactive (non-R) additives. This subdivision is denoted by the group column in Table 3.4.4, using the designation R-number and non-R-number, respectively. In addition to strontium additives, Table 3.4.4 lists estimates of RR for briquette additives. The groups for these briquette additives are denoted by bri-number. In Table 3.4.4, the additives are grouped. A given group is formed when the same additive is immersed into one metal bath and at different temperatures. For example, group R-1 refers to the immersion of pure strontium cylinders immersed in aluminum baths at three different temperatures namely, 675, 725, and 775 °C. In a similar manner, group non-R-1 refers to the immersion of a nonreactive strontium alloy, 10 wt%Sr–90 wt%Al, into an aluminum bath held at three different temperatures namely, 775, 725, and 670 °C. The focus is on examining the RR for the so-called reactive strontium alloys, presented in Table 3.4.4 as groups R-1, R-2, R-3, and R-4. For a given group of these reactive additives, a negative temperature dependence of strontium on RR is observed. For example, for the group R-1 of additives, by increasing the bath temperature from 675 to 725 °C and to 775 °C, the RR drops from 4.46 to 2.73 and 1.25, respectively. Similar trends are observed for groups of additives R-2, R-3, and R-4. These alloy additives are characterized by the following dissolution behavior [2]:

(1) Exothermic behavior as evidenced by a sudden heat release during dissolution;

(2) Intermetallic compound formation;

Table 3.4.4 The Rate of Recovery Index for Different Additions

No.	Alloy Type	Group	Form	Bath Type	Bath Temperature (°C)	Rate of Recovery (RR) (Percent Recovery Change per min)
1	Pure Sr	R-1	Cylinder	Aluminum	675	4.46
2	Pure Sr	R-1	Cylinder	Aluminum	725	2.73
3	Pure Sr	R-1	Cylinder	Aluminum	775	1.25
4	Pure Sr	R-2	Cylinder	A356	673	7.71
5	Pure Sr	R-2	Cylinder	A356	690	3.03
6	Pure Sr	R-2	Cylinder	A356	725	0.52
7	90Sr–10Al	R-3	Cylinder	Aluminum	680	1.96
8	90Sr–10Al	R-3	Cylinder	Aluminum	725	1.56
9	90Sr–10Al	R-3	Cylinder	Aluminum	776	0.8
10	90Sr–10Al	R-4	Cylinder	A356	675	2.96
11	90Sr–10Al	R-4	Cylinder	A356	720	2.33
12	90Sr–10Al	R-4	Cylinder	A356	775	1.63
13	10Sr–90Al	non-R-1	Cylinder	Aluminum	775	13
14	10Sr–90Al	non-R-1	Cylinder	Aluminum	725	7
15	10Sr–90Al	non-R-1	Cylinder	Aluminum	670	0.46
16	10Sr–90Al	non-R-2	Cylinder	A356	775	10.87
17	10Sr–90Al	non-R-2	Cylinder	A356	725	2.66
18	10Sr–90Al	non-R-2	Cylinder	A356	676	1.5
19	10Sr–14Si–Albalance	non-R-3	Cylinder	Aluminum	775	8.19
20	10Sr–14Si–Albalance	non-R-3	Cylinder	Aluminum	725	2.23
21	10Sr–14Si–Albalance	non-R-3	Cylinder	Aluminum	675	0.83
22	10Sr–14Si–Albalance	non-R-4	Cylinder	A356	775	3.06
23	10Sr–14Si–Albalance	non-R-4	Cylinder	A356	725	2.2
24	10Sr–14Si–Albalance	non-R-4	Cylinder	A356	673	0.4

Table 3.4.4 The Rate of Recovery Index for Different Additions—cont'd

No.	Alloy Type	Group	Form	Bath Type	Bath Temperature (°C)	Rate of Recovery (RR) (Percent Recovery Change per min)
25	55Sr–45Al	non-R-5	Cylinder	Aluminum	725	3.54
26	55Sr–45Al	non-R-5	Cylinder	Aluminum	675	1.9
27	55Sr–45Al	non-R-6	Cylinder	A356	775	0.96
28	55Sr–45Al	non-R-6	Cylinder	A356	725	0.63
29	55Sr–45Al	non-R-6	Cylinder	A356	673	0.1
30	75Mn–25Al	bri-1	Briquette	Aluminum	700	9.8
31	75Mn–25Al	bri-1	Briquette	Aluminum	725	12.66
32	75Mn–25Al	bri-1	Briquette	Aluminum	760	9
33	75Mn–25Al	bri-1	Briquette	Aluminum	860	4.83
34	75Mn–25Al (defective)	bri-1	Briquette	Aluminum	700	3.44
35	75Fe–25Al	bri-2	Briquette	Aluminum	760	19.6
36	75Fe–25Al	bri-2	Briquette	Aluminum	700	12
37	75Cr–25Al	bri-3	Briquette	Aluminum	760	24.5
38	75Cr–25Al	bri-3	Briquette	Aluminum	700	5.41
39	75Ni–25Al	bri-4	Briquette	Aluminum	760	14
40	75Ni–25Al	bri-4	Briquette	Aluminum	725	5.54
41	75Co–25Al	bri-5	Briquette	Aluminum	725	17.63
42	75Co–25Al	bri-5	Briquette	Aluminum	760	13.42

(3) The dissolution time made up of three stages; (1) incubation; (2) exothermic reaction and compound formation; and (3) dissolution of intermetallic compounds;
(4) A negative temperature dependence of strontium recovery;
(5) An adverse effect of surface oxidation, merely by extending the incubation time, sometimes indefinitely.

The trends shown in Table 3.4.4 indicating negative bath temperature dependence on RR can be explained on the basis of the negative temperature dependence of reactive strontium recovery identified in Ref. [2]. In contrast to the reactive strontium additives, the nonreactive strontium additives exhibit positive temperature dependence of RR. This positive dependence is seen in each group of nonreactive strontium alloys (i.e.,

non-R-1 to non-R-6) seen in Table 3.4.4. In this case, the recoveries of these non-reactive additives appeared to observe a positive temperature dependence [3].

The results for groups bri-1 to bri-5, seen in Table 3.4.4, refer to recovery tests performed on various types of briquettes. Examining the various briquetted compacts of the bri-1 group, it is clear that there is an optimum temperature (i.e., 725 °C) at which the RR is maximum (i.e., 12.66). In the same group of additives, there is one finding referred to as a defective briquette No. 34 in Table 3.4.4. This briquette was made from oxidized metal powders. As seen, among the various results shown from the bri-1 group, the one with the defective briquette exhibited the smallest number of RR (i.e., 3.44). This finding can be attributed to the fact that this defective briquette exhibits smaller amounts of "microexothermicity" when it is used as an alloying agent in liquid aluminum. As a result, this defective briquette has smaller recoveries than the other briquettes of group bri-1. It takes also a longer time for this defective briquette to reach the highest recovery.

Figures 3.4.39 and 3.4.40 display the observed recoveries of large (Figure 3.4.39) and small (Figure 3.4.40) Mn–Al compacts in liquid metals such as Al and Mg. For both of these figures, the recovery is presented as a function of Mn composition in the compact. As seen, for both sizes of compacts, the recoveries in liquid Al are very high, in the range of 90%. However in the case of liquid Mg, the detected recoveries are low. In fact, for small-size compacts (Figure 3.4.40), the witnessed recoveries exhibit a maximum of 70% at around 50 wt%Mn. The large-size compacts in liquid Mg display even lower

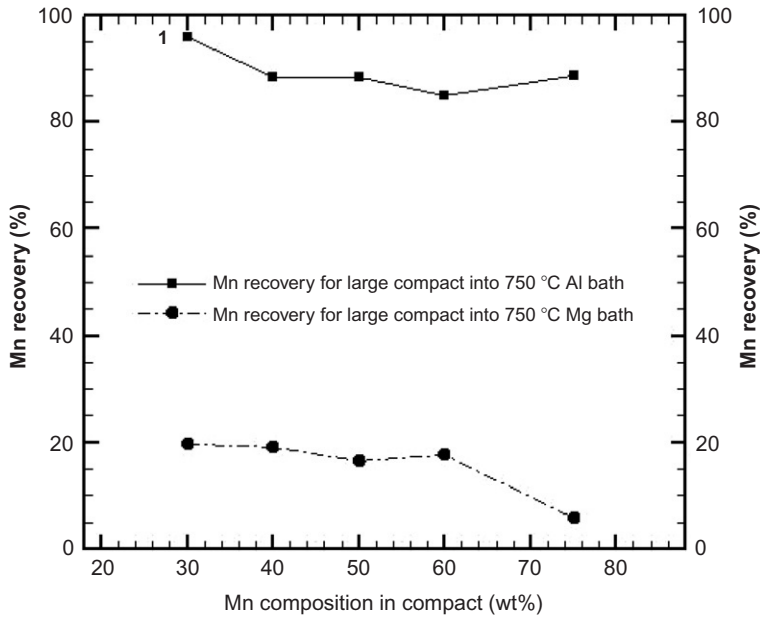


Figure 3.4.39 Recovery of large Mn–Al compacts in liquid metals such as Al and Mg as a function of Mn concentration in the compact.

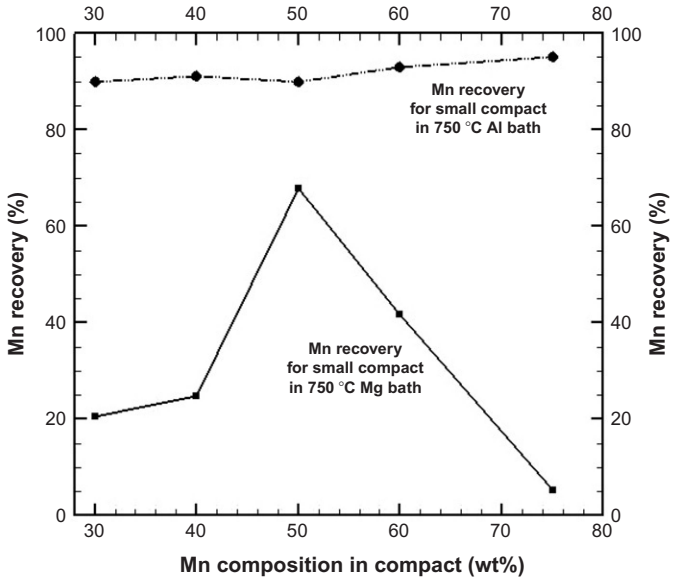


Figure 3.4.40 Recovery of small Mn–Al compacts in liquid metals such as Al and Mg as a function of Mn concentration in the compact.

recoveries than the small-size compacts. The preferential development of some phases during the assimilation process is responsible for the observed difference in recoveries between large and small compacts in liquid Mg [107,108]. The very large difference in recoveries between liquid Al and liquid Mg was attributed to the fact that the Mn–Al compacts were assimilated into liquid Mg under conditions of Al deficiency. This shortage in Al does not exist when the Mn–Al compacts are assimilated into liquid Al because there is more than enough Al for the microexothermic reactions in the Al bath. In the case of immersion of Mn–Al compacts into liquid Al, the bath acts as a heat source as well as mass source of Al. For the case of Mn–Al compacts immersed into liquid Mg, the bath acts only as a heat source [107,108].

3.4.5.2. Liquid Steel

Elder and Kendrick [142] have published observed recoveries of various ladle furnace alloy additions. Table 3.4.5 displays their results. As seen, among the five additions examined, C, FeMn, FeSi, FeCr, and FeMo, C was observed to have the lowest average recovery 79.7% while FeMo exhibited the highest average recovery 95.6%. The same authors also report that their observed calcium recoveries are in the range of 20–22%.

The concept of rate of recovery has been applied to additions in liquid steel. Figure 3.4.41 displays the maximum recovery of different grades of ferrovanadium alloys over time [76]. Table 3.4.6 displays the various rates of recovery for different ferrovanadium alloys [76].

Table 3.4.5 Ladle Furnace Alloy Additions and Recoveries [142]

Alloy	Recovery Statistics %	Typical Addition	Aim and Resulting Pick-Up at 1 σ	
			% Aim	% Result
C	$\overline{X}=79.7$ $\sigma=7.7$	90.7 kg (200#)	0.045	0.04–0.05
FeMn	$\overline{X}=93.7$ $\sigma=5.4$	317.5 kg (700#)	0.14	0.13–0.15
FeSi	$\overline{X}=82.7$ $\sigma=7.8$	317.5 kg (700#)	0.08	0.07–0.09
FeCr	$\overline{X}=92.1$ $\sigma=5.5$	136.1 kg (300#)	0.055	0.05–0.06
FeMo	$\overline{X}=95.6$ $\sigma=6.0$	65.8 kg (145#)	0.025	0.02–0.03

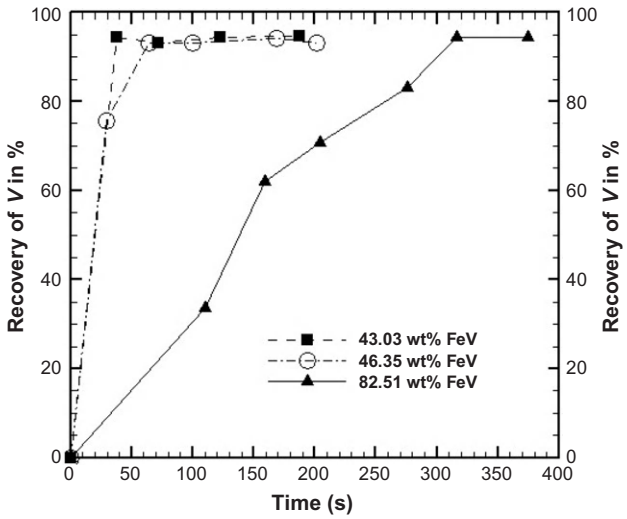


Figure 3.4.41 Recovery of various FeV addition grades in liquid steel at a temperature of 1600 °C.

Table 3.4.6 Rate of Recovery of Various Ferrovanadium Alloys

Addition	Rate of Recovery (Percent Recovery Change per min)
43.0 wt%FeV	141
46.0 wt%FeV	84.6
82 wt%FeV	17.82

3.4.6. CONCLUSIONS

A comprehensive compilation of assimilation experiments of solid metals and alloys in ferrous as well as nonferrous liquid metals is presented and reviewed. Liquid metal temperature, type of solid specimen utilized, method used, and assimilation mechanism were the parameters examined. For the majority of cases, LPD was determined as the most common assimilation mechanism.

Various additions in liquid metals were classified as belonging to one of three groups. Their assimilation in liquid metals follows six routes. The conditions promoting each route were presented. Their exothermic behavior governed by microexothermicity and/or macroexothermicity was an important factor affecting their kinetics. Experimental and mathematical modeling work encompassing a wide variety of additions was introduced. The rate of recovery index, aimed at monitoring the time required to reach maximum recovery, was introduced as a useful concept.

REFERENCES

[1] T.-T. Ikeshoji, Y. Watanabe, A. Suzumura, T. Yamazaki, JSME Int. J. Ser. A 48 (4) (2005) 346–351.
[2] M.O. Pekguleryuz, J.E. Gruzleski, Metall. Trans. B 20B (December 1989) 815–831.
[3] M.O. Pekguleryuz, J.E. Gruzleski, Can. Metall. Q. 28 (1) (1989) 55–65.
[4] M.O. Pekguleryuz, Strontium dissolution in liquid aluminium and A356 alloys (Ph.D. Thesis), Department of Mining and Metallurgical Engineering, McGill University, Montreal, Quebec, Canada, March 1987.
[5] S. Minowa, M. Kosaka, Tetsu-to-Hagane 50 (1964) 56.
[6] S. Minowa, M. Kosaka, M. Mizuta, Tetsu-to-Hagane 50 (1964) 644.
[7] M. Kosaka, S. Minowa, Tetsu-to-Hagane 51 (1965) 218.
[8] M. Kosaka, S. Minowa, Tetsu-to-Hagane 52 (1966) 536.
[9] M. Kosaka, S. Minowa, Tetsu-to-Hagane 52 (1966) 539.
[10] M. Kosaka, S. Minowa, Tetsu-to-Hagane 52 (1966) 1748.
[11] J.B. Darby Jr., D.B. Jugle, O.J. Kleppa, Trans. AIME 227 (1963) 179.
[12] V.N. Eremenko, Y.V. Natanzon, V.P. Titov, Sov. Mater. Sci. 14 (6) (1978) 579–584.
[13] V.N. Eremenko, Y.V. Natanzon, V.P. Titov, Russ. Metall. (6) (1980) 193–197.
[14] N. Tunca, G.W. Delamore, R.W. Smith, Metall. Trans. A 21A (1990) 2919–2928.
[15] M. Niinomi, Y. Ueda, M. Sano, Trans. Jpn. Inst. Met. 23 (12) (1982) 780–787.
[16] M. Niinomi, Y. Suzuki, Y. Ueda, Trans. Jpn. Inst. Met. 25 (6) (1984) 429–439.
[17] L.N. Shibanova, A.A. Vostryakov, B.M. Lepinskikh, Prot. Met. 25 (4) (1990) 519–521.
[18] V.N. Eremenko, Y.V. Natanzon, V.R. Ryabov, Fiziko-Khimicheskaya Mekhanika Materialov 4 (3) (1968) 286–290.
[19] V.I. Dybkov, J. Mater. Sci. 28 (1993) 6371–6380.
[20] V.N. Eremenko, Y.V. Natanzon, V.I. Dybkov, J. Less-Common Met. 50 (1976) 29–48.
[21] P.K. Gairola, R.K. Tiwari, A. Ghosh, Metall. Trans. 2 (1971) 2123.
[22] V.N. Eremenko, Y.V. Natanzon, V.P. Titov, Russ. Metall. (2) (1986) 52–55.
[23] H.G. Katayam, T. Momono, M. Doe, H. Saitoh, ISIJ Int. 34 (2) (1994) 171–176.
[24] C.M. Craighead, E.W. Cawthorne, R.I. Jaffee, Trans. AIME 203 (1955) 81.
[25] M. Kosaka, M. Machida, Y. Hirai, J. Jpn. Inst. Met. 33 (4) (1969) 465–470.
[26] Y. Shoji, S. Uchida, T. Ariga, Trans. Jpn. Weld. Soc. 12 (1) (1981) 19–24.
[27] T.L. Sri Krishna, M.A. Dayananda, R.E. Grace, Metall. Trans. 2 (1971) 3355–3359.
[28] T. Sano, T. Konishi, M. Miyake, Tech. Rep. Osaka Univ. 10 (1960) 815.

[29] A.G. Ward, J.W. Taylor, J. Inst. Met. 85 (Pt. 4) (1956) 145.
[30] A.G. Ward, J.W. Taylor, J. Inst. Met. 86 (Pt. 1) (1957) 36.
[31] M. Miyake, T. Konishi, T. Sano, Tech. Rep. Osaka Univ. 10 (1960) 453.
[32] J.K. Jackson, R.E. Grace, Met. Soc. Conf. AIME 7 (1961) 633.
[33] F.N. Strel'tsov, A.E. Erofeev, Izvestiya Akademii Nauk SSSR, Metally (4) (1986) 46–52.
[34] R. Ohno, M. Kagawa, T. Hasumi, Trans. Jpn. Inst. Met. 14 (2) (1973) 140–147.
[35] G.R. Cappleman, Trans. Indian Inst. Met. 36 (4–5) (1983) 368–375.
[36] R. Ohno, Metall. Trans. 4 (1973) 909–915.
[37] N.E. Fokina, I.A. Montil'o, Y.P. Nikitin, M.I. Belousova, A.D. Ionov, Russ. Metall. (6) (1986) 76–78.
[38] F.W. Hinzner, D.A. Stevenson, J. Phys. Chem. 67 (1963) 2424.
[39] L.F. Epstein, in: Chem. Eng. Progr. Symp. Series, No. 20vol. 53, 1957, p. 67.
[40] W.E. Dunn, C.F. Bonnilla, C. Ferstenberg, B. Gross, AIChE J. 2 (2) (1956) 184.
[41] J.A.R. Bennett, J.B. Lewis, AIChE J. 4 (1958) 418.
[42] A.S. Moshkevich, A.A. Ravdel, J. Appl. Chem. USSR 43 (1) (1971) 71–75.
[43] D.A. Stevenson, J. Wulff, Trans. AIME 221 (1961) 279.
[44] T.K. Lee, S. Zhang, C.C. Wong, A.C. Tan, Mater. Sci. Eng. A 427 (2006) 136–141.
[45] Y. Shoji, S. Uchida, T. Ariga, Trans. Jpn. Inst. Met. 21 (12) (1980) 819–823.
[46] Y. Shoji, S. Uchida, T. Ariga, Metall. Trans. B 13B (1982) 439–445.
[47] J.M. Lommel, B. Chalmers, Trans. AIME 215 (1959) 499.
[48] P.-Y. Yeh, J.-M. Song, K.-L. Lin, J. Electron. Mater. 35 (5) (2006) 978–987.
[49] Y. Shoji, S. Uchida, T. Ariga, Trans. Jpn. Inst. Met. 21 (6) (1980) 383–389.
[50] L. Snugovsky, M.A. Ruggiero, D.D. Perovic, J.W. Rutter, Mater. Sci. Technol. 19 (2003) 866–874.
[51] T. Ishida, Trans. Jpn. Inst. Met. 14 (1) (1973) 37–44.
[52] G.A. Pribytkov, V.I. Itin, E.M. Savitskii, Y.V. Efimov, B.P. Mikhailov, E.A. Moroz, A.G. Repina, Sov. Non-Ferrous Met. Res. 7 (2) (1979) 205–210.
[53] S.K. Kang, Metall. Trans. B 12B (1981) 620–622.
[54] T. Ishida, Metall. Trans. B 17B (1986) 281–289.
[55] N.J. Hoffman, I. Minkoff, J. Cryst. Growth 6 (1969) 53–60.
[56] M.-L. Giorgi, P. Durighello, R. Nicolle, J.-B. Guillot, J. Mater. Sci. 39 (2004) 5803–5808.
[57] M. Kosaka, S. Minowa, Tetsu-to-Hagane 50 (1964) 1424.
[58] D.E. Langberg, M. Nilmani, Metall. Mater. Trans. B. 27B (1996) 780–787.
[59] V.N. Eremenko, Y.V. Natanzon, Poroshkovaya Metallurgiya 8 (92) (1970) 39–54, Translated in English 1970 by Consultants Bureau, A division of Plenum Publishing Corporation, 227 West 17th Street, New York.
[60] G.N.K. Iyengar, R.D. Pehlke, Met. Trans. 1 (1970) 2235.
[61] P.M. Shurygin, V.D. Shantrin, Izv. Akad. Nauk SSSR Met. (2) (1964) 38.
[62] V.D. Shantarin, P.M. Shurygin, Liteinoe Proizv (7) (1964) 19–21, Russian Castings Production, No. 7, 309-311, 1964.
[63] K. Bungardt, K. Wiebking, H. Brandis, H. Schmalzried, DEW. Tech. Ber 9 (3) (1969) 407–438, Discussion 431–437 (in German).
[64] L.I. Krupman, V.I. Yavoiskii, Izv. V.U.Z. Chernaya Metall. 7 (9) (1964) 35–42, (in Russian), English Translation in British Library, Boston Spa, Wetherby, Yorkshire, UK.
[65] G.S. Ershov, V.M. Bychev, Izvest. Akad. Nauk SSSR. Metally 1 (1975) 62–63, (in Russian).
[66] I.P. Kazachkov, I.B. Parimonchik, Steel USSR (1973) 123–124.
[67] B. Miroslav, Neue Hutte 29 (4) (1984) 130–133.
[68] Z.D. Khong, V.A. Krivandin, R.B. Gutnov, Y.P. Filimonov, B.N. Sukhotin, A.P. Buslakov, Izv. V. U.Z. Chernaya Metall. 1 (1980) 54–56.
[69] S.A. Argyropoulos, The kinetics of ferro-alloy solution in liquid steel (Master Thesis), Department of Mining and Metallurgical Engineering, McGill University, August 1977.
[70] P.G. Terziyan, Stal 2 (1973) 126–127.
[71] S.A. Argyropoulos, Iron Steelmaker 11 (11) (1984) 48–57.
[72] S.A. Argyropoulos, in: Electric Furnace Conference Proceedings, vol. 42, 1984, pp. 133–148.

[73] P.G. Sismanis, S.A. Argyropoulos, Iron Steelmaker 16 (7) (1989) 39–47.
[74] S.A. Argyropoulos, R.I.L. Guthrie, Can. Metall. Q. 18 (1979) 267–281.
[75] S.A. Argyropoulos, Dissolution of high melting point additions in liquid steel (Ph.D. Thesis), Department of Mining and Metallurgical Engineering, McGill University, August 1981.
[76] S.A. Argyropoulos, A. Biswas, Iron Steelmaker 21 (10) (1994) 89–97.
[77] A.P. Buslakov, Y.P. Filimonov, Izv. V. U. Z. Chernaya Metall. (5) (1985) 70–72.
[78] S.A. Argyropoulos, P.G. Sismanis, Metall. Trans. B 22B (1991) 417–427.
[79] S.A. Argyropoulos, R.I.L. Guthrie, Metall. Trans. B 15B (1984) 47–58.
[80] V.I. Zhalybin, Y.G. Volovich, G.D. Danchenko, B.P. Vishncvskiy, Russ. Metall. (6) (1979) 75–78.
[81] S.A. Argyropoulos, P.G. Sismanis, Steel Res. 68 (8) (1997) 345–354.
[82] P.G. Sismanis, The dissolution of niobium and zirconium in liquid steel (Ph.D. Thesis), Department of Mining and Metallurgical Engineering, McGill University, April 1987.
[83] L. Gourtsoyannis, H. Henein, R.I.L. Guthrie, in: J. Farrel (Ed.), Physical Chemistry of Production or Use of Alloy Additives: Proceedings of Session from the 103rd AIME Annual Meeting, 1974, pp. 45–67.
[84] K. Niwa, M. Shimei, R. Shina, Nippon Kinzok Gakkai-Si 30 (1966) 329.
[85] A. Simkovich, K. Li, C.L. McCabe, Trans. AIME 245 (1969) 897.
[86] A.V. Kaibichew, B.M. Lepinskikh, E.E. Shretsov, B.I. Sergin, Russ. Cast. Prod. (3) (1968) 108.
[87] A.V. Klibus, B.M. Lepinskikh, A.A. Gorshkow, Dop. Akad. Ukrain. R. S. R. 6A (1967) 536.
[88] R.G. Olsson, V. Koump, T.F. Perzak, Trans. AIME 233 (1965) 1654.
[89] Y.-U. Kim, R.D. Pehlke, Metall. Trans. 5 (1974) 2527–2532.
[90] V.O. Dahlke, O. Knacke, Arch. Eisenhuttenw. 26 (1955) 373.
[91] R.G. Olsson, V. Koump, T.F. Perzak, Trans. AIME 236 (1966) 426.
[92] M. Kosaka, S. Minowa, Tetsu-to-Hagane 53 (1967) 1467.
[93] A. Mihajlovic, B. Marincek, Arch. Eisenhuttenw. 44 (7) (1973) 507–512.
[94] R.B. Gundlash, R.D. Pehlke, Met. Trans. AIME 3 (1972) 2337–2342.
[95] V.D. Shantarin, P.M. Shurygin, V.V. Utochkin, Izvest. Akad. Nauk SSSR, Metally 3 (1966) 31–33.
[96] S. Minowa, M. Kosaka, Tetsu-to-Hagane 50 (1964) 1175.
[97] J.W. Robison Jr., A.B. Draper, Dissolution of silicon carbide in liquid gray irons, TMS Paper Selection A78-21, TMS-AIME, Warrendale, PA, 1978.
[98] M. Kosaka, S. Minowa, Tetsu-to-Hagane 53 (1967) 983.
[99] H. Ooi, Y. Oguchi, H. Nakato, Tetsu-to-Hagane 56 (1970) 991.
[100] C. Wu, V. Sahajwalla, Metall. Mater. Trans. B. 31B (2000) 243–251.
[101] V.M. Surovsky, N.K. Nekrasov, Izv. V.U.Z. Chernaya Metall. (1) (1971) 164, Steel USSR 75 (1) (1971).
[102] R.D. Pehlke, P.D. Goodell, R.W. Dunlap, Trans. AIME 233 (1965) 1420.
[103] J. Szekely, Y.K. Chuang, J.W. Hlinka, Metall. Trans. 3 (1972) 2825–2833.
[104] R.I.L. Guthrie, P. Stubbs, Can. Metall. Q. 12 (4) (1973) 465–473.
[105] P.G. Sismanis, S.A. Argyropoulos, Can. Metall. Q. 27 (2) (1988) 117–122.
[106] S.A. Argyropoulos, N.J. Goudie, M. Trovant, in: N. El-Kaddah, D.G.C. Robertson, S.T. Johansen, V.R. Voller (Eds.), Proceedings of the International Symposium in Fluid Flow Phenomena in Metals Processing organized by TMS, held at the 1999 TMS Annual Meeting in San Diego, CA, February 28–March 4, 1999, pp. 535–542.
[107] Z. Li, S.A. Argyropoulos, Mater. Trans. Jpn. Inst. Met. 51 (8) (2010) 1371–1380.
[108] Z. Li, S.A. Argyropoulos, Can. Metall. Q. 48 (4) (2009) 399–418.
[109] P.G. Sismanis, S.A. Argyropoulos, P.D. Deeley, in: Electric Furnace Conference Proceedings, 155, vol. 44, 1986, pp. 39–55.
[110] G.H. Rodway, J.D. Hunt, J. Mater. Sci. 23 (1988) 814–822.
[111] K.N. Tu, Ann. Rev. Mater. Sci. 15 (1985) 147–176.
[112] C.M. Brown, N.J. Pappas, H.J. Brown, Method for adding metal to molten metal baths, U.S. Patent No. 3,592,637, Patented July 13, 1971.
[113] S.A. Argyropoulos, P.D. Deeley, Exothermic alloy for addition of alloying ingredients to steel, U.S. Patent No. 4,472,196, Patented September 18, 1984.

[114] O. Kubaschewski, W.A. Dench, Acta Metall. 3 (1955) 339–346.
[115] Z. Li, S.A. Argyropoulos, Assimilation of zirconium-aluminum powder compacts in liquid aluminum, Unpublished research work, Department of Materials Science and Engineering, University of Toronto, Canada, 2010.
[116] K. Sun, S.A. Argyropoulos, Can. Metall. Q. 45 (2) (2006) 223–232.
[117] S.A. Argyropoulos, Transactions of the ISS, I&SM, July 1996, pp. 65–80.
[118] J. Shade, S.A. Argyropoulos, A. McLean, in: M. Koch, J.C. Taylor (Eds.), Conference Proceedings on Productivity and Technology in the Metallurgical Industries, The Minerals, Metals & Materials Society, Warrendale, PA, 1989, pp. 281–300.
[119] J. Shade, S.A. Argyropoulos, A. McLean, in: Transactions of ISS, Iron and Steelmaker, January 1990, pp. 53–65.
[120] E.V. Barrera, F.D.S. Marquis, W.E. Frazier, S.G. Fishman, N.N. Thadhani, Z.A. Munir (Eds.), Proceedings of a symposium held during the 124th TMS Annual Meeting, Las Vegas, Nevada, February 12–16, 1995.
[121] Y. Iguchi, S. Nobori, K. Saito, T. Fuwa, Tetsu-to-Hagane 68 (6) (1982) 89–96.
[122] W. Helber, On the dissolving of chromium metal and deep carbonized ferrochrome in iron melts (Doctoral Thesis), Faculty for Mining and Metallurgy of RWTH, Aachen University, 1969.
[123] Y.O. Esin, M.G. Valishev, A.F. Ermakov, P.V. Gel'd, Russ. Metall. (3) (1981) 15–17.
[124] G.K. Sigworth, J.F. Elliott, Met. Sci. 8 (1974) 298–310.
[125] J.A. Dean, Lange's Handbook of Chemistry, 13th ed., McGraw-Hill, New York, 1985.
[126] R.H. Perry, D.W. Green, J.O. Maloney, Perry's Chemical Engineers' Handbook, sixth ed., McGraw-Hill, New York, 1984.
[127] J. Lacaze, B. Sundman, Metall. Trans. A 22A (1991) 2211–2223.
[128] H.T. Angus, Cast Iron: Physical and Engineering Properties, Butterworths, London, 1976.
[129] T. Iida, R.I.L. Guthrie, The Physical Properties of Liquid Metals, Clarendon Press, Oxford, 1988.
[130] Properties of Silicon, The Institution of Electrical Engineers, New York, 1988.
[131] H. Hu, S.A. Argyropoulos, Int. J. Heat Mass Transf. 39 (5) (1996) 1005–1021.
[132] H. Hu, S.A. Argyropoulos, Metall. Trans. B 28B (1997) 135–148.
[133] V. Alexiades, A.D. Solomon, Mathematical Modeling of Melting and Freezing Processes, Hemisphere Publishing Corporation, Washington, 1993.
[134] Y. Cao, A. Faghri, W. Chang, Int. J. Heat Mass Transf. 32 (1989) 1289–1298.
[135] S.V. Patankar, Numerical Heat Transfer and Fluid Flow, McGraw-Hill, New York, 1980.
[136] S.A. Argyropoulos, H. Hu, S. Ferenczy, in: N. El-Kaddah, D.G.C. Robertson, S.T. Johansen, V.R. Voller (Eds.), Proceedings of the International Symposium in Fluid Flow Phenomena in Metals Processing organized by TMS, held at the 1999 TMS Annual Meeting in San Diego, CA, February 28–March 4, 1999, pp. 149–156.
[137] J. Szekely, Y.K. Chuang, Chem. Eng. Sci. 27 (1972) 2300–2304.
[138] W.J. Minkowycz, E.M. Sparrow, J. Heat Transf. 96 (1974) 178–183.
[139] W.M. Rohsenow, H.Y. Choi, Heat, Mass and Momentum Transfer, Prentice-Hall, Inc., Englewood Cliffs, N.J., 1961, pp. 155–159.
[140] S.A. Argyropoulos, H.H. Hu, Steel Res. 73 (11) (2002) 467–479.
[141] S.A. Argyropoulos, M. Pekguleryuz, CIM Bull. 95 (1062) (2002) 83–86.
[142] R.H. Elder, V.C. Kendrick, Iron Steelmaker 12 (7) (1985) 42–45.



CHAPTER 4

Metallurgical Process Technology

Roderick I.L. Guthrie and Mihaiela Isac
McGill Metals Processing Centre (MMPC), Montreal, Canada

Contents

4.1. Process Kinetics, Fluid Flow, Heat and Mass Transfer, in Process Metallurgy 428
4.2. Turbulence Modeling and Implementation 445
4.3. Computational Fluid Mechanics 453
4.4. Solidification 497
4.5. Computational and Physical Modeling of Solidification in CCC and TSC 515
4.6. Single Phase, Two Phase, and Multiphase Flows, and Methods to Model these Flows 527
4.7. The Design of a New Casting Process; From Fundamentals To Practice 555
4.8. Conclusion 585

CHAPTER 4.1

Process Kinetics, Fluid Flow, and Heat and Mass Transfer, in Process Metallurgy

Roderick I.L. Guthrie
McGill Metals Processing Centre (MMPC), Montreal, Canada

All metallurgical processing operations to produce and refine metals and alloys, and to then render them into useful shapes, invariably involve the transfer of mass (species) and/or heat, and momentum, between one or more phases. The transfer of heat and mass can involve diffusion, thermal conduction, radiation, plus convective transport. The two diffusive transport phenomena can be expressed through Fourier's and Fick's first laws for heat and mass transport, while the Stefan–Boltzmann equation handles radiant heat transfer. The two diffusive equations basically determine the overall kinetics, and kinetic paths, followed by many metallurgical processes before they reach a final, end, result. This is because the kinetics of most pyrometallurgical reactions are transport controlled (rather than controlled by chemical kinetics), so the rate-limiting feature will be the diffusive and/or conductive processes. One can therefore normally assume that chemical equilibrium exists at the reacting interfaces separating phases, but only there.

By contrast, chemical thermodynamics represents a study of chemical equilibrium between bulk phases, in which the lowest energy state between reactants and potential products is assumed to prevail, independent of any kinetic restraints. As such, time does not appear in any thermodynamic representation. Thermodynamics can be considered as representing a basic first step, *en route* to a more realistic kinetic description of an actual process. Nonetheless, the thermodynamic approach can be incorporated into simplified kinetic models, provided that equilibrium exists between the bulk phases at all intermediate stages between the start and finish of a processing operation.

So, in terms of diffusive heat, diffusive mass, and diffusive (viscous) momentum transfer processes, in the absence of any convection, the three fundamental equations describing (one dimensional) heat conduction, mass diffusion, and viscous momentum transport, for the conduction of heat, the diffusion of species A in solvent B, and for molecular viscous shearing flows, are:

$$\text{Fourier's first law of heat conduction (a)}: \dot{q}_x'' = -k\frac{\mathrm{d}\theta}{\mathrm{d}x}, \tag{4.1.1}$$

$$\text{Fick's first law (b)}: \dot{N}_{A,x}'' = -D_{AB}\frac{\mathrm{d}CA}{\mathrm{d}x} \tag{4.1.2}$$

Treatise on Process Metallurgy, Volume 2
http://dx.doi.org/10.1016/B978-0-08-096984-8.00007-0
© 2014 Elsevier Ltd.
All rights reserved.

$$\text{Newton's law of viscosity (c)}: \boldsymbol{\tau}_{y,x} = -\mu \frac{\mathrm{d}U_x}{\mathrm{d}y} \text{ for a shearing parallel flow} \quad (4.1.3)$$

Here, $\boldsymbol{\tau}_{y,x}$ represents the x-directed viscous shear force caused by a velocity gradient of U (or U_x) in the y-direction. Additionally, $\boldsymbol{\tau}_{y,x}$ may be viewed as the transfer of x-momentum per unit time in the y-direction. Tau, or $\boldsymbol{\tau}$, is a tensor product, having a normal shear stress component, $\boldsymbol{\tau}_{xx}$, and two shear stress components, $\boldsymbol{\tau}_{yx}$ and $\boldsymbol{\tau}_{zx}$, for a total of nine components in a Cartesian system. For irrotational flows, for example, one can write that $\boldsymbol{\tau}_{y,x} = \boldsymbol{\tau}_{x,y}$, etc. These general laws are presented in textbooks on Heat, Mass, and Momentum Transport, as well as Chapter 4 of this treatise, and therefore will not be presented here [1–6].

The three equations state that the amount of heat conducted through a solid or stationary liquid, or the mass of solute diffusing through it, or the transfer of x-momentum down a velocity gradient of U_x in the y-direction, per unit time, and unit cross-sectional area, is proportional to the temperature, concentration, or velocity gradients, through the solid or stationary fluid. In the case of Newton's law of viscosity, the velocity gradient, $\mathrm{d}U_x/\mathrm{d}y$ is finite, and we can generally assume that U_y is zero across a stationary interface. Most metallurgical fluids obey Newton's law of viscosity. However, alloy systems during freezing will show deviations. The constants of proportionality are defined as the thermal conductivity (J/m K s), molecular diffusivity (m^2/s), and molecular viscosity (Pa s) [1–6].

Beyond these laws for molecular transport/diffusion processes, the role of fluid mechanics can be extremely important, as it determines the speed at which dissolved reactants or heat can pass through a bulk liquid or gas phase, to reach these reacting interfaces. Only there do the diffusive flows allow thermal heat or diffusive mass to pass through the boundary layers, to the reacting interfaces. As such, the fluid dynamics of bulk flows, as well as flows in boundary layers, generally enter into many aspects of process metallurgy. Similarly, it allows one to incorporate all the interfacial transport phenomena involved, and to have a complete description of the process, as a function of time, and space. For quantifying these situations, one has the convective and diffusive transport expressions, embodied in the Navier–Stokes Equation, together with the diffusive heat and mass transport equations [1–5].

Additionally, in actual systems that engineers encounter, turbulence phenomena are usually present. For this we have the Reynolds turbulence equation, which is equivalent to the N–S equation, but incorporates the important handling of turbulence effects. Turbulent microflows can enhance molecular transport processes, by factors of 10–10,000 times! One normally expresses the shearing stresses generated by these small-scale turbulent motions as being given by an equivalent expression to Newton's law for molecular viscosity, in which μ_m is replaced by μ_e, the turbulent eddy viscosity. As such, $\mu_\mathrm{total} = \mu_\mathrm{m} + \mu_\mathrm{e}, = \mu$, in the equation $\overline{\boldsymbol{\tau}}_{x,y} = -\overline{\mu}\frac{\mathrm{d}Ux}{\mathrm{d}y}$, where $\overline{\boldsymbol{\tau}}_{x,y}$ is the time averaged shear stress, U_x is the time averaged velocity at a point in the flow, and μ_e is equal to the sum of

the eddy viscosity (which is normally dominant in the bulk of the flow zone), and $\mu_{m,}$ the molecular viscosity.

Many metallurgical processing operations typically involve convective flows in metal extraction, refining, and casting operations. The transport of heat, or mass, or particles, is also often associated with these convective flows.

In iron making, for example, optimizing bulk gas flows through the burden of a blast furnace is a key factor in assuring high productivity and good CO gas utilization by the sinter, or pellets, comprising the burden [7]. Similarly, mixing rates of molten steel in a BOF furnace, or in a teeming ladle, during additions of alloying materials, play a key role in optimizing the local chemistry of a steel grade, and in assuring that chemical, and thermal, homogeneity is finally reached, within a specified time limit [8]. Fluid mechanics even enters the field of solidification, in that steel and slag flows within the liquid sump of conventional continuous casting machines help determine the quality of the final solidified product. These include the cast microstructure, macrosegregation of carbon and other solute components, the amounts of entrapped inclusions, and even the surface characteristics of the solidified products.

Similar examples can be cited for the relevance of fluid dynamics for the nonferrous industries, such as the successes achieved in the field of magnetohydrodynamics (MHD) for the production of aluminum in the Hall-Heroult Electrolytic Cell, and in the "contactless" casting of aluminum ingots in the electromagnetic DC (Direct Chill) casting process [10]. These electromagnetic effects can be expressed quantitatively, thanks to the development of the Maxwell equations for electric fields and forces at the turn of the twentieth century, which are solved in conjunction with the hydrodynamic equations for fluid flows, first developed by Navier and Stokes in the eighteenth century.

Over the last 40 or so years, significant strides have been made in the improvement and redesign of metallurgical processing operations. These advances have been based on a growing understanding and appreciation of fluid mechanics in such systems, together with its intrinsic coupling with process kinetics and MHD. The advent of computing power has helped greatly in this endeavor, leading to the development of computational fluid dynamics (CFD). This has now become a very common tool, helping to unify our knowledge and understanding of metallurgical reactor systems.

4.1.1. THEORY OF FLUID FLOWS

The subject of fluid mechanics dates back to at least the Ancient's times in Egyptian, Greek, and Chinese civilizations. For example, the theory of hydrostatics, or static fluids, was well advanced at those times. This leads to Archimedes' moment of insight in Syracuse, circa 260 BC, while sitting partially submerged in a bath, and contemplating how to quantify the exact proportion of gold versus copper in the "golden" crown of the King of Macedonia. He realized that a submerged body experiences an

upward displacement of force equal to the weight of the fluid displaced by it. This is now known as Archimedes' principle. Given the different densities of copper and gold, he was able to deduce how much copper had been added to the crown.

Nonetheless, the defining feature of a *true fluid* is its *inability* to withstand any *shearing stresses*, without being set in motion. Thus, once a fluid is in motion, pressure gradients will exist, and a "dynamic pressure," or "P_d," can be identified. This dynamic component of pressure can be defined as the absolute pressure, P_{ab}, less the static pressure, P_s. In defining a static pressure, P_s, for a fluid in motion, this is customarily taken as the mean of three orthogonally directed pressures (or normal stresses $\boldsymbol{\tau}_{xx}$, $\boldsymbol{\tau}_{yy}$, $\boldsymbol{\tau}_{zz}$). Thus:

$$P_d = P_{ab} - P_s, \quad \text{where } P_s = \left(\tau_{xx} + \tau_{yy} + \tau_{zz}\right)/3 \tag{4.1.4}$$

In many fluid flow situations, the dynamic components of pressure that are responsible for driving a given flow are much smaller, numerically, than the static components, such as the static atmospheric pressure and the hydrostatic or ferrostatic pressures, acting on the flow system. In the art of CFD, to be addressed later, it is therefore more expedient to rewrite the equations of motion governing fluid flows, so as to emphasize the important influence of the dynamic pressure field on a resulting flow.

4.1.2. THE CONTINUITY AND MOMENTUM EQUATIONS

The differential equations for fluid motion derive from mathematical statements of conservation of mass and momentum. The continuity equation is a statement of mass conservation, while the momentum equation is an embodiment of Newton's second law of motion. This states that the sum of the forces acting on a body is equal to the product of its mass and its resultant acceleration, or more generally, rate of momentum change, i.e.,

$$\Sigma F_x = Ma_x, \quad \text{or} \quad \Sigma F_x = \mathrm{d}(MV_x)/\mathrm{d}t \tag{4.1.5}$$

Equation (4.1.5) is for unidirectional motion, where ΣF_x represents the sum of the x-directed forces on an imaginary element of fluid, M is its mass, and a_x is its resulting acceleration, or deceleration. Alternatively, the equation may be expressed as restated as ΣF_x is equal to the rate of change of momentum $\mathrm{d}(MV_x)/\mathrm{d}t$.

In CFD analyses, it is customary to imagine the flow field as comprising an infinite number of infinitesimally small volume elements of that flow field, that are fixed in space, or stationary, through which the fluid is flowing. An individual element itself can be idealized as being a cube, a pyramid, a hexagon, etc., depending on the coordinate system being used to delineate the flow field. The latter systems can be expressed in rectangular, cylindrical, spherical, or any other convenient systems, for which body-fitted coordinates can be used.

A stationary frame of reference is termed a Eulerian frame of reference and is the flow that one would see, if one were to be a stationary observer (i.e., not moving). An alternative frame of reference would be for an observer to move at the same speed and in the same direction as the fluid. That is referred to as a Lagrangian frame of reference. Each has its own advantages. Typically, one is more likely to choose a Eulerian frame of reference to describe a flow field, since one is normally at rest, or stationary, with respect to the fluid motions. However, if you wish to sit on a particle moving through the liquid, then you will choose the Lagrangian coordinate system and enjoy a moving experience!

In order to understand these two frames of reference better, and the fundamental relevance of Newton's second law of Motion in Fluid Mechanics, we will consider the example of a jet of liquid steel issuing from the bottom of a tundish into one of the moulds of a four-strand casting machine. Figure 4.1.1 shows a schematic of the flow system to be analysed, where we can follow the movement of a cylindrical element of the jet from position 1 at time t_1, to position 2, at time t_2. We can correctly take a large "chunk" of liquid, rather than an infinitesimally small element, provided there are no

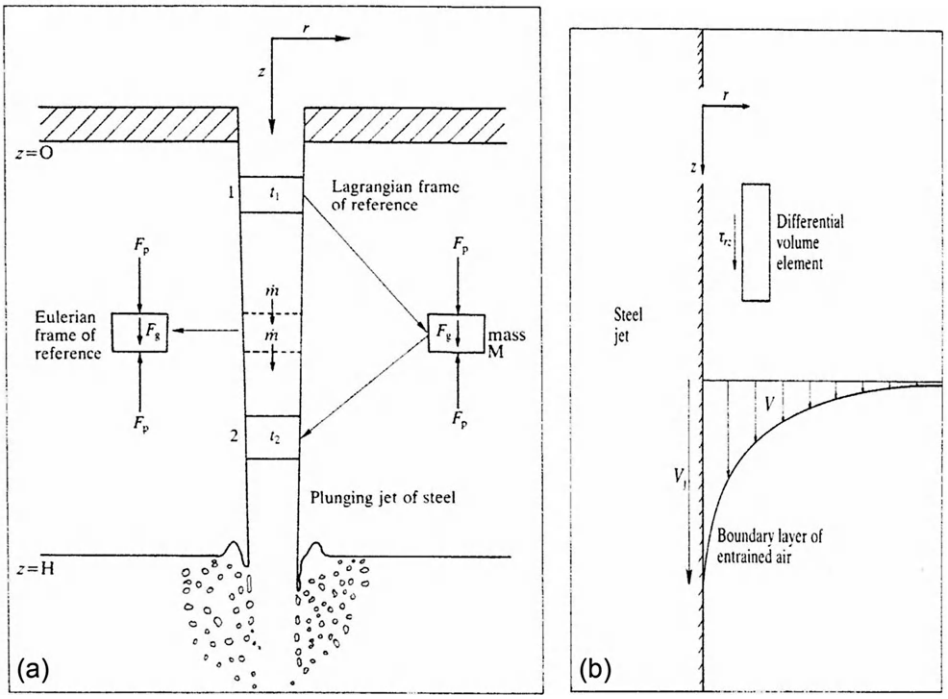


Figure 4.1.1 (a) Momentum transport processes in fluids, illustrated by a plunging jet of liquid steel, in laminar flow. Distinction between differential volume elements fixed in space (Eulerian; left-hand side) or moving with the flow (Lagrangian; right-hand side of jet). (b) The entrainment of air into a boundary layer of air adjacent to the plunging jet, owing to viscous shear. As the density of steel is 7000 times greater than air, the effect on the steel flow is zero.

shear stresses being generated between the air and the liquid steel, provided there is no turbulence, and provided the flow is laminar. All these conditions are reasonably true for the flow being considered.

However, we note that the liquid is accelerating at g, or 9.81 m/s every second, so the shape of the chunk of fluid we are following will become longer, and narrower, as it speeds up, as shown in Figure 4.1.1. Replacing the weight of the chunk, or element, by Mg, and applying Newton's second law of motion to the mass, M, we have that

$\Sigma F_x = F_p + F_g - F_p$, so that $F_g = M\,g = M\,a_x$, so that $a_x = g$

However, $a = \frac{dV}{dt} = \frac{dV}{dx}\,\frac{dx}{dt} = \frac{dV}{dx}\,V$.

Equation (4.1.4) then becomes $F_g = MV\frac{dV}{dx}$, which can be integrated from $x = 0$ to $x = \mathrm{H}$, and $V = V_0$ to V_f to give:

$$F_g H = \frac{1}{2}M\left(V_f^2 - V_0^2\right) \tag{4.1.6}$$

The integrated form of this momentum balance shows that the decrease in potential energy of the steel moving from $x = 0$ to $x = \mathrm{H}$, or ρgH, is exactly compensated by an increase in kinetic energy.

Substituting $\rho A\mathrm{d}x$ for M, and $\rho A\mathrm{d}xg$ for F_g, where ρ is the fluid density,

$$\rho gH = \frac{1}{2}\rho V_f^2 - \frac{1}{2}\rho V_0^2 \tag{4.1.7}$$

This equation therefore represents a special case, or particular form, of the steady flow energy equation, SFEE. Also, since no energy is lost, it also represents a special form of the Bernouilli Equation, which states that kinetic, pressure, and kinetic energies are conserved, and interconvertible, in a friction-free system.

However, we can also write that the net force acting on the macroscopic control volume element in Figure 4.1.1 is equal to the rate of momentum change, for a constant mass flow rate of MV, or $\dot{m}$

$$F_g = MV\int_0^f \frac{\mathrm{d}V}{\mathrm{d}x} = \rho A\mathrm{d}x\,V\int\frac{\mathrm{d}V}{\mathrm{d}x} = \dot{m}\mathrm{d}V = \dot{m}\left(V_f - V_0\right) \tag{4.1.8}$$

This can be rewritten as the relevant form of the momentum equation for this system, where $\dot{m}$ represents the (constant) mass flow rate (kg/s) through the Eulerian volume element fixed in space (left-hand side element appearing in Figure 4.1.1). The last equation is a particular form of the momentum equation, and both derive from Newton's second law of motion.

Taking a flow of steel exiting a tundish filled to 500 mm of liquid steel, its maximum exit velocity would be 3.13 m/s, and it would accelerate over a 1 m drop to the mold to an impact velocity of 5.4 m/s.

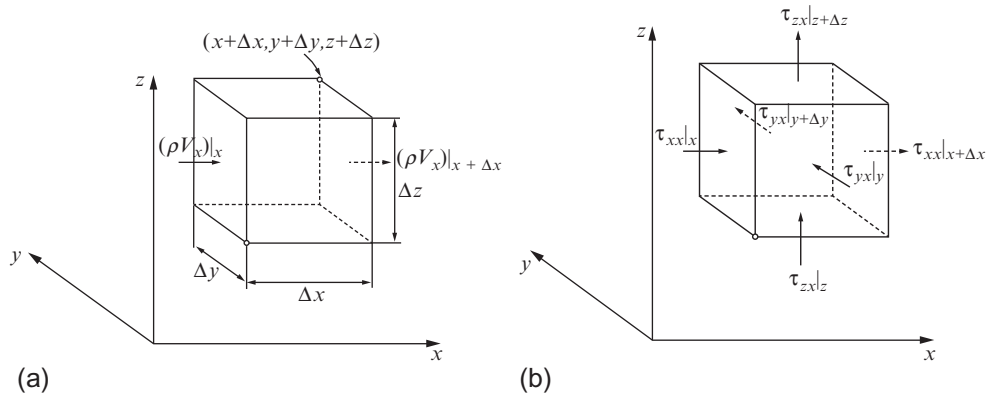


Figure 4.1.2 Volume element of fluid, $\triangle x \triangle y \triangle z$, fixed in space and time. The arrows in (a) indicate the direction in which the *x*-component of mass. Arrows in (b) indicate the diffusive components of *x*-momentum being transported through the imaginary surfaces. *Reproduced from Guthrie [1] by permission from Oxford University Press.*

Figure 4.1.2a illustrates a more generalized Eulerian situation for three-dimensional flows, in which mass enters and leaves the six surfaces of an imaginary cubic element of fluid. An accounting of inputs and outputs of mass, plus any accumulation of mass in the case of a compressible fluid, leads to the continuity equation for the conservation of mass. For a Cartesian-based coordinate system therefore

$$\frac{\partial \rho}{\partial t} + \frac{\partial}{\partial x}(\rho V_x) + \frac{\partial}{\partial y}(\rho V_y) + \frac{\partial}{\partial z}(\rho V_z) = 0 \tag{4.1.9}$$

Alternatively, in shorthand vector format:

$$\frac{\partial \rho}{\partial t} = -\nabla \cdot (\rho U) \tag{4.1.10}$$

where ∇ (nabla) represents the differential operator, acting on the general vector variable, ϕ:

$$\nabla \cdot \phi = \frac{\partial \phi_x}{\partial x} + \frac{\partial \phi_y}{\partial y} + \frac{\partial \phi_z}{\partial z}$$

The vector variable $\phi = \boldsymbol{i}\phi_x + \boldsymbol{j}\phi_y + \boldsymbol{k}\phi_z$.

We can now consider the momentum equation, or equation of motion, which is a special form of Newton's second law of motion, combined with Newton's law of viscosity, for a Eulerian system. Again, using rectangular coordinates, in which we can write the *x*-component, by way of example:

$$\rho\left(\frac{\partial V_x}{\partial t}+V_x\frac{\partial V_x}{\partial x}+V_y\frac{\partial V_x}{\partial y}+V_z\frac{\partial V_x}{\partial z}\right) = -\frac{\mathrm{d}P}{\mathrm{d}x}-\left(\frac{\partial \tau_{xx}}{\partial x}+\frac{\partial \tau_{yx}}{\partial y}+\frac{\partial \tau_{zx}}{\partial z}\right)+\rho g_x+F_{e,x}+F_{a,x} \tag{4.1.11}$$

For this momentum equation, the forces on the cube will act at the center of a similar cubic element into which momentum enters and leaves the imaginary cube in Eulerian (stationary) space, i.e., $\rho V_x V_x$, $\rho V_y V_y$, and $\rho V_z V_z$. The body forces will include (1) pressure, (2) gravity, (3) electromagnetic, (4) added mass for accelerating flows, as well as include other forces such as buoyancy (thermal and/or mass induced). Similarly, the normally directed stresses acting on the *surfaces* of the imaginary "momentum" cube, $\Delta x \Delta y \Delta z$, shown in Figure 4.1.2b, for example, will include the normal stresses, $\boldsymbol{\tau}_{xx}$, $\boldsymbol{\tau}_{yy}$, $\boldsymbol{\tau}_{zz}$. Similarly, the tangential shearing stresses, represented by the second term on the right-hand side of the momentum equation, can be represented as $\boldsymbol{\tau}_{xy}$, $\boldsymbol{\tau}_{xz}$, $\boldsymbol{\tau}_{yx}$, $\boldsymbol{\tau}_{yz}$, $\boldsymbol{\tau}_{zx}$, $\boldsymbol{\tau}_{zy}$.

In defining these shear stresses, it is customary to define the direction in which the shearing stress is acting as the second subscript, while the first subscript defines the direction of the velocity gradient generating the molecular stress. Thus $\boldsymbol{\tau}_{yx}$ represents the x-directed stress owing to a velocity gradient of V_x in the y-direction. It is also useful to note that the shear stress components, such as $\boldsymbol{\tau}_{yx}$ and $\boldsymbol{\tau}_{zx}$, for example, can also be interpreted as a transfer of x-momentum in the y-direction and of x-momentum in the z-direction, respectively. This is in keeping with similar interpretations for shear stresses based on the kinetic theory of gases; these diffusive components of momentum flux are represented in Figure 4.1.2b. As with mass conservation, or continuity, an accounting of inputs and outputs of momentum then leads to a general expression for the momentum equation (x-component) explicitly taking into account gravity, electromagnetic, and added mass forces, together with normal and shear stress forces associated with the viscosity of the fluid.

4.1.3. NEWTONIAN LIQUIDS

In single-phase fluid dynamic analyses, these two partial differential equations for continuity of mass and momentum must be solved using the particular boundary conditions applying to a given flow situation, if one can provide expressions for the various normal and shear stresses acting within the fluid system. These stresses are both property and flow dependent. Liquid metals, liquid slags, molten salts, and gases (Mach < 0.2) can all be categorized as being incompressible Newtonian fluids. For such fluids:

$$\tau_{xx} = -\mu\left(2\frac{\partial U}{\partial x}\right) \tag{4.1.12}$$

and

$$\tau_{xy} = \tau_{yx} = -\mu\left(\frac{\partial U}{\partial y} + \frac{\partial V}{\partial x}\right) \tag{4.1.13}$$

where τ_{yx} denotes the x-directed shear stress (N/m^2) acting on the y-surface (area $\Delta x \Delta z$), caused by a y-directed velocity gradient in U, ($=V_x$). In fact, different textbooks of fluid mechanics use different expressions for velocity components, for example, ($U = V_x$, $V = V_y$, and $W = V_z$) in the present case.

The property-dependent quantity, μ, is the Newtonian coefficient of viscosity, which for most liquid metals range between 1 and 10 mPa s, and between 300 and 10 Pa s, or more, for high silica-based slags. Note that for a parallel flow between x-directed plates, $\frac{\partial V}{\partial x}$ or $\frac{\partial V_y}{\partial x}$, is equal to zero, so we obtain the more familiar expression for viscous shear stresses developed for the laminar flow of liquid between two shearing, x-directed, parallel plates, as normally presented in textbooks, for Newton's law of viscosity:

$$\tau_{yx} = -\mu\left(\frac{\partial U}{\partial y}\right) \tag{4.1.14}$$

Basically, this is a definition of the viscosity of a fluid, which states that a liquid in shearing motion will offer a resistance to flow that is directly proportional to the rate of shearing flow. Substituting expressions for the shearing and normal stresses in the momentum equation leads to the three x,y,z components of the momentum equation. They take the form:

$$\rho U\frac{\partial U}{\partial x} + \rho V\frac{\partial U}{\partial y} + \rho W\frac{\partial U}{\partial z} = -\frac{\mathrm{d}P}{\mathrm{d}x} + \mu\left(\frac{\partial^2 U}{\partial x^2} + \frac{\partial^2 U}{\partial y^2} + \frac{\partial^2 U}{\partial z^2}\right) + \rho g_x \tag{4.1.15}$$

This x,y,z set of equations are referred to as the Navier–Stokes equations, in honor of two early researchers in the field of hydrodynamics. They can be summarized in *vector form* as

$$\frac{\partial(\rho V)}{\partial t} + [\nabla\cdot\rho VV] = -\nabla P - [\nabla\cdot\tilde{\tau}] + \rho g \tag{4.1.16}$$

where emboldened symbols represent vector quantities (magnitude and direction). We can summarize this equation even more compactly as

$$\frac{\mathrm{D}\rho V}{\mathrm{D}t} = -\nabla P - [\nabla\cdot\tilde{\boldsymbol{\tau}}] + \rho g \tag{4.1.17}$$

where $\mathrm{D}/\mathrm{D}t$ represents the substantial time derivative, summarizing the left-hand side of the previous equation.

4.1.4. ELECTROMAGNETICALLY DRIVEN FLOWS

The discovery of electricity and the flows of electricity, and its connections with magnetism, at the end of the eighteenth century, had a large effect on the metals community, starting with Faraday's law for the equivalence of joules of energy of electrical work for the deposition of metals from a solution containing its ions, according to $\Delta G^{o} = -zEF$. Similarly, Ohms law was discovered. This states that the voltage generated across a body-conducting electricity is equal to the current flowing (in amperes), times the electrical resistance offered by the body-conducting electricity, $\Delta V = I\Delta R$. This resistance (in ohms) is defined as the resistivity of the body times the length of passage, divided by the cross-sectional area: $\Delta R = [\rho_e L/A]$. Other experimental laws discovered at that time were the Biot–Savart law which allows us to calculate the magnetic field H generated by an electrical current, and the equivalent Ampere's circuital law, as well as Faradays law, linking a magnetic field to the generation of electrical current or voltage, and Lenz's law linking induced voltage to oppose the flux change producing it. Maxwell was able to bring all these various experimental laws of electricity into one coherent set of equations, termed the *Maxwell equations* [4,10].

In terms of electromagnetic theory and its importance to applications in process metallurgy, it is essential to many aspects of the subject. For instance, we use electromagnetic fields to inductively heat and melt metals using induction furnaces, or to levitate metals (used in cold crucible melting of reactive metals), or in ladle mixing processes, etc. It is commonly understood that if a current is passed through conducting coils that surround a ladle or mold, containing an electrical conductor (i.e., liquid steel or liquid aluminum), then that primary current through the coils will induce a magnetic force field, which, in turn, will produce the motion and heating within the melt. Thus Maxwell's equations, using the MHD approximation, can be written [5]

$$\nabla \times \mathbf{E} = \frac{\partial \mathbf{B}}{\partial t} \tag{4.1.18}$$

where $\mathbf{E}$ is the electric field vector (V/m), and $\mathbf{B}$ represents the magnetic flux density vector (Weber/m^3, or Tesla). $\mathbf{H}$, the magnetic field (amperes/meter), is related to the magnetic flux density, according to the relation $\mathbf{B} = \mu\mathbf{H}$, where μ represents the magnetic permeability of the material (H/m). Continuing,

$$\nabla \times \mathbf{H} = \mathbf{J} \tag{4.1.19}$$

$$\nabla \cdot \mathbf{J} = 0 \tag{4.1.20}$$

$$\nabla \cdot \mathbf{B} = 0 \tag{4.1.21}$$

Equations (4.1.20) and (4.1.21) represent statements of conservation for $\mathbf{J}$ and $\mathbf{B}$ for steady-state flows of electrical and magnetic fluxes. Thus $\mathbf{J}$ in Equation (4.1.19) represents

the conduction current density or flux (A/m^2). The latter is related to a form of Ohm's law that includes the flux of electrical current carried by the moving fluid, or rather liquid:

$$\mathbf{J} = \sigma_e[\mathbf{E} + \mathbf{U} \times \mathbf{B}] \tag{4.1.22}$$

where σ_e represents the liquid's electrical conductivity ($(\text{ohms m})^{-1}$). The second term, however, is often relatively insignificant for typical metal stirring applications and can commonly be ignored.

The Lorentz, or body force, generated on an element of conducting liquid by the electromagnetic force field is given by the cross product of the conduction current density, **J**, and the magnetic flux density, **B**:

$$\mathbf{F}_{em} = \mathbf{J} \times \mathbf{B} \tag{4.1.23}$$

In MHD analyses therefore, the electric and magnetic fields within the system have first to be solved, and the resulting computations for the magnetic force field incorporated into the Reynolds, or Navier–Stokes equation, to solve for the resulting flow fields. Fortunately, the two can be treated as uncoupled partial differential equations since the $U \times B$ product is not usually significant.

4.1.5. PHYSICAL MODELING

It is well known that physical models of processes can be very helpful, and far more convenient for simulating processes that do not lend themselves readily to direct analysis and measurement. This is very true of high-temperature metallurgical systems, which are opaque, very hot, and inevitably quite dangerous for humans! As a result, process metallurgists have been very adept at constructing low-temperature models of all manner of high-temperature systems, particularly at universities, where students are involved in studying process metallurgy. In fact, one can model many high-temperature fluid flow systems, using water rather than a liquid metal. The danger is that one may be viewed as being a hydrometallurgist! While water and oils to simulate liquid metals and slags have their drawbacks, such as not conducting heat too readily, nor mimicking surface tension effects too well, one can normally circumvent these problems and arrive at useful analogues. This is very true of steelmaking operations involving reactors, such as BOF and Q-BOP furnaces, complex tundish designs, teeming ladles, and continuous casting molds, where all the generalized fluid mechanics can be studied, if not the whole process itself. As such, there has been much research carried out in universities and industry, modeling ladle systems, modeling tundish metallurgy, and modeling continuous casting operations. This research has been summarized in a number of review articles by the authors of this chapter.

Thus, we may write the Navier–Stokes equation (4.1.17) in the dimensional form:

$$\frac{\rho U}{t}+\frac{\rho U^2}{L}=\frac{\Delta P}{L}+\frac{\mu U}{L^2}+\rho g$$

where L represents a characteristic length scale of the system. We can then render it dimensionless by dividing by the inertial force term, $\frac{\rho U^2}{L}$, togive $\Delta P/\rho U^2$, or take the ratio of the inertial to viscous forces, to give the dimensionless grouping $\rho UL/\mu$, the Reynolds number. We are therefore able to recast a form of the Navier–Stokes equation for incompressible flow of a viscous fluid in the dimensionless form:

$$f\left(\frac{\rho UL}{\mu},\frac{U^2}{gL},\frac{\Delta P}{\rho U^2}\right)=0 \text{ or } f(Re,Fr,Eu)=0 \tag{4.1.24}$$

where *Re*, the Reynolds number of a flow system, represents the ratio of inertial to gravity forces; *Fr* is the Froude number, representing the ratio of inertial forces to potential (or gravity) forces; and *Eu* is the Euler (or Newton) number, representing the ratio of pressure difference (or drag) forces to inertial forces. The so-called inertial forces are generated by acceleration or deceleration of fluid elements within the boundaries of the flow field. Metallurgical examples would include the accelerating flow of metal into a teeming nozzle as illustrated in Figure 4.1.1, or metal flow around injected lime particles or around argon bubbles rising within a filled ladle of steel, etc.

These last sets of dimensionless parameters are very useful when setting up a physical model of a liquid steel flow system. For example, in modellng flows within a water model of a steelmaking tundish, it is important that one has geometrical similarity, and that the ratios of the Reynolds and Froude numbers of the two systems are perfectly matched. If this is so, then one has a perfect physical model, all other matters being equal, or rather negligible.

As a final note, it is worth mentioning that MHD effects such as ladle stirring and EMBR (electromagnetic braking) of liquid metals are not conducive to being modeled in water, owing to its low electrical conductivity versus liquid metals. Conductivities are typically a million times higher in liquid (and solid) metals. For these problems, such as EMBR of metal flows entering a slab caster mold from a submerged entry nozzle, one can use low melting point metals such as mercury, gallium, indium, and tin and overcome their opacity through the use of ultrasonic probes, or equivalent, to monitor velocity fields. Alternatively, one can use saline aqueous solutions to very much approximate flows in liquid metals, by respecting Hartmann and magnetic Reynolds numbers, etc., or by using other methods to induce forces into the liquid equivalent to magnetic fields.

4.1.6. PHYSICAL AND COMPUTATIONAL MODELS

As a note to aspiring process metallurgists, if one carries out a water model experiment of a high-temperature steelmaking tundish operation, one can expect some reluctance by practicing steelmakers to accept your results and recommendations for improvements. However, if these experiments are backed up with computational models, which produce the same answers and recommendations, one has a solid case to bring to their attention. This has proved to be a very successful way to proceed, using the much more convenient low-temperature models, to devise better ways, or new processes. Once all the problems at low temperature have been addressed, then one can trial a new process using high-temperature prototype models, in collaboration with the metallurgical industry.

4.1.7. COMPUTATIONAL FLUID DYNAMICS

The techniques whereby one translates all the partial differential equations into a computer program and then solves the resultant set of equations, to arrive at particular solutions, rest on the subject of numerical analysis and on the discretization of the relevant partial differential equations. These describe all aspects of the flow, heat, mass, and concentration flows, occurring within a flow system, or a reactor. We also need to have a good model, which can account for turbulent interactions within the system.

Prior to the advent of computers, we were unable to resolve the detailed flows and processes within a flow system and had to use the "Macroscopic Control Volume" approach. This meant that we had to use integrated forms of the SFEE and to experimentally determine friction factors, or coefficients of discharge, or drag factors, within the black box, or "Macroscopic Control Volume," in order to arrive at useful generic solutions, and accompanying flowcharts and diagrams. While these are still useful, they are gradually making way for CFD solutions which provide much "richer" information. Similarly, numerical analysis was a sophisticated branch of applied mathematics in 1965, but not at all helpful for solving fluid flow problems. However, the combination of increasing computer power and the discretization of the partial differential equations, into very simplified algebraic expressions, changed all that.

Professor Spalding's Group at Imperial College, and Dr. Hirt's research group at the Los Alamos Laboratories, were pioneers in the application of CFD to engineering.

Figure 4.1.3a–c shows an early CFD example of a typical finite volume discretization scheme using the MAC (Marker and Cell) technique [1,4,8]. This was applied to a cylindrical teeming ladle system, into which liquid steel is entering through a central vertical jet.

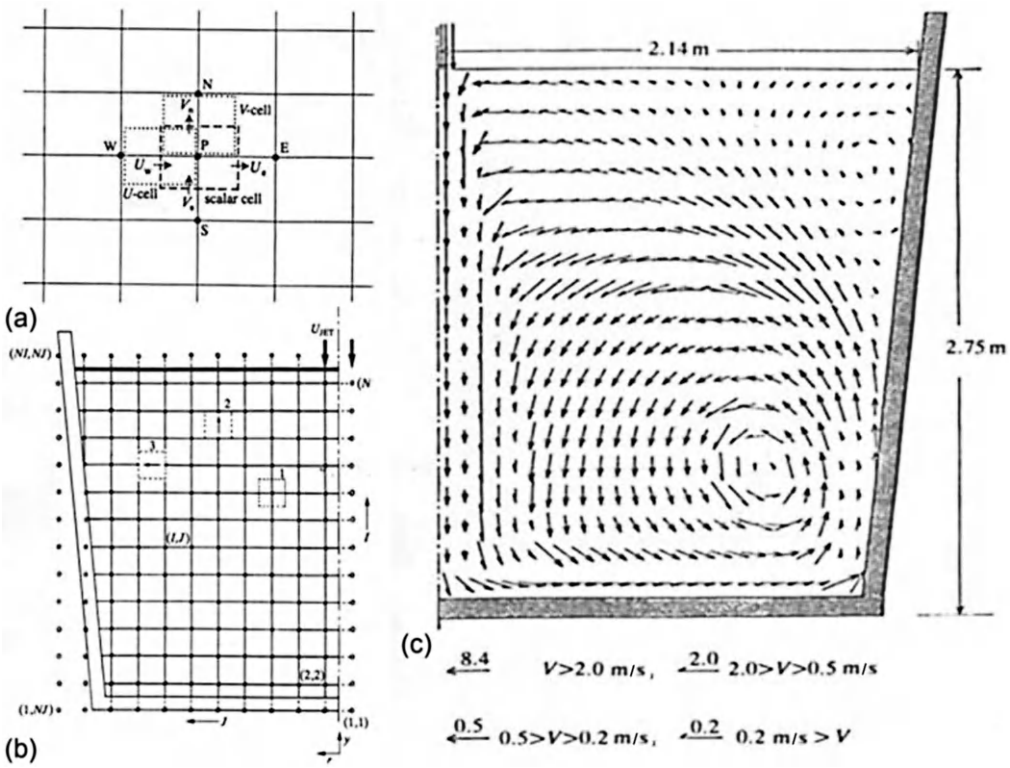


Figure 4.1.3 (a–c) An example of a transient CFD problem involving an idealized, plunging, vertical, jet of steel, filling up a teeming ladle with steel, using the MAC technique of Hirt *et al.* [1,4]..

Figure 4.1.3a shows this computational scheme incorporated a displacement of the scalar and velocity volume elements, so as to allow for upwind flows into a given cell, to dominate over the downwind outflows. Similarly, one has to choose a grid system, such that the Courant number ($U\Delta t/\Delta x \leqslant 0.4$) for reasons of numerical flow stability. Thus, one cannot have liquid moving right through a cell in one time step!

We see that the vectors for fluid flowing in and out of the generic discrete volume element shown in Figure 4.1.3a and scalar cell 1 in Figure 4.1.3b are located on each of the faces of the six sides of the scalar (central) cell (U_w, U_E. V_S, V_N). In addition to these, there are potential rotational velocity components, W_θ, $W_{\theta+1}$, not shown in Figure 4.1.3a, and not modeled in this idealized flow system. Scalar quantities, such as pressure, P, (shown), or temperature, concentration, turbulence kinetic energy, and turbulence energy dissipation rate, are located at the center of this volume element, termed *nodal points*. At these nodes, the values for the scalars represent volume averages of that scalar within the fluid bounded by the imagined volume element surrounding each node.

Given that all partial differential equations for continuity, momentum, heat and mass flows, kinetic energy of turbulence, turbulent dissipation rates, and electrical force fields, magnetic fields, and inductance, etc., that may need to be solved can be written in the general form:

$$\text{Convection terms} = \text{diffusion terms} + \text{source term}$$

One can therefore write the general equation, whose origin can be attributed to Spalding and coworkers [9]:

$$\frac{\partial}{\partial t}(\rho\phi) + \text{div}(\rho U\phi) = \text{div}\left(\boldsymbol{\Gamma_\phi grad \phi}\right) + S_\phi \tag{4.1.25}$$

in which ϕ can represent U, V, W, k, ε, C, θ, H, F_e, etc. The term $\boldsymbol{\Gamma_\phi grad}\,\phi$ represents the diffusive flux of ϕ_i; S_ϕ represents a so-called source term, which essentially involves those residual elements which do not fit into the other three groupings. Discretization of this formula over adjacent finite volume elements shown in Figure 4.1.3a–c, together with a one dimensional tridiagonal matrix algorithm for the implicit, line by line solution of nodal ϕ values, plus a Gauss–Siedel routine linking adjacent lines of nodes, provided for an efficient computational scheme for numerical integration. Figure 4.1.3c shows the computed flow patterns, or "particular solutions" for a nearly filled ladle of liquid steel, 2.75 m height, and 4.3 m in diameter at the surface. It reveals a strong vortex flow, churning deep within the filling ladle. A version of the SOLA-MAC code was written for this transient filling simulation [1,4,8] to assess the efficiency of adding alloy additions to the filling bath of steel.

Forty years on, one now has a number of commercially competitive computer programs such as FLUENT ANSYS, CFX, PHOENICS, and COMSOL that can provide the necessary platforms for easy access to CFD for students and practitioners. This is now far different from the situation where one had to develop one's own codes. For instance, we chose to develop the 3D METFLO code at McGill in the 1980s. It considered only rectangular and cylindrical coordinate systems at the time. This tended to constrain us to simple flow geometries, which were nonetheless still very useful in simulating tundish flows, flows in ladles, twin roll casting, and horizontal single belt casting. Similarly, these days, there is much easier access to gridding routines, to set up a given flow domain, and to provide differently shaped volume elements such as tetrahedral and hexagonal, as well as quadrilateral elements, so as to allow for complex three-dimensional shaped vessels to be fully researched. Similarly, one can readily increase the number density of grid nodes close to regions of strong shear, etc., such as in the vicinity of wall boundaries. These developments have gone hand in hand with increased computer power and improved algorithms. In conclusion, CFD has now become a mainstay of engineering design. It has been embraced by the major consulting companies, and advanced steel and aluminum manufacturers, in quests to improve, understand, and develop all manner of processes.

REFERENCES

[1] Roderick I.L. Guthrie, Engineering in Process Metallurgy, Oxford University Press, Oxford, 1989, ISBN: 0-19-856222-5, 0-19-856367-1.
[2] R.B. Bird, W.E. Stewart, E.N. Lightfoot, Transport Phenomena, John Wiley and Sons, Inc., New York, London, ISBN: 0 471 07392 X, 1960.
[3] D.R. Geiger, G.H. Poirier, A publication of TMS, The Minerals, Metals and Materials SocietyTransport Phenomena in Materials Processing, vol. 420, Commonwealth Drive, Warrendale, 1994.
[4] N. Sano, W.-K. Lu, P. Ribaud, Advanced Physical Chemistry, In: R.I.L. Guthrie (Ed.), Fluid Dynamics in metallurgical processes, Academic Press, ISBN: 0-12-618920-X, 1997 (Chapter 4).
[5] D. Mazumdar, J.W. Evans, Modelling of Steelmaking Processes, CRC Press, ISBN: 978-1-4200-6243-4, 2010.
[6] Takamichi Iida, Roderick I.L. Guthrie, The Physical Properties of Liquid Metals, Oxford University Press, Clarendon Press, Oxford, ISBN: 0-19-856331-0, 1988.
[7] N. Standish, Blast Furnace Aerodynamics, Proceedings organized by the Illawarra Branch of the A.I.M.M., Wollongong, Australia, 25–27 September, 1975.
[8] M. Salcudean, R.I.L. Guthrie, A three dimensional representation of fluid flow induced in ladles or holding vessels by the action of liquid metal jets, Metallurg. Trans. B 10B (1979) 423–428.
[9] S.V. Patankar, Numerical Heat Transfer and Fluid Flow, Series in Computational Methods in Mechanics and Thermal Sciences, Hemisphere Publishing Corporation, 1980.
[10] D. Jiles, Introduction to Magnetism and Magnetic Materials, Chapman and Hall, London, ISBN: 0 412 38630 5, 1991.

CHAPTER 4.2

Turbulence Modeling and Implementation

Kinnor Chattopadhyay[a] **and Roderick I.L. Guthrie**[b]
[a]HATCH (formally PDF with the MMPC)
[b]McGill Metals Processing Centre (MMPC), Montreal, Canada

NOMENCLATURE

$\boldsymbol{\delta_{ij}}$ Kronecker delta and $\delta_{ij} = \begin{cases} 0 \text{ for } i \neq j \\ 1 \text{ for } i = j \end{cases}$
$\boldsymbol{\varepsilon}$ rate of energy dissipation, m^2/s^3
$\boldsymbol{\tau_0}$ timescale
$\boldsymbol{v_0}$ velocity scale
$\boldsymbol{v_x}$ **or** $\boldsymbol{u}$ X-component of velocity of the fluid, m/s
$\boldsymbol{v_y}$ **or** $\boldsymbol{v}$ Y-component of velocity of the fluid, m/s
$\boldsymbol{v_z}$ **or** $\boldsymbol{w}$ Z-component of velocity of the fluid, m/s
$\boldsymbol{A_0}$ **and** $\boldsymbol{A_s}$ realizable κ–ε model constants
$\boldsymbol{C_1}$, $\boldsymbol{C_2}$, $\boldsymbol{C_\mu}$, $\boldsymbol{\sigma_k}$, **and** $\boldsymbol{\sigma_\varepsilon}$ empirical constants
$\boldsymbol{G_k}$ rate of production of k, kg/m s^3
$\boldsymbol{\kappa}$ kinetic energy of turbulence per unit mass, m^2/s^2
$\boldsymbol{l_0}$ length scale
$\boldsymbol{L}$ characteristic length, m
$\boldsymbol{L_m}$ Prandtl's mixing length
$\boldsymbol{P}$ pressure at any point, Pa
$\boldsymbol{Pr}$ Prandtl's number
$\boldsymbol{Re}$ Reynolds number
$\boldsymbol{R_{ij}}$ Reynolds stress tensor
$\boldsymbol{t}$ time, s
$\boldsymbol{T}$ temperature, K
$\boldsymbol{U}$ average velocity of the fluid, m/s
$\boldsymbol{Ui}$ instantaneous velocity component, m/s
$\bar{U}_i$ Reynolds-averaged velocity component, m/s
$\boldsymbol{U^*}$ friction velocity or shear velocity, m/s
$\boldsymbol{v}$ velocity vector, m/s
$\boldsymbol{V_f}$ **and** $\boldsymbol{V_r}$ fluid and Stokes rise velocities, respectively, m/s
$\boldsymbol{\mu}$ viscosity of the fluid, kg/m s
$\boldsymbol{\rho}$ density of the fluid, kg/m^3
$\boldsymbol{\sigma}$ surface tension at any interface
$\boldsymbol{\tau}$ shear stress on the fluid, N/m^2

Treatise on Process Metallurgy, Volume 2
http://dx.doi.org/10.1016/B978-0-08-096984-8.00008-2
© 2014 Elsevier Ltd.
All rights reserved.

4.2.1. INTRODUCTION

Heat, mass, and fluid flows associated with large-scale liquid metal processing operations are predominantly turbulent and thus turbulence modeling has been of great interest to process metallurgists. Turbulence is essentially a 3D phenomenon that is quite random both in space and time. Since turbulence represents 3D motions comprising a wide range of eddy sizes, it is absolutely necessary to use very fine numerical grids to capture the turbulent flows accurately over the entire spectrum of eddy sizes. Using the Navier–Stokes equation to calculate turbulence in very large computational domains will need huge amount of computational time and memory. To resolve this problem, given limited computational power and speed, the time averaged form of the Navier–Stokes equation is generally employed and the Reynolds stresses are approximated using appropriate turbulence models. In order to model a processing operation correctly, it is necessary to choose the correct turbulence model and this is ensured by a proper understanding of turbulent flows and the experience of the mathematical modeler. There are a variety of turbulence models including the algebraic or zero-order model, a one-equation model, a two-equation model, the Reynolds stress model, the large eddy simulation model, etc. They are explained in great detail in standard texts [1]. In this chapter, the implementation of different turbulence models to simulate process metallurgical operations is discussed in detail.

4.2.2. TURBULENCE MODELS

Of the different methods for simulating turbulence and its effects on transport processes, the most widely used concepts in present-day turbulence modeling for practical engineering applications is the "Eddy viscosity" concept. In analogy to the viscous stresses in laminar flows, Boussinesq suggested that the turbulent stresses are proportional to the mean gradients of velocity. In this concept, the "Reynolds stress tensor," R_{ij}, can be expressed using Equation 4.2.1:

$$R_{ij} = -\upsilon_t\left(\frac{\partial \bar{U}_i}{\partial x_j} + \frac{\partial \bar{U}_j}{\partial x_i}\right) + \frac{2}{3}\kappa\delta_{ij} \tag{4.2.1}$$

where δ_{ij} represents the Kronecker delta and $\delta_{ij} = \begin{cases} 0 \text{ for } i \neq j \\ 1 \text{ for } i = j \end{cases}$

The eddy viscosity, υ_t, has units of length multiplied by velocity and can be expressed as:

$$\upsilon_t \propto \nu_0 l_0 \; or \; \upsilon_t \propto l_0^2/\tau_0 \tag{4.2.2}$$

ν_0 is the velocity scale, l_0 is the length scale, and τ_0 is the timescale.

The models adopting the eddy viscosity concept are distinguished according to how they plan to estimate υ_t. So, the RANS (Reynolds-Averaged Navier–Stokes) equations in the eddy viscosity model become:

$$\frac{\partial \bar{U}_i}{\partial t}+\bar{U}_j\frac{\partial \bar{U}_i}{\partial x_j}=-\frac{\partial}{\partial x_i}\left(\frac{\bar{P}}{\rho}+\frac{2}{3}\kappa\delta_{ij}\right)+\upsilon\nabla^2\bar{U}_i+\frac{\partial}{\partial x_j}\left[\upsilon_t\left(\frac{\partial \bar{U}_i}{\partial x_j}+\frac{\partial \bar{U}_j}{\partial x_i}\right)\right] \tag{4.2.3}$$

Of the different turbulent models available in literature, only a few were used in tundish modeling. Prandtl's "Mixing Length Model," is one of the early turbulence models used in tundish modeling. In this model, Prandtl defined the mixing length, l_{m}, as the distance traveled by a fluid lump in the transverse direction, before the mean velocity changes by an amount equal to the transverse fluctuation velocity. He also postulated that: the turbulence length scale, l_{o}, is equal to the mixing length l_{m}, and the velocity scale, v_0, is equal to the mean velocity gradient times the mixing length. Accordingly, Equation (4.2.2) becomes:

$$\upsilon_t=l_{\mathrm{m}}^2\left|\frac{\mathrm{d}\bar{U}}{\mathrm{d}y}\right| \tag{4.2.4}$$

This model is closed when the mixing length is specified. In a very early modeling attempt, Debroy and Sychterz [2] used this turbulence model for their numerical studies of flow patterns in a tundish and specified a mixing length $l_{\mathrm{m}}=0.4d$ where d is the distance from the nearest wall. But later investigations showed that the mixing length, l_{m}, which according to the Prandtl's postulate equals to the turbulent length scale, varies within the turbulent boundary layer. So, assignment of a single value for l_{m} throughout the flow field is questionable and is one of the weaknesses of this turbulent model. Though this model was not used in any further tundish modeling approach in later years, the "Law of the Wall," which is used for boundary conditions for more sophisticated turbulence models, has been used frequently.

To date, the most popular approach using eddy viscosity models are the two-equation models. In these models, two separate transport equations are solved, to determine the length and velocity scales for eddy viscosity υ_t. There are many types of two-equation models. Of them all, the κ–ε models are the most popular and widely used.

A review of the literature on mathematical modeling in tundishes reveals that most of the researchers used the standard κ–ε model of Launder and Splading [3] to calculate eddy viscosity. In this model, the length and the timescales are built up from the turbulent kinetic energy, κ, and the turbulent dissipation rate, ε, using dimensional arguments:

$$l_0\propto\frac{\kappa\sqrt{\kappa}}{\varepsilon}\quad\text{and}\quad\tau_0\propto\frac{\kappa}{\varepsilon} \tag{4.2.5}$$

$$\upsilon_t=C_\mu\frac{\kappa^2}{\varepsilon} \tag{4.2.6}$$

where C_μ is an empirical constant.

The turbulent kinetic energy (κ) and the dissipation rate (ε) are obtained by solving the modeled transport equations (4.2.7) and (4.2.8), respectively:

$$\frac{\partial \kappa}{\partial t}+\bar{U}_j\frac{\partial \kappa}{\partial x_j}=\upsilon_t\frac{\partial \bar{U}_i}{\partial x_j}\left(\frac{\partial \bar{U}_i}{\partial x_j}+\frac{\partial \bar{U}_j}{\partial x_i}\right)-\varepsilon+\frac{\partial}{\partial x_i}\left[\left(\upsilon+\frac{\upsilon_t}{\sigma_\kappa}\right)\frac{\partial \kappa}{\partial x_i}\right] \tag{4.2.7}$$

$$\frac{\partial \varepsilon}{\partial t}+\bar{U}_j\frac{\partial \varepsilon}{\partial x_j}=C_{\varepsilon 1}\frac{\varepsilon}{\kappa}\upsilon_t\frac{\partial \bar{U}_i}{\partial x_j}\left(\frac{\partial \bar{U}_i}{\partial x_j}+\frac{\partial \bar{U}_j}{\partial x_i}\right)-C_{\varepsilon 2}\frac{\varepsilon^2}{\kappa}+\frac{\partial}{\partial x_i}\left[\left(\upsilon+\frac{\upsilon_t}{\sigma_\varepsilon}\right)\frac{\partial \varepsilon}{\partial x_i}\right] \tag{4.2.8}$$

Some researchers have used another κ–ε model, which is derived from the instantaneous Navier–Stokes equation, using a mathematical technique termed "Renormalization Group" (RNG) methods. This RNG κ–ε model results in some different constants with different values. Equations (4.2.9) and (4.2.10) are the model equations for κ and ε, respectively, used in this model:

$$\frac{\partial \kappa}{\partial t}+\bar{U}_i\frac{\partial \kappa}{\partial x_i}=\upsilon_t S^2-\varepsilon+\frac{\partial}{\partial x_i}\left(\alpha\upsilon_t\frac{\partial \kappa}{\partial x_i}\right) \tag{4.2.9}$$

$$\frac{\partial \varepsilon}{\partial t}+\bar{U}_i\frac{\partial \varepsilon}{\partial x_i}=C_{\varepsilon 1}\frac{\varepsilon}{\kappa}\upsilon_t S^2-C_{\varepsilon 2}\frac{\varepsilon^2}{\kappa}-R+\frac{\partial}{\partial x_i}\left(\alpha\upsilon_t\frac{\partial \varepsilon}{\partial x_i}\right) \tag{4.2.10}$$

Here S is the modulus of the mean rate of strain tensor, defined as $S^2=2S_{ij}S_{ij}$. Comparing with ε equation of standard κ–ε model, one extra term R arises in this model. It is expressed as: $R=\frac{C_\mu\eta^3(1-\eta/\eta_0)}{1+\beta\eta^3}\frac{\varepsilon^2}{\kappa}$.

For turbulent viscosity calculations, this model uses the relation: $\upsilon_t=0.084(\kappa^2/\varepsilon)$. The constant 0.084 could be treated as C_μ, as in the standard κ–ε model, but with a different value.

The values of the different constants appearing in the standard κ–ε model and RNG κ–ε model are reported in the literature.

To evaluate the effect of different turbulence models on the prediction of different parameters, many researchers have carried out comparative studies. Schwarze *et al.* [4,5] used different turbulence models in their prediction of flow field and dispersed phase behavior. Though their predicted velocity field using standard κ–ε and RNG κ–ε models does not seem to vary much, the mean turbulent quantities differed significantly. Comparing the results with the available experimental data, they concluded that the RNG model approximates the turbulence in flow situations with a high curvature of streamlines better than other models. Though the literature survey shows that most of the simulation works have been carried out using the standard κ–ε turbulence model, they [6] argued that this model overpredicts κ values because it does not take into account the fact that the strain rate of the flow field influences turbulence.

Hou and Zou [6] came to the same type of conclusion. They compared the standard κ–ε turbulence model with the RNG κ–ε turbulence model, while numerically simulating a swirling flow tundish (already mentioned earlier). They also obtained convergent result more easily using the RNG κ–ε turbulence model and concluded that this model is more appropriate for swirling motion. By far, the most elaborate computational study on tundish performance predictions has been done by Jha *et al.* [7]. They studied the effect of different turbulence models on residence time distribution predictions. Apart from these, to the present authors' knowledge, they have been the only researchers who applied LES (large eddy simulation) in tundish modeling. Turbulence models such as the standard κ–ε, RNG κ–ε, Chen–Kim (CK) κ–ε, LES, etc., predict gross flow properties fairly well, while others like Lam–Bremhorst low Reynolds number κ–ε model predicts initial variations better than the others.

More recently, some researchers [8–10] have used the "Realizable κ–ε model" of Shih *et al.* [11]. This is basically a new eddy viscosity model, which consists of a new dissipation rate equation and a new eddy viscosity formulation. The ε model equation and the eddy viscosity formulation are given by Equations (4.2.11) and (4.2.12), respectively:

$$\frac{\partial \varepsilon}{\partial t} + \bar{U}_j \frac{\partial \varepsilon}{\partial x_j} = C_{\varepsilon 1} \frac{\varepsilon}{\kappa} C_{3\varepsilon} \beta g_i \frac{\upsilon}{Pr} \frac{\partial T}{\partial x_j} + C_1 S\varepsilon - C_2 \frac{\varepsilon^2}{\kappa + \sqrt{\upsilon \varepsilon}} + \frac{\partial}{\partial x_j} \left[\left(\upsilon + \frac{\upsilon_t}{\sigma_\varepsilon} \right) \frac{\partial \varepsilon}{\partial x_j} \right] \quad (4.2.11)$$

$$\upsilon_t = C_\mu \frac{\kappa^2}{\varepsilon} \quad (4.2.12)$$

Unlike the standard κ–ε or RNG κ–ε models, C_μ is not a constant, but is defined as shown below in Equation (4.2.13):

$$C_\mu = \frac{1}{A_0 + A_s \frac{\kappa U^*}{\varepsilon}} \quad (4.2.13)$$

where A_0 & A_s are model constants and U^* values are to be calculated in terms of the mean rate of rotation and mean rate of strain tensor. $A_0 = 4.04$, and $A_s = \sqrt{6}\cos\varphi$, where φ is a function of strain tensors.

Nonetheless, the most widely used turbulence model is the standard κ–ε. In general, as stated earlier, the standard κ–ε model tends to overestimate mixing situations where highly turbulent and essentially laminar regions coexist, such as in a tundish flow. To adequately predict such situations, the model must be able to represent the probability of existence of turbulent fluid at a particular location. Realizing this fact, Ilegbushi [12] used a two-fluid model of turbulence to predict flow behavior in a tundish. This model essentially considers the system to be composed of two interpenetrating fluids (turbulent and nonturbulent fluid). They are allowed to exchange mass, momentum, and energy at the interface. At any location, transport equations would be solved for the

characteristics of each fluid, including velocity components, temperature, and volume fractions. The volume fraction of the turbulent fluid provides a measure of the intermittency or turbulence. The model is therefore well suited to represent the whole tundish domain, the intermittency factor being high in the turbulent inlet region and low in the quiescent region. Salcudean and Guthrie [13,14] used an adjusted laminar flow model, where they increased the viscosity of the liquid by a factor of 1000 to simulate the influence of turbulence on flow field velocities. They later compared the results with a steady-state turbulent flow model and showed that the adjusted laminar model predicted the velocity field reasonably well, apart from the fact that the entrainment of recirculating fluid was more extensive and the radial velocity gradients less steep with the turbulent flow model.

In wall-bounded turbulent flows, like in a tundish, the presence of solid walls has a strong effect on flow characteristics. So all researchers, who have tried to model flows within a tundish, have had to use special treatments such as the wall function approach or the low Reynolds number model approach, in order to tackle the boundaries. However, when there are strong reattaching and separating flows, the wall function approach is not recommended.

Only a very few researchers [15,16] have used the low Reynolds number method. In this approach, computations are carried out all the way to the walls and hence a very fine grid is required near the wall, on account of the boundary layer, where steep velocity gradients are located. Some researchers [16] used the low Reynolds number model of Launder and Jones to study the residence time distribution in a 6-strand tundish, and found better agreement with experimental result, while the low Reynolds number models such as that of Lam and Bremhorst (used by Refs. [15,16]) and the CK low Reynolds number model (with and without Yap correction) (used by Ref. [7]) were used only for comparison purposes.

Apart from the above-mentioned models, there are some other turbulence models such as the length velocity algebraic model (used by Refs. [17,18]), the κ–ω turbulence model (used by Ref. [19]), the CK, and more recently the Reynolds stress model (RSM) (used by Refs. [10,19–21]) have also been used. A discussion of all these models would require a separate review.

4.2.3. CONCLUSIONS

This chapter has given an overview of the use of different turbulence models while simulating metallurgical processing operations (steelmaking and casting). It is observed that the predominantly used turbulence models are the two-equation models and variants. For isotropic problems, the standard κ–ε model performs a decent job. However, for precise results, it is recommended to use the low Re κ–ε models where calculations are done up to the wall, rather than using wall functions. To model swirling and rotational flows efficiently, the RNG κ–ε model is preferred over the standard κ–ε model because,

in the RNG approach, a modified form of the epsilon equation is used which attempts to account for the different scales of motion through changes to the production term rather than using a single turbulence length scale. For nonisotropic problems, the realizable κ–ε model does a better job than the standard κ–ε model because the coefficient C_μ is not a constant but a function of the flow (κ, U^*, and ε). For modeling cases involving impinging jets, large pressure gradients, and impinging flows, the κ–ω model should be used. The capabilities of RANS models are limited. Under certain conditions, these models can be very accurate, but these are not suitable for transient flows, because the averaging process wipes out most of the important characteristics of a time-dependent solution. On the other hand, *Direct Numerical Simulation (DNS)*, which is a direct solution of the turbulent Navier–Stokes equation, is not practicable for 99.9% of CFD problems because of its requirement of unrealistically high computational power and time. As a result, a new simulation technique called the *Large eddy simulation* (LES) has also become very popular. In *LES*, the contribution of the large-scale eddies to the momentum and energy transfer is computed exactly as DNS, while the effect of the small eddies is modeled. The distinction between the large and small eddies is done by a filtering operation. Some new turbulence models such as the nonlinear eddy viscosity models and the $v^2 - f$ models have been proposed by different researchers but their robustness in modeling process metallurgical operations is yet to be tested.

REFERENCES

[1] D.C. Wilcox, Turbulence Modelling for CFD, second ed., D C W Industries, California, 2002.
[2] T. Debroy, J.A. Sychterz, Metall. Mater. Trans. B 16B (1985) 497–504.
[3] B.E. Launder, D.B. Splading, Lectures in Mathematical Models of Turbulence, Academic Press, New York, 1972.
[4] R. Schwarze, F. Obermeier, J. Hantusch, A. Franke, D. Janke, Steel Res. 72 (5 + 6) (2001) 215–220.
[5] R. Schwarze, F. Obermeier, D. Janke, Model. Simul. Mater. Sci. Eng. 9 (2001) 279–287.
[6] H. Qinfu, Z. Zongshu, ISIJ Int. 45 (3) (2005) 325–330.
[7] P.K. Jha, R. Ranjan, S.S. Mondal, S.K. Dash, Int. J. Numer. Methods Heat Fluid Flow 13 (8) (2003) 964–996.
[8] H.-J. Odenthal, R. Bolling, H. Pfeifer, Steel Res. Int. 74 (1) (2003) 44–55.
[9] H.-J. Odenthal, R. Bolling, H. Pfeifer, J.-F. Holzhauser, F.-J. Wahlers, Steel Res. 72 (11 + 12) (2001) 466–476.
[10] H.-J. Odenthal, H. Pfeifer, M. Klaas, Steel Res. 71 (6 + 7) (2000) 210–219.
[11] T.-H. Shih, W.W. Liou, A. Shabbir, Z. Yang, J. Zhu, A New κ-ε Eddy Viscosity Model for High Reynolds Number Turbulent Flows—Model Development and Validation, 1994), NASA TM 106721.
[12] O.J. Ilegbushi, ISIJ Int. 34 (9) (1994) 732–738.
[13] M. Salcudean, R. Guthrie, Metall. Trans. B 9B (1978) 181.
[14] M. Salcudean, R. Guthrie, Metall. Trans. B 9B (1978) 673.
[15] P.K. Jha, S.K. Dash, Int. J. Numer. Methods Heat Fluid Flow 12 (5) (2002) 560–584.
[16] A. Robert, D. Mazumdar, Steel Res. 72 (3) (2001) 97–105.
[17] H. Solhed, L. Jonsson, P. Jonsson, Metall. Mater. Trans. B 33B (2) (2002) 173–185.
[18] H. Solhed, L. Jonsson, Scand. J. Metall. 32 (1) (2003) 15–32.
[19] G. Solorio-Diaz, R.D. Morales, A. Ramos-Banderas, Int. J. Heat Mass Transf. 48 (17) (2005) 3574–3590.
[20] A. Kumar, S.C. Koria, D. Mazumdar, ISIJ Int. 44 (8) (2004) 1334–1341.
[21] G. Solorio-DIAZ, R.D. Morales, J. Palafox-Ramos, A. Ramos-Banderas, ISIJ Int. 45 (8) (2005) 1129–1137.

CHAPTER 4.3

Computational Fluid Mechanics

Kinnor Chattopadhyay[a] **and Roderick I.L. Guthrie**[b]
[a]HATCH (formally PDF with the MMPC)
[b]McGill Metals Processing Centre (MMPC), Montreal, Canada

NOMENCLATURE

acfm actual cubic feet per minute
C_1, C_2, C_μ, σ_κ, **and** σ_ε empirical constants
DRI directly reduced iron
ε rate of energy dissipation, m^2/s^3
ε rate of dissipation of k, m^2/s^3
F_b body force, N
FCD flow control device
Γ diffusivity, m^2/s
G_K rate of production of K, kg/m s^3
Gr Grashoff number
H enthalpy, J/mol
k kinetic energy of turbulence per unit mass, m^2/s^2
L characteristic length, m
μ viscosity of the fluid, kg/m s
ϕ variable of interest
P pressure at any point, Pa μ
PCI pulverized coal injection
ρ density of the fluid, kg/m^3
Re Reynolds number
RTD residence time distribution
σ surface tension at any interface, N/m
SEN submerged entry nozzle
T temperature, K
t time, s
τ shear stress on the fluid, N/m^2
$\bar{u}_i$ Reynolds averaged velocity component, m/s
u_i Instantaneous Velocity of inclusion component, m/s
U average velocity of the fluid, m/s
U, V, **and** W x, y, and z components of velocity, m/s
v velocity vector, m/s
v_x **or** u X-component of velocity of the fluid, m/s
v_y **or** v Y-component of velocity of the fluid m/s
v_z **or** w Z-component of velocity of the fluid m/s

Treatise on Process Metallurgy, Volume 2
http://dx.doi.org/10.1016/B978-0-08-096984-8.00009-4
© 2014 Elsevier Ltd.
All rights reserved.

4.3.1. INTRODUCTION

All operations in process metallurgy involve complex phenomena comprising momentum, heat, and/or mass transport. Transport phenomena, i.e., fluid flows, heat transfer, and mass transfer, play a dominant role, since their respective laws govern the kinetics of the various physical phenomena occurring in metallurgical processing operations. These phenomena include such events as three-phase reactions, entrainment of slag and gas in liquid steel, vacuum degassing, alloy melting and mixing, the movements and flotation of inclusions, melt temperature losses, residence times in a metallurgical reactor, and erosion of refractory linings. Computational fluid dynamics (CFD) and computational heat and mass transfer have been a very effective tool over the past three decades, for modeling various processes, starting from the blast furnace up to continuous casting and beyond. With the advent of commercial CFD packages and ever-increasing computational power through parallel processing, CFD has now become the dominant approach for predicting various aspects in iron- and steelmaking processes, and equivalent nonferrous processes.

Process simulations incorporating CFD codes can give detailed information of fluid flow, heat, and mass transfer in metallurgical reactors, and this can lead to a better understanding of a given process. During the past three decades, the range and power of CFD codes have been developed considerably, and CFD simulations are now extensively applied in order to help in understanding a given process and in guiding new process developments. Thanks to the contributions of Professor Spalding and coworkers [1] at Imperial College, London, in the 1960s, a generalized transport equation was formulated, which was capable of being used to describe all manner of transport phenomena. This was a great help in obtaining iterative solutions to a series of Partial Differential Equation(s) (PDEs) requiring simultaneous solutions. In turn, it spawned the formulation of general purpose computer codes that have become increasingly user-friendly and robust. The general transport equation formulated by Spalding and coworkers was:

$$\frac{\partial(\rho\phi)}{\partial t} + \mathrm{div}\left(\rho\vec{u}\emptyset\right) = \mathrm{div}(\Gamma \mathrm{grad}\phi) + S \tag{4.3.1}$$

where ϕ is the variable of interest (U, V, W, C, T, k, ε, ...) according to the type of phenomena being considered (momentum, continuity, turbulence, species conservation, energy, temperature, etc.). S represents a source term for the partial differential equation, allowing for nonconvective and nondiffusive terms, to be incorporated. Then, in 1972, Launder and Spalding [2,3] introduced the famous k–ε model for turbulent flows which represented yet another breakthrough for solving turbulent flow problems. Later, other researchers introduced variants of this model, such as the Renormalisation Group (RNG) k–ε model [4] and the realizable k–ε model [5].

For tackling the boundary problems in turbulent flows, some researchers developed the low *Re* number k–ε model [6–10] using damping factors. Launder and Spalding [3] also gave the concept of wall functions for boundary treatments. Patankar and Spalding for the first time paved the way for solving pressure-linked equations by introducing the famous SIMPLE [11] algorithm. Later on, other algorithms, such as SIMPLER, SIMPLEST, SIMPLEC, and PISO, were proposed by various researchers. These have been thoroughly discussed by Versteeg and Malalasekera [12]. Based on the above concepts, many software packages, such as PHOENICS, CFX, FLOW-3D, FIDAP, FLUENT, and COMSOL, were marketed and have allowed CFD to become an increasingly common tool for use by "nonexperts." However, it is essential that one learns the physics behind these software packages before blindly using them. As the nature of the flows associated with process metallurgical operations is very complex, the people involved in process modeling are extensively using CFD codes to design reactors, to analyze the performance of these reactors, to optimize process variables, to predict metal quality and cleanliness, etc.

Due to the complex nature of the governing equations and geometries of the metallurgical vessels, analytical solutions for the equations are not possible in a practical sense. So, different numerical techniques are devised to solve these transport equations. The numerical solution aims to provide the values of the variables at some discrete number of points in the domain of interest. These points are called grid points, nodes, or cell centroids, depending on the scheme it follows. The conversion of differential equations into a set of discrete algebraic equations requires the discretization of the domain. This is called mesh generation or meshing.

The different techniques are:

1. Finite difference method (FDM)
2. Finite element method (FEM)
3. Spectral methods
4. Hybrid schemes (such as the control volume FEM and the control volume FDM)

All the techniques perform three basic steps. Namely:

- **(i)** Approximation of unknown flow variables by means of simple functions.
- **(ii)** Discretization by substitution of the approximations into the governing flow equations.
- **(iii)** Subsequent mathematical solutions.

Close examination of the three components of the momentum equation and continuity equation shows that they are closely coupled because all velocity components appear in each momentum and continuity equation. The basics of CFD, discretization techniques, numerical methods, coupling, etc., are already presented in standard texts [1,13] and hence are not repeated here. In this chapter, the applications of CFD in process metallurgy (ironmaking, steelmaking, and casting) are highlighted, reviewed, and critiqued.

4.3.2. APPLICATIONS OF CFD IN PROCESS METALLURGY

4.3.2.1. Blast Furnace

The blast furnace is a countercurrent heat and mass exchanger, in which the hot rising reducing gases lose most of their heat, leaving the furnace at around 200 °C. Meantime, the descending cold iron oxides are heated and reduced and fully converted to molten iron, while the gangue material is absorbed into a fusible slag phase. This slag phase accumulates in the hearth, over the iron phase. Modern blast furnaces are generally massive reactors, towering up to 100 m over a steel plant. It is not easy to perform experiments in such massive high-temperature reactors, operating under commercial conditions. As such, researchers have used flow modeling experiments using CFD tools. The Blast Furnace Aerodynamics Symposium (B.F.A.) in Wollongong in 1975, organized by Prof. Nicholas Standish, was perhaps the turning point at which researchers from around the globe collectively considered blast furnace aerodynamics and associated transport phenomena. Guthrie and Storey addressed the aerodynamic aspects of auxiliary fuel injection procedures in such blast furnaces [14]. Ghiglione *et al.* [15], in the same symposium, reported on fluid dynamic aspects in blast furnaces. After these initial ideas were presented in the mid-1970s, researchers have used CFD to study inner hearth wear profiles, refractory erosion, pulverized coal injection (PCI), the dynamics of the "deadman" coke regime, drainage behavior in the blast furnace hearth, and unsteady gas, particle, and liquid flows (e.g., flooding and fluidization) through the furnace. With respect to the latter, some researchers have coupled discrete element modeling, with CFD, to study multiphase flows and movements of solids, liquids, and gases, within the blast furnace.

If the evolution of blast furnace mathematical models is considered, then it began from *1D steady-state models* [16,17], to *transient 1D models* [18–20], onto *steady-state 2D models* [21–24]. In 1998, Takatani *et al.* [25] had developed a 3D dynamic mathematical model to simulate a real blast furnace for the first time. The model was based on mass, momentum, and energy conservation. The boundary conditions were set in the same way as in the actual blast furnace. The compositions and particle diameters of ore and coke were given at the top of the furnace. Heat transfer coefficients were given for the outer surfaces of the furnace wall and the hearth. Gas flow rates, blast temperatures, and compositions were given at the tuyeres. A boundary-fitted coordinate system was adopted to treat the shape of the blast furnace precisely [26]. For that, computational grids are transformed from a physical to a computational domain, as shown in Figure 4.3.1. The algorithm adopted in solving gas flows was the SOLA [27] method, and the governing equations were discretized using a staggered grid system. The equations of energy and mass conservation for gas, solid, and liquid phases were solved by the point Successive Over-Relaxation (SOR) method, and the time integration was conducted under the fully implicit method. The model could quantitatively estimate the

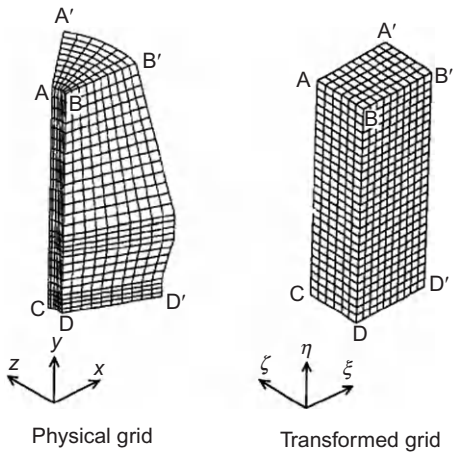


Figure 4.3.1 Grid system.

inner behavior of different blast furnaces and was also very useful in optimizing blast furnace design.

The flows of hot metal and heat transfer in a hearth have now been studied, both theoretically and experimentally, for many years. Most researchers used an uncoupled approach [28–33], while very little research has been devoted to a coupled analysis [34–36]. Furthermore, the nonpacked region of coke formed over the "deadman" in the furnace hearth, which can be presumed to affect hot metal flows, has received scant attention. Similarly, there are only a few data, obtained by blast furnace dissection studies, talking about this.

Shibata *et al.* [37] studied the dynamics of the "deadman" coke region and hot metal flow in a blast furnace hearth. They reported on the effect of the shape of the free space, the packing structure of the deadman, and the depth of a tap hole, on the flow of molten iron and on heat transfer in a hearth, using the general purpose 3D heat and mass transfer code "STREAM." The basic equations involved in this code are the continuity equation, the equation of motion, and the equation for energy/heat transfer, i.e.:

$$\text{Continuity equation}: \quad \nabla\cdot(\rho\,\varepsilon\cdot v) = 0$$

$$\text{Momentum equation}: \quad \rho\frac{\mathrm{d}v}{\mathrm{d}t} = -\nabla p - \varepsilon C_{\mathrm{B}} v - \rho\beta g(T - T_{\mathrm{ref}})$$

$$\text{Energy}: \quad \rho C_{\mathrm{p}}\frac{\mathrm{d}T}{\mathrm{d}t} = k\nabla^2 T$$

Here, ε is the void fraction, k is the thermal conductivity, β is the coefficient of volume expansion, and v is the fluid velocity.

They concluded that as the storage level of molten iron rises, there is an upward motion of packed coke particles toward the raceways. Due to this motion, there is

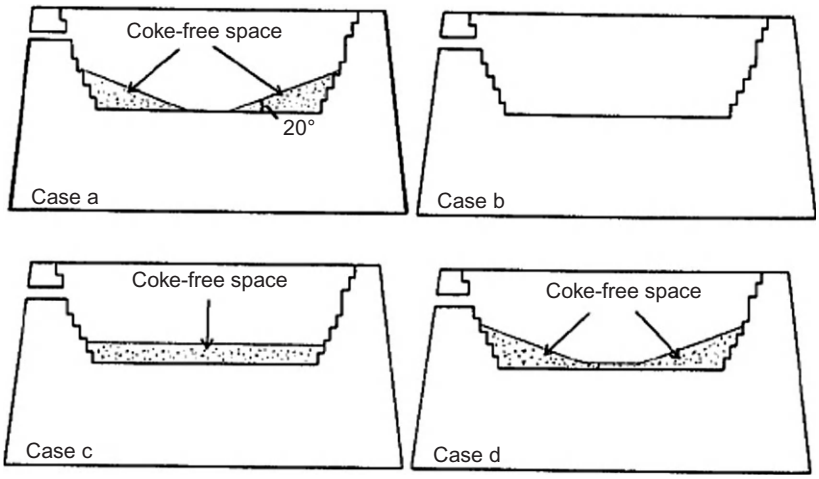


Figure 4.3.2 Representing coke-free space: (a) Free space has a gradient of 20° and the bottom of the deadman contacts the refractory at hearth bottom, (b) no free space, hearth is fully packed with coke, (c) free space has a uniform thickness at hearth bottom, and (d) free space has a gradient of 20° and bottom of the deadman does not contact the refractories at the hearth bottom.

coke-free space (Figure 4.3.2) with a specific gradient formed in the corner of the hearth's bottom. The gradient varies in the range of 0° to the horizontal, up to an angle of repose for packed particles, according to storage and drainage of molten iron. The shape of this free space significantly affects the molten iron flow and heat transfer within a hearth. They also mentioned that with a decrease in void fraction of the "deadman," the circumferential flow of molten iron becomes remarkable. In order to restrain circumferential flows and to prevent hearth erosion, proper liquid permeability in a deadman should always be ensured.

Nouchi *et al.* [38] conducted an experimental and numerical study of the two-phase flow in a particle packed bed, under conditions related to a blast furnace hearth. In these models, drainage velocities, slag/iron ratio, tapping time, and maximum slag level in the hearth were studied. The coke-free space formed at the taphole level allows a flow of circumferential slag (Figure 4.3.3) and significantly improves hearth drainage efficiency. When the coke-free space surrounds only a part of the packed bed, the effect is in proportion to the surrounded packed bed size. Such asymmetric coke-free spaces cause the imbalances in tap times and slag ratios.

Nishioka *et al.* [39] also developed a 3D model to study *drainage behavior* in the hearth of a blast furnace. Two- and three-dimensional mathematical models were developed, based on the FDM, to simulate molten iron and slag flows in the hearth of a blast furnace. A pressure drop evaluation model for a taphole was developed to reflect the effect of pressure variations in a blast furnace hearth on drainage rates of molten iron and slag, for the three-dimensional mathematical model. The two-dimensional mathematical model

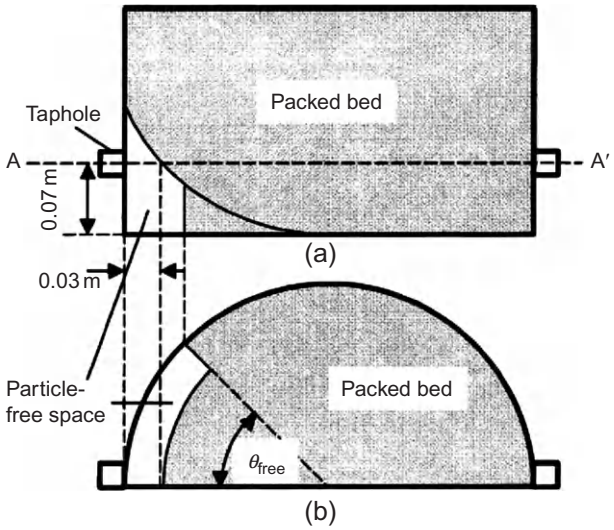


Figure 4.3.3 Schematic diagram of the free-space shape: (a) side view and (b) plan view at A–A′ plane.

results were validated with measured interface shapes obtained using a physical model. The three-dimensional mathematical model results were validated with measured total iron and slag drainage rates in Chiba No. 6 blast furnace. The results indicated how the drainage behavior and residual iron and slag volumes [40,41] were affected by the conditions in the hearth. The condition of the tap hole dominates the total drainage rate. In order to reduce the residual slag volume, the change in taphole diameter during the tap needs to be controlled. Any decreases in mean coke diameter cause increases in the residual slag volume and decreases in the residual iron volume.

In 2001, Takatani *et al.* [42] reported on a mathematical model that can estimate the transient erosion process of the blast furnace hearth. This mathematical model can treat the flow of molten iron, heat transfer, and the brick/refractory erosion at the hearth. To validate the mathematical model, computational comparisons of final erosion profiles of the hearth were made with investigatory results from dissected blast furnaces. It was found that the computational results were in good agreement with those measured. The effects of the distribution profile of the dripping molten iron flow rate into the hearth, the size of the coke-free layer, production rate of the molten iron, the thermal conductivity of the carbon brick, and the fluid flow resistance through the coke packed bed were all examined using this mathematical model.

Kumar [43] analyzed heat transfer and refractory wear in a blast furnace hearth using a FEM. Using the model and associated computer code, temperature profiles were calculated for two different designs of operating blast furnaces and maximum hearth wear, corresponding to the worst location of 1150 °C isotherm that could be experienced during operation, were predicted. A moving hot metal–refractory interface was used to

calculate hearth erosion in which the thermal properties of refractory materials were sequentially replaced by those of hot metal mixed with coke, depending upon the temperature distribution. The effects of heat load at the hot metal–refractory interface, cooling conditions at the side walls and at the bottom of the hearth, and coke-bed state (sitting or floating), on hearth wear, were all investigated.

Brannbacka *et al.* [44] developed a model to analyze the performance of a blast furnace hearth. The model was based on a set of simplifying assumptions concerning the inflow and outflow rates of iron and slag, and on a hypothesis concerning the general operating principles of liquid drainage. These assumptions have, in earlier studies, proved to be adequate for capturing the overall behavior of hearths in industrial blast furnaces. The model, which also considered the case where the "deadman coke" floats in the iron bath, could be used for "what-if" analyses of how, for example, hearth geometry, sump depth, production rate, slag ratio, and tapping time influence the drainage procedure.

Helle and Saxen [45] developed a model to simulate and study the effects of changes in tuyere parameters and boundary conditions. Variables, such as the total blast volume, blast pressure, tuyere diameter, and the degree of combustion of injected reductants into the tuyeres, were all studied. An online version of the model was developed to track how the physical conditions at the tuyere level change with time in operating blast furnaces. The model predicted the distribution of the blast and other interesting quantities, such as the gas velocity at the tips of tuyeres and the volume of gas in a given raceway, together with the raceway flame temperatures.

Dong *et al.* [46], in 2007, published a comprehensive review on multiphase modeling of blast furnaces. They classified modeling of multiphase flow in blast furnaces into two categories. One is the continuum approach at a macroscopic level and the other is the discrete element approach at a microscopic level. In the continuum approach, phases are generally considered as fully interpenetrating continuous media that can be described by separate conservation equations with appropriate constitutive relations and interaction terms representing the coupling between the phases. The continuum approach is suitable for process modeling and applied research because of its computational convenience and efficiency. Indeed, most of the Blast Furnace (BF) modeling is based on this approach. However, its effective use depends heavily on constitutive or closure relations and the momentum exchange between phases. For Newtonian fluids (gases and liquid phases here), these relations can be readily determined.

For solids and powder, general theories are not yet available. However, in the discrete element analysis approach, or DEA, phases are described based on the analysis of the motion of individual fluid elements. These are atoms for gases or liquids, and particles, for solids. So the approach can simulate fluid flow at both an atomic and a particle scale. It has the advantage that there is no need for complex constitutive relations between the stress and strain tensors acting under different flow conditions. It can generate microscopic information such as the trajectory of, and forces acting on, individual atoms or

particles. This is important to an understanding of the fundamentals. However, computationally, it is extremely demanding. For this reason, it is not possible for gas and liquid phases in any practical system. These are better handled by the continuum phase approach mentioned above. To date, the discrete approach has only been applied to solid phases. They concluded that BF models have played a significant role in integrating the knowledge and offering information for process design and control. This role will be strengthened with the rapid development of computer technology and new modeling techniques. They mentioned that it is without doubt that the development and application of reliable computer models can lead to improvements to blast furnace criteria, such as longer life campaigns, better operational control, decreased fuel consumption, improved productivity, and reduced environmental impact. However, how to make best use of this technology in practice could be a challenging task for modern iron makers.

PCI into an ironmaking blast furnace is a significant technology for economic, operational, and environmental reasons. There are compelling economic reasons for lowering the consumption rate of expensive coking coals and a parallel argument for extending the lives of coke ovens, while increasing blast furnace productivity [47,48]. A mathematical approach, especially CFD, provides a cost-effective tool for understanding the effects of these operational parameters on coal combustion. Some CFD models were developed for PCI operations and these are summarized by Shen *et al.* [49]. From a mathematical modeling perspective, the PCI process involves turbulent gas–solid two-phase flow, coupled with momentum/mass/heat transfer and various homogeneous and heterogeneous chemical reactions. In the 1980s [50–52], 1D mathematical models were developed to study PCI. By the 1990s [53–56], 2D models came into place. However, a 2D model can only generate results that are qualitatively useful in practice. To overcome this limitation, three-dimensional (3D) models are needed. To date, a few 3D studies have been reported in the literature [57–61]. Most of them have reported on the simulation of the blowpipe, with coinjections of coal and gas and modeling of PCI for raceways and tuyeres (Figure 4.3.4).

From the above discussions, it is clear that complex transport phenomena are occurring within a blast furnace and that CFD has played a significant role over the past three decades in helping us to understand and improve the process.

4.3.2.2. Direct Reduction

A dearth of good quality coking coals has led to the development of alternative ironmaking processes. Alternatives to blast furnace iron making are the direct reduction processes, which include both coal- and gas-based reduction processes. The major commercial or precommercial processes are COREX, FINEX, HIsmelt, HIsarna, and MIDREX-EAF. COREX has emerged as one of the most acceptable alternatives. It is the first commercially established, and industrially proven, smelting reduction process,

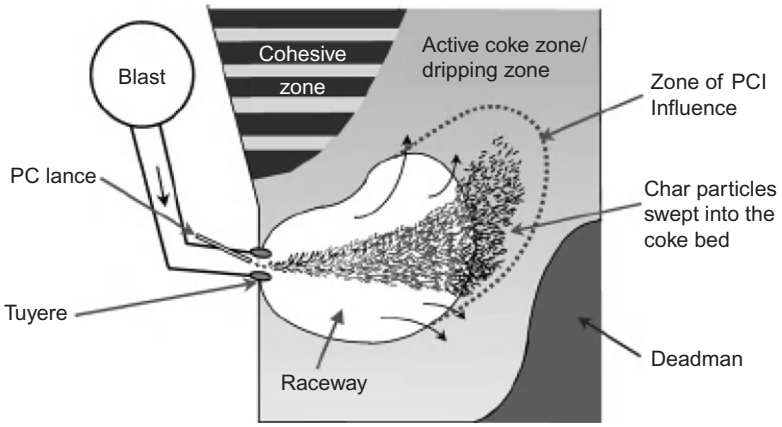


Figure 4.3.4 Schematic of Pulverised Coal Injection (PCI) process into an Iron Blast Furnace.

using noncoking coal as a fuel to produce hot metal. It allows for flexible, cost-effective, and environmentally friendly production of molten iron. Prachethan Kumar *et al.* [62] developed a computational model to optimize operational parameters of the COREX process. The model combines a set of common material and heat balance equations. Taking user-specified inputs, the model is capable of determining the consumption of raw materials and fluxes, the volume and composition of the slag, and the volume and composition of reducing gases from the melter-gasifier. The predictive accuracy of COREX operational parameters is competitive, and the model enables computation of changes in process pathways caused by modifications to input raw materials affecting slag composition, hot metal chemistry, and other parameters.

The COREX process comprises two units. The first is the reduction shaft and the second is the melter-gasifier (Figure 4.3.5).

A lot of CFD codes have been applied to model the melter-gasifier. The COREX melter-gasifier is a countercurrent reactor producing liquid iron. Partially reduced iron oxide from the reduction shaft, together with a noncoking coal, and other additives are all charged to the melter-gasifier at their respective temperatures, while pure oxygen is blown through the tuyeres. Functionally, the melter-gasifier can be divided into three zones: a moving bed, a fluidized bed, and a free board.

Lee *et al.* [63] developed a 1D model of the melter-gasifier system, taking into account the pyrolysis behavior of coal. Recently, they [64] used the model to study the effect of operational parameters such as bed height, C/O ratio, top pressure, and steam injection, on process performance. Their result shows that an increase in bed height by 0.5 m increases the hot metal temperature by 300 °C. This appears to be too high. In actual operations, it is difficult to maintain a constant bed height, but the fluctuations in the temperature of the hot metal are much less. To simplify the model, Lee *et al.* [64] assumed that combustion took place instantaneously at the tuyere plane, i.e., a zero-dimensional

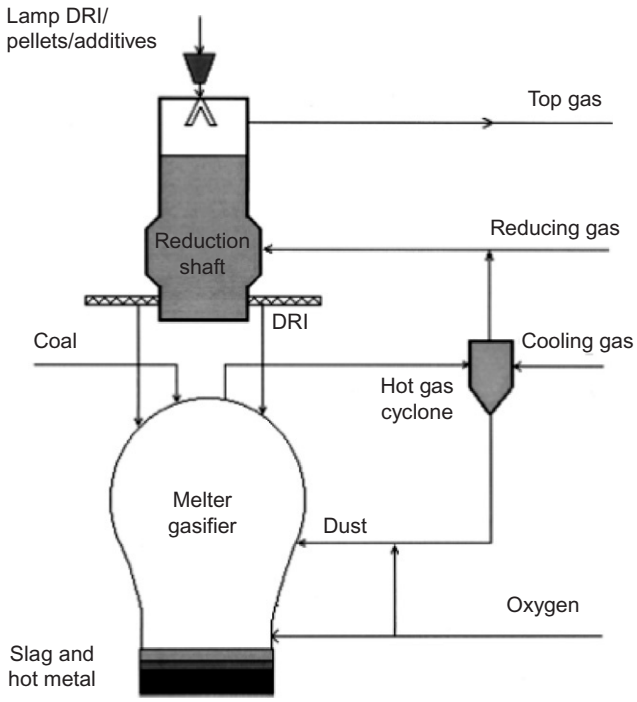


Figure 4.3.5 Schematic diagram of the COREX process.

model was assumed for the tuyere region. This reduces the combustion zone height to zero. But, the combustion zone in the COREX process can be quite large, since pure oxygen is used for combustion. As a result, the simplifying assumption ignores one of the important aspects of the process.

The size of the combustion zone in the COREX melter-gasifier smelting reduction system is quite a lot larger than that in the equivalent blast furnace process, because of the injection of pure O_2. There are large temperature and concentration gradients in the tuyere region due to the radial entry of the blast. Hence, two-dimensional (2D) modeling of the combustion zone was undertaken in their study. The 2D zone extends from the tuyere region to 0.5 m above that, while the remaining part is 1D. Viswanathan *et al.* [65] found that a pseudo 2D model, where the tuyere region is 2D but the rest is 1D, shows good agreement with the results of the 2D model for a cupola. Pal and Lahiri [66] developed a pseudo-2D model for the COREX process. The model was developed for the moving bed, where the tuyere region was two-dimensional (2D) and the rest was one-dimensional (1D). It was based on multiphase conservation of mass, momentum, and heat. The fluidized bed was treated as 1D. Partial equilibrium was calculated for the free board. The calculated temperature of the hot metal, the top gas, and the chemistry of the top gas all agreed with reported plant data. The model was used to study

the effects of bed height, injection of impure O_2, coal chemistry, and reactivity, on the process performance. The model was based on the following assumptions. Each solid has one characteristic particle size and this does not change with height. There is no temperature gradient inside the solid particles. During the fall through the free-board zone, the preheating of solids is neglected. The inertial term in the momentum-balance equation of the gas is neglected. Solid flow in the 1D region follows a plug-flow pattern. Near the tuyere region, combustion of coke and coal char creates space. The adjacent solid fills this up. The liquid moves down with constant velocity.

Pal and Lahiri [67] also developed a dynamic model of the COREX melter-gasifier to study the transient behavior of the furnace. The effect of pulse disturbances and step disturbances was investigated. Their study showed that the effect of a pulse disturbance decays asymptotically. A step change brings the system to a new steady state after a delay of about 5 h. The dynamic behavior of the melter-gasifier with respect to a shutdown/blow-on condition and the effect of tapping were also studied. The results showed that the time response of the melter-gasifier is much less than that of a blast furnace. There was a periodic fluctuation in the metal temperature, top-gas temperature, and chemistry, due to the periodic nature of tapping. These calculations can now all be more conveniently computed using MetSim software.

The first commercial COREX process was introduced to the world by ISCOR steel, in South Africa. Since then, it has also been operating at JSW steel in India and POSCO in Korea. POSCO has extended the original COREX concept and developed the FINEX process. In the latter version, the iron ore is introduced into the melter-gasifier as fine particles, eliminating the need for a pelletizer step. They have used a fluidized bed technology for the reduction of iron ore to wustite. As a comment, one cannot reduce directly to iron, as iron whiskers will form, causing clumping of the particles and collapse of the fluidized bed.

The direct smelting of iron ore fines is an alternative process for pig-iron production that is currently coming of age [68]. The HIsmelt direct ironmaking process, after a 25-year development phase, could be an alternative to the traditional iron blast furnace route. In the current group of collaborators on this extremely long-running project, Rio Tinto, together with Nucor Steel, Mitsubishi, and Shougang Steel as joint venture partners, built and operated a 0.8 Mt/a plant near PERTH in Western Australia. HIsmelt uses iron ore fines and coal fines directly, by injecting them into a molten bath at high velocity. Smelting gases (mainly CO) are released from the bath and burned in the top space by hot, oxygen-enriched, air. A fountain of metal and slag erupts from the bath. Forming iron and slag droplets, they traverse through the top space gaining heat, which they then carry back to the bath to sustain the process. This "heat pump" is the heart of the HIsmelt process.

A major enabling step in the development of the process was to understand the fluid dynamics involved, together with the associated heat and mass transfer processes. HIsmelt

initiated CFD studies in the mid-1980s and has continuously refined this capability. The flow models developed are regarded within HIsmelt as a major risk-management tool of considerable predictive power in terms of scale-up and process optimization. The paper describes one of the flow models that have been developed and provides an example of its use in process development, in process understanding, and in scale-up.

Two CFD models have been developed to describe the overall HIsmelt process: the bath model and the top space model. As the names imply, these models cover the lower and upper regions of the vessel, respectively (Figure 4.3.6).

As described elsewhere [68], this division is artificial and is made so that flow simulations can be performed in a reasonable timeframe. As the bath model is a three-dimensional, dynamic, two-phase Eulerian model, incorporating both Lagrangian tracking and the algebraic slip model (ASM) to model the bath smelting process, simulation times can be excessive. Conversely, the top space model, described in detail below, requires only moderate execution times and has therefore been used extensively in process optimization and scale-up [68]. The top space model simulates the flow of gas, liquid droplets, and particles in the volume above the iron and slag bath. Account is taken of the inflow of hot blast and bath gases, the formation of a droplet fountain above the bath surface, the flow and combustion of char and soot particles, heat transfer to the vessel walls, and radiation. The model includes the effects of droplet breakup, droplet decarburization by process gases, and droplet heat transfer. The CFD code PHOENICS was initially used as the framework for model development. A two-dimensional

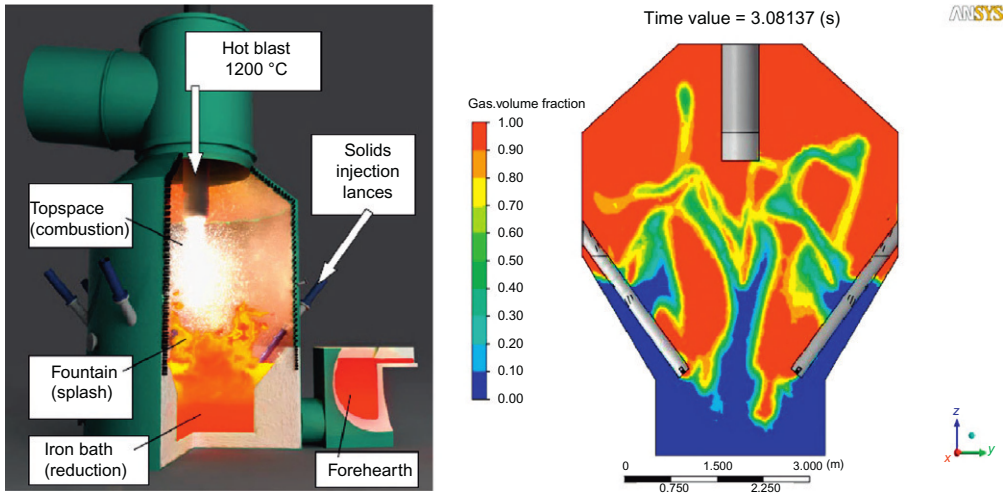


Figure 4.3.6 (a) The HIsmelt process. (b) Bath model results for a two lance configuration. Color-filled contours show gas volume fraction.

axisymmetric model was generally used for process simulations, although a three-dimensional version of the model has also been built [68]. Schwarz and Davis [69] also elaborated on the bath model. As a result of the large volumes of gas that pass through the bath, the gas voidage is often substantially >10%. Consequently, the gas phase cannot be treated as isolated bubbles simulated using a Lagrangian tracking procedure. The most appropriate computational technique for these systems is the multifluid (or "Eulerian–Eulerian") method. While the initial implementation of the multiphase model computed an average flow field and voidage distribution using an essentially steady-state approach, as computational power increased in the 1990s, the model was extended to capture transient phenomena, such as the formation of gas cavities in the bath, splashing at the surface, and slopping of the bath. To allow these transient effects to be captured, phase diffusion was not modeled, either through a turbulent diffusion term in the continuity equations, or a force in the momentum equations, since the effect of this would be to smear out the transient effects that were necessary to simulate, and also make some other adjustments to the effective eddy viscosity. The technique, which could be thought of as a "very large scale eddy simulation," was validated against experimental data obtained from physical models using water, molten tin, and molten iron as the working fluids. A technique was developed to simulate both slag and metal phases and their mixing by splitting the liquid phase into two and treating the relative motion of the two liquids by the so-called ASM. Slag moves upward relative to metal at a velocity determined by the local phase structure; e.g., for slag droplets in metal, the relative velocity is the terminal slip velocity for the local slag droplet size. Droplet size was determined by a criterion given by Hinze [70] for droplet breakup. The technique was validated using experiments conducted with oil–water systems in which entrainment of oil droplets in the underlying water was studied. Injection of coal and iron ore into the smelting reduction model was modeled by the particle-tracking technique. Coal devolatilization kinetics were treated using a version of Oeters and Orsten model [71] with parameterization of coal properties, and the volatiles generated were included as source terms in the gas phase continuity equation. Coal dissolution was treated in a similar way, with carbon as a source in the liquid phase continuity equation. Iron ore particles were assumed to react with molten iron in which carbon was dissolved, generating carbon monoxide which was included as a source in the gas phase continuity equation. The reaction kinetics were calculated using a mass transfer coefficient determined from the literature data on smelting reduction of iron ores and were assumed to be limited by carbon transfer through the melt to the particle. Flux was treated in a similar way, but did not result in gas evolution on dissolution. For particular operating conditions of interest, the bath model was run for a short period of real time (time-step limitations constrained the total period of simulation that could be achieved) and the unsteady flow fields and spatial distribution of gas, metal, and slag were analyzed to understand the likely impact on process performance. Results were also averaged over time to yield mean characteristics, such as

velocity and mass rate of slag and metal ejected into the fountain. These characteristics were used to set the boundary conditions for the fountain in the top space model. While the kinetics of the HIsmelt reactor have not yet reached expectations, the equipment in Perth has been dismantled and shipped to China, for further work there.

Meantime members of the HIsmelt team moved to Holland, where they have been collaborating with researchers from CORUS (now TATA Steel), and other European Steel Companies working under the ULCOS banner. In the most recent direct smelting attempt, the two teams have combined to create the HIsarna reactor [72]. This uses the original cyclone converter furnace (CCF) for the high-temperature reduction of iron ore fines, set on top of the HIsmelt reactor. The HIsarna reactor is now in its third campaign at the time of writing this section. The reactor (HIsarna represents a combination of HISMELT and ISARNA, which is the Celtic word for "IRON") is located in the Ijmuiden Works of TATA Steel, in Holland. The kinetics of this combined reactor is proving to be highly competitive with the iron blast furnace route, and the two teams of researchers are clearly very hopeful. Its advantages over the BF route include being able to use (a) lower grade ores, (b) nonmetallurgical grade coals, (c) much reduced CO_2 emissions, and less polluting emissions since no ore agglomeration is needed (Figure 4.3.7).

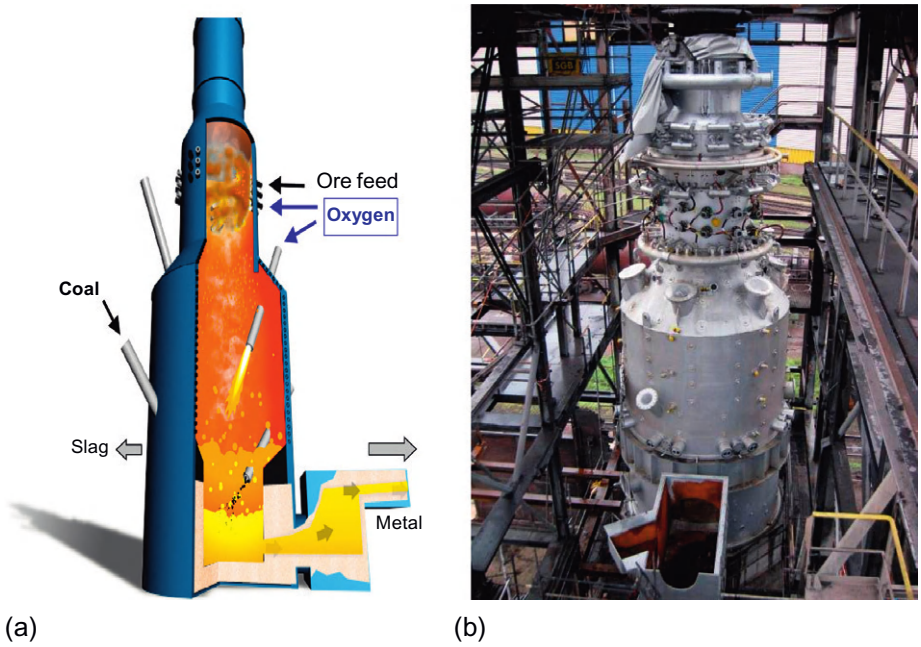


Figure 4.3.7 (a) The HIsarna project combines the CCF and SRV vessels. (b) The CCF and SRV shell [72].

4.3.2.3. Direct Reduced Iron

With rising contaminant levels (Cu, Sn, . . .) in return scrap for remelting in electric arc furnaces (EAFs), alternative clean sources of iron were, and are, needed by the mini-mills. Scrap contamination, together with environmental restrictions, and a dearth of good quality coking coals have led to the development of alternative uncontaminated sources of iron units. The MIDREX technology is the most important directly reduced iron (DRI) process, responsible for 67% of the world's total DRI production. Its main reactor, i.e., the shaft furnace, behaves as a moving bed reactor. The initial studies related to moving bed solid–gas reactors were performed by Munro and Amundson [73], Amundson [74], and Siegmund *et al.* [75]. In these works, the researchers used a linear function of the solid temperature in order to approximate the reaction rate and to obtain analytical solutions. The validity of this solution was limited to a narrow range of temperatures. Schaefer *et al.* [76] studied the heat generation in a steady-state reactor. They used a step function for the heat balance and the results showed the existence of a multiplicity of steady states. Yoon *et al.* [77] developed a model for a Lurgi-type reactor used in carbon gasification. They considered the same temperature in both phases (solid and gas) and the shrinking unreacted core model for the solid particle. Arce *et al.* [78] studied a countercurrent moving bed reactor, using a heterogeneous model for the reactor design and the shrinking core model for the solid particle. They applied both models to an irreversible, first order, exothermic reaction. Amundson and Arri [79] analyzed the same system but considering different temperatures in both phases. Rao and Pichestapong [80] developed a model for a reactor in which the reduction of iron mineral is carried out. The model considers that the controlling step is the mass transfer of the gaseous reactants in the product solid layer. The concentration of the gaseous species on the interface gas–solid is that of the equilibrium, and it was evaluated using an iterative method. As a consequence, the problem cannot be solved in terms of differential equations system. Paris and Laborde [81] modeled a countercurrent moving bed gas–solid reactor. The aim of their work was to model and simulate a solid–gas countercurrent moving bed reactor in which the reduction of iron ore pellets is performed using CO and H_2 as reducing gases. The model was based on the following assumptions. The iron ore pellet consumption is governed by the unreacted shrinking core model. Mass and heat transfer resistances through the film around the solid particle are negligible. Only steady-state operating conditions are considered. Plug flow is assumed for gas and solid phases.

Their model was validated with data obtained from at least two MIDREX® plants (Siderca SA in Argentina and Gilmore Steel Co. in the United States). In addition, they explored the behavior of the reactor for different operating conditions. This could become an important tool for controlling and modifying the shaft furnace operating conditions. Some parameters were slightly adjusted for the two different plants in order to fit the available plant data, taking into account the different types of iron ore pellets and

operational conditions. The proposed model allowed one to study abnormal operational regimes. For example, they explored the relation between degree of metallization and production of iron, and how the production is affected by the proportion of carbon monoxide used in the reducing gas. With respect to metallization, it was observed that if it were to be increased to 100% (a gain of 6% in metallization), the production rate must decrease to 70% of standard operating conditions. This is obviously not advisable. Therefore, if a plant works such that metallization levels are around 94%, it would be close to the optimum. Concerning the carbon monoxide, simulations predicted that the greater the CO proportion, the greater would be the production of iron (maintaining the total gas flow rate and the metallization level fixed). However, an optimization analysis on this subject must be done, considering a coupled simulation of both reactors: the shaft furnace and the reformer.

4.3.2.4. The Basic Oxygen Furnace

The refining of carbon-saturated liquid iron from a blast furnace is carried out in the basic oxygen furnace, or BOF. Oxidizing carbon and other metalloids are a critical part of the steel refining process. Transport phenomena in this furnace are highly complex. Many researchers have modeled component parts of the process to get a better understanding of the physical phenomena involved. Overall physical modeling of the BOF has not proved particularly effective using water models, apart from easy items such as mixing studies for combination blown converters, reported by Oymo and Guthrie [82]. Similarly, droplet production and entrainment in foaming slags have been difficult to model with low-temperature analogues (e.g., Lin and Guthrie [83], Krishnapisharody and Irons [84]). Hot models (Fruehan and coworkers) using X-ray equipment to directly observe the behavior of a foaming droplet of iron during its decarburization in an iron oxide-containing slag have proved to be very insightful, and these types of studies are still being pursued by Coley [85] at McMaster University, Canada, and Geoffrey Brooks [86,87] in Australia, using plant data and small-scale hot models. Much more needs to be done in this area, now that general CFD codes have become available, and the underlying processes of foaming, etc., are well understood. To date, there is no general CFD model of a BOF, at least in the open literature, but it would not be an impossible target/goal for the larger R&D operations of big companies such as TATA Steel, POSCO, NSSMC, etc., to attempt.

With respect to reviewing CFD analyses of steelmaking in BOFs, there has been some work conducted on analyzing the supersonic jet configurations and their effect on the liquid steel surface on which they impinge. For instance, Sambasivam *et al.* [88] at R&D Tata Steel report on the development of a new lance design for BOF steelmaking, using CFD. They mentioned that the lack of control of the foamy slag and the augmentation of interfacial area creation between the slag and metal were the major obstacles in

running the process effectively for improved turn-down steel quality. The ineffectiveness of the existing design in producing liquid metal droplets in the presence of a foaming slag was explained. In order to augment droplet generation, a new oxygen lance with a central subsonic nozzle through which flow can be controlled was designed and its blowing performances studied, using numerical and water model experiments. The jet characteristics studied in the numerical simulations showed no jet coalescence. The interferences of the jets with the bath were analyzed by aqueous model studies. It was observed that the droplet generation rate was improved significantly in the presence of the central subsonic jet. The conservative form of the governing equations was solved to obtain the jet characteristics of the compressible flow. The system of governing equations was closed using the k–ε turbulence model. It is already known that the k–ε turbulence model predicts the flow features of the multiple jets with some deviations due to the anisotropy of the turbulence [89]. Nevertheless, this model was used in this simulation because it is easy to get reasonable solutions quickly with the k–ε model with lesser computational efforts. The computational domain along with the mesh used for the simulation of the seven-hole lance design is shown in Figure 4.3.8. Slightly more than 1.3 million grid cells were generated in the computational domain. The simulations were performed with 12 processors in a Linux cluster. On average, one simulation required 72–80 h of computation.

Naji Meidani *et al.* [90] at the MMPC reported on the modeling of Co-jet technologies for BOF converters, using helium as the shroud gas, and air as the supersonic jet, to replace burning natural gas and pure oxygen in the actual system. The experimental results for three different designs of shrouded supersonic jet nozzles demonstrated that greater depths of penetration and reduced mixing times could indeed be achieved with a coaxial low-density burning subsonic jet of hydrocarbon fuel and a main jet of supersonic oxygen. Dimensional analysis indicated that the depth of penetration of a gas jet into a liquid bath might depend on the height, H, of the lance tip from the quiescent bath, and the liquid Froude, Reynolds, and Weber numbers. These reflect the ratios of gravity, viscous, and surface tension forces to the jet's inertial, or momentum, forces. Good agreement between the mathematical model including just the Froude number

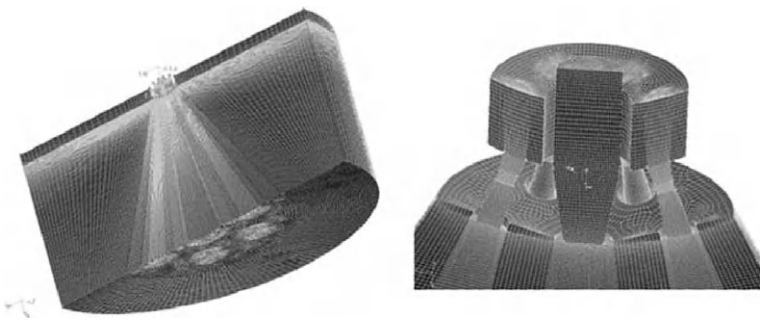


Figure 4.3.8 Computational domain and meshing of the nozzle.

and experiments was obtained, in terms of predicted and observed depths of penetration. Further efforts were made to study jet penetration into liquid metals. The effects of density of liquid metal and a wide range of gas flow rates, on the penetration depth, were investigated theoretically. The results confirmed that jet penetration depths can be increased with increasing shroud gas flow rates and decreased bath density.

Singh *et al.* [91] used CFD to optimize bottom tuyere configurations for the steelmaking vessel, in order to get a more accurate position for the bottom nozzles so that the mixing time could be further minimized. They used the two-equation k–ε turbulence model, along with a discrete phase model, to simulate the air bubbles being injected into the vessel. The mathematical modeling approach was used to solve the flow field in the bath in the presence of the bubbles arising from air being injected through the bottom nozzles. The velocity on the wall of the vessel was set to zero and the no slip condition on the wall was always prescribed. At the inlet of the nozzle, the gas velocity was prescribed because it was obtained from the experiment and the turbulence intensity was set to 2% with a turbulent viscosity ratio of 10 to start with. The top surface of the vessel was set to a zero shear stress condition, and the gas bubbles were allowed to escape through it. Once the solution reached steady state, the tracer dispersion equation was solved where the inlet of the tracer injection point was set to mass fraction of 1 for 1 s. This was achieved in five equal time steps of 0.2 s each. Then the mass fraction at the tracer inlet was set to zero for the rest of the computation. The wall of the vessel was treated as impermeable to the tracer, so the zero-flux condition was set at the walls. The momentum equation along with the turbulence closure equations was integrated over a control volume and then discretized to yield algebraic equations by using FDMs. In the discretization scheme for the convective variables, a first-order upwind scheme was used while for the diffusive fluxes, central derivative schemes were used. The pressure–velocity correlation was obtained from the SIMPLE algorithm, and the sets of algebraic equations were solved using a multigrid technique of FLUENT. For discrete particle simulations, explicit time integration was used to solve the translational motion of the particles. At each time step, a discrete particle model gave information such as the positions and velocities of individual particles. These were used to determine interaction forces, so as to determine the resulting fluid flow field, from which the fluid drag forces acting on the individual particles were again calculated. Incorporation of resulting forces into discrete particle expressions produced information about the motion of individual particles for the next time step. In this way, continuous and discrete phases were coupled via the drag forces on particles, while satisfying the momentum conservation equations. The convergence of the equations was monitored by the whole-field residual of each variable, and when this variable fell below 10^{-3}, the solution was assumed to have converged for that time step. So marching to the next time step could then be done. Steady-state solution for the velocity field could be achieved by performing the simulation for more than 60 s (real time). The comparable computer time required more than 18 h. After this, the tracer

dispersion equation was solved in the flow field, in order to determine the mixing time in the vessel. The tracer mass fraction was kept at 1 for 1 s (achieved in five time steps), and then the mass fraction was kept at 0 for all the other time steps. The dispersion equation was similarly discretized and solved by the multigrid technique, numerically, in a transient manner for more than 60 s so that steady state could be achieved in the system.

Ersson *et al.* [92] developed a fundamental mathematical model of the flow field and surface deformation caused by an impinging jet in a top-blown reactor. The results were validated against water model experiments. More specifically, the predicted penetration depth was found to agree well with surface deformation measurements and predictions using analytical equations. Furthermore, the predictions of the location of a vortex were found to agree fairly well with particle image velocimetry (PIV) measurements. Calculations were also done to compare the widely used standard k–ε model against the realizable variant of the standard k–ε model, to calculate the turbulent conditions of the flow. It was found that the penetration depth caused by the impinging jet on the liquid surface was relatively unaffected by the choice of turbulence model. However, when the main recirculation loop in the bath was investigated, there was a clear distinction in the flow fields produced when the two different turbulence models were used. They [93] also developed a novel modeling approach in which the CFD software was coupled to thermodynamic databases, in order to obtain dynamic simulations of metallurgical process phenomena. This modeling approach was used in a fundamental process model of a top-blown converter. Reactions between gas–steel, gas–slag, steel–slag, and gas–steel–slag were all considered. The results showed that the mass transport in the surface area is totally controlled by convection. These indicated that a large amount of CO produced during the decarburization might slow down the rate of decarburization in droplets ejected from the bath (which the present authors find very dubious). For the simulation conditions reflecting their laboratory experiments, it was also seen that the amount of slag (FeO and/or SiO_2) formed was close to zero, i.e., only gas ($CO + CO_2$) is created as the oxygen jet hits the steel bath in their laboratory experiments. Again, in practice, this is wrong since lime is added, silicon is oxidized, and a slag forms immediately. Nonetheless, their overall conclusion was that it was possible to make a dynamic coupling of the Thermo-Calc databases with CFD software, to make dynamic simulations of the BOF converter. This needs further investigation and verification in our opinion.

More prosaically, CFD has been used to design fume hoods in a BOF plant. Plikas *et al.* [94] at Hatch Ltd. used a CFD modeling to design fume control systems for the BOF plant. Figure 4.3.9 shows the geometry of a CFD model that was used by them to simulate secondary fugitive emissions from a BOF during charging.

This particular shop did not have a secondary hood for the control of these emissions. The primary hood, designed to capture emissions during tapping and refining operations, was also being used for the control of charging emissions. Fume originates inside the vessel and enters into the shop through the open BOF mouth. The fume flow rate at the

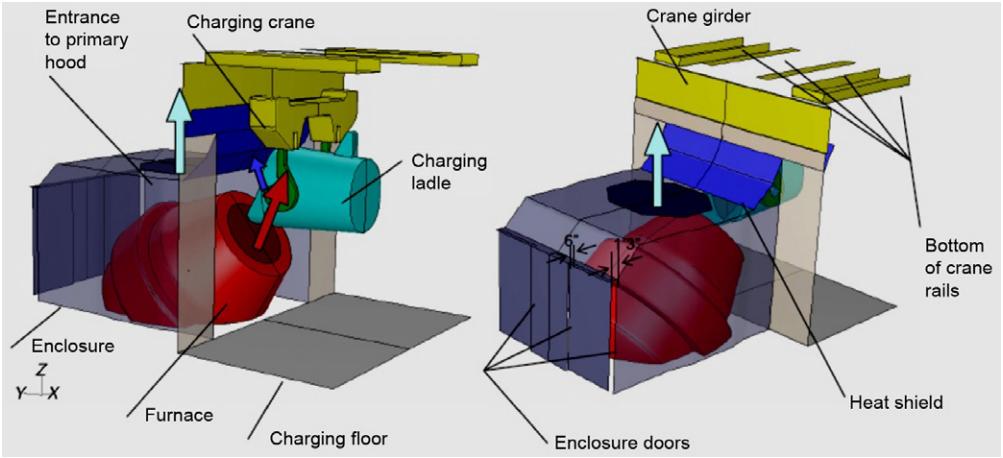


Figure 4.3.9 Model geometry of BOF charging operation.

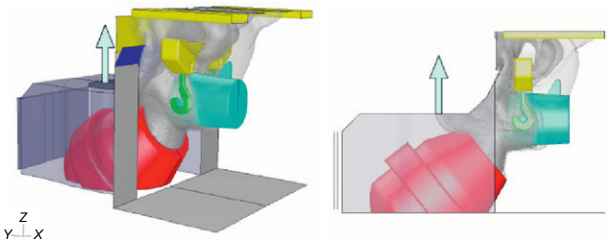


Figure 4.3.10 Predicted fume emission from the BOF during the hot metal charge.

mouth must be specified as a boundary condition in the CFD model, and a video was taken to calculate it. Several charging events were videotaped and analyzed to obtain a statistically meaningful average fume flow rate at the BOF mouth. As shown, the model included all major obstructions to the gas flow including the hot metal ladle, crane trolley, craned hooks, ductwork, etc. Figure 4.3.10 shows the predicted fume emission from the BOF during the hot metal charge. The image shows a surface of constant fume concentration equal to 1% by volume. Everywhere within this surface the concentration is >1% and everywhere outside this surface the concentration is <1%. Although the EPA defines visible emissions as those having an opacity (volume concentration) >6%, what is actually visible depends on a number of factors including particulate concentration, ambient light conditions, fume temperature, etc., and therefore, the minimum concentration at which fume becomes visible can range anywhere from 1% to 10%. For presentation of the CFD results, the lower end of 1% was used to define the extent of the plume, and any concentration <1% was considered visible. This provided a conservative estimate of the

plume extent, and therefore, it could be expected that the emissions in the plant will not be visible beyond the 1% surface plot shown by the CFD analysis. This assumption was corroborated by visually comparing the emissions observed in the shop with that predicted by the CFD model, which showed that the extent of the visible emissions roughly coincided with the 1% surface plot predicted by the model.

Their CFD model predicted that the primary hood captures only 39% of the emissions released during charging. To improve fume control during charging, the secondary hood design shown in Figure 4.3.11 was proposed. The hood was positioned directly above the BOF mouth with ductwork on both sides leading to a bag house. The size of the hood itself was limited by physical space limitations between the BOF, furnace enclosure, and crane rails. However, the ventilation flow rate to be exhausted from the hood could be varied to determine the optimum required for sufficient fume capture. The original proposed design was for an exhaust flow of 600,000 acfm, as calculated using conventional design methods. Figure 4.3.12 shows a comparison of the 1% fume surface plot and corresponding capture efficiencies between three flow rates: 300,000, 450,000, and 600,000 acfm. Exhaust at 300,000 acfm did not provide adequate control. Exhaust at 450,000 acfm was required to provide adequate fume capture, i.e., >95% capture. Increasing the exhaust to 600,000 acfm provided only marginal benefit. In terms of

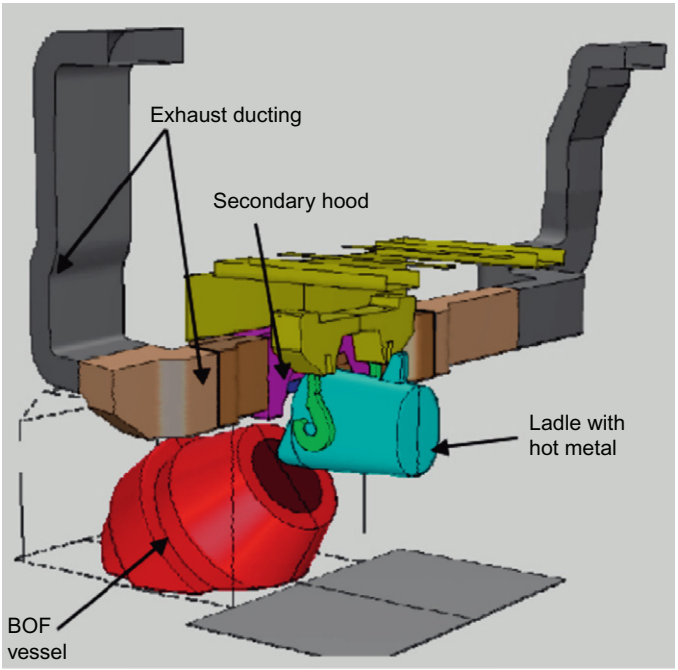


Figure 4.3.11 Proposed secondary hood design.

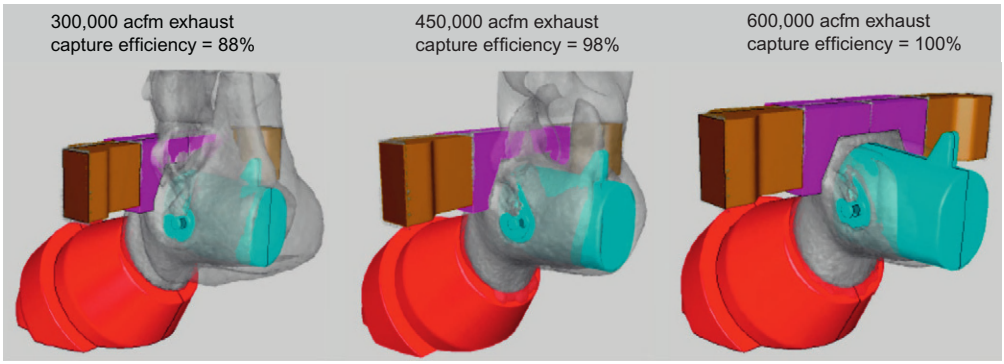


Figure 4.3.12 Performance of secondary hood in capturing fume emissions during charging.

capital cost, however, the difference between 450,000 and 600,000 acfm exhaust is significant—as much as $4,500,000 assuming US$30/acfm for a complete system. For the final design, an exhaust flow rate of 500,000 acfm was proposed to provide additional contingency, bringing the total cost saving to ~$3,000,000 from the original proposed design of 600,000 acfm. When comparing this cost saving to the cost associated with performing the analysis, $50,000, the value provided by the CFD modeling exercise was clearly demonstrated.

From the above discussions, it is clear that mostly the turbulent transport equations are solved numerically to model liquid metal flow, heat and mass transfer within the BOF. CFD has been applied to model diverse aspects of the BOF process starting from lance design, bottom tuyere configuration, to designing of fume control systems for the industry. Modeling of the supersonic jet is a very interesting subject, and here at the MMPC efforts, have been made to solve the multiphase compressible fluid flow equations to optimize the amounts of the shroud gas to be used with the oxygen jet. However, much more remains to be done in the development of a generalized CFD model of BOF steelmaking, as mentioned earlier.

4.3.2.5. Ladles

The ladle has grown in importance over the past 40 years, as steelmakers learned how to use it as a vessel for secondary steel refining. Previously used for alloy additions prior to casting, the vessel is now used for secondary refining, by successively combining it with overhead elements incorporating facilities such as an RH (or tank) degasser, a ladle furnace, and a strong stir station. Operations now include aluminum wire feeding and alloy trim additions, inclusion removal, inclusion modifications, gas stirring, and vacuum degassing. Similarly, chemical modifications to inclusions and desulfurization can be practiced for ultra-low carbon (ULC) and ultra-low sulfur steels. Many CFD researchers

have investigated phenomena such as gas–liquid interactions, turbulent fluid flows, mixing, and solid–liquid mass transfer in ladles. All these are highly complex transport processes and have been extensively modeled and analyzed by different researchers for the past three decades. Mazumdar and Guthrie [95] pointed out that many theoretical and experimental investigations had been carried out on the subject of gas injection in ladle metallurgy steelmaking operations. Symmetrically and asymmetrically placed lances/tuyeres/porous plugs have been used as gas injection devices and studies have been reported on both gas–liquid and gas–liquid–slag systems, for a wide range of vessel geometries and gas flow rates. These indicate that under ladle refining conditions, apart from the vicinity of the nozzle, well-dispersed large spherical cap bubbles can be expected in the two-phase region. Over most of the two-phase zone, nozzle configurations have little influence on bubble and liquid rise velocities, gas volume fraction distributions, plume velocities, etc., and are therefore not critical to the overall flow recirculation produced. The rising gas–liquid plume is a Froude-dominated phenomenon, which induces a recirculatory motion of liquid within the vessel. The "eye" of the large-scale toroidal vortex for a centrally placed porous plug is typically located in the upper quadrant of the ladle and is displaced toward the side walls. Under these conditions, the liquid steel in the bottom of the vessel is relatively quiescent. Furthermore, the intensity of liquid motions and liquid mixing in the vessel can become quite sluggish when there is a slag layer on top of the steel, compared to an equivalent no slag situation. The influence of operating variables (viz., gas injection rate, vessel geometry, location of gas injection nozzle, etc.) on bath hydrodynamics and associated transport processes has been extensively studied using water models and associated CFD analyses, so the influence of these variables in practical ladle refining conditions is now known with reasonable certainty. Similarly, extensive mathematical modeling of fluid flow and the associated transport phenomena (viz., mixing, slag–metal reactions, solid–liquid mass transfer, etc.) and the validation of model predictions against laboratory as well as plant scale experimental data indicate that a reasonable mathematical framework now exists to effectively carry out design and process analysis calculations in refining ladles. Madan *et al.* [96] used CFD to model mixing behavior in ladles fitted with two porous plugs at $\pm R/2$ and concluded that a discrete phase turbulent model was able to simulate experimental mixing times with a reasonable degree of certainty. A finer mesh, a seemingly small incremental time step size, together with the spherical drag law, was required to successfully model the mixing phenomena. Chattopadhyay *et al.* [97] showed that purging locations other than $\pm R/2$ can decrease mixing times even more.

A review of the history of mathematical modeling of inclusion removal in ladles shows that considerable work has been done in various areas. Numerical models for fluid flow, heat and mass transfer [98–103], subject to the conservation of mass and momentum, heat and mass transfer, have all been presented. In these models, the k–ε two-equation turbulence model has been the most commonly employed approach for solving

the problem of time-averaged Reynolds stresses in turbulent flow systems. For bubble-driven flows, various quasi-single-phase models or two-phase models of bubble plumes all give good results [104–111]. The development of turbulent models and computer technologies provides further possibilities to describe turbulent flow patterns more accurately in metallurgical containers by numerically solving conservation equations. These can then be coupled with the kinetics equations of inclusion (particle) growth and the transport equations for inclusions contained within a melt.

To provide a starting point for numerical calculations, one needs to input an initial size distribution of inclusions. This comes from either experimental measurements or assumptions. As such, the results predicted by a model for inclusion growth and removal are dependent to some extent on the validity of the initial particle size distribution (PSD) selected. Important works in this field have been tackled by Szekely [112,113], Tozawa *et al.* [114], Miki *et al.* [115], Sinha and Sahai [116], Sheng *et al.* [117], and Söder *et al.* [118]. Wang *et al.* [119] reported on the growth and removal of inclusions in a multituyere ladle during bottom gas purging. They investigated the efficiency of inclusion removal assuming three-collision mechanisms for growth, viz., Brownian, turbulence, and Stokes. They studied wall adhesion, Stokes floatation, and bubble adhesion mechanisms to remove inclusions from the bath. Kwon *et al.* [120] developed a CFD-based nucleation-growth-removal model for inclusion behavior in a gas-agitated ladle during molten steel deoxidation. In order to account for the turbulent circulating flows induced by gas bubbling through the bottom, the k–ε turbulence model was employed to evaluate time-averaged Reynolds stress, while the fluctuations of the free surface of the melt were traced by means of the volume of fluid (VOF) technique. This model enables one to couple transient flow fields and temperature fields with concentration fields of elements and inclusions in the melt. As such, it can meet the requirements of time- and space-dependent evolution of PSDs without any given initial PSD of inclusions, relying directly on the chemical reaction. The model was applied to simulate the deoxidation process in molten steel for the Fe–Al–O system in an argon gas-stirred ladle. The model successfully predicted important phenomena, including turbulent recirculation flow patterns; and the streamline structure of the steel melt, turbulence energy variations and dissipation rates, transient temperature fields, and PSDs of alumina inclusions. Comparison with some industrial data showed that the predicted PSDs were reasonable for time-dependent variations of inclusion size distribution.

Krishnapisharody and Irons [121,122] developed mathematical models to estimate slag eye size in gas-stirred ladle systems. Their model computed the eye size from the primary operating variables of the ladle and proved to be reliable in a variety of multiphase systems.

Li *et al.* [123] developed a numerical model to analyze transient three-dimensional, three-phase flows in a bottom-purged ladle with one and two off-centered porous plugs. A multiphase VOF method was used to simulate the behavior of the slag layer. Numerical

simulations were conducted to clarify the transient phenomena of gas injection into molten steel. The rising gas bubbles impinged on the slag intermittently and broke the slag layer so as to create the slag eye. Simultaneously, the wave at the slag–steel interface was formed and the wave frequency increased with the increase of argon gas flow rate for one off-centered plug case. The relationship between nondimensional areas of slag eye and the modified Froude number was in good agreement with the experimental data reported in the literature. Since significant deformation of the slag layer occurs during gas stirring operations, the thickness of the slag layer becomes thinner near the slag eye and thicker near the ladle wall, respectively. The downward flow velocity of steel at the slag eye periphery may be significantly affected by the flow rate of Ar gas. Therefore, when the downward flow velocity is larger, more emulsification of slag can be expected.

To conclude, much work has been on CFD modeling of ladle operations and most of that has focused on gas–liquid interactions, inclusion removal, and modeling of multiphase flows. As a comment, ladle wall refractory erosion due to bottom gas purging has not been modeled extensively and is an interesting topic.

4.3.2.6. Tundish

In 2000, Fan and Hwang [124] developed a mathematical model to analyze the fluid flow phenomena of liquid steel in the tundish, during initial filling stage and subsequent casting operations for the continuous casting of steel. The ultimate goal of their study was to ensure smooth initial casting operations without nozzle clogging. The mathematical model was developed using a CFD technique, named solution algorithm marker and cell (SOLA-MAC) and the famous k–ε turbulence model. SOLA-MAC has the capability of handling transient flow problems with highly distorted free surfaces. The SOLA-MAC technique uses a finite difference scheme for the mathematical analysis of fluid flow problems. Like most numerical techniques, it first divides the system, which is the configuration of the tundish under consideration, into a number of volume elements. Then a set of imaginary markers is introduced into the system to represent the location of the fluid at any instant. The velocity field of the moving fluid domain can be calculated by the application of fluid dynamics principles. Next, the markers are moved according to the calculated velocity field, in order to represent the new location of the fluid domain. The procedure can be repeated, right from the beginning when the tundish is empty, until it is filled to a predetermined height within the tundish. The mathematical model was first tested on a one-fourth scale water model. Good consistency was observed when the simulated filling patterns were compared with the water model experiments. Inclusion distributions and the amount of "dirt" exiting through the outlets of the various strands in the tundish were also analyzed using a fluid particle method. The simulated results showed that inclusion contamination was not uniformly distributed between the different strands, which was also confirmed by actual experience in the plant.

Odenthal *et al.* [125] reported results of digital particle image velocimetry (DPIV) on a one-fourth scale model of a single-strand tundish. It leads to a good interpretation of the dynamic flow phenomena. The flow separated at the bottom of the tundish and a recirculating region was developed. Simultaneously, the jet out of the ladle shroud induced a contra-rotating double vortex and a short circuit flow around the side walls. A two-equation model was developed in order to describe turbulence and the results obtained with this model corresponded well with the DPIV data. They concluded that DPIV can be used as an effective tool to determine two-dimensional velocity fields and transient velocity fields. They also suggested the use of 3D DPIV and laser Doppler anemometry (LDA) in future. LDA has an advantage that it can measure turbulent fluctuations. A transient two-fluid model was developed by Sheng and Jonsson [126] to simulate fluid flow and heat transfer in a nonisothermal water model of a continuous casting tundish. Thermal stratification in the bath was evident, and the results predicted by the two-fluid approach adopted made the effect of natural convection more clear compared with the generally used single-fluid k–ε model. The overvaluation of the conductive heat transfer in the transition region of the system found by using the single-fluid approach was eliminated by using the two-fluid k–ε model. The two-fluid approach was also found better in describing the counter-gradient diffusion phenomenon caused by the thermal buoyancy force.

Ahn *et al.* [127] predicted the concentration change during grade transition operations during steel thin slab casting based on computer simulations, a water model, and plant trials. Fluid flow and mixing patterns at various levels of fluid in the tundish and various flow rates were analyzed through 3D mathematical modeling. They correlated their results with water model experiments and developed a simple, efficient, and accurate computational model which could predict the solute concentration profiles at the outlet of the tundish. Based on the model, mixing in/below the mold was analyzed considering EMBR (electromagnetic breaking). The total amount of mixed grade steel only depended on the mixing in the tundish when EMBR was applied. They also concluded that the optimum tundish operating condition to minimize intermixed slabs greatly depended on tundish geometry. A systematic study was conducted by Sinha *et al.* [128] of the National Metallurgical Laboratory in India on the fluid flow behavior in a two-strand tundish under conditions of submerged entry nozzle (SEN) and open entry nozzle (OEN) with different levels of water in the tundish. Flow was characterized by the profiles of tracer responses at the tundish outlets. Two configurations of entry nozzle (ladle shroud), the straight tube (for SEN and OEN) and the T-shaped (for SEN only), were applied. At 34 mm immersion depth of the straight ladle shroud, the optimal level of mixed flow in the tundish was produced and thus uniformity in composition was obtained. With the OEN configuration, the greater was the height of the SEN, the less was the dead volume and the mixing was increased.

Sahai [129] made a summary on modeling of melt flows in continuous casting tundishes in the Brimacombe Memorial Symposium. He emphasized the importance of

proper melt flow in tundishes for the production of high-quality clean steel and that this can be achieved by good tundish design and optimum volumetric flow rate of liquid metal. In a full-scale model, the Reynolds and Froude similarities can be satisfied simultaneously. However, in a reduced scale model, both similarities cannot be satisfied for a water model. Froude similarity is then a sufficient and convenient similarity criterion for water modeling. In nonisothermal systems where buoyancy forces become important, the tundish Richardson number together with the Froude number are necessary and sufficient similarity criteria for modeling. Sahai also mentioned that the solution of the turbulent Navier–Stokes equation with an appropriate set of boundary conditions provides detailed information about the velocity and turbulence fields within a tundish. A coupled solution with the heat transfer equation also provides the temperature field existing in the melt.

Robert and Mazumdar [130] developed a steady-state, three-dimensional, turbulent flow model for analyzing melt flow and residence time distributions (RTDs) in a steelmaking tundish system. They used a control volume based, finite difference procedure, and the SIMPLE algorithm. To ensure that their model was consistent and sufficiently robust, they tested the model on several standard systems and obtained satisfactory results. Accordingly, their model was applied to simulate flows and RTDs in four different tundishes. The results were compared with equivalent water model experiments. Numerical modeling of RTD in the rectangular, six-strand tundish system embodying the low Reynold's number k–ε model of Launder and Jones was found to produce estimates of RTD parameters that are in reasonable agreement with the corresponding experimental results and superior to those deduced via the high Reynold's number k–ε model.

Ferro *et al.* [131] presented mathematical models for the evaluation of RTD curves for a large variety of vessels. They introduced a new volume which they named "the convection diffusion volume" to obtain a good representation of RTD curves. Two numerical models for simulation of RTD curves in different vessels were presented. The comparison of measured RTD curves with numerical results from the proposed model shows that these models can successfully represent the general behavior of a fluid inside a variety of systems. The first of the two models proved to be efficient in describing most of the one-peaked RTD curves, in spite of its simplicity. The second one, slightly more complex, successfully represented all the different RTD curves under consideration including those with double peaks. The key feature of these models was their use of a new type of volume, the convection diffusion volume. In order to find the parameters of the model for a given experimental RTD curve, a numerical algorithm was developed and also some simple mathematical relations were found that allowed the estimation of the parameters of the model from the characteristic parameters of the RTD curve.

Gardin *et al.* [132] carried out an experimental and numerical CFD study of turbulence in a tundish container. Extensive mean and fluctuating velocity measurements were performed using LDA in order to determine the flow field and these data formed the basis

for the numerical model validation. CFD modeling of this problem apparently seems easy but actually it was not. Accurate description of the jet is the most important and requires a localized fine grid, but also a turbulence model that predicts the correct spreading rates of the jet and impinging wall boundary layers. The velocities in the bulk of the tundish are generally much smaller than those of the jet, leading to damping of turbulence, or even laminar flow. They started the work with an objective of applying and validating the k–ω model of Wilcox to a tundish flow problem. This model was thought to have advantages over the k–ε model. After initial 2D studies they found that the k–ω model was diffusing the wall jet too quickly. Medium grid density 3D computations confirmed this finding. The authors developed several low-Reynolds number k–ε model variants to compute the flow and compare against measurements. The k–ε modifications proved to be very successful, with the newly developed k–ε D1 model being the best. This indicated that there is no need to use more sophisticated differential Reynolds stress models (RSMs), which are more difficult and take longer to converge. From the grid refinement, they concluded that certain turbulence models were more grid-sensitive than others. They also concluded that the large eddy simulation (LES) model might still have certain limitations for practical use.

Jha and Dash [133] employed different turbulence models to the design of optimum steel flows in a tundish. The Navier–Stokes equation and the species continuity equation were solved numerically in a boundary-fitted coordinate system, comprising the geometry of a large-scale industrial size tundish. The solution of the species continuity equation predicted the time evolution of the concentration of a tracer at the outlets of a six-strand billet caster tundish. The numerical prediction of the tracer concentration using six different turbulence models was carried out. The k–ε model predicted the closest value to the experimental observations compared to all other models. The prediction of the transient behavior of the tracer was best done by the Lam–Bremhorst model and then by the RNG model, but these models did not predict gross quantities very accurately as did the k–ε model for a single-strand bare tundish. With the help of the six turbulence models, mixing parameters, such as the ratio of mix to dead volume and the mean residence time, were computed for the six-strand tundish for different outlet positions, height of advanced pouring box (APB), and shroud immersion depth. It was found that three turbulence models show a peak value in the ratio of mixed to dead volume when the outlets were placed at 200 mm away from the side wall as shown in Figure 4.3.13.

An APB was put on the bottom of the tundish surrounding the inlet jet when the outlets were kept at 200 mm away from the wall. It was also found that there exists an optimum height of the APB where the ratio of mixed to dead volume and the mean residence time attain further peak values signifying better mixing in the tundish. At this optimum height of the APB, the shroud immersion depth was made to change from 0 to 400 mm. It was also observed that there exists an optimum immersion depth of the shroud where the ratio of mix to dead volume still attains another peak signifying slightly

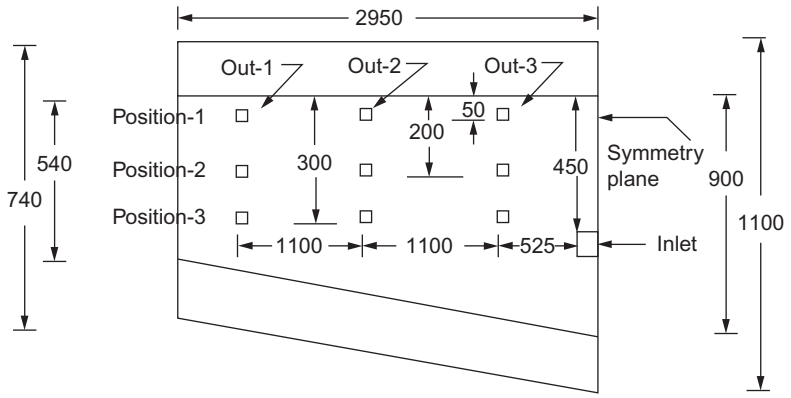


Figure 4.3.13 Top (plan) view of the tundish showing outlets on the bottom plane.

better mixing. However, none of the turbulence models predicts the same optimum height of the APB and the same shroud immersion depth, as the optimum depth. The optimum height of the APB and the shroud immersion depth were decided, rather arbitrarily, when two or more turbulence models predicted the same values.

Jha *et al.* [134] also performed a LES to study mixing in a tundish. They took the solution of the k–ε model as a starting guess for the LES. A solution for the LES could be arrived at after adapting a local refinement of the cells (twice), so that the near wall y^+ could be set <1. Such a refined grid gave a time-independent solution for the LES, which was used to solve the species continuity equation. The LES solution slightly over-predicted the mean residence time but could predict the mixed volume fairly well. However, the LES was unable to predict the two peaks in the tracer concentration, as were the k–ε, RNG, and Lam–Bremhorst models.

A comprehensive process model for fluid flow and heat transfer in the tundish was developed by Pradeshi *et al.* [135] which proved capable of capturing the transient process dynamics. The model was based on a conjugate thermal analysis of the tundish, accounting for simultaneous heat transfer through the liquid steel, refractory, steel shell, and dams. The model was validated by comparing model predictions for laminar and turbulent fluid flow conditions cited in the literature. Plant campaigns were undertaken to collect plant data for tuning and validation of the model. Kumar *et al.* [136] from their experimental and computational study on flow modeling and RTD indicated that a sufficiently small grid resolution (control volume of the order of 10^{-6} m^3) is necessary to arrive at a practical grid-independent solution. They also reported that the RSM was found to simulate RTD in the system somewhat better to the standard coefficient k–ε model. Their mathematical model was validated with experimental results and proved sufficiently robust and reliable to predict mixing parameters in tundishes with and without flow control devices (FCDs).

Ramos-Banderas *et al.* [137] performed mathematical simulations and physical modeling of unsteady fluid flows in a water model tundish mold. The LES approach used by them was able to predict qualitatively the instantaneous upper recirculating flow fields of water in the physical model. Agreement of simulated and measured jet parameters such as the jet angle and the impingement position of the entry jets in the narrow wall of the mold were acceptable. Thus, they suggested that the LES approach is well recommended to estimate jet characteristics. Changes of flow pattern with time were generated as a result of the vertical oscillation motion of the jet core. This motion was promoted by the residual Reynolds stresses that characterize turbulent flow. The same stresses caused asymmetric fluid flows. The fluid flow pattern in the jet root was unaltered by changes of the flow rate of the liquid.

Tripathi and Ajmani [138] reported on a numerical investigation of fluid flow phenomena in a curved shape tundish (Figure 4.3.14). A 3D mathematical model was developed by them. The results were compared with a conventional delta-shaped tundish. The strong role of curvature in improving fluid flow characteristics and enhancing inclusion floatation was evident from the results. They also reported a considerable increase in the plug volume and mean residence time with the use of contour-shaped pouring chambers as compared to those with sharp corners. The mathematical model was validated against experimental results for a single-strand bare tundish, for which data were available.

A novel tundish mixing model was proposed to predict the outlet concentration of the tundish during a grade transition by Cho and Kim [139]. To enhance the efficiency and replication performance, the present model was designed to minimize the number of parameters to only one that needs to be tuned for easier application to new situations, whereas the Huang and Thomas [140] model had six parameters to be tuned. Two types of water model were employed to verify Cho and Kim's model, and the real grade mixed blooms were produced through a grade transition continuous casting. When the tundish

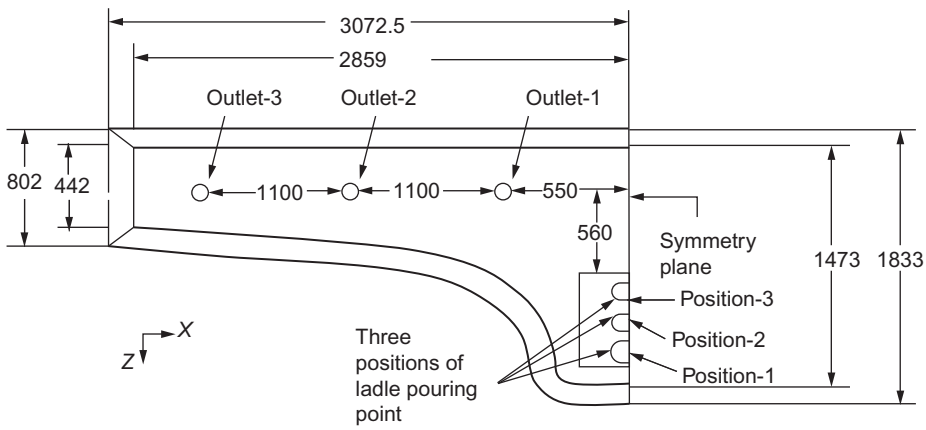


Figure 4.3.14 Top (plan) view of the curve-shaped tundish.

mixing model was applied to the cases of the water models and real bloom casting, the numerical results were found to be in good agreement with the experimental data, and the constant parameter f of their model was found to be determined depending on the shape of the tundish. Zorzut *et al.* [141] developed a mathematical model which could predict steel grade change. The model was set up on some dilution interconnecting elementary cells that describe the shroud and each strand. The cells were considered with uniform concentration. Such a model was very useful in the definition of the technological practice for the steel grade change operation.

Alkishriwi *et al.* [142] carried out LES of a continuous casting tundish to investigate the turbulent flow structure and vortex dynamics. To validate their scheme, LESs of turbulent pipe flow at $Re_T = 1280$ and cylinder flow at $Re_D = 3900$ were performed. They claimed that the good agreement obtained showed that their scheme was efficient and that it improved the accuracy for very low Mach number flows. The findings from the LES showed the presence of many intricate flow details that have not been observed before by customary Reynolds-Averaged Navier-Stokes (RANS) approaches.

Fluid flow dynamics during ladle drainage operations of steel under isothermal and nonisothermal conditions were studied using the turbulence shear stress transport k–ε model and the multiphase VOF model by Davila *et al.* [143]. At high bath levels, the angular velocity of the melt, close to the ladle nozzle, was small rotating anticlockwise and intense vertical-recirculating flows were developed in most of the liquid volume due to descending steel streams along the ladle vertical wall. These streams ascended further downstream driven by buoyancy forces. At low bath levels, the melt, which was close to the nozzle, rotated clockwise with higher velocities whose magnitudes were higher for shorter ladle holding times. These velocities were responsible for the formation and development of a vortex on the bath free surface, which entrained slag into the nozzle by shear stress mechanisms at the metal–slag interface. Sankanarayan and Guthrie [144,145] mentioned that the diameter ratio of the outlet nozzle and the ladle is important and this ratio and the critical height for vortex formation are proportional. For a constant ratio of outlet diameter to ladle diameter, the critical height becomes larger with higher initial bath heights. Understanding vortex mechanisms will be useful to design simple and efficient devices to break down the vortex flow during steel draining even at very low metal residues in the ladle.

Vayrynen *et al.* [146] modeled steady state and transient casting situations. Their work was focused on tuning and validation of a commercial CFD package which will be used to simulate tundish operations. They concluded that the software was not able to simulate the downscaled water model accurately, but on the other hand both temperature and transient casting situation results of the full-scaled tundish were satisfactory. They mentioned that one possible reason for this behavior is that areas of clearly turbulent flow in the water model are much smaller than in the actual tundish and this transition of flow type is very difficult for the present turbulence models to calculate accurately.

Hamil and Lucas [147] used an ASM which basically is a simplified form of a multiphase model to study inclusion motion and its removal. Assuming that the small particles always move at their slip velocity, which basically comes from a balance between the buoyancy and drag force, they solved separate scalar volume fraction equation for each particle species along with the basic conservation equations for multiphase (the equations are not given here). They used software CFX to compute the results and compared their results with previously published results of Joo and Guthrie [148], who used Equation (4.1) which is based on single-phase modeling approach. Joo and Guthrie [148] used the METFLO 3D software (a code developed in McGill University) to solve those equations. For the flow conditions modeled, they showed that most inclusions >100 μm should float out, independent of FCDs while all those <40 μm would not be affected by flow modifying devices, and be retained in liquid steel exiting to the strands. More recently, Hulstrung *et al.* [149] studied the influence of tundish volume on the degree of inclusion separation. Hulstrung *et al.* [149] used "discrete phase model" to predict the degree of inclusion separation and used the results as a tool for designing a higher capacity tundish. Better macroscopic cleanliness of steel slabs produced during abnormal casting condition caused due to stopping of one of the strand slab caster led them to design a tundish with a higher volume. They investigated the behavior of solid alumina particles using a Euler–Lagrangian method. In this method, the particle trajectories were computed in a Lagrangian frame of reference.This method is discussed in more detail in Section 4.6, page 8.

To simulate the chaotic effect of the turbulence eddies of the liquid phase on the inclusion trajectories, a discrete random-walk model was applied by Solorio-Diaz *et al.* [150]. In this model, a fluctuant random-velocity vector (u_i') is added to the calculated time-averaged vector ($\bar{u}_i$), in order to obtain the inclusion velocity (u_i) at each time step, as particles travel through the fluid. Each random component of the inclusion velocity is proportional to the local turbulent kinetic energy level (k_p), according to the following equation:

$$u_i' = \zeta_i \sqrt{\overline{u'^2_i}} = \zeta_i \sqrt{\frac{2k}{3}} \tag{4.3.2}$$

where ζ_i is a random number, normally distributed between −1 and 1, which changes at each integration step. The results of computations show how the inclusions can be expected to become dispersed.

Zhang *et al.* [151] proposed three modes of inclusion removal from molten steel in the tundish, viz., floatation to the free surface, collision, and coalescence of inclusions to form larger ones and adhesion to the lining solid surfaces. They studied the 3D fluid flow with and without FCDs. The results indicated that FCDs effectively control the strong stirring energy within the inlet zone. FCDs were also favorable for inclusion removal. The total

removal ratio was 51% without FCDs where inclusions with radii >72 μm were totally removed. This increased to 79% with FCDs where inclusions with radii >61 μm were totally removed. Out of this 79%, removal by floatation was 49.5% and removal by adhesion was 29.5%. The collision and coalescence mode was a better way to remove smaller size inclusions as the number of collisions per unit time per unit volume of steel was much higher for smaller inclusions than for bigger inclusions.

Thomas and Bai [152] summarized the formation mechanisms, detection methods, and prevention of tundish nozzle clogging, focusing on the role of computational models in quantifying the noncomposition-related aspects. They classified tundish clogging into four main types, viz., the transport of oxides present in the steel to the nozzle wall, air aspiration into the nozzle, chemical reaction between the nozzle refractory and the steel, and steel solidified in the nozzle. However, in practice, a clog can be a combination of two or more of the above types. They mentioned that clogging can be best detected during casting by simultaneous monitoring of several different parameters like argon back pressure, nitrogen pickup, mold-level fluctuations, and flow control position relative to casting speed. Solutions to clogging problems were also mentioned by them. They are minimizing inclusions by improved steelmaking practices, optimizing fluid flow and transfer processes, controlling steel alloy additions, slag and refractory compositions, improving nozzle material design, and avoiding air aspiration.

An extensive review of the literature shows that a large number of modeling efforts covering various aspects, such as fluid flow, RTD, effects of FCDs on flow patterns, and inclusion removal and thermal energy transport, have been reported. However, most modeling efforts have not considered interactions of the liquid steel with containing refractories and overlaying slags. One model has been developed in this regard, which took into account the steel, slag, and refractory phases. The model was also used to determine the optimal location of flow devices, making the temperature distribution in the steel more even and enhancing the removal of inclusions to the slag. In that study, the focus was to study the slag/steel interface. Predictions showed that slag is dispersed into the steel close to the interface, as well as close to the ladle shroud. A momentary interfacial solidification sampling method was developed to confirm these predictions. Analysis of the samples by ultrasonic testing, optical microscopy, and SEM confirmed the presence of nonmetallic particles close to the slag–steel interface and close to the ladle shroud. The analyses also showed that the slag–steel interface is very irregular despite low velocities. They concluded that the slag/steel interface is unstable and the liquid steel at the interface can engulf slag and can lead to the formation of inclusions in the final cast product.

An investigation of slag floatation and entrapment was studied by Solhed *et al.* [153,154] using fluid flow simulations, sampling, and physical metallurgy. A model of a continuous casting tundish, which besides the steel phase also considers refractory, slag, and flux was developed and presented together with the basic ideas behind the

development. The model was verified with velocity and temperature measurements in steel and refractory. The agreement between the measured velocities and temperatures and the corresponding predictions were good. From their computational results, it was seen that slag concentrations were very low in the regions near the walls, where flows were upwardly directed, but that near to the shroud and the stopper rod, slag concentrations were higher and the downwardly directed velocity components caused the slag to penetrate the steel. It is evident that not much work has been done on slag entrainment. So more work on slag entrainment, using both physical and mathematical modeling, needs to be done. Here at the MMPC modeling, slag entrainment both physically and numerically is being done by some researchers. In the numerical model, the VOF approach is currently used.

The effects of FCDs have also been extensively studied by a number of researchers [155–160]. The research on FCDs has been so vast in the past decade that perhaps it needs a separate review on the effect of FCDs on the performance of tundish. However, it has been seen that FCDs can have a positive effect on tundish performance if their design is properly optimized and positioning in the tundish is proper. But for inclusion removal, FCDs have failed to show their efficiency either in physical or mathematical modeling [161–163]. Also improper positioning of FCDs may result in detrimental flow patterns inside the tundish. Also, in deep large tundishes which allow sufficient residence time for inclusion floatation, FCDs are not recommended because they are inconvenient in sustaining a hot cycle tundish practice, which is quite economical. With a large tundish, the deep melt bath does not require a pour pad either.

A "swirling ladle shroud" (SLS) (Figure 4.3.15) may be very useful to reduce turbulent kinetic energy within the inlet zone. A new design of ladle shroud, obtained through water modeling, that controls turbulence of the entry jet in continuous casting tundishes

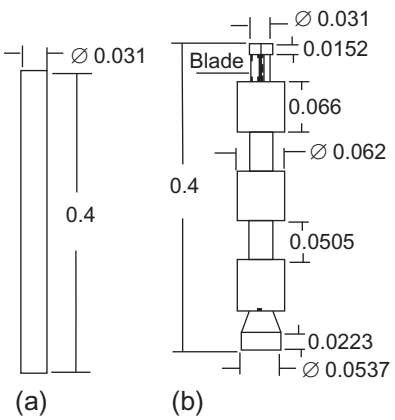


Figure 4.3.15 Geometric (internal) dimensions of the experimental shrouds, m. (a) Conventional and (b) swirling ladle shroud (SLS).

has been proposed by Diaz *et al.* [164]. PIV measurements indicated that this design decreased the impact velocity on the tundish bottom close to 1/3 of that provided by a conventional ladle shroud. This achievement was due to a swirling jet that promoted a recirculatory flow in the horizontal planes of the tundish. The swirling effects helped to dissipate the turbulence energy of the jet before it hit the tundish bottom, thereby decreasing fluid velocities impacting the back and front walls of the tundish.

Turbulence models such as k–ε, k–ω, and the RSM were applied to simulate the experimental PIV measurements of velocities in the fluid flow. Only the RSM model yielded predictions that agreed remarkably well with the experimental determinations. These results with the new ladle shroud were sufficiently good that they may allow all tundish furniture to be removed. This would include the removal of all dams, weirs, and turbulence inhibiters.

Hou and Zou [165] studied the flow patterns in a new type swirling flow tundish fitted with a swirling chamber. Numerical simulations suggested that the RNG k–ε model was the most suitable turbulence model for this new type of tundish and can get convergent results more easily than the standard k–ε model for strong curvature flows and flows with different Reynolds numbers in different areas (see Figure 4.3.16). The grid-independent feature of this RNG k–ε numerical model (Reynolds normalization group k–ε model) was verified using two kinds of grids with different node densities (Figure 4.3.17a and b). They also concluded that the asymmetrical flow patterns developed in the swirling flow tundish were mainly caused by the swirling flow exiting from the swirling chamber, and partly because of turbulent fluctuations (Figure 4.3.17).

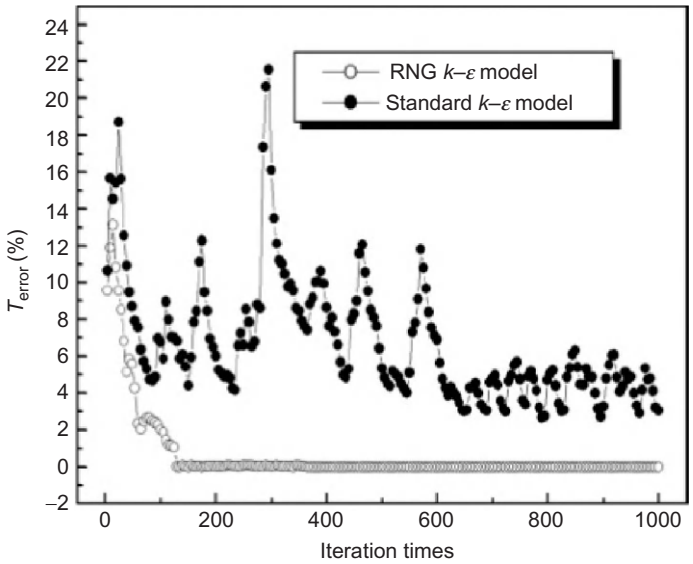


Figure 4.3.16 Variation of total error with iteration number.

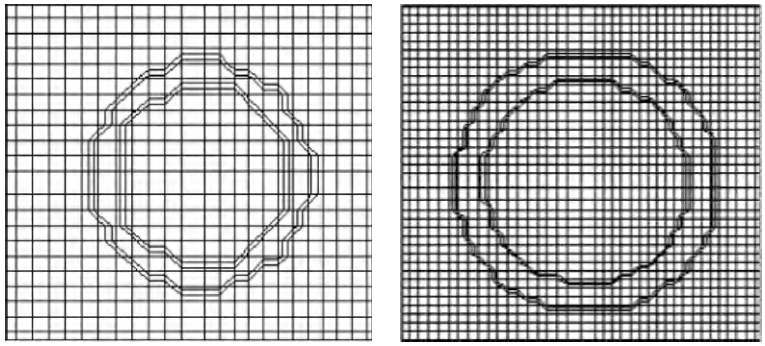


Figure 4.3.17 Grid systems of *x*–*y* plane: (a) sparse grid and (b) dense grid.

Thus the SLS is a good alternative to substitute for the FCDs available on the market. The effect of the SLS on fluid flow and mass transfer in a water model of a tundish was studied by Diaz *et al.* [166]. Experimental and mathematical simulations of liquid steel, using the water model, were presented using two kinds of ladle shroud: a conventional ladle shroud and an SLS which acts to dissipate the turbulent kinetic energy by rotational motion of the entry jet into the tundish. They used the k–ε, k–ω, and the RSM. Tracer dispersion could be accurately predicted by the RSM model, while the k–ε and k–ω models showed poor predictions. The RSM model also proved to be efficient enough to simulate acceptably well the velocity fields determined experimentally by PIV measurements. All the three turbulence models predicted close results among themselves for RTD curves, but the RSM was in best agreement with the experimental minimum residence time.

The SLS may have many advantages, but the flow fields are highly complex and may cause erosion of refractory inside the shroud. That would not be economical and would be detrimental for steel quality.

Fluid flows in the tundish are nonisothermal in reality. The nonisothermal nature of melt flows is due to energy losses that take place from the top surface and through the side walls, the top surfaces, and through bottom of the tundish. Similarly, different entry temperatures of steel from the ladle are also very probable, owing to heat losses with time within an emptying ladle, as well as temperature differences between different ladles of steel. Thus, there are many situations in actual practice where the temperature of the incoming stream from the ladle is different from that of the molten steel already present in the tundish. It was shown by Chakraborty and Sahai [167], and by Joo *et al.* [168], that the fluid flow patterns developed in such cases are quite different from those obtained under isothermal conditions. Nonisothermal conditions give rise to natural convection and buoyancy-driven flows within a tundish that are of a comparable order of magnitude to the inertially driven components. Thus, it is very useful that water modeling can

simulate the nonisothermal aspects of the fluid flow phenomena taking place in a continuous casting tundish. Damle and Sahai [169] examined the necessary modeling criteria for a nonisothermal tundish system. For nonisothermal flows, it is necessary to satisfy thermal similarity in addition to the geometric and dynamic similarities, by incorporating Tu or Gr/Re^2 effects. Fluid flows and mixing of molten steel in a twin-slab-strand continuous casting tundish were investigated using a mixing model under nonisothermal conditions by Alizadeh *et al.* [170]. This model led to a set of ordinary differential equations that were solved with a Runge–Kutta algorithm. Steady-state water modeling tests were carried out under nonisothermal conditions. Experimental data obtained from the water model were used to calibrate the mixing model. As a result of the presence of mixed convection phenomena in the nonisothermal tundish, parts of the primary fluid were mixed in with the warm incoming fluid. Due to the density difference between the two fluids, fluid channeling became evident within the tundish. The volume flow rate of the fluid in the channel was found to depend on the ratio of inertial to buoyancy forces inside the tundish. They mentioned that if the turbulent Reynolds number ($Re_T = \rho U' L/\mu$) and the Tu or Tundish Richardson number, Gr/Re^2, between two tundishes are identical (i.e., model and prototype), then the RTD curves would be in absolute accordance with each other. The mixing model results showed that the total mixed flow volume fraction in the nonisothermal tundish was lower than that for an isothermal one. Sheng and Jonsson [171] in MEFOS, Sweden, reported on convection patterns of liquid steel in the continuous casting tundish under nonisothermal conditions.

Some researchers at Baosteel [172] reported on numerical simulations of coupled fluid flow and heat transfer to enhance their tundish design. They had problems of temperature homogenization in the tundish. However, after doing a thorough investigation of fluid flow, RTD, and temperature distributions, under nonisothermal conditions, they were able to solve their problems.

Morales *et al.* [173] reported on buoyancy effects on the melt flow pattern in the molds of continuous slab casters. Thermal responses of step-input temperatures in steel for different flow rates were predicted. The molten steel velocity profiles were determined for these temperature and flow rate variations. The importance of natural flow convection was established through a dimensionless number given by the ratio Gr/Re^2, representing the ratio of buoyancy forces to inertial forces. Buoyancy forces proved to be as important as inertial forces, especially in the extremities of the tundish. The simulations indicated that these forces increase the residence time of the molten steel flowing near the slag layer, allowing more time for the nonmetallic inclusions to be captured. They also found that the turbulence inhibiting device helps to redirect the flow toward the top free surface. It was shown that this device helped to decrease turbulence near the entry zone and has a damping effect on the temperature step inputs, allowing for better control of the casting temperature. The traditional FCDs such as weirs and dams were not as effective as the turbulence inhibitor. Braun *et al.* [174] performed transient

nonisothermal numerical simulations to investigate the influence of transient boundary conditions at the outlet of the tundish on the flow structure and mixing process of fluid during the casting process. They emphasized that the tundish is a dynamic system, and hence time dependent in nature, because of the presence of transient thermal boundary conditions at all times. A positive thermal gradient is always formed along the length of the tundish until the ladle is completely drained. However, on opening up a new ladle, the thermal gradient is reversed. Miki and Thomas [175] reported on the effects of thermal buoyancy forces which significantly affect the flow pattern and thus influence inclusion separation. Sheng and Jonsson [176,177] performed physical and mathematical modeling of nonisothermal fluid flow in continuous casting tundishes. Apart from PIV and mathematical modeling, they performed tracer dispersion studies, to visualize the flow in the physical model. Tracer dispersion studies are more practical than PIV because in the latter, it is often very difficult to see the differences between isothermal and nonisothermal systems. From the above discussions, it is clear that some researchers included nonisothermal fluid flow physical and mathematical models to analyze continuous casting tundishes, but when compared to the number of papers published on isothermal fluid flow and turbulence, information published on nonisothermal melt flows is very much less. Also, another important observation is that mostly single-strand tundishes have been considered for modeling nonisothermal fluid flows. Mathematical modeling was the preferred choice for most of the researchers, while only a very few performed physical modeling of nonisothermal tundish systems.

Ray *et al.* [178] performed both physical and mathematical modeling work to analyze nonisothermal melt flows in a delta-shaped four-strand tundish. In his full-scale water modeling experiments as well as mathematical simulations, it was observed that during step inputs of hot water into a relatively cooler liquid in the tundish, the buoyancy-driven flows caused the incoming hotter fluid to move above the remaining colder fluid and to move ahead of it. However, in the physical modeling experiments, they were only able to simulate a step input of +3 °C to +4 °C. As a result, not much difference was observed between the isothermal and nonisothermal conditions.

To carry this work ahead, Chattopadhyay [179] performed experiments in a one-third scale water model tundish with higher thermal gradients. Step inputs of 5, 10, and 15 °C hotter water were introduced into the tundish through the shroud. Thermal gradients of 10–15 °C had a significant effect on the fluid flow pattern. Mathematical modeling was also performed and validated with the physical modeling experiments. During steady-state casting, i.e., when the liquid level remained constant in the tundish, buoyancy forces were generated because of the temperature differences. In the jet entry region, the inertial forces dominate because of high turbulence. The buoyancy forces become more prominent toward the ends of the tundish where the turbulence is lower. The flow patterns generated during a step-up condition are perhaps favorable for inclusion float out, since the lighter hot water tends to rise upward. On the other hand, a

step-down condition leads to stronger downward flows which in turn can worsen the liquid steel quality by entraining more inclusions into the SEN. Incorporation of flow modifiers like turbo-stops and impact pads mitigates the effects of the buoyancy forces. During a ladle change operation, the turbulence is very high because of the high refilling rate and this requires higher thermal gradients to affect the flow. For steady-state casting operations, a small temperature difference of 5 °C generated significant buoyancy-driven flows, whereas during a ladle change, a minimum of 10–15 °C temperature difference was needed to produce strong natural convection currents.

4.3.3. CONCLUSIONS

The advent of CFD and advances in computer "power" now available has created a revolution in the field of liquid metal processing. CFD has allowed researchers to challenge their limits and imaginations and to enter a world of essentially unlimited predictive capabilities. CFD models validated with actual experiments have proved to be reliable for the past three decades and will surely continue to be so. The future will surely be the development of three-dimensional multiphase mathematical simulations for each operation, starting from the blast furnace up to the mold, to final solidification. The motivation for this will be the continuing quest for a greater understanding of these processes, leading to improved product quality and process control, all made possible with an ever-increasing computational power and a decrease in computational costs.

REFERENCES

[1] S.V. Patankar, Numerical Heat Transfer and Fluid Flow, Taylor and Francis, New York, 1980, p. 15.
[2] B.E. Launder, D.B. Spalding, Lectures in Mathematical Models of Turbulence, Academic Press, New York, 1972.
[3] B.E. Launder, D.B. Spalding, Comput. Meth. Appl. Mech. Eng. 3 (1974) 269.
[4] V. Yakhot, S.A. Orszag, S. Thangam, T.B. Gatski, C.G. Speziale, Phys. Fluids A 4 (7) (1992) 1510–1520.
[5] T.-H. Shih, W.W. Liou, A. Shabbir, Z. Yang, J. Zhu, NASA TM 106721, 1994.
[6] K.-Y. Chien, AIAA J. 20 (1) (1982) 33–38.
[7] Y. Nagano, M. Tagawa, J. Fluids Eng. 112 (1990) 33–39.
[8] V.C. Patel, W. Rodi, G. Scheuerer, AIAA J. 23 (9) (1985) 1308–1319.
[9] W. Rodi, N.N. Mansour, J. Fluid Mech. 250 (1993) 509–529.
[10] B.E. Launder, B.I. Sharma, Lett. Heat Mass Transfer 1 (2) (1974) 131–138.
[11] S.V. Patankar, D.B. Spalding, Int. J. Heat Mass Transfer 15 (1972) 1787–1806.
[12] H.K. Versteeg, W. Malalasekera, An Introduction to Computational Fluid Dynamics: The Finite Volume Method, McGraw-Hill, Loughborough University, Loughborough, U.K., 1995.
[13] H.K. Versteeg, W. Malalasekera, An Introduction to Computational Fluid Dynamics—The Finite Volume Method, Pearson Education Ltd., Loughborough, U.K., 2007.
[14] R.I.L. Guthrie, A.G. Storey, in: AUS. I.M.M. Illawara Branch—B.F.A. Symposium, Wollongong, 1975, p. 30.
[15] A. Ghiglione, V. Giordano, A. Milani, G. Quintiliani, in: AUS. I.M.M. Illawara Branch—B.F.A. Symposium, Wollongong, 1975, p. 51.
[16] I. Muchi, Trans. Iron Steel Inst. Jpn. 7 (1967) 223.

[17] J. Yagi, I. Muchi, Trans. Iron Steel Inst. Jpn. 10 (1970) 392.
[18] M. Hatano, K. Kurita, H. Yamaoka, T. Yokoi, Tetsu-to-Hagane 68 (1982) 2369.
[19] R. Wartman, Stahl Eisen 95 (1975) 442.
[20] H. Kubo, T. Nishiyama, S. Taguchi, Kawasaki Steel Gillo 14 (1982) 134.
[21] J. Yagi, K. Takedaand, Y. Omori, Tetsu-to-Hagane 66 (1980) 1888.
[22] M. Hatano, K. Kurita, Tetsu-to-Hagane 66 (1980) 1898.
[23] M. Kuwabara, S. Takane, K. Sekido, I. Muchi, Tetsu-to-Hagane 77 (1991) 1593.
[24] T. Sugiyama, M. Sugata, Seitetu Kenkyu 34 (325) (1987) 34.
[25] K. Takatani, T. Inada, Y. Ujisawa, ISIJ Int. 39 (1) (1999) 15–22.
[26] K. Takatani, Tetsu-to-Hagane 74 (1988) 1546.
[27] C.W. Hirt, B.D. Nichols, N.C. Romero, in: SOLA—A Numerical Solution Algorithm for Transient Fluid Flows, Los Alamos Sci. Lab., Los Alamos, 1975LA-5852.
[28] J. Ohno, M. Tachimori, M. Nakamura, Y. Hara, Tetsu-to-Hagane 71 (1985) 34.
[29] N. Standish, P.J. Cambell, Trans. Iron Steel Inst. Jpn. 24 (1984) 709.
[30] M. Tachimori, J. Ohno, M. Nakamura, Y. Hara, Tetsu-to-Hagane 70 (1984) 2224.
[31] K. Uemura, T. Onoe, Tetsu-to-Hagane 71 (1985) S825.
[32] K. Kurita, T. Tanaka, Tetsu-to-Hagane 72 (1986) S81, Trans. Iron Steel Inst. Jpn. 26 (1986) B334.
[33] Y. Sawa, Y. Konishi, K. Takeda, S. Taguchi, H. Hamada, Y. Watanabe, T. Matsumoto, CAMP-ISIJ 1 (1988) 107.
[34] K. Kudoh, Y. Ono, H. Saito, Tetsu-to-Hagane 72 (1985) S825.
[35] Y. Seo, S. Taguchi, T. Fukutake, J.F. Elliot, Tetsu-to-Hagane 71 (1985) S68, Trans. Iron Steel Inst. Jpn. 25 (1985) B241.
[36] Y. Tomita, H. Okusu, M. Kono, CAMP-ISIJ 1 (1988) 79.
[37] K. Shibata, Y. Kimura, M. Shimizu, S.-i. Inaba, ISIJ Int. 30 (3) (1999) 208–215.
[38] T. Nouchi, M. Yasui, K. Takeda, ISIJ Int. 43 (2) (2003) 175–180.
[39] K. Nishioka, T. Maeda, M. Shimizu, ISIJ Int. 45 (5) (2005) 669–676.
[40] T. Fukutake, K. Okabe, Tetsu-to-Hagane 60 (1974) 607.
[41] T. Fukutake, K. Okabe, Trans. Iron Steel Inst. Jpn. 16 (1976) 309.
[42] K. Takatani, T. Inada, K. Takata, ISIJ Int. 41 (10) (2001) 1139–1145.
[43] S. Kumar, ISIJ Int. 45 (8) (2005) 1122–1128.
[44] J. Brannbacka, J. Torrkulla, H. Saxen, Ironmaking Steelmaking 32 (6) (2005) 479.
[45] M. Helle, H. Saxen, Ironmaking Steelmaking 33 (5) (2006) 407.
[46] X. Dong, A. Yu, J.-i. Yagi, P. Zulli, ISIJ Int. 47 (11) (2007) 1553–1570.
[47] J.G. Mathieson, J.S. Truelove, H. Rogers, Fuel 84 (2005) 1229.
[48] W.P. Hutny, G.K. Lee, J.T. Price, Prog. Energy Combust. Sci. 17 (1991) 373.
[49] Y.S. Shen, B.Y. Guo, A.B. Yu, D. Maldonado, P. Austin, P. Zulli, ISIJ Int. 48 (2008) 777.
[50] J.C. He, M. Kuwabara, I. Muchi, Tetsu-to-Hagané 72 (1986) 1847.
[51] A.S. Jamaluddin, T.F. Wall, J.S. Truelove, Ironmaking Steelmaking 13 (1986) 91.
[52] T. Suzuki, L.D. Smoot, T.H. Fletcher, P.J. Smith, Combust. Sci. Technol. 45 (1986) 167.
[53] Y.C. Guo, C.K. Chan, K.S. Lao, Fuel 82 (2003) 893.
[54] H. Aoki, H. Nogami, H. Tsuge, T. Miura, T. Furukawa, ISIJ Int. 33 (1993) 646.
[55] K. Takeda, F.C. Lockwood, ISIJ Int. 37 (1997) 432.
[56] R.J. Haywood, J.S. Truelove, M.J. McCarthy, in: Proceedings of Ironmaking Conference of AIME, ISS, Warrendale, PA, 1994, p. 437.
[57] R. Murai, M. Sato, T. Ariyama, ISIJ Int. 44 (2004) 2168.
[58] K. Goto, R. Murai, A. Murao, M. Sato, M. Asanuma, T. Ariyama, K. Goto, R. Murai, A. Murao, M. Sato, M. Asanuma, T. Ariyama, in: Proceedings of the International Blast Furnace Lower Zone Symposium, AusIMM, Wollongong, 2002, p. 1.1.
[59] S.W. Du, W.H. Chen, Int. Commun. Heat Mass Transfer 33 (2006) 327.
[60] H. Nogami, H. Yamaoka, K. Takatani, ISIJ Int. 44 (2004) 2150.
[61] B.Y. Guo, P. Zulli, H. Roger, J.G. Mathieson, A.B. Yu, ISIJ Int. 45 (2005) 1272.
[62] P. Prachethan Kumar, L.M. Garg, S.S. Gupta, Ironmaking Steelmaking 33 (1) (2006) 29–33.
[63] S.C. Lee, M.K. Shin, S. Joo, J.K. Yoon, Iron Steel Inst. Jpn. Int. 39 (1999) 319–328.

[64] S.C. Lee, M.K. Shin, S. Joo, J.K. Yoon, Iron Steel Inst. Jpn. Int. 40 (2000) 1073–1079.
[65] N.N. Viswanathan, M.N. Srinivasan, A.K. Lahiri, Iron Steel Inst. Jpn. Int. 38 (1998) 1062–1068.
[66] S. Pal, A.K. Lahiri, Metall. Mater. Trans. B 34B (2003) 103.
[67] S. Pal, A.K. Lahiri, Metall. Mater. Trans. B 34B (2003) 115.
[68] M.P. Davis, R.J. Dry, in: Ninth International Conference on CFD in the Minerals and Process Industries CSIRO, Melbourne, Australia, 10–12 December, 2012.
[69] M.P. Schwarz, M.P. Davis, in: Proceedings of the Guthrie Honorary Symposium, Montreal, Canada, 2011, p. 343.
[70] J.O. Hinze, AIChE J. 1 (1955) 289–295.
[71] F. Oeters, S. Orsten, Steel Res. 60 (1989) 145–150.
[72] D. Bhattacharjee, in: M. Isac (Ed.), Proceedings of the Roderick Guthrie Honorary Symposium, MMPC, Vaudreuil, Quebec, 2011, pp. 78–83.
[73] W.D. Munro, N.R. Amundson, Ind. Eng. Chem. 42 (1950) 1481.
[74] N.R. Amundson, Ind. Eng. Chem. 48 (1956) 26.
[75] C.W. Siegmund, W.D. Munro, N.R. Amundson, Ind. Eng. Chem. 48 (1956) 43.
[76] R.J. Schaefer, D. Vortmeyer, C.C. Watson, Chem. Eng. Sci. 29 (1974) 119.
[77] H. Yoon, J. Wei, M.M. Denn, AIChE J. 24 (1978) 885.
[78] P.E. Arce, O.M. Alfano, L.E. Arri, Rev. Latinoam. Trans. Calor. Mater. 6 (3) (1982) 99–112.
[79] N.R. Amundson, L.E. Arri, AIChE J. 24 (1978) 87.
[80] Y.K. Rao, P. Pichestapong, in: XVth CMMI Congress, Johannesburg, SAIMM, 1994, pp. 81–92.
[81] D.R. Paris, M.A. Laborde, Chem. Eng. J. 104 (2004) 35–43.
[82] D. Oymo, R.I.L. Guthrie, in: Proceedings of the 4th Process Technology Conference, 1984, pp. 45–52.
[83] Z. Lin, R.I.L. Guthrie, ISS Trans. 22 (1995) 67–73.
[84] K. Krishnapisharody, G. Irons, in: ICS 2008, 2008, pp. 367–374.
[85] M.A. Rhamdhani, G.A. Brooks, K.S. Coley, Metall. Mater. Trans. B 37B (2006) 1087–1091.
[86] G.A. Brooks, Y. Pan, D. Subagyo, K.S. Coley, Metall. Mater. Trans. B 36B (2005) 525–535.
[87] M.A. Rhamdhani, G.A. Brooks, K.S. Coley, Metall. Mater. Trans. B 36B (2) (2005) 203–227.
[88] R. Sambasivam, S.N. Lenka, F. Durst, M. Bock, S. Chandra, S.K. Ajmani, Metall. Mater. Trans. B 38B (2007) 45.
[89] Y. Tago, Y. Higuchi, ISIJ Int. 43 (2) (2003) 209.
[90] A.R. Naji Meidani, M. Isac, A. Richardson, A. Cameron, R.I.L. Guthrie, ISIJ Int. 44 (10) (2004) 1639–1645.
[91] V. Singh, J. Kumar, C. Bhanu, S.K. Ajmani, S.K. Dash, ISIJ Int. 47 (11) (2007) 1605–1612.
[92] M. Ersson, A. Tilliander, L. Jonsson, P. Jonsson, ISIJ Int. 48 (4) (2008) 377–384.
[93] M. Ersson, L. Hoglund, A. Tilliander, L. Jonson, P. Jonsson, ISIJ Int. 48 (2) (2008) 147–153.
[94] T. Plikas, J. Woloshyn, D. Johnson, Iron Steel Tech. 4 (11) (2007).
[95] D. Mazumdar, R.I.L. Guthrie, ISIJ Int. 35 (1) (1995) 1–20.
[96] M. Madan, D. Satish, D. Mazumdar, ISIJ Int. 45 (5) (2005) 677–685.
[97] K. Chattopadhyay, A. SenGupta, S.K. Ajmani, S.N. Lenka, V. Singh, Ironmaking Steelmaking 36 (7) (2009) 537–542.
[98] T. DebRoy, A.K. Majumdar, D.B. Spalding, Appl. Math. Model. 2 (1978) 146.
[99] J.S. Woo, J. Szekely, A.H. Castillejos, J.K. Brimacombe, Metall. Trans. B 21B (1990) 269.
[100] D. Mazumdar, R.I.L. Guthrie, Y. Sahai, Appl. Math. Model. 17 (1993) 255.
[101] D. Mazumdar, R.I.L. Guthrie, Metall. Trans. B 16B (1985) 83.
[102] A.H. Castillejos, M.E. Salcudean, J.K. Brimacombe, Metall. Trans. B 20B (1989) 603.
[103] J.S. Joo, R.I.L. Guthrie, Metall. Trans. B 23B (1992) 765.
[104] O.J. Ilegbusi, J. Szekely, ISIJ Int. 30 (1990) 731.
[105] P. Jönsson, L. Jonsson, Scand. J. Metall. 24 (1995) 194.
[106] J.L. Xia, T. Ahokainen, Scand. J. Metall. 32 (2003) 211.
[107] H. Turkoglu, B. Farouk, ISIJ Int. 31 (1991) 1371.
[108] S.T. Johansen, F. Boysan, Metall. Trans. B 19B (1988) 755.
[109] M. Neifer, S. Rödl, D. Sucker, Steel Res. 64 (1993) 54.

[110] D. Mazumdar, R.I.L. Guthrie, ISIJ Int. 34 (1994) 384.
[111] D. Guo, G.A. Irons, Metall. Trans. B 31B (2000) 1457.
[112] K. Nakanishi, J. Szekely, Trans. Iron Steel Inst. Jpn. 15 (1975) 522.
[113] K. Shirabe, J. Szekely, Trans. Iron Steel Inst. Jpn. 23 (1983) 465.
[114] H. Tozawa, Y. Kato, K. Sorimachi, T. Nakanishi, ISIJ Int. 39 (1999) 426.
[115] Y. Miki, Y. Shimada, B.G. Thomas, A. Denissov, Iron Steelmaker 24 (1997) 31.
[116] A.K. Sinha, Y. Sahai, ISIJ Int. 33 (1993) 556.
[117] D.-Y. Sheng, M. Söder, P. Jönsson, L. Jonsson, Scand. J. Metall. 31 (2002) 134.
[118] M. Söder, P. Jönsson, J. Alexis, Scand. J. Metall. 31 (2002) 210.
[119] L.T. Wang, Q.W. Zhang, S.H. Peng, Z.B. Li, ISIJ Int. 45 (3) (2005) 331–337.
[120] Y.-J. Kwon, J. Zhang, H.-G. Lee, ISIJ Int. 48 (7) (2008) 891–900.
[121] K. Krishnapisharody, G.A. Irons, Metall. Mater. Trans. B 38B (2007) 377.
[122] K. Krishnapisharody, G.A. Irons, ISIJ Int. 48 (12) (2008) 1807–1809.
[123] B. Li, H. Yin, C.Q. Zhou, F. Tsukihashi, ISIJ Int. 48 (12) (2008) 1704–1711.
[124] C.-M. Fan, W.-S. Hwang, ISIJ Int. 40 (11) (2000) 1105–1114.
[125] H.-J. Odenthal, H. Pfeifer, M. Klaas, Steel Res. 71 (6–7) (2000) 210–219.
[126] D.Y. Sheng, L. Jonsson, Metall. Mater. Trans. B 31B (2008) 867.
[127] J.H. Ahn, J.-E. Lee, J.K. Yoon, in: 2nd International Conference on Processing Materials for Properties TMS, 2000.
[128] S.K. Sinha, K.M. Godiwalla, D.K. Shaw, C.S. Sivaramakrishnan, Scand. J. Metall. 30 (2001) 103–107.
[129] Y. Sahai, The Brimacombe Memorial Symposium, 2000, pp. 631–641.
[130] A. Robert, D. Mazumdar, Steel Res. 72 (3) (2001) 97–105.
[131] S.P. Ferro, R.J. Principe, M.B. Goldschmit, Metall. Mater. Trans. B 32B (2001) 1185.
[132] P. Gardin, M. Brunet, J.F. Domgin, K. Pericelous, Appl. Math. Model. 26 (2002) 323–336.
[133] P.K. Jha, S.K. Dash, Int. J. Numer. Meth. Heat Fluid Flow 14 (8) (2004) 953–979.
[134] P.K. Jha, R. Ranjan, S.S. Mondal, S.K. Dash, Int. J. Numer. Meth. Heat Fluid Flow 13 (8) (2003) 964–996.
[135] R. Pradeshi, S. Basak, A.K. Singh, B. Basu, V. Mahashabde, S.K. Roy, S. Kumar, ISIJ Int. 44 (9) (2004) 1534–1540.
[136] A. Kumar, S.C. Koria, D. Mazumdar, ISIJ Int. 44 (8) (2004) 1334–1341.
[137] A. Ramos-Banderas, R. Sanchez-Perez, R.D. Morales, J. Palafox-Ramos, L. Demedices-Gracia, M. Diaz-Cruz, Metall. Mater. Trans. B 35B (2004) 449.
[138] A. Tripathi, S.K. Ajmani, ISIJ Int. 45 (11) (2005) 1616–1625.
[139] M.J. Cho, I.C. Kim, ISIJ Int. 46 (10) (2006) 1416–1420.
[140] X. Huang, B.G. Thomas, Metall. Mater. Trans. B 27B (1996) 617.
[141] M. Zorzut, F. Vecchiet, N. Kapaj, A. Paderno, BHM, 152. Jg. (2007), Heft 11.
[142] N. Alkishriwi, M. Meinke, W. Schröder, Comput. Fluid. 35 (10) (2006) 1126–1136, Institute of Aerodynamics.
[143] O. Davila, R.D. Morales, L. Gracia-Demedices, Metall. Mater. Trans. B 37B (2006) 71.
[144] R. Sankanarayan, R.I.L. Guthrie, Ironmaking Steelmaking 29 (2002) 147–153.
[145] R. Sankanarayan, R.I.L. Guthrie, in: ISS Steelmaking Conference, vol. 75, 1992, pp. 655–664.
[146] P. Vayrynen, S. Vapalahti, S. Louhenkilpi, M. Clark, T. Wagner, in: STEEL SIM 2007, Austria, 2007.
[147] I. Hamil, T. Lucas, in: Proceedings of TMS Annual Meeting on "Fluid Flow Phenomena in Metals Processing" San Diego, February 28–March 4, 1999, pp. 279–286.
[148] S. Joo, R.I.L. Guthrie, Can. Metall. Quart. 30 (1991) 261.
[149] J. Hulstrung, M. Zeimes, A. Au, W. Oppermann, G. Redusch, Steel Res. 76 (1) (2005) 59–63.
[150] G. Solorio-Diaz, R.D. Morales, J. Palafox-Ramos, A. Ramos-Banderas, ISIJ Int. 45 (8) (2005) 1129–1137.
[151] L. Zhang, S. Taniguchi, K. Cai, Metall. Mater. Trans. B 31B (2000) 253.
[152] B.G. Thomas, H. Bai, in: 18th Process Technology Division Conference Proceedings, vol. 18, Iron and Steel Society, Warrendale, PA, 2001, pp. 895–912.
[153] H. Solhed, L. Jonsson, P. Jonsson, Metall. Mater. Trans. B: Process Metall. Mater. Process. Sci. 33B (2) (2002) 173–185.

[154] H. Solhed, L. Jonsson, Scand. J. Metall. 32 (1) (2003) 15–32.
[155] S. Lopez-Ramirez, R.D. Morales, J.A. Romero Serrano, Numer. Heat Transfer A 37 (2000) 69–86.
[156] R. Schwarze, F. Obermeier, D. Janke, Model. Simul. Mater. Sci. Eng. 9 (2001) 279–287.
[157] R.D. Morales, M. Diaz-Cruz, J. Palafox-Ramos, S.L. Ramirez, J. De, J. Barreto Sandoval, Steel Res. 72 (1) (2001) 11–16.
[158] Y. Bao, W. Jang, B. Xu, H. Zhang, J. Univ. Sci. Technol. Beijing 9 (1) (2002) 13.
[159] J. Palafox-Ramos, J. De, J. Barreto, S.L. Ramirez, R.D. Morales, Ironmaking Steelmaking 28 (2) (2001) 101–109.
[160] R.D. Morales, S.L. Ramirez, J. Palafox-Ramos, D. Zacharias, Ironmaking Steelmaking 28 (1) (2001) 33–43.
[161] K.H. Tacke, J.C. Ludwig, Steel Res. 58 (1987) 262–270.
[162] A.K. Sinha, Ph.D. Thesis, The Ohio State University, USA, 1990.
[163] H. Nakajima, F. Sebo, S. Tanaka, L. Dumitru, D.J. Harris, R.I.L. Guthrie, in: Steelmaking Conference Proceedings, ISS-AIME, vol. 69, 1986, pp. 705–716.
[164] G.S. Diaz, R.D. Morales, J. Palafox-Ramos, L.G. Demedices, A.R. Banderas, ISIJ Int. 44 (6) (2004) 1024–1032.
[165] Q. Hou, Z. Zou, ISIJ Int. 45 (3) (2005) 325–330.
[166] G.S. Diaz, R.D. Morales, A.R. Banderas, Int. J. Heat Mass Transfer 48 (2005) 3574–3590.
[167] S. Chakraborty, Y. Sahai, Metall. Trans. B 23B (1992) 153–167.
[168] S. Joo, J.W. Han, R.I.L. Guthrie, Metall. Matter. Trans. B 24B (1993) 767–777.
[169] C. Damle, Y. Sahai, ISIJ Int. 36 (1996) 681–689.
[170] M. Alizadeh, H. Edris, A. Shafyei, J. Iron Steel Res. Int. 15 (2) (2008) 7–13, 22.
[171] D.Y. Sheng, L. Jonsson, Investigation on the Convection Pattern of Liquid Steel in the Continuous Casting Tundish by Theoretical Analysis, Water Model Experiment and CFD Simulation, MEFOS, Lulea, Sweden, 2011.
[172] Baosteel Group Co., Company Publications, Numerical simulation of the coupled fluid flow and heat transfer and optimization of flow control devices in a six-strand tundish, Technical Report, 2005, pp. 12–29, http://www.baosteel.com/group_e/07press/ShowArticle.asp?ArticleID=40.
[173] R.D. Morales, J. de J. Barreto, S. López-Ramirez, J. Palafox-Ramos, M. Diaz-Cruz, Model. Simul. Mater. Sci. Eng. 8 (2000) 781–801.
[174] A. Braun, M. Warzecha, H. Pfeifer, Metall. Mater. Trans. B 41B (2010) 549–559.
[175] Y. Miki, B.G. Thomas, Metall. Mater. Trans. B 30B (1999) 639–654.
[176] D.Y. Sheng, L. Jonsson, Metall. Mater. Trans. B 30B (1999) 979–985.
[177] D.Y. Sheng, L. Jonsson, Metall. Mater. Trans. B 31B (2000) 867–875.
[178] S.K. Ray, M. Isac, R.I.L. Guthrie, M. Gagne, in: AISTech—Iron and Steel Technology Conference Proceedings, vol. 1, 2009, pp. 1151–1162.
[179] K. Chattopadhyay, Modelling of Transport Phenomena for Improved Steel Quality in a Delta Shaped Four Strand Tundish, Ph.D. Thesis, McGill University, Montreal, Canada, 2011.

CHAPTER 4.4

Solidification

Mihaiela Isac and Roderick I.L. Guthrie
McGill Metals Processing Centre (MMPC), Montreal, Canada

Melting and solidification phenomena can be very complex, at both the macroscopic and the microscopic levels. In this section, we deal with solidification processes in molten metals, as they freeze against a solid substrate in near net-shape casting operations, or against a molten lubricating film of slag in conventional continuous casting machines. However, it is appropriate to first mention the fact that perfect thermal contact between liquid and solid phases is rarely established, owing to the presence, at the microscale, of surface imperfections and entrapped gases. A substrate taken at high magnification is presented in Figure 4.4.1a, while the bottom surface of a 5-mm thick aluminum alloy sheet, cast isokinetically on that horizontal surface (i.e., no relative motion), is shown in Figure 4.4.1b.

The important things to notice are the roughness of the sand-blasted surface of copper and the much smoother bottom surface of the aluminum sheet that has formed on that same copper surface. If one looks very carefully at the very flat bottom surface of the aluminum, it is possible to see what can be likened to as a few fir trees ($\sim 261/mm^2$), where the aluminum was presumably attached to some of the substrate's higher protuberances. Evidently, when the alloy is freezing, only small parts are in direct contact with the substrate, while the majority of the freezing substrate has to lose heat by conduction of heat through a 2–20-μm thick gas film, as depicted in Figure 4.4.2.

Looking at the bottom surface of the cast aluminum, one can see that these "fir trees" tend to be in the center of individual grains. These grains meet at the boundaries of other grains, where second phase particulates abound.

These spikes at, or near, the grain centers on the bottom surface of the aluminum strip are also accompanied by many small macroscopic bumps on the bottom surfaces. These, we attribute to a pulling away of the forming strip from the copper surface, owing to expansion of the gas at the interfacial substrate.

This seems to be confirmed using evidence obtained when using interfacial gases other than ambient air, or even preheated air. For instance, if one uses pure oxygen as the interfacial gas, as per the equipment shown in Figure 4.4.3, and uses shot-peened copper substrates such as those shown in Figure 4.4.4, then there can be a remarkable difference in the appearance of the bottom surfaces of aluminum strip cast onto the four substrates, as shown by comparing Figures 4.4.5 and 4.4.6.

Treatise on Process Metallurgy, Volume 2
http://dx.doi.org/10.1016/B978-0-08-096984-8.00010-0
© 2014 Elsevier Ltd.
All rights reserved.

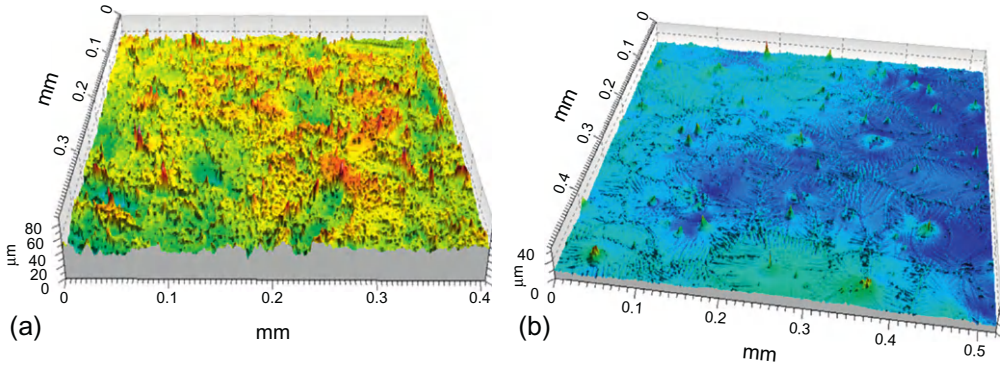


Figure 4.4.1 Three-dimensional image of AA6111 aluminum strip's bottom surface (b), cast onto the copper mold substrate (a). Note the outgrowths, or protuberances, from the strip's bottom surface (261/mm^2).

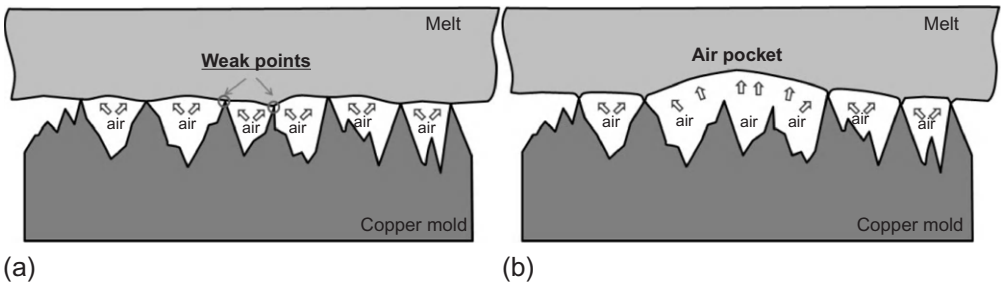


Figure 4.4.2 Proposed mechanism for dimpled surfaces generated by the formation of air pockets. (a) Entrapped air starts to expand and (b) melt loses contact with parts of mold, forming air pockets.

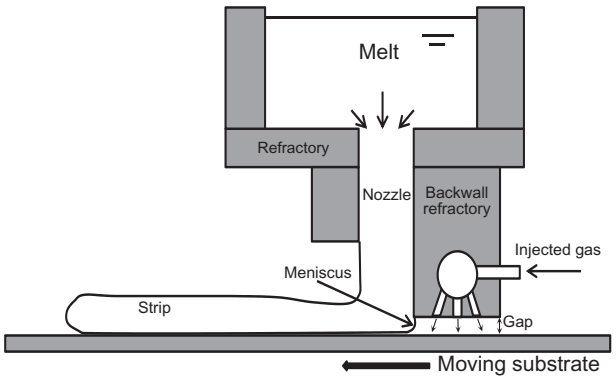


Figure 4.4.3 Configuration of backwall. Injected gas was introduced through orifices set in the bottom of the backwall.

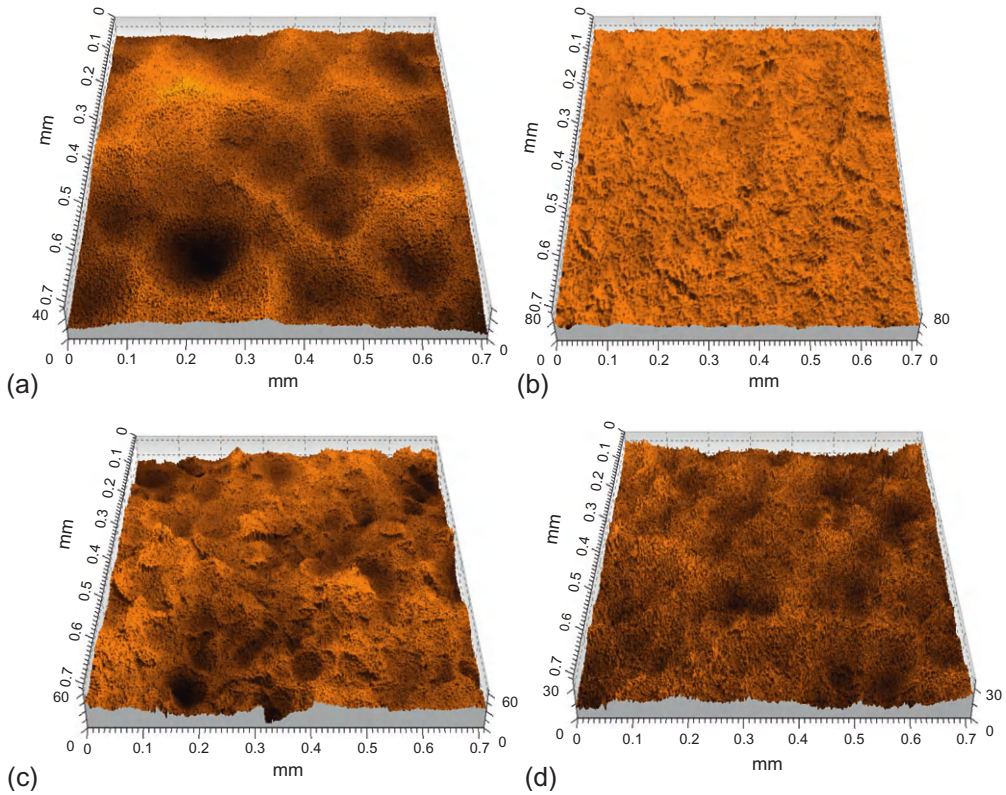


Figure 4.4.4 Surface images of sample areas of the copper block inserts in the copper substrate, sand blasted by different materials: (a) by steel shot, (b) by aluminum oxide, (c) by garnet grit, and (d) by stainless steel shot.

Figure 4.4.5 shows the effect of using preheated air, while Figure 4.4.6 illustrates the effect of an oxygen flow rate, sufficient to displace air, but insufficient to cause ingress of gas at the backwall meniscus. The reason for the better appearance of the surface in Figure 4.4.6 is due to the consumption of some of the oxygen molecules, which react with the molten aluminum, to form a coherent aluminum oxide layer on the strip. This loss of oxygen molecules compensates for the tendency of the remaining gas to expand, once and when the moving hot metal first contacts the room temperature substrate, moving at the same speed (isokinetically) as the liquid metal.

Other gases, such as helium or hydrogen, lead to increased heat extraction rates. It is interesting that these are not as high as would be expected based on relative gaseous thermal conductivities. Most commercial belt casting operations, such as the Hazelett twin-belt casters used in the aluminum, lead, zinc, and copper industries, use plasma-coated belt technologies to cut down on initial heat transfer rates. Similarly, one can coat the

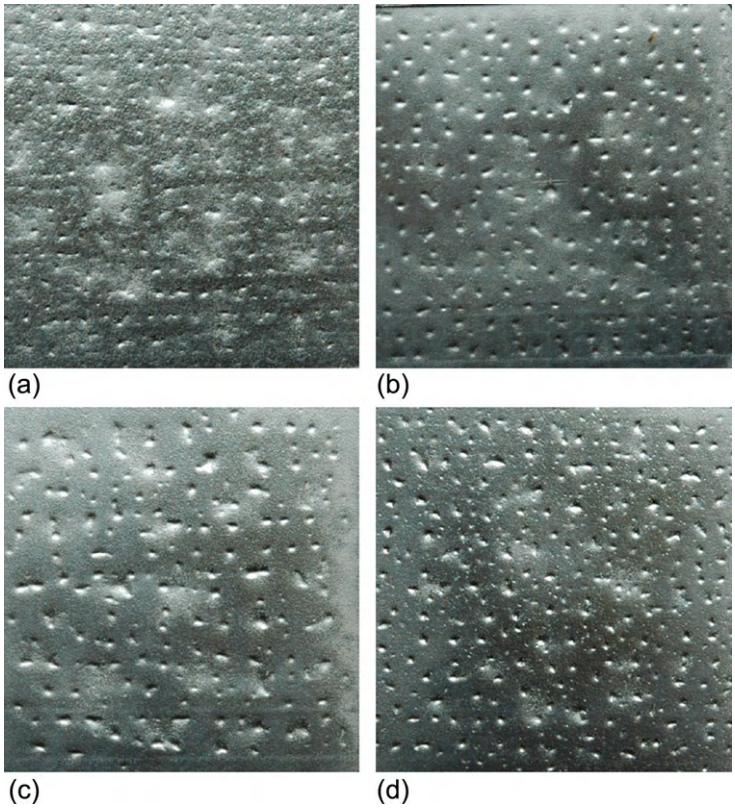


Figure 4.4.5 Photos of bottom surfaces of aluminum strip cast using preheated air in the meniscus region. (a) On Surface-I, (b) on surface-II, (c) on surface-III, and (d) on surface-IV.

steel belts with high flash point temperature oil compounds (e.g., rapeseed oil), or with graphite spray coatings. For the latter, the bottom surfaces of the cast strips are much improved, but there tends to be a loss in heat extraction capability.

Figure 4.4.7 compares the heat fluxes registered by the exposed shot blast copper surfaces versus the instantaneous heat fluxes obtained when using a graphite-coated belt. As seen, they all exceed the heat extracted by a graphite-coated belt, even though the surface topology of the latter looks to be equivalent to an uncoated belt. We therefore assume that the liquid metal/solid metal contact at the points in contact on the surface is less good, and less adherent. This would fit with the idea that graphite diminishes direct contact between the hot metal and the belt, or substrate.

The normal approach, until now, and reported in 4.4.2.1 of this section, has been to treat solidification of a steel slab or a billet against a continuous casting copper mould wall, by invoking equations of the form

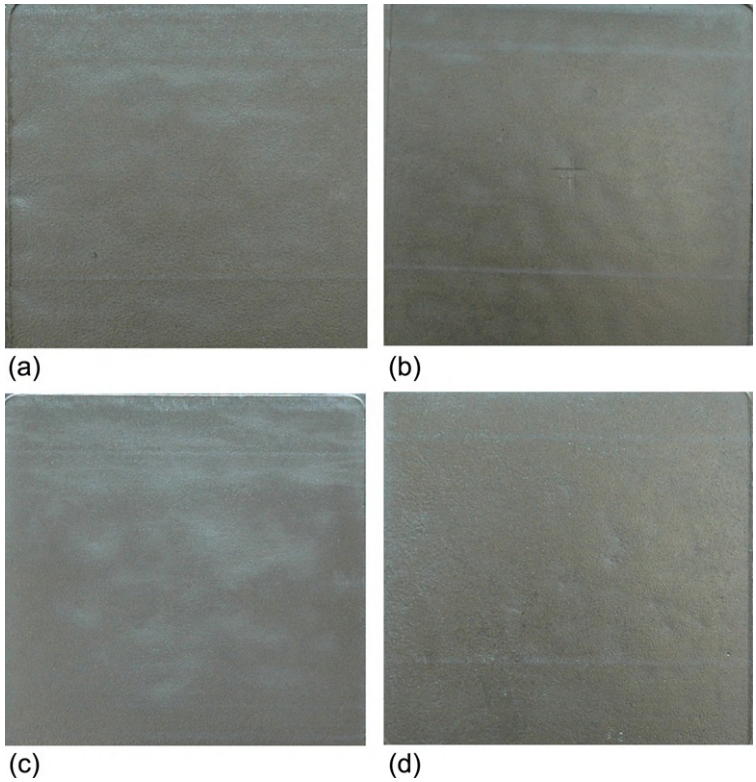


Figure 4.4.6 Photos of aluminum strip bottom surfaces, cast within oxygen atmosphere at meniscus region. (a) On Surface-I, (b) on surface-II, (c) on surface-III, and (d) on surface-IV.

$$Q = hA(\theta_{\text{steel surface}} - \theta_{\text{water}}) = -kA\frac{(\theta_{\text{mp}} - \theta_{\text{w}})}{\Delta}x = \rho LA\frac{\mathrm{d}x}{\mathrm{d}t} \qquad (4.4.4.1)$$

Here, Q represents the average rate of heat being taken up by the cooling water (e.g., kcal/s, or kJ/s, or kW) flowing through the copper mold against which steel is being cast. This heat output is set equal to the product of h (a lumped heat transfer coefficient, which bundles all the thermal resistances at the mold–metal interface, surface roughness of copper, interfacial gas, solid and liquid lubricating slag moving down the oscillating copper mold, air-gap thickness, radiant heat transfer, and conductivities of the various phases), A (the cross-sectional area), and the overall temperature driving force is ($\theta_{\text{steel at wall}} - \theta_{\text{water}}$). It is clear that h is an empirical, and potentially complex, function of many possible variables. Under quasi-steady-state conditions, these first two terms are also equal to the amount of heat being conducted through the solidified (pure) metal, and this, in turn, is equal to the heat released as latent heat evolves as the frozen steel at the solid/

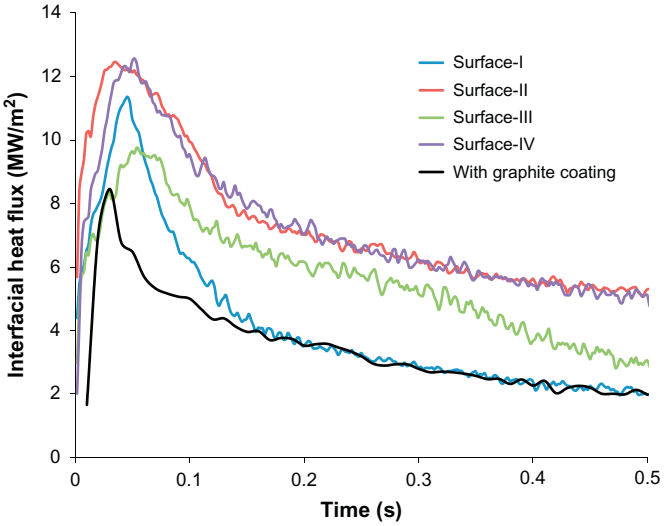


Figure 4.4.7 Interfacial heat flux curves when casting aluminum alloy strips on a copper substrate, in the presence of an oxygen atmosphere in the meniscus region.

liquid interface. This interface moves into the melt at a speed of dx/dt. The problem with this approach is that it does not get to the heart of a given solidification process. The "h" factor, or overall heat transfer coefficient, is an empirical constant deriving from heat flux measurements or rates of solidification, etc. Finally, the average Q can be calculated very conveniently, as it is equal to $M_w C[\Delta\theta]$, where M_w represents the mass flow rate of water, C its heat capacity, and $\Delta\theta$, the bulk rise in water temperature.

We will return to this a little later, but first we wish to introduce the reader to the "isokinetic contact" of a moving liquid metal, onto either a 1-cm thick copper chill mould slab, or onto a 1-mm thick, water-cooled steel belt, running below. Fundamental heat transfer analyses have been performed by Li *et al.* [1], in which we have modeled this 1D heat conduction process from first principles, using the laws of heat conduction and solidification through the aluminum, the interfacial gas phase, and the underlying cold copper substrate. In the mathematical model of interfacial heat transfer, the surface profile was simplified to have a pyramid shape, as shown in Figure 4.4.8. Only the pyramid tips contacted the melt, at their points.

Figure 4.4.9 illustrates the contact of the liquid metal with microscopic peaks on the solid substrate, resulting in conduction of heat through the roughened copper surface. This is in contact with the molten metal at a frequency of about 261 points per square millimeter, according to Figure 4.4.1b. Thermal conduction of heat through the remainder of the gas space between the points of direct contact to the cold copper substrate accounts for the remainder of the heat extracted. Note that radiation is negligible versus

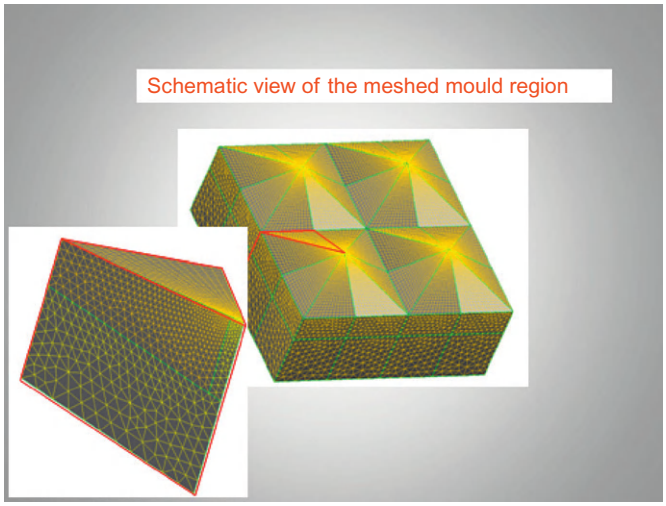


Figure 4.4.8 A schematic view of an idealized mold surface for the 3D mathematical model, illustrating the type of meshing used for predicting interfacial heat transfer fluxes from first principles. A segment of the trapezoidal pyramid for the computational mathematical model, making the assumption of symmetrical conduction of heat, is shown on the left of this figure.

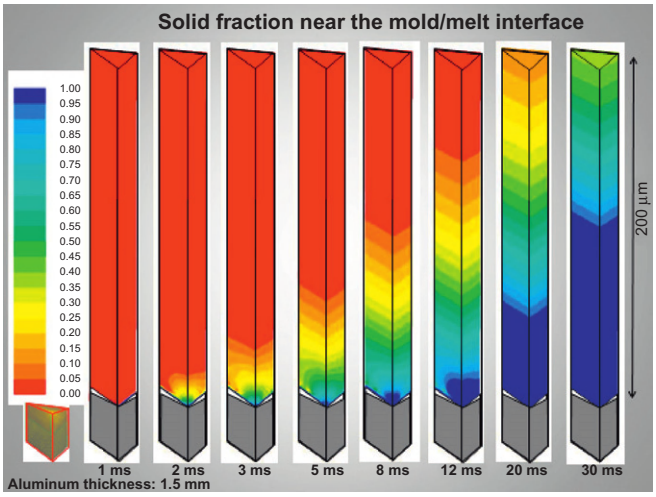


Figure 4.4.9 *Ab initio* computations of the first moments of solidification of aluminum alloy strip being cast, isokinetically, on a thick copper substrate. The copper surface comprises an array of rectangular pyramids, whose peaks contact the melt at discrete points, while the interfacial gas conducts the bulk of the heat from the freezing metal into the copper substrate.

the amount of heat transferred by conduction at these micron level interactions. Similarly, natural convection is nonexistent, again given the few microns of gap thickness. In this fundamentally new approach, aimed at quantifying and learning more about what is exactly happening at a metal interface contacted by a liquid metal (aluminum), we measure instantaneous heat fluxes into the mold interface, using instrumented thermocouples and the Inverse Heat Conduction Problem, or IHCP, solution, to compute instantaneous heat fluxes at the substrate interface. We match these against predicted freezing rates, to determine what is precisely happening at the metal–mold interface. In the present case, we are assuming that we have isokinetic feeding of liquid metal onto a horizontal moving substrate. As such, one has simple, one-dimensional, conduction of heat through a (moving) liquid metal to a cold, moving, "semi-infinite" substrate, absorbing heat from the metal above. As such, the relevant form of the 3D transient heat conduction equation for the liquid metal requiring solution is:

$$\rho C_{\mathrm{p}} \frac{\partial T}{\partial t} = k\left(\frac{\partial^2 T}{\partial x^2} + \frac{\partial^2 T}{\partial y^2} + \frac{\partial^2 T}{\partial z^2}\right) + \frac{\partial(\rho L f_{\mathrm{S}})}{\partial t} \qquad (4.4.4.2)$$

Equivalent equations for the gas and copper phases apply, but for them, they have no source terms requiring solution, so the last term is zero for those phases, and one is solving merely for unsteady-state conduction of heat through the gas phase and the copper substrate, taking into account the topology of the idealized copper surface. As anticipated, increasing the number of contact points per unit area leads to a predicted increase in the *ab initio* interfacial heat flux predictions. When the number of contact points was $268/\mathrm{mm}^2$, the initial interfacial heat flux recorded is predicted to be $7.7\ \mathrm{MW/m}^2$, whereas if the number of contact points increased to $566/\mathrm{mm}^2$, the initial heat flux would be predicted to increase to $4.4\ \mathrm{MW/m}^2$. The apex heights of the mold pyramids also have a great effect on interfacial heat fluxes. Decreasing the pyramid height from 6 to 4.5 μm is predicted to lead to an increase of initial heat fluxes, from 7.7 up to $10.2\ \mathrm{MW/m}^2$, owing to a reduction in the volume of entrapped gas. This "interfacial gas" is largely responsible for promoting the interfacial thermal resistance in all casting operations. During the first moments of solidification, one sees from the predictions that heat fluxes are at a maximum, and that solidification is initiated at the points of contact with the copper substrate. These nucleation spots grow radially outward and connect with each other after about 30 ms. After that, the bottom surface of the forming strip is fully coherent and any blemishes or imperfections will remain. The remainder of the strip is fully solid after about 2–3 s, in keeping with our data.

We have extended this analysis, using our mathematical model, and tuning the results against the carefully measured experimental heat fluxes, to evaluate the evolution of an interfacial "air gap" during initial melt contact.

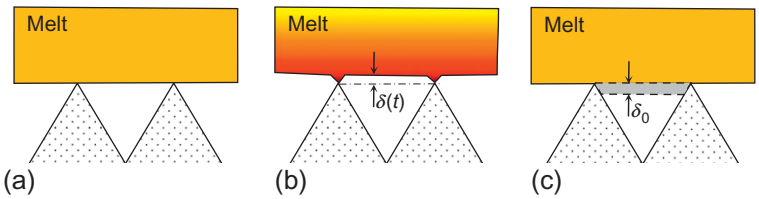


Figure 4.4.10 Evolution in the interfacial gas layer.

Thus the problem of how to conveniently model the air-gap evolution became a critical question in predicting the whole heat transfer event from first principles. In Figure 4.4.10a, we see the melt "resting" on the copper substrate, while in Figure 4.4.10b, the melt is freezing and moving upward. We denote $\delta(t)$ to represent the time-dependent increase in distance of the strip from the substrate caused by evolution of the "air gap."

A new method for modeling the air layer evolution had to be developed, in which the melt bottom surface was maintained at the same level at zero contact time, even though we recognize that the strip is lifting off the copper surface. However, by selecting a thin layer, thickness δ_0, within an entrapped air valley, we allow the real size of the air layer to become $\delta_0+\delta(t)$, at $t=t$, as per Figure 4.4.10b. During air-gap evolution, we only consider the size of this air layer. That means, at $t=0$, $\delta(t)=0$ and the air layer is δ_0, as in Figure 4.4.10(c). According to the theory of coordinates transformation, the physical domain of the air layer, $\delta_0+\delta(t)$, can be transformed into a computational domain by writing; $x'=\frac{\delta_0+\delta(t)}{\delta_0}x$, $y'=y$, $z'=z$, where x', y', z' are the coordinates in the physical domain and x, y, z are the coordinates in computational domain, x' is the vertical direction. So, for transient conduction through the air gap,

$$\frac{\partial\left(\rho C_p T\right)}{\partial t}=\frac{\partial}{\partial x'}\left(k\frac{\partial T}{\partial x'}\right)+\frac{\partial}{\partial y'}\left(k\frac{\partial T}{\partial y'}\right)+\frac{\partial}{\partial z'}\left(k\frac{\partial T}{\partial z'}\right) \tag{4.4.4.3}$$

or

$$\frac{\partial\left(\rho C_p T\right)}{\partial t}=\frac{\partial}{\partial x}\left(k\left(\frac{\delta_0}{\delta_0+\delta(t)}\right)^2\frac{\partial T}{\partial x}\right)+\frac{\partial}{\partial y}\left(k\frac{\partial T}{\partial y}\right)+\frac{\partial}{\partial z}\left(k\frac{\partial T}{\partial z}\right) \tag{4.4.4.4}$$

In this way, the general heat transfer equation for the air layer, $\delta_0+\delta(t)$, seen in Equation (4.4.4.3), can be transformed into Equation (4.4.4.4). It can be seen that Equation (4.4.4.4) is similar to Equation (4.4.4.2), but the gas thermal conductivity has anisotropic characteristics, as seen in Equation (4.4.4.5), and the computational domain is in the layer of δ_0. Similarly, the effect of air layer growth on the heat transfer process can be predicted using the general Equation (4.4.4.2), by considering anisotropic

thermal conductivity characteristics within the layer δ_0. This is preferable to considering the melt boundary to be moving upward and allows one to retain a static computational mesh during the iterative process, greatly simplifying the modeling.

$$k_{\text{air layer}} = \begin{Bmatrix} k\left(\dfrac{\delta_0}{\delta_0+\delta(t)}\right)^2 & 0 & 0 \\ 0 & k & 0 \\ 0 & 0 & k \end{Bmatrix} \tag{4.4.4.5}$$

For these computations, only the first second of contact time was modeled. Also, because of the symmetry of the computational domain, only one-eighth of the heat transfer related to one pyramid region was modeled. At all the other surfaces, the heat flux was set to zero because of symmetry. The total cell number was about 61,000. The time step was set as 1 ms, and the convergence criterion of the temperature field's residual was less than 1×10^{-15}. The predictions were made by the ANSYS FLUENT V12 software package.

Figure 4.4.11 shows a plot of the predicted interfacial heat flux versus that measured, using a very sensitive "in-house" thermocouple arrangement. It can be seen that the predicted heat flux not taking into account changes in interfacial thickness of the "air gap" was significantly higher than the experimental result. It predicts that the 1.5-mm thick aluminum melt finishes solidifying in 0.2 s. This leads to a slope change in

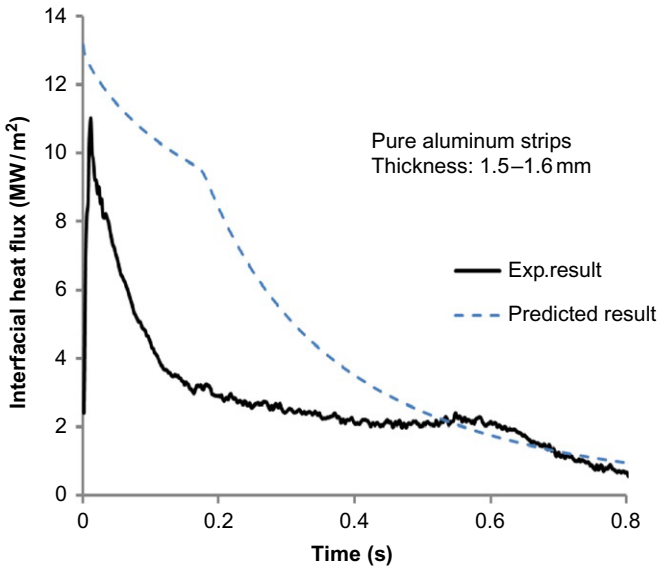


Figure 4.4.11 Comparison of predicted heat fluxes and experimental heat fluxes versus contact time.

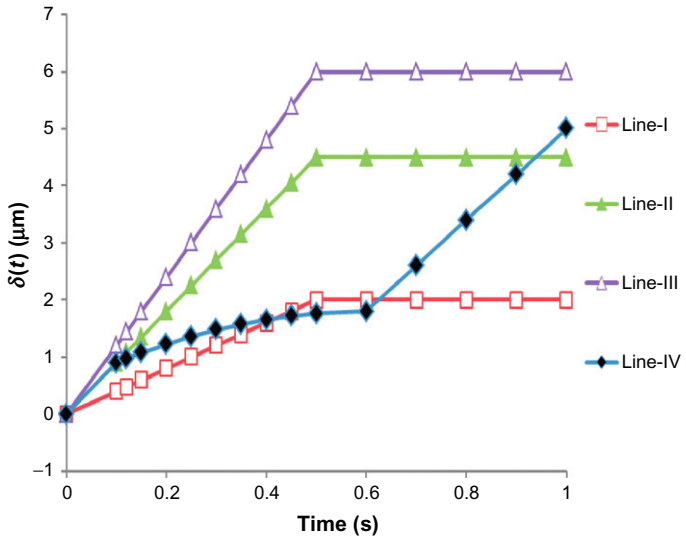


Figure 4.4.12 Various proposed curves for the growth of an air gap, following the first moment of melt contact with the copper chill substrate. These were used to predict experimental heat fluxes for comparison against actual heat fluxes measured. The results are shown in Figure 4.4.13.

instantaneous heat fluxes at that time. However, in practice, it takes about 0.6 s for such a strip to solidify. The maximum heat flux obtained in experiments was about 11.0 MW/m^2, which occurred at 6–8 ms following initial contact. This delay is related to the response time of the thermocouple. By mathematical modeling, at time $t=0$, the predicted interfacial heat flux was about 13 MW/m^2, which is close to the experimental result. It was verified that at $t=0$, the melt contacts the chill mold on the contact points, and the melt's bottom surface was smooth, without cone-shaped outgrowths. Through trial and error, we determined that the air gap increased slowly by 1.5 μm for the first 600 ms, after which the strip started to separate from the substrate, as per the line 4 scenario, in Figure 4.4.12.

4.4.1. APPLICATION OF TEXTURED COPPER SUBSTRATES FOR ENHANCING HEAT FLUXES

According to the research work above, smoothing the mold surface by reducing the pyramid height will reduce the amount of entrapped air at the melt/mold interface and can increase the interfacial heat transfer greatly. To test this hypothesis, and to obtain high interfacial heat fluxes while eliminating air pockets on the copper surface, we have researched various macroscopically textured copper mold surfaces. The copper blocks were stamped with regular triangular grooves. The grooves cross each other, at 45° to

the casting direction. All the grooves were connected together to form channels for accommodating or expelling the entrapped air at the melt–mold interfaces. The copper mold surfaces were ground down to about 0.3 μm, so as to form near perfectly smooth upper surfaces. This reduced the thickness of the interfacial air layer gap between the melt and the mold. Various patterns of grooves were made: in pattern (d), the depths of the grooves were 0.20 mm; while in pattern (e), the depths were 0.25 mm. The distance of neighboring notches in both pattern (d) and pattern (e) was 1.52 mm (Figures 4.4.13 and 4.4.14).

Figure 4.4.15 gives the interfacial heat flux obtained in subsequent casting experiments. To evaluate the interfacial heat fluxes cast onto these textured copper molds, the result of heat fluxes when casting on a sand-blasted copper mold coated with graphite spray is also given as a reference point. The aluminum strip thicknesses were all 5.0 mm, and casting temperatures 680 °C. When the melt was cast onto a sand-blasted copper substrate with the graphite coating, within 0.03 s the interfacial heat flux reached a peak value of about 4.4 MW/m^2, after which the heat flux started to decrease slowly.

When the melt was cast onto the textured copper substrate, pattern (e), the interfacial heat flux reached a maximum of 21 MW/m^2 at 0.006 s, after which the heat flux decreased quickly to about 15 MW/m^2; the transient heat flux then slowed as latent heat was released in the melt mushy zone. At 0.18 s, the interfacial heat flux suddenly dropped to <5 MW/m^2, no doubt because of contraction and deformation of the strip during solidification, followed by detachment of the strip from the copper substrate surface.

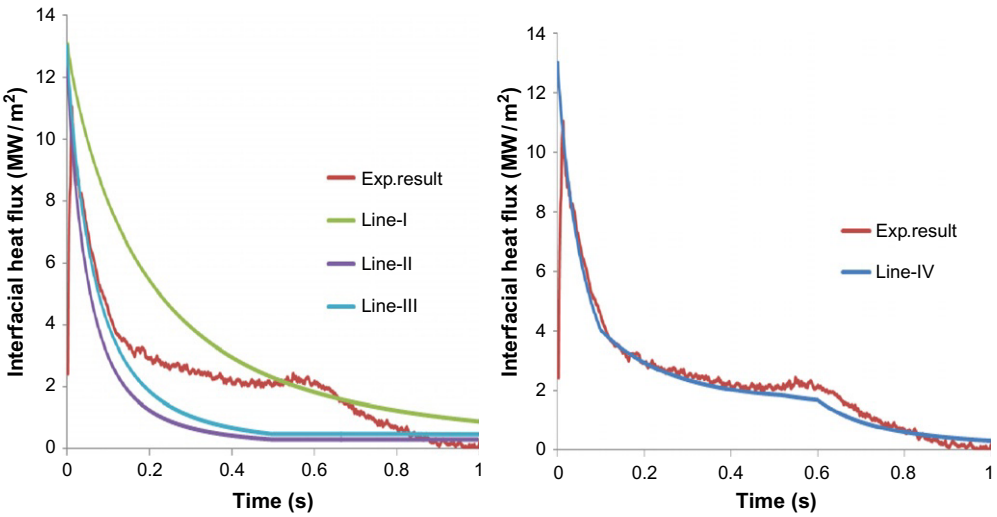


Figure 4.4.13 Predicted interfacial heat fluxes compared with the experimentally observed value, plotted versus contact time of strip on the surface of the substrate.

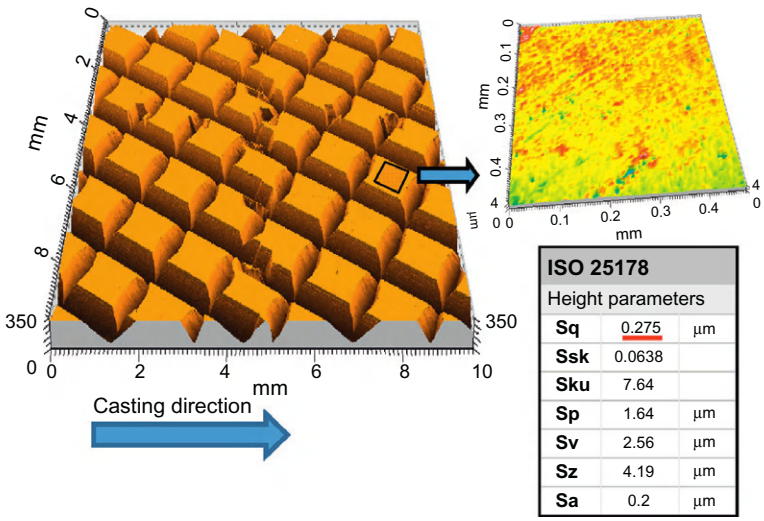


Figure 4.4.14 A 3D image of a textured copper mold surface, taken by a Nanovea 3D Profilometer from Micro Photonics Inc. The smooth surfaces of the "blocks" are shown on the right, together with their roughness ratings. $S_q = 0.275$ µm.

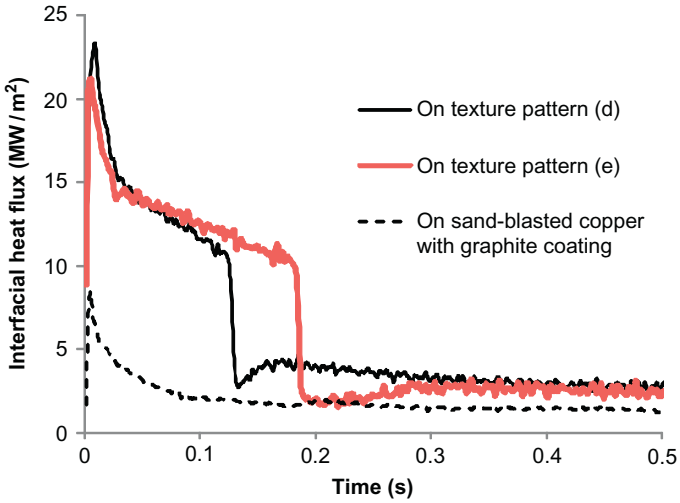


Figure 4.4.15 Instantaneous heat fluxes on textured substrates, compared with a graphite-coated, sand-blasted surface, versus contact time of AA6111 forming strip with substrates.

When an aluminum melt was cast onto textured copper, pattern (d), the interfacial heat flux curve was similar to pattern (e), but the maximum heat flux point became higher, at 23.3 MW/m^2. At 0.13 s, the strip detached from the copper surface, leading to a sudden drop of the heat flux curve. More textured copper patterns and the surface quality of the aluminum strips are reported in Ref. [2].

4.4.2. SOLIDIFICATION IN CONVENTIONAL FIXED-MOLD MACHINES

The mold and spray chamber of a continuous casting machine must fulfill important thermal requirements if steel is to be cast efficiently with a minimum of internal or external defects (Figure 4.4.16).

The water-cooled copper mold must be capable of extracting sufficient heat from the incoming metal to solidify an external shell so that it can support the liquid pool at the mold exit, and thereby minimize breakouts. It is also important that the mold be able to remove the heat uniformly, so as to avoid the formation of locally thin regions in the shell which could rupture and lead also to breakouts or surface cracks. To achieve a uniform shell with sufficient thickness for a given set of casting conditions, several mold parameters have to be regulated. The most important of these are the working length, the taper, and the corner radius.

Continuing the heat extraction process begun in the mold, the sprays must remove sufficient heat from the steel to complete the solidification of the section being cast, prior to cutting. The rate at which the heat extraction proceeds is critical to the smooth operation of the process, because insufficient cooling can result in excessively long liquid sumps of steel, while excessive cooling can lead to the formation of cracks during the bending and straightening of the strand as it exits from the caster horizontally, for cutting into longitudinal sections. The heat extraction in the sprays must also be arranged so that there is a smooth transition of the surface temperature, with a minimum of reheating, as the steel passes from the mold into the sprays and from the sprays onto the radiation cooling zones. Excessive reheating has been shown to be a primary cause of halfway cracks in strand-cast steel. There are two major variables, which can be adjusted to optimize the performance of the sprays: water flux distribution and length of the spray zone. From an operational standpoint, the optimum heat extraction can be achieved by a suitable combination of spray nozzle types, water pressures, and nozzle arrangements. It is important to realize that, in addition to the thermal requirements just outlined, a continuous casting machine has vital mechanical functions. The oscillation of the mold, the support and guidance of the strand with pinch rolls, bending and straightening rolls, and, in some cases, cutting of the strand with mechanical shears must all be carefully designed and controlled if trouble-free casting is to be achieved. The extraction of heat from the surface of the strand proceeds by different mechanisms in each of the three cooling zones. Of these, the heat extraction processes are most complex in the mold and spray regions.

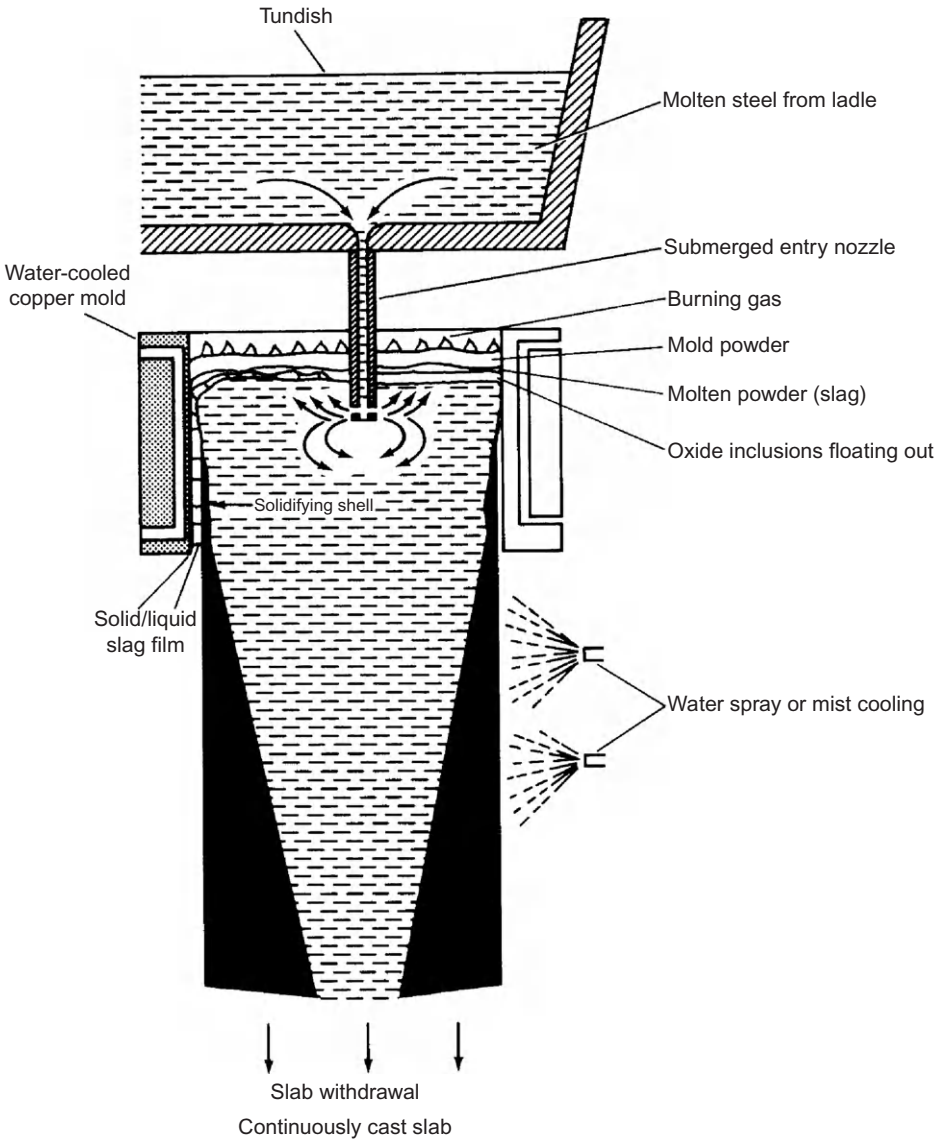


Figure 4.4.16 A typical, conventional, continuous casting machine, for the production of slabs, billets, or blooms, showing liquid steel entering the caster from a tundish, mold powder to lubricate the steel shell as it passes down a water-cooled, open-ended, fixed copper mold. Cooling is completed by banks of water sprays, until the cast is fully solid.

In the mold, heat transfer from the steel surface is influenced markedly by the formation of an air gap between the face of the mold and the solid and liquid slag films. As the width of the air gap is large (~1000 μm), heat flow from the shell surface to the mold is limited by conduction through gas in the gap, but this is mitigated somewhat by radiation mechanisms. A complication in describing the rate of heat flow arises, however, because the gap width does not appear to be constant, but varies in both vertical and horizontal directions over the mold face. However, the increasing ferrostatic pressure of liquid steel within the sump of the forming slab opposes this contraction and causes "bulging." The actual gap thickness within the mold therefore depends on many factors such as casting speed, the specific mold flux, the mold taper, steel chemistry, and mold distortion. Although both the air gap and the flux films are relatively thin compared to the thickness of the copper mold, and the freezing shell of steel, they certainly represent the major obstacles to the removal of heat. Thus, shell growth in the mold depends on the local rate of heat removal, which occurs through the following steps: (1) conduction of heat through the strand shell, (2) conduction and radiation of heat through the flux film, (3) conduction and radiation of heat across an air gap between the solidified shell and mold, (4) conduction through the (copper) mold wall, and (5) convection at the inner mold/cooling water interfaces.

4.4.2.1. Steel Shell Formation

Returning to Equation (4.4.4.1), we can make the (simplistic but useful) assumption [3] that there is a relatively constant rate of heat extraction down the face of the mold wall, according to

$$Q = \dot{q}'' A = hA(\theta_{\text{steel surface}} - \theta_{\text{water}}) \tag{4.4.4.1a}$$

where θ represents temperature, A is the surface area of the water cooled mould, $\dot{q}''$ is the heat flux, i.e., the heat extracted per unit time and area. "h" is an overall heat transfer coefficient, comprising thermal resistances in the water, the copper mold, an air(gas) gap, and the solid/molten slag layers in contact with the outside surface of the steel shell.

We know that the heat extracted through the steel shell can be written, assuming steady-state conduction through the forming shell, according to

$$\dot{q}'' = \frac{k(\theta_{\text{M}} - \theta_{\text{S}})}{x} \tag{4.4.4.1b}$$

where k is the thermal conductivity of the steel shell, and x is the shell thickness formed after time, t, of contact. Taking mold superheats of zero within the metal sump, and θ_{M} as the melting "point" or solidus temperature, θ_{S}, the outer surface temperature of the shell will remain roughly constant as the forming steel shells slide down the mold, since the slag

film/air gap largely controls the rate of heat extraction. We can therefore state that the rate of heat released during solidification balances the lateral rate of heat extraction:

$$\dot{q}''_{\text{cond}} = \rho LH \frac{\mathrm{d}x}{\mathrm{d}t} \tag{4.4.4.1c}$$

Substituting for the conductive heat flux, separating variables, and integrating from time 0 to time t, we have

$$\int_{x=0}^{x=x} x\mathrm{d}x = \frac{k(\theta_{\mathrm{M}} - \theta_{\mathrm{S}})}{\rho LH} \int_{t=0}^{t=t} \mathrm{d}t \tag{4.4.4.6}$$

Integrating:

$$\frac{x^2}{2} = \frac{k(\theta_{\mathrm{M}} - \theta_{\mathrm{S}})}{\rho LH} t \tag{4.4.4.7}$$

or the shell thickness, x, as a function of contact time with the mold, is:

$$x = \sqrt{\frac{2k(\theta_{\mathrm{M}} - \theta_{\mathrm{S}})}{\rho LH}}\, t^{1/2} \tag{4.4.4.8}$$

$$x = k'\sqrt{t} \quad \text{or} \quad x = k'\sqrt{z/U_{\text{slab}}} \tag{4.4.4.9}$$

This analysis [3] suggests that the steel shell should grow at a rate proportional to the square root of its contact time within the mold, provided our assumptions and approximations are reasonable. These include ignoring heat conduction down the vertical axis of the slab or ingot and supposing that all the heat is extracted laterally, first to the cooling water in the mold, and then to the water sprays down the remaining length of the caster. In practice, steel shell growth does turn out to be roughly a function of the square root of the dwell time in the mold, or equally (distance below meniscus/slab withdrawal velocity of slab)^{½}, and the constant k ranges from about 20 to 30 mm min$^{-0.5}$. However, as seen from Figure 4.4.17, exponents on t vary from 0.54 to 0.88 in practice, depending on specific casting conditions. In reality, we see from the first part of this section, that a first principles analysis shows that the relationship varies with the time of contact, substrate surface qualities, and substrate thermal properties, as well as those of the freezing metal, and steel grade.

Figure 4.4.17 presents a recent summary by Schwerdtfeger [4] showing how the shell thicknesses for low carbon steels increased with residence time in the mold, from a number of research groups. As seen, there are considerable deviations in shell thicknesses that formed, particularly for low dwell times. Similarly, the exponents on t vary from 0.54 from the early work of Blazek to 0.88 for Wada *et al.* Clearly, the $\sqrt{t}$ relationship can be an over-simplification of actual heat extraction events at the steel shell/liquid slag/solid slag/gas/mold "interface," and these variations are undoubtedly process, machine, and

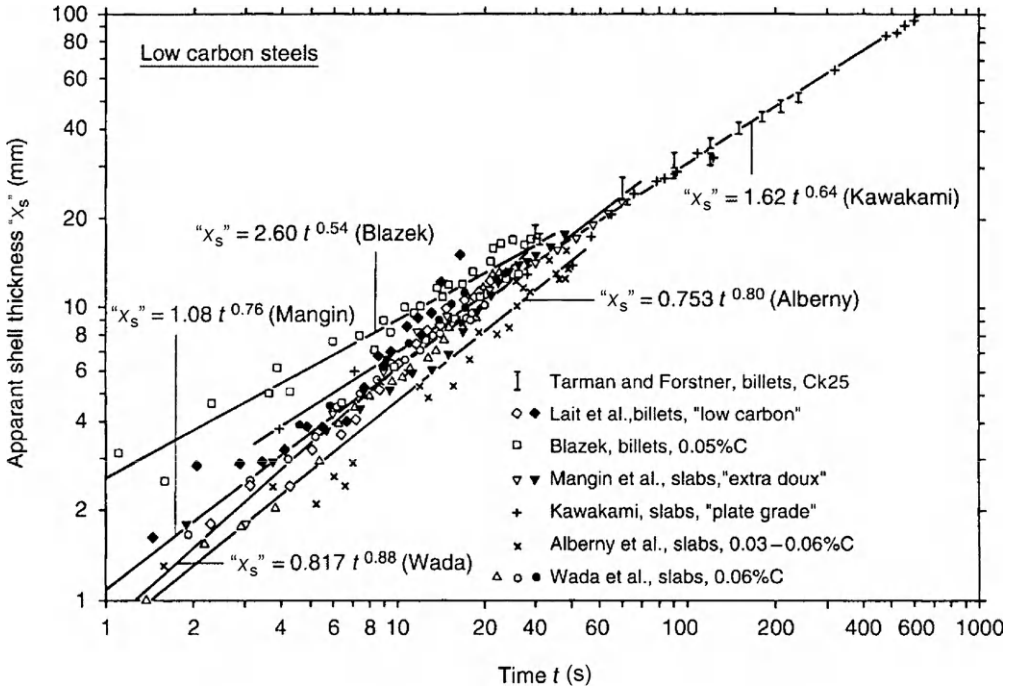


Figure 4.4.17 Logarithmic plot of apparent shell thickness plotted versus dwell time (s) in mold.

plant, specific. None of these researchers have approached the problem on a first principles basis, owing to the complex nature of the many possible interactions between a myriad of variables, and no precise measures of their properties and modes of interaction. However, we shall see in the next section that steady progress is being made in the interpretation of oscillation marks forming on the outside surfaces of thin and thick steel slabs.

REFERENCES

[1] R.I.L. Guthrie, M. Isac, D. Li, ISIJ Int. 50 (12) (2010) 1805–1813.
[2] D. Li, J. Gill, M. Isac, R.I.L. Guthrie, in: TMS 2011, 140th Annual Meeting and Exhibition, San Diego, CA, 2011, pp. 797–802.
[3] R. Guthrie and M. Isac, The Science and Practice of Steelmaking, and Steel Processing, Notes Prepared for McGill Course MIME 456, 2012 AD.
[4] K. Schwerdtfeger, in: Near Net Shape Casting Processes. J.K. Brimacombe Memorial Symposium, TMS and CIM, Vancouver, 2003.

CHAPTER 4.5

Computational and Physical Modeling of Solidification in CCC and TSC

Mihaiela Isac and Roderick I.L. Guthrie
McGill Metals Processing Centre (MMPC), Montreal, Canada

Prior to the advent of North America's first commercially successful vertical mold continuous casting machine, in 1954, for the production of stainless-steel slabs, at the Welland Plant of Atlas Steels in Ontario, all liquid steel was teemed from teeming ladles and cast into stationary ingot molds in the ingot aisle. Today, ingot casting has been largely eliminated, worldwide, and steel yields have thereby been increased by about 10%, thanks to the successful development of the slag lubricated, oscillating, and open-ended mold. One of the key contributions to the successful development of this continuous casting in the early 1960s versus the then conventional ingot casting operation was the development of oscillating molds. Typically, the molds of slab, billet, and bloom casters are oscillated sinusoidally (at 1–3 Hz), in order to prevent the newly formed shell from sticking to the copper mold. This oscillatory motion has also been thought by many to contribute toward the feeding of molten slag into the mold/strand gap, which is true, and it certainly helps with strand sticking problems, which can lead to thin shells and costly liquid steel "breakouts." Such breakouts of steel can cause freezing of molten steel onto the caster's guide rolls, and extended downtimes.

Halliday [1,2] introduced the idea of extending the period of the downward stroke in the oscillation cycle, during which the mold moves slightly faster than the strand, so as to put the thin forming shell under compression. The downstroke time, during which the mold's velocity is about 5% higher than the rate of withdrawal of the strand, was often referred to as the "healing time." During this period, any transverse cracks formed due to steel sticking to the mold, or cracks in the nascent shell forming by any other mechanisms, had the chance to heal. The upstroke, required to bring the mold back up to its reference level, was then carried out much more rapidly, as illustrated in Figure 4.5.1.

His invention helped resolve the problem of the sticking of the growing frozen steel shell to the copper mold, and it also allowed him to reach casting speeds of 14.5 m/min back in 1958, which is still a world record. These machines, now nearing process perfection in recent years, allow partially solidified slabs, blooms, or billets to be continuously withdrawn from oscillating molds at the same levels of productivity previously associated with the ingot aisles of yesteryear. As a result, Conventional Continuous Casting (CCC) techniques, nowadays, involve the use of open, vertical, sinusoidal, oscillating molds, through which steel is poured, so as to produce slabs, billets, or blooms. One uses

Treatise on Process Metallurgy, Volume 2
http://dx.doi.org/10.1016/B978-0-08-096984-8.00011-2
© 2014 Elsevier Ltd.
All rights reserved.

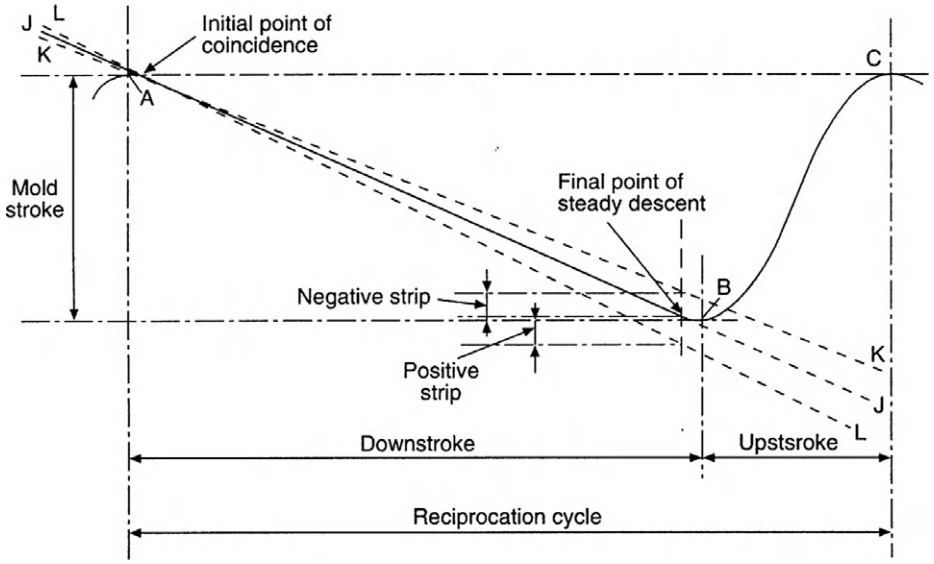


Figure 4.5.1 Schematic of the mold oscillation technique to secure continuous casting.

rectangular, round, or shaped molds, according to the shape of the semifinished products desired. Mold powders, or oils, are used to lubricate the steel shell passing down the water-cooled, oscillating, fixed copper molds, so as to prevent sticking. The steel strands are then guided through a long series of caster rolls, and spray water banks, so as to redirect the forming slab, bloom, or billet, into the horizontal direction for subsequent cutting and processing.

Over the 50 years since the development of the current CCC process, many researchers have been involved in studying the formation of the oscillation marks (OMs) generated in these machines. We know that the frequency of the OMs is exactly equal to the frequency of oscillating mold. We also understand that local variations in heat transfer and fluid flow can cause local solidification conditions to be significantly different from overall steady-state conditions. These perturbations, in turn, can lead to defects in continuous casting products, such as seams and slivers, and uneven shells caused by uneven heat extraction. Similarly, longitudinal cracks, pencil pipe defects, segregations, subsurface hooks, and deep OMs can occur [3]. In a worst-case scenario, transverse breaks in the steel shell do not reheal adequately, causing liquid steel to "breakout" from the forming strand.

In recent groundbreaking research involving three-phase computational fluid dynamics (CFD) modeling of steel–slag–mold interactions during continuous casting, Professors Ken Mills and Peter Lee, together with coauthors Ramirez-Lopez, of MEFOS and Begona Santillana, of TATA Steel, have discussed the origin of OMs [4–6]. Thus, while many plausible explanations for the appearance of OMs have been advanced in the past, the advent of CFD techniques has recently been able to shed considerable light on the true nature and reasons for the appearance of these "surface blemishes" that form on

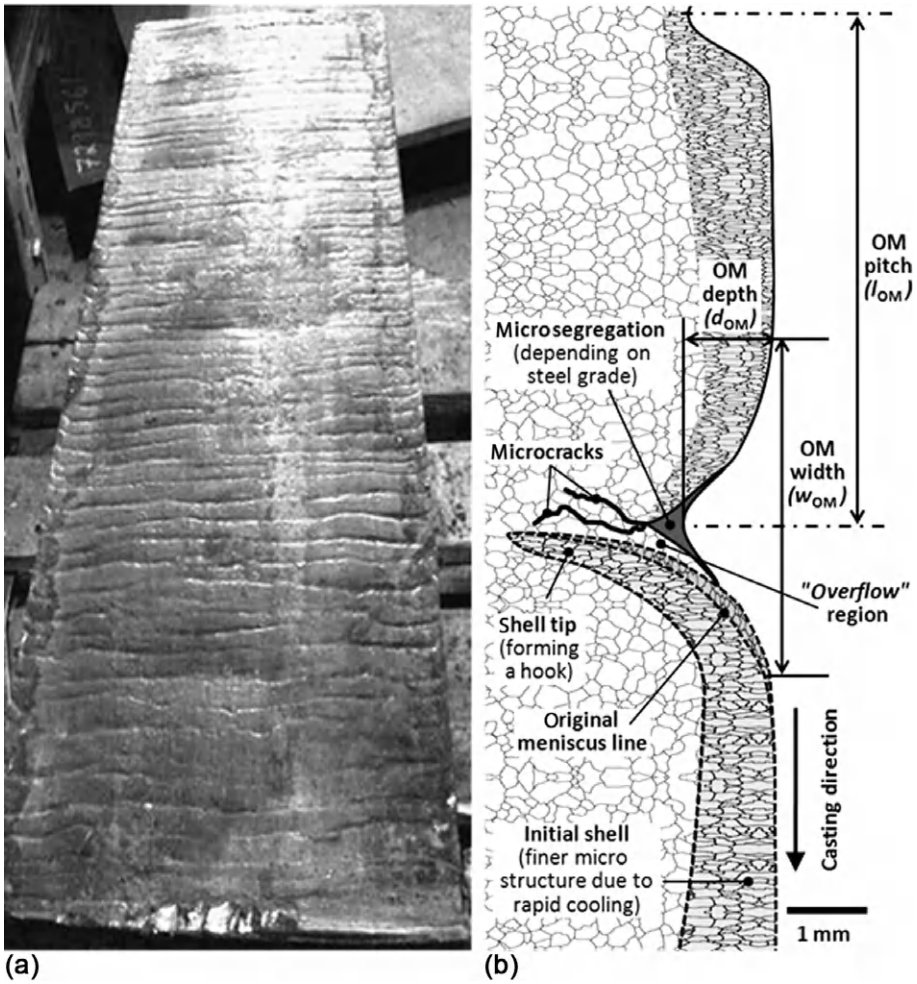


Figure 4.5.2 (a) Typical defects that can lead to oscillation marks on cast slab [3] and (b) schematic diagram showing cross section around oscillation mark [7,8].

the surfaces of slabs (Figure 4.5.2a). Thus, when liquid steel enters the mold through the submerged entry nozzle (SEN), superheat is quickly dissipated, and new liquid steel comes into contact with the freshly forming thin shells of steel, to then solidify, as described in Chapter 4.4. Heat is extracted from the liquid steel through the walls of the copper mold, via a thin layer of liquid slag (~100 μm) and a 10 times thicker shell of solidified slag (~1 mm). This flow of slag to lubricate the passage of the forming steel strand is maintained by adding mold flux powder or granules to the top surface of liquid steel in the mold. This provides thermal insulation of the upper surface of liquid steel and oxidation of the liquid steel is avoided. In return, heat from the steel causes the powder bed to sinter and to form a pool of liquid slag, as shown in Figure 4.5.3. The molten slag

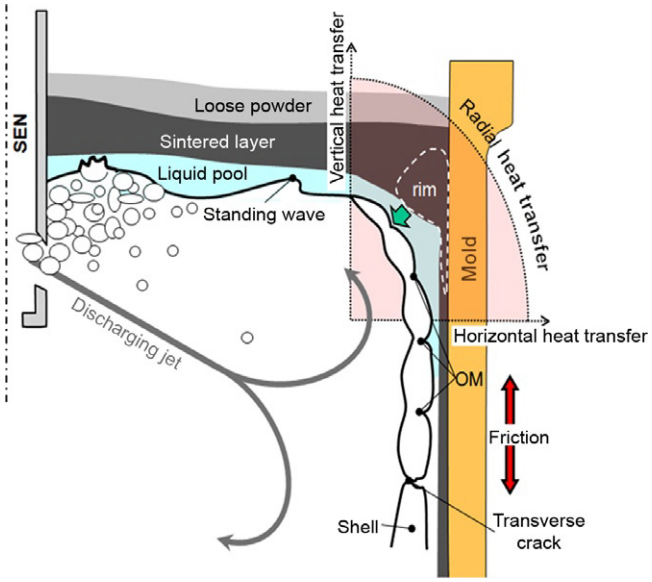


Figure 4.5.3 Initial shell formation in a continuous casting mold [4].

from this powder penetrates the steel meniscus-vertical copper mold region, where it partially freezes, but the remainder forms a thin liquid slag film that penetrates the gap between the strand and the copper mold. This is the key to providing continuous lubrication of the adjacent forming shell of solid steel.

We now understand that it is the interactions between the molten slag layer and the solid shell of steel in the meniscus region that are responsible for generating the OMs during the sinusoidal up-and-down movements of the mold. In order to cast steel without any defects, one must control the rate of heat extraction, of rate of steel shell growth, and continuously provide adequate slag lubrication. In a first-principles approach by Ramirez-Lopez *et al.* [4], continuous thin-slab casting was simulated, making no prior assumptions. The CFD model was capable of predicting the thickness of the slag film (solid and liquid), the formation of the steel shell, the rate of powder consumption, and the heat flux variations through the mold [4–6] during mold oscillation, down the length of the vertical mold, and the initial segment of secondary cooling. The model makes no prior assumptions concerning the thicknesses of the liquid- and solid slag films between mold and freezing metal, nor of the thickness of the steel shell forming, nor of the shape of the meniscus. It solves the Navier–Stokes equation coupled with a volume of fluid method for tracking the interfaces between the steel, slag (liquid and solid), and the copper mold, under transient conditions.

The 2D model was based on the commercial software FLUENT v.6.3 package. It has reportedly been applied/validated on various slab caster configurations, and those authors

suggest that it could easily be extended to billet and bloom casting. A typical model configuration for thin-slab casting computations includes the SEN, the fluid region surrounded by the mold walls, plus a half meter of the slab length after the mold exits, as shown in Figure 4.5.4. The boundary conditions are also given in this figure. Slag is supplied at this boundary, as in the real process, by calculating the mass flux required for good casting practice and optimum powder consumption, as well as the required viscosity and break temperature for the given steel grade and specific casting conditions [4].

The use of an extremely fine mesh in the meniscus region (minimum cell size ~50 μm) allowed for an explicit modeling of liquid slag infiltration into the steel shell-mold gap (Figure 4.5.5). The model was initially solved for the two-phase steel–air system operating under isothermal conditions, until a stable steel flow pattern was reached after ~1000 s of real time. Subsequently, slag was added over the molten steel, while heat transfer and solidification were calculated for at least 2000 s of real time, so as to allow both the infiltrated slag to cover the entire slab surface and to allow the steel shell to become fully developed. Convergence was reached when the residuals fell below 1×10^{-5} in time steps of 0.005 s. Typical predictions of the model are given in Figure 4.5.6 and are detailed elsewhere [4–6].

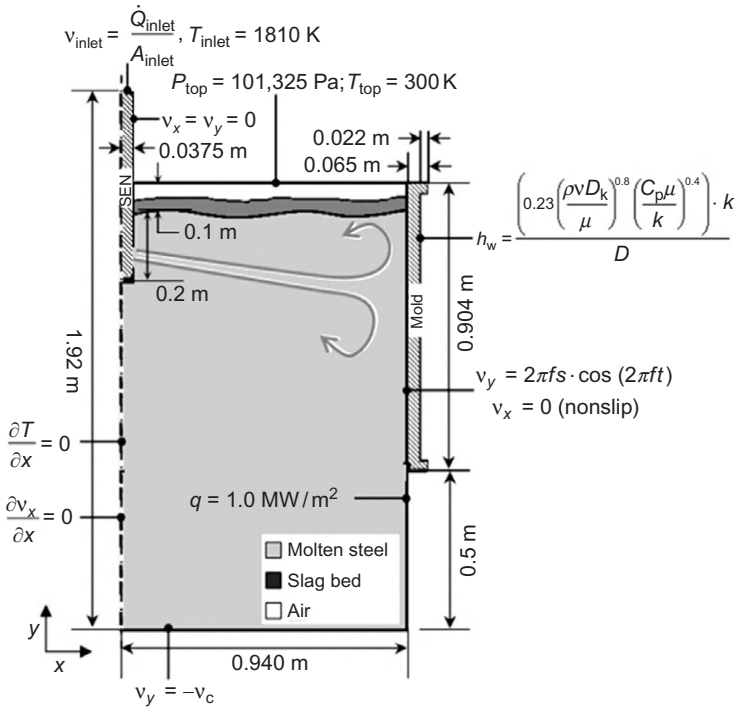


Figure 4.5.4 Model dimensions and boundary conditions [4].

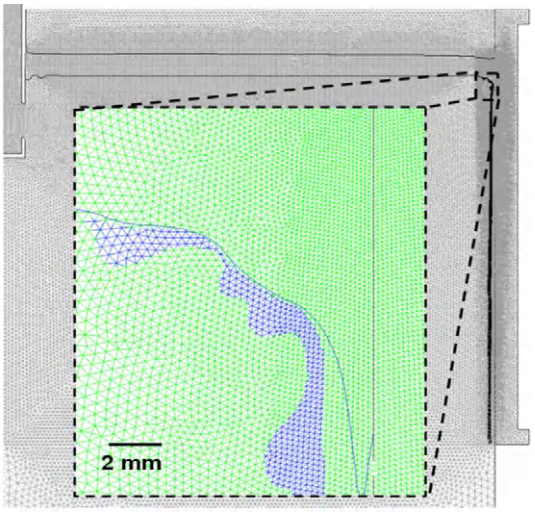


Figure 4.5.5 A very fine mesh is needed at the meniscus region to capture these events.

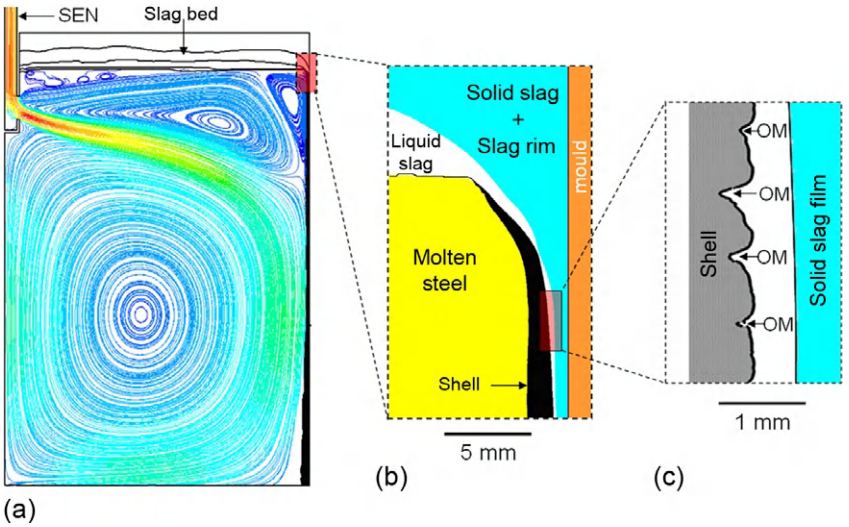


Figure 4.5.6 Typical model predictions showing (a) metal flow and bed formation, (b) initial shell solidification and slag film evolution, and (c) oscillation marks [4].

The results from the simulations confirmed the well-known double roll pattern for steel flows in the mold region (Figure 4.5.6a), together with standing waves forming at the metal/slag pool interface. Similarly, the freezing of a slag rim was predicted, and slag film thicknesses proved to be in good agreement with in-plant measurements

(Figure 4.5.6b). Values for the heat flux, powder consumption, and shell thickness are also in good agreement with plant data [6].

The model predicts the formation of regular indentations in the shell surface, which are considered to be synonymous with OMs (Figure 4.5.6c).

The model tracks the changes in heat flux, shell profiles, slag layer thicknesses, powder consumed, pressure, and velocity in the gap, through five successive oscillation cycles, based on thermocouple readings located at transverse crack (TC), 45 mm below the steel surface, as shown in Figure 4.5.7.

These results were integrated and/or averaged, so as to provide the overall peak heat flux values, total mold powder consumption, average OM depth, and pitch, for each run. A complete description of the design of experiments, statistical analysis, and regression fitting techniques can be found elsewhere [10]. Clearly, this is the type of CFD model and TC measurements that are needed to sort out the many complex interactions taking place in these machines. Thus, Figure 4.5.7 shows recorded data over five oscillation cycles where the surface rugosity (i.e., OM depth and pitch), the peak heat flux (q_{peak}), the powder consumption (Q_c), liquid/solid slag film thicknesses, and pressure in the gap were measured, 45 mm below the meniscus. That position was chosen as a control point, since the minimum slag film thickness and associated peak heat flux occur at that location. Those are the factors which are critical for the formation of OMs.

Thus the flow patterns within the liquid mold flux, or slag, during its infiltration into the meniscus region, first during an upstroke (a), followed by the downstroke (b), to the bottom of the downstroke (c), and finally near the top of the return upstroke (d), are all shown in Figure 4.5.8. One sees that the liquid slag is predicted to form a narrowing channel that goes from the slag pool to a constriction (dotted circle in Figure 4.5.8a), where the thin lubricating slag film starts. The width of the liquid slag film was determined by the distance between the surface of the shell and the break temperature (T_{br}) isotherm. Observed in Figure 4.5.8, the irregular shape of the channel, especially near the rim surface. This closely resembles rim samples obtained from in-plant experiments.

Figure 4.5.8 also illustrates how the metal–slag interface deforms to balance the forces generated by both interfacial tension and pressure exerted by the solid slag rim during the oscillation cycle. The shape and width of the channel are determined by the interaction of the various forces acting at the interface: ferrostatic pressure and slag influx pressure.

Analysis of the slag flow patterns shows that the infiltration is linked to mold velocity and displacement during the cycle, e.g., the cycle starts with an upward flow at the entry of the gap (1 in Figure 4.5.8a—mold traveling upward). Then, the upward flow decreases as the mold begins to move downward, disappearing later in the cycle. This allows partial infiltration (2 in Figure 4.5.8b). Infiltration occurs partly during the negative strip time, due to a pumping effect produced by the descending mold and slag rim (3 in Figure 4.5.8c). This infiltration of colder slag from the "arctic regions" continues through

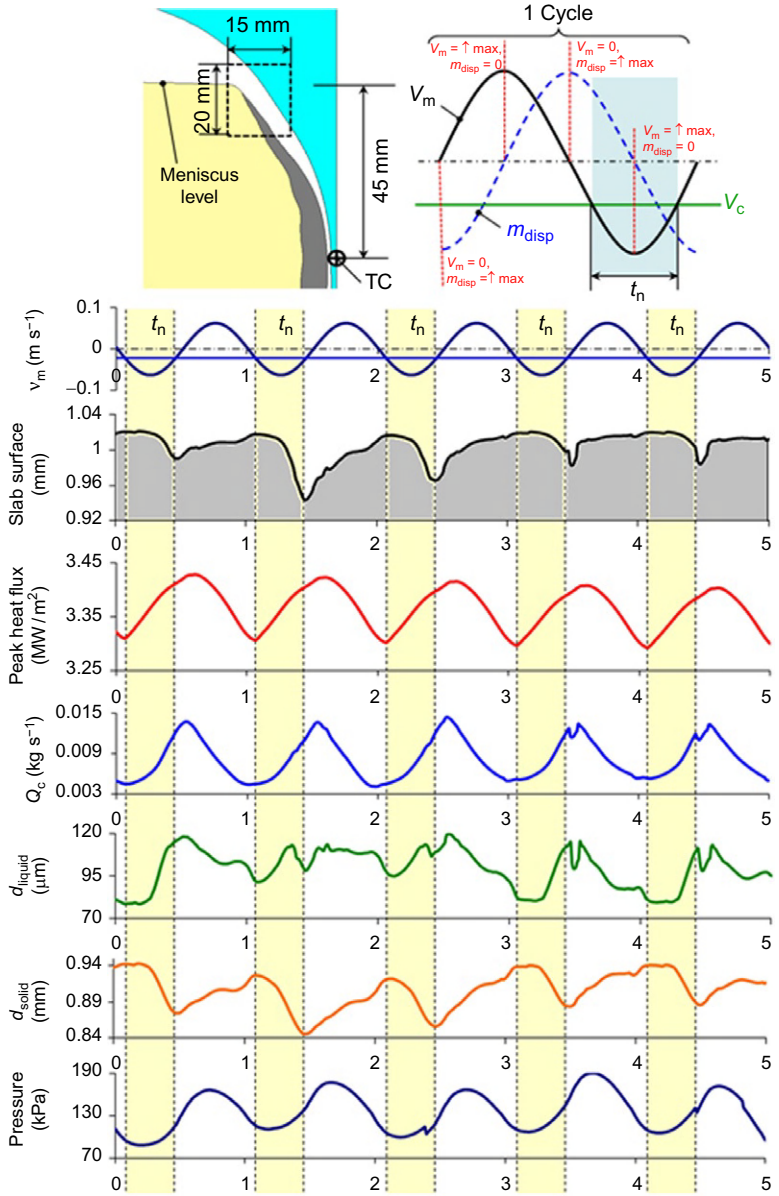


Figure 4.5.7 Recorded data for a casting speed (v_c) = 0.6 m/min, mold oscillation frequency (f) = 60 cpm and stroke (s) = 10 mm, for five consecutive mold oscillations. t_n represents the period of negative strip time, while m_d refers to mold displacement in the graph at the top right of figure.

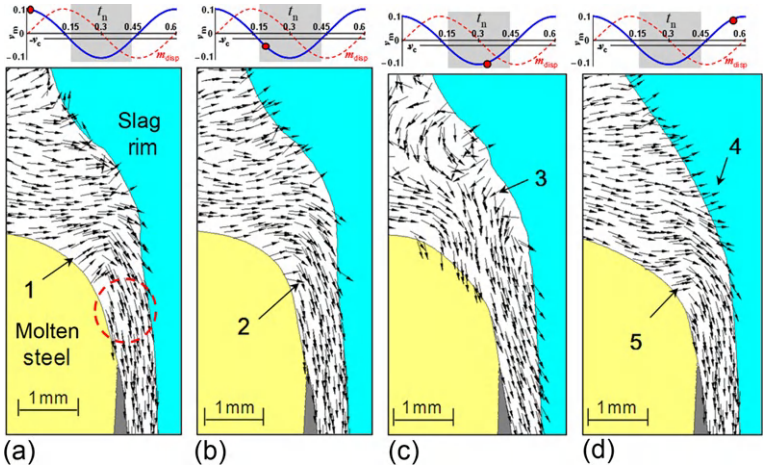


Figure 4.5.8 Predicted slag flow patterns in the slag film channel entry region during oscillation. The top figure shows a graph of the location of the figures with respect to their location in the mold oscillation cycle. The negative strip time when "arctic" flows of slag are being pumped into the slag film are marked by the shaded areas, corresponding to t_n, the negative strip time.

part of the positive strip time, until the flow is redirected upward again by the mold displacement (4 in Figure 4.5.8d). This results in a thicker "sausage" in the forming steel shell. Finally, counterflows appear at the end of the cycle, when the mold is at its highest position, and the warmer liquid slag, coming from the "equatorial" regions, flows in. This corresponds to the thinner sections of the forming steel shell being initiated. Then the cycle repeats.

The evolution of heat flux with time and the formation of OMs for different casting conditions have been compared with experimental observations made by doctoral candidate Adam Badri and professor Alan Cramb, who made use of a mold simulator [11] (Figures 4.5.9 and 4.5.10). The results showed that the predicted heat flux is strongly influenced by the mold oscillation characteristics, since the fluctuations in peak heat flux (q_{peak}) and OM pitch (l_{OM}) corresponded to the oscillation frequency. In all cases, a perfect match was observed between q_{peak} and the start of negative strip time (t_n), at point B in Figure 4.5.1. Additionally, q_{peak} was found to increase sharply during t_n ("arctic flows of slag") and the first half of the positive strip time (t_p), only to stabilize later and to then decrease during the remainder of t_p, corresponding to equatorial flows of hotter slag mold powder.

Similar trends can be observed in Badri's results (Figure 4.5.9). These changes in heat flux confirm that the variations in *cooling potential* (varying between a low of 3.30 and a peak of 3.43 MW/m^2 in Figure 4.5.7) can be mainly attributed to mold oscillation. Figures 4.5.8 and 4.5.9 present strong evidence to confirm that the main mechanism

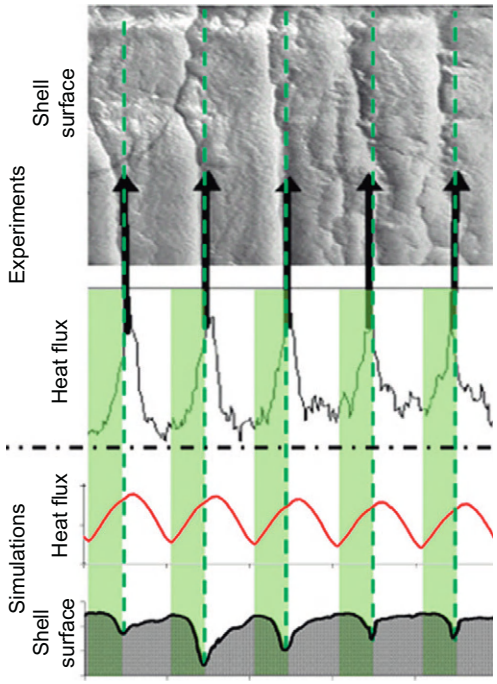


Figure 4.5.9 Predicted surface profiles and heat fluxes compared to Badri and Cramb's experiments [11].

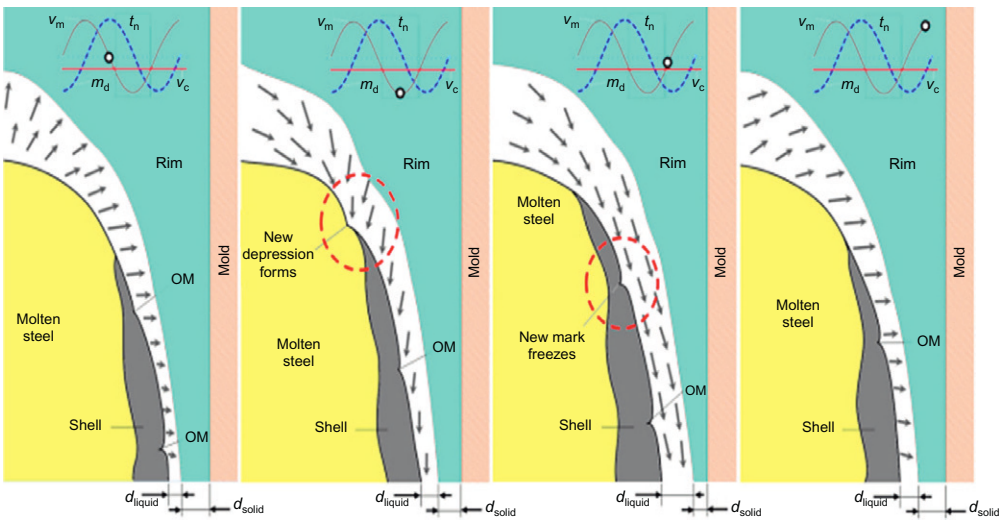


Figure 4.5.10 Updated oscillation mark formation mechanism.

for OM formation and internal undulations on the inner walls of the forming strand is the uneven solidification of the shell along the slag–metal interface during the oscillation cycle, with attendant flows of arctic (colder) and then equatorial flows (warmer) of slag, during each oscillation cycle.

It is important to note that these findings do not need a hypothesis of meniscus bending, and no stress-strain effects are included, or even needed, in the calculations. Meniscus level fluctuations can also be discarded as the main cause for the formation of OMs, since changes in steel levels do not necessarily occur at the same frequency as the mold oscillations, whereas the spacing of the marks is both consistent and regular with oscillating mold movements.

However, it is possible for the level fluctuations to interact with the shell tip to produce marks with similar spacing (determined by the oscillation pattern) but with different depths and shapes (determined by the level height). Badri and Cramb [11] suggest that there are two necessary conditions for the formation of the irregular shell shape. First, the heat flux must be high enough to produce rapid and uneven solidification. This appears in the mathematical simulations by Ramirez-Lopez *et al.* [5,6] as drastic changes in heat flux during the oscillation cycle (Figure 4.5.9).

Secondly, the slag–metal interface must deform such that the liquid comes into close proximity with the copper mold (Figure 4.5.8). This second requirement is achieved by the pushing and imprinting of an indentation in the slag–liquid metal interface during the downward movement of the mold (e.g., during t_n). This hypothesis was corroborated throughout the simulations.

4.5.1. PROPOSED NEW MECHANISM FOR THE FORMATION OF OMs

Given this recent work, it now seems certain that the key factor affecting the formation of OMs *is the change in direction of the slag flow* at the highest and lowest positions of an oscillation cycle. These periods of change reduce the heat extraction rate somewhat, for a short portion of the cycle, causing the shell to thin at that point. The local thinning of the shell is then maintained as the slab is withdrawn, since the slag film in the mark is thicker, causing the outward heat flux to the mold to be lower. These locally thinned regions are marked as OMs in Figure 4.5.10. It is the pumping action of the mold and rim and their relative movement to the shell which causes these changes in slag flow. Furthermore, there is an inherent disorder in both the metal flows and the surface waves, which also act to change the depths and shapes of the marks, but which have little influence on their spacing. These surface waves and metal flows (including SEN turbulence fluctuations) impose a lower frequency increase/decrease in OM depth. This is shown in the surface depth predictions in Figure 4.5.9a, where the second OM is significantly deeper than the others. These worst cases are caused by the additive effects of mold oscillation, surface waves, and SEN turbulence, which all combine to produce an unusually deep OM, which is likely to initiate a crack, and later, a breakout.

Referring to Figure 4.5.10, at t_n^{start}, the mold has just begun its descent and the liquid slag flow transforms from radially outward, "equatorial" to a downward "arctic" flow (Figure 4.5.10a and b). This downward flow results in increased heat flux and shell solidification, in response to the convective cooling. This can be further corroborated by observing the shell growth that occurs between t_n^{mid} and t_p^{mid}.

Later, the mold reaches its lowest point (t_p^{early}), and just before traveling upward, the slag flow changes direction from downward to outward which leads to shell thinning, as "arctic flows" of slag are replaced by "equatorial flows" (Figure 4.5.10c and d).

4.5.2. CONCLUSIONS

This recent work on the role of mold powder for continuous casting machines has finally illustrated the basic reasons for the causes of OMs and surface perturbations in cast slabs. Many factors are involved, such as steel grades, slag viscosity, interfacial tension, the speed of casting, oscillation stroke, and the speed of oscillations. It is known that an increase in the negative strip time, t_n, leads to a reduction in the depth of the OMs, but that this in turn will lead to a corresponding rise in the heat fluxes. That, in turn, means a thinner weaker shell as the strand exits the mold, or a reduced casting velocity. It is therefore no wonder that steelmakers are caught in a quandary with these machines, in terms of their optimization. Nonetheless, they have been successfully used to cast slabs, thin slabs, blooms, and billets, for the past 50 years! For the moving mold, near net-shape casting processes to compete, they do not have the latitude on surface quality that is afforded these CCC processes, since their cast thicknesses are too close to final product thickness. Their cast surfaces must be perfect from the word "go."

REFERENCES

[1] I.M.D. Halliday, JISI 191 (1959) 121–163.
[2] M.M. Wolf, On the Art of Continuous Casting, BHM Spring-Verlag, 2000, 145, heft 1, pp 35–45.
[3] C.-A. Däcker, T. Sohlgren, Steel Res. Int. 81 (10) (2010) 899–907.
[4] P. Ramirez-Lopez, B. Santillana, K.C. Mills, P.D. Lee, in: Three Phase Modelling of the Steel–Slag–Mould Interactions in Continuous Casting, Proceedings of the Roderick Guthrie Honorary Symposium on Process Metallurgy, Montreal, June 6–9, 2011, pp. 167–174.
[5] P.E. Ramirez-Lopez, et al., ISIJ Int. 50 (12) (2010) 1797–1804.
[6] P.E. Ramirez-Lopez, P.D. Lee, K.C. Mills, ISIJ Int. 50 (3) (2010) 425–434.
[7] J.M. Hill, Y.H. Wu, B. Wiwatanapataphee, Metall. Trans. A Phys. Metall. Mater. Sci. 36 (4) (1999) 311–326.
[8] K. Schwerdtfeger, H. Sha, Metall. Mater. Trans. B 31 (4) (2000) 813–826.
[9] M. Zeze, H. Tanaka, E. Takeuchi, S. Mizoguchi, in: Continuous Casting of Clad Steel slab with Level Magnetic Field Brake, Proceedings of 79th Steelmaking Conference, ISS-AIME, Pittsburgh, 1996.
[10] P.E. Ramirez-Lopez, Modelling Shell and Oscillation Mark Formation during Continuous Casting via Explicit Incorporation of Slag Infiltration, Ph.D. Thesis, Materials Dept., Imperial College, February 2010, p. 170.
[11] A. Badri, A. Cramb, Metall. Mater. Trans. B 36B (3) (2005) 373–383.

CHAPTER 4.6

Single Phase, Two Phase, and Multiphase Flows, and Methods to Model these Flows

Kinnor Chattopadhyay[a] **and Roderick I.L. Guthrie**[b]
[a]HATCH (formally PDF with the MMPC)
[b]McGill Metals Processing Centre (MMPC), Montreal, Canada

NOMENCLATURE

$\boldsymbol{\alpha_k}$ volume fraction of the kth phase
$\boldsymbol{\dot{m}_{jk}}$ mass transfer rate from phase j to phase k
$\boldsymbol{\dot{m}_{kj}}$ mass transfer rate from phase k to phase j
$\boldsymbol{S_{\alpha_k}}$ source term
$\boldsymbol{\rho_k}$ density of the kth phase, kg m^{-3}
$\boldsymbol{u_p}$ particle velocity, m s^{-1}
$\boldsymbol{u}$ fluid velocity, m s^{-1}
$\boldsymbol{m_p}$ mass of the particle, kg
$\boldsymbol{V_p}$ volume of the particle, m^3
$\boldsymbol{g}$ acceleration due to gravity, m s^{-2}
$\boldsymbol{d_p}$ diameter of the particle, m
$\boldsymbol{\mu}$ viscosity of the fluid, kg m^{-1} s^{-1}
$\boldsymbol{\rho}$ density, kg m^{-3}
$\boldsymbol{C_D}$ drag coefficient
$\boldsymbol{F_D}$ drag force, N
$\boldsymbol{F_B}$ buoyancy force, N
$\boldsymbol{F_a}$ added mass force for accelerated flows, N
$\boldsymbol{f_a}$ additional acceleration, m s^{-2}
Re Reynolds number
DPM discrete phase modeling
VOF volume of fluid
CFD computational fluid dynamics

4.6.1. INTRODUCTION

A large number of flows encountered in process metallurgy comprise a mixture of phases. Physical states of matter are generally solid, liquid, and gas, but the notion of a phase in a multiphase flow system is applied in a much wider sense. In a multiphase flow system, a phase can be defined as an identifiable class of material that has a particular

Treatise on Process Metallurgy, Volume 2
http://dx.doi.org/10.1016/B978-0-08-096984-8.00012-4
© 2014 Elsevier Ltd.
All rights reserved.

inertial response to, and interaction with, the flow and the potential field in which it is immersed [1]. For example, different-sized solid particles of the same material can be considered as different "phases" because each collection of particles with the same size will have a similar dynamical response to the flow field. In this chapter, rather than going into the fundamentals of multiphase flows, we will focus more on modeling of these flows and cite some examples which we performed in our research program at the McGill Metals Processing Centre in Canada.

4.6.2. MULTIPHASE FLOW REGIMES

Multiphase flow regimes can be classified into four categories: gas–liquid or liquid–liquid flows, gas–solid flows, liquid–solid flows, and three-phase flows [1].

4.6.2.1. Gas–Liquid or Liquid–Liquid Flows

- *Bubbly flow*: These are defined as the flows which involve discrete fluid bubbles in a continuous fluid phase.
- *Droplet flow*: These are defined as the flows which involve discrete fluid droplets in a continuous gas phase.
- *Slug flow*: These are defined as the flows which involve large bubbles in a continuous fluid phase.
- *Stratified/free-surface flow*: These are the flows which involve immiscible fluids separated by a well-defined interface.

4.6.2.2. Gas–Solid Flows

- *Particle-laden flows*: This is a flow which involves discrete particles in a continuous gas.
- *Pneumatic transport*: This is a flow pattern that depends on factors such as solid loading, Reynolds numbers, and particle properties. Typical examples are dune flow, slug flow, and homogeneous flow.
- *Fluidized bed*: This consists of vertical cylinder-containing particles, into which a gas is introduced through a distributor. The gas rising through the bed suspends the particles. Depending on the gas flow rate, bubbles appear and rise through the bed, intensifying the mixing within the bed.

4.6.2.3. Liquid–Solid Flows

- *Slurry flow*: These flows involve the transport of particles in liquids. The fundamental behavior of liquid–solid flows varies with the properties of the solid particles relative to those of the liquid. In slurry flows, the Stokes number is normally less than 1. When the Stokes number is greater than 1, the characteristic of the flow is liquid–solid fluidization.
- *Hydro-transport*: This can be described as the flow of densely distributed solid particles in a continuous liquid phase.

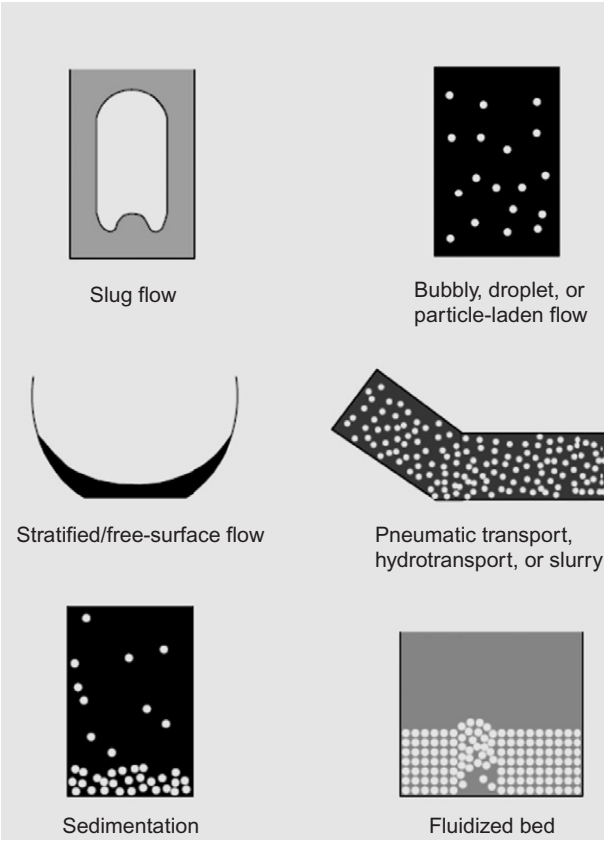


Figure 4.6.1 Multiphase flow regimes [1].

- *Sedimentation*: This can be described in terms of a tall column that initially contains a uniform dispersed mixture of particles. At the bottom, the particles will slow down and form a sludge layer. At the top, a clear interface will appear, and in the middle, a constant settling zone will exist.

4.6.2.4. Three-Phase Flows

Three-phase flows are generally regarded as combinations of the above-mentioned flow regimes (Figure 4.6.1).

4.6.2.5. Examples of Multiphase Flows in Process Metallurgical Operations

Most of the metallurgical processing operations involve the interaction between liquid metal, dissolved gasses, slag droplets, solid particles, and inclusions. For example, the blast furnace is a typical example of a counter current reactor involving hot reducing gasses,

packed layer of solids, liquid iron, and slag. The same applies to direct reduction processes and alternative ironmaking. Injection of argon bubbles in ladles as well as oxygen steel making are classic examples of bubbly and discrete phase flows. In powder metallurgical operations, the atomizer is a clear example of droplet flow where tiny metal droplets traverse in a continuous gas phase. In mineral processing operations, the transport of ore/mineral particles from the mines to the plant through large pipes is a practical example of slurry flow. Air classifiers and dust collectors in steel plants provide a practical example of particle-laden flows where dust particles are suspended in a continuous gas phase. The movement of inclusions in liquid metals is a case of discrete particle flow in a continuous liquid phase. Numerous other examples can be cited, but it is out of the scope of this chapter. It is very clear modeling of these kinds of metallurgical processes is very complicated and requires a clear understanding of the methods available and there robustness in simulating various transport phenomena.

4.6.2.6. Choice of a Proper Multiphase Model

The primary step in solving any multiphase system is to determine which of the regimes provides some broad guidelines for determining appropriate models for each regime, and how to determine the degree of interphase coupling for flows involving bubbles, droplets, or particles, and the appropriate model for different amounts of coupling.

Presently, there are two major approaches for the numerical modeling of multiphase flows, viz., the Euler–Euler approach and the Euler–Lagrange approach.

4.6.2.6.1 Euler–Euler Approach [1]

In the Euler–Euler approach, the different phases are treated mathematically as interpenetrating continua. Since the volume of a phase cannot be occupied by the other phases, the concept of phase volume fraction is introduced. These volume fractions are assumed to be continuous functions of space and time, and their sum is equal to 1. Conservation equations for each phase are derived to obtain a set of equations, which have similar structure for all phases. These equations are closed by providing constitutive relations that are obtained from empirical information, or, in the case of granular flows, by application of kinetic theory. The major Euler–Euler formulations are the volume of fluid (VOF) model, the mixture model, and the Euler model.

4.6.2.6.1.1 The VOF Method

The VOF model is a surface-tracking technique applied to a fixed Eulerian mesh. It is designed for two or more immiscible fluids where the position of the interface between the fluids is of interest. In the VOF model, a single set of momentum equations is shared by the fluids, and the volume fraction of each of the fluids in each computational cell is tracked throughout the domain. Applications of the VOF model include stratified flows, free-surface flows, filling, sloshing, the motion of large

bubbles in a liquid, the motion of liquid after a dam break, the prediction of jet breakup (surface tension), and the steady or transient tracking of any liquid–gas interface. Typical examples include the prediction of jet breakup and the motion of large bubbles in a liquid. The VOF formulation is generally used to compute a time-dependent solution, but for problems in which one is only concerned with a steady-state solution, it is also possible to perform a steady-state calculation. However, a steady-state VOF calculation is sensible only when one's solution is independent of the initial conditions and there are distinct inflow boundaries for the individual phases. For example, since the shape of the free surface inside a rotating cup depends on the initial level of the fluid, such a problem must be solved using the time-dependent formulation. On the other hand, the flow of water in a channel with a region of air on top and a separate air inlet can be solved with the steady-state formulation. The VOF formulation relies on the fact that two or more fluids (or phases) are not interpenetrating. For each additional phase that one adds to one's model, a variable is introduced: the volume fraction of the phase in the computational cell. In each control volume, the volume fractions of all phases sum to unity. The fields for all variables and properties are shared by the phases and represent volume-averaged values, as long as the volume fraction of each of the phases is known at each location. Thus the variables and properties in any given cell are either purely representative of one of the phases, or representative of a mixture of the phases, depending upon the volume fraction values. In other words, if the kth fluid's volume fraction in the cell is denoted as α_k, then the following conditions apply:

$\alpha_k = 0$: The cell is empty (of the kth fluid)

$\alpha_k = 1$: The cell is full (of the kth fluid)

$0 < \alpha_k < 1$: The cell contains the interface between the kth fluid and one or more other fluids.

Based on the local value of α_k, the appropriate properties and variables will be assigned to each control volume within the domain. The tracking of the interface (s) between the phases is accomplished by the solution of a continuity equation for the volume fraction of one (or more) of the phases. For the kth phase, this equation has the following form:

$$\frac{1}{\rho_k}\left[\frac{\partial}{\partial t}(\alpha_k \rho_k) + \nabla \cdot \left(\alpha_k \rho_k \vec{v}_k\right) = S_{\alpha_k} + \sum_{k=1}^{n}\left(\dot{m}_{jk} - \dot{m}_{kj}\right)\right] \tag{4.6.1}$$

Here, $\dot{m}_{jk}$ is the mass transfer from phase j to phase k and $\dot{m}_{kj}$ is the mass transfer from phase k to phase j.

The volume fraction equation will not be solved for the primary phase; the primary-phase volume fraction will be computed based on the following constraint:

$$\sum_{k=1}^{n} \alpha_k = 1 \tag{4.6.2}$$

The volume fraction equation may be solved through either implicit or explicit time discretization.

4.6.2.6.1.1.1 Interpolation Near the Interface The control-volume finite difference method requires that convection and diffusion fluxes through the control-volume faces be computed and balanced with source terms within the control volume itself. In the geometric reconstruction and donor–acceptor schemes, a special interpolation treatment is done to the cells that lie near the interface between the two phases. The geometric reconstruction scheme represents the interface between fluids using a piecewise-linear approach. In ANSYS FLUENT, this scheme is the most accurate and can be applied for general unstructured meshes. The geometric reconstruction scheme is generalized for unstructured meshes from the work of Youngs [2]. It assumes that the interface between two fluids has a linear slope within each cell, and uses this linear shape for calculation of the advection of fluid through the cell faces. The first step in this reconstruction scheme is calculating the position of the linear interface relative to the center of each partially filled cell, based on information about the volume fraction and its derivatives in the cell. The second step is calculating the advecting amount of fluid through each face using the computed linear interface representation and information about the normal and tangential velocity distribution on the face. The third step is calculating the volume fraction in each cell using the balance of fluxes calculated during the previous step.

In the donor–acceptor approach, the standard interpolation schemes are used to obtain the face fluxes whenever a cell is completely filled with one phase or another. When the cell is near the interface between two phases, a "donor–acceptor" scheme is used to determine the amount of fluid advected through the face [3]. This scheme identifies one cell as a donor of an amount of fluid from one phase and another (neighboring) cell as the acceptor of that same amount of fluid and is used to prevent numerical diffusion at the interface. The amount of fluid from one phase that can be advected across a cell boundary is limited by the minimum of two values: the filled volume in the donor cell or the free volume in the acceptor cell. The orientation of the interface is also used in determining the face fluxes. The interface orientation is either horizontal or vertical, depending on the direction of the volume fraction gradient of the kth phase within the cell and that of the neighboring cell that shares the face in question. Depending on the interface's orientation as well as its motion, flux values are obtained by pure upwind, pure downwind, or some combination of the two.

A schematic representation of the schemes is shown in Figure 4.6.2.

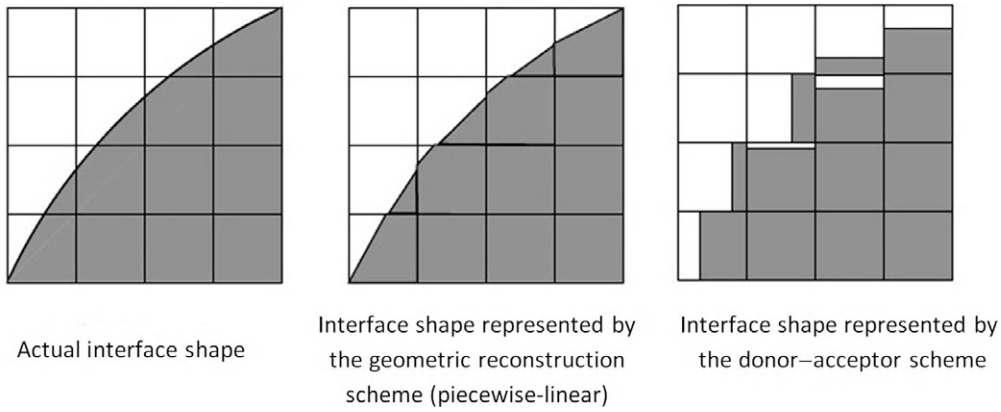


Figure 4.6.2 Different interpolation schemes used in the VOF model [1].

4.6.2.6.1.2 The Mixture Model

The mixture model is a simplified multiphase model that can be used in different ways. It can be used to model multiphase flows where the phases move at different velocities but assume local equilibrium over short spatial length scales. It can be used to model homogeneous multiphase flows with very strong coupling and phases moving at the same velocity, and lastly, the mixture models are used to calculate non-Newtonian viscosity. The mixture model can model n phases (fluid or particulate) by solving the momentum, continuity, and energy equations for the mixture, the volume fraction equations for the secondary phases, and algebraic expressions for the relative velocities. Typical applications include sedimentation, cyclone separators, particle-laden flows with low loading, and bubbly flows where the gas volume fraction remains low.

The mixture model is a good substitute for the full Eulerian multiphase model in several cases. A full multiphase model may not be feasible when there is a wide distribution of the particulate phase or when the interphase laws are unknown or their reliability can be questioned. A simpler model like the mixture model can perform as well as a full multiphase model while solving a smaller number of variables than the full multiphase model. The mixture model allows one to select granular phases and calculates all properties of the granular phases. This is applicable for liquid–solid flows. The mixture model, like the VOF model, uses a single-fluid approach. However, the mixture model is different from the VOF model in two aspects. It allows the phases to be interpenetrating and also permits the phases to move at different velocities, using the concept of slip velocities.

4.6.2.6.1.3 The Eulerian Model

The Eulerian multiphase model allows for the modeling of multiple separate, yet interacting phases. The phases can be liquids, gases, or solids in nearly any combination. An Eulerian treatment is used for each phase, in contrast to the Eulerian–Lagrangian

treatment that is used for the discrete phase model (DPM). With the Eulerian multiphase model, the number of secondary phases is limited only by memory requirements and convergence behavior. Any number of secondary phases can be modeled, provided that sufficient memory is available.

4.6.2.6.2 Euler–Lagrangian Approach [1]

In the Euler–Lagrange approach, the fluid phase is treated as a continuum by solving the Navier–Stokes equations, while the dispersed phase is solved by tracking a large number of particles, bubbles, or droplets through the calculated flow field. The dispersed phase can exchange momentum, mass, and energy with the fluid phase. A fundamental assumption made in this model is that the dispersed second phase occupies a low volume fraction, even though high mass loading is acceptable. The particle or droplet trajectories are computed individually at specified intervals during the fluid-phase calculation. This makes the model appropriate for the modeling of spray dryers, coal and liquid fuel combustion, and some particle-laden flows but inappropriate for the modeling of liquid–liquid mixtures, fluidized beds, or any application where the volume fraction of the second phase cannot be neglected.

The particle or droplet trajectories are computed individually at specified intervals during the fluid-phase calculation. The dispersed secondary phase can affect the flow in the primary phase and for that two-way turbulence coupling needs to be used. In the "two-way" turbulence coupling, as the trajectory of a particle is computed, a track of the momentum gained or lost by the particle stream that follows that trajectory is kept, and these quantities are then incorporated in the subsequent continuous phase calculations. Thus, while the continuous phase always impacts on the motion of the discrete phase, we can also incorporate the effect of the discrete phase trajectories on the continuum phase. This two-way coupling is accomplished by alternately solving the discrete and continuous phase equations, until the solutions in both phases have stopped changing [1]. The basic equations involved in DPM are presented as follows in the FLUENT handbook.

$$\frac{\mathrm{d}u_\mathrm{p}}{\mathrm{d}t} = \frac{18\mu C_\mathrm{D} Re}{24\rho_\mathrm{p} d_\mathrm{p}^2} u_\mathrm{rel} + \frac{g\left(\rho_\mathrm{p} - \rho\right)}{\rho_\mathrm{p}} + \frac{1}{2}\frac{\rho}{\rho_\mathrm{p}}\frac{\mathrm{d}}{\mathrm{d}t}u_\mathrm{rel} \tag{4.6.3}$$

$$Re = \frac{\rho d_\mathrm{p} |u_\mathrm{rel}|}{\mu} \tag{4.6.4}$$

$$u_\mathrm{rel} = u - u_\mathrm{p} \tag{4.6.5}$$

$$C_\mathrm{D} = a_1 + \frac{a_2}{Re} + \frac{a_3}{Re^2} \tag{4.6.6}$$

The original derivation of Equation (3.12) was performed by Buevich [4] in 1966. A clearer derivation of the equation is furnished below, to illustrate the traps one can fall into, if using commercial codes, blindly.

The forces acting on a particle of mass m_p are the drag force, the buoyancy force, and the force due to added mass. For a sphere, the volume of the added mass of liquid is equal to half the volume of the particle.

$$m_p \frac{du_p}{dt} = F_D + F_B + F_a \tag{4.6.7}$$

$$m_p \frac{du_p}{dt} = \frac{1}{2}\rho\left(|u-u_p|\right)^2 C_D A + m_p \frac{g\left(\rho_p-\rho\right)}{\rho_p} + \frac{1}{2}v_p\rho\frac{d}{dt}\left(u-u_p\right) \tag{4.6.8}$$

$$m_p \frac{du_p}{dt} = \frac{1}{2}\rho\left(|u-u_p|\right)^2 C_D A + m_p \frac{g\left(\rho_p-\rho\right)}{\rho_p} + \frac{1}{2}m_p\frac{\rho}{\rho_p}\frac{d}{dt}\left(u-u_p\right) \tag{4.6.9}$$

$$\left[\text{Replacing } v_p \text{ by} \frac{m_p}{\rho_p}\right]$$

$$m_p \frac{du_p}{dt} = \frac{1}{2}\rho|u_{rel}|^2 C_D A + m_p \frac{g\left(\rho_p-\rho\right)}{\rho_p} + m_p\frac{1}{2}\frac{\rho}{\rho_p}\frac{d}{dt}\left(u-u_p\right) \tag{4.6.10}$$

$$m_p \frac{du_p}{dt} = \frac{1}{2}\rho|u_{rel}||u_{rel}| C_D \frac{\pi d_p^2}{4} + m_p \frac{g\left(\rho_p-\rho\right)}{\rho_p} + m_p\frac{1}{2}\frac{\rho}{\rho_p}\frac{d}{dt}\left(u-u_p\right) \tag{4.6.11}$$

$$m_p \frac{du_p}{dt} = \frac{1}{8}\rho|u_{rel}||u_{rel}| C_D \pi d_p d_p + m_p \frac{g\left(\rho_p-\rho\right)}{\rho_p} + m_p\frac{1}{2}\frac{\rho}{\rho_p}\frac{d}{dt}\left(u-u_p\right) \tag{4.6.12}$$

$$m_p \frac{du_p}{dt} = \frac{1}{8}\rho|u_{rel}|\cdot d_p \cdot |u_{rel}|\, C_D \pi d_p \frac{\mu}{\mu} + m_p \frac{g\left(\rho_p-\rho\right)}{\rho_p} + m_p\frac{1}{2}\frac{\rho}{\rho_p}\frac{d}{dt}\left(u-u_p\right) \tag{4.6.13}$$

$$m_p \frac{du_p}{dt} = \frac{1}{8}\left(\frac{\rho|u_{rel}|d_p}{\mu}\right)\cdot|u_{rel}|\, C_D \pi d_p \mu + m_p \frac{g\left(\rho_p-\rho\right)}{\rho_p} + m_p\frac{1}{2}\frac{\rho}{\rho_p}\frac{d}{dt}\left(u-u_p\right) \tag{4.6.14}$$

$$m_p \frac{du_p}{dt} = \frac{1}{8}Re|u_{rel}|\, C_D \pi d_p \mu \frac{d_p^2/6}{d_p^2/6} + m_p \frac{g\left(\rho_p-\rho\right)}{\rho_p} + m_p\frac{1}{2}\frac{\rho}{\rho_p}\frac{d}{dt}\left(u-u_p\right) \tag{4.6.15}$$

$$\left[\text{Replacing } \frac{\rho|u_{rel}|d_p}{\mu} \text{ by } Re\right]$$

$$m_p \frac{du_p}{dt} = \frac{6}{8d_p^2}Re|u_{rel}|\, C_D \mu \frac{\pi d_p^3}{6}\frac{\rho_p}{\rho_p} + m_p \frac{g\left(\rho_p-\rho\right)}{\rho_p} + m_p\frac{1}{2}\frac{\rho}{\rho_p}\frac{d}{dt}\left(u-u_p\right) \tag{4.6.16}$$

$$m_p \frac{du_p}{dt} = \frac{6}{8 d_p^2 \rho_p} Re |u_{rel}| \, C_D \mu \frac{\pi d_p^3 \rho_p}{6} \frac{3}{3} + m_p \frac{g\left(\rho_p - \rho\right)}{\rho_p} + m_p \frac{1}{2} \frac{\rho}{\rho_p} \frac{d}{dt}\left(u - u_p\right) \quad (4.6.17)$$

$$m_p \frac{du_p}{dt} = \frac{18 \mu C_D}{24 d_p^2 \rho_p} Re |u_{rel}| \, m_p + m_p \frac{g\left(\rho_p - \rho\right)}{\rho_p} + m_p \frac{1}{2} \frac{\rho}{\rho_p} \frac{d}{dt}\left(u - u_p\right) \quad (4.6.18)$$

$$\left[\text{Replacing } \frac{\pi d_p^3 \rho_p}{6} = m_p\right]$$

$$\frac{du_p}{dt} = \frac{18 \mu C_D Re}{24 \rho_p d_p^2} u_{rel} + \frac{g\left(\rho_p - \rho\right)}{\rho_p} + \frac{1}{2} \frac{\rho}{\rho_p} \frac{d}{dt}\left(u - u_p\right) \quad (4.6.19)$$

4.6.3. EXAMPLE: MODELING OF INERT GAS SHROUDING IN A TUNDISH (THREE-PHASE FLOW INVOLVING GAS BUBBLES, LIQUID STEEL, AND SLAG)

The injection of argon gas into the ladle shroud and submerged entry nozzles is a common practice in continuous casting. The primary objective is to prevent the melt stream from reoxidation due to aspiration of ambient air. Kim [5] in 1998 in his M. Eng. thesis at McGill University discussed in detail about air aspiration in ladle shrouds. The benefits resulting from shrouding the melt stream are manifold. There is a definite reduction in the oxygen content in the bath, a lesser number of oxide inclusions, a decrease in nozzle-clogging frequency, an improvement in surface quality of slabs and billets, and a reduction of melt temperature losses from ladle to tundish [6]. Despite these benefits, too much argon gas should be avoided, as it forms an exposed eye of steel around the ladle shroud by sweeping off the protective layer of tundish slag. Many researchers have studied the injection of gas in tundish nozzles, inclusion removal by gas shrouding, etc., but no one has reported on the trajectory of these bubbles within a water model tundish, or how they affect the liquid flow field within the model tundish. Similarly, the formation of an exposed "eye" of hot steel and/or slag, due to gas injection through the shroud, has not been considered in any of the work mentioned above. Chattopadhyay *et al.* [7] have reported on the effect of inert gas shrouding on fluid flow within the tundish, and associated slag movements. In the present study, the ANSYS 12.0 package was used to develop the 3D mathematical model, and the results were compared with water model experiments, using a *full-scale* delta-shaped tundish, and a third-scale equivalent. This is a very practical example of multiphase flow (gas bubbles, slag, and steel) in metallurgical processing. An Euler–Lagrangian (DPM) model was first developed to predict liquid flow fields and bubble trajectories within a given tundish. Later on, this model was extended, using a

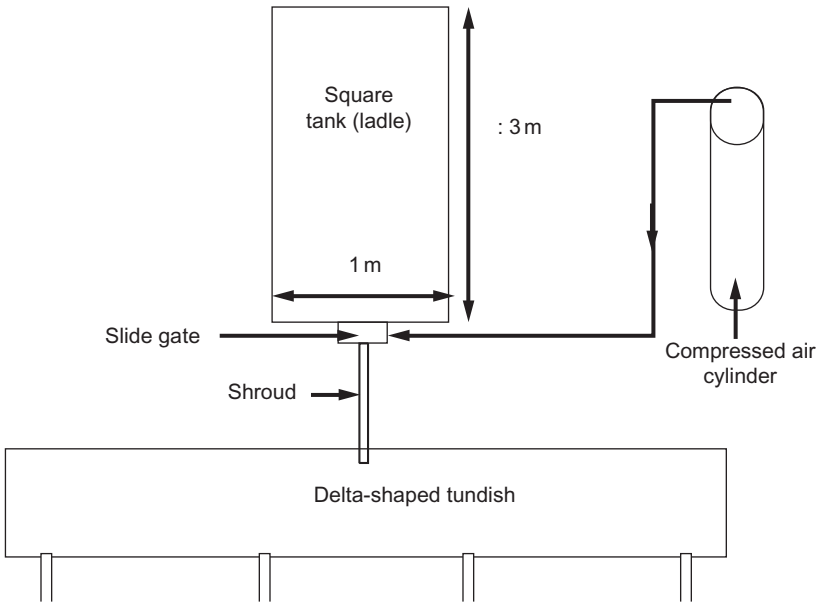


Figure 4.6.3 Schematic diagram of the experimental setup.

combined Euler–Euler (VOF) and Euler–Lagrangian (DPM) approach to simulate the formation of the exposed "eye" of steel/slag in the tundish.

4.6.3.1. Modeling Procedures

In the physical modeling research, a full-scale water model and its one-third scale equivalent was used to simulate the gas-shrouding process. Liquid steel was replaced by its low-temperature aqueous analogue (water), while argon was substituted by compressed air. A schematic diagram of our system is given in Figure 4.6.3. The square tank above the tundish was used to provide the 3-m head pressure of water and was used to control the inflow rate of water into the tundish. A flow rate of 0.17 m^3/min was maintained through the ladle shroud, so as to maintain a steady-state height of 500 mm of water within the tundish. The immersion depth of the ladle shroud was 60 mm. Air was injected from just below the slide gate, at volumetric flow rates ranging between 2 and 10 pct of water entry flows. The flow rate of air was controlled with the help of a flow meter (Cole Palmer Instrument Company, Barrington, IL).

The upper slag phase was simulated in the full-scale water model using white-colored polyethylene beads (density = 920 kg m^{-3}, diameter = 2.5–3 mm) that were poured uniformly over the free surface of water in the tundish, prior to the experiment. The thickness of the polyethylene bead layer in the vicinity of the ladle shroud was 0.02 ± 0.002 m. For the one-third scale model, a flow rate 0.01 m^3/min was maintained

from the inflow, so as to obtain a steady-state height of 167 mm, based on Froude $\left(\frac{U^2}{gL}\right)$ similitude. A 0.01-m thick layer of mineral oil (density = 870 kg m^{-3}, viscosity = 0.017 Pa s) was used to simulate the slag phase in the small-scale model. High-definition video photography was used to visualize bubble tracks, together with slag layer movements and disruptions.

The mathematical model of the two-phase gas/liquid flows in the ladle shroud was based on the following assumptions:

(1) The liquid passing down the shroud (water) is an incompressible, Newtonian fluid.

(2) The two-phase flow within the ladle shroud is predominantly bubbly; discrete bubbles are formed at the entry location, which then are evenly distributed as they move down the shroud, in conjunction with the down-flowing water. This assumption of bubbly flow holds true because the volume fraction of gas in the shroud was not greater than 10%. Above that, gas curtains are formed rather than gas bubbles and hence the discrete phase approach is incorrect.

The standard k–ε model of Launder and Spalding was used, coupled with the DPM. As noted, the present calculations were carried out using the ANSYS FLUENT 12.0. The drawing of the system and meshing were performed using GAMBIT 2.4.6. Calculations were performed in one half of the tundish, assuming a vertical plane of symmetry between the two sides of the tundish, and ignoring any potential large-scale transient turbulent motions. This was done to save on computational time. All velocity components were set to zero at the walls by using the no-slip boundary condition. At the free surface of the liquid, the shear stress was set as zero. The primary fluid was taken to be water and the discrete phase material was set as air.

In the numerical modeling, the steady-state flow field solution was first obtained in the absence of any gas injection. Once the steady state velocity field was established, inert gas injection was started under transient conditions, using a time-step size of 1 ms (10^{-3} s).

During the initial steady-state calculations, the SIMPLE algorithm, along with a first-order upwind scheme for momentum, k, and ε equations, was used. Default values of the under-relaxation factor were used, i.e., unity for body forces, density, and turbulent viscosity; 0.8 for the k and ε equations and 0.7 for the momentum equation. For pressure, the standard scheme was used, with an under relaxation of 0.3. After obtaining the steady-state velocity field, the inert gas injection was started, at which point the under-relaxation factors for k and ε were changed to 0.5. For the unsteady simulations, the PISO algorithm was used for pressure–velocity coupling and the second-order upwind scheme was used for momentum, k, and ε equations and PRESTO for pressure.

4.6.3.2. Bubble Trajectories in the Tundish

The 3D numerical model proved very effective in predicting bubble trajectories within the tundish. The gas flow rate was varied from 4% to 10% of the volumetric flow rate

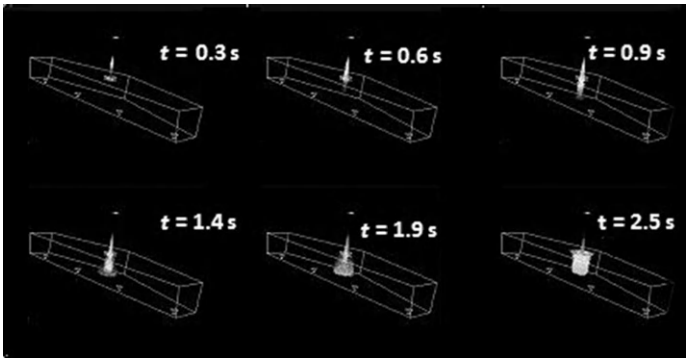


Figure 4.6.4 Numerically predicted temporal evolution of the bubble plume for gas injection at 6% of water entry flows in the full-scale tundish.

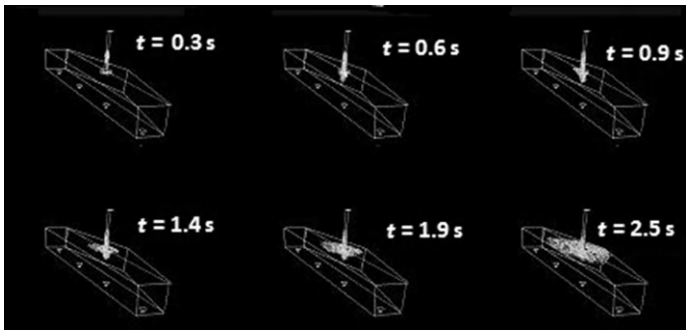


Figure 4.6.5 Numerically predicted temporal evolution of the bubble plume for gas injection at 10% of water entry flows in the full-scale tundish.

of water. The bubble tracks in the full-scale tundish for 6% gas flow are shown in Figure 4.6.4. As seen, at first the bubbles come down the ladle shroud together with the liquid and touch the base of the tundish. Then, due to their buoyancy, they rise almost straight back up to the surface, forming a bubble plume within the tundish around the ladle shroud. These rising bubbles disrupt the protective slag phase (polyethylene particles or mineral oil), creating a reverse flow, and forming an exposed "eye" of water (steel).

Figure 4.6.5 shows the temporal evolution of the bubble tracks with 10% gas injection. Here, the greater initial gas flow rate, and the larger buoyancy of the forming column, prevents the initial bubbles from reaching the bottom of the tundish. Also, once steady-state conditions are reached, the area over which the bubbles spread out around the shroud is very large, as compared to that for 6%. This is due to the overall buoyancy force, which for 10% gas injection is almost double that of 6%.

When the mathematical modeling results are compared with the physical modeling results, the same trend was observed. These are shown in Figures 4.6.6 and 4.6.7.

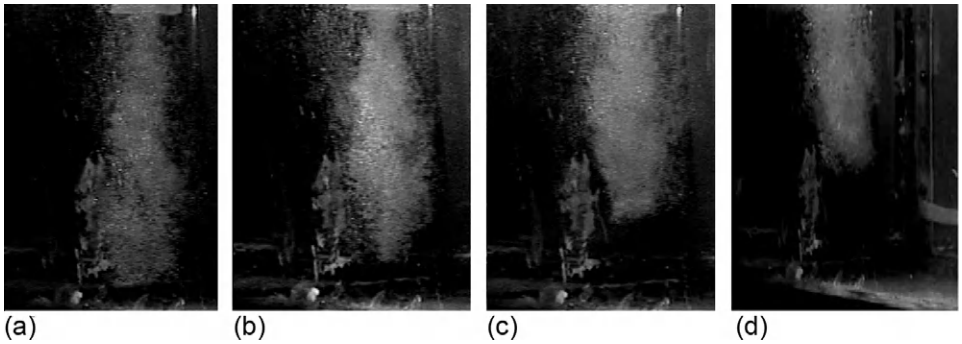


Figure 4.6.6 Bubble plume in the full-scale water model for gas injection at (a) 4%, (b) 6%, (c) 8%, and (d) 10% of water entry flows.

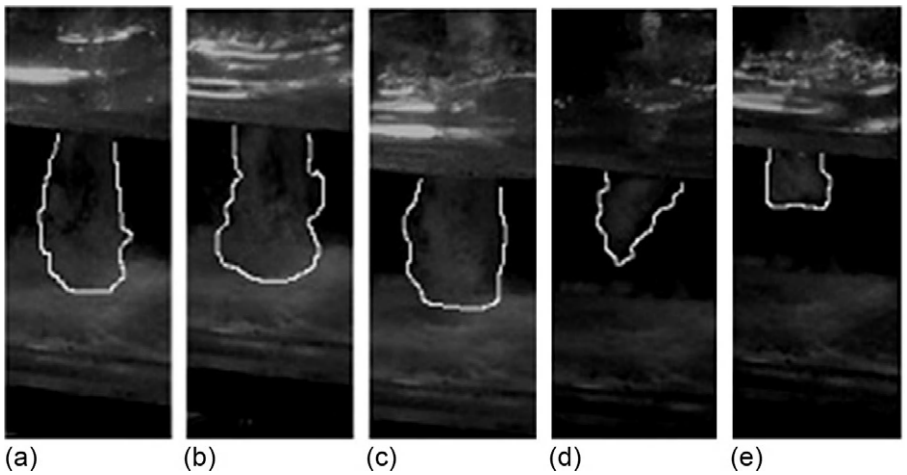


Figure 4.6.7 Bubble plume in the one-third scale water model for gas injection at (a) 2%, (b) 4%, (c) 6%, (d) 8%, and (e) 10% of water entry flows.

The depth of penetration of the bubble column varies with the volume fraction of gas injected. This was measured from the full-scale water model experiments and compared with those predicted from the mathematical model. The percentage error was also calculated and was found to be within +15%. Figure 4.6.8 shows the numerically predicted maximum depths of penetration of the bubble column (in the full-scale tundish), which decreases as the amount of gas injected in the entering liquid is increased. The corresponding experimental and computed penetration values, as a function of the percentage of gas blown, are given in Table 4.6.1. As seen, the model tends to slightly over predict the degree of penetration.

Another interesting observation was made from this 3D model. The trajectories of microbubbles in the size range 150–500 μm are totally different from those of the 3–5 mm diameter range of gas bubbles. Since microbubbles have much lower buoyancy

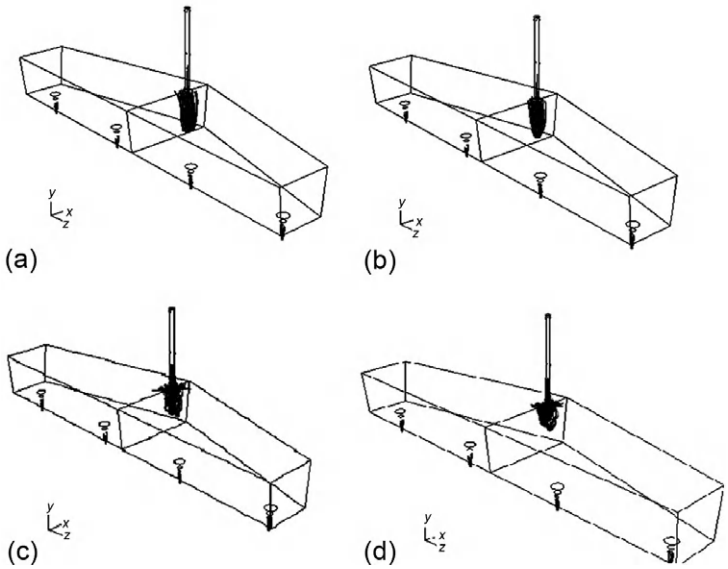


Figure 4.6.8 Numerically predicted penetration depth of the bubble column in the full-scale water model for gas injection at (a) 4%, (b) 6%, (c) 8%, and (d) 10% of water entry flows.

Table 4.6.1 Depth of Penetration of the Bubble Column from the Free Surface of the Tundish

Volume Fraction of Gas Injected (%)	Experimentally Measured Penetration Depth of the Bubble Column from the Free Surface of the Tundish (m)	Numerically Predicted Penetration Depth of the Bubble Column from the Free Surface of the Tundish (m)	Percentage Error (%)
4	0.5	0.5	0
6	0.416	0.433	+4.09
8	0.324	0.355	+9.57
10	0.267	0.294	+10.11

forces compared to 3–5 mm sized bubbles in steel, they tend to be in the Stokesian flow regime, with the bubbles fully entrained within the entering flow of liquid. They therefore spread out within the tundish with the liquid (Figure 4.6.9), rather than decoupling to form a rising bubble column. This was not reported by previous researchers. It is probable that this bubble-spreading phenomenon could be very beneficial for removing smaller inclusions from steel baths, so as to produce super clean steel.

The fluid flow modifications were validated with some water model experiments, in which surfactants were injected simultaneously with compressed air into the ladle shroud, thereby generating 0.05–0.3 mm microbubbles. The trajectories of these microbubbles were similar to our numerical predictions (Figure 4.6.10) and are quite different from the larger bubbles that are normally associated with gas bubbling in steelmaking operations.

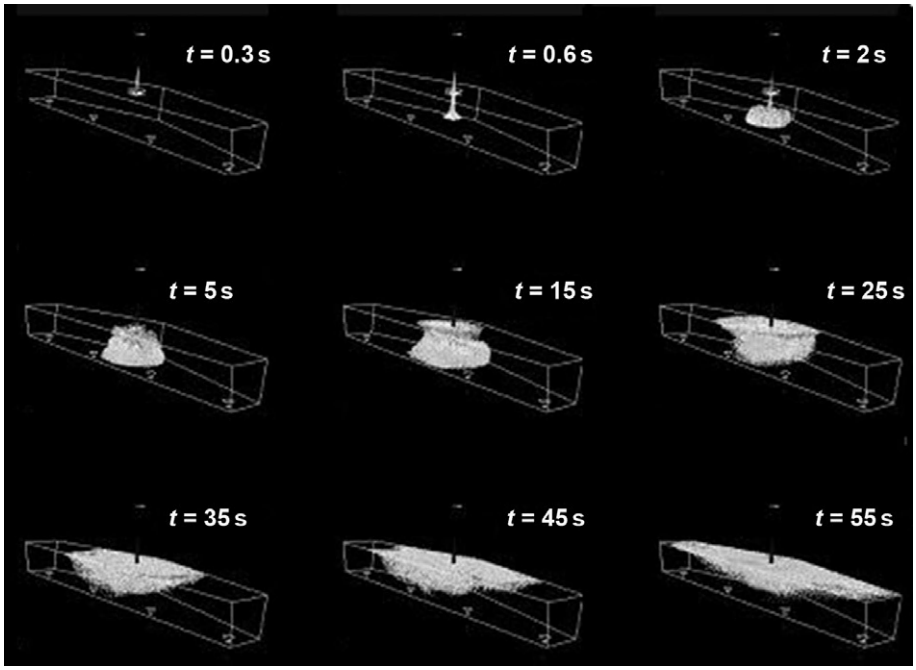


Figure 4.6.9 Predicted bubble trajectories when microbubbles of size 150–400 μm are formed in a tundish.

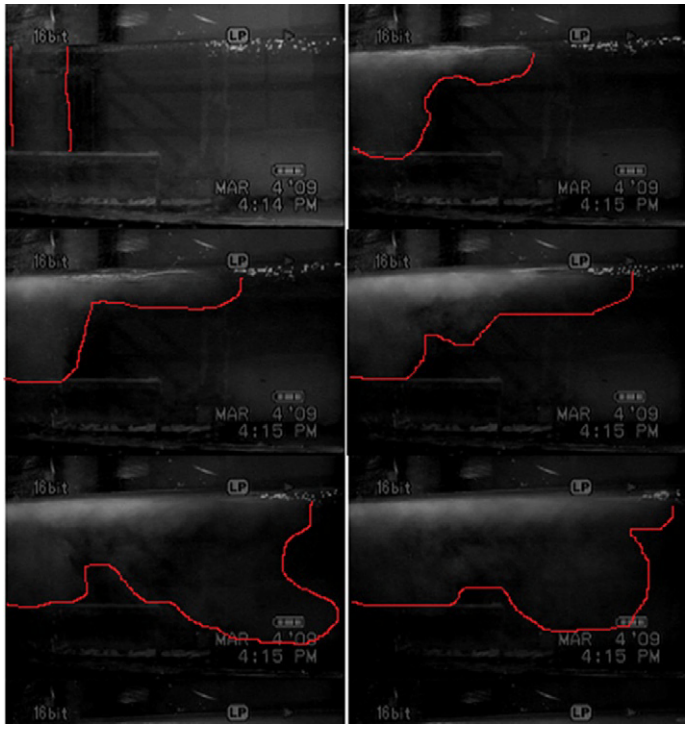


Figure 4.6.10 Experimentally observed microbubble cloud movement in the full-scale water model tundish.

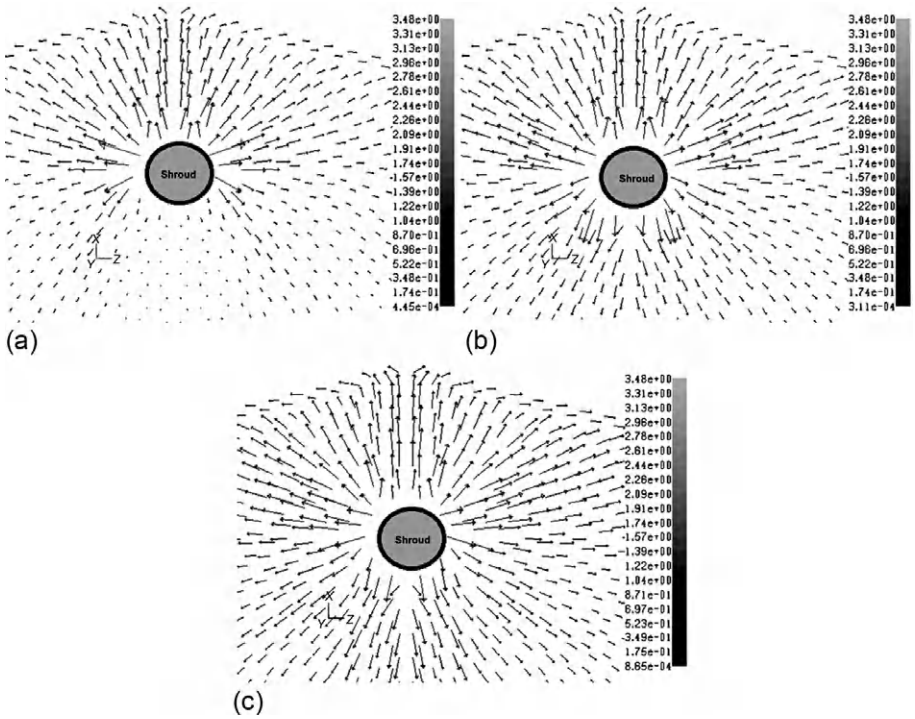


Figure 4.6.11 Predicted flow field (m s^{-1}) on the surface of the tundish (around the ladle shroud) with gas shrouding at (a) 4%, (b) 6%, and (c) 10% of water entry flows.

For these, the high surface tensions and nonwetting properties of the refractory orifices make the stability of injected microbubbles most unlikely.

4.6.3.3. Fluid Flow Patterns in the Tundish

The flow fields predicted from this 3D numerical model are next considered. Figure 4.6.11 shows the flow field at the top surface of the tundish with different amounts of gas injected. It is clearly seen that the fluid vectors are pointing away from the shroud and thus reversed flows are formed which tend to push the slag layer away from the shroud. The higher the amount of gas injected, the stronger are these reverse flows.

This fact was also validated with 2D PIV experiments in the full-scale water model. Reverse flows were detected on a plane just beside the ladle shroud and these are shown in Figure 4.6.12.

Figure 4.6.13 shows the numerically predicted flow fields around the ladle shroud on the surface of the tundish without any gas injection. It is seen that the vectors now point toward the shroud and thus prevents the formation of an "eye" around it.

The area of the exposed "eye" varies with gas flow rate, and slag thickness, and this is shown in Figures 4.6.14 and 4.6.15. Figure 4.6.14 represents full-scale water modeling with polyethylene beads as the slag phase, whereas Figure 4.6.15 represents one-third scale water

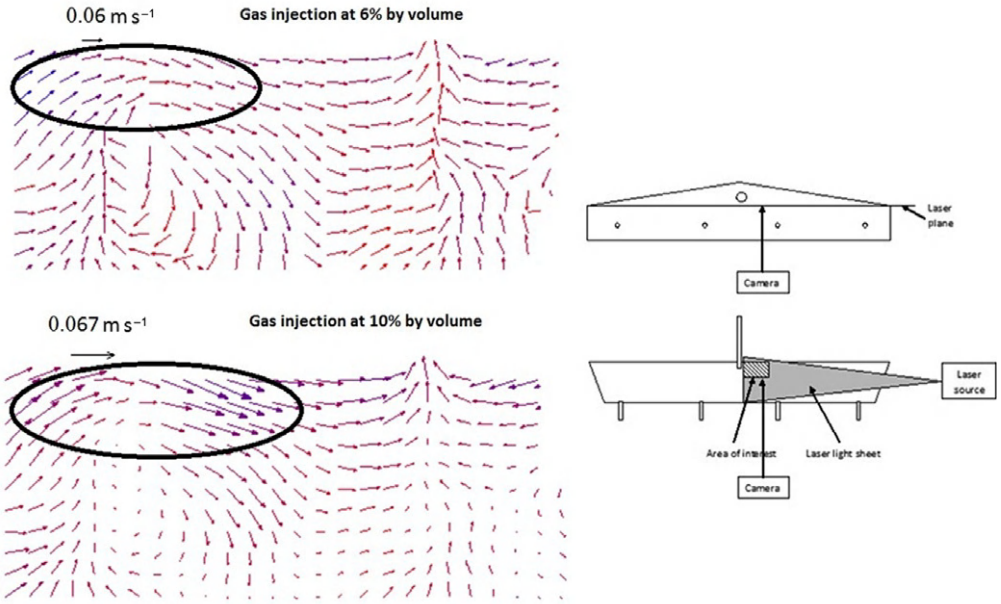


Figure 4.6.12 Velocity field (m s^{-1}) on a plane just beside the shroud measured by 2D PIV.

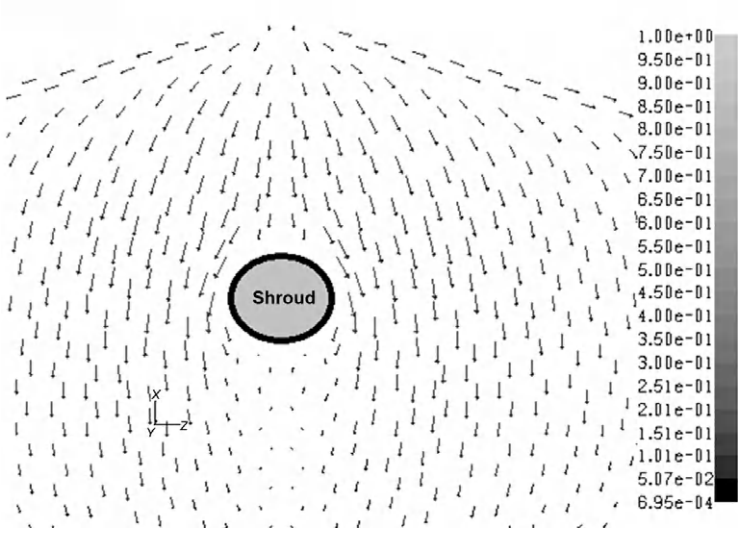


Figure 4.6.13 Predicted flow field (m s^{-1}) on the exposed liquid surface of the tundish (around the ladle shroud) without gas shrouding (no reverse surface flows).

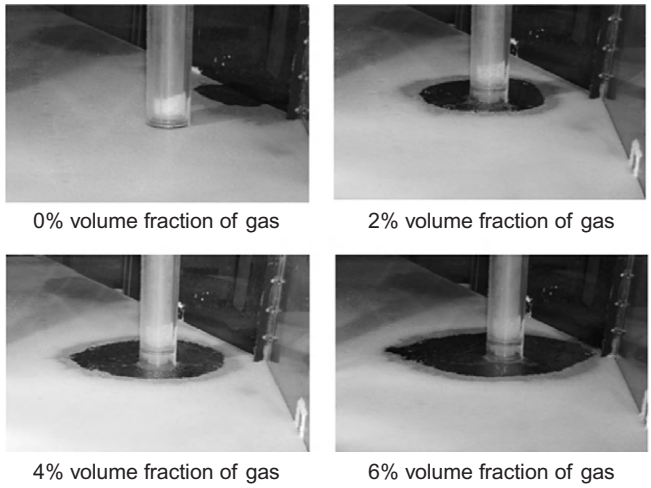


Figure 4.6.14 Showing exposed "eye" around the shroud in the full-scale water model due to inert gas shrouding.

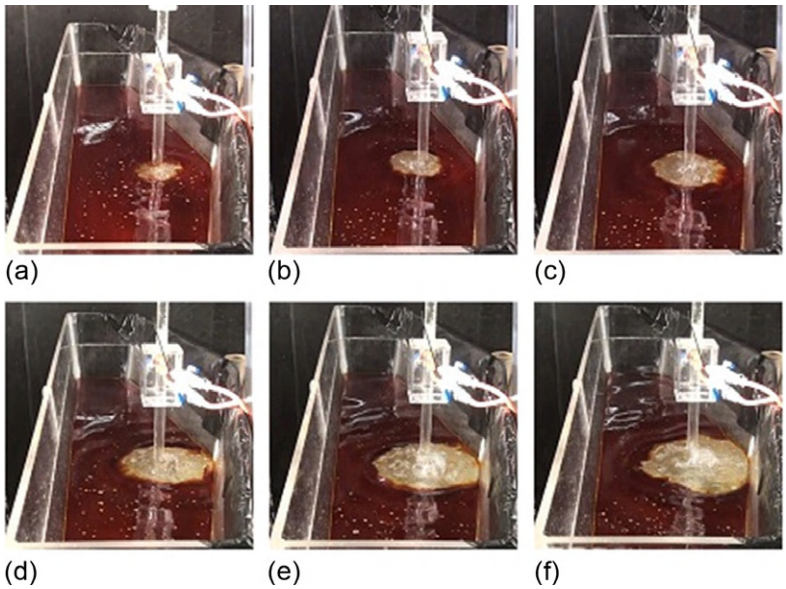


Figure 4.6.15 Showing exposed "eye" around the shroud in the one-third scale water model for gas injection at (a) 2%, (b) 4%, (c) 6%, (d) 8%, (e) 10%, and (f) 12% of water entry flows.

modeling with mineral oil as the slag phase. It is interesting to note that both systems behave similarly. Initially, without gas injection, the simulated slag phase (polyethylene beads or mineral oil) completely covers the water in the tundish. Then with increasing gas flow rate, the size of the exposed eye increases, and then when gas flow is stopped, they are restored back to their original positions. For low gas flow rates, the reverse flows are not so strong and hence the area of the exposed eye is small. For high gas flow rates, there are stronger reverse flows and so the area of the exposed eye is greater.

The size of the exposed "eye" was measured from the full-scale water model and was compared with that predicted numerically. To measure the area of the exposed "eye" from the numerical model, regions of high surface velocity were identified and the radius of the "eye" was calculated indirectly. For this, the edge of the "eye" was assumed to be located where the velocity was 10 times higher than the rest of the tundish (Figure 4.6.16).

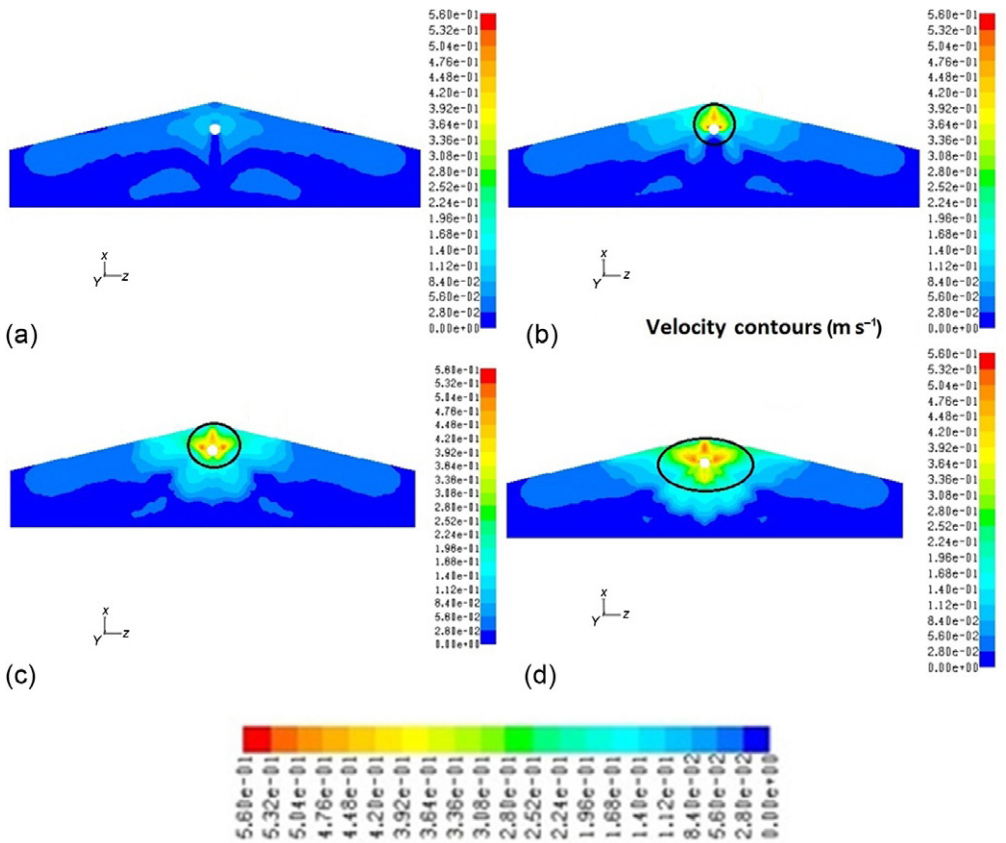


Figure 4.6.16 Numerically predicted velocity contours (m s^{-1}) on the surface of the tundish for gas injection at (a) 0%, (b) 4%, (c) 6%, and (d) 10% of water entry flows.

Table 4.6.2 Average Radius of the Slag "Eye" Measured from the Full-Scale Model

Volume Fraction of Gas Injected (%)	Experimentally Measured Average Slag "Eye" Radius (m)	Numerically Predicted Average Slag "Eye" Radius (m)	Percentage Error (%)
4	0.227	0.255	+12.55
6	0.3063	0.323	+5.45
10	0.43	0.474	+10.23

The area over which this high-velocity region extends should correspond to the area of an exposed "eye," depending on slag thickness. The values of the average radius of the exposed "eye" are given in Table 4.6.2 along with the percentage errors. The error was always less than +15%.

This amount of error can be tolerated, considering the randomness of turbulent flows. So without going into an actual multiphase model, an estimation of the "eye" diameter could be obtained.

4.6.3.4. Modeling of the Exposed "Eye" Using the Multiphase VOF Model

Modeling of the slag eye due to inert gas purging in steel ladles has been an active area of research for the past few years. Krishnapisharody and Irons [8] performed water model experiments to study the formation of spouts on the bath surface in gas stirred ladle systems. The experimental data were used to correlate the spout dimensions to the operating variables, namely, the gas flow rate and heights of water and oil layers. Nondimensional representations of the spout height revealed that factors such as the diameter of the ladle, size, and type of gas injector and physical properties of the gas–liquid system did not play any major role in the spout formation. Krishnapisharody and Irons [9,10] also developed mathematical models to estimate slag eye size in gas stirred ladle systems. Their model computed the eye size from the primary operating variables of the ladle and proved to be reliable in a variety of multiphase systems. Li *et al.* [11] developed a three-phase mathematical model to study the formation of exposed eyes in gas stirred ladle systems. Multiphase VOF method was used to simulate the behavior of the slag layer. Numerical simulation was conducted to clarify the transient phenomena of gas injection into the molten steel. When argon gas was injected into the molten steel in a ladle, the gas rising passage was formed near the plug, and then bubbles were created in the molten steel. The rising gas bubbles impinged on the slag intermittently and broke the slag layer to create the slag eye. Simultaneously, the wave at the slag–steel interface was formed and the wave frequency increased with the increase of argon gas flow rate for one off-centered plug case. Their modeling simulations showed that the diameter of slag eye changed from 0.43 to 0.81 m when the flow rate of argon gas was varied from 100 to 300 NL/min for a 220-ton ladle. The relationship between nondimensional areas of slag eye and

the modified Froude number was in good agreement with the experimental data reported in the literature. At the same total gas flow rate of 300 NL/min, the two plugs generated two eyes with diameters of around 0.6 m. Since the significant deformation of slag layer occurred during gas-stirring operation, the thickness of slag became thin near the slag eye and thick near the ladle wall, respectively. The downward flow velocity of steel at the slag eye periphery might be affected significantly by flow rate of Ar gas. Therefore, when the downward flow velocity would be larger, the more emulsification of slag could be expected. Peranandhanthan and Mazumdar [12] performed physical modeling to estimate the slag eye area in bottom purged ladles. They concluded that the slag eye area increased as the gas flow rate and the depth of bulk liquid were increased. On the contrary, the size of the exposed eye decreased with increasing thickness of the upper buoyant phase. Physical properties of the slag phase affected the area of the "eye." They developed a new simple correlation (which included three Froude number, Reynolds number, and density ratio) which could effectively predict the slag eye area in both aqueous and industrial scale ladle systems under a wide range of operating variables and upper slag phases. Mazumdar and Guthrie [13] reported on the input energy dissipation by an upper buoyant phase in gas stirred ladle systems. They mentioned that several factors such as thickness of the slag layer and its properties like viscosity and density have an important effect on the exposed eye area. A thicker slag phase would result in the formation of a smaller exposed "eye" and so is the case with a highly viscous slag phase. A highly viscous slag phase would tend to dissipate more energy due to frictional effects and viscous dissipation within, resulting in a smaller slag eye opening. Llanos *et al.* [14] developed a three-dimensional, three-phase mathematical model to study the fluid dynamics in slag covered, gas stirred ladles. Four cases were considered using one and two argon injection inlets with different configuration, where the multiphase steel/slag/argon system was simulated numerically in three-dimensional transient conditions and a water/oil/air system for the physical model was considered. The VOF model was employed to simulate the interaction between the phases considering the surface tensions. The simulation results were evaluated using a fluid dynamic analysis of the systems and by a numerical prediction of three important operational parameters, namely, mixing time, lining refractory wear, and slag opening. The implementation of two argon inlets did not reduce the mixing time; however, the slag layer opening was decreased by 30%, and the refractory wear in terms of the skin friction coefficient value was also decreased by 63%. A good agreement was obtained between the physical and mathematical modeling results, where the VOF model showed to be a powerful tool to simulate ladle gas-stirring operations. From the above discussions, it is clear that a lot of researchers have modeled exposed eyes in gas stirred ladle systems, but none of them ever tried to simulate it in a tundish. As seen in the previous section, the injection of inert gas into the shroud results in the formation of an exposed "eye" around the ladle shroud, and this is primarily caused because of reversed flows created on the bath surface. Also, when bubble trajectories were

examined, it was clear that a bubble column was formed just beneath the ladle shroud, within the tundish. However, this bubble column was not a conical plume, as in the case of bottom purged ladles. Most of the researchers, who performed mathematical modeling, used three-phase (VOF) mathematical models to simulate the formation of the "eye." In this study, the formation of the "eye" was modeled by using the DPM and a two-phase VOF model in synergy along with the k–ε turbulence model. Review of the literature reveals that this approach has never been used before to simulate the exposed "eye." Very fine mesh was necessary to obtain higher accuracy of the results. Considering this fact, the one-third scale tundish was chosen to develop this model. Around three million eight hundred thousand (3.8×10^6) tetrahedral cells were generated inside the domain and this was the maximum that could be done with the computers available. In this model, the phenomena considered were fluid flow, turbulence, discrete phase motion, and multiphase flow. Also, to efficiently track the formation of the exposed "eye," a very small time step of 10^{-5} s was used and this was the maximum allowed. Increasing the time step any further resulted in divergence of the solutions because of increased Courant number. The maximum Courant number during the solutions was 0.33. From the above discussions, it is very clear that the simulations for the exposed "eye" would require long computational times. Each simulation took around 40–45 days on a computer incorporating eight processors and 16 GB of RAM in order to simulate 6–7 s. Gas injections of 2%, 4%, and 6% by volume through the ladle shroud were considered and were modeled as discrete gas bubbles using the DPM. For the VOF model, the primary phase was taken as water and the secondary phase was taken as mineral oil (density = 870 kg m^{-3}, viscosity = 0.017 Pa s, and interfacial tension = 0.0425 Nm^{-1}). In reality, a third phase of air is present on the top of the slag, but it could not be considered here, because then the simulations were out of range of the memory available. Another interesting observation was that whenever the volume fraction of injected gas was set as 8% and higher, the computations exceeded memory after a very short period of time. The probable reason for this may be attributed to the fact that for 8–10% gas injection more bubbles need to be tracked as opposed to that for 6% and lower. So for tracking this extra amount of bubbles, some computational memory was used and this caused the overall solution to be out of memory.

In the physical model, it was seen that after the start of the gas injection, the exposed "eye" was formed in about 2 s and the size of the "eye" became stable after around 6–8 s. So for the mathematical model, for all the three gas flow cases, the simulations were done for 6 s. Figure 4.6.17 shows the exposed "eye" formed in the tundish for gas injections varying between 2% and 6% by volume after 6 s of gas injection. The red region represents mineral oil and the blue region is water. It is clearly seen that as the volume fraction of gas is increased, the area of the exposed "eye" increases. The average radius of this "eye" was measured and compared with that measured from the experiments in the one-third scale tundish. The percentage error was reported, and it was found that the

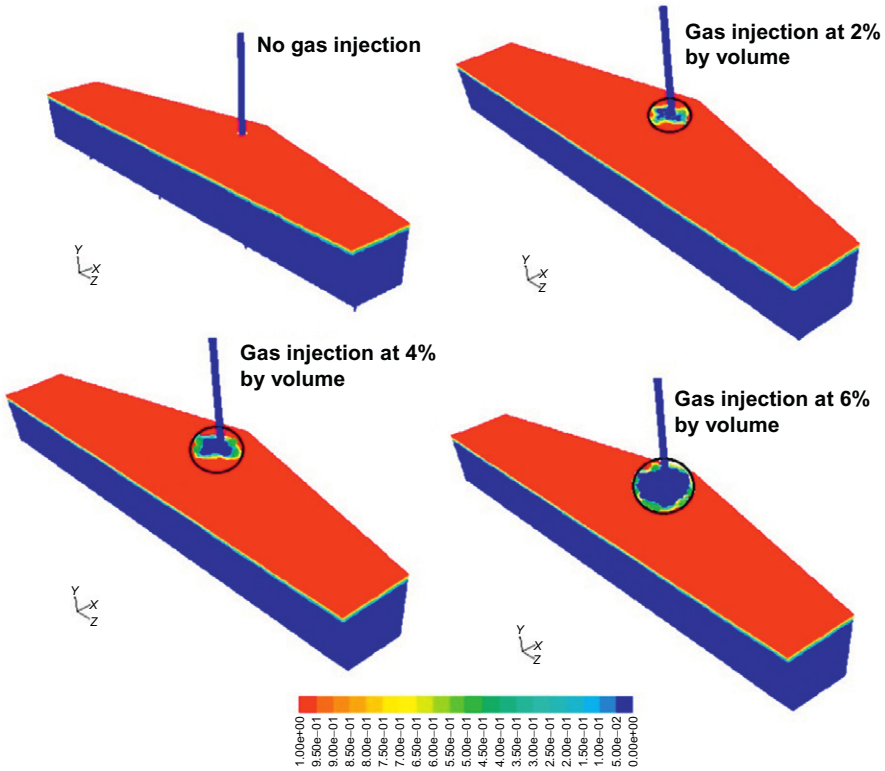


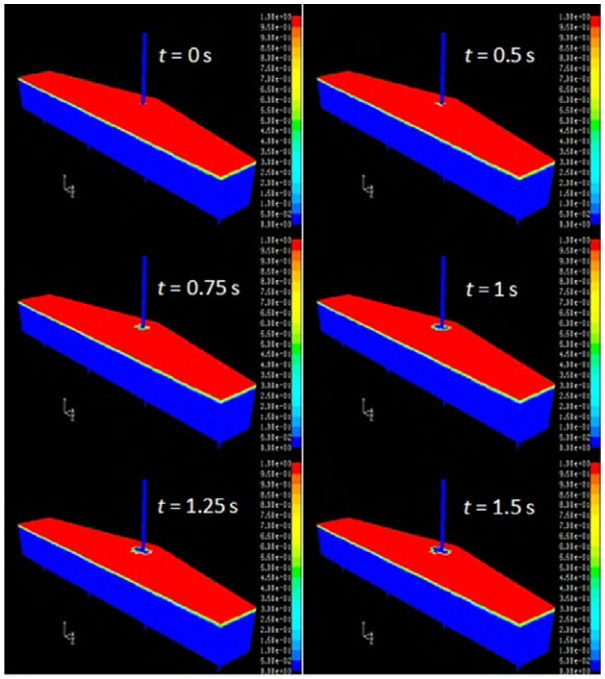
Figure 4.6.17 Predicted contours of the second phase (mineral oil) in the tundish after 6 s of gas injection.

Table 4.6.3 Average Radius of the Slag "Eye" Measured from the One-Third Scale Model

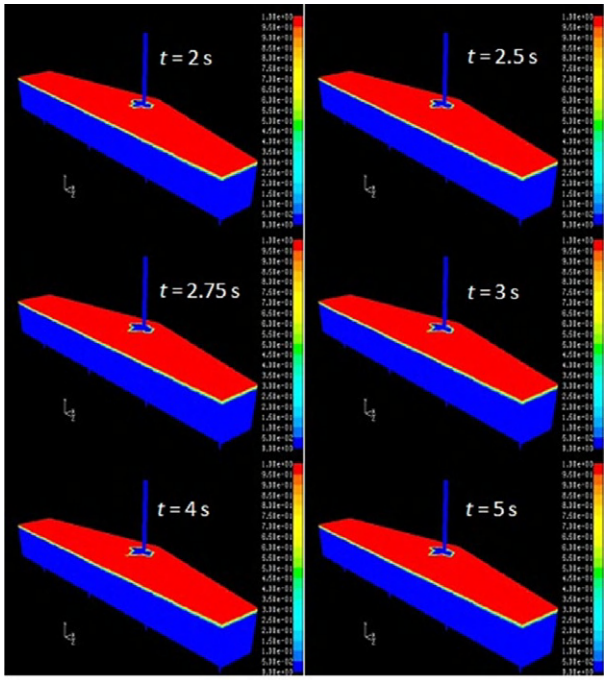
Volume Fraction of Gas Injected (%)	Experimentally Measured Average Slag "Eye" Radius (m)	Numerically Predicted Average Slag "Eye" Radius (m)	Percentage Error (%)
2	0.0527	0.0563	+6.83
4	0.0845	0.0913	+8.05
6	0.1266	0.1317	+4.02

errors are well below 10%. The mathematical model always overpredicted the "eye" radius. This error will be always present because in reality there is an upper phase of air and the free surface fluctuates. Finally, if the mesh size can be reduced further, maybe higher accuracy will be achieved (Table 4.6.3).

It should also be noted that the shape of the eye is circular, but never a perfect circle and this was evident in both the physical and the mathematical models. Figure 4.6.18a–c shows the temporal evolution of the exposed "eye" for 4% gas injection by volume. The shape of the "eye" changed with time and is evident in Figure 4.6.18. This phenomenon



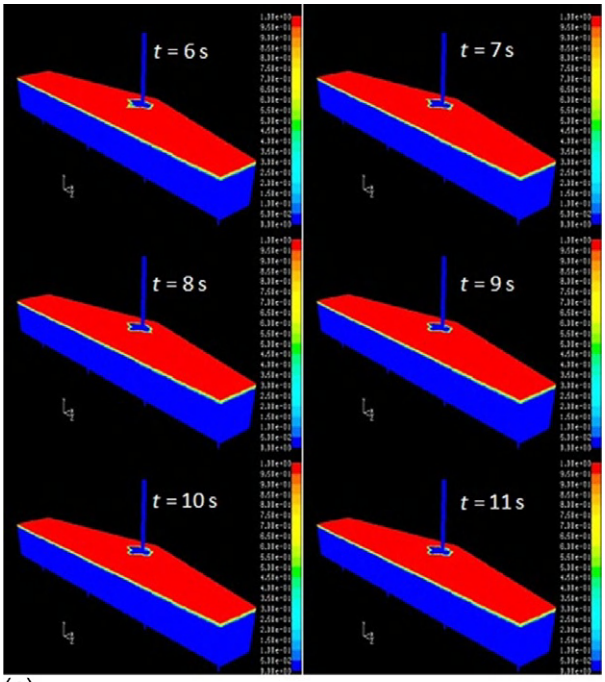
(a)



(b)

Figure 4.6.18 (a–c) Temporal evolution of the exposed "eye" due to gas injection at 4% of water entry flows.

(Continued)



(c)

Figure 4.6.18, cont'd.

was captured because of the very small time step used during the simulations. The exposed "eye" formed after about 0.5 s of gas injection. The area of the "eye" increased with time and became prominent at $t = 1$ s. After $t = 6$ s, the area of the "eye" became stable and continued to remain so till $t = 11$ s. However, the shape of the "eye" kept changing, and this is quite normal when gas bubbles are displacing a liquid phase. The bubble plume always oscillates with time, and hence the mineral oil layer also keeps on displacing.

REFERENCES

[1] ANSYS-FLUENT 12.0 Theory Guide, ANSYS Inc., USA.
[2] D.L. Youngs, in: K.W. Morton, M.J. Baines (Eds.), Numerical Methods for Fluid Dynamics, Academic Press, New York, NY, USA, 1982, pp. 273–285.
[3] C.W. Hirt, B.D. Nichols, J. Comput. Phys. 39 (1981) 201–225.
[4] Y.A. Buevich, Fluid Dyn. 1 (1966) 119.
[5] H.B. Kim, Modelling of Two Phase Gas–Liquid Flows in Ladle Shrouds, Master of Engineering Thesis, McGill University, Montreal, Canada, 1998.
[6] Y. Sahai, T. Emi, Tundish Technology for Clean Steel Production, World Scientific Publication Co. Pte. Ltd., Singapore, 2008.

[7] K. Chattopadhyay, M. Hasan, M. Isac, R.I.L. Guthrie, Metall. Mater. Trans. B 41B (2010) 225–233.
[8] K. Krishnapisharody, G.A. Irons, Metall. Mater. Trans. B 38B (2007) 367–375.
[9] K. Krishnapisharody, G.A. Irons, Metall. Mater. Trans. B 38B (2007) 377–388.
[10] K. Krishnapisharody, G.A. Irons, ISIJ Int. 48 (12) (2008) 1807–1809.
[11] B. Li, H. Yin, C.Q. Zhou, F. Tsukihashi, ISIJ Int. 48 (12) (2008) 1704–1711.
[12] M. Peranandhanthan, D. Mazumdar, ISIJ Int. 50 (11) (2010) 1622–1631.
[13] D. Mazumdar, R.I.L. Guthrie, Metall. Mater. Trans. B 41 (2010) 976–989.
[14] C.A. Llanos, S. Garcia-Hernandez, J.A. Ramos-Banderas, J. de. J Barreto, G. Solorio-Diaz, ISIJ Int. 50 (3) (2010) 396–402.

CHAPTER 4.7

The Design of a New Casting Process: From Fundamentals to Practice

Mihaiela Isac and Roderick I.L. Guthrie
McGill Metals Processing Centre (MMPC), Montreal, Canada

The last section of this chapter aims to instruct future process metallurgists on some guidelines and necessary steps needed to develop new, successful processes. In the light of the preceding sections of this chapter, one will appreciate the inexorable move toward a growing understanding and intimate knowledge of processes, of their potential for simplification, on how to improve their efficiency, how to make them better from an environmental point of view, as well as the eternal imperative to lower capital and operating costs for economic considerations. So, the first task in developing or conceiving a new process, or processing route, is to become intimately familiar with competing, or existing processes, and to then determine if there is a better way, conceptually. In the end, it is the people who are engaged in the research, and the top management who interactively determine the course of metallurgical advances.

4.7.1. CONTINUOUS CASTING MACHINES FOR THE STEEL INDUSTRY

Given the enormous tonnages of steel now being cast into flat rolled and long products, at a rate of about 1.4 billion tons per year, the market for a breakthrough technology was, and still remains, potentially enormous. This is true, provided that the introduction of any new process can satisfy all the requirements needed to usurp the present-day solution to forming metal sheets via the conventional continuous casting (CCC) approach, and then some. Even so, the penalties for a failed development can be disastrous, so this is not carried out lightly by a single steel producer in the fiercely competitive environment of steelmaking, in which one miss-step can often spell bankruptcy.

In the past 20 years, a number of Near Net Shape Casting (NNSC) technologies have appeared [1,2]. These have promised to shorten the steel production line, providing steel products with shapes and dimensions closer to the final product (Figure 4.7.1). Thus once CCC had totally usurped ingot casting practices, the first advance toward process rationalization of CCC was the development of the thin slab caster, or TSC, some 20 years later. However, meantime, the CCC became ever improved through further technical advances. While these new TSC machines were researched by the integrated mills, they were brought into the steel industry by their competitors, the scrap-melting Electric Arc

Treatise on Process Metallurgy, Volume 2
http://dx.doi.org/10.1016/B978-0-08-096984-8.00013-6
© 2014 Elsevier Ltd.
All rights reserved.

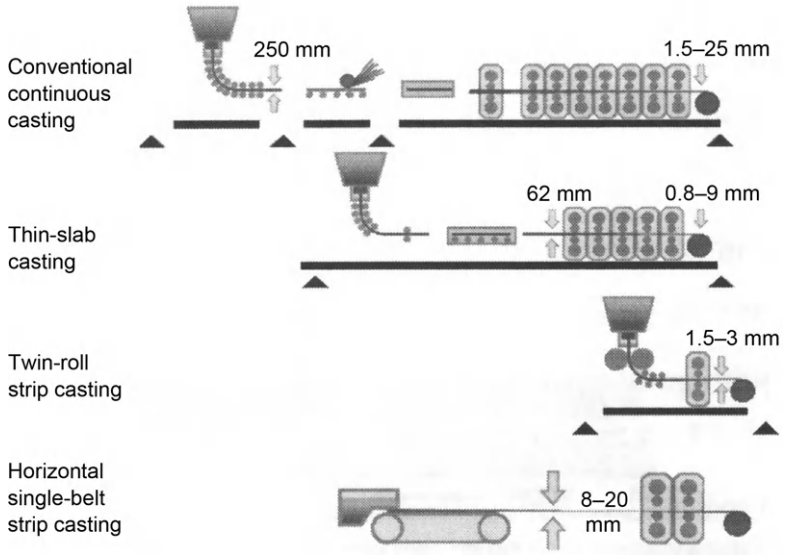


Figure 4.7.1 Typical layout and equipment for various forms of continuous casting machines.

Furnace (EAF)-based mini-mills, of North America. This allowed the latter to expand their operations out of long products, and to enter into the lucrative sheet steel market, so as to compete, head-on, with the sheet products of integrated plants!

Following the advance into TSC, there was also a burst of research activity by the large mills into the development of twin roll casting, an NNSC process. Unfortunately, these were even less suited for their company's high tonnage steel operations! However, the machines did promise to shorten the steel production lines even further, providing steel sheet products with thicknesses closer to final gauge (Figure 4.7.1).

Since the senior author of this chapter has been engaged for the past 25 years in promoting the development of a new generation of continuous casting machines suitable for integrated steelworks, as well as mini-mills, it is appropriate to consider this example of how a concept can gradually turn into a reality, provided one is prepared for the inevitable setbacks along the way.

Thus, in 1987, Dr. Guthrie was invited to take part in a Canadian workshop convened by Dr. Jock McKay, Director of the Stelco Research Laboratories, and Chairman of the Canadian Steel Industry Research Association (CSIRA). It gathered all the industrial, government, and leading academics, to brainstorm a new process for casting steels for integrated steelworks, using NNSC principles. The target was to recommend a NNSC process to produce 100–200 tons per hour per meter width for the integrated steel industry. After completing the McGill mandate of outlining the steel's physical and chemical requirements that would be needed, the author set about wrestling with the broader question of what such a machine should look like. In discussing various possible solutions and ideas with Dr. Joe Herbertson, a Research Associate at McGill who

had joined him, the HSBC (horizontal single-belt caster) process was conceived. The reaction to the proposal by CSIRA was negative, as the CSIRA steel companies had already collectively decided among themselves to develop Canada's French–English version of the twin roll caster process, under the name "Projet Bessemer." This made strategic sense, since the TRC process was, as previously noted, being investigated by many integrated steelmaking companies at that time. The workshop, in its collective wisdom, agreed that Canadians should also work on this apparently promising process. Five of Canada's largest steel companies decided to pool efforts and fund research work at the federal government laboratories at IMI, Boucherville, Quebec. The McGill Metals Processing Centre was allowed to participate on TRC, but at arm's length. This was made possible, thanks to the awarding of an NSERC strategic grant to the MMPC team. Despite this set-back, plan B was adopted by the inventors, and liquid metal delivery to an HSBC was patented in the United States and Canada [3]. Dr. Guthrie then visited his colleague, the late Dr. Geoffrey Belton, Director of Research, BHP, in Australia, who was enthusiastic. The two determined to test the new single-belt caster concept at BHP's Newcastle laboratories. To help in this effort, Dr. Joe Herbertson, who was keen to return to Australia, was recruited by Dr. Belton, all three having graduated from Imperial College, at various times. Discussions were initiated with the Hazelett Strip Casting Company and a single-belt caster was identified and delivered to BHP, Australia, to test out the proposed process. Patents were prepared, worldwide, based on the United States filing date [3]. Unfortunately, when BHP's upper management learned of this effort, they rightly decided that research on two NNSC processes was too ambitious for a single steel company. They opted to concentrate on the TRC process, which was more advanced, and involved IP agreements with IHI machine builders in Japan. Dr. Belton was upset, but was forced to stop his HSBC steel-casting trials, and send his team members down to support BHP's TRC studies in Melbourne. A few years later, Dr. Herbertson offered to send back the HSBC caster to Canada, so as to allow the MMPC team to continue further research and development on this novel casting concept.

Unbeknownst to the McGill researchers, Professor Schwerdtfeger, at TU Clausthal, in Germany, had come to exactly the same conclusion as to what such a casting machine should look like, and had also patented the DSC (direct steel casting) process [4]. Neither party knew of the other's work on DSC, or HSBC, but they were familiar with each other's reputations. When they later met, they agreed that the TRC process would not fit the requirements of an integrated steelworks, and that the single-belt caster was the most likely way forward for integrated steel plants. Unofficial collaboration began, in order to bring the concept to fruition.

4.7.1.1. Conventional Continuous Casting Machines

As shown in Figure 4.7.1, and in more detail in Figure 4.7.2, CCC operations [5] comprise a tundish, a water-cooled copper alloy mold, a mold oscillator, banks of cast strand

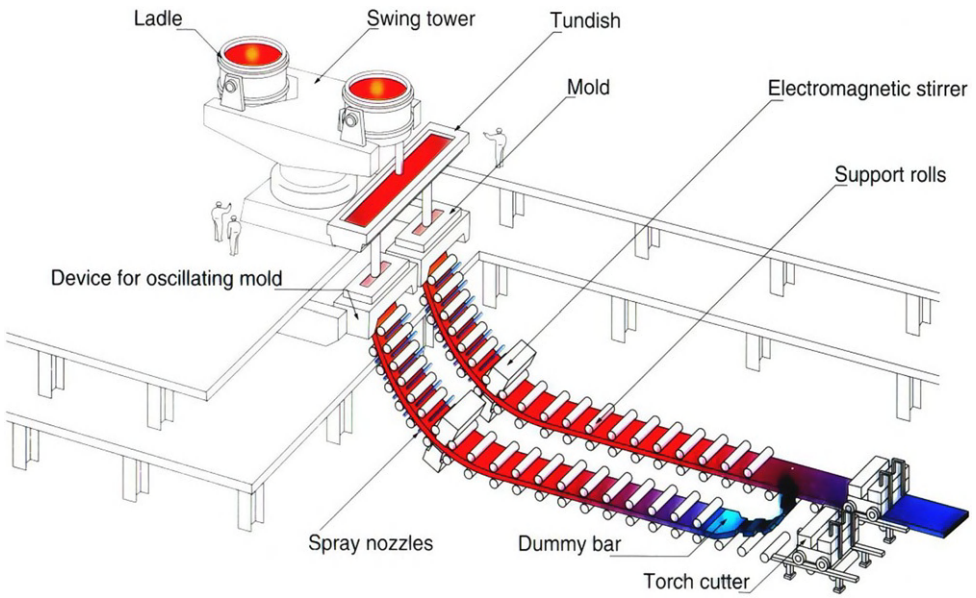


Figure 4.7.2 A two-strand continuous slab caster at Oita Works, Nippon Steel Corporation.

supporting rolls, rolls for bending and straightening the strand, rolls to pinch and withdraw the cast strands, groups of spray water nozzles to extract heat from the strand, a torch cutter for cutting the cast strand, and a dummy bar. This dummy bar fits in the bottom of the open mold at start-up, providing a starting base on which the strand can freeze. The dummy bar then extracts the cast strand, and finally moves away to "storage," once the forming strand has approached the torch cutter. The overall setup is generic, in that a "ladle" sits on a rotating "turret" or "swing tower," and empties liquid steel into a "tundish" set below via a protective ladle shroud (or tube). This tundish is used to distribute metal to one, two, four, six, or even eight, oscillating molds, set below. In the case of slab casting operations, it is common to have twin slab production. In the diagram, a SEN (submerged entry nozzle) is used so as to protect the streams entering the mold from reoxidation.

Once the ladle has been emptied of steel, the tundish is allowed to drain down somewhat, while the turret rotates a new filled ladle into position. In this way, sequence, or continuous–continuous casting can be achieved, with uninterrupted runs in the order of 1000 ladle changes being possible, using the flying tundish technique for rapid replacement of a spent one. Another popular type of fixed oscillating mold caster is the vertical and bending type caster, in which the mold and support rolls are arranged vertically so as to maximize the chances for inclusions to float out of the deep sump of molten steel, rather than being trapped in the (upper) solidifying shell. The solidified strand is then bent

and straightened to deliver the strand horizontally, and continuously. The fact that curved mold and low-head curved mold machines tend to capture a band of inclusions about mid-distance from the top surface of the strand and its central axial plane has led to the popularity of the vertical-bending machine class of casters.

In technically advanced steel mills, where surface quality is good (freedom from scabs, slivers, and deep oscillation marks), these slabs, blooms, and billets can be hot charged directly to a reheat furnace without surface inspection, prior to further size reduction. A certain amount of scale (iron oxide) forms on the slabs during their time in the reheating furnace. This can be useful, in moderation, since surface blemishes (oscillation marks, surface slivers, and seams) can be oxidized away, following passage through the high powered water jets of the descaler unit. In the case of slabs for sheet products, a roughing mill then rolls the slab down to a "transfer bar" some 25–40 mm (1–1.6 in.) thick. In most current commercial operations for sheet production, the transfer bar is then fed into a 6 or 7 stand hot strip mill, where steel sheet, 1–4 mm thick, is produced at speeds approaching 15 m/s (3000 ft./min). Strip temperatures, alloy compositions, and rates of compression are all carefully controlled so as to manipulate the solid state phase transformations, to optimize steel microstructures and physical properties [5].

4.7.1.2. Thin Slab Casting, TSC

In the past 25 years, progress toward the goal of process rationalization came through the development of thin slab casting, also based on the fixed, oscillating mold. This development was successful, and became the portal through which scrap based-EAF mini-mills were able to enter the flat products business. Thin slab-casting technology eliminates the need for a conventional rougher/breakdown mill, followed by a seven-stand hot rolling mill, using much more modest in-line rolling equipment. As a result, an integrated line comprising an advanced EAF-thin slab caster operation can produce ~500,000–800,000 tons/year. This is accomplished with lower investment costs in facilities and less energy consumption. Figure 4.7.3 illustrates the layout of such an SMS machine and the funnel shaped tapered type of mold, which allows for the placement of an SEN between its narrow faces. NUCOR brought this caster to commercial reality in order to advance its products into the sheet steel market [5].

4.7.1.3. Strip Casting, or Near Net-Shape Casting

Since about 1980, there had been many efforts to fulfill the dream of Sir Henry Bessemer, back in 1857, to cast steel strip directly from a pool of liquid steel using twin-roll casting technology. Various consortia and steel companies had researched the characteristics and potential of such machines. Then, in the millennium year 2000, Nippon Steel and Mitsubishi Heavy Industries announced the world's first commercial operation of a twin-roll caster for the production of stainless steel sheet, 2–5 mm thick, 0.76–1.3 m

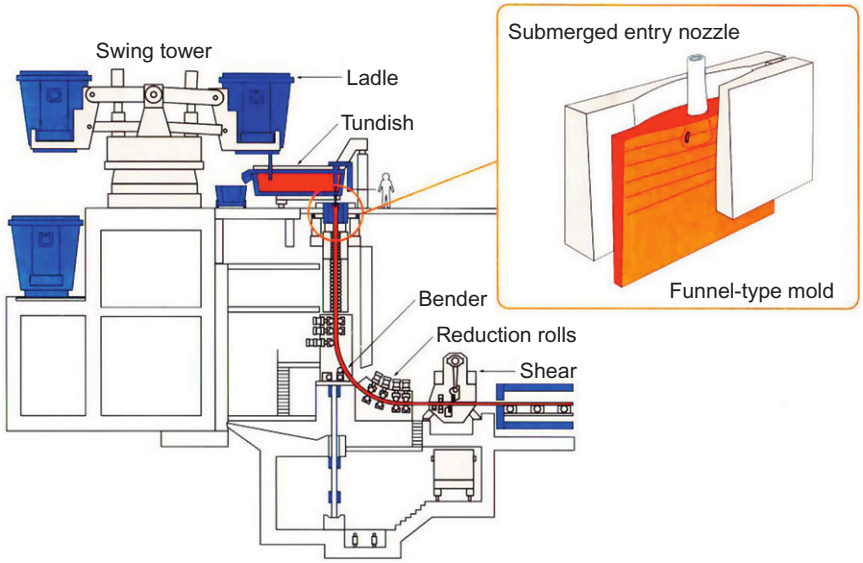


Figure 4.7.3 Thin slab caster operation.

wide, for their Hikari Works in Southern Japan. A schematic of their twin drum, or twin-roll caster, is shown in Figure 4.7.4. As seen, a conventional ladle and a single-strand tundish fed steel into a liquid sump of stainless steel created by the twin, counter-rotating rolls, and two side dams. The roll diameters were about 1.2 m, and peripheral roll speeds were in the order of 1 m/s. A pinch roll gathered the strip, which, following minimal hot working, was cooled and coiled directly into the finished product.

Similarly, following research work by BHP, Australia, under Project M, CASTRIP (NUCOR/BHP/IHI) was incorporated, and a twin roll caster was built by IHI to produce low-carbon steel strips for NUCOR. The production of the world's first commercial strip cast coils of low-carbon steel, 1.7–1.9 mm thick, was announced [6] following start-up of the caster in NUCOR's plant in Crawfordsville, Indiana, USA. Table 4.7.1 lists the CASTRIP machine's operational characteristics, while Table 4.7.2 lists its process parameters. As seen, its rolls are only 0.5 m diameter, running at speeds of 1–2 m/s.

Finally, steel makers had realized Bessemer's visionary intuition, and had apparently achieved the long sought after rationalization of the downstream processing of steel.

However, since these early successes, some companies have quietly stopped their TRC development work. These include NSC and the Eurostrip Consortium. Others are continuing. For instance, NUCOR has now built a second TRC, while POSCO (POstrip) and BaoSteel/NSC, continue on with their TRC research. Nonetheless, there is a *fivefold mismatch* in the productivity of a twin-roll caster versus current slab casting operations (e.g., 400,000 vs. 2,000,000 tpy), as illustrated in Figure 4.7.4. This, together

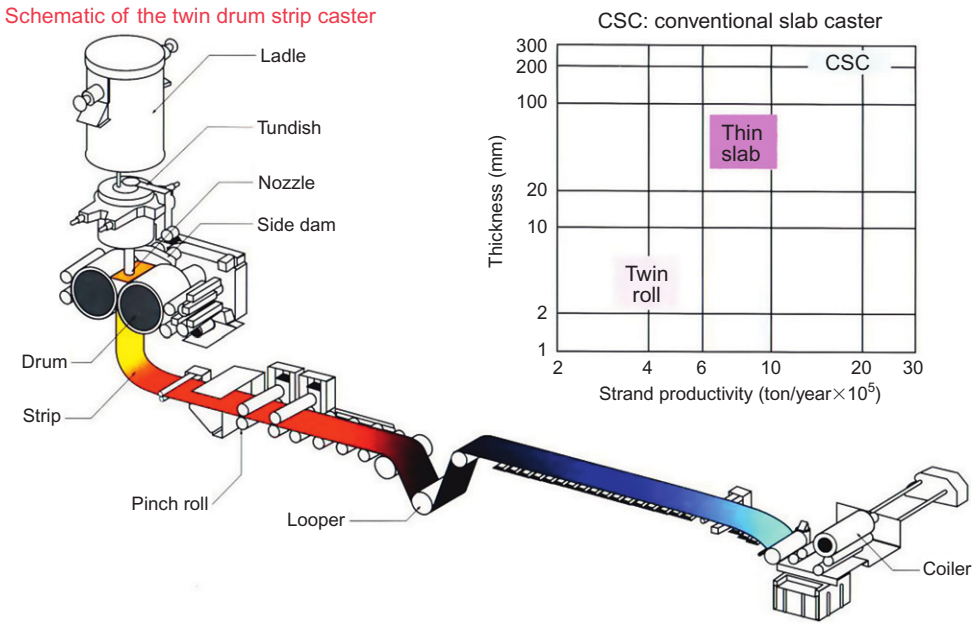


Figure 4.7.4 Schematic of the world's first commercial twin-drum caster for the strip casting of stainless steel at NSC Hikari Works. This was later stopped for "commercial reasons."

Table 4.7.1 Characteristics of NUCOR's Twin-Roll Strip Casting Facility (Metric Units)

No.	Characteristic	Specification
1.	LADLE TURRET CASTER	Twin arm turret
2.	Heat size	110 tons
3.	Mode of operation	4 Heat sequence casting
4.	Caster type	Twin roll 500 mm diameter
5.	Casting speed	80 m/min (typical), 150 m/min (maximum)
6.	Product strip thickness	0.7–2.1 mm
7.	Product strip width	2000 mm maximum
8.	Coil mass	25 tons
9.	Ladle size	110 tons
10.	Tundish	23 tons
11.	Tundish flow control	Slide gate

Continued

Table 4.7.1 Characteristics of NUCOR's Twin-Roll Strip Casting Facility (Metric Units)—cont'd

No.	Characteristic	Specification
12.	IN LINE REDUCTION MILL	
13.	Mill stand	Single stand—4 high with hydraulic AGC
14.	Work roll dimensions	475 mm × 2050 mm
15.	Backup roll dimensions	1550 mm × 2050 mm
16.	Rolling force	30 MN maximum
17.	Main drive	3500 kW
18.	Product capability	300–1000 kton/year

Table 4.7.2 Continuously Cast Products and Process Parameters

Parameters	Thick Slab	Thin Slab	CASTRIP's Twin-Roll Casting	HSBC
Cast thickness (mm)	240	60	2	2–10
Casting speed (m/min)	1–2	5	80	12–120
Average mold heat flux (MW/m^2)	1.3	2.5	15	10
Total solidification time (s)	1070	45	0.15	12
Ave., shell cooling rate (°C/s)	12	50	1700	500

with *thermomechanical considerations*, led to Guthrie's and Schwerdtfeger's joint conclusion that the horizontal single belt caster, "HSBC", or the German "DSC" caster, was a far better solution for an integrated steel plant. Thus, following a decade of pilot scale tests on HSBC casters in Australia and later Canada (BHP/McGill U.), and DSC tests at Clausthal University, Salzgitter, and later at MEFOS, Sweden, the world's first commercial HSBC caster was recently designed by SMS Siemag under the name Belt Casting Technology and delivered to the Peine Plant of Salzgitter AB. The caster is shown schematically in Figure 4.7.5 and is recently operational. It is reported to be working stably, casting one heat per week, as it is put through its paces. The entire process line is 60 m long, 11 m of which is the caster. With an 80-ton ladle capacity, the caster is designed to produce up to 1500-mm wide steel strips, at up to 30 m/min.

It was built to cast advanced high strength steels, whose production is virtually precluded from production in conventional hot rolling mills. This is because it is not possible to produce this new class of steel grades using CCC hot mill operations, owing to their high Ultimate Tensile Strength (UTSs) and strong work hardening characteristics. The endless water-cooled belts extend 11 m, far longer than those for the pilot scale casters used to trial the process. They must also stay planar, sustain thermal loading and

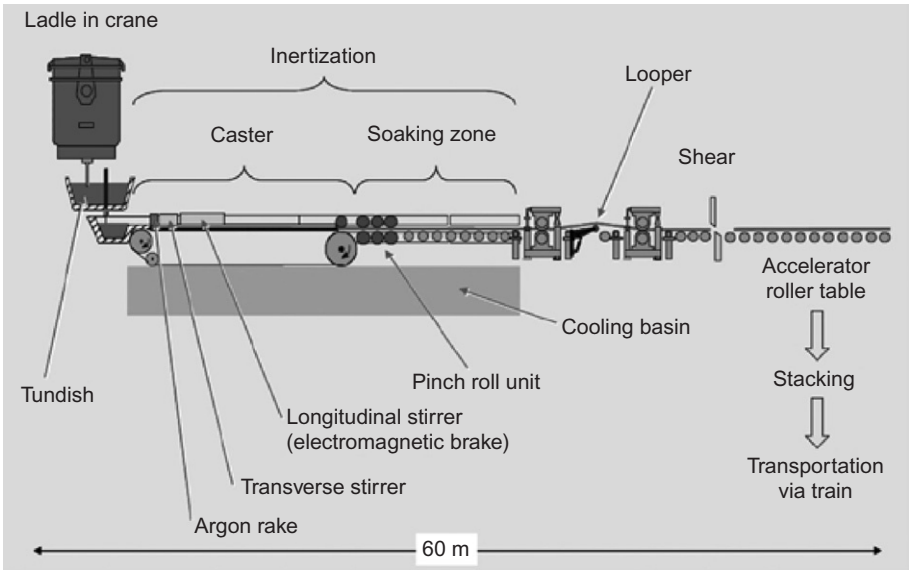


Figure 4.7.5 A schematic of the world's first commercial horizontal single-belt caster, at Salzgitter.

unloading, remain clean, and be able to function for many hours. For this, the mechanical and thermal loads acting on the belt and its guidance system will be severe. Similarly, the gasket between the moving belt and the side walls of the water chamber must be sealed perfectly for tightness, but must experience sufficiently low friction to avoid damage of the belt at its sides. For this commercial production, the width of the strip is 1.5 m, so an even delivery of metal across the width of the caster is crucial, as in the case for TRCs.

The feeding of steel onto the belt at higher speeds, however, is less difficult than feeding metal onto slower moving belts (~0.2–0.4 m/s). For the HSBC pilot casters, the metal flow on to the belt has to be throttled back, or the effective metal head values kept exceedingly small, in order to achieve iso-kinetic conditions with a slow moving belt, during the freezing of 10-mm thick strand on a 2.6 m belt. The reason for a 10-mm thick strip being targeted was to be able to provide a sufficient amount of thermomechanical conditioning to be able to produce the current grades of conventional steel grades. Other technical issues for HSBC casters, such as melt containment (side wall problems), strip edge profiles, and metal feeding, have all been successfully demonstrated on the large pilot scale caster at MEFOS, Lulea, Sweden, as discussed in articles by Carlsson *et al.* [7], and Nyström *et al.* [8]. Finally, casting with the single-belt HSBC process will have to be coupled with slow speed, in-line, hot rolling. Mathematical modeling of these issues suggests that this is feasible from a heat transfer point of view, and Salzgitter's HSBC caster at Peine will provide the answers [2].

Figure 4.7.6 shows the product thickness versus casting velocity needed to cast steel at 50 and 100 tons per hour, per meter width. Figure 4.7.7 shows the specific investment

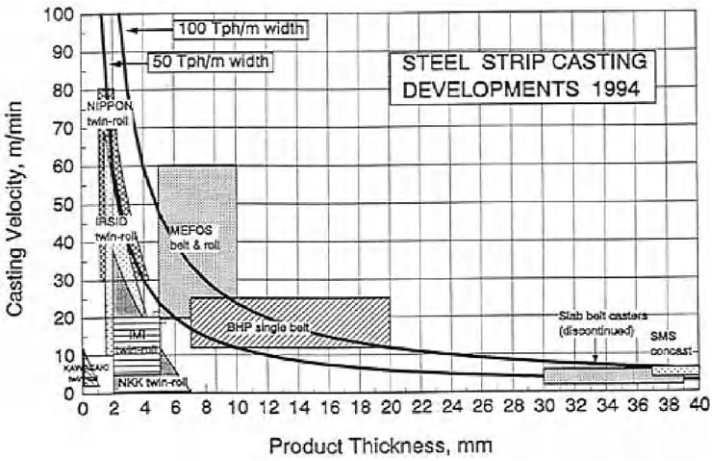


Figure 4.7.6 Various caster machines and programs 1994.

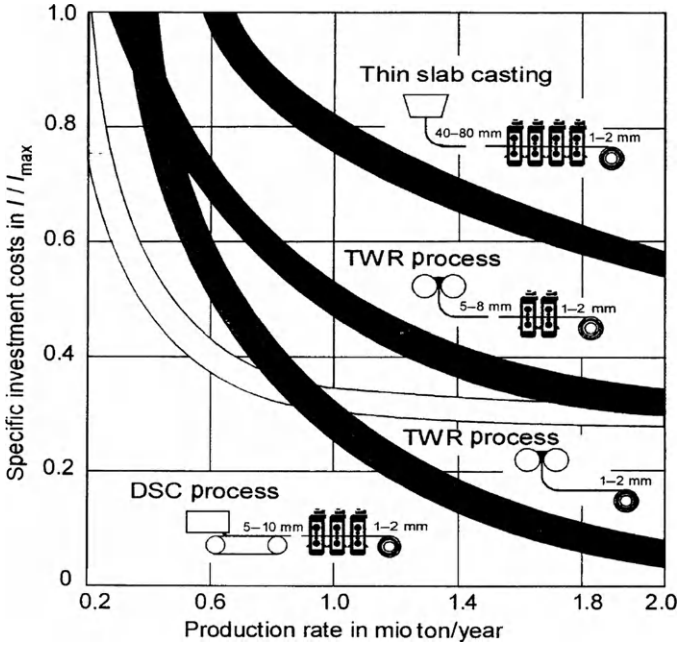


Figure 4.7.7 Specific investment costs.

costs for these NNSC machines. The higher productivity of such moving mold machines arises from the arbitrarily long lengths of water-cooled belts that can potentially be incorporated in such machine designs, versus the nonarbitrary sizes of rolls one can envision for TRC's machines.

We note that in the nonferrous industry, the Hazelett twin-belt caster is commonly used for the continuous casting of thin slabs of aluminum, copper, and zinc alloys, and their productive capacities are considerably greater than the TRC casters of Fata-Hunter.

4.7.2. FLUID FLOWS, SOLIDIFICATION, AND HEAT TRANSFER IN MOVING MOLD MACHINES

While process details of metal flow delivery systems for commercial *twin-roll casters* remain confidential to individual companies, our early mathematical and physical modeling of twin-roll casting processes pointed to a number of interesting avenues on how liquid metal should best be introduced into these machines, so as to ensure the even development of the solidification fronts across the widths of the two converging roll surfaces [9]. It also revealed inherent problems associated with the rapid grain growth of austenite immediately after the strip leaves the nip of the rolls. This can lead to relatively poor ferrite/pearlite microstructures with coarse grains.

Figure 4.7.8a depicts a half section of the sump of liquid steel and one roll surface and illustrates the predicted flow patterns that would be developed within a twin-roll caster, when a "conventional" bifurcated SEN used in slab casters delivers liquid steel to the sump. As seen, two hot jets of liquid steel pass across the sump of cooler liquid steel to either side dam losing heat as they travel and slowly mix in with the bulk liquid. They then split up to recirculate back toward the surfaces of the rotating rolls, losing superheat all the way. The net result, in terms of solidification, is that the shells of steel forming on the rolls will tend to be thicker near the mid-section of the rolls. This gives rise to the

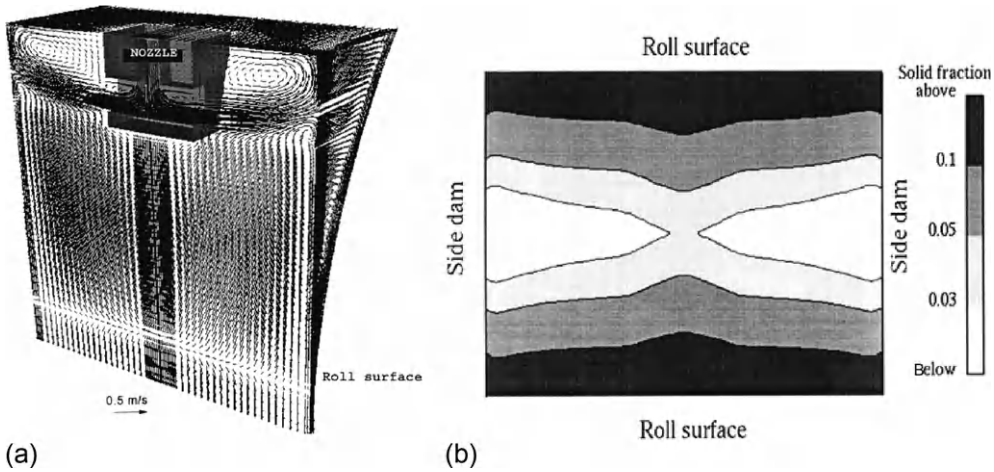


Figure 4.7.8 (a) Predicted velocity field of liquid steel within the sump of a twin-roll caster using a conventional tubular nozzle with horizontal ports; casting speed, 0.188 m/s; strip thickness, 4 mm; nozzle penetration, 5 cm. (b) Solid contour fractions 0.1 m below the top surface; superheat, 50 °C.

situation shown in Figure 4.7.8b, where the fractional amount of solidification is seen to be greater in the central region [9,10]. This will lead to uneven solidification of the forming shells, giving unstable operations, uneven microstructures, and associated variations in strip properties. Computations confirmed that the optimum way to effect solidification in an open metal delivery system to a TRC would be to arrange for a low velocity, horizontally directed flow of incoming steel from the entry nozzle, to be directed toward the two major menisci regions (or triple points) where the rotating roll surfaces first meet the pool of liquid steel. The use of a vertically slotted nozzle the full width of the rolls, as used by NSC, represented a reasonable alternative, although surface turbulence and freezing of the meniscus are predicted to be more problematic, together with a certain amount of shell remelting lower in the sump (i.e., the wedge-shaped pool of liquid steel between the rolls). A submerged cylindrical vertical shroud nozzle would be even worse, the hot vertical jet of liquid steel remelting the dendritically growing shells on the central regions of the roll surfaces. These modeling efforts pointed the way towards effective means to cast steel using TRC processes.

The *Heat Transfer* literature on twin-roll casting processes is relatively sparse. Strezov *et al.* [11] reported on instantaneous heat flux measurements made using a simulator of a TRC, in order to study the initial stages of solidification (0–100 ms) of stainless steel onto variously textured cold copper substrates. For these experiments, the copper slabs were set within a sturdy, instrumented, immersion paddle. This was rapidly plunged into an inductively stirred bath of stainless steel, and then quickly withdrawn for subsequent thermal monitoring and micro-structural analysis of the thin shells of steel so produced. The only other work on instantaneous heat fluxes was conducted in Canada, under Project Bessemer, in about 2000. For this, a TRC work roll was instrumented by McGill and IMI researchers, so as to measure heat fluxes directly [12]. This is the only set of thermal data reported in the literature concerning the direct measurement of instantaneous heat fluxes to the rolls of a twin-roll caster, which is not surprising, given that such measurements are rather challenging, particularly at high roll speeds.

On the other hand, overall values of heat fluxes and heat transfer coefficients are relatively easily measured, by measuring temperature rises in mold cooling water, together with exit strip temperatures from the roll nip. Wang and Matthys [13,14] report on various average heat transfer coefficients for thin strip casting. These are plotted in Figure 4.7.9 as a function of casting speed. While there is some scatter around the line, one sees that moving mold processes lead to increasing heat fluxes and heat transfer coefficients, as cooling substrate velocities increase. The scatter around the curve for various machines presumably relate to second order effects, such as substrate texture, mold material (i.e., copper alloy), protective coatings (e.g., plasma-coated layers of alumina or zirconia, etc.), gas environment, etc. It is to be noted that the average heat transfer coefficients obtained by Tavares *et al.* [12], determined from the integrated forms of their instantaneous measurements of $h(t)$ ($kW/m^2 K$) presented later, fit reasonably

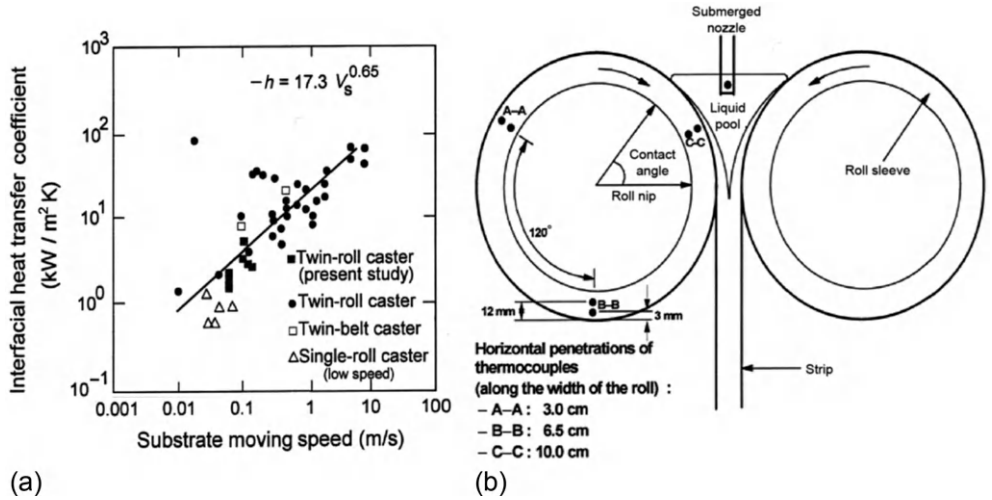


Figure 4.7.9 (a) Overall interfacial heat transfer coefficient vs. casting speed for TRC, SRC, and TBC casters. (b) Schematic of an instrumented roll for the IMI-TRC pilot scale caster.

well with the data of others, which all roughly fit on the correlation proposed by Wang and Matthys [14].

$$\overline{h_s} = 17.3 V_s^{0.65} \tag{4.7.1}$$

where V_s represents the rolls casting speed (m/s). These results show that the productivity of a strip-casting machine can be increased, the higher the rolling speed, V_s, and suggest that Equation (4.7.1) can give an adequate engineering estimate of the average heat transfer coefficient in NNSC operations, in the same way as the correlations proposed by Schwerdfeger, for fixed mold casting operations reported in Section 4.4, Figure 4.4.17.

However, any accurate evaluations of local cooling rates and temperatures across the strip during the solidification event itself, requires a knowledge of instantaneous values of interfacial heat fluxes and heat transfer coefficients during the time of contact of metal with the cooling substrate. Also, while the exponent 0.65 in Equation (4.7.2) is similar to the theoretical exponent of 0.5 for perfect thermal contact, it is to be emphasized that perfect thermal contact would have resulted in much higher solidification kinetics. The lower values can be ascribed to the imperfect contact at the mold–frozen metal interface. Thus, using embedded thermocouples, and an inverse heat transfer analysis, using the methods described by Beck, temperature–time data were used to deduce instantaneous heat fluxes to the roll surfaces during the production of steel strips. Steel strip compositions are listed in Table 4.7.3, while the experimental setup is shown in Figure 4.7.9b. There, a tubular SEN, with two horizontal ports in the direction of the side dams, was

Table 4.7.3 Chemical Analyses of the Low-Carbon Steels Used in McGill/IMI Experiments

Element/Steel	C	Mn	Si	P	S	Al	N
A	0.11	0.42	0.087	0.009	0.009	0.0004	0.0056
B	0.127	0.42	0.120	0.012	0.012	0.0030	0.0065
C	0.146	0.38	0.10	0.008	0.005	0.002	0.010

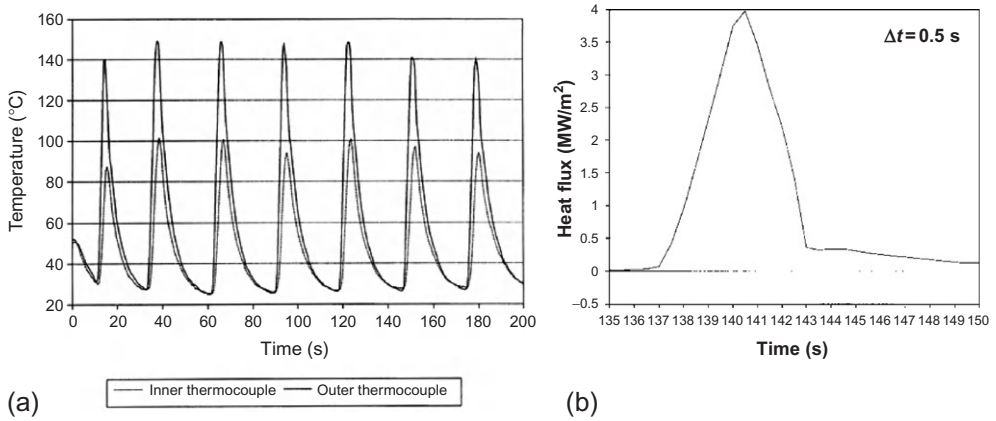


Figure 4.7.10 (a) Typical variation of the temperatures during contact of the roll surface with steel in the sump during casting of thicker strip. (b) Typical variation in heat fluxes during contact of roll surface with steel in the sump of twin-roll caster for thicker strip experiments ($u = 4$ m/min, strip 6–7.5 mm thick).

used to deliver liquid steel into the pilot scale twin-roll caster. In all experiments, the superheat in the molten steel was approximately 25 °C.

Figure 4.7.10 shows the cyclical responses of the external and internal thermocouples during rotation of the copper rolls. As seen, peak temperatures approaching 160 °C were measured by the outermost thermocouple located just beneath the roll surface, and up to 100 °C, at the inner thermocouple, 12 mm or so below the roll surface. During periods of noncontact with the liquid steel melt, temperatures returned close to cooling water temperatures of some 30 °C.

The variation in heat flux with contact time is presented in more detail in Figure 4.7.10b. There, following thermal radiation and liquid metal contact, a rapidly increasing heat flux to the roll surface was recorded. A maximum value was reached, usually after 1/2 to 2/3 of the metal sump-roll contact time. One will appreciate from Figure 4.7.10b that actual heat fluxes were quite different from those expected on the basis of quasi-perfect thermal contact, for which a maximum heat flux would have been registered at the first moment of contact between the liquid metal and the roll surface, as was demonstrated in Section 4.4, Figure 4.4.8, for the initial contact of hot metal with a cooling substrate. This delay in maximum heat fluxes was likely caused by a proprietary, thermally

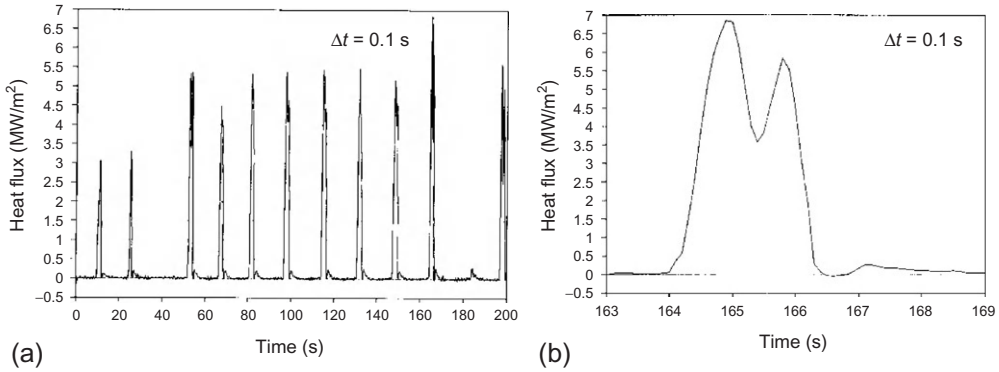


Figure 4.7.11 (a) Typical variation in heat fluxes at the roll–melt interface for thinner strip experiments. (b) Variation in heat fluxes during melt contact with the roll ($u = 7.5$ m/min, strip 3.5 mm).

insulating, thin plasma coating of unknown thickness and thermal properties that had been applied to the copper rolls, in order to reduce initial heat fluxes. This was reported to the McGill researchers by IMI scientists, much later, after repeated requests for any additional information! This illustrates the difficulties of University-Industry collaborations.

Figure 4.7.11 illustrates cyclic variations in heat fluxes during one of the "thin strip, higher speed" experiments, corresponding to 4 mm strips and roll speeds of 8 m/min. In general, the peak heat fluxes were higher than those obtained in the experiments of "thick strip/low speed" experiments, corresponding to 4 m/min and 6–7.5-mm thick strip. The higher peak heat fluxes were presumably due to the higher casting speeds.

Figure 4.7.11b presents the transient heat fluxes during one period of roll contact with the freezing shell. Up until about 70% of the contact time, the heat flux variations are similar to those shown in Figure 4.7.10b. The mechanism proposed for the experiments of the slow speed group should also apply here. However, for most of the higher speed experiments, a second peak in the heat flux was also observed during the last 30% of the contact time between the strip and the roll.

The second peak in the heat flux was probably associated with a more intense interaction of the two dendritic mushy zones formed between the rolls as the solid fraction at the center of the caster continuously increases. At some critical solid fraction, the dendrites form a cohesive network that begins to develop some strength and to exert pressure against the thin solidified shell, as the distance between the surfaces of the rolls continuously diminishes toward the roll nip.

It is believed that the relatively thinner solid shell in the second set of experiments was not able to withstand this internal pressure and was pushed against the surface of the roll, increasing the contact pressure and thereby the heat flux, as illustrated in Figure 4.7.12. Similar to what happens in rolling, the contact pressure then reduces after reaching a maximum.

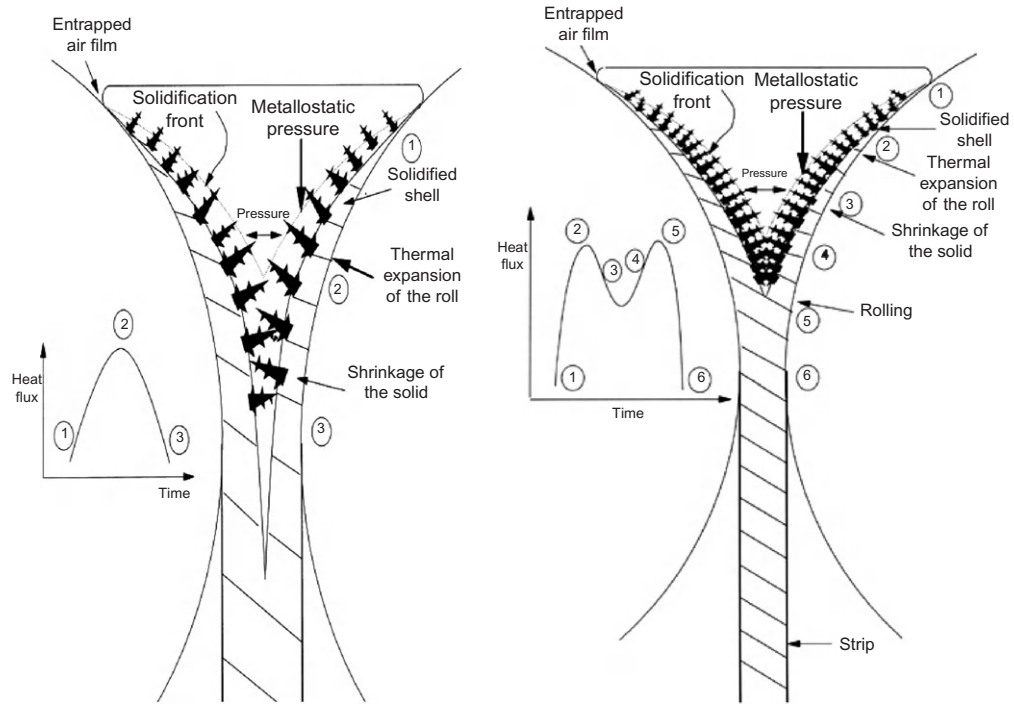


Figure 4.7.12 Mechanisms to explain transient heat flux variations in thicker (a), and thinner (b), strip experiments associated with lower (a), and higher (b) casting speeds.

The fact that a second peak was not detected in the "thick strip" experiments is probably associated with the lower cooling rate during solidification, due to the lower heat fluxes. Thus in the experiments of the low speed group, the solidified shells are thicker and did not deform to the same extent as the thinner shells associated with the thin strip set, once the rolling zone was reached. The latent heat of the mushy zone was then absorbed by the solid shells and not transferred to the working rolls. Finally, it should be noted that a constant force of 20 kN was applied to the 400-mm wide rolls at IMI, Boucherville, Quebec, independent of strip thickness being cast. It is therefore possible that the thinner shells were deformed such that better thermal contact was reestablished with the rolls.

4.7.3. THEORETICAL HEAT FLUXES, BASED ON PERFECT AND IMPERFECT, THERMAL CONTACT

While measured, interfacial heat transfer coefficients were initially low near to the melt meniscus; they increased to a maximum as the freezing shell moved down into the sump. Our time averaged values coincided quite well with the mean values obtained

by other workers, as illustrated in Figure 4.7.9a. In assessing the relative thermal resistances offered by the thin shell of freezing steel and the copper substrate, it is clear that a significant interfacial thermal resistance must have been responsible for these heat fluxes.

On the basis of much evidentiary work in the literature, and in the absence of information on plasma-coated surface rolls, which would also act to moderate initial heat fluxes, the low overall heat fluxes can be ascribed to the presence of a stabilised gas film at the interface. Within this thin-gas film, the heat is transferred by conduction, since radiation is of secondary importance (i.e., $q = h\Delta T \cong \frac{k}{\Delta x}\Delta T$). The air gap thickness, $\Delta x = \frac{k_{air}}{h}$, is related to the conductivity of the air and the heat transfer coefficient, according to $\Delta x = \frac{k_{air}}{h}$, while the heat flux between the melt and the substrate, in the presence of an interfacial resistance of negligible thermal capacity, becomes:

$$q = \frac{(T_M - T_S)}{\frac{M}{k'} + \frac{1}{h_g} + \sqrt{\frac{\pi t}{\rho C k}}} \tag{4.7.2}$$

Accepting Equation (4.7.2) for the mean interfacial heat transfer coefficient ($h_s = 17.3\, V_s^{0.65}$) and ascribing this resistance primarily to heat conduction over an air gap of thickness, δ, one can write:

$$h_g = \frac{k_g}{\delta_g} = 17.3 \times 10^3\, V_s^{0.65}\ \left(\mathrm{W/m^2K}\right) \tag{4.7.3}$$

or

$$\delta_g \approx \frac{k_g}{17{,}300 \times V_s^{0.65}}\ (\mathrm{m})$$

Taking $k_g \sim 0.08$ W/m/K at 1000 °C and $V_s \sim 1$ m/s, the mean air (or nitrogen) gap thickness would be 2.4 μm for a typical TRC operation. This is in keeping with the first principles analysis in Chapter 4.4.

4.7.4. SOLIDIFICATION AND STRIP MICROSTRUCTURES IN NNSC

In CCC operations for slabs, blooms, and billets, the as-cast microstructure is completely, or almost completely, changed during slab reheating operations. The cast structure transforms into FCC austenite, prior to hot rolling operations. However, in strip-casting processes, the as-cast structure can be of major significance in influencing the nature of the final microstructures and associated properties of the steel, since there is no "wiping of the slate clean." As such, final microstructures will be affected by instantaneous heat fluxes at the roll–strip interfaces. As with heat fluxes, little quantitative work has been published in the open literature regarding the as-cast structure of low-carbon steels strips produced by twin-roll casting. The investigation of Shiang and Wray [15]

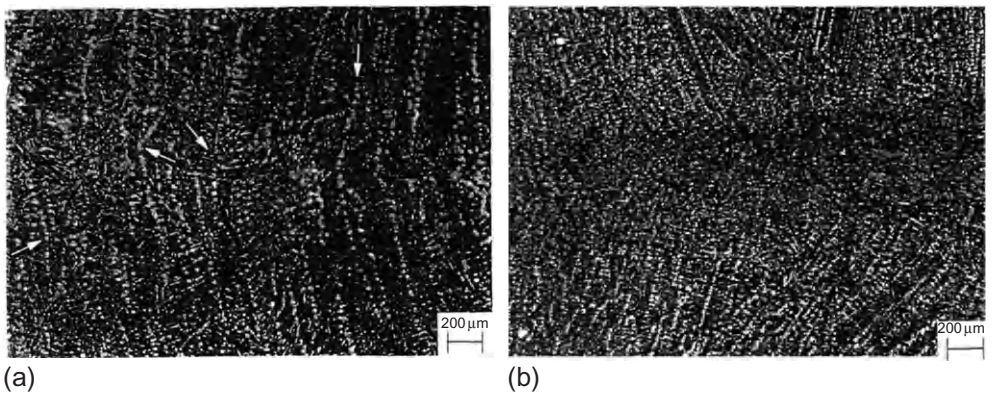


Figure 4.7.13 Typical dendritic structures revealed in a transverse section of (a) a 6-mm thick strip and (b) a 3.5-mm thick TRC strip, at casting speeds of 4 m/min and 7.5 m/min, respectively. Original dendritic microstructure revealed through use of Oberhoffer's etchant. Casting is left to right in (a), and right to left, in (b).

was mainly devoted to an analysis of how strip microstructures respond to different thermal processing operations, while Ueshima *et al.* [16] studied the effect of MnS precipitation during the strip's solidification, on ferrite grain size distribution. None of these works correlated the characteristics of the microstructures, particularly grain sizes, to the corresponding rates of heat extraction and to caster conditions.

Figure 4.7.13a shows a transverse section of the dendritic structure of 6-mm thick strip, cut from a hypo-eutectoid steel, cast at slow speed, 4 m/min, in the Bessemer twin-roll caster at IMI Boucherville. The primary solidification, or dendritic, structure was revealed using *Oberhoffer's reagent*. Basically, this etching solution reveals the different levels of microsegregation. The areas richer in iron (dendrites) appear black, while regions with higher concentrations of impurities (interdendritic spaces) appear white. The structure is essentially columnar, with the radial growth of columnar dendrites meeting approximately at the center of the strip, and angled at about 15° in the direction of casting. Signs of interaction of the columnar dendrites coming from the two surfaces of the strip can be seen; various broken and bent dendrites are apparent, as indicated by the arrows. This is more likely to occur in situations of relatively large interdendritic spaces, associated with the lower cooling rates pertaining to the thick strip experiments. A transverse section of the dendritic structure of a 3.5 mm thick, thin strip, produced at the higher casting speed ~7.5 m/min, is illustrated in Figure 4.7.13b. Again, columnar dendrites are formed close to the surfaces of the strip. The primary dendrite spacing here is much smaller, in agreement with the higher cooling rates (higher heat fluxes) for the higher speed experiments. It is also seen, in contrast to Figure 4.7.13a, that the columnar dendrites do not reach the center of the strip. Previous investigations also reported on an equiaxed zone in the center of twin-roll cast strips. This was attributed to incomplete

solidification of the strip at the roll gap. In the work of Tavares [9], simulations of heat transfer and solidification, using average heat fluxes determined experimentally, revealed that the strips were usually fully solid just above the roll gap. It is also seen in Figure 4.7.13b that the noncolumnar zone is darker than the surrounding areas. Considering that Oberhoffer's reagent causes the regions richer in impurities to appear white, this suggests that the noncolumnar zone was depleted of these impurities, possibly due to squeezing of the interdendritic liquid back into the sump. This evidence is consistent with the reverse flows of steel that are predicted to occur as the two shells of steel converge as they approach the roll nip. Excess entrained steel in the roll boundary layers are returned back up toward the surface of the steel (see Figure 4.7.8a). This suggests that a more intense interaction of dendrites, together with a certain amount of hot deformation of the strip before leaving the rolls, was responsible for the equiaxed zone and the second peak in instantaneous heat fluxes.

Figure 4.7.14 shows the as cast structure across the thickness of one TRC strip produced in a thick strip experiment as revealed by a *nital etching* solution. This section was taken from a region located approximately halfway between the center and the edge of

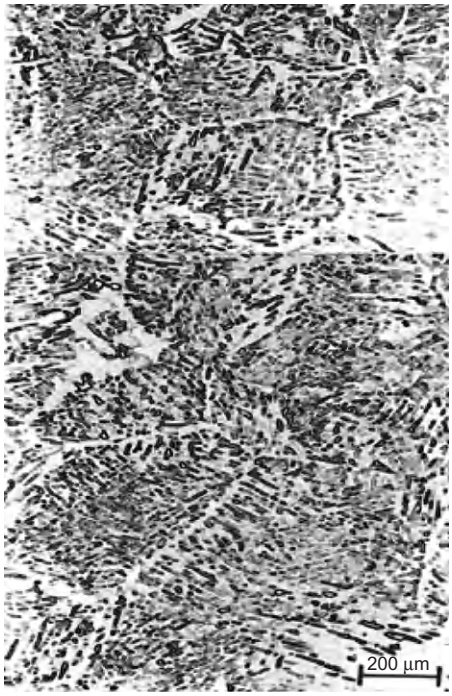


Figure 4.7.14 As-cast structure in a transverse section of a strip produced (6 mm thick, casting speed 4 m/min). Nital etch reveals grain boundaries of prior austenite, and Widmanstatten type microstructure.

the strip (along its width). As seen, the room temperature structure was mainly composed of ferrite and pearlite. The morphology of the ferrite in this sample is usually called a *Widmanstätten structure*, which is a microstructure produced when the prior austenite grains are large, and the cooling rates during transformation from austenite to ferrite and pearlite is relatively high.

The Widmanstätten plates nucleate at the austenite grain boundaries and grow along well-defined matrix planes [10]. They grow either from the grain boundaries or from preexisting ferrite allotriomorphs. Nucleation can also occur inside the grains, at the austenite twin planes. This kind of nucleation pattern, mainly at the grain boundaries, allows one to approximately identify the sizes and shapes of the prior austenite grains, prior to their transformation. These are delineated by the white network of ferrite. This feature was used to estimate the prior austenite grain sizes, which can be identified through inspection of Figure 4.7.14. The prior austenite grains are seen to be large, especially near the strip's surface (bottom of photograph), where they show a tendency to columnar shapes.

Mathematical simulations of heat transfer, solidification, and subsequent grain growth across the strip thickness, indicate that the surface region experiences significant reheating after leaving the roll gap, in much the same way as conventional casting (bloom back). This reheating also favors a more pronounced grain growth of austenite in the surface regions of the strip.

Figure 4.7.15 present predictions for the variation of austenite grain size, for the thick strip and the slow speed groups, as a function of distance below meniscus, for the surface and center of the strip. As seen, three different equations were used for calculations of austenite grain growth. Equation (10), obtained from the solidification studies of Yasumoto *et al.* [17], predicts a more pronounced and faster grain growth than those given by the equation proposed by Maehara *et al.* [18], and by the equation proposed by Ikawa *et al.* [19]:

$$D_Y^3 - D_{Yo}^3 = 3.434 \times 10^{34} \sum_{i=1}^{n} \Delta t_i \exp\left(\frac{-135767.5}{T_i}\right) \tag{4.7.4}$$

To verify these predictions, a few approximate measurements of austenite grain sizes were made. The prior austenite grains presented very irregular shapes. Two dimensions were then used to specify their sizes (Figure 4.7.16), a major and a minor length, and the following average values were obtained: major length: 780 μm (standard deviation: 328 μm, $n = 10$); minor length: 453 μm (standard deviation: 117 μm, $n = 10$).

These results are mainly for the surface region. In the center of the strip, the austenite grains that were identified presented a more equiaxed shape, with sizes ranging from 130 to 360 μm.

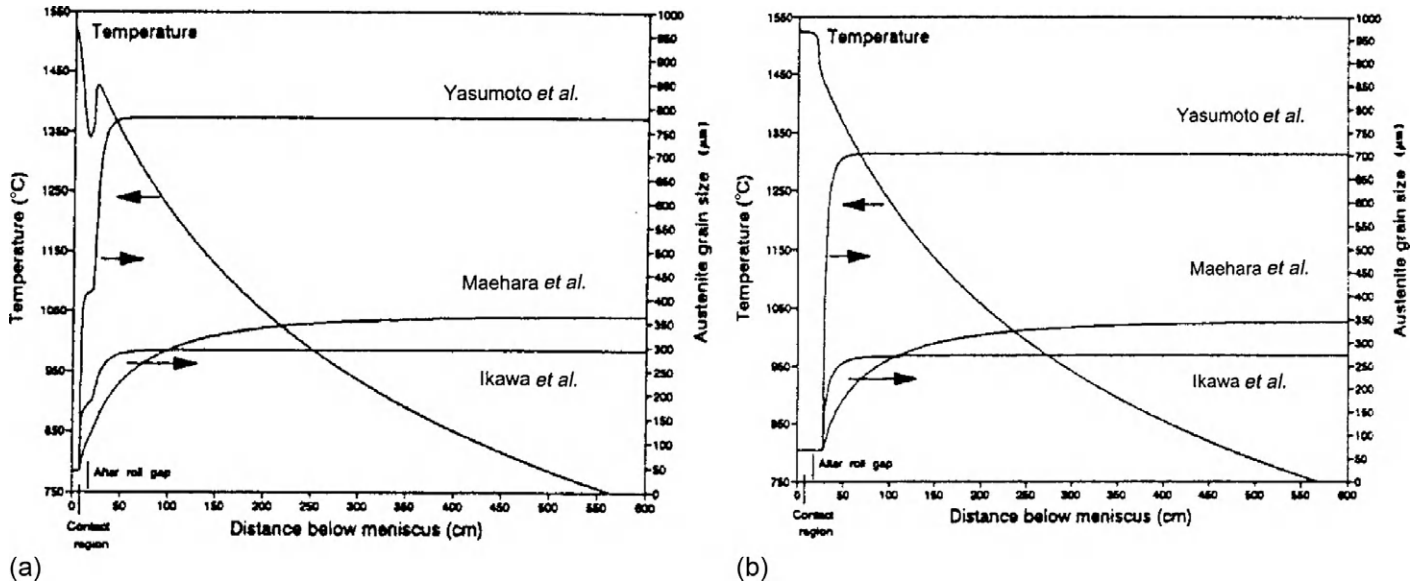


Figure 4.7.15 Predictions of austenite grains sizes and strip temperatures as a function of distance below meniscus of the IMI-TRC, for 6-mm thick strip (a: strip surface, b: strip center).

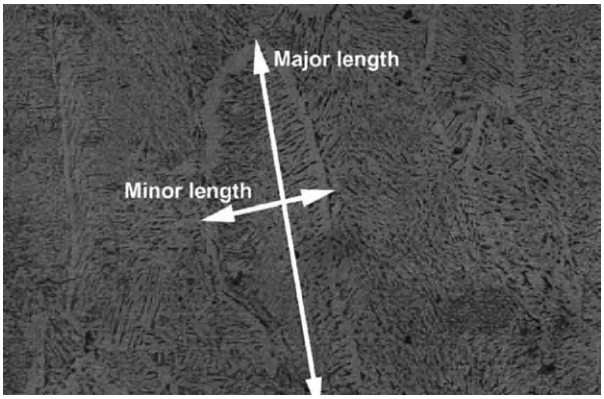


Figure 4.7.16 Dimensions used to define the prior austenite grain sizes.

4.7.5. HORIZONTAL SINGLE-BELT CASTING PROCESSES

In the single-belt process, the liquid steel is fed from the steel supply system onto a moving belt ~1 mm thick, made from steel or copper sheet, which is cooled from below by water emerging from nozzles located in the cooling chamber. "Thick strip" is produced, with thicknesses between 7 and 15 mm. Compared to twin-roll caster research, developments only recently led to a production scale installation. Table 4.7.4 gives data

Table 4.7.4 Data on Available Single-Belt Pilot Scale Casting Installations

	Clausthal II (Pilot)	**MEFOS**	**McGill**
Cooled belt length (mm)	3200	3800	2600
Belt width (mm)	500	1050	400
Belt material	Low C steel	Copper, low C steel	Copper, low C steel
Strand thickness (mm)	10–15	10–12	5–10
Cast strand width (mm)	300	450, 870	200
Realized velocity (cm/s) (at 10 mm)	18	29	20
Furnace capacity (kg)	1300	4000	250
In-line rolling	Yes	No	Yes
Roll diameter (mm)	300	–	300
Roll width (mm)	450	–	400

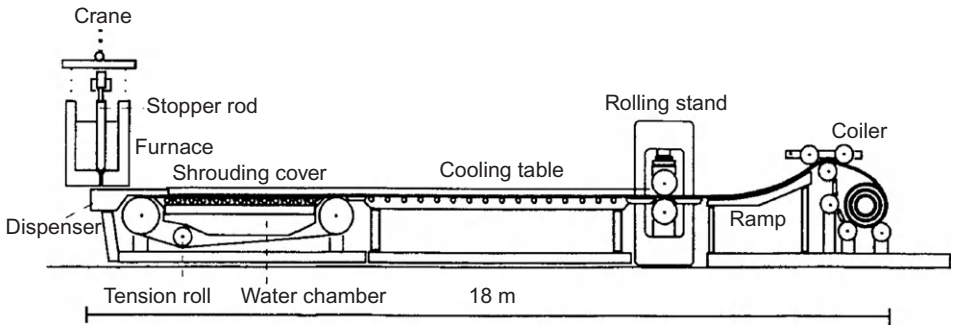


Figure 4.7.17 Pilot plant installation for the DSC single-belt casting/hot rolling process at Clausthal.

on the known casters. The most advanced program was operated at Clausthal Technical University in cooperation with Salzgitter AG, SMS Demag AG, and Thyssen Krupp Stahl AG. This caster is connected to a rolling stand for in-line hot rolling. The sketch of the installation is shown in Figure 4.7.17. It has been demonstrated that casting and hot rolling can be coupled without major difficulties [20]. The MEFOS caster was somewhat larger, and heat sizes considerably greater, allowing wider strips to be cast. The McGill caster, originally operated at BHP, Newcastle, is a research machine used for exploring high speed, thin strip casting of both ferrous and nonferrous strip material.

4.7.6. FLUID FLOWS: DESIGN OF METAL DELIVERY SYSTEMS

An obvious requirement of the flow control system to such casters is that liquid steel must emerge from a dispenser at the same mass rate as it is withdrawn by the traveling belt. At the same time, uniform solidification requires that lateral flows be minimal. Ideally, the melt should be delivered to the belt in the form of a flat stream, the same width as that of the strand. Also ideally, the metal stream should emerge from the feeding nozzle with a bulk velocity as close as possible to that of the belt (isokinetically) and with a thickness as close as possible to that of the final strand, i.e., no hydraulic jumps. Unfortunately, it is very difficult to fully realize these additional requirements at low belt velocities. For such cases, the effective head, or height difference Δh between the level of steel in the dispenser and its level in the strand level has to be made very small. Furthermore, this low head must be kept constant if the exit velocity of steel from the delivery system, v, is to equal the casting velocity, v_c.

Another problem in designing an appropriate metal delivery system is that thin flat streams with an upper free surface do not have shape or form stability; rather, they tend to contract as a result of surface tension forces, to form a narrower, thicker stream with surface waves.

If the thin stream is constrained to remain flat (and wide) by using a closed channel with upper and lower confinement (slit nozzle), local freezing may occur easily in the

narrow slit gap and cause clogging. Many types of feeding system have been proposed and explored experimentally. Two methods developed at MEFOS and at Clausthal sub-divide the feeding stream into several streams so as to make the stream area A smaller than the strand area A_c. This allows one to use a larger exit velocity v from the dispenser, with a concomitant increase in Δh to a more practical level. This general principle has been applied in the so-called zig–zag nozzle and the multihole nozzle. Unfortunately, these subdivisions of the flow into several streams lead to nonuniform solidification, for similar reasons to those for TRC using standard SENs. Similarly, it can lead to feeding, or meniscus marks, on the lower strand surface, and/or stripes of decreased strand thickness, or even nozzle clogging. Two dispenser types involving single flat streams ($A_c = A$) are depicted in Figures 4.7.18 and 4.7.19. In the kind used at Clausthal Technical University, Figure 4.7.18, the metal stream flows over a refractory weir substrate with two steps. Two so-called argon rakes are used to prevent contraction of the open stream on the weir and distribute it laterally on to the belt so that the edges are filled. The argon rakes consist of a series of argon streams emerging from bores in the gas distributors. The distributors extend over the width of the strip, are water cooled, and are made of copper. In a dispenser proposed by the McGill group (Figure 4.7.19), the feeding occurs through a reticulated medium (e.g., open pore zirconia filter) at the bottom of the dispenser chamber, or alternatively after passing through a transverse magnetic field to control the velocity field. Work on the latter system is planned, going forward.

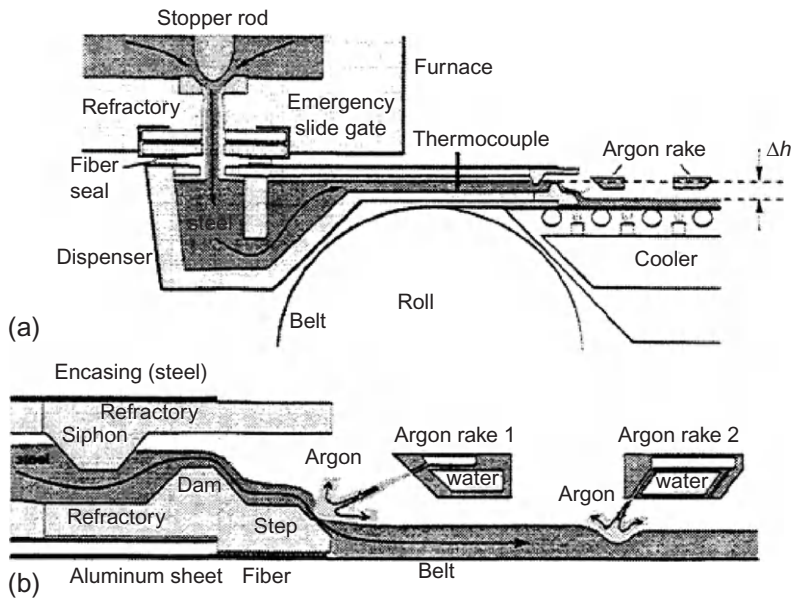


Figure 4.7.18 Feeding system with argon rakes used on the Clausthal Caster II.

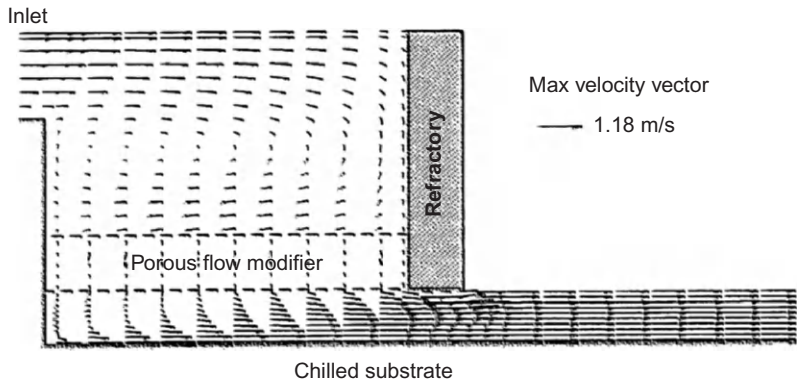


Figure 4.7.19 Predicted velocity fields in an extended pool of liquid steel placed over a water-cooled horizontal single-belt casting machine, using a porous flow modifier (belt speed 1.18 m/s, porous filter 35 ppi).

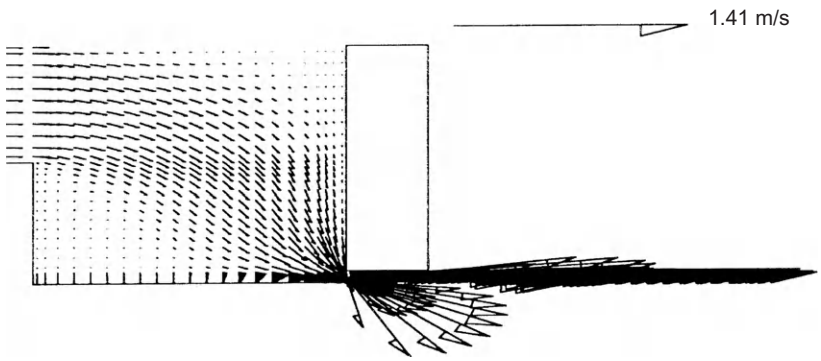


Figure 4.7.20 Predicted velocity fields in an extended pool of liquid steel placed over a water-cooled horizontal belt casting machine with no-flow modification, exit slot, $d = 4$ mm, meniscus level in extended nozzle = 80 mm.

The high Δh values ($\sim$80 mm) are isokinetically matched to belt speeds $\sim$1.2 m/s. At lower metal production rates and belt speeds associated with pilot scale casters producing 7-mm thick steel strip, flow constrictions are required to drop the effective head, Δh, in these extended metal delivery systems. While the head loss due to such flow modifiers are minimal, their role in promoting an even, pressurized, vertical flow of slowly moving liquid steel over an extended region onto the chilled moving belt below is illustrated by considering their absence. Figure 4.7.20 shows the short circuiting of metal flow to the exit slot without flow control. The extended nozzle configuration is thought to provide an optimum means for delivering steel, without significant turbulence, in a chemically controlled environment, to the moving mold below, provided it can be

engineered to avoid freezing at the back wall. The need for a flow modifier is evident when comparing Figure 4.7.19 with Figure 4.7.20.

The "no-flow modifier" case leads to recirculation, regions of high turbulence, freezing at the back wall, as well as remelting of the frozen moving shell due to short circuiting of the steel flow to the exit. Computations showed that belt lengths in the order of 10–15 m are required to produce 10-mm thick strip at belt speeds of 1–2 m/s. This particular type of advanced delivery system has yet to be fully modeled and tested on a belt caster. One prerequisite for its proper functioning is that there can be no clogging of the exit port by build-up of inclusions.

One feature that exists in all strip-casting operations is the presence of a triple point—the point where a three-phase interface forms as the liquid melt comes into contact with the solid cooling substrate in a gaseous shrouding environment. This gas can be adjacent, or not, to a refractory back wall.

Figure 4.7.21 shows the result from one such study, carried out for the MMPC–HSBC delivery system, where the effects of a back-wall gap of 0.9 mm, and various casting speeds, on meniscus shape was investigated. As mentioned earlier, the successful control of this meniscus is absolutely critical to the successful operation of the strip-casting process in terms of surface quality of the strip. Numerical modeling has been heavily used, coupled with experiments, to understand the correlation between different operating parameters and the shape and stability of that meniscus. The modeling used the Volume of Fluid (VOF) approach to model the two immiscible phases, gas and metal, described in section 4.6 of this Chapter.

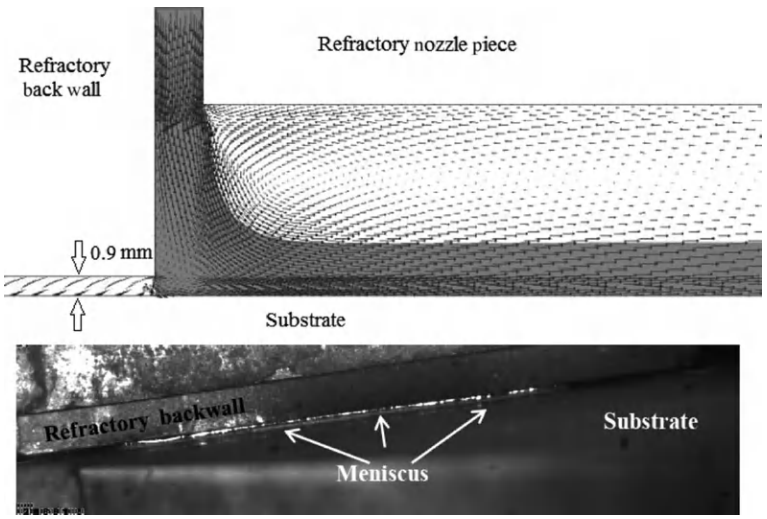


Figure 4.7.21 A comparison between predicted (top) and experimental (bottom) fluid flow and meniscus behavior in an HSBC process.

To avoid the problems associated with belt distortion created by thermal stresses generated when the molten steel first contacts the belt, which can lead to buckling, the cooling chamber of both the Clausthal and MEFOS machines were operated under partial vacuum. This represents one of the techniques that can be used for maintaining a flat belt under thermal loads. Variations of about ±1 mm at 15 mm thickness were typical of those experienced when casting peritectic grades of steel on a conventional slab caster. These variations proved to be stochastic, and practically invisible following in-line pass rolling. Owing to the different cooling rates at the lower and upper surfaces of the Direct Chill (re casting of aluminum ingots) (DC) cast strand, the dendritic structure and micro-segregation are asymmetrical with respect to the center-plane. Nonetheless, tests carried out on samples taken from the upper and lower halves of the material did not reveal significant differences in mechanical properties after hot rolling, in terms of yield and tensile strengths, elongation, and notch impact energies.

4.7.7. THE POTENTIAL OF THE HSBC CASTER: FROM FUNDAMENTALS TO PRACTICE

The peculiar advantages of the HSBC caster over CCC and TSC, and also of HSBC over TRC, are now hopefully more apparent to steelmakers. They should consider the following points:

1. The productivity of an HSBC machine is potentially able to replace CCC machines in integrated steel plants producing 2–4 Mt/year, or more, of steel strip, or sheet. In fact, the output from an HSBC is virtually unlimited, provided the length of the cooling belt can be readily extended, and/or heat extraction intensified.
2. At 2 Mt/year output, its estimated specific investment costs are *less than a tenth* those of a CCC (Figure 4.7.7).
3. It is an NNSC process, eliminating the need for mold powders, complex casting machines, slab-reheating furnaces, 7 stand hot rolling mills, but still allowing for sufficient thermomechanical working. Cast strip thicknesses can range from ~1 to 20 mm.
4. The machine is superior to both twin-roll and twin-belt processes, in that it represents unconstrained solidification.
5. It is a friction-free process, provided the liquid steel flowing on to the belt is in isokinetic flow with the endless, fast-traveling, water-cooled, belt. Similarly, research has shown how the surface quality of both the top and bottom surfaces can be controlled.
6. It is not susceptible to surface oscillation marks discussed in section 4.5 for CCC, nor is it susceptible to serious melt contraction problems as it can shrink without constraints, under low gauge pressures.
7. It can be used for handling difficult-to-cast grades of steel, such as the peritectic, 0.1% C steels, and also for bulk metallic glasses. Similarly, it can be used to cast steels that have high work hardenability, such as AHHS.

8. Its cast microstructure is much finer grained than CCC, and macrosegregation problems are mitigated.
9. Given the surface tension of liquid steel, it is likely possible to cast steels without using side dams to constrain the liquid steel, up to a thickness of approximately 7 mm thick.
10. The thickness of strand produced (~10 mm) allows for a sufficient amount of thermomechanical reduction to produce conventional steel microstructures, unlike twin roll casting NNSC processes.
11. It is very low on carbon dioxide emissions; breakouts are nonthreatening, provided it does not penetrate the water-cooled steel belt.

Finally, the process is relatively simple, requiring much less manpower than conventional caster-hot rolling mill operations.

4.7.8. CONCLUSIONS

As a result of the promised profitability of net-shape casting of steel sheet products, many research programs have been carried out on TRC aimed at developing moving mold technologies. As with NUCOR's successful commercialization of low-carbon sheet material using TRC, carried out in collaboration with BHP, IHI, and general electric, this time, Salzgitter, an integrated steel plant, is leading the charge to commercialize HSBC casters. Such casters promise to revolutionize the way steel strips will be produced in the future. As a final conclusion therefore, one can expect that these new casters will be a game-changer, and force a complete reevaluation of continuous casting machines for flat products.

REFERENCES

[1] G.E. Sa, M. Isac, R.I.L. Guthrie, ISIJ Int. 52 (12) (2012) 2109–2122.
[2] G.E. Sa, M. Isac, R.I.L. Guthrie, ISIJ Int. 53 (5) (2013) 729–742.
[3] J. Herbertson, R.I.L. Guthrie, Continuous Casting of Thin Metal Strip, Canadian Patent 536533, March 3, 1992 and U.S. Patent 4,928,748, May 29, 1990.
[4] W. Reichelt, K. Schwerdtfeger, P. Voss-Spitzer, Vorrichtung zum kontinuierlichen Gieben von Metallschmelze, isobesondere von Stahlschmelze, German Patent No. DE 3423834 C2, June 28, 1984.
[5] R.I.L. Guthrie, M. Isac, in: Handbook of Metallurgical Process Design, Marcel Dekker, New York, 2004, ISBN: 0-8247-4106-4, 2004, pp. 251–293(Chapter 8).
[6] ForeCast, vol. II(2), Castrip, July 2002 AD.
[7] G. Carlsson, R. Nystrom, H. Sandberg, W. Reichelt, U. Urlau, in: Iron and Steel—Today, Yesterday and Tomorrow, Stockholm Sweden, vol. 1, 1997, pp. 161–174.
[8] R. Nyström, E. Burström, W. Reichelt, V. Urlau, in: Metec 94, 2nd European Conference on Continuous Casting, Düsseldorf, 1994.
[9] R.P. Tavares, Vertical Twin-Roll Caster: Metal–Mould Heat Transfer, Solidification and Product Characterization, Ph.D. Thesis, McGill University, 1998, pp. 234–268.
[10] R.P. Tavares, M. Isac, R.I.L. Guthrie, ISIJ Int. 38 (1998) 1353–1361.
[11] L. Strezov, J. Herbertson, G.R. Belton, in: The Belton Memorial Symposium Proceeding, Australia, 2000, pp. 289–299.

[12] R.P. Tavares, M. Isac, F.G. Hamel, R.I.L. Guthrie, Metall. Mater. Trans. B 32B (2001) 55–67.
[13] G.-X. Wang, E.F. Matthys, Trans. ASME J. Heat Transfer 118 (1996) 157–163.
[14] G.-X. Wang, E.F. Matthys, in: E.F. Matthys, W.G. Truckner (Eds.), Melt Spinning, Strip Casting and Slab Casting, The Minerals, Metals & Materials Society, Warrendale, Pennsylvania, 1996, pp. 205–236.
[15] L.-T. Shiang, P.J. Wray, Metall. Trans. A 20A (1989) 1191.
[16] Y. Ueshima, T. Sawai, T. Mizoguchi, S. Mizoguchi, in: Proceeding of the 6th Int. Iron and Steel Cong., 1990, p. 642.
[17] K. Yasumoto, T. Nagamichi, Y. Maehara, K. Gunji, Tetsu-to-Hagane 73 (1987) 1738–1745.
[18] Y. Maehara, K. Yasumoto, Y. Sugitani, K. Gunji, Trans. ISIJ 25 (1985) 1045–1052.
[19] H. Ikawa, S. Shin, H. Osihige, Y. Mekuchi, Trans. Jpn. Weld. Soc. 8 (2) (1977) 46–51.
[20] K. Schwerdtfeger, in: The Brimacombe Symposium Proceedings, The Meteoritical Society, Vancouver, British Columbia, Canada, 2000, pp. 613–629.

CHAPTER 4.8

Conclusion

Roderick I.L. Guthrie
McGill Metals Processing Centre (MMPC), Montreal, Canada

This chapter has been concerned with the application of fluid flows with attendant heat and mass transfer processes in metallurgical processing reactors. It is aimed at describing the kinetic paths whereby reactants form products, or how phases interact with each other, to reach a new state of equilibrium, in the time considered. In other words, its purpose is to describe the kinetics of any reaction or process, in detail, and to faithfully report on the final result. This requires knowledge of the transport coefficients (diffusion, thermal conductivity, and molecular viscosity), the continuity, momentum, energy, and species conservation equations, plus equations for turbulence creation and dissipation. An important *caveat* is that one has to have an understanding of local equilibrium at reacting interfaces, plus one has to be cognizant of kinetic constraints that would cause a process to follow an alternative path, leading to a different end point. As such, time is an important consideration for kinetics, as it describes how quickly things will happen.

By contrast, thermodynamics does not contain "time" in its equations, but is still a very necessary component in any kinetic analysis of a metallurgical process, since it will determine possible local equilibrium conditions at reacting interfaces, as well as predict likely outcomes, provided kinetic constraints are not present.

The importance of computers has been emphasized, since they have allowed us to solve particular solutions to many nonlinear problems that would have defied classical analyses, given the many variables and parameters that are normally in play in a real process. Ever more powerful computers and storage capacities have evolved, while *computational fluid dynamics* (CFD) has come a long way since it began in earnest in the 1950s. It is now possible to use generic computer codes such as FLUENT ANSYS, which allow one to describe the kinetic paths that will be followed by virtually any complex flow event, involving heat and/or mass transfer, chemical reactions, etc. This is not to say that we can dispense with any further experiments. We have to do experiments to test out our theories and hypotheses, and to show they can be exactly matched by our computations. In this way, the subject can move forward, with CFD going hand in hand with experimental research.

The development of turbulence theories to model real processes was a major breakthrough in CFD analyses. Similarly, the "genius" of Dr. Brian Spalding and Associates at Imperial College, London, in casting all our transport equations into the same format, and then solving them iteratively, in three dimensions, helped our progress enormously.

Treatise on Process Metallurgy, Volume 2
http://dx.doi.org/10.1016/B978-0-08-096984-8.00014-8
© 2014 Elsevier Ltd.
All rights reserved.

In fact, one is now entering a time when modeling of a given metallurgical system is the first step toward finding an optimum solution for the product desired. We believe that this era is now upon us for the many metallurgical processes considered to date. Similarly, it is an integral component in the development of new processes such as the HIsarna direct smelting technology and the Horizontal Single Belt Caster. It will be used in the future, to develop processes yet to be conceived, or even considered.

CHAPTER 5

Computational Thermodynamics, Models, Software and Applications

Jean Lehmann[a] **and Klaus Hack**[b]
[a]ArcelorMittal, Global R&D, Maizières-lès-Metz Cedex, France
[b]GTT Technologies, Kaiserstrasse, Herzogenrath, Germany

Contents

5.1. Thermodynamics 588
5.2. Slag Viscosity Models 643
5.3. Applications 675
5.4. Process Modeling 799

CHAPTER 5.1

Thermodynamics

Jean Lehmann[a] **and In-Ho Jung**[b]
[a]ArcelorMittal, Global R&D, Maizières-lès-Metz Cedex, France
[b]Department of Mining and Materials Engineering, McGill University, Montreal, Canada

5.1.1. CALPHAD METHOD

The CALPHAD (CALculation of PHAse Diagrams [1]) method was initiated by Kaufman and Berstein in 1970 [2] to promote the mathematical calculation of phase diagrams. Previously, phase diagrams and other thermodynamic properties, as chemical potentials of components or heat of solidification, were treated separately despite the fact that the formalism necessary to derive simultaneously all these properties has been already established by J.W. Gibbs in 1875–1878 [3] whose work has been summarized by Hertz [4]. In [2], Kaufman and Bernstein summarized the general principles of the calculation of phase diagrams and gave listings of computer programs for the calculation of binary and ternary phase diagrams. In 1973, Kaufman organized the first project meeting of the international CALPHAD group and since then a CALPHAD conference has been organized every year.

The idea behind the CALPHAD method is to derive expressions of the Gibbs energy of phases from all the experimental data available (melting and other transformation temperatures, heat capacities, enthalpies of formation, chemical potentials, etc.). From these expressions and their derivatives, material properties could then be calculated as well as transformations of multicomponent materials. As it is understood now, CALPHAD method is "the technique of selecting models for phases which can be extrapolated both in composition and temperature ranges, including also metastable ranges" [5] and of fitting the parameters used in these models on all kinds of experimental and theoretical data available.

According to Schmid-Fetzer and Gröbner [6], the advantages of the Calphad approach can be summarized as follows:

- The models developed according to the Calphad approach have a good capability for extrapolating from binary assessed systems valuable information to ternary and higher order systems, which is a necessary property for application to industrial situations.
- It provides the possibility to define relevant key experiments and then to reduce the effort that has to be devoted to experimental studies in multicomponent systems.
- Stable but also metastable equilibria can be calculated simply by suspending phases that do not form under specific conditions due to kinetic reasons.

Treatise on Process Metallurgy, Volume 2
http://dx.doi.org/10.1016/B978-0-08-096984-8.00030-6
© 2014 Elsevier Ltd.
All rights reserved.

- Driving forces for all transformations can be calculated. These are important quantities for kinetic models.
- Local equilibria can be calculated. This possibility is also used in kinetic models typically when chemical equilibrium is assumed to be reached at the interface between two phases.
- The possibility for commercial pieces of software to calculate and to plot two-dimension sections of phase diagrams for multicomponent systems permit their practical use for industrial problems.

The thermodynamic databases built according to this approach should be internally consistent since they synthesize information relative to a large set of data of different types covering large domains of composition. In these databases, high-order assessments rely on lower order assessments: ternary assessments depend on binary assessments, which themselves depend on unary data for pure elements, etc. These assessments are based on the choice made by SGTE [7] for pure elements and models some 30 years ago (and especially on the tremendous work done by Dinsdale who established a standard for all chemical elements in their different states [8]). This kind of structure makes it difficult to revise models and data especially those concerning low-order systems since any modifications of these systems implies a revision of a lot of higher order systems. However, these revisions are inevitable due to the availability of new experimental data and the development of new and more powerful models [5]. A series of workshops has been organized by the Max Planck Institute in Stuttgart to lay the foundations for these new developments and papers summarizing the choices or recommendations that have been published [9–12].

5.1.2. DILUTE METALLIC SOLUTION

5.1.2.1. Liquid Fe

During the ironmaking and steelmaking processes, the thermodynamic behaviors of dilute elements such as C, O, and other metallic elements are very important. There are several models that are specially suited for handling the thermochemistry of dilute solutions.

The deoxidation reaction (Fe–M–O system) is one of the most important chemical reactions occurring in molten steel. For example, the standard Gibbs energy of M_xO_y oxide formation from pure M and O_2 is very well known:

$$xM + y/2O_2 = M_xO_y : \Delta G^o_{M_xO_y} \tag{5.1.1}$$

Using the Gibbs energy change from Raoultian to Henrian standard state, the oxidation reaction involving $\underline{M}$ and $\underline{O}$ dissolved in liquid Fe can be written as:

$$M = \underline{M} \quad \Delta G^o = RT \ln \gamma^o_M \tag{5.1.2}$$

$$1/2O_2(g) = \underline{O} \quad \Delta G^o = RT \ln \gamma_O^o \tag{5.1.3}$$

$$x\underline{M} + y\underline{O} = M_xO_y(s) \quad \Delta G^o = \Delta G^o_{M_xO_y} - RT\left(x \ln \gamma_M^o + y \ln \gamma_O^o\right) \tag{5.1.4}$$

where γ_i^o is the Henrian activity coefficient of element i. Then the equilibrium constant of the reaction (5.1.24) is:

$$K = a_{M_xO_y} / \left(f_{\underline{M}} x_M\right)^x \left(f_{\underline{O}} x_O\right)^y \tag{5.1.5}$$

where x_i is the mole fraction of element i, $f_{\underline{i}}$ is the activity coefficient of element i relative to the infinite dilution standard state, and $a_{M_xO_y}$ is the activity of M_xO_y.

The Gibbs energy of ternary Fe–M–O solution dissolving a dilute amount of $\underline{M}$ and $\underline{O}$ can be described as:

$$\begin{aligned} G^m = &\left(x_{Fe} g^o_{Fe} + x_M g^o_{\underline{M}} + x_O g^o_{\underline{O}}\right) + RT\left(x_{Fe} \ln x_{Fe} + x_M \ln x_M + x_O \ln x_O\right) \\ &+ RT\left(x_{Fe} \ln f_{\underline{Fe}} + x_M \ln f_{\underline{M}} + x_O \ln f_{\underline{O}}\right) \end{aligned} \tag{5.1.6}$$

where $g_{\underline{i}}^o$ $(= g_i^o + RT \ln \gamma_i)$ is the standard Gibbs energy of element i in the infinite dilution (Henrian) standard state.

5.1.2.1.1 Wagner Interaction Parameter Formalism

The Wagner Interaction Parameter Formalism (WIPF) [13] has been widely used for dilute solutions. This simple formalism can describe the activities of dilute elements as a function of solute compositions. For example, the activity coefficients of $\underline{M}$ and $\underline{O}$ in Equations (5.1.5) and (5.1.6) can be expressed:

$$\ln f_{\underline{M}} = \varepsilon_{MM} x_M + \varepsilon_{MMM} x_M^2 + \varepsilon_{MO} x_O + \varepsilon_{MOO} x_O^2 + \varepsilon_{MMO} x_M x_O + \cdots \tag{5.1.7}$$

$$\ln f_{\underline{O}} = \varepsilon_{OO} x_O + \varepsilon_{OOO} x_O^2 + \varepsilon_{OM} x_M + \varepsilon_{OMM} x_M^2 + \varepsilon_{OOM} x_O x_M + \cdots \tag{5.1.8}$$

where ε_{ij} and ε_{ijk} are the so-called first- and second-order interaction parameters. (ε_{ij} and ε_{ijk} are identical to the conventional notations ε_i^j and ρ_i^{jk}, respectively.) The interaction parameter can be expressed as a function of temperature, $\varepsilon = a + b/T$. The WIPF assumes that $f_{\underline{Fe}} = 1$, and $\varepsilon_{ij} = \varepsilon_{ji}$. Other interaction parameters may be included in the expansion to account for interactions with other alloying elements. The activity given in Equations (5.1.2)–(5.1.8) can be expressed as a function of the wt% of dilute elements with respect to the 1 wt% standard state. Since the WIPF is practical and easy to describe the dilute solution, it has been widely applied to the interpretation of chemical reactions occurring in the steelmaking process. The most well-known assessments of the Henrian activity coefficients and interaction parameters for dilute liquid Fe solution are those of Sigworth and Elliot [14] and the JSPS[15].

Unfortunately, the WIPF is thermodynamically sound only in infinite dilution. As pointed out by Pelton and Bale [16], the WIPF cannot satisfy the Gibbs–Duhem equation and other thermodynamic constraints except for infinite dilute solution. Thus, the WIPF cannot directly be used in a thermodynamic software package.

5.1.2.1.2 Unified Interaction Parameter Formalism

The Unified Interaction Parameter Formalism (UIPF) is a modified WIPF. In order to overcome the shortcoming of the WIPF and to be consistent with the Gibbs–Duhem equation and other thermodynamic relationships, Pelton and Bale [16–18] modified the activity coefficient forms of the Wagner formalism for the Fe-*i*–*j*–*k*, etc., solution as following and called the formula as the UIPF:

$$\ln f_{\underline{i}} = \sum_{j=1}^{N} \varepsilon_{ij} x_j + \sum_{j,k=1}^{N} \varepsilon_{ijk} x_j x_k + \ln f_{\mathrm{Fe}} \tag{5.1.9}$$

$$\ln f_{\mathrm{Fe}} = -\frac{1}{2} \sum_{j,k=1}^{N} \varepsilon_{jk} x_j x_k - \frac{2}{3} \sum_{j,k,l=1}^{N} \varepsilon_{jkl} x_j x_k x_l \tag{5.1.10}$$

This modification does not increase the number of model parameters. The parameters ε_{ij} and ε_{ijk} of the UIPF can be calculated from conventional interaction parameters from compilations [14,15] using the following standard formalisms [17]:

$$\varepsilon_{ij} = \varepsilon_{ji} = \varepsilon_i^j = \varepsilon_j^i \tag{5.1.11}$$

$$\varepsilon_{ijk} = \varepsilon_{ikj} = \varepsilon_{jik} = \varepsilon_{jki} = \varepsilon_{kij} = \varepsilon_{kji} \tag{5.1.12}$$

$$2\varepsilon_{ijj} = 2\rho_i^j + \varepsilon_j^j = \rho_j^{ij} + \varepsilon_i^j \tag{5.1.13}$$

$$2\varepsilon_{ijk} = \rho_i^{jk} + \varepsilon_j^k = \rho_j^{ik} + \varepsilon_i^k = \rho_k^{ij} + \varepsilon_i^j \tag{5.1.14}$$

where ε_i^j and ρ_i^{ij} represent the first- and second-order interaction parameters in the WIPF, respectively. The UIPF is not anymore limited to dilute solutions. It can be used to describe the complete range of binary, ternary, and multicomponent systems. Lee [19] used the UIPF to describe the thermodynamic properties of the entire ternary Mn–Fe–C liquid solution. Li and Morris [20] also applied the UIPF for the Mn–Fe–C–Si system. The UIPF can be converted to normal polynomial Gibbs energy expression [21]. For example, it can be converted to Bragg–Williams Redich–Kister polynomial model and *vice versa*.

The UIPF has been used for the dilute liquid Fe solution databases of FactSage [22], CEQCSI [23] and MTDATA [24].

5.1.2.1.3 Modified Regular Solution Model

Hillert [25] demonstrated that the Darken's quadratic formalism [26] can be transformed to a regular solution model with modification of the standard states of dilute elements:

$$G^m = x_{\mathrm{Fe}} g^{\circ}_{\mathrm{Fe}} + \sum_{i=\text{solute}} x_i \left(g^{\circ}_i + M_i\right) + RT\left(x_{\mathrm{Fe}} \ln x_{\mathrm{Fe}} + \sum_{i=\text{solute}} x_i \ln x_i\right) + \frac{1}{2} \sum_{i,j=\mathrm{Fe},\text{solute}} x_i x_j L_{ij} \tag{5.1.15}$$

where all $L_{ii} = 0$ and $L_{ij} = L_{ji}$. M_i, which is related to the change of standard states from Raoultian to Henrian solution, and the regular solution parameters, L_{ij}, can be determined from conventional interaction parameters:

$$(M_i + L_{\mathrm{Fe}\ i})/RT = \ln \gamma^{\circ}_i \tag{5.1.16}$$

$$\left(L_{ij} - L_{\mathrm{Fe}\ i} - L_{\mathrm{Fe}\ j}\right)/RT = \varepsilon^j_i \tag{5.1.17}$$

$$-2L_{\mathrm{Fe}\ i}/RT = \varepsilon^i_i \tag{5.1.18}$$

$$L_{ij}/RT = \varepsilon^j_i - \left(\varepsilon^i_i + \varepsilon^j_j\right)/2 \tag{5.1.19}$$

The dilute liquid Fe solution database in Thermo-Calc has been developed using the modified regular solution model. Since the second order interaction parameters are not well counted in the model, the reassessment of the previously compiled interaction parameters seemed to be required in many cases.

Recently, Miki and Hino [27–29] used the Redlich–Kister polynomial equation with a quadratic function of the excess parameters:

$$G^m = \sum x_i g^{\circ}_i + RT \sum x_i \ln x_i + \sum x_i x_j \left(\Omega^0_{ij} + \Omega^1_{ij}\left(x_i - x_j\right)\right) \tag{5.1.20}$$

where i and j correspond to Fe and solute elements. Instead of using the Henrian standard state, the Raoultian standard state is used for all solute elements. Since it is hard to define the Gibbs energy of pure liquid (Raoultian liquid state) for gaseous elements such as O_2, H_2 and N_2, the dissolved gaseous elements at 1 atm pressure of pure gases were selected as the standard state. In this way, the Gibbs energy of the liquid solution can be described. For example, the deoxidation equilibrium of the entire Fe–Ni–Al system [28] was described by this approach.

5.1.2.1.4 Associate Model for Deoxidation

In order to describe the deoxidation equilibria of liquid Fe solution, it is usually necessary for the cross-interaction parameters $\varepsilon^{\mathrm{O}}_{\mathrm{M}}$, $\rho^{\mathrm{O}}_{\mathrm{M}}$, $\rho^{\mathrm{M}}_{\mathrm{O}}$, $\rho^{\mathrm{M,O}}_{\mathrm{M}}$ and $\rho^{\mathrm{O,M}}_{\mathrm{O}}$ to be very negative in order to account for the very strong attractive interactions between dissolved <u>M</u> and <u>O</u> atoms. Furthermore, in order to reproduce the measured data over a range of

temperature, the interaction parameters must generally have a strong empirical temperature dependence, usually expressed as $\varepsilon = a + b/T$ (and $\rho = c + d/T$). By using many empirical parameters, the interaction parameter formula reproduces the measured deoxidation equilibria over a limited range of temperature and composition. However, the resultant equations extrapolate very poorly outside this range. In the case of very strong deoxidants such as Ca, Mg, and Ba, the interaction parameter formalism has been found to be incapable of providing a satisfactory description of the deoxidation equilibria even over the temperature and composition ranges of the measured data.

The failure of the WIPF for very strong deoxidation systems results essentially from a wrong assumption of the behavior of solute atoms in liquid Fe. Intrinsically, the WIPF assumes that all solute elements in liquid Fe are distributed randomly and separately regardless of the interaction between solutes. However, physically, it can be easily presumed that the behavior of strong deoxidation element is not independent with oxygen anymore and *vice versa*. Thus, when there is strong negative interaction between $\underline{\mathrm{M}}$ and $\underline{\mathrm{O}}$, the configurational entropy of liquid Fe solution is easily over-estimated by the WIPF. In order to overcome this problem of the WIPF, Jung *et al.* [30] considered the associate formation in liquid steel to resolve this strong deoxidation phenomena. For example, for a ternary liquid solution Fe–M–O, where Fe is the solvent and M is a metal solute, the solution is assumed to contain dissolved unassociated $\underline{\mathrm{M}}$ and $\underline{\mathrm{O}}$ atoms as well as dissolved molecules (associates) $\underline{\mathrm{M^*O}}$ and, in some systems at the highest concentrations of M, a small amount of $\underline{\mathrm{M_2{}^*O}}$ associates. The equilibria among the dissolved associates and the dissolved unassociated $\underline{\mathrm{M}}$ and $\underline{\mathrm{O}}$ atoms are represented by:

$$\underline{\mathrm{M}} + \underline{\mathrm{O}} = \underline{\mathrm{M^*O}} \quad \Delta g^{\circ}_{\underline{\mathrm{M^*O}}} \tag{5.1.21}$$

$$2\underline{\mathrm{M}} + \underline{\mathrm{O}} = \underline{\mathrm{M_2{}^*O}} \quad \Delta g^{\circ}_{\underline{\mathrm{M_2{}^*O}}} \tag{5.1.22}$$

The total amount of M and O in solution are $n_{\mathrm{M}} = n_{\underline{\mathrm{M}}} + n_{\underline{\mathrm{M^*O}}} + 2n_{\underline{\mathrm{M_2{}^*O}}}$ and n_{O} ($n_{\mathrm{O}} = n_{\underline{\mathrm{O}}} + n_{\underline{\mathrm{M^*O}}} + n_{\underline{\mathrm{M_2{}^*O}}}$). The Gibbs energies of the associate formation, $\Delta g_{\underline{\mathrm{M^*O}}}$to and $\Delta g^{\circ}_{\underline{\mathrm{M_2{}^*O}}}$ are model parameters, instead of very negative interaction parameters ($\varepsilon^{\mathrm{O}}_{\mathrm{M}}$, $\rho^{\mathrm{O}}_{\mathrm{M}}$, $\rho^{\mathrm{M}}_{\mathrm{O}}$, $\rho^{\mathrm{M,O}}_{\mathrm{M}}$ and $\rho^{\mathrm{O,M}}_{\mathrm{O}}$), which can be obtained by evaluation/optimization of available data (deoxidation equilibria) for the Fe–M–O systems. Temperature-independent (i.e., constant) values of $\Delta g^{\circ}_{\underline{\mathrm{M^*O}}}$ and $\Delta g^{\circ}_{\underline{\mathrm{M_2{}^*O}}}$ were found to be sufficient, which indicates that the configurational entropy of the systems is well described by the Associate Model. No further interaction parameters like $\rho^{\mathrm{M,N}}_{\mathrm{O}}$ are necessary to reproduce the deoxidation behavior of quaternary and higher-order Fe–M–N–$\cdots$–O systems. As shown by Jung *et al.* [30], the observed Ca deoxidation curve (Fe–Ca–O system), which is impossible to explain using the classical WIPF, can be easily

reproduced with the Associate Model with only one temperature-independent model parameter. Similar results were found for the deoxidation equilibria by Mg, Ba, etc. Moreover, the Associate Model can explain other deoxidation phenomena by less stronger deoxidants such as Al, Ti, Cr, V, Mn, Si, B, C, Ce, Nb, Zr, etc. The FTmisc-FeLq database of FactSage for liquid Fe solution is formulated using the UIPF with the embedded Associate Model for the associate formations in Fe–M–O systems. That is, all the model parameters of the liquid Fe database are formulated using the UIPF, except for the cross-interaction terms of M–O that are replaced by the associate formation energies. The same model can be used for the desulfurization equilibria for Fe–M–S solution [31].

5.1.2.2. Dilute Metallic Solution: Nonferrous Metals

The WIPF was used widely to evaluate interaction parameters between dilute elements for many non-ferrous metals such as Cu and Co [32,33]. As mentioned earlier, as the WIPF cannot satisfy the Gibbs–Duhem equation and other thermodynamic constraints except for infinite dilute solution, the WIPF cannot directly be used in a thermodynamic software package. Instead the UIPF has been used for the database development. The mathematical formalism is the same as shown in the above section. UIPF model is used for FactSage to describe dilute liquid solution of Cu, Pb, Sn, etc.

5.1.3. MODEL FOR OXIDE SOLID SOLUTIONS

The Compound Energy Formalism (CEF) [34] has been used to describe complex and extensive oxide solid solutions such as spinel, melilite, pyroxene, olivine, etc. In order to accurately describe the Gibbs energy of oxide solution over a wide temperature range, the entropy of solution should be properly described based on its crystal structure. One of the most complex oxide solid solutions encountered in steelmaking is the spinel solution.

For example, the spinel solution of the Fe–Mg–Al–Cr–O system, encompassing Fe_3O_4, $FeAl_2O_4$, $FeCr_2O_4$, $MgFe_2O_4$, $MgAl_2O_4$, $MgCr_2O_4$ and Cr_3O_4, is of great importance for refractories in steelmaking. This solution can be modeled based on its crystallographic information:

$$\left[Fe^{2+},Fe^{3+},Mg^{2+},Al^{3+},Cr^{2+},Cr^{3+}\right]^{T}\left[Fe^{2+},Fe^{3+},Mg^{2+},Al^{3+},Cr^{3+},Va\right]_{2}^{O}O_4 \quad (5.1.23)$$

where T and O represent tetrahedral and octahedral sublattices in the spinel structure. Vacancies (Va) in octahedral sublattices are also taken into account. The Gibbs energy of the spinel solution can be expressed as following using the CEF:

$$G^m = \sum_i \sum_j Y_i^T Y_j^O G_{ij}^o - TS_C + G^E \tag{5.1.24}$$

where Y_i^T and Y_j^O represent the site fractions of constituents i and j on the tetrahedral and the octahedral sublattices, G_{ij}^o is the Gibbs energy of an end member $[i]^T[j]_2^O O_4$, S_C is the configurational entropy:

$$S_C = -R\left(\sum_i Y_i^T \ln Y_i^T + 2\sum_j Y_j^T \ln Y_j^T\right) \tag{5.1.25}$$

and G^E is the excess Gibbs energy:

$$G^E = \sum_i \sum_j \sum_k Y_i^T Y_j^T Y_k^O L_{ij;k} + \sum_i \sum_j \sum_k Y_k^T Y_i^O Y_j^O M_{k;ij} \tag{5.1.26}$$

where $L_{ij;k}$ and $M_{k;ij}$ are the interaction energies between cations i and j on one sublattice when the other sublattice is occupied by k. The interaction energies, $L_{ij;k}$ and $M_{k;ij}$ can be internally set in the model as follows:

$$L_{ij} = L_{ij:k} = L_{ij:s} = \cdots \tag{5.1.27}$$

$$M_{ij} = M_{k:ij} = M_{s:ij} = \cdots \tag{5.1.28}$$

That is, the interaction between i and j in a sublattice is assumed to be the same regardless of the cations on the other sublattice.

There are 36 Gibbs energies of end-members to be determined in Equation (5.1.24). Once the Gibbs energies of the end members are well determined, the Gibbs energy function of the solution can be further modified using the interaction parameters. However, as the experimental data are mostly insufficient to determine the Gibbs energies of all end-members, certain logical and physically meaningful assumptions should be applied to fix the Gibbs energies properly.

For example, the spinel solution of the Mg–Fe–Al–O system encompasses $MgAl_2O_4$, $FeAl_2O_4$, Fe_3O_4 and $MgFe_2O_4$ stoichiometric spinels. Figure 5.1.1 shows the schematic diagram of the thermodynamic model for the Mg–Fe–Al–O system [35]. For the sake of simplicity, vacancies are not considered. 16 Gibbs energies of end-members should be determined to describe the entire spinel solution. Each stoichiometric spinel solution has four end-members. Thermodynamic and crystallographic data (cation distribution between tetrahedral and octahedral sublattices) can be used to determine the Gibbs energies of four end-members. Sometimes, more than one set of end-member Gibbs energies can be obtained to describe a stoichiometric spinel solution or two adjacent stoichiometric spinel solutions due to the lack of experimental data to fix the Gibbs energies of all end-members simultaneously. As can be seen in Figure 5.1.1, because the stoichiometric spinel solutions are connected to each other by a common end-member, the Mg–Fe–Al–O spinel solution

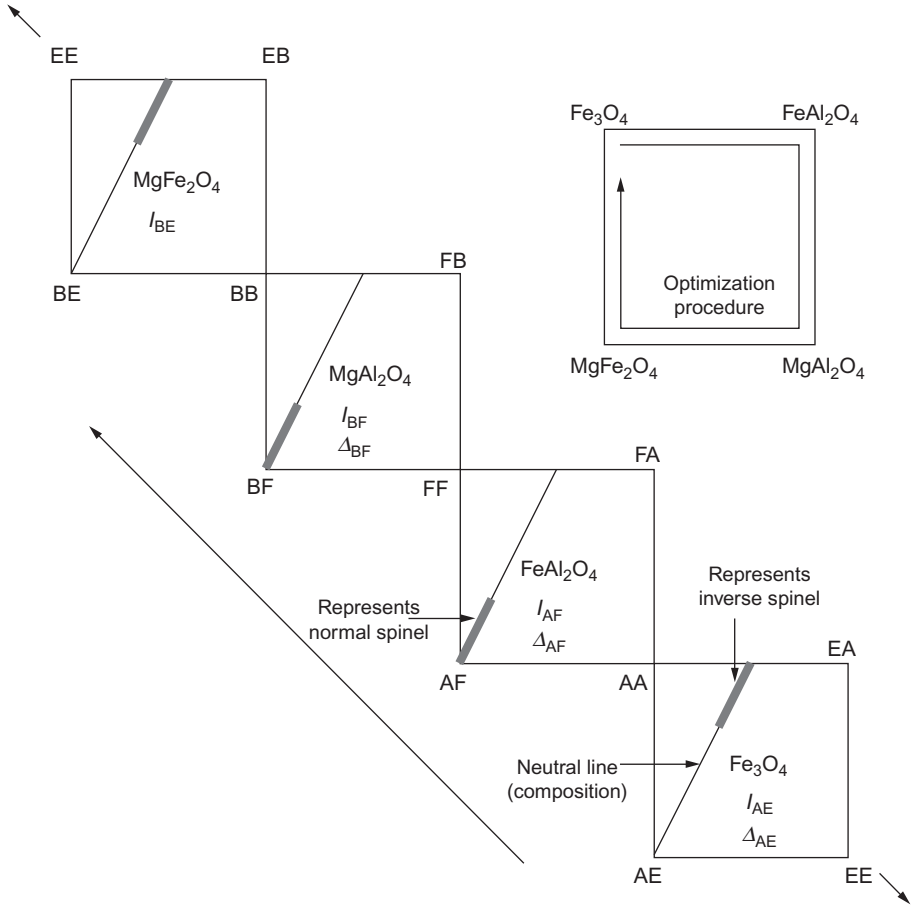


Figure 5.1.1 Schematic diagram for the structure of thermodynamic model of Fe–Al–Mg–O spinel solution. E, A, F, and B represent Fe^{3+}, Fe^{2+}, Al^{3+}, and Mg^{2+} cations in the (Fe^{2+}, Fe^{3+}, Mg^{2+}, Al^{3+})[Fe^{2+}, Fe^{3+}, Mg^{2+}, Al^{3+}]$_2O_4$ spinel solution [35].

composed of four stoichiometric spinels can form a closed loop solution structure. This closed loop structure can effectively constrain the Gibbs energies of end-members. The end-member Gibbs energies can also be properly estimated based on physically meaningful assumptions. For example, the reciprocal parameters, Δ_{ij} ($=G_{ii}+G_{jj}-G_{ij}-G_{ji}$), can be assumed to be about 40 kJ/mol, based on the extensive study on the 2–3 spinels by O'Neil and Navrotsky [36]. In addition, the magnetic properties of spinel oxide solution should be taken into account. The spinel solutions in binary, ternary, and multicomponent oxide systems have been modeled [37–47] using this approach.

Similarly, other extensive oxide solid solutions such as olivine, pyroxene, melilite, and so on have been modeled based on their crystallographic data as well as

thermodynamic properties and phase diagrams. Without proper considerations of the cation distribution, accurate entropy and Gibbs energy functions of the extensive solid solution can hardly be described.

5.1.4. THE RECIPROCAL IONIC LIQUID MODEL

The Reciprocal Ionic Liquid Model (RILM) was developed by Hillert *et al.* [48] and used as a standard model for the oxide melt database in Thermo-Calc [49]. This model supposes two sublattices in liquid oxide. For example, in the CaO–MgO–SiO_2 system [50], the liquid structure is formulated as:

$$\left(Ca^{2+},Mg^{2+}\right)_P\left(SiO_4^{4-},O^{2-},SiO_2^0\right)_Q \tag{5.1.29}$$

where P and Q indicate the number of sites on each sublattice, which can vary with composition in order to maintain electron neutrality.

$$P = 4y_{SiO_4^{4-}} + y_{O^{2-}} \tag{5.1.30}$$

$$Q = 2y_{Ca^{2+}} + 2y_{Mg^{2+}} = 2 \tag{5.1.31}$$

where y is the site fraction of species on a particular sublattice. The Gibbs energy of the ternary CaO–MgO–SiO_2 solution for 1 mol of formula unit is given by:

$$\begin{aligned} G^m = {} & y_{Ca^{2+}} y_{SiO_4^{4-}} G_{(Ca^{2+})_4\left(SiO_4^{4-}\right)_2} + y_{Mg^{2+}} y_{SiO_4^{4-}} G_{(Mg^{2+})_4\left(SiO_4^{4-}\right)_2} \\ & + y_{Ca^{2+}} y_{O^{2-}} G_{(Ca^{2+})_2(O^{2-})_2} + y_{Mg^{2+}} y_{O^{2-}} G_{(Mg^{2+})_2(O^{2-})_2} + Q y_{SiO_2^0} G_{SiO_2^0} \\ & + PRT\left(y_{Ca^{2+}} \ln y_{Ca^{2+}} + y_{Mg^{2+}} \ln y_{Mg^{2+}}\right) \\ & + QRT\left(y_{SiO_4^{4-}} \ln y_{SiO_4^{4-}} + y_{O^{2-}} \ln y_{O^{2-}} + y_{SiO_2^0} \ln y_{SiO_2^0}\right) + G^E \end{aligned} \tag{5.1.32}$$

where $G_{(Ca^{2+})_4\left(SiO_4^{4-}\right)_2}$ of the imaginary liquid $Ca_4Si_2O_8$ species is the main model parameter, $G_{(Ca^{2+})_2(O^{2-})_2}$ and $G_{SiO_2^0}$ are the Gibbs energies of liquid 2CaO and SiO_2, respectively, and G^E is the excess Gibbs energy of interaction between the species on the same sublattice:

$$\begin{aligned} G^E = {} & \sum_i \sum_j \sum_k y_i y_j y_k L_{i,j:k} + \sum_i \sum_k \sum_l y_i y_k y_l L_{i:k,l} \\ & + y_{Ca^{2+}} y_{Mg^{2+}} y_{O^{2-}} y_{SiO_4^{4-}} L_{Ca^{2+},Mg^{2+}:O^{2-}SiO_4^{4-}} \end{aligned} \tag{5.1.33}$$

where i and j are species on P sites and k and l are species on Q sites. The L parameters are expanded as Redlich–Kister polynomials:

$$L_{i,j:k} = \sum_m {}^m L_{i,j:k}\left(y_i - y_j\right)^m \text{ and } L_{i:k,l} = \sum_m {}^m L_{i:k,l}\left(y_k - y_l\right)^m \tag{5.1.34}$$

The amount of species in the anionic sublattice (SiO_4^{4-}, O^{2-} and SiO_2^0) is mainly determined by $G_{(M^{2+})_4(SiO_4^{4-})_2}$.

Many binary and ternary oxide solutions have been optimized [44,50–58] using the RILM. However, as mentioned by Hallstedt (1995), often the ionic species defined in the binary systems are not enough to reproduce the properties of ternary systems, so certain modifications of the structural formulae must often be made. That is, often the model has poor predictive ability for ternary or higher-order systems. This is because the structure is not properly taken into account in the model. The assumption of two sublattices is "artificial." Therefore, this results in difficulties in the development of multicomponent liquid oxide databases. Also as pointed out by Pelton *et al.* [59], the model cannot reproduce limiting slope rule at every dilute solution region due to the assumption of artificial ionic species.

The thermodynamic description of the RILM for binary MO–SiO_2 solution is identical to that of the Associate Model considering only M_2SiO_4 associate species.

5.1.5. QUASICHEMICAL MODELS

The quasichemical formalism as proposed by Guggenheim [60] could be simply illustrated by the case of a binary system containing N_A and N_B atoms or molecules A and B with a common coordinate number z. To derive an expression of the partition function, it models the short range ordering phenomenon (SRO) by considering all possible pairs of atoms or molecules AA, AA, and AB distributed on a quasilattice. The formation of AB pairs from AA and BB pairs is associated to a Gibbs energy change:

$$AA + BB \rightarrow 2AB \quad W_{AB} \tag{5.1.35}$$

If N_{AA}, N_{BB} and $2N_{AB}$ (we assume $N_{AB} = N_{AB}$, i.e., no long-range ordering—LRO) denote the mole numbers of the different pairs, Guggenheim proposed to correct the expression corresponding to a random mixing of pairs:

$$g = \frac{\left(\frac{1}{2}z(N_A + N_B)\right)!}{(N_{AA})!(N_{BB})!((N_{AB})!)^2} \tag{5.1.36}$$

by a multiplying factor h. Indeed, expression (Equation 5.1.36) overcounts the number of configurations since it does not take into account the interaction (overlapping) between the different pairs. h is designed in such a way that for $W_{AB} = 0$, the number of configurations must be equal to the number of random distributions of A and B:

$$h = \frac{(N_A + N_B)!}{N_A!N_B!} \Bigg/ \left(\frac{\left(\frac{1}{2}z(N_A + N_B)\right)!}{\left(N_{AA}^*\right)!\left(N_{BB}^*\right)!\left(\left(N_{AB}^*\right)!\right)^2} \right) \tag{5.1.37}$$

where

$$N_{ij}^{*} = z\frac{N_i \cdot N_j}{N_A + N_B} \tag{5.1.38}$$

If x_i denotes the mole fraction of component i and p_{ij} the fraction of pairs ij, the configurational entropy is equal to:

$$\begin{aligned} {}^{\text{conf}}S^{\text{m}} = &-R\frac{z}{2}(2p_{AB}\ \ln(p_{AB}) + p_{AA}\ \ln(p_{AA}) + p_{BB}\ \ln(p_{BB})) \\ &+ R(z-1)(x_A\ \ln x_A + x_B\ \ln x_B) \end{aligned} \tag{5.1.39}$$

One of the drawbacks of the quasichemical model is that it could lead to negative configurational entropy for high deviations from randomness, i.e., very large and negative values of W_{AB} when the coordination numbers differ from 2. Indeed, Equation (5.1.39) shows that for $p_{AB} = 0.5$ and $p_{AA} = p_{BB} = 0$ we have:

$${}^{\text{conf}}S^{\text{m}} = -R\left(\frac{z}{2} - 1\right)\ \ln(2) \tag{5.1.40}$$

Hillert *et al.* [61] propose a correction of this drawback for binary solutions with the same coordination number for the two end-members consisting in introducing an additional term function of the degree of SRO in the expression of the configurational entropy. This term is a function f of an order parameter q defined as:

$$p_{AB} = x_A x_B(1+q) \tag{5.1.41}$$

which should satisfy the three following conditions:

$$\begin{aligned} &f(0) = 0 \\ &f(1) = -R\left(\frac{z}{2} - 1\right)(x_A\ \ln x_A + x_B\ \ln x_B) \\ &f'(0) = 0 \end{aligned} \tag{5.1.42}$$

The first condition has the same purpose as the correction factor introduced by Guggenheim, the second one is to ensure that the configurational entropy remains positive, and the third one is to ensure that the Gibbs energy has the same equilibrium value at $q = 0$ as the classical quasichemical model. Hillert *et al.* recommend to choose for f a third power correction, which gives a realistic miscibility gap for positive values of W_{AB} and avoids unrealistic negative values for the configurational entropy for negative values of W_{AB}:

$$f(q) = -0.5(1+q)\cdot q^2\left(R\left(\frac{z}{2} - 1\right)(x_A\ \ln x_A + x_B\ \ln x_B)\right) \tag{5.1.43}$$

5.1.6. THE CELL MODEL

The Cell model developed by ArcelorMittal Maizières (formely IRSID) is one of the simplest models for slags derived from Guggenheim's treatment. It generalizes the approach proposed by Kapoor and Frohberg [62] for ternary system.

5.1.6.1. Structure of the Slag

Let us assume that the slag contains m cations and p anions coming from mixing $m+p-1$ independent components. Two sublattices are supposed to exist, one filled by cations in the decreasing order of their valence state, the other filled by the divalent anions. The structure is then described in terms of cells containing one central anion surrounded by two cations. A cell with an anion k as the central atom and cations i and j as neighbors of this central anion will be noted *i–k–j*. The mole number of cells is noted R_{ij}^{k}.

5.1.6.2. Partition Function

The partition function is given by:

$$\Omega = \sum_i g(E_i) \cdot \exp\left(\frac{E_i}{RT}\right) \tag{5.1.44}$$

The summation carries on all possible energetic configurations. g is the degeneracy of the configuration i, i.e., the number of microscopic configurations leading to the same energy state.

The sum can be assimilated to its largest term

$$\Omega = g(E) \cdot \exp\left(\frac{E}{RT}\right) \tag{5.1.45}$$

5.1.6.2.1 Degeneracy of the System

It is given by Guggenheim quasichemical treatment:

$$g = P_A \cdot P_C \cdot \frac{U}{U^*} \tag{5.1.46}$$

P_A is the number of possible permutations on the anionic sublattice for a random distribution, P_C the equivalent number on the cationic sublattice, U is the total possible permutations number between the different cells and U^* is the maximum value for U corresponding to a random distribution.

5.1.6.2.2 Calculation of the Permutations Number

Sublattice sites are assumed to be filled in priority by the cations with the highest charge. The cations are indexed by decreasing order of their charge. Hence, the sublattice is filled successively by cations of type 1, 2, ⋯, m.

Let us assume the cations of type 1, 2, ⋯ $(i-1)$ are already placed on the sublattice. They neutralize a mole number of anionic sites such as the remaining site mole number is equal to:

$$D_i = \sum_{j=i}^{m} V_j \tag{5.1.47}$$

With

$$V_j = \sum_{k=1}^{p} v_{jk} \cdot n_{jk} \tag{5.1.48}$$

See Table 5.1.1 for the definition of the variables.

All anions are supposed to have the same valence state:

$$a_i = \frac{u_{ik}}{v_{ik}} \quad \text{for all } k = 1 \cdots p \tag{5.1.49}$$

The mole number of possible sites for the cations I is $a_i D_i$ and they occupy $\sum_{k=1}^{p} u_{ik} \cdot n_{ik}$ sites among these sites. The mole of sites remaining unoccupied is then:

$$a_i \cdot D_i - \sum_{k=1}^{p} u_{ik} \cdot n_{ik} = a_i \cdot D_{i+1} \quad \text{for all } k = 1 \cdots p \tag{5.1.52}$$

The possible permutations number for the cations is therefore:

Table 5.1.1 Mass Balance Constraints

$$\text{Anions} \quad \sum_{i,j=1}^{m} R_{ij}^{k} = \sum_{i=1}^{m} v_{ik} n_{ik} = V_k \quad \text{for } k = 1 \cdots p \tag{5.1.50}$$

$$\text{Cations} \quad \sum_{k=1}^{p} \sum_{j=1}^{m} R_{ij}^{k} = \sum_{k=1}^{p} v_{ik} n_{ik} = V_i \quad \text{for } i = 1 \cdots m \tag{5.1.51}$$

n_{ik} is mole number of the component containing u_{ik} cations i and v_{ik} anions k.
V^k is the mole number of anions k.

$$P_i = \frac{(N \cdot a_i \cdot D_i)!}{\left(N \cdot \sum_{k=1}^{p} u_{ik} \cdot n_{ik}\right)!(N \cdot a_i \cdot D_{i+1})!} \tag{5.1.53}$$

N is the Avogadro number.

The total number of cations permutations is deduced from the preceding formula:

$$P_C = \prod_{i=1}^{m-1} P_i = \prod_{i=1}^{m-1} \frac{(N \cdot a_i \cdot D_i)!}{\left(N \cdot \sum_{k=1}^{p} u_{ik} \cdot n_{ik}\right)!(N \cdot a_i \cdot D_{i+1})!} \tag{5.1.54}$$

or after using Stirling formula:

$$\ln(P_C) = \sum_{i=1}^{m-1} a_i \cdot \left(D_i \cdot \ln \frac{D_i}{V_i} - D_{i+1} \cdot \ln \frac{D_{i+1}}{V_i}\right) \tag{5.1.55}$$

The derivation of anions and cells perturbation number can be derived straightaway (Table 5.1.2).

5.1.6.2.3 Calculation of the Maximum Cells Permutation Number

This number is obtained for a random distribution of anions and cations on their respective sublattices. The maximum probability to "meet" a cell *i–k–j* is noted $R_{ij}^{*\,k}/D_1$. It is equal to the product of the probabilities of the following events assumed to be independent:

- Meet an anion k on the anionic sublattice, probability V^k/D_1.
- Meet a cation i on the cationic sublattice, probability V_i/D_1.
- Meet a cation j on the cationic sublattice, probability V_j/D_1.

Table 5.1.2 Anions and Cells Perturbation Number

$$P_A = \frac{(N \cdot D_1)!}{\prod_{k=1}^{p} (N \cdot V^k)} \quad \text{or} \quad \ln(P_A) = \sum_{k=1}^{p} V^k \cdot \ln \frac{V^k}{D_1} \tag{5.1.56}$$

$$U = \frac{(N \cdot D_1)!}{\prod_{k=1}^{p} \prod_{i,j=1}^{m} \left(\mathrm{N} \cdot R_{ij}^{k}\right)!} \quad \text{or} \quad \ln(P_A) = \sum_{k=1}^{p} V^k \cdot \ln \frac{V^k}{D_1} \tag{5.1.57}$$

The number of cells i–j–k is then for a random distribution:

$$R_{ij}^{*k} = \frac{V^k}{D_1} \cdot \frac{V_i \cdot V_j}{D_1} \tag{5.1.58}$$

Using Stirling formula, the value of U^* is equal to:

$$\begin{aligned} \ln\left(U^*\right) &= \sum_{k=1}^{p} \sum_{i,j=1}^{m} R_{ij}^{*k} \ln \frac{R_{ij}^{*k}}{D_1} \\ &= \sum_{k=1}^{p} \ln \frac{V^k}{D_1} \sum_{i,j=1}^{m} R_{ij}^{*k} - \sum_{i=1}^{m} \ln \frac{V_i}{D_1} \sum_{k=1}^{p} \sum_{j=1}^{m} R_{ij}^{*k} \\ &\quad - \sum_{j=1}^{m} \ln \frac{V_j}{D_1} \sum_{k=1}^{p} \sum_{i=1}^{m} R_{ij}^{*k} \end{aligned} \tag{5.1.59}$$

Noticing that:

$$\sum_{i,j=1}^{m} R_{ij}^{*k} = V^k \quad \text{and} \quad \sum_{k=1}^{p} \sum_{j=1}^{m} R_{ij}^{*k} = V_i \tag{5.1.60}$$

We obtain:

$$\ln\left(U^*\right) = -\sum_{k=1}^{p} V^k \ln \frac{V^k}{D_1} - 2 \sum_{i=1}^{m} V_i \ln \frac{V_i}{D_1} \tag{5.1.61}$$

5.1.6.3. Degeneracy Calculation

Using the preceding development and after obvious simplifications, g is given by:

$$\begin{aligned} \ln(g) &= \sum_{i=1}^{m-1} a_i \cdot \left(D_i \cdot \ln \frac{D_i}{V_i} - D_{i+1} \cdot \ln \frac{D_{i+1}}{V_i} \right) + 2 \sum_{i=1}^{m} V_i \ln \frac{V_i}{D_1} \\ &\quad - \sum_{k=1}^{p} \sum_{i,j=1}^{m} R_{ij}^{k} \cdot \ln \frac{R_{ij}^{k}}{D_1} \end{aligned} \tag{5.1.62}$$

5.1.6.4. Energy of the System

The energy is a sum of two terms: a formation energy and an interaction energy:

$$E = E_{\mathrm{F}} + E_{\mathrm{I}} \tag{5.1.63}$$

5.1.6.5. Formation Energy

It is written as a function of the energies of formation of cells from a set of independent cells corresponding to the independent components of the slag. The formation energy of *i*–*k*–*j* cells is noted:

$$W_{ij}^{k} \tag{5.1.64}$$

The formation energy is then written as follows:

$$E_{\mathrm{F}} = \sum_{k=1}^{p} \sum_{i,j=1}^{m} W_{ij}^{k} \cdot R_{ij}^{k} \text{with } W_{ij}^{k} = W_{ji}^{k} \tag{5.1.65}$$

The parameter W_{ij}^{k} $(i<j)$ can depend linearly on composition:

$$W_{ij}^{k} = {}^{0}W_{ij}^{k} + {}^{1}W_{ij}^{k} \cdot X_i \tag{5.1.66}$$

X_i is the molar fraction of component i in the slag.

$$X_i = \frac{\sum_{k=1}^{p} n_{ik}}{\sum_{k=1}^{p} \sum_{j=1}^{m} n_{jk}} \tag{5.1.67}$$

5.1.6.5.1 Interaction Energy

Different assumptions allow to keep here only binary interaction parameters with only one parameter per binary (with however a possible linear dependence on composition). These assumptions are the following.

The interactions between two cells are considered. The interaction energy between a cell *i*–*k*–*j* and a cell *i*′–*l*–*j*′ is noted $E_{ikj-I'kj'}$. E_I is expressed as follows:

$$E_{\mathrm{I}} = \sum E_{ijk-i'lj'} \cdot X_{\mathrm{ikj}-i'lj'} \tag{5.1.68}$$

where $X_{ikj-i'lj'}$ is the number of associations of cells *i*–*k*–*j* and *i*′–*l*–*j*′.

We assume a random distribution of the cells. The number of associations of cells *i*–*k*–*j* and *i*′–*l*–*j*′ is the product of the respective cell mole numbers:

$$E_{\mathrm{I}} = \frac{1}{D_1} \sum E_{ikj-i'lj'} \cdot R_{ij}^{k} \cdot R_{i'j'}^{l} \tag{5.1.69}$$

The interaction energy between two asymmetrical cells is supposed to be 0:

$$E_I = \frac{1}{D_1}\sum_{k,l=1}^{p}\left(\sum_{i,i'=1}^{m} E_{iki-i'li'}\cdot R_{ii}^{k}\cdot R_{i'i'}^{l} + \sum_{\substack{i,i',j'=1\\ i'\neq j'}}^{m} E_{iki-i'lj'}\cdot R_{ii}^{k}\cdot R_{i'j'}^{l} + \sum_{\substack{i,j,i'=1\\ i\neq j}}^{m} E_{ikj-i'li'}\cdot R_{ij}^{k}\cdot R_{i'i'}^{l}\right) \tag{5.1.70}$$

In order to keep only binary parameters, we use an additivity hypothesis that allows taking into account only cells having a common cation:

$$\begin{aligned} E_{iki-i'li'} &= E_{ii'}^{k} + E_{ii'}^{l} + E_{i}^{kl} + E_{i'}^{kl} \\ 2E_{iki-i'lj'} &= E_{ii'}^{k} + E_{ij'}^{k} + 2E_{i}^{kl} \quad \text{if } i \neq j \end{aligned} \tag{5.1.71}$$

With these assumptions, the interaction energy can be rewritten:

$$\begin{aligned} E_I = \frac{1}{D_1}\sum_{k=1}^{p}\sum_{i=1}^{m} R_{ii}^{k}\cdot\Bigg(2\sum_{l=1}^{p} E_{i}^{kl}\cdot\sum_{i',j'=1}^{m} R_{i'j'}^{k} + \sum_{j'=1}^{m} E_{ij'}^{k}\cdot\sum_{l=1}^{p}\sum_{i'=1}^{m} R_{i'j'}^{l} \\ + \sum_{i'=1}^{m} E_{ii'}^{k}\sum_{l=1}^{p}\sum_{j'=1}^{m} R_{i'j'}^{l}\Bigg) \end{aligned} \tag{5.1.72}$$

Taking into account the anions and cations mass balance:

$$E_{\mathrm{I}} = \frac{2}{D_1}\sum_{k=1}^{p}\sum_{i=1}^{m} R_{ii}^{k}\cdot RT\ \ln Q_{i}^{k} \tag{5.1.73}$$

with

$$RT\ \ln Q_{i}^{k} = \frac{1}{D_1}\left(\sum_{l=1}^{p} V^{l}\cdot E_{i}^{kl} + \sum_{j=1}^{m} V_{j}\cdot E_{ij}^{k}\right) \tag{5.1.74}$$

Another assumption has been taken into account:

$$E_{ij}^{k} = 0 \quad \text{if } i > j \tag{5.1.75}$$

i.e., the interaction between a cell *i*–*k*–*i* and a cell *i*–*k*–*j* is null if *i* is more basic than *j*.

The same dependence on composition as for the formation energies is assumed for the interaction energies (Equation 5.1.66).

5.1.6.6. Gibbs Energy

Gibbs energy is equal to the minimum value of $G = E - RT\ln(g)$ corresponding to the stable microscopic state of the system. This function is:

$$G=\sum_{k=1}^{p}\sum_{i,j=1}^{m}W_{ij}^{k}\cdot R_{ij}^{k}+\frac{2}{D_1}\sum_{k=1}^{p}\sum_{i=1}^{m}R_{ii}^{k}\cdot RT\ln Q_i^k$$
$$-RT\left(\sum_{i=1}^{m-1}a_i\cdot\left(D_i\cdot\ln\frac{D_i}{V_i}-D_{i+1}\cdot\ln\frac{D_{i+1}}{V_i}\right)+2\sum_{i=1}^{m}V_i\ln\frac{V_i}{D_1}-\sum_{k=1}^{p}\sum_{i,j=1}^{m}R_{ij}^{k}\cdot\ln\frac{R_{ij}^{k}}{D_1}\right) \tag{5.1.76}$$

For a binary SiO_2–MO, the Gibbs energy is expressed as:

$$G=2\left({}^{0}W_{\mathrm{MSi}}^{\mathrm{O}}+{}^{1}W_{\mathrm{MSi}}^{\mathrm{O}}x_{\mathrm{SiO_2}}\right)\cdot R_{\mathrm{MSi}}^{\mathrm{O}}+2R_{\mathrm{SiSi}}^{\mathrm{O}}\frac{n_{\mathrm{MO}}}{(2n_{\mathrm{SiO_2}}+n_{\mathrm{MO}})}\left({}^{0}E_{\mathrm{SiM}}^{\mathrm{O}}+{}^{1}E_{\mathrm{SiM}}^{\mathrm{O}}x_{\mathrm{SiO_2}}\right)$$
$$+RT\left(\frac{1}{2}(2n_{\mathrm{SiO_2}}+n_{\mathrm{MO}})\ln(2n_{\mathrm{SiO_2}}+n_{\mathrm{MO}})-\frac{3}{2}(2n_{\mathrm{SiO_2}})\ln(2n_{\mathrm{SiO_2}})-\frac{3}{2}n_{\mathrm{MO}}\ln n_{\mathrm{MO}}\right)$$
$$+RT\left(R_{\mathrm{SiSi}}^{\mathrm{O}}\ln R_{\mathrm{SiSi}}^{\mathrm{O}}+R_{\mathrm{MM}}^{\mathrm{O}}\ln R_{\mathrm{MM}}^{\mathrm{O}}+2R_{\mathrm{SiM}}^{\mathrm{O}}\ln R_{\mathrm{SiM}}^{\mathrm{O}}\right) \tag{5.1.77}$$

where the number of cells R_{ij}^{k} must be replaced by their actual values obtained by minimizing G with their respect under the mass balance constraints:

$$\begin{aligned}2n_{\mathrm{SiO_2}}&=R_{\mathrm{SiSi}}^{\mathrm{O}}+R_{\mathrm{SiM}}^{\mathrm{O}}\\ n_{\mathrm{MO}}&=R_{\mathrm{SiM}}^{\mathrm{O}}+R_{\mathrm{MM}}^{\mathrm{O}}\end{aligned} \tag{5.1.78}$$

5.1.6.7. Calculation of the Cell Mole Numbers

The cell mole numbers are given by the minimization of G with respect to the mass balance equations (Equations 5.1.49 and 5.1.50):

$$\begin{aligned}R_{ii}^{1}\cdot R_{jj}^{1}&=\left(R_{ij}^{1}/P_{ij}^{1}\right)^{2}\cdot P_{ii}^{1}\cdot P_{jj}^{1}\\ R_{ii}^{1}\cdot R_{ii}^{k}/R_{11}^{1}&=R_{ii}^{k}/P_{ii}^{k}\\ R_{ii}^{1}\cdot R_{jj}^{1}\cdot\left(R_{11}^{k}\right)^{2}&=\left(R_{11}^{1}\right)^{2}\cdot\left(R_{ij}^{k}/P_{ij}^{k}\right)^{2}\end{aligned} \tag{5.1.79}$$

With

$$RT\ln\left(P_{ij}^{k}\right)=\frac{1}{2}\left(W_{ii}^{1}+W_{jj}^{1}\right)+W_{11}^{k}-W_{11}^{1}-W_{ij}^{k}-2\delta_{ij}\cdot RT\ln Q_i^k \tag{5.1.80}$$

The preceding equations can be expressed as:

$$\gamma_i\cdot\sum_{j=1}^{m}\sum_{k=1}^{p}P_{ij}^{k}\cdot\gamma_j\cdot\gamma^{k}=V_i\quad\text{for}\,i=1\,\text{to}\,m$$

$$\gamma^k = V^k \Bigg/ \left(\sum_{i=1}^{m} \sum_{j=1}^{m} P_{ij}^k \cdot \gamma_i \cdot \gamma_j \right) \quad \text{for } k = 2 \text{ to } p \tag{5.1.81}$$

with $\gamma_i = \sqrt{R_{ii}^1}$ and $\gamma^k = R_{11}^k / R_{11}^1$

We have then a set of $(m+p-1)$ equations with the y's as unknowns to solve in order to find the cell mole numbers.

5.1.6.8. Chemical Potentials

They are the derivatives of G with respect to the component mole numbers, the cell mole numbers having the values solution of the preceding equations:

$$\mu_{ik} = \nu_{ik} \left(\omega_i + \omega^k + 2RT \ln Q_i^k + W_{ii}^k + RT \ln \frac{R_{ii}^k}{D_1} + \omega_i' - \sum_{j=1}^{m} x_j \cdot \omega_j' \right) \tag{5.1.82}$$

With:

$$\omega_i = \frac{2}{D_1} \sum_{j=1}^{m} \sum_{l=1}^{p} R_{jj}^l \cdot \left(E_{ji}^l - RT \ln Q_j^l \right) - RT \left(a_i \ln \frac{D_i}{V_i} + \sum_{j<i} a_j \ln \frac{D_j}{D_{j+1}} \right) - 2RT \ln \frac{V_i}{D_1}$$

$$\omega^k = \frac{2}{D_1} \sum_{j=1}^{m} \sum_{l=1}^{p} R_{jj}^l \cdot E_j^{lk}$$

$$\omega_i' = \frac{1}{\sum_{j,l} n_{jl}} \left(\sum_{j=1}^{m} \sum_{l=1}^{p} {}^1W_{ij}{}^l \cdot R_{ij}^l + 2 \sum_{l=1}^{p} \frac{R_{ii}^l}{D_1} \sum_{j=1}^{m} {}^1E_{ij}{}^l \cdot V_j \right) \tag{5.1.83}$$

The terms ω_i' come from the dependence of the parameters on the composition:

$$\begin{aligned} W_{ij}^k &= {}^0W_{ij}^k + {}^1W_{ij}^k \cdot x_i \\ E_{ij}^k &= {}^0E_{ij}^k + {}^1E_{ij}^k \cdot x_i \end{aligned} \tag{5.1.84}$$

for $i < j$ and with

$$x_i = \sum_{k=1}^{p} n_{ik} \Bigg/ \sum_{j=1}^{m} \sum_{k=1}^{p} n_{jk} \tag{5.1.85}$$

For a binary MO–SiO_2:

$$\mu_{MO} = \left(\begin{array}{l} -\frac{3}{2}RT \ln \frac{n_{MO}}{2n_{SiO_2} + n_{MO}} + RT \ln \frac{R^O_{MM}}{2n_{SiO_2} + n_{MO}} \\ -x_{SiO_2} \cdot \frac{1}{n_{SiO_2} + n_{MO}} \left({}^1W S^O_{SiM} \cdot R^O_{SiM} + 2 \frac{R^O_{SiSi}}{2n_{SiO_2} + n_{MO}} {}^1E^0_{SiM} \cdot n_{MO} \right) \end{array} \right)$$

$$\mu_{SiO_2} = 2 \left(\begin{array}{l} \frac{2n_{MO}}{D_1} \left(1 - \frac{R^O_{SiSi}}{2n_{SiO_2} + n_{MO}} \right) \cdot E^O_{SiM} \\ -\frac{3}{2}RT \ln \frac{2n_{SiO_2}}{2n_{SiO_2} + n_{MO}} + RT \ln \frac{R^O_{SiSi}}{2n_{SiO_2} + n_{MO}} \\ +(1 - x_{SiO_2}) \cdot \frac{1}{n_{SiO_2} + n_{MO}} \left({}^1W S^O_{SiM} \cdot R^O_{SiM} + 2 \frac{R^O_{SiSi}}{2n_{SiO_2} + n_{MO}} {}^1E^0_{SiM} \cdot n_{MO} \right) \end{array} \right) \tag{5.1.86}$$

As an illustration, Figure 5.1.2 presents the cell numbers and the activities for the binary $CaO–SiO_2$. Due to the high formation energy associated to the reaction:

$$Ca - O - Ca + Si - O - Si \rightarrow 2Si - O - Ca$$

the number of cells Si–O–Ca reaches a sharp maximum at the composition corresponding to the stoichiometry $2CaO{\cdot}SiO_2$ and the number of cells Ca–O–Ca and Si–O–Si, respectively, decreases and increases linearly before and after this composition. The shapes of the activity curves result directly from these variations.

5.1.6.9. CSIRO's Modification

In order to correct the Cell model for systems containing simultaneously Al_2O_3 and high amounts of SiO_2, Zhang *et al.* [63] introduced more flexible polynomial functions for the cell formation energies as well as ternary model parameters For example, for the ternary $CaO–Al_2O_3–SiO_2$ system, the cell formation energy parameters W_{SiCa} and W_{SiAl} have been modified by introducing two ternary parameters W_{SiCaAl} and W_{SiAlCa} as follows:

$$W_{ij} = W^{(0)}_{ij} + W^{(1)}_{ij} x_i + W^{(2)}_{ij} x_i^2 + \sum_k W_{ijk} \frac{x_k}{(1 - x_i)} \tag{5.1.87}$$

The model extended to the system $SiO_2–P_2O_5–TiO_2–Ti_2O_3–Al_2O_3–Cr_2O_3–Fe_2O_3–FeO–CaO–MgO–CrO–NiO–MnO$ is proposed to the users through the MPE package [64].

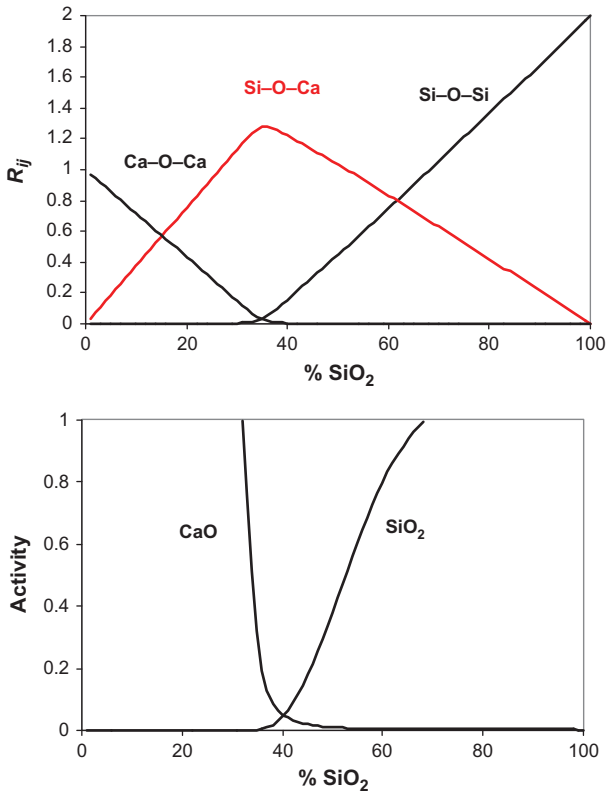


Figure 5.1.2 Cell numbers and activities in the binary CaO–SiO_2 (ref. state: pure solid).

5.1.7. THE CENTRAL ATOMS MODEL AND GENERALIZED CENTRAL ATOM MODEL

The Generalized Central Atom (GCA) model unifies in the same formalism the Central Atoms model, originally proposed by Lupis and Elliott [65] and close to the "surrounded atoms model" developed at about the same period at the LTPCM [66,67] and the Cell model. That is why the Central Atom model's specificities will be presented here as a particular case of the GCA model.

5.1.7.1. Description of the Structure

In the "unified" model, the elements are distributed between two sublattices. The first one, constituted by the substitutional sites, is filled, in the case of the liquid steel, with metallic elements whereas the other one, constituted by the interstitial sites, is filled with

non-metallic elements. In the case of the metallurgical slags, the first sublattice is filled with the different cations and the second one with the different anions. Some interstitial sites could be left unoccupied in the case of the liquid steel, contrary to the metallurgical slags where all the sites are supposed to be occupied either by anions or by cations.

The liquid structure is described in terms of cells composed of a central atom and its shell of nearest neighbors. In a system with m components with t substitutional elements, the cell will be noted as:

$i_1, i_2, \ldots i_k, \ldots i_t$	Atoms on substitutional sites
J	Central atom
$j_{t+1}, \ldots j_r, \ldots j_m$	Atoms on interstitial sites

In such a cell, around a central atom J that can be either substitutional or interstitial, there are i_1 atoms of element #1, i_2 atoms of element #2, etc., located on substitutional sites, the total number of different elements being t. On the interstitial sites, there are j_{t+1} atoms of element $\#t+1$, j_{t+2} atoms of elements $\#t+2$, etc., the total of elements on these sites being $m-t$. In the case of the metallic solutions, the index m can refer to the vacancies.

One of the main differences with the Central Atoms model is that the number of nearest neighbors can depend on the nature of the central atom. This is the case, in particular, for the metallurgical slags. The number of nearest anions (and nearest cations) of a silicon atom is four whereas the number of nearest anions (and nearest cations) of a calcium atom is two.

The total number of nearest neighbor atoms of an element i is denoted Z_i when these neighbors are placed on substitutional sites and z_i when they are placed on interstitial sites.

For the liquid metallic phases, a structure similar to the austenite has been chosen. The number of substitutional sites is equal to the number of interstitial sites and the atoms have all the same number of neighbors. An atom i on a substitutional site has $z_i=6$ neighbors located on interstitial sites and $Z_i=12$ on substitutional sites. Inversely, an atom j on an interstitial site has $z_j=12$ neighbors located on interstitial sites and $Z_j=6$ on substitutional sites. As an example, for liquid alloys Fe–Cr–Mn–Si–C–S, the substitutional sites are occupied by the solvent Fe as well as by the solutes Cr, Mn and Si. The interstitial sites are occupied by C and S, the other sites remain vacant. Thus, this solution can be represented by the formula (Fe, Cr, Mn, Si) (C, S,Va).

For the metallurgical slags, the number of nearest anions of a given cation is equal to its valence state and is also the number of its nearest anions. For an anion O^{2-}, S^{2-} or $2F^{2-}$, the number of nearest cations is 2 and the number of its nearest anions is taken constant to $Z=6$ as it has been done for the oxisulfide model.

5.1.7.2. Parameters of the Model

5.1.7.2.1 Formation Energy Parameters

The energy of a cell is noted $\phi^J_{\{i\},\{j\}}$ where J represents the central atom and $\{i\}$ and $\{j\}$ represent, respectively, the whole set of substitutional elements $i_1, \cdots, i_t$ and interstitial elements (including vacancies, if any) $j_{t+1}, \cdots, j_m$. For the sake of simplicity, we suppose that this energy is the sum of the contributions of the two sites:

$$\phi^J_{\{i\},\{j\}} = \phi^J_{\{i\}} + \phi^J_{\{j\}} \tag{5.1.88}$$

In order to reduce the number of parameters, different assumptions have been formulated to describe the energy variation of the central atom according to the composition of chemical neighborhood. We chose the following expression in order to stay compatible with what had been previously taken for the Cell model and for the Central Atoms model [68]:

$$\phi^J_{\{i\}} = \sum_{k=1}^{t} i_k \phi^J_{kk} + \frac{1}{2} \sum_{\substack{k,l=1 \\ k \neq l}}^{t} i_k i_l \phi^J_{kl} \tag{5.1.89}$$

For the metallurgical slags, the parameters ϕ^J_{kl} are inherited from the Cell model where they are associated with the formation of an "asymmetric" cell from the two corresponding symmetric ones:

$$\tfrac{1}{2}k - J - k + \tfrac{1}{2}l - J - l \rightarrow k - J - l \tag{5.1.90}$$

For the metallic solutions, as pointed out by Mathieu *et al.* [66], the quadratic contribution in [65] could be omitted for the systems exhibiting a symmetrical mixing enthalpy, as, for example, the binary Fe–Ti (Figure 5.1.3). But the quadratic terms appear to be necessary for systems with markedly asymmetrical mixing enthalpies. Figure 5.1.4 shows the typical example of the Fe–Ni binary and Figure 5.1.5 illustrates the very good fit obtained with this formalism for the activity coefficient curve.

5.1.7.2.2 Interaction Energy Parameters

Beside these formation energy parameters, additional interaction energy terms have been considered to stay compatible with the Cell model. The contribution of these terms to the Gibbs free energy has the following expression:

$$E = \frac{1}{2} kT \left(\sum_{J=1}^{m} \sum_{\{i\},\{j\}} N_J p^J_{\{i\}\{j\}} \ln Q^J_{\{i\}\{j\}} \right) \tag{5.1.91}$$

where N_J is the number of atoms J and $p^J_{\{i\}\{j\}}$ the probability to have the configuration $\{i\}\{j\}$ around the atom J.

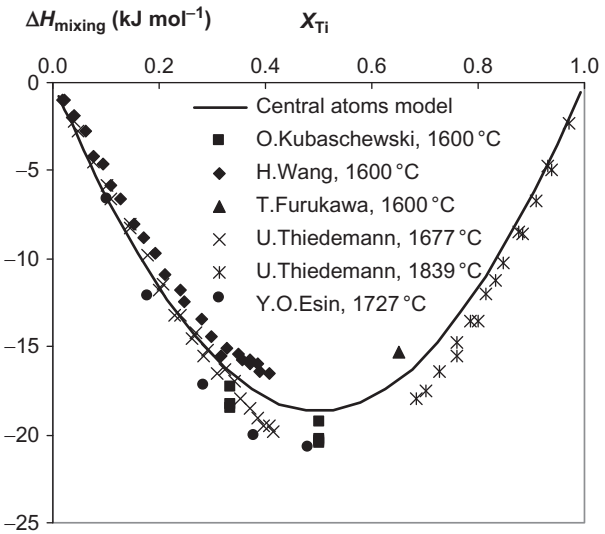


Figure 5.1.3 Mixing enthalpy of the binary Fe–Ti [69–73]. The curve symmetry is well reproduced by the linear formalism. No clear dependence on the temperature can be extracted from the data.

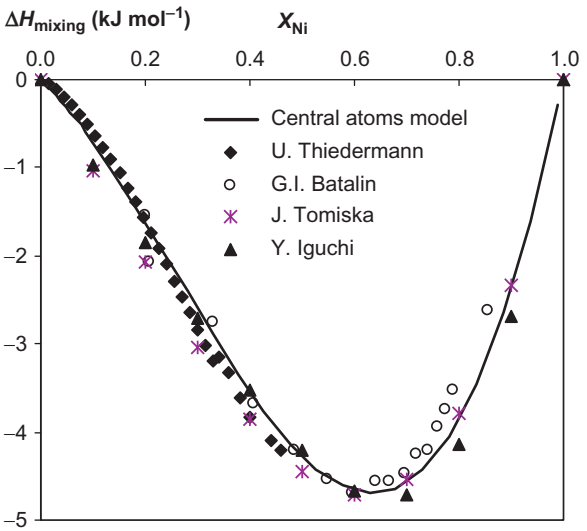


Figure 5.1.4 Mixing enthalpy of the binary Fe–Ni at 1873 K [72,74–76]. The quadratic formalism reproduces accurately the curve asymmetry.

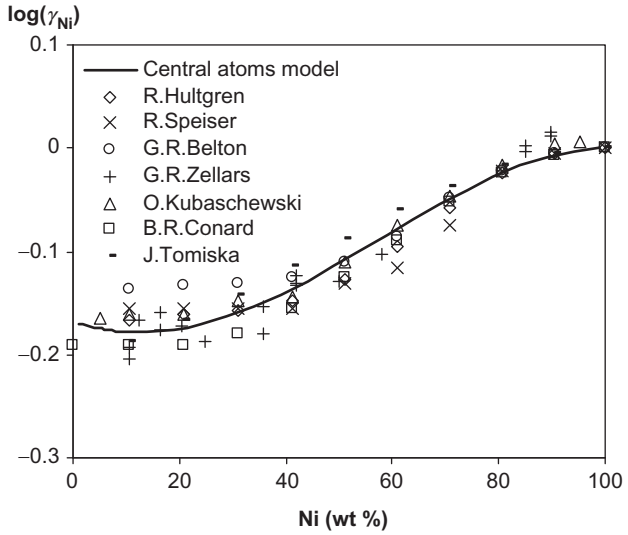


Figure 5.1.5 Ni activity coefficient on the binary Fe–Ni at 1873 K [69,75,77–81]. The reference state for Ni is pure liquid.

Some simple assumptions have been introduced for these interactions. First, interactions between cells depend only on the occupation of the first shell of neighbors. For instance, if the central atom is located on a substitutional site, the interaction depends only on the nature of the atoms situated on the closest interstitial sites. It means that, if J is located on an interstitial site ($J > t$), we have:

$$\ln Q^J_{\{i\}\{j\}} = \ln Q^J_{\{i\}} \tag{5.1.92}$$

Then, this interaction vanishes if all the atoms situated on this shell are not of the same nature:

$$\ln Q^J_{\{i\}} = \ln Q^J_k \neq 0 \quad \text{if and only if } i_k = Z_J \tag{5.1.93}$$

Finally, we have adopted for $\ln Q^J_k$ the following expression:

$$\ln Q^J_k = \frac{1}{2N_R}\left(\sum_{i=1}^{t} Z_i N_i . E^J_{ki} + \sum_{j=t+1}^{m+1} Z_j N_j . E^J_{jk}\right) \tag{5.1.94}$$

for $J > t$ and $k \leq t$ and

$$kT \ln Q^J_l = \frac{1}{2N_S}\left(\sum_{j=t+1}^{m+1} z_j N_j . E^J_{lj} + \sum_{k=1}^{t} z_k N_k . E^J_{kl}\right) \tag{5.1.95}$$

for $J \leq t$ and $l > t$.

N_R and N_S are the number of atoms on the interstitial and the substitutional sites, respectively.

5.1.7.3. Gibbs Free Energy and Chemical Potential

The formalism to derive the expression of the various thermodynamic functions is similar to what had been proposed by Foo and Lupis [82,83]. Prior to the calculation of the Gibbs free energy and of the chemical potential, the partition function must be maximized. The corresponding equations are given in Table 5.1.3. They deliver the values of the Lagrange multipliers $\beta_k^{(J)}$. These equations are quite similar to the corresponding ones given by Foo and Lupis. Differences arise from the dependence of the number of neighbors on the nature of the central atom, from the expression of the formation energy and from the interaction energy parameters.

The expression of the Gibbs free energy is given in Table 5.1.4. When compared to the Central Atoms model [82], an additional term appears that comes from the normalizing factor of the expression of the mixing entropy (terms function of the D_i's). This term is inherited from the Cell model and is, therefore, specific to the metallurgical slags. But it could also be adopted for the liquid metallic phase if, for example, it appears that, in such a phase, the number of nearest neighbors could differ from one element to the other.

The chemical potentials derived from the Gibbs free energy will have a much more complicated expression than in the Central Atoms model. In particular, specific terms will appear resulting from the variations of the neighbors' numbers as a function of the nature of the central atom and from the interaction energy.

5.1.7.4. Multicomponent Steels

The extrapolability of the Central Atoms model to multicomponent systems has been checked, in the case of the liquid steel, for three interstitial solutes: sulfur, nitrogen, and oxygen.

5.1.7.4.1 Sulfur-Bearing Systems

Figure 5.1.6 demonstrates, for the description of sulfur behavior, the relevance of the assumption of a two sublattice network for the liquid phase. Given the limited range of S contents involved (<6%), it was not necessary to introduce a quadratic dependency of the energy parameter and the assumption of a linear variation is sufficient to satisfactorily reproduce the experimental data on the binary Fe–S.

The capacity of the model to describe the sulfur behavior in multicomponent systems is illustrated by Figure 5.1.7 for high-alloyed carbon steels. Systems under consideration contain up to seven components.

Table 5.1.3 Conditions of Maximization of the Partition Function

Composition variables.
n_{kl}: Mole number of components $(C_l)_{u_l}(A_k)_{v_l}$.

$$N_k = \sum_{l=t+1}^{m} v_l n_{lk} = V_k \quad 1 \le k \le t \quad (5.1.96)$$

$$V_l = \sum_{k=1}^{t} v_l n_{lk} \quad t < l \le m \quad (5.1.97)$$

$$N_l = \sum_{k=1}^{t} u_l n_{lk} \quad t < l \le m \quad (5.1.98)$$

$$D_i = \sum_{l=i}^{m} V_l \quad \text{and} \quad D = D_{t+1} \quad (5.1.99)$$

Mass balance equations.

$$\psi_k = \sum_{J=1}^{t} N_J \frac{P_k^J}{S^J} - Z_k N_k = 0 \quad 0 < k \le t \quad (5.1.100)$$

$$\psi_l = \sum_{J=1}^{t} N_J \frac{P_l^J}{s^J} - Z_l N_l = 0 \quad t < l \le m \quad (5.1.101)$$

$$\psi'_k = \sum_{J=t+1}^{m+1} N_J \frac{P_k^J}{S^J} - z_k N_k = 0 \quad 0 < k \le t \quad (5.1.102)$$

$$\psi'_I = \sum_{J=t+1}^{m+1} N_J \frac{P_I^J}{s^J} - z_l N_l = 0 \quad t < l \le m \quad (5.1.103)$$

Expression of the different polynomials.

$$p^J_{\{i\}} = \frac{Z_J!}{\prod_{k=1}^{t} i_k!} \exp\left(-\phi^J_{\{i\}}\right) \prod_{k=1}^{t} \left(\frac{V_k}{D}\beta_k^{(J)}\right)^{i_k} \left(Q_k^J\right)^{\vartheta_{kJ}} \quad \text{and} \quad p^J_{\{j\}} = \frac{z_J!}{\prod_{l=t+1}^{m+1} j_l!} \exp\left(-\phi^J_{\{j\}}\right) \prod_{l=t+1}^{m+1} \left(\frac{V_l}{D}\beta_l^{(J)}\right)^{j_l} \left(Q_l^J\right)^{\vartheta_{lJ}} \quad (5.1.104)$$

Continued

Table 5.1.3 Conditions of Maximization of the Partition Function—cont'd

$$S^J = \sum_{\{i\}} p^J_{\{i\}} \quad \text{and} \quad s^J = \sum_{\{j\}} p^J_{\{j\}} \tag{5.1.105}$$

$$P^J_k = \sum_{\substack{i_1,\ldots,i_t=0 \\ \sum_k' i_k' = Z_J}}^{Z_J} i_k p^J_{\{i\}} \quad \text{and} \quad P^J_l = \sum_{\substack{j_{t+1},\ldots,j_{m+1}=0 \\ \sum_l' j_l' = z_J}}^{z_J} j_l p^J_{\{j\}} \tag{5.1.106}$$

ϑ_{kJ} is equal to 1 if $J > t$ and $k \leq t$ and if $i_k = Z_J$ and otherwise is equal to 0.

Note: 1. The components of the liquid metallic phase are (Fe)(Va), (Si)(Va), (Fe)(C), etc., and those of the slags are $(Si)(O)_2$, $(Al)_2(O)_3$, etc.
2. When an exponent is put into brackets (as it is the case for $\beta_k^{(J)}$), the value of the corresponding variables is the same for all elements in brackets as long as they belong to the same site. Thus the variables β have two sets of values (β_k, β_l) for $J \leq t$ and (β'_k, β'_l) for $J > t$.

Table 5.1.4 Expression of the Gibbs Free Energy

$$G/RT = -\sum_{l=t+1}^{m} \frac{u_l}{v_l}\left(D_l \ln \frac{D_l}{V_l} - D_{l+1} \ln \frac{D_{l+1}}{V_l}\right) + \sum_{k=1}^{t} N_k \ln \frac{V_k}{D} - \sum_{J=1}^{m+1} N_J \ln S^J s^J + \sum_{J=1}^{m+1}\left(Z_J \exp\beta_J + z_J \exp\beta'_J\right)\cdot N_J \qquad (5.1.107)$$

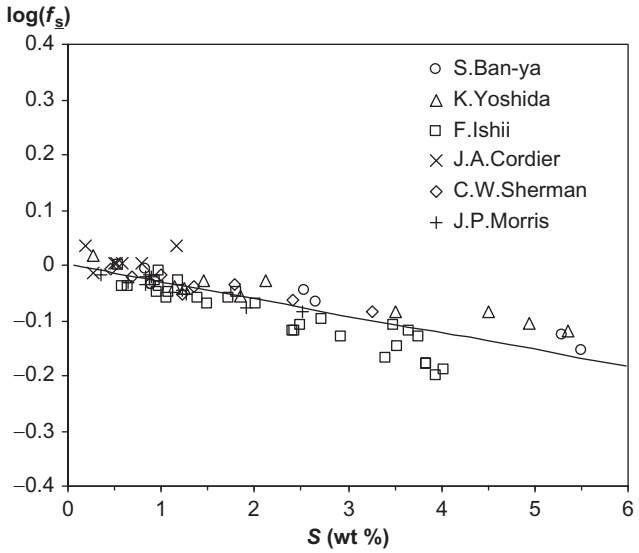


Figure 5.1.6 Comparison between the calculated (line) and experimental values [84–90] of the sulfur activity coefficient for the binary Fe–S at 1873 K. The reference state for S is 1 wt% dilute solution.

5.1.7.4.2 Nitrogen-Bearing Systems

For nitrogen, the extrapolability has been checked for domains interesting for the production of stainless steels, i.e., for systems containing Cr and Ni. Figure 5.1.8 illustrates the fit obtained by assessing the parameters ϕ^{N}_{FeCr} and ϕ^{N}_{FeNi} on the two ternaries Fe–Cr–N and Fe–Ni–N. The scatter of the experimental points reflects the uncertainty on the determination of the nitrogen solubility. For example, for a Fe–18%Cr alloy, the values collected from the literature range from 2400 to 3050 ppm at 1873 K.

Such an assessment of the ternary parameters has been done for all Fe–X–N systems for which experimental data were available. Then, the model has been applied to four- and five-component systems. The good quality of the results obtained on these systems is

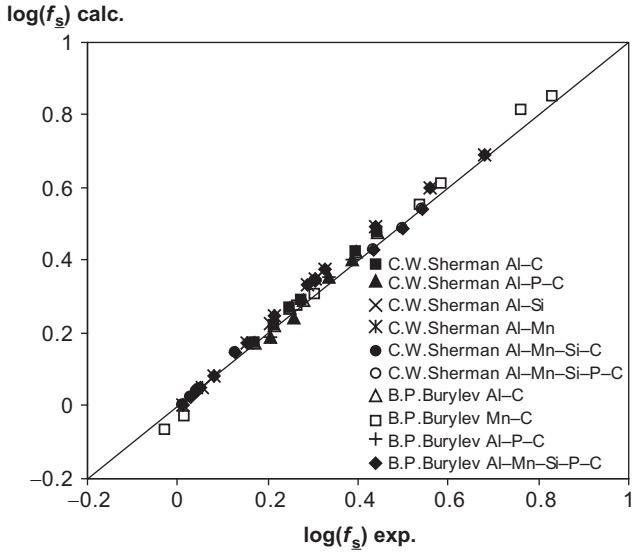


Figure 5.1.7 Comparison between calculated and experimental sulfur activity coefficients for high-alloyed carbon steels at 1873 K [90,91]. The reference state for S is 1 wt% dilute solution.

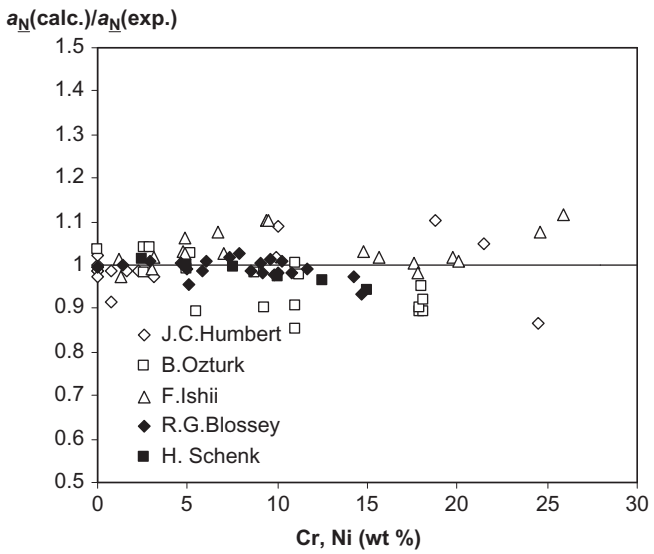


Figure 5.1.8 Comparison between calculated and experimental values of the nitrogen activity for two ternary systems Fe–Cr–N (open symbols) and Fe–Ni–N (filled symbols) at 1873 K [92–96]. The reference state for N is 1 wt% dilute solution.

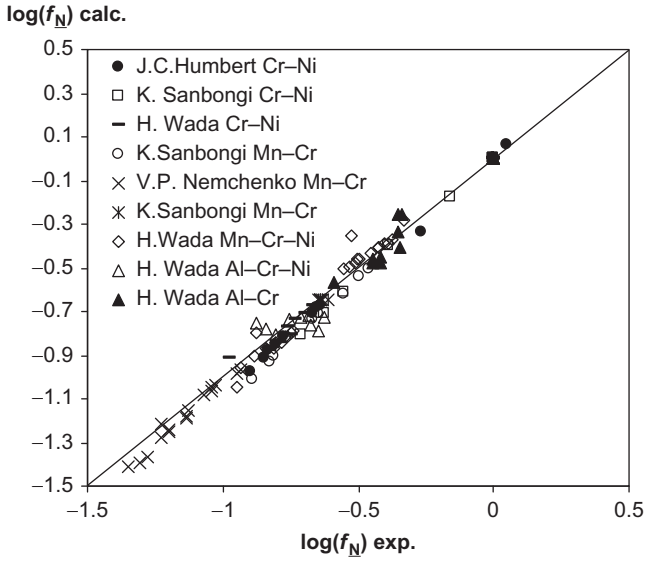


Figure 5.1.9 Comparison between calculated and experimental nitrogen activity coefficients (Cr and Ni contents, respectively, up to 30% and 15%) [96–99]. The reference state for N is 1 wt% dilute solution.

presented in Figure 5.1.9 that compares the calculated and the experimental nitrogen activity coefficients.

Figure 5.1.10 provides a more direct comparison between the predictions of the model and the experimental data. This figure gives the evolution of the nitrogen solubility as a function of the temperature for two alloy compositions. As we can see, the extrapolation of the model yields values in close agreement with Wada *et al.* data [98] whereas Sanbongi *et al.* [97] give a value significantly smaller by 350 ppm for the 18% Cr–8%Ni composition.

5.1.7.4.3 Oxygen-Bearing System

The prediction of the oxygen behavior brought by the model has also been checked for Cr-bearing system since this element is known for having a strong effect on its activity. Figure 5.1.11 shows that the model predicts correctly this effect for the range of Cr contents that has been experimentally studied.

Figure 5.1.12 illustrates the combined effect of Cr and Al. Al tends also to decrease the oxygen activity. Here also, the agreement is satisfactory.

5.1.7.5. Multicomponent Slags

The improvement that has been brought to the description of the multicomponent slags by the GCA model when compared to the Cell model is illustrated in Figure 5.1.13 with

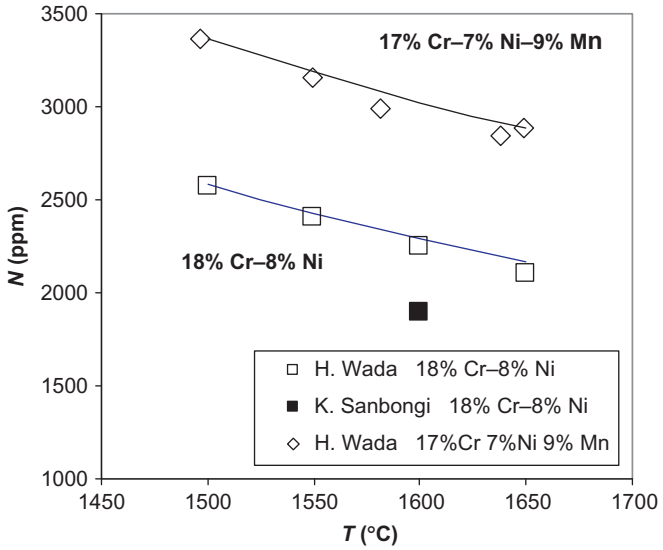


Figure 5.1.10 Evolution of the nitrogen solubility as a function of the temperature for Cr–Ni alloys [97,98].

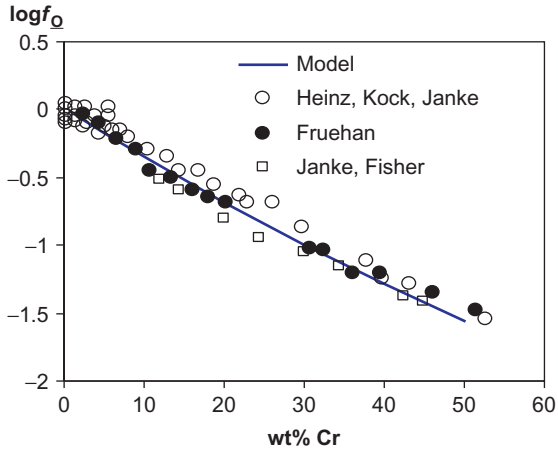


Figure 5.1.11 Oxygen activity coefficient in the Fe–Cr–O system at 1873 K [100–102].

the example of the binary SiO_2–Al_2O_3. One of the main weaknesses of the Cell model was the abnormally low eutectic point of silica and mullite which is corrected by the GCA. The shape of the activity curve (Figure 5.1.14) shows that the vicinity of a miscibility gap at low temperature in the metastable liquid is also correctly predicted by the model. Finally, Figure 5.1.15 depicts the variation of all the cells with the composition.

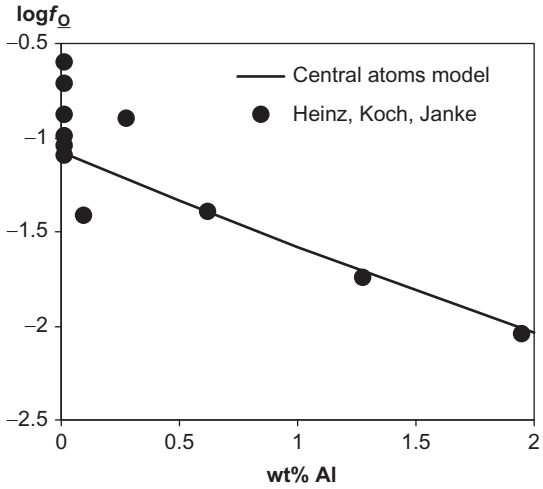


Figure 5.1.12 Oxygen activity coefficient in the Fe–25% Cr–2% Si–0.7% Mn system at 1873 K [102].

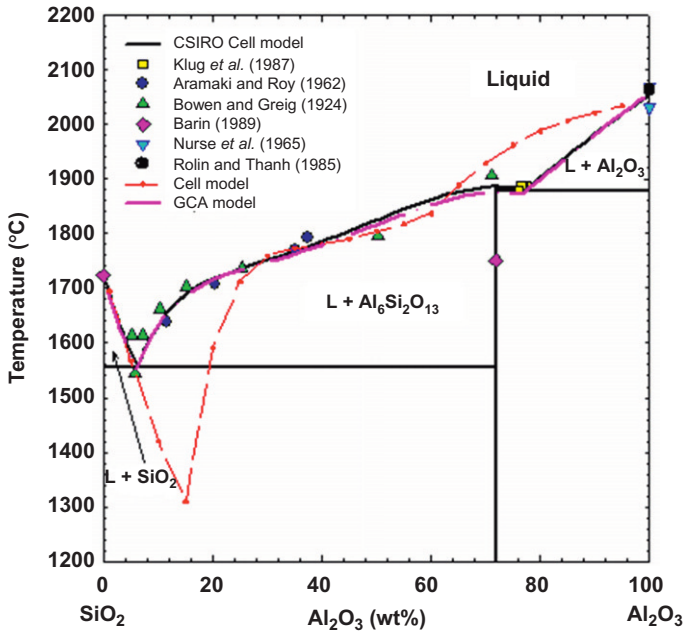


Figure 5.1.13 Al_2O_3–SiO_2 phase diagrams calculated by the cell model (and its modified version by CSIRO) and by the GCA model compared to the experimental data.

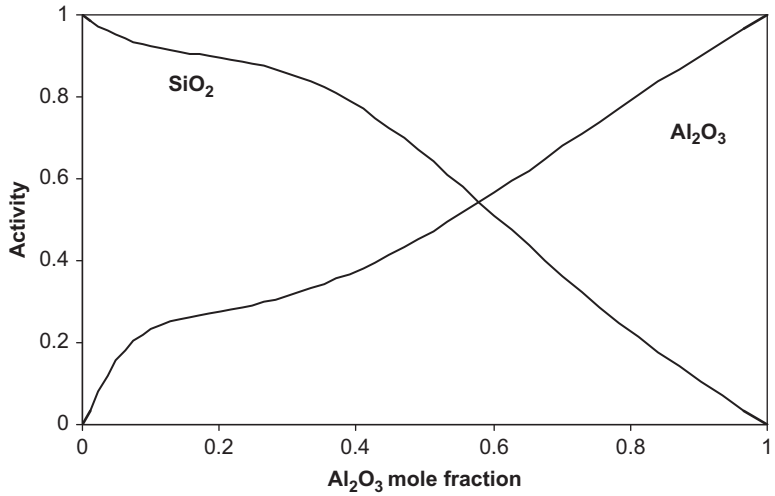


Figure 5.1.14 Activities in the binary Al_2O_3–SiO_2 at 1873 K calculated with the GCA model. Reference state: Pure liquid.

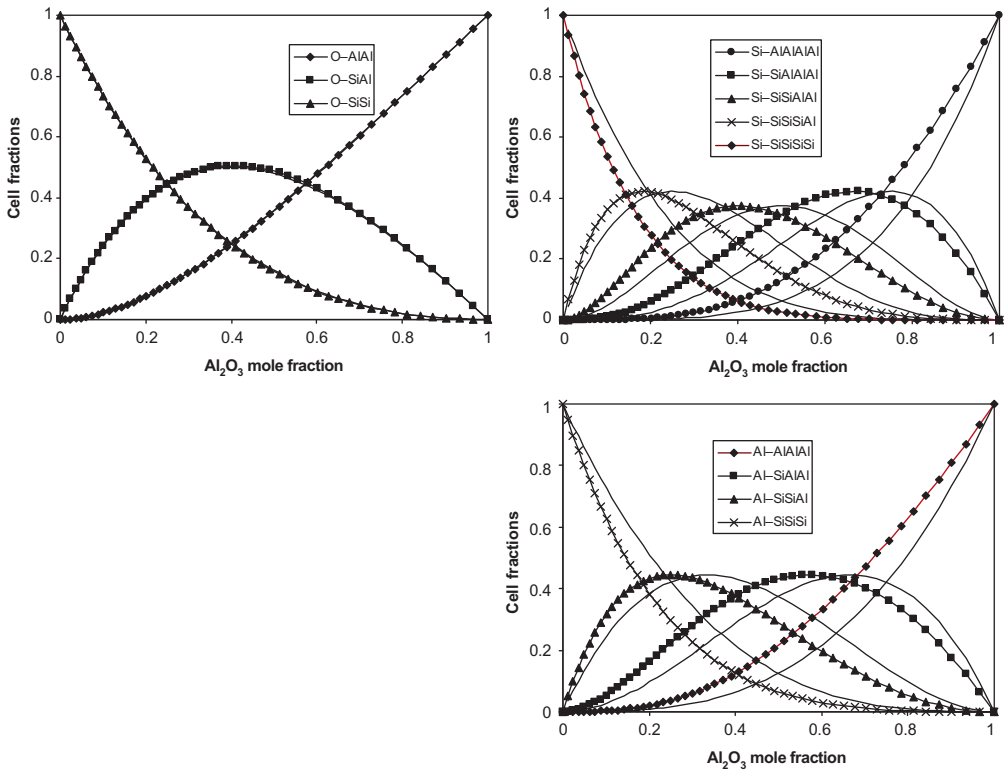


Figure 5.1.15 Cell fractions in the binary Al_2O_3–SiO_2 at 1873 K calculated with the GCA model. The light lines figure a random distribution.

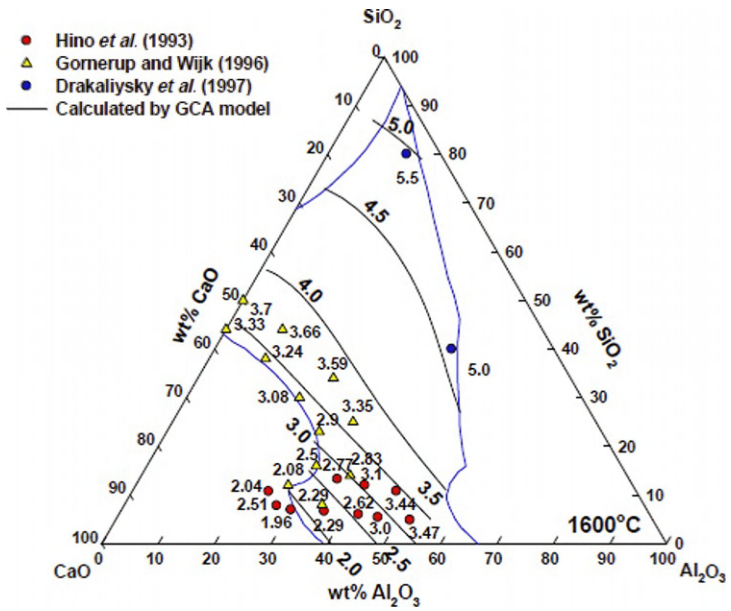


Figure 5.1.16 Comparison between experimental values of sulfide capacities ($-\log C_S$) and values calculated with the GCA model for the system Al_2O_3–CaO–SiO_2 at 1873 K.

Figure 5.1.16 gives another example of the quality of the predictions delivered by the GCA model for the sulfide capacities for the Al_2O_3–CaO–SiO_2 system at 1873 K.

5.1.8. THE MODIFIED QUASICHEMICAL MODEL

The Modified Quasichemical Model for short-range ordering has been developed by Pelton and Blander [103,104].

For a binary system, consider the formation of two 1–2 pair bonds from a 1–1 and a 2–2 pair:

$$(1-1)+(2-2)=2(1-2) \tag{5.1.108}$$

Let the molar Gibbs energy change for this reaction be $\Delta g_{12}=(\omega-\eta T)$. Let the coordination numbers of 1 and 2 atoms or molecules be Z_1 and Z_2. The total number of bonds emanating from an i atom, ion or molecule is Z_iX_i. Hence, mass balance equations can be written as

$$\begin{aligned} Z_1X_1 &= 2n_{11}+n_{12} \quad Z_2X_2 = 2n_{22}+n_{12} \\ Z_1X_1 &= 2n_{11}+n_{12} \quad Z_2X_2 = 2n_{22}+n_{12} \end{aligned} \tag{5.1.109}$$

where n_{ij} is the number of i–j bonds in 1 mol of solution. Equivalent fractions may be defined as

$$Y_1 = 1 - Y_2 = \frac{Z_1 X_1}{Z_1 X_1 + Z_2 X_2} \tag{5.1.110}$$

where the total number of pairs in 1 mol of solution is $(Z_1 X_1 + Z_2 X_2)/2$. Letting X_{ij} be the fraction of i–j pairs in solution, Equation (5.1.109) may be written as

$$2Y_1 = 2X_{11} + X_{12} \quad 2Y_2 = 2X_{22} + X_{12} \tag{5.1.111}$$

The molar enthalpy and excess entropy of mixing are assumed to be directly related to the number of 1–2 pairs:

$$\Delta H - TS^{\text{non-conf}} = (Z_1 X_1 + Z_2 X_2) X_{12} (\omega - \eta T)/4 \tag{5.1.112}$$

An approximate expression for the configurational entropy of mixing is given by a one-dimensional Ising model:

$$\begin{aligned} \Delta S^{\text{conf}} = &-R(X_1 \ln X_1 + X_2 \ln X_2) - \frac{R}{2}(Z_1 X_1 + Z_2 X_2) \\ &\left[X_{11} \ln\left(X_{11}/Y_1^2\right) + X_{22} \ln\left(X_{22}/Y_2^2\right) + X_{12} \ln\left(X_{12}/2Y_1 Y_2\right)\right] \end{aligned} \tag{5.1.113}$$

Thus, the Gibbs energy of solution can be written as:

$$G^m = \left(g_1^{\circ} X_1 + g_2^{\circ} X_2\right) + \Delta H - TS^{\text{non-conf}} - T\Delta S^{\text{conf}} \tag{5.1.114}$$

The equilibrium distribution is calculated by minimizing G^m with respect to X_{12} at constant composition. This results in a quasichemical equilibrium constant for reaction (5.1.108):

$$\frac{X_{12}^2}{X_{11} X_{22}} = 4 \exp\left(-\frac{\Delta g_{12}}{RT}\right) \tag{5.1.115}$$

When $\Delta g_{12} = 0$ the solution of Equations (5.1.110) and (5.1.111) gives a random distribution with $X_{11} = Y_1^2$, $X_{22} = Y_2^2$, and $X_{12} = 2Y_1 Y_2$, and Equation (5.1.113) reduces to the ideal Raoultian entropy of mixing. When Δg_{12} becomes very negative, 1–2 pairs predominate and the plot of $\Delta H - TS^{\text{non-conf}}$ versus composition becomes V-shaped and ΔS^{conf} becomes m-shaped with minima at $Y_1 = Y_2 = 1/2$. When Δg_{12} is positive, (1–1) and (2–2) pairs predominate. The quasichemical model can thus also treat such clustering that accompanies positive deviations from ideality. The Δg_{12} parameter is usually expanded as a polynomial in the equivalent fractions.

$$\Delta g_{12} = \Delta g_{12}^{\circ} + \sum \Delta g_{12}^{ij} Y_1^i Y_2^j \tag{5.1.116}$$

Recently, the model has been extended more flexibly by Pelton *et al.* [105] and Pelton and Chartrand [106]. The main changes are:

(i) The excess model parameter can be expressed by bond fraction rather than equivalent fraction: $\Delta g_{12} = \Delta g^{o}_{12} + \sum \Delta g^{i0}_{12} X^{i}_{11} + \sum \Delta g^{0j}_{12} X^{j}_{22}$

(ii) Coordination number can be changed for each binary system to reproduce the short range ordering of each binary solution more correctly.

The Modified Quasichemical Model has been applied to the molten slag phase since 1984. In a binary silicate melt, MO_x–SiO_2 (M = Ca, Mg, Na, Fe, Mn, etc.), the tendency to short-range ordering can be identified with the tendency to form SiO_4^{4-} ions, or with the break-up of the silicate network and the resultant formation of second-nearest-neighbor M–Si pairs. At the orthosilicate composition, $M_{2/x}SiO_4$, a completely ordered solution can be considered to consist of only M^{2x+} cations and SiO_4^{4-} anions. This is equivalent to saying that there are only M–Si pairs and no M–M or Si–Si pairs. An Si–Si pair can be considered to be joined by a doubly-bonded (bridged) oxygen and an M–M pair is a pair of cations separated by an O^{2-} ion. Hence the quasichemical reaction is applied for second-nearest-neighbor pairs:

$$(\mathrm{M}-\mathrm{M})+(\mathrm{Si}-\mathrm{Si})=2(\mathrm{M}-\mathrm{Si}):\Delta g_{\mathrm{MSi}} \tag{5.1.117}$$

and this is identical to the well-known equilibrium between free, broken (singly-bonded), and bridged (doubly-bonded) oxygens:

$$\left(\mathrm{M}-\mathrm{O}^{2-}-\mathrm{M}\right)+\left(\mathrm{Si}-\mathrm{O}^{0}-\mathrm{Si}\right)=2(\mathrm{A}-\mathrm{O}^{-}-\mathrm{Si}) \tag{5.1.118}$$

$$\mathrm{O}^{2-}+\mathrm{O}^{0}=2\mathrm{O}^{-} \tag{5.1.119}$$

For optimizing a given binary MO_x–SiO_2 system, the model parameters of the Gibbs energy of the quasichemical reaction, Δg_{MSi} are optimized, using a minimum number of parameters, in order to reproduce all reliable phase diagram data and thermodynamic data in the system.

Due to the coordination numbers Z_{M} and Z_{Si}, the maximum second-nearest neighbor ordering of the M–Si can occur at $x_{\mathrm{SiO_2}} = Z_{\mathrm{M}}/(Z_{\mathrm{M}} + Z_{\mathrm{Si}})$. For example, the maximum ordering for the CaO–SiO_2 slag occurs at the Ca_2SiO_4 composition. The very negative Δg_{CaSi} results in $x_{\mathrm{CaSi}} \approx 1$ near $x_{\mathrm{SiO_2}} = 1/3$, and virtually all Ca atoms have Si atoms as second-nearest neighbors and *vice versa*; that is, the calculated structure of the melt is equivalent to $Ca_2^{2+}SiO_4^{4-}$. Although the relative value of coordination numbers of M^{2+} and Si^{4+} in the silicate melts is $Z_{\mathrm{M}}/Z_{\mathrm{Si}} = 1/2$ which reflects the silicate network structure, the actual values of Z_{M} (1.3774) and Z_{Si} (2.7548) used in the model are not exactly reflecting the network structure. Thus, the coordination number in the MQM is to some extent arbitrary.

The thermodynamic properties of ternary solutions can be calculated using a proper interpolation technique from binary model parameters, Δg_{MSi}. Depending on the

chemistry of the given ternary system, different kind of interpolation techniques can be applied [107]. For example, the thermodynamic properties of the $CaO–MgO–SiO_2$ solution [108] can be well calculated using the Toop-like interpolation technique with SiO_2 as an asymmetric component. In the case of $CaO–Al_2O_3–SiO_2$ alumino-silicate system, either the Kohler or the Toop-like interpolation technique can be used (in fact, the MQM uses the Toop-like interpolation technique for ternary alumino-silicate melts with SiO_2 as an asymmetric component [109]). The Kohler type of interpolation technique is used for ternary solutions like CaO–MgO–FeO [37]. Because the MQM permits a flexible choice of interpolation techniques for any given ternary systems, high predictive ability can be obtained in the multicomponent systems. Many binary, ternary, and multicomponent slags [37–43,108–129] have been successfully modeled with the MQM.

As the Modified Quasichemical Model is based on the slag structure, the slag structure can be back-calculated from the model with optimized model parameters. For example, as can be seen in Figure 5.1.17, the compositions of free oxygen, broken oxygen bridges, and bridged oxygens calculated from the Quasichemical model are in good agreement with the experimental data from XPS of Park and Rhee [130]. The calculated trend of the fractions of the broken oxygen bridges for various binary silicate systems is also quite reasonable from the viewpoint of the basicity of basic oxides. These oxygen bond concentrations are used for the calculation of the concentrations of structural units for our new structural viscosity model of FactSage system. In summary, the thermodynamic model used for the molten oxide phase, in the present study, the Modified Quasichemical Model, adequately represents the actual structure of liquid slags and also has very high predictive ability for multicomponent systems.

Recently, the two-sublattice MQM [131,132] has been developed with quadruplet approximation. The previously optimized model parameters for oxide melts can be easily included in the two-sublattice MQM without losing any accuracy. The two-sublattice model has been successfully applied to molten slag containing sulfur [133] and fluorine [134]. This model has been widely used for molten salts containing different cations and anions.

5.1.9. MODIFIED QUASICHEMICAL MODEL FOR MATTE

Liquid metal-sulfide solutions exhibit a high degree of short-range ordering resulting from the fact that metal–sulfur nearest-neighbor pairs are energetically favored over metal–metal and sulfur–sulfur pairs. In particular, in the systems iron–sulfur, at compositions around 50 mol% sulfur, this strong ordering results in a change of sulfur potential several orders of magnitude over a narrow composition range, with an inflection point near 50 mol% sulfur. Simple empirical expansions of the excess thermodynamic properties as polynomials in the component mole fractions, as are often used to describe

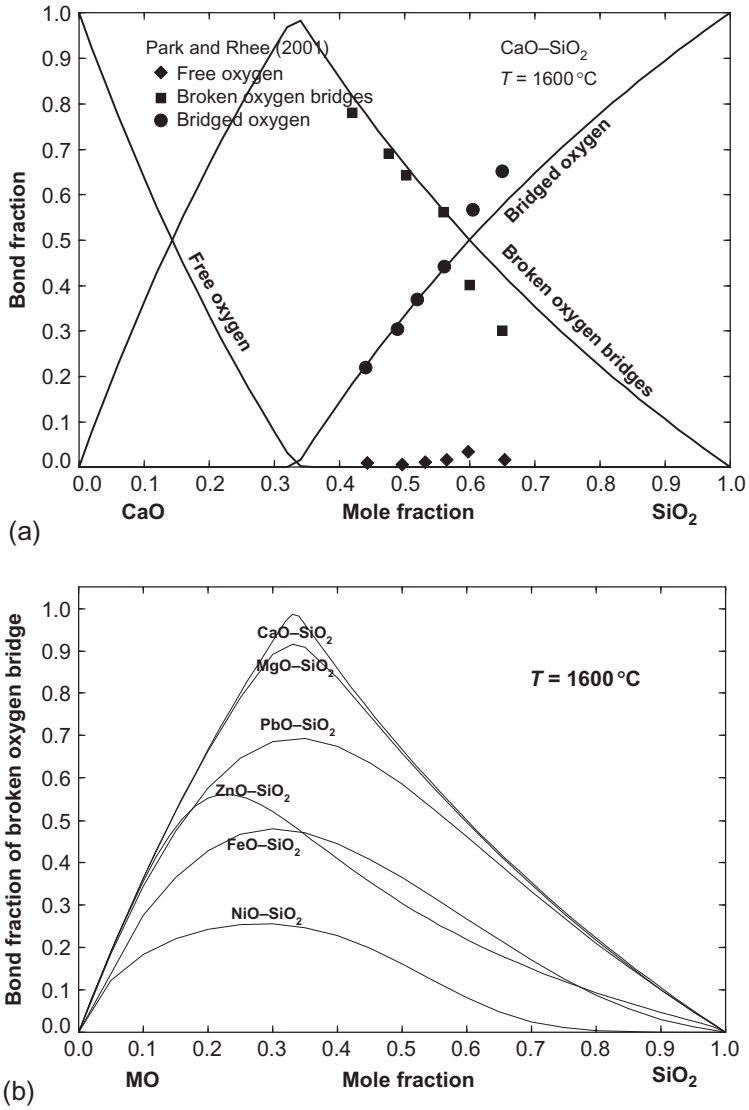


Figure 5.1.17 Calculated structural data from modified Quasichemical model parameters. (a) Comparison of calculated bond fractions of O^{2-}, O^{-} and O^{0} for the $CaO–SiO_2$ system with experimental data of Park and Rhee [130], and (b) calculated bond fractions of O^{-} for various binary silicate systems at 1600 °C.

molten alloys, do not provide an adequate description for liquid sulfide solutions. "Associate models" that assume the existence of molecular-like species are better than simple polynomial models and can correctly describe the observed curves of sulfur partial pressure versus composition in binary metal–sulfur systems. However, because such models

are not physically realistic, they do not give good predictions of the properties of ternary and multicomponent solutions from the optimized binary parameters, and generally require several empirical ternary and quaternary model parameters in order to reproduce the properties of multicomponent solutions. The Modified Quasichemical Model [103–106] used in the present study gives a more realistic description of short-range ordering in liquid metal–sulfur solutions. The details of the Modified Quasichemical Model are already discussed in the section for molten slag. In this section, the brief discussion on the model for ternary Fe–Ni–S system will be introduced as an example.

First, consider the binary Fe–S liquid solution. The atoms Fe and S are distributed over the sites of a quasi-lattice. The following pair exchange reaction is considered:

$$(\mathrm{Fe}-\mathrm{Fe})+(\mathrm{S}-\mathrm{S})=2(\mathrm{Fe}-\mathrm{S}) \tag{5.1.120}$$

where (Fe–S) represents a first-nearest-neighbor pair. The non-configurational Gibbs energy change for the formation of two moles of (Fe–S) pairs according to reaction (Equation 5.1.120) is Δg_{FeS}. The analytical description of the Gibbs-energy is given by:

$$G=\left(n_{\mathrm{Fe}}G^{\circ}_{\mathrm{Fe}}+n_{\mathrm{S}}G^{\circ}_{\mathrm{S}}\right)-T\Delta S^{\mathrm{config}}+(n_{\mathrm{FeS}}/2)\Delta g_{\mathrm{FeS}} \tag{5.1.121}$$

where G°_{Fe} and G°_{S} are the molar Gibbs energies of the pure components, $\Delta S^{\mathrm{config}}$ is the configurational entropy of mixing given by a random distribution of the (Fe–Fe), (S–S) and (Fe–S) pairs in the one-dimensional Ising approximation, n_{Fe} and n_{S} are the numbers of moles of iron and sulfur atoms, and n_{FeS} is the number of moles of iron–sulfur pairs.

Because the model parameter Δg_{FeS} is negative, reaction (Equation 5.1.120) is displaced to the right, with (Fe–S) pairs being favored. The "equilibrium constant" of this "quasichemical reaction" (Equation 5.1.120) becomes larger as Δg_{FeS} becomes more negative. At 50 mol% sulfur, the melt contains mainly (Fe–S) pairs. At sulfur contents below 50 mol%, the melt contains principally (Fe–S) and (Fe–Fe) pairs. Δg_{FeS} is expanded as a polynomial in terms of the pair fractions $X_{\mathrm{FeFe}}=n_{\mathrm{FeFe}}/(n_{\mathrm{FeFe}}+n_{\mathrm{SS}}+n_{\mathrm{FeS}})$ and $X_{\mathrm{SS}}=n_{\mathrm{SS}}/(n_{\mathrm{FeFe}}+n_{\mathrm{SS}}+n_{\mathrm{FeS}})$, where n_{FeFe}, n_{SS}, and n_{FeS} are the numbers of moles of each kind of pairs, as follows:

$$\Delta g_{\mathrm{FeS}}=\Delta g^{\circ}_{\mathrm{FeS}}+\sum_{i\geq 1} g^{i0}_{\mathrm{FeS}}X^{i}_{\mathrm{FeFe}}+\sum_{j\geq 1} g^{0j}_{\mathrm{FeS}}X^{j}_{\mathrm{SS}} \tag{5.1.122}$$

where $\Delta g^{\circ}_{\mathrm{FeS}}$, g^{i0}_{FeS}, and g^{0j}_{FeS} are the adjustable model parameters, which can be functions of temperature. Since the Fe-rich melts (with less than 50 mol% S) contain mainly (Fe–Fe) and (Fe–S) pairs, X_{SS} is small in this composition range, and so the parameters g^{0j}_{FeS} have little influence. Similarly, in melts containing over 50 mol% S, X_{FeFe} is small, and the parameters g^{i0}_{FeS} have little influence. Hence, the two composition regions can be modeled nearly independently. As a result, all model parameters affected the entire

composition range, thereby making it more difficult to obtain a satisfactory optimization, as well as generally necessitating a larger number of parameters.

The second change to the original Modified Quasichemical Model is that the "coordination numbers" of iron and sulfur, Z_{Fe} and Z_S, can now vary with composition as follows:

$$\frac{1}{Z_{Fe}} = \frac{1}{Z_{FeFe}}\left(\frac{2n_{FeFe}}{2n_{FeFe}+n_{FeS}}\right) + \frac{1}{Z_{FeS}}\left(\frac{n_{FeS}}{2n_{FeFe}+n_{FeS}}\right) \tag{5.1.123}$$

$$\frac{1}{Z_S} = \frac{1}{Z_{SS}}\left(\frac{2n_{SS}}{2n_{SS}+n_{FeS}}\right) + \frac{1}{Z_{SFe}}\left(\frac{n_{FeS}}{2n_{SS}+n_{FeS}}\right) \tag{5.1.124}$$

where Z_{FeFe} is the value of Z_{Fe} when all nearest neighbors of an iron atom are iron atoms, and Z_{FeS} is the value of Z_{Fe} when all nearest neighbors are sulfur atoms. Z_{SS} and Z_{SFe} are defined in an analogous manner. The composition of maximum short-range ordering is thus determined by the ratio (Z_{FeS}/Z_{SFe}) which, in the present case, is set at 1/1. Values of the binary coordination numbers Z_{FeS} and Z_{SFe} are unique to the iron–sulfur binary system, while the values of the unary coordination numbers Z_{FeFe} and Z_{SS} are common to all systems containing iron or sulfur as a component. This gives greater flexibility in treating multicomponent solutions compared to the previous version of the model [103,104] in which Z_{FeS} and Z_{SFe} were necessarily equal to Z_{FeFe} and Z_{SS}, respectively.

Since the composition of maximum short-range ordering is at 50 mol% sulfur, the binary "coordination numbers" Z_{FeS} and Z_{SFe} are set equal to each other. It was found that a value of two for the binary coordination numbers Z_{FeS} and Z_{SFe} and a value of six for the unary coordination numbers Z_{SS} and Z_{FeFe} give the best optimization results. The "non-physical" character of the coordination numbers results from the use of the one-dimensional Ising approximation for the configurational entropy.

An identical model applies to the binary liquid Ni–S phase to obtain the optimized model parameters. For molten binary Fe–Ni solutions, short-range ordering is negligible, and a random-mixing approximation of the molar Gibbs energy is used, with:

$$G = X_{Fe}G^{o}_{Fe} + X_{Ni}G^{o}_{Ni} + RT(X_{Fe}\ln X_{Fe} + X_{Ni}\ln X_{Ni}) + G^{ex} \tag{5.1.125}$$

where G^o_i and X_i are the molar Gibbs energies and mole fractions of Fe and Ni, and the excess Gibbs energy, G^{ex}, is expanded as:

$$G^{ex} = X_{Fe}X_{Ni}\sum_{n\geq 0}{}^{n}L_{(Fe,Ni)}(X_{Fe}-X_{Ni})^n \tag{5.1.126}$$

The Gibbs energy of the ternary Fe–Ni–S liquid phase is estimated using the ternary interpolation technique [107] from the binary parameters. In the M–N–S systems where M and N are metallic elements, the Toop-like interpolation technique with S as asymmetric component can provide good estimation of the Gibbs energy for

the ternary system. If this interpolation technique is used, the Gibbs energy, Δg_{FeS}, of forming (Fe–S) pairs according to reaction (Equation 5.1.120) is given in the ternary system by:

$$\Delta g_{FeS} = \Delta g^{0}_{FeS} + \sum_{i\geq 1} g^{i0}_{FeS}(X_{FeFe} + X_{NiNi} + X_{FeNi})^{i} + \sum_{j\geq 1} g^{0j}_{FeS} X^{j}_{SS} \tag{5.1.127}$$

Equation (5.1.127) reduces to Equation (5.1.122) in the Fe–S binary system. A similar equation can be written for the energy, Δg_{NiS}, of forming Ni–S pairs.

In the ternary system, Equation (5.1.126) for the Fe–Ni interactions becomes:

$$G^{ex} = X_{Fe}X_{Ni}\sum_{n\geq 0} {}^{n}L_{(Fe,Ni)}\left(\frac{X_{Fe} - X_{Ni}}{X_{Fe} + X_{Ni}}\right)^{n} \tag{5.1.128}$$

That is, the Fe–Ni interaction energies are assumed to remain constant along lines of constant X_{Fe}/X_{Ni} ratio.

An important new feature of the extended Modified Quasichemical Model for multicomponent solutions [106] is this ability to combine, in one multicomponent solution, binary solutions that have been modeled with the quasichemical model with others that have been modeled using the random mixing approximation.

Finally, in order to reproduce the available data for the ternary system within the experimental error limits, empirical "ternary terms" of the form

$$g^{ijk}_{FeS(Ni)}(X_{FeFe} + X_{NiNi} + X_{FeNi})^{i} X^{j}_{SS}(X_{Ni}/(X_{Fe} + X_{Ni}))^{k} \tag{5.1.129}$$

can be added to Equation (5.1.127). These give the effect of added nickel upon the energy of forming (Fe–S) pairs. Similarly, terms involving ternary parameters $g^{ijk}_{NiS(Fe)}$ can be added to the expansion for Δg_{NiS}. Finally, ternary terms of the form:

$$g^{ijk}_{FeNi(S)}\left(\frac{X_{Fe}}{X_{Fe} + X_{Ni}}\right)^{i}\left(\frac{X_{Ni}}{X_{Fe} + X_{Ni}}\right)^{j} X^{k}_{S} \tag{5.1.130}$$

can be added to account for the influence of sulfur on the Fe–Ni interaction energy.

The Modified Quasichemical Model has been used for the description of matte for S–Cu–Fe–Ni–Co–Pb–Zn–As and S–Cu–Fe–Ni–Co–Cr–Mn systems. The examples of the thermodynamic modeling can be found elsewhere [135–141].

5.1.10. THERMODYNAMIC PACKAGES AND DATABASES

There are several commercial thermodynamic software with their own critically evaluated/optimized thermodynamic databases of gases species, stoichiometric solids, and solid and liquid solution phases such as oxides, sulfides, salts, alloys, etc. Many of

these software can perform the multi-component equilibrium calculations with several doses of components and also provide the phase diagram calculations for multicomponent systems. A brief summary of several commercially available thermodynamic software in particular for pyrometallurgical applications is provided in Table 5.1.5. CEQCSI (Chemical Equilibrium Calculation for the Steel Industry) is a non-commercial software, which was originally developed at IRSID, France, and has been developed continuously in ArcelorMittal Maizières, France for their internal usage.

Table 5.1.5 Summary of Thermodynamic Databases Relevant to Pyrometallurgical Applications Available in Commercial Software

Software	Databases and Thermodynamic Model/Calculation Modules
FactSage	FTOxid Slag containg limited concentrations of S, H, C, N and F (MQM) Ceramic solutions (CEF) FTmisc Dilute solution: FeLq, CuLq, SnLq, PbLq, AlMgLq, etc., (UIPF, asscociate model) Matte (MQM) FTOxCN Slag for reciprocal oxycarbonitride (MQM) Ceramic solutions (CEF) FTSalt Molten Salts of halide–chloride containing limited range of oxide (MQM) Solid salt solutions (CEF) FTHall Molten cryolite solution for Al Hall–Héroult process (MQM) Solid solution (CEF) User-friendly interface for equilibrium and phase diagram calculations
MPE	Slag containing limited concentration of S (cell model/GCA) Cermaic solution (CEF) Matte Liquid Fe (CEF), liquid Cu (CEF) User-friendly interface for equilibrium calculation
MTDATA	NPLOX Slag containing limited concentrations of H, S, and C (associate model) Ceramic solutions (CEF) MTFEDLSL Liquid Fe (UIPF) User-friendly interface for equilibrium and phase diagram calculations

Continued

Table 5.1.5 Summary of Thermodynamic Databases Relevant to Pyrometallurgical Applications Available in Commercial Software—cont'd

Software	Databases and Thermodynamic Model/Calculation Modules
Thermo-Calc	SLAG Slag containing limited concentrations of S and F (cell model) Ceramic solutions (CEF) Liquid Fe (modified regular solution model; CEF) TCOX Slag (reciprocal ionic solution model) Ceramic solutions (CEF) User-friendly interface for equilibrium and phase diagram calculations

MQM, modified Quasichemical model; CEF, compound energy formalism; UIPF, unified interaction parameter formalism; GCA, general central atom model.

5.1.10.1. FactSage (www.factsage.com)

FactSage [142] is a commercially available software, which was introduced in 2001 as the fusion of the F*A*C*T/FACT-Win (Thermfact, Canada) and ChemSage (GTT-Technology, Germany) thermochemical packages. This software can perform complex equilibrium calculations with up to 32 elements, 40 non-ideal solution phases, and over 1500 stoichiometric compounds simultaneously. FACT thermodynamic database has been developed for pyrometallurgial applications since 1976 and it was largely expanded toward alloy design and other areas since 2001.

5.1.10.1.1 Databases for Slags/Oxides for Pyrometallurgical Applications

FactSage has thermodynamic databases for various pyrometallurgical applications including iron/steelmaking, Cu/Ni smelting, Pb/Zn production, Al smelting, glassmaking, cement, combustion, etc.

5.1.10.1.1.1 FToxid

The FACT oxide solution database (FToxid) contains consistently assessed and critically evaluated thermodynamic data for the molten slag phase, numerous extensive ceramic solid solution phases and all available stoichiometric compounds containing SiO_2–CaO–MgO–Al_2O_3–FeO–Fe_2O_3–MnO–TiO_2–Ti_2O_3–CrO–Cr_2O_3–ZrO_2–NiO–CoO–Na_2O–K_2O–B_2O_3–Cu_2O–As_2O_3–GeO_2–PbO–SnO–ZnO. The core Al_2O_3–CaO–FeO–Fe_2O_3–MgO–SiO_2 system has been fully optimized from 25 °C to above the liquidus temperatures at all compositions and oxygen partial pressures. Components like B_2O_3, K_2O, Na_2O, CoO, CrO, Cr_2O_3, Cu_2O, MnO, NiO, PbO, SnO, TiO_2, Ti_2O_3, ZnO, and ZrO_2 were added to this core six-component system and the relevant subsystems were optimized over the composition ranges important for industrial applications. The molten slag phase is described using the

Modified Quasichemical Model (MQM) [103–106,131,132]. The dilute solubilities of gaseous species such as F, S, SO_4, PO_4, H_2O, OH, C, CO_3, CN, Cl, and I are also modeled using the Blander–Reddy Model [143–146]. Recently, the composition of S in molten oxide slag has been extended up to pure sulfide using new two-sublattice MQM [133]. The same approach is applied to other gaseous species like F [134]. The extensive solid solutions such as spinel, olivine, melilite, monoxide, perovskite, wollastonite, etc., are modeled in the framework of the CEF [34], taking into account the crystal structure of each solution. Over 50 solid oxide solutions are available in FToxid database.

Viscosity database [147–149] for multicomponent molten slags containing entire the composition range of SiO_2–CaO–MgO–Na_2O–K_2O–Al_2O_3–FeO–Fe_2O_3–MnO–NiO–CoO–PbO–ZnO–TiO_2–Ti_2O_3–B_2O_3–CaF_2 system is also available.

5.1.10.1.1.2 FTmisc

FTmisc database contains various solution thermodynamic databases for pyrometallurugical applications covering matte solution, dilute metallic liquid solutions such as FeLq, CuLq, PbLq, SnLq, and AlMgLq, aqueous solution, etc.

The Matte database (MATT) covers liquid S–Cu–Fe–Ni–Co–Pb–Zn–As sulfide system important for nonferrous extractive metallurgy. This database can be selected with other databases mainly for matte/slag/metal/speiss equilibrium calculations involved in Cu-, Pb-, and Zn-smelting and processing. Recently, new Matte database (MAT2) covering entire range of S–Cu–Fe–Ni–Co–Cr–Mn system (from metal to sulfur and all solid stoichiometric sulfides and solutions) has been added. This new database can be particularly useful for calculating metal/liquid sulfide/solid sulfide/gas equilibria related to steelmaking (hot corrosion and sulfide inclusion formation), recycling of matte, etc. Both matte solutions were modeled with Modified Quasichemical Model to describe the strong short-range-ordering in liquid sulfide solution. The solid sulfide solutions were described with the CEF.

Dilute metallic liquid solutions are prepared for the pyrometallurgical extractive and refining process. All the solutions were modeled using the Unified Interaction Paramater Formalism (UIPF) [16–18]. The liquid Fe solution (FeLq) database was developed based on the well-known interaction parameters recommended by the JSPS [15]. This database covers 30 dilute elements in liquid Fe solution (Fe–Ag–Al–B–C–Ca–Ce–Co–Cr–Cu–H–La–Mg–Mn–Mo–N–Nb–Ni–O–P–Pb–Pd–S–Si–Sn–Ta–Ti–U–V–W–Zr). The deoxidation behaviors of Fe–M–O (M = Ca, Mg, Ba, Al, Ti, Cr, V, Mn, Si, B, C, Ce, Nb, Zr, etc.) systems are described by the Associate Model [30] in order to more accurately describe deoxidation phenomena in liquid steel and to have high predictive ability for the deoxidation in multicomponent systems. FactSage also provides a dedicated steel database (FSStel), which is an updated version of the SGTE solution database [150] and is similar to TCFE database in Thermo-Calc. Liquid Cu solution also for

speiss (CuLq) covers the minor impurity elements of liquid Cu during Cu smelting process, Cu–Pb–Zn–As–Fe–Ni–Au–S–O. Liquid Pb solution (PbLq) contains Ag–As–Au–Bi–Cu–Fe–Na–O–S–Sb–Sn–Zn for Pb smelting and purification process. Liquid Sn (SnLq) contains Al–Ca–Ce–Co–Cr–Cu–Fe–H–Mg–Mo–Na–Ni–O–P–S–Se–Si–Ti in dilute solution. Liquid alloy liquid solution mainly for liquid Al and Mg alloy process covers Al–Mg–Sr–Ca–Mn–Na–K–Be–Si with dilute C–O–Cl–F–Fe.

Aqueous solution database (Pitz) contains Pitzer parameters for non-ideal aqueous solution of 96 solutes only accurate around room pressure and temperature. More extensive aqueous solution database (FThelg) contains infinite dilution properties for over 1400 aqueous solute species taken from the GEOPIG-SUPCRT Helgeson public database. These incorporate the Helgeson equation of state for temperatures up to 350 °C and pressures up to 165 bar. The aqueous solution can be also generally valid up to 0.5 molal concentration by incorporating the extended Debye–Huckel (Davies) equation.

5.1.10.1.1.3 Other Databases

FTsalt database contains liquid and solid salts covering a wide range of chloride, halide, and mixtures, which are useful for light alloy-refining processes. FTOxCN database is new oxycarbonitride database for Al–Si–Ca–Mg–Fe–C–O–N system important for ceramic refractories and the Al carbo-thermic reduction process. The FThall database has been developed for thermodynamic and phase equilibrium calculations involving liquid Al/cryolitic bath/Al_2O_3-based oxides in alumina reduction electrolysis cells (Hall–Héroult process), and for molten aluminum treatment with fluoride fluxes.

5.1.10.1.2 Databases for Other Applications

There are accurate thermodynamic data available for many different types of materials such as various steels/Fe-alloys, Al-, Mg-, Cu-, Pb-, high purity Si-, noble metal-based alloys, solder alloys, nuclear materials, etc. The liquid solution in each alloy database can also be used for the pyrometallurgical process calculations.

5.1.10.2. MPE (www.csiro.au)

MPE (Multicomponent Phase Equilibria) package [151,152] is a commercially available thermodynamic package developed by the CSIRO, Australia. The package has been developed for applications related to ferrous and non-ferrous pyrometallurgical processes.

5.1.10.2.1 Databases for Slags/Oxides for Pyrometallurgical Applications

The MPE oxide database contains consistently accessed binary and ternary thermodynamic parameters for molten slags, extensive solid solutions, and stoichiometric solids containing SiO_2–P_2O_5–TiO_2–Ti_2O_3–Al_2O_3–Cr_2O_3–Fe_2O_3–FeO–CaO–MgO–CrO–NiO–MnO. The thermodynamic properties of molten slag are described by the Cell Model [153] like CEQCSI, although MPE database has been developed separately.

Extensive solid solutions such as halite, spinel, corundum, olivine, melilite, pyroxene, pseudo-brookite are also available to describe the oxide phase diagram accurately. The limited solubility of S in molten slag can be also calculated. Recently the database for molten slags of the SiO_2–Al_2O_3–Fe_2O_3–FeO–MnO–MgO–CaO–Na_2O–K_2O system is being developed based on the GCA (General Central Atom) Model in collaboration with CEQCSI group [154]. Viscosity database [155–157] for multicomponent slags containing SiO_2–CaO–MgO–Al_2O_3–FeO–Fe_2O_3–MnO–NiO–CoO–PbO–ZnO–TiO_2–Ti_2O_3–Cu_2O is available.

The liquid Fe solution database covering Fe–Al–C–Ca–Cr–H–Mg–Mn–N–Ni–P–O–S–Si–Ti is available in the MPE package. The liquid database is modeled based on the random mixing Bragg–Williams Redlich–Kister model and the database is accurate for dilute concentrations of all elements except Mn, Ni, and C, which can be accurately modeled up to a high concentration range.

For Cu-smelting process, matte database covering Fe–Cu–Ni–Co–Cr–S and liquid Cu containing O and S are available.

5.1.10.3. MTDATA (www.npl.co.uk)

MTDATA [158] is a commercially available thermodynamic package developed by the National Physical Laboratory (NPL), UK. The software can perform complex equilibrium calculations with up to 30 different components and 500 phases simultaneously.

5.1.10.3.1 Databases for Slags/Oxides for Pyrometallurgical Applications

5.1.10.3.1.1 NPLOX

The oxide database (NPLOX) in MTDATA includes liquid oxide, solid solutions, and stoichiometric compounds within the K_2O–Na_2O–CaO–MgO–FeO–Fe_2O_3–Al_2O_3–SiO_2–Cu_2O–S system with additions of B_2O_3, CaF_2, CoO, CrO, Cr_2O_3, Li_2O, Nb_2O_5, NiO, MnO, P_2O_5, PbO, V_2O_5, ZnO and ZrO_2. Dilute solutions of OH^-, SO_4^{4-} and CO_3^{2-} are also modeled for selected liquid oxide systems. The Associate Model is used for the liquid oxide phase, and the extensive solid solutions such as spinel, olivine, melilite, monoxide, perovskite, wollastonite, etc., are modeled in the framework of the CEF [34]. Calculations of volume [159] and density changes in the CaO–MgO–FeO–Fe_2O_3–Al_2O_3–SiO_2 system are possible.

5.1.10.3.1.2 MTFEDLSL

The dilute liquid Fe solution database (MTFEDLSL) contains 26 elements in liquid Fe (Fe–Ag–Al–B–C–Ca–Co–Cr–Cu–H–Mg–Mn–Mo–N–Nb–Ni–O–P–Pb–S–Si–Sn–Ti–U–V–W–Zr), which is described by the UIPF [16–18] with accessed interaction parameters. TCFE liquid and solid steel database developed by Thermo-Calc group can also be used for high alloyed steel calculations.

5.1.10.3.2 Databases for Other Applications

There are accurate thermodynamic data available for many different types of materials such as various steels/Fe-alloys, Al, salts, aqueous solution, solder, semiconductors, and cements.

5.1.10.4. Thermo-Calc (www.thermocalc.com)

Thermo-Calc is a commercially available software package developed at KTH and Thermo-Calc Software, Stockholm, over the past 35 years [49]. Incorporated in Thermo-Calc are numerous models for thermodynamic properties of elements, compounds, solid solution phases, liquid, aqueous solutions, gaseous mixtures, polymers and more. Combining this with a powerful calculation engine and a flexible post-processor, Thermo-Calc is capable of performing different kinds of calculations for an alloy containing up to 40 components.

5.1.10.4.1 Databases for Slags/Oxides for Pyrometallurgical Applications

5.1.10.4.1.1 SLAG3

The SLAG (Fe-containing slag database) database contains a liquid slag phase, an Fe-rich liquid phase (dilute solution), a gaseous mixture phase, and many solid oxide, sulfide, and fluoride phases. Thermodynamic data for the liquid slag phase in the Al_2O_3–CaO–CrO–Cr_2O_3–FeO–Fe_2O_3–MgO–MnO–Na_2O–SiO_2–TiO_2 system were critically assessed by IRSID (1984) and Thermo-Calc Software (since 1997), using the Kapoor–Frohberg–Gaye Quasichemical Cell Model, i.e., the Kapoor–Frohberg Slag Model with the extensions introduced by Gaye and Welfringer [153] for complex multicomponent liquid slag systems. Data for the additional components Sulfur and Fluorine in the liquid slag phase and some S/F-bearing solid slag phases, which were critically assessed by IRSID (1997) and Thermo-Calc Software (since 1997), have been added to the database, and it thus allows calculations of sulfide capacities and many other specific properties within the Al_2O_3–CaO–CrO–Cr_2O_3–FeO–Fe_2O_3–MgO–MnO–Na_2O–SiO_2–TiO_2–S–F system. In this database, all the solid phases are simply treated as pure stoichiometric phases.

Data for a dilute solution of many elements in the Fe-rich liquid phase are critically assessed and converted to regular solution parameters according to Hillert [25], with modified dilute solution parameters in Fe-rich liquid from Sigworth and Elliot [14], so that it becomes a consistent thermodynamic model and also generally improves the agreements of calculated results with available experimental data obtained from steelmaking metallurgical processes. The following 26 components are included in the FE_LIQUID solution phase: Ag–Al–B–C–Ca–Co–Cr–Cu–H–Mg–Mn–Mo–N–Nb–Ni–O–P–Pb–S–Si–Sn–Ti–U–V–W–Zr. For high alloyed steels, the liquid phase from the TCFE (TCS Steels/Fe-Alloys Database) database should be used instead. The TCFE database, containing Al–B–C–Ca–Co–Cr–Cu–Fe–H–Mg–Mn–Mo–N–Nb–Ni–O–P–S–Si–Ta–Ti–V–W–Zr, is specifically applicable for various types of steels/Fe-based

alloys. The TCFE database is based on complete assessments of binary and many ternary systems as well as some critical quaternary systems and is suitable to predict different thermodynamic properties with high accuracy for concentrated solution phases.

The SLAG database (most recent updated slag database is called SLAG3) is suitable and efficient for various equilibrium calculations of activities, phase equilibria, phase diagrams, and many other properties in a wide range of metallurgical slag systems, especially for (but not limited to) steel-making processes. It can be used not only for slag system (liquid slag and solid slag phases) but also for alloy–slag–gas heterogeneous interaction processes.

5.1.10.4.1.2 TCOX

TCOX is Thermo-Calc's own oxide database. TCOX (TCS Metal Oxide Solutions Database) has been developed at KTH and Thermo-Calc Software since 1992. The TCOX database was earlier called ION. TCOX has been developed in a CALPHAD spirit with all of the oxygen-containing binary systems assessed for their full range of composition including all phases, plus all of the O-ternary systems and many other binary and ternary systems as well.

The core Al_2O_3–CaO–Cr–Fe–MgO–Mn–Ni–O–SiO_2 system has been fully optimized from room temperature to above the liquidus temperatures at all compositions [44,50–58]. The liquid metal and slag phase is treated as one phase and described using the ionic two-sublattice liquid model (RILM) [48]. Y_2O_3 and ZrO_2 were added to the core system and relevant subsystems (Al_2O_3–CaO–MgO–SiO_2 + Y_2O_3–ZrO_2) were optimized over the composition ranges important for modeling CMAS-TBC (yttria partially stabilized zirconia) interaction.

There are 106 different phases included in the database. Many oxides are modeled as solution phases (in all cases where it is meaningful). The solid solution phases such as spinel, mullite, corundum, halite, olivine etc., are modeled within the framework of the Compound Energy Formalism.

5.1.10.4.2 Databases for Other Applications

There are accurate thermodynamic data available for many different types of materials such as various steels/Fe-alloys, Ni-, Al-, Mg-, Ti-, Zr-based alloys, solder alloys, semiconductor alloys, nuclear materials, hard materials, ceramics, molten salts, minerals, aqueous solutions, etc., DICTRA is a general software package for simulation of Diffusion Controlled TRAnsformations in multicomponent alloys. DICTRA, coupled with Thermo-Calc and databases, is applied to solve problems such as solidification and micro segregation in steels, carburization and decarburization of steels, austenite/ferrite diffusional transformations in steels, interdiffusion in coating/substrate compounds, and much more.

REFERENCES

[1] http://www.calphad.com.
[2] L. Kaufman, H. Bernstein, Computer Calculation of Phase Diagrams with Special Reference to Refractory Materials, Academic Press, New York, 1970.
[3] W. Gibbs, On the Equilibrium of Heterogeneous Substances, Transactions of the Connecticut Academy of Arts and Sciences, Vol. III, 1878, p. 1875.
[4] J. Hertz, J. Phase Equilib. 13 (1992) 450.
[5] H. Lucas, S. Fries, B. Sundman, Computational Thermodynamics, Cambridge University Press, 2007, p. 313.
[6] R. Schmid-Fetzer, J. Gröbner, Adv. Eng. Mater. 3 (2001) 947.
[7] http://www.sgte.org/.
[8] A. Dinsdale, Calphad 15 (1991) 317.
[9] F. Adlinger, B. Sundman, H.J. Seifert (Eds.), Calphad 19 (1995) 433.
[10] F. Adlinger, B. Sundman, H.J. Seifert (Eds.), Calphad 21 (1997) 139.
[11] F. Adlinger, B. Sundman, H.J. Seifert (Eds.), Calphad 24 (2000) 15.
[12] F. Adlinger, B. Sundman, M. Zinkevich (Eds.), Calphad 31 (2007) 2.
[13] C. Wagner, Thermodynamics of Alloys, Addison-Wesley, Reading, MA, 1962.
[14] G.K. Sigworth, J.F. Elliott, Met. Sci. 8 (1974) 298.
[15] Steelmaking Data Sourcebook, in: JSPS, 19th Committee on Steelmaking, Gordon & Breach Science, New York, NY, 1988.
[16] A.D. Pelton, C.W. Bale, Metall. Trans. A 17A (1986) 1211.
[17] C.W. Bale, A.D. Pelton, Metall. Trans. A 21A (1990) 1997.
[18] A.D. Pelton, Metall. Mater. Trans. B 28B (1997) 869.
[19] Y.E. Lee, ISIJ Int. 43 (2003) 144.
[20] H. Li, A. Morris, Metall. Mater. Trans. B 28B (1997) 553.
[21] M.-C. Heuzey, A.D. Pelton, Metall. Mater. Trans. B 27B (1996) 810.
[22] FactSage. www.factsage.com, Montreal, Canada.
[23] CEQCSI. www.arcelormittal.com, Maizières, France.
[24] MTDATA. www.npl.co.uk, Teddington, UK.
[25] M. Hillert, Metall. Trans. A 17A (1986) 1878.
[26] L.S. Darken, Trans. Metall. Soc. AIME 239 (1967) 80.
[27] T. Miki, M. Hino, ISIJ Int. 45 (2005) 1848.
[28] A. Hayashi, T. Uenishi, H. Kandori, T. Miki, M. Hino, ISIJ Int. 48 (2008) 1533.
[29] S.-H. Seok, T. Miki, M. Hino, ISIJ Int. 49 (2009) 804.
[30] I.-H. Jung, S.A. Decterov, A.D. Pelton, Metall. Mater. Trans. B 35B (2004) 493.
[31] I.-H. Jung, McGill University, Montreal, QC, Canada, unpublished research.
[32] G.K. Sigworth, J.F. Elliott, Can. Metall. Q. 13 (1974) 455.
[33] G.K. Sigworth, J.F. Elliot, Can. Metall. Q. 15 (1976) 123.
[34] M. Hillert, J. Alloys Compd. 320 (2001) 161.
[35] I.-H. Jung, Ph.D. Thesis, Ecole Polytechnique, Montreal, Canada, 2004.
[36] H.S.C. O'Neill, A. Navrotsky, Am. Mineral. 69 (1984) 733.
[37] S.A. Decterov, I.-H. Jung, E. Jak, Y.-B. Kang, P. Hayes, A.D. Pelton, in: VII Int'l. Conference on Molten Slags, Fluxes and Salts, South African Inst. Mining & Metallurgy Johannesburg, 2004, p. 839.
[38] I.-H. Jung, S.A. Decterov, A.D. Pelton, J. Phase Equilib. Diffus. 25 (2004) 329.
[39] I.-H. Jung, S. Decterov, A.D. Pelton, J. Am. Ceram. Soc. 88 (2005) 1921.
[40] I.-H. Jung, S.A. Decterov, A.D. Pelton, J. Phys. Chem. Solids 65 (2004) 1683.
[41] S.A. Decterov, I.-H. Jung, A.D. Pelton, J. Am. Ceram. Soc. 85 (2002) 2903.
[42] I.-H. Jung, S.A. Decterov, A.D. Pelton, H.-M. Kim, Y.-B. Kang, Acta Mater. 52 (2004) 507.
[43] I.-H. Jung, Solid State Ionics 177 (2006) 765.
[44] B. Hallstedt, J. Am. Ceram. Soc. 75 (1992) 1497.
[45] J.R. Taylor, A.T. Dinsdale, Z. Metallkd. 84 (1993) 335.
[46] J.R. Taylor, A.T. Dinsdale, Z. Metallkd. 81 (1990) 354.
[47] B. Sundman, J. Phase Equilib. 12 (1991) 127.

[48] M. Hillert, B. Jansson, B. Sundman, J. Aagren, Metall. Trans. A 16A (1985) 261.
[49] J.O. Andersson, T. Helander, L. Hoglund, P. Shi, B. Sundman, CALPHAD: Comput. Coupling Phase Diagrams Thermochem. 26 (2002) 273.
[50] W. Huang, M. Hillert, X. Wang, Metall. Mater. Trans. A 26A (1995) 2293.
[51] H. Mao, M. Hillert, M. Selleby, B. Sundman, J. Am. Ceram. Soc. 89 (2006) 298.
[52] H. Mao, O. Fabrichnaya, M. Selleby, B. Sundman, J. Mater. Res. 20 (2005) 975.
[53] M. Selleby, Metall. Mater. Trans. B 28B (1997) 577.
[54] B. Hallstedt, J. Am. Ceram. Soc. 78 (1995) 193.
[55] M. Hillert, B. Sundman, X. Wang, Metall. Trans. B 21B (1990) 303.
[56] M. Hillert, M. Selleby, B. Sundman, Metall. Trans. A 21A (1990) 2759.
[57] B. Hallstedt, J. Am. Ceram. Soc. 73 (1990) 15.
[58] B. Hallstedt, J. Phase Equilib. 14 (1993) 662.
[59] A.D. Pelton, in: VII Int'l. Conference on Molten Slags, Fluxes and Salts, South African Inst. Mining & Metallurgy Johannesburg, 2004, p. 607.
[60] E.A. Guggenheim, Mixtures, Clarendon Press, Oxford, 1952, 270 pp.
[61] M. Hillert, M. Selleby, B. Sundman, Acta Mater. 57 (2009) 5237–5244.
[62] M.L. Kapoor, M.G. Frohberg, in: Chemical Metallurgy of Iron and Steel, Iron and Steel Institute, London, 1973, pp. 17–22.
[63] L. Zhang, S. Sun, S. Jahanshahi, J. Phase Equilib. Diffus. 28 (2007) 121–129.
[64] L. Zhang, S. Jahanshahi, S. Sun, C. Chen, B. Bourke, S. Wright, M. Sommerville, JOM (2002) 51–56.
[65] C.H.P. Lupis, J.F. Elliott, Acta Meter. 15 (1967) 265–276.
[66] J.C. Mathieu, F. Durand, E. Bonnier, J. Chim. Phys. 62 (1965) 1289–1296.
[67] B. Pascal, J.C. Mathieu, P. Hicter, P. Desré, E. Bonnier, J. Chim. Phys. 68 (1971) 774–781.
[68] J. Lehmann, F. Bonnet, M. Bobadilla, H. Gaye, in: Proc. of the Metal Separation Technology III Conference, Colorado, June 20–24, 2004.
[69] O. Kubaschewski, W.A. Dench, Acta Meter. 3 (1955) 339–346.
[70] H. Wang, R. Luck, B. Predel, Z. Metallkd. 82 (1991) 659–665.
[71] T. Furukawa, E. Kato, Tetsu-to-Hagane 61 (1975) 22–30.
[72] U. Thiedemann, J. Qin, K. Schaefers, M. Rosner-Kuhn, M.G. Frohberg, ISIJ Int. 35 (1995) 1518–1522.
[73] Yu.O. Esin, M.G. Valishev, A.F. Ermakov, P.V. Gel'd, M.S. Petrushevskiy, Russ. Metall. 3 (1981) 15.
[74] G.I. Batalin, E.A. Beloborodova, V.A. Stukalo, L.V. Goncharuk, Zhur. Fiz. Khim. 45 (1971) 2007.
[75] J. Tomiska, Z. Metallkd. 76 (1985) 532–537.
[76] Y. Iguchi, Y. Tozaki, M. Kakizaki, T. Fuwa, S. Ban-Ya, Tetsu-to-Hagane 67 (1981) 925.
[77] R. Hultgren, P.D. Desai, D.T. Hawkins, M. Gleiser, K.K. Kelly, Am. Soc. Met. (1973).
[78] R. Speiser, A.J. Jacobs, J.W. Spretnak, Trans. Met. Soc. AIME 215 (1959) 185.
[79] G.R. Belton, R.J. Fruehan, J. Phys. Chem. 71 (1967) 1403–1409.
[80] G.R. Zellars, S.L. Payne, J.P. Morris, R.L. Kipp, Trans. Met. Soc. AIME 215 (1959) 181.
[81] B.R. Conard, T.B. McAneney, R. Sridhar, Met. Trans. 9B (1978) 463.
[82] E-Hsin Foo, C.H.P. Lupis, Acta Meter. 21 (1973) 1409–1430.
[83] C.H.P. Lupis, Chemical Thermodynamics of Materials, Elsevier Science Publishing Co. Inc, 1983p. 482.
[84] S. Ban-ya, J. Chipman, Trans. Met. Soc. AIME 245 (1969) 391.
[85] S. Ban-ya, J. Chipman, Trans. Met. Soc. AIME 242 (1968) 940.
[86] S. Ban-ya, J. Chipman, Trans. Met. Soc. AIME 245 (1969) 133.
[87] F. Ishii, T. Fuwa, Tetsu-to-Hagane 67 (1981) 736.
[88] J.A. Cordier, J. Chipman, J. Met. 7 (1955) 905.
[89] J.P. Morris, A.J. Williams, Trans Am. Soc. Met. 41 (1949) 1425.
[90] C.W. Sherman, J. Chipman, J. Met. 4 (1952) 597.
[91] B.P. Burylev, L.S. Tsemekham, L.P. Mojsov, Izv. Russ. Akad. Nauk Met. 4 (2002) 17–19.
[92] B. Ozturk, R.J. Fruehan, Met. Trans. B 21B (1990) 879.
[93] F. Ishii, Y. Iguchi, S. Ban-ya, Tetsu-to-Hagane 69 (1983) 913.
[94] R.G. Blossey, R.D. Pehlke, Trans. Met. Soc. AIME 236 (1966) 566.

[95] H. Schenck, M.G. Frohberg, H. Graf, Arch. Hüttenwesen Eisen 30 (1959) 533–537.
[96] J.C. Humbert, J.F. Elliott, Trans. Met. Soc. AIME 218 (1960) 1076.
[97] K. Sanbongi, M. Othani, Tetsu-to-Hagane 47 (1961) 841.
[98] H. Wada, R.D. Pehlke, Met. Trans. B 9 (1978) 441–448.
[99] V.P. Nemchenko, I.P. Malkin, S.I. Popel, Isz. Vyssh. Uchelon. Zaved. Chern. Metall. (12) (1968) 5.
[100] R.J. Fruehan, Trans. TMS-AIME 245 (1969) 1215.
[101] D. Janke, W.A. Fisher, Arch. Hüttenwesen Eisen 47 (1976) 147.
[102] M. Heinz, K. Koch, D. Janke, Steel Res. 60 (1989) 246.
[103] A.D. Pelton, M. Blander, in: Proc. AIME Symposium on Metallurgical Slags and Fluxes, Warrendale, PA, 1984, p. 281.
[104] A.D. Pelton, M. Blander, Metall. Trans. B 17B (1986) 805.
[105] A.D. Pelton, S.A. Degterov, G. Eriksson, C. Robelin, Y. Dessureault, Metall. Mater. Trans. B 31B (2000) 651.
[106] A.D. Pelton, P. Chartrand, Metall. Mater. Trans. A 32A (2001) 1355.
[107] A.D. Pelton, CALPHAD: Comput. Coupling Phase Diagrams Thermochem. 25 (2001) 319.
[108] I.-H. Jung, S.A. Decterov, A.D. Pelton, J. Eur. Ceram. Soc. 25 (2005) 313.
[109] G. Eriksson, A.D. Pelton, Metall. Trans. B 24B (1993) 807.
[110] I.-H. Jung, S.A. Decterov, A.D. Pelton, Metall. Mater. Trans. B 35B (2004) 877.
[111] E. Jak, P. Hayes, A.D. Pelton, S.A. Decterov, Molten 2009, Santiago, Chile, 2009, p. 473.
[112] E. Jak, P. Hayes, A. Pelton, S. Decterov, Int. J. Mater. Res. 98 (2007) 847.
[113] P. Wu, G. Eriksson, A.D. Pelton, J. Am. Ceram. Soc. 76 (1993) 2065.
[114] P. Wu, G. Eriksson, A.D. Pelton, J. Am. Ceram. Soc. 76 (1993) 2059.
[115] G. Eriksson, A.D. Pelton, Metall. Trans. B 24B (1993) 795.
[116] G. Eriksson, P. Wu, A.D. Pelton, CALPHAD: Comput. Coupling Phase Diagrams Thermochem. 17 (1993) 189.
[117] G. Eriksson, P. Wu, M. Blander, A.D. Pelton, Can. Metall. Q. 33 (1994) 13.
[118] S. Degterov, A.D. Pelton, J. Phase Equilib. 17 (1996) 476.
[119] S. Degterov, A.D. Pelton, J. Phase Equilib. 17 (1996) 488.
[120] S. Degterov, A.D. Pelton, Metall. Mater. Trans. B 28B (1997) 235.
[121] I.-H. Jung, Y.-B. Kang, S.A. Decterov, A.D. Pelton, Metall. Mater. Trans. B 35B (2004) 259.
[122] Y.-B. Kang, I.-H. Jung, S.A. Decterov, A.D. Pelton, H.-G. Lee, ISIJ Int. 44 (2004) 975.
[123] Y.-B. Kang, I.-H. Jung, S.A. Decterov, A.D. Pelton, H.-G. Lee, ISIJ Int. 44 (2004) 965.
[124] Y.-B. Kang, I.-H. Jung, Molten 2009, Santiago, Chile, 2009, p. 459.
[125] Y.-B. Kang, I.-H. Jung, H.-G. Lee, CALPHAD: Comput. Coupling Phase Diagrams Thermochem. 30 (2006) 235.
[126] Y.-B. Kang, I.-H. Jung, H.-G. Lee, CALPHAD: Comput. Coupling Phase Diagrams Thermochem. 30 (2006) 226.
[127] S.A. Decterov, V. Swamy, I.-H. Jung, Int. J. Mater. Res. 98 (2007) 987.
[128] S. Arnout, M. Guo, I.-H. Jung, B. Blanpain, P. Wollants, J. Am. Ceram. Soc. 92 (2009) 1831.
[129] V. Swamy, I.-H. Jung, S.A. Decterov, J. Non-Cryst. Solids 355 (2009) 1679.
[130] J.-H. Park, P.C.-H. Rhee, J. Non-Cryst. Solids 282 (2001) 7.
[131] P. Chartrand, A.D. Pelton, Metall. Mater. Trans. A 32A (2001) 1397.
[132] A.D. Pelton, P. Chartrand, G. Eriksson, Metall. Mater. Trans. A 32A (2001) 1409.
[133] Y.-B. Kang, A.D. Pelton, Metall. Mater. Trans. B 40B (2009) 979.
[134] I.-H. Jung, in: Asia Steel Conference, Pusan, Korea, 2009, p. S3.
[135] F. Kongoli, Y. Dessureault, A.D. Pelton, Metall. Mater. Trans. B 29B (1998) 591.
[136] S.A. Degterov, A.D. Pelton, Metall. Mater. Trans. B 30B (1999) 1033.
[137] S.A. Degterov, A.D. Pelton, Metall. Mater. Trans. B 30B (1999) 661.
[138] F. Kongoli, A.D. Pelton, Metall. Mater. Trans. B 30B (1999) 443.
[139] S.A. Degterov, Y. Dessureault, A.D. Pelton, Can. Metall. Q. 39 (2000) 43.
[140] P. Waldner, A.D. Pelton, Metall. Mater. Trans. B 35B (2004) 897.
[141] P. Waldner, A.D. Pelton, Z. Metallkd. 95 (2004) 672.
[142] C.W. Bale, E. Belisle, P. Chartrand, S.A. Decterov, G. Eriksson, K. Hack, I.H. Jung, Y.B. Kang, J. Melancon, A.D. Pelton, C. Robelin, S. Petersen, CALPHAD: Comput. Coupling Phase Diagrams Thermochem. 33 (2009) 295.

[143] A.D. Pelton, G. Eriksson, A. Romero-Serrano, Metall. Trans. B 24B (1993) 817.
[144] A.D. Pelton, Glass Sci. Technol. (Frankfurt/Main) 72 (1999) 214.
[145] I.-H. Jung, ISIJ Int. 46 (2006) 1577.
[146] I.-H. Jung, ISIJ Int. 46 (2006) 1587.
[147] A.N. Grundy, H. Liu, I.-H. Jung, S.A. Decterov, A.D. Pelton, Int. J. Mater. Res. 99 (2008) 1185.
[148] A.N. Grundy, I.-H. Jung, A.D. Pelton, S.A. Decterov, Int. J. Mater. Res. 99 (2008) 1195.
[149] S.A. Decterov, A.N. Grundy, A.D. Pelton, Molten 2009, Santiago, Chile, 2009, p. 423.
[150] SGTE database, www.sgte.org.
[151] L. Zhang, S. Jahanshahi, S. Sun, C. Chen, B. Bourke, S. Wright, M. Somerville, JOM 54 (2002) 51.
[152] S. Jahanshahi, S. Sun, L. Zhang, J. S. Afr. Inst. Min. Metall. 104 (2004) 529.
[153] H. Gaye, J. Welfringer, in: Proc. AIME Symposium on Metallurgical Slags and Fluxes, TMS AIME, Warrendale, PA, 1984, p. 357.
[154] L. Zhang, J. Lehmann, Molten 2009, Santiago, Chile, 2009, p. 403.
[155] L. Zhang, S. Jahanshahi, Metall. Mater. Trans. B 29B (1998) 177.
[156] L. Zhang, S. Jahanshahi, Metall. Mater. Trans. B 29B (1998) 187.
[157] L. Zhang, S. Jahanshahi, Scand. J. Metall. 30 (2001) 364.
[158] R.H. Davies, A.T. Dinsdale, J.A. Gisby, J.A.J. Robinson, S.M. Martin, CALPHAD: Comput. Coupling Phase Diagrams Thermochem. 26 (2002) 229.
[159] J.A.J. Robinson, A.T. Dinsdale, P.N. Quested, in: 2nd Inter. Cong. Sci. Tech. Steelmaking, U. Wales, Swansea, 2001.

CHAPTER 5.2

Slag Viscosity Model

In-Ho Jung[a], Evgueni Jak[b] and Jean Lehmann[c]
[a]Department of Mining and Materials Engineering, McGill University, Montreal, Canada
[b]School of Chemical Engineering, University of Queensland, Queensland, Australia
[c]ArcelorMittal, Global R&D, Maizières-lès-Metz Cedex, France

5.2.1. FactSage STRUCTURAL VISCOSITY MODEL FOR MULTICOMPONENT SLAG

In order to calculate viscosity of molten slag with multicomponent system, the structural viscosity model has been developed since 1999. In this model, viscosity is related to the structure of the melt, which in turn is calculated from the thermodynamic description of the melt using the Modified Quasichemical Model [1,2] and the optimized FactSage database [3]. The model predicts within experimental error limits the viscosity of multicomponent slags from just a few model parameters fitted to the viscosities of the binary system and alumino-silicate ternary systems. The viscosity of slag of all other ternary and multicomponent slags are then predicted well within the experimental error limits because the structural change in the multicomponent slag is automatically counted in the viscosity model by calculating the structural units (SUs) from the Modified Quasichemical Model. Now the FactSage software provides a viscosity calculation module based on a structural viscosity model with optimized database applicable for the slag containing Al_2O_3–B_2O_3–CaO–MgO–FeO–Fe_2O_3–MnO–NiO–PbO–ZnO–Na_2O–K_2O–TiO_2–Ti_2O_3–SiO_2–F. The viscosity calculation module in the FactSage software also provides the viscosity model for glasses valid down to glass transition temperature. The details of the structural model equations and accuracy of the model prediction in comparison to the binary, ternary, and multicomponent experimental data can be found elsewhere [4–9]. Several examples are presented here with a brief model description.

5.2.1.1. Viscosity Model

The structure of silicate melts is characterized by the bridging behavior of oxygen. An oxygen atom separating an M–M pair is a free oxygen, O^{2-}; an oxygen separating an M–Si pair is a nonbridging oxygen, O^{-}; and an oxygen separating an Si–Si pair is called

Treatise on Process Metallurgy, Volume 2
http://dx.doi.org/10.1016/B978-0-08-096984-8.00031-8
© 2014 Elsevier Ltd.
All rights reserved.

a bridging oxygen, O^0. The silicon atoms in silicate melts are always tetrahedrally bonded to four oxygen ions. Basic silicate melts consist mainly of M^{n+}, O^{2-}, and SiO_4^{4-} ions. As the silica content increases above the orthosilicate composition, the SiO_4^{4-} tetrahedra start to polymerize, forming more and more bridging oxygens, and gradually a three-dimensional network is formed. The structural change taking place upon formation of the SiO_2 network can be characterized by the amounts of so-called Q^i-species [10], which are defined as Si atoms linked to i bridging oxygens and $(4-i)$ nonbridging oxygens. In pure SiO_2, all four oxygens surrounding each Si are bridging oxygens and the fraction of Q^4-species is 1.0. An isolated SiO_4^{4-} ion is a Q^0-species.

The Modified Quasichemical Model [1,2] and the optimized FactSage thermodynamic database [3] can be used to calculate the numbers of M–M, M–Si, and Si–Si second-nearest-neighbor pairs, which correspond to the fractions of free oxygens, broken bridges, and bridging oxygens respectively, as functions of temperature and composition. Then, the amount of Q^i-species per mole of silicon (i.e., the probability that a given silicon is a Q^i-species) can be calculated using a binomial distribution of the bond fraction of broken bridge and bridging oxygen. Figure 5.2.1 compares the calculated Q^i-fractions with the experimentally determined Q^4 fractions for the system $NaO_{0.5}$–SiO_2.

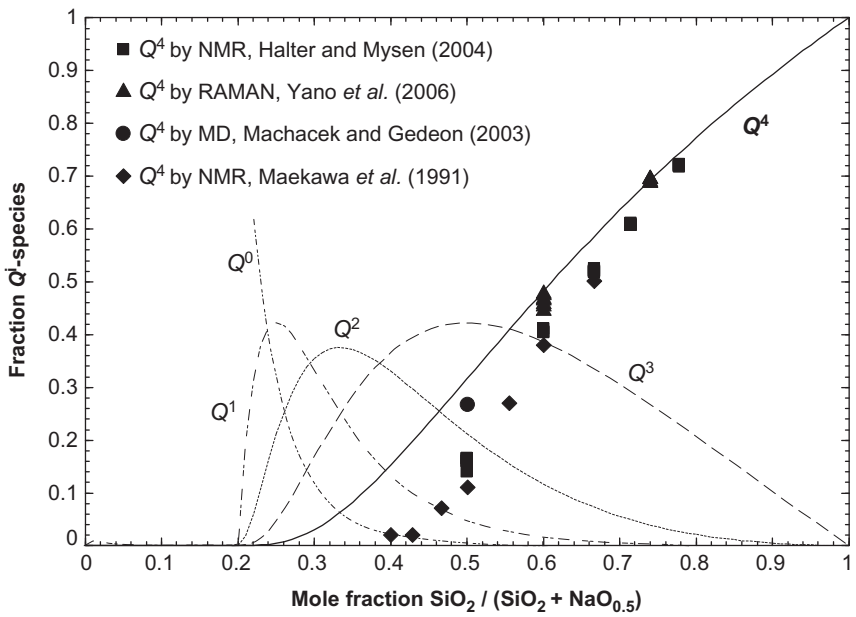


Figure 5.2.1 Calculated concentrations of Q-species compared to experimental values of Q^4 species for the system $NaO_{0.5}$–SiO_2. [65, 66, 67, 68].

5.2.1.1.1 Basic Formula of the Viscosity Model

Let us define p as the probability that a particular pair emanating from a given Si atom is an Si–Si pair. Then, as a first approximation, p can be calculated by dividing the number of Si–Si pairs emanating from all Si atoms by the number of all Si–Si and Si–M pairs:

$$p = \frac{2n_{\mathrm{Si-Si}}}{2n_{\mathrm{Si-Si}} + \sum_{\mathrm{M}} n_{\mathrm{Si-M}}} \tag{5.2.1}$$

where n_{i-j} is the number of i–j pairs. Note that every Si–Si pair is counted twice as emanating from one and from the other Si atom in the pair.

Then, the probability that a given Si atom is a Q^4-species is p^4 because four Si–Si pairs emanate from this Si atom. Similarly, the probability that a given Si atom is part of a cluster of at least n interconnected Si–Si pairs is proportional to p^n. This is only an approximate relation. Clearly there are restrictions on the arrangement of bonds because of the local structure of the melts, which is similar to the diamond lattice structure of cristobalite. The approximation becomes better for larger values of n. In any case, the function p^n is clearly a measure of the connectivity of the network. We postulate that a certain critical cluster size can be defined that mimics the formation of a percolating SiO_2 network. When this cluster size is reached, the viscosity will increase dramatically. The analysis of the viscosity data indicates that a group of 40 interconnected Si–Si pairs is a good choice for the critical cluster size.

Consider a liquid oxide melt with the composition given by the metal mole fractions X_{M}. For example, for a binary system MOx–SiO_2, the mole fractions of M and Si are

$$X_{\mathrm{M}} = \frac{n_{\mathrm{MO}_x}}{n_{\mathrm{MO}_x} + n_{\mathrm{SiO_2}}}, \quad X_{\mathrm{Si}} = \frac{n_{\mathrm{SiO_2}}}{n_{\mathrm{MO}_x} + n_{\mathrm{SiO_2}}} \tag{5.2.2}$$

where n_i are the mole fractions of the components.

The following equations were proposed for the viscosity of liquid melts:

$$\ln \eta = A + \frac{E}{RT} \tag{5.2.3}$$

$$E = \sum_{\mathrm{M}} \left(X_{\mathrm{M}} E_{\mathrm{M}}\right) + X_{\mathrm{Si}} \left\{ E^*_{\mathrm{Si}} + E^{\mathrm{E}}_{\mathrm{Si}} p^{40} + \left(p^4 - p^{40}\right) \frac{\sum_{M} \left(X_{\mathrm{M}} E^{\mathrm{R}}_{\mathrm{M-Si}}\right)}{\sum_{\mathrm{M}} X_{\mathrm{M}}} \right\} + \sum_{\mathrm{M}} \left(X_{\mathrm{M}} X_{\mathrm{Si}} E_{\mathrm{M-Si}}\right) \tag{5.2.4}$$

$$A = \sum_{\mathrm{M}} (X_{\mathrm{M}} A_{\mathrm{M}}) + X_{\mathrm{Si}} \left\{ A^{*}_{\mathrm{Si}} + A^{\mathrm{E}}_{\mathrm{Si}} p^{40} + \left(p^{4} - p^{40}\right) \frac{\sum_{\mathrm{M}} \left(X_{\mathrm{M}} A^{\mathrm{R}}_{\mathrm{M-Si}}\right)}{\sum_{\mathrm{M}} X_{\mathrm{M}}} \right\} + \sum_{\mathrm{M}} (X_{\mathrm{M}} X_{\mathrm{Si}} A_{\mathrm{M-Si}}) \tag{5.2.5}$$

where η is the viscosity in Pa s, R is the gas constant, and T is temperature in Kelvin. The parameters A_{M} and E_{M} give the viscosity of the pure liquid oxides MO_x, which are not network formers:

$$\ln \eta_{\mathrm{MO}_x} = A_{\mathrm{M}} + \frac{E_{\mathrm{M}}}{RT} \tag{5.2.6}$$

Similarly, $\ln \eta^{*}_{\mathrm{Si}} = A^{*}_{\mathrm{Si}} + \frac{E^{*}_{\mathrm{Si}}}{RT}$ represents the hypothetical viscosity of SiO_2 if it behaved as a basic oxide and did not form a network. An excess contribution per Si atom of large clusters of Q^4-species, which contain at least 40 interconnected Si–Si pairs, is proportional to p^{40}. This contribution is represented by the parameters $E^{\mathrm{E}}_{\mathrm{Si}}$ and $A^{\mathrm{E}}_{\mathrm{Si}}$. This is the contribution of the silica network that is assumed to be independent of other cations M. Therefore, the viscosity of pure SiO_2 is:

$$\ln \eta_{\mathrm{Si}} = \left(A^{*}_{\mathrm{Si}} + A^{\mathrm{E}}_{\mathrm{Si}}\right) + \frac{\left(E^{*}_{\mathrm{Si}} + E^{\mathrm{E}}_{\mathrm{Si}}\right)}{RT} \tag{5.2.7}$$

An excess contribution per Si atom of the rest of the Q^4-species, that is, of smaller clusters that contain less than 40 interconnected Si–Si pairs, is proportional to $(p^4–p^{40})$. This contribution is represented by binary parameters $E^{\mathrm{R}}_{\mathrm{M-Si}}$ and $A^{\mathrm{R}}_{\mathrm{M-Si}}$. Since these clusters are smaller, the M cations are located closer to a given Si atom so that the contribution of this Si atom depends on M.

Finally, the last term in Equations (5.2.4) and (5.2.5) contains the additional binary parameters $E_{\mathrm{M-Si}}$ and $A_{\mathrm{M-Si}}$ to account for small nonlinearities of the viscosity, if any, as a function of composition in the basic regions of the binary systems M–Si.

It should be noted that parameters $A^{\mathrm{R}}_{\mathrm{M-Si}}$ and $A_{\mathrm{M-Si}}$ are almost never needed and can almost always be set equal to zero. So far the model has been applied to multicomponent oxide liquids containing Si, B, Al, Ca, Mg, Li, Na, K, Mn, Ni, Fe^{2+}, Fe^{3+}, Pb, Zn, and Ti; only one nonzero parameter, $A^{\mathrm{R}}_{\mathrm{Al-Si}}$, was introduced, and even in this case, the description was already very good without it.

Figure 5.2.2 shows the viscosity of the CaO–SiO_2 system. The steep increase of the viscosity of the binary silicate system in the high SiO_2 region can be well reproduced by the introduction of Q_{40} SUs containing 40 interconnected second-nearest-neighbor

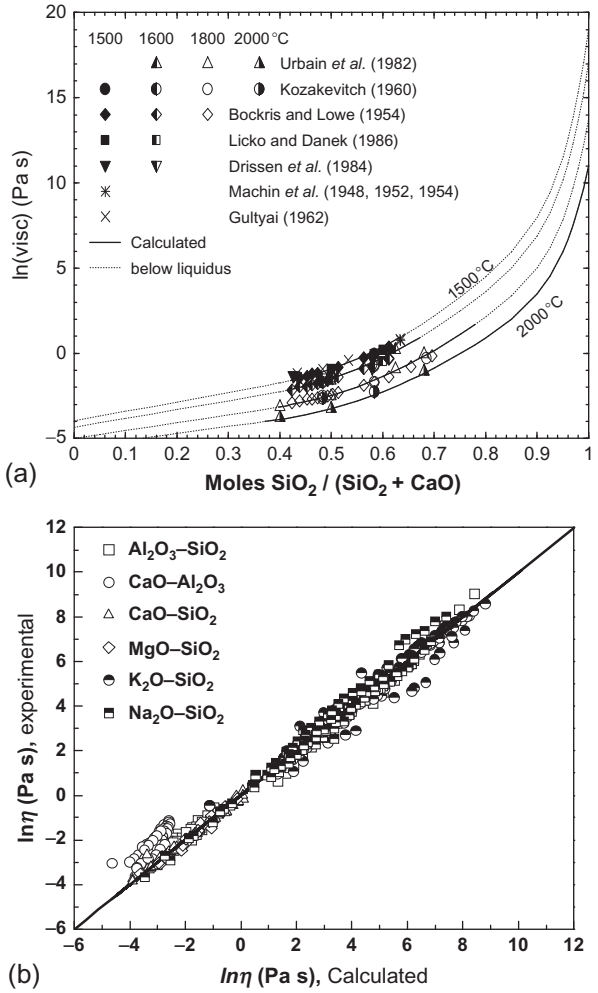


Figure 5.2.2 Calculated viscosity of (a) the binary $CaO–SiO_2$ system and (b) various binary systems along with experimental data.

Si–Si pairs (i.e., bridged oxygens). The model can accurately reproduce the experimental viscosity from basic oxides to SiO_2 with a small number of model parameters.

The viscosity of ternary MO_x–NO_y–SiO_2 systems (silicate slag with two network modifiers MO_x and NO_y) or multicomponent systems without an amphoteric component like Al_2O_3 is well predicted with binary viscosity parameters. Of course, in the viscosity calculations, the structure of the melt for ternary and higher order systems are always calculated from the Modified Quasichemical Model, which can give a proper SU reflecting the chemical nature of the melt.

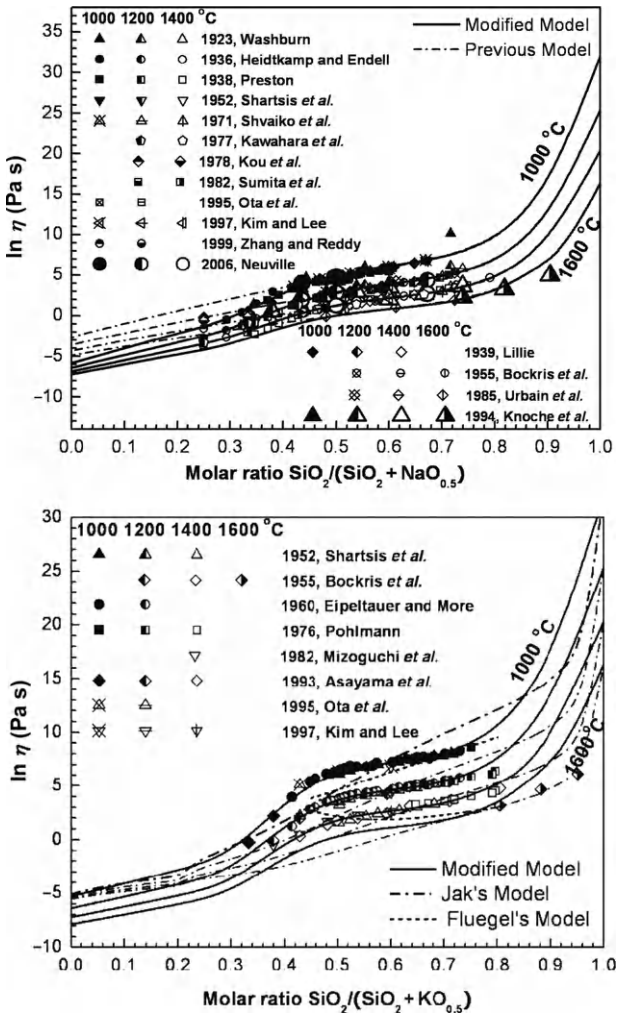


Figure 5.2.3 Viscosity of Na_2O–SiO_2 and K_2O–SiO_2 melts: Comparison with the previous original model without considering ring formation, the modified model considering the effect of ring structure and the other models like Jak's model [13] and Fluegel's model [14].

5.2.1.1.2 Modification of the Model for Melts Containing Alkali Oxides

There is experimental evidence for complex behavior of the viscosity on the alkali-rich side of the $MO_{0.5}$–SiO_2 systems where M is an alkali, as can be seen in Figure 5.2.3. In this composition region, mostly Q^2- and Q^3-species are present. In particular, rings formed by Q^2- and Q^3-species have been reported to form in binary alkali oxide–silica systems based on evidence from nuclear magnetic resonance and Raman spectroscopy [11,12]. Formation of these rings is facilitated by monovalent alkali cations, which are very strong network breakers. On the other hand, for a divalent cation, such as Ca^{2+}, no complex

behavior has been reported. Therefore, for alkali oxide–silica systems, an additional excess contribution of Q^2- and Q^3-species polymerized into large rings has been added to the viscosity formula, in particular to activation energy term in Equation (5.2.4):

$$E = \sum_{M}(X_M E_M) + \sum_{M}(X_M X_{Si} E_{M-Si}) + X_{Si}\left\{ E^*_{Si} + E^E_{Si} p^{40} + \left(p^4 - p^{40}\right)\frac{\sum_{M}\left(X_M E^R_{M-Si}\right)}{\sum_{M} X_M} + p^7(1-p)^3\frac{\sum_{M=Alkali}\left(X_M E^{Ring}_{M-Si}\right)}{\sum_{M} X_M}\right\} \quad (5.2.8)$$

where E^{Ring}_{M-Si} is a binary parameter which is nonzero only for alkali oxide–silica systems. It should be noted that a similar additional term was never needed in Equation (5.2.5) for A. That is, all parameters $A^{Ring}_{M-Si} = 0$. Therefore, Equation (5.2.5) can still be used with Equations (5.2.3) and (5.2.8).

In summary, for most binary systems MO_x–SiO_2 only two binary parameters, E^R_{M-Si} and E_{M-Si}, were required to fit the experimental viscosity data, while for each alkali oxide–SiO_2 system one additional binary parameter, E^{Ring}_{M-Si}, was needed. The example of the effect of the modification of the model can be shown in Figure 5.2.3 for Na_2O–SiO_2 system. Any other viscosity models available in literature can reproduce this complex behavior of viscosity in alkali-oxide silicate systems.

5.2.1.1.3 Charge Compensation Effect for Alumino-Silicate System

Certain amphoteric oxides such as Al_2O_3 can behave in profoundly different ways in a silicate melt depending on the overall composition. When added to a pure silica melt, Al_2O_3 acts as a network-modifier, breaking the oxygen bridges of the pure silica network, thereby substantially decreasing the viscosity. On the other hand, when Al_2O_3 and MO or M_2O are added simultaneously to SiO_2, some of the Al cations assume tetrahedral coordination and replace Si in the liquid network, so that Al acts as a network former. The missing charge is compensated by M cations that stay close to the Al ions. Due to this "Charge Compensation Effect" [10], there is a maximum in the viscosity when the molar ratio of Al_2O_3 to MO or M_2O is unity.

The thermodynamic database of Modified Quasichemical Model parameters, upon which the viscosity model is based, does not explicitly consider the different structural roles of Al. Hence, in order to model the viscosity maximum, the amount of network-forming Al must be evaluated a posteriori. This is done as follows. Consider, for example, the Al_2O_3–CaO–Na_2O–SiO_2 system. Two reactions can be considered to form tetrahedrally coordinated Al that enters the silica network and is charge-compensated by either Na or Ca:

$$Al + Na \rightleftarrows NaAl \quad (5.2.9)$$

$$2\mathrm{Al} + \mathrm{Ca} \rightleftarrows \mathrm{CaAl_2} \tag{5.2.10}$$

It is assumed that the NaAl and $CaAl_2$ "species" have the same effect on the viscosity as one or two Si atoms, respectively. The model parameters in our model are simply the Gibbs energies of reactions (5.2.9) and (5.2.10). These Gibbs energies are not dependent on temperature, but are found to vary linearly as a function of SiO_2 content, becoming more negative at higher SiO_2 concentrations. Hence, only two parameters are required to model the Charge Compensation Effect in each ternary system MO_x–Al_2O_3–SiO_2 (including the limiting MO_x–Al_2O_3 binary systems).

The equilibrium constants for reactions (5.2.9) and (5.2.10) can be written as

$$K_{\mathrm{NaAl}} = \exp\left(\frac{-\Delta G_{\mathrm{NaAl}}}{RT}\right) = \frac{X'_{\mathrm{NaAl}}}{X'_{\mathrm{Na}} X'_{\mathrm{Al}}} \tag{5.2.11}$$

$$K_{\mathrm{CaAl_2}} = \exp\left(\frac{-\Delta G_{\mathrm{CaAl_2}}}{RT}\right) = \frac{X'_{\mathrm{CaAl_2}}}{X'_{\mathrm{Ca}} \left(X'_{\mathrm{Al}}\right)^2} \tag{5.2.12}$$

At each given overall composition X_{Na}, X_{Ca}, X_{Al}, and X_{Si}, Equations (5.2.11) and (5.2.12) can be solved, taking into account the mass balance constraints to obtain $X'_{\mathrm{Na}}, X'_{\mathrm{Ca}}, X'_{\mathrm{Al}}, X'_{\mathrm{Si}}, X'_{\mathrm{NaAl}}, \text{and } X'_{\mathrm{CaAl_2}}$.

Here $\left(X'_{\mathrm{NaAl}} + 2X'_{\mathrm{CaAl_2}}\right)$ gives the amount of network-forming Al, while X'_{Al} gives the amount of network-modifying Al.

Since it is assumed that NaAl and $CaAl_2$ species have exactly the same effect on the viscosity as one or two Si atoms respectively, the viscosity can be calculated by substituting the following adjusted mole fractions into Equations (5.2.3), (5.2.5), and (5.2.8):

$$\begin{aligned}
X^*_{\mathrm{Si}} &= \left(X'_{\mathrm{Si}} + X'_{\mathrm{NaAl}} + 2X'_{\mathrm{CaAl_2}}\right)/N^*_{\mathrm{tot}} \\
X^*_{\mathrm{Al}} &= X'_{\mathrm{Al}}/N^*_{\mathrm{tot}} \\
X^*_{\mathrm{Ca}} &= X'_{\mathrm{Ca}}/N^*_{\mathrm{tot}} \\
X^*_{\mathrm{Na}} &= X'_{\mathrm{Na}}/N^*_{\mathrm{tot}} \\
\text{where } N^*_{\mathrm{tot}} &= X'_{\mathrm{Na}} + X'_{\mathrm{Ca}} + X'_{\mathrm{Al}} + X'_{\mathrm{Si}} + X'_{\mathrm{NaAl}} + 2X'_{\mathrm{CaAl_2}}
\end{aligned} \tag{5.2.13}$$

Obviously, this proposed treatment of the Charge Compensation Effect is a simplification. Strictly speaking, the charge-compensated Al that enters the silica network does not form chemically distinct species such as NaAl and $CaAl_2$; the contribution of network-forming Al to the viscosity may be different from that of Si and, finally, mole fractions are used in Equations (5.2.11) and (5.2.12) instead of activities. However, the proposed treatment gives a qualitatively correct functional dependence of the viscosity on temperature and composition, and the description is made quantitative by fitting the

Gibbs energies of reactions (5.2.9) and (5.2.10) to experimental viscosity data in the ternary MO_x–Al_2O_3–SiO_2 systems.

Figure 5.2.4 shows the calculated iso-viscosity for the two alumino-silicate systems, CaO–Al_2O_3–SiO_2 and Na_2O–Al_2O_3–SiO_2 from the present model. The local maximum can occur near MO_x/Al_2O_3. The calculated viscosities are compared with experimental data in Figure 5.2.5. As can be seen in figure, the experimental viscosity data are accurately reproduced by considering the formation of associate $CaAl_2O_4$ and $NaAlO_2$. All experimental data of other alumino-silicate system are also well reproduced as can be seen in Figure 5.2.6 in the wide viscosity and temperature ranges. Typically it is assumed that the addition of alkaline oxide to normal metallurgical slag can decrease the viscosity of the slag. However, in some cases, the viscosity can be even increased by the addition of Na_2O or K_2O. For example, Figure 5.2.7 shows the effect of addition of Na_2O or K_2O to the CaO–Al_2O_3–SiO_2 melts, which shows that K_2O addition can increase the viscosity of slag while Na_2O decreases the viscosity. These complex effects are well predicted by the present structural model.

5.2.1.1.4 Addition of Fluoride in Oxide Slag

The viscosity model for oxide slag was extended to oxy-fluoride melts containing MF_x (M = Ca, Mg, Na, K, and Al), which are important for pyrometallurgical applications. A simple solution database using a polynomial solution model with Gibbs energies of each pure liquid oxide and fluoride was developed to roughly calculate the overall "equilibrated composition" from given initial compositions of oxyfluoride melts. Structural roles of MF_x (M = Ca, Mg, Na, K, and Al) are reviewed and regarded as network modifiers in silicate or borate melts and simply approximated to have the same breaking effects on silicate or borate networks as basic oxides containing the same cations. No charge compensation effect from available viscosity data of the system containing MF_x and

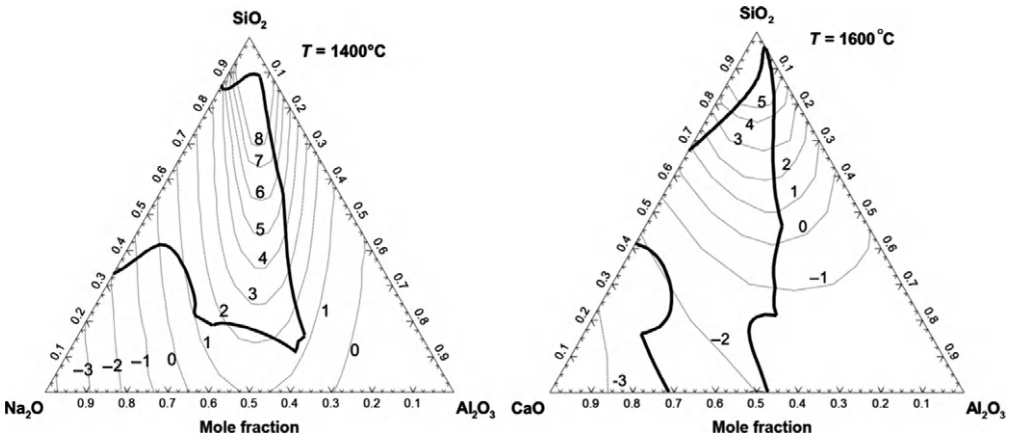


Figure 5.2.4 Iso-viscosity lines for CaO–Al_2O_3–SiO_2 and Na_2O–Al_2O_3–SiO_2 systems calculated from the present viscosity model. Thick lines: liquidus lines at given temperature. Thin lines: iso-viscosity lines of ln (viscosity (Pa s)).

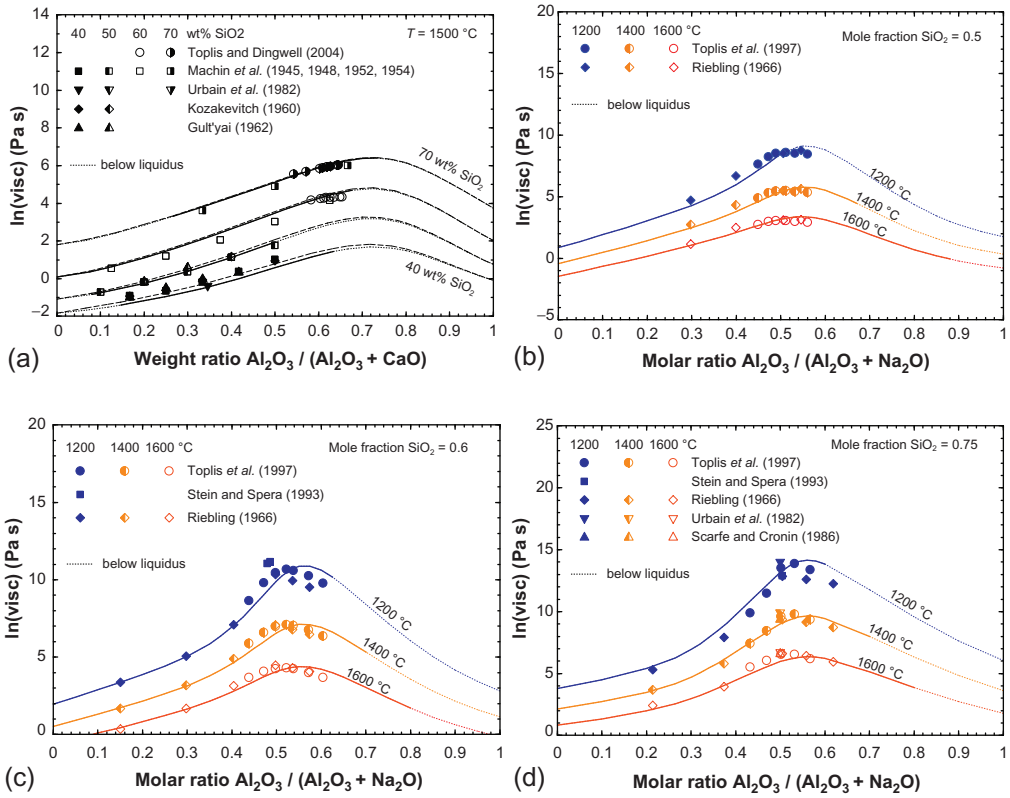


Figure 5.2.5 Calculated viscosities from the model in comparison to the experimental data for (a) $CaO–Al_2O_3–SiO_2$ system and for (b), (c), and (d) $Na_2O–Al_2O_3–SiO_2$ system.

Al_2O_3 was observed, and thus the model reproduces the experimental data for binary and ternary melts without applying charge compensation effect. The available viscosity data for all subsystems of $MF_x–SiO_2–B_2O_3–Al_2O_3–CaO–MgO–Na_2O–K_2O–PbO–MnO–TiO_y$ melts (M = Ca, Mg, Na, K, and Al) are reviewed and modeled. The details of the model equations can be found elsewhere [9].

There is a large discrepancy between experimental data in the literature for the viscosity of CaF_2. After reviewing all binary, ternary, and multicomponent slag containing CaF_2, the most optimum values were selected for the pure CaF_2 as can be seen in Figure 5.2.8. The ternary viscosity is predicted from the binary model parameters. For example, the calculated viscosities for two ternary systems $CaF_2–CaO–SiO_2$, and $CaF_2–Al_2O_3–CaO$ are compared with the experimental data in Figure 5.2.9. Several experimental data for the real mold flux systems were collected and compared with the calculations in Figure 5.2.10. The prediction of the viscosity for the multicomponent oxyfluoride melts shows an excellent agreement with the experimental data.

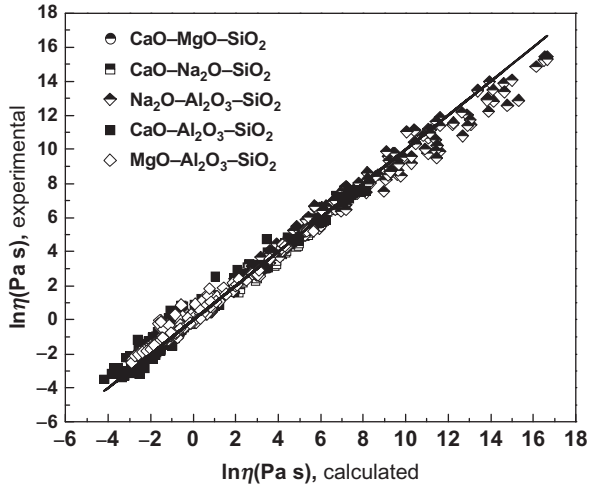


Figure 5.2.6 Comparison of the experimental and calculated viscosity data for various MO_x–Al_2O_3–SiO_2 systems.

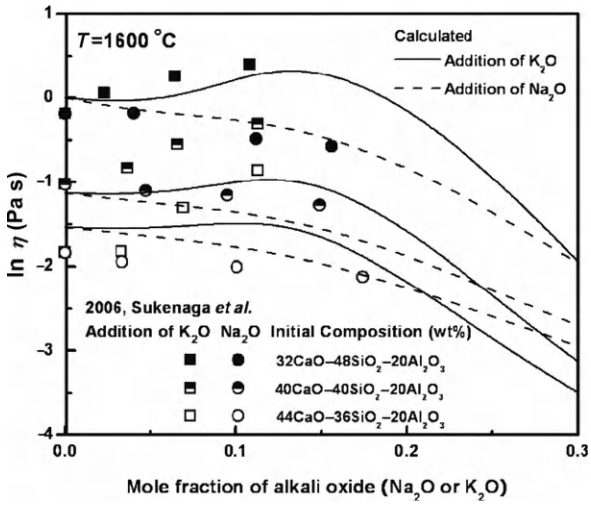


Figure 5.2.7 Changes in the viscosity of CaO–Al_2O_3–SiO_2 melts resulting from additions of Na_2O or K_2O.

5.2.2. VISCOSITY OF SLAGS

Viscosity is a physical property that is related to the structural properties of the melt. In slags, viscosity is dominated by the silicate structure and all models available in the literature are related to a description of this structure (see, for instance, Ref. [15]).

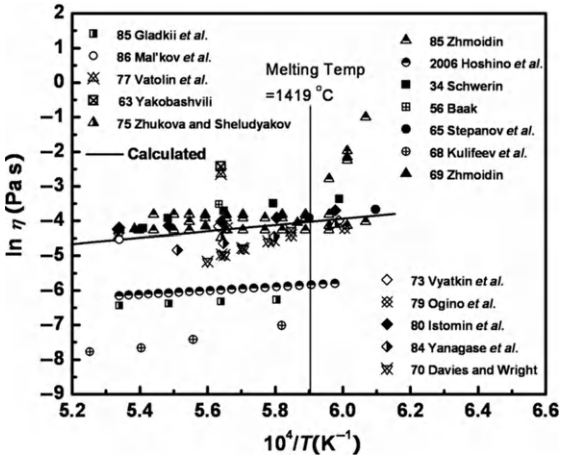


Figure 5.2.8 Calculated viscosity of CaF_2 along with all available experimental data in literature.

Silicate slag has a network structure, made of the bonding of SiO_4^{4+} units, in which SiO_4^{4+} ions are combined with each other through bridging oxygen O^0 (connecting two SiO_4^{4+} units), i.e., the vertex oxygen in tetrahedron structure of SiO_4^{4+} units. When some basic oxides such as CaO and Na_2O are added in the silicate slag, the network structures are partially cut off by oxygen ions decomposed from basic oxides to produce some numbers of nonbridging oxygen O^- (connected to one SiO_4^{4+} unit) and free oxygen ion O^{2-}. It has been suggested that as the degree of polymerization of the melt diminishes owing to the cutting-off of the network structure, there is a corresponding decrease in the viscosity of the slag. An acid slag with large polymerized silicate ions is highly viscous whereas a basic slag with small depolymerized silicates is much more fluid. For example, the effect of basic compounds such as Li_2O, Na_2O, K_2O, BaO, and MgO on the viscosity of SiO_2–Al_2O_3–CaO melts has been very recently studied by Santhy *et al.* [16]. Spectroscopic analysis performed by these authors confirms the effects of these oxides on melt polymerization.

SiO_2 and other oxides as P_2O_5 that contribute to the polymerization of the slags are called network formers. Basic oxides such as CaO, MgO, and Na_2O are called network modifiers. Oxides, such as Al_2O_3, which can act as network formers or network modifiers according to the overall melt composition, are designated as amphoteric oxides. It is a common phenomena that viscosity shows a maximum value at intermediate ratios of amphoteric to basic oxides. This is usually attributed to the so-called "charge compensation effect" — ability of a three-valent amphoteric cation (e.g., Al^{3+}) to take a tetrahedral interstitial site between oxygen anions provided that the excess charge is compensated by the alkali or alkali earth metal cations (e.g., Ca^{2+}, Mg^{2+}, Na^+, K^+).

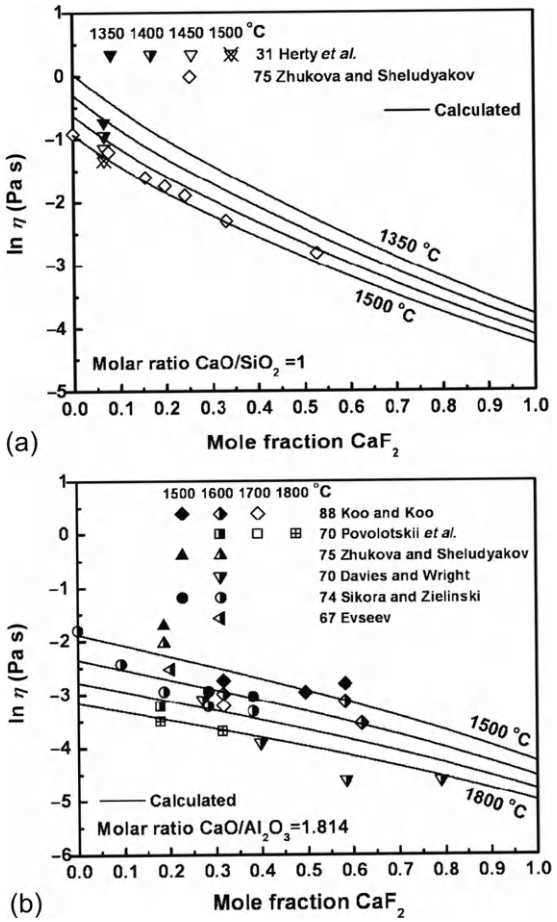


Figure 5.2.9 Calculated viscosities of (a) CaF_2–CaO–SiO_2 melts with a molar $CaO/SiO_2 = 1$ and (b) CaF_2–Al_2O_3–CaO melts with a molar ratio $CaO/Al_2O_3 = 1.814$ compared to experimental data.

Viscosity models can be classified according to the way in which they are connected to this description of the slag structure:

- A first class of model that will be called hereafter "explicit models" only distinguish compounds according to their network forming, modifying or amphoteric character. The various parameters of these models are explicit functions of the mole fractions of these various compounds. A typical example of such models is Urbain's pioneer work [17] in which no distinction is made between the roles of the different compounds belonging to the same group (i.e., network formers and modifiers).
- A second class of models uses the same concepts as the thermodynamic quasichemical models of slags. These thermodynamic models start from the structural description of the slags given before and develop an expression of the Gibbs free energy through the

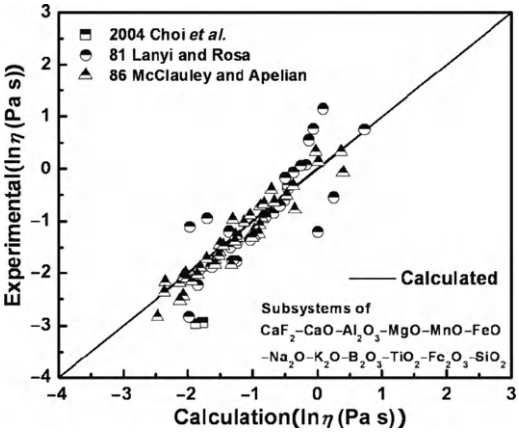


Figure 5.2.10 Comparison between calculation and experimental data for the viscosity of liquid mold fluxes.

quasichemical approach proposed by Guggenheim [18]. Therefore, all the models in this category refer to one of the two thermodynamic models of slags based on this approach: the IRSID slag model or the Modified Quasichemical Model [19]. This class of models will be referred hereafter as "structural models." The main quantities extracted from the thermodynamic models and used by the "structural models" are the numbers of cells. The cells are elements describing the short range order in the metallurgical slags. They consist in a central anion (O^{2-}, S^{2-}...) surrounded by two cations.

– In a third class, we will gather miscellaneous models in which the structure of the slags is not taken into account or at least not in such a straightforward way.

Table 5.2.1 lists the slag viscosity models reviewed in this chapter.

5.2.2.1. Nomenclature

h Planck constant
k Boltzmann constant
Λ optical basicity
Λ_I optical basicity of oxide *i*
μ viscosity in Pa s (Pl) or in poise (10^{-1} Pa s)
N Avogadro' number
R gas constant (8.31431 J K^{-1} mol^{-1}, 1.987 cal K^{-1} mol^{-1})
T temperature in K
X_i mole fraction of oxide *i*

5.2.2.2. Explicit Models

5.2.2.2.1 Model due to Urbain et al. *[17,19,20]*

Chemical system: SiO_2–P_2O_5–TiO_2–Cr_2O_{3t}–Al_2O_{3t}–CrO–FeO_t–MnO–MgO–CaO–K_2O–Na_2O–CaF_2

Table 5.2.1 Slag Viscosity Models Reviewed in This Chapter

Authors	Type of Model	Chemical System	Applicability Domains
Urbain *et al.* [17,20,21]	Explicit	SiO_2–P_2O_5–TiO_2–Cr_2O_{3t}–Al_2O_3–FeO_t–MnO–MgO–CaO–K_2O–Na_2O–CaF_2	Blast furnace, steelmaking, ladle slags
Mudersbach *et al.* [22]	Explicit	SiO_2–Al_2O_3–FeO_t–MgO–CaO···	Blast furnace, steelmaking, ladle slags
Tan and Vix [23]	Explicit	SiO_2–Al_2O_3–FeO–CaO–ZnO	Lead–Zinc smelting slags
Riboud *et al.* [24]	Explicit	SiO_2–Al_2O_3–FeO_t–MnO–MgO–CaO–K_2O–Na_2O–CaF_2	Mold slags
Koyama *et al.* [25]	Explicit	SiO_2–Al_2O_3–MgO–CaO–Li_2O–Na_2O–CaF_2	Mold slags
Kim *et al.* [26]	Explicit	SiO_2–Al_2O_3–B_2O_3–MgO–CaO–Li_2O–Na_2O–CaF_2	Mold slags
Iida [27–29]	Explicit	SiO_2–Al_2O_3–MgO–CaO–Li_2O–K_2O–Na_2O–CaF_2	Mainly blast furnace and mold slags
Reddy and Hebbar [30]	Explicit	SiO_2–FeO	
KTH model [31]	Explicit	SiO_2–Al_2O_3–FeO–MnO–CaO···	Blast furnace, steelmaking, ladle slags
Jak and Kondratiev [32–35]	Explicit	SiO_2–Al_2O_3–FeO_t–CaO	Coal ash slags, steelmaking, ladle slags,
Jak *et al.* [36–43]	Structural	SiO_2–Al_2O_3–FeO_t–MgO–CaO–Na_2O–K_2O	Blast furnace, steelmaking, ladle slags, coal ash slags
Zhang *et al.* [44]	Structural	SiO_2–Al_2O_3–MnO_t–MgO–CaO···	General
Nakamoto *et al.* [45]	Structural	SiO_2–Al_2O_3–FeO_t–CaO	Steelmaking slags
NPL [46]	Miscellaneous (optical basicity)	SiO_2–P_2O_5–TiO_2–Al_2O_3–Fe_2O_3–B_2O_3–FeO–MnO–MgO–CaO–BaO–SrO–K_2O–Na_2O–Li_2O–CaF_2	All kinds of slags
Pal *et al.* [47]			All kinds of slags

Continued

Table 5.2.1 Slag Viscosity Models Reviewed in This Chapter—cont'd

Authors	Type of Model	Chemical System	Applicability Domains
	Miscellaneous (optical basicity)	SiO_2–P_2O_5–Al_2O_3–Fe_2O_3–B_2O_3–FeO–MnO–MgO–CaO–BaO–SrO–K_2O–Na_2O–Li_2O–CaF_2–Cs_2O–Cr_2O_3–CoO–NiO–ZnO–PbO	
Hanao *et al.* [48]	Miscellaneous (Neural Network)	SiO_2–Al_2O_3–CaO–MgO–Na_2O–F–FeO_t–ZrO_2–TiO_2–BaO–MnO–B_2O_3–S–C	Blast furnace, steelmaking, ladle slags

Applicability: Blast furnace, steelmaking, ladle slags

Urbain *et al.*'s model is one of the most widely used slag viscosity models and is based on the application of polynomial functions of slag composition to describe the pre-exponential and exponential terms in the Weymann–Frenkel [49,50] equation:

$$\mu = AT\exp(1000B/T) \tag{5.2.14}$$

where μ is the viscosity (in Pa s). B is related to the activation energy E_w by the relation $1000B = E_w/R$.

Urbain expressed B as a third power polynomial of the network formers concentration X (calculated from the mole fractions of SiO_2 and P_2O_5):

$$B = B_0 + B_1 \cdot X + B_2 \cdot X^2 + B_3 \cdot X^3 \tag{5.2.15}$$

Each coefficient B_i is itself a polynomial function of the mole fraction of network modifiers. Finally, A is supposed to be a linear function of B:

$$-\ln A = mB + n \tag{5.2.16}$$

Experimental data indicate presence of the maximum in viscosity at intermediate ratios of amphoteric to basic oxides commonly attributed to the so-called charge compensation effect—ability of the amphoteric cation such as Al^{3+} to take tetrahedral coordination that is described by Urbain with the second-power polynomial.

Urbain *et al.* assessed their model's parameters on the binary systems silica-oxide and alumina-oxide and on the ternary systems Al_2O_3–MgO–SiO_2, Al_2O_3–MnO–SiO_2, and Al_2O_3–CaO–SiO_2. Details about the model are given in Appendix 5.2.3.1 along with the values of the different parameters.

Significant discrepancies have been found between the prediction of the model and experimental values as reported in Ref. [44] for the ternaries CaO–MgO–SiO_2 and

$CaO–MnO–SiO_2$. It is attributed to the fact that, in Urbain's model, all the network modifiers, for instance CaO and MgO, have the same contribution to the viscosity, which is not in agreement with the experimental values.

5.2.2.2.2 Model due to Mudersbach et al. [22]

Chemical system: $SiO_2–Al_2O_3–FeO_t–MgOCaO...$

Applicability: Blast furnace, steelmaking, ladle slags

It is a modification of Urbain's model. The coefficients have been changed and A is no more a function of B only, and the coefficients m and n in Equation (5.2.16) depend on the slag basicity CaO/SiO_2. The numerical values of the different coefficients are not given by the authors. They have been assessed on a database of 54 oxide-silicate and alumina-silicate melts.

5.2.2.2.3 Model due to Tan and Vix [23]

Chemical system: $SiO_2–Al_2O_3–FeO–CaO–ZnO$

Applicability: Lead–zinc smelting slags

Tan and Vix modified and extended Urbain's model to model blast furnace slags that contain roughly five components ZnO (10–25%)–$CaO–SiO_2–Al_2O_3–FeO$. The modification consisted in expressing the B factor as an explicit function of all components' mole fractions (i.e., the contribution of ZnO, FeO, CaO... are distinguished) and of the network former mole fraction (Appendix 5.2.3.8). The values of the different coefficients are not available.

5.2.2.2.4 Model due to Riboud et al. [24,51]

Chemical system: $SiO_2–Al_2O_3–FeO_t–MnO–MgO–CaO–K_2O–Na_2O–CaF_2$

Applicability: Mold slags

Riboud *et al.* corrected the Urbain formalism to describe the viscosities of some industrial mold fluxes (in the $Al_2O_3–CaO–Na_2O–SiO_2–CaF_2$ system). In their model, the slag components are now classified according to five groups:

- "SiO_2" = $SiO_2 + P_2O_5 + TiO_2 + ZrO_2$
- "CaO" = $CaO + MgO + FeO + BO_{1.5}$
- "Al_2O_3" = Al_2O_3
- "CaF_2" = CaF_2
- "Na_2O" = $Na_2O + K_2O$

And the values of A and B of the Weyman equation (5.2.14) are expressed as polynomials of the mole fraction of these five groups (see Appendix 5.2.3.2). Unlike to Urbain's model, A is no more a simple function of B.

5.2.2.2.5 Model due to Koyama et al. [25]

Chemical system: $SiO_2–Al_2O_3–MgO–CaO–Li_2O–Na_2O–CaF_2$

Applicability: Mold slags

Koyama *et al.*'s model is based on the Arrhenius equation:

$$\mu = A\exp(B/T) \tag{5.2.17}$$

and, contrary to what is assumed in Riboud's model, CaO and MgO are no more supposed to belong to the same group. The model is used for mold slags. See Appendix 5.2.3.4 for details.

5.2.2.2.6 Model due to Kim et al. [26]

Chemical system: SiO_2–Al_2O_3–B_2O_3–MgO–CaO–Li_2O–Na_2O–CaF_2

Applicability: Mold slags

Kim *et al.*'s model is formally identical to Koyama *et al.*'s model. Only the values of the different parameters are changed. See Appendix 5.2.3.5.

5.2.2.2.7 Model due to Iida et al. [27–29]

Chemical system: SiO_2–Al_2O_3–MgO–CaO–Li_2O–K_2O–CR–Na_2O–CaF_2

Applicability: Mainly blast furnace and mold slagsIida viscosity model is based on an Arrhenius type of equation:

$$\mu = A\mu_0 \exp\left(\frac{E}{Bi^*}\right) \tag{5.2.18}$$

A and E are functions of temperature only. μ_0 is a linear function of the mole fractions of the different components:

$$\mu_0 = \sum_{i=1}^{n} \mu_{0i} X_i \tag{5.2.19}$$

Each coefficient μ_{0i} depends only on the properties of the pure component i and on the temperature.

The coefficient Bi^* is called the modified basicity index. It is a function of the slag composition:

$$Bi^* = \frac{\sum (\alpha_i W_i)_B + \alpha^*_{Fe_2O_3} W_{Fe_2O_3}}{\sum (\alpha_i W)_A + \alpha^*_{Al_2O_3} W_{Al_2O_3} + \alpha^*_{TiO_2} W_{TiO_2}} \tag{5.2.20}$$

α_i are, respectively, specific coefficients only dependent on the temperature. W_i are the weight percentages. The indexes A and B represent the acidic oxides and the basic oxides or fluoride, respectively. α_i^* is the specific coefficient for the amphoteric oxide i. It is given as a function of the basicity index Bi and of the weight percentage of the amphoteric oxide W_i.

The calculation details are given in Appendix 5.2.3.3. The values of all coefficients can be found in Ref. [27].

This model has been used, for instance, by Holappa *et al.* [52] on $CaO–SiO_2–CrO_x$ and has been shown to be able to reproduce satisfactorily their measurements.

5.2.2.2.8 Model due to Reddy and Hebbar [30]

Chemical system: SiO_2–FeO

Applicability: limited to the SiO_2-FeO binary system

Reddy and Hebbar used the whole theory to derive the following expression of the viscosity:

$$\mu = 4.9 \times 10^{-10} N_{O^0} T^{1/2} \exp\left(\frac{E}{RT}\right) \tag{5.2.21}$$

N_{O^0} is the fraction of bridging oxygen and is evaluated starting from the melt composition and from the free enthalpy variation value associated to the depolymerization reactions. For example, on the binary $FeO–SiO_2$, the depolymerization reaction is:

$$\frac{1}{2}SIO_2 + FeO \rightarrow \frac{1}{2}Fe_2SiO_4 \tag{5.2.21}$$

The values of the corresponding free enthalpy variations are taking from Refs. [53,54].

E is developed as a fourth order polynomial of the bridging oxygen fraction whose coefficients have been assessed against experimental values for the binary SiO_2–FeO (Appendix 5.2.3.11).

5.2.2.2.9 KTH model [31,55,56]

Chemical system: $SiO_2–Al_2O_3$–FeO–MnO–CaO...

Applicability: Blast furnace, steelmaking, ladle slags

The KTH viscosity model is based on the Eyring equation:

$$\mu = \frac{hN\rho}{M} \exp\left(\frac{\Delta G^*}{RT}\right) \tag{5.2.23}$$

ρ and M are the density and molecular weight both the melts expressed as a linear function of the components mole fractions. ΔG^* is the Gibbs energy of activation for viscosity. The authors have given to that quantity an expression similar to what is taken for the Gibbs free energy in the sublattice formalism: it is expressed as a sum of the contribution of the end-members of the solution and of a mixing term:

$$\Delta G^* = \sum X_i \Delta G_i^* + \Delta G_{\text{mix}}^* \tag{5.2.24}$$

The mixing term is expressed as polynomials of cation fractions and temperature. This model is included in the commercially available code THERMOSLAG sold by the Royal Institute of Technology of Stockholm.

The limited comparison reported by the authors themselves between the predictions and the experimental data showed a good performance of the model.

5.2.2.2.10 Modified Urbain Model by Jak and Kondratiev [32–35]

Chemical system: SiO_2–Al_2O_3–FeO–CaO...

Applicability: Blast furnace, steelmaking, ladle slags, coal ash slags

Jak and Kondratiev expanded the Urbain formalism (Equations 5.2.14–5.2.16) to allow separate individual contributions of the amphoteric and network-breaking metal oxides. Model parameters were systematically optimized using all experimental data available at the time including experimental viscosity results for all binary, ternary, and quaternary systems. These modifications enabled the discrepancies of the original Urbain model to be reduced. Model parameters are given in Appendix 5.2.3.

5.2.2.3. Structural Models

As mentioned before, these models use the same concepts as the thermodynamic quasichemical models of slags.

5.2.2.3.1 Model due to Nakamoto et al. [45]

Chemical system: SiO_2–Al_2O_3–FeO_t–CaO

Applicability: Steelmaking slags

Nakamoto *et al.* propose a model that considers the flow mechanism of the slags. It is based on an estimation of the number of "cutting-off" points in the slag network, which are weakness points of the structure. The points are adjacent to nonbridging and free oxygen. Under these considerations, the authors derived the following expression of the viscosity:

$$\eta = A \exp\left(\frac{E}{1 + (\alpha_m)^{1/2}}\right) \tag{5.2.25}$$

α_m is a function of the numbers of cells as they are given by IRSID slag model (Appendix 5.2.3.10). Good agreement between the model predictions and the experimental data was reported by the authors for a limited range of compositions. In Ref. [57], it is reported that Tanaka mentioned in a private communication that his model needs further development. See Appendix 5.2.3.10 for details.

5.2.2.3.2 Model due to Zhang et al. [44,58,59]

Chemical system: SiO_2–Al_2O_3–MnO_t–MgO–CaO...

Applicability: All slags

Zhang's model is based on the Weymann–Frenkel equation and links the slag viscosity to the internal structure of the slag expressed through the concentrations of bridging, nonbridging, and free oxygens derived from the cell thermodynamic model. These numbers are deduced from IRSID thermodynamic slag model. As mentioned before, in this kind of models, the structure of the slags is described in terms of cells. The number of bridging oxygens (or anions) can be simply calculated from the number of cells containing two network-forming cations, the number of nonbridging oxygens from the number of cells containing only one network-forming cation, etc.

This model performs well in a number of slag systems according to the reported comparison with the experimental data on coal-ash-type slags and TiO_2-containing blast furnace slags.

5.2.2.3.3 *Model due to Jak* et al. *[36–43]*

Chemical system: SiO_2–Al_2O_3–FeO–MgO–CaO–Na_2O–K_2O

Applicability: Blast furnace, steelmaking, ladle slags, coal ash slags

Jak *et al.* developed the quasichemical viscosity model for the system Al_2O_3–CaO–"FeO"–MgO–SiO_2–Na_2O–K_2O. It is based on the Eyring approach [60] in which the viscosity is determined by the ability of the molecules or of SUs to move from their positions to the adjacent holes of the structure. Jak *et al.* assume that, for the silicate and other oxide melts (slags), the SUs are the cells as defined by the quasichemical models of slags, i.e., oxygen anions with metal cations partly associated with them (see Refs. [36–43]). Under this assumption, viscosity can be expressed as follows:

$$\mu = \frac{2RT}{\Delta E_v} \frac{(2\pi m_{\mathrm{SU}} kT)^{1/2}}{v_{\mathrm{SU}}^{2/3}} \exp\left(\frac{E_a}{RT}\right) \text{in Pa s} \tag{5.2.26}$$

where m_{su} and v_{SU} are the average weight and volume of an SU, E_a is the integral molar activation energy (J mol^{-1}) and ΔE_v is an integral molar energy term (J mol^{-1}) related to the concentration of the holes, all expressed as functions of the SU concentrations X_{i-j} calculated by the Modified Quasichemical Model [19].

m_{Su} and v_{SU} are expressed as linear function of the SU concentrations X_{i-j}:

$$m_{\mathrm{SU}} = \sum_{i,j} m_{i-j} X_{i-j} \tag{5.2.27}$$

$$v_{\mathrm{SU}} = \sum v_{i-j} X_{i-j} \tag{5.2.28}$$

where X_{i-j} is the mole fraction of the SUs i–O–j, m_{i-j} and v_{i-j} are the weights and volumes of the i–O–j SUs. The vaporization and activation energies are more complex but still expressed as explicit functions of these SU mole fractions (Appendix 5.2.3.12). Model parameters were developed through systematic optimization of all available experimental

data on low and higher order systems. Special attention is given to the description of the maximum of the viscosity at intermediate ratios of amphoteric (e.g., Al^{3+}) to basic metal oxide cations commonly referred to as the "charge compensation effect." The initial formalism [36–41] was significantly modified and extended to the Na_2O- and K_2O-containing systems [42] and is currently being further improved [43].

5.2.2.4. Other Models

5.2.2.4.1 *Model due to Hanao* et al. *[48]*

Chemical system: SiO_2–Al_2O_3–CaO–MgO–Na_2O–F–FeO_t–ZrO_2–TiO_2–BaO–MnO–B_2O_3–S–C.

Applicability: Blast furnace, steelmaking, ladle slags

This model uses the neural network technique to compute slag viscosity (and solidification temperatures). The authors showed that their model gives better results than Iida's model on the selection of 142 slag of the Round Robin test project of Mills *et al.* [61].

5.2.2.4.2 *Model due to Mills* et al. *[46]*

Chemical system: SiO_2–P_2O_5–TiO_2–Al_2O_3–Fe_2O_3–B_2O_3–FeO–MnO–MgO–CaO–BaO–SrO–K_2O–Na_2O–Li_2O–CaF_2

Applicability: All kinds of slags

The National Physical Laboratory (NPL) viscosity model is based on the structurally related optical basicity (OB) concept and the Arrhenius equation (Appendix 5.2.3.6). OB is a function of the mole fractions of the different components (x_i is the mole fraction of component i, n_i refers to the number of oxygen atoms in the molecule, e.g., 3 for Al_2O_3):

$$\Lambda^{\text{corr}} = \frac{\sum x_i n_i \Lambda_i}{\sum x_i n_i} \tag{5.2.29}$$

The values of the OB of the various components are taken from Refs. [62,63].

The model is said to provide a good estimation of the viscosities of iron blast furnace slags. However, it is well known that the extrapolability of models based the OB outside a limited domain of composition can be problematic as it has been shown for some thermodynamic properties such as sulfide capacities [64].

5.2.2.4.3 *Model due to Pal* et al. *[47]*

Chemical system: SiO_2–P_2O_5–Al_2O_3–Fe_2O_3–B_2O_3–FeO–MnO–MgO–CaO–BaO–SrO–K_2O–Na_2O–Li_2O–CaF_2–Cs_2O–CoO–NiO–ZnO–PbO

Applicability: All kinds of slags

This model is based on the same approach as Urbain's model but the expression of the parameter B is given as a function of the OB of the slag and the coefficients connecting A

to B are different (Appendix 5.2.3.7). Let us note that the relation linking OB values to the parameter B is not given explicitly, only a graph is provided.

5.2.3. APPENDICES

Appendix 5.2.3.1. Urbain's Model for Steelmaking Slags [17,20,21]

$$\mu = 100AT\,\exp\left(1000B/T\right)\text{in poise}$$

$$\alpha = \frac{X_{\mathrm{M}}}{X_{\mathrm{M}} + X_{\mathrm{A}}}$$

$$X_{\mathrm{A}} = X_{\mathrm{Al_2O_3}} + X_{\mathrm{Cr_2O_3}} + X_{\mathrm{Fe_2O_3}}$$

$$X_{\mathrm{M}} = X_{\mathrm{FeO}} + X_{\mathrm{CaO}} + 2X_{\mathrm{TiO_2}} + X_{\mathrm{MgO}} + X_{\mathrm{MnO}} + X_{\mathrm{CrO}} + X_{\mathrm{K_2O}} + X_{\mathrm{Na_2O}} + 3X_{\mathrm{CaF_2}}$$

$$X_{\mathrm{T}} = X_{\mathrm{SiO_2}} + 1.6X_{\mathrm{P_2O_5}}$$

$$\Omega = \begin{pmatrix} 1 & 1 & 1 & 1 \\ 1 & 1 & 1 & 1 \\ 1 & 1 & 1 & 1 \end{pmatrix} \cdot \begin{pmatrix} 13.2 \\ 30.5 \\ -40.4 \\ 60.8 \end{pmatrix} + \alpha \cdot \begin{pmatrix} 15.9 & -54.1 & 138 & -99.8 \\ 41.5 & -117.2 & 232.1 & -156.4 \\ 20 & 26 & -110.3 & 64.3 \end{pmatrix} + \alpha^2 \cdot \begin{pmatrix} -18.6 & 33 & -112 & 97.6 \\ -45 & 130 & -298.6 & 213.6 \\ -25.6 & -56 & 186.2 & -104.6 \end{pmatrix}$$

$$B = \frac{1}{X_{\mathrm{MgO}} + X_{\mathrm{CaO}} + X_{\mathrm{MnO}}} \begin{pmatrix} X_{\mathrm{MgO}} \\ X_{\mathrm{CaO}} \\ X_{\mathrm{MnO}} \end{pmatrix}^{\mathrm{T}} \cdot \Omega \cdot \begin{pmatrix} 1 \\ X_{\mathrm{T}} \\ X_{\mathrm{T}}^2 \\ X_{\mathrm{T}}^3 \end{pmatrix}$$

$$A = \exp(-0.2693B - 11.6725)$$

Appendix 5.2.3.2. Riboud's Model [24]

$$\mu = AT\,\exp\left(B/T\right)\text{in Pas}$$

$$A = \exp\begin{pmatrix} -19.81 + 1.73\left(X_{\mathrm{CaO}} + X_{\mathrm{MnO}} + X_{\mathrm{MgO}} + X_{\mathrm{FeO}}\right) + \\ 5.82X_{\mathrm{CaF_2}} + 7.02\left(X_{\mathrm{Na_2O}} + X_{\mathrm{K_2O}}\right) - 36.76X_{\mathrm{Al_2O_3}} \end{pmatrix} \text{in PasK}^{-1}$$

$$B = 31140 - 23896\left(X_{\mathrm{CaO}} + X_{\mathrm{MnO}} + X_{\mathrm{MgO}} + X_{\mathrm{FeO}}\right)\text{in K}$$

Appendix 5.2.3.3. Iida's Model [27–29]

$$\mu = A\mu_0 \exp\left(\frac{E}{Bi^*}\right)\text{ in Pas}$$

$$A = 1.745 - 1.962 \times 10^{-3} T + 7.000 \times 10^{-7} T^2$$

$$E = 11.11 - 3.65 \times 10^{-3} T$$

(Different values for $A = 1.029\text{–}2.078 \times 10^{-3} T + 1.05 \times 10^{-6} T^2$ and $E = 28.46\text{–}2.0884 \times 10^{-2} T + 4 \times 10^{-6} T^2$ are reported in Ref. [15].)

μ_0 is the viscosity of nonnetwork-forming (hypothetical) melts:

$$\mu_0 = \sum_{i=1}^{n} \mu_{0i} X_i$$

$$\mu_0 = 1.8.10^{-7} \frac{\left[M_i (T_m)_i\right]^{1/2} \exp(H_i / RT)}{(V_m)_i^{2/3} \exp\left(H_i / R(T_m)_i\right)} \text{Pas}$$

$$H_i \equiv 5.1 (T_m)_i^{1/2}$$

M_i is the formula weight of component i
$(V_m)_I$ is the molar volume of component i
$(T_m)_I$ is the melting temperature of component i
X_i is the mole fraction of component i
Bi^* is the modified basicity index

$$Bi^* = \frac{\sum (\alpha_i W_i)_B + \alpha^*_{Fe_2O_3} W_{Fe_2O_3}}{\sum (\alpha_i W_i)_A + \alpha^*_{Al_2O_3} W_{Al_2O_3} + \alpha^*_{TiO_2} W_{TiO_2}}$$

where α and W are specific coefficient and weight percentage; A and B represent acidic oxide and basic oxide or fluoride, respectively.

α_i^* is a modified specific coefficient indicating the interaction of the amphoteric oxide with other components in slags, and would be given as a function of the basicity index Bi and the weight percentage of the amphoteric oxide W_i. Thus the modified basicity index Bi' can be obtained by taking account of the characteristic features of amphoteric oxides: the value for $a'i$ will widely vary with slag.

The values of all coefficients are given in Ref. [27].

Appendix 5.2.3.4. Koyama *et al.*'s Model [25]

$$\mu = A \exp(B/T) \text{ in poise}$$

$$\ln A = -24.2 X_{Al_2O_3} - 6.1 X_{CaO} - 12.1 X_{MgO} + 6.3 X_{CaF_2} - 19 X_{Na_2O} - 4.81560$$

$$B = \begin{pmatrix} -9259 X_{SiO_2} + 28318.6 X_{Al_2O_3} - 16563.5 X_{CaO} \\ -41364.6 X_{CaF_2} - 45510.3 X_{Li_2O} + 29012.564 \end{pmatrix}$$

Appendix 5.2.3.5. Kim *et al.*'s Model [26]

$$\mu = A\exp(B/T)\,\text{in Pa s}$$

$$\ln A = -0.046X_{SiO_2} - 0.185X_{Al_2O_3} - 0.07X_{CaO} - 0.041X_{MgO} + 0.035X_{CaF_2} - 0.095X_{B_2O_3} - 2.307$$

$$B = \begin{pmatrix} 70.68X_{SiO_2} + 312.65X_{Al_2O_3} + 32.58X_{CaO} - 176.1X_{CaF_2} \\ -34.77X_{Na_2O} - 167.4X_{Li_2O} + 59.7X_{B_2O_3} + 6807.2 \end{pmatrix}$$

Appendix 5.2.3.6. NPL's Model [46]

$$\mu = A\exp(B/T)\,\text{in Pa s}$$

$$\frac{\ln B}{1000} = -1.77 + \frac{2.88}{\Lambda^{corr}}$$

$$\ln A = -232.69(\Lambda^{corr})^2 + 357.32\Lambda^{corr} - 144.17$$

$$\Lambda^{corr} = \frac{\sum x_i n_i \Lambda_i}{\sum x_i n_i}$$

x_i is the mole fraction of component i, n_i refers to the number of oxygen atoms in the molecule, e.g., 3 for Al_2O_3.

The values of the OB Λ_I are listed in Table 5.2.2.

Appendix 5.2.3.7. Pal *et al.*'s Model [47]

$$\mu = AT\exp(1000B/T)\,\text{in poise}$$

$$-\ln A = 0.2056B + 12.492$$

B is a function of the OB not given explicitly but extracted from a graph presented by the authors. The OB is calculated as in the NPL's model (Appendix 5.2.3.6) with the coefficients given in Tables 5.2.2 and 5.2.3.

Table 5.2.2 Values of the Optical Basicity of the Different Slag Components

K_2O	Na_2O	BaO	SrO	Li_2O	CaO	MgO	Al_2O_3	TiO_2	SiO_2	B_2O_3	P_2O_5	FeO	Fe_2O_3	MnO	CaF_2
1.4	1.15	1.15	1.10	1.0	1.0	0.78	0.60	0.61	0.48	0.42	0.40	1.0	0.75	1.0	1.2

The values are taken from Refs. [62,63] except for CaF_2, for which the adopted value is 1.2.

Table 5.2.3 Values of the Optical Basicity of the Different Slag Components not Listed in Table 5.2.2

Cs_2O	Cr_2O_3	CoO	NiO	ZnO	PbO
1.7	1.0	0.95	0.9	0.95	1.15

Appendix 5.2.3.8. Tan and Vix's Model [23]

$$\mu = AT\exp(1000B/T)$$

$$-\ln A = mB + n$$

$$B = \sum_{i=1}^{3} b_i^{SiO_2} X_{SiO_2}^i + \sum_{i=0}^{3}\sum_{j=1}^{2}\left(\frac{b_i^{ZnO,j}X_{ZnO} + b_i^{CaO,j}X_{CaO} + b_i^{FeO,j}X_{FeO}}{X_{ZnO} + X_{CaO} + X_{FeO}}\right)\left(\frac{X_{ZnO} + X_{CaO} + X_{FeO}}{X_{ZnO} + X_{CaO} + X_{FeO} + X_{Al_2O_3}}\right)X_{SiO_2}^i$$

$$m = m_{ZnO}X_{ZnO} + m_{Al_2O_3}X_{Al_2O_3} + m_{CaO}X_{CaO} + m_{SiO_2}X_{SiO_2} + m_{FeO}X_{FeO}$$

Appendix 5.2.3.9. Jak and Kondratiev Model [32]

$$\mu = AT\exp(1000\mathrm{B}/\mathrm{T})$$

$$-\ln A = mB + n$$

$$B = \sum_{i=1}^{3} b_i^0 X_{SiO_2}^i + \sum_{i=0}^{3}\sum_{j=1}^{2}\left(\frac{b_i^{CaO,j}\times X_{CaO} + b_i^{FeO,j}\times X_{FeO}}{X_{CaO} + X_{FeO}}\right)\left(\frac{X_{CaO} + X_{FeO}}{X_{CaO} + X_{FeO} + X_{Al_2O_3}}\right)^j X_{SiO_2}^i$$

$$m = m_{Al_2O_3}X_{Al_2O_3} + m_{CaO}X_{CaO} + m_{FeO}X_{FeO} + m_{SiO_2}X_{SiO_2}$$

Model parameters (10^{-1} Pa s) [32].

	j/i	0	1	2	3		
b_i^0	0	13.31	36.98	−177.70	190.03	n	9.322
$b_i^{CaO,j}$	1	5.50	96.20	117.94	−219.56	m_F	0.665
	2	−4.68	−81.60	−109.80	196.00	m_C	0.587
$b_i^{FeO,j}$	1	34.30	−143.64	368.94	−254.85	m_A	0.370
	2	−45.63	129.96	−210.28	121.20	m_S	0.212

Appendix 5.2.3.10. Nakamoto *et al.*'s model [45]

$$\eta = A\exp\left(\frac{E_V}{S}\right)$$
$$A = 4.80\times10^{-8}(\text{Pas})$$
$$E_V = \left(\frac{E}{1+(\alpha_m)^{1/2}}\right)$$
$$E = 5.21\times10^{5}(\text{J})$$

$$\alpha_m = \sum_{i=1}^{m}\alpha_{(M_i)_{u_i}O_{v_i}}(N_{Si-O-M_i}+N_{M_i-O-M_i}) + \sum_{i=1}^{m-1}\sum_{j=i+1}^{m}\frac{\left(\alpha_{(M_i)_{u_i}O_{v_i}}+\alpha_{(M_j)_{u_j}O_{v_j}}\right)}{2}N_{M_i-O-M_j}$$

where m is the number of oxides (excluding SiO_2), $N_{M_i-O-M_j}$ is the number of cells M_i–O–M_j as given by IRSID slag model, $\alpha_{(M_i)_{u_i}O_{v_i}}$ is a constant equal to 2 for CaO, 3.8 for FeO, and 0.95 for Al_2O_3

Appendix 5.2.3.11. Reddy and Hebbar's Model [30]

$$\mu = 4.9\times10^{-10}N_{O^0}T^{1/2}\exp\left(\frac{E}{RT}\right)\text{in Pas}$$
$$N_{O^0} = \frac{4-4X_{MO}-N_{O^-}}{2(2-X_{MO})}$$

where X_{MO} is the mole fraction of the metal oxide, N_{O^-} is calculated using the following equation:

$$\left(1-\exp\left(\frac{\Delta G^0}{RT}\right)\right)(N_{O^-})^2+(2X_{MO}-4)N_{O^-}+8X_{MO}(1-X_{MO})=0$$

ΔG^0 is the free enthalpy variation of the depolymerization reaction (−19193.55 to 2.96T J mol^{-1} for FeO–SiO_2)

$$E = \alpha+\beta N_{O^0}+\gamma(N_{O^0})^2+\delta(N_{O^0})^3+\varepsilon(N_{O^0})^4$$

For FeO–SiO_2:

$$\alpha = 703820.4981 - 1222.06 \times 10^{6}/T + 78587.57 \times 10^{-7}/T^{2}$$

$$\beta = 1/\left(-1103.44 \times 10^{-15}(-839.0098 + T)^{2} - 1870.26 \times 10^{-9}\right)$$

$$\gamma = 954182.1129 + 1921.929T - 0.7953T^{2}$$

$$\delta = 1077387.1 - 5732.0204T + 1.8542T^{2}$$

$$\varepsilon = -809470.4 + 3459.2634T - 1.0581T^{2}$$

Appendix 5.2.3.12. Jak *et al.*'s Model [42]

$$\mu = \frac{2RT}{\Delta E_v}\frac{(2\pi m_{\mathrm{SU}} kT)^{1/2}}{v_{\mathrm{SU}}^{2/3}}\exp\left(\frac{E_a}{RT}\right)\mathrm{in\,Pas}$$

where m_{SU}, v_{SU}, E_a, and ΔE_v are expressed through the molar fractions of the structural units X_{i-j} and "i" and "j" indicate Al, Ca, Fe, K, Mg, Na, KAl, and NaAl metal cations of SUs.

The average mass and volume of SU are expressed as $m_{\mathrm{SU}} = \sum_{i,j} m_{i-j}X_{i-j}$ and $v_{\mathrm{SU}} = \sum v_{i-j}X_{i-j}$:

The integral molar viscosity energies terms coefficients (J mol^{-1}) in the equations $E_a = \sum E_{a,i-j}X_{i-j}$ and $\Delta E_v = \exp(\sum \varepsilon_{v,i-j}X_{i-j})$, respectively, are:

$$\begin{aligned}E_{a,\mathrm{Si-Si}} = {} & 80{,}900 + 464{,}963X^{2}{}_{\mathrm{Si-Si}} + 498{,}451X_{\mathrm{Si-Al}} + 233{,}696X_{\mathrm{Si-Ca}} \\ & + 516{,}645X_{\mathrm{Fe-Si}} + 277{,}000X_{\mathrm{Mg-Si}} + 210{,}000X_{\mathrm{Si-K}} - 320{,}000X^{1/5}{}_{\mathrm{Si-K}}X^{5}{}_{\mathrm{Si-Si}} \\ & + 500{,}000X^{2}{}_{\mathrm{Na-Si}} - 270{,}000X^{1/5}{}_{\mathrm{Na-Si}}X^{5}{}_{\mathrm{Si-Si}} + 436{,}800X_{\mathrm{Si-KAl}} \\ & + 600{,}000X_{\mathrm{Si-NaAl}};\end{aligned}$$

$$E_{a,\mathrm{Al-Al}} = 129{,}911;\quad E_{a,\mathrm{Ca-Ca}} = 82{,}126;\quad E_{a,\mathrm{Fe-Fe}} = 49{,}504;\quad E_{a,\mathrm{K-K}} = 35{,}000;$$

$$E_{a,\mathrm{Mg-Mg}} = 105{,}890;\quad E_{a,\mathrm{Na-Na}} = 30{,}000;$$

$$E_{a,\mathrm{Si-Al}} = 277{,}533 + 73{,}759X_{\mathrm{Si-Ca}} - 270{,}000X_{\mathrm{Fe-Si}} + 562{,}671X_{\mathrm{Al-Ca}} + 743{,}000X_{\mathrm{Al-Fe}};$$

$$\begin{aligned}E_{a,\mathrm{Si-Ca}} = {} & 119{,}885 - 7300X_{\mathrm{Fe-Si}} - 20{,}000X_{\mathrm{K-Si}} + 18{,}540X_{\mathrm{Mg-Si}} - 90{,}000X_{\mathrm{Na-Si}} \\ & + 29{,}000X_{\mathrm{Al-Ca}} + 37{,}000X_{\mathrm{Fe-Ca}};\end{aligned}$$

$$E_{a,\mathrm{Si-Fe}} = 28{,}120 + 95{,}145X_{\mathrm{Mg-Si}} + 120{,}000X_{\mathrm{Fe-Al}} - 753{,}000X_{\mathrm{Fe-Ca}} - 180{,}000X_{\mathrm{Mg-Fe}};\quad E_{a,\mathrm{Si-K}} = 50{,}000;\quad E_{a,\mathrm{Si-Na}} = 50{,}000;$$

SU	Si–Si	Al–Al	Ca–Ca	Fe–Fe	K–K	Mg–Mg	Na–Na	KAl–KAl	NaAl–NaAl	Si–Al	Si–Ca	Fe–Si	Si–K	Mg–Si	NaSi
m, SU $\times 10^{-26}$ kg	4.99	5.64	9.31	11.93	15.64	6.69	10.29	16.29	13.61	5.32	7.15	8.46	10.32	5.84	7.64
v, SU $\times 10^{-29}$ m^3	1.92	3.03	5.79	4.34	9.00	3.99	5.94	14.98	10.81	2.43	3.50	2.96	4.58	2.83	3.56

MP, SU	Si–KAlO	Si–NaAl	Ca–Al	Fe–Al	Al–K2	Al–KAlO	Mg–Al	Na–Al	Al–NaAl	Fe–Ca	Ca–K	Ca–KAlO	Mg–Ca	Na–Ca	Ca–NaAl
m, SU $\times 10^{-26}$ kg	10.64	9.30	7.48	8.79	8.79	10.97	6.17	7.97	9.63	10.62	12.48	12.80	8.00	9.80	11.46
v, SU $\times 10^{-29}$ m^3	6.29	5.15	4.27	3.65	5.49	7.49	3.49	4.32	6.12	5.03	7.28	9.67	4.84	5.86	8.04

MP, SU	Fe–K	Mg–Fe	Fe–Na	Mg–K	Na–K	Mg–Na	Fe–KAlO	K–KAlO	Na–NaAl	Fe–NaAl	K–NaAl	Mg–KAlO	Mg–NaAl	Na–KAlO	KAl–NaAl
m, SU $\times 10^{-26}$kg	13.79	9.31	11.11	11.17	12.97	8.49	14.11	15.96	11.95	12.77	14.63	11.49	10.15	11.95	14.95
v, SU $\times 10^{-29}$ m^3	6.39	4.16	2.40	6.16	7.47	4.90	8.59	11.74	8.13	7.09	9.88	8.41	6.84	9.88	12.91

$$E_{a,\mathrm{Si-Mg}} = 100{,}420 + 150{,}000X_{\mathrm{Mg-Al}} + 100{,}000X_{\mathrm{Mg-Ca}} + 270{,}000X_{\mathrm{Mg-Fe}};$$
$$E_{a,\mathrm{Al-Fe}} = 99{,}708; \quad E_{a,\mathrm{Al-Mg}} = 132{,}651;$$

$$E_{a,\mathrm{Si-KAl}} = 403{,}200 - 70{,}000X_{\mathrm{Si-Al}} + 10{,}000X_{\mathrm{Si-Ca}} - 200{,}000X_{\mathrm{Fe-Si}}; \quad E_{a,\mathrm{Ca-Al}} = 183{,}400 - 1780X_{\mathrm{Fe-Al}} + 55{,}771X_{\mathrm{Al-Mg}};$$

$$\text{the rest } E_{a,i-j} = 0.5\left(E_{a,i-i} + E\varepsilon_{a,j-j}\right).$$

$$\varepsilon_{a,\mathrm{Si-Si}} = 17.34 + 11.12X_{\mathrm{Si-Si}} - 6.22X^2{}_{\mathrm{Si-Si}} + 1.06X_{\mathrm{Si-Al}} + 0.06X_{\mathrm{Fe-Si}} + 0.05X_{\mathrm{Mg-Si}} + 1.80X_{\mathrm{Si-K}} + 1.80X_{\mathrm{Si-Na}};$$

$$\varepsilon_{a,\mathrm{Al-Al}} = 13.59; \quad \varepsilon_{a,\mathrm{Ca-Ca}} = 13.02; \quad \varepsilon_{a,\mathrm{Fe-Fe}} = 11.25; \quad \varepsilon_{a,\mathrm{K-K}} = 11.00;$$
$$\varepsilon_{a,\mathrm{Mg-Mg}} = 13.85; \quad \varepsilon_{a,\mathrm{Na-Na}} = 11.00;$$

$$\varepsilon_{a,\mathrm{Si-Al}} = 20.08 + 9.00X_{\mathrm{Ca-Si}}; \quad \varepsilon_{a,\mathrm{Si-Ca}} = 14.46; \quad \varepsilon_{a,\mathrm{Si-Fe}} = 9.60 + 6.00X_{\mathrm{Mg-Si}};$$
$$\varepsilon_{a,\mathrm{Si-K}} = 11.00; \quad \varepsilon_{a,\mathrm{Si-Mg}} = 13.33;$$

$$\varepsilon_{a,\mathrm{Si-Na}} = 12.30; \quad \varepsilon_{a,\mathrm{Si-KAl}} = 22.50; \quad \varepsilon_{a,\mathrm{Si-NaAl}} = 22.70; \quad \varepsilon_{a,\mathrm{Al-}} = 16.88;$$

$$\text{the rest } \varepsilon_{a,i-j} = 0.5\left(\varepsilon_{a,i-i} + \varepsilon_{a,j-j}\right).$$

REFERENCES

[1] A.D. Pelton, S.A. Degterov, G. Eriksson, C. Robelin, Y. Dessureault, Metall. Mater. Trans. B 31B (2000) 651.
[2] A.D. Pelton, P. Chartrand, Metall. Mater. Trans. A 32A (2001) 1355.
[3] C.W. Bale, E. Belisle, P. Chartrand, S.A. Decterov, G. Eriksson, K. Hack, I.H. Jung, Y.B. Kang, J. Melancon, A.D. Pelton, C. Robelin, S. Petersen, Comput. Coupling Phase Diagrams Thermochem. 33 (2009) 295.
[4] A.N. Grundy, H. Liu, I.-H. Jung, S.A. Decterov, A.D. Pelton, Int. J. Mater. Res. 99 (2008) 1185.
[5] A.N. Grundy, I.-H. Jung, A.D. Pelton, S.A. Decterov, Int. J. Mater. Res. 99 (2008) 1195.
[6] W.-Y. Kim, X. Yang, L. Yan, A.D. Pelton, S.A. Decterov, Comput. Coupling Phase Diagrams Thermochem. 35 (2011) 542.
[7] E. Brosh, A.D. Pelton, S.A. Decterov, Int. J. Mater. Res. 103 (2012) 537.
[8] W.-Y. Kim, A.D. Pelton, S.A. Decterov, Metall. Mater. Trans. B 43 (2012) 325.
[9] W.-Y. Kim, Ph.D. Thesis, Ecole Polytechnique de Montreal, Montreal, Canada, 2011.
[10] B. Mysen, Eur. J. Mineral. 15 (2003) 781.
[11] W.J. Malfait, W.E. Halter, Y. Morizet, B.H. Meier, R. Verel, Geochim. Cosmochim. Acta 71 (2007) 6002.
[12] D.W. Matson, S.K. Sharma, J.A. Philpotts, J. Non-Cryst. Solids 58 (1983) 323.
[13] E. Jak, in: Molten Slags and Salts 2009, Santiago, Chile, 2009, p. 434.
[14] A. Fluegel, Glass Technol. Eur. J. Glass Sci. Technol. A 48 (2007) 13.
[15] T. Matsushita, M. Hayashi, S. Seetharaman, Int. J. Mater. Prod. Technol. 22 (2005) 351.
[16] K. Santhy, T. Sowmya, S.R. Sankaranarayanan, ISIJ Int. 45 (2005) 1014.
[17] G. Urbain, Trans. J. Br. Ceram. Soc. 80 (1981) 139.
[18] E.A. Guggenheim, Mixtures, The Clarendon Press, Oxford, 1952.

[19] M. Blander, A.D. Pelton, in: 2nd International Symposium on Metallurgical Slags and Fluxes, TMS-AIME, Warrendale, PA, 1984, p. 295.
[20] G. Urbain, Steel Res. 58 (1987) 111.
[21] G. Urbain, M. Boiret, Mémoires et Etudes Scientifiques Revue de Métallurgie, 1989), p. 209.
[22] D. Mudersbach, P.M. Drissen, M. Kühn, J. Geiseler, Steel Res. 72 (2001) 86.
[23] P. Tan, P. Vix, in: EPD Congress TMS, 2005, p. 713.
[24] P.V. Riboud, Y. Roux, D. Lucas, H. Gaye, Fachber. Huttenprax. Metallweiterverarb. 19 (1981) 859.
[25] K. Koyama, Y. Nagano, T. Nakano, Seitetsu kenkyu Nippon Steel Technical Report 324 (1987) 39.
[26] J.W. Kim, J. Choi, O.D. Kwon, I.R. Lee, Y.K. Shin, J.S. Park, in: Proceedings of 4th International Conference on Molten Slags and Fluxes, ISIJ, Sendaï, 1997, p. 468.
[27] T. Iida, H. Sakai, Y. Kita, K. Shigeno, ISIJ Int. 40 (Suppl.) (2000) S110.
[28] T. Iida, H. Sakai, T. Kawasima, Y. Kurihara, in: Proceedings of 5th International Conference on Molten Slags, Fluxes and Salts' 97, Iron & Steel Society, Sydney, Australia, 1997, p. 877.
[29] T. Iida, H. Sakai, Y. Kita, K. Murakami, High Temp. Mater. Proc. 19 (2000) 153.
[30] R.G. Reddy, K. Hebbar, Miner. Metall. Proc. (USA) 18 (2001) 195.
[31] F.Z. Ji, Du Sichen, S. Seetharaman, Ironmaking Steelmaking Slags 25 (1998) 309.
[32] A. Kondratiev, E. Jak, Metall. Mater. Trans. 32B (2001) 1015.
[33] A. Kondratiev, E. Jak, Metall. Mater. Trans. 32B (2001) 1027.
[34] A. Kondratiev, E. Jak, P. Hayes, JOM 54 (2002) 41.
[35] E. Jak, A. Kondratiev, S. Christie, P.C. Hayes, Metall. Mater. Trans. 34B (2003) 595.
[36] A. Kondratiev, E. Jak, Metall. Mater. Trans. 36B (2005) 623.
[37] A. Kondratiev, P. Hayes, E. Jak, ISIJ Int. 46 (2006) 359.
[38] A. Kondratiev, P. Hayes, E. Jak, ISIJ Int. 46 (2006) 368.
[39] A. Kondratiev, P. Hayes, E. Jak, ISIJ Int. 46 (2006) 375.
[40] A. Kondratiev, P. Hayes, E. Jak, ISIJ Int. 48 (2008) 7.
[41] A. Kondratiev, P. Hayes, E. Jak, Curr. Adv. Mater. Process. 18 (2005) 821.
[42] E. Jak, in: VIII International Conference on Molten Slags, Fluxes and Salts, GECAMIN, Santiago, Chile, 2009, , ISBN: 978-956-8504-205, 2009, p. 433.
[43] M. Suzuki, E. Jak, in: MOLTEN 12, The 9th International Conference on Molten Slags, Fluxes and Salts, Beijing, China, 2012, paper # w68.
[44] L. Zhang, S. Jahanshahi, Metall. Mater. Trans. 29B (1998) 177.
[45] M. Nakamoto, J. Lee, T. Tanaka, ISIJ Int. 45 (2005) 651.
[46] K. Mills, S. Sridhar, Ironmaking Steelmaking 26 (1999) 262.
[47] S.K. Pal, P. Choudhury, S. Sircar, H.S. Ray, Trans. Indian Ceram. Soc. 64 (2003) 213.
[48] M. Hanao, M. Kawamoto, T. Tanaka, M. Nakamoto, ISIJ Int. 46 (3) (2006) 346.
[49] H.D. Weyman, Kolloid Z. Z. Polym. 181 (1962) 131.
[50] J. Frenkel, Kinetic Theory of Liquids, Clarendon Press, Oxford, United Kingdom, 1946.
[51] P. Riboud, M. Larrecq, NOH-BOS Conference, AIME, Detroit, 1979.
[52] L. Holappa, L. Forsback, Z. Han, ISIJ Int. 46 (2006) 394.
[53] E.T. Turkdogan, Physical Chemistry of High Temperature Technology, Academic Press Inc, New York, 1980.
[54] R.G. Reddy, K. Hebbar, in: TMS EPD Congress, 1991, p. 523.
[55] S. Seetharaman, Du Sichen, Metall. Mater. Trans. B 25B (1994) 5895.
[56] S. Seetharaman, Du Sichen, J.Y. Zhang, JOM 51 (1999) 38.
[57] S. Seetharaman, K. Mukai, Du Sichen, Steel Res. Int. 76 (2005) 267.
[58] L. Zhang, S. Jahanshahi, S. Sun, C. Chen, B. Bourke, S. Wright, M. Somerville, JOM 54 (2002) 51.
[59] S. Jahanshahi, S. Sun, L. Zhang, J. S. Afr. Inst. Min. Metall. (2004) 529.
[60] H. Eyring, J. Chem. Phys. 4 (1936) 283.
[61] K.C. Mills, L. Chapman, A. Fox, S. Sridhar, Scand. J. Metall. 30 (2001) 396.
[62] D. Sommerville, Y. Yang, Aust. IIM Proc. 306 (2001) 71.
[63] M. Susa, K. Mills, Slag Atlas, Second ed., Verlag Stahleisen GmbH, Düsseldorf, 1995.
[64] J. Lehmann, H. Gaye, Rev. Int. Hautes Temp. Réfract. Fr. 28 (1992-1993) 81.

[65] W.E. Halter, B.O. Mysen, Melt speciation in the system Na_2O–SiO_2, Chem. Geol. 213 (2004) 115–123.
[66] T. Yano, S. Shibata, T. Maehara, Structural equilibria in silicate glass melts investigated by Raman spectroscopy. J. Am. Ceram. Soc. 89 (2006) 89–95.
[67] J. Machacek, O. Gedeon, Q-species in alkali-disilicate glasses. Ceramics 47 (2003) 45–49.
[68] H. Maekawa, T. Maekawa, K. Kawamura, T. Yokokawa, The structural groups of alkali silicate glasses determined from silicon-29 MAS-NMR, J. Non-Cryst. Solids 127 (1991) 53–64.

CHAPTER 5.3

Applications

In-Ho Jung[a], Jean Lehmann[b] and Evgueni Jak[c]

[a]Department of Mining and Materials Engineering, McGill University, Montreal, Canada
[b]ArcelorMittal, Global R&D, Maizières-lès-Metz Cedex, France
[c]School of Chemical Engineering, University of Queensland, Queensland, Australia

LIST OF SYMBOLS

$[wt\%S(t)]_{metal}$ steel sulfur content at time t
$(wt\%S(t))_{slag}$ slag sulfur content at time t
$[wt\%S]_{metal}$ and $(wt\%S)_{slag}$ sulfur content in steel and slag, respectively. When the subscript "metal" is omitted **[wt%S]** refers to the steel S-content
A surface of the slag/metal interface (m^2)
$a_{\underline{O}}$, $a_{\underline{S}}$ activity in oxygen and sulfur, respectively, in liquid steel (reference state 1 wt% diluted solution in liquid Fe)
B kinetic desulfurization parameter
C'_S sulfide capacity of the slag at the treatment temperature (reference states: 1 wt% diluted solution in liquid iron)
C_S sulfide capacity of the slag at the treatment temperature (reference states: pure gaseous species)
$f_{\underline{S}}$ activity coefficient of sulfur in liquid steel ($a_S = f_S$[wt%S])
K_S desulfurization kinetic coefficient (m/s)
R desulfurization ratio (−)
T absolute temperature (K)
V metal volume (m^3)
λ thermodynamic desulfurization parameter: $\lambda = L_S M$ = sulfur metal–slag equilibrium partition coefficient · slag mass (t per ton of steel)

5.3.1. APPLICATIONS TO STEELMAKING PROCESSES

5.3.1.1. Overview of Steelmaking Processes and Chemistry

5.3.1.1.1 Steelmaking Process

Liquid iron called pig iron is produced from the Blast Furnace (BF) where iron ores are reduced by coals (cokes) and injected air. During the reduction process, the gangue forms a molten oxide phase called slag. In order to enhance the slagging in the BF, $CaCO_3$, and others are also added as fluxes. Molten iron tapped from the BF contains a high level of impurities (3–5C, 0.2–0.3Mn, 0.2–1.5Si, 0.06–0.12P, 0.02S in wt%). Pig iron is then transferred to the Basic Oxygen Furnace (BOF) using a so-called torpedo car. The dephosphorization and desulfurization processes are frequently carried out in the torpedo car during the transfer to the BOF in order to reduce the burden for BOF

Treatise on Process Metallurgy, Volume 2
http://dx.doi.org/10.1016/B978-0-08-096984-8.00032-X
© 2014 Elsevier Ltd.
All rights reserved.

and secondary steelmaking processes. This is called the hot metal pretreatment. The main role of the BOF process is the reduction of carbon (decarburization) and phosphorus (dephosphorization) contained in molten iron by blowing oxygen. After the BOF process, liquid steel containing $C < 0.05$ wt% is tapped in a ladle. Since liquid steel after the BOF still contains a high amount of oxygen (>0.05 wt%) and other impurities such as C, S, P, and H, a secondary steelmaking process (also called ladle refining process) is necessary to produce clean steels. Various unit equipments are used in the secondary refining process to remove impurities. For example, oxygen can be reduced by adding deoxidants such as Al, Mn, and Si directly into molten steel. Gaseous elements like C and H can be further reduced in a vacuum degasser (RH). P and S can be further removed through chemical reactions with the top slag covering molten steel. The liquid steel temperature can be increased and the chemical composition of molten steel can be homogenized in a Ladle Furnace (LF). After the refining process, the steel chemistry can be adjusted by the addition of alloying elements to meet various steel grades. Molten steel is finally transferred to a tundish for casting in forms of slab, billet, or broom. In the continuous casting process, oxyfluoride mold flux is normally used as a lubricant between steel and the water-cooled Cu mold. When molten steel is produced from an Electric Arc Furnace (EAF) using steel scraps, it is directly moved to the secondary refining process. In the case of stainless steel production, primary stainless steel is generally produced from an EAF. It is further refined to mainly reduce C and P using special degasser equipments such as an argon oxygen degasser (AOD) and a vacuum oxygen degasser (VOD).

5.3.1.1.2 Overview of Chemistry

Obviously, the most important phases and chemical constituents involved in the steelmaking process are Fe-rich metallic phases, oxide, oxysulfide, and oxyfluoride phases. The important chemical systems for each steelmaking process can be listed up as follows:

(1) Molten slag for refining process
- **(a)** $CaO–FeO–Fe_2O_3–SiO_2–MgO–P_2O_5$ system: BOF process
- **(b)** $CaO–MgO–Al_2O_3–SiO_2–FeO–Fe_2O_3$ system: ladle refining process
- **(c)** $CaO–MgO–SiO_2–CaF_2$ system: stainless steel refining
- **(d)** $CaO–CrO–Cr_2O_3–MgO–SiO_2$ system: AOD and VOD process for stainless steel
- **(e)** $CaO–MgO–SiO_2–MnO–CrO–Cr_2O_3$ system: high Mn stainless steel

(2) Mold flux for casting process
- **(a)** $CaO–MgO–Al_2O_3–SiO_2–Na_2O–Li_2O–F$ system: conventional process
- **(b)** $CaO–MgO–Al_2O_3–SiO_2–Na_2O–Li_2O–B_2O_3$ system: new candidate

(3) Nonmetallic inclusions
- **(a)** $CaO–Al_2O_3–MgO–CaS$: conventional low carbon steels
- **(b)** $MnO–SiO_2–Al_2O_3–CaO–MnS$: wire steels and free cutting steels
- **(c)** $MnO–SiO_2–Ti_2O_3–TiO_2–Al_2O_3$: high-strength steels

(d) Al_2O_3–Ti_2O_3–TiO_2: interstitial-free (IF) steels
(e) Ti–Nb–C–N: high-strength low-alloy (HSLA) steels containing Ti and Nb

(4) Refractories
(a) MgO–C: BOF and RH vessel refractories, ladle slag line
(b) MgO–Al_2O_3: ladle castable
(c) MgO–Cr_2O_3–FeO–Fe_2O_3–Al_2O_3: VOD and AOD refractories
(d) Al_2O_3–ZrO_2–SiO_2–C: nozzle refractories and tundish plugs

The followings are important slag and solid oxide phases which can be encountered in steelmaking process:

(a) slag (molten oxide): SiO_2–CaO–MgO–Al_2O_3–FeO–Fe_2O_3–MnO–TiO_2–Ti_2O_3–CrO–Cr_2O_3–Na_2O–Li_2O–B_2O_3 with minor gas solubilities of S, P, F, H, C, and N.
(b) monoxide (halite): CaO–MgO–FeO–MnO with limited solubilities of Al_2O_3 and Fe_2O_3, which encompasses well-known lime (CaO), periclase (MgO), and wustite (FeO). A solid miscibility gap exists between CaO- and MgO-rich monoxides.
(c) α- and α′-Ca_2SiO_4: $(Ca,Mg,Fe,Mn)_2SiO_4$, which is a Ca_2SiO_4-rich phase.
(d) olivine: $(Mg,Fe,Ca,Mn)[Mg,Fe,Ca,Mn]SiO_4$, which covers forsterite (Mg_2SiO_4), fayalite (Fe_2SiO_4), γ-Ca_2SiO_4, monticellite $CaMgSiO_4$, and tephroite Mn_2SiO_4.
(e) corundum: $(Al,Cr,Fe)_2O_3$, which is a solution of Al_2O_3, Cr_2O_3, and Fe_2O_3. Solid miscibility gaps exist between the constituents below about 1100 °C.
(f) spinel: $(Mg,Fe^{2+},Cr^{2+},Mn^{2+},Al^{3+},Fe^{3+})[Mg,Fe^{2+},Cr^{2+},Al^{3+},Fe^{3+},Cr^{3+},Mn^{3+},Va]_2O_4$, which is an extensive solid solution containing $MgAl_2O_4$, $MgCr_2O_4$, $MgFe_2O_4$, $FeCr_2O_4$, Fe_3O_4, $FeAl_2O_4$, Cr_3O_4, $MnAl_2O_4$, $MnCr_2O_4$, $MnFe_2O_4$, etc.
(g) mullite: nonstoichiometric $3Al_2O_3{\cdot}2SiO_2$ phase.
(h) wollastonite: $(Ca,Mg,Mn)SiO_3$, which is a $CaSiO_3$ rich phase stable below 1300 °C. Pseudo-wollastonite is stoichiometric $CaSiO_3$ stable below 1550 °C.
(i) melilite: $Ca_2[Mg,Fe^{2+},Fe^{3+},Al](Fe^{3+},Al,Si)_2O_7$. Akermanite $Ca_2MgSi_2O_7$ and gehlenite $Ca_2Al_2SiO_7$ form the melilite solid solution stable below 1590 °C.
(j) pyroxene: $(Mg,Ca,Fe)[Mg,Fe]Si_2O_6$, which is a $MgSiO_3$-rich phase stable below 1560 °C. proto-, ortho-, and low-clino-pyroxenes exist. Clino-pyroxene is a $CaMg_2SiO_6$-rich phase, which is stable below 1390 °C.
(k) pseudo-brookite: $(Fe,Mg,Mn,Ti^{3+})[Ti^{3+},Ti^{4+}]_2O_5$, which is a solution of Ti_3O_5, $MnTi_2O_5$, $MgTi_2O_5$, and $FeTi_2O_5$.
(l) ilmenite: $(Fe,Mg,Mn,Ti^{3})[Ti^{3+},Ti^{4+}]O_3$, which is a solution of Ti_2O_3, $MnTiO_3$, $MgTiO_3$, and $FeTiO_3$.
(m) rhodonite: $(Mn,Ca)SiO_3$, which is a $MnSiO_3$-rich solid stable below 1300 °C.
(n) (Ti,Nb)(C,N): solid precipitates form during or after solidification of steels. FCC solution of TiC, TiN, NbC, and NbN with miscibility gaps.
(o) various stoichiometric compounds including SiO_2, $xCaO{\cdot}yAl_2O_3$, anorthite $CaAl_2Si_2O_8$, CaS, CaF_2, cuspidine $Ca_4Si_2F_2O_7$.

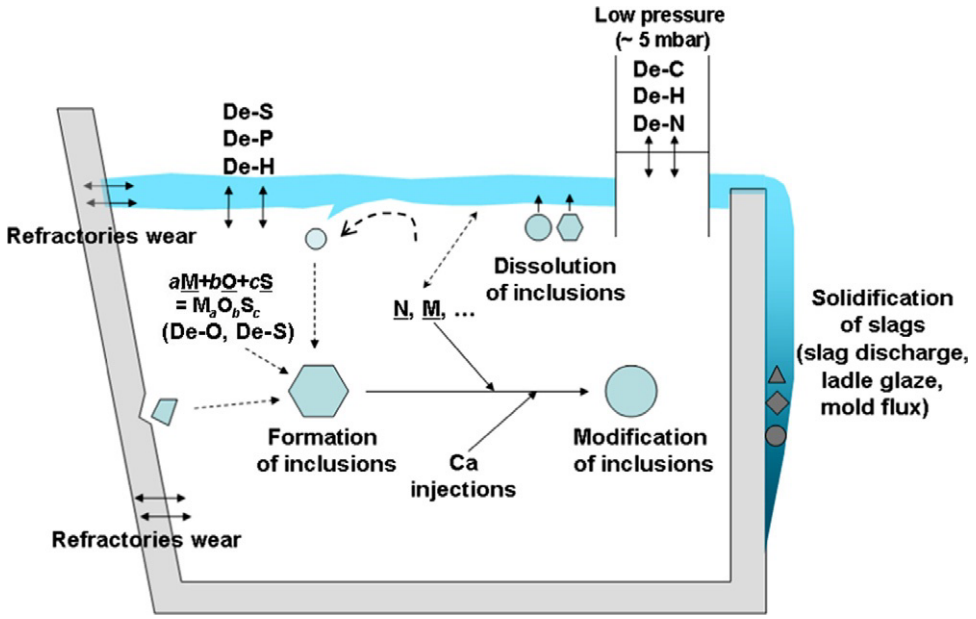


Figure 5.3.1 Schematic diagram for major chemical reactions occurring in the steelmaking process.

5.3.1.1.3 Chemical Reactions

Figure 5.3.1 shows a schematic diagram of the main chemical reactions occurring in the steelmaking process: (1) liquid iron/inclusion, (2) liquid iron/slag, (3) slag/refractories, (4) slag/inclusion, and (5) liquid iron/refractories.

5.3.1.2. Liquid Steel Desulfurization

Desulfurization is an important step in the refining of high-quality steels for various applications. In solid steel, sulfur is mainly present as manganese sulfide (MnS) inclusions. The MnS inclusions affect the processing and properties of steel. Their volume fraction, size, shape, and distribution depend on many factors. The most important factors are the S-content, the solidification rate, the degree of hot and cold deformation, and the hot working temperatures. Since the inclusions are more plastic than steel, they act as crack initiation sites and zones of weakness during deformation. Therefore, S is detrimental to bendability, ductility, toughness, formability, weldability, and corrosion resistance. The maximum S-content that is acceptable for high-quality steel grades, such as *advanced high-strength steel* sheets, wheels, and tubes, has decreased over the years, in a context of always more severe conditions applied to steel due to thickness reduction and increase in deformation rate.

The most demanding applications of steel especially for flat products (used for car body, wheels, packaging applications, etc.) require very low levels of S (<0.003 to <0.001 wt%). It is necessary to decrease the S-content during secondary steelmaking operations (i.e., during ladle refining, before casting) in order to satisfy the ultra-low S specifications.

However, S is beneficial to machinability. Thus, higher S-levels are required for applications which are extensively machined during manufacturing. Inclusion population must be carefully adjusted, so that oxides and sulfides that precipitate remain plastic and protect carbide cutting tools from abrasion during steel product manufacturing.

5.3.1.2.1 Partitioning of Sulfur Between Slag and Metal Melts

5.3.1.2.1.1 Sulfide Capacity

During secondary steelmaking operations (i.e., alloying operations following the transformation of hot metal into steel in converters), the control of the steel S-content at very low levels requires knowledge of the properties of metallurgical slags. At the low oxygen activities prevailing during iron and steel making operations, the presence of sulfates can be excluded [1], and the reaction controlling the S partitioning between steel and slag can then be written as:

$$\mathrm{M}p\mathrm{O}(\mathrm{slag}) + \mathrm{S}(\mathrm{metal}) \rightarrow \mathrm{M}p\mathrm{S}(\mathrm{slag}) + \mathrm{O}(\mathrm{metal}) \tag{5.3.1}$$

where M stands for any cation present in the slag, p is the stoichiometric coefficient of the corresponding oxide/sulfide in the slag, and O(metal) and S(metal) are dissolved oxygen and sulfur, respectively, in the liquid metal. The capacities of a slag to extract S from a gas phase can be expressed through a reaction analogous to Equation (5.3.1) but involving gas species:

$$\mathrm{M}p\mathrm{O}(\mathrm{slag}) + \frac{1}{2}\mathrm{S}_2(\mathrm{g}) \rightarrow \mathrm{M}p\mathrm{S}(\mathrm{slag}) + \frac{1}{2}\mathrm{O}_2(\mathrm{g}) \tag{5.3.2}$$

Fincham and Richardson [2] have introduced the concept of sulfide capacity C_S defined as:

$$C_S = \left(\frac{P_{O_2}}{P_{S_2}}\right)^{1/2} (\mathrm{wt\%S})_{\mathrm{slag}} \tag{5.3.3}$$

where P_{O_2} and P_{S_2} are the partial pressures of O_2 and S_2 in the gas phase. For steelmaking applications, this quantity is often modified to refer to diluted solutions containing 1 wt% of the respective species in liquid iron:

$$C'_S = \left(\frac{a_O}{a_{\underline{S}}}\right) (\mathrm{wt\%S})_{\mathrm{slag}} \tag{5.3.4}$$

where a_i is the activity of species i in the liquid metal. The relationship between the two quantities depends only on the temperature [3]:

$$C'_S = \exp\left(-\frac{2154}{T} + 3.166\right) \cdot C_S \tag{5.3.5}$$

The usefulness of the definition appears when expressing the sulfur partition coefficient at slag/metal equilibrium L_S:

$$L_S = \frac{(\text{wt\%S})_{\text{slag}}}{[\text{wt\%S}]_{\text{metal}}} = C'_S \frac{f_{\underline{S}}}{a_{\underline{O}}} \tag{5.3.6}$$

where $f_{\underline{S}}$ is the activity coefficient for sulfur in the liquid metal, defined as $f_{\underline{S}} = a_{\underline{S}}/[\text{wt\%S}]_{\text{metal}}$, and $a_{\underline{O}}$ is the oxygen activity prevailing at the slag/metal interface where the desulfurization reaction takes place. This relation enlightens the role of the different factors controlling the reaction:

- The sulfide capacity depends only on the slag composition and on the temperature.
- $f_{\underline{S}}$ depends only on the metal composition and on the temperature. This coefficient is close to 1 for low-alloyed steel but can differ markedly from this value for other metallic liquids. For example, for hot metal (C-saturated liquid iron), this factor has a value close to 6 around 1773 K due to the effect of carbon on S activity. Such a large value favors the desulfurization reaction.
- In low-alloyed steel, $a_{\underline{O}}$ value is practically equal to the content of dissolved oxygen in the steel expressed in wt%. This activity of oxygen $a_{\underline{O}}$ depends both on metal and slag compositions and on temperature. It emphasizes that an efficient desulfurization can only take place under very reducing conditions.

5.3.1.2.1.2 Modeling

Different approaches have been proposed to correlate the sulfide capacity with the composition of slags. Among the most popular models are those that are based on the optical basicity concept as in Sosinsky and Sommerville [4] which expresses the sulfide capacity as a linear function of slag compositions. The merit lies in the simplicity of the mathematical expressions. The use on large composition domains however can lead to large prediction errors [5]. Other models use more rigid thermodynamic concepts, e.g., the model proposed by Nzotta *et al.* [6], which takes into account the possible interactions among the different components of the melt. Zhang and Toguri [7] built their approach on the concept of Flood *et al.* [8], which restricts the application domain to basic slags that contain iron oxides in equilibrium with liquid iron. Reddy and Blander [9] used the Flory polymerization model to describe the structure of the melt and to derive the expression of the sulfide capacity. This approach was later modified by Pelton *et al.* [10].

The most precise and promising models are those that are based on a comprehensive thermodynamic approach as in Lehmann and Gaye [11] and Kang and Pelton [12] in which the sulfide capacity is derived from a formulation of the Gibbs free energy of mixing in the melt.

5.3.1.2.1.3 Desulfurization During Secondary Metallurgy Operations

One of the interests to develop precise prediction models is that they provide robust tools to extrapolate experimental data which can then be used to produce useful diagrams for chemically complex systems.

Figure 5.3.2 compares the desulfurization power of some common oxides used in ferrous pyrometallurgy. It shows why lime is the most common desulfurization agent. MnO and FeO also have good desulfurizing properties, but their concentrations in slag are limited owing to the reducing conditions prevailing during desulfurization operations.

In Figure 5.3.3, isovalue lines for the quantity "$-\log(C'_S)$" calculated with the cell model are drawn at 1773 K in the Al_2O_3–CaO–SiO_2 system (which is the basic system for secondary steelmaking operations) for composition domains corresponding to completely liquid slags at this temperature. The diagram shows that the maximum values of the sulfide capacity are reached for compositions that are saturated with lime (lower part of the diagram) and that these isovalue lines remain parallel to the lime saturation isotherm for compositions of slags that are poor in silica.

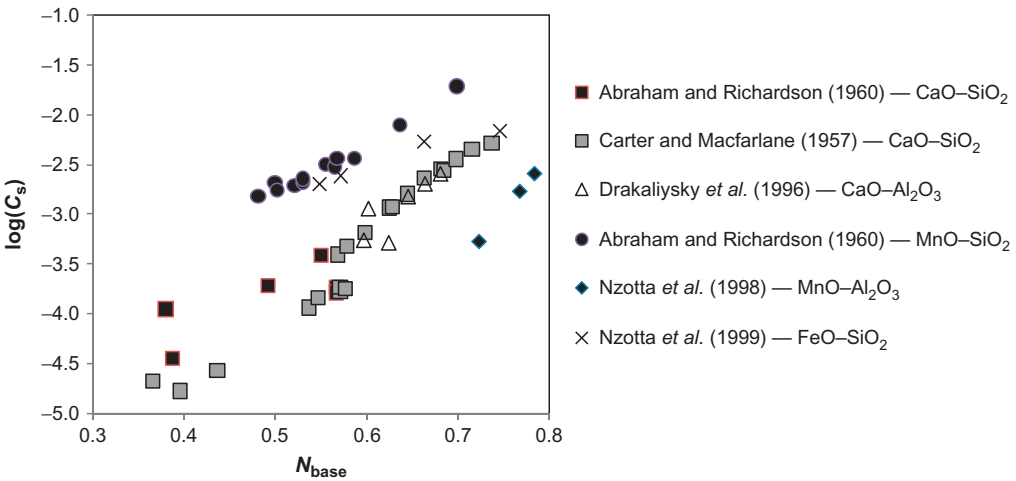


Figure 5.3.2 Variation of the sulfide capacities with the mole fraction of the basic end-member at 1773 K for binary oxide systems, composed by a basic oxide (CaO, MnO, MgO) and either an acid (SiO_2) or an amphoteric (Al_2O_3) oxide.

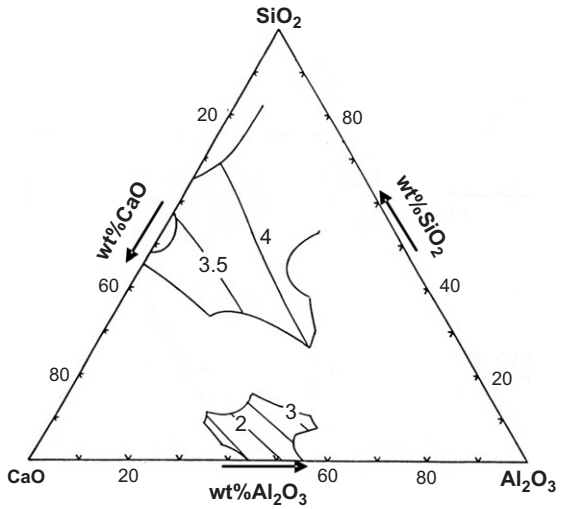


Figure 5.3.3 Calculated (cell model) iso"$-\log(C'_S)$" lines in Al_2O_3–CaO–SiO_2 melts at 1773 K. "2" on the diagram means that $\log(C'_S) = -2$.

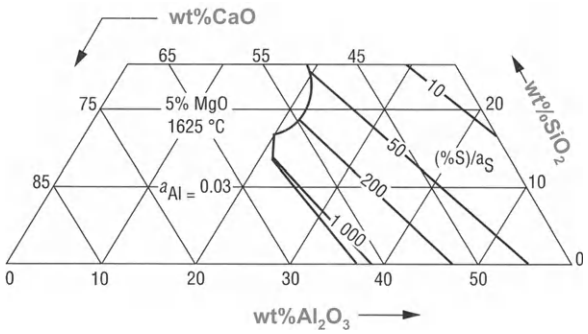


Figure 5.3.4 Sulfur partition coefficients between slag and metal at equilibrium for a metal with an Al activity of 0.03 which corresponds to a low-alloyed steel containing 0.03% Al [13].

Figure 5.3.4 has even a more straightforward practical application since it provides information about the equilibrium partitioning of S between slag and metal. In this case, the oxygen activity $a_{\underline{O}}$ at the slag/metal interface is controlled by the Al content of the steel. Steelmakers refer to this kind of grade as "Al-killed" steels since Al additions are used to deoxidize the steel. For each point on the diagram, the activity of Al_2O_3 has been calculated with the cell model and the oxygen activity has then been computed through the reaction:

$$2\mathrm{Al(metal)} + 3\mathrm{O(metal)} \rightarrow \mathrm{Al_2O_3(slag)} \tag{5.3.7}$$

The sulfur activity in the metal has been kept constant in the expression of the partition coefficient $(\mathrm{wt\%S})_{\mathrm{slag}}/a_{\underline{S}} = C'_S/a_{\underline{O}}$ in order to have a diagram applicable to any composition of steel.

Figure 5.3.4 has been plotted for slags containing 5 wt% of MgO since this content is not far from the saturation value for very basic slags. Approaching such a value is a consequence of the partial dissolution of the ladle refractory lining or is a result of the deliberate addition of magnesia or dolomite to avoid as much as possible any refractory erosion. Close to the lime saturation line (bottom of the diagram), the partition coefficient can exceed 1000, but decreases very rapidly when the slag gets enriched in Al_2O_3 and/or in SiO_2. As for the sulfide capacity, the isovalue lines of the partition coefficients are nearly parallel to the lime saturation line.

The simplified formalism developed by Riboud *et al.* [14] can be used as a very simple first approach to describe desulfurization of liquid metals. As a first approximation, the decrease of the S concentration in steel can be described as:

$$\frac{\mathrm{d}[\mathrm{wt\%S}]_{\mathrm{metal}}}{\mathrm{d}t} = -K_{\mathrm{S}} \times \frac{A}{V} \times \left([\mathrm{wt\%S}(t)]_{\mathrm{metal}} - \frac{(\mathrm{wt\%S}(t))_{\mathrm{slag}}}{L_{\mathrm{S}}} \right) \tag{5.3.8}$$

with t = treatment time (s), K_{S} = desulfurization kinetic coefficient (m/s), A = surface of the slag/metal interface (m_2), V = metal volume (m^3), $[\mathrm{wt\%S}(t)]_{\mathrm{metal}}$ = steel S-content at time t, $(\mathrm{wt\%S}(t))_{\mathrm{slag}}$ = slag S-content at time t. Hereafter, the subscript "metal" will be omitted: "wt%S" into square brackets will refer to the S-content of the metal.

The integration of the kinetic equation allows one to calculate the desulfurization ratio R, assuming first-order kinetics, a constant sulfur partition coefficient L_{S}, no S in the slag at the beginning of desulfurization, and no S loss to the gas phase:

$$R = \frac{[\mathrm{wt\%S}]_{\mathrm{final}} - [\mathrm{wt\%S}]_0}{[\mathrm{wt\%S}]_0} = \frac{1 - \exp(-B \times (1 + 1/\lambda))}{1 + 1/\lambda} \tag{5.3.9}$$

where λ is a thermodynamic parameter with

$$\lambda = L_{\mathrm{S}} \cdot M \tag{5.3.10}$$

M is the slag mass (t) per ton of steel, B is a kinetic parameter defined as:

$$B = -K_{\mathrm{S}} \times \frac{A}{V} \times t \tag{5.3.11}$$

The desulfurization kinetics is favored by a high stirring intensity. Assuming a constant L_{S}, the desulfurization ratio R depends on two parameters [14]:

- The thermodynamic parameter λ that corresponds to the slag desulfurization potential, taking into account the S equilibrium partition coefficient between slag and steel L_{S} and the specific amount of slag M in ton of slag per ton of steel.
- The kinetic parameter B that depends on the stirring time and Ar flow rate. This parameter includes the effect of stirring on the increase of interfacial area through the formation of slag droplets entrapped in steel.

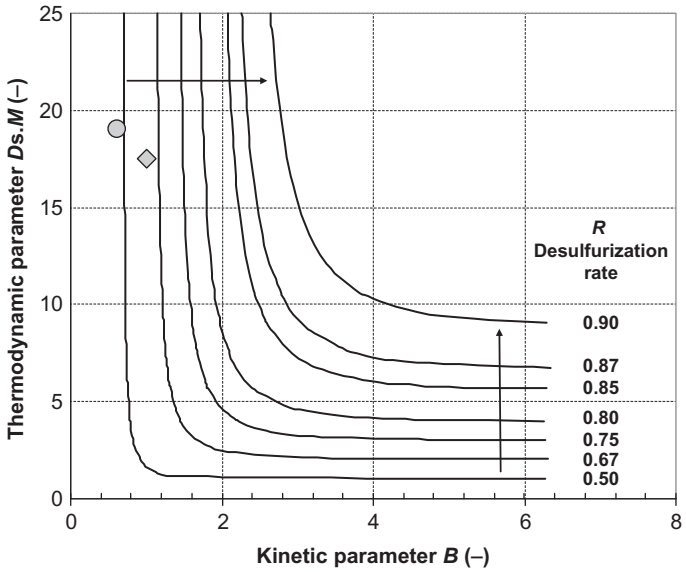


Figure 5.3.5 Desulfurization by steel–slag stirring: Example of positioning in (L_S·M, B) plane.

Figure 5.3.5 illustrates the factors which can limit the performance of this treatment. For instance, if the value of L_S·M is too low (insufficient slag mass or inappropriate slag composition), the desulfurization ratio will not exceed a certain value regardless of the intensity of the duration of the stirring.

To analyze steel desulfurization performances, thermodynamic software (as CEQCSI) can be used to determine the L_S between steel and slag. Slag mass is evaluated by multiple mass balances based on slag components and the consumption of deoxidizers. The B parameter is evaluated based on the stirring and geometrical conditions [14].

Figure 5.3.5 shows an example of positioning for steel–slag stirring at atmospheric pressure (8 min desulfurization stirring with 1500 L/min STP through a porous plug and 2000 L/min STP through a lance). To enhance desulfurization in such a case, it is not necessary to increase the specific amount of slag, or L_S, but rather to optimize desulfurization kinetics. Numerical modeling with computational fluid dynamics (CFD) codes, such as Fluent© (www.ansys.com), is a help for optimizing steel flow in ladles.

5.3.1.2.2 Future Work

Ultra-low S-grades with <0.001–0.003 wt%S are required for demanding applications as advanced high-strength steels for automotive (for reduction of vehicles weight and CO_2 footprint) and HIC (hydrogen-induced cracking) grades for plates and long distance pipes.

With the progress of basic knowledge and thermodynamic modeling to describe the partitioning of S between steel and slag, steelmakers have powerful tools to define

adequate steel and slag process to achieve good desulfurization from a thermodynamics point of view. To face the increase of ultra-low-S product share, it is necessary to still enhance the kinetics of desulfurization by steel–slag stirring at atmospheric pressure. One of ways to resolve this task is the development of coupled thermodynamic and CFD modeling taking into account the fluid flow in the ladle, considering that the liquid steel in the ladle is not any more a chemical homogeneous medium, and the local reactions [15–21].

5.3.1.3. Ca Treatment

Calcium treatment on aluminum-killed steels can be performed during secondary metallurgy operations with two main objectives:

- To improve steel castability in continuous casting, i.e., minimize nozzle blockage and therefore minimize inclusion-related surface defects in billet, bloom, and slab castings.
- To modify the shapes of the sulfides, which has several beneficial effects depending on steel grades:
  - It improves steel machinability at high cutting speeds and increases the carbide tool life.
  - It minimizes the susceptibility of steel to re-heat cracking, as in the heat-affected zones of welds.
  - It prevents lamellar tearing in large restrained welded structures.
  - It minimizes the susceptibility of HSLA linepipe steels to HIC in sour gas or sour oil environments.
  - It increases both tensile ductility and impact energy in the transverse and through-thickness directions in steels with tensile strengths below 1400 MPa.

5.3.1.3.1 The "Theory"

The principle of the Ca treatment can be best understood by looking at the phase diagram Al_2O_3–CaO (Figure 5.3.6). This diagram presents a "deep" eutectic point between the stoichiometric compounds $C_{12}A_7$ ($12CaO–7Al_2O_3$) and C_3A ($3CaO–Al_2O_3$) at a composition close to 50% Al_2O_3–50% CaO. Let us note that according to some sources, the compound is not stable [22]. The eutectic temperature is around 1673 K that is well below the liquidus temperatures of conventional steels. The Ca treatment aims at transforming alumina inclusions ($\theta_{fusion} = 2326$ K) into liquid Ca silicates inclusions close to the composition of the compound $C_{12}A_7$ in order for them to remain liquid well under the liquidus of the steel grades. Steelmakers often speak, by misnomer, of a transformation into $C_{12}A_7$, which is inappropriate since this formula refers to a solid oxide. Let us note that most of the time the inclusions will contain some amounts of other oxides as SiO_2 and MgO which modify their liquidus temperatures. These elements can be due to the

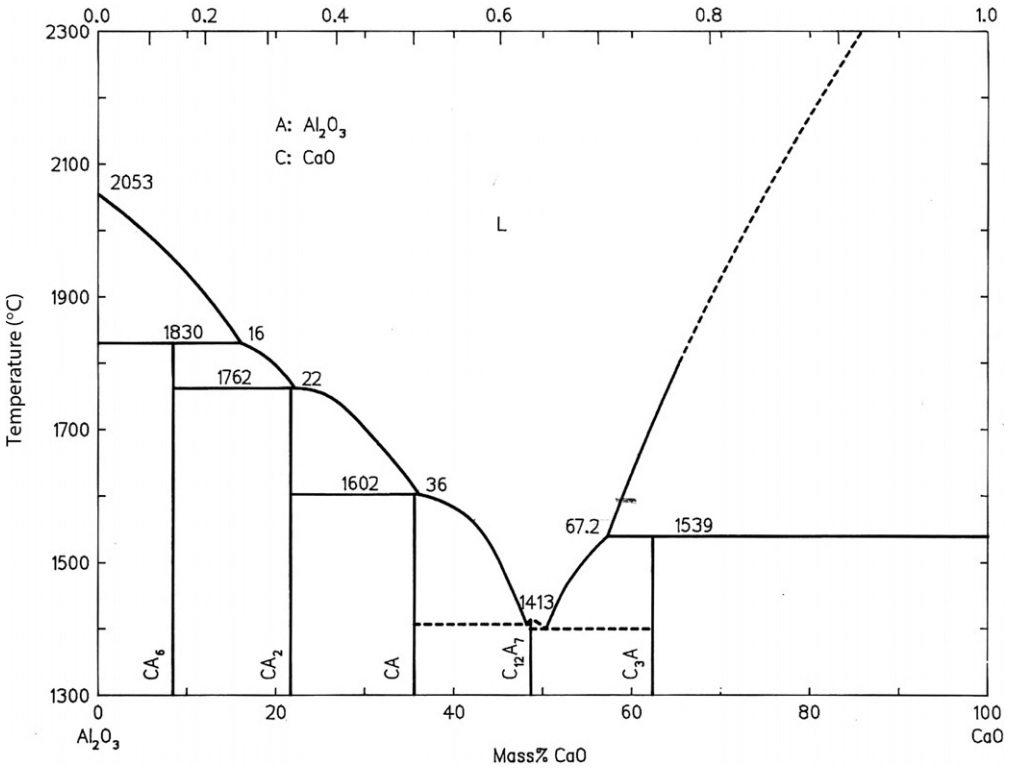


Figure 5.3.6 Phase diagram of Al_2O_3–CaO.

composition of the steel (this will be the case for silica) or by a pollution coming from the slag, refractory, etc., as typically for MgO.

The challenge for the steelmaker is to add the right quantity of Ca in order to obtain the right composition for the inclusions and not insufficiently transformed Ca-aluminates such as the compounds CA_6 or CA_2. Faulring [23] has shown that the formation of such compounds is even more detrimental to the castability of the steel than pure alumina (Figure 5.3.7).

Another issue could arise from a too large addition of Ca. In this case, depending on the amount of sulfur contained in the grade Ca sulfides can precipitate above the liquidus of the steel and provoke also some clogging issue.

These two issues—consequences of a too weak and a too large addition—are now classically represented in diagrams such as the one displayed in Figure 5.3.8. In this figure, the physical state of the inclusions is plotted as a function of the total contents (i.e., dissolved contents and contents trapped in inclusions) of calcium and oxygen. The region where the inclusions are liquid at the liquidus temperature of the grade is limited for high-Ca contents by the appearance of solid Ca sulfides and for low calcium contents

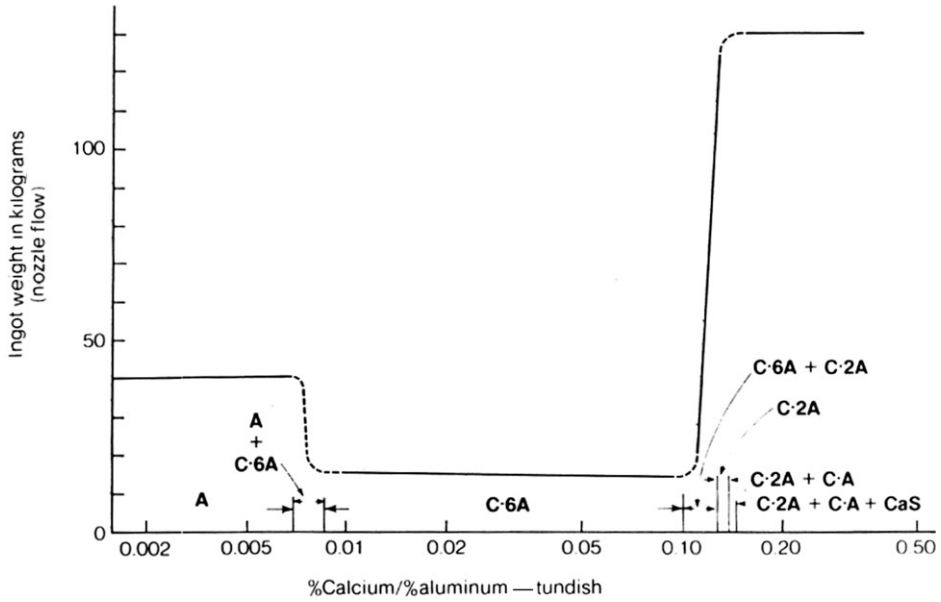


Figure 5.3.7 Castability as a function of the nature of the oxide inclusions. *After Ref. [23].*

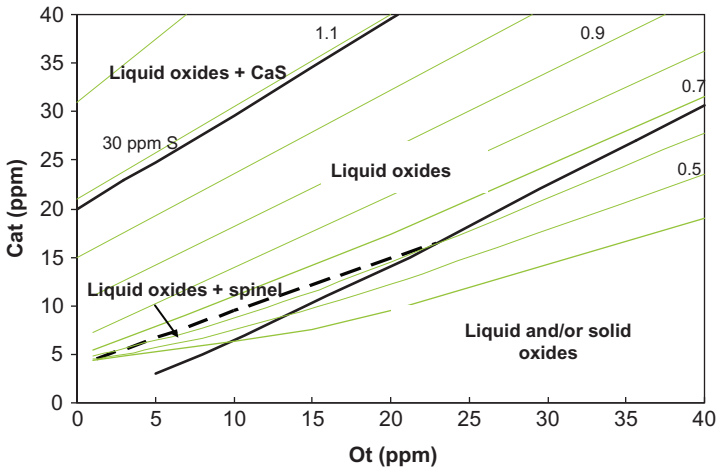


Figure 5.3.8 Nature of the inclusions at the function of the total oxygen and calcium contained in steel. The green lines give the ratio wt%CaO/wt%Al_2O_3 in the inclusions.

by the precipitation of solid oxides. The domain where liquid oxides coexist with spinel ($MgAl_2O_4$) has been drawn for a total Mg content of 2 ppm and treated differently: this domain is limited by a dotted line since the effect of spinel on nozzle clogging is still controversial.

The wt%CaO/wt%Al_2O_3 iso-ratios have been also drawn in Figure 5.3.8. In regions where several nonmetallic phases are stable, the "global" ratios have been considered and, for instance, when CaS coexists with oxides, the Ca content trapped in sulfides has been counted as CaO. These lines are almost parallel to the limit of the liquid oxides domain but not exactly since other components than only CaO and Al_2O_3 enter in the inclusions such MgO, SiO_2 but also MnO and FeO whose amounts increase with increasing oxygen content.

Let us note that one often considers that the success of the Ca treatment is dictated by the ratio Ca_{total}/O_{total}. Figure 5.3.8 shows that if, for the grade and the temperature considered for this specific calculation, the lower boundary of the liquid domain follows a line of constant Ca_{total}/O_{total} ratio (i.e., "nearly" going through the origin), it is not true for the upper limit. Therefore, for this example, the Ca_{total}/O_{total} ratio must be higher than a given value to ensure the success of the treatment, but too high-Ca and O contents, even if they are in a "suitable" ratio, can lead to the formation of CaS.

As stated before, Ca treatment can have an objective other than nozzle clogging prevention that is sulfide "globularization." Without Ca addition, S precipitates usually as MnS which are very deformable and take elongated shapes during rolling operations. This behavior can be altered by the formation of solid solutions (Ca,Mn)S.

Figure 5.3.9 provides an insight into the mechanism of sulfide transformation. Most of the time, sulfides nucleate on the surface of the preexisting oxides. Sulfur "extracts" Ca from the oxides which, in turn, get more alumina rich.

This mechanism can be summarized by the following chemical reaction:

$$S + pCaO{\cdot}nAl_2O_3 + 2/3Al \rightarrow CaS + (p-1)CaO{\cdot}(n+1/3)Al_2O_3$$

and is substantiated by the complete thermodynamic calculation illustrated in Figure 5.3.10. In this case, the oxides that appear in the liquid steel are liquid and sulfides start to precipitate well below the liquidus temperature of the grade which should guarantee a good castability. As soon as sulfides precipitate, the nature of the oxides changes: liquid oxides are transformed into solid oxides CA and then CA_2. Spinel also appears together with solid Ca-aluminates.

5.3.1.3.2 The Practice

The Ca-treatment industrial practice consists in injecting Ca-containing flux cored wires.

The challenge for the steelmaker when performing the Ca treatment is to control the Ca addition yield. Figure 5.3.11 gives an idea of the order of magnitude of Ca addition yield for various kinds of Ca-alloys. The maximum is around 30%. These low figures are the consequence of the low solubility of Ca in steel and of its high vapor pressure which explains the violent reactions which take place during its injection.

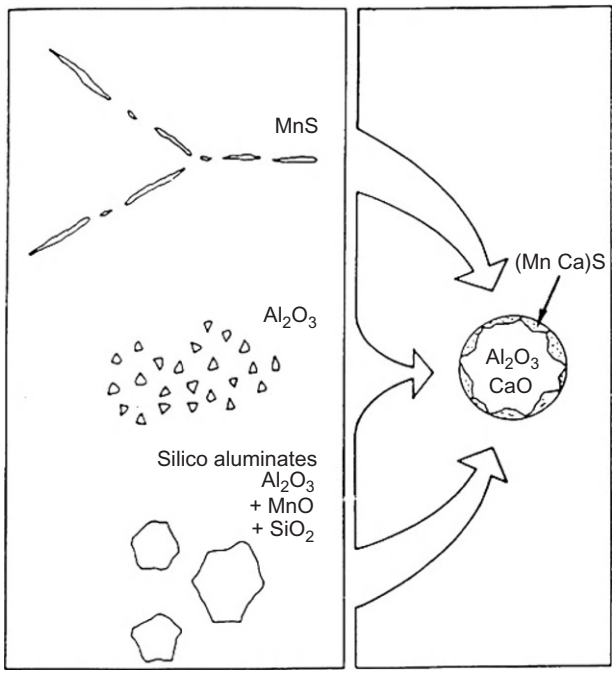


Figure 5.3.9 Ca treatment and sulfide transformation.

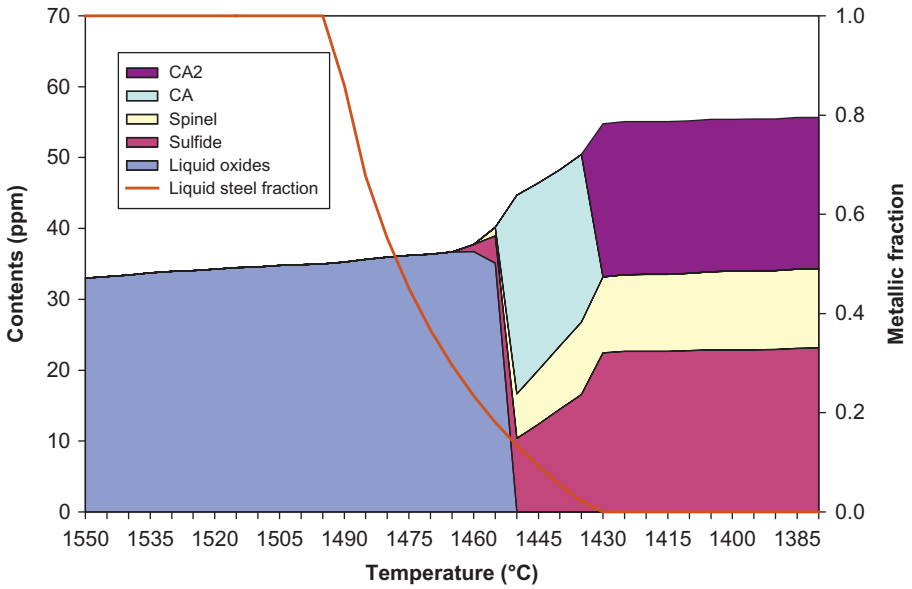


Figure 5.3.10 Evolution of the nature and of the quantity of oxides and sulfides during steel cooling and solidification.

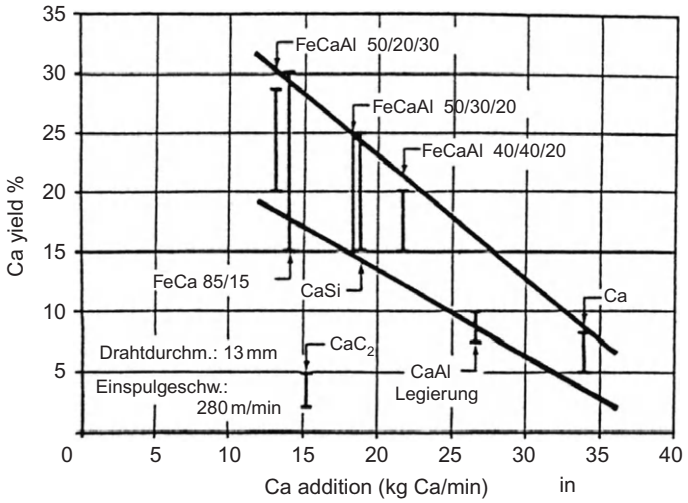


Figure 5.3.11 Comparison between yields for different kinds of Ca-containing flux cored wires [24].

In the first half of the twentieth century, different addition methods were tried [25] as:

- Tapping the liquid steel onto the calcium alloy placed in the bottom of the ladle.
- Adding the calcium alloy to the surface of the liquid steel.
- Adding alloy lumps at the end of a rod which is dipped into the liquid steel.
- Adding alloy inside a steel pipe with holes in the side and plunging the pipe into the liquid steel.
- Adding Ca briquettes made with sponge iron or steel chips.
- Wrapping Ca alloy in bags added in the steel stream.

In the 1960s, a pneumatic injection process was developed by Thyssen-Nuederrhein [26] and further improved by Scandinavian Lancers System [27]. The main drawbacks of these systems were frequent slopping problems and unreliable operations due to lance plugging.

Nowadays, these techniques have been widely replaced by wire feeding techniques in which iron-clad calcium wire is fed into the ladle by a wire feeder. The technical idea is always to inject Ca or Ca alloy as deep as possible into the melt in order to have the highest possible ferrostatic pressure in order to minimize the vaporization and to increase the residence time of Ca in the melt.

Different alloys of calcium as CaSi or mixtures as CaFe are commercially available. Using true alloys instead of "mechanical" mixtures can have a beneficial effect due to a decrease of Ca activity and thus a lower propensity to vaporize but their use can be prohibited by constraints on steel chemistry.

Figure 5.3.11 shows that these alloys lead to very different yields which decrease when the addition rate increases. If the maximum is situated around 30%, it can be as low as a few percents.

5.3.1.4. Mold Flux Design

The development of continuous casting mold flux keeps pace with the development of new steel grades. Mold flux is a key ingredient in the continuous casting process to improve the quality of the cast slabs. In a typical mold flux, cuspidine ($Ca_4Si_2F_2O_7$) precipitation occurs at about 1200 °C and about 40–50% of liquid remains at 1000 °C. It should be noted that the melting temperature of pure cuspidine is about 1400 °C. Once cuspidine is formed, the heat flux through the mold walls is reduced drastically. The controlled formation of cuspidine can reduce longitudinal cracks formed during the $\delta \rightarrow \gamma$ transformation of steel. Thus, the effect of additional components such as Na_2O, Li_2O, Al_2O_3, and MgO on the liquidus temperature of the cuspidine phase is one of the most important parameters for the development of new mold fluxes customized for new steel grades. Recently, a thermodynamic database for oxyfluoride systems has been developed for applications to mold flux design [28]. The thermodynamic database covers a wide range of compositions of the $CaO–SiO_2–MgO–Na_2O(<20\%)–Li_2O(<15\%)–Al_2O_3(<5\%)–F(<50\%)$ system.

5.3.1.4.1 Solidification Behavior of Commercial Mold Flux

Based on new oxyfluoride database, the equilibrium solidification behavior of several commercial mold fluxes was calculated and the results are in good agreement with phase diagram studies and experience in industrial trials [29]. As examples, the calculations for two commercial fluxes are presented in Figure 5.3.12.

The phase distribution during rapid Scheil cooling is calculated for the flux of Figure 5.3.12b in Figure 5.3.13a. The solidification behavior is similar to equilibrium cooling. The change of equilibrium gas pressure during the solidification is shown in Figure 5.3.13b. As can be seen, the pressure of NaF is the highest among the gaseous species. Thus, if there is a possible carrier gas in the mold flux system, NaF gas can evaporate and condense as solid NaF at the cold mold side.

5.3.1.4.2 Mold Flux Design Using the Phase Diagrams

The phase diagram information can provide an overview of the mold flux solidification. In order to understand the temperature history of the phase formation, isoplethal diagrams (temperature vs. composition) should be calculated. Isopleths of the $CaO–SiO_2–CaF_2–Na_2O$ system with fixed Na_2O (10 and 15 wt%) and CaF_2 (15, 20, and 25 wt%) contents are calculated in Figure 5.3.14.

From the calculated isopleths, it is possible to estimate the change of liquidus temperature of the cuspidine phase depending on the basicity ($B = wt\%CaO/wt\%SiO_2$). For example, the cuspidine liquidus temperature is highest (1250 °C) at $B = 0.95$ at 10 wt%Na_2O + 20 wt% CaF_2. The slag basicity at the maximum cuspidine formation temperature changes with the Na_2O content at fixed CaF_2 concentration. That is, the

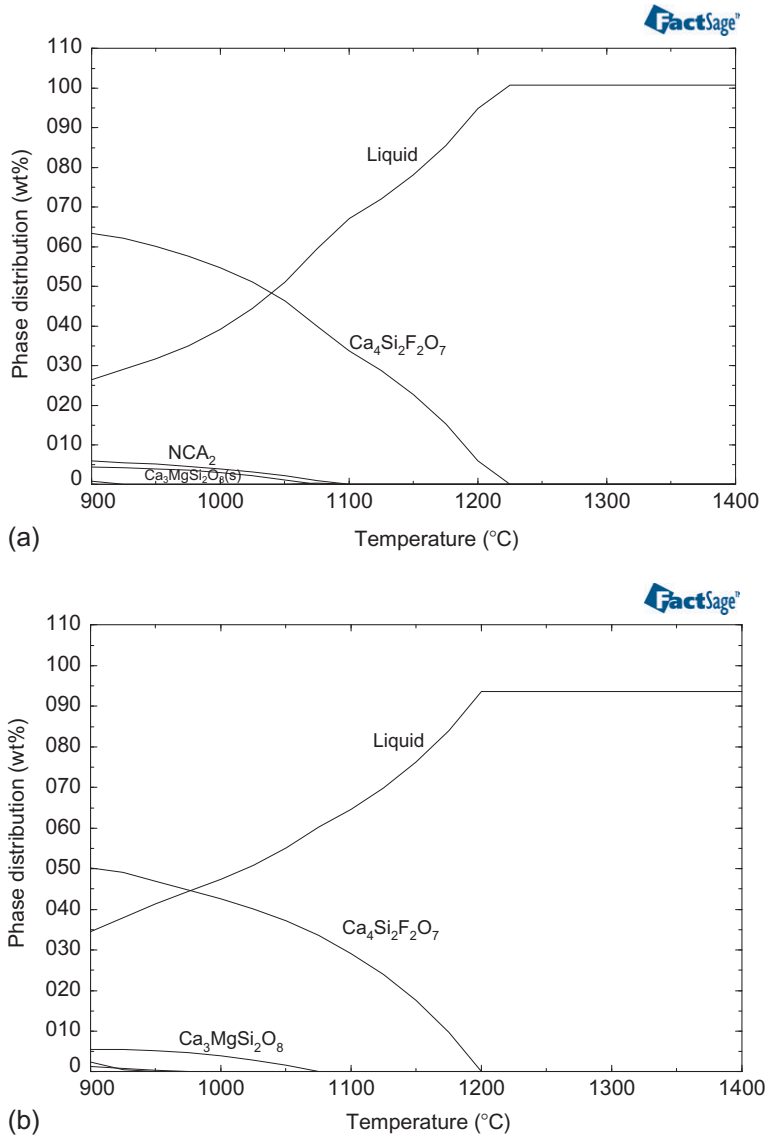


Figure 5.3.12 Calculated phase distribution during equilibrium solidification of mold flux (a) $32SiO_2$–37.4CaO–0.67MgO–$6.8Al_2O_3$–$7.4Na_2O$–$15.39CaF_2$–$1.0Li_2O$ and (b) $31.8SiO_2$–32.5CaO0.9MgO–$5.3Al_2O_3$–$9.5Na_2O$–$12.9CaF_20.7Li_2O$ (in wt%) [29].

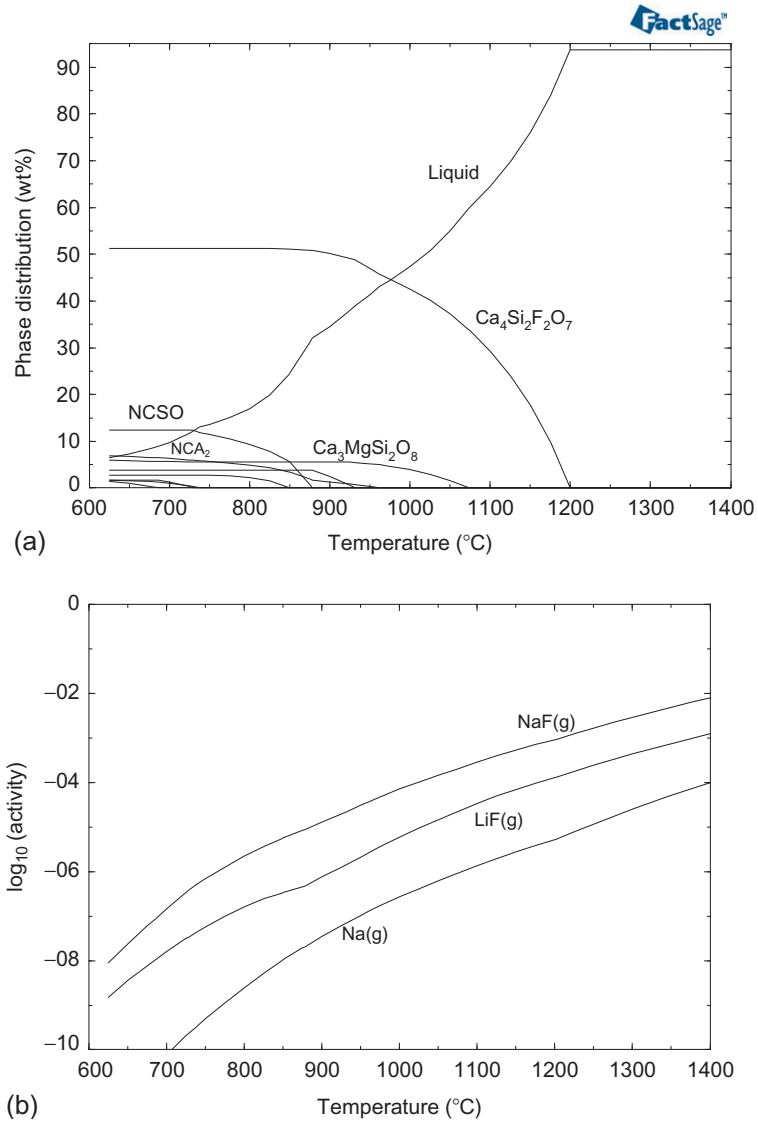


Figure 5.3.13 Calculated phase distribution during rapid Scheil cooling of the mold flux and the equilibrium pressures of major gaseous species [29].

basicity decreases with increasing Na_2O content: $B = \sim 0.95$ at 10 wt% Na_2O and $B = \sim 0.76$ at 15 wt% Na_2O. On the other hand, the influence of CaF_2 on the slag basicity at the maximum cuspidine liquidus temperature is negligible up to 25 wt% CaF_2 addition. The calculated diagrams also show that $CaSiO_3$ and SiO_2 can be formed as primary crystalline phases with increasing the SiO_2 content. It should be also noted that between

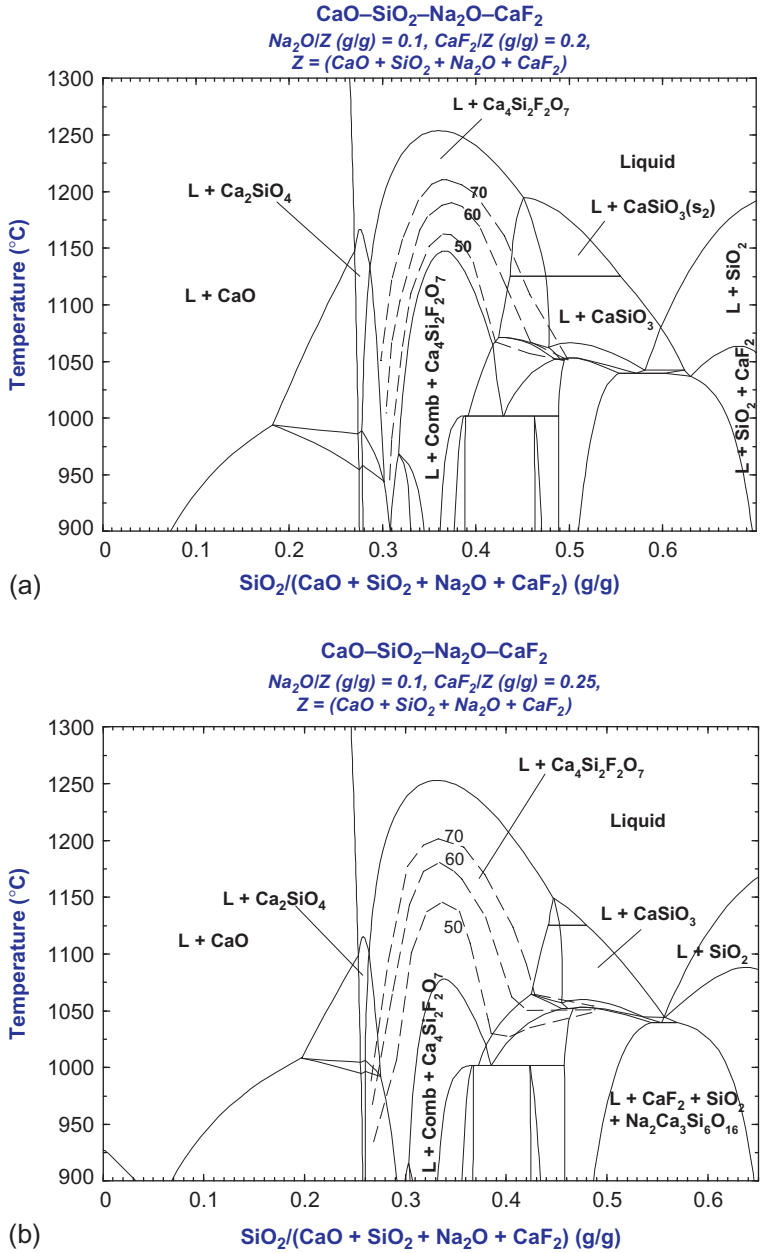


Figure 5.3.14 Calculated isopleths of the $CaO–SiO_2–CaF_2–Na_2O$ system. (a) 10 wt% $Na_2O + 20$ wt% CaF_2, (b) 10 wt% $Na_2O + 25$ wt% CaF_2,

(Continued)

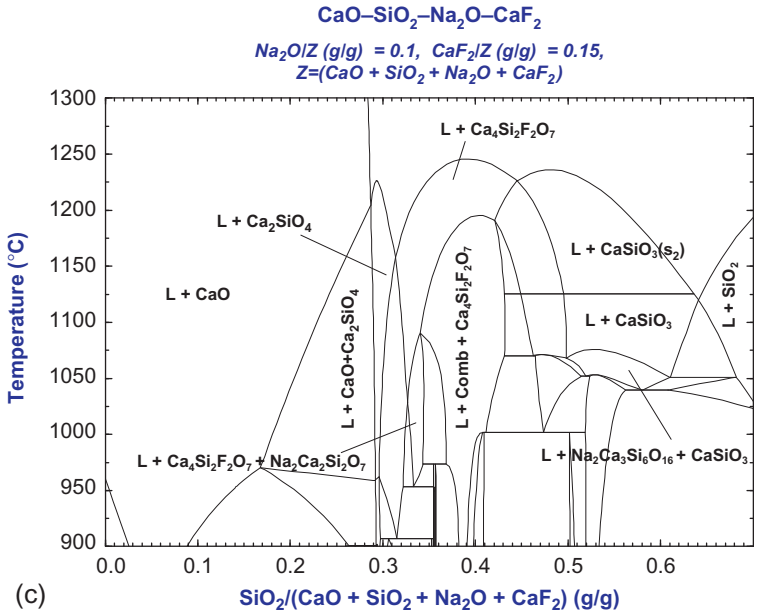


Figure 5.3.14, cont'd (c) 10 wt% $Na_2O + 15$ wt% CaF_2, (d) 15 wt% $Na_2O + 15$ wt% CaF_2, and

(Continued)

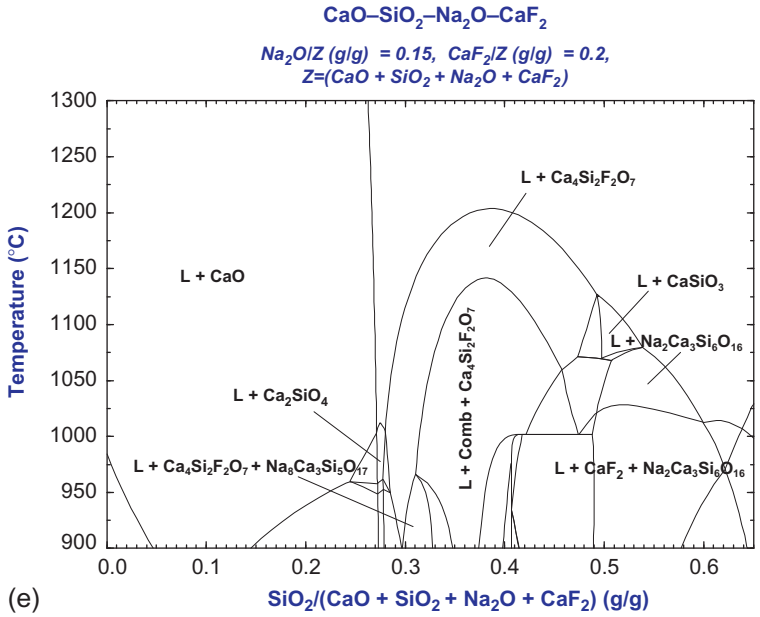


Figure 5.3.14, cont'd (e) 15 wt% $Na_2O + 20$ wt% CaF_2. Comb is the combeite solid solution [29].

the CaO and cuspidine primary crystalline regions, a deep liquid well can exist. The depth of the well becomes larger with an increase in CaF_2 content.

In Figure 5.3.14, the calculated fraction (wt%) of liquid in the cuspidine primary phase region is also indicated: iso-fraction lines of 50, 60, and 70 wt% liquid are represented by the dashed lines in Figure 5.3.14. The iso-fraction lines are decreased by about 20–30 °C upon increasing the CaF_2 content from 20 to 25 wt% at the same slag basicity.

As can be seen from comparison of Figure 5.3.14a–c, the addition of CaF_2 at a fixed Na_2O content of 10 wt% increases slightly the cuspidine liquidus temperature by about 20 °C. Surprisingly, 10 wt% CaF_2 addition decreases noticeably the liquidus temperature of combeite solid solution by 125 °C. In addition, the liquidus temperature of $CaSiO_3$ is decreased with increasing CaF_2 content.

The effect of Na_2O at fixed CaF_2 concentration can be understood from comparison of Figure 5.3.14a and e and 5.3.14c and d. An increase of Na_2O content can reduce the liquidus temperature of cuspidine; 5 wt% Na_2O reduces the temperature by about 50 °C. However, the influence of Na_2O on the combeite liquidus is negligible (about 10 °C decrease with 5 wt% increment of Na_2O). It should be noted that the stabilities of Ca_2SiO_4 and $CaSiO_3$ can be significantly reduced with an increase of Na_2O content.

5.3.1.5. Slag Crystallization

One of the first concerns of the steelmaker about metallurgical slags is their physical state, i.e., are they completely liquid or not and if not what is the effect of an addition of such or such component on their physical state? Thermodynamic models could help answering this kind of question.

5.3.1.5.1 Slag Liquidus Temperatures and Solid Proportions

The first example presented here refers to the usage of a slag for its coating properties. When emptying a liquid steel vessel, part of the slag could remain "stuck" to the refractory layer and thus protect it from a too fast erosion. In order to have this kind of behavior, experience has shown that the slag should contain a certain proportion of solids. When evaluating this ability of a slag to protect the refractory, one could be tempted to rely only on its liquidus temperature, thinking that slags having the highest liquidus temperatures will have the highest proportion of solids for temperatures below these temperatures. Figure 5.3.15, which compares the crystallization path of two slags differing by Al_2O_3–CaO proportions, demonstrates that it is not always the case. Slag on the left-hand side has the smaller liquidus temperature but at 1350 °C, and it has a higher proportion of solids. Calculations have been done with the GCA model of slags.

5.3.1.5.2 Effect of Oxide Additions on Slag Liquidus Temperatures

A simplistic approach for appreciating the effect of some oxide addition on the liquidus temperature of a given slag would be to consider that, as long as the addition remains moderate and as long as the oxide does not belong to the list of components of the slag, it will decrease its liquidus. The examples displayed below show that the reality is more complex.

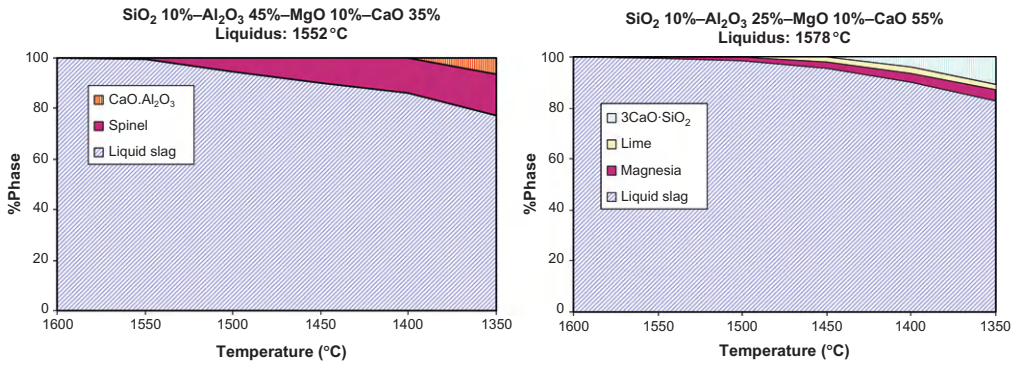


Figure 5.3.15 Comparison between the liquidus temperatures and the crystallization paths of two slags with different Al_2O_3–CaO ratios.

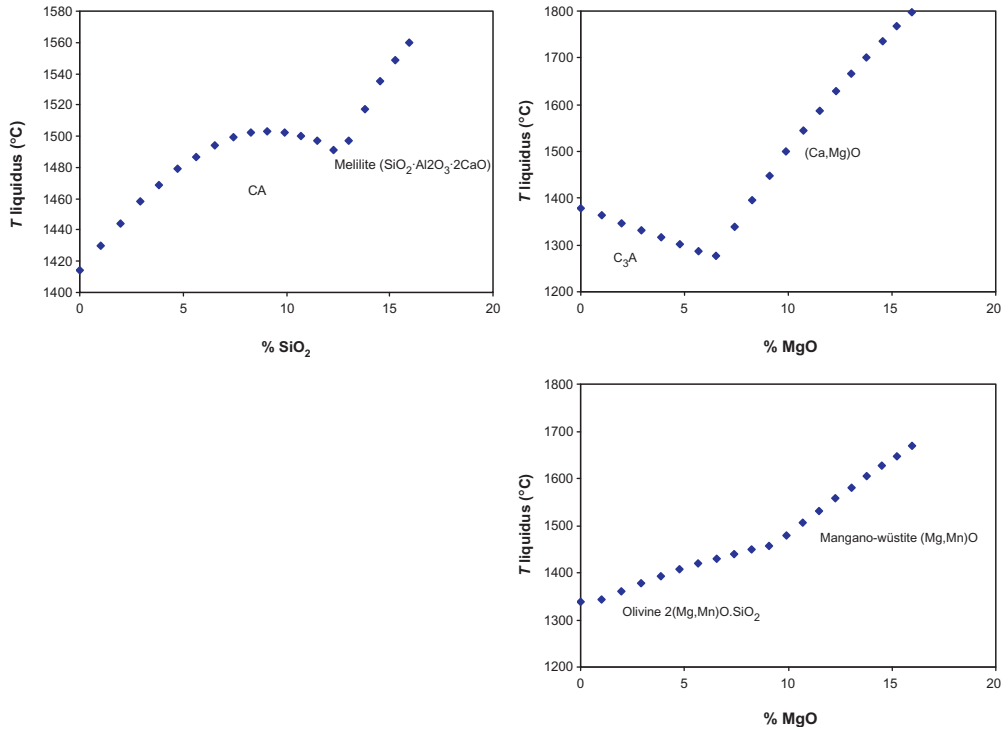


Figure 5.3.16 Effect of different additions on binary slags liquidus temperatures. Clockwise:
- SiO_2 additions to 52% Al_2O_3–48% CaO
- MgO additions to 50% Al_2O_3–50% CaO
- MgO additions to 30% SiO_2–70% MnO.

Figure 5.3.16 shows the effect of different additions on the liquidus temperatures of different binary compositions of slags as calculated with the GCA model:
- SiO_2 additions to 52% Al_2O_3–48% CaO
- MgO additions to 50% Al_2O_3–50% CaO
- MgO additions to 30% SiO_2–70% MnO

SiO_2 additions to the composition 52%Al_2O_3–48% CaO first increase (up to a percentage of around 12%) the liquidus temperature even if the primary does not contain any silica. On the contrary, MgO additions to a composition 50% Al_2O_3–50% CaO decrease the liquidus as it is usually expected and, as in the first example, the primary does not contain any magnesia. Finally, the third example, MgO additions to 30% SiO_2–70% MnO, shows an increase of the liquidus temperature, but in this case, MgO enters the composition of the primary phase which is a solid solution 2(Mg,Mn)O·SiO_2.

5.3.1.5.3 Mineralogy of As-Solidified Slags

BF, BOF, and secondary steelmaking slags can be recycled to produce cements, road-construction materials and even steelmaking slag after proper treatments. In order to be suitable for recycling, the solidified slag products must have certain mechanical, physical, and chemical properties, which are directly related to slag mineralogy. The mineralogy of solid slags is determined by the chemistry and the solidification process of slags.

Durinck *et al.* [30] performed solidification experiments of $CaO–MgO–SiO_2$ slags and compared the results with Scheil solidification calculations. As can be seen in Figure 5.3.17, the observed mineralogy of the solidified slags is quite different from that calculated by a traditional equilibrium model but reasonably close to the Scheil solidification calculation results, which shows that the Scheil solidification model is more suitable to predict the solidification behaviors of molten slags. The same approach has been used to explain the solidification behaviors of the $CaO–SiO_2–MgO–Al_2O_3–CaF_2$ slags [31] and the $CaO–SiO_2–CrO_x$ slags with controlled oxygen partial pressure [32].

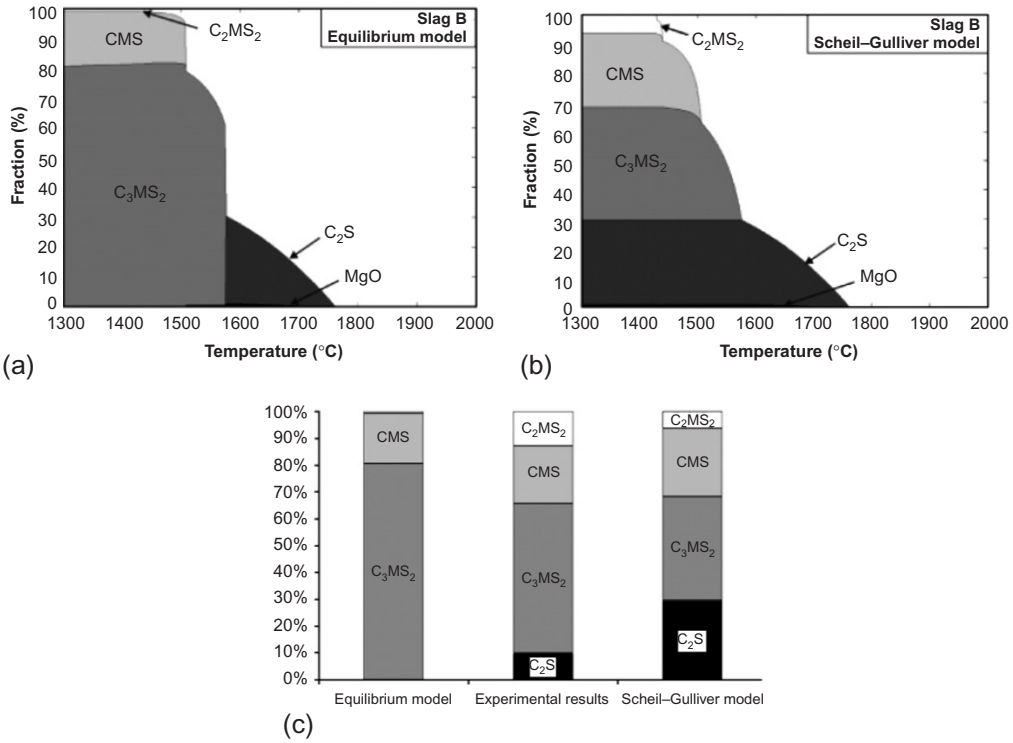


Figure 5.3.17 Solidification simulation of the $47CaO–15MgO–38SiO_2$ (in wt%) slag using the Scheil–Gulliver cooling calculations with FactSage FToxid database [30]. Evolution of the phase fractions during the solidification with (a) equilibrium model, (b) Scheil–Gulliver model, and (c) the comparison with experimentally observed mineralogy of the solidified slag.

5.3.1.5.4 Heat Evolution During Solidification

The heat evolution of solidification or melting is an important design issue for process. The enthalpy change from solid to liquid can be easily calculated using the thermodynamic database. In this calculation, the enthalpy change of solids from room temperature to their melting temperature and the enthalpy of mixing of liquid are automatically taken into account. For example, the enthalpy changes for solid mixture of MgO, FeO, and SiO_2 to equilibrium phase (liquid slag or mixture of solid solutions) at 1600 °C are calculated with the variation of MgO content at fixed 30 wt% of SiO_2. As can be seen in Figure 5.3.18, the calculated amount of enthalpy (ΔH) to form liquid slag can be varied with MgO content. The maximum value can be found at about 25 wt% MgO. That is,

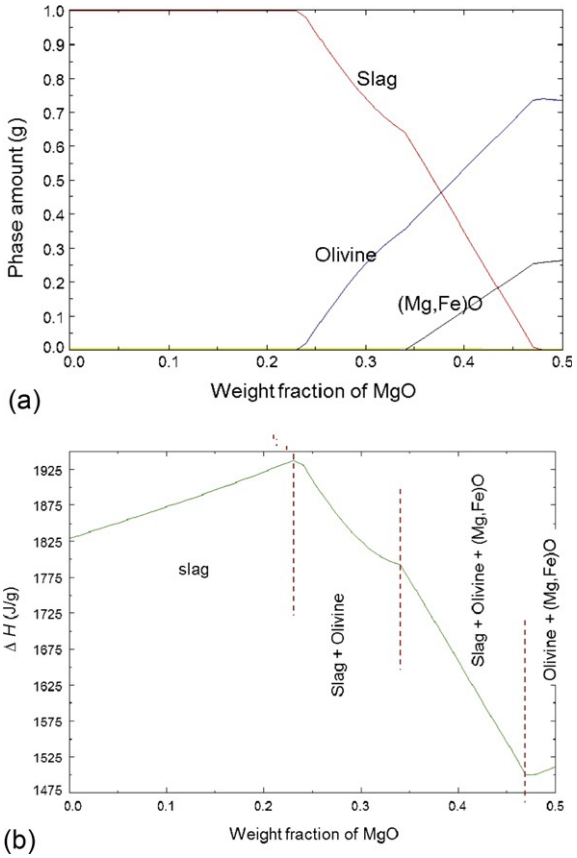


Figure 5.3.18 Calculated enthalpy change (ΔH) for the MgO–FeO–SiO_2 system (xMgO + (0.7 − x) FeO + 0.3SiO_2 in (g) from solid mixture at room temperature to equilibrium liquid and solid solution phase at 1600 °C with the variation of MgO amount. (a) Equilibrium phase distribution at 1600 °C and (b) variation of ΔH with MgO content.

the similar amount of enthalpy can be produced with solidification. Strictly speaking, the enthalpy of solidification can be changed depending on final solidified phases. Scheil cooling calculation can be performed to calculate the enthalpy produced during the solidification.

5.3.1.6. Chemical Interaction of Refractory with Molten Slag, Steel, and Inclusion

All furnaces, vessels, and nozzles used in contact with liquid Fe and molten slag are all lined with refractories. Refractories must have sufficient thermal and chemical stabilities to withstand attack by liquid Fe, molten slag, and even gases. In addition, refractories intended for iron and steel production must have a high resistance to thermal shock caused by abrupt changes in temperature.

Various types of refractories are used in ironmaking and steelmaking process depending on the operation environment. Refractories can be classified into shaped refractories (bricks) and unshaped refractories (monolithics or castable). Although physicochemical properties of refractory brick are superior to that of monolithics refractories, the usage of monolithic refractories is increasing due to the easy maintenance and remedy. Among many refractories, most common bricks for steel operation are:

Slag line: MgO–C, magnesia-chromite, and dolomite-carbon bricks

Steel bath: High alumina brick/castable, magnesia-chromite brick

Continuous casting and nozzle: MgO–C, Al_2O_3–C, $MgAl_2O_4$–C, Al_2O_3–SiO_2–C, ZrO_2–C

In this section, several case studies for the applications of the thermodynamic database to the refractory stability and its interactions with molten slag, steel, and inclusion will be discussed.

5.3.1.6.1 Thermal Stability of Refractories

MgO–C refractories are widely used during primary steelmaking in both basic oxygen and EAFs owing to their excellent resistance against thermal shock and slag attack, and their low cost. As the wetting behavior between C and molten slag is low, C contained in the refractory can effectively protect it from chemical attack by molten slag. However, the oxidation of C can deteriorate the physicochemical properties of the refractories. In order to retard C oxidation, so-called antioxidants are added to refractories. In addition to the prediction of the antioxidant behavior at high temperatures, thermodynamic calculations can assist in the selection of proper antioxidants for carbon-containing refractories. Zhang *et al.* [33] conducted thermodynamic calculations to predict the chemical reactions at high temperatures between MgO–C refractories containing various antioxidants such as Al, Si, and B_4C and atmosphere. Figure 5.3.19 shows the calculated phase changes of a MgO–C brick containing 5 wt%Al or Si at 1500 °C

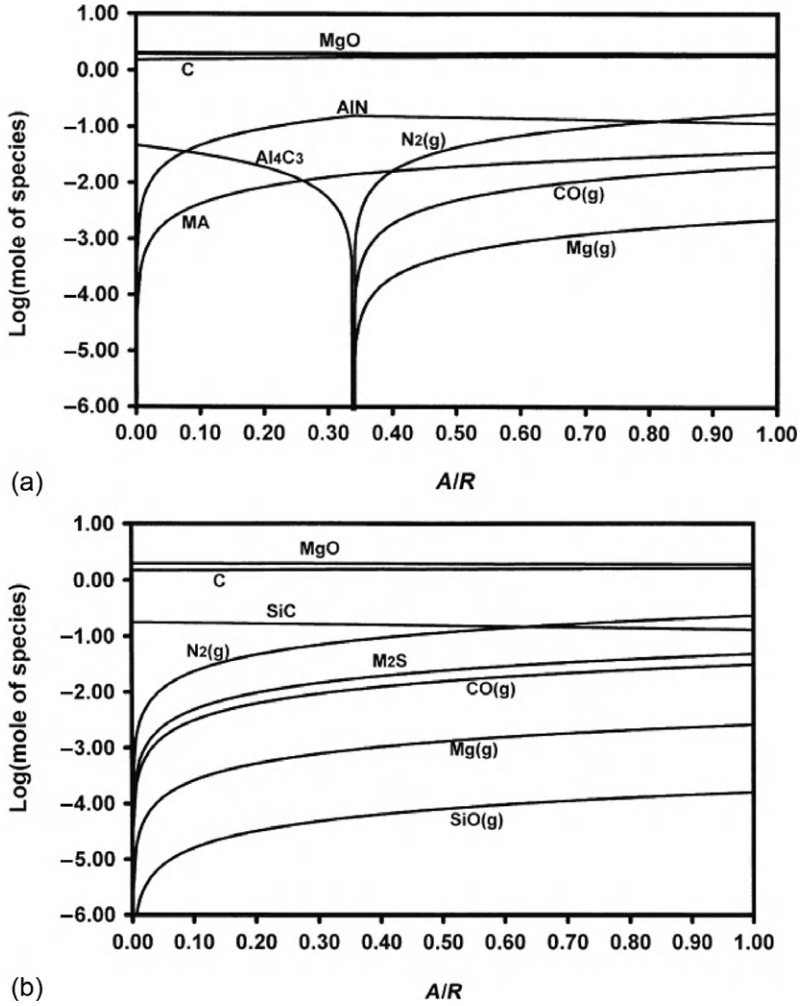


Figure 5.3.19 Calculated phase changes in MgO–C refractory brick containing antioxidants: (a) 5 wt% Al and (b) 5 wt% Si at 1500 °C. *A/R* represents the atmosphere/refractories ratio where atmosphere is 35%CO + 65%N_2 and refractories is composed of 40 wt% fused MgO, 40 wt% sintered MgO, and 20 wt% graphite. Calculations were performed using FactSage FToxid/FTmisc database.

with air/refractory (*A/R*) ratio. As the refractories react with atmosphere, various solid oxides, carbides, and nitrides and gaseous phases were predicted to form or vanish, which was in good agreement with observed microstructures. Chan *et al.* [34,35] calculated the thermal behavior of Al_2O_3–SiO_2–SiC–C bond system containing Al, Si, Si_3N_4, BN, B_2O_3, or B_4C under reducing condition and also the chemical reactions between refractories and molten slag. The thermodynamic calculations were in good agreement with experimental results on refractories/slag reactions.

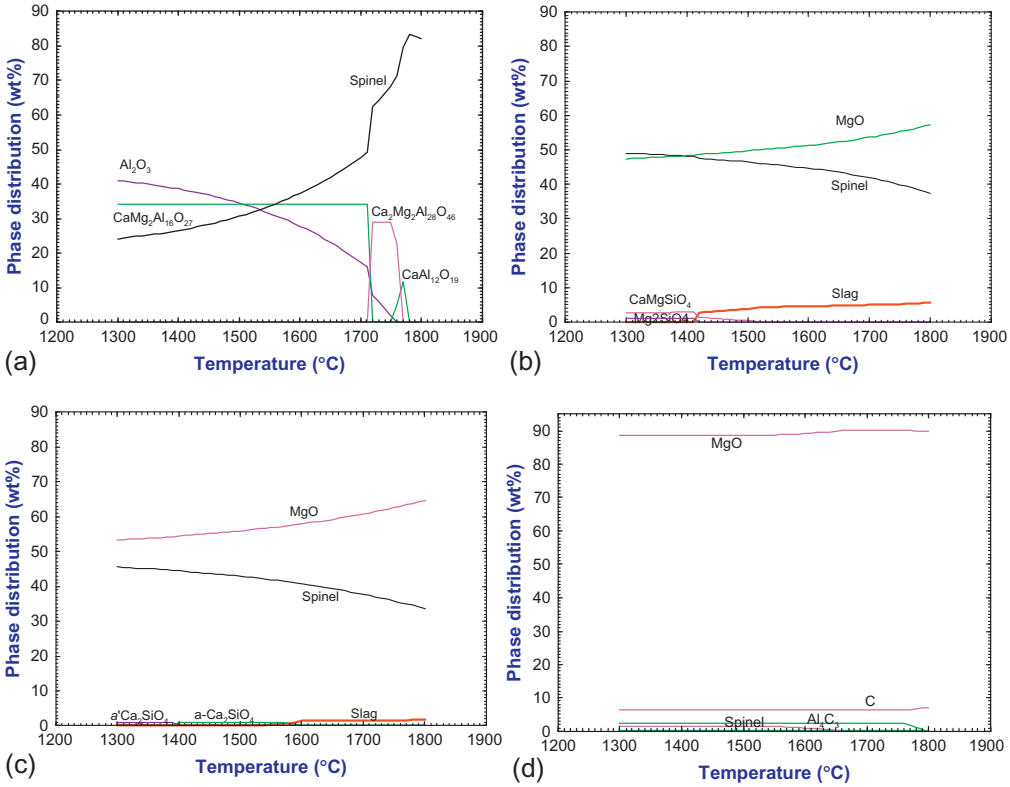


Figure 5.3.20 Calculated thermal stability of various refractories using FactSage FToxid database [36]. (a) $88Al_2O_3$–9MgO–3CaO, (b) 11 Al_2O_3–58MgO–0.9CaO–$20Cr_2O_3$–$8.8Fe_2O_3$–$1.6SiO_2$, (c) $4Al_2O_3$–61MgO–0.7CaO–$29Cr_2O_3$–$4.8Fe_2O_3$–$0.4SiO_2$, and (d) $0.5Al_2O_3$–89MgO–$0.5SiO_2$–7C in wt%.

The thermal stabilities of various high alumina-spinel type and magnesia-chromite-type refractories were calculated by Cho and Jung [36] for application to the lining at the RH bottom vessel. Part of the results is presented in Figure 5.3.20. As seen in the figure, certain commercially available refractories are thermally unstable at about 1650–1700 °C and, therefore, cannot be candidates for high-temperature applications in RH or VOD vessels. In certain cases, very small amount of CaO and SiO_2 can induce partial melting of refractories even below 1600 °C. In addition, a significant change in the refractory phases with temperature may result in large volume variations, which can subsequently cause thermal stresses in refractories and refractory wear.

5.3.1.6.2 Slag/Refractories Reactions

In order to understand the complex chemical reactions between molten slags and refractories, phase diagram information is indispensible [37–39]. However, phase diagrams for

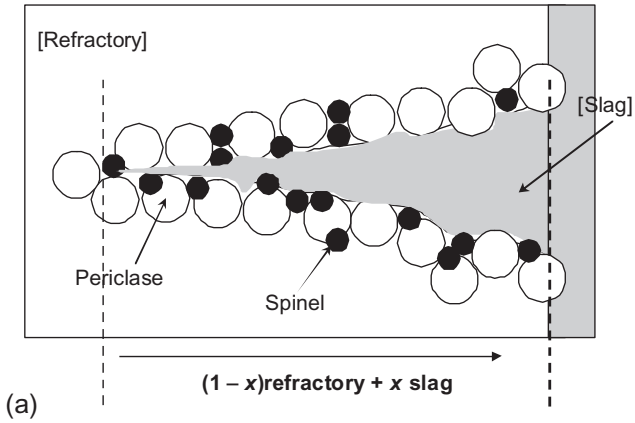
specific "molten slag–refractory" systems are unavailable in many cases. Thermodynamic database can be used to calculate any phase diagram sections within the accuracy of the database. FactSage and MTDATA have been frequently used for this purpose [40–54].

5.3.1.6.2.1 Interaction with Various Slags

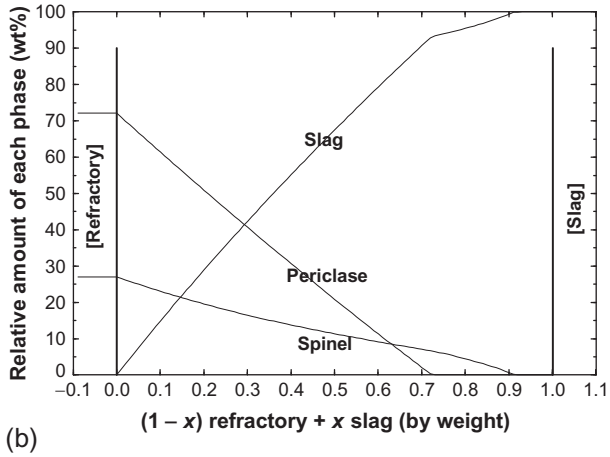
The complex chemical reactions between magnesia-chromate refractories and $CaO–SiO_2–Al_2O_3$ slags in VOD stainless steelmaking processes were calculated by Jung *et al.* [40]. According to the calculation results, magnesia-chromite spinel refractories with overall composition $58MgO–6.5Al_2O_3–21Cr_2O_3–13.5FeO$ (in wt%) consist of periclase and spinel phases at 1650 °C under reducing condition (in contact with liquid steel): 73 wt% periclase (composition: $72.8MgO–0.6Al_2O_3–9.1Cr_2O_3–17.5FeO$ in wt%) and 27 wt% spinel (composition: $21.5MgO–22.5Al_2O_3–53.4Cr_2O_3–2.6FeO$ in wt%). Figure 5.3.21 shows a thermodynamic simulation of the refractory corrosion by a $50CaO–40SiO_2–10Al_2O_3$ (in wt%) slag at 1650 °C. In the calculations, x gram of slag and $(1-x)$ gram of refractory were assumed to be completely equilibrated in order to simulate corrosion with slag penetration into the refractory. That is, the calculation assumes that the diffusion rates of all oxide elements in molten slag are the same and that the amount of penetrated slag varies linearly with the depth of penetration. The resultant equilibrium amounts of all phases and their compositions are plotted versus x in Figure 5.3.21. The periclase phase is more severely corroded compared to the spinel phase. Various silicate phases such as Ca_2SiO_4, merwinite, and monticellite (olivine) observed in reacted refractories can form during cooling of the penetrated slag. When the refractory and slag compositions are changed, different corrosion reactions can be calculated.

Similar approach was used by Goto *et al.* [41] to simulate the corrosion of $MgO–MgAl_2O_4$ spinel refractory bricks by calcium aluminosilicate slags at about 1450 °C. The mineralogy of refractories revealed the formation of secondary spinel, monticellite, and merwinite phases with the slag penetration depth, which was well explained by thermodynamic calculations using the FACT oxide database [55]. Corrosion of high alumina refractories by ladle slag was calculated and compared with experimental microstructures by Melcher *et al.* [42]. In order to understand the degradation of MgO refractories by $CaO–SiO_2–MgO–Al_2O_3–FeO$ slags, Nightingale *et al.* [43] calculated the phase diagram of the MgO–molten slag system using MTDATA [56]. The degradation mechanism was well explained by the calculated phase diagram. Reiter *et al.* [44] performed thermochemical calculations for various refractories with EAF slags at controlled oxygen partial pressure to prescreen the suitable refractories for EAF process. Park [31] and Kaiser *et al.* [46] also conducted thermodynamic calculations to understand the degradation of zirconia ceramic nozzle by mold flux.

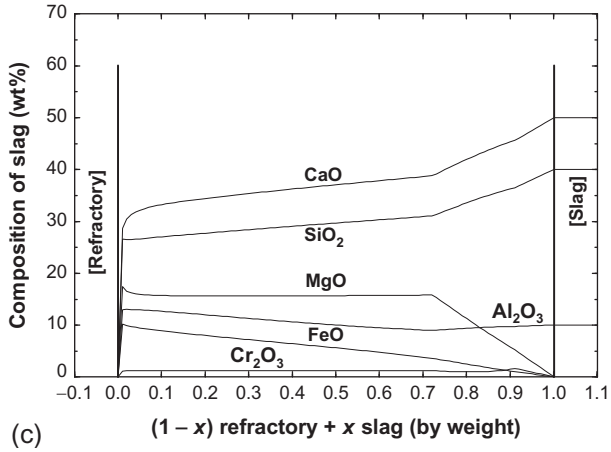
Van Ende *et al.* [49] performed an experimental study on the degradation of MgO–C refractories by $CaO–SiO_2–MgO–MnO–Al_2O_3–Cr_2O_3$ stainless steel slags at 1600 °C



(a)



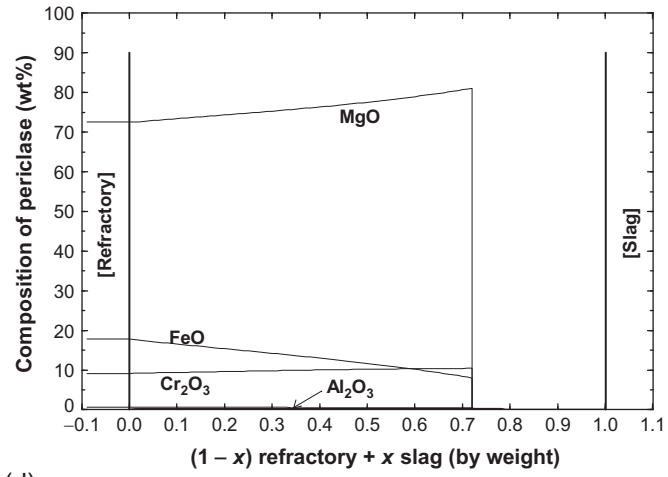
(b)



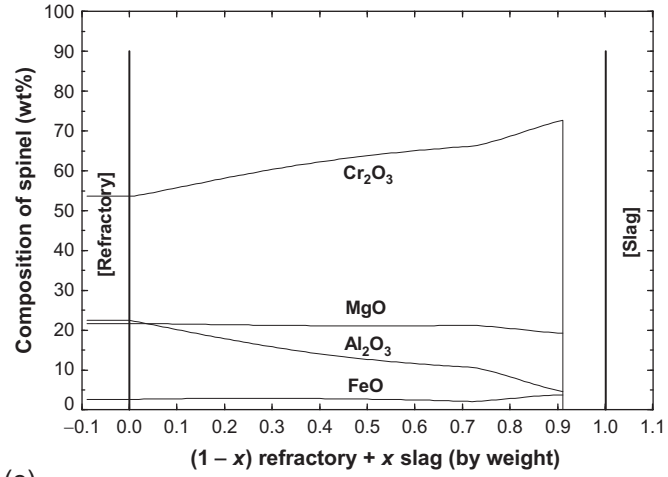
(c)

Figure 5.3.21 Simulation of slag penetration into refractories for VOD in stainless steelmaking using FactSage FToxid database [40]. Initial compositions: refractories: 58MgO–6.5Al_2O_3–21Cr_2O_3–13.5FeO and slag: 50CaO–40SiO_2–10Al_2O_3 in wt%. (a) Schematic of slag penetration, (b) relative amounts of slag, periclase and spinel phases with slag penetration, and their composition of (c) slag,

(Continued)



(d)



(e)

Figure 5.3.21, cont'd (d) periclase, and (e) spinel.

and compared the experimental results with thermodynamic calculations performed with FactSage. According to the experiment results, the refractory degradation was highly dependent on the basicity and MnO content of the slag. As can be seen in Figure 5.3.22, the thermodynamic calculations using FactSage can well predict the final slag compositions and assist in the interpretation of the degradation mechanisms.

The dissolution of MgO refractory (MgO–C) by CaF_2-containing slag is a great concern in steelmaking. In order to understand the chemical corrosion by the slag, phase diagram information is indispensable. Unfortunately, phase diagrams of the CaO–SiO_2–Al_2O_3–MgO–F system are very rare and unreliable.

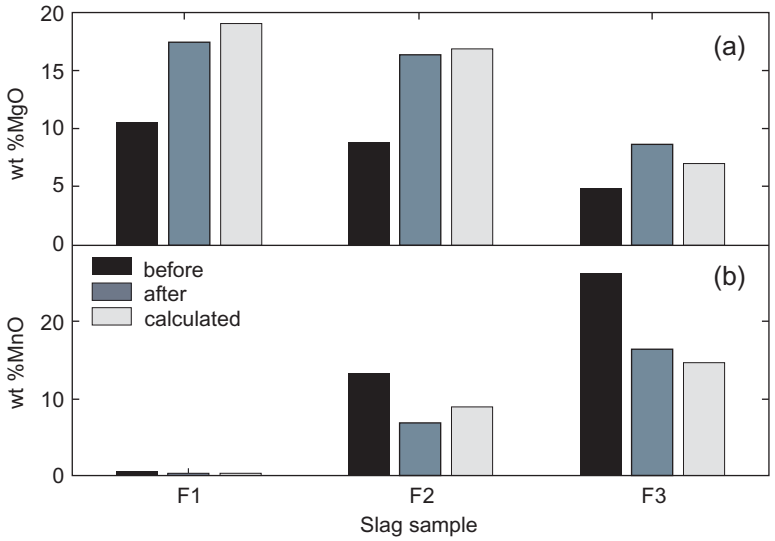


Figure 5.3.22 The comparison of observed concentrations of (a) MgO and (b) MnO in molten slags after reaction with MgO–C refractory with thermodynamic calculations [49]. F1–3 represent different slags used in the experiments. Thermodynamic calculations were performed using FactSage FToxid database.

Figure 5.3.23 shows the effect of MgO content on the calculated phase diagram of the $CaO–SiO_2–CaF_2$ slag system at 1600 °C [57]. In order to superimpose all the phase diagrams with different MgO contents on the same diagram, normalized axes are used. That is, the diagram is a projection of the quaternary system onto a ternary $CaO–SiO_2–CaF_2$ section. As can be seen, the MgO saturation line moves toward lower CaO/SiO_2 with increasing MgO content. In addition, the slag composition cosaturated with MgO and Ca_2SiO_4 moves toward lower CaF_2 and lower CaO/SiO_2 with increasing MgO content. (Symbols in Figure 5.3.23b correspond to the co-saturation points: circles, triangles, and diamonds are 5, 10, and 15 wt% MgO condition, respectively.) These co-saturation points are in general considered as the best slag composition for both high refining capacity such as S and P removal and optimal MgO refractory life.

In order to investigate the influences of CaF_2 and Al_2O_3 on the MgO and Ca_2SiO_4 saturation lines in the $CaO–MgO–SiO_2$ system at 1600 °C, phase diagram calculations were performed using the present thermodynamic database. The results are summarized in Figure 5.3.24 [57]. The ternary phase diagram of the $CaO–MgO–SiO_2$ system at 1600 °C is presented as reference diagram in Figure 5.3.24a. The slag compositions at MgO saturation and Ca_2SiO_4 saturation can be easily read from the diagram. For example, the co-saturation of MgO and Ca_2SiO_4 can be found at about 18 wt% MgO.

The influence of CaF_2 up to 20 wt% is calculated in Figure 5.3.24b. The addition of CaF_2 to the slag moves the MgO saturation toward lower SiO_2 regions. This is due to the

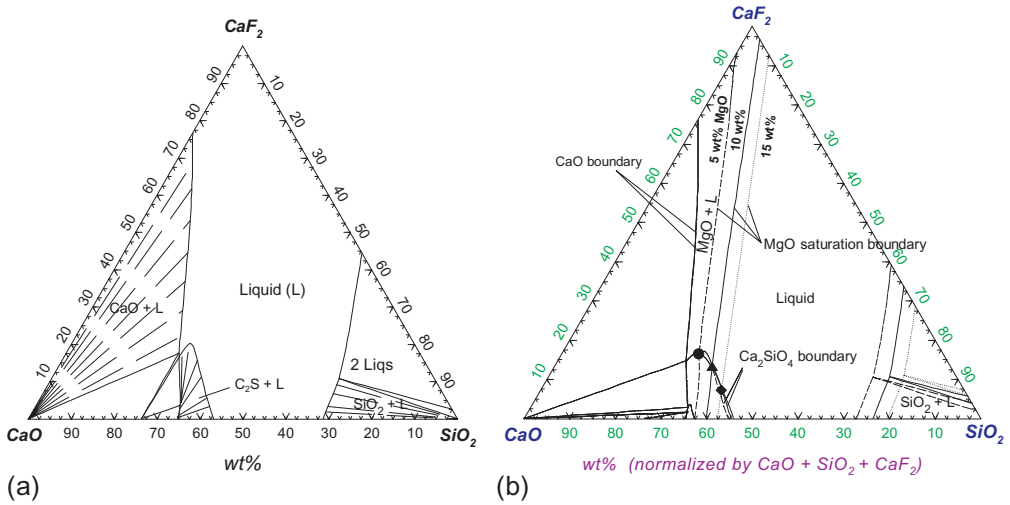


Figure 5.3.23 Calculated phase diagrams for the CaO–SiO_2–MgOCaF_2 system at 1600 °C. (a) CaO–SiO_2–CaF_2 and (b) CaO–SiO_2–CaF_2 with 5, 10, and 15 wt%MgO [57].

expansion of the liquid area in the CaO–MgO–SiO_2–CaF_2 system with increasing CaF_2. In addition, the co-saturation point of MgO and Ca_2SiO_4 moves toward lower MgO and lower SiO_2 regions with increasing CaF_2 content. The shift of the liquidus of the CaO–MgO–SiO_2–10 wt%CaF_2 system with the addition of Al_2O_3 (10, 15, and 20 wt%) is calculated in Figure 5.3.24b. Increasing the Al_2O_3 content in the slag shifts the MgO and CaO liquiduses toward lower SiO_2 regions. It should be noted that the Ca_2SiO_4 region appears at 10 wt% Al_2O_3 addition, but disappears with further Al_2O_3 addition. That is, no co-saturation point of MgO and Ca_2SiO_4 exists in the CaO–MgO–SiO_2–10 wt% CaF_2–Al_2O_3 system when the Al_2O_3 content is higher than 10 wt%. Instead, co-saturation with MgO and CaO can occur, as can be seen in Figure 5.3.24b.

5.3.1.6.2.2 Interaction with Ladle Glaze

Beskow *et al.* [50–52] and Son *et al.* [53] investigated the so-called ladle glaze, which is a solidified slag film formed on ladle refractories during the discharge of the steel in ladle. They reported that liquid slags can react with ladle refractories even within 2 min, resulting in the degradation of the refractory linings and eventually the contamination of molten steel with nonmetallic inclusions. The chemical reactions between ladle refractories (MgO–C and high alumina magnesia) and top slags can be readily understood using thermodynamic calculations. Figure 5.3.25 shows the formation of ladle glaze on the surface of high Al_2O_3 castable (88.2Al_2O_3–8.6MgO–2.4CaO–0.8SiO_2 in wt%) after dipping into liquid slag (50CaO–7MgO–22Al_2O_3–10SiO_2 in wt%) for 2 min. The ladle glaze can be clearly shown in the EPMA area mapping image in particular Ca mapping

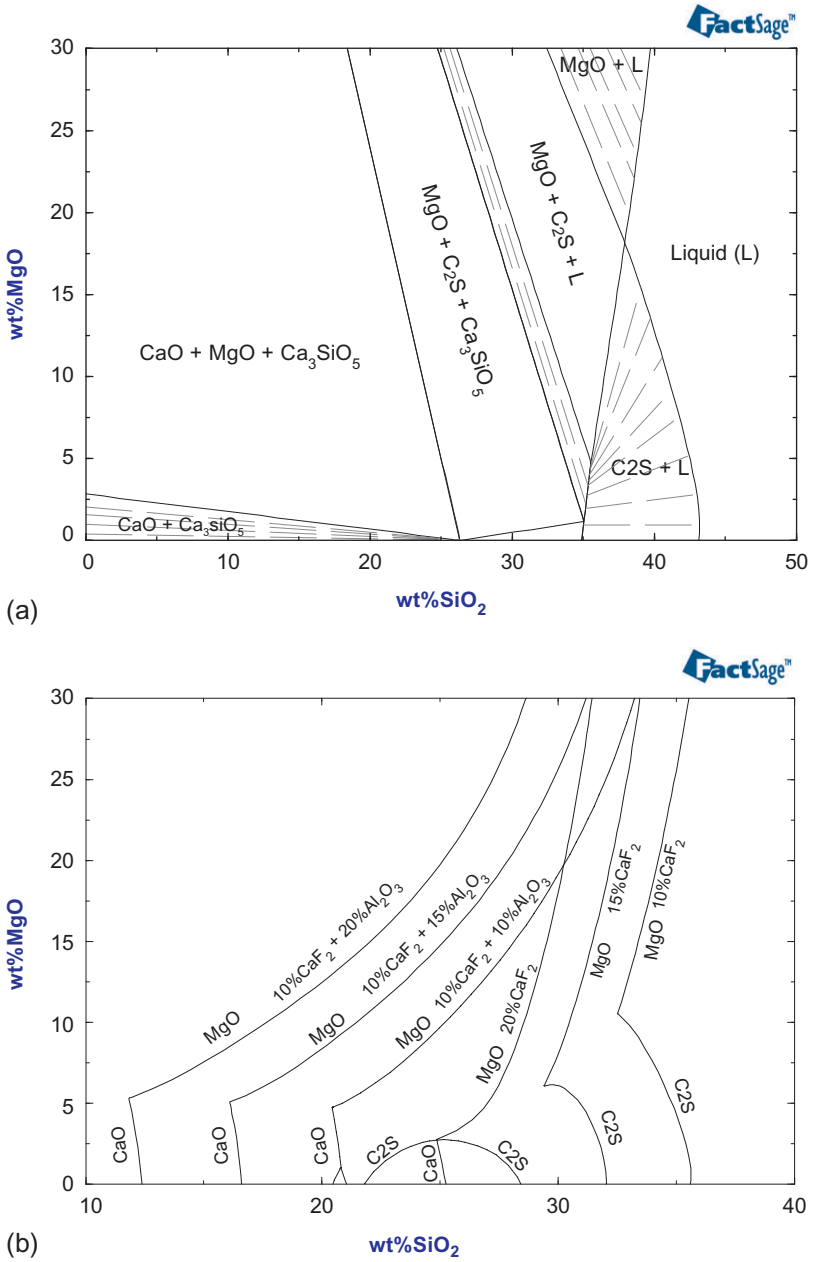


Figure 5.3.24 Calculated phase diagram and liquidus for the $CaO–SiO_2–MgO–Al_2O_3–CaF_2$ system at 1600 °C from the present thermodynamic database. (a) Phase diagram of the $CaO–MgO–SiO_2$ reference system, and (b) influences of CaF_2 and Al_2O_3 on the liquidus of the $CaO–MgO–SiO_2$ system [57].

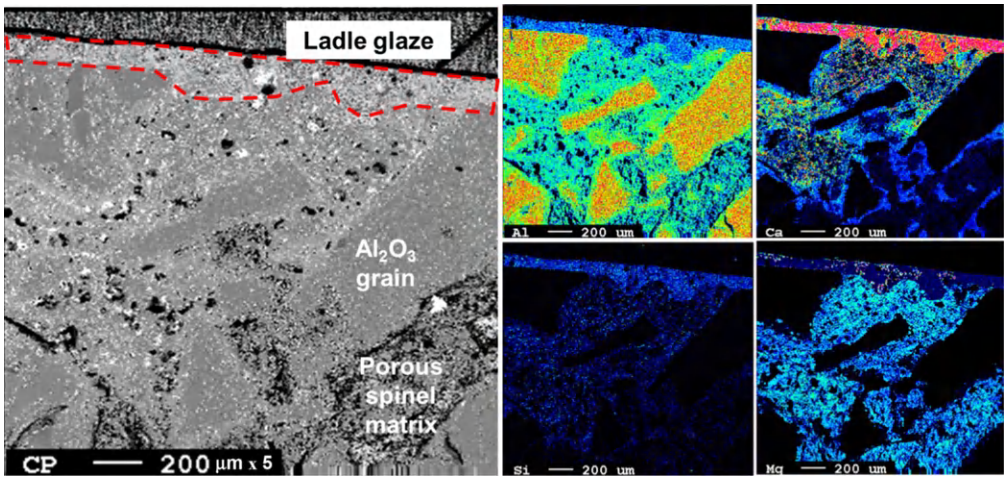


Figure 5.3.25 Formation of ladle glaze on the high Al_2O_3 castable refractory after dipping of the refractory into molten ladle slag at 1600 °C for 2 min.

image. The close microstructural examination of the ladle glaze showed the glaze was saturated with spinel. Chemical reaction between ladle slag and high alumina castable refractory calculated in Figure 5.3.26 using the FactSage FToxid database, and the results are in good agreement with experimental data. The details of the experimental results are discussed in the reference by Son *et al.* [53].

5.3.1.6.2.3 Interaction with RH Vacuum Degasser Slag

Recently, Cho *et al.* [58] performed the experimental study on the corrosion of two typical types of RH refractories, magnesia-carbon, and magnesia-chromite refractories against five different slags at 1600 °C to understand the refractory degradation mechanisms during the RH process: a typical ladle slag, two FeO-rich slags containing 20 and 40 wt%FeO, and two CaO–Al_2O_3 slags. Microstructural investigations of the as-delivered and worn refractories were carried out to study the interactions between slag and refractory. In addition, thermodynamic calculations using the FactSage FToxid database were performed to assist with the interpretation of the experimental results.

An example for the thermodynamic calculations in comparison with the experimental data is presented in Figures 5.3.27 and 5.3.28. High FeO slag was chosen to simulate the chemical reactions between RH refractory and high FeO slag in RH vessel after oxygen blowing before Al deoxidation. High Al_2O_3 slag is representative of the RH slag composition after Al deoxidation until the end of the RH process. Figure 5.3.27 shows the SEM–BSE images of magnesia-chromite refractories reacted with high FeO slag and high Al_2O_3 slag for 10 min at 1600 °C. The refractory samples, which are about 1 cm diameter, were completely infiltrated by both slags. In Figure 5.3.27, the light-gray phase in

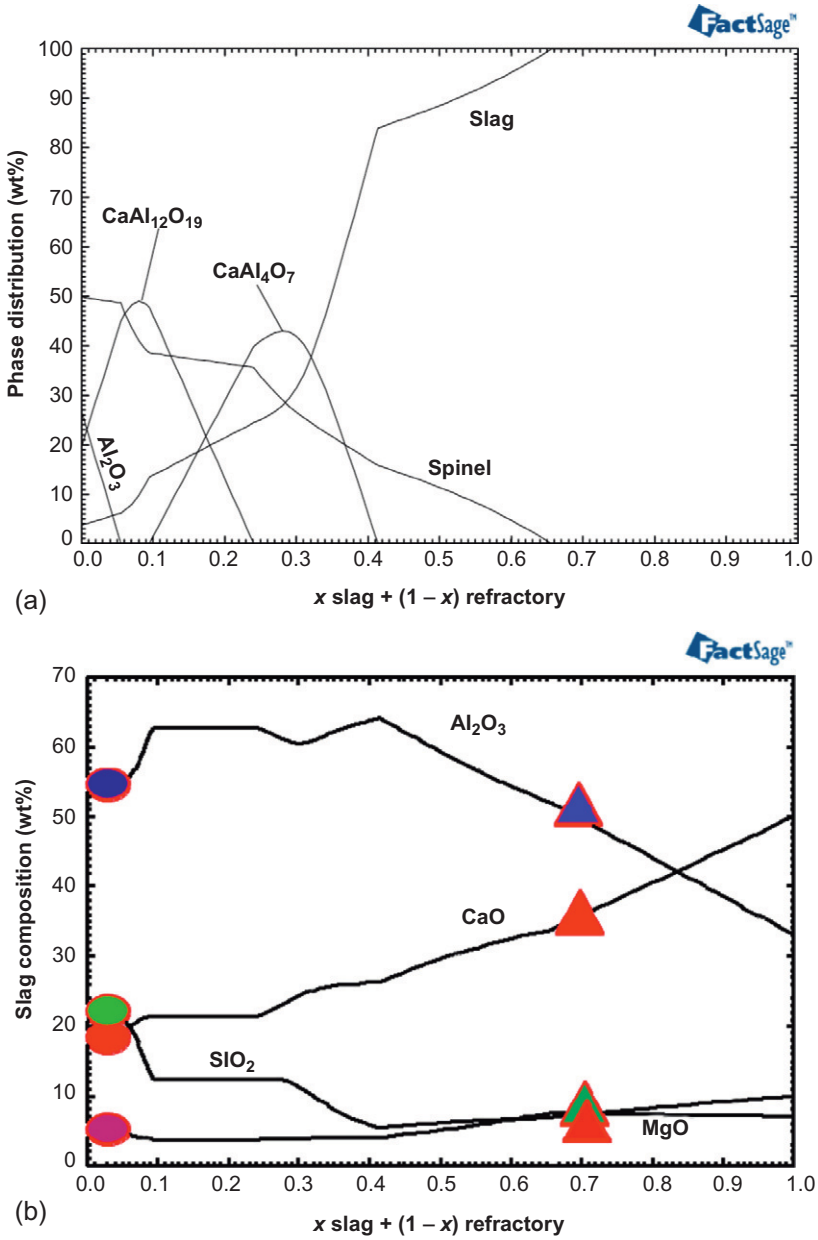


Figure 5.3.26 Chemical reactions between ladle slag and high Al_2O_3 castable refractory at 1600 °C to form ladle glaze. (a) Overall phase assemblage by the interaction between slag and refractory and (b) compositions of original ladle slag (circles) and glaze (triangles).

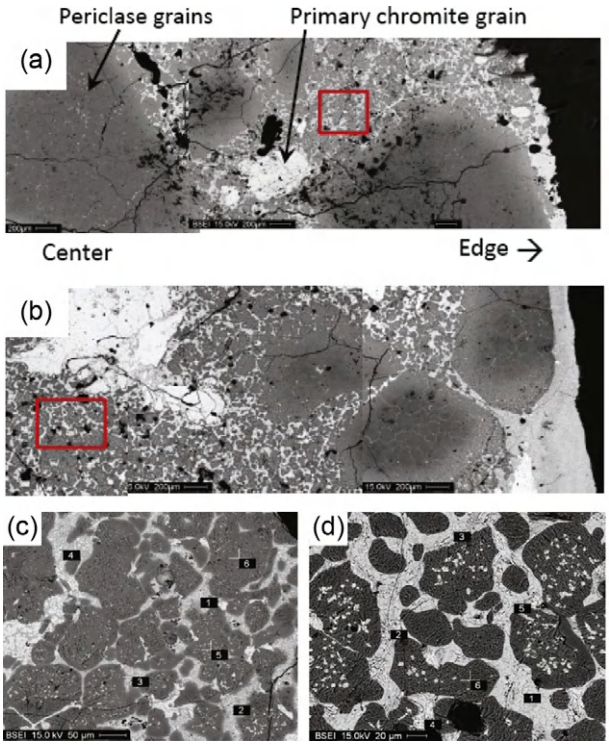


Figure 5.3.27 SEM–BSE images of magnesia-chromite refractories (55.8MgO–22.9Cr_2O_3–2.1SiO_2–8.2$Al_2O_3$11.0Fe_tO in wt%) reacted with (a) high FeO slag (43.2CaO–21.3Al_2O_3–20Fe_tO–8.3SiO_2–7.3MgO in wt%) and (b) high Al_2O_3 slag (51.2CaO–41.8Al_2O_3–7.0MgO in wt%) for 10 min at 1600 °C. Images (c) and (d) are enlarged views of the microstructure of the square regions in (a) and (b), respectively.

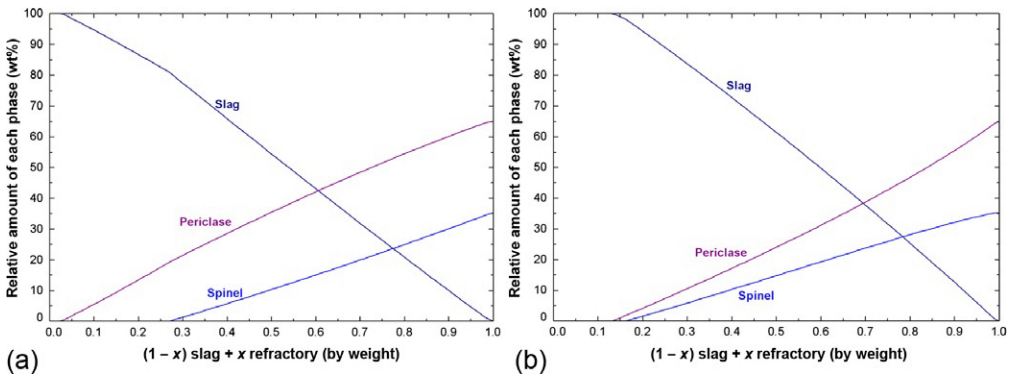


Figure 5.3.28 Thermodynamic calculations for the corrosion of magnesia-chromite refractories by (a) high FeO slag (43.2CaO–21.3Al_2O_3–20Fe_tO–8.3SiO_2–7.3MgO in wt%) and (b) high Al_2O_3 slag (51.2CaO–41.8Al_2O_3–7.0MgO in wt%) at 1600 °C.

between the dark-gray periclase (MgO) grains is the infiltrated slag. The main difference between two experimental results is as follows: (i) periclase grains are more fragmented in the high Al_2O_3 slag and (ii) spinel particles are more dissolved in the high FeO slag.

5.3.1.6.2.4 Interaction with Mold Flux

Fox *et al.* [54] performed Confocal Scanning Laser Microscope (CSLM) experiments to observe the dissolution behavior of ZrO_2, Al_2O_3, MgO, and $MgAl_2O_4$ particles in fluoride-free mold flux ($CaO–SiO_2–Na_2O–MgO–Al_2O_3–B_2O_3$). As can be seen in Figure 5.3.29, they computed the phase diagram of "ZrO_2–mold flux" system using MTDATA in order to understand the dissolution mechanism of ZrO_2. The calculation result shows that ZrO_2, a common submerged entry nozzle (SEN) material, can directly dissolve into the mold flux at 1500 °C without producing any protective layer, which was confirmed by CSLM experiments. This means that ZrO_2 is not the optimum SEN material for the fluoride-free mold flux from the chemical corrosion viewpoint.

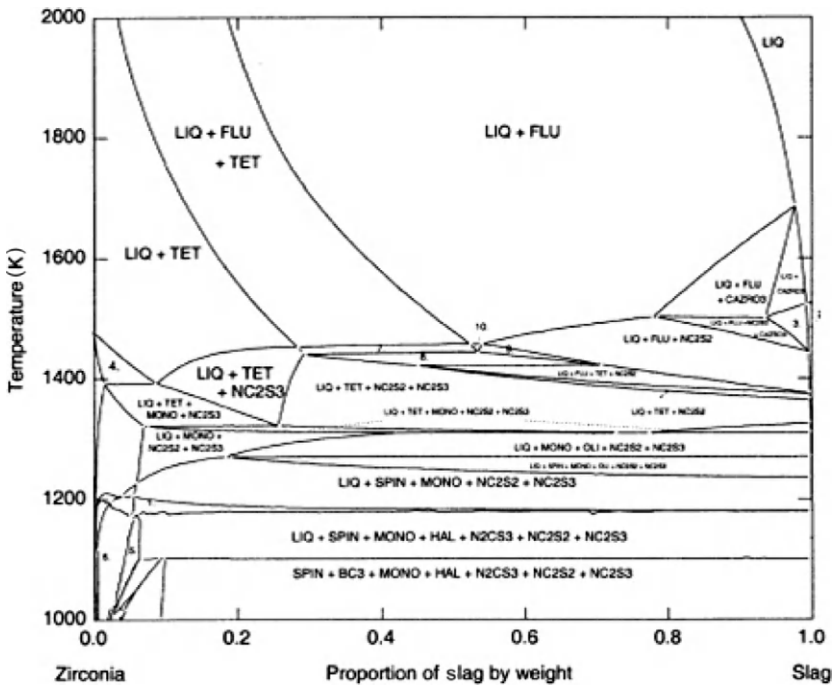


Figure 5.3.29 Calculated phase diagram of "ZrO_2–slag" system using MTDATA [54]. The composition of slag is $20CaO–9Al_2O_3–40SiO_2–9MgO–20Na_2O–0.5Li_2O–1.5B_2O_3$ in wt%. FLU, TET, and LIQ represent cubic ZrO_2 solution, tetragonal ZrO_2 solution, and liquid, respectively.

5.3.1.6.3 Metal/Refractory Interactions

Refractories used in the secondary metallurgy and continuous reactors are complex materials. In industrial conditions, their structure and composition can be modified either because the constituting phase assemblage at room temperature is not stable at high temperature or because of the interaction with the slag and/or with the metal.

Thermodynamics is used to analyze these stability problems and to understand their consequences on the purity and cleanliness of the metal. Because of the complexity of the involved chemical reactions, the use of thermodynamic models able to handle multicomponent problems is required.

5.3.1.6.3.1 Tundish Refractory

In continuous casting tundishes, the most widely used refractory products are constituted by a mixing of two phases: magnesia and olivine (solid solution $2(MgO,FeO)–SiO_2$). In laboratory experiments performed at Irsid [59], several specimen of this kind of product, with different olivine to magnesia ratios, have been tested by immersion in an aluminum-killed steel at 1600 °C in a 1 kg induction furnace. The main consequence of the reactions with the refractory is an Al loss of the metal. That means the formation of an additional amount of alumina inclusions which, even if, for kinetic reasons in industrial conditions, it remains quite limited, could be all the more detrimental to the steel cleanliness and castability since it takes place in the tundish that is to say downstream from the liquid metal elaboration line. Figure 5.3.30 shows that the main reaction causing this reoxidation is the reduction of the iron oxides which content increases with the silica content of the refractories, i.e., with their olivine proportion. This figure also confirms that the water content is also an important factor. Refractory products fired at 1200 °C

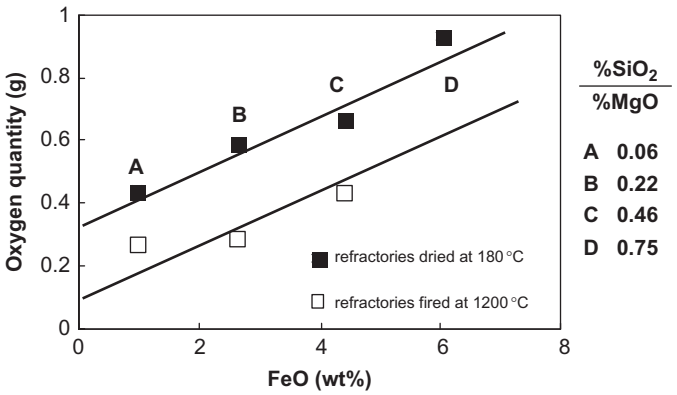


Figure 5.3.30 Relation between the oxygen fixed by the aluminum of the bath (1 kg metal) after an hour and the FeO content of the refractories.

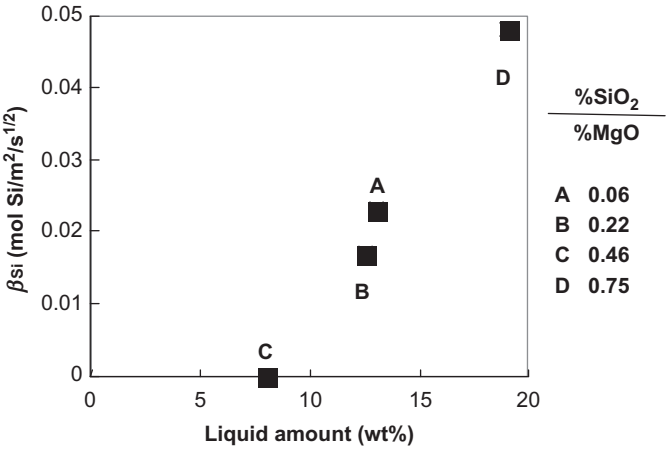


Figure 5.3.31 Effect of the amount of liquid silicate contained in the refractories on the transfer kinetics of Si pickup by the metal (it has been observed that the Si pickup is a linear function of the square root of time for all the refractories and β_{Si} is the slope of this function).

before the immersion in the metallic bath provoke less reoxidation than refractories simply dried at 180 °C.

Another consequence of the reaction on the metal analysis is a small increase of the silicon content. Unlike reoxidation, Si pickup is not a simple function of refractory composition.

Figure 5.3.31 shows that the transfer kinetics of Si pickup by the metal (β_{Si}) is related to the amount of liquid silicate contained in the different refractories. This liquid amount has been evaluated with the cell model. It depends not only on the oxide contents of the main phases, SiO_2, MgO, and FeO, but also on the oxides, notably CaO and Al_2O_3, brought by the interstitial phases (like monticellite SiO_2–MgO–CaO) of the refractories.

The transposition to the industrial scale shows that this transfer, in the case of the tested refractories, will not provoke any noticeable Si pickup. But these results emphasize the role of the liquid oxide and it will be shown later that its presence can also induce the precipitation of potentially harmful inclusions.

5.3.1.6.3.2 Effect of Antioxidant Additions to MgO–C on the Steel Cleanliness

If the addition of an antioxidant (Al, SiC, etc.) protects the magnesia-graphite from a too rapid oxidation during preheating, the very low oxygen activity that it imposes in its vicinity can cause the precipitation of (Ca,Mg) sulfides even if the sulfur content remains quite low. This precipitation of sulfides has been systematically observed on the dense layer which always covers the refractory product after laboratory experiments conducted on a MgO–C refractory product with Al addition as antioxidant immersed in Al-killed steels with sulfur contents as low as 60–80 ppm.

The presence of sulfides is due to the reduction of magnesium and calcium oxides of the dense layer according to the reactions:

$$CaO + \underline{S} \rightarrow CaS + \underline{O} \tag{5.3.12}$$

$$MgO + \underline{S} \rightarrow MgS + \underline{O} \tag{5.3.13}$$

As mentioned before, Ca comes from the interstitial phases of magnesia refractory. At high temperature, besides being fixed by the sulfides, this element is dissolved as CaO in the liquid oxide phase that is present in the dense layer. Therefore, to calculate the sulfides stability domain, we have used the value of the CaO activity calculated with the cell model for the liquid oxide in equilibrium with magnesia and spinel ($MgO{\cdot}Al_2O_3$) in the system Al_2O_3–CaO–MgO.

Figure 5.3.32 gives the minimum values of the sulfur activity for which (Ca,Mg)S will precipitate in the vicinity of the dense layer as a function of the aluminum content of the steel. In the case of a refractory without any antioxidant, the aluminum content of steel near the refractory will be equal or even smaller than the bulk Al content of the bath. Figure 5.3.32 shows that, in this case, for a steel containing 0.03% aluminum, sulfides will appear only for a sulfur content larger than 0.015%. On the contrary, if the refractory contains metallic Al as an antioxidant, the Al activity near the interface will be much larger than the nominal activity of the bath. In this case, sulfides will precipitate for smaller sulfur content. Figure 5.3.32 shows that they precipitate for 0.008% as soon as the Al activity reaches 0.08%.

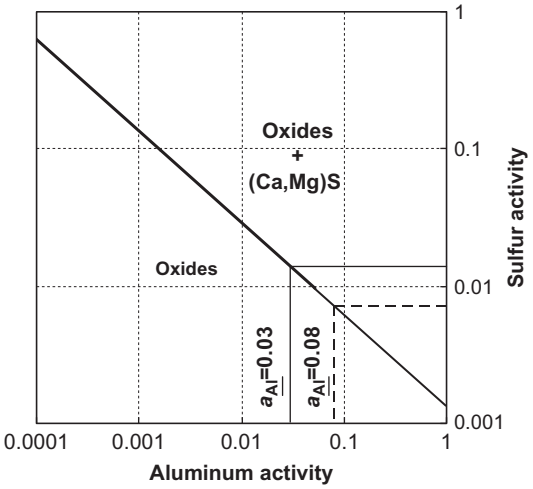


Figure 5.3.32 Minimum sulfur activities for which a precipitation of (Ca,Mg)S will occur at 1600 °C as a function of the aluminum activity of a liquid steel in equilibrium with spinel, magnesia, and the equilibrium liquid oxide of the system Al_2O_3–MgO–CaO. All the activities are referenced to the 1 wt% dilute solution in liquid iron. The solid solution (Ca,Mg)S is considered to be ideal.

5.3.1.6.3.3 Reaction of Refractories and High Mn Steels

Recently, high Mn steel like TWIP (TWin-Induced Plasticity) steel and other advanced high-strength Mn steels containing more than 10 wt% of Mn are produced and under development. One of the critical issues in the production of the steels is their chemical reactions with refractory materials in ladle treatment. Figures 5.3.33 and 5.3.34 show the

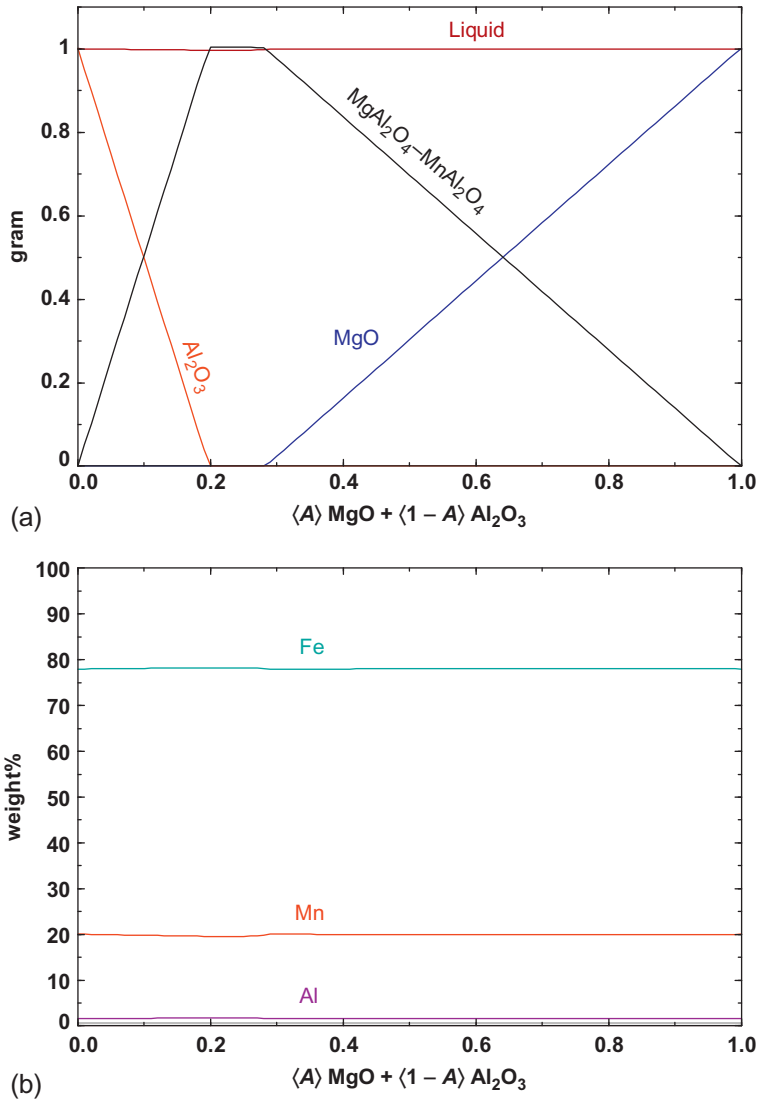


Figure 5.3.33 Chemical reaction between TWIP steel and MgO–Al_2O_3 refractory at 1500 °C. (a) Overall phase distribution and (b) chemical composition of molten steel depending on the refractory composition.

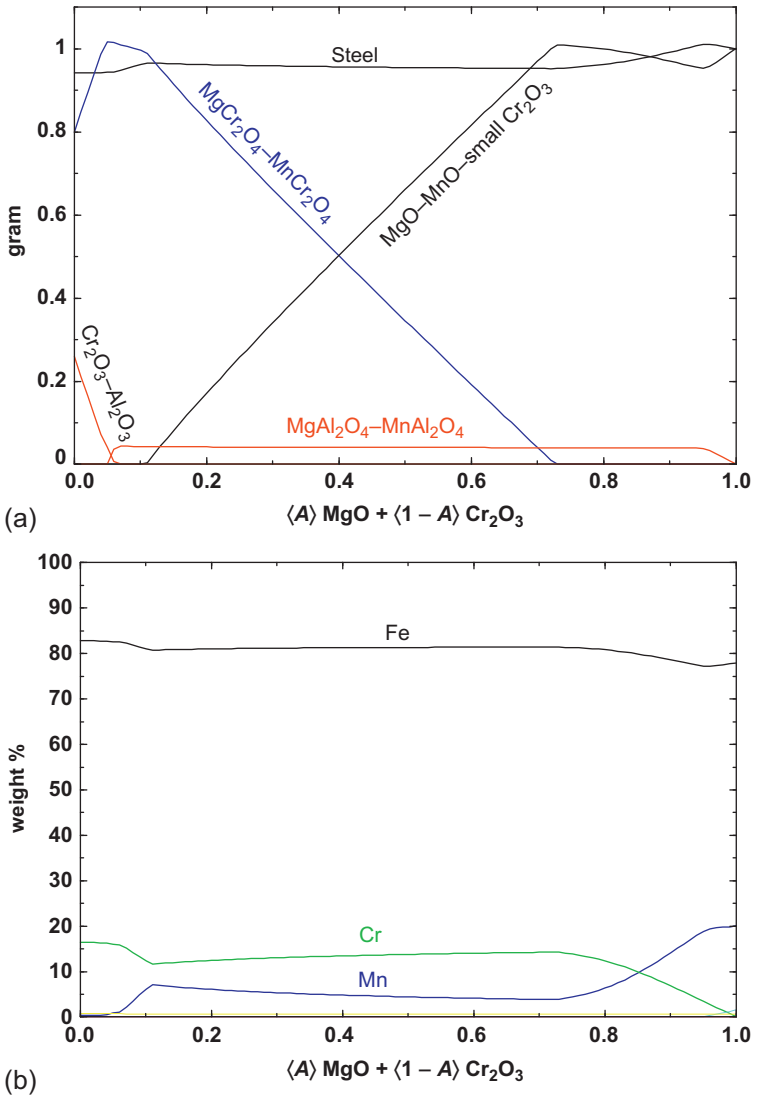


Figure 5.3.34 Chemical reaction between TWIP steel and MgO–Cr_2O_3 refractory at 1500 °C. (a) Overall phase distribution and (b) chemical composition of molten steel depending on the refractory composition.

possible chemical reactions between molten steel (Fe–20Mn–1.5Al–0.6C in wt%) and two types of refractories, MgO–Al_2O_3 and magnesia-chromite at 1500 °C, respectively, calculated from FactSage FToxid database [60]. As can be seen in Figure 5.3.32, the refractory made of MgO–Al_2O_3 has nearly no severe chemical reaction with molten steel. However, Mn in the steel can induce severe corrosion of MgO–Cr_2O_3 refractory.

Cr_2O_3 and $MgCr_2O_4$ can be reacted by Mn and Al in molten steel due to the following chemical reactions:

$$3\underline{Mn} + 4Cr_2O_3 = 3MnCr_2O_4 + 2\underline{Cr} \quad (5.3.14)$$

$$3\underline{Mn} + 6\underline{Al} + 4Cr_2O_3 = 3MnAl_2O_4 + 8\underline{Cr} \quad (5.3.15)$$

$$\underline{Mn} + 2MgCr_2O_4 = 2MgO + MnCr_2O_4 + 2\underline{Cr} \quad (5.3.16)$$

Thus, the special attention can be required to select the refractory materials for high Mn production.

5.3.1.6.4 Corrosion of Nozzle Refractories by Liquid Inclusion in High Oxygen Steels

Most of the continuous casting refractories including SEN, slide gate nozzle plate (SN plate), and tundish stopper contain a significant amount of carbon and are highly subject to the corrosion by high oxygen steel and liquid inclusions [61–65]. Typical refractory materials for the nozzle and stoppers are spinel–C, Al_2O_3–C, ZrO_2–C, MgO–C, and Al_2O_3–SiO_2–C (alumina–mullite–C). There are several types of liquid inclusions occurring at secondary steelmaking process: CaO–Al_2O_3–SiO_2-based inclusion after Al deoxidation and Ca treatment, MnO–Al_2O_3–SiO_2 inclusion after Mn/Si deoxidation, and MnO–SiO_2–MnS-based inclusion forming in high oxygen steels with high concentrations of Mn and S. In particular, as high oxygen steels contain a large amount of liquid oxide inclusions, the buildup of liquid inclusion around nozzle and stopper head can be inevitably more severe. For example, the stopper head made of Al_2O_3–C refractory corroded after series of continuous casting of high oxygen steel is presented in Figure 5.3.35. The original stopper head of hemisphere shape is irregularly eroded, which causes difficulty in accurate control of molten metal flow during casting process and eventually induces casting defects of the steel products. The erosion of the stopper is considered as the result of the corrosion of stopper refractories by liquid inclusions in the molten

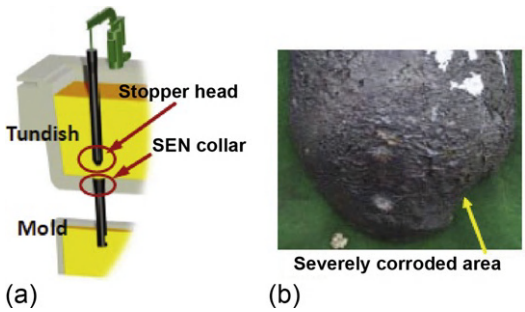


Figure 5.3.35 Refractories in continuous casting process. (a) Schematic of the stopper system and (b) example of corroded stopper after continuous casting of high oxygen steel (Al_2O_3–C refractory).

steel. All the calculations in this study were performed using the FactSage FToxid and FTmisc database [55].

5.3.1.6.4.1 Liquid Inclusion in High Oxygen Steel

The chemical composition of high oxygen steel investigated in this study is Fe–0.08C–1.2Mn–0.3S–0.01Si–O-minor P, Bi, etc., in wt%. Due to high sulfur and oxygen content, oxysulfide inclusions can form at ladle by Mn–Si deoxidation and at tundish due to temperature drop. The calculated inclusions are plotted in Figure 5.3.36. When the concentrations of all other alloying elements are fixed, the amount of inclusion forming in the molten steel can be varied with oxygen content. Thermodynamic calculations show that liquid inclusion can form in the entire temperature and oxygen concentration ranges considered in this study. According to the calculations (Figure 5.3.36a), liquid inclusion can form at 1550 °C when oxygen content in the molten steel becomes higher than 122 wt ppm, and the amount of the liquid inclusion increases linearly with increasing oxygen content. Once the inclusion is generated, the composition of inclusion is constant regardless of total oxygen content (Figure 5.3.36b): 62MnO–25SiO_2–7FeO–5MnS–1FeS in wt%. When total oxygen content is fixed to be 200 wt ppm, the inclusion can begin to form even at 1600 °C and the amount of liquid inclusion can increase linearly with decreasing of temperature (Figure 5.3.36c). The composition of liquid inclusion (Figure 5.3.36d) is also almost independent with temperature except that MnO concentration slightly increases with decreasing temperature. When small amount of Al is considered in the calculation, MnO–SiO_2–Al_2O_3–MnS inclusion can be calculated.

The liquid inclusion calculated in this study agrees with the inclusion observed in real plant steel sample. As mentioned earlier, the liquid inclusion of 62MnO–25SiO_2–7FeO–5MnS–1FeS was prepared for simulating the chemical reaction between the inclusion and refractories.

5.3.1.6.4.2 Chemical Reaction Between Liquid Inclusion and Refractories

In order to test the corrosion of refractory by liquid inclusion, the inclusion of 62MnO–25SiO_2–7FeO–5MnS was placed on various refractories including spinel–C, Al_2O_3–C, ZrO_2–C, MgO–C, and Al_2O_3–SiO_2–C and their interfacial reactions were experimentally observed. The chemical analysis results for Figures 5.3.37 and 5.3.38 are listed in Table 5.3.1. The details of experimental techniques and results can be found elsewhere [65].

5.3.1.6.4.2.1 $MgAl_2O_4$–C Refractory In order to test the corrosion behavior of spinel refractories containing both low (4 wt%) and high (13 wt%) amount of carbon were investigated in this study. As can be seen in Figure 5.3.37, the wetting behavior of liquid inclusion on $MgAl_2O_4$–C refractories was significantly changed with carbon content.

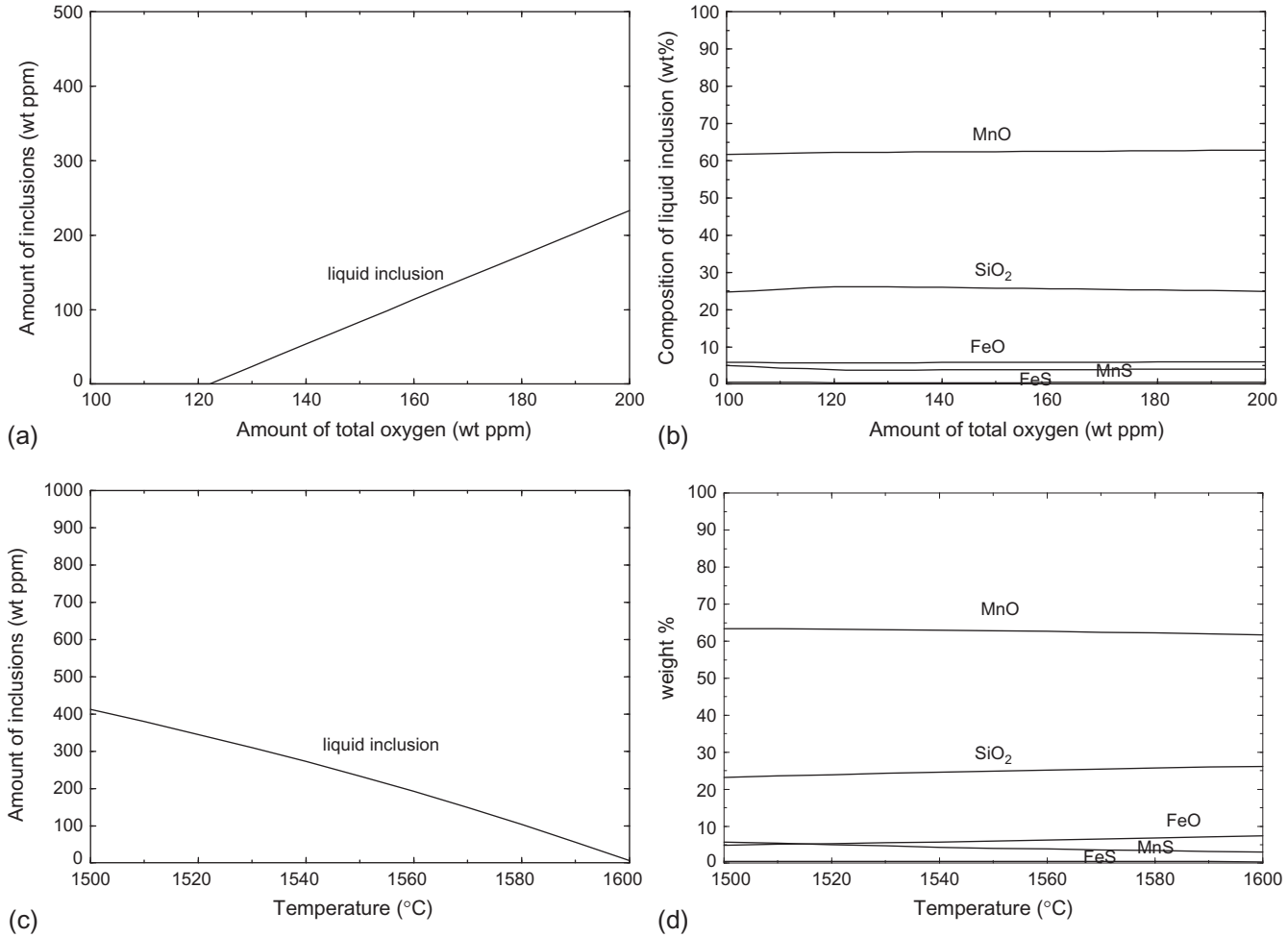


Figure 5.3.36 Calculated inclusions formed in high oxygen steel (Fe–0.08C–1.2Mn–0.3S–0.01Si–O–minor P, Bi, etc., in wt%) during continuous casting process. (a) and (b) Amount and composition of liquid inclusion varied with total oxygen content in steel at 1550 °C; (c) and (d) amount and composition of liquid inclusion in molten steel containing 200 wt ppm oxygen varied with temperature.

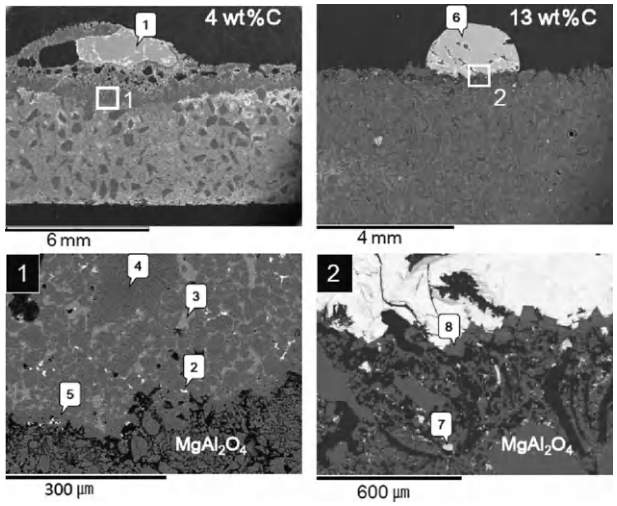


Figure 5.3.37 Microstructure of the $MgAl_2O_4$–C refractories (low carbon = 4 wt% and high carbon = 13 wt%) reacted with liquid inclusion. Overview of the cross section of the refractories and the zoom-up views of reaction interfaces between liquid inclusion and the refractories. 1 to 2 are the zoomed up views of refractory in top. See the table 5.3.1 for the chemical analysis.

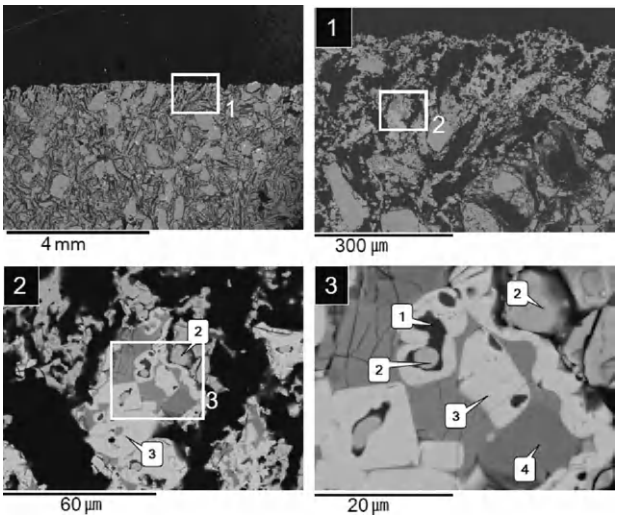


Figure 5.3.38 Microstructure of the ZrO_2–C refractory reacted with liquid inclusion. Overview of the cross section of the refractory (metallic droplet is detached during the postsample treatment) and the zoom-up view of reaction interface between liquid inclusion and the refractory. 1 to 3 are the zoomed up views of refractory in top left. See the table 5.3.1 for the chemical analysis.

The liquid inclusion was relatively well wetted on $MgAl_2O_4$–low C refractory, while no significant wetting behavior of liquid inclusion on the $MgAl_2O_4$–high C refractory was observed. The wetting behavior and liquid inclusion penetration into the refractories seem to be highly related to the reduction of inclusion by carbon in the refractories.

Table 5.3.1 Chemical Compositions of Various Phases After the Reaction Between Liquid Inclusion and Refractories, Determined by EPMA

	Oxide (mol%)							Metal/Sulfide (Atom%)			
#	MnO	SiO_2	FeO	Al_2O_3	MgO	CaO	ZrO_2	Fe	Mn	Si	S
Figure 5.3.37											
1								52	40	8	
2									68		32
3	18	50		9	23						
4	3			50	47						
5	2			52	46						
6								48	32	20	
7								4	92	4	
8	6			51	43						
Figure 5.3.38											
1		24		16		32	28				
2						7	93				
3							100				
4								59	8	33	

The $MgAl_2O_4$–low C refractory produced a large metallic particle in the middle of liquid inclusion sample, as shown in Figure 5.3.37. But there is still a large amount of liquid inclusion remained after the reduction by carbon. The remaining liquid inclusion penetrated well into the decarburized refractory and reacted with $MgAl_2O_4$ grain to form $(Mg,Mn)Al_2O_4$ spinel phase where MnO is about 2–3 mol% and liquid $18MnO–50SiO_2–23MgO–9Al_2O_3$ (in mol%) phase. Many pores can also be observed in the liquid inclusion area and the reaction area between liquid inclusion and $MgAl_2O_4$ refractory, which should be generated by CO gas bubbles.

In the case of $MgAl_2O_4$–high C refractory, the original liquid inclusion was almost completely transformed to a metallic droplet Fe–Mn–Si (48Fe–32Mn–20Si in at.%) as shown in Figure 5.3.37. The reaction interface shows a sharp distinction between metallic phase (originally liquid inclusion) and spinel refractory. Small amount of MnO oxide is reacted with spinel at the interface to form $(Mg,Mn)Al_2O_4$ spinel solution ($MnO < 7$ mol%), and small amount of metallic Mn–Fe–Si (94Mn–4Fe–2Si in at.%) phase is also observed. This microstructure tells that most of liquid inclusion was already

reduced to metallic phase by C in refractory before it reacted with spinel refractory. Small amount of liquid inclusion could penetrate into spinel refractory, but it was immediately reduced by C after the penetration.

5.3.1.6.4.2.2 ZrO_2–C Refractory The microstructure of ZrO_2–C refractory after the reaction with liquid inclusion is shown in Figure 5.3.38. Like $MgAl_2O_4$–C refractory above, no significant wetting of liquid inclusion happened on the refractory surface. The surface of the refractory is very flat and no noticeable chemical reaction is observed. Unfortunately, metallic droplet on the surface of the refractory like in Figure 5.3.37 was detached during the sample treatment. The metallic droplet composition was almost identical to that of $MgAl_2O_4$–high C case. Small amount of Fe–Mn–Si metallic phase can be observed near the interface between inclusion and the refractory. Among all other refractories, the ZrO_2–C refractory showed the least refractories wear by the liquid inclusion.

5.3.1.6.4.3 Corrosion Mechanism of Refractories by Liquid MnO–SiO_2–FeO Inclusion

The corrosion of continuous casting refractories by liquid inclusion can occur in two-stage processes: (i) reduction of liquid inclusion by carbon in refractories and (ii) the wetting and chemical reaction of the remaining liquid inclusion with refractory mineral phases.

In order to understand the reduction of liquid inclusion by carbon, thermodynamic calculations were performed and the results are presented in Figure 5.3.39. Two types of calculations were performed: (a) assuming the reduced metal can be continuously in equilibration with remaining liquid inclusion (solid line in Figure 5.3.39), and (b) assuming the reduced metal can be separated away from the remaining liquid inclusion during the reduction process (dashed line in Figure 5.3.39). The reality should be in between these two calculation conditions. According to the calculations, FeO can be firstly reduced and MnO and SiO_2 can be reduced afterward. The concentration of the resultant liquid metal is, therefore, changed with the degree of reduction (amount of carbon reacted). The more reduction of liquid inclusion by carbon, the higher concentrations of Mn and Si in liquid metal. Thus, the composition of metallic phase can give a reasonable estimate for the degree of reduction of liquid inclusion.

The possible corrosion mechanism of the refractories by liquid inclusion in high oxygen steels is presented in Figure 5.3.40. After the inclusion is attached to refractories, the inclusion can be partially reduced by C directly from refractories or the dissolved C (highly concentrated in steel near the refractories) in high oxygen steels. The degree of reduction can be mainly dependent on carbon content in refractories. The remaining inclusion (MnO–SiO_2) can attack decarburized region of refractories. The metallic phase produced by reduction (in particular, the large metal droplet on high C refractories) can be washed away by being dissolved into surrounding liquid steel. New liquid inclusion

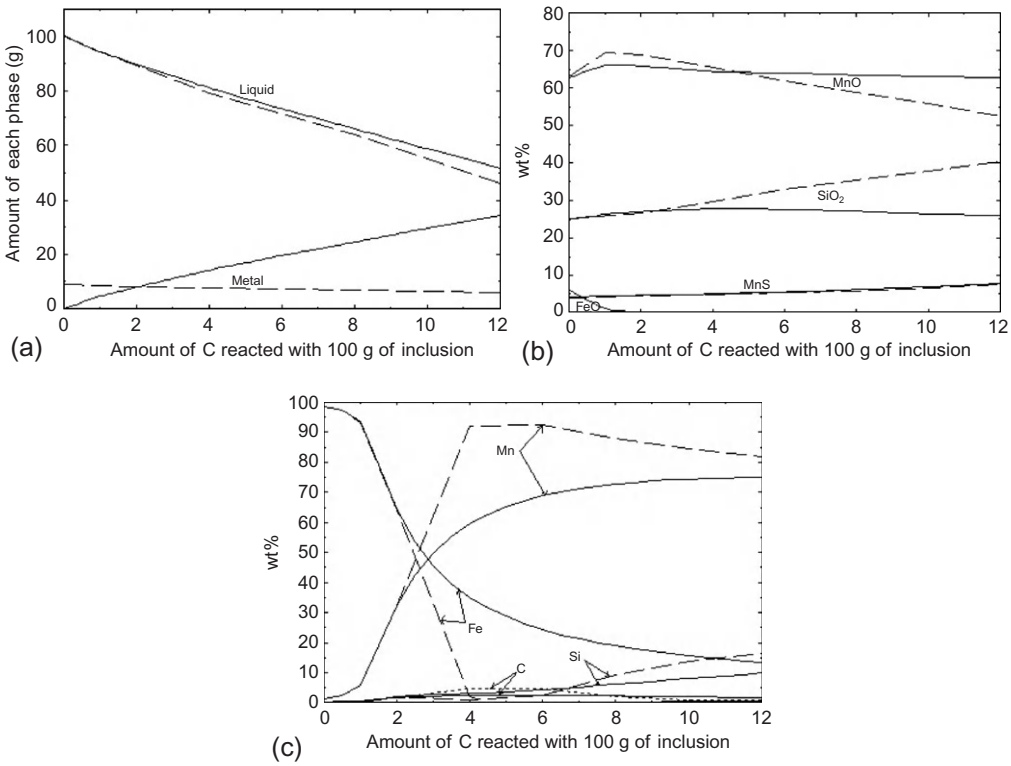


Figure 5.3.39 Reduction of 100 g of liquid inclusion ($MnO–SiO_2–FeO–MnS$ in wt%) with increasing amount of carbon. (a) Amount of liquid inclusion and metal, (b) composition of liquid inclusion, and (c) liquid metal. Solid lines were calculated with the assumption that the reduced metal can be continuously in equilibration with remaining liquid inclusion and dashed lines were calculated with the assumption that reduced metal cannot participate in further reaction with remaining liquid inclusion during the reduction process.

can be accumulated on the prereacted surface of the refractories and the similar reactions can occur repeatedly.

The following three factors can be important in the refractory corrosion in high oxygen steels, if the refractories have all same microstructure (size of oxide refractory grains, porosity, etc.):

- Amount of remaining liquid inclusion after the reduction by C in refractories
- The chemical solubility of refractory materials to the remaining liquid inclusion
- The wetting tendency and penetration force of the remaining liquid inclusion into the refractory (the penetration force can be related to the viscosity of liquid inclusion)

The more reduction of liquid inclusion by carbon remains, the less liquid inclusion to react with refractories. Therefore, in general, the high C containing refractory can be less corrosive and have longer life time. The chemical solubility (stability) of refractories

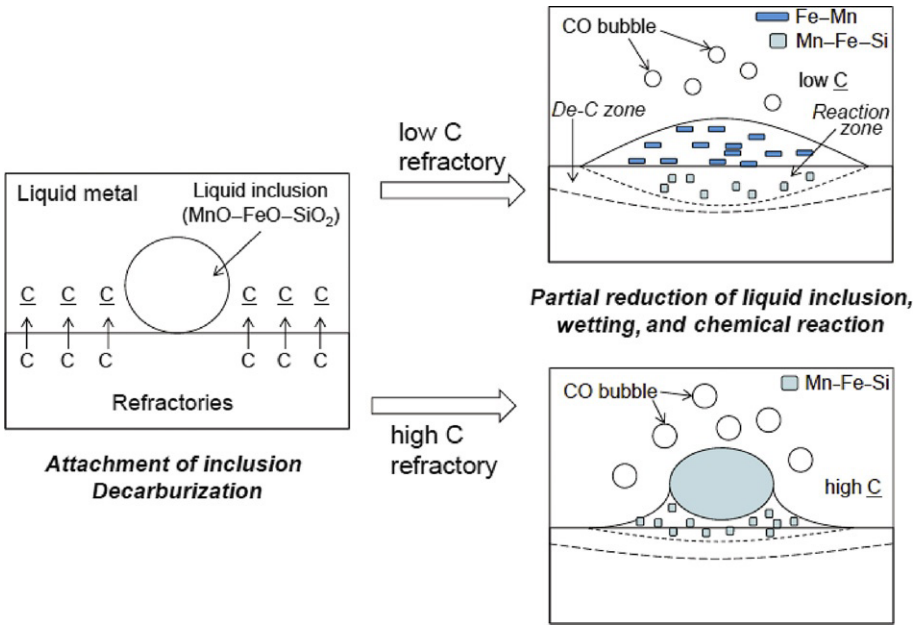


Figure 5.3.40 Refractory corrosion mechanism by liquid inclusion in high oxygen steels.

to the remaining liquid inclusion can be determined by phase diagram between refractories and liquid inclusion. The ternary phase diagrams of refractory oxide–MnO–SiO_2 systems at 1550 °C were calculated for the various refractory oxides, Al_2O_3, MgO, $MgAl_2O_4$, and ZrO_2 in Figure 5.3.41. As mentioned above, the MnO/SiO_2 ratio in the inclusion remained after the reduction is depending on the degree of reduction (mainly C content in refractory): (wt%MnO)/(wt%SiO_2) in the remaining inclusion can be about 3 and 1.5 (or even below 1.0) after low and high degree of reduction, respectively. If the decarburized zone in refractories was already developed, the remaining liquid inclusion can readily penetrate and react with oxide refractory grains. The viscosity of liquid inclusion can increase with decreasing basicity MnO/SiO_2. However, the change of the viscosity of the MnO–SiO_2-based liquid inclusion is slightly increasing but not significant when the basicity (wt%MnO)/(wt%SiO_2) of the inclusion varies from 3 to 1.5. Therefore, factors (i) and (ii) would be most important parameters for the corrosion of refractories by liquid inclusions in high oxygen steels.

According to the calculated phase diagrams in Figure 5.3.41, Al_2O_3–C refractory can be weak after both low and high degree of reduction. In case of the spinel–C refractory, the chemical stability of spinel phase can be weaker after high reduction than low reduction but the amount of remaining liquid inclusion after high reduction is much lower. Therefore, the corrosion tendency is lower at high reduction condition (high carbon

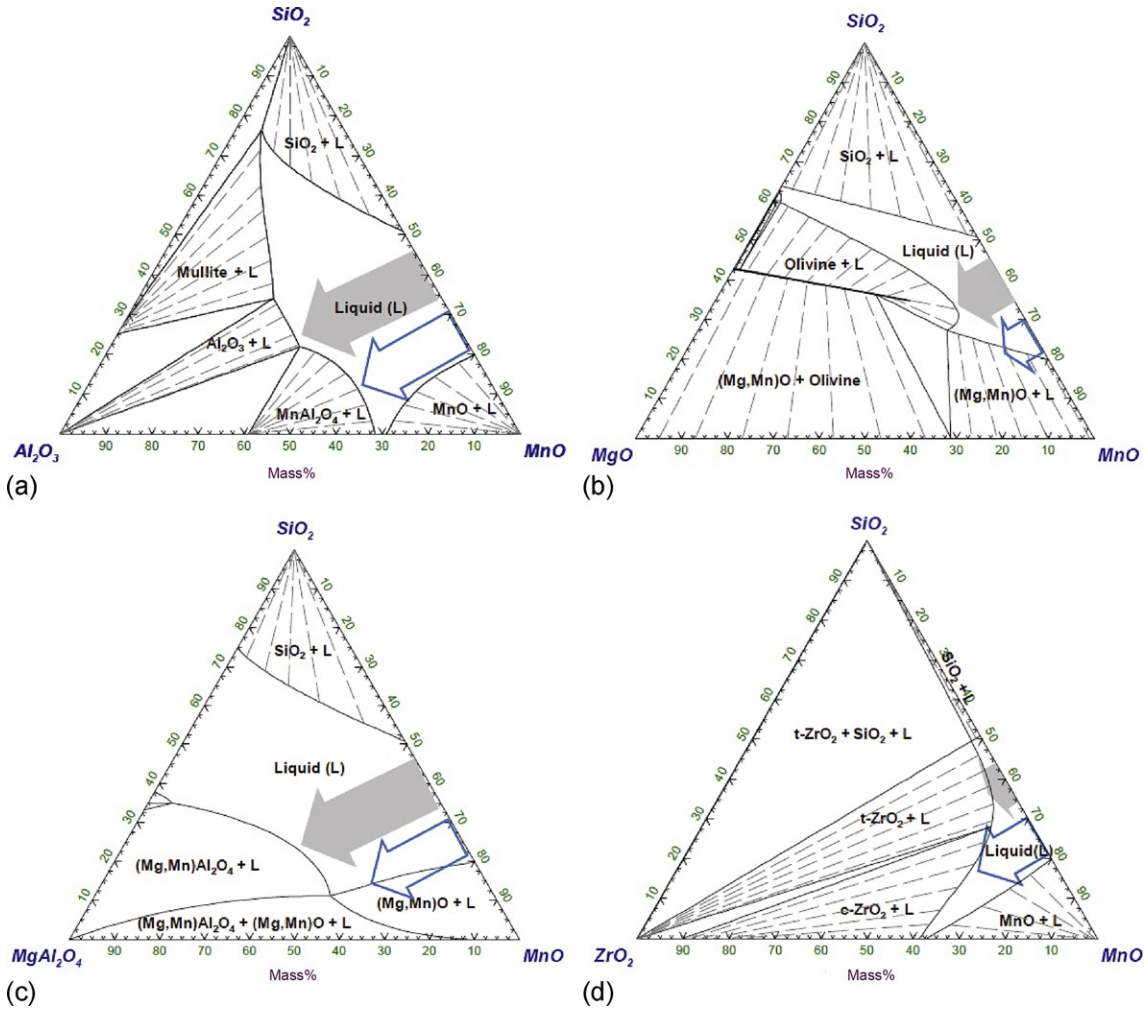


Figure 5.3.41 Thermodynamic stability of the refractory components against liquid inclusion (MnO–SiO_2) at 1550 °C. The arrows (gray arrow represents high degree of reduction, and empty arrow represents low degree of reduction) in phase diagrams represent the possible amount of dissolution of each refractory component.

spinel refractory). MgO–C refractory can be more stable than Al_2O_3–C and spinel–C refractory, but it can produce $(Mg,Fe)_2SiO_4$ olivine silicate as reaction product after high reduction. ZrO_2 refractory is very stable after high reduction of initial liquid inclusion, but less stable at no or less reduction of liquid inclusion.

If liquid inclusion in high oxygen steel contained a certain amount of Al_2O_3 (Al can be dissolved in molten steel from top slag, ladle refractories, and impurity from ferro-alloy, which can change the inclusion composition in return), the thermal stability of various oxide refractories can be different from the calculated results in Figure 5.3.41. For example, Al_2O_3–C refractory can be more stable than MgO–C refractory against the $MnO–SiO_2–Al_2O_3$ slag, as reported by Xie *et al.* [64] because the liquid slag can be readily saturated with Al_2O_3 with small amount of Al_2O_3 dissolution but a large amount of $MgAl_2O_4$ should be dissolved until the slag is saturated with $(Mg,Mn)Al_2O_4$.

In real continuous casting process, the influence of molten steel cannot be neglected. As Nomura *et al.* [61] reported from the microstructure of the Al_2O_3–C refractories dipped in molten steel (Fe–0.3Mn–0.004C–0.001Si–0.06O in wt%), the solute elements such as Mn can be reacted with the refractory oxide. For example, Nomura *et al.* interpreted the results as two-stage processes: (i) the formation of $(Mn,Fe)Al_2O_4$ by the reaction of $Al_2O_3 + \underline{Mn}$ (or $\underline{Fe}$) $+ 2\underline{O} \rightarrow (Mn,Fe)Al_2O_4$ and (ii) the modification of the oxide products by (Mn,Fe)O inclusion to produce $MnO–FeO–Al_2O_3$ liquid phase on the surface of Al_2O_3–C refractory. Even though this corrosion mechanism is considered for the present steel grade, the highly concentrated solutes Mn (1.2 wt%) and Si (0.01 wt%) in high oxygen steel can form liquid $MnO–SiO_2$–refractory phase on the surface of refractories in the early stage and then this liquid oxide can react with liquid $MnO–SiO_2$ inclusion. The resultant stability of refractories can be similar to the calculations in Figure 5.3.41.

5.3.1.6.4.4 In Plant Tests

Al_2O_3–AlN–C and ZrO_2–C refractories were tested for the stopper head refractories at Posco, Pohang work, Korea. The corrosion resistance of the refractories was evaluated by two casting process indexes typically used for stopper: mold level auto control and average profile distance during the casting. Both indexes show that the stopper of ZrO_2–C is superior to that of Al_2O_3–AlN–C. The number of continuous casting heats for high oxygen steels can be improved with the employment of ZrO_2–C stopper by 20–50% more compared to the casting heats with Al_2O_3–AlN–C stopper.

5.3.1.7. Inclusion Engineering

Inclusion control is the key to the production of clean or ultra clean steel. Inclusions appear in steel at various stages of its production and cause serious problems like nozzle clogging, crack initiation sites, degradation of surface quality, and so on. Inclusions can

be classified into two types: endogenous and exogenous. Endogenous inclusions are mainly formed during deoxidation, while exogenous inclusions are caused by slag entrapment, ladle glaze, erosion of refractories, and steel reoxidation. In addition, inclusion precipitation can occur upon cooling and solidification of steel owing to the change in solubility of dilute elements with temperatures. Although nonmetallic inclusions can move to the steel surface where they are captured by top slag, the removal of inclusions is very limited during the process due to the short process time and the continuous circulation of liquid steel in the ladle. Since the presence of inclusions cannot be avoided, it is essential to modify their composition to render them less harmful in modern steelmaking process. In some cases, composition-controlled inclusions can even be beneficial to steel properties.

Thermodynamically, the inclusion composition is very sensitive to the concentrations of even dilute elements in steel. Moreover, since the inclusions are composed of complex oxides, sulfides, and/or nitrides, accurate thermodynamic databases for both steel and inclusion are essential to perform complex thermodynamic calculations. In order to find out which inclusion phases is stably formed at a given molten steel, so-called inclusion diagrams (inclusion stability diagrams) have been widely used for inclusion engineering [66] in steelmaking.

5.3.1.7.1 Mn/Si Deoxidation

Although Al is one of the most common deoxidants widely used in steelmaking process, undeformable Al_2O_3 inclusions are generated during Al deoxidation, which may provide crack initiation sites during deformation of steel. In order to avoid the harmful Al_2O_3 inclusions, Mn/Si complex deoxidation, which results in the formation of inclusions of low melting temperature, is indispensable for the production of many high-value steels such as tire-cord steel, high-strength steel, and invar steel. The main goal of Mn/Si deoxidation is to obtain fully or partially liquid oxide inclusions even below 1200 °C. In actual steelmaking processes, Mn/Si deoxidation usually produces liquid $MnO–Al_2O_3–SiO_2$ inclusions as the deoxidation products. The inclusion chemistry is closely related to that of molten steel. The $MnO–Al_2O_3–SiO_2$ inclusions can gradually change to the $CaO–MnOAl_2O_3–SiO_2$ inclusions by indirect reaction with top slag containing CaO.

Figure 5.3.42 shows the calculated liquidus projection of the $MnO–Al_2O_3–SiO_2$ system [67]. In order to obtain liquid oxide below 1200 °C, the concentrations of Mn, Si, and Al in molten steel should be tightly controlled. Figure 5.3.43a shows the variation of the $MnO–Al_2O_3–SiO_2$ inclusion composition with Mn/Si ratio in molten steel along with experimental data [68]. In addition, the concentrations of Al and O in equilibrium with the oxide inclusion are calculated in Figure 5.3.43b. In order to obtain liquid $MnO–Al_2O_3–SiO_2$ inclusions at 1200 °C, the Mn/Si ratio and the Al concentration should be controlled tightly: $2 < (\text{wt\%Mn/wt\%Si}) < 10$ and $0.1 < \text{wt ppm Al} < 0.5$.

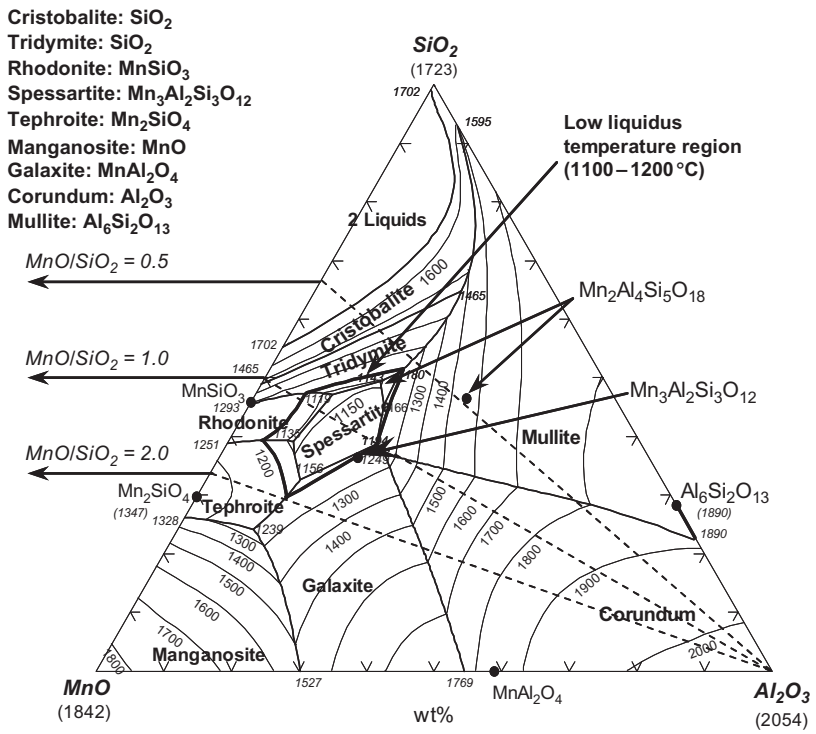


Figure 5.3.42 Calculated liquidus surface of the MnO–SiO_2–Al_2O_3 system using FactSage FToxid database [67]. Temperature in °C.

In actual steelmaking practice, $2.0 < Mn/Si < 3.0$ is used in the deoxidation process. However, the Al content is hardly controlled within this range to obtain fully liquid oxide inclusions.

After deoxidation, the chemistry of the nonmetallic inclusions can be indirectly modified by top slag chemistry via molten steel. The chemistry of top slag can influence the chemistry of the molten steel, which can in turn alter the inclusion chemistry. In reality, the Al content in molten steel after Mn/Si deoxidation can be controlled by top slag. Figure 5.3.44 shows the chemical equilibrium between top slag and MnO–Al_2O_3–SiO_2 inclusion via molten steel. The top slag saturated with Ca_2SiO_4 and containing 15 wt% Al_2O_3 can provide about 3–5 wt ppm Al in molten steel at 1550 °C, which can subsequently produce liquid MnO–Al_2O_3–SiO_2 inclusions saturated with Al_2O_3 [69]. The chemistry of ladle slag is therefore very important to control the inclusion composition.

The inclusion chemistry can be further modified during the LF treatment. Figure 5.3.45 shows the calculated compositional trajectory of the MnO–Al_2O_3–SiO_2 inclusions produced by the Mn/Si deoxidation process by indirect reaction with top slag composed of 55CaO–15Al_2O_3–SiO_2 (in wt%) [70]. As can be seen in the diagram, the

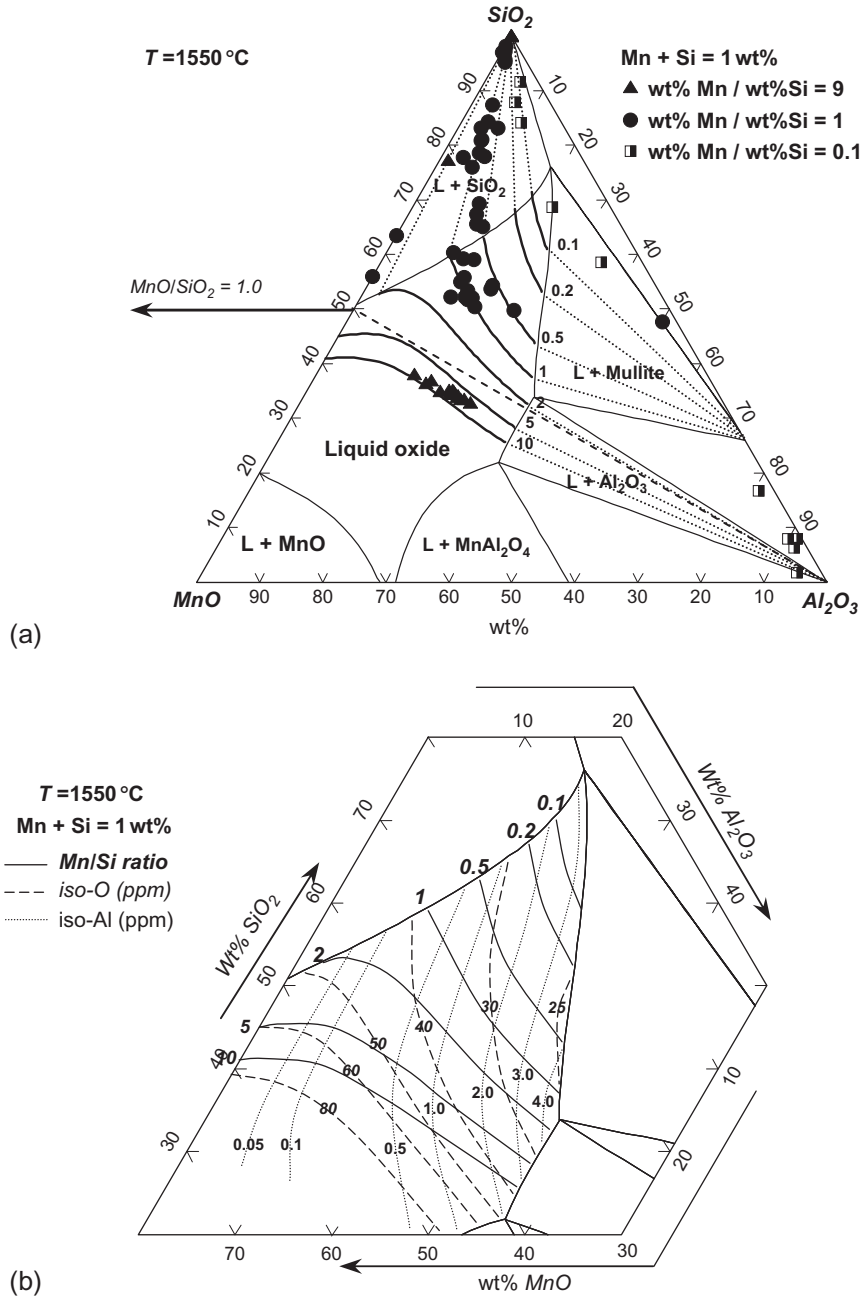


Figure 5.3.43 Computed $MnO–Al_2O_3–SiO_2$ inclusion composition in equilibration with Mn/Si deoxidized steels at 1550 °C [67,68]. The lines with values indicate the composition of Mn/Si deoxidized steel. (a) Calculated inclusion composition in comparison with experimental data, and (b) calculated Mn/Si ratio, iso-oxygen and iso-aluminum in steels. Calculations were performed using FactSage FToxid/FTmisc database.

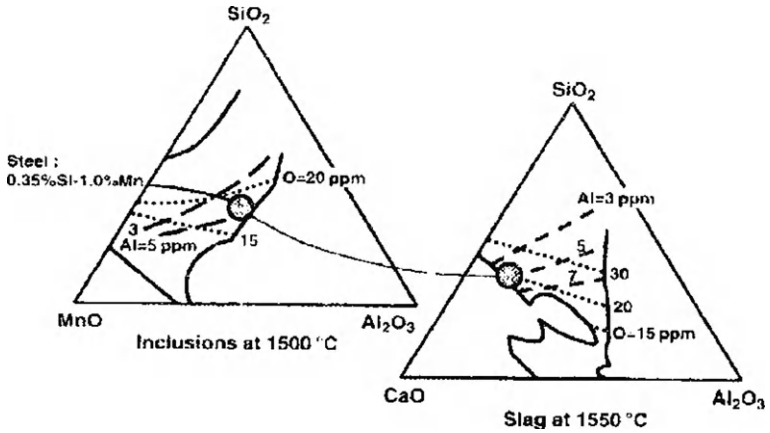


Figure 5.3.44 The calculated isothermal sections of the phase diagram at $CaO–SiO_2–Al_2O_3$ at 1550 °C and $MnO–SiO_2–Al_2O_3$ at 1500 °C [69]. The dotted lines represent the Al and O in steel in equilibrium with the slag and inclusion. The circles indicated in both diagrams present the liquid $MnO–Al_2O_3–SiO_2$ inclusion composition produced by the $CaO–SiO_2–Al_2O_3$ top slag. Calculations were performed using CEQCSI.

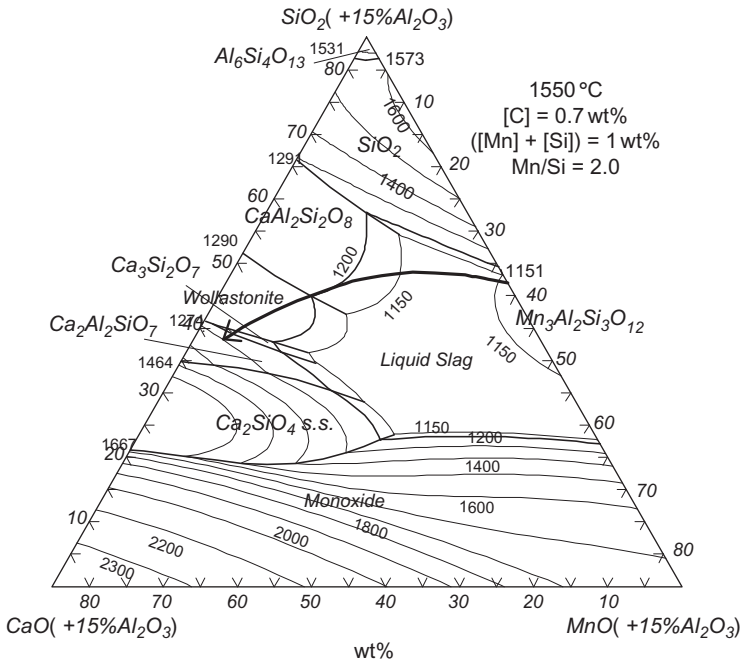


Figure 5.3.45 Calculated change of composition of inclusions formed during Mn/Si deoxidation (as shown by arrows) when the Mn/Si ratio equals 2.0 for tire-cord steel ([C] = 0.7 wt%) by reaction with CaO-containing top slag at 1550 °C (top slag composition: $55CaO–15Al_2O_3–30SiO_2$ in wt%). Predicted liquidus isotherms (T in °C) are also plotted [70]. Calculations were performed using FactSage FToxid/FTmisc database.

evolution of the inclusion composition in the course of the treatment can lead to a further decrease of their melting temperature.

5.3.1.7.2 Formation of Oxisulfide Inclusions

Free cutting steels frequently contain high amount of sulfur in order to distribute a large amount of oxysulfide precipitates, which can limit the machining chip length and form protective films on machining tools when steels are machined. Recently, accurate thermodynamic databases for various oxysulfide systems are available both in CEQCSI and in FactSage. For example, the liquidus projection and isothermal section of the MnO–SiO_2–MnS oxysulfide system of importance for free cutting steels are calculated [69,71] in Figure 5.3.46.

The formation of oxide, oxysulfide, and sulfide inclusions in free cutting steel Fe–0.07C–1.35Mn–0.014Si0.35S–0.006O (in wt%) was calculated [74]. The calculated distributions of oxygen and sulfur between different inclusion types during steel solidification are shown in Figure 5.3.47. The machinability of free cutting steels can be changed with the variation of inclusion type and relative amount of the inclusions, which can be well calculated using thermodynamic databases.

5.3.1.7.3 Inclusion Diagram of Al/Ti Deoxidation

High probability of nozzle clogging events has been reported during the production of IF steels containing a relatively high amount of Ti. The clog is formed by the accumulation of Al–Ti–O (Al_2O_3–TiO_2–Ti_2O_3) inclusions. Many experimental and thermodynamic studies [75–80] have been performed to understand the transitions of Al_2O_3 oxide inclusions, the reoxidation of IF steels, and the inclusion diagram of the Fe–Al–Ti–O system.

Figure 5.3.48 shows the predicted phase diagram of the Al_2O_3–TiO_2–Ti_2O_3 system [79] at 1600 °C from the FactSage thermodynamic database. No comprehensive phase diagram study has been performed under steelmaking conditions. According to the predicted diagram, a liquid phase can exist at 1600 °C under low oxygen partial pressure ($P_{O_2} \sim 10^{-13}$). The inclusion diagrams for Al/Ti complex deoxidation [75,79] are calculated in Figure 5.3.49 using thermodynamic databases from, respectively, CEQCSI and FactSage. Although the calculation results are slightly different (for example, the well-known Ti_3O_5 was not taken into account in CEQCSI calculation), the existence of a liquid oxide phase is predicted in both calculated diagrams. Usually, deoxidation of IF steels by Al addition is performed first, followed by Ti alloying (Ti = 0.07–0.2 wt% and Al = 0.03–0.05 wt%). According to the thermodynamic calculations in Figure 5.3.49, inclusions in IF steel should be composed of solid Al_2O_3. However, liquid and solid Al–Ti–O inclusions can be observed in the tundish, as a result of steel reoxidation by tundish slag. Liquid steel reoxidation can be caused by the reduction of less stable oxide components in slag

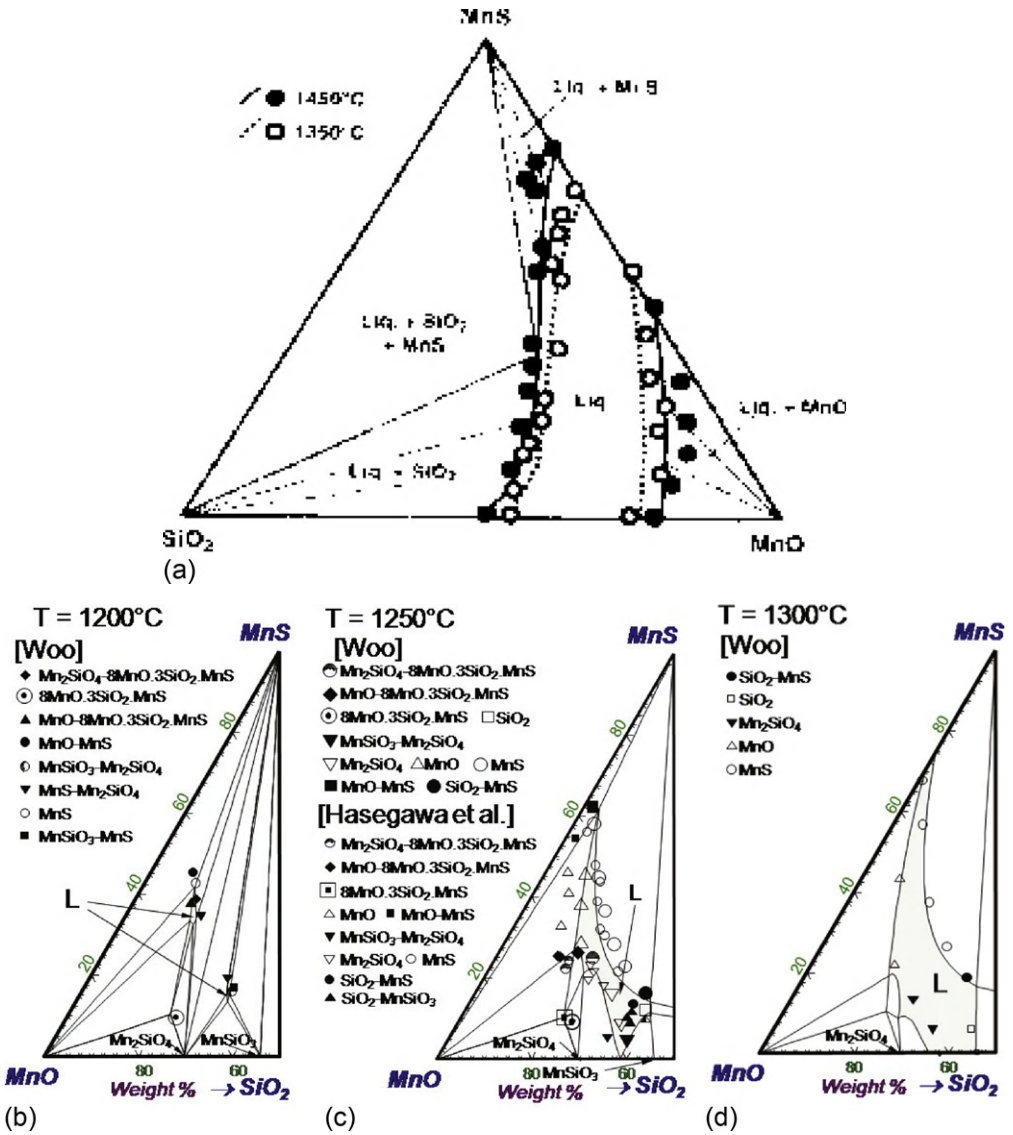


Figure 5.3.46 The calculated phase diagrams of the MnO–SiO_2–MnS oxysulfide system in comparison with experimental data [72,73]. (a) Calculated from CEQCSI [74] and (b)–(d) calculated from FactSage FToxid database [71].

such as SiO_2 and FeO by Al in molten steel [78,79]. As a result, the Al content in molten steel is locally decreased and may become sufficiently low for the formation of Al–Ti–O inclusions, as can be seen in Figure 5.3.49. These Al–Ti–O inclusions can be readily attached to the SEN wall resulting in the nozzle clogging phenomena.

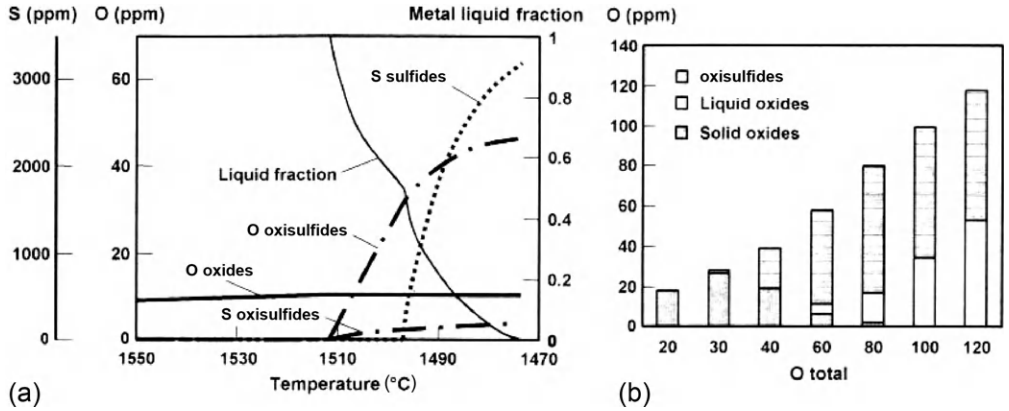


Figure 5.3.47 The distributions of oxygen and sulfur between different inclusion types during solidification of free cutting steels [74] calculated using CEQCSI. (a) Sequence of equilibrium precipitates in steel Fe–0.07C–1.35Mn–0.014Si–0.35S–0.006O (in wt%) and (b) calculated distribution of oxygen among oxides and oxysulfide inclusions in solidified steels as function of total oxygen content in steels.

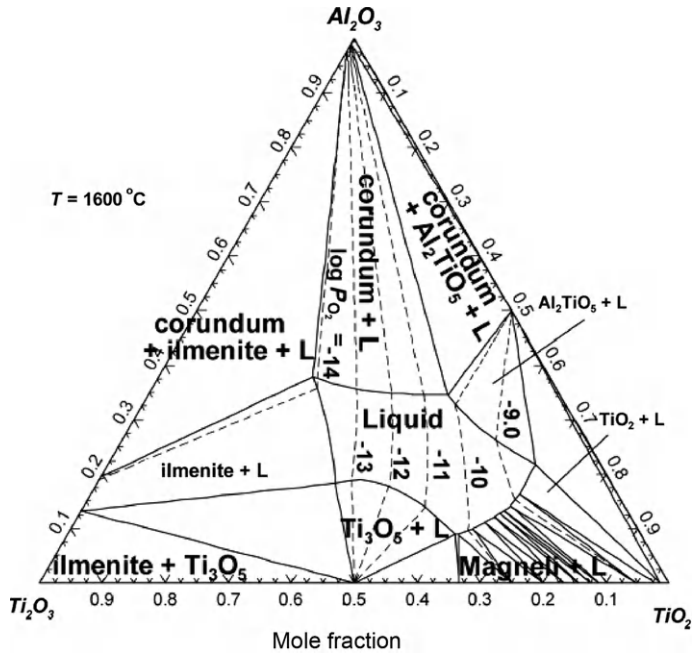


Figure 5.3.48 Predicted phase diagram of the Al_2O_3–TiO_2–Ti_2O_3 system at 1600 °C with oxygen partial pressure isobars (bar) from FactSage FToxid database [79].

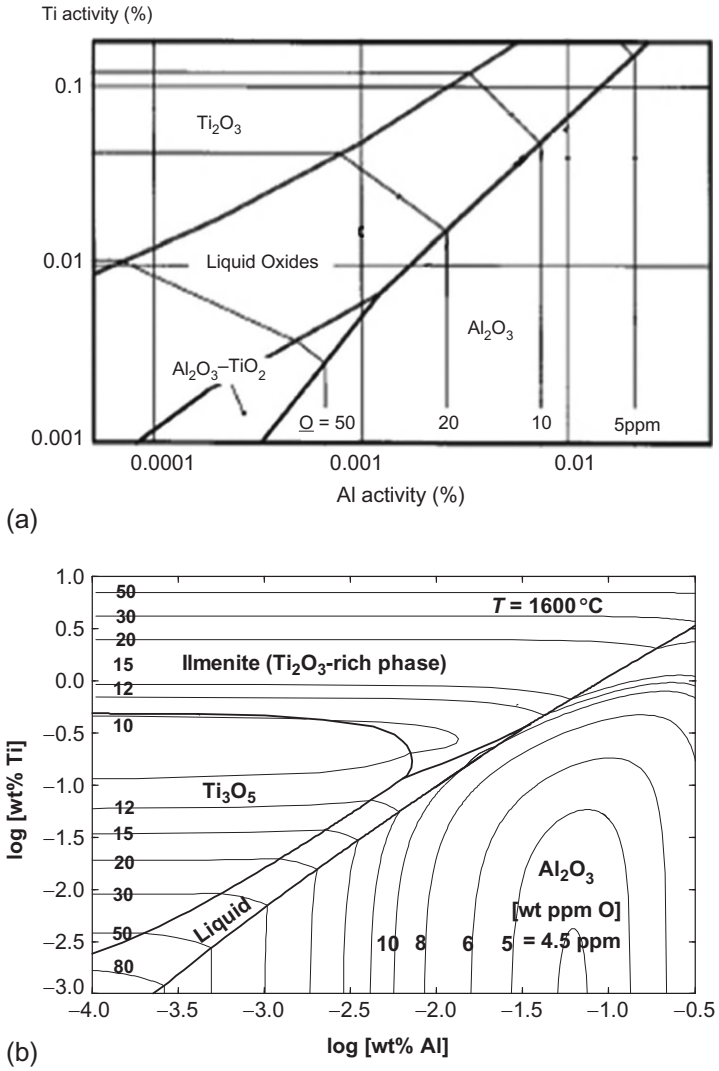


Figure 5.3.49 Inclusion diagram of the Fe–Al–Ti–O system at 1600 °C, calculated using CEQCSI [75] and FactSage FToxid/FTmisc database [79]. Axes indicate the amounts of Ti and Al dissolved in the liquid steel. Stable inclusion phases are labeled, and iso-oxygen content lines in the liquid Fe are also plotted.

5.3.1.7.4 Acicular Ferrite Formation

Although nonmetallic inclusions are in general detrimental to the mechanical properties of steels, certain nonmetallic inclusions can serve as nucleation sites for acicular ferrite formation, resulting in a significant improvement of the mechanical properties of steels. Various nonmetallic inclusions including $MnO–TiO_2$, $MnO–SiO_2–MnS$, $TiO_2–TiN$,

and VN are known to promote acicular ferrite formation. Recently, Sarma *et al.* [81] reviewed the influence of nonmetallic inclusions on acicular ferrite formation.

Many thermodynamic calculations [82–91] have been performed to describe the evolution of nonmetallic inclusions with steel grades and temperature. Figure 5.3.50 shows the changes in chemistry and morphology of nonmetallic inclusions with the addition of various alloying elements in steels [85]. For example, the evolution of the inclusion chemistry with Ti content in Fe–0.1C–1.5Mn–0.1Si–0.01O–0.007S steel is calculated [85] in Figure 5.3.51. According to the calculations using FactSage, the portion of liquid phase among the inclusions decreases with increasing Ti content. In the case of Ti = 104 and 122 ppm, the fraction of liquid inclusions becomes less than 20 mass% at 1200 °C. During the cooling process, ilmenite phase becomes dominant with increasing Ti content. When Ti = 34 and 61 ppm, MnS precipitates can form from liquid inclusions after steel solidification. On the contrary, when Ti = 104 and 122 ppm, MnS precipitation takes place during steel solidification. The calculation results were in agreement with

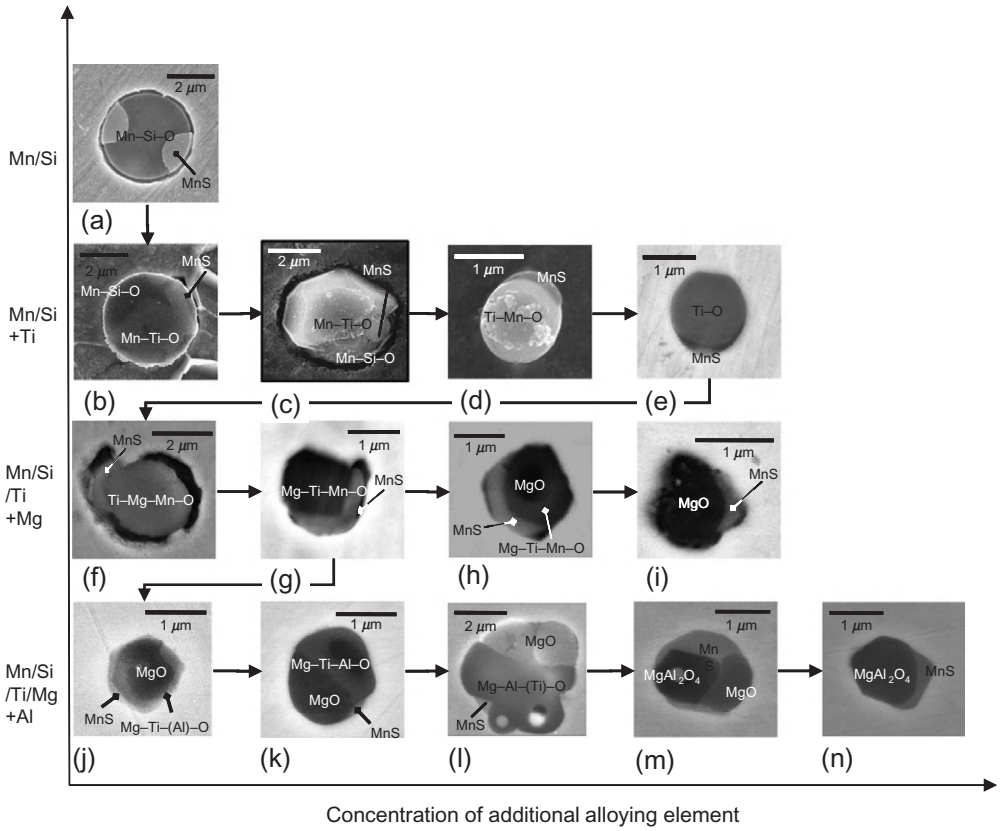


Figure 5.3.50 Change of morphology and chemistry of typical inclusions found in Fe–C–Mn–Si–O–S–N (in wt%) steel with additions of Ti, Mg, and Al [82–91].

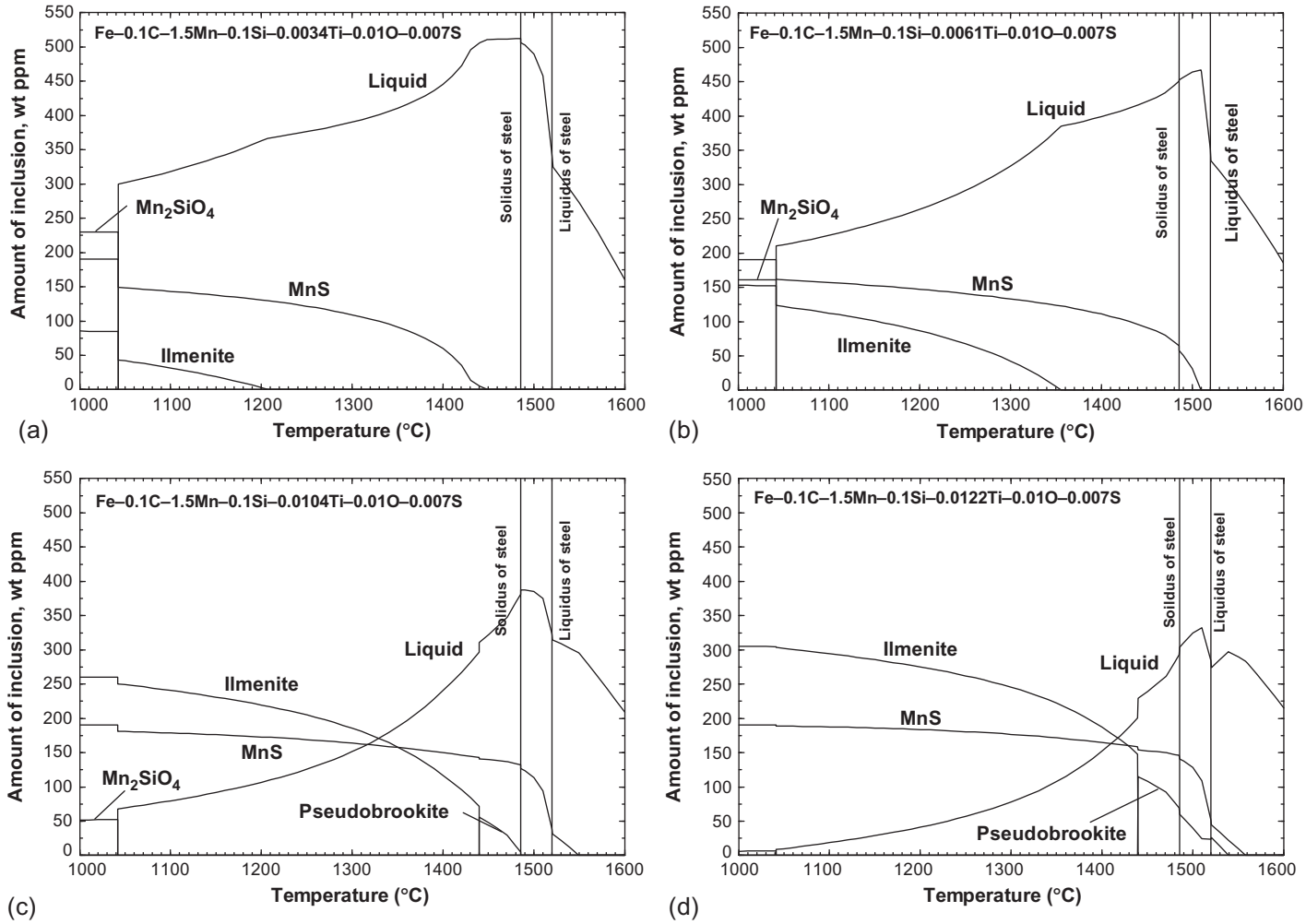


Figure 5.3.51 Evolution of inclusions in Fe–0.1C–1.5Mn–0.1Si–0.01O–0.007S (in wt%) steel with addition of Ti during solidification, calculated from FactSage FToxid/FTmisc database [85]. (a) 34 ppm Ti, (b) 61 ppm Ti, (c) 104 ppm Ti, and (d) 122 ppm Ti.

the morphology of the observed inclusions in Figure 5.3.50. That is, in the case of MnS precipitation from liquid inclusions, MnS was embedded in oxide inclusions, while, when MnS precipitation occurred during steel solidification, MnS wrapped oxide inclusions. The evolutions of nonmetallic inclusion chemistry with varying Mg [83] and Al [84] contents in steel were also well explained by thermodynamic calculations.

Byun *et al.* [89] performed thermodynamic calculations using Thermo-Calc [92] with SGTE database [93] to investigate the evolution of $MnO–SiO_2$ inclusions with increasing Ti concentration in Fe–0.08C–1.7Mn–0.2Si–0.004O–0.001N at 1477 °C. As can be seen in Figure 5.3.52a, the predictions revealed that $MnSiO_3$ inclusions gradually change to Mn_2TiO_4, $MnTiO_3$, and Ti_2O_3 with increasing Ti content, which was consistent with experimental observations. Similarly, Shim *et al.* [87] calculated the evolution of inclusions in Fe–0.14C–1.84Mn–0.18Si–0.011Ti–0.003O–0.001N steel with decreasing temperature (Figure 5.3.52b). They found that a Mn-depleted zone (MDZ) forms around Ti_2O_3 ilmenite particles due to the absorption of Mn into ilmenite to form ilmenite solution $Ti_2O_3–MnTiO_3$. The presence of an MDZ near inclusions is considered to facilitate the austenite to ferrite transformation with acicular ferrite structure.

Kang and Lee [86] performed the thermodynamic calculations to analyze the MDZ formation around Ti oxides in the temperature range between 1000 and 1500 °C as shown in Figure 5.3.53. According to the calculations, the solubility of Mn in Ti_2O_3 ilmenite becomes maximized at 1175 °C, resulting in largest MDZ formation. Based on the thermodynamic analysis, they suggested an optimal thermal process to maximize intergranular ferrite (IGF) development associated with MDZ.

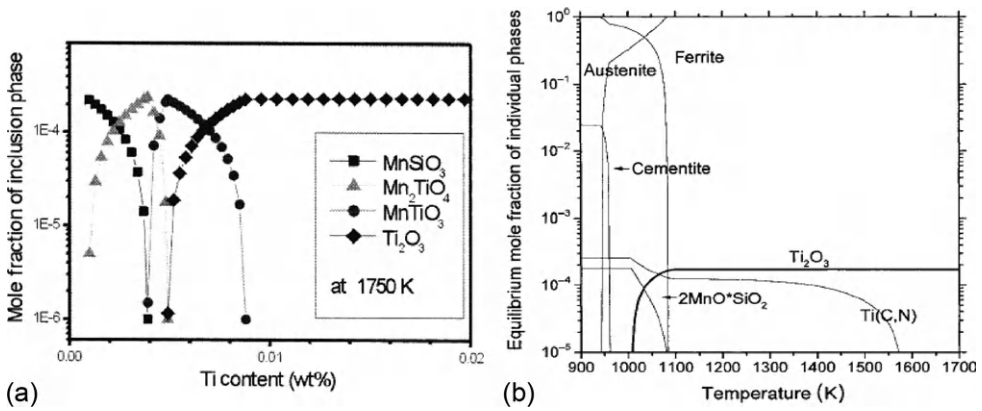


Figure 5.3.52 The evolution of oxide inclusions in high-strength steels [87,89] calculated using SGTE database. Evolutions of inclusions (a) with increasing Ti content in Fe–0.08C–1.7Mn–0.2Si–0.004O–0.001N (in wt%) at 1477 °C, and (b) with temperature in Fe–0.14C–1.84Mn–0.18Si–0.011Ti–0.003O–0.001N (in wt%) steel.

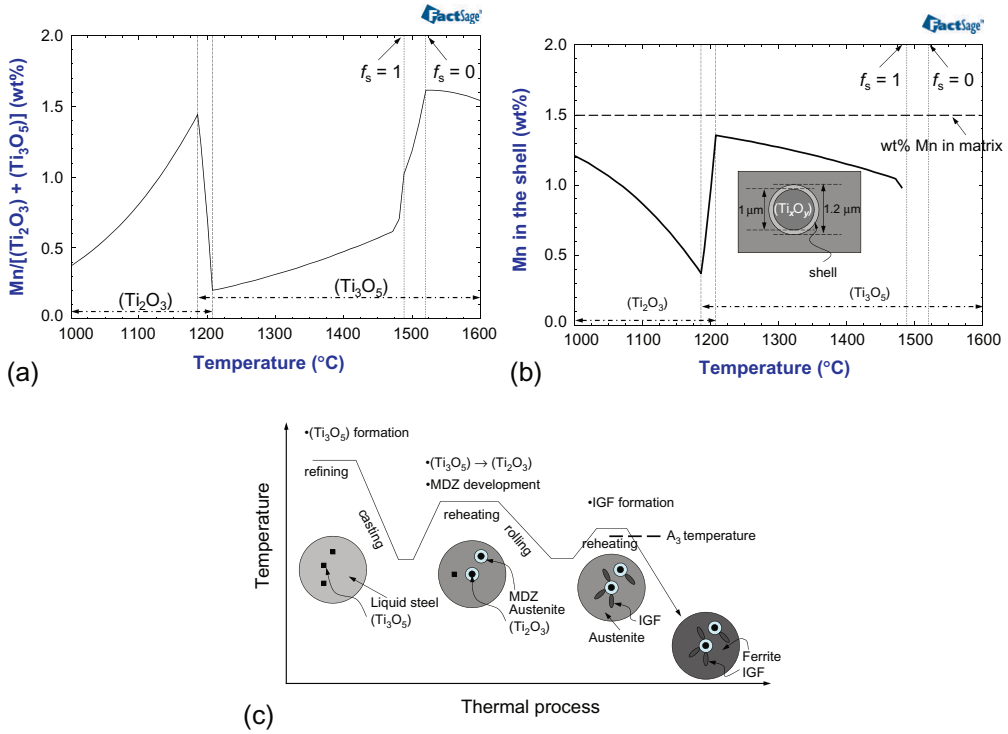


Figure 5.3.53 Calculated Mn concentrations (a) in TiO_x inclusions and (b) in a shell around the TiO_x inclusion in equilibrium with Fe–0.1C–1.5Mn–0.1Si–0.007S–0.005O–0.015Ti (in wt%), and (c) proposed optimum thermal process in order to maximize IGF development associated with MDZ [86]. Calculations were performed using FactSage FToxid/FSStel database.

5.3.2. APPLICATION OF ADVANCED MODELING IN NONFERROUS METALLURGY

5.3.2.1. Introduction

The purpose of this section is to summarize and to systematically present different ways that thermodynamic modeling tools can be applied to assist technologists and researchers in resolving various issues in the nonferrous pyrometallurgical processes. The information provided in this section is derived from extensive experiences of the application of thermodynamic and physical properties modeling in various operations.

A general approach to the way that the thermochemistry of the nonferrous processes is analyzed and modeled is presented.

There are several features specific to the nonferrous pyrometallurgical processes that require attention and can be assisted with the advanced analysis based on computer

modeling of the properties and of the processes. These specific features include but are not limited to the presence of complex multicomponent nonideal solutions, liquids, and solids, that have to be taken into account, the importance of oxygen partial pressure in controlling metal recovery and the partitioning of major species between gas/liquid/solid phases, and the partitioning of minor impurities between process streams.

5.3.2.2. Generic Overview of Nonferrous Smelting Chemistry

5.3.2.2.1 Value Metals, Minerals, and Other Input Chemistry

Section key points

- sulfides, carbonates, hydroxides
- Fe—common metal element
- SiO_2—common main gangue (and fluxing) material
- CaO, Al_2O_3, MgO—common minor gangue elements
- Minor elements
  - As, Sb, Bi, and other common "penalty" impurities
  - Ag, Au, and other common value-adding "bonus" minor elements
- CaO—common flux together with SiO_2

The nonferrous value metals, e.g., Cu, Pb, Zn, Ni, and others, are mined in the form of stable compounds, such as sulfides, carbonates, and hydroxides; examples of the principal value minerals are:

- Pb sulfide—galena PbS;
- Zn sulfide—sphalerite ZnS;
- Cu sulfides—chalcopyrite $CuFeS_2$, bornite Cu_5FeS_4; chalcocite Cu_2S; covellite CuS;
- Ni sulfides—pentlandite, $(Fe,Ni)_9S_8$ with variable Ni:Fe ratio, usually close to 1:1;
- Pb carbonate/sulfate–cerussite ($PbCO_3$) and anglesite ($PbSO_4$) [94];
- Ni hydroxides—laterite–limonite ores $(Fe,Ni)(OOH)_2$
- Ni hydrated silicates—laterite–saprolite ores
  - e.g., serpentine $(Mg,Fe,Ni)_2{\cdot}3(Si,Al,Fe)_2O_5(OH)_4$.

The obsolete man-made materials such as electronic scrap, batteries, and others are also a source of valuable metals treated through nonferrous pyrometallurgical recycling processes.

Most nonferrous metal concentrates have high proportion of iron chemically bound together with the value metal, such as chalcopyrite $CuFeS_2$ for copper. Iron cannot be separated physically at the mineral processing stage and therefore is removed during the pyrometallurgical treatment.

The secondary recycling materials have become important sources of valuable nonferrous metals. These secondary recycling materials include lead acid battery paste (predominantly sulfate $PbSO_4$ and lead oxide PbO_2), plates and other lead metal components, zinc oxide-rich EAF dust that originates from the treatment of the obsolete Zn-galvanized steel, various types of batteries, and fast-increasing electronic wastes.

The recycling of many other hazardous and valuable materials, such as hydrometallurgy process residues, is another important value metal source inputs for the nonferrous pyrometallurgy.

Silica SiO_2 (quartz) is a common main gangue material. The CaO, Al_2O_3, and MgO oxides are common minor elements present in the gangue and in the concentrates—these elements form stable oxides.

There are several unwanted "penalty" impurities: the main is arsenic As, and others include antimony Sb, bismuth Bi, etc., present in different forms. For example, common As compounds in copper concentrates include tennantite $Cu_{12}As_4S_{13}$ and arsenopyrite FeAsS, but As can also be present in a solid solution in the main copper sulfide minerals.

The common value-adding "bonus" minor elements are, for example, Ag, Au, Mo, Pt, and others—these elements frequently are essential for the economic operation of the process.

The common fluxes added during operation are silica SiO_2 and CaO (added as a limestone $CaCO_3$ or a calcined lime CaO).

5.3.2.2.2 Brief Generic Description of Some Nonferrous Pyrometallurgical Smelting Process and Common Process Stages

Section key points

- Staged production—overview of the process description and basis for staged process
  - Oxidation + reduction
    - Pb sinter or top lance oxidation + blast furnace reduction
    - Cu direct-to-blister smelting + reduction
  - Cu smelting + converting
  - Zn smelting/fuming

Most of the nonferrous pyrometallurgy processes involve (a) the separation of the major gas-forming elements (such as sulfur in case of sulfides, CO_2 in case of carbonates, etc.) into the gas phase (e.g., predominantly as SO_2 gas in case of sulfides) and (b) the separation into the slag (molten oxide) phase of iron (transformed into the oxide form) along with the gangue materials present in the concentrate (such as silica SiO_2, CaO, Al_2O_3, MgO, and several other impurities) combined with fluxes. The final by-product is usually a benign discard slag that has iron oxide and silica as the base components, where iron is separated from the value metal into the oxide form in the slag, and silica comes from the gangue as well as flux additions to ensure the high-iron-oxide slag is liquid at the process temperature. The Fe/SiO_2 ratio in the slag is usually an important operational parameter that is controlled (mostly by the silica flux additions) to ensure the slag is liquid. The slags usually also contain CaO, which, in addition to some amount introduced with the gangue material, is frequently added as a flux to lower the slag melting temperatures as well as to increase value metal oxide activity coefficients, to decrease slag viscosity, and therefore to increase recovery of a value metal. The benign slag is used as building or

other useful materials, or discarded. The sulfur dioxide SO_2 is removed from the gas stream to produce sulfuric acid as by-product. Noticeable proportion of dust is usually generated as (a) mechanical carryover of fine feed particles or (b) through the vaporization/condensation mechanism for elements with high vapor pressure. The dust is separated from the gas stream on cooling in the waste heat boiler (WHB) and then in electrostatic precipitators (ESP) and usually is recirculated.

The processes are carried out at high temperatures, which are essential for the fast kinetics of processes and for the formation of a liquid slag phase. The exothermic heat from the selective oxidation of some elements from the concentrates is used in the process to heat up the products to high temperatures and to compensate heat losses from the reactors. It is due to the use of this exothermic oxidation heat that these pyrometallurgical processes usually are significantly more environmentally friendly and have low CO_2 emissions per the unit of a value metal produced. The remaining balance of heat is usually achieved by the burning of the hydrocarbons, such as coke, coal, oil, and natural gas, and frequently by oxygen enrichment. Air- or oxygen-enriched air are used for oxidation of gas-forming elements (e.g., $S + O_2 \rightarrow SO_{2,gas}$) and of iron (e.g., $Fe + O_2 \rightarrow$ "FeO" slag). The oxygen enrichment of air is used to meet the heat balance requirements by saving the enthalpy needed to heat the nitrogen, to increase concentration of SO_2, and to reduce gas volume and thus make it easier to clean the gas and to save on expenses for installation and running of the gas cleaning equipment.

The process flow sheets and technologies selected for the nonferrous pyrometallurgical smelting processes are critically dependent on the chemistries of the particular systems. In some cases, for example, high-grade Cu and Pb concentrates, it is possible to produce the metal product directly from the sulfide feed. In the case of Ni, Zn, and most of the Cu and Pb concentrates (that contain significant concentrations of Fe), it is not possible to achieve metal production in a single reaction step and is commonly carried on in two or more stages. The staged nonferrous pyrometallurgical smelting processing is illustrated in the following examples. The principal aim in these examples is the separation of S and Fe from the metal values. The reason for the staged processing is as follows. The *simultaneous* separation of the value metal into one stream and removal of several other elements, in particular iron, into different stream(s) *at the same time* determines the selection of a production route. For example, the removal of sulfur into SO_2 gas for the sulfides input requires oxidation conditions that on the other hand result in the adverse processes of (a) the oxidation of the value metal into the slag and (b) increasing stability of the high-iron spinel–magnetite Fe_3O_4 solution. These latter two processes frequently determine the limiting conditions achievable for a given production stage—how far the oxidation can be "pushed" forward. The extent of the oxidation for a given stage is frequently controlled by the oxygen to feed ratio. It is due to these reasons that many nonferrous smelting processes are separated into two or more stages.

5.3.2.2.2.1 Oxidation + Reduction Routes

The common first stage in the oxidation/reduction processes used for Pb/Zn sulfide metallurgy is performed in the oxidizing conditions; sulfur is oxidized and separated into SO_2 gas and iron—into Fe^{2+}/Fe^{3+} oxides into the slag. The stream with the value metals predominantly in an oxide form (e.g., slag or sinters) is then treated in the next stage where further separation is undertaken in more reducing conditions producing a benign slag low in the value metal. Figure 5.3.54 schematically illustrates oxidation + reduction process route for the Pb/Zn sulfide smelting.

5.3.2.2.2.2 Smelting/Converting Route

Most sulfide copper is produced through the multistage smelting/converting route. The *smelting stage* involves oxidation of sulfur into SO_2 gas and iron into oxide in the silicate slag, producing matte (Cu_2S–FeS-based solution) with ~50–70% copper grade. Formation of the high-melting temperature spinel solid solution (predominantly magnetite Fe_3O_4) is one of the main barriers which determine the selected temperature, fluxing, and the oxygen to feed ratio for a given selected final matte grade. Information on the liquidus temperatures of the smelting slag is essential for the selection of the process parameters, such as smelting temperatures and fluxing strategy. Most of the stable oxide-forming impurities Al_2O_3, MgO, and others are removed into the smelting slag. Copper loss into the slag in the form of (a) chemically dissolved predominantly Cu^{1+} and (b) physically entrained matte is an essential parameter that determines copper recovery and therefore strongly influences financial viability of the processes.

The *converting stage*—production of the copper metal blister from the matte—is mostly done through the Peirce–Smith converting process. The Peirce–Smith is a batch process that gradually, in several stages, removes iron into the iron-silicate slag and sulfur into SO_2 gas; the main components of the slag phase in the Peirce–Smith process are ferrous and ferric iron oxides, silica, and some copper oxide. Continuous converting can be

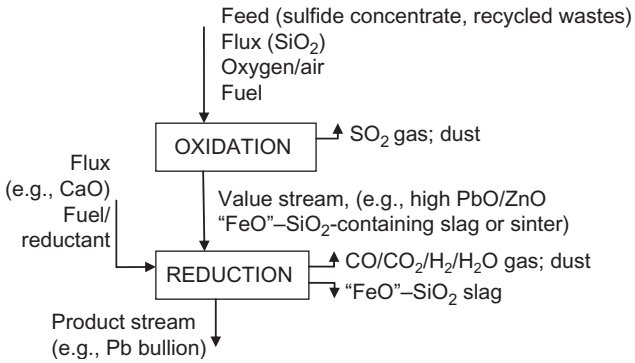


Figure 5.3.54 Schematic process flow diagram for the sulfide oxidation/reduction route for processing of Pb/Zn concentrates.

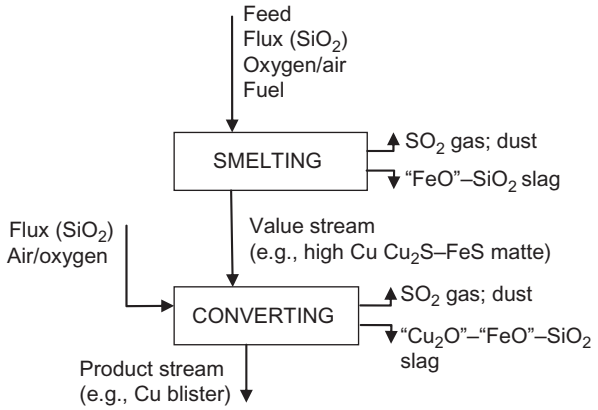


Figure 5.3.55 Schematic of the copper smelting/converting route.

carried out in a number of different technologies, such as Flash converting, Mitsubishi process, and top submerged lance processes. Calcium ferrite slags used in some continuous converting can be presented by the "Cu_2O"–CaO–FeO–Fe_2O_3 system. The conditions during converting are oxidizing; formation of spinel (predominantly magnetite Fe_3O_4) liquidus is one of the main limiting issues in converting.

Figure 5.3.55 schematically illustrates the smelting and converting process route for copper sulfides.

5.3.2.2.2.2.1 Common Features of Base-Metal Sulfide Systems Complex multicomponent systems require staged removal/separation of elements. In smelting processes, these result in:

- Fe, Mg, Si, Al partition preferentially into the slag phase,
- S partition to the gas phase, and
- Partition of value metal product into molten metal or molten sulfide solutions.

Some of the common phase chemistry features important for the modeling of the processes include:

- Fe removal as ferric or ferrous oxide into slag is one of the common targets of the processes
- Spinel (predominantly magnetite Fe_3O_4) solid solution liquidus is one of the key limiting parameters that determine the oxidizing stage of the process characteristics such as the type of the process, temperature, fluxing, and degree of oxidation (controlled by the oxygen to feed ratio)
- Wustite solid solution liquidus is usually present in the reducing stages of the processes, unless the spinel phase is stabilized by impurities such as Al_2O_3 and MgO
- Tridymite steep liquidus usually determines maximum silica flux addition

- Melilite or dicalcium silicate liquidus usually limit CaO flux addition for the high-CaO slags
- High-silica-iron oxide slags are commonly used and are frequently called "fayalite" slags
- Low-silica calcium ferrite slags are used in some processes
- Vapor pressure, vaporization/dust formation

Examples of common stages in some of the nonferrous processes are given in Table 5.3.2.

Table 5.3.2 Examples of Oxidation/Reduction Route

Metal Production Route	Stage	Chemistry of the Main Output Streams
Lead sulfide oxidation + blast furnace reduction	1. Oxidation in sinter machine	Heterogeneous sinter with 20–40 wt% Pb, 10–15% Zn, balance iron oxide, SiO_2, CaO and impurities, CaO/SiO_2 from ~0.6 to 1.2
	2. Oxidation in top lance smelting furnace	Pb–Zn-high slag 30–50 wt% Pb, 10–15 wt% Zn, balance iron oxide, SiO_2, CaO and impurities, CaO/SiO_2 from ~0.3 to 0.6
	3. Reduction in blast furnace	Pb-low (1–2 wt% Pb), Zn-high (10–20 wt% Zn) fayalite slag, lead bullion
	4. Zn fuming	Zn is removed into the gas phase and later reoxidizes to ZnO dust on cooling; the by-product is predominantly "FeO"–CaO–SiO_2 slag with Al_2O_3, MgO, and other impurities
Conventional copper sulfide smelting/converting	1. Direct-to-blister smelting—oxidation	Predominantly Cu_2S–FeS matte with usually 50–73% copper (matte grade) and the low copper (0.5–3 wt% Cu) "Cu_2O"–"FeO"–SiO_2 slag with possible CaO from fluxing, as well as Al_2O_3, MgO, and other impurities
	2. Converting in Peirce–Smith or alternative reactor	Copper blister and mostly "FeO"–SiO_2 slag
Direct-to-blister copper smelting + reduction	1. Direct-to-blister smelting—oxidation	Low Fe and relatively low S blister as a value stream and the high copper (up to 20–25% Cu) "Cu_2O"–"FeO"–SiO_2 slag with possible CaO from fluxing, as well as Al_2O_3, MgO and other impurities, blister copper
	2. Reduction in electric furnace	Mostly "FeO"–CaO–SiO_2 slag with Al_2O_3, MgO and other impurities, blister copper

5.3.2.2.3 Major Phases and Output Stream Chemistries

Section key points

- Value streams—bullion/matte/speiss/gas
- Slag
- Solids
  - Spinel/wustite
  - Tridymite
  - Melilite
  - Fayalite
  - Olivine
  - Pyroxene
  - $CaSiO_3$ and Ca_2SiO_4
  - Feldspars
- Gas
- Dust

In addition to the "value" stream (metal bullion, matte, or other), the main output streams include slag (molten oxides), crystalline solids suspended in the slag, gas phase, and the dust separated from the gas phase.

5.3.2.2.3.1 Value Stream Chemistries

The value stream depends on the nature of the value element and usually is a metal bullion with some wanted and unwanted impurities as the final product. Intermediate value streams may be matte represented by the main components Cu_2S–FeS or Cu_2S–FeS–NiS in case of the copper or nickel production, high-PbO and -ZnO sinter, or PbO–ZnO–"FeO"–CaO–SiO_2 slag in case of lead and zinc smelting, ZnO dust precipitated from the gas phase in case of Zn-fuming processes and some other (e.g., speiss).

5.3.2.2.3.2 Slag Chemistry

Most of the nonferrous smelting processes have slag as by-product. The common slag chemistry may be represented by the "FeO"–SiO_2–CaO system where iron oxide is separated in a ferrous Fe^{2+} and ferric Fe^{3+} forms into the slag from the value stream, silica comes from gangue and as additional flux to "bind" iron oxide into a liquid slag phase, and CaO mostly coming as a flux to reduce liquidus as well as to increase activity coefficient of a value metal oxide and to reduce viscosity to increase recovery. Common other minor slag-forming elements include Al_2O_3 coming from the gangue as well as from the coke and coal ash, magnesium, sodium, potassium, titanium, and other stable oxides.

The slag phase also contains (a) some of the chemically dissolved value metal oxide and (b) physically entrained value phase (metal or matte) droplets.

Calcium ferrite (CaO–FeO–Fe_2O_3) slags with low silica concentrations are alternative slag chemistry used in some processes.

5.3.2.2.3.3 Common Solid Chemistry

Spinel (Fe^{2+}, Mg^{2+}, Ni^{2+}, Zn^{2+}...)O·(Fe^{3+}, Al^{3+}, Cr^{3+},...)$_2O_{3+\gamma}$ and *wustite* (Fe, Mg, Ni, Zn)O_{1+z} are the most common iron oxide-rich crystalline phase encountered in high-temperature smelting processes.

Spinel is a complex solution phase having end-members such as magnetite Fe_3O_4, hercynite $FeAl_2O_4$, spinel $MgAl_2O_4$, gahnite $ZnAl_2O_4$, franklinite $ZnFe_2O_4$, magnesioferrite $MgFe_2O_4$, and other.

The spinel solid solution phase is found in most of the nonferrous pyrometallurgical processes. It is usually rich in iron oxide close to the composition of magnetite Fe_3O_4 and therefore is quite commonly referred to as just "magnetite." It is important to note that there are two meanings of the word "magnetite" that are used in practice; these should be clearly distinguished. The first meaning is related to the "magnetite" as a phase: the magnetite—(Fe_3O_4)—rich spinel solid solution. The second meaning of the word "magnetite" is related to the control of the level of reducing/oxidizing conditions that in industrial practice are frequently monitored by regular measurement of magnetic susceptibility of the slag, is expressed as the Fe_3O_4 concentration, and is frequently called "magnetite concentration" as indication of the ferric iron Fe^{3+} concentration in the slag phase.

The magnetite—(Fe_3O_4)—rich spinel solid solution phase is less stable at more reducing conditions, whereas it is more stable at more oxidizing conditions and frequently present as precipitate in the slag as a separate solid phase. Note that at more oxidizing conditions, the "magnetite concentration" indicating the ferric iron Fe^{3+} concentration in the slag phase is also high. These two meanings magnetite (a) as a measure of oxidizing conditions and the ferric iron Fe^{3+} concentration in the slag phase and (b) as spinel (close to the magnetite Fe_3O_4 composition) precipitates should not be confused.

To maximize the removal of iron, high-iron slags are commonly formed with spinel as a primary phase. The liquidus temperatures of spinels are high; most end-members melt at 1873 K (1600 °C) and higher. Presence of MgO, Al_2O_3, and Cr_2O_3 in the chemical system generally increases the stability of the spinels and therefore increases liquidus temperatures. More reducing conditions reduce the spinel liquidus temperatures. More oxidizing conditions stabilize spinel and result in higher liquidus temperatures. Spinel is the most common solid phase that determines liquidus temperatures of slags and therefore influences many process routes that are designed to separate Fe from the value metal and specifically designed to avoid and "go around" the spinel formation.

At relatively reducing conditions, *wustite* solid solution is a stable iron oxide-rich phase in place of the spinel. The pure FeO_{1+z} wustite liquidus in equilibrium with metallic iron is 1644 K (1371 °C) and is by ~200 K lower compared to the spinel Fe_3O_4 in oxidizing conditions. Wustite can form extensive solid solutions with a number of Me^{2+} oxides including MgO, NiO, ZnO, CaO, and other. Presence of MgO increases wustite stability and therefore liquidus temperatures, and the effects of other Me^{2+} oxides depend

on bulk chemistry. Me^{3+} oxides do not form extensive solutions in wustite; Al_2O_3 does not dissolve significantly in wustite and therefore the presence of Al_2O_3 in the bulk composition marginally reduces wustite liquidus.

Silica SiO_2 is a major flux used to "chemically bind" iron oxide into a liquid slag phase; excessive silica additions result in the formation of crystalline *tridymite* SiO_2 that has high-melting temperature (pure SiO_2 melts at 1723 °C) and steep liquidus.

Melilite $(Ca^{2+},Pb^{2+})_2(Zn^{2+}, Mg^{2+}, Fe^{2+}, Al^{3+}, Fe^{3+})(Si^{4+}, Al^{3+}, Fe^{3+})_2O_7$ is a complex solid solution with three sublattices. Importantly, the liquidus temperatures of the high-Ca melilites are relatively high (for example, hardystonite $Ca_2ZnSi_2O_7$ melts at 1425 °C), and this phase therefore commonly determines the limit for the CaO flux additions.

The *fayalite* Fe_2SiO_4 is stable at reducing conditions, and it has relatively low liquidus temperature—pure fayalite melts in equilibrium with metallic iron at 1478 K (1205 °C). The fayalite has an olivine crystal structure and forms extensive solid solutions with Me^{2+} oxides $(Fe^{2+}, Ca^{2+}, Mg^{2+}, Zn^{2+} \ldots)_2SiO_4$. The addition of CaO reduces the fayalite liquidus temperatures that can be as low as below 1373 K (1100 °C) in the "FeO"–CaO–SiO_2 system in equilibrium with metallic iron; the range of compositions with low liquidus temperatures in the fayalite primary phase field is wide, and these are called "fayalite" slags. The addition of MgO increases the stability of this phase and therefore the fayalite liquidus temperatures are significantly increased.

The *olivine* $(Mg,Fe)_2SiO_4$ is the magnesium—iron orthosilicate solution with the forsterite Mg_2SiO_4 end-member having high liquidus temperature of 2163 K (1890 °C).

In high-MgO systems, *pyroxene* $MgSiO_3$ may form; this phase has relatively high (over 1823 K (1550 °C)) liquidus temperatures.

Dicalcium silicate Ca_2SiO_4 melts at temperatures over 2373 K (2100 °C) and is the stable phase at high-CaO concentrations with high liquidus temperatures, thus limiting fluxing with CaO. Dicalcium silicate forms solid solutions with a number of Me^{2+} oxides $(Ca^{2+}, Fe^{2+}, Pb^{2+}\ldots)_2SiO_4$, particularly with metals having high cation radius such as Pb^{2+} that can substitute half Ca^{2+} in this phase.

The formation of these solids is a common limitation in selection of the slag chemistry and frequently determines the actual operational route. Table 5.3.3 gives a list of some common solid phases. Deer *et al.* [95] is a convenient source of the information on the chemistry of common crystalline solid phases.

5.3.2.2.3.4 Common Gas Chemistry

The composition of the gas phase in sulfide smelting, in particular, the N_2 partial pressure, is directly determined by the oxygen enrichment, and if the process is run at total pressures close to 1 atm., the reminder of the gas would consist of the predominant species corresponding to the particular process; for example, in sulfide oxidation/smelting, the

Table 5.3.3 Mineralogy of the Typical Solid Phases in Lead and Zinc Smelting

Phase Name	Phase Chemistry	End-member/T Liquidus [a]
High-melting temperature multicomponent solid solutions		
Spinel	($FeO{\cdot}Fe_2O_3$–$ZnO{\cdot}Fe_2O_3$–$ZnO{\cdot}Al_2O_3$–$FeO{\cdot}Al_2O_3$–$MgO{\cdot}Fe_2O_3$–$MgO{\cdot}Al_2O_3$) E.g., Fe_3O_4 = magnetite; $ZnFe_2O_4$ = franklinite; $FeAl_2O_4$ = hercynite; $ZnAl_2O_4$ = gahnite	Fe_3O_4/>1873 K (1600 °C)
Wustite	(FeO–Fe_2O_3–CaO–ZnO–MgO–···)	FeO_x/1644 K (1371 °C)
Zincite	(ZnO–FeO–Fe_2O_3–···)	ZnO/2198 K (1925 °C)
Melilite	($Pb_2ZnSi_2O_7$–$Ca_2ZnSi_2O_7$–$Ca_2FeSi_2O_7$–$Ca_2Fe_2O_7$–$Ca_2Al_2SiO_7$) E.g., Hardystonite $Ca_2ZnSi_2O_7$	$Ca_2ZnSi_2O_7$/1698 K (1425 °C)
Willemite	(Zn_2SiO_4–Fe_2SiO_4)	Zn_2SiO_4/1823 K (1550 °C)
Wollastonite	($CaSiO_3$–$FeSiO_3$)	$CaSiO_3$/1828 K (1555 °C)
Olivines	(Fe_2SiO_4–Ca_2SiO_4–Zn_2SiO_4–Mg_2SiO_4–···) e.g. Fe_2SiO_4–fayalite	Fe_2SiO_4/1478 K (1205 °C)
α′ Dicalcium silicate	(Ca_2SiO_4–Fe_2SiO_4–Pb_2SiO_4–Zn_2SiO_4–···)	Ca_2SiO_4/2373 K (2100 °C)
Pyroxenes	($MgSiO_3$–$FeSiO_3$–$CaSiO_3$)	$MgSiO_3$/1823 K (1550 °C)[b]
Feldspars	$CaAl_2Si_2O_8$–$NaAlSi_3O_8$–$KAlSi_3O_8$	$CaAl_2Si_2O_8$/1828 K (1555 °C)
Low-melting temperature solids		
Pb-silicate	$(Ca,Pb)_2Pb_3Si_3O_{11}$	$(Ca,Pb)_2Pb_3Si_3O_{11}$/<1323 K (1050 °C)[b]
Pb-silicate	$CaPb_8Si_6O_{21}$	$CaPb_8Si_6O_{21}$/<1153 K (880 °C)[b]
Larsenite	$PbZnSiO_4$	$PbZnSiO_4$/<1383 K (1010 °C)[b]
Pb/Zn melilite	$Pb_2ZnSi_2O_7$	$Pb_2ZnSi_2O_7$/<1083 K (810 °C)[b]
Melanotekite	$Pb_2Fe_2Si_2O_9$	$Pb_2Fe_2Si_2O_9$/<1173 K (900 °C)[b]
Pb/Fe silicate	$Pb_{10}Fe_2Si_2O_{17}$	$Pb_{10}Fe_2Si_2O_{17}$/<1073 K (800 °C)[b]

[a]Liquidus temperature is given for the congruently melting end member.
[b]Peritectic temperature is given for the incongruently melting compound.

SO_2 is the predominant species in oxidizing conditions, and the SO_2 partial pressure P_{SO_2} is determined by the oxygen enrichment.

In case hydrocarbons are used in the process, then the CO/CO_2 and H_2/H_2O depend on the oxidation/reduction level of the process.

Common volatile metal impurities such as As, Bi, and Hg can vaporize into the gas phase at higher temperatures and then recondense on cooling, forming fine dust, that is separated and treated later.

It is important to note that there are several stable gaseous species that have to be included in the analysis of systems. For example, PbS is a stable gaseous species at reducing conditions in lead/zinc operation; Zn has high vapor pressure at reducing conditions and high temperature. Omission of these stable gaseous species from analysis can result in erroneous predictions. If the gas phase is not included into the analysis at all, that can also result in erroneous predictions.

Application of thermodynamics to modeling of actual industrial processes requires introduction of some kinetic factors, e.g. such as very slow C graphitization on cooling of the CO/CO_2 gas mixtures.

5.3.2.2.3.5 Dust Chemistry

Dust is another common output stream in the nonferrous processes commonly separated in the WHB and in the ESP. Dust consists of two main components: (1) "mechanically" carried-over particles originating from the main feed material; and (2) fine particles rich in volatile elements (As, Bi, Hg, etc.) condensed on cooling. The condensation of the volatile components can take place on the surface of the mechanically entrained dust particles.

The compositions of the dust particles are expected to be determined by the reactions with the gas phase; for example, the dust would contain sulfur in a sulfate form in the sulfide smelting processes due to the relatively oxidizing gas atmosphere.

5.3.2.2.4 Summary—Main Issues Assisted with Advanced Modeling in Nonferrous Pyrometallurgy

Section key points

- Slag liquidus and phase equilibria
  - Removal of Fe and gangue
  - Degree of recovery of valuable metal
- Value-metal partitioning—final recovery
  - P_{O_2}
  - chemically dissolved and physically entrained
- Heat balance and oxidation state
  - Reductant and fuel are frequently the same element
  - Decoupling through electrical energy, plasma injection

- Major gas-forming elements' partitioning $C/CO/CO_2$, $S/S_2/SO_2$, H/H_2O
- Minor elements' distribution
  - As, etc.
  - Ag, Au, etc.

The chemistries of the input feed stocks as well as the compositions of the output streams are complex, and the selection of the process conditions requires overcoming many different restrictions and therefore satisfying many various parameters. The advanced modeling tools are used at many stages of the process parameter selection. The following main issues that are commonly assisted with theoretical modeling tools can be identified.

Slag liquidus and phase equilibria are common starting points in selection of process conditions such as fluxing, temperature, and others and frequently assisted with the computer modeling tools. The usual conditions that have to be satisfied include, but not limited, to the need to:

- maintain slag liquid,
- ensure furnace integrity,
- ensure stability of the process,
- minimize fuel use, and
- minimize fluxing and discard slag rates.

The selection of the slag chemistry and of the overall process characteristics usually has the following aims:

- removal of Fe and gangue into the liquid slag,
- optimum degree of recovery of valuable metal and of valuable minor elements,
- removal of unwanted impurities,
- further use or discard of the final slag, and other.

Variables that are commonly controlled to determine the slag phase equilibria and corresponding process temperature usually include:

- Fe/SiO_2 is controlled by the silica flux addition,
- CaO/SiO_2 is controlled by the lime/limestone flux additions,
- Al_2O_3, MgO, and other impurity levels are usually determined by the feedstock,
- concentrations of valuable metal oxides (e.g., PbO, ZnO, "Cu_2O"), and
- related effective oxygen partial pressure through the oxygen to feed ratio.

Value-metal partitioning and final recovery of the value metal includes (a) chemically dissolved oxidized metal in the slag and (b) physically entrained high-value metal or matte phase in the slag. The concentration of the value metal oxide chemically dissolved in the slag depends on the reduction/oxidation state controlled principally by the oxygen to feed and reductant/fuel to feed ratios, by kinetic factors (rates of reduction reactions), and by slag composition and temperature. The amount of the high-value metal phase physically entrained in the slag depends on viscosity, residence time, mixing intensity, and a number of other factors. Slag chemistry determines the physicochemical properties such as slag viscosity, density, and interfacial tension that in turn determine entrainment.

Heat balance and corresponding oxidation state are principally controlled by the oxygen enrichment, oxygen to feed ratio, reductant/fuel to feed ratio, and some other parameters.

The reductant and fuel in pyrometallurgical processes are frequently the same element—this imposes restrictions and introduces difficulties in the optimum selection and control of these parameters. In case of the sulfide smelting additional hydrocarbon fuels (coke/coal, oil, natural gas) are used to finely tune (trim) the heat balance. The decoupling of fuel/reductant and oxygen requirements through alternative chemically relatively neutral sources of enthalpy is used in some cases including electrical energy (FSFE, Kivcet), plasma injection (e.g., Zn fuming [96,97]), and other. Various feed streams can introduce additional oxygen (e.g., limestone $CaCO_3$) or additional reductant (e.g., Fe residue) that has to be taken into account. The number of parameters to select and control the heat balance and the oxidation state is large, and the thermochemical relations are complex. Simplifications have previously been used in solution of the heat balance; complex computer-driven thermodynamic modeling tools can significantly increase the accuracy and efficiency of the operational parameters selection since the heat balance and final chemical partitioning can now be predicted in a single model for complex multicomponent multiphase systems with complex nonideal solution phases. *Major gas-forming species concentration including* CO/CO_2, S_2/SO_2, and H/H_2O can now be predicted at the same time taking into account interactions with the complex nonideal solutions condensed phases using the advanced thermodynamic models.

Minor elements distribution between gas, value-metal, and by-product (e.g., slag) streams is another major issue that has to be resolved as part of the process parameters selection and optimization that can now be assisted with the computer thermodynamic modeling tools. The common unwanted elements include As, Sb, and Bi. The common value-adding elements include Ag, Au, and Pt.

The partitioning of minor elements is one of the key issues in optimization of the nonferrous pyrometallurgical processes and involves several routes including (i) vaporization into hot gas followed by condensation and separation as a WHB and ESP dusts, and by recirculation or bleeding; and (ii) partitioning between slag and a condensed value stream such as metal and matter. The degree of partitioning depends on thermodynamic (equilibrium) properties as well as on kinetics. Advanced computer-aided modeling tools including thermodynamic predictions can greatly assist in optimization of the process with respect to the minor elements distribution. Mechanical dust carryover can also be an additional noticeable mechanism for partitioning of minor elements between streams, but the dust mechanical carryover for the minor elements and major elements is unlikely to be different.

The partitioning of minor elements between phases directly depends on the effective oxygen partial pressure defined by the oxidation/reduction level controlled by the oxygen to feed ratio; the partitioning of minor elements is frequently taken into account in

selection of the oxidation/reduction level of the actual process; again, advanced modeling tools are used to assist in this issue.

5.3.2.2.5 Selection of Multicomponent Sections

Section key points

- Selection of the right section can help a lot

Most of the input and output streams in nonferrous pyrometallurgy are multicomponent and have complex chemistry restrictions; the analysis of the trends of the key properties including phase equilibrium, thermodynamic and physicochemical properties, as a function of composition and temperature therefore is essential.

The representation of phase equilibria in one- and two-component systems as a function of temperature, composition, and pressure is relatively straightforward. Ternary systems are readily represented using phase diagrams having Gibbs triangular coordinates on a compositional plane and a temperature axis normal to this plane.

Four-component compositional space can be represented in a tetrahedron. To simplify the visualization of phase relations in these systems, and to be able to present the effects of changing temperature, sections of the quaternary are commonly used including sections through the quaternary at fixed ratios of the components (Figure 5.3.56a), sections through the quaternary at fixed compositions of the fourth component (Figure 5.3.56b) and pseudo-ternary subsystems defined by Alkemade compositional triangles (Figure 5.3.56c). For oxide systems containing transition metal species of variable oxidation state, the phase equilibria can be described by considering each oxidation state as a separate chemical component, for example, $FeO–CaO–SiO_2$ and $Fe_2O_3–CaO–SiO_2$ in Figure 5.3.56d. This is achieved by the projection of the composition from the oxygen apex onto a plane in compositional space. For example, in Figure 5.3.56d, the slag of composition a may be represented as a′ on the $FeO–CaO–SiO_2$ section. Pseudo-ternary sections in higher order systems are constructed by the introduction of further compositional restrictions. For example, a multicomponent system can be represented in a tetrahedron by combining several components at fixed ratios in one or several apexes in Figure 5.3.56a and b; say, D may represent a three-component composition made of E, F, and G chemical components at fixed E/F and E/G ratios. Clearly, the bulk composition of each point on the diagram must be fully defined so that to have a pseudo-ternary section in the n-component system $(n-3)$ additional compositional or thermodynamic (e.g., activity of a component) restrictions must be introduced.

Various methods in which phase equilibria in complex chemical systems can be correctly presented are discussed further by Pelton [98] and Hillert [99].

Additional factors that affect the choice of section in compositional space include changes in composition of the slag during processing due to, for example, flux addition, reactions, or crystallization.

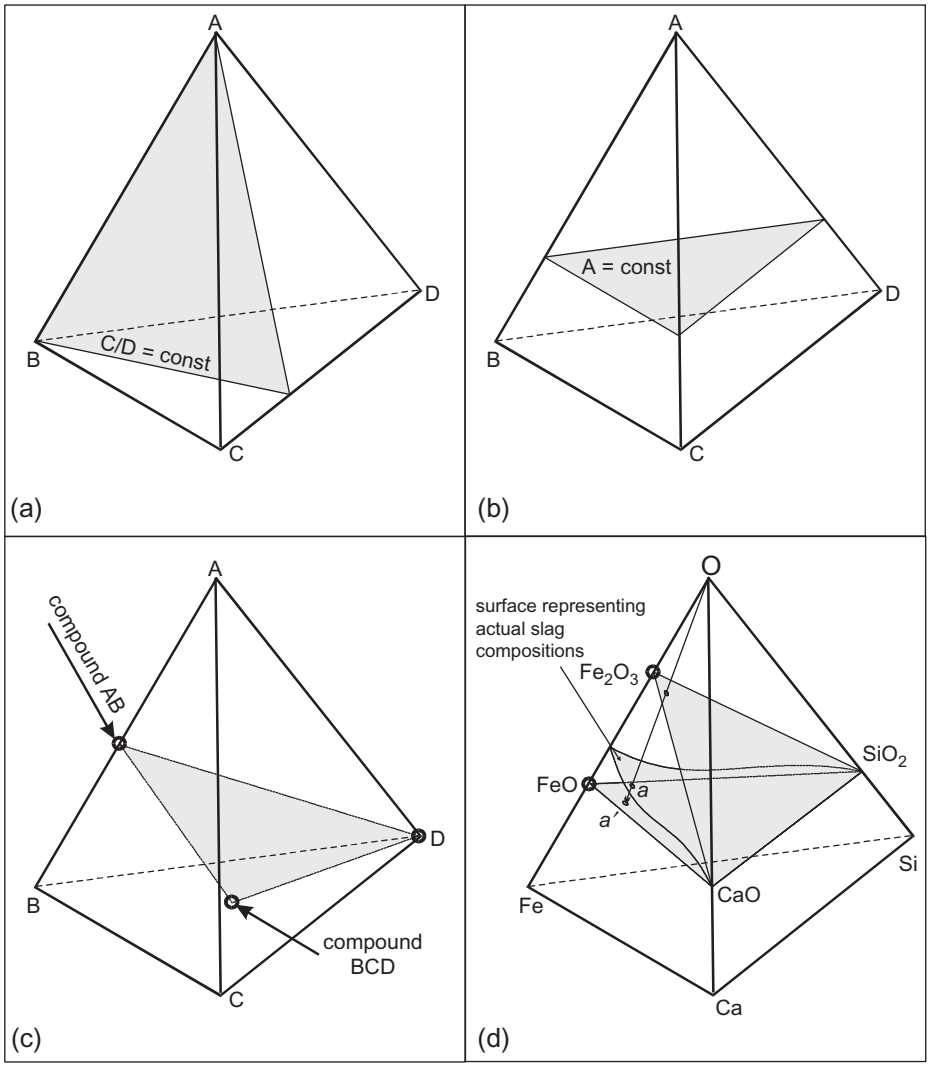


Figure 5.3.56 Projections and sections in compositional space: (a) section at constant ratio of two components in a quaternary system; (b) section at constant value of A in a quaternary system; (c) alkemade compositional triangle in a quaternary system; (d) projections in compositional space.

An example of the selection of the pseudo-ternary section to represent liquidus in the six-component system PbO–ZnO–SiO_2–CaO–FeO–Fe_2O_3 in air [100] is given below in Figure 5.3.57. Pseudo-ternary sections in the multicomponent systems are essential to describe the phase equilibria in the range of compositions of interest so that the liquidus temperatures can be uniquely described as a function of composition and can be projected as isotherms on a two-dimensional equilateral triangular base. The appropriate choice of

end members can result in the construction of joins that could be used similar to the ternary systems. If all of the crystalline phases have compositions in the plane of the section, then these ternary sections can be interpreted in the same way as ternary phase diagrams; e.g., the lever rule can still be applied to determine the proportions of the phases present at any temperature. The crystallization path of any liquid therefore can be traced. If compounds are formed that do not contain the same stoichiometric ratios as end members, then this part of the system does not obey the general rules of a ternary diagram.

Analysis of number of degrees of freedom is important for the correct section construction and further interpretation. For this example, air is assumed to consist of only oxygen and nitrogen, and the number of elements C in the present system Pb–Zn–Ca–Si–Fe–O–N is equal to seven. For a liquid in equilibrium with one solid phase and the gas phase (total three phases in equilibrium), the number of degrees of freedom $F = C + 2 - P = 7 + 2 - 3 = 6$. In open air two more degrees of freedom—total pressure and oxygen potential—are fixed, then for two more restriction-fixed CaO/SiO_2 and $PbO/(CaO + SiO_2)$ ratios in the liquid, only two degrees of freedom remain. This means that the compositions of all liquids, which have certain CaO/SiO_2 and $PbO/(CaO + SiO_2)$ ratios, in equilibrium with one solid at fixed oxygen activity lie on a two-dimensional curved surface which can be referred to as the "liquidus surface" illustrated schematically in Figure 5.3.57. The "liquidus surface" is located within the

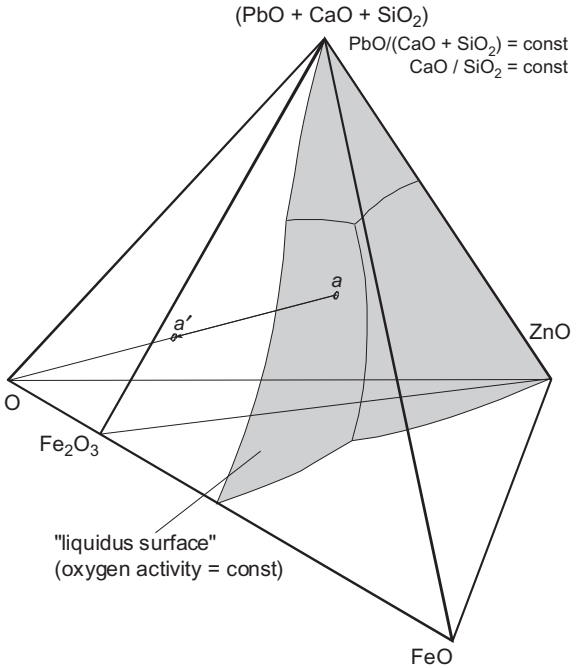


Figure 5.3.57 Composition tetrahedron with the constant $PbO/(CaO + SiO_2)$ and CaO/SiO_2 ratios.

composition tetrahedron ZnO–(PbO + CaO + SiO_2)–FeO–Fe_2O_3. The composition of each particular point on the "liquidus surface" is fully defined and determines the primary phase, liquidus temperature, and the FeO/Fe_2O_3 ratio. Similarly, the compositions of the liquids in equilibrium with two solids and the gas phase will form a line which can be called "boundary line." The "two-dimensional liquidus surface" with isotherms, "univariant lines," and "invariant points" can be projected onto the composition plane ZnO–(PbO + CaO + SiO_2)–Fe_2O_3 by recalculating all iron as Fe_2O_3 for the presentation purposes—this is illustrated with the projection of point "a" from the liquidus surface onto the point "a" on the pseudo-ternary plane (section) in Figure 5.3.57.

5.3.2.2.6 Suggestions on the Use of Advanced Thermodynamic Software Tools

The availability of more powerful and advanced research tools in combination with the significantly improved control of the operations introduces new opportunities and a new range of the applications of predictions in industrial practice.

There are common points that are advisable in the application of the advanced predictive tools and derived from experiences in this field:

1. It is a good practice to envisage ("picture") a prediction as a particular high-temperature experiment or a particular process with clear planning of input and a hypothesis of the expected output of the model. "Visualizing" or "imagining" the prediction as an actual physical process is always beneficial.
2. Clearly identify the purpose of the calculations. For example, is the purpose to characterize the phase assemblage which is primarily determined by the major components, or is the distribution or partitioning of minor elements between these major phases the key target?
3. Find experimental data or other independent reliable information and undertake first pass simple calculations to test predictions, to identify what major gaseous, liquid, and solid phases can be formed or what is the range of process conditions of interest.
4. Examine and select appropriate thermodynamic and other models for complex solutions from available databases. It is common to attempt to use ideal solution for liquid and stoichiometric solids—this can easily result in inadequate predictions since the presence of complex multicomponent nonideal liquid and solid solutions is a particular feature of the nonferrous pyrometallurgical streams. The limits to these solutions, both actual solubility limits and limitations of model descriptions, must be carefully examined and taken into account.
5. Complex gaseous species in vapor phases should not be ignored; noninclusion of appropriate gaseous species into the thermodynamic treatment of the gas solution phase can result in erroneous predictions. Multiple examples include the gaseous PbS species that is particularly stable in reducing conditions with high Pb and S concentrations; gaseous SiO species in reducing conditions at high temperatures.

6. Predictions should be tested and compared to the available information, such as selected reliable experimental sources. For example, multicomponent phase equilibria predictions should be tested against selected key low-order phase diagrams before calculations for a real complex system. It should not be assumed that all databases are equally accurate or that the accuracy of predictions is uniform across all compositions and process conditions.
7. The validity of theoretical predictions in the multicomponent system is better being tested against specially performed targeted experiments as well as selected industrial measurements.
8. It is important to set a good structure of the calculations, the process variable to be examined, and how the results are to be presented to facilitate interpretation of trends.

5.3.2.3. Examples of Applications/Case Studies

5.3.2.3.1 Analysis of Slag Chemistry for Lead and Zinc Industrial Slags—Liquidus and Subliquidus "Fluxing" Diagrams for the Pb and Zn Blast Furnace Slags

The potential environmental problems and increasing costs associated with the disposal of zinc-containing wastes have grown to an important sustainability issue, facing the metallurgical industry. Pyrometallurgical processes are used to produce benign materials for disposal. Improvements of existing and development of new pyrometallurgical processes for these systems are dependent on the detailed analysis of key properties of the slag system. An example of such an analysis [101,102] is given below. The treatment of recycling materials using existing nonferrous pyrometallurgical processes introduces changes in the process chemistry that require adjustments in fluxing or other process characteristics—knowledge of the slag system properties therefore is essential to incorporate these changes into practice. The liquidus, proportions of phases, Zn and O_2 partial pressures, slag viscosities, and the lead solubility in slag are predicted in the PbO–ZnO–FeO–Fe_2O_3–CaO–SiO_2–Al_2O_3 system in the range of conditions relevant to a selected lead BF slag over a range of compositions (Table 5.3.4). A trend analysis has been carried out to systematically determine the effects of changes to the slag chemistry. Of particular

Table 5.3.4 Selected Conditions

	Average	Range
ZnO	24 wt%	20–30 wt%
Al_2O_3	5 wt%	0–8 wt%
FeO/SiO_2	1.27	1.0–1.8
CaO/SiO_2	0.71	0.5–0.9
Temperature	1473 K (1200 °C)	1446–1488 K (1175–1215 °C)

interest is the variation in the properties of the system with CaO/SiO_2 and FeO/SiO_2 ratios. Corresponding fluxing diagrams therefore are constructed. Information on the liquidus temperature enables the optimum flux conditions to maintain fully liquid slags to be identified. The liquidus temperatures are presented in Figure 5.3.58a. The lead BF slag is close to the boundary between the wustite and zincite primary phase fields. According to the predictions, an increase of CaO/SiO_2 ratio at constant FeO/SiO_2 ratio would result in an increase in the liquidus temperatures. Changing FeO/SiO_2 at constant CaO/SiO_2 from the average values would result in an increase in the liquidus temperatures. If the reactor is operated below the liquidus, the relative importance of changes in slag composition can be assessed by predicting the % solids in isothermal sections. The phases predicted to be stable in the range of conditions investigated are listed in Table 5.3.5 and are indicated with the corresponding name or letter on the diagrams. The proportions of solids at 1473 K (1200 °C) (see Figure 5.3.58b) are predicted to be insensitive to variations of FeO/SiO_2 or to a decrease of CaO/SiO_2, but increasing CaO/SiO_2 would result in the formation of melilite solid solution in addition to wustite and zincite, with an accompanying sharp increase in the proportions of solids. Control of the zinc partial pressures is essential for these Pb/Zn pyrometallurgical operations. The variation of the zinc partial pressure with bulk composition at 1473 K (1200 °C) (Figure 5.3.58c) is not what might intuitively be expected—P_{Zn} is found to be insensitive to changes in the FeO/SiO_2 ratio and decreases as the CaO/SiO_2 ratio increases. The main factors effecting P_{Zn} at constant temperature are the activity of ZnO and the oxygen partial pressure P_{O_2}. Predictions in this study were made for the condition of $a_{Pb} = 1$ at PbO = 1 wt% in the slag so that, as the bulk composition changes, both P_{O_2} and a_{ZnO} change. Figure 5.3.58d shows P_{O_2} at 1473 K (1200 °C). It would normally be anticipated that an increase of CaO/SiO_2 would result in an increase of P_{Zn}. However, a decrease of P_{O_2} with an increase of CaO/SiO_2 (see Figure 5.3.58d) results in decreasing P_{Zn}. These results provide an important basis for trend analysis of slag behavior for a lead BF slag to assist with the selection of fluxing and waste recycling. The viscosities of these slags are given in Figure 5.3.58e. PbO solubilities in the slag system at fixed oxygen partial pressure in equilibrium with metallic lead are given in Figure 5.3.58f.

Predictions of the type illustrated in Figure 5.3.58 provide necessary background information to assist in selection of the optimum process characteristics.

5.3.2.3.2 Liquidus and Subliquidus "Fluxing" Diagrams for the Electric Arc Furnace Dust Recycling Slags

An analysis of the phase equilibria in the $ZnO–FeO–Fe_2O_3–CaO–SiO_2$ system undertaken at conditions of importance to the recycling of the EAF dusts to assist in selection of the optimum conditions for the pyrometallurgical processing [103] is presented in Figure 5.3.59.

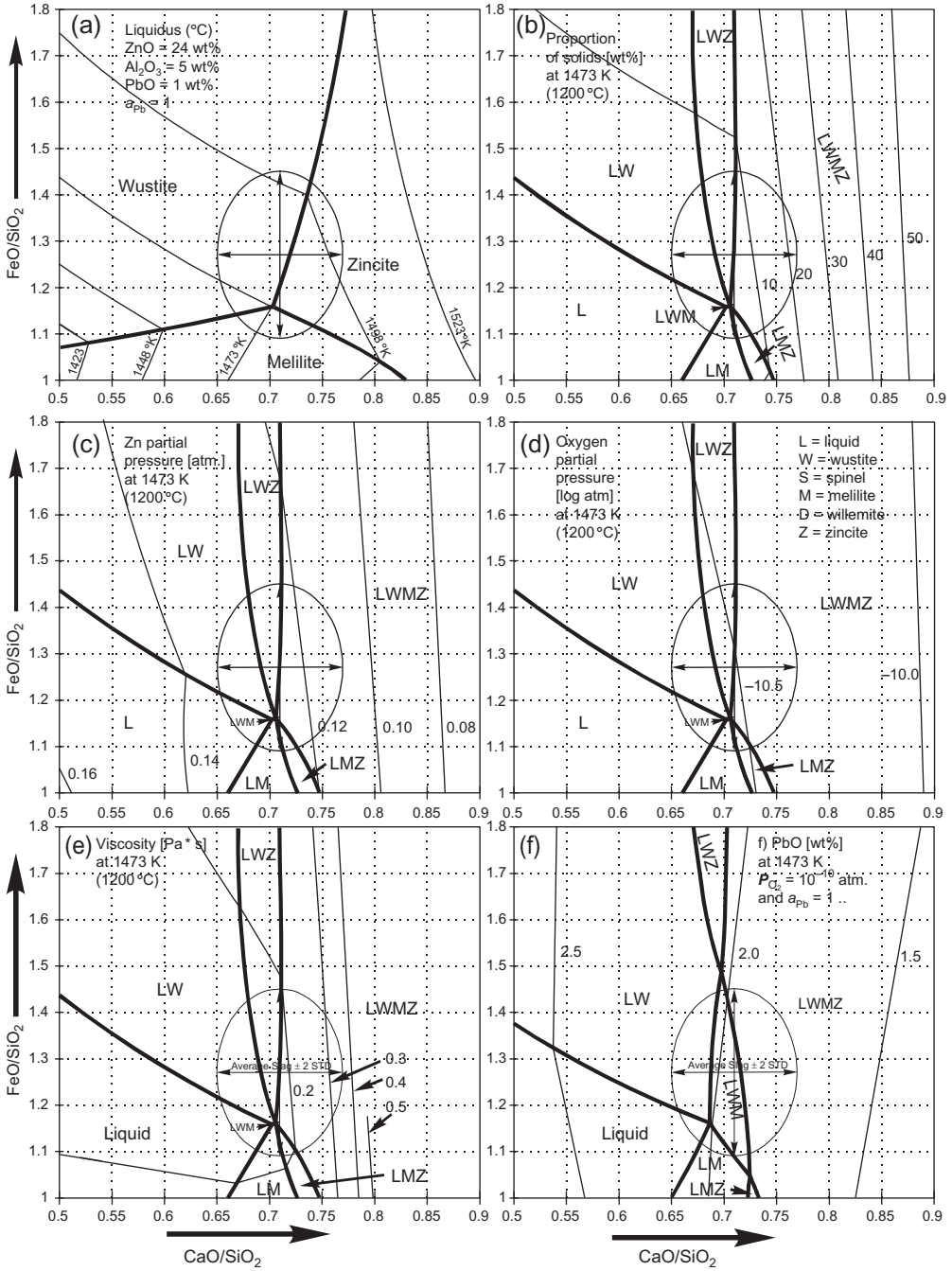


Figure 5.3.58 (a) Liquidus (°C), (b) proportion of solids (wt%), (c) Zn partial pressure (atm.), and (d) oxygen partial pressure (atm.) at 1473 K (1200 °C) in a slag system with ZnO = 24 wt%, Al_2O_3 = 5 wt%, PbO = 1 wt%, and a_{Pb} = 1 [101].

Table 5.3.5 Phases Predicted to Be Stable in the Investigated Range

Name	Chemical Formulae	ID
Liquid		L
Wustite	(Fe,Zn)O	W
Spinel	$(Fe,Zn)(Fe^{3+},Al^{3+})_2O_4$	S
Melilite	$(Ca,Pb)_2(Fe^{2+},Zn^{2+})Si_2O_7$	M
Willemite	$(Zn,Fe)_2SiO_4$	D
Zincite	(Zn,Fe)O	Z

Recent trends in the supply of the metals indicate the growing recovery of metals from secondary materials [104]. For example, in 1997, approximately 77% of the total lead output and 62% of the zinc output in the United States were produced from secondary sources [105]. Most lead and zinc secondaries are recycled via pyrometallurgical smelting processes [105]. Production of refined lead from all secondary materials outside China now accounts for 75% of the lead output [106].

EAF dust is an important source of secondary zinc production. A number of pyrometallurgical processes are being used to recover zinc from EAF dust [107–110]. In all cases, this involves fluxing of the EAF dust by CaO and SiO_2 to obtain liquid slag. Systematic analysis of phase equilibria is important to optimize the selection of flux additions.

The EAF dusts contain mostly Fe and Zn oxides in various proportions. For example, a number of authors ([107–110]) reported Zn/Fe weight ratios in the range of 0.504–1.421.

Phase equilibria conditions were predicted in the $ZnO–FeO–Fe_2O_3–CaO–SiO_2$ system for Zn/Fe weight ratios of 0.504 and 1.421. The results of predictions are presented in Figure 5.3.59a–f in the form of pseudo-ternary sections with zinc and iron oxide combined in one apex of the compositional triangle, and CaO and SiO_2 in the other two. This form of section is selected because both lime and silica may be used for the fluxing of EAF dust. The calculations were performed for the oxygen partial pressures of 10^{-9} and 10^{-3} atm. so that the Fe^{2+}/Fe^{3+} ratios predicted by FactSage [111] vary with composition and temperature. Two types of calculations were performed: liquidus temperatures (Figure 5.3.59a–d) and isothermal sections (Figure 5.3.59e and f).

The sum of the weight percentages of ZnO, FeO, and Fe_2O_3 (all iron was accounted as FeO) at fixed Zn/Fe ratio are used to represent compositions in Figure 5.3.59a–f. That is, the projection is made from the oxygen corner onto the plane $CaO–SiO_2–(ZnO+FeO)$. The "weight of FeO" is actually $(0.900m_{Fe_2O_3}+m_{FeO})$, where $m_{Fe_2O_3}$

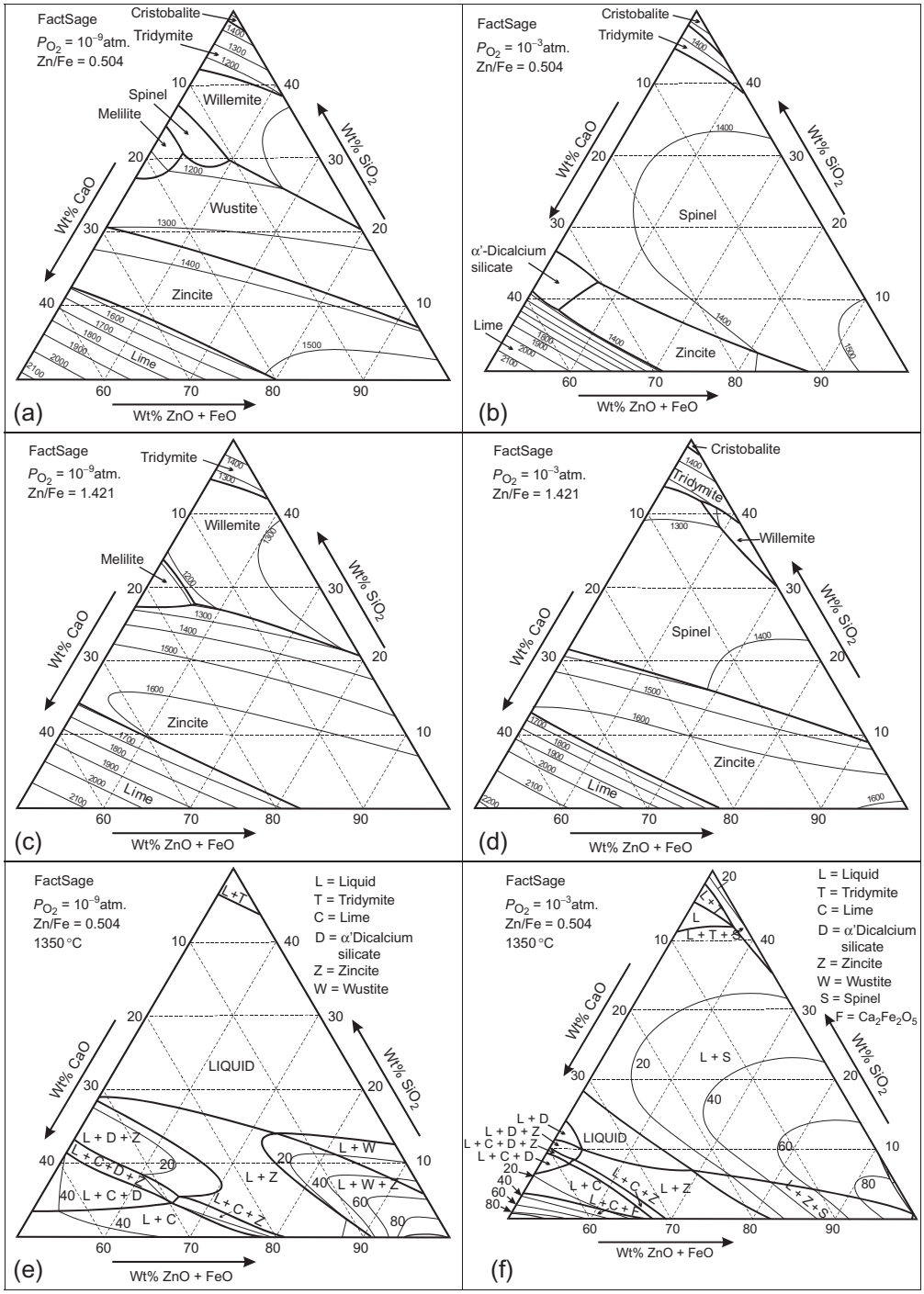


Figure 5.3.59 Phase relations in the CaO–FeO–Fe_2O_3–SiO_2–ZnO slag predicted with FactSage: liquidus surface (a) for Zn/Fe = 0.504 at $P_{O_2} = 10^{-9}$ atm., (b) Zn/Fe = 0.504 at $P_{O_2} = 10^{-3}$ atm.; (c) Zn/Fe = 1.421 at $P_{O_2} = 10^{-9}$ atm.; (d) Zn/Fe = 1.421 at $P_{O_2} = 10^{-3}$ atm.; and proportions of solids on the isothermal section (e) for Zn/Fe = 0.504 at $P_{O_2} = 10^{-9}$ atm. and (f) Zn/Fe = 0.504 at $P_{O_2} = 10^{-3}$ atm., showing the phases present at equilibrium and the proportion of solids (20, 40, 60, and 80 wt %) (°C, wt%) [103].

and m_{FeO} are the weights of the components in a phase, and 0.900 is the ratio of the molecular weights of 2FeO and Fe_2O_3.

Figure 5.3.59a and b present predictions for the EAF dust with Zn/Fe weight ratio of 0.504 at the oxygen partial pressures of 10^{-9} and 10^{-3} atm., respectively. The liquidus temperature for the zinc and iron oxide mixture alone is above 1773 K (1500 °C) for both the oxygen partial pressures, but the primary phase for the zinc/iron-rich compositions changes from the zincite solid solution for $P_{O_2} = 10^{-9}$ atm. to spinel for $P_{O_2} = 10^{-3}$ atm. Liquidus temperatures below 1623 K (1350 °C) can be achieved at $P_{O_2} = 10^{-9}$ atm. by the addition of CaO and/or SiO_2 in weight proportion of CaO/SiO_2 of approximately 0.5 and lower. The addition of approximately 30 wt% $CaO + SiO_2$ with CaO/SiO_2 weight ratio of 0.5 (so that ZnO + FeO is ~70 wt%) results in liquidus temperatures below 1623 K (1350 °C) at $P_{O_2} = 10^{-9}$ atm. (see Figure 5.3.59a). At $P_{O_2} = 10^{-3}$ atm., however, the liquidus temperature of the slag with 70 wt% ZnO + FeO and the CaO/SiO_2 weight ratio of 0.5 is approximately 100 K higher (see Figure 5.3.59b).

Figure 5.3.59c and d predictions of the liquidus temperatures for slags with the Zn/Fe weight ratio of 1.421. Increase of the zinc content results in substantially higher liquidus temperatures at high ZnO + FeO contents at both oxygen partial pressures of 10^{-9} atm. (compare Figure 5.3.59c and a) and 10^{-3} atm. (compare Figure 5.3.59d and b).

In industrial practice slags can contain solid as well as liquid phases. The slag composition and operating temperature should be such that a small temperature decrease in the reactor or a small variation in slag chemistry does not lead to a large increase in the fraction of solids in the slag. This is an important consideration because the viscosities of solid/liquid slurries can increase dramatically with increasing solids content, particularly beyond 10–20% solids. The slag should at all times be maintained under conditions where it is sufficiently fluid to be readily tapped from the reactor.

Although the proportion of solids can readily be derived from the phase diagram for binary systems, deriving the same information for a complex slag system is not possible without a complete thermodynamic model of the system.

Isothermal sections of the form $CaO–SiO_2–(ZnO + FeO)$ at 1623 K (1350 °C) at fixed Zn/Fe weight ratio of 0.504 and fixed oxygen partial pressures of 10^{-9} and 10^{-3} atm. are presented in Figure 5.3.59e and f, respectively. The amount of addition or removal of CaO or SiO_2 required to achieve a certain slag chemistry can be easily worked out from these diagrams. The areas of bulk compositions with certain phase assemblages are bounded with thick solid lines. The slag is predicted to be completely liquid at 1623 K (1350 °C) when the composition is within the phase region marked L.

The proportions of solid phases at temperatures below the liquidus are presented on these pseudo-ternary sections. In Figure 5.3.59e and f, the thin solid lines represent compositions for which the proportion of solids at fixed temperature is the same (20, 40, 60, and 80 wt% solids).

5.3.2.3.3 Spinel Liquidus in lead Smelting Slags—Complex Combination of "Fluxing" and Oxidizing Conditions Resulting in a Local Maximum in the Spinel Liquidus

The chemistries of lead smelting and sintering systems are complex, and the sequence and proportions of phases formed under equilibrium conditions in subliquidus temperatures are not readily determined experimentally although the sequence can be qualitatively understood using phase diagrams of low-order systems. At this point, it is necessary to turn to chemical thermodynamic models of the systems [112]. All of the experimental data available on the ZnO–FeO–Fe_2O_3–PbO–CaO–SiO_2 system have been incorporated into the FactSage database [102,103,113–119]. The use of sophisticated tools of this type enables the liquidus temperatures, phase assemblages and compositions, and the proportions of all phases in the system to be predicted as a function of temperature, bulk composition, and oxygen pressure.

Figures 5.3.60 and 5.3.61 illustrate the effect of PbO concentration on liquidus, % solids, and oxygen partial pressure P_{O_2} in lead smelting slags in equilibrium with liquid lead metal for a range of CaO/SiO_2 ratios. Figure 5.3.60 presents predictions for one slag composition, and Figure 5.3.61 presents predictions for a range of compositions illustrating the effect of the CaO/SiO_2 ratio. Figures 5.3.60 and 5.3.61 characterize slag system properties as a function of the PbO concentrations—as PbO is reduced from the slag into the Pb metal bullion phase in various operations, for example, in lead batch reduction processes.

At high lead concentrations, the liquidus temperature is low and the slag is completely liquid at 1493 K (1220 °C). As lead is reduced and the PbO concentration is progressively lowered, the liquidus temperatures increase and the spinel primary phase becomes stable, the proportion of this solid phase increasing with decreasing PbO concentration. The increasing stability of the spinel relative to the liquid slag phase is due to the removal of the PbO—strong fluxing agent. The maximum liquidus in the spinel primary phase field is approximately 1533 K (1260 °C) at approximately 30–35 wt% PbO in slag (see Figures 5.3.60a and 5.3.61a). Note that the maximum proportion of solids at 1493 K (1220 °C) in equilibrium with metallic lead metal is predicted to be at bulk PbO concentrations between ~12 and 19 wt% PbO (Figures 5.3.60b and 5.3.61b). As PbO is reduced further to concentrations below ~30 wt% PbO, more reducing conditions result in lower spinel stability, and the liquidus temperatures decrease reaching minimum between ~12 and 18 wt% PbO in liquid slag (Figures 5.3.60a and 5.3.61a). This range of concentrations, however, corresponds to the maximum proportion of solids (Figures 5.3.60b and 5.3.61b). At low PbO concentrations, solid zincite is formed, and the liquidus temperatures and proportions of solids increase rapidly with decreasing PbO concentration. If the smelting process is operated at subliquidus conditions, e.g., 1493 K (1220 °C), the % solids in the spinel primary phase field increases with increasing CaO/SiO_2 ratio, beyond a critical value the liquidus temperature and % solids starts to

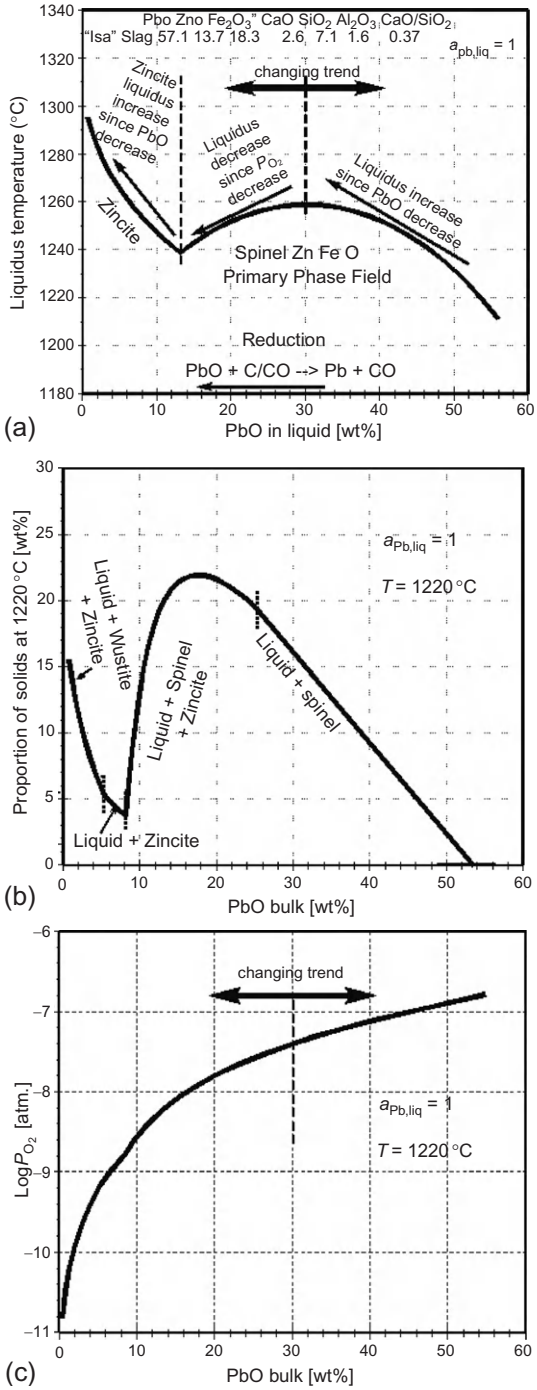


Figure 5.3.60 Liquidus, oxygen partial pressure, and proportion of solids as a function of bulk concentration of lead oxide in equilibrium with metallic lead for the "Isasmelt" slag, showing changes with reduction of lead. *Predicted with FactSage 6.1.*

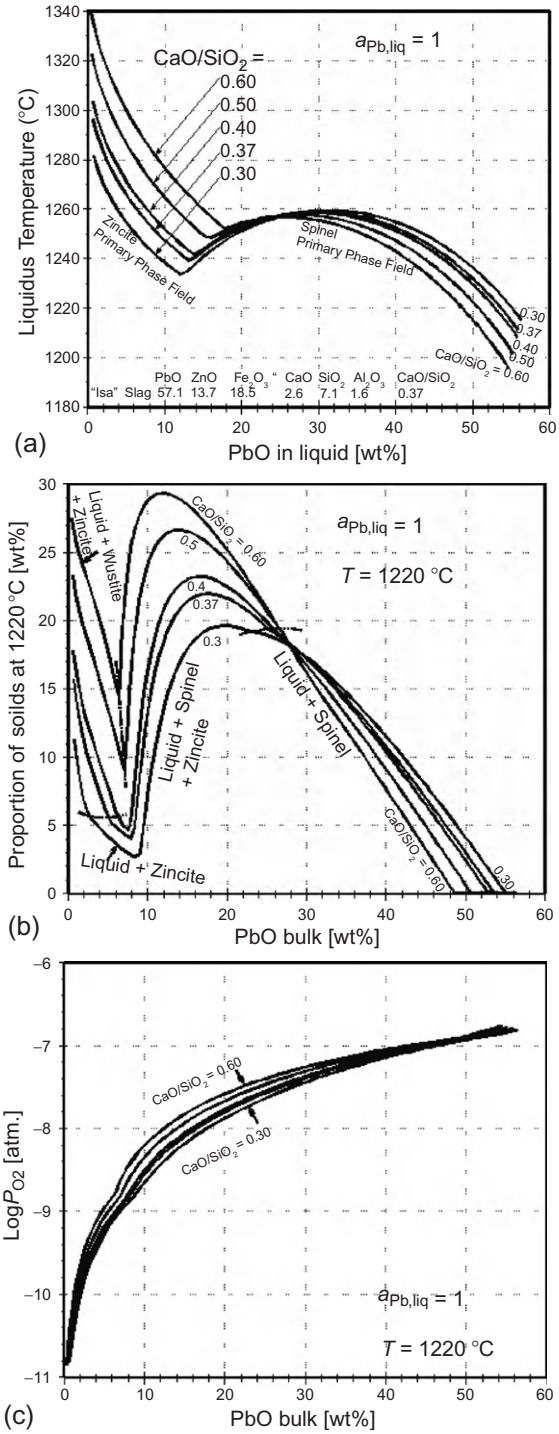


Figure 5.3.61 Predicted (a) liquidus, (b) proportion of solids, and (c) oxygen partial pressure in lead smelting slags in equilibrium with liquid lead metal as a function of CaO/SiO_2 ratio. *FactSage 6.1 databases [118].*

decrease. In a batch reactor, the effect of reducing lead from the slag is to increase the viscosity of the slag through removal of lead oxide species and increased % solids.

These figures illustrate a very important phenomenon frequently observed in the nonferrous smelting and is related to the behavior of the spinel solid—stability of the spinel $Zn_xFe_{3-x}O_{4+y}$ relative to the liquid depends on two competing factors:

1. Fluxing with PbO: decrease of PbO at fixed P_{O_2} increases spinel stability relative to the liquid slag.
2. Oxygen partial pressure: decrease of P_{O_2} decreases spinel stability relative to the liquid slag.

Both PbO concentration and P_{O_2} are directly linked at the condition of equilibrium with metallic lead through the reaction:

$$Pb + 0.5O_2 \rightarrow PbO$$

As PbO concentration is reduced, the oxygen partial pressure is also reduced. The extent of the changes of % PbO and P_{O_2} is complex and depends on slag chemistry (see Figures 5.3.60c and 5.3.61c). The extent of the effect of % PbO and P_{O_2} on the stability of the spinel relative to the liquid slag is also complex, but can be characterized with the advanced thermodynamic computer packages.

Important practical implication is that the fluxing cannot be selected solely on the information of the initial oxidation slag and final reduced slag—the maximum of the spinel stability at intermediate PbO concentrations can strongly affect process performance. This phenomenon of the spinel stability at intermediate PbO concentrations is not commonly recognized.

5.3.2.4. Spinel Liquidus in Copper Smelting Slags

The maximum stability of spinel at intermediate stages of the extraction of a value metal in nonferrous processes is a common phenomenon. The following section outlines this typical issue in the copper smelting described by Hidayat *et al.* [120].

Figure 5.3.62 presents a pseudo-ternary diagram of "Cu_2O"–"Fe_2O_3"–SiO_2 in equilibrium with metallic copper [120] using experimental measurements from that study as well as the information on the pseudo-binary "Cu_2O"–"Fe_2O_3" [121,122] and "Cu_2O"–SiO_2 [123] systems in equilibrium with metallic copper. Other data reported by Ruddle *et al.* [124] and Oishi *et al.* [125] are included in the ternary and are indicated by cross and plus symbols, respectively.

The system has four primary phase fields between 1373 and 1573 K (1100 and 1300 °C), i.e., tridymite, cuprite, spinel, and delafossite. The oxygen partial pressure in the system in equilibrium with metallic copper decreases according to the reaction $Cu_2O_{slag} \rightarrow 2Cu_{metal} + 0.5O_{2,gas}$ as the composition of the slag moves away from "Cu_2O" corner and approaches the iron oxide–silica binary. For instance, the spinel

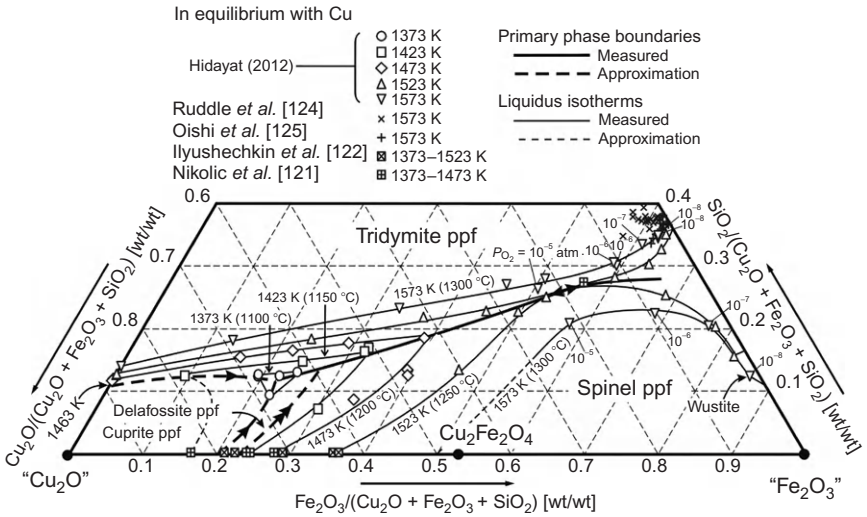


Figure 5.3.62 Liquidus isotherms in the "Cu_2O"–"Fe_2O_3"–SiO_2 system in equilibrium with metallic copper–iron alloy [120], oxygen partial pressures in atm.

liquidus point at 1573 K (1300 °C) containing 21.6 wt pct "Cu_2O" corresponds to experiments at $P_{O_2} = 10^{-5}$ atm. At the same temperature, the spinel liquidus point containing lower copper oxide concentration of 2.8 wt pct "Cu_2O" corresponds to the experiment at lower $P_{O_2} = 10^{-7}$ atm. Figure 5.3.63a illustrates that the oxygen isobars lie almost parallel to the "Fe_2O_3"–SiO_2 join. The 10^{-7} and 10^{-8} atm. oxygen isobars are located relatively close to the "Fe_2O_3"–SiO_2 join, but the 10^{-5} and 10^{-6} atm. oxygen isobars are located at significant copper concentrations. The $CuO_{0.5(l)}$ activity coefficients in the "Cu_2O"–"Fe_2O_3"–SiO_2 ternary are also provided in Figure 5.3.63b, showing that the activity coefficient of $CuO_{0.5(l)}$ in the slag increases as the slag compositions approach the "Fe_2O_3"–SiO_2 join.

Figures 5.3.62 and 5.3.63 illustrate the maximum of the spinel stability relative to the slag at intermediate copper oxide concentrations. For the system with a given Fe/SiO_2 ratio, the spinel liquidus is (a) low at high copper oxide concentrations due to the strong "Cu_2O" fluxing effect, and (b) low at low copper oxide concentrations due to the significant decrease in the oxygen partial pressure in that compositional area. This phenomenon has important practical implication for the reduction of copper oxide in the "direct-to-blister" processes.

With the decreasing availability of "clean" copper concentrate resources, operations are moving generally to slag systems containing more impurities, such as MgO, CaO, and Al_2O_3. The effects of these elements on slag phase equilibria are complex, and their potential to create processing problems that lead to increased operational costs are not

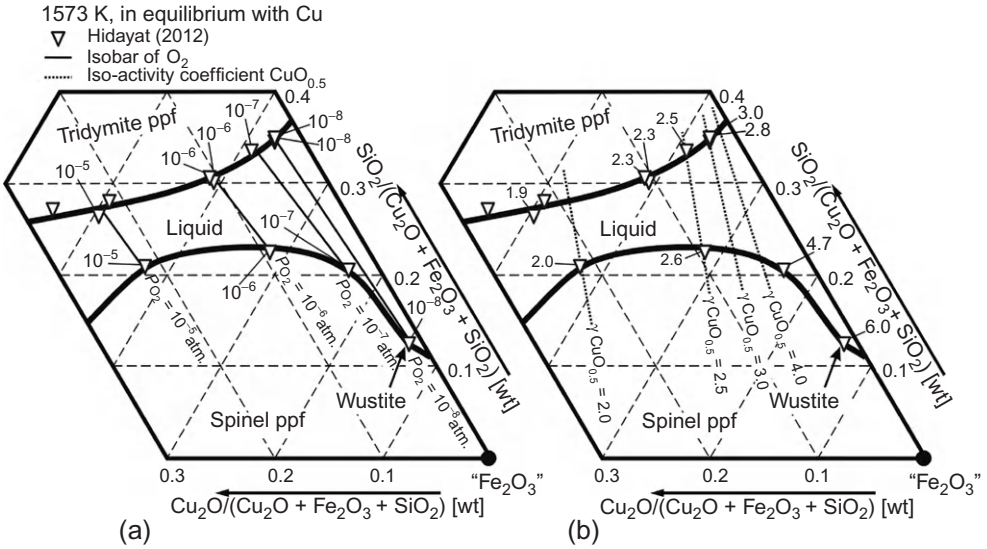


Figure 5.3.63 A section of the "Cu_2O"–"Fe_2O_3"–SiO_2 system in equilibrium with metallic copper at 1573 K (1300 °C) [120], showing (a) O_2 isobars (atm.) and (b) lines of isoactivity coefficient of $CuO_{0.5}$ (pure $CuO_{0.5(l)}$ standard state) [120].

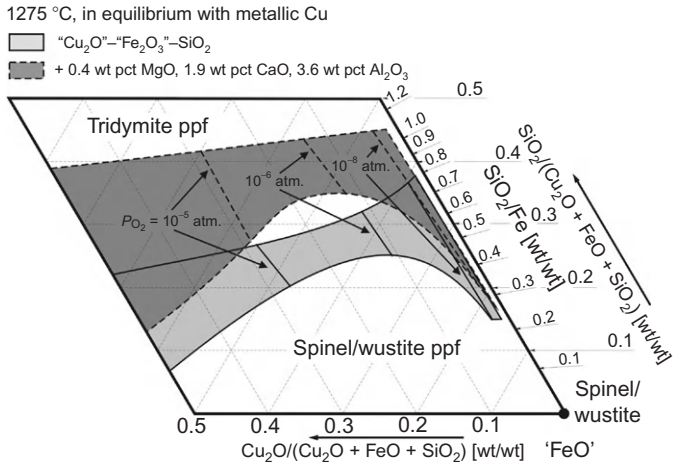


Figure 5.3.64 The effect of impurities on the Cu–Fe–O–Si slag in equilibrium with metallic copper at 1548 K (1275 °C) [126].

well characterized. The availability of thermodynamic databases developed with FactSage [111] of the relevant slag system means that it is now possible to obtain good estimates of the effects of impurities on the consumption of flux and extent of copper losses during the process. An example of such analysis is given in Figure 5.3.64.

The spinel/wustite and tridymite liquidus, and the O_2 isobars are predicted in the "Cu_2O"–FeO–Fe_2O_3–SiO_2 system at 1548 K (1275 °C) over a range of compositions as shown in Figure 5.3.64 [126]. The effects of addition of 0.4 wt pct MgO, 1.9 wt pct CaO, and 3.6 wt pct Al_2O_3 on the liquidus and O_2 isobars are also provided in this figure. According to the predictions, the addition of the MgO, CaO, and Al_2O_3 into the Cu–Fe–O–Si slag system results in the shift of the fully liquid area toward higher SiO_2 concentration. This means that if the operation was carried out in the spinel primary phase field, appropriate adjustments to the Fe/SiO_2 ratio in the slag and corresponding SiO_2 flux additions have to be introduced to avoid excessive solids formation and buildups. Figure 5.3.64 also indicates differences in the positions of P_{O_2} isobars between impurity-free and impurity-containing slag systems. With the presence of 0.4 wt pct MgO, 1.9 wt pct CaO, and 3.6 wt pct Al_2O_3 in the slag, the P_{O_2} isobars slightly shift toward higher Cu_2O concentration.

These results provide an important basis for trend analysis of slag behavior for a copper smelting/converting slag to assist with the selection of fluxing and prediction of copper loss in the slag. Later, the new thermodynamic database can also be used to predict partitioning of major and minor elements between phases, activities, vapor pressure, and other thermodynamic properties over a wide range of process conditions in copper production.

There is a general tendency to simplify the representation of the phase equilibria data, such as into rectangular compositional coordinates for both axes with different basis such as Fe/SiO_2 ratio and CaO/SiO_2 ratio. Although the simplified representation is a convenient way to indicate fluxing or other industrial parameters, it results in a loss of scientific information that would be present if the data were presented in the Gibbs triangle diagrams. For example, in the graph with the rectangular compositional coordinates, the "lever rule" cannot be applied and the solidification/crystallization path of a given slag composition cannot be tracked.

5.3.2.4.1 Copper Smelting and Cleaning Slags—Effect of Oxygen Partial Pressure

The system FeO–Fe_2O_3–CaO–SiO_2 forms the basis for smelting and refining slags in most nonferrous smelting processes; the effect of oxygen partial pressures on the phase equilibria in this system is important and is systematically analyzed using thermodynamic predictive tools [127]. The experimental phase equilibrium studies that have been carried out on various aspects of this system have been widely reported in the literature [128–130].

The necessity to obtain more detailed information on the phase chemistry of these systems is driven by the need to take practical steps to optimize metallurgical outcomes, and to reduce operating costs. In particular, the issues of use and selection of flux additions, refractory wear, and control of solid phase formation are of general concern from a pyrometallurgical viewpoint.

The chemical and physicochemical properties of the slag are intimately linked to the phases present and their compositions. Properties such as the liquidus and proportion of solids, important to many aspects of the process, are controlled by variables, such as bulk composition, temperature, and oxygen partial pressure.

To date, prediction of the effects of these process variables has largely been carried out with the aid of ternary or pseudo-ternary phase diagrams, determined under particular experimental conditions. While these diagrams are very useful as a guide to the general behavior of the slags, they are limited in the range of conditions which can be accurately described. These difficulties, largely stemming from the number of compositional and process variables that have to be considered, can be overcome by constructing chemical thermodynamic models of the slag.

The following examples illustrate the ways in which thermodynamic predictive packages can be used to systematically analyze and predict the effects of process variables on the phases present, their proportions and their compositions.

The selected examples refer primarily to the conditions encountered generally in copper smelting and converting technologies [130], but the use of the FactSage model can be extended to applications in any set of composition, temperature, and oxygen partial pressure conditions in the system.

5.3.2.4.1.1 Liquidus

Of principal concern to copper smelting operations is the liquidus of the slag. In flash smelting, the slag is exposed to a range of oxygen pressures, highly oxidizing conditions are present in the smelting shaft and these oxygen pressures are lowered by contact with the matte phase [130,131]. The liquidus at 1523 K (1250 °C) for the system $FeO–Fe_2O_3–CaO–SiO_2$ at oxygen partial pressures 10^{-6}, 10^{-8}, and 10^{-10} atm. as predicted using the FactSage model is given in Figure 5.3.65. It can be seen that the liquidus does not vary significantly with oxygen pressure in the tridymite, wollastonite, and dicalcium silicate primary phase fields. The liquidus of iron-rich slags is, however, very sensitive to oxygen partial pressure. At low oxygen pressures, e.g., $P_{O_2} = 10^{-10}$ atm., the bounding primary phase field of iron-rich slags is wustite. At higher oxygen partial pressures, the spinel (in this case magnetite) phase becomes stable. The extent of the spinel field increases with increasing oxygen partial pressure, and the range of compositions at which the slags are completely liquid becomes smaller.

The formation of magnetite during smelting operations is widely recognized as a major problem in industrial practice [130]. The formation of this solid phase impedes slag/matte separation and ultimately reduces bath volume due to the buildup of magnetite deposits on the reactor walls. To select operating conditions that avoid or minimize these undesirable effects, further detail on the slag chemistry is required.

The influence of SiO_2/Fe weight ratio, CaO/SiO_2 weight ratio, and oxygen partial pressure on the liquidus temperatures of the slags is illustrated in Figure 5.3.66.

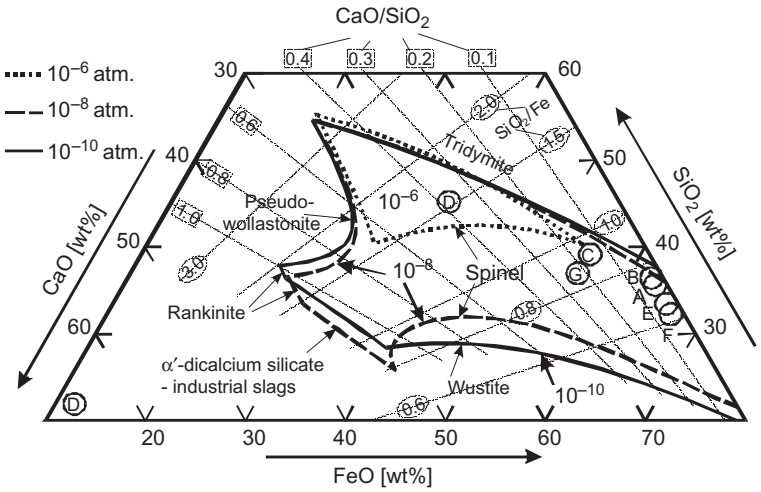


Figure 5.3.65 Liquidus isotherms at 1523 K (1250 °C) in the system FeO–Fe_2O_3–CaO–SiO_2 for oxygen partial pressures of 10^{-6} (solid line), 10^{-8} (dashed line), and 10^{-10} atm. (dotted line) [127]. *Predicted by FactSage model.*

The predicted slag liquidus as a function of SiO_2/Fe ratio for the CaO/SiO_2 weight ratios of 0, 0.1, 0.2, and 0.3 at an oxygen partial pressure of 10^{-4} atm. is given in Figure 5.3.66a. The predictions show that increasing SiO_2/Fe ratio leads to a decrease in slag liquidus in the spinel primary phase field. The liquidus increases with increasing SiO_2/Fe ratio in the tridymite (SiO_2) primary phase field. A feature of the equilibria at this relatively high oxygen partial pressure is that the liquidus temperatures are, in general, above 1573 K (1300 °C).

The general shape of the liquidus is retained on lowering the oxygen partial pressures progressively to 10^{-6}, 10^{-8}, and 10^{-10} atm. (Figure 5.3.66b–d). The absolute and relative values of the liquidus temperatures change with changing oxygen pressure. In the iron oxide primary phase fields, lowering the oxygen pressure is accompanied by the lowering of liquidus temperatures, while the liquidus temperatures for the tridymite and fayalite primary phase fields remain almost unaffected by P_{O_2}. At 10^{-10} atm., there is a significant range of compositions that are fully liquid at 1473 K (1200 °C). This is associated primarily with the appearance of the fayalite or olivine primary phase field.

By way of comparison, the liquidus for the pseudo-ternary system FeO_x–CaO–SiO_2 at iron saturation is given in Figure 5.3.66e.

The effect of the CaO/SiO_2 weight ratio in the slag on the liquidus (Figure 5.3.66a–e) is also dependent on the primary phase field. Note that increasing CaO/SiO_2 generally increases slightly the liquidus in the magnetite and wustite primary phase fields, but reduces the liquidus in the olivine or fayalite, and tridymite (SiO_2) primary phase fields.

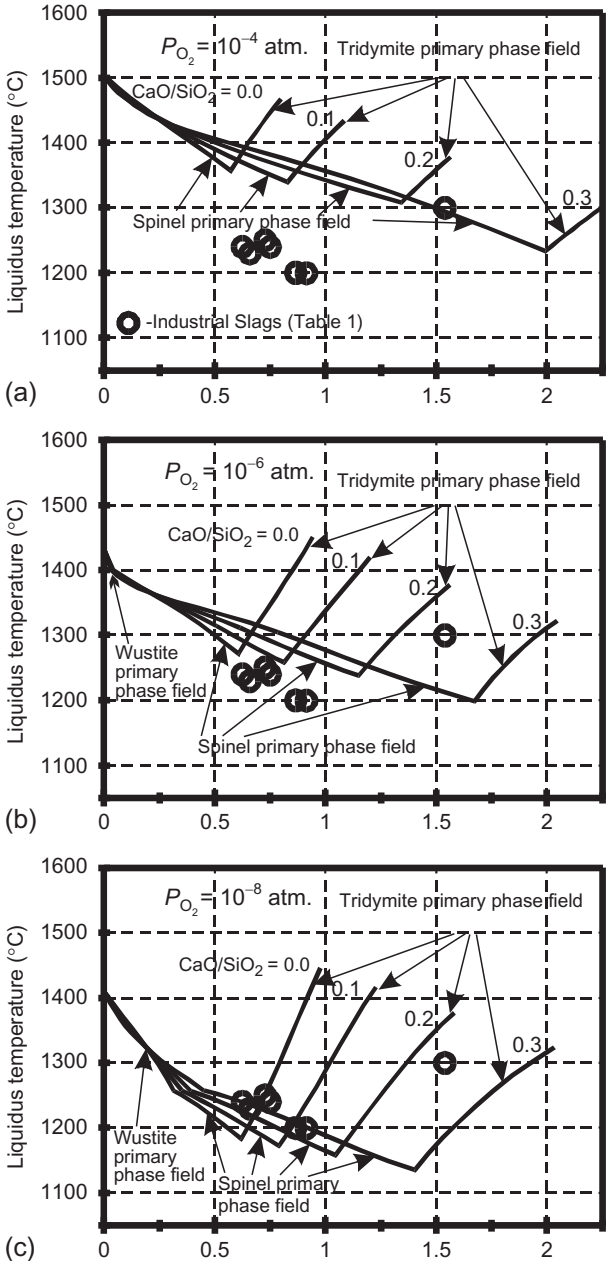


Figure 5.3.66 Slag liquidus as a function of SiO_2/Fe weight ratio for CaO/SiO_2 weight ratios of 0, 0.1, 0.2, and 0.3 at oxygen partial pressures of (a) 10^{-4}, (b) 10^{-6}, (c) 10^{-8},

(Continued)

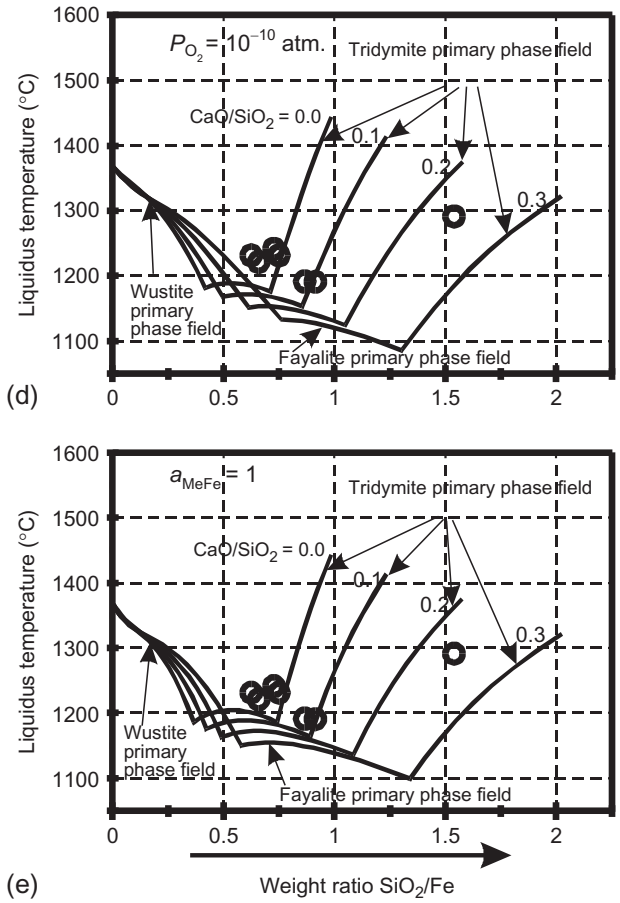


Figure 5.3.66, cont'd (d) 10^{-10} atm., and (e) at metallic iron saturation [127]. *Predicted by FactSage model.*

5.3.2.4.1.2 Subliquidus

Figures 5.3.67 and 5.3.68 show the weight proportion of liquid at 1523 K (1250 °C) as a function of oxygen partial pressure for SiO_2/Fe weight ratios of 0.6 and 1.0, respectively, at various CaO/SiO_2 ratios. The data at SiO_2/Fe = 0.6 show that the slags with CaO/SiO_2 less than 0.3 are fully liquid for oxygen pressures below 10^{-8} atm. With no lime additions, solids formation does not occur until oxygen pressures exceed approximately 3×10^{-7} atm., once this critical oxygen pressure has been achieved; however, there is a dramatic reduction in the proportion of liquid present in the system. As lime is added to these slags, the critical oxygen pressures for the appearance of solid spinel decrease. From the point of view of operating above the liquidus at high oxygen pressures, lime addition does not appear to be useful for this SiO_2/Fe ratio.

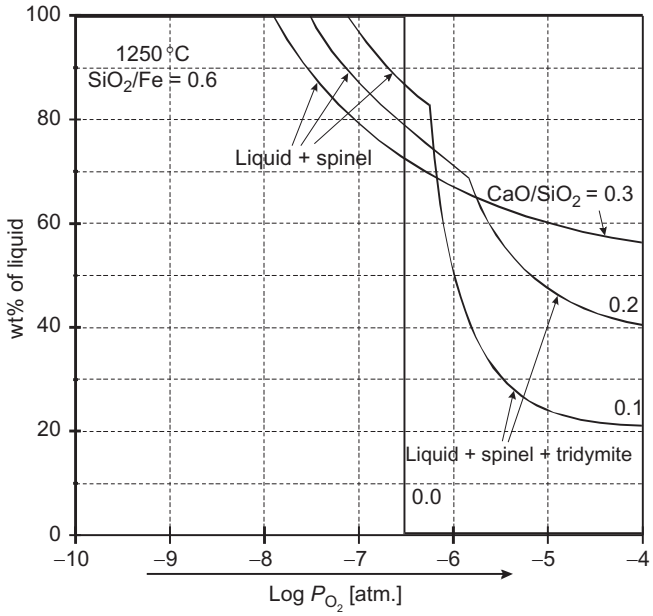


Figure 5.3.67 Weight% of liquid at 1523 K (1250 °C) as a function of oxygen partial pressure for SiO_2/Fe weight ratio of 0.6 and CaO/SiO_2 weight ratios of 0, 0.1, 0.2, and 0.3 [127]. *Predicted by FactSage model.*

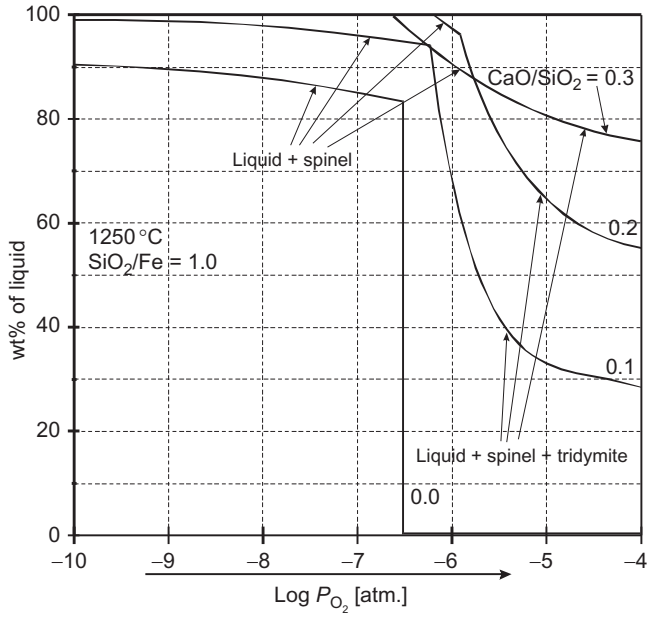


Figure 5.3.68 Weight% of liquid at 1523 K (1250 °C) as a function of oxygen partial pressure for SiO_2/Fe weight ratio of 1.0 and CaO/SiO_2 weight ratios of 0, 0.1, 0.2, and 0.3 [127]. *Predicted by FactSage model.*

In contrast, the data at SiO_2/Fe weight ratio of 1.0 show that the slags with no lime contain approximately 10 wt% solids for oxygen pressures in the range 10^{-12}–10^{-7} atm. Small additions of lime lower the proportions of solids present over the same range of oxygen partial pressures and extend the range of oxygen pressures under which the system can be operated without the catastrophic precipitation of the solid phase. In general, low slag fluidity, high viscosity, is to be expected if the solids content of the slag exceeds 20 wt%.

The presence of Al_2O_3 also significantly reduces the critical oxygen pressure for the formation of the spinel solid phase. As an example (Figure 5.3.69), at the oxygen partial pressure of 10^{-8} atm., with no Al_2O_3, the slag is completely liquid; with 6 wt%Al_2O_3 under the same conditions, over 20 wt% solids are present.

5.3.2.4.1.3 Further Comments

Most copper smelting processes operate with slags having SiO_2/Fe weight ratios in the range 0.6–1.0. The slag compositions and process conditions used in various copper smelting operations are given in Table 5.3.6 [130] and marked in Figures 5.3.65 and 5.3.66. In general, those smelters that operate with SiO_2/Fe weight ratios of approximately 0.6 use low CaO additions. Those smelters that operate with SiO_2/Fe weight ratios of approximately 1.0 and higher have slags containing significant CaO

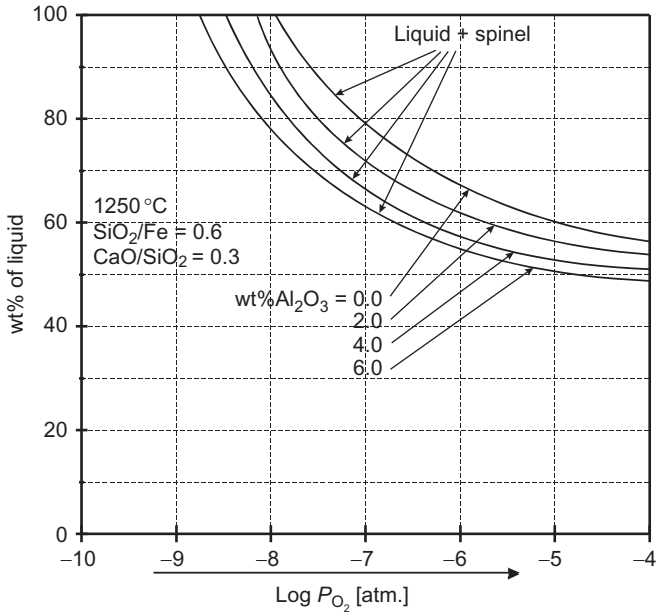


Figure 5.3.69 Effect of Al_2O_3 and oxygen partial pressure on the slag liquidus for SiO_2/Fe weight ratio of 0.6 for CaO/SiO_2 weight ratio of 0.3 at metallic iron saturation [127].

Table 5.3.6 Compositions of Copper Smelting Slags [wt%], and Process Conditions for Various Smelting Processes [130]

	Smelter	Process	Cu	SiO_2	Fe Tot.	Fe^{3+}	Al_2O_3	CaO	MgO	S	SiO_2/Fe	CaO/SiO_2	Slag *T* (°C)
A	Magma	Outokumpu Flush	2.75	32	44	2	4	1		1	0.73	0.03	1250
B	Chino	Inco Flash	0.9	33	44	1	3	1		1	0.75	0.03	1240
C	Ilo	Reverberatory Furnace	0.6	33	36	2	8	5		1	0.92	0.15	1200
D	Mufulira	Electric Furnace	0.7	37	24	1	5	14	5	0.3	1.54	0.38	1300
E	Southern Copper	Noranda Furnace	2.6	29	44	5	2	1	3	1	0.65	0.03	1230
F	Caletones	Teniente Furnace	7	25	40	4	6	1		5	0.63	0.04	1240
G	Mt Isa	Isasmelt	0.5	32.6	37.6	5.6	4.3	7.4	1.9	1	0.86	0.22	1200

concentrations. These compositions have been selected by operators following plant trials to suit the particular process technologies and operating practices in each case. It is, however, interesting to compare these practices to the predictions made using the slag model.

The calculated liquidus temperatures in the system $FeO–Fe_2O_3–CaO–SiO_2$ at iron saturation, shown in Figure 5.3.66e, indicate that at SiO_2/Fe weight ratio of 0.6, CaO addition will result in a lowering of the liquidus. The system under these conditions is operating in the region described by the fayalite primary phase field. The equilibrium oxygen partial pressures in copper matte smelters are reported to be in the range 10^{-11}–10^{-9} atm. [130]; however, local excursions above these values occur as the concentrates are contacted with oxidizing gases [130]. In direct smelting, the oxygen partial pressures in equilibrium with copper metal are approximately 10^{-5} atm. Figure 5.3.66a–d shows that, for SiO_2/Fe weight ratio of 0.6, as the oxygen partial pressure increases the extent of the iron oxide primary field expands, the slag moves into the region of influence of this new phase field and the liquidus temperatures increase dramatically. In addition, while CaO additions are beneficial in lowering the liquidus at SiO_2/Fe weight ratio of 0.6 for oxygen partial pressures below 10^{-9} atm., above this oxygen pressure the addition of CaO increases the liquidus temperatures, making it more likely that solid spinel will form.

In contrast for those smelters operating at SiO_2/Fe weight ratios of approximately 1.0, in the tridymite primary phase field, the liquidus is largely unaffected by oxygen partial pressure, i.e., local over oxidation does not lead to dramatic increases in the proportion of solids and magnetite is not the first solid formed. In this operating regime, the addition of CaO is beneficial in reducing the liquidus temperatures and may lead to improved operability. The calculations, in fact, indicate that the liquidus temperatures for the SiO_2/Fe weight ratio of 1.0 and the CaO/SiO_2 weight ratio of 0.15 are the same as for SiO_2/Fe weight ratio of 0.6 with no lime additions.

The thermodynamic modeling can be used to carry out trend and sensitivity analysis of the system, to explore the effects of changes in composition, temperature, and oxygen pressure and therefore provides a powerful predictive tool that can be used in the selection of optimum process conditions in metallurgical smelting systems.

5.3.2.4.2 Cu Smelting Predominance Diagram

The application of predominance diagrams to illustrate and characterize main processes taking place in pyrometallurgical reactors has been an essential approach widely used by metallurgists and developed and introduced into the use by many scientists; the contribution of Yazawa [132] is particularly important in this area. Following Yazawa's [132] approach, parts of the predominance diagram related to the main copper pyrometallurgical production steps have been predicted [133] using the new FactSage thermodynamic model of the slag phase [126] along with the model for matte and Cu metal models taken from the FactSage public database [134] (see Figure 5.3.70). The set of constant total pressure (sum of the partial pressures of the O- and S-containing gaseous species) solid lines

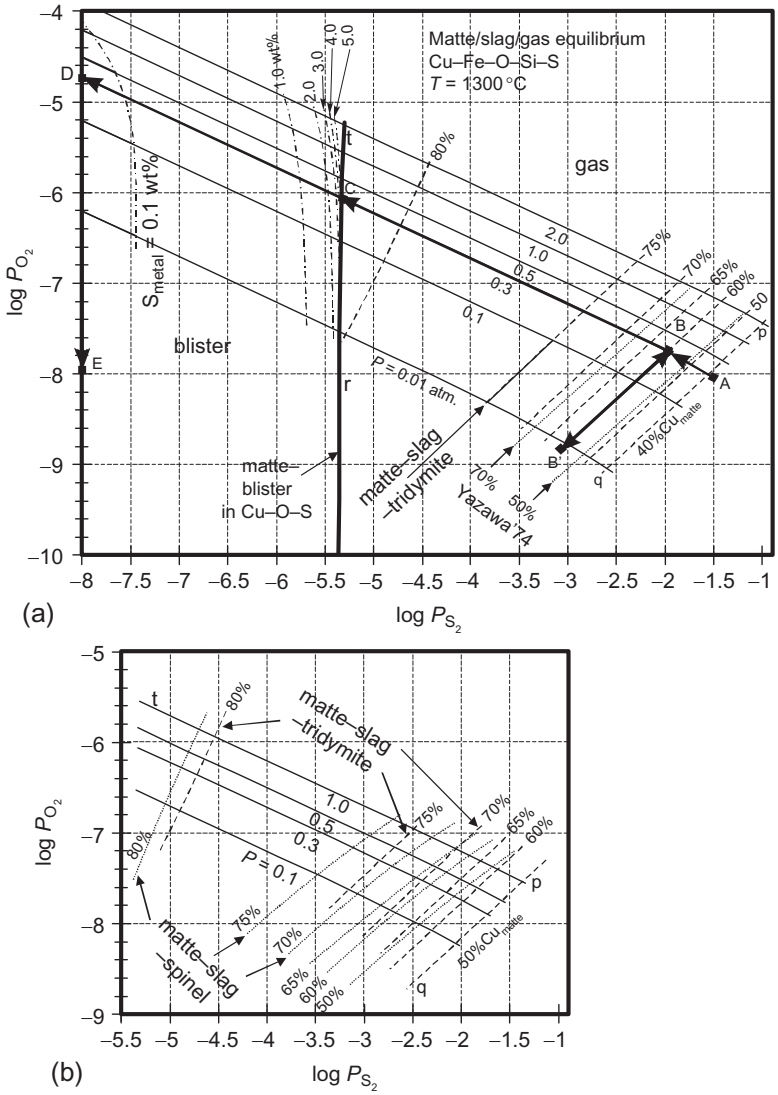


Figure 5.3.70 (a) S–O predominance diagram for the system Cu–Fe–Si–O–S calculated with FactSage using new slag model [126] for 1573 K (1300 °C). (b) Effect of the change in Fe/SiO_2 in slag between the tridymite and spinel liquidus [133].

(parallel to the lines p–t for $P_{total} = 1$ atm. and A–D for $P_{total} = 0.3$ atm.) is close to the conventional constant P_{SO_2} lines. The set of constant matte grade dashed lines (parallel to the lines q–p for 40 wt% Cu and B′B for 60 wt% Cu matte) were predicted for the equilibrium with tridymite. The corresponding positions of the 50 and 70 wt% Cu matte grade dotted lines reported by Yazawa [132] are given for comparison.

The phase field boundary r–t (see Figure 5.3.70) corresponding to the equilibrium between gas, white metal, and blister, as well as the set of dash–dot lines for fixed sulfur concentrations in the blister are predicted for the Fe-free Cu–O–S system. The main copper production path ABB′BCDE is indicated here for the $P_{\text{total}} = 0.3$ atm., which approximately corresponds to 50% oxygen enrichment—details are discussed in Figure 5.3.70. Tables 5.3.7 and 5.3.8 summarize the conditions for some lines and some production steps in the "Yazawa" predominance diagram (Figure 5.3.70).

The thermodynamic model [126] was used to further investigate the behavior of the system and to predict important trends. For example, predicted effect of the higher Fe/SiO_2 slag ratio corresponding to the equilibrium with the spinel (magnetite) solid phase on the location of these constant matte grade lines is illustrated in Figure 5.3.70b. The increase of the Fe/SiO_2 in the slag toward equilibrium with spinel results in increase of the P_{O_2} necessary to achieve the same matte grade at a given total pressure of the O- and S-containing gaseous species.

Thermodynamic models can now be used to further investigate complex effects of some of the important operational input parameters on the key smelting process output parameters. The following examples demonstrate such thermochemistry analyses.

The predicted effect of the total pressure, temperature, primary phase (actually Fe/SiO_2 in the slag), and common impurities including CaO, Al_2O_3, and MgO on the Cu chemically dissolved in slag phase and on the equilibrium P_{O_2} and Fe/SiO_2 in slag as a function of equilibrium matte grade is illustrated in Figure 5.3.71. Note that the maximum total pressure of the O- and S-containing gaseous species of 2 atm. is selected for this analysis, reflecting possible conditions generated by hydrostatic pressure of the matte and slag liquid layers.

Figure 5.3.71a demonstrates that the increase of the total pressure for a given matte grade affects the P_{O_2} and does not affect the Cu solubility in the slag. The Cu solubility increases with the increase of matte grade. The trend of the Fe/SiO_2 in the slag ion equilibrium with tridymite as well as with the gas and matte phases is shown in the top part of Figure 5.3.71a, as well as corresponding top parts of Figure 5.3.71b–d.

An increase in process temperature (see Figure 5.3.71b) results in a small increase of the Cu dissolved in slag—this is a cumulative effect of the changing P_{O_2} and the Fe/SiO_2 in the slag in equilibrium with the tridymite phase.

The effect of the slag chemistry—the Fe/SiO_2 change from the tridymite to spinel equilibria—is predicted to result in the increase of the Cu solubility in slag. This trend may be related to the reaction $Cu_2S + FeO \leftrightarrow Cu_2O + FeS$ and $K_{\text{eq}} = \frac{a_{Cu_2O} a_{FeS}}{a_{Cu_2S} a_{FeO}}$ so that $a_{Cu_2O} = \frac{K_{\text{eq}} a_{Cu_2S}}{a_{FeS}} \times a_{FeO}$, where the first term of the product $\frac{K_{\text{eq}} a_{Cu_2S}}{a_{FeS}}$ is approximately constant for a given matte grade, and a_{FeO} increases with Fe/SiO_2 ratio in slag.

The effect of CaO, Al_2O_3, and MgO impurities is illustrated in Figure 5.3.71d, where Al_2O_3 and MgO are predicted to decrease the Fe/SiO_2 in slag in equilibrium with tridymite, but to have insignificant effects on the Cu solubility in slag. The increase of

Table 5.3.7 Reactions and Corresponding Conditions for Specific Lines in the Predominance Diagram (Figure 5.3.70)

Equilibria	Reactions	Equilibrium Constant	Equation for the Line
Matte–slag p–q	$FeS(l) + 1/2O_2(g) = FeO(l) + 1/2S_2(g)$	$K_{eq} = \frac{P_{S_2}^{1/2} a_{FeO}}{P_{O_2}^{1/2} a_{FeS}}$	At fixed %Cu in matte: $\log P_{O_2} = \log P_{S_2} + \text{constant}$
Matte–gas t–p	$1/2S_2 + O_2 = SO_2$	$K_{eq} = \frac{P_{SO_2}}{P_{O_2} P_{S_2}^{1/2}}$	For a constant P_{SO_2} $\log P_{O_2} = \text{const} - 1/2 \log P_{S_2}$
Matte–blister r–s	$Cu_2S_{liq} = 2Cu_{blister} + x\underline{S}_{blister} + 1/2(1-x)S_2$	$K_{eq} = \frac{a_{Cu,blister}^2 a_{S,blister}^x P_{S_2}^{(1-x)/2}}{a_{Cu_2S}}$	
Blister–as C–D	$S_{blister} + O_2 = SO_2$		
Blister–gas D–E	$O_{blister} + CO = CO_2$		

Table 5.3.8 Reactions During Copper Production (Figure 5.3.70)

Production Step	Reaction
A → B—Smelting	$2CuFeS_2(concentrate) + (4 - 1.5\gamma)O_2(g) + xSiO_2(s) \rightarrow \{Cu_2S + \gamma FeS(l,matte)\} + \{(2-\gamma)FeO + xSiO_2(l,slag)\} + (3-\gamma)SO_2(g)$
B → B′—Slag/matte separation	$O_{condensed}$ in matte, sulfates, oxides, slag (e.g., Fe_2O_3, Cu_2O, $CuSO_4$) $O_{condensed} + S_{matte} + Fe_{matte} + xSiO_{2(s)} \rightarrow FeO–xSiO_2(l) + 3/2SO_{2(g)}$
B → C—Converting 1. Slag blow from matte to white metal	$1.\ FeS(l) + 1.5O_2(g) + xSiO_2(s) \rightarrow FeO–xSiO_2(l) + SO_2(g)$
B → C—Converting 2. Blister blow	$2.\ Cu_2S(l) + O_2(g) \rightarrow 2Cu(l) + SO_2(g)$
C → D—Refining: S blow–oxidation (S, removal, gas/liquid)	$1.\ S(in\ Cu) + O_2(g) \rightarrow SO_2(g)$
D → E—Refining: O blow–reduction (O removal, gas/liquid)	$2.\ O(in\ Cu) + CH_4 \rightarrow CO/H_2O(g)$
Side reaction—oxidation of Cu into slag	$2Cu(l, metal/matte) + 0.5O_2(g) \rightarrow Cu_2O(slag)$

CaO in slag by 1 wt% is predicted to decrease the Fe/SiO_2 in slag in equilibrium with tridymite and also results in some decrease of the Cu dissolved in slag at a given matte grade.

The effect of Fe/SiO_2 (in the range between the equilibrium with tridymite and with spinel) on the chemically dissolved Cu in slag and on the equilibrium P_{O2} predicted with the current thermodynamic databases for given temperatures, matte grades, and total pressures is illustrated in Figure 5.3.72. In general, the figure demonstrates that the Fe/SiO_2 in the slag in equilibrium with the matte having 55–60 wt% Cu has relatively small effect on the Cu solubility in the slag.

Note that the proportion of Cu dissolved in slag in the form of Cu_2S is predicted to be negligible.

These predictions of the key input and output operational parameters are given here to illustrate the opportunities for advanced analysis created by the integrated research program that involves a combination of experimental studies and computer thermodynamic modeling.

5.3.2.4.3 Mass and Energy Balance Predictions

The use of the advanced experimental and thermodynamic modeling research tools has enabled a high cumulative level of information on the thermochemistry and phase

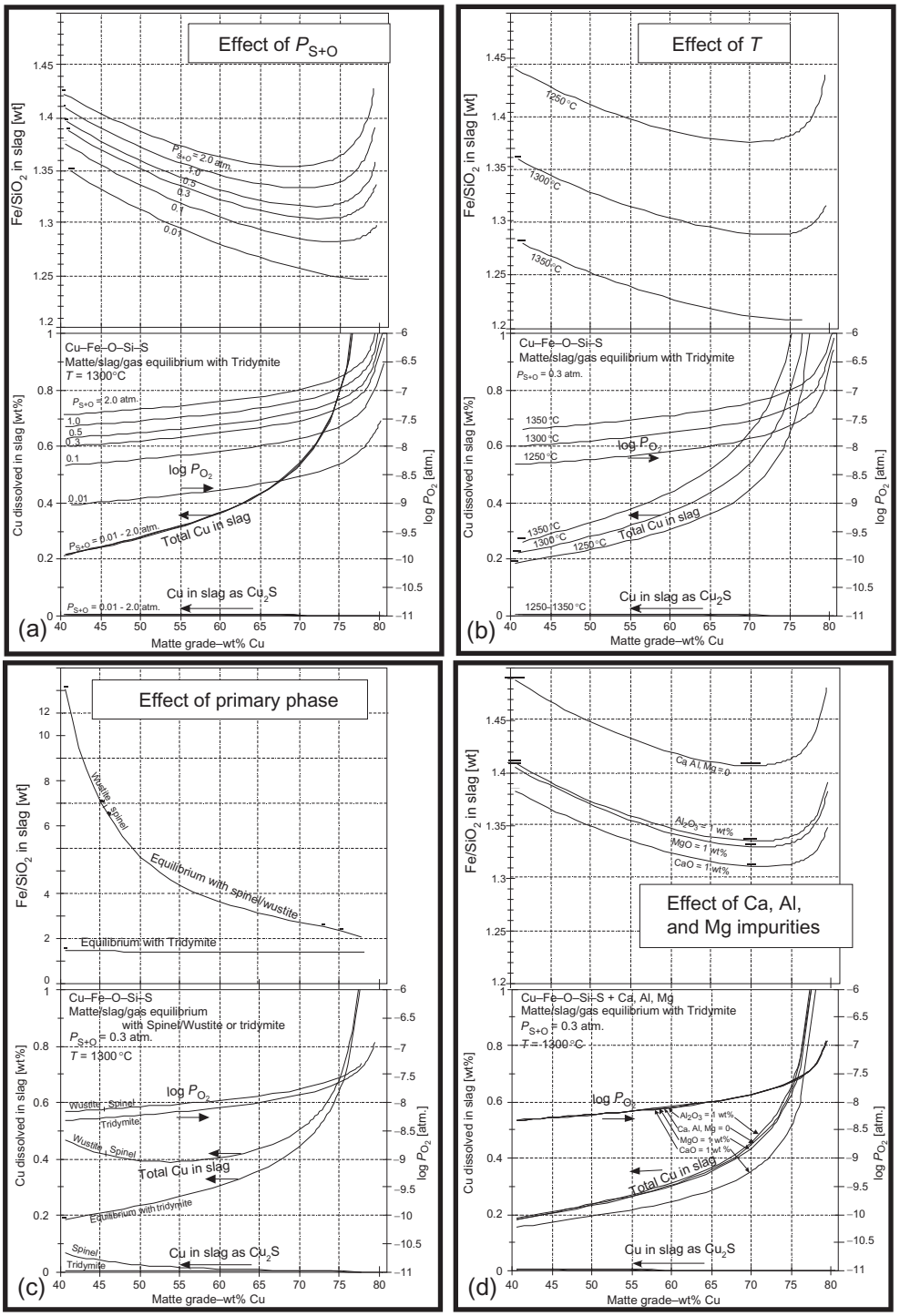


Figure 5.3.71 Sensitivity analysis [133] of key smelting process output parameters including chemically dissolved Cu in slag, P_{O_2}, and Fe/SiO_2 in slag in equilibrium with tridymite or spinel, on important input parameters (including (a) total pressure = oxygen enrichment, (b) temperature, (c) primary phase = Fe/SiO_2 in slag, and (d) CaO, Al_2O_3, and MgO impurities) for the Cu smelting predicted with FactSage using new slag model [126].

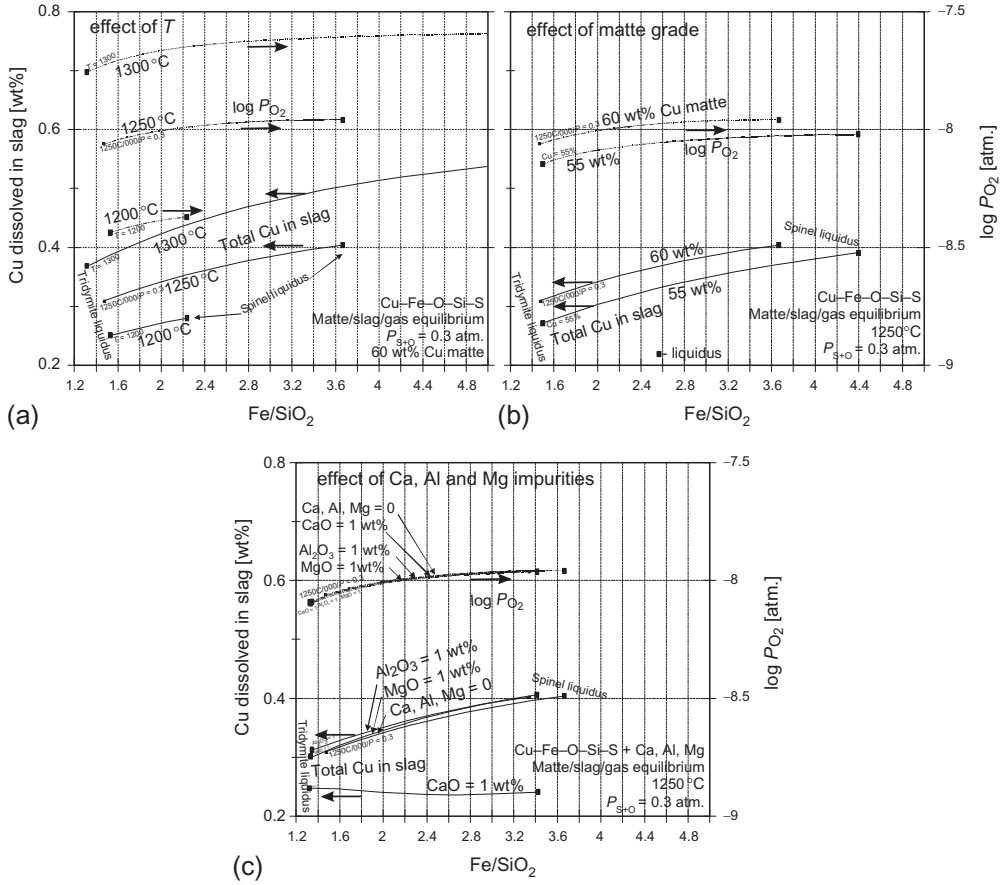


Figure 5.3.72 The effects of the Fe/SiO_2 ratio (in the range between equilibrium with tridymite and with spinel) on the chemically dissolved Cu in slag and on the equilibrium P_{O_2} predicted with the current thermodynamic databases for the matte + slag + gas equilibria at given temperatures, matte grades, and total pressures [133].

equilibria of the copper smelting systems and with it improved understanding of reactions and processes to be achieved. These tools can be used in a different way. For example, they can be involved in identification of priorities of optimization of the operations—the search for the most efficient direction in improvements of the industrial operations can be assisted using thermodynamic modeling. For this purpose, a simplified one-step reactor thermodynamic model of the Flash Smelting Furnace was assembled and used for the analysis. Figure 5.3.73 illustrates simplified schematic of this one-step reactor model. Main input and output parameters are given in Table 5.3.9. The one-step reactor model incorporates concentrate, coal, flux, as well as air and oxygen blast as an input.

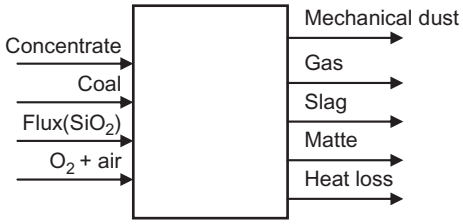


Figure 5.3.73 One-step reactor model for copper smelting.

Table 5.3.9 Flash Smelting Furnace Thermodynamic Modeling [133]

	Parameter	Changed Parameter				
		Base	Fe/SiO_2	*T*	Heat Losses	Entrained Cu
1	Value of the change	0	+0.4	+10°K	+0.5MW	−0.1%
2	Total feed (t/h)	100.0	100.0	100.0	100.000	100.000
3	Concentrate feed (t/h)	87.389	89.917	87.317	87.460	87.389
4	O_2 efficiency	1.000	1.000	1.000	1.000	1.000
5	%Mechanical (physical) dust carryover	4.500	4.500	4.500	4.500	4.500
6	Dust added to the fresh feed (t/t)	0.0450	0.0450	0.0450	0.0450	0.0450
7	%O_2 enrichment	50.00	50.00	50.00	50.00	50.00
8	%Cu in matte	60.00	60.00	60.00	60.00	60.00
9	Availability of furnace	0.9	0.9	0.9	0.9	0.9
10	Coal added to the feed (t/t feed)	0.0057	0.0022	0.0065	0.0049	0.0057
11	Enriched air (Nm^3/h)	33,251	33,223	33,457	32,986	33,251
12	SiO_2 flux added to the concentrate (t/t conc.)	0.1378	0.1096	0.1378	0.1378	0.1378
13	Fe/SiO_2 in the slag	1.60	**2.00**	1.60	1.60	1.60
14	*T* (°K (°C))	1523 (1250)	1523 (1250)	**1533 (1260)**	1523 (1250)	1523 (1250)
15	Heat losses (MW)	−11.11	−11.11	−11.11	**−10.61**	−11.11
16	log P_{O_2}	−7.96	−7.91	−7.89	−7.96	−7.96
17	P_{SO_2}	0.40	0.42	0.40	0.41	0.40
18	Generation of slag kg/h	36,245	34,920	36,214	36,271	36,245
19	%Cu chemically dissolved in slag	0.32	0.35	0.34	0.32	0.32

Continued

Table 5.3.9 Flash Smelting Furnace Thermodynamic Modeling [133]—cont'd

	Parameter	Changed Parameter				
		Base	Fe/SiO_2	*T*	Heat Losses	Entrained Cu
20	%Cu physically entrained in slag (assumed)	0.50	0.50	0.50	0.50	**0.4**
21	Cu in slag (t/year)	2350	2350	2386	2352	2065
22	Saved Cu compared to the base (t/year)	0	−64	37	0	−286
23	Total Cu production (t/year)	234,380	240,859	234,183	234,540	234,666
24	Variation of the Cu production compared to the base case (t/year)	0	6479	−197	160	+266
25	Saved Cu compared to the base (% from production)	0	−0.03	+0.015	0	−0.12
26	Energy variation primary–electrowinning refining (GJ/year)[a]	0	−7423	4292	−4	−32,916
27	Coal used (t/year)	4479	1765	5136	3840	4479
28	Coal used (t/t copper produced)	0.0191	0.0073	0.0219	0.0164	0.0191
29	Variation of coal (t/year) (<0 = saving)	0	−2839	661	−643	−5
30	Variation of CO_2 (t/year) (<0 = saving)	0	−10,409	2423	−2356	−20
31	Variation of energy at 24 MJ/kg coal (GJ/year) (<0 = saving)	0	−68,130	15,856	−15,421	−131
32	Variations of wind mills (at 14,191 GJ/year per mill[b]) (<0 = saving)	0	−5.3	1.4	−1.1	−2.3

[a]Total energy for primary Cu (GJ/t) = 116; energy used for electrorefinery of Cu (GJ/t) = 0.81; energy variation (primary–electrowinning refining) (GJ/t) = 115.
[b]Wind mill year production 1.5 MW at 30% capacity (GJ/year) = 14,191 GJ/year.

A certain proportion of the solid feed is assumed to be physically carried over as a mechanical dust after oxidation in the gas to corresponding sulfates and oxides states. Oxygen efficiency was assumed to be 100% for analysis purposes only (with full understanding this may not be the case; however, the fact that no ingress of air due to the negative draft pressure was introduced may offset this). The materials remaining after the mechanical dust carry over, and corresponding reactions of gas with the dust is assumed to reach equilibrium producing gas, matte, and slag. The total feed of 100 t/h of chalcopyrite with 50 vol% oxygen enrichment producing 60 wt% Cu matte and $Fe/SiO_2 = 1.6$ slag was taken as the base case (some data are taken from the example given

by Davenport [135]). The addition of SiO_2 flux, coal, and air was used to adjust the output to a targeted matte grade, Fe/SiO_2 in slag, and temperature at a given heat loss (40,000 MJ/h = 11.11 MW per 100 t/h feed rate [135]). Several variants were predicted starting from the base case, then increasing Fe/SiO_2 in slag, increasing temperature by 10°K, decreasing heat losses (this may be also viewed as adding enthalpy though air preheat or other measures), and decreasing Cu entrained in slag. Most of the predicted input and output values are listed in Table 5.3.9 and are self-explanatory. The concentration of Cu chemically dissolved in slag (row 19) is predicted with the thermodynamic model, and the concentration of Cu physically entrained in slag (row 20) was assumed to be 0.5 wt% for analysis purpose. The total Cu lost into the smelting slag and comparison of Cu losses to the base case are given in rows 21 and 22, respectively. The corresponding Cu production and comparison relative to the base case are given in rows 23 and 24, respectively. The energy saving or consumption due to the Cu lost into slag given in row 26 (no further flotation or other slag cleaning was assumed) is evaluated using the values on total energy for primary Cu production less energy for electrorefining taken from Hayes [136]. The total coal used, coal per 1 t of Cu produced and corresponding saved coal, and saved CO_2 emissions are given in rows 27 through 30, respectively. Note that the variation in coal use given in row 29 is related to the Cu produced. The corresponding energy saved was evaluated assuming calorific value of coal used in electric stations to be 24 MJ/kg coal. The number of the 1.5 MW wind mills at 30% capacity equivalent to the energy savings compared to the base case is given in row 32.

Results clearly indicate that relatively modest adjustments and optimization of operational practices can give significant increase of the Cu production and significantly decreased use of energy and CO_2 footprint. This analysis also demonstrates how the selection of priorities in optimization of the operations can be assisted with advanced theoretical tools. The important advantage of this approach to the modeling of the metallurgical reactors is the fact that the mass and energy balance is predicted together with partitioning of the major and minor elements between phases. Chemical reactions and the final phase compositions predicted using complex thermodynamic models of the multicomponent solution phases. The demonstrated approach therefore is superior compared to the common solution of the heat and mass balance based on the use of spreadsheets with fixed partition coefficients.

A one-step reactor approaching equilibrium outlined in the previous section is a common first approximation of some pyrometallurgical processes. Any process, however, represents a combination of areas with different reactions and different conditions in various parts (or locations) of the reactor. The optimization of any process requires identification of a limiting condition—the "bottle neck" that restricts possible changes of input parameters. This "bottle neck" would appear in one particular location of a reactor with a specific reaction and a condition that can differ from other locations and from the average condition. The one-step reactor approximation assumes the average condition over the

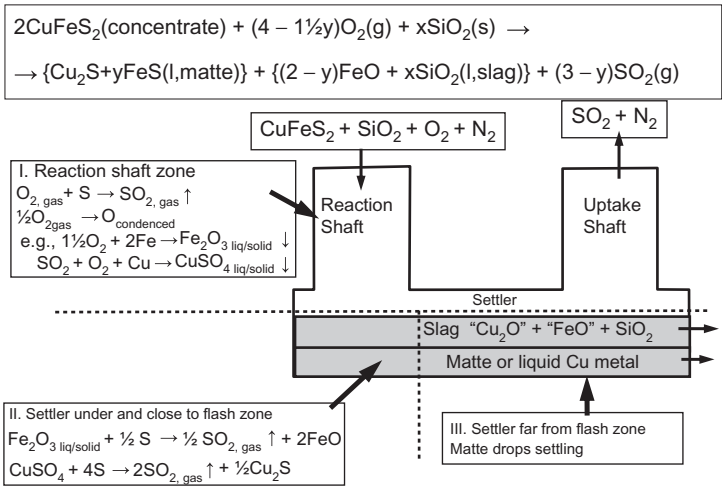


Figure 5.3.74 Schematic of the Cu Flash Smelting Furnace [133].

whole reactor, and this is clearly an oversimplification. Analysis of the reactions taking place in different locations in the furnace with the purpose to identify the limiting condition (so-called bottle neck) represents the next essential step of process optimization; and an example of such an analysis of difference in conditions in various locations in a reactor is given in this section. Important factor is that this analysis must be accompanied by the experimental and analytical supporting research.

Different reactions taking place in different locations in a Flash Smelting Furnace are illustrated in Figure 5.3.74. The flash smelter may be viewed as a three-stage reactor: *I. Reaction shaft*: The oxidation takes place in the reaction shaft. Part of the feed (surface of larger particles and whole small particles) is overoxidized so that the excess of oxygen in the condensed form is produced (e.g., ferric iron Fe_2O_3, CuO, Cu_2O, $CuSO_4$, etc.), and at the same time, the core of larger particles may remain unreacted due to kinetic limitations and stay underoxidized (e.g., FeS, Cu_2S, etc.). The over- and underoxidized particles do not practically react with each other in the reaction shaft due to the low chances of coalescence and relatively slow diffusion of main reactants through the gas phase. *II. Settler under reaction shaft*: After most of the material from the reaction shaft (including over- and underoxidized particles) is plunged into the bath underneath the reaction shaft, all particles are forced in direct contact together resulting in establishing condensed phase interactions, reactions, convective and diffusive mass transfer, etc. The condensed oxygen from the overoxidized particles will react with underoxidized material including unreacted sulfides, thus producing SO_2 gas. A description of some of these reactions and further references can be found in Taskinen [137]. *III. Settler far from reaction shaft*: After most of the oxidation/reduction reactions are completed in the settler area close to the reaction shaft, decantation of the matte droplets from the slag layer may take place

in the rest of the settler. Some further particles may still fall down onto the slag from the gas area above the settler and, some further reactions may take place between the gas and slag phases and further down in the bath—occurrence and extent of those are expected to be significantly less important than the reactions in and underneath the reaction shaft, and the former are yet to be identified; if significant, then four or more stages would have to be introduced into analysis of the flash smelter in order to identify specific conditions deviating from the average over the reactor, and therefore particular locations in the reactor that could determine the limit for a possible optimization of the process (a "bottle neck").

The improved level of knowledge as well as the advanced level of the research tools now provides new opportunities in detailed and quantitative investigation of the complex reactions, taking place in the industrial furnaces; this can greatly assist in the identification of the limits in optimization of the processes, help to understand the reasons for some operation instability, and therefore increase availability and decrease costs of the operations.

5.3.2.4.4 Modeling Zinc-Fuming Process

The following section describes an example of application of thermodynamic modeling of the zinc-fuming process [138]. Extensive plant data have been collected at Pasminco Port Pirie plant during operation of the zinc-fuming process [139–141]. The data reported by Grant [139] for charge 198 are summarized in Table 5.3.10. In brief, the plant dataset [139] includes temperature and slag composition measurements taken at 10 min intervals starting after all the slag had been charged (at 59th minute for charge 198 [139]); complete specification and charging rates of the coal as well as of the primary and secondary air used in the process (see Table 5.3.10). The FactSage computer package with the new thermodynamic database was used to predict the fuming as a function of the process time. The initial slag charge and the process conditions data specified by Grant [139] were used as an input. The following assumptions were made (similar to the assumptions accepted by Grant [139]):

- whole slag charge participates in the reaction (effect of the slag frozen on the furnace jackets is neglected),
- air, coal, and slag achieve equilibrium at any given moment, and
- equilibrated gas is removed from the reactor and this gas does not participate in any further reaction.

Only gas/liquid slag equilibrium was considered during the FactSage modeling. A time increment of 1 min was selected for each iteration. The amounts of the air and coal added per each time step (one minute) were calculated from the data reported by Grant [139] (see Table 5.3.10). Coal and air charged during each time interval were assumed to reach equilibrium with the slag. At each time step, the resulting equilibrium gas was excluded from further reaction, and the resulting slag mass and composition were used as input for

Table 5.3.10 Measured Data and Process Conditions in Zinc-Fuming Plant Trial [139]

Plant Data for Charge 198 [139]

Time (Min)	Bath T (°C)	ZnO (wt%)	PbO	FeO	Fe_3O_4	SiO_2	MgO	CaO	Al_2O_3	S	Total
59	1195	14.6	0.101	24.5	2.90	25.6	5.2	15.2	7.6	0.60	96.3
68	1190	13.5	0.043	23.6	4.08	25.8	5.2	15.6	7.6	0.64	96.1
78	1200	11.4	0.022	24.0	4.94	26.8	5.7	16.0	6.6	0.64	96.1
88	1200	9.9	0.009	25.3	3.54	27.0	5.7	16.2	7.6	0.45	95.7
99	1210	7.8	0.009	25.3	4.30	28.1	5.6	16.7	7.9	0.64	96.3
109	1215	6.2	0.009	26.1	4.30	28.4	5.9	16.9	7.6	0.68	96.1
119	1230	4.8	0.022	27.5	3.33	29.2	5.8	17.5	7.5	0.64	96.3
129	1240	3.1	0.009	26.6	4.62	29.6	6.1	17.7	7.7	0.70	96.1
140	1250	2.4	0.013	26.4	4.94	30.0	6.1	17.7	7.7	0.66	95.9

Coal Data–Coal Rate = 57.7 kg/min

C	O	H	N	S	Ash	FeO	CaO	SiO_2	Al_2O_3	MgO	H_2O
(wt% on Dry Basis)						(wt% of Ash)					(wt% Wet Basis)
72.3	4.02	3.85	0.93	0.3	18.6	52.69	3.76	2.69	34.41	6.45	2.66

Air Input

	Rate (m^3/min)	*T* (°C)	*P* (Torr)	H_2O (Torr)
Primary	4.96	28.3	758	10.9
Secondary	260.51	28.3	758	10.9

Coal and Air Weight Input per Minute (kg/min)

Total Coal + Air	C	O	H	N	S	FeO	CaO	SiO_2	Al_2O_3	MgO
365.0	40.607	77.014	2.645	234.112	0.168	5.504	0.393	0.281	3.595	0.674

Initial Slag Charge (kg)

Total Slag	ZnO	PbO	FeO	Fe_3O_4	SiO_2	MgO	CaO	Al_2O_3	S
45,320	6870.9	47.5	11529.9	1364.8	12047.6	2447.2	7153.2	3576.6	282.4

the next step in the iterative calculation with the new "fresh" addition of the coal and air. The temperature during the process was entered for each time step according to those measured during the plant trial (see Table 5.3.10). The FactSage output (composition and weight of the gas and slag phases) was recorded, analyzed, recalculated to the same

basis, and compared to the plant data. A comparison of the model predictions with the plant measurements is given in Table 5.3.11, these data are plotted in Figure 5.3.75 [138].

Excellent agreement between model predictions and plant measurements can be seen in Table 5.3.11 and Figure 5.3.75. As zinc and lead are fumed off from the slag and coal mineral matter is incorporated into the molten bath, the contents of all elements but Zn and Pb gradually increase, whereas the zinc and lead contents decrease. The predicted and measured values for almost all elements agree to within 1 wt pct. The slight deviation of the aluminum content may be attributed to the coal ash variability (note that Al_2O_3 is one of the major components of the coal ash, and ash content was taken constant during the process). The difference between actual (measured) and equilibrium (predicted) zinc contents of the slag is within 1 wt pct—this difference may be attributed to the inherent uncertainties of the assumptions, measurements, and predictions. From this comparison, it may be concluded that, provided all assumptions are correct, the process is principally controlled by the equilibrium considerations.

The predicted zinc concentrations, however, are slightly lower than the measured values, and the difference between measured and predicted Zn contents systematically increases with time (and, consequently, with the decrease of the total zinc in slag).

The difference between measured and equilibrium (calculated) zinc concentration relative to the equilibrium Zn concentration in slag (in pct) as a function of time are presented in Figure 5.3.76. From the data, it could be concluded that at earlier stages of the process (and therefore at higher Zn concentrations) the Zn-fuming process is principally equilibrium controlled. As Zn fuming progresses and reaches lower Zn concentrations in the slag, the gap between the actual (measured) and equilibrium (predicted) concentrations becomes significant and the reaction becomes increasingly limited by kinetic factors.

It is important to stress that these conclusions depend on the accepted assumptions, accuracy of measurements, and reliability of predictions.

While the conditions favorable for zinc fuming are widely recognized in general terms, providing accurate quantitative predictions of the optimum conditions has been limited by the absence of adequate thermodynamic information, particularly on the activity coefficient of zinc oxide in the slags. The new FactSage model clearly provides this capability, and enables the limiting case from a thermodynamic viewpoint, to be firmly established. The new FactSage model will enable more accurate process models to be developed to describe zinc-fuming operation and, for processes which are rate limited, will enable the maximum rates which can be attained to be accurately established.

5.3.2.5. Concluding Statement

Using the advanced thermodynamic databases and computer software packages, it is now possible to describe the complex multicomponent, multiphase systems that are

Table 5.3.11 Comparison of the F*A*C*T Predictions [138] with the Plant Measurements

Time	Bath *T*	Elemental Slag Plant Data [139] Normalized to 100%									Elemental Slag Data Predicted by FactSage								
min	°C	Zn wt%	Pb	Fe	Si	Mg	Ca	Al	O	S	Zn wt%	Pb	Fe	Si	Mg	Ca	Al	O	S
59	1195	12.2	0.10	22.0	12.4	3.3	11.3	4.2	34.0	0.62									
68	1190	11.3	0.04	22.2	12.6	3.3	11.6	4.2	34.2	0.67	11.3	0.01	22.4	12.6	3.3	11.5	4.3	34.0	0.59
78	1200	9.5	0.02	23.1	13.0	3.6	11.9	3.6	34.5	0.67	9.5	0.00	23.0	12.9	3.4	11.7	4.4	34.3	0.61
88	1200	8.3	0.01	23.2	13.2	3.6	12.1	4.2	34.9	0.47	7.8	0.00	23.6	13.2	3.5	12.0	4.6	34.7	0.62
99	1210	6.5	0.01	23.6	13.6	3.5	12.4	4.3	35.3	0.66	6.0	0.00	24.2	13.5	3.6	12.3	4.7	35.0	0.63
109	1215	5.2	0.01	24.4	13.8	3.7	12.6	4.2	35.5	0.71	4.5	0.00	24.8	13.7	3.6	12.5	4.8	35.3	0.64
119	1230	4.0	0.02	24.7	14.2	3.6	13.0	4.1	35.7	0.66	3.2	0.00	25.3	14.0	3.7	12.7	5.0	35.6	0.64
129	1240	2.6	0.01	25.0	14.4	3.8	13.2	4.2	36.1	0.73	2.0	0.00	25.7	14.1	3.8	12.9	5.1	35.8	0.65
140	1250	2.0	0.01	25.1	14.6	3.8	13.2	4.2	36.3	0.69	1.0	0.00	26.0	14.3	3.8	13.0	5.2	36.0	0.65

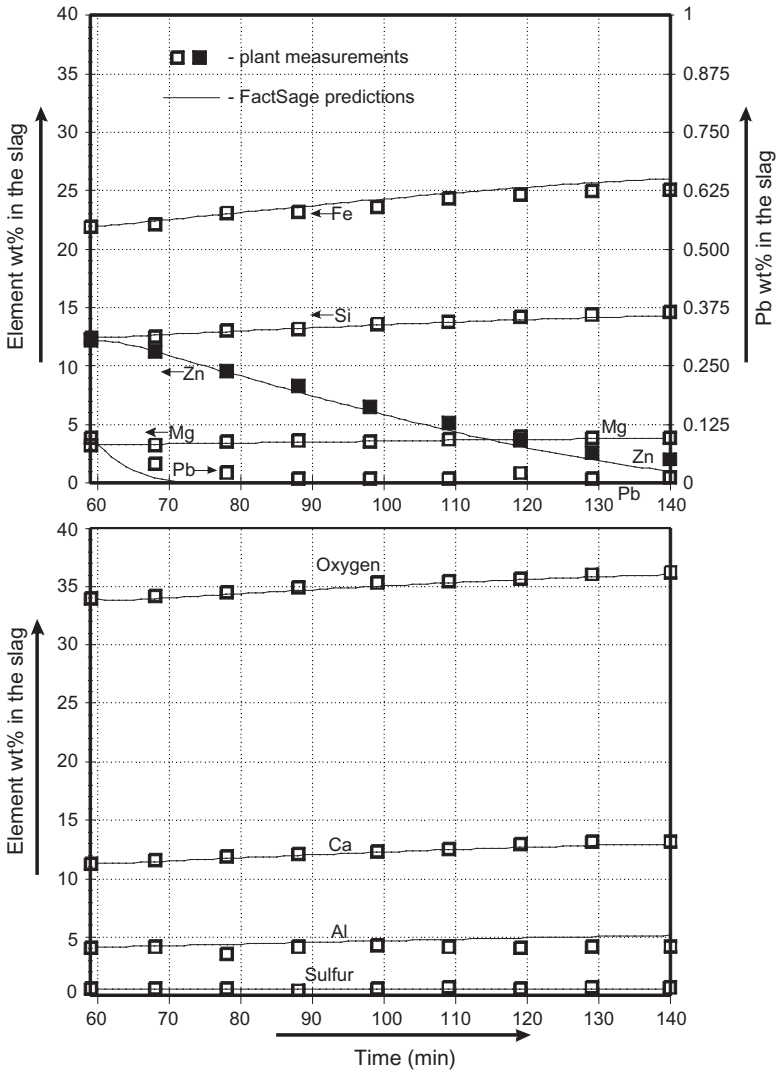


Figure 5.3.75 Comparison between FactSage predictions [138] (equilibrium assumption) and plant measurements [139].

commonly encountered in nonferrous smelting systems. The existing databases provide adequate descriptions of the major chemical components in these systems, although the models are not yet optimized for the whole range of elements, compositions, and conditions. Since these pyrometallurgical smelting systems approach equilibrium, these tools are particularly useful for (a) exploring phase equilibria for compositions that are not easily measurable, (b) providing trend analysis to determine the relative influences of process variables, and hence (c) identifying optimum process conditions.

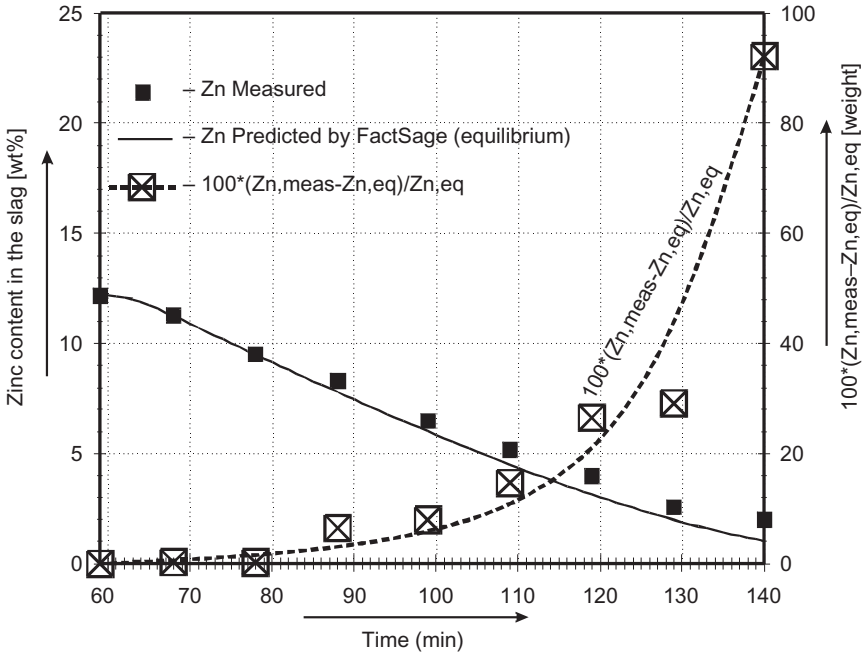


Figure 5.3.76 Comparison of the actual (measured [139]) and equilibrium (predicted with FactSage) Zn content—an indication of the achievement of equilibrium [138].

Advanced research tools have become available. There is an opportunity now to use these powerful outcomes to improve metallurgical operations. This can only be done through implementation stage. The latter, though, requires high level of expertise and most likely can only be successful if the efforts of technologists with high level of metallurgical expertise are joined together with the experienced researchers in a close collaborative effort.

The combination of several approaches is believed to be the most efficient and promising strategy that should include the following:

(a) continuous laboratory-based fundamental and applied experimental research,
(b) theoretical modeling,
(c) plant tests and experiments, and
(d) systematic implementation program combining collaborative efforts of technologists and researchers.

New opportunities and the need for the application of accurate fundamental information on phase equilibria, thermodynamic, and physicochemical properties of the complex multicomponent systems in metallurgical and recycling industries are enhanced by (a) stronger economical competition, (b) stricter environmental regulations, and (c) advanced equipment and options in process control. Many other factors also

contribute to the need for predictive tools, including increasing complexity of ores, the number of available smelting technology options, and others. The availability of the advanced tools increases due to (a) new experimental techniques based on modern advanced analytical techniques, dramatic improvement of their capabilities and availability, and (b) new theoretical modeling approaches utilizing increased computer power.

ACKNOWLEDGMENTS

The author of Section 5.3.8 would like to acknowledge a significant direct contribution by Prof. Peter C. Hayes to many components and analysis presented in this Section 5.3.8, to discussions, and revision of the text.

REFERENCES

[1] F.O. Richardson, C.J.B. Fincham, J. Iron Steel lnst. 178 (1954) 4–14.
[2] C.J.B. Fincham, F.O. Richardson, The behaviour of sulphur in silicate and aluminate melts, Proc. R. Soc. Lond. A 223 (1954) 40–62.
[3] A. Rist, M.F. Ancey-Moret, C. Gatellier, P. Riboud, Équilibres thermodynamiques en sidérurgie, 1974, Techniques de l'ingénieur, m1730.
[4] D.J. Sosinsky, I.D. Sommerville, Metall. Trans. 17B (1986) 331–337.
[5] H. Gaye, J. Lehmann, P.V. Riboud, J. Welfringer, J. Mem. Et. Sci. Rev. Métall. 4 (1989) 237–244.
[6] M.M. Nzotta, M. Andreasson, P. Jönsson, S. Seetharaman, Scand. J. Metall. 29 (2000) 177–184.
[7] X.F. Zhang, J.M. Toguri, Can. Met. Quart. 26 (1987) 117–122.
[8] H. Flood, T. Förlan, K. Grojtheim, The Physical Chemistry of Melts, IMM, London, 1953, pp. 46–62.
[9] R.G. Reddy, M. Blander, Metall. Trans. 18B (1987) 591–596.
[10] A.D. Pelton, G. Eriksson, A. Romero-Serrano, Metall. Trans. 24B (1993) 817–825.
[11] J. Lehmann, H. Gaye, Rev. Int. Hautes Tempér. Réfract. Fr. 28 (1992–1993) 81–90.
[12] Y.B. Kang, A.D. Pelton, Metall. Trans. 40B (2009) 979–999.
[13] Le livre de l'acier, Technique et Documentation, Lavoisier, ISBN: 2-85206-981-4, 1994.
[14] P. Riboud, R. Vasse, CIT Rev. Métall. 82 (11) (1985) 801–810.
[15] M.A.T. Andersson, L.T.I. Jonsson, P.G. Jönsson, ISIJ Int. 40 (2000) 1080–1088.
[16] M.A.T. Andersson, M. Hallberg, L.T.I. Jonsson, P.G. Jönsson, Ironmaking Steelmaking 29 (3) (2002) 224–232.
[17] M.A.T. Andersson, L.T.I. Jonsson, P.G. Jönsson, in: 6th International Conference on Clean Steel, 10–12 June 2002, 2002, pp. 144–153.
[18] M. Hallberg, L.T.I. Jonsson, P.G. Jönsson, P. Undvall, Stahl u. Eisen 125 (5) (2005) 39–48.
[19] M. Al-Harbi, H.V. Atkinson, S. Gao, in: C.A. Gandin, M. Bellet (Eds.), Modeling of Casting, Welding and Advanced Solidification Processes—XI, TMS (The Minerals, Metals & Materials Society), 2006, pp. 1089–1096.
[20] M. Al-Harbi, H.V. Atkinson, S. Gao, in: 7th International Conference on Clean Steel, Balatonfüred, Hungary, 4–6 June 2007, 2007, pp. 238–245.
[21] J. Lehmann, N. Bontems, M. Simonnet, P. Gardin, in: Scanmet III, Lulea, 9-11/06/2008, 2008.
[22] Slag Atlas.
[23] Faulring, Farrell, Hilty, I&SM, 1980.
[24] Bannenberg, Harste, Bode, Scaninject 1992.
[25] D. Lu, Kinetics: Mechanisms and Modelling of Calcium Treatment of Steel, Thesis 1992.
[26] E. Förster, W. Klapdar, H. Richter, H.W. Rommerswinkel, E. Spetzler, J. Wendroff, Stahl Eisen 94 (1975) 474.
[27] K.E. Oeberg, F.J. Weiss, in: 36th EAF Conference, Toronto, December 5–8, 1978.
[28] I.-H. Jung, McGill University, Montreal, QC, Canada, unpublished research, 2012.

[29] I.-H. Jung, A.D. Pelton, in: International Symposium on Clean Steel in the Future: H.-G. Lee Symposium, Pohang, South Korea, 2012, p. 121.
[30] D. Durinck, P.T. Jones, B. Blanpain, P. Wollants, G. Mertens, J. Elsen, J. Am. Ceram. Soc. 90 (2007) 1177.
[31] J.H. Park, Comput. Coupling Phase Diagrams Thermochem. 31 (2007) 428.
[32] D. Durinck, P.T. Jones, B. Blanpain, P. Wollants, J. Am. Ceram. Soc. 91 (2008) 3342.
[33] S. Zhang, N.J. Marriott, W.E. Lee, J. Eur. Ceram. Soc. 21 (2001) 1037.
[34] C.-F. Chan, B.B. Argent, W.E. Lee, J. Am. Ceram. Soc. 81 (1998) 3177.
[35] C.-F. Chan, B.B. Argent, W.E. Lee, Comput. Coupling Phase Diagrams Thermochem. 27 (2003) 115.
[36] M.K. Cho, I.H. Jung, in: Symposium on Steelmaking Technologies—Refractories in Steelmaking. KIMM, Pohang, Korea, May 2009, 2009.
[37] S. Zhang, W.E. Lee, Int. Mater. Rev. 45 (2000) 41.
[38] W.E. Lee, S. Zhang, M. Karakus, J. Mater. Sci. 39 (2004) 6675.
[39] W.E. Lee, B.B. Argent, S. Zhang, J. Am. Ceram. Soc. 85 (2002) 2911.
[40] I.-H. Jung, S.A. Decterov, A.D. Pelton, Taikabutsu 56 (2004) 382.
[41] K. Goto, B.B. Argent, W.E. Lee, J. Am. Ceram. Soc. 80 (1997) 461.
[42] F. Melcher, V. Reiter, H. Harmuth, in: UNITECR, 2007, p. 230.
[43] S.A. Nightingale, G.A. Brooks, B.J. Monaghan, Metall. Mater. Trans. B 36B (2005) 453.
[44] V. Reiter, F. Melcher, H. Harmuth, in: UNITECR, 2007, p. 170.
[45] J.H. Park, Comput. Coupling Phase Diagrams Thermochem. 31 (2007) 149.
[46] A. Kaiser, R. Telle, M. Lober, in: UNITECR, 2007, p. 272.
[47] R. Artir, W.E. Lee, B.B. Argent, P.H. Larsen, High Temp. Mater. Sci. 34 (1995) 69.
[48] W.E. Lee, S. Zhang, Int. Mater. Rev. 44 (1999) 77.
[49] M.-A. Van Ende, M. Guo, P.T. Jones, B. Blanpain, P. Wollants, Ceram. Int. 35 (2009) 203.
[50] K. Beskow, J. Jia, C.H.P. Lupis, D. Sichen, Ironmaking Steelmaking 29 (2002) 427.
[51] K. Beskow, D. Sichen, Ironmaking Steelmaking 31 (2004) 393.
[52] K. Beskow, D. Sichen, N. Sano, Iron Steel Technol. 3 (2006) 103.
[53] J.-H. Son, I.-H. Jung, S.-M. Jung, H. Gaye, H.-G. Lee, ISIJ Int. 48 (2008) 1542.
[54] A.B. Fox, M.E. Valdez, J. Gisby, R.C. Atwood, P.D. Lee, S. Sridhar, ISIJ Int. 44 (2004) 836.
[55] C.W. Bale, E. Belisle, P. Chartrand, S.A. Decterov, G. Eriksson, K. Hack, I.H. Jung, Y.B. Kang, J. Melancon, A.D. Pelton, C. Robelin, S. Petersen, Comput. Coupling Phase Diagrams Thermochem. 33 (2009) 295.
[56] R.H. Davies, A.T. Dinsdale, J.A. Gisby, J.A.J. Robinson, S.M. Martin, Comput. Coupling Phase Diagrams Thermochem. 26 (2002) 229.
[57] I.-H. Jung, E.M.-A. Van, D.-G. Kim, in: UNITECR, Kyoto, Japan, 2011.
[58] M.-K. Cho, E.M.-A. Van, T.-H. Eun, I.-H. Jung, J. Eur. Ceram. Soc. 32 (2012) 1503.
[59] J. Lehmann, M. Boher, M.C. Kaerle, in: 2nd International Symposium on Advances in Refractories for the Metal. Industry, Montreal, Canada, 1996, p. 25.
[60] I.-H. Jung, McGill University, Montreal, Quebec, Canada, unpublished research, 2012.
[61] O. Nomura, S. Uchida, W. Lin, Shinagawa Technical Report 42 (1999) 31.
[62] W. Lin, O. Nomura, S. Uchida, CAMP-ISIJ 11 (1998) 868.
[63] P. Guillo, J. Simoes, in: Proceedings of the Third International Conference on Continuous Casting of Steel in Developing Countries, Beijing, China, 2004, 2004, p. 122.
[64] D. Xie, C. Garlick, T. Tran, ISIJ Int. 45 (2005) 175.
[65] M.-K. Cho, I.-H. Jung, ISIJ Int. 52 (2012) 1281.
[66] I.-H. Jung, S.A. Decterov, A.D. Pelton, ISIJ Int. 44 (2004) 527.
[67] I.-H. Jung, Y.-B. Kang, S.A. Decterov, A.D. Pelton, Metall. Mater. Trans. B 35B (2004) 259.
[68] Y.-B. Kang, H.-G. Lee, ISIJ Int. 44 (2004) 1006.
[69] H. Gaye, M. Faral, J. Lehmann, Rev. Metall./Cah. Inf. Tech. 100 (2003) 125.
[70] I.-H. Jung, S. Degterov, A.D. Pelton, Y.-B. Kang, H.-G. Lee, in: Proceedings of CIM Symposium, Ladle and Tundish Technology, Canadian Institute of Metallurgy, Montreal, Canada, 2002, p. 131.
[71] Y.-B. Kang, A.D. Pelton, Metall. Mater. Trans. B 40B (2009) 979.
[72] D.-H. Woo, Ph.D. Thesis, Postech, Pohang, Korea, 2010.

[73] A. Hasegawa, K. Morita, N. Sano, Tetsu to Hagane 81 (1995) 1109.
[74] H. Gaye, J. Lehmann, P. Rocabois, F. Ruby-Meyer, Steel Res. 72 (2001) 446.
[75] F. Ruby-Meyer, J. Lehmann, H. Gaye, Scand. J. Metall. 29 (2000) 206.
[76] H. Matsuura, C. Wang, G. Wen, S. Sridhar, ISIJ Int. 47 (2007) 1265.
[77] D.-C. Park, I.-H. Jung, P.C.H. Rhee, H.-G. Lee, ISIJ Int. 44 (2004) 1669.
[78] S. Basu, S.K. Choudhary, N.U. Girase, ISIJ Int. 44 (2004) 1653.
[79] I.-H. Jung, G. Eriksson, P. Wu, A. Pelton, ISIJ Int. 49 (2009) 1290.
[80] E.M.-A. Van, M. Guo, R. Dekkers, M. Burty, D.J. Van, P.T. Jones, B. Blanpain, P. Wollants, ISIJ Int. 49 (2009) 1133.
[81] D.S. Sarma, A.V. Karasev, P.G. Joensson, ISIJ Int. 49 (2009) 1063.
[82] H.S. Kim, H.-G. Lee, K.-S. Oh, Metall. Mater. Trans. A 32A (2001) 1519.
[83] C.H. Chang, I.H. Jung, S.C. Park, H.S. Kim, H.G. Lee, Ironmaking Steelmaking 32 (2005) 251.
[84] S.-C. Park, I.-H. Jung, K.-S. Oh, H.-G. Lee, ISIJ Int. 44 (2004) 1016.
[85] Y.-B. Kang, C.-H. Chang, S.-C. Park, H.-S. Kim, I.-H. Jung, H.-G. Lee, Iron Steel Technol. (10) (2006) 154.
[86] Y.-B. Kang, H.-G. Lee, ISIJ Int. 50 (2010) 501.
[87] J.H. Shim, J.S. Byun, Y.W. Cho, Y.J. Oh, J.D. Shim, D.N. Lee, Scr. Mater. 44 (2001) 49.
[88] J.H. Shim, Y.J. Oh, J.Y. Suh, Y.W. Cho, J.D. Shim, J.S. Byun, D.N. Lee, Acta Mater. 49 (2001) 2115.
[89] J.S. Byun, J.H. Shim, Y.W. Cho, D.N. Lee, Acta Mater. 51 (2003) 1593.
[90] D.E.C. Van, O. Grong, J. Walmsley, Mater. Sci. Technol. 16 (2000) 55.
[91] D.E.C. Van, Ph.D. Thesis, NTNU, Trondheim, Norway, 1999.
[92] J.O. Andersson, T. Helander, L. Hoglund, P. Shi, B. Sundman, Comput. Coupling Phase Diagrams Thermochem. 26 (2002) 273.
[93] SGTE database, www.sgte.org.
[94] A.F. Holleman, E. Wiberg, N. Wiberg, Lehrbuch der Anorganischen Chemie, 91–100, Walter de Gruyter, ISBN: 3-11-007511-3, 1985, p. 801.
[95] W.A. Deer, R.A. Howie, J. Zussman, Introduction to the Rock-Forming Minerals, second ed., Longman Group (FE) Limited, 1992.
[96] K. Verscheure, M. Van Camp, B. Blanpain, P. Wollants, P.C. Hayes, E. Jak, Metall. Mater. Trans. B Process Metall. Mater. Process. Sci. 38B (2007) 13.
[97] K. Verscheure, M. Van Camp, B. Blanpain, P. Wollants, P.C. Hayes, E. Jak, Metall. Mater. Trans. B Process Metall. Mater. Process. Sci. 38B (1) (2007) 21.
[98] A.D. Pelton, in: G. Kaiura, C. Pickles, T. Utigard, A. Vahed (Eds.), J.M. Toguri Symposium, Fundamentals of Metallurgical Processing, Ottawa, 2000, Met. Soc. CIM, Montreal, Ottawa, 2000, p. 45.
[99] M. Hillert, Phase Equilibria, Phase Diagrams, and Phase Transformations—Their Thermodynamic Basis, Cambridge University Press, 1998.
[100] E. Jak, P. Hayes, Metall. Mater. Trans. B 33B (2002) 851.
[101] E. Jak, B. Zhao, S. Nikolic, P.C. Hayes, in: International Conference on EMC2007, Dusseldorf, Germany, 2007, p. 1789.
[102] E. Jak, P.C. Hayes, A.D. Pelton, S.A. Decterov, in: 8th International Conference on Molten Slags, Fluxes and Salts, Santiago, Chile, 2009, p. 473.
[103] E. Jak, S. Degterov, B. Zhao, A.D. Pelton, P.C. Hayes, Metall. Mater. Trans. B 31B (2000) 621.
[104] C. Hassal, H. Roberts, in: Proceedings of the Zinc and Lead Processing Symposium, Calgary, Canadian Institute of Mining, Metallurgy and Petroleum, Quebec, Canada, 1998, p. 3.
[105] P.B. Queneau, S.E. James, J.P. Downey, G.M. Livelli, in: Proceedings of the Zinc and Lead Processing Symposium, Calgary, Canadian Institute of Mining, Metallurgy and Petroleum, Quebec, Canada, 1998, p. 127.
[106] C. Hassall, H. Roberts, in: A. Siegmund et al., (Ed.), International Conference on Lead-Zinc 2010, TMS (The Minerals, Metals & Materials Society), 2010, p. 17.
[107] G. Assis, in: Proceedings of the Zinc and Lead Processing Symposium, Calgary, Canadian Institute of Mining, Metallurgy and Petroleum, Quebec, Canada, 1998, p. 243.
[108] L.M. Southwick, in: Proceedings of the Zinc and Lead Processing Symposium, Calgary, Canadian Institute of Mining, Metallurgy and Petroleum, Quebec, Canada, 1998, p. 277.

[109] M. Olper, in: Proceedings of the Zinc and Lead Processing Symposium, Calgary, Canadian Institute of Mining, Metallurgy and Petroleum, Quebec, Canada, 1998, p. 545.
[110] W.D. Schneider, B. Schwab, in: Proceedings of the Zinc and Lead Processing Symposium, Calgary, Canadian Institute of Mining, Metallurgy and Petroleum, Quebec, Canada, 1998, p. 229.
[111] FactSage ver. 6.3. 2010, CRCT-Thermfact Inc & GTT-Technologies: Montreal, Canada.
[112] E. Jak, P.C. Hayes, in: International Conference on Lead-Zinc 2010, Vancouver, Canada, TMS (The Minerals, Metals & Materials Society), 2010, p. 1161.
[113] S.A. Degterov, E. Jak, P.C. Hayes, A.D. Pelton, Metall. Mater. Trans. B 32B (2001) 643.
[114] E. Jak, S.A. Degterov, A.D. Pelton, P.C. Hayes, Metall. Mater. Trans. B 32B (2001) 793.
[115] M. Kudo, E. Jak, P.C. Hayes, K. Yamaguchi, Y. Takeda, Metall. Mater. Trans. B 31B (2000) 15.
[116] E. Jak, S.A. Degterov, P.C. Hayes, A.D. Pelton, Can. Metall. Q. 37 (1) (1998) 41.
[117] E. Jak, S.A. Degterov, P. Wu, P.C. Hayes, A.D. Pelton, Metall. Mater. Trans. B 28B (1997) 1011.
[118] E. Jak, S.A. Degterov, P.C. Hayes, A.D. Pelton, in: Proceedings of the 5th International Symposium on Metallurgical Slags and Fluxes, Sydney, Iron and Steel Society, AIME, Warrendale, PA, 1997, p. 621.
[119] S. Decterov, I.H. Jung, E. Jak, P.C. Hayes, A.D. Pelton, in: 7th International Conference on Molten Slags, Fluxes and Salts, Cape Town, SAIMM, Johannesburg, South Africa, 2004, p. 839.
[120] T. Hidayat, H.M. Henao, P.C. Hayes, E. Jak, Metall. Mater. Trans. B 43B (2012) 1034.
[121] S. Nikolic, P.C. Hayes, E. Jak, Metall. Mater. Trans. B 40B (2009) 892.
[122] A. Ilyushechkin, P.C. Hayes, E. Jak, Metall. Mater. Trans. B 35B (2) (2004) 203–215.
[123] T. Hidayat, H.M. Henao, P.C. Hayes, E. Jak, Metall. Mater. Trans. B (2012), http://dx.doi.org/10.1007/s11663-012-9735-2.
[124] R.W. Ruddle, B. Taylor, A.P. Bates, Trans. Inst. Mining Metall. C 75 (1966) C1.
[125] T. Oishi, M. Kamuo, K. Ono, J. Moriyama, Metall. Mater. Trans. B 14B (1982).
[126] T. Hidayat, E. Jak, in: MOLTEN 12, The 9th International Conference on Molten Slags, Fluxes and Salts, Beijing, China, 2012, paper # 81.
[127] E. Jak, B. Zhao, P.C. Hayes, in: Presented at 6th International Conference on Slags, Fluxes and Molten Salts, Stockholm/Helsinki, June 2000, Mineral Processing and Extractive Metallurgy (TIMM C), vol. 117(3), 2008, p. 147.
[128] E.F. Muan, A. Osborne, Phase Equilibria Among Oxides in Steelmaking, Addison Wesley, 1965.
[129] Slag Atlas, second ed. Verlag Stahleisen GmbH, 1995, pp. 79–80, 126–130, 154–156.
[130] A.K. Biswas, W.G. Davenpor, Extractive Metallurgy of Copper, third ed., Pergamon, 1994.
[131] R. Sridhar, J. Toguri, S. Simeonov, Metall. Mater. Trans. B 28B (1997) 191–200.
[132] A. Yazawa, Can. Metall Q. 13 (1974) 443.
[133] E. Jak, in: MOLTEN 12, The 9th International Conference on Molten Slags, Fluxes and Salts, Beijing, China, 2012, paper # w77.
[134] S.A. Degterov, A.D. Pelton, Metall. Mater. Trans. B 30B (1999) 661–669.
[135] W.G. Davenport, D.M. Jones, M.J. King, E.H. Partelpoeg, Flash Smelting: Analysis, Control and Optimisation, The Minerals, Metals and Materials Society, TMS, 2001, p. 59.
[136] P.C. Hayes, Process Principles in Minerals and Materials Production, third ed., Hayes Publishing Co, Australia, 2003.
[137] P. Taskinen, in: L. Ragnarsson, P. Jonsson (Eds.), The Seetharaman Seminar 2010, Department of Materials Science and Engineering, Royal Institute of Technology, KTH, Sweden, 2012, pp. 110–120.
[138] E. Jak, P.C. Hayes, Phase Equilibria and Thermodynamics of Zinc Fuming Slags, Can. Metal. Q. 41 (2) (2002) 163.
[139] R.M. Grant, in: Proceedings of Australia/Japan Extractive Metallurgy Symposium, Australasian Institute of Mining and Metallurgy, Melbourne, Australia, 1980, p. 75.
[140] R.M. Grant, L.J. Barnett, Proceedings of the South Australia Conference, Australasian Institute of Mining and Metallurgy, Melbourne, Australia, 1975, p. 247.
[141] D.H. Ward, in: MINPREX 2000, International Congress on Mineral Processing and Extractive Metallurgy, AusIMM, Carlton, Victoria, Australia, 2000, p. 471.

CHAPTER 5.4

Process Modeling

Klaus Hack[a] **and Marie-Aline Van Ende**[b]
[a]GTT Technologies, Kaiserstrasse, Herzogenrath, Germany
[b]Department of Mining and Materials Engineering, McGill University, Montreal, Canada

LIST OF SYMBOLS FOR SECTION 5.4.3

A area of phase boundary
c_x, c_i concentration of component x, i
c_0 critical carbon concentration
k_x reaction rate constant
$K_{x,\mathrm{eff}}$ transport coefficient
m_{total} $m_{\mathrm{Hotspot}} + m_{\mathrm{Metal-Slag}} + m_{\mathrm{Bath}}$
m_{total} total mass flow rate through the converter
m_{Hotspot} mass flow rate through the hot spot
$m_{\mathrm{Metal-Slag}}$ mass flow rate through the metal–slag reaction zone
m_{Bath} mass flow rate through the bath
m_x mass flow rate of component x
M_x molar mass of component x
n_x molar flow rate of component x
N number of droplets
$\dot{N}$ droplet flow rate
R_x reaction rate
t' droplet residence time in the slag
V volume of droplet
[ ] dissolved in liquid iron
( ) dissolved in slag
{ } in gas phase
Δt time increment
ρ density

Treatise on Process Metallurgy, Volume 2
http://dx.doi.org/10.1016/B978-0-08-096984-8.00033-1
© 2014 Elsevier Ltd.
All rights reserved.

5.4.1. PRODUCTION OF METALLURGICAL GRADE SILICON IN AN ELECTRIC ARC FURNACE*

5.4.1.1. Summary

In this study, the thermochemistry of the production of metallurgical grade silicon in an electric arc furnace will be discussed in three calculation steps of increasing complexity, a stoichiometric reaction approach, a complex equilibrium calculation, and a steady state counter-current flow model.

5.4.1.2. Introduction

Metallurgical grade silicon is produced in an electric arc furnace. The process is shown schematically in Figure 5.4.1. Quartz, sand, and carbon are fed in appropriate proportions through the top and liquid silicon is extracted at the bottom. The temperature in the production zone is approximately 2200 K. This is achieved through an electric arc burning between a graphite electrode and the metal bath. Hot gases are produced in the bottom zone of the reactor during the formation of silicon under input of energy from the electric arc. These gases flow upward as a convective flux. On their way up, heat exchange with condensed matter falling downward takes place. To what extent can this process be understood on the grounds of equilibrium thermodynamics?

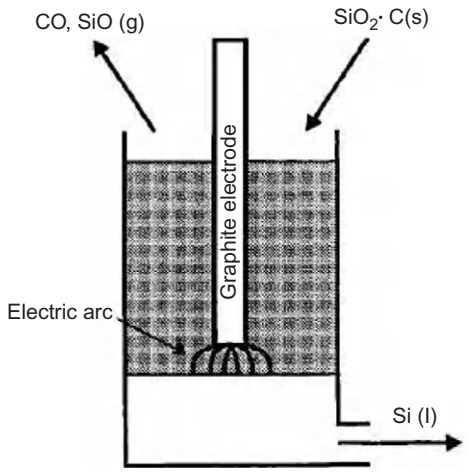


Figure 5.4.1 A schematic drawing of the silicon arc furnace.

*This chapter is a reproduction from the SGTE-Casebook with kind permission of Woodhead Publishers. Gunnar Eriksson and Klaus Hack, GTT-Technologies, Herzogenrath, Germany.

5.4.1.3. The Stoichiometric Reaction Approach

It is often claimed that the production of silicon is governed by the simple stoichiometric reaction:

$$SiO_2 + 2C = Si + 2CO\langle G\rangle \qquad 5.4.1$$

At equilibrium, the Gibbs energy change of the reaction must be zero. As all four phases can be considered as stoichiometric pure substances, the equilibrium constant is equal to unity. (The process takes place at atmospheric pressure, and CO is assumed to be the only gas species involved.) Thus the standard Gibbs energy change of the reaction must be zero too,

$$K = 1 \rightarrow \Delta G^\circ = 0 \quad \text{where } K \text{ is the equilibrium constant} \qquad 5.4.2$$

Figure 5.4.2 shows ΔG° as a function of temperature. Indeed, there is a value of T for which the curve changes sign $T \approx 1940\,K$. However, this value is far below the one known from the process. Such a difference cannot be explained by deviations from unit activities or errors in the thermodynamic data. There must be other reasons.

5.4.1.4. The Complex Equilibrium Approach

If quartz is permitted to react freely with carbon in a system with a given total pressure and temperature, a different type of calculation must be carried out. All phases possible must be considered for set values of temperature, total pressure and system composition.

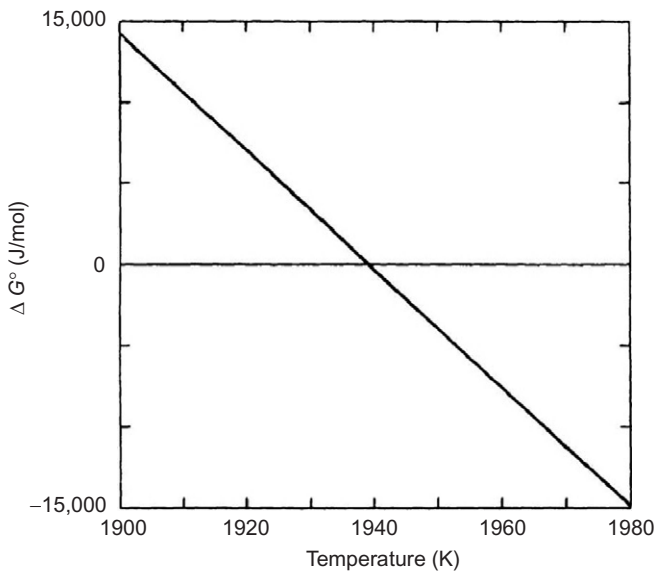


Figure 5.4.2 ΔG° for the reaction $SiO_2 + 2C = Si + 2\,CO(g)$ as a function of T.

Especially, all possible gas species have to be introduced into the calculation. A databank search reveals the following list of phases and phase components for the system Si–O–C:

Gas: $Si, Si_2, Si_3, SiO, SiO_2, C, O, O_2O_3, CO, CO_2$

Stoichiometric condensed: C (graphite), SiC, SiO_2 (quartz), SiO_2 (tridymite), SiO_2 (cristobalite), SiO_2 (liquid)

Assuming stoichiometric behavior of the reaction 1 mol of SiO_2 and 2 mol of carbon are needed as input, together with the values for the total pressure (=1 bar) and the temperature. The complex equilibrium calculation will describe a reaction

$$SiO_2(\text{quartz}) + 2C \rightarrow \eta\text{Gas} + \eta_{SiO_2(x)} SiO_2(x) + \eta_{SiC} SiC + \eta_{Si} Si \qquad 5.4.3$$

If the temperature is varied through an interval from below the value of equilibrium for the simple stoichiometric reaction (Equation 5.4.1) to a value high enough to obtain liquid silicon, the resulting yield factors can be plotted as in Figure 5.4.3. From this figure it is obvious that the gas phase in this system contains SiO as an essential species. Thus, the simple stoichiometric reaction initially given cannot be right. On the other hand, the assumption that the process can be described as a single although complex equilibrium state is also disproved. The temperature at which silicon would be produced is near 2900 K and the yield is not more than 50%. This is not in agreement with values known from the real process.

5.4.1.5. The Counter-Current Reactor Approach

In order to simulate the arc furnace as a whole, it is necessary to take into account the fact that the substances taking part in the process move in a temperature field while reacting. Cold condensed matter is fed through the top of the furnace, falling downward, and hot gases flow rapidly upward. On their way, they meet and exchange heat or even react with

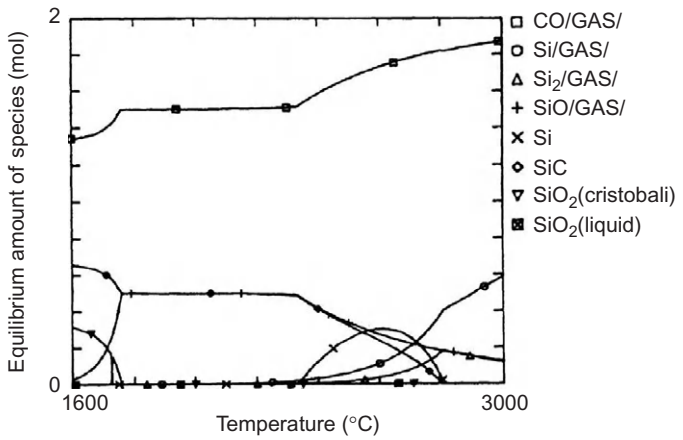


Figure 5.4.3 One-dimensional phase map for 1 mol SiO_2 + 2 mol C as a function of *T*.

each other. Thus, the local mass balances must not be identical to the overall mass-balance of the process. Additionally, the temperature at different levels of the furnace is not controlled from outside, but is mainly determined by the heat exchange and the reactions taking place. Such a complex situation can only be simulated by a thermodynamic equilibrium approach if several separate zones of local equilibrium that are interconnected by materials and heat exchange are assumed.

For the silicon arc furnace, it was found that a reactor with four stages which are controlled by the internal heat-balance is well suited for the modeling. The flow scheme, the values for the heat-balances in each stage, the input substances, their amounts, and initial temperatures as well as the distribution coefficients for the non-ideal flow between the stages are given in Figure 5.4.4. It should be emphasized that all values are the result of a series of parameter optimizations. This set of parameters represents best the process data obtained from the silicon arc furnace of KemaNord at Ljungaverk, Sweden.

Using the above flow data and a set of initial estimates of the elementary abundances in each stage derived from Figure 5.4.3, the converged solution of the reactor simulation is given by the set of Tables 5.4.1–5.4.4.

Each of the tables represents one stage of the reactor, stage 1 being the top and stage 4 the bottom stage. The tables contain information on the local equilibrium state (T, P and the phase amounts and compositions), the flow of matter between the stages (inflowing and outflowing substance amounts as well as elementary flows), and the boundary conditions (adiabatic behavior (stage 1–3) or constant enthalpy input (stage 4)).

The most important information for the derivation of a materials flow diagram of the reactor (Figure 5.4.5) is given in the column "Boundary Flow." If an ordinate is chosen, which shows in arbitrary units the width and sequence of the four stages, the calculated

	↑ Gas	
Stage 1	*DH/KJ = 0.000 ↑ T/K = 1784.12 ↓ P/bar = 1.0000	← chem. Inputs C SiO_2(quartz)
Stage 2	*DH/KJ = 0.000 ↑ T/K = 2058.82 ↓ P/bar = 1.000	
Stage 3	*DH/KJ = 0.000 ↑ T/K = 2080.17 ↓ P/bar = 1.0000	
Stage 4	*DH/KJ = 8.750×10^2 ↑ T/K = 2245.88 ↓ P/bar = 1.0000	
	* Regulated quantity ↓	Pure phases

Figure 5.4.4 Flow diagram for the silicon arc furnace.

Table 5.4.1 Converged Solution of the Reactor Simulation, Stage 1

Stage 1

$T^a = 1784.12$ K					
$P = 1.00000$ bar					
$V = 2.3002 \times 10^2$ dm^3					
	Input Amount mol		**Gas Flow mol**		**Condensed Flow mol**
C	2.8378		1.8000		1.2948
O	3.8187		2.0000		2.2679
Si	1.7810		1.9988×10^{-1}		1.7733
Gas	**Input Amount mol**	**Equil Amount mol**	**Mole Fraction mol**	**Fugacity bar**	**Flow mol**
CO	1.0377	1.5428	9.9494×10^{-1}	9.9494×10^{-1}	1.7999
SiO	7.8081×10^{-1}	7.7238×10^{-3}	4.9810×10^{-3}	4.9810×10^{-3}	1.9985×10^{-1}
CO_2	9.1223×10^{-5}	1.2212×10^{-4}	7.8751×10^{-5}	7.8751×10^{-5}	1.4525×10^{-4}
Total	1.5507	1.0000	1.0000	1.0000	
	mol	**mol**	**Activity**	**mol**	
SiO_2 (cristobali)	0.0000	1.1339	1.0000	1.1339	
C	1.8000	6.5550×10^{-1}	1.0000	6.5550×10^{-1}	
SiC	0.0000	6.3932×10^{-1}	1.0000	6.3932×10^{-1}	
SiO_2 (tridymite)	0.0000	0.0000	9.9978×10^{-1}	0.0000	
SiO_2 (liquid)	0.0000	0.0000	9.3374×10^{-1}	0.0000	
SiO_2 (quartz) T	1.0000	0.0000	9.1635×10^{-1}	0.0000	
Si	0.0000	0.0000	2.0937×10^{-2}	0.0000	

[a]The value of T was found such that it satisfies the fixed value of the heat balance.
Enthalpy of reaction = 0.0000 J; entropy of reaction = 1.1262×10^2 J K^{-1}; the cutoff limit has been specified to 1.000×10^{-5}; data on one species identified with "T" have been extrapolated.

materials flow can be marked for the up-flowing gases on the upper abscissa in each segment, and for the down-flowing condensed phases on the lower abscissa in each segment.

Thus, continuous curves are obtained which represent the total materials flow through the reactor relative to 1 mol of silica and 1.8 mol of carbon in the feed. The most important result, the silicon yield, can be read on the lowest abscissa to be 0.8 mol mol^{-1} of silica. The total elementary mass balance of the reactor (Table 5.4.5) is readily obtained from the values on the outermost abscissae.

As a mass balance with respect to phases on obtains:

$$SiO_2 + 1.8C > 0.8Si + 1.8Si + 0.8Si + 1.8CO\langle G\rangle + 0.2SiO\langle G\rangle \qquad 5.4.4$$

Note that this is not an isothermal reaction equation as silica and carbon enter the reactor at room temperature, silicon leaves the reactor at 2200 K and the gas-phase leaves at 1874 K.

Table 5.4.2 Converged Solution of the Reactor Simulation, Stage 2

Stage 2

T[a] = 2058.82 K					
P = 1.00000 bar					
$V = 3.0467 \times 10^2$ dm^3					
	Input Amount mol		**Gas Flow mol**		**Condensed Flow mol**
C	2.0703		1.2948		9.8154×10^{-1}
O	4.1050		2.2679		2.3251
Si	2.8352		9.7313×10^{-1}		2.1441
Gas	**Input Amount mol**	**Equil Amount mol**	**Mole Fraction mol**	**Fugacity bar**	**Flow mol**
CO	7.7540×10^{-1}	1.0887	3.8824×10^{-1}	6.1166×10^{-1}	1.2947
SiO	1.0616	6.9100×10^{-1}	4.9810×10^{-3}	3.8824×10^{-1}	9.7295×10^{-1}
CO_2	5.7548×10^{-5}	9.9487×10^{-5}	5.5897×10^{-5}	5.5897×10^{-5}	1.1436×10^{-4}
Si	3.1171×10^{-4}	7.3605×10^{-5}	4.1355×10^{-5}	4.1355×10^{-5}	1.6745×10^{-4}
Total		1.7798	1.0000	1.0000	
	mol	**mol**	**Activity**	**mol**	
SiO_2 (liquid)	0.0000	1.1626	1.0000	1.1626	
SiC	6.3932×10^{-1}	9.8154×10^{-1}	1.0000	9.8154×10^{-1}	
SiO_2 (cristobali)	1.1339	0.0000	9.8254×10^{-1}	0.0000	
SiO_2 (tridymite) T	0.0000	0.0000	9.8012×10^{-1}	0.0000	
SiO_2 (quartz) T	0.0000	0.0000	8.7802×10^{-1}	0.0000	
Si	0.0000	0.0000	5.0165×10^{-1}	0.0000	
C	6.5550×10^{-1}	0.0000	1.2585×10^{-1}	0.0000	

[a]The value of T was found such that it satisfies the fixed value of the heat balance.
Enthalpy of reaction = 0.0000 J; entropy of reaction = 1.3954×10^1 J K^{-1}; the cutoff limit has been specified to 1.000×10^{-5}; data on two species identified with "T" have been extrapolated.

The temperature distribution that results from the energy input in the production zone ($\Delta H = +875$ kJ/mol SiO_2) and the assumed adiabatic behavior ($\Delta H = 0$) of the three upper zones is also given in the diagram. The highest temperature is reached in the production zone. Its value (2245 K) is higher than that for which the standard Gibbs energy change of the simple reaction in the first paragraph changes sign (1940 K); but, it is also considerably lower than the value for which the single cell complex equilibrium calculation shows a maximum of the silicon yield ($\approx$2900 K).

A thermochemical understanding of the different reactions taking place at different levels within the reactor can be obtained from the materials flow between stages 3 and 4 and stages 1, 2, and 3, respectively. The reactor can obviously be split into two

Table 5.4.3 Converged Solution of the Reactor Simulation, Stage 3

Stage 3

$T^a = 2080.17$ K					
$P = 1.00000$ bar					
$V = 3.2259 \times 10^2$ dm^3					
	Input Amount mol		**Gas Flow mol**		**Condensed Flow mol**
C	1.762		9.8155×10^{-1}		9.7589×10^{-1}
O	4.1654		2.3251		2.3003
Si	3.2049		1.3440		2.1261
Gas	**Input Amount mol**	**Equil Amount mol**	**Mole Fraction mol**	**Fugacity bar**	**Flow mol**
SiO	1.0596	1.0786	5.7831×10^{-1}	5.7831×10^{-1}	1.3435
CO	7.8063×10^{-1}	7.8630×10^{-1}	4.2157×10^{-1}	4.2157×10^{-1}	9.8145×10^{-1}
Si	1.0190×10^{-3}	1.5081×10^{-4}	8.0856×10^{-5}	8.0856×10^{-5}	4.0555×10^{-4}
CO_2	3.0834×10^{-5}	6.4708×10^{-5}	3.4693×10^{-5}	3.4693×10^{-5}	7.2417×10^{-5}
Total		1.8652	1.0000	1.0000	
	mol	**mol**	**Activity**	**mol**	
SiO_2 (liquid)	1.1626	1.1502	1.0000	1.1502	
SiC	9.8154×10^{-1}	9.7589×10^{-1}	1.0000	9.7589×10^{-1}	
SiO_2 (cristobali)	0.0000	0.0000	9.7691×10^{-1}	0.0000	
SiO_2 (tridymite) T	0.0000	0.0000	9.8738×10^{-1}	0.0000	
SiO_2 (quartz) *T*	0.0000	0.0000	8.7109×10^{-1}	0.0000	
Si	0.0000	0.0000	7.7554×10^{-1}	0.0000	
C	0.0000	0.0000	8.7603×10^{-2}	0.0000	

[a]The value of *T* was found such that it satisfies the fixed value of the heat balance.
Enthalpy of reaction = 0.0000 J; entropy of reaction = 2.2424×10^{-1} J K^{-1}; the cutoff limit has been specified to 1.000×10^{-5}; data on two species identified with "*T*" have been extrapolated.

distinct zones that are governed by two separate processes. In the bottom zone, silicon is produced according to the mass balance equation

$$SiO_2 + SiC \rightarrow Si + SiO\langle G\rangle + CO\langle G\rangle \qquad 5.4.5$$

In the top zone, the up-flowing silicon monoxide reacts with the carbon according to the mass balance equation

$$C + SiO\langle G\rangle \rightarrow {}^2/_3\, SiO_2 + {}^1/_3\, SiC + {}^2/_3 CO\langle G\rangle \qquad 5.4.6$$

This reaction is, however, usually incomplete because the amount of incoming carbon is too low to allow all $SiO\langle G\rangle$ to react. Thus, a loss of silicon (20%) cannot be avoided.

Table 5.4.4 Converged Solution of the Reactor Simulation, Stage 4

Stage 4

T^a = 2245.88 K					
P = 1.00000 bar					
$V = 4.2980 \times 10^2$ dm^3					
	Input Amount mol		**Gas Flow mol**		**Condensed Flow mol**
C	9.7589×10^{-1}		9.7589×10^{-1}		0.0000
O	2.3003		2.3003		0.0000
Si	2.1261		1.3259		8.0012×10^{-1}
Gas	**Input Amount mol**	**Equil Amount mol**	**Mole Fraction mol**	**Fugacity bar**	**Flow mol**
SiO	0.0000	1.3245	5.7544×10^{-1}	5.7544×10^{-1}	1.3245
CO	0.0000	9.7578×10^{-1}	4.2395×10^{-1}	4.2395×10^{-1}	9.7578×10^{-1}
Si	0.0000	1.2737×10^{-3}	5.5340×10^{-4}	5.5340×10^{-4}	1.2737×10^{-3}
Si_2C	0.0000	6.9523×10^{-5}	3.0206×10^{-5}	3.0206×10^{-5}	6.9523×10^{-5}
CO_2	0.0000	3.8543×10^{-5}	1.6746×10^{-5}	1.6746×10^{-5}	3.8543×10^{-5}
Si_2	0.0000	2.4640×10^{-5}	1.0705×10^{-5}	1.0705×10^{-5}	2.4640×10^{-5}
Total		2.3017	1.0000	1.0000	
	mol	**mol**	**Activity**	**mol**	
Si	0.0000	8.0012×10^{-1}	1.0000	8.0012×10^{-1}	
SiC	9.7589×10^{-1}	0.0000	8.2082×10^{-1}	0.0000	
C	0.0000	0.0000	9.3929×10^{-2}	0.0000	
SiO_2 (liquid)	1.1502	0.0000	5.9571×10^{-2}	0.0000	
SiO_2 (cristobali)	0.0000	0.0000	5.5865×10^{-2}	0.0000	
SiO_2 T (tridymite)	0.0000	0.0000	5.5186×10^{-2}	0.0000	
SiO_2 T (quartz)	0.0000	0.0000	4.8820×10^{-2}	0.0000	

[a]The value of T was found such that it satisfies the fixed value of the heat balance.
Enthalpy of reaction = 8.7500×10^5 J; entropy of reaction = 4.1861×10^2 J K^{-1}; the cutoff limit has been specified to 1.000×10^{-5}; data on two species identified with "T" have been extrapolated.

It is worth noting that SiC is both formed and consumed within the reactor and, therefore, does not occur in the total mass-balance. However it is an essential phase in the whole process!

A more detailed analysis of the process was given by Eriksson and Johansson [1]. They have also employed modifications of the above set of calculation parameters, e.g., to study the influence of the energy supply and the amount of carbon fed into the process. Figure 5.4.6 shows the silicon yield as a function of energy supply for two different amounts of carbon feed. The lower curve (1.8 mol *carbon*) shows that the optimum value for the silicon yield (80%) is obtained for 875 kJ mol^{-1} of silica. This value was used in the calculations discussed above.

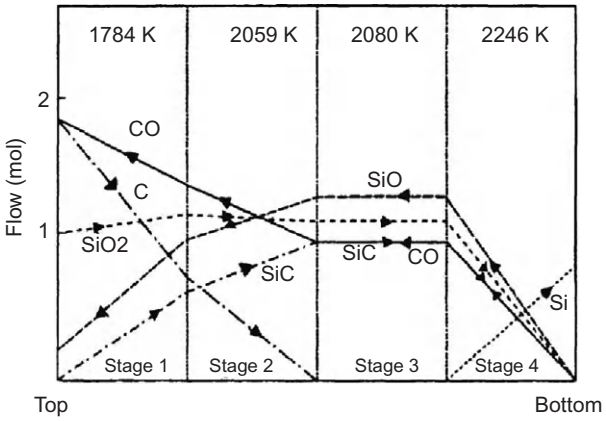


Figure 5.4.5 The materials flow for the calculated steady state.

Table 5.4.5 Total Elementary Mass Balance of the Reactor

Component	Input (mol)	Output (mol)
Si	1 SiO_2	0.8 Si + 0.2 SiO<G>
C	1.8 C	1.8 CO<G>
O	2 SiO_2	1.8CO<G> + 0.2 SiO<G>

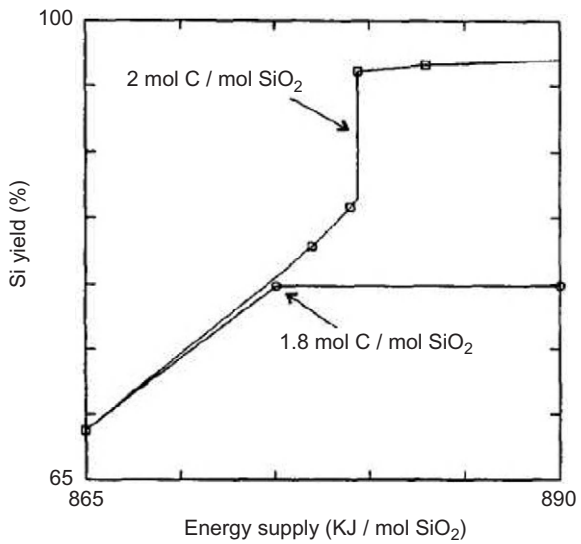


Figure 5.4.6 The silicon yield for two different amounts of carbon feed.

A higher energy supply will not raise the silicon yield. For a higher carbon feed (2 mol mol^{-1} of silica), the upper curve indicates a possible silicon yield of more than 95%. However, the resulting temperature level in the bottom stage (>2700 K) would make such a combination of process parameters technologically unfeasible.

The calculations for this case study have been performed using SimuSage [2].

5.4.2. MODELING TiO_2 PRODUCTION BY EXPLICIT USE OF REACTION KINETICS*

5.4.2.1. Introduction

Titanium dioxide (TiO_2) is a bulk commodity, which is used as a white pigment, e.g., for paints, plastics, paper, and rubber. TiO_2 pigment is produced by two major industrial routes from its ore, which is either ilmenite (ferrous titanate) or either natural or synthetic rutile. Ilmenite-based raw materials are being used for the wet sulfuric acid process, while rutile is the major input for the high-temperature chloride process. After years of development, both manufacturing processes remain in extensive use and represent both economically effective and environmentally sound industrial practice. In the following examples, the combined reaction rate–multiphase calculation has been applied to two characteristic unit processes of TiO_2 production.

5.4.2.2. Anatase–Rutile Transformation: A Simple Example of the Constrained Gibbs Energy Method

The first example presents the formation of titanium dioxide in a calciner, which is one of the final stages of the sulfate process. To simplify the treatment here, the feed is supposed to consist of titanium oxyhydrate slurry without sulfuric acid or sulfate residues. The chemical composition of the oxyhydrate is approximated as $TiO(OH)_2 * nH_2O$. During calcination, the slurry is dried and finally the hydrate decomposes, leaving the product titanium dioxide into the bed. From the oxy-hydrate, at relatively low temperatures (~200 °C) the crystalline form anatase, TiO_2(An), is formed first, and only in the high temperature zone of the furnace end, the thermodynamically stable rutile form TiO_2(Ru) appears as the desired product. The reactions are as follows:

$$TiO(OH)_2 \times nH_2O \leftrightarrow TiO_2(An) + (n+1)H_2O(gas) \quad (5.4.7)$$

$$TiO_2(An) \leftrightarrow TiO_2(Ru) \quad (5.4.8)$$

As rutile is the more stable form of the two titanium dioxide species Gibbs free energy minimization would at all temperatures result in rutile and water. This would lead to a 100% rutilization of the titania already at temperatures where the Ti-oxyhydrate is but calcined by *reaction* (5.4.7). It is however well known from practical experience, that the rutilization reaction (5.4.8) is slow and only takes place with a finite rate at elevated temperatures (above 850 °C). The simulation of the calcination process must take this feature into account.

*This chapter is a reproduction from the SGTE-Casebook with kind permission of Woodhead Publishers. Pertti Koukkari and Risto Pajarre, VTT, Helsinki, Finland; Klaus Hack, GTT-technologies, Herzogenrath, Germany

Table 5.4.6 Stoichiometric Matrix for $TiO(OH)_2$ Calcination with Kinetically Constrained Rutilization

Index (*k*)	Species	O	H	Ti	R
1	O_2-gas	2	0	0	0
2	H_2O-gas	1	2	0	0
3	$TiO(OH)_2$	3	2	1	0
4	TiO_2(An)	2	0	1	0
5	TiO_2(Ru)	2	0	1	1
6	R+	0	0	0	1
7	R−	0	0	0	−1

The gray shaded part of the table indicates the stoichiometric matrix of the unconstraint system. The additional lines and columns are needed to incorporate the kinetic constraints into the standard Gibbs energy minimization.

In the shaded area of Table 5.4.6, the equilibrium system is presented. The additional system component (R) represents the kinetically constrained rutile content, the amount of which is set by using R+ or R− inputs. These two additional constituents are used for input amounts, yet they are not allowed to form in the calculated (restricted) equilibrium.

As R+ or R− are defined as pseudoconstituents in the multicomponent system, it is necessary to define an input value for their chemical potentials. They are not supposed to affect the energy or entropy balances of the system, and thus the essential input condition is $\mu^0_{R+} = \mu^0_{R-} = 0$ [3]. Here again, the reaction constraint must not affect the mass balance of the system, and the molecular mass of the system component R is also set to zero (MR = 0). With these input settings, the Gibbs'ian method can again be used to solve for both the equilibrium conditions and the condition for a kinetically constrained multicomponent system. The conditions for the chemical potentials of anatase and rutile are received for the kinetically constrained system [3]:

$$\mu_4 - 2\pi_O - \pi_{Ti} = 0 \tag{5.4.9}$$

$$\mu_5 - 2\pi_O - \pi_{Ti} - \pi_R = 0 \tag{5.4.10}$$

The chemical potential of a constituent species is denoted as μ^k and the chemical potential of a system component as π_j; subscripts 4 and 5 are used for anatase and rutile, respectively. The kinetic condition for the anatase–rutile transformation then becomes

$$\mu_5 - \mu_4 = \pi_R \tag{5.4.11}$$

which gives the affinity of reaction (5.4.8) in terms of the component potential π_R. At equilibrium, this affinity is zero, as can be seen if Equation (5.4.10) is applied for the equilibrium system (shaded part of the matrix). For reaction (5.4.7), both the shaded and the extended matrix give the zero affinity condition. The additional constraint in the calculation follows the deviation of the affinity of anatase–rutile transformation from zero and can be used as a control for the extent of this reaction. In practice, this is done algorithmically through the addition of the pseudoconstituent R+ in each calculation step.

At the unrestricted equilibrium there is $\pi_R = 0$, so that with $\mu^0_{R+} = \mu^0_{R-} = 0$ also the chemical potentials of R+ and R− become zero. This is equal to the condition that the activities of these two "phases," as defined by Eriksson [4], equal unity. This kind of equilibrium condition is then directly applicable to calculations using standard Gibbs energy minimizers.

The reaction rate can be presented in the form of rutile fraction x, which is measured as function of time at constant temperature and pressure. For example, the following formula has been presented for rutile fraction in an anatase–rutile calcination system without additives [5]:

$$x = 1 - (1 - k \cdot t)^3 \tag{5.4.12}$$

Here, x is the fraction of rutile in the reaction mixture, t is time (h), and k is the reaction rate constant ($h-1$). This formula was used in the multicomponent system to calculate the respective molar amount for R+, which determines the kinetic conversion rate from anatase to rutile.

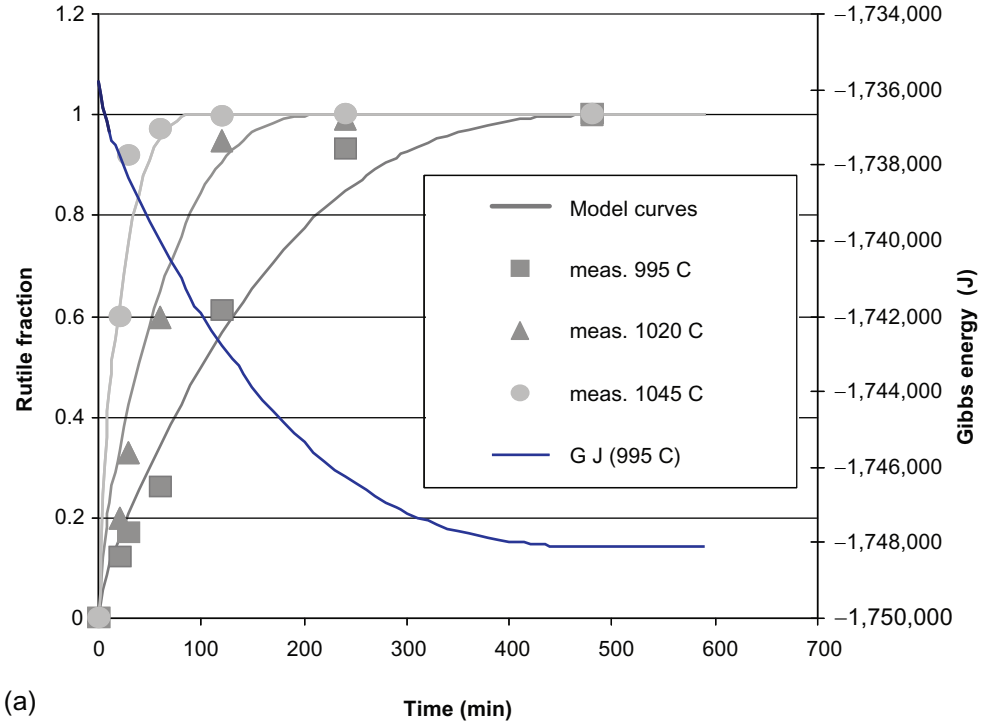
The input data of the calculation system have been collected to Table 5.4.7. The parameters for the rate constant are given in terms of the Arrhenius equation [$k = A \exp(-E_a/RT)$], where A is the frequency factor and E_a is the activation energy.

The thermodynamic (Gibbs energy) data for the species are received from standard sources (Ref. [6], see also Ref. [7]). The calculation is then performed in 60 steps with 10 min intervals to cover the experimental data of McKenzie [5], covering in total 10 h at 995 °C. For each step, the Gibbs energy of the system is minimized and as a result the composition and the Gibbs energy of the system is calculated.

Figure 5.4.7a shows the anatase–rutile transformation curves for the $TiO(OH)_2 - O_2$ system for three different temperatures. The curves represent the degree of rutilization (rising from zero to 1) and the total, decreasing Gibbs energy of the system during the course of the reaction. At each temperature, the Gibbs energy is a monotonically descending curve as a function of time, reaching its minimum value at equilibrium. As the Gibbs energy model inherently calculates other thermodynamic properties, such as heat capacities, enthalpies, and entropies, it is usually beneficial to use Gibbs energy based modeling in process calculations. As an example, the exothermal heat effect of the rutilization reaction has been deduced from the Gibbs energy model at the three reaction temperatures and is presented in Figure 5.4.7b. As for non-isothermal systems, the entropy production could be used to assess the thermodynamic consistency of the coupled kinetic–thermodynamic models [8].

Table 5.4.7 Input Data for the $TiO(OH)_2$ Calcination Model

O_2 (mol)	$TiO(OH)_2$ (mol)	R+ (mol)	Temperature (C)	Pressure (atm)	A (h^{-1})	E_a (KJ mol^{-1})
0.5	1.0	Equation (5.4.12)	995–1045	1	1.8×10^{17}	442



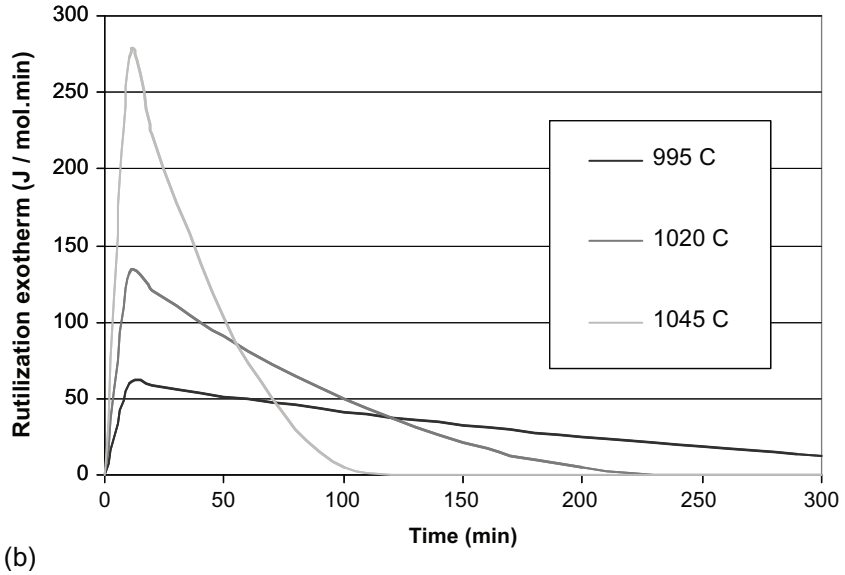


Figure 5.4.7 (a and b) Anatase–rutile transformation kinetics in a Gibbs free energy model at 995 – 1045 °C. The kinetic data is reproduced from McKenzie [5]. (a) Shows additionally the descending Gibbs energy of the system at 995 °C. (b) Shows the exotherms of the rutilization reaction as received from the thermodynamic Gibbs energy model.

The presented method can include more complex mechanisms in a multicomponent calculation [9]. The matrix must then be extended with one column and two rows for each linearly independent kinetically restricted reaction. The method of the extended matrix is now directly applicable in the commonly used Gibbs free energy routines, such as ChemApp. In fact, a particular data-assembling program is available from the developers of the ChemApp program library, so that the appropriate Gibbs energy data-files can be adapted to solve problems including kinetic constraints.

5.4.2.3. Model for the $TiCl_4$-Burner: Comparison with the Image Component Technique

An early approach to combine reaction rates with the multiphase Gibbs'ian calculations was that of Koukkari [10] while modeling of the production process for TiO_2 pigment production with the chloride process. The main reaction is burning of $TiCl_4$ in a plug flow reactor. The original work was based on the use of the image component technique discussed briefly in [3] (chapter III.5 of the SGTE-Casebook), the calculations have been performed here both with the constrained Gibbs energy method and with the image technique in view of the computation of the entropy of mixing.

The particular reactor modeled in this work is the titanium (IV) chloride oxidation burner, well known for its use in the high temperature TiO_2 pigment production. In this process, rutile (either natural or synthetic) is used as raw material. In a reducing fluidized bed the ore is chlorinated at ca. 900 °C. The ore consists of 94–96% TiO_2, the rest being oxides of other metals. The impurity chlorides from these other cations become separated in a series of condensers and the pure $TiCl_4$ is then gasified, heated, and fed to a tubular burner together with a flow of superheated oxygen. A vigorous oxidation reaction then follows between the 'tetra-chloride' and oxygen, the overall reaction being as follows:

$$TiCl_4(g) + O_2(g) \leftrightarrow TiO_2(s) + 2Cl_2(g) \tag{5.4.13}$$

The two gaseous reactants produce an aerosol, with titanium dioxide as the condensed phase in a gas stream consisting of the reactants, chlorine, and gaseous intermediates. The activation energy of reaction (5.4.13) is quite high (average: 88 kJ mol^{-1}), and thus the preheating of the reactant streams is essential.

In an industrial burner, the ignition takes place at 850–900 °C (mixed reactant temperature). Furthermore, the oxidation is an exothermic reaction with $\Delta_R H = -177\,kJ/mol\,(1000\,°C)$. The Gibbs energy change is $-102\,kJ/mol\,(1000\,°C)$ and $-54\,kJ/mol$ $(1500\,°C)$. Thus, increase of temperature in the reaction mixture may become a limiting factor for the overall conversion of titanium (IV) chloride to TiO_2.

To avoid excessive heating of the mixture, the reactor is provided with a cooling jacket with water circulation. Thermodynamic studies, e.g., that performed by Karlemo *et al.* [11], show that gaseous chlorine dissociates significantly at temperatures exceeding 1100 °C. This dissociation is an endothermic process and thus is an additional factor

affecting the temperature of the process. The reaction rate parameters for the consumption of $TiCl_4$ in the oxidation were determined by Pratsinis *et al.* [12]. The overall reaction rate equation was given as follows:

$$\frac{d[TiCl_4]}{dt} = -\left(k + k'\sqrt{[O_2]}\right)[TiCl_4] \tag{5.4.14}$$

$$k = A \cdot \exp(-E_a/RT) \tag{5.4.15}$$

$$k' = A' \cdot \exp\left(-E'_a/RT\right) \tag{5.4.16}$$

where k and k' are given in the usual Arrhenius form.

The numerical values for the frequency factors $A(=8.26 \cdot 10^{-4}\,s^{-1})$ and $A'\left(=1.4{\cdot}10^5\sqrt{dm^3\,mol^{-1}}/s\right)$ and the activation energy $E_a\,(=E'_a=88\,kJ/mol)$, average, were taken from Pratsinis *et al.* [12]. One may conclude that at close to stoichiometric compositions, $k'[O_2]^{1/2} \ll k$ and the reaction rate is practically 1st order in terms of the $TiCl_4$ concentration.

As there is no measured data of the reassociation of chlorine to Cl_2 in the burner conditions, it is a viable assumption that chlorine atoms and molecular chlorine coexist in mutual equilibrium according to the reaction:

$$Cl_2(g) \leftrightarrow 2Cl(g) \tag{5.4.17}$$

With the overall reaction rate of Equation (5.4.13), by using the rate parameters measured by Pratsinis *et al.* [12] and by using the partial equilibrium assumption for chlorine dissociation, a thermodynamic model controlled by reaction kinetics can be presented for the $TiCl_4$ oxidation.

To simulate the operation of the burner, the extent of reactions and the enthalpies of reaction must be combined with the heat transfer from the reaction mixture to the surrounding cooling media. A schematic representation of the one-dimensional reactor model is given in Figure 5.4.8. In the recent modeling work performed by Koukkari *et al.* [13], different values of the activation energy E_a in the range $71 - 102\,kJ/mol$ were tested.

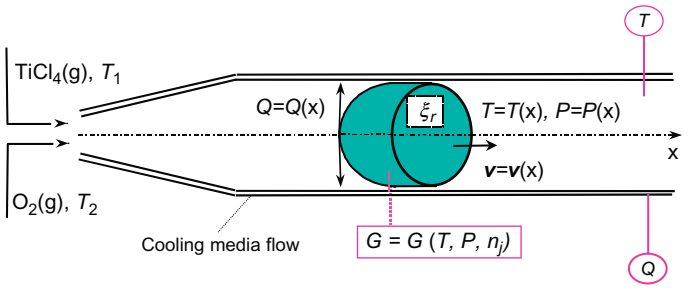


Figure 5.4.8 The schematic presentation of the one-dimensional $TiCl_4$ burner model.

The best agreement with the measured heat transfer and temperature data from the process could actually be achieved by low E_a values, and thus $E_a = 71$ kJ/mol was adopted for the actual model (see Figures 5.4.9 and 5.4.10). The measured gas temperatures [14] were also in satisfactory agreement with the results of the model calculations.

The $TiCl_4$ burner model is a practical example of the usefulness of the image component technique. The reactant $TiCl_4$ is introduced to the model as an image (unreactive) constituent, which is then algorithmically transferred to its reactive counterpart. The latter is stoichiometrically connected with the rest of the system in the stoichiometric matrix of the system.

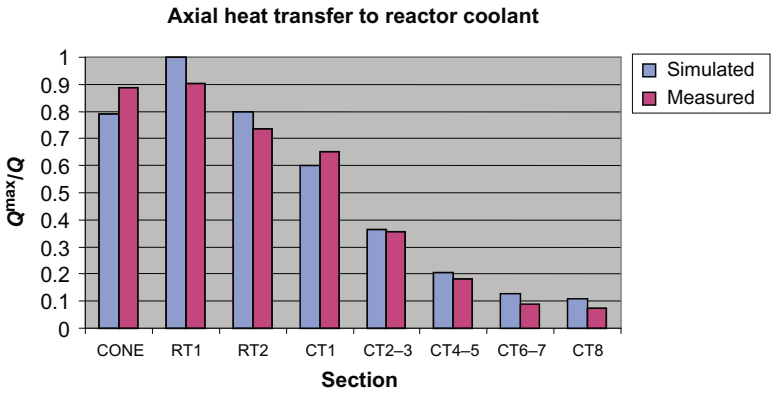


Figure 5.4.9 The calculated and measured heat transfer of the reactor for predefined segments along the reactor's longitudinal axis.

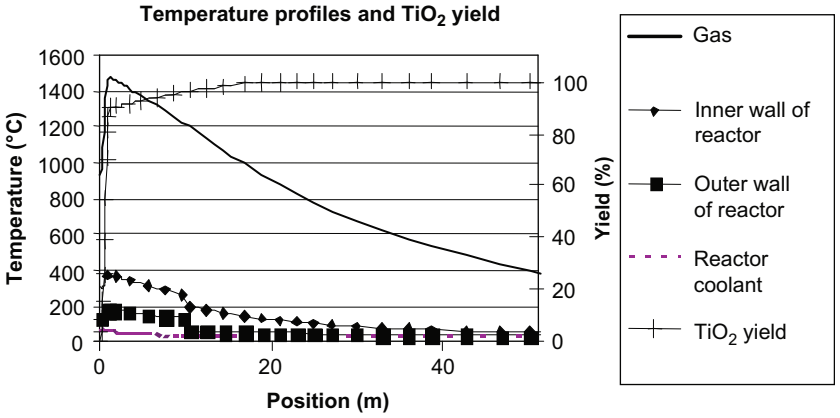


Figure 5.4.10 The calculated temperature and TiO_2 yield profiles. The O_2:$TiCl_4$-mole ratio was 1.1 and the initial mixing temperature ca. 950 °C. For measured gas temperatures see [14]. The reaction is slightly retarded due to the thermodynamic conversion limit at high temperatures. Additional heat transfer completes the reaction. The exothermal behavior can also be utilized for a secondary $TiCl_4$ injection.

As all the reactive $TiCl_4$ is readily consumed to form TiO_2, Cl_2, Cl, and (minor amounts) of oxychlorides in the minimization calculation, the image reactant $TiCl_4$, with its thermophysical properties equal to those of the actual reactant provides for the necessary upkeep of the heat and material balances in the sequential calculation.

When the temperature is raised to $\sim 1300\,^{\circ}C$, however, part of the reactive $TiCl_4$ remains thermodynamically stable in the reactant stream, and a situation is encountered, where both the active and the image constituent can be present as species in the calculated gas phase. Their combined amount equals the physical amount of $TiCl_4$ at those temperatures, and thus heat and material balances are not violated. However, there is a deviation in the entropy of mixing due to the "double presence" of a single constituent in this high temperature range.

The "entropy-of-mixing" effect of the image component method in the $TiCl_4$ burner model is illustrated in Figure 5.4.11. When the image component is used, its mole fraction in the reactive mixture can be presented with X_I whereas its reactive counterpart has a mole fraction of X_R. The image component is transferred to its reactive counterpart with discrete increments $\Delta n_R = \Delta n_I$ (expressed in molar amounts).

When all of the Δn_R is consumed in the subsequent reaction, it follows that $X_R \approx 0$, and only the terms due to X_I contribute to the entropy of mixing at each stage of the calculation. This gives a result for ΔS_{MX} which is physically justified. If, however, the thermodynamic procedure leaves some of the Δn_R unreacted in the mixture, both terms, the one involving

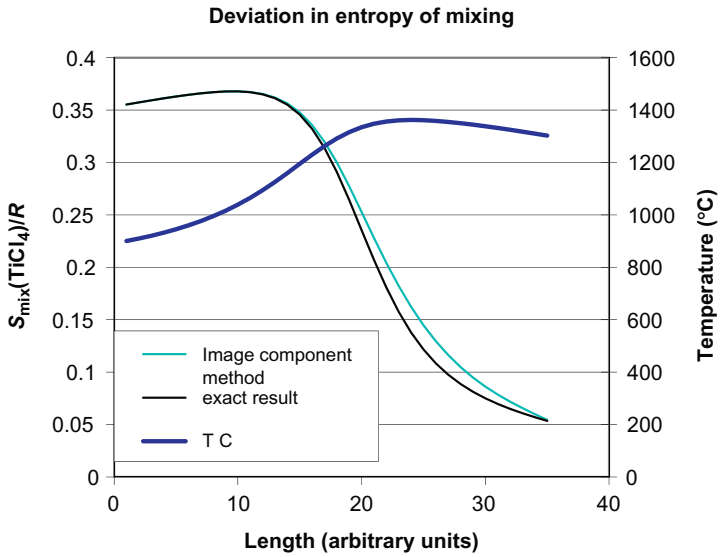


Figure 5.4.11 The deviation of the entropy of mixing in the $TiCl_4$ burner model when the image model is compared with the single reactant approach.

X_R and the one involving X_I, contribute to the value of ΔS_{MX} as if they were different constituents of the mixture. The error in the calculated ΔS_{MX} is thus due to the unreacted amount of the reactive species at such stages of the calculation, where Δn_R is not entirely consumed. In such cases, which prevail in the intermediate stages of the $TiCl_4$-reactor, the entropy using the image component is calculated too high (see Figure 5.4.11). When, on the other hand, using the constrained Gibbs energy method, the changing chemical state can be described entirely with well-defined functions and the erroneous entropy effect is eliminated.

The image component method remains applicable for cases, where either the driving force of the consumption of the reactive species is sufficiently large to prevent any remnants of this constituent to appear in the mixture or the reactive species and its image component are stoichiometric condensed substances. For the practical process modeling purpose, the image approach is often advantageous, as it provides an easy method to maintain the correct mass and heat balances for the reactor.

5.4.3. NON-EQUILIBRIUM MODELING FOR THE LD-CONVERTER*

5.4.3.1. Introduction

In the LD converter process, pure oxygen is blown on a molten iron bath for refining purposes. Elements dissolved in the molten iron, e.g., C, Si, Mn, P, etc., but also part of the molten iron, are oxidized. They either form a slag phase covering the hot metal or, in case of C, gas bubbles containing CO and CO_2.

Several reaction zones can be identified in Figure 5.4.12. In the hot spot, the oxygen directly reacts with iron and dissolved elements. Due to the impact of the oxygen jet, iron

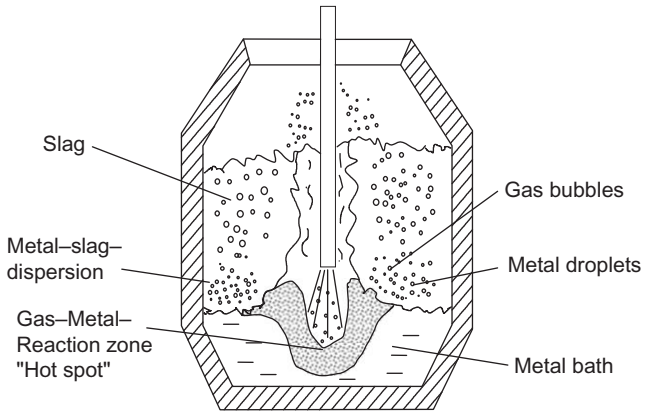


Figure 5.4.12 LD converter process.

*This chapter is a reproduction from the SGTE-Casebook with kind permission of Woodhead Publishers. Michael Modigell, Institut für Verfahrenstechnik, RWTH Aachen, Germany; Anke Güthenke, Daimler-Chrysler, Stuttgart, Germany; Peter Monheim, SMS-Demag, Düsseldorf, Germany; Klaus Hack, GTT-Technologies, Herzogenrath, Germany

droplets are dispersed in the slag phase as well as slag droplets in the metal bath. The metal–slag dispersion is mixed further by CO and CO_2 bubbles and serves as the main reaction zone. A third zone contains the hot metal which is not dispersed in the slag but forms the bath underneath. Droplets from the dispersion fall back into this bath.

5.4.3.2. Process Model Development

The task of developing a suitable converter model will be discussed based on the decarburization reaction of the iron melt. Obviously, the rate of the decarburization reaction depends on the reaction rate of

$$[\mathrm{C}] + (\mathrm{O}) = \{\mathrm{CO}\} \tag{5.4.18}$$

and the transport conditions in the converter. Thereby, these are determined by oxygen blowing conditions and CO-formation. On the other hand, CO-formation is influenced by the decarburization reactions.

Intermediary formation of FeO in the hot spot is the main oxygen source for the decarburization. FeO is dispersed in the slag and the metal bath as well as Fe–C droplets, which are accelerated by the oxygen jet. The subsequent reaction of FeO with carbon dissolved in iron occurs in both phases. In the slag phase, dissolved FeO reacts with dispersed Fe–C droplets, in the metal bath FeO droplets form the disperse phase. For the decarburization several reaction routes can be formulated:

$$(\mathrm{FeO}) + [\mathrm{C}] = [\mathrm{Fe}] + \{\mathrm{CO}\} \tag{5.4.19}$$

$$(\mathrm{FeO}) + \{\mathrm{CO}\} = [\mathrm{Fe}] + \{\mathrm{CO_2}\} \tag{5.4.20}$$

$$\{\mathrm{CO_2}\} + [\mathrm{C}] = 2\{\mathrm{CO}\} \tag{5.4.21}$$

Reaction (5.4.19) is kinetically inhibited [15]. The time for the complete reduction of a FeO-droplet with a diameter of 1 mm (equaling 4.7×10^{-5} mol) in a Fe–C melt amounts to between 30 and 175 s. The same amount of FeO reacts with pure CO according to Equation (5.4.20) in only 0.2 s. The consecutive reaction (5.4.21) takes place in only 2×10^{-3} s.

From these data it can be concluded that the direct reaction between FeO and C contributes little to the decarburization due to its kinetic limitation. However, reaction (5.4.20) and (5.4.21) can only occur spontaneously when CO_2 bubbles come into contact with Fe droplets in the slag phase or CO bubbles with FeO droplets in the metal phase respectively. The probability for such contacts depends on the transport conditions in the slag and metal bath respectively.

In principle, the conditions close to the phase boundary of the droplets can be modeled by transport and reaction equations. In a simple two-layer model, a transport equation according to Ficks' law can be stated for every component x:

$$n_x = K_{x,\mathrm{eff}}\, A \left(c_{x,\mathrm{metal}} - c_{x,\mathrm{phase\,boundary}}\right) \tag{5.4.22}$$

The transport coefficients $K_{x,\text{eff}}$ are functions of the macroscopic and the local microscopic fluid movement, which is caused by the stirring of the gas bubbles. Additionally, the increase of the diffusion boundary layer during the reaction due to the formation of a pure Fe phase has to be taken into consideration for all three reaction routes 19, 20, and 21. For the reaction rate, Equation (5.4.21) can be stated:

$$-R_x = k_x \prod c_i^{n_i} \qquad 5.4.23$$

However, there is no reliable information on transport coefficients, reaction rate constants, and concentration ratios that are needed for solving Equations (5.4.22) and (5.4.23). Hence, a process model based on these equations is not promising. Instead, the process will be modeled on a less detailed level employing a cell model, which is based on the concept of local equilibrium.

As shown in Figure 5.4.13, according to the main reaction zones, the converter is divided into three sections. These are treated assuming complete (local) equilibrium: the hot spot, where the reaction between oxygen and iron melt takes place, the metal–slag zone, where the conversion of the FeO from the hot spot with melt droplets takes place, and the metal bath. The fourth zone, the slag, as shown in Figure 5.4.13 is needed for the temporal discretization of the model. It is assumed that the total amount of FeO formed in the hot spot is transported to the metal–slag zone, where it reacts with carbon containing iron melt and already available slag. This assumption is reasonable as reactions taking place in the bath zone can be transferred to the metal–slag zone.

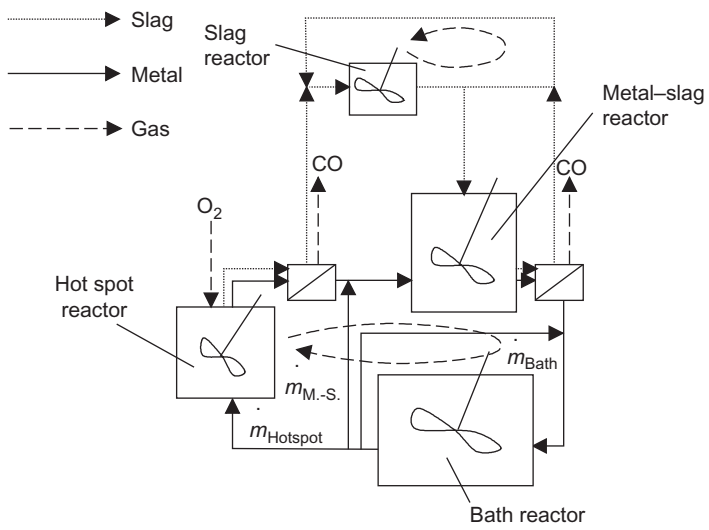


Figure 5.4.13 Cell model for the LD converter process.

The individual ideal reaction zones are interlinked by material streams in a way that a circular flow through these zones results. This flow models the circulation of the material in the converter and the stream of metal droplets through the slag phase as they have been observed in experimental studies. With a given oxygen blow rate and lance height, the circulation rate between bath reaction zone and hot spot reaction zone can be defined. This also determines the mass flow between the assumed reaction zones, for which a boundary condition can be stated. Assuming the experimentally proven full conversion of oxygen in the hot spot leads to

$$2n_{O_2} \leq \frac{m_{Fe,Hotspot}}{M_{Fe}} \tag{5.4.24}$$

Between the bath and the metal–slag zone mass transfer of Fe droplets takes place. During a wide part of the process, the decarburization reaction is limited by the oxygen supply. After reaching the critical point, it is limited by the carbon transport to the reaction zone. Therefore at the critical point, Equation (5.4.25) holds:

$$2n_{O_2} \leq \frac{N * V}{t'} * c_0 = N * V * c_0 = \frac{m_{Fe,Metal-slag}}{\rho_{Fe}} * c_0 \tag{5.4.25}$$

These mass flows are a function of the oxygen blow rate and conditions as well as the gas production, which are constant over the main process time. Toward the end of the process, gas formation depends on carbon concentration and therefore the mass transfer conditions change.

As the kinetic and transport limitations of the process are modeled by the interlinking of the reaction zones, the zones themselves can be treated assuming thermochemical equilibrium. Though derived with regard to the decarburization reaction, the present model is at the same time also valid for other chemical components with similar behavior present in hot metal and slag. Processes determined by other kinetic phenomena, such as the melting of scrap and the dissolution of lime, need to be modeled separately.

The dissolution of fluxes, especially lime, is limited by the formation of a dicalcium silicate layer around the particles for a major part of the process. This behavior is mainly dependent on the composition and temperature of the slag and mixing between metal and slag [16]. A dissolution function was implemented into the model regulating lime participation in reactions leading to the formation of slag. With this function, the heating up of the lime prior to its dissolution and the withdrawal of energy from bath and slag due to this heating up is treated as well.

A similar problem exists for the addition of steel scrap. Scrap melting does not only depend on its temperature but also on its carbon concentration. Diffusive carbon transport to the scrap/metal bath-interface is therefore an important factor for the melting behavior. A function was implemented which treats the melting as well as the heating up of the scrap prior to melting.

Not only material streams to and from ideal reaction zones are defined in the model, but energy streams as well. Energy losses are calculated and appropriate amounts of enthalpy are withdrawn from the ideal reaction zones throughout the simulation. Thus radiation losses from the converter mouth as well as radiation and convection losses through the converter walls are regarded. Furthermore, enthalpy losses due to the hot off-gas stream are directly taken into account in the reaction zone model as the hot off-gas stream is removed throughout the process.

A temporal discretization of the described model is needed for simulation purposes. According to a chosen time increment Δt and the determined mass flows between the ideal reaction zones, in every time step the mass exchange between the reaction zones and the reaction progress is calculated. Hence, a step-by-step transport and conversion of the different mass streams results.

5.4.3.3. Modeling Tool

The process modeling tool SimuSage is a combination of the thermochemical programmers library ChemApp and a library of additional graphical components for Borland's programming environment Delphi. Initially developed by Mannesmann Demag Metallurgy as an in-house tool under the name ProMoSys, it is now codeveloped by GTT-Technologies and SMS-DEMAG under the new name SimuSage. It consists of flow sheeting components, which add to Borland Delphi's powerful programming language the capability to easily generate stand-alone flow-sheeting models with a sound thermodynamic basis. The elements of the reaction zone model shown in Figure 5.4.13, for example material streams and equilibrium reactors, are readily available in SimuSage as graphic components. This has made it possible to set up the converter model and to test modifications and additions to the model very quickly.

As indicated above, the ChemApp programmers' library (in form of a Dynamic Link Library, DLL) has been used to form the thermodynamic backbone of SimuSage. The general concept is represented in Figure 5.4.14. The ChemApp library permits the easy use of full complex equilibrium calculations within the software by way of a set of interface routines. These interface routines are used to define the conditions for a "local" equilibrium calculation, to execute the equilibrium calculation, and to extract information from the calculated equilibrium state (such as phase amounts or phase internal concentrations) that is needed for the process model to proceed.

The equilibrium calculations in ChemApp are performed by the same Gibbs energy minimization code as in the well-known interactive software ChemSage4, now FactSage5, and are thus of proven reliability. The thermodynamic data used in the present modeling have been taken from the extensive file store of GTT-Technologies. 109 phases and altogether 202 species have been included in the calculations. The gas phase (60 species) has been treated as ideal, while the liquid Fe-phase (dilute solution approach,

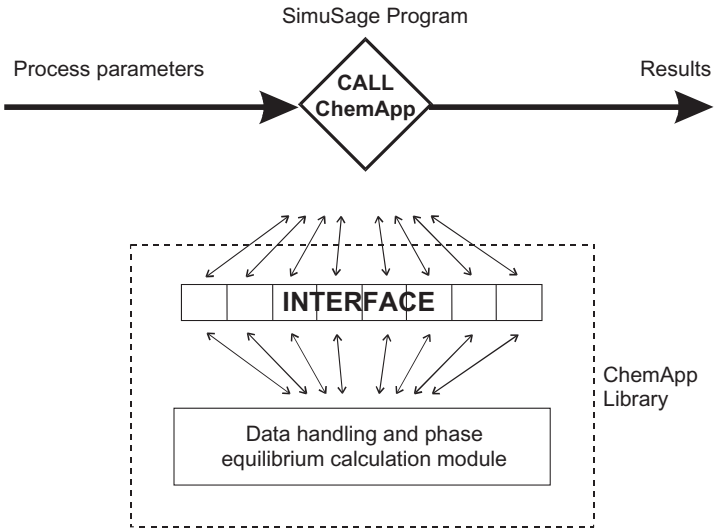


Figure 5.4.14 Integration of ChemApp into SimuSage.

14 species) and the liquid slag (Gaye–Kapoor–Frohberg model, 8 species) have been treated as nonideal chemical solutions.

5.4.3.4. Simulation Results

For the simulation calculations, the following process conditions are assumed according to Asai and Muchi [17]:

150 *t* Converter

Oxygen blow rate 10.87 kg O_2/s for 0th to 15th min, from 15th min 7.99 kg O_2/s

5 *t* Scrap input

10 *t* CaO input

From the experimental results [17] shown in Figure 5.4.15 and the corresponding process conditions stated above, model parameters can be calculated. The lower limit for the exchange ratio between the bath and hot spot reaction zone defined as $m_{\text{Hotspot}}/m_{\text{total}}$ is calculated with Equation (5.4.24), it amounts to 0.023. The exact value for this exchange ratio is derived by comparing measured and calculated decarburization results. Other reactions, for example of Si, and the temperature development also have to be considered. From the comparison of experimental and calculated results, the exchange ratio between the bath and hot spot reaction zone is found to be 0.04.

In Figure 5.4.15 the critical point, where the change from a constant decarburization rate to a rate controlled by carbon concentration takes place, is found to be at 13.5 min at a carbon concentration of 0.006. From this, the exchange ratio between bath and metal–slag reaction zone defined as $m_{\text{Metal-slag}}/m_{\text{total}}$ is calculated to be 0.7.

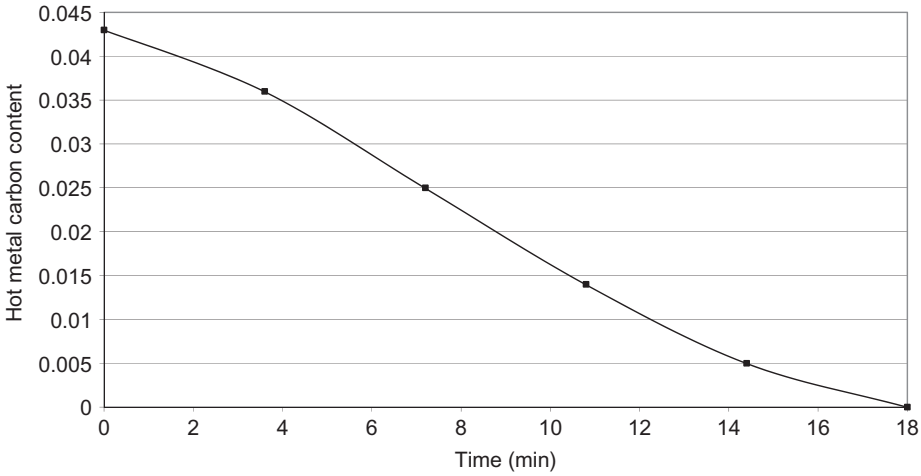


Figure 5.4.15 Carbon content in hot metal.

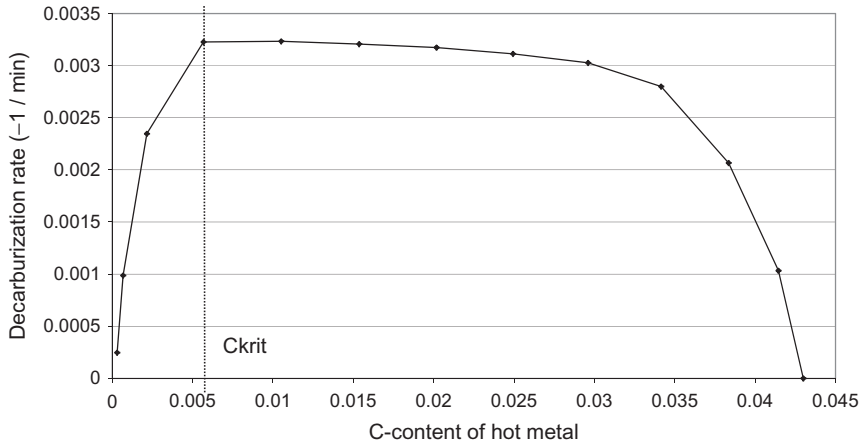


Figure 5.4.16 Decarburization rate.

The results of the calculation with these parameters are shown in Figure 5.4.16. The decarburization reaction, the critical point, and carbon content are modeled correctly as can be seen from the calculation of the decarburization rate. With the calculated exchange ratio between bath and metal–slag reaction zone, a critical carbon content of 0.006 results as expected.

As discussed above, Equation (5.4.25) is valid for the process conditions up to the critical point. The decrease in decarburization rate from the critical point onward results in a decrease in CO-production and therefore less stirring is caused by the gas bubbles. Hence mass transfer in form of metal droplets in the slag decreases.

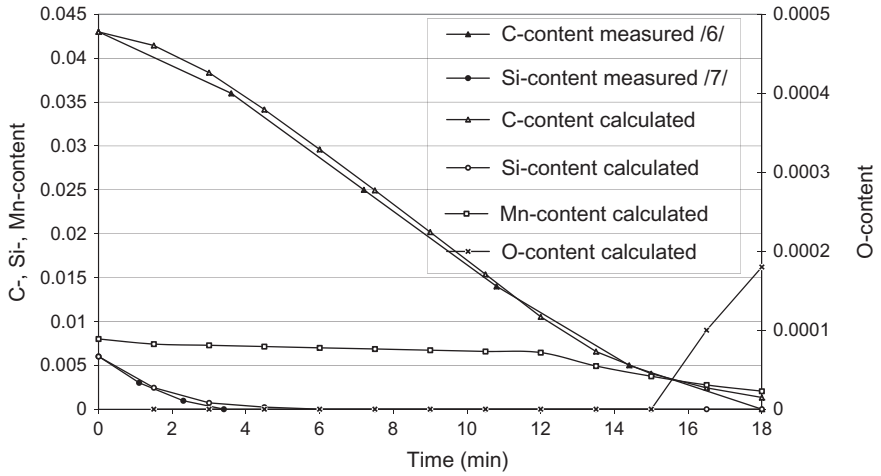


Figure 5.4.17 Components in hot metal.

In Figure 5.4.17, this effect is taken into account and modeled by a decrease of the bath/metal–slag reaction zone exchange ratio from the critical point onward. After reaching the critical point, the exchange ratio is set to 0.35. Obviously, the decrease in decarburization rate can be modeled quite well with this set of parameters. The calculated carbon content of the metal phase shows good agreement with measured values [17].

At the beginning of the process, the oxidation of Si from the hot spot is limited by the transport of Si to the phase boundary. Hence decarburization starts though normally Si is oxidized preferentially to carbon.

The limitation of transport to the phase boundary is modeled by a limited mass flow through the hot spot reaction zone and therefore limited amount of Si in this reaction zone. The resulting excess oxygen reacts to form CO and FeO-rich slag. This slag facilitates the dissolution of lime and forms the main reaction zone for further reactions.

The oxidation of Si therefore not only takes place in the hot spot but also in the metal–slag reaction zone. The amount of Si calculated in the metal phase shows a good agreement with measured values [18]. Additionally, the content of Mn and O in the metal phase was calculated. Both components show a qualitatively good agreement with measured values. Mn is oxidized toward the end of the process, the oxygen content of the metal phase increases.

Figure 5.4.18 shows the composition of the slag phase, which shows a qualitatively good agreement with measured values. The FeO-content rises toward the end of the process resulting in iron losses.

The calculated gas production is shown in Figure 5.4.19. The shift of the main reaction zone from the hot spot to the metal–slag dispersion in the course of the process

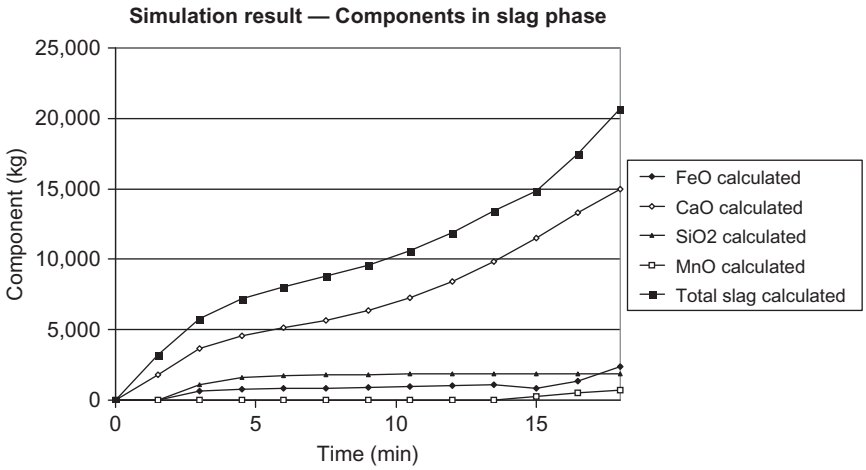


Figure 5.4.18 Components in slag phase.

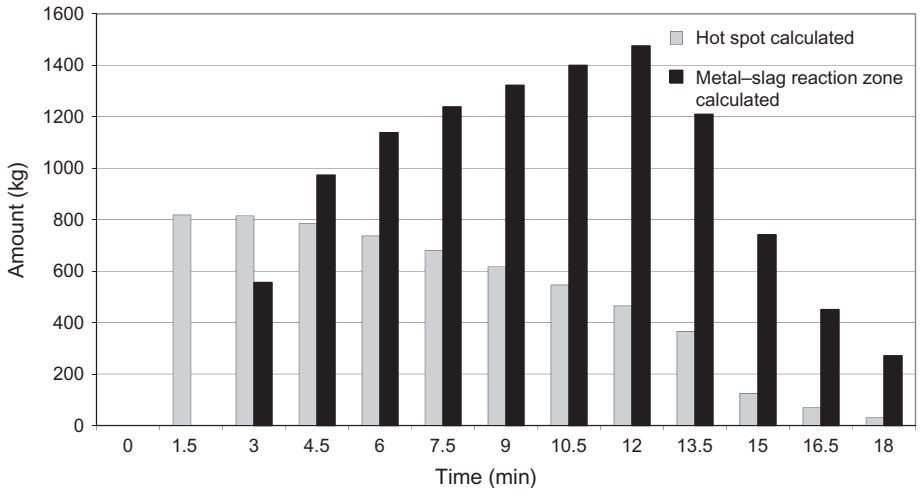


Figure 5.4.19 Gas production.

is modeled well, as can be seen from the gas production decreasing in the hot spot while increasing in the metal–slag reaction zone. The decreasing gas production at the end of the process is caused by the change of the oxygen blow rate and the slower decarburization.

As discussed above, the ideal reaction zones in the cell model are not only coupled by defined mass transfer but by heat transfer as well. Energy losses from the converter are calculated in every time step and enthalpy is withdrawn from various the reaction zones, mainly from the metal–slag reaction zone. In Figure 5.4.20, the evolution of the

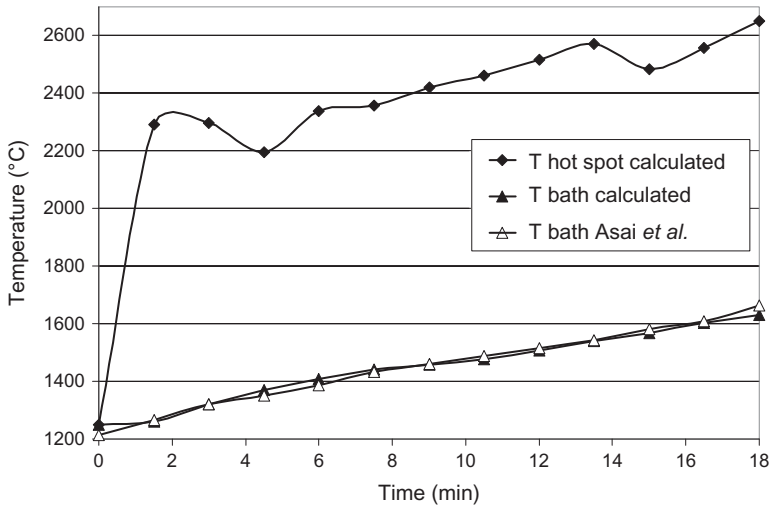


Figure 5.4.20 Temperature evolution.

temperature in the hot spot and the mean temperature of the hot metal bath are shown. The temperature in the hot spot is well described. Measurements give values of 2300–2400 °C for the first 8 min of the process [19]. The mean temperature shows a very good quantitative agreement with the experiments [17].

5.4.3.5. Conclusions

The aim of the research presented in this paper is the evaluation of a technique for modeling metallurgical processes. In the long term, the process models developed by use of this technique shall be used to improve process design. A special focus is set on modeling non-equilibrium phenomena which are caused, e.g., by transport limitations or dissolution processes. The objective is to model the process with a relatively simple model structure and only few model specific parameters.

The LD-converter process was modeled according to this intention. Based on experimental results for the decarburization reaction and possible reaction routes, a simple cell model was developed which describes well the transport limitations of the decarburization. Simple relationships were deduced which define the mass transfer between the cells (reaction zones) and thus the model parameters. Only little further adjustment is needed. Energy losses from the process are calculated throughout the simulation. The resulting temperatures of the hot spot show good agreement with real process data. Regarding the reactions, the model does not only describe the decarburization but also the behavior of other elements dissolved in metal and slag. The temperature of the metal bath could also be reproduced by the model. Altogether, these facts show that, although only a

simple model structure was employed, the physical and chemical conditions in the converter process are handled correctly.

5.4.4. SIMULATION OF THE RH–OB AND BOF PROCESSES USING THE EFFECTIVE EQUILIBRIUM REACTION ZONE MODEL

5.4.4.1. Concept of the Effective Equilibrium Reaction Zone Model

The evolution of the metal and slag composition during the RH treatment was treated using a *effective equilibrium reaction zone model*. This model differs from the "reaction interface models," in which the reactions are assumed to reach equilibrium only at the interface (Figure 5.4.21a). As a consequence, mass transfer coefficients and reaction rates must be considered at the interface. The main difficulty of this approach lies in the determination of the mass transfer coefficients and reaction interface areas depending on the composition, temperature, and flow pattern. In the effective equilibrium reaction zone model, all phases within the "effective" reaction zone located at the interface (Figure 5.4.21b) are assumed to reach equilibrium. With this approach, an effective reaction volume is used instead of mass transfer coefficients. This approach allows easy linkage of the multicomponent thermodynamic database to the kinetic simulation. Depending on the process conditions, the extent of the effective reaction zone volume changes to consider the variations in reaction kinetics.

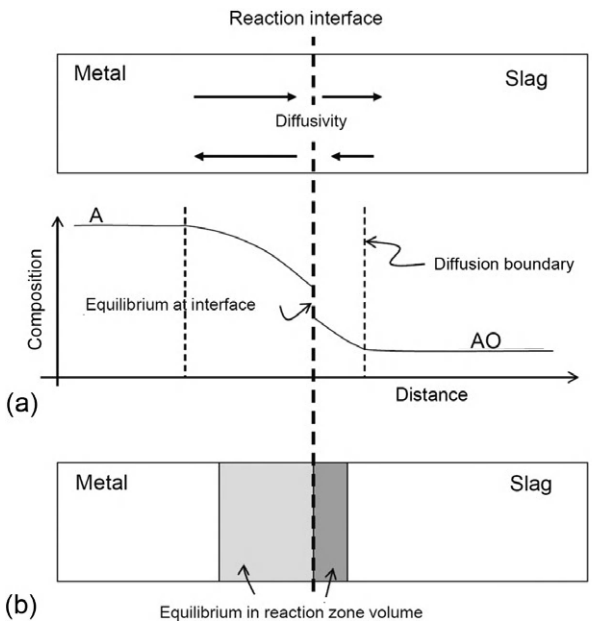


Figure 5.4.21 Schematic representation of the concept of (a) the reaction interface model and (b) the reaction equilibrium model applied to a metal/slag reaction [20].

5.4.4.2. Calculation Procedure

Thermodynamic equilibrium at each reaction zones and each cycle was calculated using FactSage software and database [21]. FactSage combined a large number of thermochemical data with powerful calculation to solve complex chemical equilibria involving multiple phases. Equilib calculation files were prepared to describe the reactions occurring in each reaction zone. As large and repetitive Equilib calculations are involved in the kinetic models, the Equilib calculations were automated by the Macro Processor available with FactSage software. FactSage Macro Processing enables to edit and run Equilib files as background job, save reaction products as streams, access any Equilib calculation results, etc. through a series of commands and functions written in a macro file. In addition, FactSage Macro Processing allows interacting with Microsoft Excel™ Worksheets to read input conditions, write calculation results, and generate graphics.

5.4.4.3. Simulation of the RH–OB Process

The Ruhrstahl Heraeus (RH) degasser is the most widely used vacuum decarburization unit in the secondary steelmaking process. The RH process is designed to treat molten steel for decarburization to low C content (<10 ppm), deoxidation and desulfurization in vacuum, H and N removal, efficient alloying, rapid homogenization of the ladle steel and inclusion removal. The RH process is therefore an important metallurgical reactor involving complex reactions between molten steel, gas, slag, inclusions and refractory. The RH unit consists in a pair of snorkels immersed into the steel bath and an evacuated vessel (1–3 torr) [22]. Argon is injected into the steel in one of the snorkels (up leg), lowering the steel density and forcing the steel to flow upward into the unit. The steel returns to the ladle through the other leg (down leg), creating a very large steel recirculation. Oxygen can be injected through a top lance in the vessel (RH–OB) to facilitate decarburization and to reheat by oxidation of aluminum.

Many mathematical modeling studies [23–31] have been performed to understand the influence of various operation parameters on RH decarburization reaction: RH vacuum pressure, lifting gas (Ar or Ar–N_2) flow rate and configuration, O_2 blowing rate, dimension of RH vessel and snorkel, etc. However, in all previous investigations, a simple chemical reaction $\underline{C} + \underline{O} = CO(g)$ and a simplified Fe–C–O steel system were taken into account. No other chemical reactions were considered. Recently, Van Ende *et al.* [20] built a kinetic model for the RH process which combines FactSage thermodynamic software and multicomponent database, FactSage Macro Processing and mathematical expressions of the reaction kinetics based on the concept of the effective equilibrium reaction zone model. Previous numerical simulation and empirical relations were combined to construct the kinetic model. It was validated with C and O contents in ladle steel measured during industrial operation. The model can reproduce successfully the behavior of the RH degassing process for various steel compositions and process conditions.

The results of the model were used to clarify the decarburization behavior observed during the treatment. In particular, the observed deviation of the C and O contents from the stoichiometry of the decarburization reaction could be explained by the chemical reaction between steel and slag in the RH vessel, which was considered for the first time.

Based on the predicted evolution of the slag composition in the RH vessel, the chemical stability of two typical RH refractories, magnesia–carbon, and magnesia–chromite refractories, in contact with the RH slags were predicted [32].

The kinetic model was applied to the simulation of ferromanganese addition in the RH process to reproduce the C pickup in steel [33]. The results of the process simulation highlighted the significant changes on the steel and RH slag chemistry following the ferromanganese addition. The additional C brought to the steel by the ferromanganese caused a significant drop in the O content of the ladle steel and the reduction of the Fe_tO content of the RH slag. The time at which the ferromanganese is added must be carefully chosen to allow an effective removal of the additional C from the ferroalloy.

5.4.4.3.1 Determination of the Reaction Zones

The RH degassing process was divided into 14 effective reaction zones, as depicted in Figure 5.4.22. In the RH vessel, seven effective reaction zones were identified to deal with the decarburization, deoxidation, alloying, and slag/steel/refractory reactions. The steel in the ladle was divided into two effective reaction zones to take into account

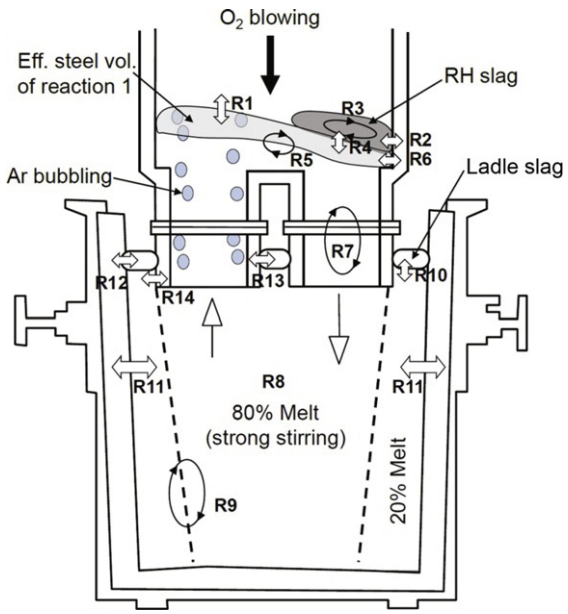


Figure 5.4.22 Schematic representation of the reaction zones in the RH degassing process [20].

strong mixing in the recirculating zone. Also, effective reaction zone volumes were added to consider the reactions between steel, slag, and refractory in the ladle.

To simulate the decarburization reaction in the RH degasser, the mechanism of the decarburization process in the RH vessel was described based on three reaction sites [23,27,29,34–37]:

(i) Spontaneous CO bubbles formation in bulk steel, when the equilibrium partial pressure of CO gas becomes larger than the local hydrostatic pressure of molten steel;

(ii) Hot spot formation in bulk steel during O_2 blowing stage, the hot spot being the area in which oxygen penetrates into molten steel during the O_2 blowing stage [36];

(iii) Bath surface and Ar bubble surface reactions.

The effective reaction zone volumes involved at the three reaction sites were determined as a function of the RH process conditions such as vacuum pressure in vessel, O_2 blowing rate, Ar flow rate in upper snorkel, RH vessel dimensions, steel composition entering the RH vessel, steel temperature, etc. based on simplified mathematical functions and empirical relations derived from mathematical hydrodynamic simulations and plant data. The volume of the other above mentioned reactions zones were expressed in a similar way, based on simplified mathematical functions, empirical relations found in literature and plant data. The equations for each reaction zone volume can be found in [20].

5.4.4.3.2 Model Validation

The decarburization phenomena of a 270-ton ladle under various RH processing conditions were calculated using the model and compared with $\underline{C}$ and $\underline{O}$ data from industrial runs at POSCO Gwangyang Works. The initial compositions of steel and ladle slag, and operation conditions, which were used as input data to predict the course of the RH treatment, are listed in Table 5.4.8.

The evolution of the ladle steel composition calculated with the model (solid lines) is compared with the O and C contents measured in the plant (triangle and square symbols, respectively) in Figure 5.4.23. The evolution of the decarburization reaction, which is represented by the variation of $\underline{C}$ and $\underline{O}$ with operation time, is well simulated by the model. The Al content after Al deoxidation is also in good agreement with the observed data. The O and C content during the first minute of the process are barely changing as the RH vessel pressure is close to 1 atm and O_2 is not blown. Once O_2 is blown, the O content increases while C content remains unchanged in the beginning of O_2 blowing. Once the RH vessel pressure is low enough, decarburization starts and the C content begins to decrease significantly. In the end of O_2 blowing, the O content decreases along with the C content. Upon reaching approximately 380 s, the O content remains mostly constant, whereas the C content keeps decreasing.

The originality of the kinetic model is the presence of a slag in the RH vessel and its influence on the decarburization reaction. This slag was formed in the RH vessel by entrainment of ladle slag during the immersion of the RH snorkels at the beginning

Table 5.4.8 Process Conditions and Dimensions of the RH Degassing System

	C	Al	O	Mn	Cr
Initial steel composition (ppm)	193	0	415	260	90
Final steel composition after RH treatment (ppm)	9	430	0	900	100
Total melt in ladle	270,000 kg				
Initial steel temperature	1596 °C				

	SiO_2	Al_2O_3	FeO	CaO	MgO	MnO
Initial ladle slag composition (wt%)	9.0	22.1	6.8	53.6	6.5	2.0
RH slag amount	265 kg					
Additional amount of FeO	170 kg					
Al addition	287 kg (14 min after the start of the RH process)					
Al purity	92%					
O_2 blowing	18 $Nm^3\ min^{-1}$ between 1st and 3rd minute					
O_2 blowing yield	80%					

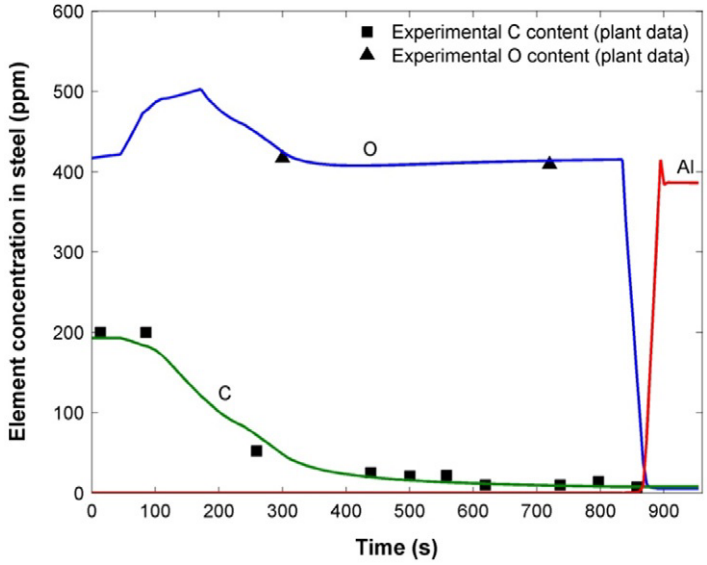


Figure 5.4.23 Evolution of the calculated ladle steel composition (solid lines) during the RH degassing treatment compared with observed C and O contents (plant data) [20].

of the treatment and by dissolution of Fe_tO into the RH slag. The authors suggested that Fe_tO arose from oxidation of steel droplets ejected on the RH wall and oxidation of the steel skull left during draining of the RH vessel.

The predicted evolution of the RH slag composition and that of steel equilibrated with the RH slag (reaction zone 4 in Figure 5.4.22) is shown in Figure 5.4.24.

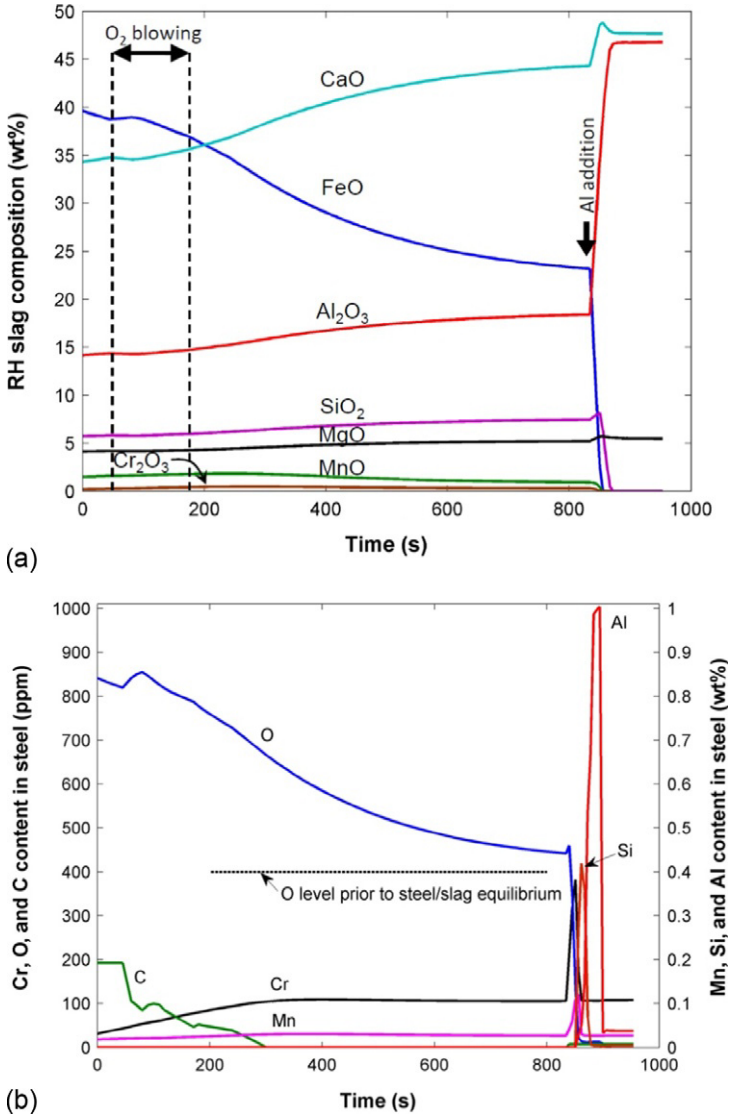


Figure 5.4.24 Evolution of (a) RH slag composition and (b) RH steel composition in the effective volume of reaction zone 4 [20].

Interestingly, the FeO content in the RH slag decreases continuously during the decarburization process (Figure 5.4.24a), while the O content in the RH steel in reaction zone 4 (Figure 5.4.24b) significantly increases after reaction with the RH slag. It was suggested that O is continuously transferred from the RH slag into molten steel during the RH process through the decomposition of Fe_tO from the RH slag:

$$Fe_tO_{(RH\,slag)} \rightarrow t\underline{Fe} + \underline{O} \tag{5.4.26}$$

The RH slag is, therefore, an oxygen reservoir to the steel. When Al is added in the RH vessel for steel deoxidation, a large amount of Al in steel is consumed to reduce all remaining Fe_tO in the RH slag to Fe in a very short time, which explains the low Al yield observed at the plant.

As seen in Figure 5.4.25, industrial data (triangle markers in Figure 5.4.26) shows a considerable deviation from the stoichiometric decarburization trajectories ($\underline{C} + \underline{O} = CO(g)$, 1 torr, 1600 °C, dotted lines in Figure 5.4.26), toward an increase of the O content. This deviation cannot be reproduced without considering an additional O source during the reaction (model prediction, solid line in Figure 5.4.25). While the decarburization reaction consumes both C and O from the steel, the RH slag continuously supplies O to the steel by decomposing Fe_tO. Thus, the O content remains virtually constant, whereas the C content still decreases.

The kinetic model has been applied to more than 12 different RH operation conditions at POSCO Gwangyang Works without changing any model parameters. The predicted results were quite satisfactory for all cases in comparison with plant data. Though the concept is relatively simple, the model could successfully reproduce the plant data over a wide range of process conditions. By dividing the complex process into a

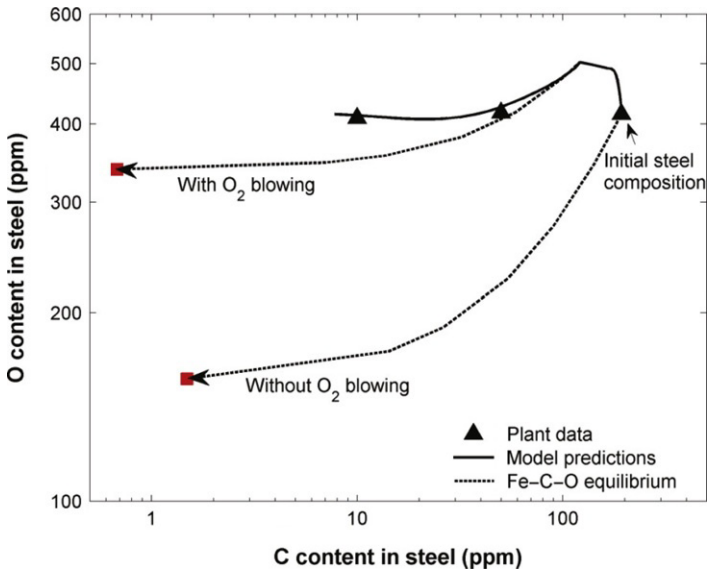


Figure 5.4.25 Evolution of the relation between C and dissolved O contents of steel in the ladle during the RH degassing treatment and comparison between observed and equilibrium values and those calculated with the present model [20].

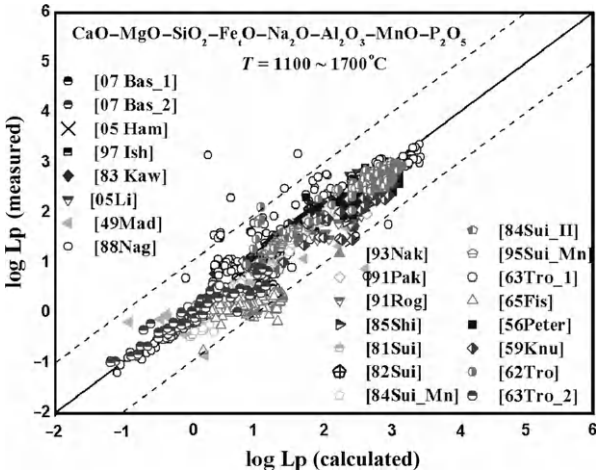


Figure 5.4.26 Comparison between experimental and calculated L_p values for binary, ternary, and multicomponent slags [38].

series of smaller reactors and carefully analyzing the plant data, reactions taking place in particular areas of the process, where sampling is almost impossible, could be predicted.

5.4.4.4. Simulation of the BOF Process

In the Basic Oxygen Steelmaking (BOS, BOF, or LD converter) process, the hot metal produced in the Blast Furnace is refined into raw liquid steel. The main functions of the process consist in decarburization and dephosphorization of the hot metal and optimization of the steel temperature. The hot metal is charged into the Basic Oxygen Furnace (BOF) vessel and poured onto the metal scrap. Oxygen is blown at supersonic speed through a top lance. In other variations of the process, oxygen is blown through bottom tuyeres solely (OBM, Q-BOP, LWS) or through a combination of top lance and bottom tuyeres (LBE, LET, K-BOP, K-OBM). Oxygen is blown for about 14–25 min during which the lance is moved to different heights. At the beginning of the blowing period, the lance is high to safely establish the oxidizing reactions. The lance is soon lowered to increase the reaction rates and slag formation. At its lowest position, maximum decarburization is achieved. Fluxes (CaO, MgO, CaF_2, etc.) are added soon after oxygen blowing to control the chemistry and S and P capacity of the slag. After the blowing period, the steel is sampled for chemical analysis and temperature measurement. Corrective actions are performed if necessary (reblowing or coolants addition). The steel is then tapped into the ladle and further refined in the secondary steelmaking process. The slag is typically splashed on the furnace wall to coat the lining and dumped in a slag pot.

During the blowing period, a large number of metal droplets are ejected into the slag emulsification by the high speed gas, accelerating the reaction kinetics by the formation

of large interfacial areas. A rapid oxidation of Si from the hot metal occurs at first, while S, P, and Mn are transferred from the metal to the slag over the entire blowing period. The decarburization reaction exhibits usually a delay due to the competition with other metallic elements. The slag is rich in FeO and SiO_2 at the beginning of the blowing period when the lance is high. The CaO content in slag increases progressively as the flux dissolves. Decarburization of the hot metal takes place at a high rate as the lance is lowered, resulting in the reduction of FeO from the slag. Slag foaming and emulsification is of significant importance during the middle blowing period, when large amount of CO(g) are produced. Toward the second half of the blowing period, P and Mn show a tendency to reverse to the melt bath. The FeO content increases once the decarburization reaction slows down.

The BOF process is characterized by multiphase regions in which gas and fluid dynamics, fluid properties, mass transfer, and overall kinetics are complex. Jung *et al.* [39] presented a preliminary kinetic model based on the effective equilibrium reaction zone model and on an accurate P_2O_5-containing database [38,40]. The accuracy of the phosphorus distribution, L_p, between slag and molten metal calculated with the database is excellent, as seen in Figure 5.4.26.

5.4.4.4.1 Determination of the Reaction Zones

The BOF process was divided into two main periods [41]: the soft blowing period and the medium and hard blowing periods. During the soft blowing period, the oxygen lance is high, which promotes the oxidation of the metal surface. The decarburization rate is low. The reactions are limited to slag formation and reaction between slag and bulk hot metal. During the medium and hard blowing periods, the oxygen lance is low, which promotes the formation of a hot spot and the ejection of a significant amount of metal droplets in the slag. Effective decarburization and dephosphorization take place in the emulsion. Melting of scrap, flux, and other solids was taken into account throughout the process. The reaction zones that consider the reactions between hot metal, scrap, oxygen jet, slag, fluxes, metal droplets, and solid oxides are shown in Figure 5.4.27a and b for, respectively, the soft blowing period and the medium and hard blowing periods.

5.4.4.4.2 Model Validation

The model was validated with the industrial data reported by Cicutti *et al.* [42,43] which provides operating conditions and composition variations of slag and hot metal during the blow. The initial hot metal and scrap compositions, amount and temperature, flux addition and blowing conditions from the industrial process [42,43] were used as input for the model. The typical evolution of the hot metal and slag composition was reproduced with the kinetic model. Figures 5.4.28 and 5.4.29 show the results of the preliminary kinetic modeling using the effective equilibrium reaction zone model. Many aspects of the BOF

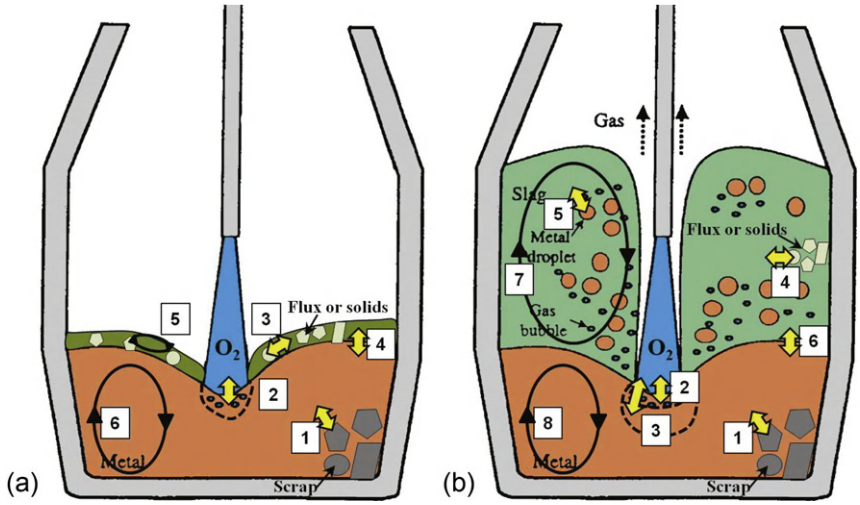


Figure 5.4.27 Schematic representation of the reaction zones in the BOF process: (a) soft blowing period and (b) medium and hard blowing periods [41].

process are successfully simulated: the evolution of the decarburization reaction, rapid Si oxidation, reversion of Mn and P (Figure 5.4.28a), slag and metal temperature, and slag chemistry change over the process (Figures. 5.4.28b and 5.4.29).

The results of the process simulation are in good agreement with the industrial measurements and observations [42,43]. At the beginning of the process, Si from the hot metal is quickly oxidized, forming a SiO_2 and FeO-rich slag. FeO originates from oxidation of the hot metal surface since the oxygen lance is high. Meanwhile, the CaO content in the slag increases progressively as the CaO flux dissolves into the slag. Mn and P are oxidized soon after. C removal from the hot metal takes place after an incubation period. Then, the FeO content in the slag drops as it is consumed by the decarburization reaction. Toward the half of the blowing period, Mn and P reverse from the slag to the metal, which is in agreement with the industrial observations reported by Cicutti *et al.* [42]. The predicted hot metal and slag temperatures at the end of the blow and the evolution of the slag mass during the process are in good agreement with practice. Also, the slag path (Figure 5.4.29) follows the general trend observed at the plant [43,44]. Such model is important to understand the changes in slag and metal compositions during the blow, such as P reversion, and propose alternatives to improve the process.

5.4.5. ROTARY CEMENT KILN MODEL

Thompson and Argent [45] built a kinetic model for a cement Kiln based on the thermodynamic data provided in the MTOX database and the MTDATA software

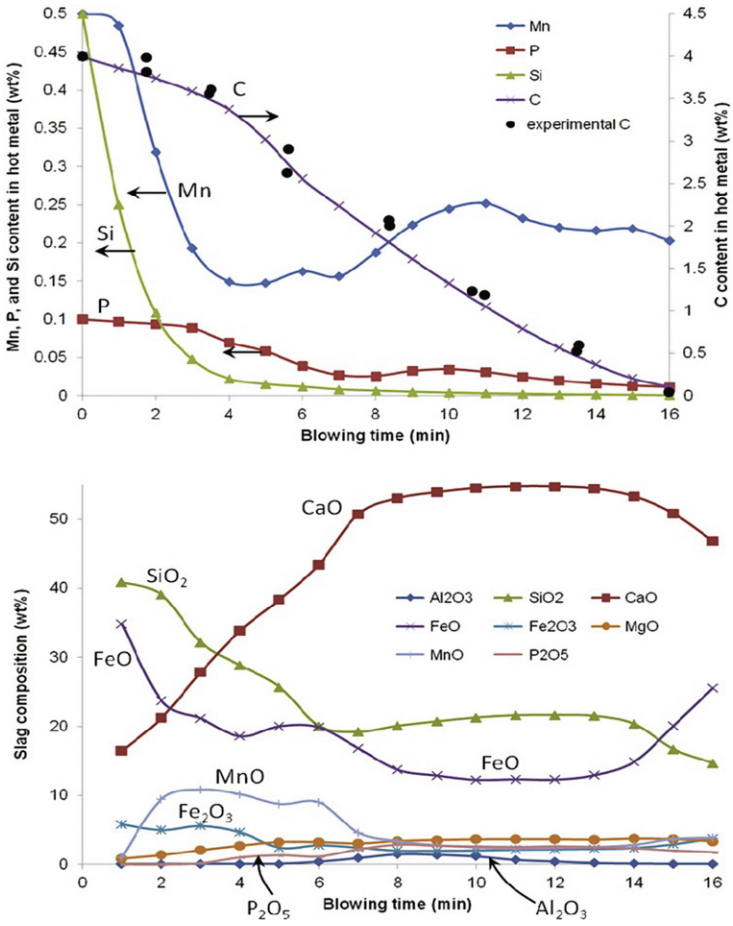


Figure 5.4.28 Simulation results of a typical BOF process using the effective equilibrium reaction zone model: (a) change in hot metal composition and (b) change in slag composition during the blow [39].

package. Portland cement is produced in rotary kilns, where the dried and preheated raw materials are heated to about 1200–1450 °C. The rotary kiln is a rotating cylindrical vessel, inclined at an angle of 3–4° to the horizontal, in which the raw materials are continuously fed into the upper end and fuel plus combustion air are fired at the lower end. As the kiln slowly rotates, the materials move gradually toward the lower end. The hot gasses pass along the kiln in the opposite direction as the materials, creating a continuous counter-current process. In the rotary kiln, the materials are partially melted and undergo chemical reactions resulting in the formation of the four main components of the Portland cement: tricalcium silicate ($3CaO{\cdot}SiO_2$), dicalcium silicate ($2CaO{\cdot}SiO_2$), tricalcium aluminate ($3CaO{\cdot}Al_2O_3$), and tetracalcium alumino-ferrite ($4CaO{\cdot}Al_2O_3{\cdot}Fe_2O_3$). Trace elements

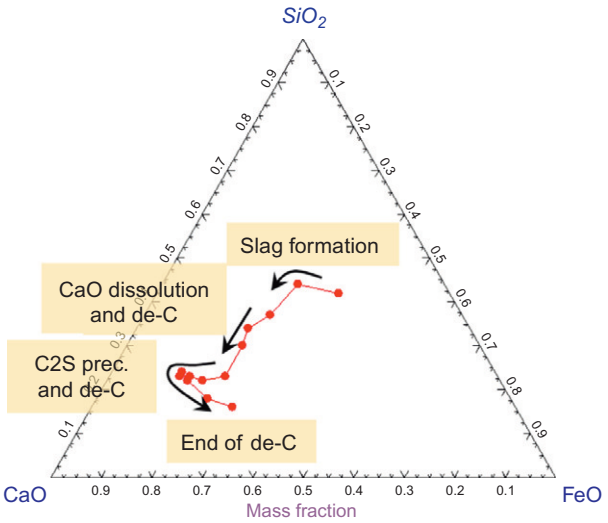


Figure 5.4.29 Calculated slag path during the BOF process [39].

such as Cr, Ni, Cd, Co, Cu, and Zn are naturally present in the raw materials and fuels. They can significantly affect the manufacturing process, the quality of the cement itself, and be potentially harmful to human health and the surrounding environment. These trace elements, by inducing a change in phase stability, can alter the fine balance of cement phases. Trace elements that volatilize significantly at the hotter end of the rotary kiln can condensate at the cooler end as they are transported by the combustion gases. They reenter the materials, creating a buildup of trace element in the rotary kiln. Therefore, Thompson and Argent [45] built a model of the cement phases that include the minor elements. They were treated as dilute components of a Henrian solution. Their solubility in the main cement phases were considered based on published data. The solution models and thermodynamic properties were taken from MTOX database, and transferred to FactSage to facilitate the implementation through the use of FactSage macro processing.

5.4.5.1. Description of the Model

In Thompson and Argent's model [45], the rotary kiln was divided into 16 zones depicted in Figure 5.4.30: zones 1–8 representing the raw materials transferred from the cooler (zone 1) to the hottest end (zone 8), and zones 9–16 representing the combustion gas transfer from the hottest end (zone 9) to the cooler end (zone 16). Bypass streams for gas and materials were created to consider the slow decomposition or reaction of certain species. The material zones add material to the adjacent gas zone (toward hotter end) and the gas zone deposits material in the next material zone (toward cooler end). The process is then iterated.

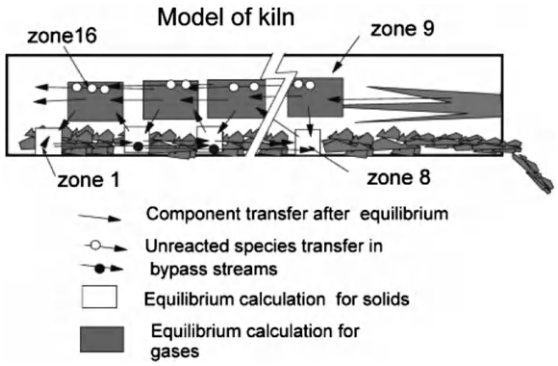


Figure 5.4.30 Concept of rotary kiln model [45].

FactSage Equilibrium calculations combined with an Excel spreadsheet were used to represent each computational zone of the rotary kiln. The Excel spreadsheet contained the input composition and the fractions to be passed to the bypasses (gas and solids) and to the adjacent zones (gas and solids). The temperatures in the computational zones are based on informed guesses.

5.4.5.2. Results of the Rotary Kiln Model

Based on the model results, the behavior of mobile elements was predicted and compared to laboratory tests results and reports from full scale cement plants. Significant potassium buildup in the kiln was predicted, as illustrated in Figure 5.4.31a. Potassium is retained as the species $K_2Ca_2(SO_4)_3$ until the formation of $3CaO{\cdot}SiO_2$. Sodium concentration was found to buildup too (Figure 5.4.31b), but to a lesser extent than potassium. Chlorine was largely transferred to the gas (Figure 5.4.31c). A little zinc buildup was reported with a limited degree of volatilization as element (Figure 5.4.31d). Similar immobility was observed for chromium and nickel. The buildup of potassium, sodium, and zinc was increased when taking into account the transfer of solids from the feedstock to the gas. The predicted behavior of the trace elements was found to be in excellent agreement with the experimental observations.

5.4.6. KINETIC SIMULATION OF LADLE REFINING AND SMELTING USING SOFTWARE

5.4.6.1. METSIM

METSIM is a chemical and metallurgical process simulation program designed to perform detailed mass and energy balances, chemical reactions, process controls, equipment sizing, operating cost estimations, and process analysis [46,47]. It is capable of performing dynamic simulations for many diverse processes. METSIM is programmed in APL,

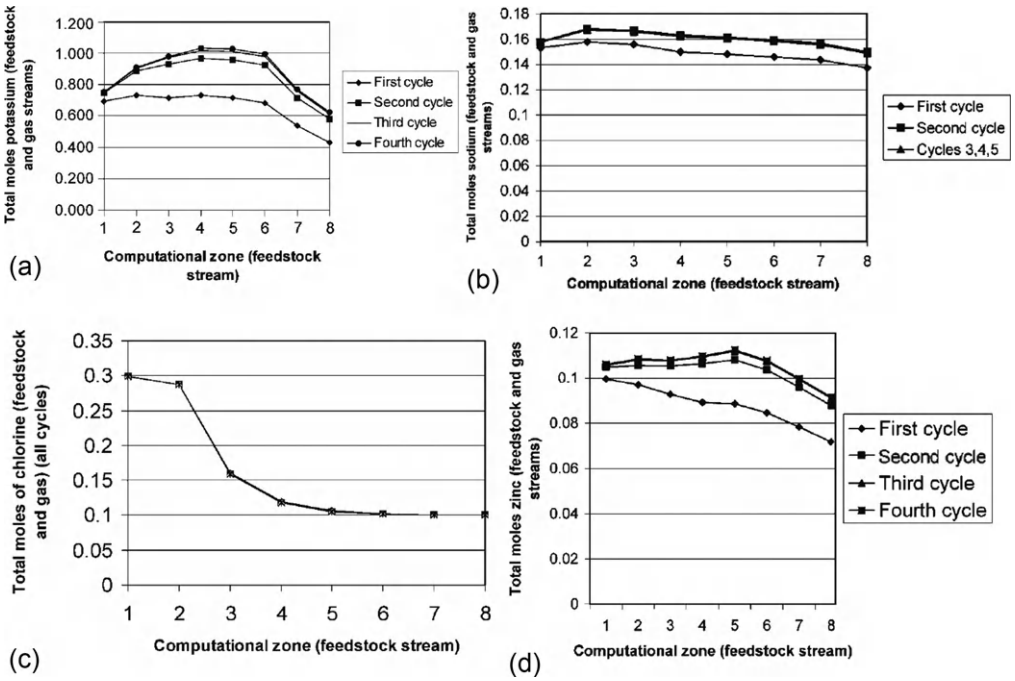


Figure 5.4.31 Total (a) potassium, (b) sodium, (c) chlorine, and (d) zinc in feedstock zone and adjacent combustion gas zone [45].

which provides interactive and fast calculation capabilities. The sequential modular approach is employed to solve the set of equations.

METSIM has a long list of users worldwide. However, published process modeling studies using METSIM are limited compared to the number of users. METSIM has a wide range of applications including ore concentrators [48–51], gold and copper heap leaching [52–55], zinc leaching [56], lead desilverizing by zinc [57], carbon dioxide sequestration [58–60], iron chloride pyrohydrolysis [61], smelting of copper concentrates [62–64], nickel and chromium smelting [65–67], ferromanganese smelting [68–70], and ironmaking [71] and steelmaking [72–75] processes. METSIM is employed in the role of process feasibility studies, pilot plant data evaluation, full scale plant design, operating plant improvements, actual plant operations, and alternative flowsheet evaluations.

A detailed model of a complex process can be easily constructed by linking unit operation modules in a flowsheet. More than 200 unit operations are available in METSIM, each of them containing a complete mathematical model of that particular unit operation. Unit operations are linked by streams that transfer matter and energy. METSIM can handle multiphase, high temperature systems that are undergoing phase changes and chemical reactions. Solids, molten metals, slags, mattes, and gases can be accommodated in METSIM. Standard unit operations include the stream mixer, splitter for streams,

splitter for phases, Gibbs free energy minimizer (FEM), etc. Chemical reactions must be specified for each unit operation and must be written in the order in which they will be performed. The degree of conversion of each reaction must also be specified by the user. In the Gibbs FEM unit operation, the chemical reactions do not need to be entered. Chemical equilibrium is calculated by minimizing the Gibbs free energy. This unit operation should only be used when the actual conditions can be approximated by equilibrium. In conformance with the sequential modular approach, METSIM solves the equations subset for each module, allowing for an individual analysis of each unit operation in the flowsheet. Each module calculates the output streams, which can be passed as input streams for the next process step. The program provides a graphical representation of the flowsheet.

Users can easily define input and output interfaces, process controllers, incorporate thermodynamic data and solution models, etc. The program is supplied with an extensive database of components for which chemical and thermodynamic data are provided. The users can upgrade, customize, and expand the database according to their needs. Solution densities, which are essential in hydrometallurgical processes, can be calculated based on specific gravity functions and database in METSIM.

In the present section, two kinetic models using METSIM will be described. The first one presents ladle refining simulation as a part of the secondary steelmaking process [75] and the second one is dedicated to modeling of the ferromanganese smelting process [68,69].

5.4.6.2. Simulation of Ladle Refining at Two Ladle Metallurgy Furnaces

Peter *et al.* [75] modeled and simulated the ladle refining at two different Ladle Metallurgy Furnaces (LMF's). The mass transfer rate constants of twenty heats were determined based on the METSIM model. The effect of the argon flow rate, ladle geometry, ambient pressure, and steel temperature on the reaction kinetics was investigated.

The primary functions of the LMF (also called ladle arc furnace or ladle furnace) are temperature adjustment achieved by electric power through graphite electrodes, homogenization of temperature and chemistry through inert gas stirring, alloy additions, desulfurization, dephosphorization, inclusion removal and modification, as well as buffer for downstream steelmaking equipments. Gas stirring is provided by porous plugs at the bottom of the ladle. Fumes are collected by a hood mounted on the water-cooled roof of the LMF. The graphite electrodes are lowered into the slag layer, above the molten steel surface.

5.4.6.2.1 Description of the Kinetic Model

The model of the ladle built by Peter *et al.* [75] was created by using the Gibbs FEM, stream mixer, and splitter modules from METSIM. Streams carry the material flow between the modules. The METSIM model of the LMF is illustrated in

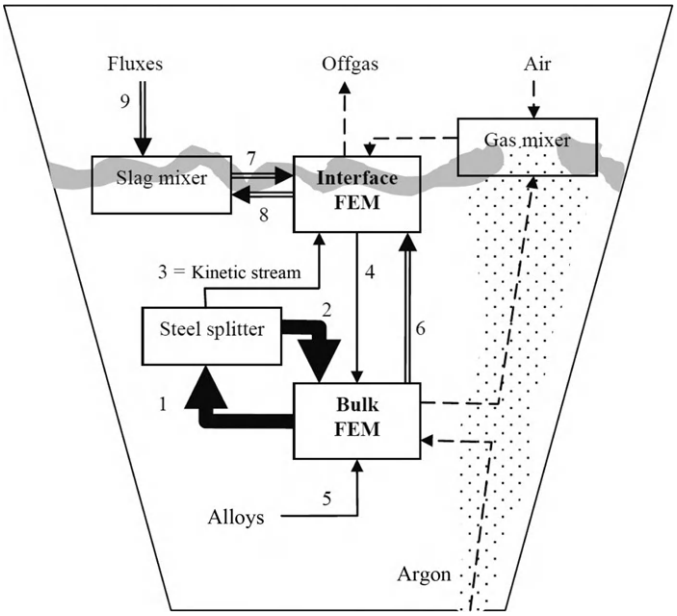


Figure 5.4.32 Illustration of METSIM model used for simulation of steel treatment in the ladle [75].

Figure 5.4.32. Two interface Gibbs FEM modules were created to calculate the reactions at the slag/steel interface (Interface FEM) and the reactions in the bulk steel (Bulk FEM). Activity coefficients were obtained from FactSage calculations after numerous iterations of the METSIM simulations. Some activity coefficients, such as that of FeO, were changed during the calculations. The pressure was set at 1.3 atm in the bulk steel and 1 atm at the slag/metal interface, and the temperature was that measured during the trials.

Streams 1 and 2 in Figure 5.4.32 represent the bulk flow of steel which does not take part in the reaction with the slag during one calculation. Stream 3 (Kinetic stream) corresponds to the fraction of steel reacting with the slag and is the product of the total steel mass and the mass transfer rate constant. The latter was adjusted within the model until the calculated concentrations agreed with the measured data for all components of the steel and slag. The steel flow after reaction with the slag is sent back to the bulk and is represented by stream 4. Alloys are added to the bulk steel through stream 5. The removal of nonmetallic inclusions from the bulk to the steel/slag interface is represented by stream 6. Slag is carried between the Interface FEM and the slag mixer by streams 7 and 8. Gas streams are represented by dashed lines. Fluxes additions are carried out by means of stream 9.

Based on previous studies and plant observations, argon stirred ladles were found to enable the formation of large slag/steel emulsions and to provide vigorous mixing of the slag. The limiting factors for reaction kinetics under such conditions are the bulk

transport of the steel to the slag/steel interface and the thermodynamic equilibrium at the slag/steel interface. The overall mass transfer rate constant is determined by the mass transfer rate within the steel.

5.4.6.2.2 Simulation Results

The METSIM simulation results were compared to two representative heats from each LMF, LMF1 and LMF2, in terms of change of slag and steel composition during the treatment. The comparison is shown in Figure 5.4.33. The simulations could reproduce very well the measured steel and slag concentrations for all heats.

LMF1 represents the treatment of an Al-killed steel (Figure 5.4.33a–d) stirred with 50 standard cubic feet per min (scfm). Al was added during the first 3 min of the treatment. Lime additions were performed after the 1st, 8th, and 15th min to aid the desulfurization reaction. Desulfurization actively took place during the first 5 min (Figure 5.4.33a), when the FeO content of the slag decreased due to the Al addition (Figure 5.4.33c). The decrease in Al content of the steel (Figure 5.4.33a) was reproduced by the addition of Fe_2O_3 in the model. The C and P contents of the steel remained unchanged during the treatment (Figure 5.4.33a), whereas the Si and Mn contents in the steel slightly increased (Figure 5.4.33a and b) through the reduction of SiO_2 and MnO from the slag by Al (Figure 5.4.33c and d). According to the plant data (Figure 5.4.33a), reversion of Si was observed around the 8th min, which could not be reproduced in the simulations. The large variation in the measured total O was attributed to slag entrapment in steel (Figure 5.4.33b). The N content in steel slightly increased due to the formation of an open-eye (Figure 5.4.33b).

Si-deoxidized steel was produced in LMF2 with 7 scfm stirring. The N content in steel was found to increase at the same rate ($\sim$0.25 ppm min^{-1}) as in LMF1 (Figure 5.4.33f), though the stirring intensity is much lower. The variation of the measured total O in Figure 5.4.33f is less than that in LMF1 (Figure 5.4.33b), which could indicate a more significant slag/steel emulsification with increasing the stirring intensity. C boiling was achieved during the first 7 min of the treatment (Figure 5.4.33e), where Ar stirring and lime addition was carried out. The FeO content of the slag was predicted to increase during that period (Figure 5.4.33g). SiMn, FeSi, spar and lime were added at the 7th min, resulting in a decrease of the FeO content of the slag (Figure 5.4.33g). The C and P contents increased due to their occurrence in the SiMn and FeSi alloys (Figure 5.4.33e). P reversion from the slag occurred simultaneously (Figure 5.4.33g). The onset of the desulfurization reaction took place around the 12th min when the FeO content in slag was sufficiently low (Figure 5.4.33e). V and MgO were incorporated after the 14th min (Figure 5.4.33f and h). Fe_2O_3 was added in the model at the 20th min to reproduce the sudden fall of part of the skull from the LMF roof into the steel. The Fe_2O_3 addition caused a decrease in the Si content of steel and a slowdown of the desulfurization rate (Figure 5.4.33e). CaSi wire was added as counter-measure 2 min later.

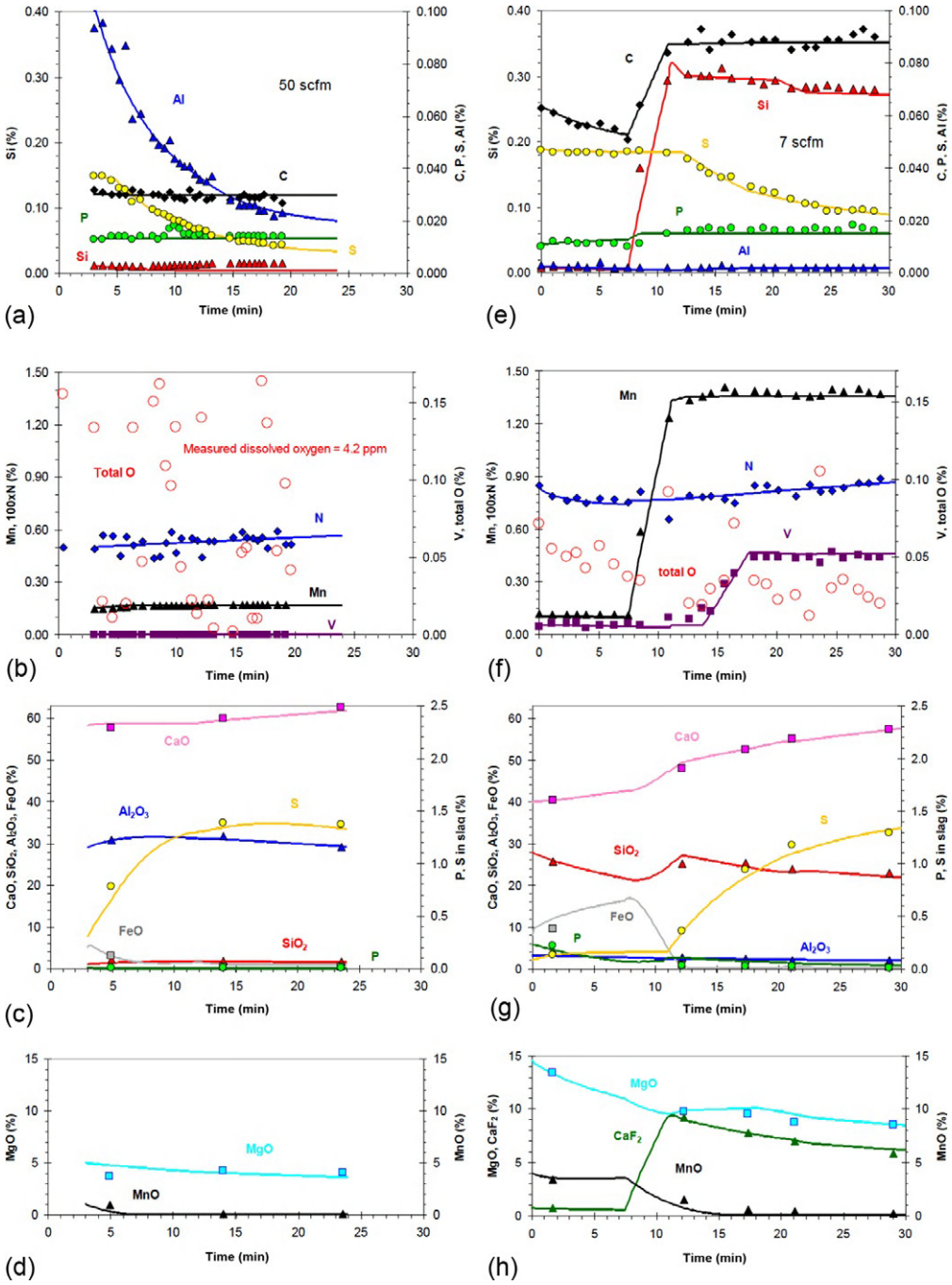


Figure 5.4.33 Comparison between measured data (markers) and METSIM simulation results (continuous lines) from (a) to (d) LMF1 and (e) to (h) LMF2 [75].

The calculated mass transfer rate constants were 0.18 and 0.06 min^{-1} for, respectively, LMF1 and LMF2. Based on the comparison of the mass transfer rate constants for the 20 heats, Peter *et al.* [75] reported that the specific stirring power was mainly function of the Ar flow rate and steel mass, as the other factors such as ambient pressure, absolute temperature, and injection depth were identical or varied little between the heats. The relationship between the mass transfer rate constant and the stirring power was described by a power function with an exponent of 0.47, which is in good agreement with power functions by previous researchers.

A dimensional analysis was carried out, during which a square-root relationship between the mass transfer rate constant and the argon flow rate was predicted. The results of the dimensional analysis provided a better description of the relationship between the mass transfer rate constant (k) and the argon flow rate (Q), steel mass (m), steel temperature (T), top area of ladle (A_{top}), number of porous plugs ($N^{1/4}$), injection depth of Ar (h) and ambient pressure (P_0) according to the following relation:

$$k = \frac{0.08}{m}\sqrt{14.23\frac{QTA_{top}}{N^{1/4}}\log_{10}\left(1+\frac{h}{1.5P_0}\right)}.$$

Thermodynamic equilibrium at the slag/steel interface also affects the reaction kinetics during ladle refining. Different desulfurization rates were observed for heats with similar mass transfer rate constant. FeO has to be reduced by the deoxidant (Al) for the desulfurization reaction to proceed. The desulfurization rates were found to increase if the FeO in slag is reduced before the slag basicity is increased by lime addition. Lime addition lowers the activity coefficient of FeO, slowing down the reduction of FeO by Al.

This experimental and kinetic study is a good example of an approach to kinetic modeling of a complex process combined with METSIM process simulation software and FactSage thermodynamic calculations. The results of the simulations allowed deriving mass transfer rate constants and obtaining a greater understanding of the relationship between common production conditions and the reaction kinetics during ladle refining. The refining time can be decreased and the slag composition can be optimized to maximize the desulfurization rate.

5.4.6.3. Simulation of the Ferromanganese Smelting Process

The ferromanganese smelting process commonly consists in the carbothermic reduction of manganese and iron oxides from ores in submerged electric arc furnaces [76]. Blending of ores from different sources to obtain a specific Mn to Fe ratio is a common practice. Carbonaceous agent (typically coke) and fluxing materials such as limestone and/or dolomite are fed with the ores in the furnace. The role of the fluxing materials is to provide suitable chemical properties, smelting temperature, and viscosity of the slag for good

furnace operation and high manganese recovery. The control of the ferromanganese slag composition is crucial as it determines the slag/metal equilibrium relations including the MnO content in slag and the manganese yield. High carbon ferromanganese is produced in the submerged arc furnace, and typically contains around 78 wt% Mn and 7 wt% C. A further refining step is performed to obtain medium and low carbon ferromanganese alloys.

The furnace is divided in a low temperature pre-reduction zone, where the higher oxides of Mn are reduced in solid state to Mn_3O_4 and MnO by CO(g), and the high temperature coke bed zone. In the coke bed zone, the pre-reduced ores and fluxes melts around 1250–1300 °C to form a ferromanganese slag, whereas coke remains solid. After further reduction by C, the metal is collected at the bottom of the furnace where it is tapped with the slag. Reduction of other minor elements (Si, P, etc.) also occurs in the furnace.

The reactions taking place in the process are complex. Temperatures, CO/CO_2 ratios in the gas, chemical reactions can vary greatly in the different zones of the furnace.

5.4.6.3.1 Development of the Multistage Reactor Model for Ferromanganese Smelting

In Li *et al.*'s multistage reactor model for the ferromanganese smelting process [68,69], the furnace was divided into four major zones. Each zone was represented by a different unit operation with its individual chemical reactions to represent the typical reaction zones in the ferromanganese furnace. The schematic diagram of the model is shown in Figure 5.4.34.

Zone 1 (OP4 in Figure 5.4.34) represents the drying and calcining zone, where drying, reduction of MnO_2 to Mn_2O_3 and decomposition of $MgCO_3$ take place. The pre-reduction zone (OP6 in Figure 5.4.34) is assigned to zone 2, where reduction of Fe_2O_3 to Fe_3O_4 and partly to FeO, reduction of Mn_2O_3 to Mn_3O_4 and partly MnO, and condensation of vapor species such as K, Mn, and Mg occur. Direct reduction of all Fe_3O_4 to FeO and partly to Fe, reduction of all Mn_3O_4 to MnO, condensation of vapor species such as K, Mn, and Mg, and decomposition of $CaCO_3$ take place in zone 3, the direct reduction zone (OP8 in Figure 5.4.34). Zone 4, the smelting reduction zone or hearth zone (OP10 in Figure 5.4.34), consists in the reduction of all FeO to Fe and most of the MnO to Mn, reduction of small amount of SiO_2, and formation of ferromanganese and slag phases. Zones 1–3 were defined as splitter for phases (SPP) unit operations in METSIM. The thermodynamic data for all species included in the model were taken directly from the METSIM database. A FEM unit operation was used to define zone 4.

As illustrated in Figure 5.4.34, a total of 14 unit operations (OP1 to OP14 in Figure 5.4.34) were defined to simulate the furnace and were connected by 81 streams to allow material and gases to flow. In addition to the four core zones of the process described above (OP4, OP6, OP8, and OP10), the other 10 unit operations were designed to mix the raw materials (OP1 and OP2 in Figure 5.4.34), and to simulate

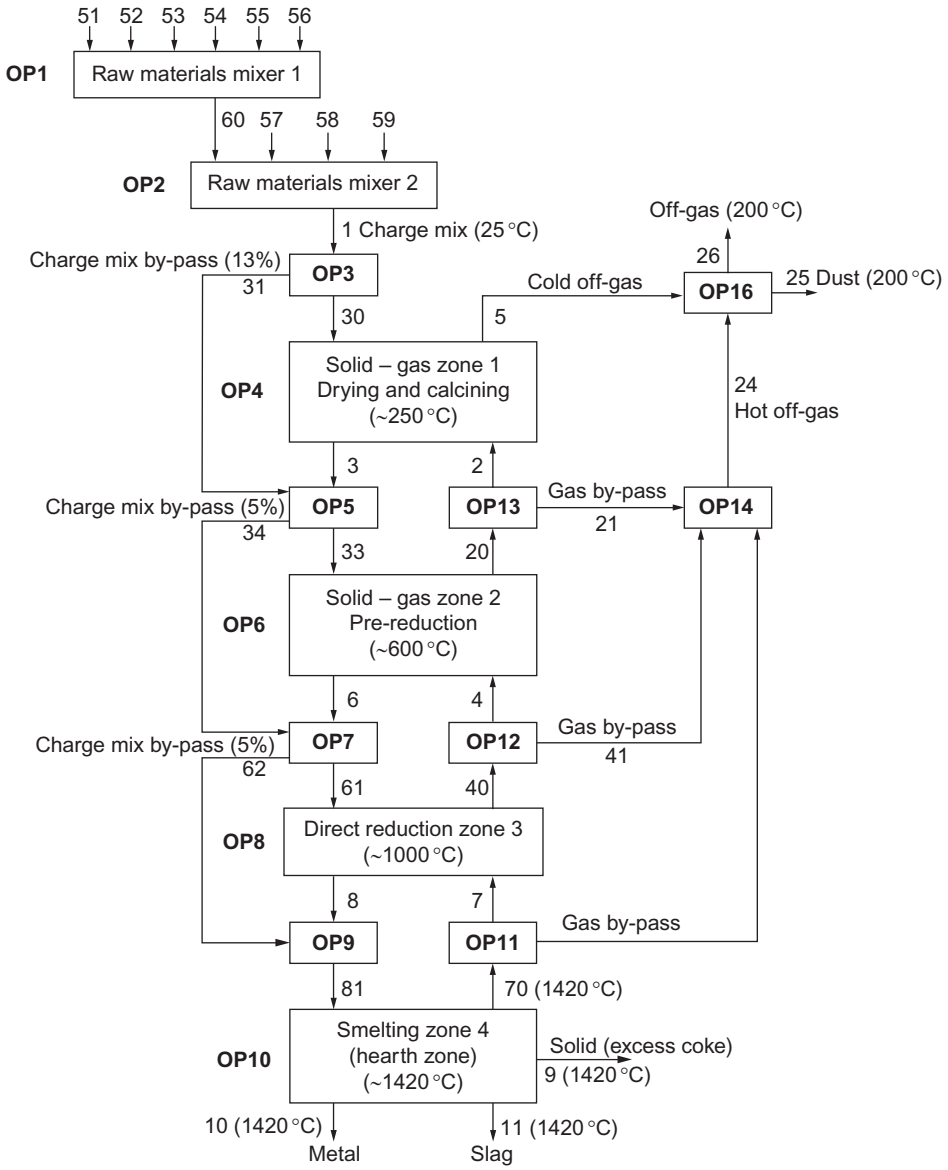


Figure 5.4.34 Schematic diagram of the process model for ferromanganese smelting [68,69].

the by-pass of solids (OP3, OP5, and OP7) and gases (OP9, OP11, OP12, and OP13) from the upper zone to the lower zones without taking part in the reactions. Chemical reactions in the gas by-pass were represented by a unit operation (OP14), where reactive species such as K form dusts upon cooling in the upper part of the furnace. It was assumed that the dusts are fine and removed from the furnace by the off-gas. These 10 unit

operations were incorporated in the METSIM model by splitter for streams (SPS) unit operations.

The chemical reactions in splitter for phases and splitter for streams unit operations need to be defined within the unit operation for METSIM to calculate the chemical reactions. These calculations are performed sequentially according to the reaction order and the conversion degree defined by the user. In zone 4, the chemical reactions are not specified since the equilibrium calculations are based on Gibbs free energy minimization (FEM unit operation). Nonideal solution models were employed for the slag and metal phases in zone 4 (hearth zone): the Cell model for the slag phase and the Unified Interaction Parameter Model (UIPM) for the metal phase. As METSIM does not include nonideal solution models, activity coefficient equations for the species in both slag and metal phases derived from the Cell model and UIPM were coded in the reactor model.

5.4.6.3.2 Results of the Kinetic Simulation

The calculated metal and slag compositions, and the distribution of Mn, K, P, and As between metal, slag, and dust were compared with plant data [69]. The hearth temperature was set at 1400 °C. As seen in Tables 5.4.9 and 5.4.10, the agreement between the model calculations and the plant data was fairly good. The model calculations also predicted the recirculation of K inside the furnace. The K content in the solid mix coming down to the earth zone was predicted to be, at steady state, 10 × larger than that in the raw materials, which is in good agreement with plant data.

Table 5.4.9 Comparison Between Calculated and Measured Metal and Slag Compositions (wt%) [69]

Metal	Mn	Fe	C	Si	P	As	
Calculated	80.14	12.62	6.78	0.14	0.21	0.11	
Plant data	79.5	12.4	6.9	0.2	0.2	0.07	
Slag	**MnO**	**SiO_2**	**Al_2O_3**	**CaO**	**MgO**	**K_2O**	**BaO**
Calculated	50.62	19.54	22.71	1.69	1.25	3.14	1.01
Plant data	48.85	19.35	22.77	1.67	0.60	3.10	0.96

Table 5.4.10 Comparison Between Calculated and Measured Distribution of Mn, K, P, and As (wt%) [69]

Element	Calculated			Plant data		
	Metal	Slag	Dust	Metal	Slag	Dust
Mn	76.89	21.49	1.62	75.27	18.94	1.98
K	0.00	85.75	14.25	0.00	87.54	12.46
P	88.05	0.00	11.95	87.01	0.00	12.99
As	88.43	0.00	11.57	88.87	0.00	11.13

Various aspects of the ferromanganese smelting process were investigated with the model. In Li *et al.*'s study [68], the influence of the hearth temperature and gas by-pass ratios on the process performance in terms of slag and metal amount and compositions, distribution of elements between phases and energy consumption were investigated. Typical raw materials charge at the plant was used in the simulations.

Three hearth temperatures (1350, 1420, and 1500 °C) were selected based on the hearth temperature profile given in literature (~1500 °C at the electrode and ~1350 °C at the furnace wall). The gas and solid by-pass ratios were fixed at 5%. An increase of the hearth temperature resulted in an increased hearth gas volume and amount of gaseous K, Mn, and SiO, and an increased recirculation of K inside the furnace. According to the simulation results, at 1350 °C, the degree of reduction is low due to the low temperature, resulting in a low Si concentration in metal (0.01 wt%), high MnO and K_2O content in slag, and high slag and low metal amounts. As a result of the limited reduction at 1350 °C, the coke fed in the furnace was not completely consumed, resulting in a buildup of coke in the coke bed. In contrast, at 1500 °C, the simulation predicted a high degree of reduction, resulting in a high Si content in metal (0.6 wt%), low MnO and K_2O in slag, and low slag and high metal amounts. Under these conditions, the coke bed was found to be completely consumed by the reduction reactions, leaving insufficient amount of C to saturate the metal. The calculations results at 1420 °C were found to represent better the plant data.

Based on the simulation results and the temperature profile in the hearth, an estimation of the phase distribution and composition through the furnace was obtained. The results indicated that the coke bed would be consumed and the metal would be richer in Si in the area near the electrode as a result of the high temperature. Near the furnace wall, where the temperature is lower, solid coke and MnO-rich slag would be present.

Three values of the gas by-pass ratio, 0%, 5%, and 10%, were selected to investigate its effect on the process outputs with a fixed hearth temperature of 1420 °C. With a higher gas by-pass ratio, a larger fraction of gaseous species such as K leaves the furnace as dusts in the off-gas without taking part in the reactions. The K recirculation is, therefore, maximum when the gas by-pass ratio is 0% since a larger fraction of the gaseous K reacts with CO_2, condensates in the colder zone of the furnace and reenters the hearth. For that reason, the concentration of K in the hearth gas and in the slag is the highest when the gas by-pass ratio is 0%. At steady state, the calculated K content in the solids entering the hearth zone reaches 18.6 wt% without gas by-pass, against 7.7 wt% with a gas by-pass ratio of 10% and 1 wt% in the raw materials. Due to the increased consumption of C to reduce K_2O to K(g) when the gas by-pass ratio is low, less C is available for reducing MnO. The slag amount and the MnO content in the slag are higher at lower gas by-pass ratio.

The ferromanganese smelting process was successfully simulated using a multistage reactor model and the METSIM metallurgical simulator. The results of the simulation

show reasonable agreement with plant data. The effect of the hearth temperature and the gas by-pass ratio could be investigated and quantified. These two parameters were found to have a significant effect on the K recirculation in the furnace.

REFERENCES

[1] G. Eriksson, T. Johansson, Scand. J. Metallurgy 7 (1978) 264–270.
[2] S. Petersen, K. Hack, P. Monheim, U. Pickartz, Int. J. Mat. Res. 98 (10) (2007) 946–953.
[3] P. Koukarri, R. Pajarre, K. Hack, III.5 Setting Kinetic Controls for Complex Equilibrium Calculations, second ed., The SGTE Casebook—Thermodynamics at WorkWoodhead Publishing, 2008, pp. 359–367.
[4] G. Eriksson, Chem. Scr. 8 (1975) 100.
[5] K.J.D. McKenzie, Trans. J. Brit. Ceram. Soc. 74 (1975) 77.
[6] FACT database Edition 2001, in FactSage 5.0, CRCT, Montreal, Canada and GTT Technologies, Herzogenrath, Germany, 2001.
[7] M. Ketonen, P. Koukkari, PenttiläK., in: The European Control Conference, ECC 97, Brussels, Belgium 1–4 July, 1997.
[8] P. Koukkari, S. Liukkonen, Industrial & Engineering Chemistry Research 41 (12) (2002) 2931.
[9] P. Koukkari, R. Pajarre, Comput. Chem. Eng. 30 (2006) 1189.
[10] P. Koukkari, Computers Chem. Engng. 17 (12) (1993) 1157.
[11] B. Karlemo, P. Koukkari, J. Paloniemi, Plasma Chemistry Plasma Proc. 16 (1996) 59.
[12] S.E. Pratsinis, H. Bai, M. Frenkloch, S.V.R. Mastrangelo, J. Am. Ceram. Soc. 73 (1990) 2158.
[13] P. Koukkari, M. Keegel, K. Penttilä, in: K. Hilpert, F.W. Froben, L. Singheiser (Eds.), High Temperature Materials Chemistry, Schriften des Forschungszentrum Julich, 15, Part I, 2000, p. 253.
[14] P. Koukkari, J. Niemelä, Computers Chem. Eng. 21 (3) (1996) 245.
[15] I. Barin, M. Modigell, F. Sauert, Metall. Trans. B 18 B (1987) 347–354.
[16] V.I. Baptizmanskii, et al., Steel in the USSR 8 (1973) 634–638.
[17] S. Asai, I. Muchi, Transactions ISIJ 10 (1970) 250–263.
[18] A.I. van Hoorn, J.T. van Konyenburg, P.J. Kreyger, in: W.-K. Lu (Ed.), Role of slag in basic oxygen steelmaking, McMaster University Press, Hamilton, Ontario, 1976.
[19] K. Koch, W. Fix, P. Valentin, Archiv für das Eisenhüttenwesen 47 (10) (1976) 583–588.
[20] M.-A. Van Ende, Y.-M. Kim, M.-K. Cho, J.H. Choi, I.-H. Jung, Metall. Mater. Trans. B 42B (2011) 477.
[21] C.W. Bale, E. Bélisle, P. Chartrand, S.A. Decterov, G. Eriksson, K. Hack, I.H. Jung, Y.B. Kang, J. Melançon, A.D. Pelton, C. Robelin, S. Petersen, Calphad 33 (2009) 295.
[22] D.H. Hubble, R.O. Russell, H.L. Vernon, R.J. Marr, in: R.J. Fruehan (Ed.), The Making, Shaping and Treating of Steel, AISE Steel Foundation, Pittsburgh, PA, 1998, p. 285.
[23] T. Kuwabara, K. Umezawa, K. Mori, H. Watanabe, Trans. ISIJ 28 (1988) 305.
[24] R. Tsujino, J. Nakashima, M. Hirai, I. Sawada, ISIJ Int. 29 (1989) 589.
[25] Y. Kato, H. Nakato, T. Fujii, S. Ohmiya, S. Takatori, ISIJ Int. 33 (1993) 1088.
[26] Y.G. Park, W.C. Doo, K.W. Yi, S.B. An, ISIJ Int. 40 (2000) 749.
[27] Y.G. Park, K.W. Yi, ISIJ Int. 43 (2003) 1403.
[28] S.K. Ajmani, S.K. Dash, S. Chandra, C. Bhanu, ISIJ Int. 44 (2004) 82.
[29] J.F. Domgin, P. Gardin, H. Saint-Raymond, F. Stouvenot, D. Huin, Steel Res. Int. 76 (2005) 5.
[30] J.H. Wei, H.T. Hu, Steel Res. Int. 77 (2006) 32.
[31] D.Q. Geng, H. Lei, J.C. He, Metall. Mater. Trans. B 41 (2010) 234.
[32] M.K. Cho, M.A. Van Ende, T.H. Eun, I.H. Jung, J. Eur. Ceram. Soc. 32 (2012) 1503.
[33] M.A. Van Ende, Y.M. Kim, M.K. Cho, J. Choi, I.H. Jung, in: The 6th European Oxygen Steelmaking Conference, Jernkontoret, 2011, p. 3.14.
[34] S. Kitamura, K. Miyamoto, R. Tsujino, Tetsu-To-Hagané 80 (1994) 101.
[35] S. Kitamura, M. Yano, K. Harashima, N. Tsutumi, Tetsu-To-Hagané 80 (1994) 213.
[36] T. Kitamura, K. Miyamoto, R. Tsujino, S. Mizoguchi, K. Kato, ISIJ Int. 36 (1996) 395.
[37] H. Saint-Raymond, D. Huin, F. Stouvenot, Mater. Trans. JIM 41 (2000) 17.

[38] I.H. Jung, P. Hudon, W.Y. Kim, M.A. Van Ende, M. Rahman, G.G. Curiel, High Temp. Mater. Processes 32 (2013) 247.
[39] I.H. Jung, M.A. Van Ende, W.Y. Kim, CAMP-ISIJ 25 (2012) 199.
[40] I.H. Jung, P. Hudon, J. Am. Ceram. Soc. 95 (2012) 3665.
[41] M.A. Van Ende, I.H. Jung, Montreal, Canada, unpublished research, 2011.
[42] C. Cicutti, M. Valdez, T. Pérez, J. Petroni, A. Gomez, R. Donayo, L. Ferro, in: S. Seetharaman, S. Du (Eds.), Sixth International Conference on Molten Slags, Fluxes and Salts, Division of Metallurgy, KTH, Stockholm, Sweden, 2000, p. 367.
[43] C. Cicutti, M. Valdez, T. Pérez, R. Donayo, J. Petroni, Lat. Am. Appl. Res. 32 (2002) 237.
[44] S. Basu, A.K. Lahiri, S. Seetharaman, J. Halder, ISIJ Int. 47 (2007) 766.
[45] D. Thompson, B.B. Argent, Trans. Inst. Min. Metall. Sect. C: Miner. Process. Extr. Metall. 116 (2007) 115.
[46] METSIM Process Simulator. http://www.metsim.com (accessed February 2013).
[47] METSIM—Chemical & Metallurgical Process Simulation. http://members.ozemail.com.au/ozmetsim/ (accessed February 2013).
[48] C. Panaou, M. Bellino, M. Greyling, in: D.G. Nixon, M.J. Dry (Eds.), Proceedings of the International Symposium on Computational Analysis in Hydrometallurgy, Canadian Institute of Mining, Metallurgy and Petroleum, Montreal, QC, 2005, p. 145.
[49] P.C. Hernandez, M.E. Taboada, T.A. Graber, H.R. Galleguillos, Ind. Eng. Chem. Res. 48 (2009) 10522.
[50] J.P. Glynn, Randol Gold Forum Vancouver '92, Randol Int, Golden, CO, 1992, p. 101.
[51] N. Haque, T. Norgate, W. Bruckard, Publ. Australas. Inst. Min. Metall. 7/2010 (2010) 3217.
[52] J. Bartlett, F.L. Bazzanella, in: G.V. Jergensen II (Ed.), Copper Leaching, Solvent Extraction, and Electrowinning Technology, Society for Mining, Metallurgy, and Exploration, Littleton, CO, 1999, p. 3.
[53] L.M. Dufour, D.M. Hladun, Randol Gold Forum '96, N. McPherson Nilles (Ed.), Randol International, Golden, CO, 1996, p. 221.
[54] V.F. Swanson, Publ. Australas. Inst. Min. Metall. 7/94 (1994) 69.
[55] M. Botz, A. Kaczmarek, S. Orser, Miner. Metall. Process. 28 (2011) 133.
[56] G. Holcroft, L. Rosato, S. Seyer, in: V.G. Papangelakis, G.P. Demopoulos (Eds.), Int. Symp. Modell., Simul. Control Hydrometall. Processes, The Canadian Institute of Mining, Metallurgy and Petroleum, Montreal, QC, 1993, p. 93.
[57] T.R.A. Davey, K.J. Charlesworth, J.T. Bartlett, in: R.G. Reddy, R.N. Weizenbach (Eds.), The Paul E. Queneau International Symposium on Extractive Metallurgy of Copper, Nickel and Cobalt—Vol. 1: Fundamental Aspects, Miner. Met. Mater. Soc., Warrendale, PA, 1993, p. 153.
[58] V.L. Richards, C.H. Rawlins, S.N. Lekakh, K.D. Peaslee, in: N.R.R. Neelameggham, G. Ramana (Eds.), Carbon Dioxide Reduction Metallurgy, Proceedings of a Symposia Held During the TMS 2008 Annual Meeting & Exhibition, Minerals, Metals & Materials Society, Warrendale, PA, 2008, p. 95.
[59] S.N. Lekakh, D.G.C. Robertson, C.H. Rawlins, V.L. Richards, K.D. Peaslee, Metall. Mater. Trans. B 39 (2008) 484.
[60] J.-Q. Shi, S. Durucan, M. Fujioka, Int. J. Greenhouse Gas Control 2 (2008) 47.
[61] K. Adham, C. Lee, D. Small, in: J.E. Dutrizac, P.A. Riveros (Eds.), Iron Control Technologies, Proceedings of the International Symposium on Iron Control in Hydrometallurgy, Canadian Institute of Mining, Metallurgy and Petroleum, Montreal, QC, 2006, p. 815.
[62] P. Chamveha, K. Chaichana, A. Chuachuensuk, S. Authayanun, A. Arpornwichanop, Ind. Eng. Chem. Res. 48 (2009) 1120.
[63] C. Caballero, A. Moyano, P. Morales, C. Toro, H. Jara, L. Guzman, R. Diaz, in: J. Kapusta, T. Warner (Eds.), International Peirce-Smith Converting Centennial Held During the TMS 2009 Annual Meeting & Exhibition, Minerals, Metals & Materials Society, Warrendale, PA, 2009, p. 263.
[64] H. Joshi, S. Thakre, B. Basu, D. Shah, S. Chauhan, R.S. Chugh, K. Khandelwal, Copper 2010, GDMB Informations GmbH, Clausthal-Zellerfeld, Germany, 2010, p. 2381.
[65] A.G. Hunt, E.J. Grimsey, N.B. Gray, Publ. Australas. Inst. Min. Metall. 7/91 (1991) 251.
[66] T.E. Norgate, S. Jahanshahi, Publ. Australas. Inst. Min. Metall. 2/2004 (2004) 97.

[67] N. Tripathi, P. Coursol, M. Kreuh, D. Tisdale, P. Mackey, in: J. Kapusta, T. Warner (Eds.), International Peirce-Smith Converting Centennial Held During the TMS 2009 Annual Meeting & Exhibition, Minerals, Metals & Materials Society, Warrendale, PA, 2009, p. 251.
[68] H. Li, A. Morris, D. Robertson, Electr. Furn. Conf. Proc. 54 (1997) 227.
[69] H.J. Li, D.G.C. Robertson, A.E. Morris, Proc. - Electrochem. Soc. 97-39 (1997) 171.
[70] J. Nell, I. Nolet, in: A. Vartiainen (Ed.), The Twelfth International Ferroalloys Congress, Outotec Oyj, 2010, p. 579.
[71] H.Y. Sohn, M.E. Choi, in: TMS 2010, Annual Meeting & Exhibition, Supplemental Proceedings, Minerals, Metals & Materials Society, Warrendale, PA, 2010, p. 347.
[72] D.G.C. Robertson, in: G.W. Warren (Ed.), EPD Congress 1995, Symp. TMS Annual Meeting, Miner. Met. Mater. Soc, Warrendale, PA, 1995, p. 347.
[73] K.N. Swamy, D.G.C. Robertson, Process Technol. Conf. Proc. 13 (1995) 357.
[74] P.C. Pistorius, M.K.G. Vermaak, S. Afr. J. Sci. 95 (1999) 377.
[75] J. Peter, K.D. Peaslee, D.G.C. Robertson, B.G. Thomas, in: AISTech 2005, Proceedings of the Iron & Steel Technology Conference, Association for Iron & Steel Technology, Warrendale, PA, 2005, p. 959.
[76] S.E. Olsen, M. Tangstad, T. Lindstad, Production of Manganese Ferroalloys, Tapir Academic Press, Trondheim, 2007, pp. 43–50.

INDEX

Note: Page numbers followed by "*f*" indicate figures, and "*t*" indicate tables.

A

AA6111 aluminum strip, 497, 498*f*
Ab initio computations, 502–504, 503*f*
Absorption of surfaces, 160–161
Acceleration of assimilation, 408–410
Acicular ferrite formation, 736–739
AC-SM. *See* Auxiliary coil-stirring modifier (AC-SM)
Activity determinator
  cleanliness control, 275–276
  desulfurization control, 275
  ferrous oxide, 273–275
  manganese control, 276–277
Adsorption and electrocapillary curves, 83–84
Advanced thermodynamic software tools, 757–758
Air bubble in water, quasi-stationary growth, 180, 180*f*
Air gaps, 504, 505, 506–507
Air pockets, 497, 498*f*
AISI. *See* American Iron and Steel Institute (AISI)
Algebraic slip model (ASM), 465–467
Alkaline–halide ionic mixtures, 42, 43*f*
Alloy-slag interface, emulsification, 114–115, 117*f*
Al_2O_3-C refractories, 293–295, 298
Al_2O_3–SiO_2 phase, 621*f*, 622*f*
Alumina-graphite immersion nozzles, 302–303
Alumina–graphite refractory, 127, 128*f*
Aluminum, 68, 75*f*
Aluminum sphere, 380*f*
American Iron and Steel Institute (AISI), 217
Amphoteric oxides, 654
Anatase–rutile transformation kinetics, 809–813, 812*f*
ANSYS FLUENT V12 software package, 506
ANSYS 12.0 package, 536–537
AOD. *See* Argon–oxygen decarburization (AOD) process
Argon–oxygen decarburization (AOD) process, 230–233
Argon-stirred steel, 233–238
Ascending velocity of single bubbles, 133–134, 134*f*
ASEA-SKF ladle furnace, 236, 237*f*
ASM. *See* Algebraic slip model (ASM)
Assimilation, 376–377
Austenite grains sizes and strip temperatures, 574, 575*f*
Auxiliary coil-stirring modifier (AC-SM), 271
Average radius of exposed eye, 546–547, 547*t*

B

Backwall configuration, 497, 498*f*
Base-metal sulfide systems, 745–746
Basic oxygen furnace (BOF), 214–215, 469–475
  medium and hard blowing periods, 835
  model validation, 835–836
  reaction zones determination, 835
  RH degassing treatment and comparison, 833*f*, 835
  soft blowing period, 835
  steelmaking, 305–306
Basic oxygen steelmaking (BOS), 834
Bath smelting furnace, 213–214
Behaviors of small gas bubbles, 131
Bench-scale experiments, 335–338
Blast furnace, 456–461, 834
Bodenstein-number Bo*, 99–100, 100*f*
BOF. *See* Basic oxygen furnace (BOF)
BOS. *See* Basic oxygen steelmaking (BOS)
Boundary and initial conditions, 403–408
Boussinesq approximation, 401
"Bridge over the Atlantic", 248, 249*f*
Bubble breakup and coalescence, 181–184
Bubble detachment size, 181
Bubble diameter *vs.* gas flow rate, 182, 182*f*
Bubble formation, 179–184
Bubble rupture, 187–188
Bubble shapes, 184
Bubble size, foaming index, 208, 208*f*
Bubble trajectories, tundish, 538–543
Bubbling–jetting transition, 189–192
Buoyancy forces, 490–491
Butler's model, 37–38

C

Calcination process, 809–810
Calcium treatment
  Ca-containing flux cored wires, 690, 690*f*
  nature, oxide inclusions, 686, 687*f*
  nonmetallic phases, 687*f*, 688
  phase diagram, Al_2O_3-CaO, 685–686, 686*f*
Calculation, cell mole numbers, 606–607
CALculation of PHAse Diagrams (CALPHAD) method, 588–589
Canadian Steel Industry Research Association (CSIRA), 556–557
CaO–MgO–SiO_2 slags, 260*f*, 261*f*, 264*f*
Capillary number, 112–113, 113*f*
Capillary rise method, 31
Carbon banding and elongated manganese sulfide inclusions, 251–252, 252*f*
Carbon content, hot metal, 822, 823*f*
Cartesian-based coordinate system, 434
CCC. *See* Conventional continuous casting (CCC)
CCF. *See* Cyclone converter furnace (CCF)
CEF. *See* Compound energy formalism (CEF)
Cell model, 600–608
Central atoms model, 609–623
CFD. *See* Computational fluid dynamics (CFD)
CFX, computer programs, 442
Charge compensation effect
  alumino-silicate system, 649–651

Charpy tests, 252, 253*f*
ChemApp library, 821, 822*f*
Chemical attack by slag, 328
Chemical kinetics
  GPMT, 171–172
  LPMT, 172–174
Chemical reaction, liquid inclusion and refractories
  MgAl2O4-C refractory, 720–724
  ZrO2-C refractory, 724
ChemSheet program, 57
Cleavage and elastic deformation, 12, 12*f*
Clogging in casting processes, 90
Cl_2 reaction with nickel, 149–151
Coal- and gas-based reduction processes, 461–467
CO, H_2, C_2 H_6 and CH_4 reaction, liquid iron, 169
Coke-free space, 457–458, 458*f*
Commercial software FLUENT v.6.3 package, 518–519
Common gas chemistry, 749–751
Completely stirred tank reactor (CTSR), 307, 309–310
Complex equilibrium approach, 801–802
Compound energy formalism (CEF), 594–597
Computational and physical models, 440
Computational fluid dynamics (CFD), 430, 440–442, 456–492
Computers, 585
COMSOL, 442
Concentration profile of solute *i, ci* (mol/m^3), 2–3, 3*f*
Constrained Gibbs energy minimization approach, 53–57
Contact angle, 14–16
Continued decarburization by slag, 323
Continuity and momentum equations, 431–435
Continuous casting machines
  CCC, 557–559
  NNSC, 559–565
  TSC, 559
Continuous nonintrusive monitoring, 278–280
Continuous reduced iron steelmaking process (CRISP), 314
Continuous refining, steel, 309–310
Continuous steelmaking technologies, 307, 307*t*, 309*f*
Contours of droplets, Bi, Sn and Ga, 21–23, 22*f*
Control-volume finite difference method, 532
Conventional continuous casting (CCC)
  initial shell formation, 516–518, 518*f*
  metal–slag interface, 521–523, 523*f*
  OMs (*see* Oscillation marks (OMs))
  seams and slivers, 516
  steel mills, surface quality, 559
  water-cooled copper alloy mold, 557–558, 558*f*
Conventional fixed-mold machines, 510–514
Copper smelting slags, spinel liquidus
  chemical and physicochemical properties, 771
  one-step reactor model, 782–784, 785*f*
  oxygen partial pressure, 770–778
  predominance diagrams, 778–782, 781*t*
  and process conditions, 776–778, 777*t*
CO_2 reaction, liquid Fe–C, 167–168
COREX process, 462, 463*f*
Correlation of surface tension
  liquid metals, 36, 37*f*
  Molten salts, heat of evaporation, 37, 38*f*
Corrosion testing, refractories, 290–292
Counter-current reactor approach, 802–809
Coupled kinetic–thermodynamic models, 811
Coupled mass transfer, 151–153
CRISP. *See* Continuous reduced iron steelmaking process (CRISP)
CSIRA. *See* Canadian Steel Industry Research Association (CSIRA)
CSIRO's modification, 608
CTSR. *See* Completely stirred tank reactor (CTSR)
Cu flash smelting furnace, 788–789, 788*f*
Curve-shaped tundish, 483, 483*f*
Curve symmetry, 612*f*
Cyclone converter furnace (CCF), 467, 467*f*
Cylindrical polar coordinate system, 399–400

D

DEA. *See* Discrete element analysis (DEA)
Decarburization rate, 823, 823*f*
Degeneracy, 600, 603
Delta-shaped tundish, 483
Dendritic structure of 6-mm thick strip and 3.5-mm thick TRC strip, 572–573, 572*f*
Deoxidation, 592–594
Design of metal delivery systems, 577–581
Desulfurization kinetics, 221–225
Desulfurization mass transfer constant, 224–225
Detachment method, 27–29
Development of turbulence theories, 585
Diethylether droplet, 97–98, 98*f*
Diffusive carbon transport, 820
Digital particle image velocimetry (DPIV), 479
Dilute metallic solution, 589–594
Dilute solution approach, 821–822
Dimensional analysis, foaming index, 209–211
DIOS. *See* Direct iron ore smelting (DIOS)
DIOS 100-t smelter, 218, 219*f*
Direct ironmaking, 217–221
Direct iron ore smelting (DIOS), 217
Direct reduced iron (DRI), 468–469
  based continuous steelmaking, 313–316
  description, 310–311
  melting and decarburization, 316–324
  in steelmaking, 311–313
Discrete element analysis (DEA), 460–461
Dissociation of CO2, solid iron, 172, 173*f*
Dissolution of refractories, 125–130
3D mathematical model, 502, 503*f*
3D METFLO code, 442
Donor–acceptor schemes, 532
DPIV. *See* Digital particle image velocimetry (DPIV)
DRI. *See* Direct reduced iron (DRI)

Drop weight (DW), 26–27
Dual-coil electromagnetic stirring system, 271, 271*f*
Dust chemistry, 751
DW. *See* Drop weight (DW)
Dynamic Link Library (DLL), 821
Dynamic tests, 292

E

EAF. *See* Electric arc furnace (EAF)
EBT. *See* Eccentric bottom tapping (EBT)
Eccentric bottom tapping (EBT), 295*f*
Effect of interfacial flow
  liquid-gas reactions, 101–102
  liquid-liquid reactions, 98–101
  liquid-solid reactions, 102–105
  solidification processes and crystal growth, 105–108
Electric arc furnace (EAF), 212–213, 294*t*, 295*f*, 305–307, 327–329
  dust recycling slags, 759–763
  secondary zinc production, 761
Electrocapillary curves
  CaO/SiO_2 and SiO_2/Al_2O_3, 84–85, 86*f*
  low alloyed steel and copper, 84–85, 87*f*
  shapes, 91–92, 92*f*
Electrocapillary equation, 83
Electrocapillary phenomena, 82–92
Electrochemical double layer, 81–82
Electrochemical equilibrium, 79–80
Electromagnetically driven flows, 437–438
Electromagnetic stirring, 271–272
Electromotoric force (EMF), 82
Elementary mass balance, reactor, 804, 808*t*
EMF. *See* Electromotoric force (EMF)
Emulsification of metal and slag, 90–91
Endothermic process, 813–814
Energy consumption, U.S. steel industry, 305, 306*f*
Energy, system, 603
Equilibrium contact angles, 14–15, 14*f*, 15*f*
Equilibrium reaction zone model, 827
Equilibrium solidification behavior, 691, 692*f*
Erosion, 328
Euler–Euler approach, 530–534
Eulerian model, 533–534
Euler–Lagrange and Euler–Euler (two-fluid) models, 194–195, 195*f*
Euler–Lagrangian approach, 534–536
Evaluation of Molten ionic mixtures, 39–42
Exothermic assimilation, 397
Exothermic heat, 400

F

FACT oxide (FToxid) solution database, 632–633
FactSage, 632–634
  software and database, 828
  structural viscosity model, 643–652
FactSage™ thermodynamic modeling package, 334–335
FCDs. *See* Flow control devices (FCDs)
Fe–Al–O system, 477
Fe-Cr alloys, interfacial tension, 68, 68*f*
Feeding system, Clausthal Caster II, 577–578, 578*f*
Fe–Mn compacts, 388–391
FeO reduction, Fe–C–S metal surface, 175–176, 175*f*
Ferromanganese and silicomanganese cylinders
  inflection points, 377–378
  liquid steel, 380*f*, 381*f*
Ferromanganese smelting process, 845–850
Ferrosilicon shell, 392*f*
Ferrous liquid metals, 361–376, 370*t*
Ferrous oxide in molten slag, 272–277
Fick's First Law, 145
Firebrick, 283
Flag signals, 246, 246*f*
Flash Smelting Furnace Thermodynamic Modeling, 782–784, 785*t*
Floating zone (FZ) method, $NaNO_3$ liquid bridge, 105*f*, 106–107
Flow control devices (FCDs), 485–486, 487
Flow pattern in sulfur content, 121–122, 123*f*
FLUENT ANSYS, 442
Fluid flow dynamics, 484
Fluid flow patterns, tundish, 543–547
Fluid flows theory, 430–431
Fluid movement, 819
Flux and metal reaction, casting process, 98–99, 99*f*
Foam drainage, 200–202
Foam height
  $CaO–SiO_2–FeO$ slag, 201–202, 201*f*
  and foam layer thickness, 203, 204*f*
  and superficial gas velocity, 203–204, 204*f*
Foaming index
  $CaO–SiO_2–FeO–MgO–Al_2O_3$ slags, 206–207, 207*f*
  foam life, $CaO–SiO_2–FeO$ slags, 206, 206*f*
  reciprocal of average bubble diamete, 206, 207*f*
  variation, $CaO–SiO_2–FeO–MgO_{sat}$ slags, 206, 207*f*
Foam stability, 199–200
Formation energy
  interaction and parameters, 611–614
  parameters, 611
Formation of liquid oxides, Gibbs free energy, 51–52
The Forth Bridge, 244, 244*f*, 245*f*
Forward and reverse reactions, 163–164
Free-space shape, 458, 459*f*
Free vaporization, 154–155
Frequency spectrum, levitation drop method, 32, 33*f*
FTmisc database, 633–634
FTsalt database, 634
Fume emission, 472–474, 473*f*

G

Gas and matte phases, 780
Gas bubble formation, liquid steel, 132–134
Gaseous intermediates, 174–176
Gases and mass transfer coefficient relationships, 147–148
Gas–liquid and liquid–liquid reaction, rules, 144
Gas–liquid/liquid–liquid flows, 528
Gas-phase mass transfer (GPMT), 145–154
Gas production, 824–825, 825*f*

Gas–solid flows, 528
Gaye–Kapoor–Frohberg model, 821–822
GCA model. *See* Generalized central atom (GCA) model
Generalized central atom (GCA) model, 609–623
Gibbs Absorption Isotherm, 160, 161*f*
Gibbs adsorption isotherm, 5–7
Gibbs energy, 605–606, 614
Gibbs energy minimizer, surface equilibria calculations, 55–57
Gibbs free energy routines, 813
Gibbs free energy, sublattice formalism, 661
GPMT. *See* Gas-phase mass transfer (GPMT)
GPMT-controlled reactions, 149
Grid system, 456–457, 457*f*

H

Hall-Heroult Electrolytic Cell, 430
Hazelett twin-belt casters, 499–500
HCLI. *See* High carbon liquid iron (HCLI)
Healing time, 515
Heat and mass transfer processes, 585
Heat balance and oxidation, 753
Heat evolution, solidification, 700–701
Heat fluxes, 507–510
  prediction, 397, 398*f*
  variations, 568–569, 569*f*
Heat of vaporization, 36, 37
Heat-to-heat variations, weldability, 121
Heat transfer control, 159–160
Heat transfer equations, 410–414
Heat transfer, twin-roll casting processes, 566
Helmholtz layer, 81–82, 81*f*
High carbon liquid iron (HCLI), 407–408, 414, 414*f*
High quality processing (HQPs), 247, 247*f*
HIsmelt process, 217, 465, 465*f*
Hood design, 474–475, 474*f*, 475*f*
H_2O reaction, liquid iron–carbon alloys, 168–169
Horizontal single-belt casting (HSBC)
  advantages, 581–582
  pilot plant installation, 576–577, 577*f*
HOTLINK®, 313
HQPs. *See* High quality processing (HQPs)
HSBC. *See* Horizontal single-belt casting (HSBC)
HYTEMP®, 313

I

Ice–sulfuric acid system, 413*f*
IHCP. *See* Inverse Heat Conduction Problem (IHCP)
Iida's model, 665–666
Image component technique, 813–817
Inclusion engineering
  acicular ferrite formation, 736–739
  Al/Ti deoxidation, 733–735
  classification, 728–729
  Mn/Si deoxidation, 729–733
  stages, production, 728–729
Incubation period, 319–320
Industrial burner, 813
Industrial practice slags, 763
Inert gas shrouding, tundish, 536–552
Innovation process, 241–249
Instantaneous heat fluxes, 508, 509*f*
Interaction coefficient and formation energy difference, 52–53, 52*f*
Interface of molten slag, SiO_2 refractory, 127, 128*f*
Interfacial convection basics, 95–98
Interfacial energy, 5
Interfacial free energy between solid and liquid phases
  in binary alloys, 63, 65*f*
  in metals, 63, 64*t*
Interfacial gas layer, 505, 505*f*
Interfacial heat flux curves, 500, 502*f*
Interfacial heat transfer coefficient *vs.* casting speed, 566–567, 567*f*
Interfacial tension, liquid steel and molten slag, 50–53
  contact angle, 66, 67*f*
  drop weight method, 66–68, 67*f*
  sessile drop method, 66, 66*f*
Intermetallic reactions, 389*f*
Inverse Heat Conduction Problem (IHCP), 502–504
Ionic radii data, 46
Iron carburization, $CO–H_2$ gas mixtures, 170–171, 171*f*
Iso-sulfide capacity lines, 262, 263*f*
Isothermal saturation diagrams, 326–327, 326*f*
Iso-water vapor capacity lines, 264–265, 265*f*

J

Jak and Kondratiev model, 668
Jak et al.'s model, 670–672
Jet breakup, 192

K

Kelvin-Helmholtz instability model, 114–115, 116*f*
Kim et al.'s model, 667
Kinetic effects, 223–224
Kinetic–thermodynamic models, 811
Koyama et al.'s model, 666

L

Ladle desulfurization kinetics, 221–225
Ladle furnace alloy, 422*t*
Ladle metallurgy, 279
Ladle metallurgy furnaces (LMFs)
  description, 841–843
  FactSage thermodynamic calculations, 845
  METSIM simulation, 843–845
  primary functions, 841
  Si-deoxidized steel, 843
  thermodynamic equilibrium, 845
Ladle refining and smelting, 839–850
Ladles, 475–478
Ladle transfer, 266–267
Langmuir's isotherm, 7–10
Large drop method, 21–23, 21*f*
Large eddy simulation (LES) model, 482
Laser and CCD camera equipment, SD method, 20–21, 21*f*
Laser microscope, solid-liquid interface, 105–106
LD converter process, 817–818, 817*f*
Lead and zinc industrial slags, 758–759
LES model. *See* Large eddy simulation (LES) model
Levitation drop method, 31–33
Lippmann equation, 83
Liquid Al alloys, 415–421
Liquid Bi—Sn alloy, 57, 57*f*
Liquid Fe, 589–594

Liquid Fe-Al alloy and molten silicate slag, 113–114, 114*f*
Liquid Fe-Si-S alloy and molten Cao-based slag, 115, 118*f*
Liquid inclusion
  chemical reaction, 720–724
  high oxygen steel, 720
Liquid metals (M) and solid oxides (XO), wettability of, 62
Liquid MnO-SiO2-FeO inclusion, 724–728
Liquid-phase mass transfer (LPMT), 155–158
Liquid–solid flows, 528–529
Liquid steel, 395–396, 396*t*
Liquid steel desulfurization
  binary oxide systems, 681, 681*f*
  cell model, 681, 682*f*
  modeling, 680–681
  secondary metallurgy operations, 681–684
  steel-slag stirring, 684, 684*f*
  sulfide capacity, 679–680
  sulfur partition coefficient, 682, 682*f*
Liquid surface contour method, 29–30
Liquidus, 771–773
LMFs. *See* Ladle metallurgy furnaces (LMFs)
Local corrosion, refractories, 299–303
LPMT. *See* Liquid-phase mass transfer (LPMT)
Lull period, 322–323

M

MAC. *See* Marker and Cell (MAC) technique
Macroexothermic phenomenon, 394–397
Magnetohydrodynamics (MHD), 430
Marangoni effect, 300–302
Marangoni flow, welding process, 119–124
Marker and Cell (MAC) technique, 440
Mass and energy balance, 782–789
Mass-limited foaming, 211
Mass transfer correlation relationships, 148–149
Mathematical formulation and computational approach, 397–403
Matte database (MATT), 626–630
Maximum bubble pressure (MBP), 23–25
Maxwell equations, 437
MBP. *See* Maximum bubble pressure (MBP)
Measurements of sessile drop, 20–21
Mechanism, sulfide transformation, 688
Melting and decarburization, DRI, 316–324
Melting and spalling, 329
Melt penetration, 284–287
Melt polymerization, 654
Metal droplets, liquid metal surface, 188, 189*f*
Metal drop weight method, 84–85, 88*f*
Metal-electrolyte interfaces, 81–82, 81*f*
Metallic droplets, 130
Metallurgical and recycling industries, 794–795
Metallurgical grade silicon, 800
Metallurgical processes
  liquid metal cleanliness, 277–278
  operations, 529–530
  steelmaking operations, 278–280
Metallurgy, 456–492
Metal/refractory interactions
  antioxidant additions, MgO-C, 715–716
  reaction, high Mn Steels, 717–719
Metal–slag reaction zone, 825–826, 826*f*
Metal surface, oxidation/reduction, 101, 102*f*
METFLO 3D software, 485
METSIM, 839–841
MgO-C composite refractory, 293, 294*f*
MgO-C corrosion mechanism, 296–299
MgO solubility, FCSM slags, 331–333, 331*f*
MHD. *See* Magnetohydrodynamics (MHD)
Microbubbles, 540–543, 542*f*
Micro-emulsion, 113
Microexothermic phenomenon, 391–394
Mineralogy, lead and zinc smelting solid phases, 749, 750*t*
Mixed controlled, 288
Mixing Length Model, 447
Mixing time, 187
Mixture model, 533
MMPC–HSBC delivery system, 580, 580*f*
Mn–Al compacts, 390*f*, 420*f*, 421*f*
Modeling of exposed eye, 547–552
Modeling zinc-fuming process, 789–791
Modified quasichemical model (MQM), 623–626
Modified regular solution model, liquid Fe, 592
Mold flux design
  calculated isopleths, 694*f*, 696
  equilibrium solidification behavior, 691, 692*f*
  phase diagram information, 691–696, 693*f*
Mold oscillation technique, 515, 516*f*
Molten ionic materials, 39–49
Molten PbO-SiO_2, Marangoni flow, 103–104, 103*f*
Molten SiO_2—Al_2O_3—CaO system, 46–47, 47*f*
Molten SiO_2—Al_2O_3—MnO system, 46–47, 48*f*
Molten SiO_2 based binary and ternary slag, 42–49
Molten SiO_2—CaO—CaF_2 system, 46–47, 49*f*
Molten SiO_2—CaO—FeO system, 46–47, 48*f*
Molten SiO_2—CaO—MgO system, 45–46
Molten SiO_2—CaO—Na_2O system, 46–47, 50*f*
Molten SiO_2—FeO—MgO system, 46–47, 49*f*
Molten slag, steel and inclusion, 699
Molten steel, 253–256
Momentum equations, 401
Movement of drops, electrocapillary, 91–92, 92*f*
Movement velocity, 100–101
MQM. *See* Modified quasichemical model (MQM)
MTDATA, 635–636
MTFEDLSL, 635
Mudersbach et al. model, 659
Multicomponent
  slags, 619–623
  steels, 614–619
Multicomponent phase equilibria (MPE) package, 634–635

Multistage reactor model, ferromanganese smelting, 846–848

N

Nakamoto et al.'s model, 669
$NaNO_3$ melt, Czochralski growth conditions, 106*f*, 107–108
Nanovea 3D Profilometer from Micro Photonics Inc, 507–508, 509*f*
Natural gas- and coal-based produced DRI, 310, 310*t*
Navier–Stokes equation, 429, 481
NDMV. *See* Nondimensional mass velocity (NDMV)
Near net-shape casting (NNSC)
  investment costs, 563–564, 564*f*
  NUCOR's twin-roll strip casting facility, 560, 561*t*
  solidification and strip microstructures, 571–575
Network formers, 654
Newtonian liquids, 435–436
Ni activity coefficient, 611, 613*f*
Nitrogen-bearing systems, 617–619
NNSC. *See* Near net-shape casting (NNSC)
Nodal points, 441–442
Nondimensional mass velocity (NDMV), 189–190
Non-equilibrium modeling, 817–827
Nonferrous liquid metals, 361–376, 362*t*
Nonferrous metallurgy
  duction, 740–741
  minor elements distribution, 753
Nonferrous metals, 594
Non-isothermal systems, 811
Nonmetallic inclusions and gas bubbles, 130–132
Nonwetting condition, 180, 181*f*
Noyes-Nernst equation, 288–289
NPLOX, 635
NPL's model, 667
N_2 reaction with liquid iron, 164–167
NUCOR's twin-roll strip casting facility, 560, 561*t*

O

OEN. *See* Open entry nozzle (OEN)
OMs. *See* Oscillation marks (OMs)
Online sensors, 277–278
Open entry nozzle (OEN), 479
Optical basicity (OB) concept, 256, 257, 664
Oscillation marks (OMs)
  evolution, heat flux, 523, 524*f*
  formation, mechanism, 525–526
  surface blemishes, 516–518, 517*f*
Oxide-carbon refractories, 292–303, 297*f*
Oxide solid solutions, 594–597
Oxisulfide inclusion formation, 733
Oxygen and sulfur activity, electrocapillary measurement, 85–88, 89*f*
Oxygen and sulfur contents, nitrogen reaction, 156–157
Oxygen-bearing system, 619
Oxygen content *vs.* interfacial tension, molten iron, 68, 68*f*
Oxygen steelmaking process, 117

P

Padday's cone technique, 28, 28*f*
Pal et al.'s model, 667
Particle image velocimetry (PIV), 472
Particle-tracking technique, 465–467
Partition function
  cells permutation number, 602–603
  degeneracy, 600
  maximization, 614, 615*t*
  permutations number calculation, 601–602
Pauling electronegativities, 258
PCI. *See* Pulverized coal injection (PCI)
PCR. *See* Postcombustion ratio (PCR)
Pellet positions, 317, 317*f*
Pendent drop, 25–26
Penetration depth, bubble column, 540, 541*f*, 541*t*
PFR. *See* Plug flow reactor (PFR)
Phases and output stream chemistries, 747–751
PHOENICS, 442
Physical interface θ between α and β phases, 2–3, 3*f*
Physical modeling, 438–439
Physical model of slag foaming, 202
Physicochemical properties, ionic melts, 42, 42*f*
Pilot trials
  description, 338–353
  phase I, 339–344
  phase II, 344–353
PIV. *See* Particle image velocimetry (PIV)
Plant tests, 728
Plasma-coated surface rolls, 571
Plug flow reactor (PFR), 307
Plume shape, 184–186
Postcombustion ratio (PCR), 220
PR. *See* Production rate (PR)
Predicted slag flow patterns, 521–523, 523*f*
Process analysis, 353–355
Process characteristics, DRI, 313–315
Process modeling tool SimuSage, 821–822
Process requirements, DRI, 315–316
Production rate (PR), 218
Pulverized coal injection (PCI), 461, 462*f*
Pyrometallurgical applications, 632–634, 651–652
Pyrometallurgical smelting process
  description, 742
  flow sheets and technologies, 743
  multistage smelting/converting route, 744–746
  oxidation+reduction routes, 744, 746*t*
  selection, multicomponent sections, 754–757
  smelting/converting route, 744–746

Q

Quasichemical models, 598–599
Quasichemical viscosity model, 663
Quasi-stationary bubbling, 179–181

R

Radial distributions, bubble plume, 186, 186*f*
RANS. *See* Reynolds-Averaged Navier–Stokes (RANS)
Rapid gas evolution period, 320–322
Rate-controlling process, 143–144
Rate equations and activated complexes, 161–162
Rate of recovery (RR), 416
Reaction mechanism and kinetics, 318–323
Reaction of CO_2 with carbon, 153–154
Reaction of nickel with HCl, 151–153
Reactions in process metallurgy, 142
Reaction zone model, 821
Reactive strontium alloys, 416–419

Reactor simulation
stages 1 and 2, 803, 804*t*, 805*t*
stages 3 and 4, 803, 806*t*, 807*t*
Realizable κ–ε model, 449
Reciprocal ionic liquid model (RILM), 597–598
Reddy and Hebbar's model, 669–670
Refining slags, 256–259
Refractory corrosion, 103–104, 329–331
melt penetration, 284–287
oxide-carbon refractories, 292–303
refractory/melt interfaces, 287–290
testing, 290–292
Refractory degradation, 327–333
Refractory/melt interfaces, 287–290
Refractory stability, 351–353
Renormalization Group (RNG), 448, 449
Residence time distributions (RTDs), 480
Residual reactions in gas-liquid reactions, 10, 10*f*
Reynolds and Weber numbers, bubble shapes, 184, 185*f*
Reynolds-Averaged Navier–Stokes (RANS), 447, 450–451
Reynolds stress models (RSMs), 480–481
Reynolds stress tensor, 446
RH degassing system, 830, 831*t*
Riboud et al.'s model, 659
Riboud's model, 665
RILM. *See* Reciprocal ionic liquid model (RILM)
RNG. *See* Renormalization Group (RNG)
ROMELT, 217
Rotary Cement Kiln model, 836–839
Routes of assimilation
route five, 387–388
route four, 383–387
route one, 377–378
route six, 388–391
route three, 381–383
route two, 378–380
RR. *See* Rate of recovery (RR)
RSMs. *See* Reynolds stress models (RSMs)
RTD curves, 489–490
RTDs. *See* Residence time distributions (RTDs)
Ruhrstahl Heraeus (RH) degasser, 828–834

S

Scrap melting, 820
Scrap/metal bath-interface, 820
SD. *See* Sessile drop (SD)
Semi-implicit method for pressure linked equations revised (SIMPLER), 400, 401
SEN. *See* Submerged entry nozzle (SEN)
Sessile drop (SD), 19–23
Setup of maximum pressure method, 24–25, 25*f*
Shell period, 377
Short range ordering (SRO), 623–626
Silicon cylinder immersion, 407*f*
SIMPLE algorithm, 471–472
SIMPLER. *See* Semi-implicit method for pressure linked equations revised (SIMPLER)
SiO_2 refractory–(PbO—SiO_2) slag–liquid Pb, 126, 127*f*
SLAG3, 636–637
Slag crystallization
liquidus temperatures and solid proportion, 697
mineralogy, as-solidified slags, 699
oxide additions, liquidus temperatures, 697–698
Slag foaming, 138, 325–327
CaO–SiO_2 slag, 197–198, 198*f*
and emulsification, 834–835
experimental setup, 197, 198*f*
slag–metal reactions, 199, 199*f*
Slag-metal interfaces, 84–89, 302–303, 302*f*
Slag/refractories reactions
ladle glaze interaction, 708–710
mold flux interaction, 713
slags interaction, 704–708
Slags
chemistry, 747, 780
designs, 333–353
liquidus and phase equilibria, 752
multicomponent, 619–623
oxidizing power, 323–324
phase components, 824, 825*f*
structure, 600
Slag viscosity model
addition of fluoride, oxide slag, 651–652
basic formula, 645–647
classification, 655–656
explicit models, 656–662
KTH, 661–662
melts containing alkali oxides, 648–649
nomenclature, 656
structural models, 662–664
SLS. *See* Swirling ladle shroud (SLS)
Smelting system, nonferrous, 791–793
Smith's equation, 14–15
Software for evaluation of surface tension, SD, 33–34
SOLA-MAC. *See* Solution algorithm marker and cell (SOLA-MAC)
SOLA-MAC code, 442
Solid chemistry, common, 748–749
Solidification
conventional fixed-mold machines, 510–514
process, nucleation, 135–138
textured copper substrates, heat fluxes, 507–510
Solid–liquid interface, 2, 3*f*
Solution algorithm marker and cell (SOLA-MAC), 478
Species and components, matrix form, 56, 56*t*
Spinel liquidus
copper smelting slags, 767–791
lead smelting slags, 764–767
SRO. *See* Short range ordering (SRO)
Stability of interface, liquid steel and molten slag, 111–118
Stainless steel production, AOD, 230–233
Static corrosion tests, 291–292
Steel cooling and solidification, 688
Steelmaking operations. *See* Refractory corrosion
Steelmaking process
chemical reactions, 678
phases and chemical constituents, 675–676
Steel nitrogen content and slag foaming, 350–351
Steel quality
evaluation of, 272–280
oxygen control, molten steel, 253–256
preservation of, 265–272
refining slags, 256–259
slag chemistry and sulfur control, 259–262
water vapor dissolution, molten slags, 262–265
Steel–refractory–slag and slag–refractory–air, 127–130, 129*f*

Steels
multicomponent, 614–619
shell formation, 512–514
strip compositions, 567–568, 568*t*
Stefan-Boltzmann equation, 428
Steinmetz-number Ste, 98–101
Stirring power, 183
Stoichiometric reaction approach, 801
Strontium alloys, 416–419
Subliquidus, 774–776
Submerged entry nozzle (SEN), 479
Submerged entry nozzle material, slag/steel, 127–130, 129*f*
Sulfide capacity of slag, 259
Sulfur-bearing systems, 614–616
Sulfur distribution coefficient, 222
Sulfur effect, D/W ratio in weld pool, 121, 121*f*
Sulfuric acid–ice experimental setup, 398, 399*f*
Sump of liquid steel, twin-roll caster, 565–566, 565*f*
Suppression of foaming, 215
Surface blemishes, 516–518, 517*f*
Surface layer and isotropic bulk, 54
Surface poisoners, 160, 162
Surface roughness, 15–16
Surfaces and interfaces, definition of, 2–5
Surface tension
definition of, 11–12
driven flow, 97, 97*f*
of liquid alloys, 37–39
of liquid iron, 8, 9*f*
of liquid pure metals and molten salts, 35–37
Surface velocities, 410*f*
Swirling ladle shroud (SLS), 487–488, 487*f*
Synergistic interactions, 247, 248*f*
Szyszkowski's equation, 8

T

Tan and Vix's model, 668
TCOX, 637
Temperature and composition, Gibbs energy, 38–39
Temperature and entrained liquid, sonic velocity, 190–192
Temperature coefficient, oxygen and sulfur concentrations, 119–120, 120*f*
Temperature dependence of surface tension, 12–14, 46, 46*t*
Temporal evolution, bubble plume, 539, 539*f*
Theoretical modeling approaches, 794–795
Thermal Marangoni convection, 96
Thermal stability, refractories, 701–703
Thermo-Calc, 636–637
Thermochemistry analyses, 780
Thermodynamic database and software
model validation, 830–834
reaction zones determination, 829–830
stoichiometric decarburization trajectories, 833
Thermodynamic evaluation, 333–335
Thermodynamic packages, 630–637
Thermodynamic predictive packages, 771
Thermodynamic software tools, 757–758
Thermodynamics *vs.* kinetics, 144–145
Thin slab casting (TSC), 559
Three-phase flows, 529
$TiCl_4$-burner model, 813–817
"Tigh-Na-Truish", 248
TiO_2 production modeling, 809–817
Titanium cylinder, 386*f*
Topographies of weld pool surface, 121–122, 123*f*
Total pressure P_{max} , bubble detachment, 23
Transfer operations, 252–253, 254, 280
Trapping of liquid oil into liquid water, 124–125, 125*f*
Triumvirate, knowledge exchange, 242, 242*f*
TSC. *See* Thin slab casting (TSC)
Tundish, 478–492
Tundish refractory, 714–715
Tundish to mold transfer, 269–272
Tundish transfer, 267–268
Turbulence models, 446–450
Turbulent forces *vs.* surface tension forces, 183
"Two-film" model, 224
Two-phase gas/liquid flows, mathematical model, 538
Two-phase LPMT, 158
Two-phase steel–air system, 519
Two-way turbulence coupling, 534

U

UIPF. *See* Unified interaction parameter formalism (UIPF)
Unified interaction parameter formalism (UIPF), 591
Unshaped/monolithic refractory, 283
Urbain's model, steelmaking slags, 665

V

Vacuum argon degassing (VAD), 225
Vacuum degassing, 225–229
VAD. *See* Vacuum argon degassing (VAD)
Value-metal partitioning and final recovery, 752
Value metals, minerals and input chemistry, 741–742
Value stream chemistries, 747
Van der Waals ionic metal–oxygen bonding, 51
Vaporization and activation energies, 663–664
Volume of fluid (VOF) model, 530–532, 547–552

W

Wagner interaction parameter formalism (WIPF), 590–591
Water vapor dissolution, molten slags, 262–265
Wettability, 61–62, 299–300
Wettability and wear, refractory materials, 90
Wetting, 16–17, 17*f*
Widmanstätten structure, 573–574
WIPF. *See* Wagner interaction parameter formalism (WIPF)

X

X-ray transmission apparatus, 292, 293*f*

Y

Young's equation, 14

Z

Zero interface, 4
Zinc-fuming plant trial, 789–791, 790*t*
Zr–Al compacts, 393, 393*f*, 394*f*